

Ground and Non-Ground Filtering for Airborne LIDAR Data

Suchita Yadav

National Institute of Technology, Allahabad, Uttar Pradesh, India

Publication Date: 9 February 2016

DOI: <https://doi.org/10.23953/cloud.ijarsg.41>



Copyright © 2016 Suchita Yadav. This is an open access article distributed under the **Creative Commons Attribution License**, which permits unrestricted use, distribution, and reproduction in any medium, provided the original work is properly cited.

Abstract Automatic ground filtering for Light Detection and Ranging (LIDAR) data is a critical process for Digital Terrain Model and three-dimensional urban model generation. Various methods have been proposed in literature to separate ground from non-ground, but sometimes problem has been occurred due to the similar characteristics possessed by ground and non-ground objects. The proposed approach in this paper is based on neighborhood based approach. Hierarchy of preprocessing is done for LIDAR data using various essential tools. K-D tree is used to distinguish the bare ground and non-ground objects using nearest neighbor search. Experimental results show the effectiveness of the proposed approach.

Keywords *LiDAR, Airborne LiDAR, K-D tree, Point Clouds*

1. Introduction

LiDAR (Light Detection and Ranging) could be a remote sensing technique supported optical device technology. It measures the period of time of the emitted optical device pulses to work out the space between the device and also the ground. Combined with a world Positioning System (GPS) and a mechanical phenomenon measure Unit (IMU), measuring system will generate a three-dimensional (3D) dense, geo-referenced purpose clouds for the reflective parcel of land surface. Mobile lightweight detection and travel (LiDAR) has bit by bit become a thought tool for aggregation elevation info of surface targets by scheming the time of flight taken for optical device pulse travel between a measuring system device and a target scene. Compared with ancient photogrammetric technique. Measuring system will penetrate through vegetation to get parcel of land elevation in biological science areas. The raw measuring system information contains tremendous points came from numerous objects, like buildings, trees, vehicles etc. measuring system has 2 major blessings over photogrammetric systems: (1) the acquisition of vertical info over an oversized space is additional cost-effective; and (2) there are fewer necessities for information preprocessing.

In terms of DTM creation, measuring system has taken the place of ancient photogrammetric ways and become the first technique for manufacturing regional or national DTMs in some countries.

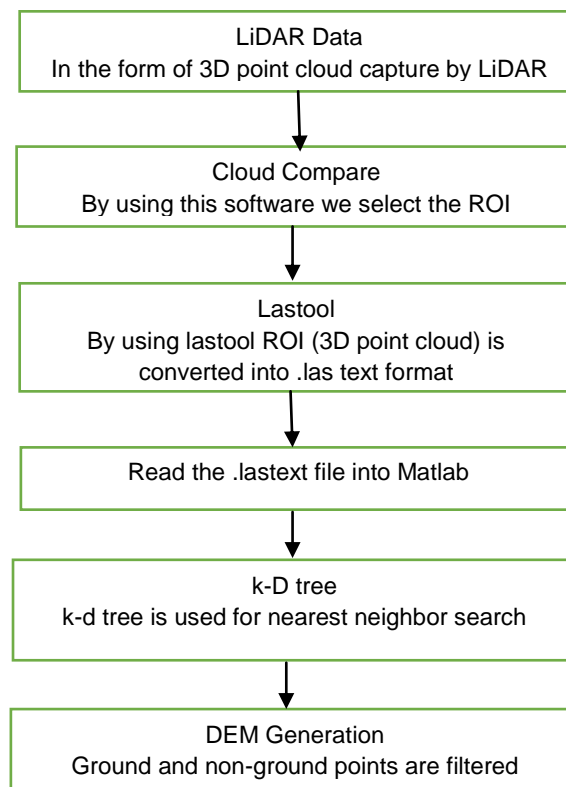
Modern mobile measuring system technology will map the Earth's surface at a 15–20-cm horizontal resolution, and future generations of measuring system scanners are expected to come up with even

higher resolution maps. The big volume of scanned information that are manipulated once process a measuring system purpose cloud has been one amongst the main challenges in processing.

In raw measuring system information, each bare-ground and non-ground objects, like trees, buildings, vehicles, and electrical wires, generate disperse. Non-ground points got to be known and eliminated from measuring system measurements before constructing added product like DTMs [3]. Likewise, ground points got to be removed to accurately establish non-ground objects, like buildings and trees. In either case, an economical and correct ground filtering is needed. Existing algorithms have achieved some success, however typically have problem on steep slopes or ridges. To the present finish, our goal is to develop a stronger ground filtering algorithmic program to facilitate DTM creation. Ground filtering algorithms treat either raw measuring system purpose clouds or gridded elevation values [3] that are derived by interpolation of data. However sorting out neighbors in an irregular basis distributed purpose cloud will be long and hard, particularly once users apply the algorithms to broader areas. Most ground filters are supported the idea that natural parcel of land variations ar gradual, instead of abrupt. Therefore, ground elevation and slope ought to vary swimmingly once moving from one ground purpose to a different neighboring ground purpose. In distinction, the boundary between ground and non-ground points ought to exhibit an abrupt amendment in elevation and slope. The joint use of slopes, elevation variations, and native elevations will discriminate ground points from non-ground points [4].

2. Proposed Approach

Proposed approach is briefly described in following chart.



Step used in proposed approach is described following:

Step 1

First we take the raw LiDAR input data which is captured by airborne LiDAR. The input is in the form of 3D point cloud. These point clouds consists the points of both ground and non-ground objects.

Step 2

We select ROI (region of interest) from taken input with the help of Cloud Compare software. Selected ROI must consist both ground and non-ground point, which is helpful for further processing.

Step 3

We have to convert the ROI which is in 3D point cloud, into text format so that we can easily read the input data by using Matlab and can process our algorithm on that data.

Step 4

Now we use k-D tree data structure which is useful for nearest neighbor search. k-D tree is the type of multidimensional BST. A k dimensional tree is a space partitioning data structure in a k-dimensional space.

2.1. Nearest Neighbor Search

The nearest neighbor search formula aims to seek out purpose within the tree that's nearest to a given input point.

- 1) Starting with the foundation node the formula moves down the tree recursively, within the same manner that it might if the search purpose were being inserted (goes left or right, depends).
- 2) Once the formula reaches a leaf node, it that leaf node purpose because the "current best".
- 3) The formula unwinds the rule of the tree, activity the subsequent steps at every node:
 - a. If the present node is nearer than the present best, then it becomes the present best.
 - b. The formula checks whether or not there may well be any purposes on the opposite aspect of the ripping plane that are nearer to the search point than the present best. In concept, this is often done by crossed the ripping hyper plane with a hyper sphere round the search purpose that encompasses a radius up to the present nearest distance. Since the hyper planes are all axis-aligned this is often enforced as a straightforward comparison to check whether or not the distinction between the ripping coordinate of the search purpose and current node is lesser than the space (overall coordinates) from the search purpose to the present best. (1) If the hyper sphere crosses the plane, there may well be nearer points on the opposite aspect of the plane, therefore the formula should move down the opposite branch of the tree from the present node probing for nearer points, following identical algorithmic method because the entire search. (2) If the hyper sphere does not cross the ripping plane, then the formula continues walking up the tree, and also the entire branch on the opposite aspect of that node is eliminated.

- 4) 4- Once the formula finishes this method for the foundation node, then the search is complete.

Range search: a spread search searches for ranges of parameters as an example, if a tree is storing values akin to financial gain and age, then a spread search can be one thing like probing for all members of the tree that have associate age between twenty associated fifty years and an financial gain between 50,000 and 80,000. Since k-d trees divide the vary of a site in at every level of the tree, they're helpful for activity vary searches.

2.2. Algorithm

Input: 3 Dimensional Coordinates of all 3d points

Output: Bare Ground with removed object

Assumption: (1) x, y, z, β and μ are NULL vectors.

- (2) R is radius that is 0.3.
 (3) n is number of 3d points.
 (4) α is object created by K-D Tree Algorithm.

2.3. Procedure

OBJECT REMOVAL (All Coordinates)

$x \leftarrow$ X coordinates of all 3d points

$y \leftarrow$ Y coordinates of all 3d points

$z \leftarrow$ Z coordinates of all 3d points

$\alpha \leftarrow$ **KD Tree**($x, y,$)

For $i \leftarrow 1$ to n

$\beta \leftarrow$ **RangeSearch**($\alpha, \alpha(i), R$)

$s \leftarrow z(\beta(1,1))$

$\mu \leftarrow$ Standard Deviation($s(1,1)$)

If $\mu \leq R1$

$x(i) \leftarrow x(i)$

$y(i) \leftarrow y(i)$

$z(i) \leftarrow z(i)$

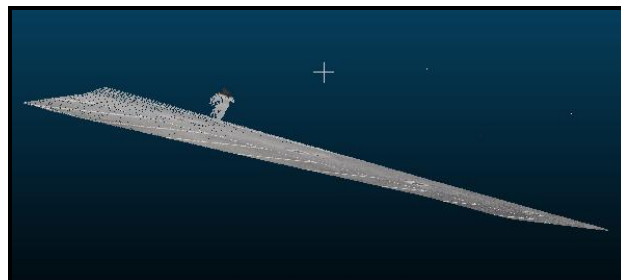
End If

End For

End Procedure

3. Experimental Result

3.1. Input Data



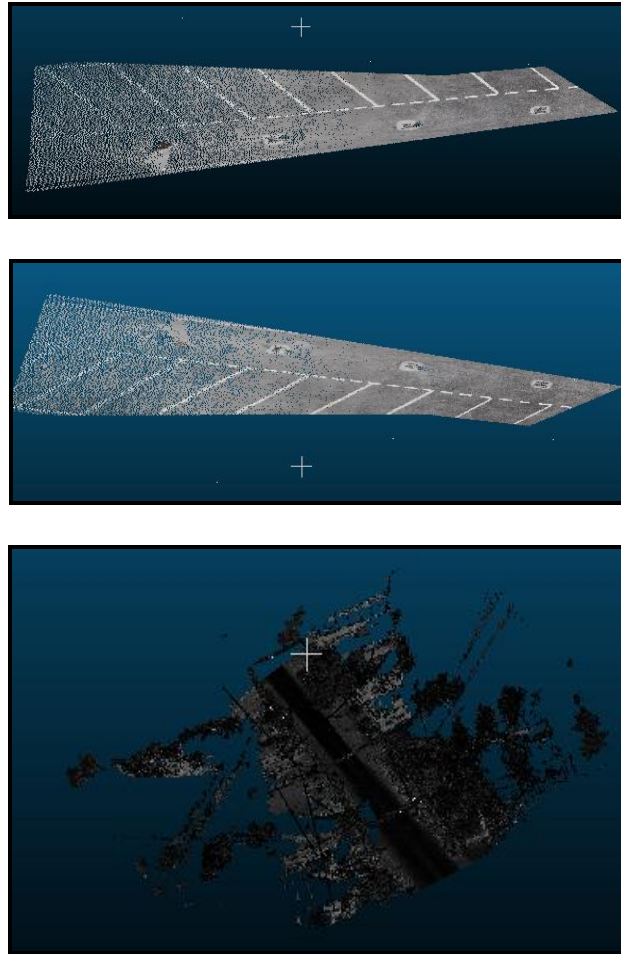


Figure 1: 3D Data Point Cloud Captured by Airborne LiDAR

3.2. Output

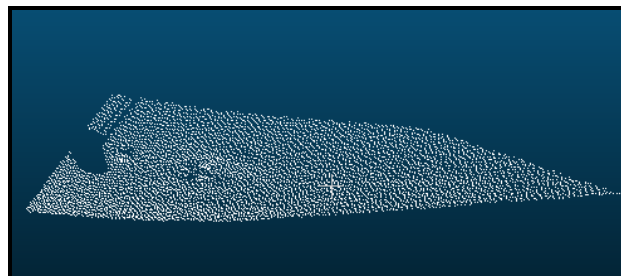


Figure 2: 3D Data point Cloud Output

4. Dataset and Accuracy Measure

The dataset was sampled by ALTM scanner, and both the first and last return was available. For the study site, the ground point are already identified and available for assessing accuracy. We use the ground reference data to optimize our selection of slope and elevation difference thresholds and test the sensitivity of our algorithms to changes in thresholds.

Table 1: Kappa Coefficient for Various Algorithms

| Sample Data | Kraus and Pfeifer | Sithole and Vosselman | Zhang and Whitman | Jie Shan and Sampath | Meng et al. | Ground and Non-Ground Filtering |
|-------------|-------------------|-----------------------|-------------------|----------------------|-------------|---------------------------------|
| Data1 | 65.05 | 51.24 | 80.01 | 78.48 | 91.24 | 90.63 |
| Data2 | 90.10 | 78.86 | 56.78 | 81.97 | 60.13 | 89.14 |
| Data3 | 91.01 | 90.44 | 92.51 | 74.71 | 54.89 | 67.73 |
| Data4 | 47.09 | 87.61 | 86.11 | 36.29 | 89.17 | 98.7 |
| Data5 | 75.26 | 41.21 | 61.21 | 49.00 | 90.05 | 88.03 |
| Data6 | 66.75 | 19.81 | 46.31 | 54.21 | 31.22 | 41.19 |

5. Conclusion

The proposed approach is based on neighborhood of the cloud points. Hierarchy of preprocessing is done for LIDAR data using various essential tools. ROI is selected and cropped by a specific tool. Coordinates of all three dimensions of cloud points are processed by nearest neighborhood processing algorithm. K-D tree is used to distinguish the bare ground and non-ground objects using nearest neighbor search. Experiments have been performed on various LIDAR data sets. Kappa coefficient is used to compare the accuracy and effectiveness of the proposed approach. Experimental results show the effectiveness and usefulness of the proposed approach.

References

- [1] Kraus and Pfeifer. *Determination of Terrain Models in Wooded Areas with Airborne Laser Scanner Data*. ISPRS Journal of Photogrammetry & Remote Sensing. 1998. 53; 193-203.
- [2] Keqi Zhang et al. *A Progressive Morphological Filter for Removing Non-Ground Measurements from Airborne LIDAR Data*. IEEE Transactions on Geoscience and Remote Sensing. April 2003. 41 (4).
- [3] Sithole and Vosselman. *Experimental Comparison of Filter Algorithms for Bare-Earth Extraction from Airborne Laser Scanning Point Clouds*. ISPRS Journal of Photogrammetry & Remote Sensing. 2004. 59; 85-101.
- [4] Zhang and Whitman. *Comparison of Three Algorithms for Filtering Airborne LiDAR Data*. Photogrammetric Engineering & Remote Sensing. March 2005. 71 (3) 313-324.
- [5] Jie Shan and Aparajithan Sampath. *Urban DEM Generation from Raw LiDAR Data: A Labeling Algorithm and Its Performance*. Photogrammetric Engineering & Remote Sensing. February 2005. 71 (2) 217-226.
- [6] Xulien Meng et al. *A Multi-Directional Ground Filtering Algorithm for Airborne LIDAR*. ISPRS Journal of Photogrammetry and Remote Sensing. 2009. 64; 117-124.
- [7] Xulien Meng et al. *Ground Filtering Algorithms for Airborne LiDAR Data: A Review of Critical Issues*. Remote Sensing. 2010. 2; 833-860.
- [8] Dehvari and Heck. *Removing Non-Ground Points from Automated Photo-Based DEM and Evaluation of Its Accuracy with LiDAR DEM*. Computers & Geosciences. 2012. 43; 108-117.
- [9] Chen and Li. *A Robust Method of Thin Plate Spline and Its Application to DEM Construction*. Computers & Geosciences. 2012. 48; 9-16.

- [10] Chen, Z., Devereux, B., Gao, B. and Amable, G. *Upward-Fusion Urban DTM Generating Method Using Airborne LiDAR Data*. ISPRS Journal of Photogrammetry and Remote Sensing. 2012. 72; 121-130.
- [11] Chen et al. *A Multiresolution Hierarchical Classification Algorithm for Filtering Airborne Lidar Data*. ISPRS Journal of Photogrammetry and Remote Sensing. 2013. 82; 1-9.

Evaluation of Shadow Reconstruction Algorithm for Very High Resolution Satellite Imagery

Panchal Anjali Jayant^{1,2}, Rizvi Imdad A.² and Kadam M.M.²

¹Department of Electronics and Telecommunication Engineering, Konkan Gyanpeeth College of Engineering, Karjat, Maharashtra, India

²Department of Electronics and Telecommunication Engineering, Terna Engineering College, Navi Mumbai, Maharashtra, India

Publication Date: 9 February 2016

DOI: <https://doi.org/10.23953/cloud.ijarsg.38>



Copyright © 2016 Panchal Anjali Jayant, Rizvi Imdad A. and Kadam M.M. This is an open access article distributed under the **Creative Commons Attribution License**, which permits unrestricted use, distribution, and reproduction in any medium, provided the original work is properly cited.

Abstract The Very High Resolution images have opened a new era for remote sensing applications such as object detection, classification, object mapping and change detection. However, the effects of shadow in these images are remarkable. The objective of this paper is to propose algorithm for shadow reconstruction. The primer stage, shadow detection and classification are carried out which separates shadow from rest of environment. For doing reconstruction the preprocessing is done by morphological operations which extract image components such as region and shape. It is followed by border creation and finally the reconstructed of an original image is accomplished border interpolation. The reconstruction accuracy is calculated by using Kappa Coefficient. Here Experimental results are obtained on three VHR images representing different shadow conditions. The performance analysis is carried out which shows better sensitivity and specificity.

Keywords *Cast Shadow; Self-Shadow; Shadow Detection; Sensitivity; Specificity; VHR Satellite Images*

1. Introduction

The resolution of VHR image distinguishes very well defined features from small objects like building structures, trees, vehicles and roofs (Rizvi and Buddhiraju, 2011, 2012). But high spatial resolution causes some problems like presence of shadows particularly in urban areas where there are larger changes in surface elevation due to the presence of buildings, bridges, towers and longer shadows. (Lorenzi, Melgani and Mercier, 2012). However the analysis of these images also requires new digital image processing techniques to deal with challenges such as the problem of shadows (Jindong and Marvin, 2012).

In high resolution imagery presence of shadow leads to the reduction or total loss of spectroradiometric information which carry problems in the interpretation of land cover and the evaluation of ground condition depend (Susaki, 2012). To estimate the effects of shadow reconstruction, both pixel-based and object-oriented methods were used (Jindong and Marvin, 2013).

An invariant color space based non-linear transformation was projected, while histogram thresholding was performed to differentiate shadows from non-shadow areas in QuickBird and IKONOS images (Salvador et al., 2001), radiance ratio with digital numbers (Liu and Yamazaki, 2010) and with three dimensional models (Tsai and V.J.D, 2006; Chung et al., 2009). Additionally if the a priori knowledge of the sensor, the illumination, and the 3-D geometry of the scene are available, three-dimensional models have been developed (Scott and Narayanan, 2012).

The several radiometric restoration methods were compared to get rid of shadow areas in the original satellite imagery, (Sarabandi, 2004), with gamma correction, linear correlation correction (Chen, 2007) and histogram matching (Tsai and V.J.D, 2006). To swap shadow pixels in one image with non-shadow pixels of the same area from another image, multisource data fusion has also been used (Yuan, 2008). The shadow areas were easily extracted from the Quick Bird imagery by using the segmentation of a panchromatic image and a calculated radiance ratio between the shaded and sunlit areas (Liu and Yamazaki, 2012). Similarly to prepare an initial shadow mask, thresholding is adopted and then for shadow detection the noise and wrong shadow regions are isolated by the morphological phases (Song et al., 2013) and then reconstruction is carried out by linear correlation method.

The classification is also better approach for shadow reconstruction, considering most spectroradiometric restoration algorithms were not designed to optimize classification performance, a support vector machine approach (Buddhiraju and Rizvi, 2010) was used to classify shadows for shadow pixels in satellite imagery (Panchal et al., 2014).

Similarly the object-oriented methods produces better classifications because of its capacity of subdividing images into individual homogeneous regions (i.e., image objects) at scales that are appropriate to the inherent landscape (Rizvi and Buddhiraju, 2010) and establishing the context information and topological network of these image objects for accurate classification (Benz et al., 2004).

2. Proposed Method

In this case, the more interest is given in the land cover that casts the shadows (e.g., buildings and trees) than the land cover shaded by shadows (e.g., grass and impervious surfaces). In this work three satellite images are used which has impervious shadow structure. Most of the shadow structure is almost in rectangular shape as they cast on building, aircraft etc. The flowchart with principal steps of proposed system is shown in Figure 1. This is the extended work of (Panchal et al., 2015) in which shadow detection is already explained in detail. The brief review of shadow detection is explained further.

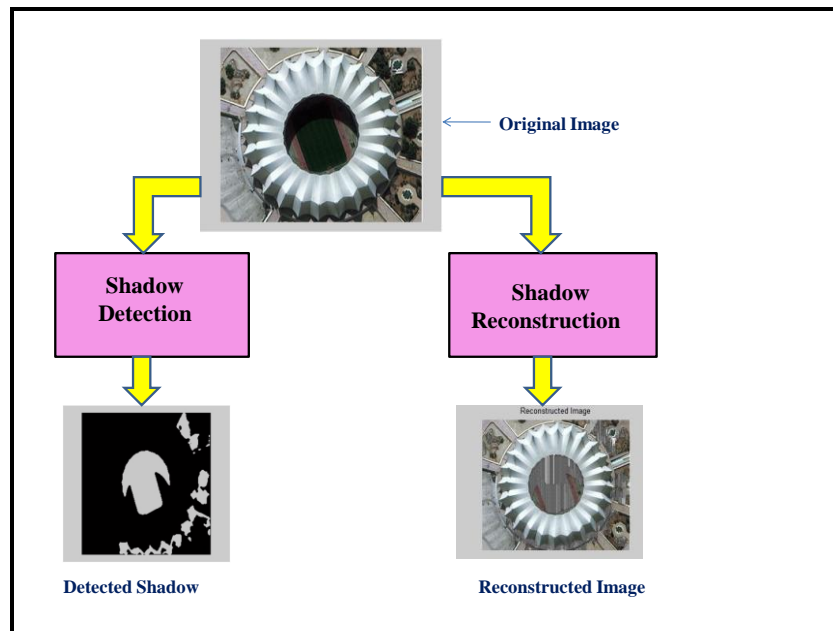


Figure 1: Flowchart of Proposed System

2.1. Shadow Detection Approach

In this paper, spectral values of satellite images are taken into consideration. To perform shadow detection the basic processing are done by following stages.

2.1.1. Thresholding

Threshold value is calculated from the same satellite images. Thresholding is simply the method of converting an image to binary format by setting all pixels whose values are greater than some threshold level to “high” and the remaining pixels to “low”. It represents binary mask of a satellite image.

2.1.2. Morphological Filtering

The morphological operators are required in order to separate isolated shadow pixels in a non-shadow area and also isolated non-shadow pixels in a shadow area. Then the operations of erosion, dilation and morphological operation are performed. Erosion finds the correct points of shadow which are placed in neighborhood. The points which are found by erosion are connected by dilation.

2.1.3. Border Creation

The border is to be defined which shows transition in between the shadow and non-shadow areas. Otherwise it can raise problems such as boundary ambiguity, color inconstancy, etc. Therefore canny edge detection algorithm is used, so bordered image is found.

2.2. Shadow Reconstruction Approach

Here morphological operations are used for extracting image components such as region and shape. The structuring elements adopted to perform morphological opening operation and morphological closing operations are shown in Figure 2.

| | | | | |
|---|---|---|---|---|
| 1 | 1 | 1 | 1 | 1 |
| 1 | 1 | 1 | 1 | 1 |
| 1 | 1 | 1 | 1 | 1 |
| 1 | 1 | 1 | 1 | 1 |
| 1 | 1 | 1 | 1 | 1 |

Figure 2: Structuring element for Opening operation and Closing operation

The opening operation smoothes the contour of an image whereas closing fuse the narrow breaks, eliminates small holes and fill gaps in contour. The output of these operations is post processed mask of an image. After this process again structuring element is applied of 10×10 matrix to have dilation of an image.

In this case, for doing reconstruction the simple step is carried out i.e. as we know the shadow is also surrounded by non-shadow region. It means if we calculate average value of non-shadow region in the neighborhood and then assign into shadow region, it will be seen as an image without shadow.

To do so, border $h[x, y]$ is created by subtracting dilated image with closing operation of an image and final mask is created with border.

$$h[x, y] = \partial[x, y] - \text{Eclosebw}[x, y] \quad (1)$$

The connected components of shadow region are searched out and assigned the pixel value to shadow region. In this case shadow values and non-shadow values are taken into consideration. The shadow values are selected and these intensity values should be replaced with non-shadow. For this purpose, nearest location of non-shadow value is calculated by considering the region of shadow pixel value added with 50 and shadow pixel value subtracted with 50. Within the same region, minimum value of non-shadow pixel is calculated and it replaces the shadow pixel. If minimum value is not identified then shadow pixel is replaced by nearby non shadow pixel within the region.

3. Results and Discussions

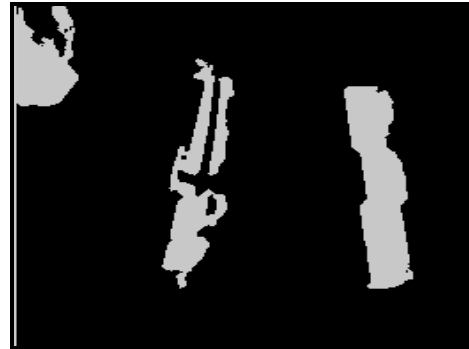
To evaluate the results of proposed method, three images were used. They differ from the properties (distribution and size) of the shadows which depend on the kinds of shaded land covers and the acquisition time. The aircraft image is of 634×403 dimensions with 69 dpi resolution as shown in Figure 3(a). The circular image is of 260×210 dimensions with 300 dpi resolution as shown in Figure 4(a). The road image is of 738×533 dimensions with 96 dpi resolution as in Figure 5(a).

3.1. Shadow Detection Output

As described in the previous section, the first task of the proposed methodology is to generate a mask image useful to localize the shadow, the non-shadow, and the border areas. Therefore to capture shadow, thresholding is carried out which create binary mask of an image. Similarly shadow detection outputs are shown in Figures 3(b), 4(b) and 5(b).



(a) Aircraft Image



(b) Detected Shadow

Figure 3: (a) Aircraft Image (b) Detected Shadow



(a) Circular Image

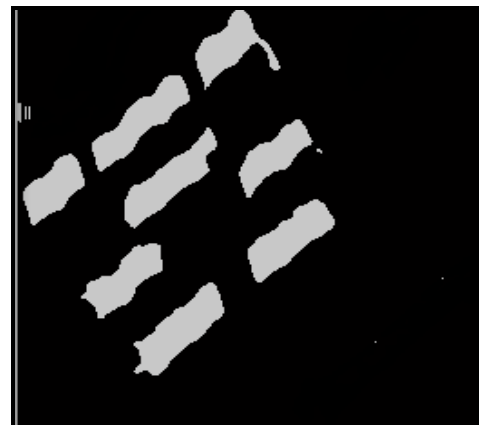


(b) Detected Shadow

Figure 4: (a) Circular Image (b) Detected Shadow



(a) Road Image



(b) Detected Shadow

Figure 5: (a) Road Image (b) Detected Shadow

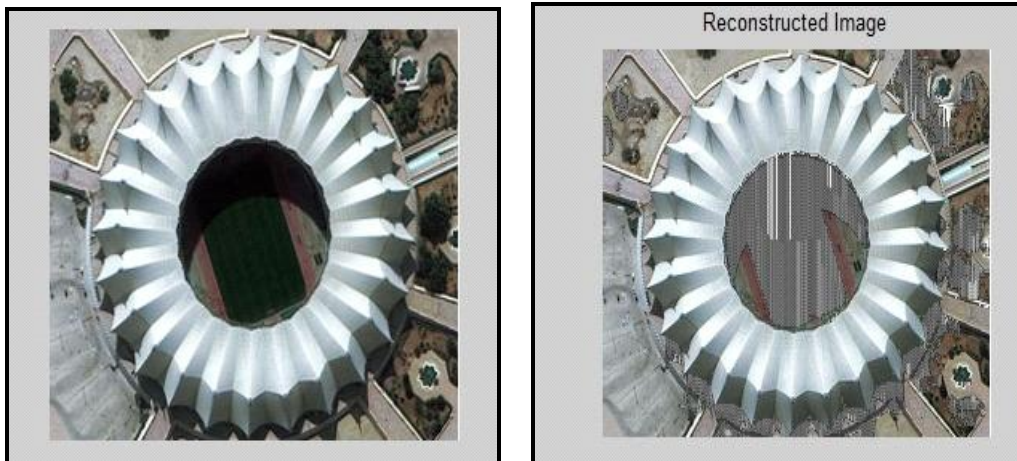
3.2. Shadow Reconstruction Output

The shadow reconstruction output is shown with original images. The first image shows shadow structures in rectangular manner, therefore they are more properly reconstructed. But second image and third image, the dark vegetation areas are mistakenly represented as shadow area, so these

portions of an image is also reconstructed with shadow part. The figures are shown in 6(a), 6(b) and 6(c).



(a) Aircraft Image



(b) Circular Image



(c) Road Image

Figure 6: Image Reconstruction output (a) Aircraft image (b) Circular image (c) Road image

The reconstruction output's accuracy is also calculated in following manner i.e. by neural network. The User's Accuracy and producer's accuracy are observed weak. But Kappa Coefficient and Classification accuracy i.e. overall accuracy are observed in better manner.

Table 1: Classification Evaluated for Image Reconstruction

| | User's Accuracy | Producer's Accuracy | Kappa Coefficient | Classification Accuracy |
|----------------|-----------------|---------------------|-------------------|-------------------------|
| Aircraft Image | 30 | 42.5 | 0.496 | 72.5 |
| Circular Image | 31 | 33 | 0.734 | 85 |
| Road Image | 25.8 | 40.8 | 0.493 | 74.5 |

4. Performance Analysis

To evaluate the performance of the given method, the following procedure is used. The classified output is compared with ground truth information to validate the results. The assumption is made that shadow pixels are of white as foreground and non-shadow pixels are black pixels as background in the ground truth. The following terms are used for doing analysis.

True positive (TP): pixels correctly classified as foreground

False positive (FP): pixels falsely classified as foreground

True negative (TN): pixels correctly detected as background

False negative (FN): pixels falsely detected as background

These metrics are then used to calculate sensitivity, specificity and accuracy as:

Sensitivity: The sensitivity of the method is proportion of positive pixels correctly predicted (i.e. the probability that a pixel belonging to shadow is correctly identified). This is calculated as $TP / (TP+FN)$.

Specificity: The specificity of the method is proportion of negative pixels correctly predicted (i.e. the probability that a pixel belonging to non-shadow is correctly identified). This is calculated as $TN / (TN+FP)$. Thus models with high sensitivity can correctly predict positive pixels (pixels belonging to the category of interest) and models with high specificity can correctly predict negative pixels (pixels not belonging to the category of interest). High sensitivity is usually associated with poor specificity, which manifests as an overestimate of area in the category of interest.

Accuracy: Accuracy is biased estimates that depend on the proportion of pixels actually belonging to each class. It is $(TP+TN) / (TP+FP+TN+FN)$.

Table 2: Performance Parameters Evaluation

| | TP | FP | TN | FN |
|----------------|------|------|-------|------|
| Aircraft Image | 7435 | 1049 | 55618 | 1434 |
| Circular Image | 3048 | 9085 | 53384 | 19 |
| Road Image | 2236 | 3079 | 53781 | 6442 |

Table 3: Performance Accuracy Evaluation

| | Sensitivity | Specificity | Accuracy |
|-----------------------|-------------|-------------|----------|
| Aircraft Image | 96.21 | 83.83 | 98.15 |
| Circular Image | 86.10 | 99.38 | 85.46 |
| Road Image | 85.47 | 25.77 | 94.58 |

The aircraft image is evaluated with correct shadow pixels classified as 3048, correct non shadow pixels 19. The non-shadow pixels 20995 are classified as shadow and 37525 shadow pixels are classified as non-shadow. Therefore sensitivity says that the correctly shadow pixels identified are 86.10%. Similarly specificity observed that the correctly non shadow pixels identified are 99.38% and accuracy 85.46%. Note that first image have larger shadow structure, therefore the result is good.

For the circular image is evaluated with correct shadow pixels classified as 7435, correct non shadow pixels 1434. The non-shadow pixels 1049 are classified as shadow and 55618 shadow pixels are classified as non-shadow. For this case image with sensitivity 96.21%, specificity 83.83%, 98.15% accuracy is observed.

The road image is evaluated with correct shadow pixels classified as 2236, correct non shadow pixels 6442. The non-shadow pixels 3079 are classified as shadow and 53781 shadow pixels are classified as non-shadow. Therefore sensitivity says that the correctly shadow pixels identified are 85.47%. Similarly specificity observed that the correctly non shadow pixels identified are 25.77% and accuracy 94.58%.

5. Conclusion

From obtained results, following points can be considered,

- The proposed method works well for grayscale images where shadows are in rectangular shapes. Therefore this method can be used for urban areas.
- The shadow reconstruction output is calculated by using neural network. It is observed that the Kappa Coefficient values for three images are greater than 50% and Classification Accuracy for three images gave above 70%.
- An optimum classification model would be one with the highest possible value of both sensitivity and specificity. From performance analysis, the classification accuracy, sensitivity, specificity are observed greater than 80%.

References

Benz, U.C., Hofmann, P., Willhauck, G., Lingenfelder, L. and Heynen, M. *Multi-Resolution, Object-Oriented Fuzzy Analysis of Remote Sensing Data for GIS-Ready Information*. ISPRS Journal of Photogrammetry Remote Sens. 2004. 58; 239-258.

Buddhiraju, K.M. and Rizvi, I.A., 2010: *Comparison of CBF, ANN and SVM Classifiers for Object-Based Classification of High Resolution Satellite Images*. Proc. IGARSS. 40-43.

Chung, Liang Kuo, Lin Yi-Ru, and Huang Yong-Huai. *Efficient Shadow Detection of Color Aerial Images Based on Successive Thresholding Scheme*. IEEE Transaction on Geosciences and Remote Sensing. 2009. 47 (2).

Chen, Y., Wen, D., Jing, L. and Shi, P. *Shadow Information Recovery in Urban Areas from Very High Resolution Satellite Imagery*. International Journal of Remote Sensing. 2007. 28; 3249-3254.

- Jindong Wu and Marvin E. Bauer. *Evaluating the Effects of Shadow Detection on QuickBird Image Classification and Spectroradiometric Restoration*. Journal of Remote Sensing. 2013. 5; 4450-4469.
- Lorenzi Luca and Melgani Farid, and Mercier Grégoire. *A Complete Processing Chain for Shadow Detection and Reconstruction in VHR Images*. IEEE Transaction on Geosciences and Remote Sensing. 2012. 50 (9).
- Liu Wen and Yamazaki Fumio. *Shadow Extraction and Correction from Quick Bird Images*. IEEE J. Sel. Top. Appl. Earth Obs. Remote Sens. 2010. 978-1-4244-9566 5/10.
- Liu, W., and Yamazaki, F. *Object-Based Shadow Extraction and Correction of High Resolution Optical Satellite Images*. IEEE J. Sel. Top. Appl. Earth Obs. Remote Sens. 2012. 5; 1296-1302.
- Panchal, A.J., Rizvi, I.A. and Kadam, M.M., 2014: *Shadow Detection of Very High Resolution Satellite Images Using Support Vector Machine*. ISPRS TC VIII Mid-Term Symposium 2014.
- Panchal, A.J., Rizvi, I.A. and Kadam, M.M. *Proposed Algorithm for Shadow Identification and Classification in VHR Satellite Imagery*. Journal of Remote Sensing & GIS. 2015. 6 (3) 2015.
- Rizvi, I.A. and Buddhiraju, K.M. *Object-Based Image Analysis of High Resolution Satellite Images using Modified Cloud Basis Function Neural Network and Probabilistic Relaxation Labeling Process*. IEEE Transaction on Geosciences and Remote Sensing. 2011. 49 (12) 4815-4820.
- Rizvi, I.A. and Buddhiraju, K.M., 2012: *Object-Based Analysis of Worldview-2 Imagery of Urban Areas*. IEEE International Geoscience and Remote Sensing Symposium, Munich, Germany.
- Rizvi, I.A. and Buddharaju, K.M. *Improving the Accuracy of Object-Based Supervised Image Classification using Cloud Basis Functions Neural Network for High Resolution Satellite Images*. International Journal of Image Processing. 2010. 4 (4) 342-353.
- Susaki, J. *Segmentation of Shadowed Buildings in Dense Urban Areas from Aerial Photographs*. IEEE Transaction on Geosciences and Remote Sensing. 2012. 4; 911-933.
- Salvador, E., Cavallaro, A., and Ebrahimi, T. *Shadow Identification and Classification Using Invariant Color Models*. Proc. IEEE Int. Conf. Acoust., Speech, Signal Process. 2001. 3; 1545-1548.
- Scott Papson and Narayanan Ram M. *Classification via the Shadow Region in SAR Imagery*. IEEE Transactions on Aerospace and Electronic Systems. 2012. 48 (2I).
- Sarabandi, P., Yamazaki, F., Matsuoka, M. and Kiremidjian, K., 2004: *Shadow Detection and Radiometric Restoration in Satellite High Resolution Images*. In Proceedings of IEEE International Geoscience and Remote Sensing Symposium (IGARSS '04), Anchorage, AK, USA, 20-24 September 2004. 6; 3744-3747.
- Song Huihui, Huang Bo and Zhang Kaihua. *Shadow Detection and Reconstruction in High Resolution Satellite Images via Morphological Filtering and Example-Based Learning*. IEEE Transaction on Geosciences and Remote Sensing. 2013. 52 (5) 2545-2554.
- Tsai, V.J.D. *A Comparative Study on Shadow Compensation of Color Aerial Images in Invariant Color Models*. IEEE Transaction on Geosciences and Remote Sensing. 2006. 44 (6).

Wu Jindong, and Marvin E. Bauer. *Estimating Net Primary Production of Turf Grass in an Urban-Suburban Landscape with Quickbird Imagery*. Journal of Remote Sensing. 2012. 4; 849-866.

Yuan, F. *Land-Cover Change and Environmental Impact Analysis in the Greater Mankato Area of Minnesota using Remote Sensing and GIS Modeling*. International Journal of Remote Sensing. 2008. 29; 1169-1184.

Multi-temporal Analysis of Vegetation Dynamics Over Three Decades for Sustainable Management of Woody Vegetation: The Case of Abaya-Gelana Area, Borena Zone, Southern Ethiopia

Birhane Gebrehiwot

Department of Land Administration, Dilla University, Gedeo, Ethiopia

Publication Date: 21 April 2016

DOI: <https://doi.org/10.23953/cloud.ijarsg.53>



Copyright © 2016 Birhane Gebrehiwot. This is an open access article distributed under the **Creative Commons Attribution License**, which permits unrestricted use, distribution, and reproduction in any medium, provided the original work is properly cited.

Abstract Up-to-date and reliable land use/land cover (LULC) information forms an essential component of local and regional planning. So, the aim of the present study is to analyze and quantitatively evaluate LULC changes in Abaya-Gelana area between 1986 and 2015 using remotely sensed data and techniques. To realize the aforementioned objective, cloud free orthorectified multispectral land sat 5 thematic mapper (TM) acquired in 1986 and land sat 8 operational land imager (OLI) acquired in 2015 were used for LULC change detection. In addition to the land sat images, collateral information was obtained from topographic maps, field data, and Google earth images. After digital image processing and visual interpretation of the land sat images, supervised classification with maximum likelihood algorithm was applied and LULC maps for 1986 and 2015 were produced. Finally, post-classification comparison was made to analyze LULC changes over the past three decades. The results of the change detection analysis show that there is obvious deforestation problem in the study area which is manifested by the reduction of bushland by 46.89% and an increase in bareland by 253.34% within 29 years. Besides, a reduction in grass land, a remarkable increase in cultivated land, urban expansion, an increase in water surface are among the major LULC changes over the past three decades.

Keywords *LULC Change; Land Sat Images; Maximum Likelihood Algorithm; Post-Classification Comparison; Supervised Classification*

1. Introduction

1.1. Background of the Study

Forests are increasingly recognized for the wide range of products and essential ecosystem services they provide at all spatial scales. According to Ellen (2010), forested catchments which account for three quarters of the earth's accessible freshwater resources reduce its quality as forest conditions worsen. Forest area is declining across the globe due to logging activities and conversion of habitats to croplands. Agricultural expansion accounts for up to 43% of tropical forest losses (Ellen, 2010). Specifically, a study conducted by FAO on global forest land-use change from 1990–2005 indicate that

next to South America, Africa had the second highest net forest loss which is 1.6 million hectares annually during the study period (Lindquist et al., 2012). As a result, conversions of land use/land cover (hereafter LULC) from one to another have become recognized as a major cause of global environmental changes.

Similarly, deforestation and the resulting environmental degradation is a major problem in Ethiopia and after several years of deforestation, the remaining forest is estimated to be about 12 percent of the country's surface area (Zenebe, 2007). Likewise, Ellen (2010) points out that within a quarter of a century (1955-1979), over 77% of the country's forested area was disappeared and continued at the rate of 8% (about 140,000 hectares) annually. In addition, conversion of rangelands into cultivated land is one of the main challenges affecting the management of rangelands in Ethiopia (Elias et al., 2015) which has led to a severe land degradation in the Ethiopian highlands (Binyam, 2015). On the other hand, scientific information regarding growth rates, natural regeneration, or other related forest dynamics is lacking in the country (Desta, 2001).

Other studies also indicate that majority of the Ethiopian population is dependent on fuel wood for its energy consumption. JICA (2012) states that while the electricity coverage in Ethiopia reached 41%, the main source of energy for 85% of the Ethiopian population is still fuel wood. Among other things, the dependence of urban centers for their fuel on the rural hinterlands has also aggravated deforestation problems (Barnes et al., 2004).

As far as the study area is concerned, there is a continuous supply of fire wood and charcoal to the surrounding towns especially to the Dilla town which is located at the eastern part of the study area. In addition, there is conversion of rangeland into agriculture because many people who were pastoralists in the past are becoming agro-pastoralists and small scale farmers. Besides, investors have also taken large area of rangeland for crop production. However, although deforestation is evident in the study area, little prior knowledge exists with regard to the rate and the spatial pattern of deforestation over time (BoFED of National Regional Government of Oromia, 2015). On the other hand, at global level, the last few decades have witnessed considerable developments in the use of remotely sensed data as a means to follow-up and scrutinize the changes imposed on the environment (Ayache et al., 2015). Since up-to-date and reliable LULC information forms an essential component of local and regional planning (Campbell and Randolph, 2011), the aim of the present study is to analyze and quantitatively evaluate the LULC changes in Abaya-Gelana area over the past three decades using remotely sensed data and techniques.

2. Materials and Methods

2.1. Description of the Study Area

In the Federal Democratic Republic of Ethiopia, the administrative structure divides the regional states into divisions called *Woredas*. A *Woreda* is an administrative division equivalent to a district. It is composed of a number of subdivisions, which are the smallest administrative units called *Kebeles*. So in this study, a *Kebele* refers to a peasant association (PA) within a *Woreda*/district.

The current study was conducted in two *woredas* namely Abaya and Gelana which are located in the Oromiya Regional State, Borena zone. It was a single *Woreda* (district) in the past but they have been administratively split into two and each of them formed an independent *woreda* currently. The geographic coverage of the study area extends from 5°44'10" to 6°40'10"N and from 37°44'10" to 38°19'40"E (Figure 1). It is bordered by Hagere Mariam *Woreda* in the south, and in the west, north and east by the Southern Nations Nationalities and Peoples Region (SNNPR). Specifically, it is bordered by lake Abaya in the west. According to the central statistical agency of Ethiopia (1994), the total surface area of Abaya-Gelana is 3240 square kilometers and estimated numbers of human

population in 2009 for Abaya and Gelana *woredas* were 110,086 and 81210 respectively (BoFED of National Regional Government of Oromia, 2015). The capital center of Abaya *woreda* is Guangua town which is found at 365 kilo meters south of Addis Ababa along the Addis Ababa-Moyale international road and the capital of Gelana *woreda* is Tore town which is located to the south west of Guangua town.

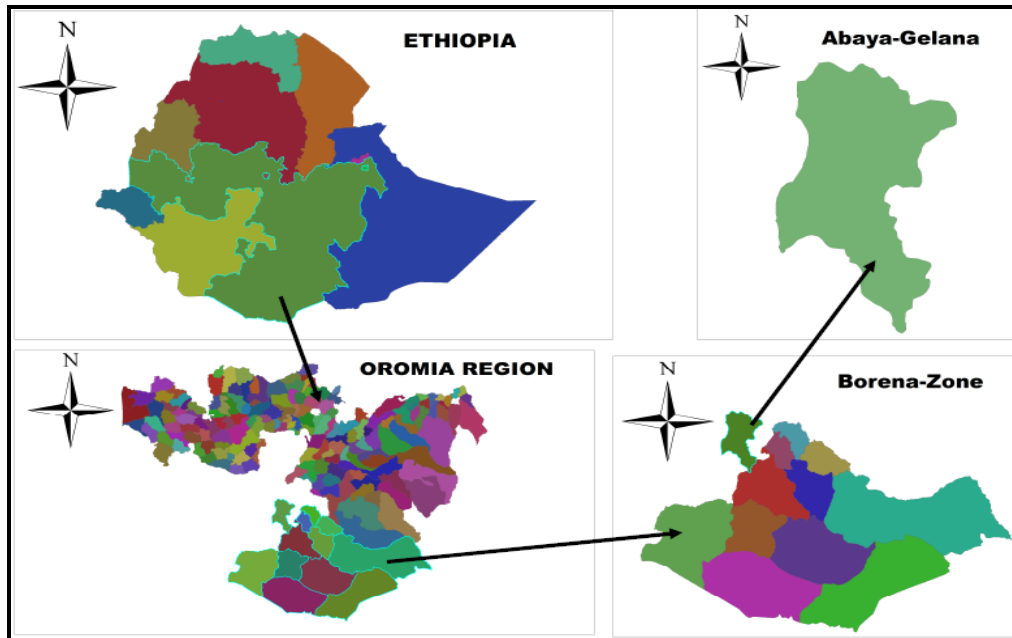


Figure 1: Location Map of the Study Area

The elevation of Abaya *woreda* ranges from 1100 to 2060 meters above sea level and it has two types of agro-climatic zones, 'Weyna Dega' or midland (about 40%) and 'Kola' or lowland (about 60%). Its average annual rainfall ranges from 900 mm to 1200 mm and its temperature ranges from 16°C to 28°C. Likewise Gelana *woreda* has elevation ranges of 1280 to 1860m above sea level. Generally, the study area has bi-modal rainy seasons from the mid of March to the end of May and from the mid of September to the end of November (BoFED of National Regional Government of Oromia, 2015).

The study area is covered by different types of vegetation, predominantly shrubs, bushes, and grass including natural and plantation forests which are protected by the government. The major land uses are shrub land, forest, water, swamp, cultivated and barelands. Crops such as maize, barley, teff, sorghum, haricot bean, wheat, enset (*ensete ventricosum*) and chickpea are grown in the study area. However, in both *woredas*/districts, there are problems regarding up to date, reliable and adequate information on the existing condition, current level of exploitation, and degradation of natural resources (BoFED of National Regional Government of Oromia, 2015).

2.2. Methods of Data Collection

In this study, different types of data collection methods were employed. These are remote sensing, GIS, and field data collection methods.

2.2.1. Remote Sensing and GIS Data Collection

Cloud free orthorectified multispectral land sat 5 TM image which was acquired on January 18/1986 and Land sat 8 OLI image acquired on January 05/2015 were downloaded from the USGS website. These images were selected for the study as the land sat program has the longest continuous time-

series of similar remotely sensed data which is a critical component in the analysis of changes in LULC since the 1970s (Williams et al., 2006). The time of acquisition of the images was in a similar time of the year to minimize the effects of seasonality so as to keep the data quality. In addition, topographic maps with the scale of 1:50,000 and 1:250,000 which were produced in 1979 were obtained from the Ethiopian Mapping Agency (EMA) and they were found to be useful in reconstructing the past image of the study area.

Table 1: Remotely Sensed Data Used for the Study

| Type of Sensor | Path/row | Spatial Resolution | Date of Acquisition | Source of Data |
|---|----------|--------------------|---------------------|----------------|
| Landsat 5 Thematic mapper (TM) | 168/056 | 30m X 30m | January 18/1986 | USGS archive |
| Landsat 8 operational land imager (OLI) | 168/056 | 30m X 30m | January 05/2015 | USGS archive |

2.2.2. Collection of Ground Truths / Land Cover Samples

To improve the satellite image interpretation and accuracy of LULC classification, a detailed field observation was conducted in order to take representative ground truths for each land cover class and the location of each ground truth data was recorded with Global Positioning System (GPS). Finally, during the training stage, these ground truth data were overlaid as training areas or land cover samples so as to train the software.

2.3. Methods of Data Analysis

2.3.1. Digital Image Processing and Visual Image Interpretation

Image enhancement and transformation techniques were applied in order to make the image ready for visual interpretation. Specifically, normalized difference vegetation index (NDVI), principal components analysis (PCA) and spectral ratio were applied using EARDAS Imagine 2013 and ENVI 4.5 softwares so as to accurately interpret the image. Finally, visual image interpretation was applied by overlying the ground truth data on the current image to improve the accuracy of image interpretation, classification, and change detection results. Similarly, the previous (1986 image) was interpreted by comparing its spectral reflectance with the one acquired in 2015. Moreover, the topographic map with 1:50,000 scale was found useful in interpreting the 1986 image because the map was produced in 1979 which is very close to the image acquisition time. In addition to EARDAS Imagine 2013 and ENVI4.5 softwares, ArcGIS 10.1 was used in order to integrate the various spatial data with GIS.

2.3.2. Training Stage and Digital Image Classification

After digital processing and visual interpretation of both the 1986 and 2015 land sat images, training areas were overlaid as region of interests using the ground truth data as reference. Accordingly, supervised classification was adopted to match the spectral classes to their corresponding information classes using EARDAS imagine 2013 software. Supervised classification was selected because it does not suffer from the problem of matching spectral classes to their corresponding information classes on the final map (Campbell and Randolph, 2011). As the quality of the training process determines the success of the classification stage and the value of the information generated from the entire classification effort, representative and complete samples were taken carefully for all information classes (Lillesand et al., 2004).

In order to distinguish between similar land cover classes and to achieve better accuracy of classification, masking technique was applied for the agroforestry and urban classes, because the spectral reflectance of agroforestry was similar with the forest class and the spectral reflectance of urban was similar with bare land reflectance. Finally, the images were classified using Gaussian maximum likelihood classification algorithm.

2.3.3. Accuracy Assessment

"A classification is not complete until its accuracy is assessed (Lillesand et al., 2004)." For that reason, the accuracy of the classification was assessed using error matrix (confusion matrix) which is one of the most common means of expressing classification accuracy. As a result, by comparing with 137 ground truth data, an overall accuracy of 93.88% and 94.44% was achieved for the 1986 and 2015 images respectively.

2.3.4. Change Detection

Ideally, change detection procedures require data acquired by the same (or similar) sensor and be recorded using the same spatial resolution, viewing geometry, spectral bands, radiometric resolution, and time of the day. However, in reality, it might be difficult to find images which fulfill all these requirements. Due to these difficulties, one way of discriminating changes between two dates of imaging is to employ post-classification comparison (Lillesand et al., 2004). Thus, in order to compensate for variations of sensor characteristics, post-classification change detection approach was applied (Figure 2).

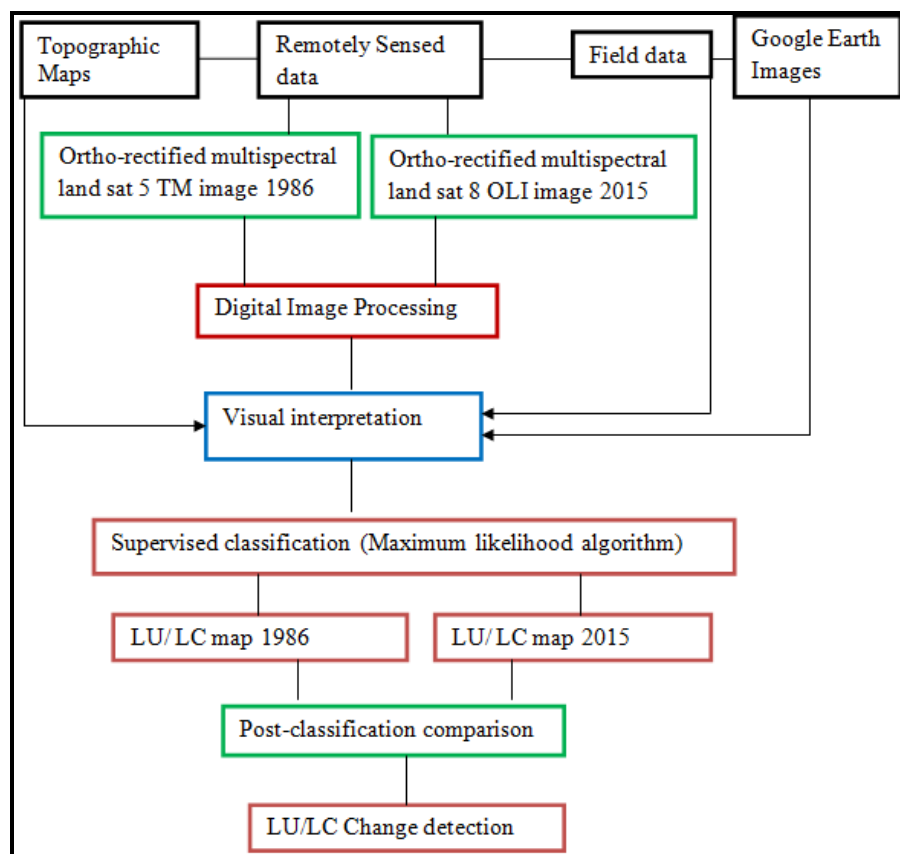


Figure 2: Flow Chart of Digital Image Analysis and LULC Change Detection

3. Results and Discussion

3.1. Land use/Land Cover Classes of the Study Area in 1986 and 2015

The total surface of the study area is 257,442.20 hectares. However, in order to keep the quality of the information, cloud free area of 238,385.11 hectares (92.6%) was considered in the current study. The LULC classes were defined based on the Global Forest Resources Assessment (2010) and by

considering the biophysical characteristics of the study area (Table 2). Accordingly, the 1986 image was classified into seven (Figure 3) while the one acquired in 2015 was divided into eight LULC classes (Figure 4).

Table 2: Description of the LULC Classes of the Study Area

| No | LULC Class | Description |
|----|--------------|---|
| 1 | Agroforestry | Refers to the complex land use pattern with natural and plantation trees at the top, inset in the middle, coffee in the lower layer and other herbaceous plants on the ground layer. In some parts of the study area, it is mixed with small parcels of cereals, pulses, vegetables, root crops, and scattered rural settlements where it is impossible to map each layer separately. |
| 2 | Annual crops | Refers to rainfed and irrigated crops mainly maize, wheat, barely, teff, and haricot bean out of the agroforestry area. |
| 3 | Bareland | Degraded or devegetated land including rock outcrops |
| 4 | Bushland | Land composed of bush or shrubs mainly acacia species which are lower than 5 meters in height. |
| 5 | Forest | Land spanning more than 0.5 hectares with trees higher than 5 meters and a canopy cover of more than 10 percent. It also includes areas with young trees that have not yet reached but which are expected to reach a canopy cover of more than 10 percent and tree height higher than 5 meters. |
| 6 | Grassland | Land cover dominated by grass and herbs with scattered trees and shrubs mainly used for grazing purpose. |
| 7 | Urban | Refers to towns including residential areas, infrastructures such as roads, various institutions, factories, and cemetery. |
| 8 | Water | Refers to water bodies mainly lakes and rivers. |

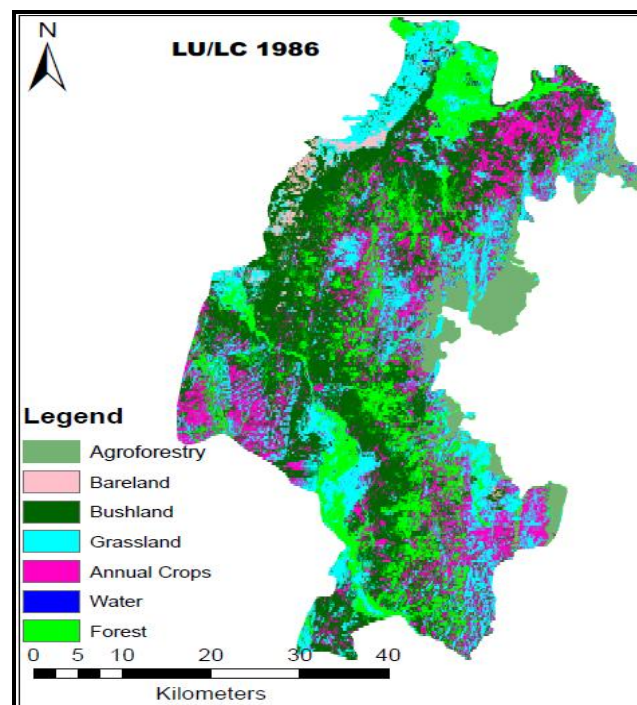


Figure 3: LULC Classes of the Study Area in 1986

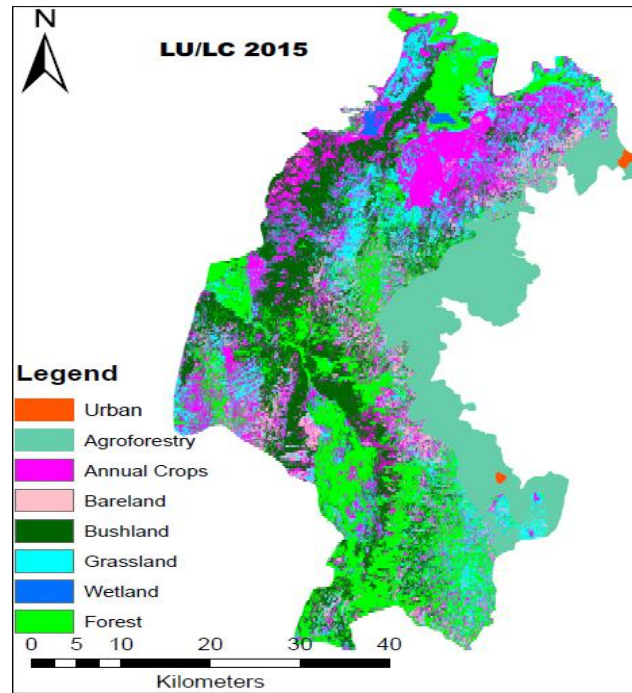


Figure 4: LULC Classes of the Study Area in 2015

Table 3: Surface Area of LULC Classes in 1986

| No | LU/LC Class | Area (inha) | Percent |
|----|--------------|------------------|-------------|
| 1 | Agroforestry | 12780.22 | 5.36% |
| 2 | Annual crops | 40467.54 | 16.96% |
| 3 | Bareland | 5284.98 | 2.22% |
| 4 | Bushland | 88891.12 | 37.29% |
| 5 | Forest | 38273 | 16.06% |
| 6 | Grassland | 52527.51 | 22.04% |
| 7 | Water | 160.74 | 0.067% |
| | Total | 238385.11 | 100% |

Table 4: Surface Area of LULC classes in 2015

| No | LU/LC Class | Area (inha) | Percent |
|----|--------------|------------------|-------------|
| 1 | Agroforestry | 38579.87 | 16.18% |
| 2 | Annual crops | 51108.8 | 21.44% |
| 3 | Bareland | 18674.19 | 7.83% |
| 4 | Bushland | 47209.59 | 19.80% |
| 5 | Forest | 38961.76 | 16.34% |
| 6 | Grassland | 42359.31 | 17.77% |
| 7 | Urban | 381.89 | 0.16% |
| 8 | Water | 1109.7 | 0.47% |
| | Total | 238385.11 | 100% |

3.2. Change Detection Results

The result of the post classification comparison by subtracting the surface area of each LULC class in the 1986 from that of the 2015 is shown below (Table 5).

Table 5: LU/LC Changes between 1986 and 2015

| No | LU/LC Classes | Area (ha) 1986 | Area (ha) 2015 | LU/LC change (2015-1986) | | Rate of change | |
|----|---------------|-------------------|-------------------|-----------------------------|---------|----------------|---------|
| | | | | Area (ha) | Percent | Area (ha/yr) | Percent |
| 1 | Agroforestry | 12780.22 | 38579.87 | 25799.65 | 201.87% | 889.64 | 6.96% |
| 2 | Annual crops | 40467.54 | 51108.8 | 10641.26 | 26.30% | 366.94 | 0.91% |
| 3 | Bareland | 5284.98 | 18674.19 | 13389.21 | 253.34% | 461.70 | 8.74 |
| 4 | Bushland | 88891.12 | 47209.59 | -41681.53 | -46.89% | -1437.29 | -1.62 |
| 5 | Forest | 38273 | 38961.76 | 688.76 | 1.80% | 23.75 | 0.06 |
| 6 | Grassland | 52527.51 | 42359.31 | -10168.20 | -19.36% | -350.63 | -0.67 |
| 7 | Urban | 0 | 381.89 | 381.89 | 381.89% | 13.17 | 3.45 |
| 8 | Water | 160.74 | 1109.7 | 948.96 | 590.37% | 32.72 | 20.36 |

3.3. Major LU/LC changes between 1986 and 2015

Over the past three decades, there is a remarkable change in the agroforestry class (Table 5). The area of land under agroforestry has increased by 201.87% within the past 29 years with average annual increment of 6.96%. Likewise, the land area covered with annual crops which consist of mainly maize, teff, barley, wheat, and haricot bean has also expanded although at relatively lower rate as compared to the agroforestry. Within three decades, the surface area of annual crops has raised by 26.30% with an average annual expansion of 0.91%. Generally cultivated land including both agroforestry and annual crop classes has expanded from 53,247.76 hectares in 1986 to 89,688.67 hectares in 2015 which has risen by 168.43% between the two study periods.

The agroforestry area is located in the eastern part of the study area bordered by the Gedeo zone. The Gedeo people are famous for their management of indigenous agroforestry. So the agroforestry practice at the immediate border of the Gedeo zone shows the cultural dissemination to previously pastoral areas of the study area. The most common vegetation species in the agroforestry class include *Millettia ferruginea*, *Cordia africana*, *Croton macrostachyus*, *Ficus sur Forssk*, *Erythrina brucei*, *Ficus vasta*, Enset (*Ensete ventricosum*), Coffee (*Coffea arabica*), Banana (*Musa paradisiaca*), Avocado (*Persea americana*), and Mango (*Mangifera indica*). In some parts, these trees are combined with small parcels of cereal crops such as maize, wheat and barley. The farmers keep diversified trees species to play various roles in the agroforestry system. Some of these trees such as *Erythrina brucei*, *Millettia ferruginea*, *Cordia africana*, *Ficus sur Forssk* and *Ficus vasta* are preferred for coffee shade. In addition to their role as a shade for coffee, the farmers witnessed that *Erythrina brucei* and *Millettia ferruginea* are also preferred for soil fertility enhancement as they are nitrogen fixing plants. Enset (*ensete ventricosum*) is used as a staple food in the agroforestry area while tree crops such as coffee, avocado, mango, and banana are grown for fruit production for market and household consumption. Specifically, coffee production in the agroforestry area is primarily market-oriented. Other tree species such as *Croton macrostachyus* are also grown for firewood. These diverse multipurpose trees species and the enset fulfill production and protection purposes which act as cornerstones, holding the whole agro-ecosystem intact (Tadesse, 2002). Due to the cultivation of integrated and diversified species, farmers in the agroforestry area are less vulnerable for hazards such as drought as compared to the cereal crop producers.



Figure 5: Typical Agroforestry Site in Foge kebele, Abaya district

In 1986, the landuse/landcover of the study area was dominated by bush land (37.29%) and grassland (22.04%) as shown in (Table 3 and 5), but in 2015 it is dominated by cultivated land (37.62%) which is the combination of agroforestry and annual crops (Table 4 and 5). Over the past three decades, the decline in grass land and bushland is evident but the rate of change is higher for bushland (Table 5) since it is primarily cleared for market-oriented charcoal making (Figure 6) but also for agricultural expansion by both small scale farmers and agricultural investors. Similarly, Worku and Csaplovics (2015) found that about 52 % of woodland area was converted to other land uses, primarily cropland in the northwestern part of the country between 1972 and 2010.

In the study area, the bushland class predominantly consists of thorny acacia species which are highly preferred by the local community for charcoal production. Different groups of the local community including children are engaged in market-oriented charcoal making for income generation (Figure 6). Charcoal making is an attracting business in the study area due to high demand for charcoal in the nearby towns. Firewood collection is also another factor contributing to the diminishing of the bush land (Figure 7) as the main source of energy for 85% of the Ethiopian population is still fuel wood (JICA, 2012). After they fell the trees, they use the branches for fire wood while the stem and root parts are used for charcoal making (Figure 6 and 7). While charcoal is produced primarily for sale, firewood wood is collected for both domestic consumption and for market.



Figure 6: Traditional Method of Charcoal Making in Gololcha Kebele, Abaya district

Some studies in other parts of the Borena zone indicate that there is an increase in the bushland area due to bush encroachment of invasive acacia species which resulted in the decline of forage production and also prohibited human and livestock access to the underlying grass (Dessalegn et al., 2003; Berhanu and Suryabhagavan, 2014). In contrast, the bush encroachment in the study area has created employment opportunity and majority of the local community are engaged in market-oriented charcoal production from the bushland. This job opportunity is created mainly due the geographic location of the study area which is bordered by Dilla town in east. Huge amount of charcoal and fire wood is continuously supplied to the town (Figure 7) and those engaged in this activity claimed that the price of charcoal and fire wood is rising from time to time due to shortage of wood for charcoal production. Consequently, the area of the bush land has declined from 88,891.12 hectares in 1986 to 47,209.59 hectares in 2015 which is a reduction by 46.89% within 29 years. Similarly, Elias et al. (2015) reported a reduction of bushland in other parts of the Borena zone mainly attributed to agricultural expansion.



Figure 7: Supply of Firewood and Charcoal from Abaya district to Dilla town

On the other hand, the increase in cultivated lands (Figure 8) and decline in grass lands in the current study is consistent with the findings of Mesele et al. (2006) who found dramatic declines in the extent of grasslands while a five-fold increase in croplands in Yabelo district of the Borena zone. Similarly

Elias et al. (2015) found a remarkable increase in cultivated land in some parts of the Borena rangeland due to the conversion of woodland, bushland, and grassland. Thus the significant increase in cultivated lands probably indicates that the pastoral communities in the study area are shifting from heavier livelihood dependence on livestock to crop production to cope up with population pressure and food insecurity (Mesele et al., 2006). Previous pastoralists are becoming agro-pastoralists or there is a change from pastoralism to mixed farming system. The people have started stable life instead of moving with their animals from one place to another place. As a result, they keep both cultivated lands and livestock together.



Figure 8: Area Cleared for Agricultural Investment

Bareland categories in this study include non-vegetated and non-agricultural lands including rock outcrops and degraded areas. The surface area of the bare land class has shown an increase within the study period (Table 5) which could be the indication of land degradation (Berhanu and Suryabhagavan, 2014; Elias et al., 2015).

Another important LULC in the study area is the forest class which consists of mixed natural and plantation vegetation species such as *Olea europaea*, *Juniperus procera*, *Combretum molle*, *Croton macrostachyus*, *Acacia* and *Ficus vasta*. Although reduction of the forest land as a result of deforestation activity is observed in some parts of the study area, there is a slight net increase in this class due to area closure or enclosure of previously degraded communal lands for rehabilitation with natural regeneration and reforestation programs (Figure 9). Area enclosure was introduced in order to protect degraded lands from anthropogenic interference and further degradation which is implemented on mountains and hillsides. As a result, previously degraded lands are being rehabilitated by natural regeneration and reforestation which resulted in a slight gain in the area of forest land. Similarly, Bokutache (2011) also reported the existence of area closures and Elias et al. (2015) found slight gains of woodland vegetation on mountain escarpments in the Borena zone.



Figure 9: Area Closure at Semero Kebele, Abaya District with Emerging and Diversified Vegetation Species

The urban class which refers to the permanent settlement in particularly two emerging towns has a total area of 381.89 hectares in 2015. These two small towns are newly emerged and it was absolutely impossible to map them using the land sat image in 1986.

Other changes in land use/land cover in the past three decades are the increase in number and surface area of water bodies. One of the reasons behind the increase in the surface area of water bodies is due to the over flow of the Abaya lake, which is one of the largest rift valley lakes in the country located in the western border of the study area. As a result of the overflow, a new small lake is formed around the Abaya lake (Figure 10). Consequently, more than 2000 households were displaced from their original settlement in 2013. In addition, there was an increase in the surface area of another previously existing lake. The overflow and expansion of these lakes might be associated with the accumulation of sediment as a result of soil erosion from the upper stream as Seleshi (2007) reported that the major challenges in the Abaya and Chamo lakes basin are deforestation, over grazing, poor tillage, severe soil erosion, and flooding of areas surrounding the rivers.

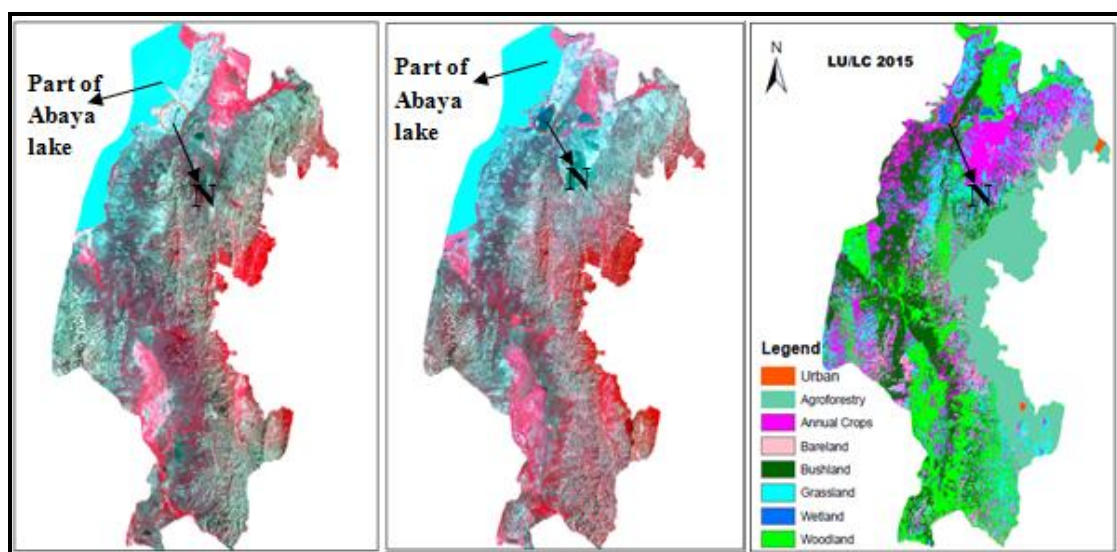


Figure 10: The Location of the New Lake Formed by the Overflow of the Abaya lake is labeled 'N'
a) Land sat 5 TM 1986 b) Land sat 8 OLI 2015 c) Classified image 2015

4. Conclusion

In the study area, there is obvious deforestation problem as a result of charcoal making, firewood collection, and agricultural expansion which is manifested by the reduction of bushland by 46.89% and an increase in bare land by 253.34% within 29 years. Similarly, there is reduction in grass land mainly due to conversion into agricultural lands. As a result, a remarkable expansion of cultivated land including agroforestry and annual crops was observed over the past three decades. Perhaps, the reduction in grassland and the rise in the area of cultivated land is the manifestation of livelihood change from high dependence on livestock husbandry to mixed farming system.

In some parts of the study area, previously deforested and degraded communal lands are enclosed or legally protected from human and livestock interference. These enclosed areas mainly mountains and hillsides are being rehabilitated by natural regeneration and reforestation, which resulted in a slight gain of the forest land. Other important LULC changes observed in the study area include urban expansion and an increase in the water bodies mainly due the overflow of Abaya lake which resulted in the displacement of more than 2000 households from their settlement area.

References

- Ayache, A., Ayad, N., Hellal, B., Benhanifia, K., and Gacemi, M. *Study of the Temporal Evolution of Land Use in the Steppe South of Tlemcen Province for the Period 1987 and 2010 using Remote Sensing and GIS Techniques*. International Journal of Remote Sensing & Geoscience. 2015. 4 (4) 28-34.
- Barnes, D.F., Krutilla, K., and Hyde, W., 2004: *The Urban Household Energy Transition: Energy, Poverty, and the Environment in the Developing World*. World Bank.
- Berhanu, K., and Suryabhadgavan, K.V. *Multitemporal Remote Sensing of Landscape Dynamics and Pattern Change in Dire District, Southern Ethiopia*. Indian Society of Geomatics. 2014. 8 (2).
- Binyam Alemu. *The Effect of Land Use Land Cover Change on Land Degradation in the Highlands of Ethiopia*. Journal of Environment and Earth Science. 2015. 5 (1) 1-12.
- Bokutache Dida, 2011: *Range Enclosures in Southern Oromia, Ethiopia: An Innovative Response or Erosion in the Common Property Resource Tenure?* Future Agricultures.
- Bureau of Finance and Economic Development of Oromiya Region, 2015. The National Regional Government of Oromia, Regional Statistics.
- Campbell, B.J., and Randolph, H.W., 2011: *Introduction to Remote Sensing*. Fifth Edition. New York: The Guilford Press.
- CSA, 1994: Central Statistical Agency of Ethiopia National Census Data.
- Dessalegn Gurmessa, Sileshi Nemomissa, Girma Tadesse, 2003: *Borana Rangeland Change from 1986-2003: The Application of Remote Sensing and GIS*.
- Desta Hamito, 2001: *Research Methods in Forestry: Principles and Practices with Particular Reference to Ethiopia*, Larenstein University of Professional Education, Deventer, the Netherlands.

Elias, M., Hensel, O., Richer, U., Hulsebusch, C., Kaufmann, B., and Wasonga, O. *Land Conversion Dynamics in the Borana Rangelands of Southern Ethiopia: An Integrated Assessment Using Remote Sensing Techniques and Field Survey Data*. *Environments*. 2015. 2 (3) 385-387.

Ellen, W., 2010: *Participatory Forest Management in Ethiopia, Practices and Experiences*. Food and Agriculture Organization Sub Regional Office for Eastern Africa (SFE), Addis Ababa.

Global Forest Resources Assessment, 2010: Terms and Definitions, Food and Agriculture Organization of the United Nations, Forest Resources Assessment Programme, Working Paper 144/E Rome.

Japan International Cooperation Agency (JICA, 2012). Energy Policy of Ethiopia, Country Report, Tokyo Japan June 24-July 14, 2012.

Lillesand, T.M., Kiefer, R.W., and Chipman, J.W., 2004: *Remote Sensing and Image Interpretation*. 5th ed. USA: John Wiley and Sons.

Lindquist, E.J., D'Annunzio, R., Gerrand, A., MacDicken, K., Achard, F., Beuchle, R., Brink, A., Eva, H.D., Mayaux, P., San-Miguel-Ayanz, J., and Stibig, H.J., 2012: *Global Forest Land-Use Change 1990–2005*. FAO Forestry Paper No. 169. Food and Agriculture Organization of the United Nations and European Commission Joint Research Centre, Rome.

Mesele, S., Heluf Gebrekidan, Lemma Gizachew, and Coppock, D.L., 2006: *Changes in Land Cover and Soil Conditions for the Yabelo District of the Borana Plateau, 1973-2003*. Research Brief 06-06-PARIMA. Global Livestock Collaborative Research Support Program. University of California, Davis. 4.

Seleshi Bekele. *Abaya-Chamo Lakes Physical and Water Resources Characteristics, Including Scenarios and Impacts*. Catchment and Lake Research. LARS 2007. 162-167.

Tadesse Kippie, 2002: *Five Thousand Years of Sustainability? A Case Study on Gedeo Land Use (Southern Ethiopia)*. Heelsum. The Netherlands: Treemail Publishers.

Williams, D.L., Goward, S., and Arvidson, T. *Landsat: Yesterday, Today, and Tomorrow*. *Photogram. Eng. & Remote Sens.* 2006. 72 (10) 1171-1178.

Worku Zewdie and Csaplovics, E. *Remote Sensing Based Multi-Temporal Land Cover Classification and Change Detection in Northwestern Ethiopia*. *European Journal of Remote Sensing*. 2005. 48; 121-139.

Zenebe Gebreegiabher, 2007: *Household Fuel Consumption and Resource Use in Rural-Urban Ethiopia*. PhD Thesis, Wageningen University, Netherlands.

Assessment Integration of GF-1 MSS Multispectral and PAN Panchromatic China satellite Images for Producing Image Map and Updating Information Content in Egyptian Map Scale 1:25 000

Ahmed Ibrahim Ramzi

Digital Mapping Department, National Authority of Remote Sensing and Space Science (NARSS) Egypt

Publication Date: 9 February 2016

DOI: <https://doi.org/10.23953/cloud.ijarsg.37>



Copyright © 2016 Ahmed Ibrahim Ramzi. This is an open access article distributed under the **Creative Commons Attribution License**, which permits unrestricted use, distribution, and reproduction in any medium, provided the original work is properly cited.

Abstract The investigation of interpretability of panchromatic satellite image GF-1 integrated with multispectral image with the purpose of producing image map and updating Egyptian topographic map topo has been described. A main objective of this research is to evaluate china GF-1 images for producing and updating topographic maps. The study has been chosen the area of the topographic map sheet at the scale of 1:25000 located in Cairo Governorates and made in 1977 and updated in 1990. In this study, the high resolution GF-1 MSS and PAN satellite images covering Cairo City, Egypt have been used. The proposed methodology based on producing image sheet map and evaluation updating topographic maps according to Egyptian specifications using GF-1 MSS, GF-1 PAN and the integration of GF-1 MSS and PAN. Results are discussed with reference to the specifications required for the scale 1: 25 000 Egyptian topographic maps. The results of these evaluations show that integration of GF-1 MSS and PAN images, from the point of geometric accuracy and Information content have the capability of 1:25,000 scale maps revision with difficulties in identification and extraction some features can be completed using other mapping methods.

Keywords *GF-1 Satellite Image; Image Map; Topographic Map Updating; Satellite Images; Feature; Extraction*

1. Introduction

Most developing countries have great difficulties in systematic updating of their maps. Maps are essential database for both planning and fieldwork operation. Up-to-date maps are necessary because obsolete maps creates so many problems to engineers, planners and other professionals who need to develop their work based on updated records (Ajayi, 1992; Abdel Mageed, 2000). In the past mapping using digital aerial photos has become very popular several years, but now the use of satellite images for cartographic and updating maps was limited by image resolution (Cheng, P. and Toutin, T., 1997). The application of remote sensing data could be an alternative method of supplying information relevant to topographic map production, revision, and updating, which is repetitive, cost-effective and relatively fast operational monitoring system (Pohl, 1996). In Egypt, National mapping agencies the Military Survey Department (MSD) and the Egyptian Survey

Authority (ESA), are confronted with the problem of producing and/or updating topographic maps. Egyptian topographic maps are many years out of date more than 25 years old; the main issue is the rapid development of urban areas and lack of adequate and up to date maps. (Abdel Mageed, 2000). Nowadays, there is useful information, provided by remote sensing satellites, in the form of single and overlapped images, which can be used for the underlined purpose of large-scale mapping (Diefallah, 1989). The Chinese government pays great attention to the development of space industry. Many Chinese sensor types used for remote sensing applications. GF1 Images can be used for City management: urban and rural planning and monitoring, scenic and landscaping area monitoring, etc. The horizontal position of any terrain point on the map is usually expressed by 2D two coordinates of the point known as planimetric map. Topographic or contour map 3D coordinates produced from planimetric map by adding the vertical position of the terrain point, is usually expressed by one coordinate, relative to well defined vertical control datum, which is internationally adopted to be the geoid (Nassar, 1977). Horizontal or planimetric maps accuracy and standardization according to the American the National Map Standards Accuracy (NMAS), (NMAS; 1947) still the official standards for map accuracy. The cost of mapping generally increases rapidly with increasing scale and accuracy requirements. Higher accuracy and closer contour interval usually increases the cost of mapping so, it is very important to consider carefully what scale, contour interval and accuracy are necessary to satisfy the requirements (R.I.C.S, 1980). Revision of mapping can be made in three main methods: cyclic revision, selective revision and continuous revision (Jamebozorg, et al., 2003; Aisanont, S., 1990). Evaluations Egypt Sat-1 images show that from the point of geometric accuracy has the capability of producing and revision 1:25,000 scale maps (Yasser G.M., et al., 2012). Also, Information content and feature extraction capability from Egypt Sat-1 has been evaluated (Abd Elwahed, et al., 2011). Visual comparison of different images over the test area have been carried out for specific features such as roads, railways, watercourses and boundaries of urban areas (Abd Elwahed, et al., 2012). Geometric correction results and information contents of VHR space images are very important factor to get spatial information and extract objects from images. A comparison of information contents of high resolution Space Images has been done (Topan, H., et al., 2004). A Proposed Approach to update large scale maps in developing countries using IKONOS high resolution satellite imagery (Jacobsen, K., 2002; Shaker, A., et al., 2002). Large scale topographic databases have been updated and detection of urban features in urban areas with sub-meter QuickBird images and GIS (Marco, G., 2008; Marangoza, A.M., and Alkisb, Z., 2012). The urban features such as buildings and roads in the images have been detected, recognized and extracted visually by the method of on-screen digitizing using ArcGIS software. The proposed methodology includes producing image sheet map, updating topographic maps according to Egyptian specifications using GF-1 MSS, GF-1 PAN and the integration of GF-1 MSS and PAN. Also, the methodology includes evaluation information extracted from GF-1 images; find the solutions to extract all requirements according to Egyptian specifications.

2. Used Satellite Images GF-1 Satellite

2.1. The Technical Specification of GF-1 (GF= Gao) Satellite Images

P/MS Camera

- P/MS camera has four multi-spectral bands and a panchromatic band. The multi-spectral data with a spatial resolution of 8m which contained Red band (R), Green band (G), Blue band (B) and Near Infrared band (NIR).
- The panchromatic band has a spatial resolution of 2m.

WFV Camera

Four wide field view (WFV) camera has the same design in spectral rang with the P/MS camera, whereas it has a wide swath which covers no less than 800 kilometers after the four cameras data combined.

GF-1 Satellite

- GF-1 launched 26th April 2013
- 5-8 years design life
- Life time: 5-8 years
- Platform: CAST-2000
- Orbit Sun synchronous recurrent frozen orbit
- Altitude 645km
- Inclination 98.0506°
- Repetition cycle 41/4 days
- Descending node (Local time) 10:30 AM

MSS Bands

0.45—0.52 μ m 0.45—0.52 μ m
 0.52—0.59 μ m 0.52—0.59 μ m
 0.63—0.69 μ m 0.63—0.69 μ m Spatial Resolution (m) MSS 8m

PAN Bands

0.77—0.89 μ m 0.77—0.89 μ m
 Spatial Resolution (m) PAN 2m, 16m

(Wei Xiangqin, et al. 2015; (Lei Wang, et al., 2015) Figure 1 Shows Chinese GF-1 Satellite.



Figure 1: Chinese GF-1 Satellite

3. Study Area ND Used Data

Cairo city is one of the fastest growing urban areas in Egypt. The study area consists of various land covers such as, urban, rural, water, mountainous and agriculture. This study is applied on part of Cairo city the capital of Egypt. Figure 2 shows location map.

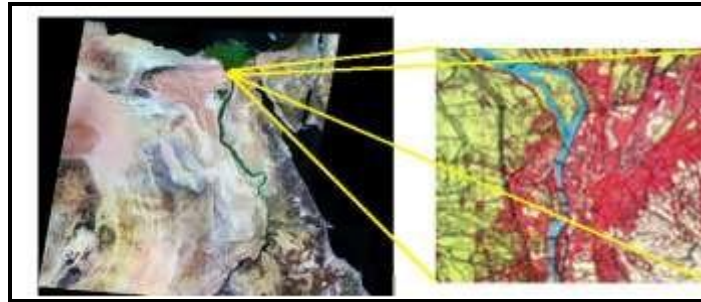


Figure 2: Location Map

3.1. Used Data

3.1.1. Used Satellite Images GF-1

In this study, the high resolution GF-1 MSS and PAN satellite images covering Cairo City, Egypt have been used.

Image date: 29/6/2014

PAN Resolution 2m

MSS data Resolution 8m

Figure 3 shows GF-1 PAN image and 2 images 1 & GF-1 MSS image 1 and 2

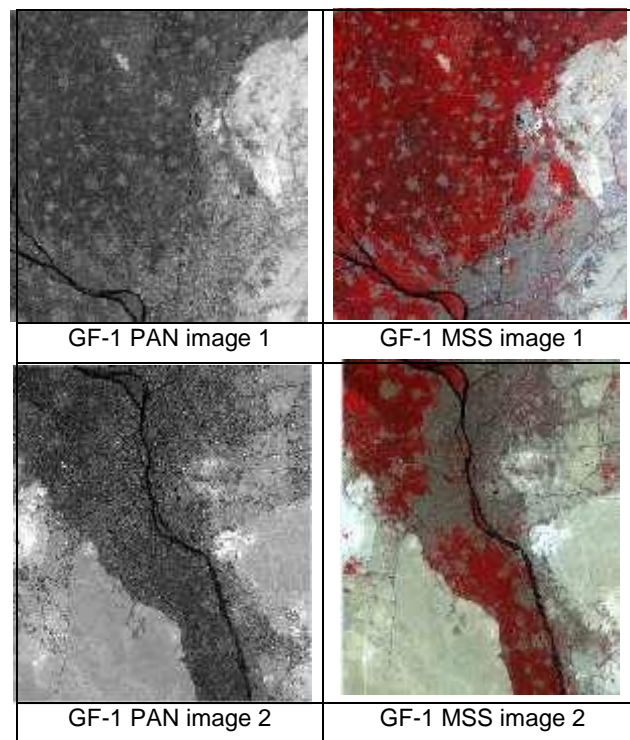


Figure 3: GF-1 PAN image and 2 image 1 & GF-1 MSS image 1 and 2

3.1.2. Image Support Data

4 DEM supplied with the data 2 for GF-1 image 1 MSS and PAN & 2 DEM 2 for GF-1 image 1 MSS and PAN. Figure 4 shows example of DEM supplied with the data.

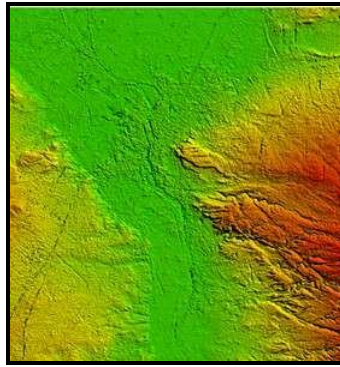


Figure 4: Example of DEM Supplied with the Data

3.2. Used Map

There is available in hand large scale map for the study area scale 1:5000, and 1:10 00. Also, there are medium and small scale topographic map compiled from aerial photographs at scale 1:25,000, covering the study area is obtained used as a basis for comparison and assessment.

- 1:5000 large scale map cover the same area of study produced in 2004 from aerial photographs acquired in 2006. The map is produced by the Egyptian Survey Authority (ESA).
- 1:10 000 large scale map cover the same area of study produced in 2004 from aerial photographs acquired in 2006. The map is produced by the Egyptian Survey Authority (ESA).
- A 1:25 000 topographic maps over the same area of study produced in 1930 from aerial photographs acquired in 1945. The map is produced by the Egyptian Survey Authority (ESA), two sheet maps are:

1- Sheet no. 81/630

Scale 1:25 000

Size 60cm x 40 cm cover area 15km x 10km

2-Sheet no. 82/630

Scale 1:25 000

Size 60cm x 40 cm cover area 15km x 10km

Figure 5 shows enlarged part of *two topographic maps sheets scale 1:25,000*

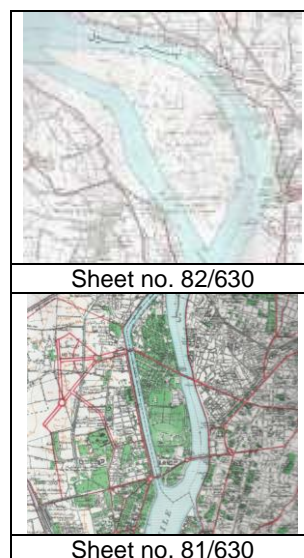


Figure 5: Enlarged Part of Two Topographic Maps Sheets Scale 1:25,000

3.3. Ground Control Points

GCPs ground control points extracted from maps 1:5000 and check points CPs extracted from maps 1:10 000.

4. Methodology

The proposed methodology based on producing image sheet map and evaluation updating topographic maps according to Egyptian specifications using GF-1 MSS, GF-1 PAN and the integration of GF-1 MSS and PAN. In general, high accurate ground control points derived from DGPS. Taken into consideration the number of GCPs and CPs and the cost these points in additional to the other processing to produce image map and up-dating maps. In this study, Nine GCPs ground control points for planimetric features has been derived from maps 1:5000 taken into consideration these points well defined and clearly interpretable on the satellite image. Also, 15 check points CPs for planimetric features has been used derived from maps 1:10 000 taken into consideration these points well defined and clearly interpretable on the satellite image. The Methodology of producing and updating topographic map process using GF-1 satellite imagery main procedures as following:

4.1. Producing Up-To-Date One Sheet 1:25 00 Image Map

- Data collection
- Rectification of GF-1 PAN image based on DEM and ground control points extracted from maps 1:5000 RMS is $\pm 0.5\text{m}$
- Best rectified PAN image based on RMS
- Producing rectified PAN image 1&2
- Producing PAN mosaic
- Rectification of GF-1 MSS image based on DEM and ground control points extracted from maps 1:5000 RMS is $\pm 0.5\text{m}$
- Best rectified PAN image based on RMS

4.2. Producing Rectified MSS Image 1&2

- Producing MSS mosaic
- Obtaining the image coordinates of x , y , z of ground points, ground control points (GCPs) and check points (CPs) from the rectified mosaics
- Accuracy check of GCPs and CPs, calculation of residuals in x and y directions and RMSE.
- PAN mosaic subset to meet 1:25 000 sheet map
- MSS mosaic subset to meet 1:25 000 sheet map

4.3. Map Updating

- Geo-reference 1:25 000 old sheet map
- Co-registration of MSS multispectral mosaic and PAN mosaic with old geo-reference 1:25 000 sheet map
- Subset co-registration MSS multispectral and PAN mosaic
- Vectrization of Geo-reference 1:25 000 old sheet map
- Overlaying co-registration MSS multispectral mosaic and old vector layers.
- Updating vector layer
- Assessment of cartographic potential and information extracted from of Gf1 MSS mosaic
- PAN mosaic with old geo-reference 1:25 000 sheet map
- Overlaying co-registration PAN mosaic and old vector layers

- Updating vector layer
- Assessment of cartographic potential of information extracted from of GF1 PAN mosaic
- Studying integration of subset co-registration Gf1 PAN mosaic and MSS mosaic to complete the vector layers otherwise find the low cost and time solution to complete the vector map

4.4. After that

- Field Revision and Verification Purposes
- Data revision process
- Revision of map vector data Integration of vector and raster data Image processing
Topology editing
- Contour line editing in built-up areas
- Production of the Final updating topographic maps

5. Results

The proposed methodology carried out step by step to achieve the objectives from this research.

Rectification of Geometric Correction of MSS and PAN Image

The planimetric allowable accuracy or Total root mean square error TRMS in coordinate (X or Y) m for different map scales based upon the specifications of the National Map Standards Accuracy (NMAS),

$$\text{Total root mean square error TRMS in (E or N)} = 0.50 \text{ mm} * \text{map scale}$$

Dealing Since the main concern herein deals with medium scale maps, the lower limit of scale will be 1:25,000, and hence, the allowable limit for horizontal positioning error will be 12.5 m for this scale. For large scale maps, the lower limit of scale will be 1:10,000, and hence, the allowable limit for horizontal positioning error will be 5.0 m for this scale. Several experiments were performed to rectify PAN image using models 2D-first order polynomial, 2D- second order polynomial non-parametric mathematical models with different distribution of GCPs. The best geometric accuracy of PAN GF-1 PAN and MSS was obtained using 2D second order polynomial with 15 GCPs.

5.1. Accuracy check of GCPs and CPs

5.1.1. Accuracy check of GCPs

Accuracy assessment of using 9 GCPs well distributed.

- The RMSE of GF-1 PAN in GCPs in X and Y directions RMSE_x, RMSE_y and TRMSE are 1.285m, 1.012m and 1.636m respectively.
- The RMSE of GF-1 MSS in GCPs in X and Y directions are RMSE_x, RMSE_y and TRMSE are 3.667m, 3.267m and 4.911m respectively.

5.1.2. Accuracy Check of CPs

Accuracy assessment of the produced image map and validated have been done using 15 CPs well distributed check points.

- The RMSE error of GF-1 PAN in CPs in X and Y directions RMSE_x, RMSE_y and TRMSE are 2.625m, 2.334m and 3.512m respectively which meets large scale map 1:10 000 or smaller according to specifications.

- The RMSE error of GF-1 MSS in CPs in X and Y directions are RMSE_x, RMSE_y and TRMSE are 7.114m, 6.961m and 9.953m respectively which meets large scale map 1:25 000 or smaller according to specifications.

GF-1 PAN mosaic and GF-1 MSS mosaic have been produced from rectified image 1 and image 2. Figure 6 shows produced GF-1 PAN mosaic and GF-1 MSS mosaic. Sub set of GF-1 PAN mosaic and GF-1 MSS to meet one sheet from topographic map 1:25,000 have been produced.

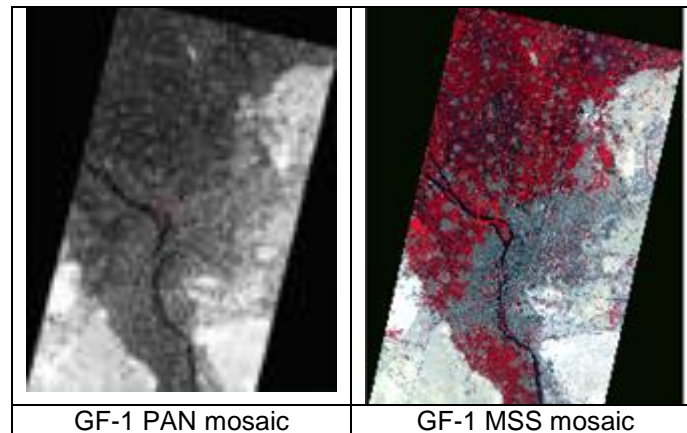


Figure 6: Produced GF-1 PAN mosaic and GF-1 MSS mosaic

5.2. Qualitative Evaluation of Information Content in GF-1 Images

Features exist on the actual surface of the Earth, within the area of interest can be classified as natural features (e.g. mountains, hills, rivers, deserts, forests.....etc) and artificial features (e.g. roads, railways, bridges, tunnels, buildings...etc). Features extracted from satellite images can be summarize as first: detect, second: identify and finally: recognize.

Main Information content in one sheet of topographic map is:

- Built up area
- Un-built Areas
- Bridge
- Wall
- Roads
- Rail Way
- Tower
- Boundary line
- Transition lines
- Water features
- Green areas

Figure 7 shows enlarged part of *two parts of*: GF-1 PAN mosaic, GF-1 MSS mosaic and part *topographic maps scale 1:25,000* Sheet no. 81/630 & Part of Sheet no. 82/630. Figure 8 shows example of information content appeared in the multispectral MSS and panchromatic PAN GF-1 image map. Degree of recognize features exist on GF-1 images can be categorized:

- Easy recognize
- Medium recognize
- Difficult recognize

- Impossible recognize

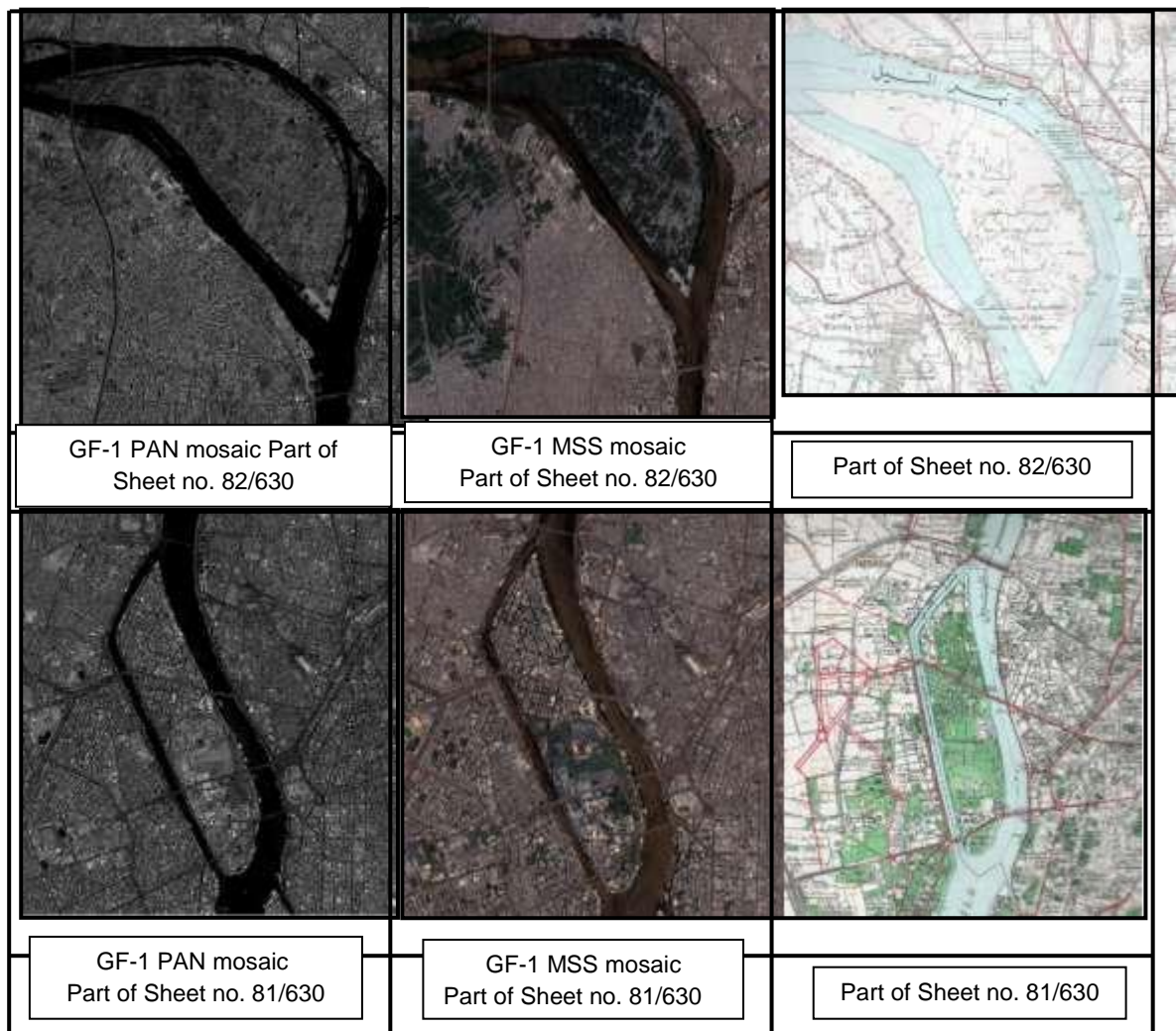


Figure 7: Enlarged Part of Two Parts of: GF-1 PAN Mosaic, GF-1 MSS Mosaic and Part Topographic Maps
Scale 1:25,000 Sheet no. 81/630 & Part of Sheet no. 82/630

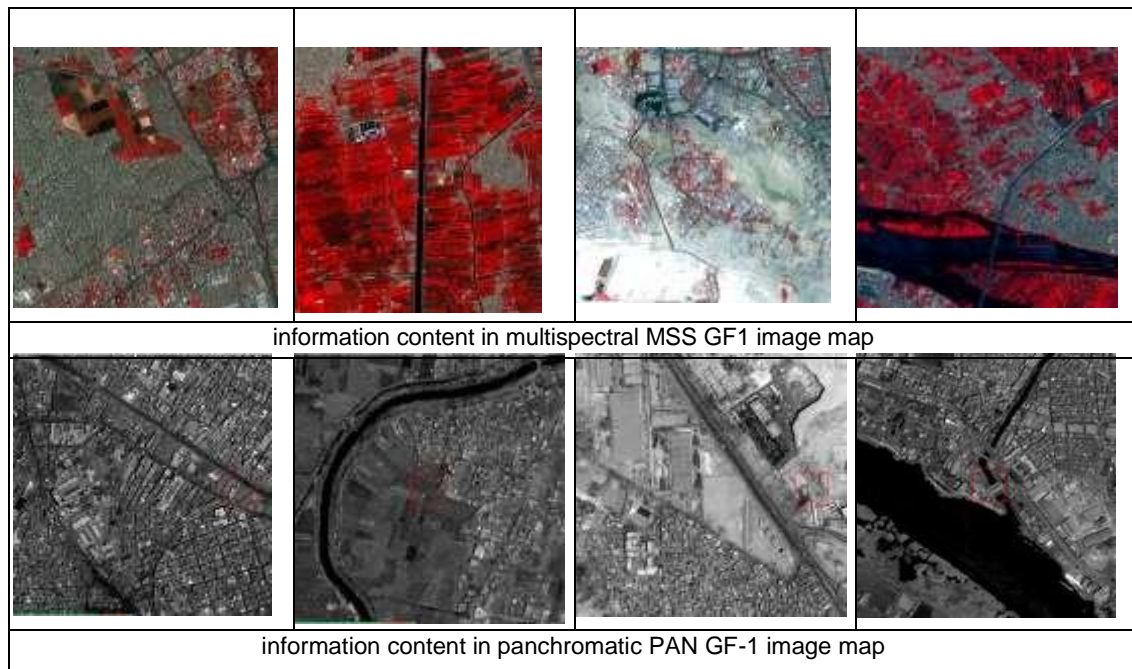


Figure 8: Example of Information Content Appeared in the Multispectral MSS and Panchromatic PAN Gf-1 Image Map

The Results of Evaluation Information Content appeared in the Multispectral MSS and Panchromatic PAN GF-1 Image for updating maps at 1:25,000 scale showed that:

- The contrast between the features and background is relatively low.
- Features that is impossible to be detected and identified on the image such as overhead power transmission lines and the railway.
- In general ability of details by GF-1 MSS to be recognized such as building and building blocks with dimension less than 6m; linear feature with width less than 6m.
- Also, ability of details by GF-1 PAN to be recognized such as building and building blocks with dimension less than 2m; linear feature with width less than 2m.

Solutions

To product complete map from GF-1 images according to the Egyptian specifications, one must find alternative methods or solutions to complete the rest of requirements. The sources of information which can be used:

- Very high resolution satellite images or SAR data
- Field survey

6. Conclusions

In Egypt, the production or updating of large scale surveying maps is considered as an important topic to be investigated. The investigation should be oriented towards the best rapid, informative, and economical way, for the replace of out-of-date maps, as well as updating existing acceptable maps, on the medium and large scale level. On the basis of the research carried out about cartographic potential of GF-1 MSS multispectral combined with GF-1 PAN panchromatic china satellite images used for updating Egyptian map scale of 1:25 000, the following conclusion could be drawn:

- There is always an urgent requirement, for regular updating of information of basic topographic maps, needed for both economical reasons, as well as supporting scientific investigations.
- The geometric accuracy of China GF-1 MSS meet the requirement of 1:25 000 image map or smaller according to the National Map Accuracy Standards (NMAS).
- The geometric accuracy of China GF-1 PAN meets the requirement of 1:10 000 map or smaller according to the National Map Accuracy Standards (NMAS).
- Integration of GF-1 MSS and PAN provides a large amount of information that can be used for updating features exists on 1:25 000 Egyptian maps.
- There are difficulties in extracting some features from GF-1 MSS images such as linear features with width less than pixel size (gas lines, canals, power transmission lines and the railway extension in some area with weak contrast background)
- The comparison of information content China GF-1 PAN image with China GF-2 MSS image shows that still there are some features that remain impossible to be recognized. The remaining features may be added from other mapping methods such as very high resolution satellite images such as China GF-2 images or ground survey methods.

Recommendations

Next paper will focus on producing pansharpened image from GF-1 PAN and GF-1 MSS using different fused image techniques which expect improve the produced image map and extracted information content from it.

References

- Abdel Mageed, K., 2000: *Applications of GPS Kinematic Techniques in Medium Scale Surveying Maps*. M.Sc. Thesis, Department of Public Works, Faculty of Engineering, Ain Shams University, Cairo, Egypt.
- Abd Elwahed, A., Farrag, A., and Moustafa, Y. *Evaluation of Information Content and Feature Extraction Capability from Egypt Sat-1 Images*. Journal of Engineering Sciences, Assiut University. 2011. 39 (3) 529-538.
- Abd Elwahed, A., Farrag, A., and Moustafa, Y. *The Potentials of Satellite Images for Map Updating With Emphasizes on Egypt Sat-1 Images*. Journal of Engineering Sciences, Assiut University. July 2012. 40 (4) 989-1003.
- Aisanont, S. 1990: *Base Map Revision Using High Resolution Satellite Data*. Royal Thai Survey. Department, Bangkok. 10200, Thailand, GISdevelopment.net, ACRS 1990.
- Ajayi, G.E. *Topographic Mapping from Satellite images: How Feasible in Developing Countries?* ISPRS. 1992. XXIX; Part B4.
- Cheng, P. and Toutin, T. *Planning Using Data Fusion of Satellite and Aerial Photo Images*. In Proceedings of the IEEE International Geoscience and Remote Sensing Symposium on Remote Sensing. 1997. 2; 839-841.

Diefallah, M. *Assessment of Mapping Capabilities of Space Imagery*. Engineering Bulletin. 1989. 24 (2). Dep. of Public Works, Faculty of Engineering, Ain Shams University, Cairo.

Jacobsen, K. Mapping with IKONOS images, EARSeL, Prag 2002 Geoinformation for European-wide Integration. Millpress. 2002. 149-156.

Jamebozorg, G., Valadan, Z., and Sadeghian, S., 2003: *The Revision of Iranian 1:25000 Scale Topographic Maps by KVR- 1000 Image Using Rational Function Model*. Proceedings of the Joint ISPRS Workshop on High Resolution Mapping from Space, 2003, 6-8 Oct. Hannover, Germany.

Lei Wang, Ranran Yang, Qingjiu Tian, Yanjun Yang, Yang Zhou, Yuan Sun and Xiaofei Mi. *Comparative Analysis of GF-1 WFV, ZY-3 MUX, and HJ-1 CCD Sensor Data for Grassland Monitoring Applications*. Remote Sensing. 2015. 7; 2089-2108.

Marangoza, A.M. and Alkısib, Z., 2012: *Detection of Urban Features and Map Updating from Satellite Images using Object-Based Image Classification Methods and Integration to GIS*. Proceedings of the 4th GEOBIA, May 7-9, 2012 - Rio de Janeiro - Brazil. 315.

Marco, G., 2008: *Updating Large Scale Topographic Databases in Italian Urban Areas with Submeter QuickBird Images*. International Journal of Navigation and Observation. 2008; 9.

Nassar, M., 1977: *Gravity Field and Leveled Heights in Canada*. Department of Surveying Engineering, University of New Brunswick, Canada. Fredericton N.B, Technical Report No. 41.

NMAS, 1947: *United States National Map Accuracy Standards*. National Mapping Program Maintained by the U.S. Department of Interior, U.S.

Pohl, C., 1996: *Geometric Aspects of Multisensor Image Fusion for Topographic Map Updating in the Humid Tropics*. Ph. D. Thesis, ITC Publication No. 39, Netherlands.

Shaker, A., Zahran, M., and ElSagheer, A. *A Proposed Approach to Update Large-Scale Maps in Developing Countries Using High-Resolution Satellite Imagery*. CERM. Jun. 2002. 24 (1) 344-362.

R.I.C.S., 1980: *Maps Standardization*. Royal Institution of Chartered Surveyors and the British Air Survey Association and presented by L. Scott to the X1V the International Congress of Photogrammetry, Hamburg, 1980. Commission 1.

Topan, H., Büyüksalih, G. and Jacobsen, K., 2004: *Comparison of Information Contents of High Resolution Space Images*. ISPRS XXth Congress, Istanbul.

Wei Xiangqin, Gu Xingfa, Meng Qingyan, Yu Tao, 2015: *Review of Chinese GF-1 Satellite Data and Its Application*. IGIT 2015 International Conference Program January 17, 2015.

Assessment of Land Degradation Status and Its Impact in Arid and Semi-Arid Areas by Correlating Spectral and Principal Component Analysis Neo-Bands

Alfred Homère Ngandam Mfondoum^{1,3}, Joachim Etouna^{2,3}, Buji Kindess Nongsi^{3,4}, Fabrice Armel Mvogo Moto^{3,4}, and Florine Gustave Noulouape Deussieu^{3,4}

¹ Laboratory of Natural Resources Management, Department of Geography, University of Yaoundé I, Cameroon

² Laboratory of Remote Sensing and Spatial Analysis, National Institute of Cartography, Yaoundé, Cameroon

³ Technical Committee of Geospatial Techniques, ILG Asso., Centre of Handicapped Street, Yaoundé, Cameroon

⁴ Master's Research Unit of Remote sensing and GIS Applied to Territorial Planning, Department of Geography, University of Yaoundé I, Yaoundé, Cameroon

Publication Date: 22 February 2016

DOI: <https://doi.org/10.23953/cloud.ijarsg.77>



Copyright © 2016 Alfred Homère Ngandam Mfondoum, Joachim Etouna, Buji Kindess Nongsi, Fabrice Armel Mvogo Moto, and Florine Gustave Noulouape Deussieu. This is an open access article distributed under the **Creative Commons Attribution License**, which permits unrestricted use, distribution, and reproduction in any medium, provided the original work is properly cited.

Abstract This paper aimed to assess the status of land degradation in arid and semi-arid areas based on a correlation analysis between spectral and statistical neo-bands. The methodology uses vegetation and soil spectral indices as the second Modified Soil Adjusted Vegetation Index (MSAVI2), Normalized Difference Bare Soil Index (NDBSI), Texture Index (NDTeI), Crust Index (CI), Top Soil Grain Size Index (GSI), Normalized Difference Sand Dune Index (NDSDI) and the first Specific Principal Component of the red, near infrared, shortwave infrared bands stacking ($SPC1_{R-NIR-SWIR1-SWIR2}$). The vegetation is considered here as the main object of soil sub-surface. Thus after all the spectral and the statistic neo-bands are performed on Landsat8 OLI sensor image, a linear regression is generated to assess their correlation with MSAVI2. Based on the visual interpretation and the regression curves the results show that the determination coefficient R^2 and the P values all significant as less than 0.0001. Each neo-band is weighted with its R^2 to improve its contribution to the model and the synthesis image obtained enhances the land degradation sensing in six classes; these are respectively named as “severe” (3139 km²), “high” (6763 km²), “moderate” (8341 km²), “low” (7454 km²), “very low” (6947 km²) and “close to nil” (5437 km²). This last image is summed with population layer to produce a decision map helpful for further government decision. At the end the degradation image has given interesting results for the detection of land degradation comparatively to derivation and comparison of individual indices.

Keywords *Correlation Analysis; Decision Map; Linear Regression; Specific Principal Component; Spectral Indices*

1. Introduction

Land degradation refers to a change in soil health condition that causes a reduction in the ecosystem's ability to provide goods and services for its beneficiaries (Barrow, 1991; Conacher and Sala, 1998; Biancalani, n.y.). It is also defined as the loss of soil production by either chemical or physical processes (Singer and Munns, 2002; Blaikie and Brookfield, 1987). It thus covers the various types of soil degradation as physical, chemical and biological (Brabant, 2010), adverse human impacts on water resources, deforestation, and lowering of the productive capacity of rangelands (Metternicht, 2006; UNEP, 1992). Brabant (2009) testify that fighting this process is now a priority, particularly in developing countries which host 75% of the world's population and where 3/4 people work in agriculture; but the main obstacle to achieve such evaluations has been the lack of a standard streamlined international assessment procedure. Further, the UNCCD (1994) and Fadhil (2009) have listed several biophysical but also socio-economic causes to that phenomenon as marketing, income, human health, institutional support, poverty, undermining food production and political stability. From a holistic point of view and in its extreme form, land degradation is followed by a severe deterioration of vegetation cover and soil production capacity reduction takes the connotation of desertification, particularly in those semi-dry arid or arid areas (Warren and Agnew, 1988; Begzsuren, 2007).

Assuming the importance of land in several scientific fields it is necessary to know the actual and available tools belonging to the field of remote sensing and GIS, in order to assess the early detection of "Soil Degradation" or to take up any preventive measures (Rojas, 2013). Several studies and models have been devoted to the prediction of erosion risk based on the USLE (Universal Soil Loss Equation) of Wischmeier and Smith (1978), and the RUSLE (Revised Universal Soil Loss Equation of Renard et al., 1991). Concerning the analysis of the state of land degradation it is encouraged and supported by projects such as LADA (Land Degradation in Drylands Assessment) which aims to develop an integrated assessment methodology for land degradation to understand the degradation processes at different scales (global, national and local) by identifying the status and trends of land degradation, the root causes, effects and consequences. On that point of view, MSAVI has been used in correlation with field data to assess vegetation cover (Senseman et al., 1996a; Senseman et al., 1996b; Chen, 1999), biomass and/or leaf area index (Smith et al., 2005; Phillips et al., 2009), or as one indicator to monitor desertification (Liu and Wang, 2005). Pandey et al. (2013) have used some spectral indices such as CI (Crust Index), NDSDI (Normalized Difference Sand Dune Index), GSI (Top Soil Grain Size Index) compare to NDVI (Normalized Difference Vegetation Index) to assess land degradation and sand encroachment in Western India. Also, Raina et al. (1991) have used Landsat TM imagery to map the type, extent and degree of degradation. The soils affected by fires and their capacity for regeneration has been studied from images Landsat TM and Digital Elevation Model (DEM) (González and Rodríguez, 2013).

Based on these applications and experimentations, the main objective of this article is to assess the state of land degradation through the correlation analysis of vegetation and soils spectral indices, and SPC neo-band, followed by their crossing.

2. Research Location

The area chosen for this study is the far-north of Cameroon in Central Africa. It is situated between the longitude 13°30'-15°40' East and longitude 10°-13° North (Figure 1). It covers a total area of about 38086 km² and six departments are concerned. Several reasons explain this choice. This is indeed a bioclimatic milieu naturally predisposed to several forms of soils damages due to the dry hot climate and low rainfall. As consequences vegetation cover gradually changes from weak dense grassy savannah in the south to very sparse dry savannah or steppe as one moves in latitude. The soils are typically arid including ferruginous, alluvial, sandy, also latosols and vertisols, all barren and yellowish, skeletal and therefore poor (Raunet, 1993).

In addition the 3,300,324 inhabitants (BUCREP, 2010) of the area are facing landholding conflicts and live from agriculture and transhumant breeding with some practices as bushfire and irrigation by pumping or pouring (MINEF-UNCCD, 2004; COMIFAC-CEEAC, 2007). All these bioclimatic and human characteristics expose the concern area to many forms of land degradation such as rock levelling, gullying, valleys silting, banks sapping, wind and water erosion, the extension of dune banks, drying and induration due to cattle trampling, armoring or crusting (Figure 2). In 2003 the GLADA was estimating the total of degraded area in Cameroon to 151605 km² which represent 31.89% of national territory (Bai et al., 2008).

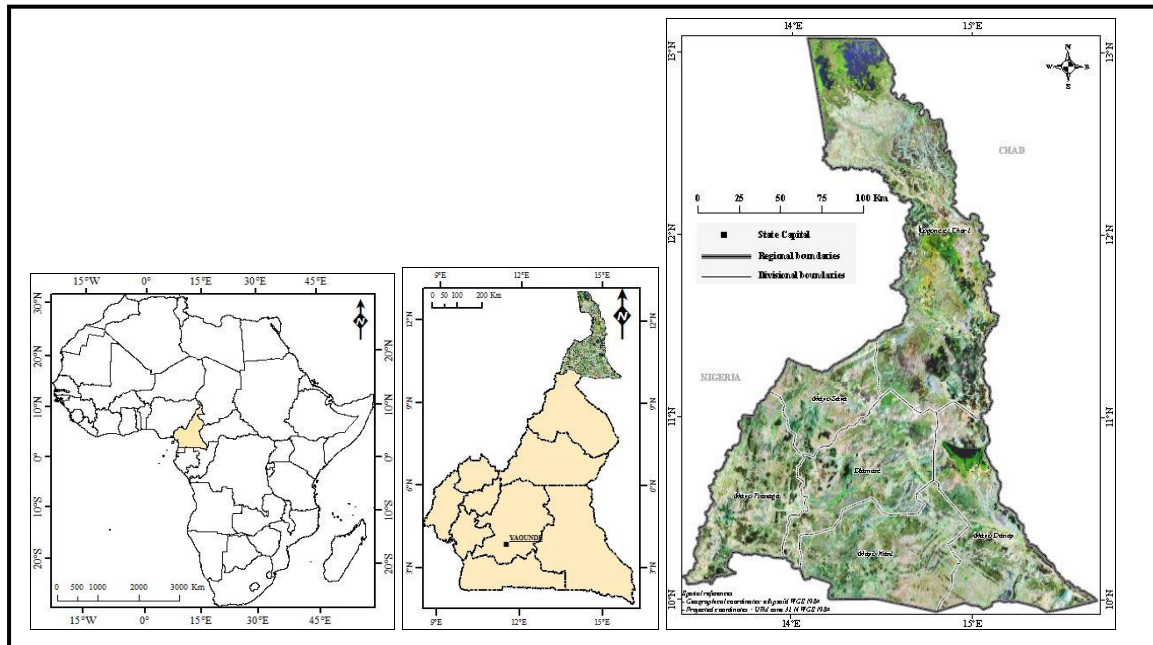


Figure 1: The Study Area in Background of Landsat Image Bands Composition 5-4-3



Mountainous Rock Levelling



Bare and Burned Fallow Lands



Gullying



Valley Silting



Cattle Trampling



Bank Sapping

Figure 2: Some Features of Land Degradation

3. Materials and Methods

3.1. Satellite Image Acquisition and Preprocessing

Satellite images of Landsat 8 OLI sensor were downloaded at the middle of the dry season, characterized by the absence of rainfall and very slow chlorophyll activity; thus implicitly declining agricultural activities. This is a total of seven scenes acquired on January 2015, on the official website of NASA <http://earthexplorer.usgs.gov/> (Table 1). Each scene is composed by eleven bands covering the electromagnetic spectrum between 0.433 μm and 12.50 μm . The bands stacked are blue, green, red, near infrared, and the two shortwave infrared with a spatial resolution of 30 meters, while the panchromatic band is at 15 meters (Table 2).

Table 1: List of Scenes used

| Scene ID | Date of Acquisition |
|-----------------------|---------------------|
| LC81830532015014LGN00 | 14/01/2015 |
| LC81840512015021LGN00 | 21/01/2015 |
| LC81840522015021LGN00 | 21/01/2015 |
| LC81840532015005LGN00 | 05/01/2015 |
| LC81850512015012LGN00 | 12/01/2015 |
| LC81850522015012LGN00 | 12/01/2015 |
| LC81850532015028LGN00 | 28/01/2015 |

Table 2: Spectral and Spatial Characteristics of Bands Used

| Spectral Band | Wavelength (μm) | Spatial Resolution (M) |
|---------------------------|------------------------------|------------------------|
| Aerosol / Coastal | 0.433 - 0.453 | 30 |
| Blue | 0.450 - 0.515 | 30 |
| Green | 0.525 - 0.600 | 30 |
| Red | 0.630 - 0.680 | 30 |
| Near Infrared | 0.845 - 0.885 | 30 |
| Short Wavelength Infrared | 1.560 - 1.660 | 30 |
| Short Wavelength Infrared | 2.100 - 2.300 | 30 |
| Panchromatic | 0.500 - 0.680 | 15 |

Preprocessing operations were performed to prepare the images. This step starts by the radiometric calibration and atmospheric corrections by Chavez (1996) low COST method on each scene. Then a spatial enhancement to 15m has been applied to merge the multispectral image with the panchromatic band. The process used has been the wavelet resolution merge that can be considered as an improvement of the classical IHS (Intensity Hue Saturation) method and it is expected to better preserve the spectral characteristics of the multispectral image (Ferrerres et al., no year). It processes the signals of the image as the Fourier Transform for better readability of a phenomena and uses short discrete “wavelets” instead of a long wave (King and Wang, 2001; ERDAS, 2003; Klonus and Ehlers, 2009; Zaydan, 2012). Finally, the entire data set of seven scenes was mosaicked and clipped to the limits of the study area as the final step in the preprocessing sequence.

2.2. Presentation of Spectral Indices Generated

Spectral indices have proved efficiency to highlight the indicators of land degradation mentioned above. Applications of remote sensing for assessing and monitoring land degradation is mainly related to spectral reflectance of soil and vegetation (Al-Bakri, 2012). The approach used here has been implemented using two entrances.

The first entrance is the characterization of the land surface cover through a vegetation density index. Indeed the determination of soil recovery rate by vegetation is a fundamental indicators to measure soil protection rate (Deschamps, 1983). So far the most frequently used method employing EO datasets is trend analysis of vegetation index data, most commonly the Normalized Difference Vegetation Index (NDVI) (Higginbottom and Symeonakis, 2014). In this study, the Second Modified Soil-Adjusted Vegetation Index, MSAVI2 of (Qi et al., 1994) has been used. This index describes the state and the density of the vegetation while separating it from the ground effects especially when the canopy is sparse and Leaf Area Index, LAI, is low (Table 3, Figure 5a). It is advantageous in the assessment of the top soil elements on arid and semi-arid surfaces according to the formula (1):

$$MSAVI2 = \frac{(2 \cdot NIR + 1 - \sqrt{(2 \cdot NIR + 1)^2 - 8 \cdot (NIR - R)})}{2} \quad (1)$$

Where NIR and R, are respectively values of reflectance in the near infrared (band 5: 0845-0885 μm) and Red (band 4: 0630-0680 μm) electromagnetic spectrum.

The second entrance has been that to characterize the state of topsoil cover. It then important to remember that apart from the degree of coverage by vegetation, soil reflectance is influenced by intrinsic factors such as moisture, roughness (Barnes and Zalewski., 2003; Thomasson et al., 2001) stoniness, microrelief and texture thinness (Madeira et al., 1991; Touriño Soto, 2005). It is admitted that the most important interaction of soils and electromagnetic radiation is in the range of 0.3 to 3 μm (Zaydan, 2012). Then in arid and semiarid areas, spectral reflectance of soil is mainly controlled by the dominant particle size and the content of minerals, including accumulated salts (Al-Bakri, 2012). Five indices and one statistical neo-band were chosen to highlight these factors:

- The Normalized Difference Bare Soil Index, NDBSI, aims at enhancing bare soil areas, fallow lands, and vegetation with marked background response. It is a normalized difference using the Near and the Short wavelength infrared as follows in formula (2):

$$NDBSI = \frac{SWIR - NIR}{SWIR + NIR} + 0,001 \in [-1, 1] \quad (2)$$

Where SWIR refers to the reflectance values in the short wavelength infrared (band 6: 1560-1660 μm) Landsat OLI sensor. It is useful for predicting and assessing bare soil characteristics such as roughness, moisture content, amount of organic matter, and relative percentages of clay, silt, and sand (Roy et al., 1997) (Table 3). In general condition NDBSI > -0.20 is a strong necessary, but not sufficient indication of the presence of bare soil areas (Baraldi et al., 2006).

- The normalized difference between the two bands of the Short Wavelength infrared, important to enhance the contrast of texture or roughness of tropical soils. It was originally used to express the content of gibbsite and kaolinite in latosols, and therefore allows to distinguish the sandy soils from clay soils in tropical areas (Madeira, 1993). It particularly enhance clay soils, sandy soils, rocks leveling, vertisols and latosols in tropical areas under or over the vegetation as it is the case in the study area (Table 3). It will be named in this study the Normalized Difference Texture Index, NDTel, that uses the spectral domain of the infrared with the formula (3):

$$NDTel = \frac{SWIR1 - SWIR2}{SWIR1 + SWIR2} \in [-1, 1] \quad (3)$$

Where SWIR2 is the reflectance values the second Short Wavelength infrared Landsat OLI sensor (band 7: 2100-2300 μm).

- The Topsoil Grain Size Index, GSI, is used to characterize the surface texture of the soil. Taking in account the fact that soil physical degradation involves thinning of the organic layer, destabilization of aggregate structure in the topsoil, surface crusting and topsoil compaction (Brabant et al., 1996), this index is increasingly coupled to vegetation indices to indicate degradation, based on the fact that the increase in this index is indicative of a rough surface texture (Xiao et al., 2006) (Table 3). The higher values indicate that the soil is coarse and close to degradation. The formula (4) is based on the reflectance values of the spectral bands of the visible as follow :

$$\text{GSI} = \frac{R - B}{R + B + G} \quad (4)$$

Where B and G express the reflectance values in the blue band (band 2: 0450-0515 μm) and the green band (0525-0600 μm) OLI Landsat sensor. GSI value is close to 0 or a smaller value in vegetated area, and for a body of water it is a negative value. Higher positive values of GSI represent the sand affected region.

- The Crust Index, CI, is a normalized difference between the red and blue domain of electromagnetic spectrum. It is mainly used to map geological features, and has the ability to detect and differentiate lithological/morphologic units such as active crusted sand areas (Karnieli, 1997) (Table 3). The formula of the CI is:

$$\text{CI} = 1 - \left(\frac{R - B}{R + B} \right) \in [0, 1] \quad (5)$$

- The Normalized Difference Sand Dune Index, NDSDI, is used to identify and assess the existence of the sand dune accumulations and sand spread (Fadhil, 2009). This normalized difference is calculated between the Red and the short wavelength infrared (SWIR) spectral values following the formula (6):

$$\text{NDSDI} = \frac{R - \text{SWIR2}}{R + \text{SWIR2}} \in [-1, 1] \quad (6)$$

This index mainly distinguishes vegetation and non-vegetation, water and arid surface, sandy or bare soil, while reflectance in the red and SWIR bands can discriminate the mineral and rock types as it is sensitive to the moisture content of soil and vegetation (Table 3). Value of the NDSDI ranges between -1 and +1, whereas the sand dune accumulations and drifting sands often give values below zero and vegetative cover produces values greater than zero.

- The first Selective Principal Component R-NIR-MIR-SWIR: the Principal Component Analysis (PCA) also named Hotelling transform is a mathematical transformation used in remote sensing to develop the image signal on the basis of orthogonal functions of these (Bonn et al., 1992; Joly, 1986; Baccini, 2010; Gonzalez, no year). It looks for a better representation of numerous information, n , in a sub-space F_k in space R_p of k dimension. Thus k new variables which are linear combinations of p initial variables and that minimize the loss of information are defined (Figure 3).

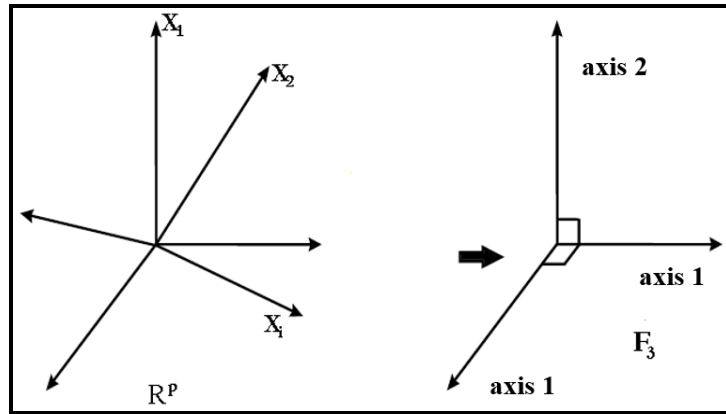


Figure 3: Schematic Explanation of the PCA [Smith et al., 2005]

This technique works to search axes larger variances in the space of radiometry of an image (Youan, 2009). Some authors have derived the selective principal component, SPC, to enhance lithological lineaments. The bands of the visible and the ones of the infrared part of the electromagnetic spectrum are compiled separately to produce the selective principal component of blue-green-red, SPC_{BGR} and the selective principal component of near infrared-shortwave infrared one and two, $SPC_{NIR-SWIR1-SWIR2}$. Then the first SPC of the results is chosen to proceed with the analysis. In this study the $SPC_{R-NIR-SWIR1-SWIR2}$ have been used to generate new axes of images information; this is according to the fact that the red band coupled to the NIR easily separate soils from vegetation; while the spectral curve of soil is more distinct in the infrared domain (Figure 4).

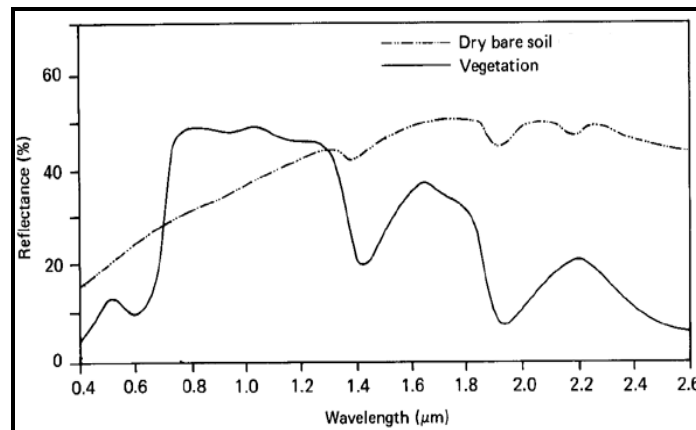


Figure 4: Generalized Spectral Signatures for Soil and Vegetation (Source: Wageningen University)

With an eigenvalue of 21870.68 over 22016.39, that is an explained variance of 99, 33 %, the $SPC1_{R-NIR-SWIR1-SWIR2}$ concentrates the essential of information contained in the four bands and has been selected to continue the process. Then the soil surface characteristics enhanced are rough lithological features considered as a part of land degradation (Table 3).

Table 3: Contribution of Neo-Bands Used To the Detection of Degraded Lands

| Neo-Bands | Main Contribution To Degraded Lands Detection | Significant Values And Threshold | |
|---------------|---|------------------------------------|-------------------------------------|
| | | ≤ 0 | > 0 |
| MSAVI2 | Vegetation density | Absence of vegetation | Presence of vegetation |
| NDBSI | bareness, roughness, fallow lands ; | Absence of Bare soil (< -0.20) | Presence of bare soil (> -0.20) |
| NDTel | Soil surface texture, roughness; | Low texture and roughness | High texture and roughness |

| CI | Actives encrusting | Low encrusting | High encrusting |
|-----------------------------------|--|--|--|
| GSI | Sand and rocks grains size, stoniness, surface texture | Body of water (<0); vegetated area (=0) | Sand affected area and bare soil surface |
| NDSDI | Sandbank, sand spread, dune accumulation, drifting sands | Sand dune accumulations, drifting sands; | Vegetative cover |
| SPC1 _{R-NIR-SWIR1-SWIR2} | Rough and lithological elements of top soil | Non-significant | Important |

2.3. Experimentations

2.3.1. Calculation of Indices Correlations

Two indices are considered equivalent if the decision made on the basis of one index could have been made equally well on the basis of the other index (Perry and Lautenschlager, 1984). Moreover binary discrimination between classes of vegetation and non-vegetation requires at least a pair of indexes, to guarantee separability of these two land cover types in feature space (Baraldi et al., 2006). Thus the six indices and the PCA have been generated through the Erdas imagine 2014 software model maker (Figure 5).

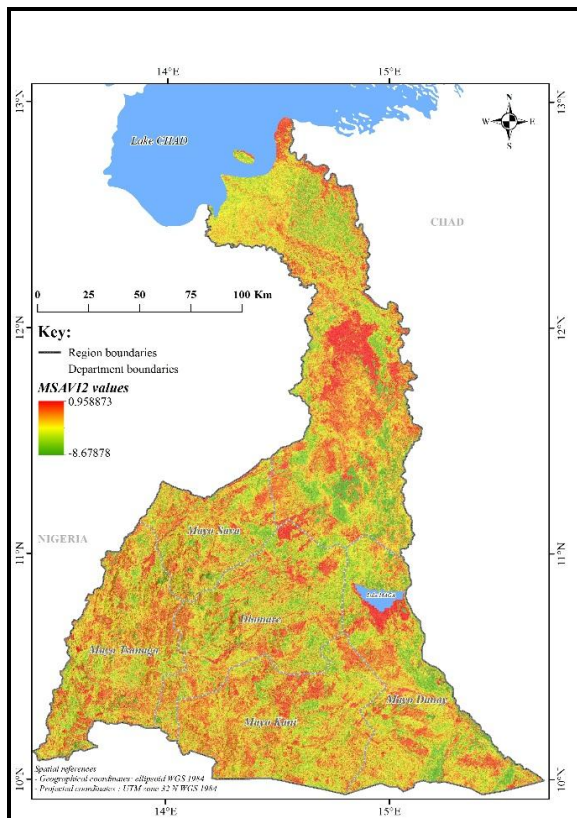
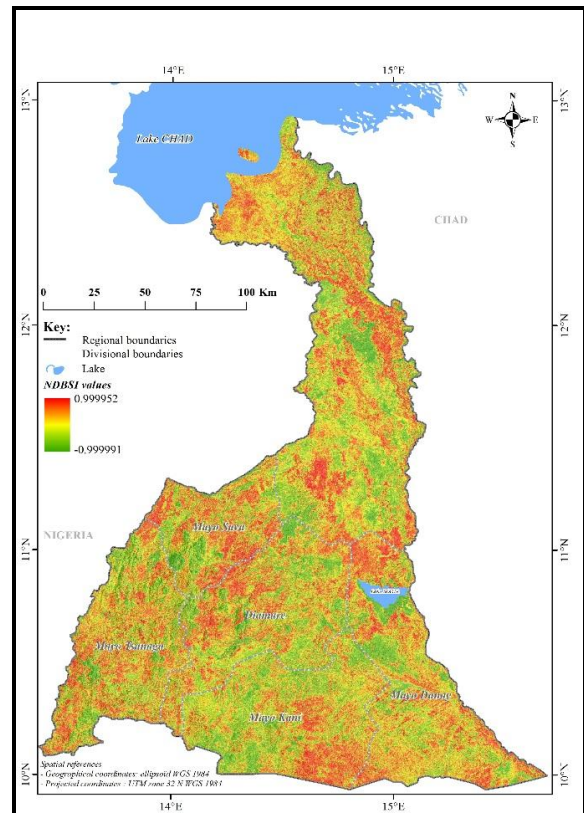


Figure 5a: MSAVI2 (i)



NDBSI (ii)

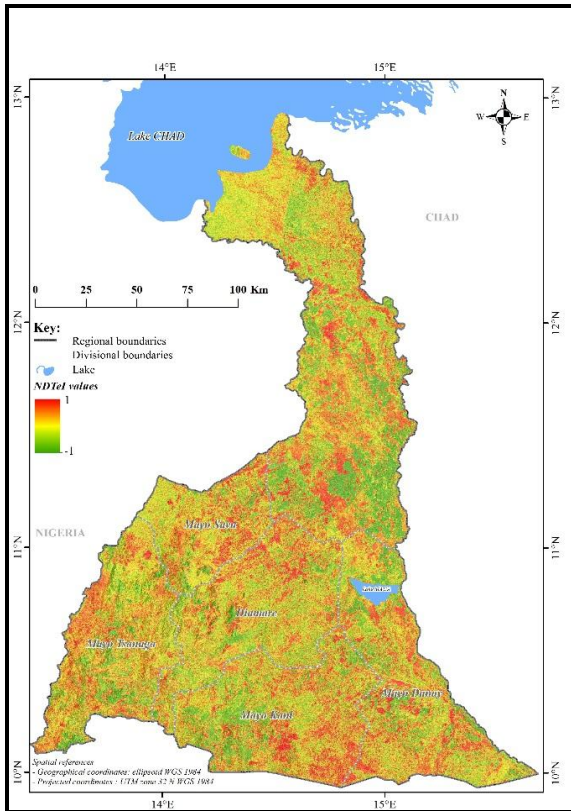
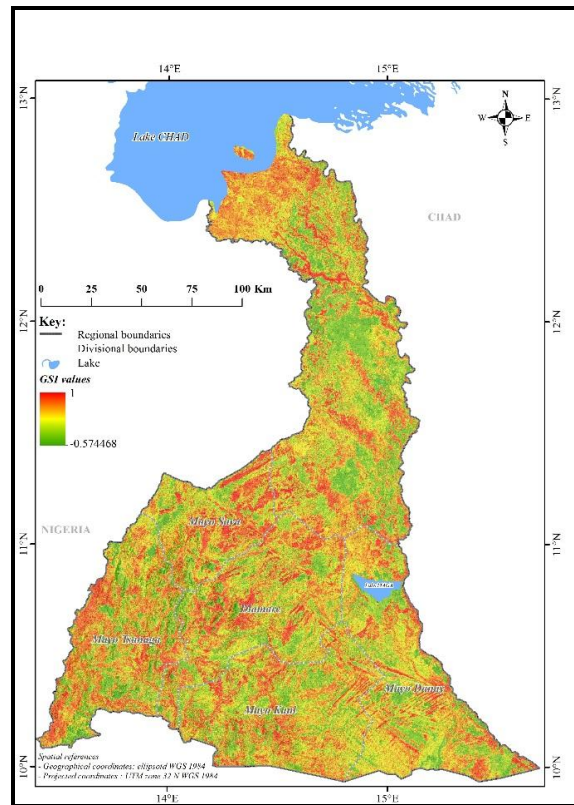


Figure 5b: NDTeI (iii)



GSI (iv)

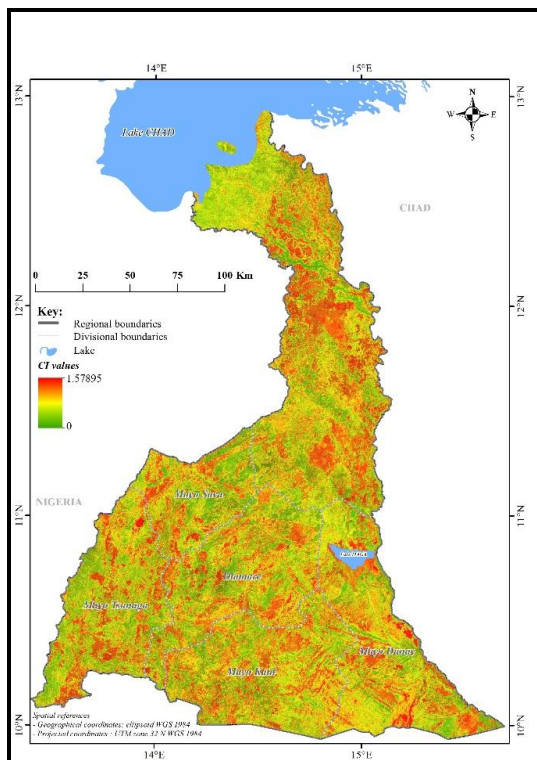
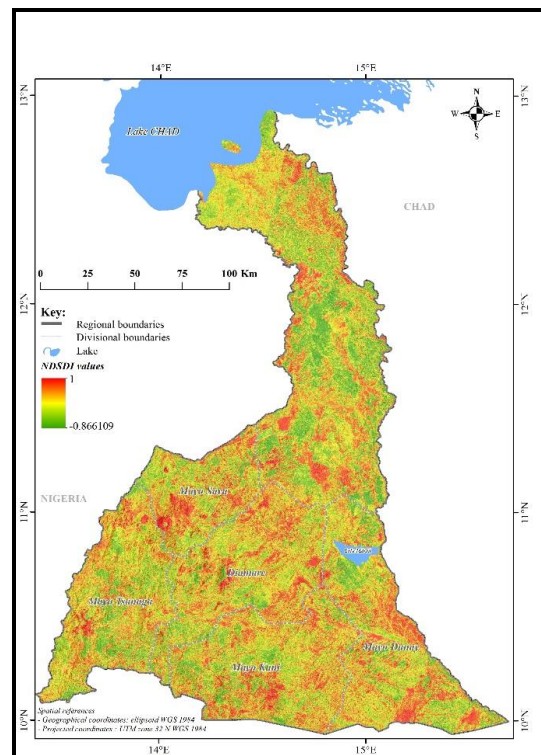


Figure 5c: CI (vi)



NDSDI (vii)

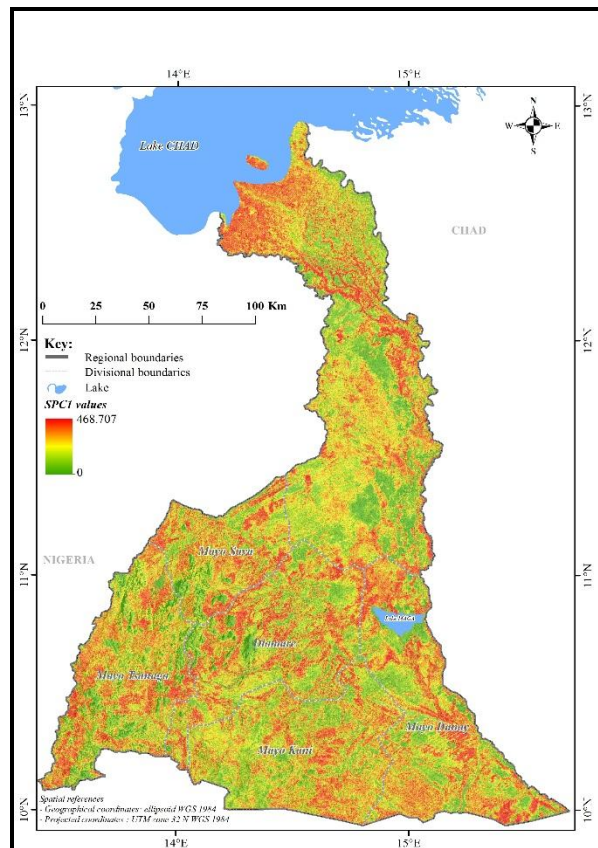


Figure 5d: SPC1

After it has been proceeded to a comparison between each index and $SCP1_{R-NIR-SWIR1-SWIR2}$ on one hand as the dependent variables, with the MSAVI2 on the other hand as the independent variable. This was done considering the lack of vegetation as the first indicator of soil exposition to degradation. The comparison was made by the method of simple linear regression. The goal of this statistic method is to determine the equation model of the line that fit better the observed points in an (x, y) plan (Dagnelie, 2009). The equation is generally presented in the form:

$$y = ax + b$$

A correlation test has been also calculated to show the level of that linear relation between the others neo-bands and the MSAVI2. It just appears that the $SCP1_{R-NIR-SWIR1-SWIR2}$ is most strongly determined by the MSAVI2 with a coefficient of determination R^2 up to 0.3134 (Figure 6, Table 4). Also the highest negative correlation coefficient with the MSAVI2 is the $SCP1_{R-NIR-SWIR1-SWIR2}$ up to -0.5599; while the highest positive value is the GSI with -0.4493 (Table 4). All the P-values generated are strictly less than 0.0001 (Table 4) and knowing that P-values less than 0.05 are often reported as “statistically significant” (Sellke et al., 2001) all the neo-bands are then important for the analysis process.

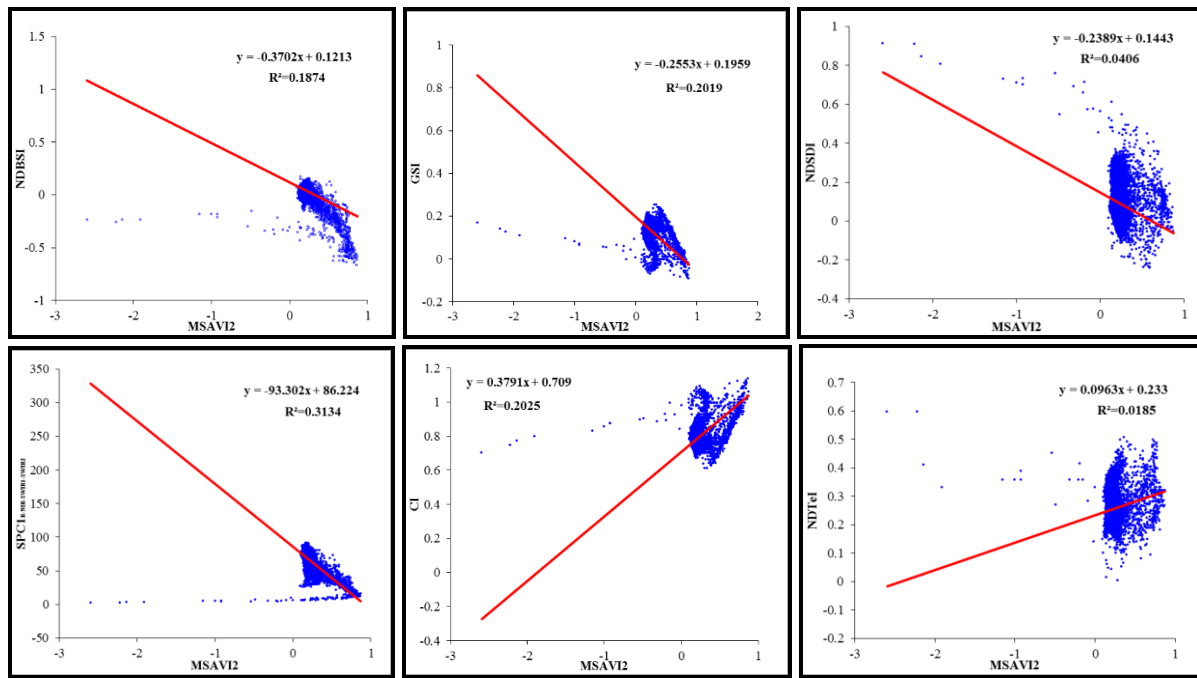


Figure 6: The Correlation between MSAVI2 and the others Neo-Bands

Table 4: Statistic Relation between MSAVI2 and the others Neo-Bands

| Indicators of Correlation Neo-bands | Correlation Coefficient | Determination Coefficient R ² | P-values | |
|-------------------------------------|-------------------------|--|-----------|-------------|
| | | | Threshold | Test |
| NDBSI | -0.43271964 | 0.18740843 | < 0.0001 | Significant |
| NDTel | 0.13637548 | 0.01859827 | < 0.0001 | Significant |
| GSI | -0.44937944 | 0.20194188 | < 0.0001 | Significant |
| CI | 0.45007158 | 0.20256443 | < 0.0001 | Significant |
| NDSDI | -0.20150989 | 0.04060623 | < 0.0001 | Significant |
| SPC1 _{R-NIR-SWIR1-SWIR2} | -0.55990621 | 0.31349319 | < 0.0001 | Significant |

2.3.2. The Neo-Bands Couples Reflectance Trends

The indices were grouped together in three pairs of indices according to their relation in characterizing land degradation (Figure 7). The visual overlay of the indices images generated can be observed and concluded on the basis of the contrast of reflectance values sampled for 40000 pixels distributed on all the features of bareness, roughness, encrusting, rough lithology, sand spread and implicitly a first pre-definition of degradation areas. The MSAVI2 appears then effectively negatively correlated to NDBSI, the contrast appearing therefore as a strong indicator of soil bareness. At same time GSI and NDTel are also negatively correlated what supposes that they bring different additional information to enhance top soil texture. At last CI and NDSDI have a negative correlation and it is an indicator that any image adds different information to the model relatively to the encrusting and the sand.

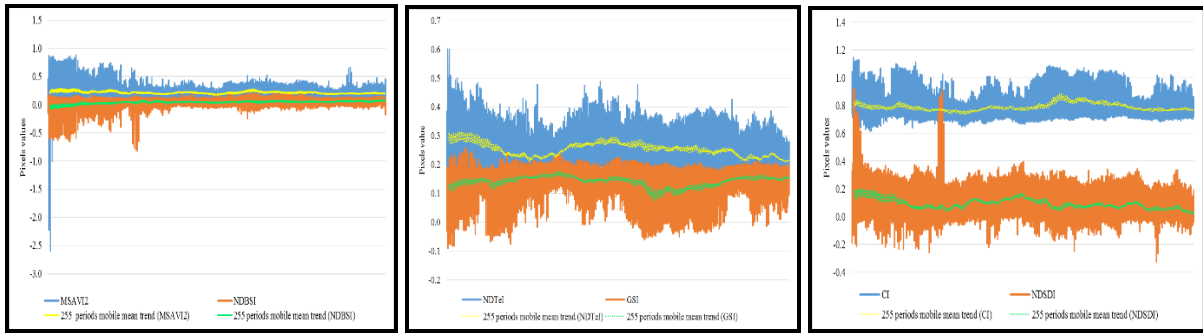


Figure 7: Reflectance Trends between the Three Couples of Spectral Indices

2.3.3. The Simple Weighted Sum Method

The indices were crossed following the weighted sum method. These were grouped together and crossed in three pairs of indices according to their relation and their explained proximity in characterizing the state of land degradation. They are each represented by six classes of information. Initially, the MSAVI2 and NDBSI were decomposed and crusaders with a view to characterize or confirm the state of soils bareness. This assumes in the synthetic image obtained that the low values of MSAVI2 correspond to high values of NDBSI to confirm the bare surfaces (Table 5). After the NDTel and the GSI were crossed to appreciate the soil texture in terms of surface undulations and grain size. In this case, the six classes of these indices and the synthetic image obtained reflect the strong values to the coarser texture and low values for the less pronounced texture (Table 5). Furthermore the CI and the NDSDI were crossed to highlight areas of high attendance and sand crusts together. It therefore appears that the synthetic image spring for high values highly silted areas and much encrusted resulting high values of two crossed indices (Table 5). At last the three images obtained have been crossed with the $SPC1_{R-NIR-SWIR1-SWIR2}$ to obtain a synthetic image. This allowed a first assessment of the state of land degradation.

Table 5: Numerical Interpretation of the Weighted Sum Algorithm

| Level of Degradation Indices for Degradation | Level of Degradation | | | | | |
|---|----------------------|----------------------|----------------------|--------------------|---------------------|----------------------|
| | Low | | | | | High |
| MSAVI2 (High to low vegetation cover) | 0.958 – 0.354 | 0.354 – 0.165 | 0.165 – - 0.023 | -0.023 – -0.439 | -0.439 – -1.271 | -1.271 – -8.678 |
| NDBSI (Low to high soil bareness) | - 0.999 – - 0.349 | -0.349 – -0.176 | - 0.176 – - 0.066 | -0.066 – 0.011 | 0.011 – 0.082 | 0.082 – 0.999 |
| NDTel (Low to high soil texture and roughness) | - 1 – 0.043 | 0.043 – 0.145 | 0.145 – 0.223 | 0.223 – 0.286 | 0.286 – 0.372 | 0.372 – 1 |
| CI (Low to high soil encrusting) | 0 – 0.743 | 0.743 – 0.804 | 0.804 – 0.873 | 0.873 – 0.947 | 0.947 – 1.034 | 1.034 – 1.572 |
| GSI (Low to high soil grain size and texture) | - 0.574 – - 0.037 | - 0.037 – - 0.024 | - 0.024 – 0.080 | 0.080 – 0.123 | 0.123 – 0.166 | 0.166 – 0.993 |
| NDSDI (Low to high sand spread) | - 0.866 – 0.119 | -0.119 – 0.004 | 0.004 – 0.092 | 0.092 – 0.187 | 0.187 – 0.319 | 0.319 – 1 |
| $SPC1_{R-NIR-SWIR1-SWIR2}$ (Low to high soil roughness) | 0 – 20.218 | 20.218 – 34.923 | 34.923 – 49.627 | 49.627 – 64.332 | 64.332 – 104.769 | 104.769 – 468.706 |

2.3.4. The Weighted Overlay Sum Method

In ArcGIS 10.2.2 software this method uses proportion as percentages. The image resulting from the weighted sum crossing has been analyzed statistically. The linear regression has been once more used for this purpose (Figure 7). The objective has been to improve the contribution of any neo-band

to the pre-detection of degraded lands. On the basis of the R^2 generated on the scatterplot it is observed that the synthesis image is more determined by the $SPC1_{R-NIR-SWIR1-SWIR2}$ up to 99.99%, contrarily to NDSDI that slightly determined it to 7.42% (Figure7, Table 6). Therefore the last step of the analysis was to weight of each index or neo-band by its determination coefficient R^2 with the synthesis image in order to enhance its contribution in the land degradation detection model and minimize any bias. The resulting image is considered optimal for contextual sensing of land degradation in arid and semi-arid regions.

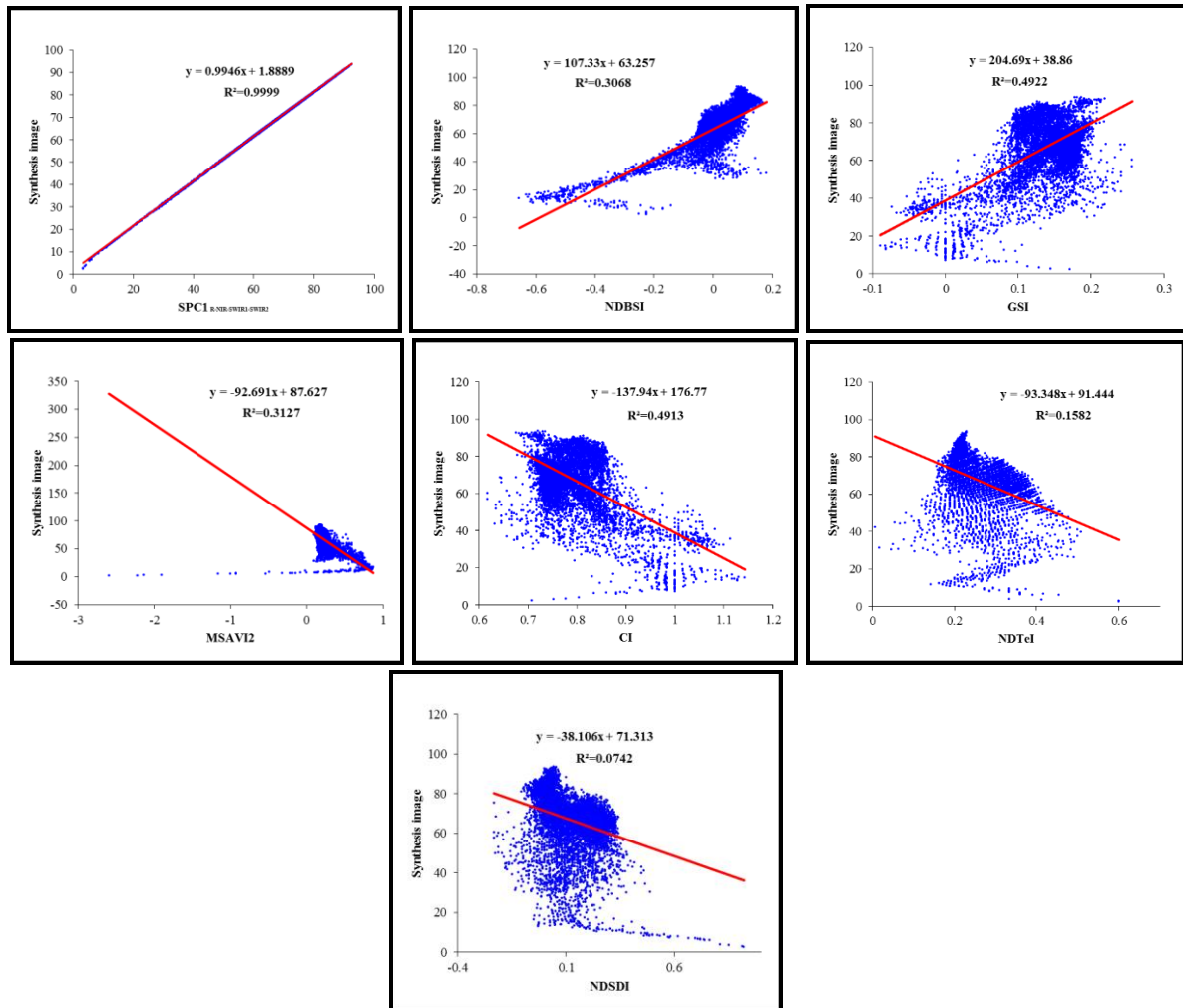


Figure 7: The Correlation between the Synthesis Image and the Neo-Bands Crossed

Table 6: Statistic Relation between Synthesis Image and the others Neo-Bands

| Indicators of Correlation Neo-bands | Linear Model Full Equation (a + bx) | Determination Coefficient Full Value (R^2) | P-values | |
|-------------------------------------|-------------------------------------|--|-----------|-------------|
| | | | Threshold | Test |
| MSAVI2 | $63.256523+107.328965*0.107784$ | 0.31271896 | < 0.0001 | Significant |
| NDBSI | $87.627229-92.690587*0.187408$ | 0.30680340 | < 0.0001 | Significant |
| NDTel | $91.443515-93.347721*0.225165$ | 0.15823584 | < 0.0001 | Significant |
| GSI | $38.859672+204.694035*0.085173$ | 0.49221143 | < 0.0001 | Significant |
| CI | $176.771284-137.941105*0.874418$ | 0.49130331 | < 0.0001 | Significant |
| NDSDI | $71.312706-38.105661*0.016806$ | 0.07428657 | < 0.0001 | Significant |
| $SPC1_{R-NIR-SWIR1-SWIR2}$ | $1.888909+0.994648*77.067878$ | 0.99993701 | < 0.0001 | Significant |

2.4. The Analysis of Exposition to Degradation

The increase in population is one of the significant factors that influence and accelerate land degradation by creating a great pressure on the land and other natural resources (Fadhil, 2009). The villages and population layers point format of the study area has been used to perform this step of the process. The analysis has been performed via ArcGIS 10.2.2 software toolbox. The first part has consisted to convert the considered layers into density of surface using the *point density* function of *spatial analyst tool*. It calculates a magnitude per unit area from point features that fall within a neighborhood around each cell. Afterwards the result obtained has been reclassified to six classes and crossed to the image of degradation. The image obtained is the one considered as the decision or action map for government concerning the fight against arid land degradation. A general diagram resumes the methods used in this study (Figure 9).

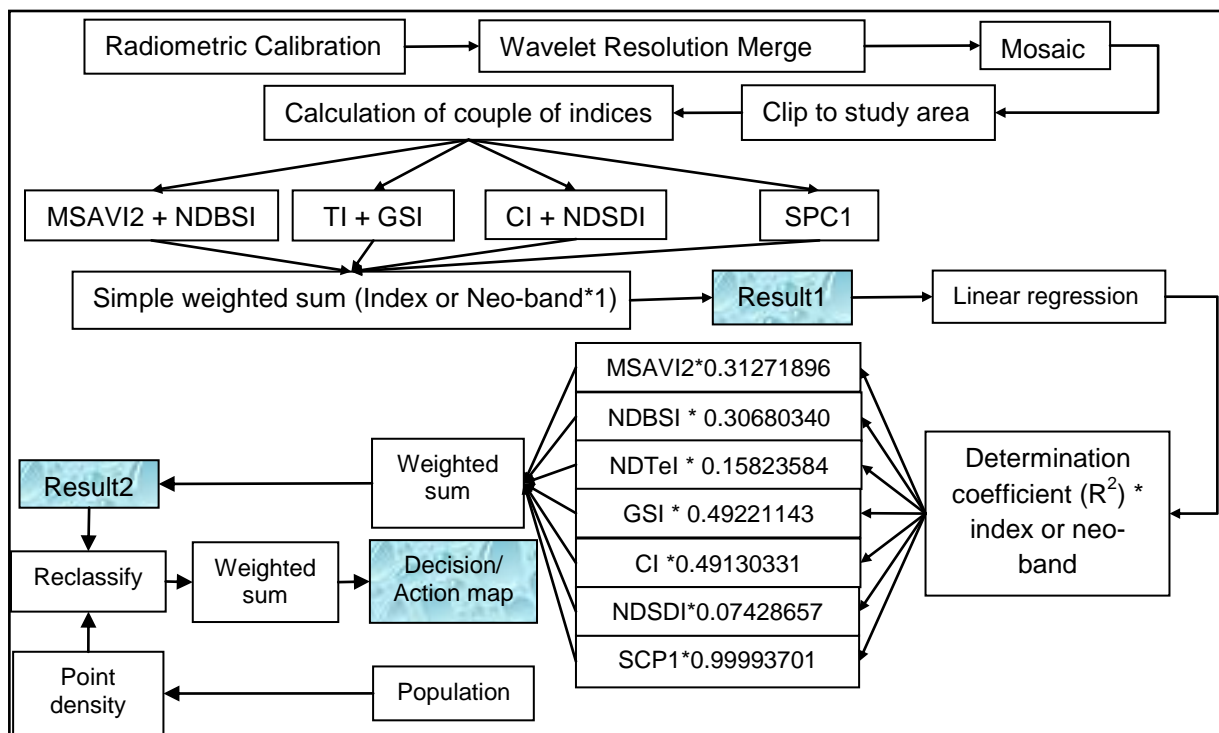


Figure 9: Flowchart Illustrating the Methodology

3. Results

3.1. Visual and Statistical Patterns of the Degradation Image

The results show six classes of land degradation on a nominal decreasing graduated scale that is arranged from the severe to the nil (Figure 10). The first remark is that a visual and statistic close relation between $SPC1_{R-NIR-SWIR1-SWIR2}$ and the degradation image; and this is confirmed by comparing the areas on each image class of degradation. Then the areas are evaluated respectively for $SPC1$ and resulting image to 3796 and 3139 km² for the class “severe”; 7483 and 6763 km² for the class “high”; 7984 and 8341 km² for the class “moderate”; 7424 and 7454 km² for the class “low”; 6291 and 6947 km² for the class “very low”; 5101 and 5437 km² for the class “close to nil” (Table 7, Figure 10).

Likewise the total areas per indices and neo-bands have shown slight difference in total areas concerned by degradation. The most important difference is recorded between $SPC1_{R-NIR-SWIR1-SWIR2}$ and NDSI; that is a residual of 9 km².

The quality of the model can also be analyzed still based on the areas per class for the different spectral and statistical neo-bands. It thus appears for the class “severe” that the MSAVI2 and the GSI with respectively 12235 km² and 5644 km² (Table 7, Figure 10) are the more explained; what probably indicates that the largest areas of bares soils severely degraded are constitutes from top soil grains size sandy or rocky humanly directly unusable. With 3139 km², the degradation image respectively 25.65% and 55.61% of MSAVI2 and GSI, explaining that all the vegetative uncover, sandy and rocky surfaces of this class are not degraded. The class “high” shows that the indices MSAVI2 and NDBSI with 20212 km² and 12661 km² more influences the model and thus lack of vegetation and bareness are the two main causes of degradation. The degradation image value recorded for this class is 6763 km², corresponding respectively to 33.46% and 53.41% of degraded land in MSAVI2 and NDBSI. For the class “moderate”, NDTel and NDSDI have the more large areas, respectively 12156 km² and 11113 km² which supposes that roughness and sand spread are the main causes of degradation at this level. The portion of degraded land expressed by the degradation image for this class is 8341 km² that is 68.61% and 75.05% of the NDTel and NDSDI. The class “low” is more represented by the NDSDI and CI, with respectively 9909 km² and 9057 km² and the two main causes of degradation are then sand spread and encrusting. The total of land degraded expressed by the degradation image is 7454 km² that is 75.22% and 82.30 % of the NDSDI and CI. The class “very low” records the more highest areas values from CI and SPC1_{R-NIR-SWIR1-SWIR2} respectively 11946 and 6291 km²; that supposes the importance of encrusting and rough lithology for this class. The degradation image for this class is 6947 km², representing 58.15% and 110.4 % of the CI and the SPC1_{R-NIR-SWIR1-SWIR2}. At last the “close to nil” class shows that the SPC1_{R-NIR-SWIR1-SWIR2} and the CI with respectively 5101 km² and 4020 km² record the highest areas which supposes that rough lithology and encrusting enhanced by these two neo-bands slightly influences the state of soil degradation in the study area. Comparatively to the degradation image which scored 5437 km² for this class it represent 106.5% and 135.2% for SPC1_{R-NIR-SWIR1-SWIR2} and CI.

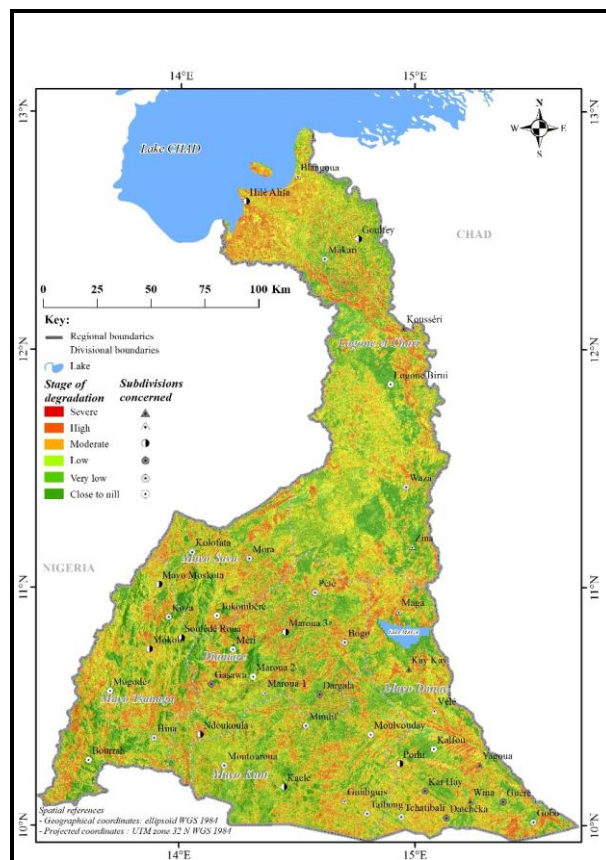


Figure 10: Land Degradation Image

Table 7: Degraded Areas per Neo-Bands and Per Classes

| Neo-bands Classes | MSAVI2 | NDBSI | GSI | NDTeI | CI | NDSDI | SPC1 | Crossed Image | Two Main Causes of Degradation |
|-------------------|--------------|--------------|--------------|--------------|--------------|--------------|--------------|---------------|----------------------------------|
| Severe | 12235 | 3642 | 5644 | 4222 | 1711 | 2590 | 3796 | 3139 | Bareness and top soil grain size |
| High | 20212 | 12661 | 12434 | 10718 | 5193 | 6624 | 7483 | 6763 | Fallow and roughness |
| Moderate | 4379 | 11090 | 7540 | 12156 | 6159 | 11113 | 7984 | 8341 | Roughness and sand spread |
| Low | 842 | 6925 | 6715 | 7246 | 9057 | 9909 | 7424 | 7454 | Sand spread and encrusting |
| Very low | 394 | 3019 | 4617 | 2712 | 11946 | 5961 | 6291 | 6947 | Encrusting and rough lithology |
| Close to nil | 20 | 751 | 1137 | 1032 | 4020 | 1889 | 5101 | 5437 | Rough lithology and encrusting |
| Total | 38082 | 38088 | 38087 | 38086 | 38086 | 38086 | 38079 | 38081 | |

3.2. Human Exposition and Spaces of Public Action

The vulnerability map obtained after crossing population density with degradation map shows that some spaces principally those dominated by the severe, high and moderate class of degradation have the priority of government action to initiate land rehabilitation and protection (Figure 11). The first is situated between the three departments of Diamare, Mayo-Sava and Mayo-Tsanaga. The second is mainly between the departments of Mayo-Kani and Mayo-Danay around the “duck-beak” very important for irrigated rice cultivation. The third area is situated in the division of Logone-Chari around the Lake Chad concerned with desertification and conflicts about land and water access.

The statistics extracted show that 279293 inhabitants live within the surface severely damaged (Table 8). At same time 548418 inhabitants are slightly concerned by the degradation (Table 8). When taking in consideration administrative limits of divisions, two of them are severely concerned by the degradation, notably the Mayo-Danay and the Logone-Chari, with respectively 178047 and 101246 inhabitants (Table 8).

Table 8: Population Exposition per Class of Degradation and Per Administrative Division

| Division Classes | Diamare | Mayo-Danay | Mayo-Kani | Mayo-Sava | Mayo-Tsanaga | Logone-Chari | Total per class |
|---------------------------|---------------|---------------|---------------|---------------|---------------|---------------|-----------------|
| Severe | 0 | 178047 | 0 | 0 | 0 | 101246 | 279293 |
| High | 330410 | 126793 | 43632 | 0 | 0 | 75970 | 576805 |
| Moderate | 32091 | 0 | 144313 | 0 | 307310 | 218278 | 701992 |
| Low | 51296 | 112836 | 0 | 0 | 0 | 0 | 164132 |
| Very low | 132355 | 85182 | 134333 | 257634 | 124831 | 198017 | 932352 |
| Close to nil | 86834 | 26203 | 82368 | 91256 | 201490 | 331242 | 819393 |
| Total per division | 632986 | 529061 | 404646 | 348890 | 633631 | 924753 | 3473967 |

4. Discussions

Nevertheless other field components can interfere with the indices results such as landscape position (Demattê and al., 2009) and that effects are to be reduced. While in regions with a varied topography, elements as slope length and inclination named as LS factor in the USLE (Wischmeier and Smith, 1978) and RUSLE (Renard and al., 1991) formula are relevant to be introduced into the model. This is important to minimize and even subtract spectral values of each index due to the relief, when enhancing at same time some features of soil degradation.

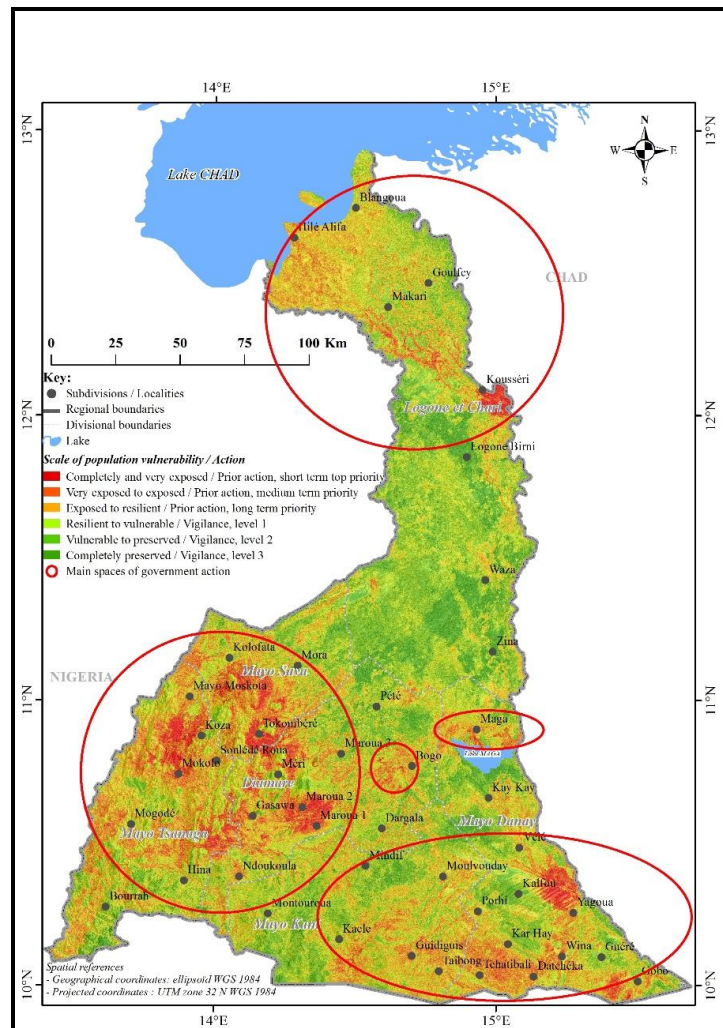


Figure 11: People Exposition Map to Degradation

Another bias can be introduced by human settlements like houses in sand materials and straw roof. These building materials strongly impact the top soil reflectance and can influence the values of indices to falsify the results of land degradation detection. No method has used to avoid such confusion during this experimentation.

Further apart from measuring and characterizing the degradation in laboratory before a deep field campaign verification it can also be important to integrate new instruments as mobile and portable spectroradiometers that have not been used in this study. They can facilitate a more precise measure of soil reflectance, color and composition (Escadafal et al., 1993), for a complementary comment on its degradation and the different noises and speckle around.

5. Conclusions

On the basis of laboratory test performed in this paper it is possible to detect the state of soil degradation in a semi-arid and arid tropical zone through the calculation and the crossing of spectral indices and statistical neo-band. Then the remote sensing techniques used are based on the visual and statistical comparison on one hand, and crossing of vegetation and soil indices with a statistical neo-band on the other hand to result in generating the land degradation image. The indices used in this study are MSAVI2, NDBSI, NDTel, GSI, CI and NDSI, and $SPC1_{R-NIR-SWIR1-SWIR2}$. And the generated index has been used to improve the accuracy of land degradation with regard to enhance

characteristics as bareness, texture, roughness, sand spread and encrusting in arid and semi-arid zone.

Considering the soil cover or bareness as the first entrance, a vegetation index adapted to the area of study has to be calculated and correlated with the soil and top soil indices indicators of degradation. Thus the MSAVI2 has been correlated with the others neo-bands. Their p values obtained were strictly lower than 0.0001, and appeared then significant for the analysis. After they were summed following a simple weighted sum method a linear regression has been performed between every of them and the resulting image to assess the contribution of any neo-band to the model. Then each index or neo-band was weighted by its determination coefficient R^2 with the synthesis image in order to enhance its contribution and minimize any bias in the degradation image building model. It then appears that the final image corresponding to the degradation image is visually and statistically highly correlated to $SPC1_{R-NIR-SWIR1-SWIR2}$.

Nevertheless this experimentation has some limitations. The first one is the unused of the slope because of the plain relief in the study areas; which supposes that in topographic varied areas these elements are to be integrated in the model. In second point the sand materials and straw roof buildings can introduce bias in some indices calculation as NDSI in desert and Sahel regions as the study areas; a method to avoid these confusion have to be found. The accuracy of the degradation image can be improved by field experimentations based on portable spectroradiometers.

Acknowledgments

The authors gratefully acknowledge the material and technical assistance of the National institute of cartography. The discussions with the technical members of the laboratory of image processing of the association ILG (I Love Geomatics) as well as those of the private consulting firm GEOVECTORIX are to be noted for the improvement of the content of this paper. The authors also highly appreciate all the facilities offered by the public administrations as Ministry of Environment, Nature protection and Sustainable Development, and the Central Bureau of Population Census concerning all the data provides.

Author Contributions

Alfred Homère NGANDAM MFONDOUM is the main author who co-initiated the idea and wrote the manuscript. Joachim ETOUNA co-initiated the idea, provided review and comments.

MBUJI Kindness Nongsi, Fabrice Armel MVOGO MOTO, and Florine Gustave NOULAQUAPE DEUSSIEU have contributed to technical processing and discussions.

References

Al-Bakri, J., Saoub, H., Nickling, W., Suleiman, A., Salahat, M., Khresat, S., and Kandakji, T. *Remote Sensing Indices for Monitoring Land Degradation in a Semiarid to Arid Basin*. In Jordan. Proc. of SPIE. 2012. 8538; 1-10.

Baccini, A. *Statistique Descriptive Multidimensionnelle*. Publications de l'Institut de Mathématiques de Toulouse, mai. 2010. 33.

Bai, Z.G., Dent, D.L., Olsson, L., and Schaepman, M.E., 2008: *Global Assessment of Land Degradation and Improvement 1. Identification by Remote Sensing*. In: GLADA Report 5, Version November 2008. 78.

- Baraldi, A., Puzzolo, V., Blonda, P., and Bruzzone, L., and Tarantino C. *Automatic Spectral Rule-Based Preliminary Mapping of Calibrated Landsat TM and ETM+ Images*. IEEE Transactions on Geoscience and Remote Sensing. 2006. 44 (9) 2563-2586.
- Barnes, R.A., and Zalewski, E.F. *Reflectance-Based Calibration of SeaWiFS-II*. Conversion to Radiance. Applied Optics. 2003. 42 (9) 1648-1660.
- Barrow, C.J., 1991: *Land Degradation: Development and Breakdown of Terrestrial Environments*. Cambridge University Press, Cambridge, UK. 300.
- Begzsuren, S., 2007: *Integrated Desertification Assessment in Southern Mongolia*. Dr. Thesis, University of Bonn. 141.
- Biancalani, R. No Year: *Land Degradation Assessment in Drylands*. LADA Team, FAO-UNEP. 46.
- Blaikie, P., and Brookfield, H., 1987: *Land Degradation and Society*. Methuen, London. 296.
- Bonn, F., and Rochon, G., 1992: *Précis de télédétection*. Vol.1. Principes et méthodes. Ed. AUPELF-UREF, Presses Universitaires du Québec, Montréal.
- Brabant, P., Darracq, S., Égué, K., and Simonneaux, V., 1996: *Togo: Human-Induced Land Degradation Status – Explanatory Notes on the Land Degradation Index*. ORSTOM editions, Paris 66.
- Brabant, P. *A Global Land Degradation Assessment and Mapping Method. A Standard Guideline Proposal*. Les Dossiers Thématiques du CSFD. July 2009. (8) 2.
- Brabant, P. *Une Méthode D'évaluation Et De Cartographie De La Dégradation Des Terres. Proposition De Directives Normalisées*. Les dossiers thématiques du CSFD. Août 2010. (8) 52.
- BUCREP, 2010: *Rapport De Présentation Des Résultats Définitifs*. BUCREP, Cameroun, 22 avril 2010. 67.
- Chavez, Jr. P.S. *Image-Based Atmospheric Corrections - Revisited and Improved*. Photogrammetric Engineering & Remote Sensing. 1996. 62 (9) 1025-1036.
- Chen, Y., 1999: *Correlation of Saltbush Cover Measurements to TM Wavebands and Vegetation Indices*. Geoscience and Remote Sensing Symposium, IEEE IGARSS '99.
- COMIFAC-CEEAC, 2007: *Programme D'Action Sous-Régional de Lutte Contre la Dégradation des terres et la Désertification en Afrique Centrale (PASR/LCD-AC)*. Jun 2007, 65. Available on www.unccd.int/ActionProgrammes/rms-fre2007.pdf
- Conacher, J., and Sala Wiley, M., 1998: *Land Degradation in Mediterranean Environments of the World: Nature and Extent, Causes and Solutions*. Chichester. 491.
- Dagnelie, P. *De La Régression Linéaire Simple Et L'analyse De La Variance Aux Modèles Linéaires Généralisées: Synthèse Et Chronologie*. Revue MODULAD. 2009. 39; 107-136.
- Demattê, J.A.M., Huete, A.R., Laerte Guimarães, F. Jr., Nanni, M.R., Alves, M.C., and Ricardo Fiorio, P. *Methodology for Bare Soil Detection and Discrimination by Landsat TM Image*. The Open Remote Sensing Journal. 2009. 2; 24-35.

Deschamps, P.Y., Duhaut, P., Rouquet, M.C., and Tanre, O., 1983: *Mise En Évidence, Analyse Et Correction Des Effets Atmosphériques Sur Les Données Multispectrales De Landsat Ou Spot*. Inra-CNES. Coll. Int. Signatures spectrales d'objets en Télédétection, Bordeaux, France. 709-722.

ERDAS, 2003: *ERDAS Field Guide, Seventh edition*. Leica Geosystems, Atlanta, Georgia. 698.

Escadafal, R., Gouinaud, C., Mathieu, R., and Pouget, M. *Le Spectroradiomètre De Terrain: UN Outil De La Télédétection Et De La Pédologie*. Cah. Orstom, sér. Pédol. 1993. XXVIII (1) 15-29.

Fadhil, A.M. *Land Degradation Detection Using Geo-Information Technology for Some Sites in Iraq*. Journal of Al-Nahrain University. 2009. 12 (3) 94-108.

Ferreres Mora, L., Ruiz Fernández, L.A., Artero Verdú, F., and Soo Kyun, Ik. *Using a Wavelet Based Method for High Resolution Satellite Image Fusion*.

Available on [http://www.cgat.webs.upv.es/bigfiles/Ferreres_et_al\(SNRFAl01\).pdf](http://www.cgat.webs.upv.es/bigfiles/Ferreres_et_al(SNRFAl01).pdf)

González, E.P., and Rodríguez, P.G. *Use of Remote Sensing in Soil Degradation*. Boletín de la Asociación de Geógrafos Españoles. 2013. 61; 425-427.

Gonzalez, P.L. No Year: *L'Analyse en Composantes Principales (ACP)*. 37. Available on maths.cnam.fr/IMG/pdf/A-C-P-.pdf

Higginbottom, T.P., and Symeonakis, E. *Assessing Land Degradation and Desertification using Vegetation Index Data: Current Frameworks and Future Directions*. Remote Sens. 2014. 6; 9552-9575.

Joly, G., 1986: *Traitements Des Fichiers Images*. Collection Télédétection satellitaire, n°3, Paradigme, Caen. 137.

Karnieli, A. *Development and Implementation of Spectral Crust Index over Dune Sands*. Int. J Remote Sensing. 1997. 18 (6) 1207-1220.

King, R., and Wang, J., 2001: *A Wavelet Based Algorithm for Pansharpening Landsat-7 Imagery*. Proceedings of the Geoscience and Remote Sensing Symposium, IGARSS. 2; 849-851.

Klonus, S., and Ehlers, M., 2009: *Performance of Evaluation Methods in Image Fusion*. 12th International Conference on Information Fusion, Seattle, WA, USA. July 6-9, 2009. 1409-1416.

Liu, A., and Wang, J., 2005: *Monitoring Desertification in Arid and Semi-Arid Areas of China with NOAA-AVHRR and MODIS Data*. Geoscience and Remote Sensing Symposium. IEEE, IGARSS '05.

Madeira, J., Pouget, M., Bedidi, A., and Cervelle, B. *Relations entre les constituants minéraux d'Oxisols brésiliens et leurs signatures spectrales du visible à l'infra-rouge moyen: application à des données satellitaires (Landsat TM): I- Les oxydes de fer. - II. La kaolinite et la gibbsite. Implications sur la texture*. Télédétection, ORSTOM, Paris. 1991. 6.

Madeira, J., 1993: *Etude qualitative des relations constituants minéralogiques-réflectance, diffusion des latosols brésiliens: applications à l'utilisation pédologiques des données satellitaires TM (région de Brasilia)*. Coll. Etudes et Thèses. Orstom éd. 1993. Paris. 236.

Metternicht, G., 2006: *Current Developments of Remote Sensing for Mapping and Monitoring Land Degradation at Regional Scale*. UN-Zambia-ESA Regional Workshop on the Applications of GNSS in Sub-Saharan Africa, Zambia. June 2006. 40.

Ministère de l'environnement et des forêts (Cameroun), UNCCD, 2004: Rapport National sur la mise en œuvre de la convention des Nations Unies sur la lutte contre la désertification. Novembre 2004. UNCCD. 53.

Pandey, P.C., Rani, M., Srivastava, P.K., Sharma, L.K., and Nathawat, M.S. *Land Degradation Severity Assessment with Sand Encroachment in an Ecologically Fragile Arid Environment: A Geospatial Perspective*. In Q Science Connect. 2013. 43; 17.

Perry, C. Jr., and Lautenschlager, L.F. *Functional Equivalence of Spectral Vegetation Indices*. Remote Sensing of Environment. 1984. 14 (1-3).169-182.

Qi, J., Chehbouni, A., Huete, A.R., Kerr, Y.H., and Sorooshian, S. *A Modified Soil Adjusted Vegetation Index*. Remote Sens. Environ. 1994. 48; 119-126.

Raina, P., Joshi, D.C., and Kolarkar, A.S. *Land Degradation Mapping By Remote Sensing in the Arid Region of India*. Soil Use Manage. 1991. 7 (1) 47-51.

Raunet, M. *Quelques clés morphopédologiques pour le Nord Cameroun à l'usage des agronomes*. Cirad, France. September 1993. 21.

Renard, K.G., Foster, G.R., Weesies, G.A., and Porter, J.P. *RUSLE, Revised Universal Soil Loss Equation*. J. Soil Water Conserv. 1991. (1) 30-33.

Rojas, N., 2013: *An Overview of the Geospatial Methodologies used in Order to Assess the Soil Erosion Risk by Water*. Aplicaciones Espaciales de Alerta y Respuesta a Emergencias. February 2013. 41.

Roy, P., Miyatake, S., and Rikimaru, A. *Biophysical Spectral Response Modeling Approach for Forest Density Stratification*. ACRS 1997.
Available on <http://www.a-a-r-s.org/aars/proceeding/ACRS1997/Papers/FR97-7.htm>

Sellke, T., Bayarri, M.J., and Berger, J.O. *Calibration of P Values for Testing Precise Null Hypotheses*. The American Statistician. February 2001. 55 (1).

Smith, A., Freemantle, J., Nadeau, C., Wehn, H., Zwick, H., and J. Miller. 2005: *Leaf Area Index Map Generation Using CHRIS Data*. Presentation given at the 3rd CHRIS Proba Workshop. 2005.

Senseman, G.M., Bagley, C.F., and Tweddale, S.A. *Correlation of Rangeland Cover Measures to Satellite-Imagery-Derived Vegetation Indices*. Geocarto International. 1996. 11 (3) 29-38.

Senseman, G.M., Tweddale, S.A., Anderson, A.B., and Bagley, C.F., 1996: *Correlation of Land Condition Trend Analysis (LCTA) Rangeland Cover Measures to Satellite-Imagery-Derived Vegetation Indices*. US Army Corps of Engineers USACERL. Technical Report 97/07.

Singer, M.J., and Munns, D.N., 2002: *Soils: An Introduction*. 5th Edition. Upper Saddle River, New Jersey: Prentice Hall Publishers.

Thomasson, J.A., Sui, R., Cox, M.S., and Al-Rajehy, A. *Soil Reflectance Sensing for Determining Soil Properties in Precision Agriculture*. Trans. ASAE. 2001. 44 (6) 1445-1453.

Touriño Soto, I., 2005: *Mise En Relation De La Cartographie Du Rendement Avec La Distribution Spatiale De L'état De Surface Du Sol Observée Par Télédétection*. Application dans un contexte d'agriculture de précision. Th. Dr. L'Institut National Polytechnique de Toulouse. 259.

UNCCD, 1994: *United Nations Convention to Combat Desertification in Those Countries Experiencing Serious Drought and/or Desertification, Particularly in Africa*. UN, Paris, France.

UNEP, 1992: *World Atlas of Desertification*. Edward Arnold, London.

Warren, A., and Agnew, C. *An Assessment of Desertification and Land Degradation in Arid and Semi-Arid Areas*. Drylands Program, Issues Envelope. April 1998. 2.

Wischmeier, W.H., and Smith, D.D. 1978: *Predicting Rainfall Erosion Losses: A Guide to Conservation Planning*. USDA, Agriculture Handbook 537. U.S. Government Printing Office, Washington, DC.

Xiao, J., Shen, Y., Tateishi, R., and Bayaer, W. *Development of Topsoil Grain Size Index for Monitoring Desertification in Arid Land Using Remote Sensing*. Int. J. Remote Sensing. 2006. 27 (12) 2411-2422.

Youan, T.M., 2008: *Contribution de la télédétection et des systèmes d'informations géographiques à la prospection hydrogéologique du socle précambrien d'Afrique de l'Ouest: Cas de la région de Bondoukou Nord Est de la Côte d'Ivoire*. Thèse de doctorat unique, Université de Cocody-Abidjan (Côte d'Ivoire), 236.

Zaydan, A.H. *Using a Wavelet Based Method for High Resolution Satellite Image Fusion*. Iraqi Journal of Science. 2012. 53 (4) 999-1005.

Morphometric Analysis of Abdan Basin, Almahfid Basement Rock, Yemen: using Remote Sensing and GIS

Syed Ahmad Ali, Mohsen Alhamed, and Umair Ali

Department of Geology, Aligarh Muslim University, Aligarh, India

Publication Date: 5 March 2016

DOI: <https://doi.org/10.23953/cloud.ijarsg.47>



Copyright © 2016 Syed Ahmad Ali, Mohsen Alhamed, and Umair Ali. This is an open access article distributed under the **Creative Commons Attribution License**, which permits unrestricted use, distribution, and reproduction in any medium, provided the original work is properly cited.

Abstract To achieve the morphometric analysis of Abdan basin, Survey of Yemen Geological Survey and Mineral Resources Board (YGSMRB) topomaps in 1:100000 scales are procured and the boundary line has been extracted by joining the ridge points. The drainage map is prepared with the help of GIS tool and morphometric parameters such as linear, aerial and relief aspects of the basin have been determined. For detailed study we used SRTM data for preparing DEM, elevation and slope map. GIS was used to estimate the linear, aerial and relief aspects of morphometric parameters. The result indicate that the drainage area is 922.933 km², perimeter 163.115 km, basin length 54.156 km, drainage texture 1.974, constant of channel maintenance 1.145, the stream frequency 0.349, drainage density 0.873, length over flow 0.572. Mean bifurcation ratio 4.355 so the drainage pattern has not been disturbed by structural disturbance. Form factor 0.315 and circulatory ratio 0.436 indicate that the basin is sub-circular to elongate in shape.

Keywords *Abdan Basin; Almahfid Basement; Geographic Information System; Morphometry*

1. Introduction

Drainage basins are the fundamental units to understand geometric characteristics of fluvial landscape, such as topology of stream networks, and quantitative description of drainage texture, pattern, shape and relief characteristics (Obi Reddy et al., 2004; Subba Rao, 2009). Morphometric analysis is an important technique to evaluate and understand the behaviour of hydrological system. Morphometric analysis of a river basin offers a quantitative description of the drainage system, which is an important aspect of the characterization of basins (Strahler, 1964). According to Clarke (1996), geomorphometry is the measurement and mathematical analysis of the configuration of the Earth's surface, shape and dimensions of its landforms.

The morphometric analysis is performed through measurement of linear, aerial, relief, gradient of channel network and contributing ground slope of the basin (Ali, 1988; Nautiyal, 1994; Nag and Chakraborty, 2003; Magesh et al., 2012b). Morphometric analysis of a river basin comprises of discrete morphologic region and has special relevance to drainage pattern and geomorphology (Strahler, 1957; Dornkamp and King, 1971).

Remote sensing and GIS utility provides useful source for the preparation of various thematic layers for morphometric analysis. Morphometric and other characteristics (elevation, slope etc.) of landscape can be evaluated to any extent using Digital Elevation model. SRTM data has been used in spatial environment (GIS) to assess the morphometric behaviour with ease, accuracy and cost effective way. Remote sensing and GIS technology has been used for morphometric analysis of river basins carried out using (Ali et al., 2013; Ali & Ali, 2014)

In the present study, evaluation of various morphometric parameters is described using ArcGIS10.2 software for Abdan Basin, YEMEN. The mathematical calculation of linear, aerial and relief aspects were done to decipher the various geomorphometric parameters for planning and development of Abdan Basin.

2. Materials and Methods

2.1. Study Area

The Abdan basin covers an area of 922.933 km² with basin length of 54.156 kms. The greater portion of Abdan basin is located in Nisab and Hatib districts, Shabwah governorate, and a small part is located in Jayshan district, Abyan governorate, Republic of Yemen. This basin lies between longitudes 46° 10' to 46° 40' and latitudes 14° 00' to 14° 40' (Figure 1). The climate of the study area is tropic-arid. It is essentially affected by the monsoon winds of the Indian Ocean. The climate is moderate in summer and cold in winter. The vegetation in some parts of the surface is limited either in terms of quantity or type and it is almost exclusively in certain types of grasses and small plants that abound during the rainy seasons as well as some old trees scattered near the valleys and mountain passes and the most important of these trees are lotus, acacia tortilis and acacia nilotica and some trees of acacia gummifera, tamarisk and boxthorn.

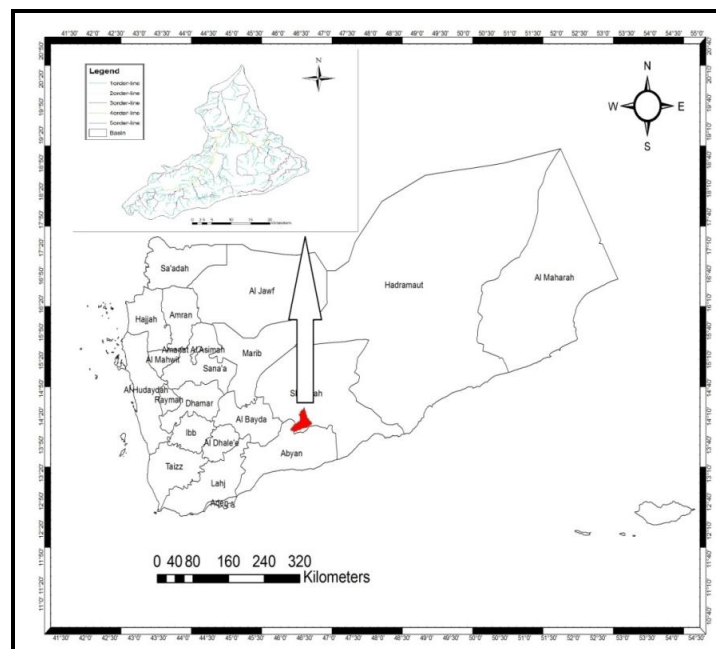


Figure 1: Location Map of Abdan Basin

2.2. Geology of Study Area

Abdan basin is part of Almafidi zone which in this basin consists of Barak subzone which is lower Proterozoic and Hatib subzone which is higher Proterozoic. The Barak group comprises Biotite-

Plagioclase Schist, Biotite-Amphibole Gneisses, a part of which is granitized. The Hatib group complete sequence is subdivided into the Hogl, Wasr, Medwa, Ayan and Samaq formation.

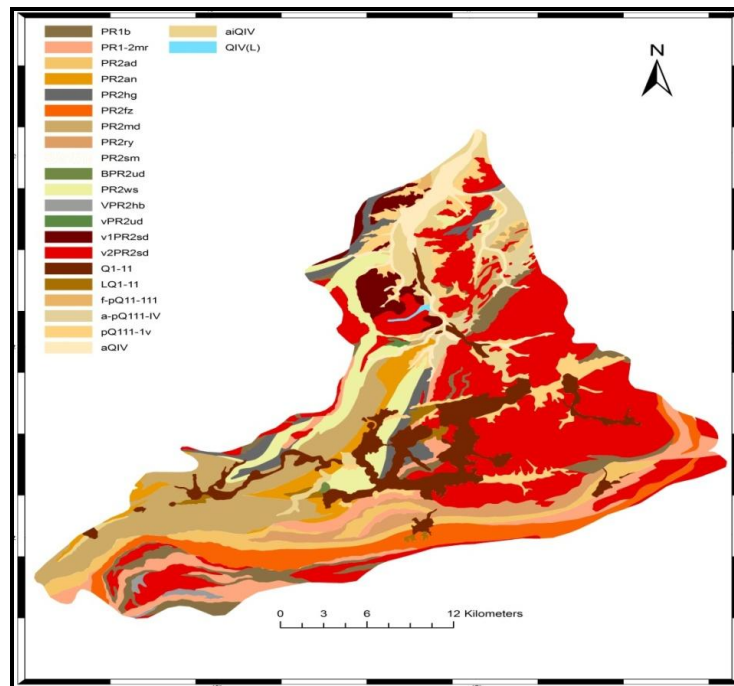


Figure 3: Geological Map of Study Area

2.3. Methodology and Data Source

The study of Abdan basin is based on Yemen Geological Survey Board (YGSMRB) toposheet maps on a 1:100000 scale. The toposheet maps (D-38-57, D-38-58, D-38-69 and D-38-70) and also an SRTM data were used. The SRTM was an 11 day space shuttle mission in February 2000 (Figure 7 & 8). The drainage network (Figure 3) and morphometric analysis was carried out at the basin in Arc GIS 9.3. The morphometric parameters were divided into three categories: linear, areal and relief aspects of the basin.

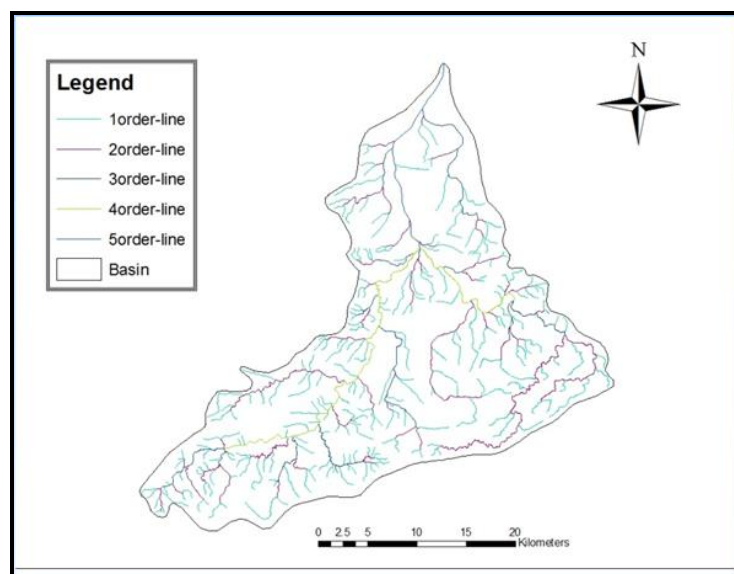


Figure 2: Drainage Map of Abdan Basin

Table 1: Description Geological Map of Study Area

| S/O | Symbol | Description | Period |
|-------|------------|--|-----------------------|
| I | PR1b | Biotite-Plagioclase Schist, Biotite-Amphibole Gneisses, a part of which is granitized. Barak Group | Lower Proterozoic |
| II | PR1-2mr | Mash'ar formation | Lower Proterozoic |
| III | PR2ad | 'Ads formation. Fahman Group. | Upper Proterozoic |
| IV | PR2an | Ayan formation. Hatib Group. | Upper Proterozoic |
| V | PR2hg | Hogl formation. Hatib Group. | Upper Proterozoic |
| VI | PR2fz | Fayzum formation. Fahman Group. | Upper Proterozoic |
| VII | PR2md | Medwa formation. Hatib Group. | Upper Proterozoic |
| VIII | PR2ry | Ray formation. Fahman Group | Upper Proterozoic |
| IX | PR2sm | Samaq formation. Hatib Group. | Upper Proterozoic |
| X | BPR2ud | Metadiabase. Uddamar Magmatic Complex. | Upper Proterozoic |
| XI | PR2ws | Wasr Formation. Hatib Group. | Upper Proterozoic |
| XII | VPR2hb | Metagabbro, Gabbro-Amphibolite. Hatib Group. | Upper Proterozoic |
| XIII | vPR2ud | Metagabbro. Uddamar Magmatic Complex | Upper Proterozoic |
| XIV | v1PR2sd | Older Granite. Sa'id Magmatic Complex. | Upper Proterozoic |
| XV | v2PR2sd | Younger Granite, Mainly Syenogranite. Sa'id Magmatic Complex | Upper Proterozoic |
| XVI | Q1-11 | Lower-Middle Quaternary Basaltic Rocks | Quaternary Volcanites |
| XVII | LQ1-11 | Lacustrine Loam, Sand, Gravel And Gruss. Lower-Middle Quaternary | Quaternary Volcanites |
| XVIII | f-pQ11-111 | Fluvial-Proluvial Pebble Gravel, Boulders, Conglomerate. Middle-Upper Quaternary | Quaternary |
| XIX | a-pQ111-IV | Alluvial-Proluvial Pebble Gravel, Boulders, Conglomerate. Upper Quaternary-Recent. | Quaternary |
| XX | pQ111-1V | Proluvial Rubble, Pebble Gravel. Upper Quaternary-Recent | Quaternary |
| XXI | aQIV | Alluvial Pebble Gravel, Gravel And Sand. | Quaternary |
| XXII | aiQIV | Agro-Irrigation Loesslike Loam. Recen | Quaternary |
| XXIII | QIV(L) | Basalt. Recent | Quaternary |

3. Results and Discussion

The Morphometric characteristics of study area are examined with reference to linear, aerial and relief aspects.

Table 2: Formulae Adopted for Computation of Morphometric Parameters

| S. No. | Morphometric Parameters | Formula | Reference |
|--------|------------------------------|--|-----------------|
| 1 | Stream order | Hierarchical rank | Strahler (1964) |
| 2 | Stream length (L.u) | Length of the stream | Horton (1945) |
| 3 | Mean stream Length (L. sm) | $L.sm = L.u / Nu$ where L.sm = Mean stream length L.sm = Total stream length of order 'u' N.u = Total no. of stream segment of order 'u' | Strahler (1964) |
| 4 | Stream length Ratio (R.L) | $R.L. = L.u / Lu-1$ Where R.L = Stream length Ratio L.u = The Total stream length of order 'u' L.u.1 =The total stream length of its next lower order | Horton (1945) |
| 5 | Bifurcation Ratio (Rb) | $Rb. = Nu/Nu + 1$ Where Rb = Bifurcation Ratio Nu = Total no. of steam segments of order 'u' N.u.1 =The total stream length of its next higher order | Schumn (1956) |
| 6 | Mean bifurcation ratio (Rbm) | Rbm. = Average of bifurcation ratios of all orders | Strahler (1957) |

| | | | |
|----|----------------------------------|--|-----------------------|
| 7 | Relief Ratio (Rh) | $Rh = H/L.b$ where Rb = Relief Ratio H =Total relief (Relative relief) of the basin in Kilometer) Lb = Basin length | Schumn (1956) |
| 8 | Drainag Density (D) | $D = L.u / A$ where, D = Drainage Density Lb = Total stream length of all orders. A =Area of the Basin (Km ²) | Horton (1932) |
| 9 | Stream Frequency (Fs) | $Fs = Nu / A$ where, Fs = Stream Frequency Nu = Total no. of streams of all orders A =Area of the Basin (Km ²) | Horton (1932) |
| 10 | Drainage Texture (Dt) | $Dt = Nu / A$ where, Dt = Drainage Texture Nu = Total no. of streams of all orders P =Perimeter (km) | Horton (1945) |
| 11 | Form Factor (Rf) | $Rf = A / L.b^2$ where, RF = Form Factor A =Area of the Basin (Km ²) Lb ² =Square of Basin length | Horton (1932) |
| 12 | Circularity Ratio (Rc) | $Rc = 4 * A / P^2$ where, RC = Circularity Ratio Pi = 'Pi' Value i.e. 3.14 A =Area of the Basin (Km ²) P = Perimeter (km) | Miller (1953) |
| 13 | Elongation Ration (Re) | $Re = 2V (A / Pi / L.b)$ where, Re = Elongation Ratio A =Area of the Basin (Km ²) Pi ="Pi" value i.e. 3.14 L.b =Basin length | Schumn (1956) |
| 14 | Length of overland flow (Lg) | $L.g = 1 / D*2$ Where, Lg = Length of overland flow D =Drainage Density. | Horton (1945) |
| 15 | Constant channel Maintenance (C) | $C = 1/D$ | Schumn (1956) |
| 16 | Slope | $Sb = \frac{H-h}{L}$ | Mesa (2006) |
| 17 | Gradient Ratio | $Gr = \frac{H-h}{L}$ | Sreedevi et al (2005) |
| 18 | Infiltration number (If) | $If = D*Fs$ Where, If = Infiltration number, D = Drainage Density, Fs = Stream frequency. | |

3.1. Linear Aspects

Linear aspects includes drainage parameters such as stream order (Nu), stream length (Lu), Mean Stream Length (Lsm), Stream Length Ratio (RI), Bifurcation Ratio (Rb) and Mean Bifurcation Ratio (Rbm).

Table 3 (a): Linear Aspect of Abdan Basin

| Basin | Stream Number in Different Orders | | | | | Total | Orders Total Stream Length (Km) | | | | | total |
|-------------|-----------------------------------|-----------------------|-----------------------|-----------------------|-----------------------|-------|---------------------------------|-----------------------|-----------------------|-----------------------|-----------------------|-------|
| | 1 st order | 2 nd order | 3 rd order | 4 th order | 5 th order | | 1 st order | 2 nd order | 3 rd order | 4 th order | 5 th order | |
| Abdan Basin | 248 | 58 | 14 | 2 | 1 | 322 | 455.9 | 186.6 | 88.19 | 54.03 | 21.26 | 806 |

Table 3 (b): Linear Aspect of Abdan Basin

| Basin | Perimeter (Km) | Mean stream length (Km) | | | | | Stream length ratio (RI) | | | | | Bifurcation ratio (Rb) | | | | Mean bifurcation ratio (Rbm) |
|-------------|----------------|-------------------------|-----------------------|-----------------------|-----------------------|-----------------------|--------------------------|-------|-------|-------|-------|------------------------|-------|-------|-------|------------------------------|
| | | 1 st order | 2 nd order | 3 rd order | 4 th order | 5 th order | total | 2/1 | 3/2 | 4/3 | 5/4 | RI | 1/2 | 2/3 | 3/4 | |
| Abdan Basin | 163.115 | 1.838 | 3.275 | 6.299 | 27.015 | 21.269 | 0.409 | 0.479 | 0.613 | 0.397 | 0.472 | 4.276 | 4.276 | 7.143 | 2.143 | 4.355 |

3.1.1. Stream Order (U)

The designation of stream orders is the first step in drainage basin analysis. It is based on hierarchic ranking of streams proposed by Strahler (1964). The first order streams have no tributaries. The second order streams have only first order streams as tributaries. Similarly, third order streams have first and second order streams as tributaries and so on. In present study, Abdan watershed has fifth stream order. With increasing stream order the number of stream is decreases (Figure 4, Table 3a).

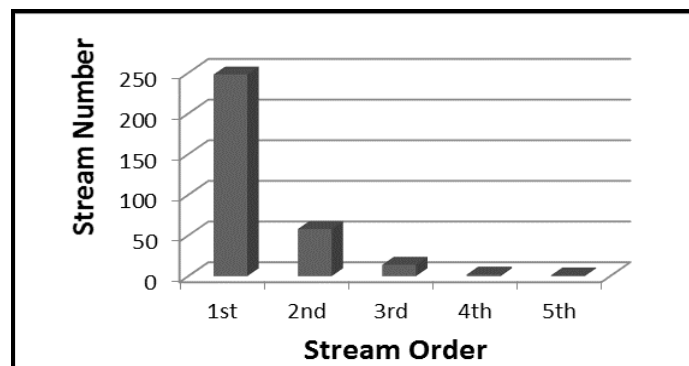


Figure 4: Stream Number Vs Stream order

3.1.2. Stream Length (Lu)

It is the total length of streams in a particular order. The numbers of streams of various orders in watershed were counted and lengths were measured with help of ArcGIS 9.3. Generally, the total length of stream segments decreases with stream order. The maximum length of the total basin is 806.093 km. Generally the total length of stream segments decreases with increasing stream order (Figure 5, Table 3a).

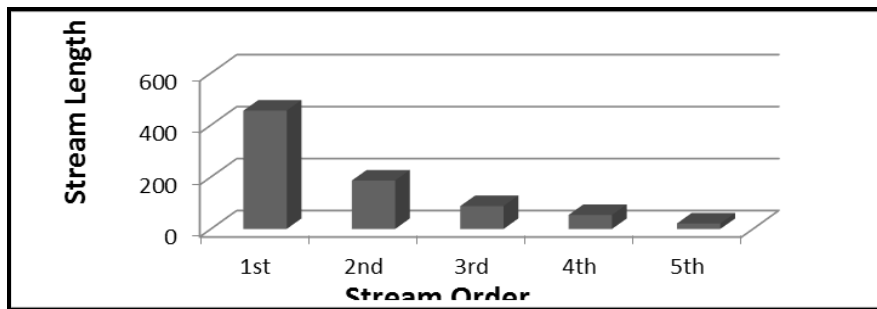


Figure 5: Stream length Vs Stream order

3.1.3. Mean Stream Length

The mean stream length of a channel is a dimensional property and reveals the characteristic size of drainage network components and its contributing basin surfaces (Strahler, 1964). The mean stream length (L_{sm}) is calculated by dividing the total stream length of order by the number of streams.

3.1.4. Stream Length Ratio (RI)

The stream length ratio (RI) is defined as the ratio of mean stream length (L_u) of segment of order u , to mean stream segment length (L_{u-1}) of the next lower order $u-1$. The stream length ratios (RI) are changing haphazardly at the basin and sub-basin levels. The values of the RI vary from 0.394 to 0.613. It is noticed that the RI between successive stream orders of the basin vary due to differences in slope and topographic conditions. The RI has an important relationship with the surface flow discharge and erosional stage of the basin (Table 3b).

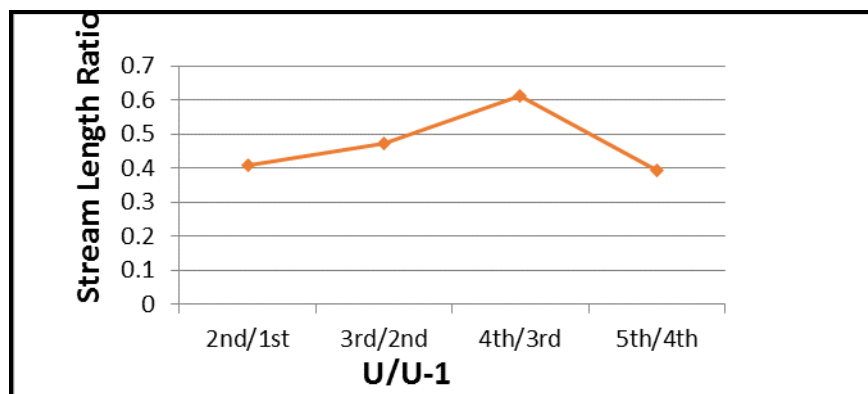


Figure 6: Stream Length Ratio Vs U/U-1

3.1.5. Bifurcation Ratio (Rb)

It is the ratio of the number of a given order to the number of streams of the next higher order (Schumm, 1956). Horton (1945) considered bifurcation ratio (R_b) as an index of relief and dissection. Strahler (1957) demonstrated that R_b show only a small variation for different regions on different environment except where powerful geological control dominates. Lower R_b values are the characteristics of structurally less disturbed watersheds without any distortion in drainage pattern (Nag, 1998). In this study area, mean R_b varies from 2 to 7 and the mean R_b of the entire basin is 4.355.

3.2. Aerial Aspects

Aerial Aspect includes drainage parameters such as Drainage Density (Dd), Drainage Texture (Dt), Stream Frequency (Fs), Form Factor (Rf), Circulatory Ratio (Rc), Elongation Ratio (Re).

Table 4: Aerial Aspect of Abdan Basin

| Basin | Drainage Density (D) | Stream Frequency (Fs) | Circularity Ratio (Rc) | Form Factor (Rf) | Elongation ratio (Re) | Drainage Texture(Rt) |
|-------------|----------------------|-----------------------|------------------------|------------------|-----------------------|----------------------|
| Abdan Basin | 0.873 | 0.349 | 0.436 | 0.315 | 0.633 | 1.974 |

3.2.1. Drainage Density (Dd)

Drainage density (Dd) expresses the closeness of spacing of channels. It is the measure of the total length of the stream segment of all orders per unit area. It is affected by factors which control the chrematistics length of the stream like resistance to weathering, permeability of rock formation, climate, vegetation etc (Langbein, 1947).

Slope gradient and relative relief are the main morphological factors controlling drainage density.

Strahler (1964) noted that low Dd is favored where basin relief is low, while high Dd is favored where basin relief is high. The Dd for the whole basin is 0.873 km/km².

3.2.2. Drainage Texture (Dt)

It is the total number of stream segment of all orders per perimeter of that area (Horton, 1945). Horton recognized infiltration capacity as the single important factor which influences drainage texture (Rt) and considered the drainage texture to include drainage density and steam frequency. The Rt of the whole basin is 1.974, shown in Table 3. Smith (1950) classified drainage density into five different texture i.e. very coarse (<2), coarse (2-4), moderate (4-6), fine (6-8), and very fine (>8). In the present study Basin has very coarse drainage texture as its drainage density is 1.974.

3.2.3. Stream Frequency (Fs)

Horton introduced stream frequency (Fs) or channel frequency which is the total number of stream segments of all orders per unit area (Horton, 1932). Hypothetically, it is possible to have the basin of same drainage density differing in stream frequency and basins of same stream frequency differing in drainage density. Reddy et al. (2004b) state that low values of Fs indicate permeable sub-surface material and low relief. The Fs of the whole basin is 0.349.

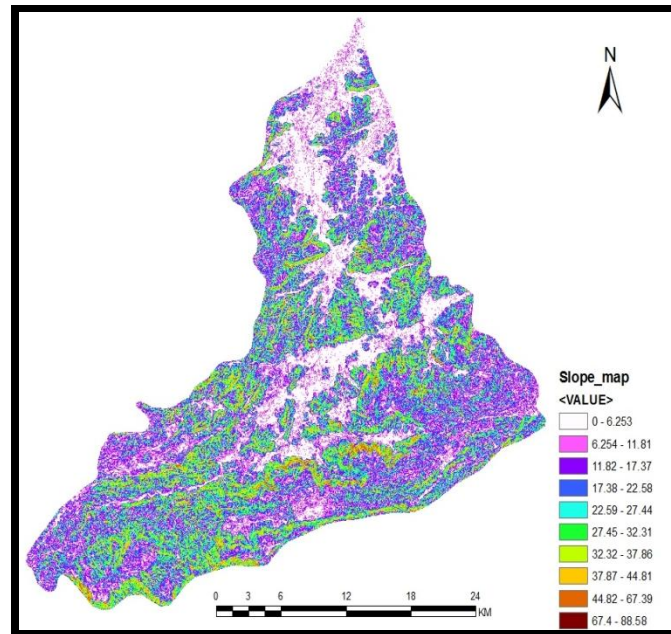


Figure 7: Slope Map of Abdan Basin

3.2.4. Form Factor (Rf)

Horton (1932) defined Form factor (Rf) as a dimensionless ratio of basin area (A) to the square of basin length (Lb). The value of Form factor would always be less than 0.7854 (for a perfectly circular basin). Smaller the value of form factors have high peak flows for shorter duration, whereas elongated basins with lower values of form factor have lower peak flow for longer duration. Flood flows of elongated basins with low form factor are easier to manage than those of the circular basins with higher values of form factor (Nautiyal, 1994). The Rf of the whole basin is 0.315.

3.2.5. Circularity Ratio (Rc)

Miller (1953) defined circulatory ratio (Rc) as the ratio of the area of the basin (A) to the area of circle having the same circumference as the perimeter of the basin (P). The circulatory ratio (Rc) is influenced by the length and frequency of streams, geological structures, land use/land cover, climate, relief and slope of the basin (Chopra et al, 2005). The circulatory ratio remained remarkably uniform in the range 0.6 to 0.7 for first order and second order basins in homogeneous shales and dolomites, indicating the tendency of small drainage basins in homogeneous geologic material to preserve geometrical similarity. However, first and second order basins situated on flanks of moderately dipping strata are strongly elongated with circularity ratio between 0.4 and 0.5 (Chow, 1964). The Rc of the whole basin is 0.436.

3.2.6. Elongation Ratio (Re)

It is the ratio between the diameter of the circle with the same area as that of the basin (A) and the maximum length (L) of the basin. A circular basin is more efficient in run-off discharge than an elongated basin (Singh and Singh, 1997). The value of elongation ratio (Re) generally varies from 0.6 to 1.0 associated with a wide variety of climate and geology. Values close to 1.0 are typical of regions of very low relief whereas that of 0.6 to 0.8 are associated with high relief and steep ground slope (Strahler, 1964). These values can be grouped into three categories, namely circular (>0.9), oval (0.9-0.8) and less elongated (<0.7). The Elongation Ratio (Re) for the basin is 0.633. The Re value indicated the basin to be elongated with high relief and steep slope.

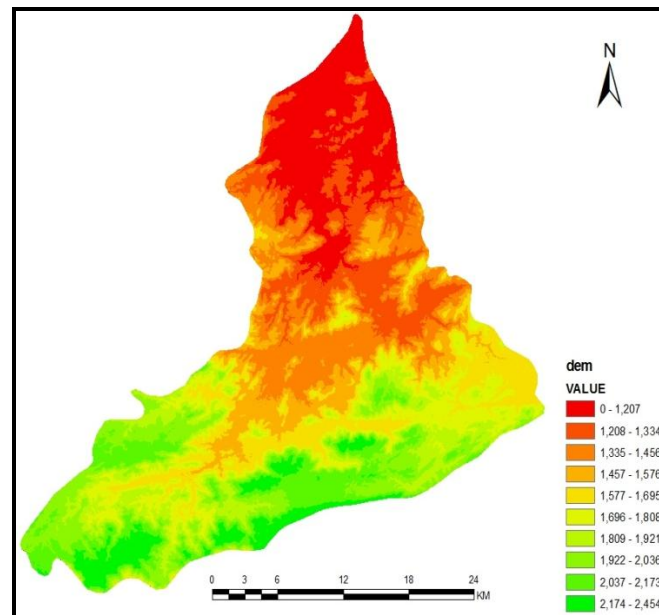


Figure 8: Digital Elevation Model of Abdan basin

3.2.7. Relief Aspect

Relief Aspect includes Relief Ratio, Length of Overland Flow, and Constant of Channel Maintenance (Table 5).

3.2.8. Relief Ratio (Rh)

The elevation difference between the highest and lowest points on the valley floor of a sub-watershed is its total relief, whereas the ratio of maximum relief to horizontal distance along the longest dimension of the basin parallel to the principal drainage line is Relief Ratio (Rh) (Schumm, 1956). It measures the overall steepness of a drainage basin and is an indicator of intensity of erosion processes operating on the slopes of the Basin. The Rh normally increases with decreasing drainage area and size of a given drainage basin (Gottschalk, 1964). Rh for the basin is 0.0216.

3.2.9. Length of Overland Flow

It is the length of water over the ground before it gets concentrated into definite stream channels (Horton, 1945). This factor relates inversely to the average slope of the channel and is quite synonymous with the length of sheet flow to a large degree. It approximately equals to half of reciprocal of drainage density (Horton, 1945). The Length of over land flow for whole basin is 0.572.

3.2.10. Constant of Channel Maintenance

Schumm (1956) has used the inverse of drainage density as a property termed constant of channel maintenance. It tells the number of sq.ft of watershed surface required to sustain one linear feet of channel. The Constant of channel maintenance of whole basin is 1.145.

Table 5: Relief aspects of Abdan Basin

| Basin | Infiltration number (If) | Elevation (km) | | Longest dimension of basin length(Km) | Relief (Km) | Relief Ratio (Rr) | Gradient Ratio (Gr) | Constant channel maintenance (C) | Length of overland flow (Lg) |
|-------------|--------------------------|----------------|-------|---------------------------------------|-------------|-------------------|---------------------|----------------------------------|------------------------------|
| | | Max | Min | | | | | | |
| Abdan Basin | 0.305 | 2.241 | 1.070 | 54.143 | .171 | 0.0216 | 0.022 | 1.145 | 0.572 |

4. Conclusion

The study of morphometric analysis of Abdan basin using Remote sensing and GIS software which are very help full to analysis the drainage basin easily and accurately. The study of linear aspects shows that the basin has formed subdendritic to subparallel type drainage pattern with highest order fifth. The study of area concluded that areas drained by drainage orders of 1st, 2nd and 4th have Bifurcation ratio between 2 to 4.276, indicating that these are not distorted by geological structures. The Bifurcation ratio in case of the 3rd order is 7. It is noted, in the drainage basin that this area is dominated by the presence of lineaments. The Drainage density (Dd) is 0.873 reveals that the subsurface strata are impermeable in Abdan basin. This is a characteristic feature of coarse drainage as the density values are less than 5.0. Lower order streams mostly dominate the basin. The form factor and elongation ratio value of the Abdan basin is 0.315 and 0.633 respectively, which indicated that the basin is sub-circular to elongate in shape and the major part of basin is of high relief. The length of overland flow is 0.572 which indicated young topography of the study area.

Acknowledgement

The corresponding author is very much thankful to Mohammad Alkutini, Ministry of Oil and Minerals, Shabowah Branch, Yemen. I am also very much thankful to Shadi Fadhl. I am also thankful to Department of Geology, Aligarh Muslim University for providing me lab facility.

References

- Ali, S.A. and Khan, N. *Evaluation of Morphometric Parameters- A Remote Sensing and GIS Based Approach*. Open Journal of Modern Hydrology. 2013. 3; 20-27.
- Ali, S.A., 1988: *Morphometric Analysis of the Hiyuni River Basin at Rishikesh, Garhwal Himalayas, India*. Proceedings of the IX Asian Conference on Remote Sensing, Bangkok, 23-29 November, B-9-1-B-9-8.
- Ali, U., and Ali, S.A. *Analysis of Drainage Morphometry and Watershed Prioritization of Romushi - Sasar Catchment, Kashmir Valley, India using Remote Sensing and GIS Technology*. I. Jour. of Advanced Research. 2014. 2 (12) 5-23.
- AL-Khribash, S., Takla, M., Abdul Wahed, M.S., and Sakran, Sh. *Tectonic Evolution of the Southeast Precambrian Basement Complex, Yemen*. Faculty of Science Bulletin-Sana'a University. 2001. 14; 67-83.
- Chow V.T., 1964: *Handbook of Applied Hydrology*. New York: McGraw Hill Inc.
- Clarke, J.I., 1966: *Morphometry from Maps*. Essays in Geomorphology. New York: Elsevier Publ. Co., 235-274.

Dornkamp, J.C., and King, C.A.M., 1971: *Numerical Analyses in Geomorphology, an Introduction*. New York: St. Martin's Press, 372.

Geological Survey & Minerals Resources-Yemen (GSY), 1990, 1978: Geological and Topographical maps of Abdan Area D-38-57, D-38-58, D-38-69, and D-38-70.

Gottschalk, L.C., 1964: Reservoir Sedimentation. In: Chow, V.T. (ed.) *Handbook of Applied Hydrology*, New York: McGraw Hill Book Company Section. 7-1.

Horton, R.E. *Drainage Basin Characteristics*. Transaction of American Geophysical Union. 1932. 13; 350-361.

Horton, R.E. *Erosional Development of Streams and their Drainage Basins: Hydrophysical Approach to Quantitative Morphology*. Bulletin Geological Society of America. 1945. 56; 275-370.

Langbein, W.B. *Topographic Characteristics of Drainage Basins*. Geological Survey of America. Water-Supply Paper. 1947. 986 (C) 157-159.

Magesh, N.S., Jitheshlal, K.V., Chandrasekar, N., and Jini, K.V. *GIS based Morphometric Evaluation of Chimmini and Mupily Watersheds, Parts of Western Ghats, Thrissur District, Kerala, India*. Earth Sci Inform. 2012b, 5; 111-121.

Mesa, L.M., *Morphometric Analysis of a Subtropical Andean Basin (Tucumam, Argentina)*. Environmental Geology. 2006. 50 (8) 1235-1242.

Miller, V.C. *A Quantitative Geomorphic Study of Drainage Basin Characteristics in the Clinch Mountain Area*. Virginia and Tennessee, Project Number 389-402. Technical Report-3, Columbia University, Department of Geology, New York, 1953.

Nag, S.K. *Morphometric Analysis using Remote Sensing Techniques in the Chaka Sub-Basin, Purulia District, West Bengal*. Journal of the Indian Society of Remote Sensing. 1998. 26 (1&2) 69-76.

Nag, S.K., and Chakraborty, S. *Influence of Rock Types and Structures in the Development of Drainage Network in Hard Rock Area*. Journal of the Indian Society of Remote Sensing. 2003. 31 (1) 25-35.

Nautiyal, M.D. *Morphometric Analysis of a Drainage Basin Using Aerial Photographs: A Case Study of Khairkuli Basin, District Dehradun, U.P.* Journal of the Indian Society of Remote Sensing. 1994. 22 (4) 251-261.

Obi Reddy, G.P., Maji A.K., and Gajbhiye K.S. *Drainage Morphometry and its Influence on Landform Characteristics in a Basaltic Terrain, Central India- A Remote Sensing and GIS approach*. Int J Appl Earth Obs Geoinfo. 2004. 6; 1-16.

Rajiv Chopra, Raman Deep Dhiman and Sharma, P.K. *Morphometric Analysis of Sub-Watersheds in Gurdaspur District, Punjab Using Remote Sensing and GIS Techniques*. Journal of the Indian Society of Remote Sensing. 2005. 33 (4) 531-539.

Rakesh, K., Lohani, A.K., Sanjay, K., Chatterjee, C., and Nema, R.K. *GIS Based Morphometric Analysis of Ajay River Basin up to Sarath Gauging Site of South Bihar*. Journal of Applied Hydrology. 2001. 14 (4) 45-54.

Reddy, O.G.P., Maji, A.K., and Gajbhiye, S.K. *Drainage Morphometry and its Influence on Landform Characteristics in a Basaltic Terrain, Central India- A Remote Sensing and GIS Approach*. International Journal of Applied Earth Observation and Geoinformatics. 2004b. (6) 1-16.

Schumm, S.A. *Evolution of Drainage Systems and Slopes in Badlands at Perth Amboy, New Jersey*. Bulletin of the Geological Society of America. 1954. 67; 597-646.

Singh, S., and Singh, M.C. *Morphometric Analysis of Kanhar River Basin*. National Geographical Journal of India. 1997. 43 (1) 31-43.

Sreedevi, P.D., Subrahmanyam, K., and Shakeel, A. *The Significance of Morphometric Analysis for Obtaining Groundwater Potential Zones in a Structurally Controlled Terrain*. Environmental Geology. 2005. 47 (3) 412-420.

Strahler, A.N. *Quantitative Analysis of Watershed Geomorphology*. Transactions of American Geophysical Union. 1957. 38; 913-920.

Strahler, A.N. *Quantitative Geomorphology of Drainage Basins and Channel Networks*. In: Chow, V.T. (ed). Handbook of Applied Hydrology. New York: McGraw Hill Book Company. 1964, Section 4-11.

Subba, Rao. *A Numerical Scheme for Groundwater Development in a Watershed Basin of Basement Terrain: A Case Study from India*. Hydrogeology Journal. 2009. 17; 379-396.

Soil Erosion and Sediment Yield Analysis Using Prototype & Enhanced SATEEC GIS System Models

Narasayya Kamuju

CWPRS, Pune, Maharashtra, India

Publication Date: 9 January 2016

DOI: <https://doi.org/10.23953/cloud.ijarsg.39>



Copyright © 2016 Narasayya Kamuju. This is an open access article distributed under the **Creative Commons Attribution License**, which permits unrestricted use, distribution, and reproduction in any medium, provided the original work is properly cited.

Abstract Rapid propagation of soil erosion is a severe worldwide problem because of its economic and environmental impacts. Thus various efforts have been made to evaluate soil erosion and sediment yield spatially and temporarily to develop effective soil erosion best management practices. To effectively estimate soil erosion and to establish soil erosion management plans, many computer models have been developed and used. In the past couple of decades, these soil erosion models have been integrated with Geographic Information System (GIS) for spatiotemporal analysis of generation and transport of soil erosion and sediment. The Revised Universal Soil Loss Equation (RUSLE) has been used in many countries, and input parameter data for RUSLE have been well established over the years. Thus, the GIS-based Sediment Assessment Tool for Effective Erosion Control (SATEEC) was developed to estimate soil loss and sediment yield for any location within a watershed using RUSLE and a spatially distributed sediment delivery ratio. In this paper SATEEC GIS System Ver.1.6 and version 1.8 were used for estimation of soil erosion and sediment yield. Moore & Burch 'LS' factor method and slope based SDR were used for estimation of soil erosion and sediment yield. The simulation results are reveals that SATEEC ver.1.6 exhibits 3 times more in quantity of soil erosion and sediment yield to SATEEC ver. 1.8.

Keywords SATEEC GIS System; R-Factor; RUSLE; Land Use/Land Cover; DEM

1. Introduction

Basically, soil erosion is a natural process by which materials are entrained and transported across the surface. As such, soil loss is the amount of material removed from a particular slope due to changes in topography, vegetation, and soil characteristics. Therefore, assessment of sediment yield is necessary to quantify the amount of eroded material that is actually transported from plot, field, channel or watershed [15]. Many soil erosion models like Universal Soil Loss Equation (USLE) [17], Soil and Water Assessment Tool (SWAT) [2], Water Erosion Prediction Project (WEPP) [3], and European Soil Erosion Model (EUROSEM) [9] have been developed to estimate soil erosion. Geographical Information System (GIS) enable users to analyze and manipulate the spatial data easily and it also helps users to identify the spatial locations vulnerable to soil erosion [7]. USLE Model has been widely used because the model is relatively easy to implement and its input data are available in most

countries [11]. Therefore USLE model has been integrated with GIS for spatio-temporal analysis of soil erosion by many researchers worldwide [18]. A GIS integrated prototype version of the 'Sediment Assessment Tool for Effective Erosion Control (SATEEC) [6] was developed with GIS interface to estimate soil erosion and sediment yield without additional input parameters other than those for the USLE model. With simple thematic maps as used for USLE, the SATEEC GIS system can estimate soil erosion and sediment yield at any point within the watershed. To reflect precipitation pattern for soil erosion estimate monthly and annual the enhanced SATEEC Ver. 1.8 was utilized. The most useful modification in SATEEC ver. 1.8 is time-variant soil erosion simulation with temporal USLE factors to reflect surface condition of land and precipitation in the form of 'C' and 'R' factors [11]. In the present study soil erosion estimation and sediment yield comparison has been performed using SATEEC GIS System Versions 1.6 and 1.8. For soil erosion calculations Moore & Burch method used for calculation of 'LS' factor for both versions of SATEEC GIS System models. To compare sediment yield slope based module was used for SATEEC GIS System Ver. 1.6 and Ver. 1.8 models.

2. Study Area

The study area is located in the western part of Doon valley, Dehradun district and Uttarakhand state in India. The sub-watershed 'SitlaRao', which is a sub-basin in 'Asan' watershed, is selected to run the erosion model. It belongs to Asan river system, which is tributary of Yamuna River. Geographical location of the study area covers (a total of) an approximately 50 sq km and lies between $77^{\circ}45'33''$ and $77^{\circ}57'46''$ and $30^{\circ}24'39''$ and $30^{\circ}29'05''$ as shown in Figure 1. The sub-basin of Sitlarao falls in SOI toposheet map no. 53F/15. The study area falls in western part of the Doon valley of Dehradun district having large area under hilly tract. The climate is humid to sub-tropical varying from valley to the high mountain ranges of Himalayas. During rainy season 1625 mm rainfall is observed in the year 2004. The mean temperature Ranges from 15.8° in winters to 33.3° in summer. The area has a favorable climate for the growth of abundant vegetation due to reasonably good rainfall & elevation Dense & moderate mixed forest, shrubs, agriculture crops. In the study area river terraces are mainly confined to narrow river valley and consisted of alluvium parent material derived from lesser Himalayas & comprises of sedimentary and meta-sedimentary rocks. It composed of gravels, pebbles, cobbles & boulders mainly of quartzite with fine sandy & silty matrix and fragments of shale, slate, phyllite, limestone, sandstone etc. Soils of the study area are found to be derived from alluvium parent material. These were observed, well to excessively drain with low to medium permeability and having texture sandy loam to clay loam with low to medium productivity.

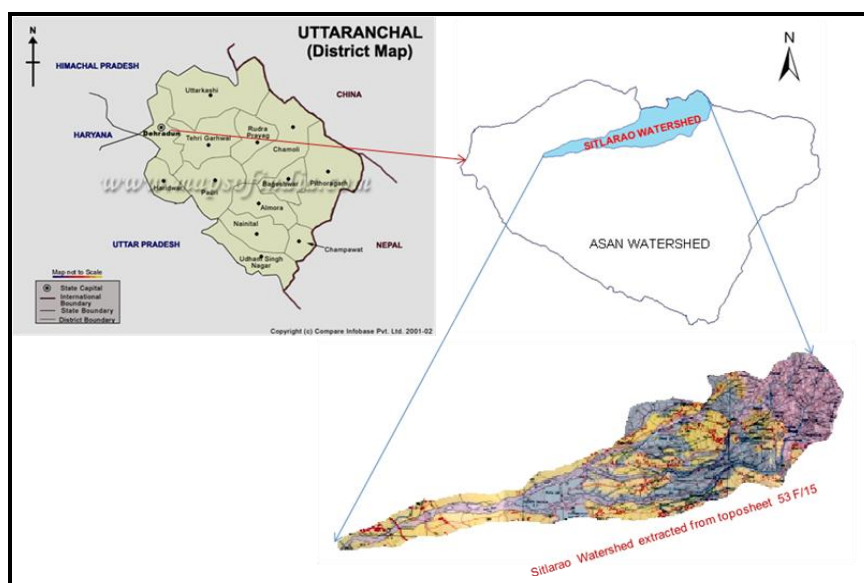


Figure 1: Location Map of Sitlarao Watershed

3. Materials

The successful running of the model depends on the preparation of data in the form of thematic layers. Basically SATEEC model required boundary map of the study area, digital elevation model (DEM), Land uses-land cover and soil data. Based on this basic data, thematic layers are prepared in ArcGIS environment and ERDAS imagine software. These thematic layers named as Rain erosivity factor map (R-factor), Soil erodability factor map (K-factor), Crop cover factor map (C-factor), Crop management factor map (P-factor). From DEM the 'LS factor' map derived from Moore & Burch method by SATEEC GIS system itself. All the thematic layers are arranged in Figure 2 as shown.

3.1. Climatic Data

Climatic data prepared from rain gauge stations available in the Sitlarao watershed. In order to prepare Rfactor map, rainfall data available from a Self-recording rain gauges at Langha village [5]. From the average annual rainfall, 'R-factor' is calculated from raster calculator available in spatial analyst tool. The rain gauge available in the watershed is shown in Figure 2a.

3.2. Soil Data

Soil data gathered form textural properties of soils covered in the watershed. A soil thematic layer prepared by using soil data available from Sitlarao watershed. A polygonised soil map prepared based on the types of soils covered in the catchment as shown in Figure 2b. There are 6 varieties of soil textural classes are identified from 'Sitlarao' sub-basin. These are Loam, Silt Loam, Sandy Loam, Sandy clay Loam, Gravelly clay loam, Loam to Sandy Clay Loam. The higher portion of the catchment covered with Loamy soils and a least area of soils are covered with loam to sandy clay loam.

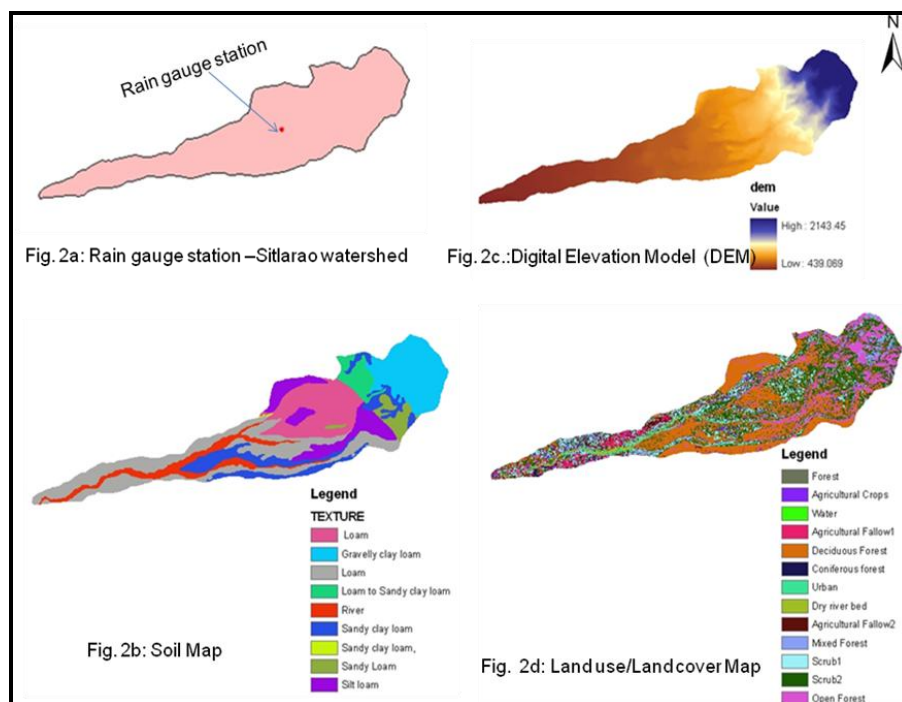


Figure 2: Input Thematic Layers Prepared for SATEEC GIS System Model

3.3. Dem

Dem the contour lines having vertical intervals of 20-meters were traced on tracing sheet by visual interpretation method from a toposheet No. 53 F/15 (scale 1:50,000 scale). This manually traced contour map was exported into GIS and digitized to prepare vector layer. Surfacing function in 'Image Interpreter' was used to generate a DEM & to represent as a surface or one-band image file where the value of each pixel was a specific elevation value. A gray scale was used to differentiate variations in terrain as shown in Figure 2c.

3.4. Land Use–Land Cover

Land use classification is prepared using a satellite image of Landsat TM acquired on 14 Nov 2004. There are 7 basic classes are identified under 'supervised classification' with ground truth data in sitlarao watershed as shown in Figure 2d. The basic classes are Agricultural crops, Fallow, Forest, Scrubland, Settlements, dry river bed sand, water and Tea gardens. The Land use-Land cover map is the basis for preparation of Crop cover (C-factor) and Crop Management (P-factor) factor maps.

4. Methodology

Development of effective erosion control plans requires the identification of areas vulnerable to soil erosion and quantification of the amounts of soil erosion from various areas. The RUSLE model does not consider the runoff process explicitly, nor soil detachment, transport, and deposition individually [14]. Eq. (1) shows how the RUSLE computes the average annual soil loss.

$$\text{Average annual soil loss, } A = R * K * L * S * C * P \quad \text{Eq. (1)}$$

Where,

A = average annual soil loss (ton/ha/year)

R = rainfall/runoff erosivity

K soil erodability

LS = slope length and steepness

C = cover management

P = support practice

The R-factor in RUSLE is composed of total storm kinetic energy (E) times the maximum 30 min intensity (I_{30}), and the numerical value of R is the average annual value for storm events for at least 22 years ([15] [17]). Hence, RUSLE cannot be used to estimate soil erosion and sediment yield for a single storm event. Rambabu et al. [13] developed a relationship between EI_{30} and daily and monthly rainfall amounts for Dehradun (India) region as given below:

$$EI_{30} = 3.1 + 0.533 * R_d \text{ (for daily rainfall in mm)}$$

$$EI_{30} = 1.9 + 0.640 * R_m \text{ (for monthly rainfall in mm)}$$

Based on regression equation, R can be determined from Eq. (2)

$$R = 22.8 + 0.6400 * R_a \quad \text{Eq. (2)}$$

Where,

R = Rainfall erosivity factor (in metric unit), and

R_a = Annual rainfall (mm)

Rain gauges installed at various meteorological observatories give depth of rainfall at that place. This point information can be converted to spatial distribution by IDW method in GIS environment. Once this IDW map is derived then by above formula, R factor map can be drawn and shown in Figure 3a.

RUSLE K factor indicating soil erodibility index (g / J) is the weight of soil detached from the soil mass per unit of rainfall energy. It is integrated effect of the processes that regulate rainfall acceptance and the resistance of the soil to particle detachment and subsequent transport. These processes are influenced by soil particle, of which soil texture is an important factor that influences erodibility. In this study soil erodibility factor are taken from [1].

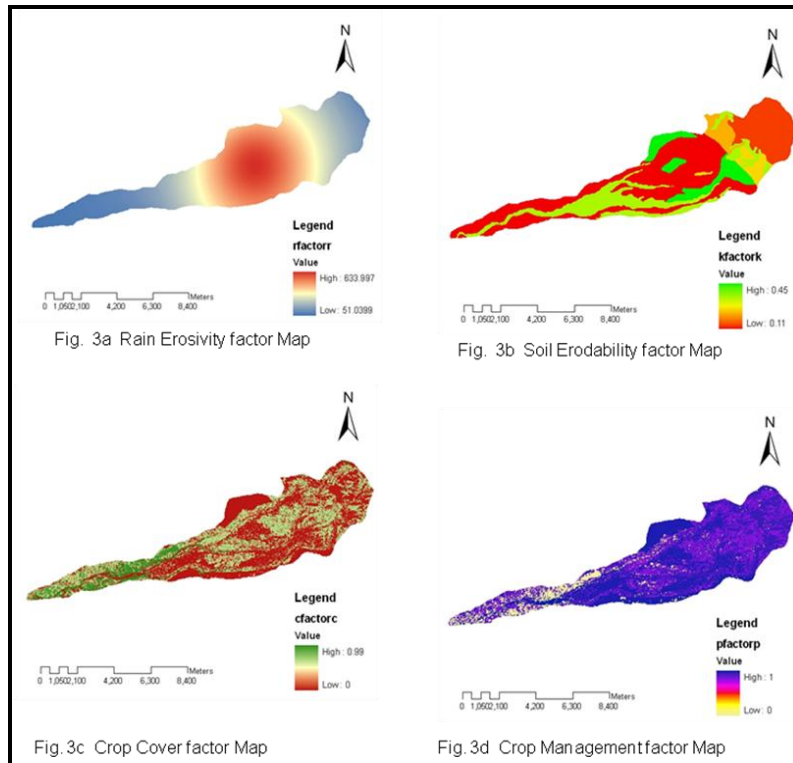


Figure 3: RUSLE Factor Maps

SATEEC computed the LS factor map based on DEM and the method suggested by Moore and Burch 1986 [8]. In this study Moore and Burch LS factor is used for the entire computations both in versions of SATEEC GIS system. The length of hill slope in the USLE experimental plots ranged from 10.7 m (35ft) to 91.4 m (300 ft), thus, it was recommended to use of slope lengths less than 122 m (400 ft) because overland flow becomes concentrated into the rills in less than 122 m (400 ft) under natural condition. The equation 3 (Eq. 3) utilized in this study [4].

$$LS = \left(\frac{A}{22.13} \right)^{0.6} \times \left(\frac{\sin \theta}{22.13} \right)^{1.3} \quad \text{Eq. (3)}$$

Then the RUSLE crop cover management (C-factor) reflects the effects on soil erosion of surface condition of watershed, rainfall drop impact and flow velocity are affected by the surface condition of watershed in real field. It has the range 0 to 1 as a fraction lower value indicates that the surface is covered well so that less soil erosion occurs, while higher value indicates that the surface is covered roughly which has higher possibility of much soil erosion. The prepared C-factor map is shown in Figure 3c. The overall methodology applied is drawn in flow chart and shown in Figure 4.

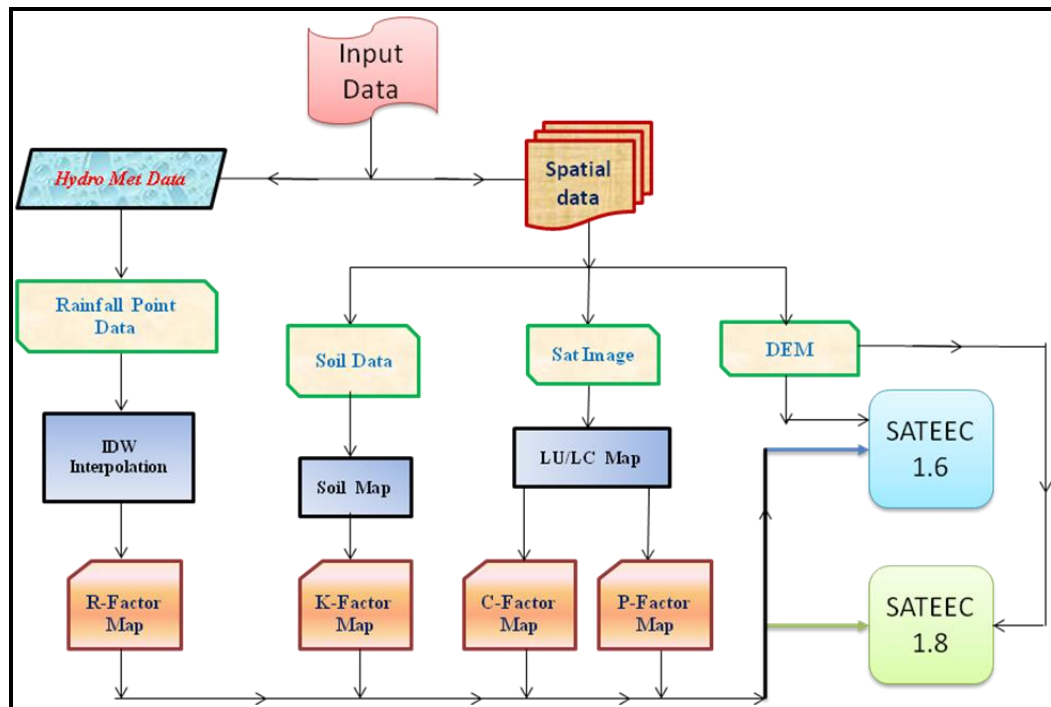


Figure 4: Flow Chart of Methodology

Conservation practice factor (P-factor) in the RUSLE model expresses the effect of conservation practices that reduce the amount and rate of water runoff, which reduce erosion. A “P factor” map was derived from the land use/land cover map, and each value of P was assigned to each land use/cover type and slope [1]. The attribute table in ArcGIS was used to reclassify the land use/cover according to its ‘P’ value. P-factor map which was prepared similar to ‘C’ factor map. The spatial distribution of P-factor map is shown in Figure 3d.

4.1. SDR

RUSLE is a field scale model, thus it cannot be directly used to estimate the amount of sediment reaching downstream areas because some portion of the eroded soil may be deposited while traveling to the watershed outlet, or the downstream point of interest. To account for these processes, the Sediment Delivery Ratio (SDR) for a given watershed should be used to estimate the total sediment transported to the watershed outlet. The SDR can be expressed from equation 4 as follows

$$\text{SDR} = \frac{\text{SY}}{\text{E}} \quad \text{Eq. (4)}$$

Where,

SDR = Sediment Delivery Ratio,

SY = Sediment Yield,

E = Gross Erosion for Entire Watershed.

The total soil loss for a given area is not the same as the sediment yield measured at a point of interest, such as a watershed outlet. To explain the possible deposition of eroded materials while they travel to the channel networks and eventually to the watershed outlet, the spatially distributed SDR is computed in the SATEEC GIS system. The SDR is related with physical characteristics of the watershed, such as size and shape of watershed, rainfall patterns, direct runoff, peak runoff, land use, cover crop, slope, particle size, and channel density [10]. Area-based SDR module provides convenience to estimate SDR with limited data collection for a given watershed. The SDR in the

watershed is affected by various geomorphologic properties such as average channel slope than watershed area. Thus, slope-based SDR module was incorporated into the SATEEC system to supplement limitation of area-based SDR module. The equation 5 for SDR based on slope of the watershed is given by [16]

$$\text{SDR} = 0.627 \times S^{0.403} \quad \text{Eq. (5)}$$

Where, S is slope of watershed.

However, the SDRs by slope-based SDR module were from 0.553 to 0.999 with varying slope from 0.73 % to 3.17 %. It indicates that the SDR is one of watershed-specific conditions, thus, better ways to estimate SDR needs to be developed based on various characteristics of watershed and measured data, not just based on single parameter such as only area or only slope. Three area based methods are used in SATEEC to compute the spatially distributed SDR map and it is out of scope study to discuss in details. In this study channel slope based-SDR values are utilized for both versions of SATEEC GIS system modules.

5. Application of SATEEC GIS System

The SATEEC GIS system acts as an extension for ArcView GIS 3.2a, with easy to use commands. The SATEEC GIS system estimates annual average soil loss by multiplying all USLE input parameter maps (e.g. R, K, LS, C, and P maps). The two erosion modules consist of SATEEC Soil Loss. All the procedures are fully automated with Avenue, CGI, and database programming; thus the enhanced SATEEC system does not require experienced GIS users to operate the system.

5.1. SATEEC ver. 1.6

The prototype version of the SATEEC GIS system was developed by 'Kyoung Jae Lim and Bernard A. Engel' Purdue university to provide an easy to use sediment assessment tool for soil erosion decision makers with Avenue programming within the ArcView GIS software. Thus, with several clicks of the mouse button with SATEEC menus, users can estimate the sediment yield for every cell within a watershed [6]. An overview of the prototype version of the SATEEC GIS system shown in Figure 5. Soil loss is estimated with RUSLE, and a spatially distributed sediment yield map is generated with RUSLE estimated soil loss multiplied by the spatially distributed sediment delivery ratio map.

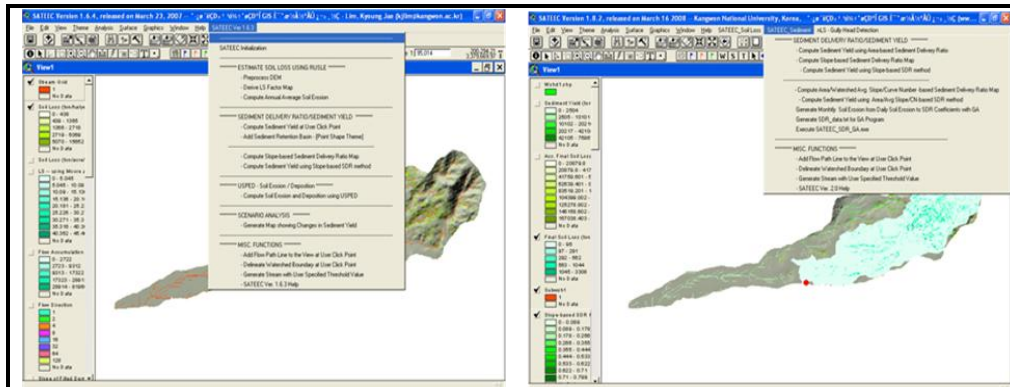


Figure 5: Over view of SATEEC GIS System ver. 1.6

Figure 7: Over view of SATEEC GIS System ver. 1.8

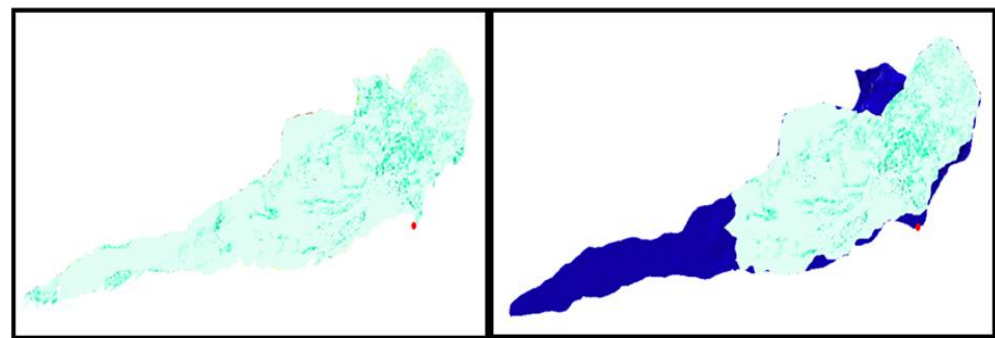


Figure 6: Spatial distribution of Sediment yield map - SATEEC ver. 1.6

Figure 8: Spatial distribution of Sediment yield map - SATEEC ver. 1.8

The total soil loss for a given area is not the same as the sediment yield measured at a point of interest, such as a watershed outlet. To explain the possible deposition of eroded materials while they travel to the channel networks and eventually to the watershed outlet, the spatially distributed SDR is computed in the SATEEC GIS system. In this study slope based SDR value has been used to compute and thus sediment yield estimated. The result map of sediment yield as shown in Figure 6.

5.2. SATEEC ver. 1.8

In similar way, SATEEC Ver. 1.8 is used for estimation of soil erosion and sediment yield for entire watershed by using Moore & Burch LS factor and channel-slope based SDR. The enhanced version of the SATEEC GIS system provides an overview as shown in Figure 7. The SATEEC estimated soil loss can be used to identify spatial locations vulnerable to soil erosion within the study area. This study carried with slope based SDR value to estimate sediment yield of the sitlarao watershed by dividing the entire basin into 20 sub-basins. The resultant spatially distributed sediment yield map is generated with RUSLE as shown in Figure 8.

6. Results and Discussions

The study aims to evaluate the applicability of an erosion model in mountainous terrain of Sitlarao watershed. In addition, it aims to determine spatial distribution of soil loss and sediment yield to analyze the utilization of different versions of ATEEC GIS system. The soil erosion obtained from SATEEC Ver. 1.6 a maximized value of 11,76,936 (ton/yr) and a lower value of 4,76,328 (ton/yr) soil erosion obtained from SATEEC ver. 1.8. The entire basin is divided into 20 sub-basins. The overall results are summarized and arranged in tabular format shown in Table 1.

Table 1: Summary of Results from both versions of SATEEC GIS System

| Sub-Basins | Area sq. km | SATEEC 1.6 | | | SATEEC 1.8 | | |
|------------|-------------|-------------|-----------|----------------|-------------|-----------|----------------|
| | | SDR | Soil Loss | Sediment Yield | SDR | Soil Loss | Sediment Yield |
| | | slope-based | (ton/yr) | (ton/yr) | slope-based | (ton/yr) | (ton/yr) |
| 1 | 27.1095 | 0.9611 | 911947 | 361231 | 0.39611 | 369399 | 146323 |
| 2 | 8.9323 | 0.276256 | 118205 | 32654.8 | 0.276256 | 47833.8 | 13214.3 |
| 3 | 9.50371 | 0.184922 | 20254.4 | 3745.48 | 0.184932 | 8206.68 | 1517.76 |
| 4 | 1.61823 | 0.468864 | 103664 | 48604.1 | 0.468864 | 41940.1 | 19664.2 |
| 5 | 0.012642 | 0.181522 | 1455.84 | 264.266 | 0.181522 | 589.651 | 107.034 |
| 6 | 0.279062 | 0.426928 | 4538.21 | 1937.49 | 0.426816 | 1836.36 | 783.788 |
| 7 | 0.23388 | 0.160657 | 39.6999 | 6.37806 | 0.14811 | 16.7769 | 2.48484 |
| 8 | 0.09 | 0.115591 | 17.9065 | 2.06983 | 0.115591 | 7.07621 | 0.81795 |
| 9 | 0.152155 | 0.17966 | 51.859 | 9.31696 | 0.17966 | 21.1954 | 3.80796 |
| 10 | 0.112289 | 0.106506 | 64.7158 | 6.8926 | 0.106506 | 25.6139 | 2.72803 |
| 11 | 0.21129 | 0.158134 | 46.9754 | 7.42839 | 0.158134 | 19.2021 | 3.0365 |
| 12 | 0.206639 | 0.148857 | 46.0784 | 6.8591 | 0.148857 | 21.3283 | 3.17487 |
| 13 | 0.151823 | 0.0898823 | 12.7903 | 1.14962 | 0.0898823 | 2.65773 | 0.238883 |
| 14 | 0.192353 | 0.124513 | 37.5737 | 4.67842 | 0.124513 | 14.983 | 1.86558 |
| 15 | 0.154813 | 0.18082 | 37.4408 | 6.77003 | 0.18082 | 15.5145 | 2.80533 |
| 16 | 0.145179 | 0.106552 | 44.3841 | 4.72924 | 0.106552 | 17.736 | 1.89382 |
| 17 | 0.164115 | 0.189607 | 167.072 | 31.678 | 0.189607 | 67.008 | 12.7052 |
| 18 | 0.112621 | 0.452129 | 7757.29 | 3507.29 | 0.442986 | 2835.7 | 1256.18 |
| 19 | 0.199994 | 0.402586 | 8478.03 | 3413.14 | 0.402586 | 3429.93 | 1380.84 |
| 20 | 0.094682 | 0.214496 | 70.2305 | 15.0641 | 0.214496 | 28.1055 | 6.02851 |

The highest sub-basin area of 27.10 sq.km contains a soil loss of 911947 (ton/yr) with SATEEC ver. 1.6 and for the same area of sub-basin delivered a soil loss of 369399 (ton/yr). The results obtained from both these SATEEC versions reveals that Prototype of SATEEC ver. 1.6 gives higher values as shown in Figure 9.

In this article slope based sediment delivery ratio value is used to estimate sediment yield at outlet point of the basin. The total sediment yield delivered at outlet of sitlarao basin is 455460 from SATEEC ver.1.6 and comparatively a lower value of 1,84,288 (ton/yr) obtained from SATEEC ver. 1.8. For the higher area of sub-basin, the sediment yield obtained 3,61,231 (ton/yr) from SATEEC ver. 1.6 and for the same area of sub-basin a value of 1,46,323 (ton/yr) from SATEEC ver.1.8. The comparison graph of sediment yield drawn in logarithmic scale for better discrimination visually between these two versions of SATEEC GIS system as shown in Figure 10.

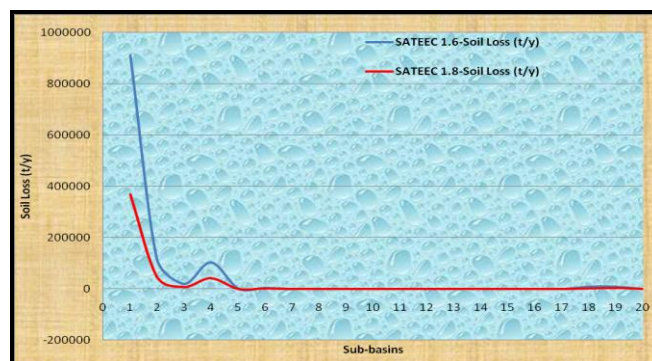


Figure 9: Soil Erosion Graph - SATEEC ver. 1.6 Vs SATEEC ver. 1.8

In all 20 sub-basins of sitlarao, SATEEC ver. 1.6 values of sediment yield is higher than SATEEC ver. 1.8. The higher sediment yield occur for higher SDR for SATEEC ver. 1.6. In case of SATEEC ver. 1.8 the highest sediment yield not occurred with highest SDR value. As per the basic equation of SDR, sediment yield is directly proportional to sediment delivery ratio.

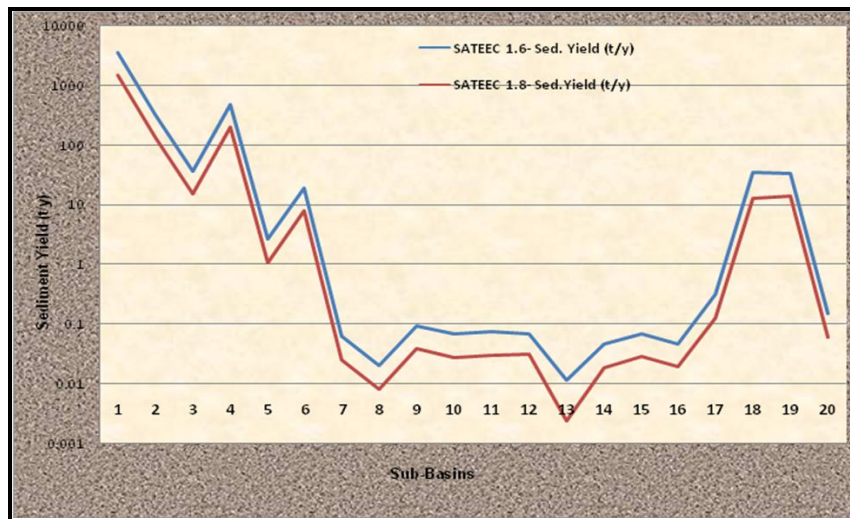


Figure 10: Sediment Yield Graph - SATEEC Ver. 1.6 Vs SATEEC ver. 1.8

As such, a comparative sediment delivery ratio (SDR) graph drawn between SATEEC ver. 1.6 and SATEEC ver. 1.8 as shown in Figure 11. The graph shows that prototype SATEEC version gives higher values at first two sub-basins. And these SDR values are slightly higher values than SATEEC ver. 1.8. A tremendous variation shown in SDR value at first sub-basin as 0.9611 in SATEEC ver. 1.6 and 0.3961 for SATEEC ver. 1.8

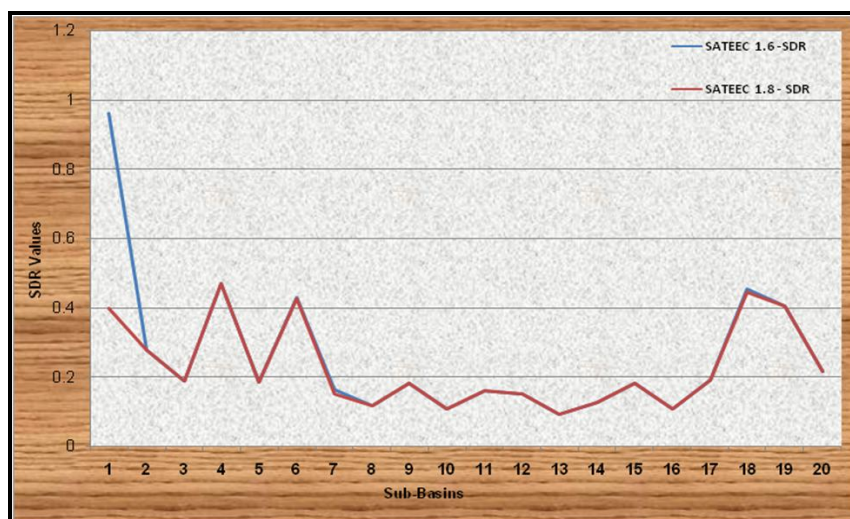


Figure 11: SDR Graph - SATEEC ver. 1.6 Vs SATEEC ver. 1.8

7. Conclusions

The Sitlarao watershed which is a sub-watershed of ASAN basin is taken to study for soil erosion and sediment yield using SATEEC GIS systems of versions 1.6 and 1.8. The average annual soil erosion from RUSLE equation obtained nearly 59.52% higher erosion takes place from SATEEC ver.1.6 than SATEEC ver. 1.8. Interestingly, 59.53% more sediment yield obtained than SATEEC ver. 1.8. The

overall results reveal that SATEEC ver. 1.6 gives higher values in terms of Average Annual Soil erosion and Sediment yield. The manual calculation of soil erosion and sediment yield using RUSLE for large areas or many sub-basins could be cumbersome and time consuming process, therefore an advanced GIS tool such as SATEEC GIS system is an appropriate application. However, soil erosion decision makers can be used to estimate soil loss and sediment yield, to identify areas vulnerable to soil loss, and to establish efficient erosion control plans with a fully automated menu driven system available in advanced GIS based geospatial tools of SATEEC ver. 1.6 & SATEEC ver. 1.8.

References

- [1] Pandey, V.M. Chowdary and B.C. Mal. *Identification of Critical Erosion Prone Areas in the Small Agricultural Watershed Using USLE, GIS and Remote Sensing*. Water Resources Management. 2007. 21. 729-746.
- [2] Arnold, J.G., Srinivasan, R., Muttiah, R.S., and Williams, J.R. *Large Area Hydrologic Modeling and Assessment Part I: Model Development*. Journal of American Water Resources Association. 1998 34 (1) 73-89.
- [3] Flanagan, D.C., and Nearing, M.A. 1995: *USDA Water Erosion Prediction Project: Hill Slope Profile and Watershed Model Documentation*. NSERL Report No. 10. USDA-ARS National Soil Erosion Research Laboratory, West Lafayette, IN 47907-1194.
- [4] Foster, G.R., Renard, K.G., Yoder, D.C., McCool, D.K. and Weesies, G.A., 1996: *RUSLE User's Guide*. Soil and Water Cons. Soc.
- [5] Kalpana O. Bhaware, 2006: *Soil Erosion Risk Modelling and Current Erosion damage Assessment using Remote Sensing and GIS Techniques*. M.Tech Thesis. Andhra University, T. 130.
- [6] Lim, K.J., Choi, J., Kim, K., Sagong, M., and Engel, B.A. *Development of Sediment Assessment Tool for Effective Erosion Control (Sateec) in Small Scale Watershed*. Transactions of the Korean Society of Agricultural Engineers. 2003. 45 (5) 85-96.
- [7] Lufafa, A., Tenywa, M.M., Isabirye, M., Majaliwa, M.J.G., and Woomer, P.L. *Prediction of Soil Erosion in a Lake Victoria Basin Catchment using a GIS-based Universal Soil Loss Model*. Agricultural Systems. 2003. 76; 883-894.
- [8] Moore, I. and Burch, G. *Physical Basis of the Length-Slope Factor in the Universal Soil Loss Equation*. Soil Science Society of America Journal. 1986. 50; 1294-1298.
- [9] Morgan, R.P.C., Quinton, J.N., Smith, R.E., Govers, G., Poesen, J.W.A., Auerswald, K., Chisci, G., Torri, D., and Styczen, M.E. *The European Soil Erosion Model (EUROSEM): A Dynamic Approach for Predicting Sediment Transport from Fields and Small Catchments*. Earth Surface Processes and Landforms. 1998. 23; 527-544.
- [10] Ouyang, D., and Bartholic, J., 1997: *Predicting Sediment Delivery Ratio in Saginaw Bay Watershed*. Proceedings of the 22nd National Association of Environmental Professionals Conference. May 19-23, 1997, Orlando, FL. 659-671.
- [11] Ouyang, D., and Bartholic, J., 2001: *Web-Based GIS Application for Soil Erosion Prediction*. Proceedings of an International Symposium—Soil Erosion Research for the 21st Century Honolulu, HI. Jan. 3-5.

- [12] Park, Y.S., Kim, J., Kim, N., Kim, K.S., Choi, J., and Lim, K.J. *Analysis of Sediment Yields at Watershed Scale using Area/Slope-Based Sediment Delivery Ratio in SATEEC*. Journal of Korean Society on Water Quality. 2007. 23 (5) 650-658 [in Korean].
- [13] Rambabu, Tejwani, K.K., Agrawal, M.C. and Bhusan, L.S., 1979: *Rainfall Intensity Duration-Return Equation and Nomographs of India*. CSWCRTI, ICAR, Dehradun, India.
- [14] Renard, K.G., Foster, G.R., Yoder, D.C., and McCool, D.K. *RUSLE Revisited: Status, Questions, Answers, and the Future*. Journal of Soil Water Conservation. 1994. 49; 213-220.
- [15] Renard, K.G., Foster, G.R., Weesies, G.A., McCool, D.K., and Yoder, D.C., 1997: *Predicting Soil Erosion by Water: A Guide to Conservation Planning With the Revised Soil Loss Equation (RUSLE)*. U.S. Dept. of Agriculture, Agric. Handbook No. 703.
- [16] Williams, J.R., and Berndt, H.D. *Sediment Yield Prediction Based on Watershed Hydrology*, Trans. of the ASAE. 1977. 20; 1100-1104.
- [17] Wischmeier, W.H., and Smith, D.D. 1978: *Predicting Rainfall Erosion Losses. A Guide to Conservation Planning*. The USDA Agricultural Handbook No. 537.
- [18] Yitayew, M., Pokrzywka, S.J., and Renard, K.G. *Using GIS for Facilitating Erosion Estimation*. Applied Engineering in Agriculture. 1999. 15 (4) 295-301.

Water Body Extraction Research Based on S Band SAR Satellite of HJ-1-C

Liu Liang^{1,2,3}, Zhang Wei^{2,3}, Jiang Xiaoguang¹, Li Xianbin⁴, Huo Hongyuan⁵, and Zhang Xuehua^{2,3}

¹University of Chinese Academy of Sciences, Beijing, China

²National Disaster Reduction Center of China, MCA, Beijing, China

³Satellite Application Center for Disaster Reduction, MCA, Beijing, China

⁴Institute of Optics and Electronics, Chinese Academy of Sciences, Chengdu, China

⁵College of Urban and Environmental Sciences, Tianjin Normal University, Tianjin, China

Publication Date: 10 February 2016

DOI: <https://doi.org/10.23953/cloud.ijarsg.43>



Copyright © 2016 Liu Liang, Zhang Wei, Jiang Xiaoguang, Li Xianbin, Huo Hongyuan, and Zhang Xuehua. This is an open access article distributed under the **Creative Commons Attribution License**, which permits unrestricted use, distribution, and reproduction in any medium, provided the original work is properly cited.

Abstract The C Satellite of Environment and Disaster Monitoring and Forecasting Small Satellite Constellation (HJ-1-C) was launched successfully on 19 November 2012. It is the first Synthetic Aperture Radar (SAR) satellite for civil use in China and the only S-band SAR satellite on orbit in the world at present. One of its applications is to extract water body, which can be used for assessing the severity of floods or drought. As the user of the S Band SAR Satellite of HJ-1-C, the National Disaster Reduction Center of China (NDRCC) has the responsibility to assess its water body extraction capability and precision. This study validates the water extraction precision using the HJ-1-C by means of comparison with water body delineation using optical images of the HJ-1-B and ZY-3. The result shows that, the C Satellite has a prominent advantage in extracting details of water bodies as compared with the HJ-1-A and HJ-1-B.

Keywords *HJ-1; SAR; S-Band; Water Body*

1. Introduction

Environment and Disaster Monitoring and Forecasting Small Satellite Constellation (HJ-1) is the first small satellite constellation that is specifically used on environment and disaster monitoring and forecasting, and the first civilian earth observation system with multiple satellites and multiple payloads in China. The “2+1” constellation consists of two small optical satellites (HJ-1-A, HJ-1-B) and one small radar satellite (HJ-1-C) [1]. HJ-1-A carries optical payloads and HJ-1-B carries multi-spectral camera (CCD), super-spectral camera (HSI), and infrared camera (IRS). After more than seven years’ operation, HJ-1-A and HJ-1-B have become irreplaceable data resources in the Chinese comprehensive disaster prevention and reduction operation system.

On 19 November 2012, the HJ-1-C was launched successfully in Taiyuan (Performance index as shown in Table 1). HJ-1-C is the first SAR satellite for civil use in China and currently the only on-orbit operation S-band SAR satellite in the world [2, 3]. At present, HJ-1-A, HJ-1-B, and HJ-1-C, the three

state-owned satellites that are specialized in Chinese disaster management work, stably operate on-orbit. This marks the establishment of environmental and disaster reduction satellite “2+1” constellation, which continuously provides remotely, sensed data in these fields.

Table 1: Performance Index of HJ-1-C

| Index | Performance |
|--------------------------|---|
| Polarization Mode | VV Polarization |
| Frequency | S-band |
| Spatial Resolution/Width | Scan : 20 m/100 km Strip : 5 m/40 km |
| Radiation Resolution | 3 dB |
| Observation Mode | Right side looking. Visual Angle: 25°–47° |

Flood disaster is one of the most important natural disasters in China. Flooding and waterlogging are the two main types of flood disasters. Flooding is caused by excessive water volume in rivers, lakes and coastal areas and water level rise and flashfloods due to heavy rains, snow and ice melting, dam bursts, storm surges, and other reasons. Waterlogging is due to excessive water and insufficient drainage, which is caused by heavy rains, rainstorms, or long-term concentrated water accumulation [4].

In order to assess the water monitoring capability of HJ-1-C, the Poyang Lake region in China is chosen as the study area in this study [5]. The Poyang Lake region is a typical flood-afflicted area. The lake is in the northern part of Jiangxi Province, on the southern bank of the middle and lower reaches of the Yangtze River. The lake is connected with the Ganjiang River, Fu River, Xinjiang River, Rao River, and Xiu River, receiving inflow from these five rivers and discharge water to the Yangtze River.

2. Method and Evaluation Standard of Water Extraction Accuracy Analysis

2.1. Water Extraction and Accuracy Analysis Method

The flow chart of the water extraction accuracy test is shown in Figure 1.

The specific method and process are as follows:

2.1.1. Image Processing

➤ Speckle Noise Suppression

Use speckle noise suppression algorithm based on the image features to suppress speckle noises in the images and improve the identification of targets.

➤ Geometric Correction and Registration

Use 1:50,000 topographic map, ground control points (GCP), or the same type of remote sensing data after geometric correction to correct geometric precision of HJ-1-C. GCP of each image should be uniformly distributed. Re-sample images of strip mode or scan mode to specify projection, directing and resolution.

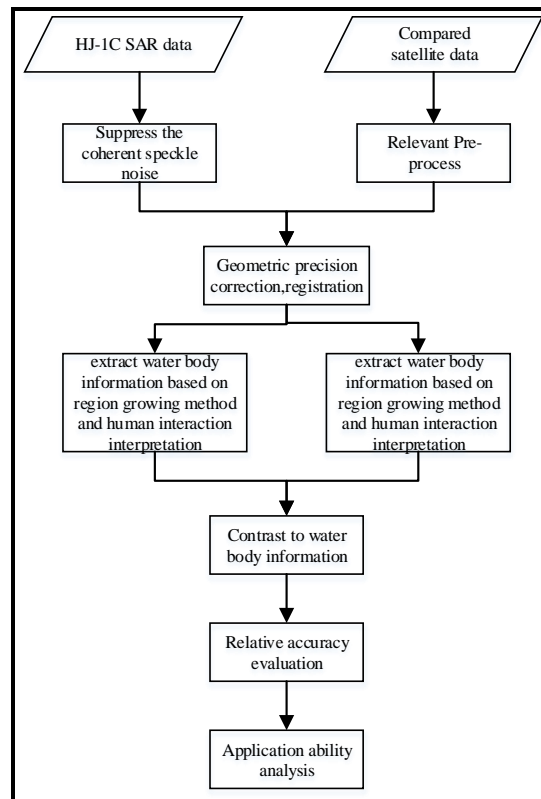


Figure 1: Flow Chart of Water Extraction Accuracy Analysis

2.1.2. Extraction of Water Body

Interpreting the data and extracting water bodies based on the region-growing method and threshold value method or interactive interpretation

2.1.3. Accuracy Analysis and Result Evaluation

Select monitoring results of HJ-1-B CCD image and ZY-3 optical images to relative precision analysis and result evaluation according to the situation actual damage, satellite transit and data quality. The overlapping area of water bodies extracted through the test data and in the reference data is drawn. Through comparison analysis, the relative precision of water extraction using HJ-1-C is evaluated.

2.1.4. Application Capability Analysis

Applicability of flood water extraction using HJ-1-C data for disaster monitoring and assessment is analyzed in the final step.

2.2. Evaluation Standard

Integrity rate, accuracy rate, false rate and missing rate are selected as evaluation standard in this study.

2.2.1. Test Data

(A) Scan Mode

Parameters of the test data of HJ-1-C in scan mode is shown in Table 2. The data used for precision validation of the extraction result is HJ-1-B CCD optical image with 30 m spatial resolution, which were obtained on 8 March 8 2013, when the most recent cloud-free HJ-1-C data for the study area were acquired.

Table 2: Test Data Parameters, HJ-1-C (Scan Mode)

| Parameter Type | Value |
|---------------------------|---------------------------------|
| Imaging time | 2013-03-11 18:12:18 |
| Imaging mode | Scan |
| Incidence angle (degrees) | 34.0616,36.1216,37.8016,39.3716 |
| Orbital direction | Rising Orbital |
| Equivalent number | 2.081 |
| Radiation resolution(dB) | 3.879 |
| Dynamic range (dB) | 24.984 |

(B) Strip Mode

Parameters of the test data of HJ-1-C (strip mode) is shown in Table 3. The data used for precision validation of the extraction result is ZY-3 optical image with 5.8 m spatial resolution, which were obtained on 18 January 2013, when the most recent cloud-free HJ-1-C data for the study area were acquired.

Table 3: Test Data Parameters, HJ-1-C (Strip Mode)

| Parameter Type | Value |
|---------------------------|---------------------|
| Imaging time | 2013-01-22 06:15:46 |
| Imaging mode | Strip |
| Incidence angle (degrees) | 37.2712 |
| Orbital direction | Falling Orbital |
| Equivalent number | 0.768 |
| Radiation resolution(dB) | 2.733 |
| Dynamic range (dB) | 108.165 |

2.2.2. Test Results

(A) Scan Mode

Remote sensing monitoring of the HJ-1 constellation for the Poyang Lake test area (scan mode) is shown in Figure 2. Comparison of the SAR and CCD extraction results and analysis are shown in Figure 3. Statistics of water extraction result is shown in Table 4. Error result is shown in Table 5.

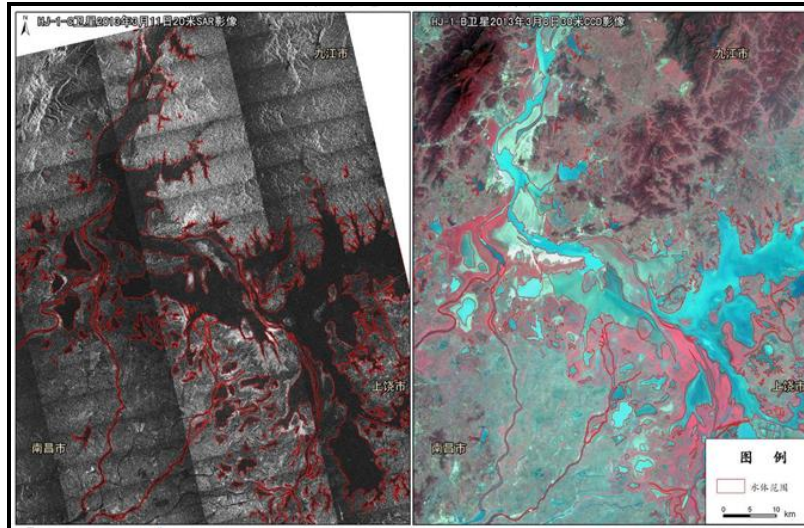


Figure 2: Remote Sensing Monitoring of Water Bodies in the Poyang Lake Area – Scan Mode
 (Left: Water Body Extraction Result of HJ-1-C SAR Image; Right: Water Body Extraction Result of False Color Composite Image of HJ-1-B CCD with Red: Band4, Green: Band3, Blue: Band2)

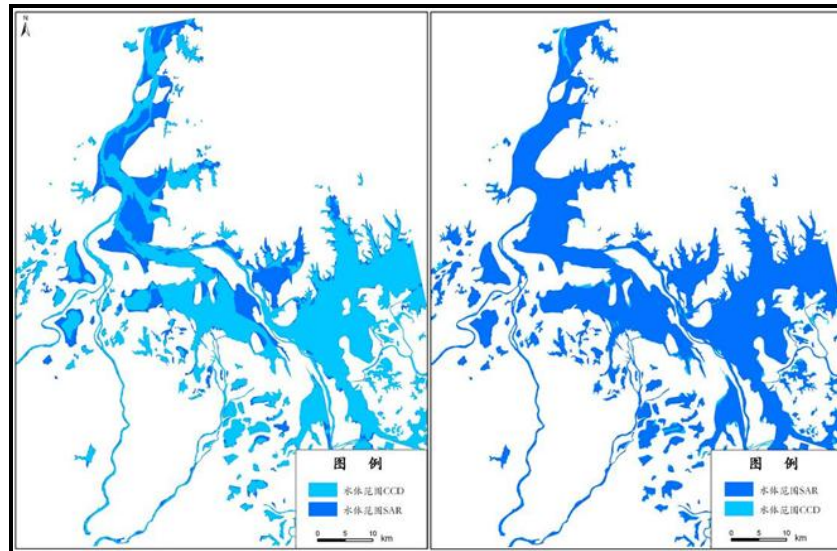


Figure 3: Water Range of the Poyang Lake Area – Scan Mode

Table 4: Water Extraction Result Statistical Table – Scan Mode (Unit: km²)

| | HJ-1-C 2013-03-11 | HJ-1-B 2013-03-08 |
|--|----------------------|----------------------|
| Extracted water record (number) | 218 | 306 |
| Water area (km ²) | 1591.79 | 1286.88 |
| Minimum effective water area (m ²) | 14909 | 269 |
| Accurate extracted area (km ²) | 1150.54 | |

Table 5: Error Table – Scan Mode

| Integrity Rate | Accuracy Rate | False Rate | Missing Rate |
|------------------|------------------|------------|--------------|
| =1150.54/1286.88 | =1150.54/1591.79 | =1-72.28% | =1-89.41% |
| =89.41% | =72.28% | =27.72% | =10.59% |

The acquisition time of the HJ-1-C SAR data was three days after the HJ-1-B CCD. Assuming the change of water scope in the test area over these three days was negligible, the water body extraction result of the HJ-1-B CCD was used as reference for comparison/validation. Through contrasting the extracted water bodies from the HJ-1-C SAR and HJ-1-B CCD, two types of errors in the result of the HJ-1-C SAR are identified.

The first type of error of extraction is false information, which indicated no water in the water body extraction result of CCD but water in the extraction result of SAR. In the SAR image, these areas are the flood plains or the margin of the water bodies without very clear water and land boundary. These two types of areas both have higher soil moisture, which are dark in the SAR image, so they are falsely interpreted as water area (Figure 4).

The second type of error of extraction is missing information, which indicated water in the extraction result of CCD, but no water in the extraction result of SAR. In the CCD image, these areas are shows as narrow river channels, small water areas, or the area of poor image SNR are regarded as water area, which cannot be identified by image intensity contrast difference of beam adjacent area of scan mode image. These areas are misinterpreted in the SAR image as no water (Figure 5). So it can be inferred that in this test area, under the data quality of the test image (HJ-1-C SAR of 20 m spatial resolution with scan mode) and by using the region-growing method, threshold value method, or interactive interpretation, the extracted water area is slightly smaller than the HJ-1 constellation CCD image of 30 m spatial resolution.

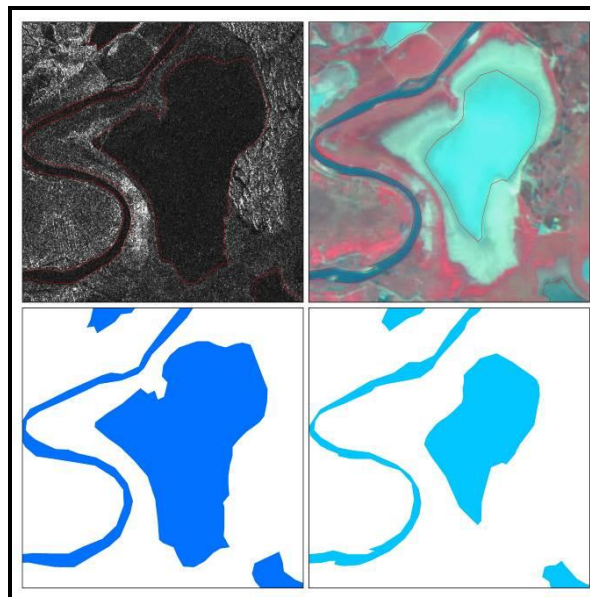


Figure 4: Extraction Error: False Information – Scan Mode
(Upper Left: SAR Image; Upper Right: Optical Image; Lower Left: Extraction Result of SAR Image; Lower Right: Extraction Result of Optical Image)

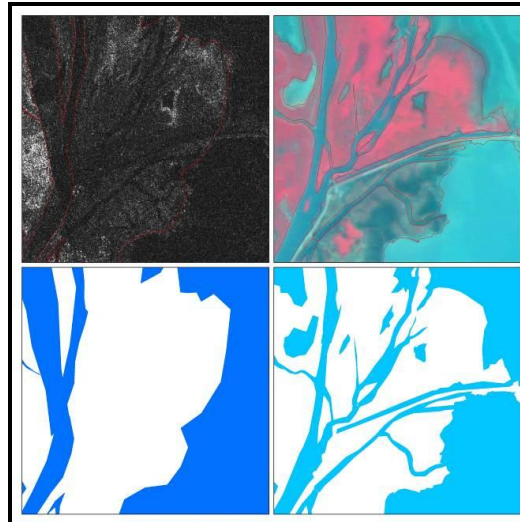


Figure 5: Extraction Error: Missing Information – Scan Mode

(Upper Left: SAR Image; Upper Right: Optical Image; Lower Left: Extraction Result of SAR Image; Lower Right: Extract Result of Optical Image)

(B) Strip Mode

Remote sensing monitoring of HJ-1 constellation for the Poyang Lake test area (strip mode) is shown in Figure 6. We compared and analyzed the extraction results of the SAR and multispectral image. Contrast analysis of the extraction results of water range is shown in Figure 7. Statistics of water extraction result is shown in Table 6. Error result is shown in Table 7.

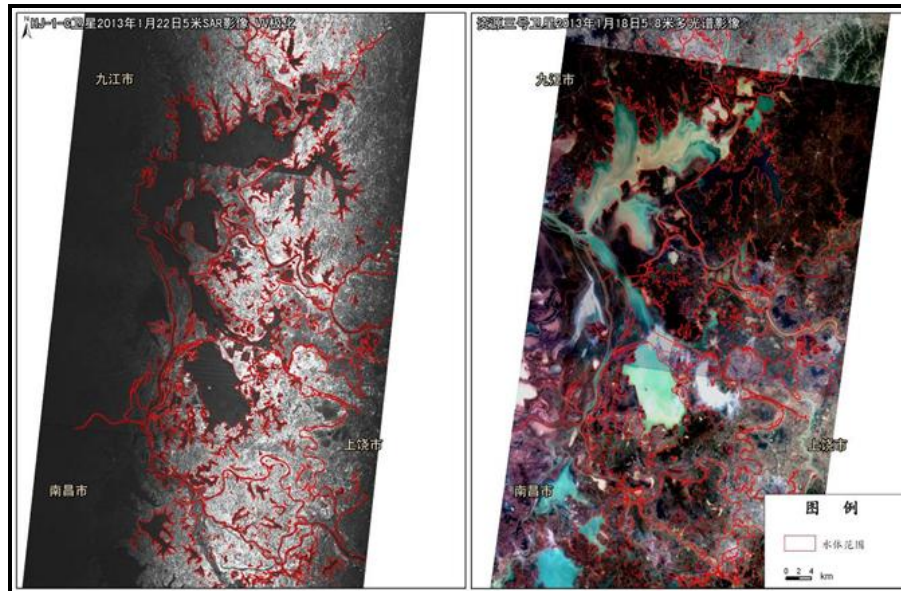


Figure 6: Remote Sensing Monitoring of Water Bodies in the Poyang Lake Area – Strip Mode

(Left: Water Body Extraction Result of HJ-1-C SAR Image; Right: Water Body Extraction Result of True Color Composite Image of ZY-3 with Red: Band3, Green: Band2, Blue: Band1)

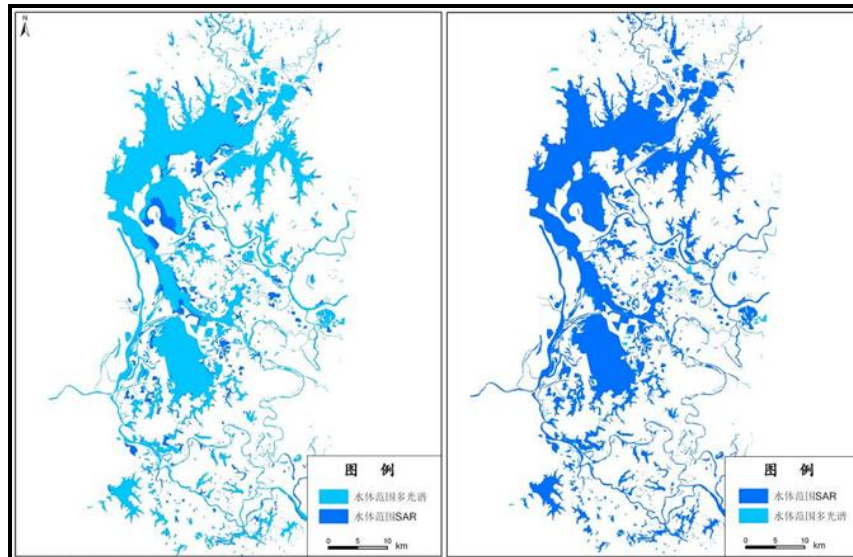


Figure 7: Water Range of the Poyang Lake Area – Strip Mode

Table 6: Water Extraction Result Statistical Table – Strip Mode (Unit: km²)

| | HJ-1-C 2013-01-22 | ZY-3 2013-01-18 |
|---|----------------------|--------------------|
| Extracted water record (number) | 1077 | 1645 |
| Water area (km ²) | 879.29 | 779.40 |
| Minimum effective water area(m ²) | 734 | 296 |
| Accurate extracted area(km ²) | 746.20 | |

Table 7: Error Table – Strip Mode

| Integrity Rate | Accuracy Rate | False Rate | Missing Rate |
|----------------|----------------|------------|--------------|
| =746.20/779.40 | =746.20/879.29 | =1-84.86% | =1-95.74% |
| =95.74% | =84.86% | =15.14% | =4.26% |

The acquisition time of the HJ-1-C SAR was four days later than the optical image from ZY-3. Disregarding the change of water scope in the test area over these four days and misinterpretation of water information because of cloud cover for small areas in the ZY-3 optical image, the extraction result of ZY-3 optical image was considered more accurate. Through the comparison of water body extraction results of HJ-1-C SAR and ZY-3 optical images, two types of errors in the result of HJ-1-C SAR are identified.

The first type is false information, which indicated no water in the extraction result of the multispectral image, but water in the extraction result of the SAR. In the SAR image, these areas are flood plains or the margin of water bodies without very clear water and land boundary. These areas both have higher soil moisture, which are dark in the SAR image, so they are falsely interpreted as water area (Figure 8).

The second type of error is missing information, which indicates water in the extracting results of multi-spectral image, but indicates no-water in the extracting results of SAR. In multi-spectral image, these area shows as the thin river or small water area, which are missing to be interpreted in SAR image (Figure 9). So it can be inferred, in this test area, under the data quality of this image, by using region-growing method and threshold value method or interactive interpretation, according to water

information extracting, the information extraction fine degree of HJ-1-C SAR of 5m spatial resolution of strip mode is slightly less than ZY-3 CCD multi-spectral image of 5.8m spatial resolution.

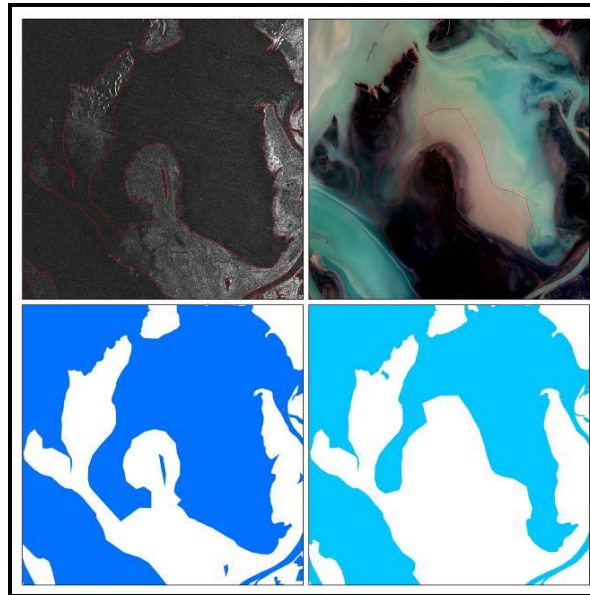


Figure 8: Extraction Error: False Information – Strip Mode
(Upper Left: SAR Image; Upper Right: Optical Image; Lower Left: Extraction Result of SAR Image; Lower Right: Extraction Result of Optical Image)

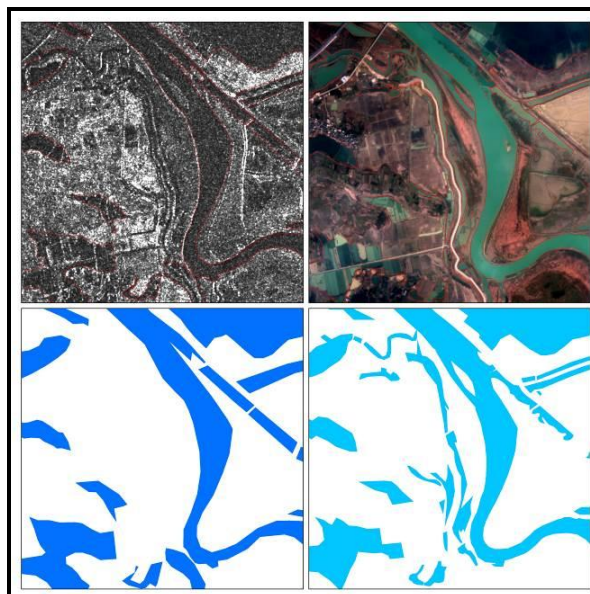


Figure 9: Extraction Error: Missing Information – Strip Mode
(Upper Left: SAR Image; Upper Right: Optical Image; Lower Left: Extraction Result of SAR Image; Lower Right: Extract Result of Optical Image)

3. Conclusions and Prospects

In this study, the scan mode and strip mode of HJ-1-C SAR data were both selected to extract water body range in the Poyang Lake area. A HJ-1-B CCD image and a ZY-3 multispectral image were selected to validate the monitoring result of HJ-1-C. The results indicate that the HJ-1-C satellite generally respond well to water bodies, which is shown as dark regions. It can be effectively used for

the delineation of water distribution, and can accurately distinguish low soil humidity areas and floodplains, so it has good application potentials in monitoring flood inundated areas. At the same time, areas of relatively high soil humidity or flat floodplains that show the same spectral characteristics as water bodies can easily lead to false judgment, resulting in larger water area than is the actual case. Information extraction from image of the strip mode presents the flooding situation much better than the scan mode.

In the future, we will continue to carry out research in the following areas to further explore the application potential of the S-band SAR satellite in disaster reduction: (1) Field validation and joint interpretation of multiple data sources to examine the false interpretation areas in order to increase the precision of water range extraction; (2) Calculation of soil humidity through analyzing the backscatter coefficient and inference of water area post-flood disaster to fully take advantage of the SAR for disaster reduction and relief applications.

References

- [1] Bai, Z.G. *HJ-1A and HJ-1B of Environment and Disaster's Monitoring and Forecasting Small Satellite Constellation*. Aerospace China. 2009. 5; 10-15.
- [2] Wang, L. and Zhang, W. *The Operation Management and Disaster Reduction Application Potential Analysis for HJ-1-C*. Disaster Advances. 2014. 7 (7) 28-34.
- [3] Liu, Y.T., 1999: *Radar Imaging Technology [M]*. Harbin: Harbin Institute of Technology Press.
- [4] Zhang, W., Yang, S.Q. and Wang, L. *Review on Disaster Reduction Application Potentiality of Synthetic Aperture Radar*. Remote Sensing and Application. 2012. 27 (6)100-107.

Assessment of Groundwater Vulnerability – A Case Study

Mohamed R. El Tahlawi, Mohamed Abo-El Kassem, Gamal Y. Baghdadi, and Hussein A. Saleem

Mining and Metallurgical Engineering Department, Faculty of Engineering, Assiut University, Assiut City, Egypt

Publication Date: 22 February 2016

DOI: <https://doi.org/10.23953/cloud.ijarsg.79>



Copyright © 2016 Mohamed R. El Tahlawi, Mohamed Abo-El Kassem, Gamal Y. Baghdadi, and Hussein A. Saleem. This is an open access article distributed under the **Creative Commons Attribution License**, which permits unrestricted use, distribution, and reproduction in any medium, provided the original work is properly cited.

Abstract Two DRASTIC models have been used in this study, which are generic and pesticide to get the groundwater vulnerable levels to pollution in the Nile aquifer along Assiut governorate. Groundwater vulnerability maps were produced using Geographic Information Systems (GIS). It has been found in map of generic DRASTIC model that the most of the study area is covered by moderate vulnerable and high vulnerable; where 55.2 % of the area is moderately vulnerable and 35.4 % has high level of vulnerability. However in the vulnerability map generated by pesticide DRASTIC model, the results concluded that about 64% of the study area has an extreme to high vulnerability to contamination, 34.6% has a moderate vulnerability and small areas occupy about 1.4% and has a low vulnerability.

Keywords *Groundwater Vulnerability; Generic DRASTIC; Pesticide DRASTIC; Geographic Information Systems (GIS)*

1. Introduction

There is a rising awareness of monitoring groundwater pollution since consumption of groundwater in agriculture, industry, and domestic use has increased. Due to the high-cost of groundwater contamination monitoring in huge parts, the usage of modeling methods such as DRASTIC model with GIS has become a must to assess groundwater potential to pollution. Groundwater resources of Assiut, Egypt face a very serious problem which is contamination from agricultural and urbanization activities. In the previous decades, researchers working in groundwater pollution assessment have focused on limited areas in Assiut governorate by using traditional methods such as chemical and bacterial analysis (Sobih et al., 1988) [1]; Abdel-Lah and Shamrukh, 2001 [2]), and electrical resistivity measurement (Bakheit et al., 1993 [3]; Ebrahim, 1997 [4]; Sebaq et al., 2003 [5]; Mohamaden et al., 2009 [6]). Ebrahim (1997) [4] used Schlumberger geoelectrical depth soundings and horizontal geoelectrical profiling to determine the distribution of the contaminated and uncontaminated zones of groundwater in (El-Madabegh) area, northwest of Assiut city. Sebaq et al. (2003) [5] used surface geoelectrical methods for delineation of groundwater pollution in Beni Ghaltib area, northwest of Assiut city. Mohamaden et al. (2009) [6], carried out Forty-two vertical electrical soundings (VES.'s), using Schlumberger array in Assiut area in order to elucidate hydrogeological information and delineate

subsurface structural elements. However in this paper groundwater pollution potential is being studied all over Assiut governorate though using newly updated method represented in DRASTIC model and geographic information systems (GIS).

A groundwater vulnerability analysis classifies areas where groundwater is possible to be polluted as an effect of different activities. The purpose of vulnerability investigation is to protect groundwater quality through spotting the light on those vulnerable areas by decision makers. Groundwater vulnerability can be assessed throughout three different ways: (1) site-specific evaluation by hydrogeologists, (2) pesticide destiny, and (3) index methods [7]. DRASTIC model has been chosen as one of the most well-known index methods because it is more flexible and economic.

DRASTIC model has been developed by the U.S. Environmental Protection Agency in 1987 as an implement to evaluate groundwater vulnerability. The word DRASTIC is an acronym formed the initial letters of the seven factors which are used for determining relative rankings. (D) refers to Depth to water, (R) refers to net Recharge, (A) refers to Aquifer media, (S) refers to Soil media, (T) refers to Topography, (I) refers to Impact of the vadose zone media, and (C) refers to hydraulic Conductivity of the aquifer [8]. For GIS is “a powerful set of tools for storing and retrieving at will, transforming and displaying spatial data from the real world for a particular set of purposes” [9], it has been used for assessing groundwater vulnerability based on DRASTIC model.

The factors used to assess groundwater vulnerability differ according to available data. Schmidt (1987) [10] used five factors to develop a GIS weighting model which are type of bedrock, depth to bedrock, depth to water table, soil characteristics, and surficial deposit characteristics. Nebert and Anderson (1987) [11] used another five factors which are land cover, soil media, precipitation, geological properties, and shallow aquifers to evaluate groundwater contamination potential through pesticides by GIS to build a database. Petersen et al. (1991) [12] applied GIS to assess non-point pollution using topography, farm animal density, soils, precipitation, land cover, and a rainfall-runoff factor. Atkinson et al. (1992) [13] used seven factors representing the DRASTIC model and a GIS to evaluate groundwater vulnerability. Zhang et al., (1996) [14] used DRASTIC model and GIS to determine groundwater pollution potential through applying several parameters which are groundwater depth, net recharge, Aquifer media, impact of vadose zone, soil media, topography, and hydraulic conductivity.

Al-Adamat et al., (2003) [15], used GIS and DRASTIC model to generate groundwater vulnerability map and risk map by including six factors out of seven DRASTIC factor except the hydraulic conductivity of the aquifer because of sufficient quantitative data shortage, while Thapinta and Hudak (2003) [16] used five factors including soil media, topography, land use map, depth to water, and rainfall in Geographic information systems (GIS) to estimate groundwater vulnerability to pesticide pollution. GIS as a technique can be used alone or accompanied by other image processing software such as ILWIS "Integrated Land and Water Information System" and ERDAS imagine "Earth Resources Data Analysis System". Rahman (2008) [17] used Arcview 3.2a as GIS software with (ILWIS 3.0) to determine the groundwater vulnerable zones in shallow aquifers using the DRASTIC model. It is obvious that GIS play a significant function in assessing and expecting the groundwater pollution potential.

2. Study Area

Assiut governorate is considered as a part of the Nile Valley, Egypt. It reaches the northern edge of Sohag Governorate at latitude 27°37' N and extends the southern edge of El-Minia Governorate at latitude 26° 47' N. It is bordered between longitudes 30° 37' - 31° 34' E, as shown in Figure 1. The total area of Assiut governorate is 25,926 km². The length of the River Nile along Assiut governorate area is approximately 125 km, and the valley width varies between 16 and 60 km [18].

The study area includes populated and agriculture areas in Assiut governorate cover up an area of about 2674.54 km². River Nile divides the study area into a western and an eastern part. In general, the land surface in the fringes of both parts slopes towards the River Nile. The sharp declination is the main feature of the fringes of the study area because of the limestone plateau which limits the area from the east and the west, except of the Northwestern part that has a moderate slope [19]. There are some wadies joined with the study area like: Wadi El-Assiuti and Wadi El Ibrahimy in the central east, Wadi Abu Shih in the south east.

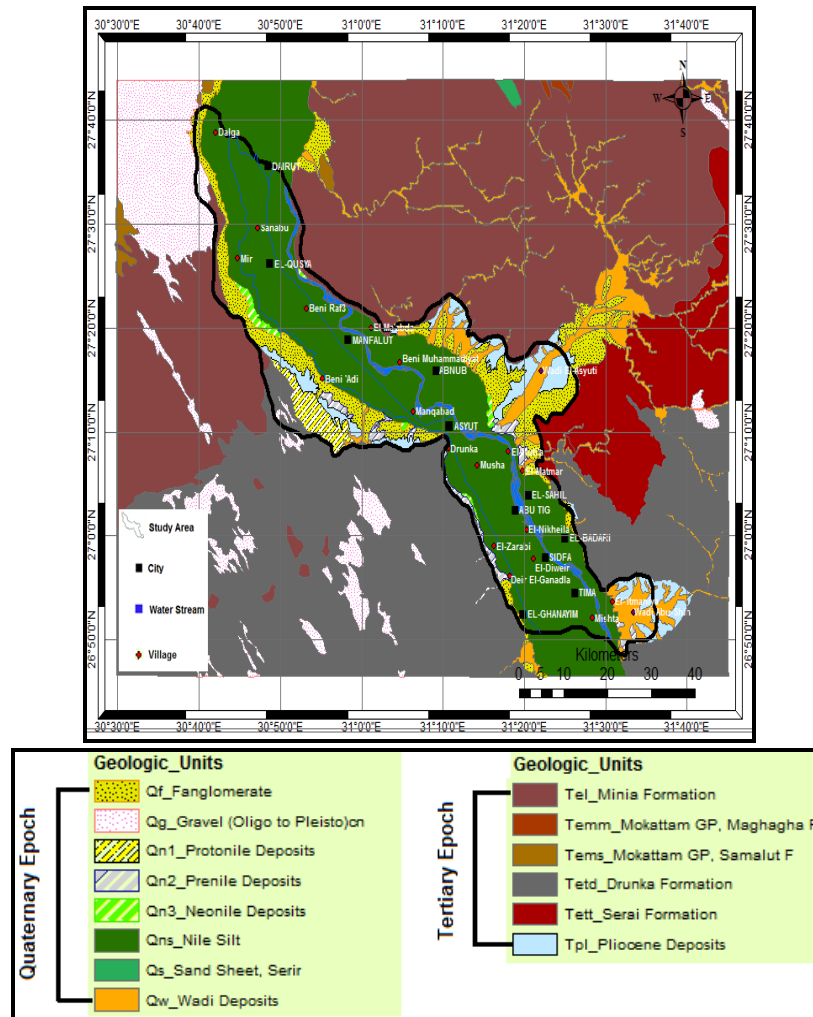


Figure 1: Geological Map of Assiut Region [20]

3. Methodology

In recent decades, modeling has grown to be an essential tool for managing groundwater resources, predicting the current and future conditions impact on groundwater and pollutant movement and assessing aquifer susceptibility.

3.1. The DRASTIC Model

DRASTIC is "an empirical groundwater model that estimates groundwater contamination vulnerability of aquifer systems based on the hydrogeological settings of that area" [8]. DRASTIC uses a statistical ranking system that gives relative weights to different factors. Each one of DRASTIC factors is specified a certain weight according to its relative importance in affecting pollution possibility. The

standard ratings vary between 1 and 10 while weights between 1 and 5.

The DRASTIC Index [DI] can be expressed numerically through calculating algebraic sum of the ratings and weights outcomes of each factor (see Equation 1). Whenever DI value is higher, groundwater becomes more vulnerable [8].

$$DI = D_r D_w + R_r R_w + A_r A_w + S_r S_w + T_r T_w + I_r I_w + C_r C_w \quad (1)$$

Where; r: rating of the factor & w: weight assigned to the factor

In the following Table 1, weights significance for factors in general and pesticide DRASTIC models have been assigned [8].

Table 1: Weights of DRASTIC Factors [8]

| Factors | Weight Significance | |
|----------------------------|---------------------|-------------------|
| | General DRASTIC | Pesticide DRASTIC |
| Depth to water (D) | 5 | 5 |
| Net Recharge (R) | 4 | 4 |
| Aquifer Media (A) | 3 | 3 |
| Soil Media (S) | 2 | 5 |
| Topography (T) | 1 | 3 |
| Impact of Vadose Zone (I) | 5 | 4 |
| Hydraulic Conductivity (C) | 3 | 2 |

3.2. Implementation of DRASTIC Model using GIS

The DRASTIC model has been applied to create the map of groundwater vulnerability of Nile aquifer along Assiut governorate. Two DRASTIC models have been used by adopting their weights and ratings which generic DRASTIC model and pesticide DRASTIC model. The water wells data has been used to get the DRASTIC factors values. From these wells data, three parameters have been gotten which are depth to water (D), permeability, and hydraulic conductivity (C). Permeability layer will overlay with geology layer and water depth layer to attain aquifer media (A) and impact of vadose zone (I) respectively. The topography (T) has been produced from the Digital Elevation Model (DEM) of Assiut area. However, no data was available for soil media S, landuse layer has been employed instead of soil media. In regard to recharge (R) of the Nile River quaternary aquifer, Dawoud, M.A., Ewea, H.A., (2009) [19] mentioned that "it ranges from 0.5 to 0.8 mm/day in the old agriculture land and ranges from 1.0 to 1.5 mm/day in the desert fringes for new reclaimed lands".

Application of GIS technique for implementation of DRASTIC model of River Nile quaternary aquifer along Assiut governorate is described as follows:

a) Identification of Data Layers

This paper spotlighted on seven factors influencing movement of contaminants to groundwater. The following table illustrates the data format for each variable.

Table 2: List of Data Layers Affected in this Paper

| Data Layer | Variables Affected | Data Feature | Conversion into GIS Format |
|----------------------------|--|-----------------|-----------------------------------|
| Depth to water (D) | Depth of water wells map | point | Resulted as surface raster format |
| Net Recharge (R) | Annually Recharge rate map | polygon | Converted from vector to raster |
| Aquifer media (A) | Permeability of Aquifer media map + Geological map | point + polygon | Resulted as surface raster format |
| Soil media (S) | Land use map | polygon | Converted from vector to raster |
| Topography (T) | Digital Elevation Model map (DEM map) | polygon | Already in raster format |
| Impact of vadose zone (I) | Permeability of soil media map+ Depth to water map | point | Resulted as surface raster format |
| Hydraulic conductivity (C) | Hydraulic conductivity map | point | Resulted as surface raster format |

b) Add X, Y Data

This method is applied to add a new object to an analysis of any GIS project [21]. Firstly, longitude and latitude of groundwater wells at Assuit governorate must be added to GIS software by this tool. Three factors were tabulated as numbers and related to x and y coordinates which considered as point feature; these factors are depth to water, permeability, and Hydraulic conductivity. This theme contained forty four points representing depth to water, permeability, and Hydraulic conductivity of wells as shown in Figure 2.

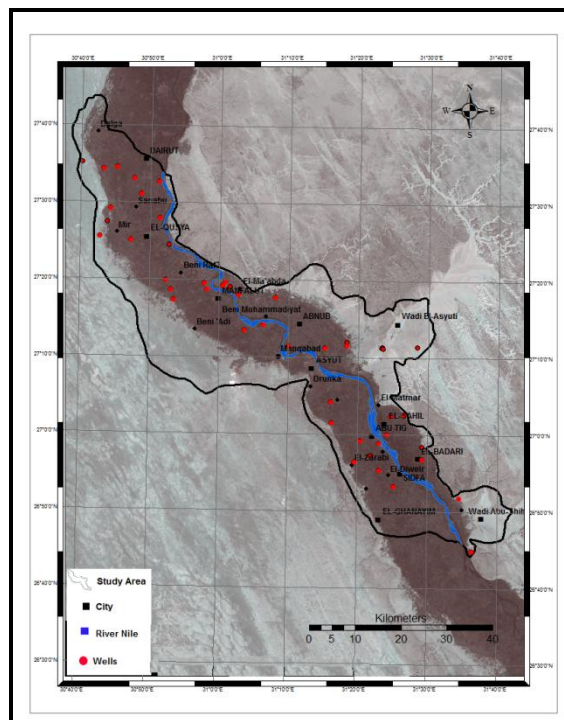


Figure 2: Well Location Map Overlaid Assiut Satellite Image [16]

c) Management of Data Layers

Every one of data layers affected groundwater vulnerability has to manipulate by three main methods as the following [22].

- 1) Data layer must be converted from vector feature such as point, line, or polygon, to raster data because the last one is relatively easier than vector data.
- 2) The data layers in the form point feature must be converted into surface raster grid by interpolation methods such as kriging or inverse distance weighting (IDW).
- 3) All data layers need to be factorial data by reclassification method. This method is used in order to unify the criteria that will be applied on all layers and to diminish the number of classes of each data layer.

d) Rasterization of Vector Data

Rasterization is defined as "the process of converting a polygon feature theme from vector to raster data structure" [23]. By this process polygons were converted to grid cells or pixel. The cell values belonging to each polygon are equal to each others.

e) Interpolation of Point Data

Interpolation can be known as "the function used to predict unknown values of any geographic point data to generate a continuous surface from sampled point values" [24]. There are three interpolation methods included in GIS software. They are Inverse Distance Weighted (IDW), Spline, and Kriging. It is not important what method is applied, whenever the data samples are more, the results are more dependable [24]. In this paper, IDW interpolation method was applied for interpolating all parameters which are included in physicochemical analysis of wells. IDW calculates the value of all pixels by computing the average of a set of sample points in a point feature theme. The computed average value is depending on the values of sample point and the distance between point to be estimated and other points. Thus, the closer the sample points to the cell which to be calculated, the more effect on the interpolated value [25].

f) Reclassification of Data Layers

The reclassification process can be elucidated as "replacing input cell values with new output cell values" [24]. In this paper, every data layer has been reclassified according to a general scale illustrating its effect to cause groundwater pollution. This scale includes ten classes for each data layer ranging from 10 to 1 where 10 is the highest potential to pollution and 1 means the lowest pollution potential. Spatial analyst included in ArcGIS software has been used to reclassify all data layers as shown below in the following clarification.

- Depth to water was reclassified by the obtained data wells into seven classes as shown in Table 3:

Table 3: *Reclassification of Depth to Water (D)*

| Depth, m | Rating |
|-------------|--------|
| 0.02 - 1.5 | 10 |
| 1.5 - 4.5 | 9 |
| 4.5 - 9.5 | 7 |
| 9.5 - 15.2 | 5 |
| 15.2 - 22.9 | 3 |
| 22.9 - 30.5 | 2 |
| 30.5 - 42 | 1 |

The pollution potential is inversely proportional with depth of wells, thus the highest depth was assigned by 1 and the lowest depth was assigned by highest rating 10.

- Net Recharge (R): recharge has been reclassified into two classes as shown in Table 4.

Table 4: Reclassification of Net Recharge (R)

| Land Use | Recharge, mm/Day | Rating |
|--------------------------------------|------------------|--------|
| Old agriculture lands | 0.5 to 0.8 | 8 |
| Desert fringes (new reclaimed lands) | 1.0 to 1.5 | 9 |

The two classes took rating 8 and 9 according to DRASTIC rating standard which determined by (Aller, et al., 1987) [8] as shown in Table 5.

Table 5: DRASTIC Rating Standard [8]

| Recharge (inch/year) | Rating | Recharge (mm/year) | Rating |
|----------------------|--------|--------------------|--------|
| 0 – 2 | 1 | 0 – 51 | 1 |
| 2 – 4 | 3 | 51 – 102 | 3 |
| 4 – 7 | 6 | 102 – 178 | 6 |
| 7 – 10 | 8 | 178 – 254 | 8 |
| >10 | 9 | >254 | 9 |

- Aquifer media: To identify aquifer media precisely, permeability and geology of aquifer were used to reclassify it. Moulton, (1992) [26] summarized that Quaternary alluvial deposits were given higher DRASTIC ratings than Tertiary sedimentary deposits, and young deposits were given higher ratings than old deposits. Table 6 and Table 7 illustrate the classes of permeability and geology of aquifer respectively.

Table 6: Reclassification of Permeability

| Permeability, Millidarcy | Rating |
|--------------------------|--------|
| 7.98 – 2876.96 | 2 |
| 2876.96 – 5232.61 | 4 |
| 5232.61 – 8924.22 | 6 |
| 8924.22 – 15165.9 | 8 |
| 15165.9 – 28256.5 | 10 |

Table 7: Reclassification of Geology Types

| Geology Type | Age | Rating |
|--------------------------|--|--------|
| Nile Silt (Qns) | Quaternary | 10 |
| Fanglomerate (Qf) | Quaternary | 9 |
| Wadi deposits Qw | Quaternary | 8 |
| Neonile deposits Qn3 | Quaternary | 7 |
| Prenile deposits (Qn2) | Quaternary | 6 |
| Protonile deposits (Qn1) | Quaternary | 6 |
| Pliocene deposits (Tpi) | Tertiary (Pliocene) | 5 |
| Samalut Fm. (Tems) | Tertiary (Middle Eocene- Mokattam group) | 1 |
| Minia Fm. (Tei) | Tertiary(Middle Eocene) | 4 |
| Drunka Fm. (Tetd) | Tertiary(Lower Eocene- Thebes group) | 3 |
| Seria(Thebes) Fm. (Tett) | Tertiary(Lower Eocene- Thebes group) | 1 |

- The soil data layer has been reclassified by its landuse, which can be categorized into six groups as shown in Table 8. Due to lack of soil data, landuse map was used instead of soil layer. The new reclaimed lands were assigned highest rating because the degree of pesticide usage is high and the soil of new reclaimed lands has higher permeability than old agriculture lands.

Table 8: *Reclassification of the Soil Data Layer*

| Landuse | Rating |
|-----------------------|--------|
| New reclaimed lands | 8 |
| Water | 7 |
| Old agriculture lands | 6 |
| Islands | 6 |
| Buildings | 5 |
| Desert, | 3 |

- The topography data layer has been reclassified by percent slope of land surface as shown in Table 9.

Table 9: *Reclassification of Percent Slope Layer*

| Range, % | Rating |
|------------------------|--------|
| 0 – 2 (very flat) | 10 |
| 2 – 6 (flat slope) | 9 |
| 6 – 12 (medium slope) | 5 |
| 12 – 18 (steep slope) | 3 |
| >18 (very steep slope) | 1 |

- The Vadose Zone for the purposes of the Nile aquifer vulnerability map incorporates soil permeability and depth to water. The equation used incorporates the factors believed to be important to the Vadose Zone as shown in Equation 2 [27].

$$\text{Impact of Vadose Zone} = \text{Soil Permeability} + \text{Depth to Water} \quad (2)$$

The more the impact of vadose zone, the more rating of pollution potential as clarified in Table 10.

Table 10: *Ranges and Ratings for Vadose Zone Impact*

| Ranges | Rating |
|---------|--------|
| 4 – 5 | 2 |
| 5 – 7 | 4 |
| 7 – 10 | 6 |
| 10 – 12 | 8 |
| 12 - 17 | 10 |

- Hydraulic conductivity is strongly related to contamination potential; the higher the hydraulic conductivity, the higher contamination potential [8]. Hydraulic conductivity in the study area varies between 9 and 164 m/day. Table 11 shows that five categories of hydraulic conductivity are existed.

Table 11: Ranges and Ratings for Hydraulic Conductivity

| Ranges | Rating |
|--------------|--------|
| 9.1 – 12.5 | 2 |
| 12.5 – 28.5 | 4 |
| 28.5 – 40.5 | 6 |
| 40.5 – 81.5 | 8 |
| 81.5 – 163.9 | 10 |

a) Analysis of Data Layers

This process is the last step of GIS technique in this paper to analyze data through overlaying all layers. Overlay process is defined as "the spatial operation in which a thematic layer is placed over another to form a new layer" [23]. During this process, all data layers have been overlain to produce a groundwater vulnerability map.

By these actions, all cells values in each layer were multiplied by their weight. The total result of adding the values of one layer that place at the same location to the values of the others was an output expressing DRASTIC index (DI).

4. Results and Discussion

The vulnerability results will be presented in the following steps.

4.1. Ratings for the DRASTIC Factors

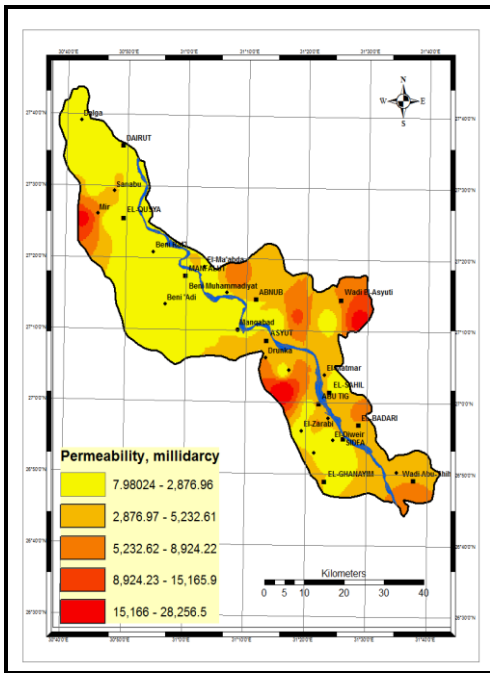
a) Depth to Water (D)

This layer was classified into seven classes as shown in Figure 3b. Spatial analyst (reclassify tool) was then applied on depth to water layer to reclassify it into 7 classes ranging from 1 (the highest depth) to 10 (the lowest depth). The majority of study area varies between two categories; the first one ranges from 1.6 to 4.5 m which has rating equal 9, the second category ranges from 4.5 to 9.5 m assigning 7 as rating value.

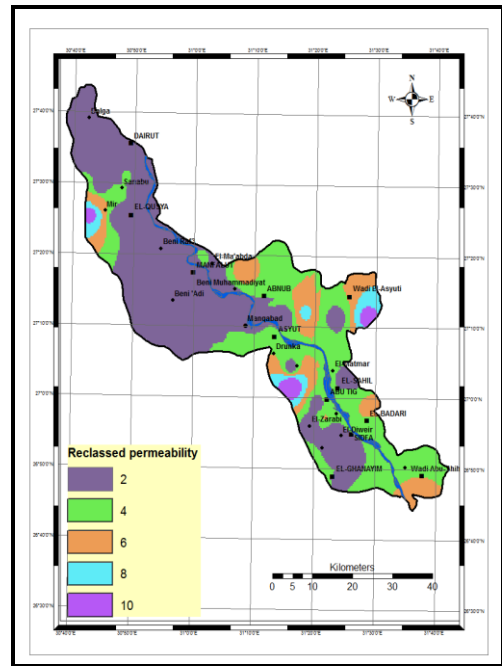
b) Net Recharge (R)

The spatial distribution layer of net recharge of the Nile aquifer has been reclassified into two classes. The two classes assigned rating 8 and 9 according to DRASTIC rating standard as shown in Figure 4a and Figure 4b.

they were combined together by raster calculation tool - which including in spatial analyst - to get integrated view of aquifer media as shown in Figure 7.

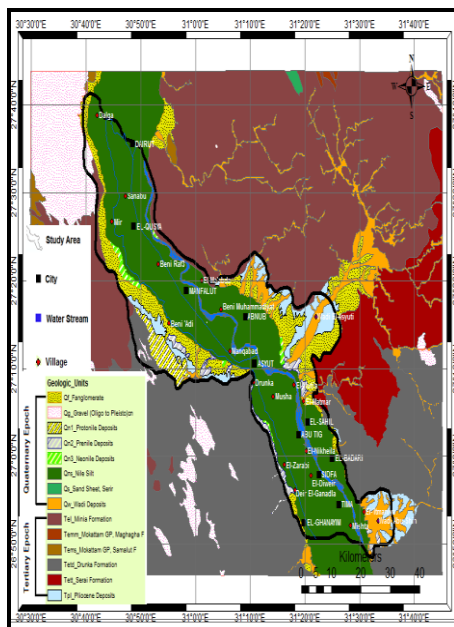


(a) Raw Data

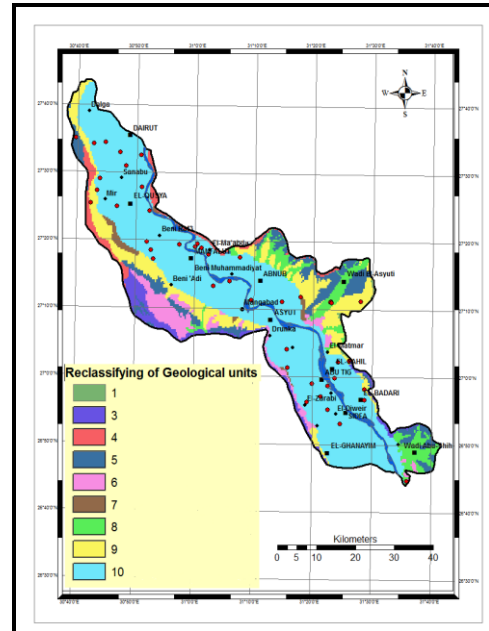


(b) After Reclassification

Figure 5: Spatial Distribution Map of Permeability of the Nile Aquifer



(a) Original Map



(b) After Reclassification

Figure 6: Geology Map of Assiut Region

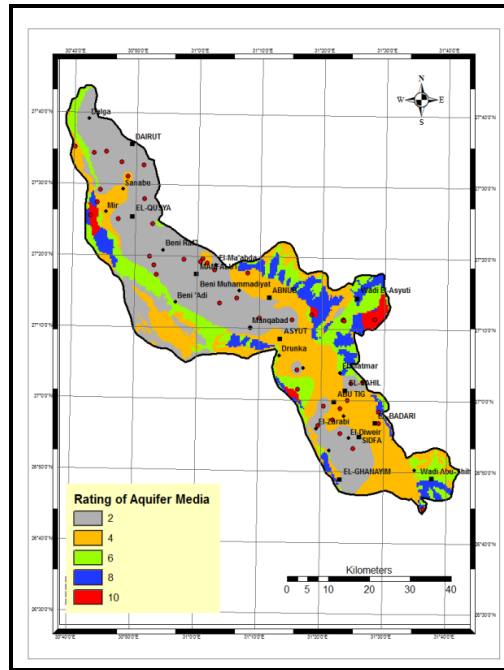


Figure 7: Geology Layer Incorporated with Permeability Layer in Study Area

d) Soil (S)

For the reason that there is lack of soil data, landuse map was used instead of soil layer. The soil data layer was reclassified by its landuse, which can be categorized into six groups as shown in Figure 8. Landuse map has been reclassified according to rating shown in Table 8, the highest rating was distinguished the new reclaimed land since high degree usage of pesticides in it. The desert land has been assigned with lowest rating because annually rate of rain is very low in the way that it doesn't affect the groundwater properties in desert lands.

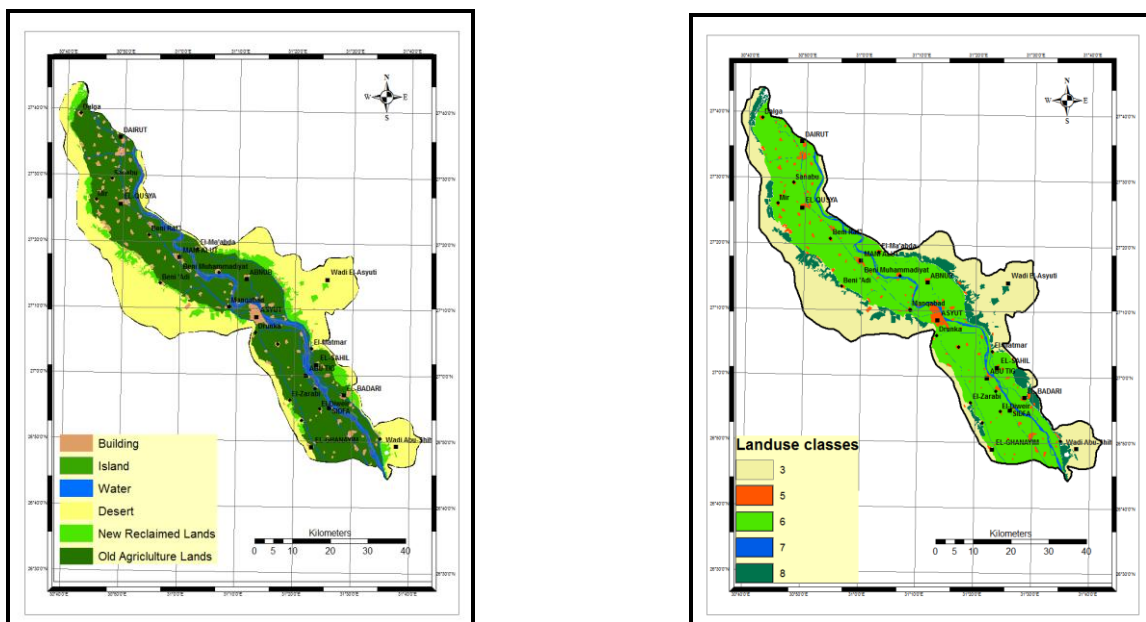
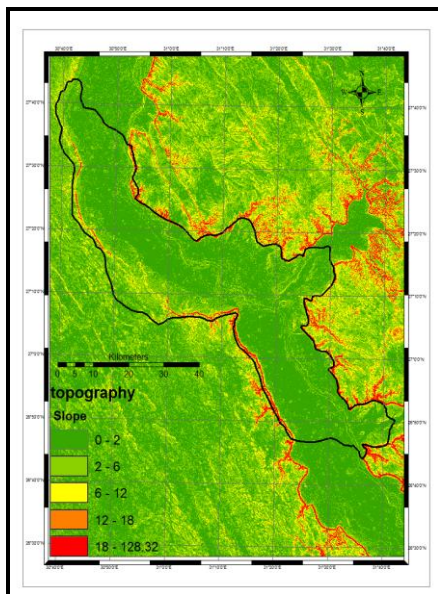


Figure 8: Landuse Map of Study Area

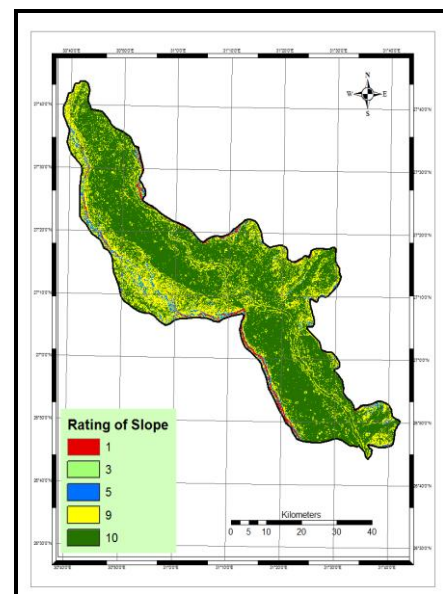
e) Topography (T)

The slope data layer represents topography map of study area. The slope map can be produced as percent from digital elevation model (DEM) of Assiut area using spatial analyst tool in ArcGIS 9.3. Classification of slope including five classes which are: very flat slope (0-2), flat slope (2-6), medium slope (6-12), steep slope (12-18), and very steep slope (18-128.32) as shown in Figure 9a.

Slope map has been reclassified by percent slope of land surface as displayed in Figure 9b. The reclassification of slope was based upon the rule that "The higher the slope, the lower the rating". Accordingly, the cell which is very flat slope was assigned 10 rating, whereas, the cell has very steep slope was assigned rating 1.



(a) Raw Data

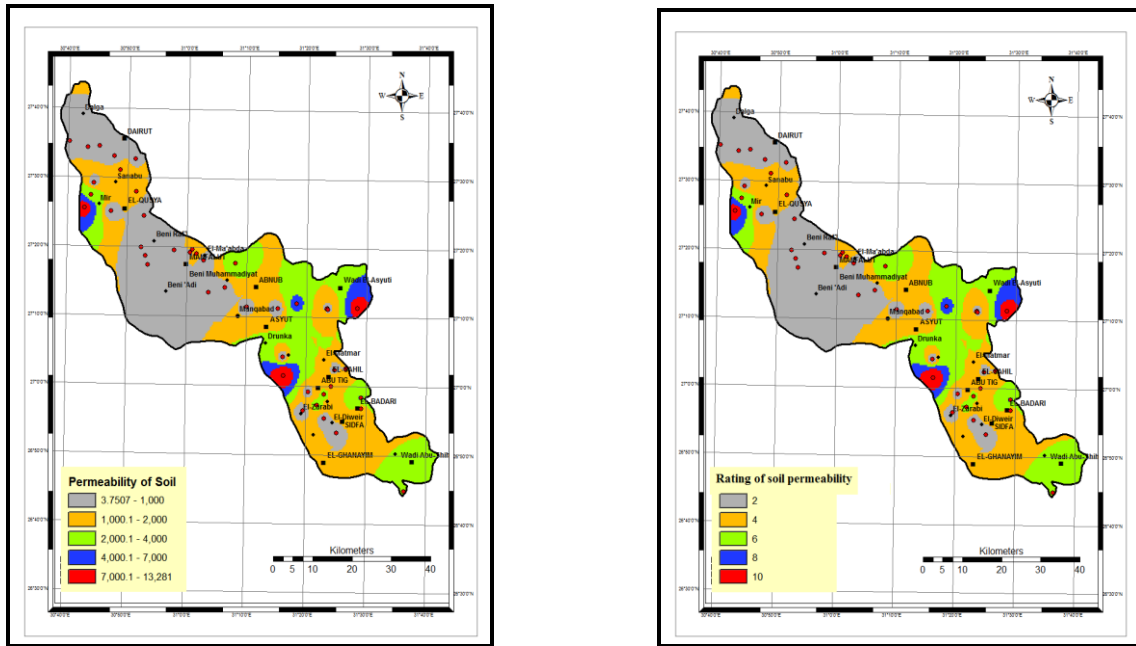


(b) After Reclassification

Figure 9: Slope Map of Study Area Generated from DEM

f) Impact of Vadose Zone (I)

The Vadose Zone for the purposes of the Nile aquifer vulnerability map incorporates soil attenuation type and depth to water. Depth to water has previously been displayed in Figure 3a and Figure 3b, but soil attenuation type is unavailable; hence soil permeability is used. Figure 10a demonstrates the soil permeability map of study area.



(a) Raw Data

(b) After Reclassification

Figure 10: Soil Permeability Map of Study Area

Soil permeability map was reclassified according to "the higher the permeability, the higher the potential of pollution". Impact of vadose zone layer has been created as shown in Figure 11.

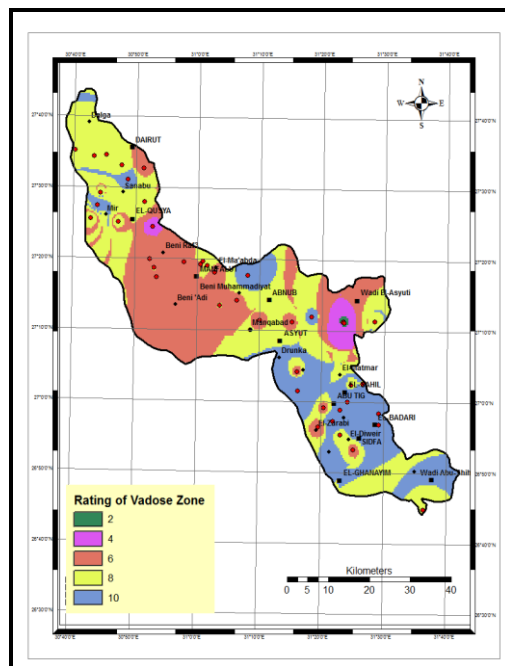


Figure 11: Impact of Vadose Zone Layer After Incorporating and Reclassification

g) Hydraulic Conductivity (c)

There are five categories of hydraulic conductivity index values. According to DRASTIC standard rating these values were assigned for the rating where a higher rating is referring to a higher hydraulic

conductivity; i.e., high hydraulic conductivity values ranked as 10, and lower values as 1 as displayed in Figure 12a and Figure 12b.

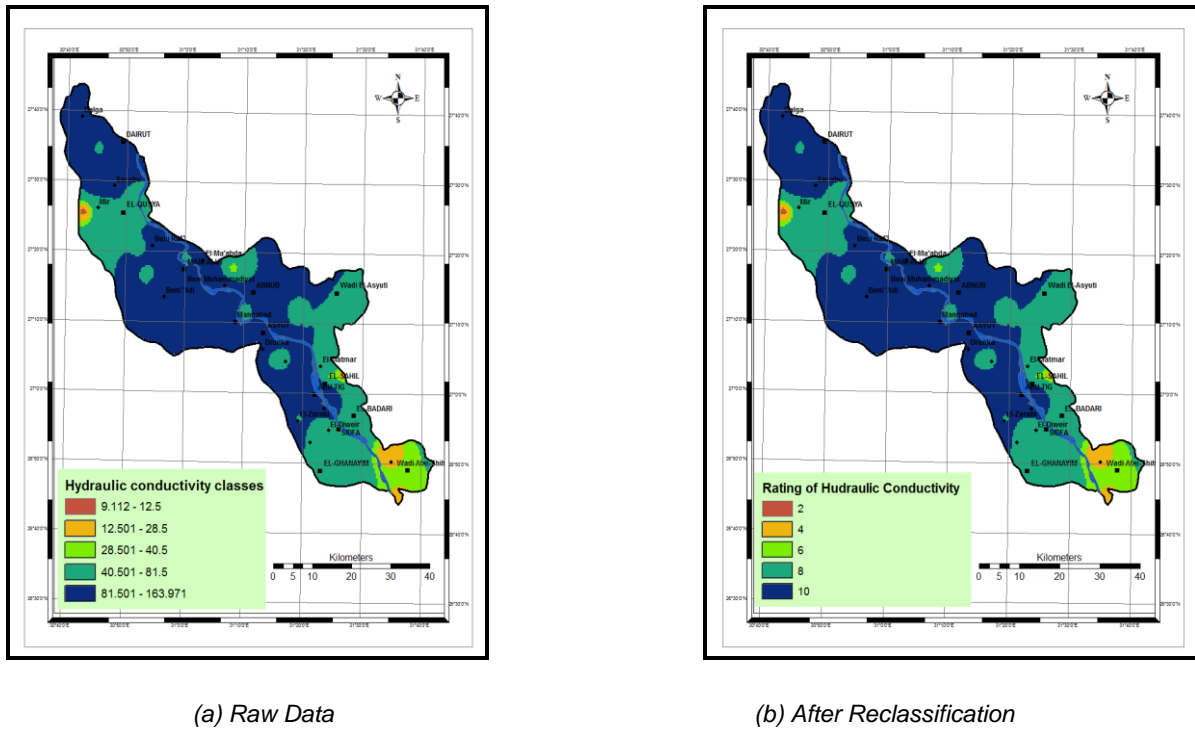


Figure 12: Spatial Distribution of Hydraulic Conductivity of Study Area

4.2. Generation of Vulnerability Map

To create vulnerability map, the DRASTIC Index [DI] must be computed by summation of the products of ratings and weights of each factor as shown in Figure 13. If the value of DI is becoming higher, the relative pollution potential or aquifer vulnerability will be greater. The weights and ratings were adopted as specified in the generic DRASTIC model and pesticide DRASTIC model to generate two vulnerability maps.

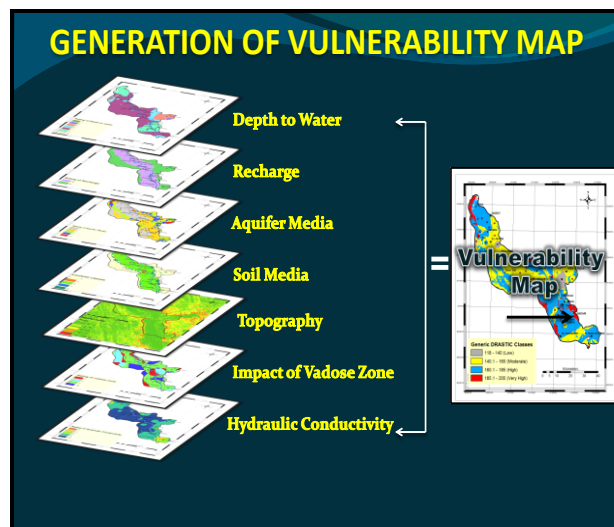


Figure 13: Generation Process of Vulnerability Map

a) Groundwater Vulnerability Implemented By Generic DRASTIC Model

The vulnerability map generated by generic DRASTIC Model as shown in Figure 14, while Table 12 demonstrates the summary of vulnerability level and the areas percent of each class.

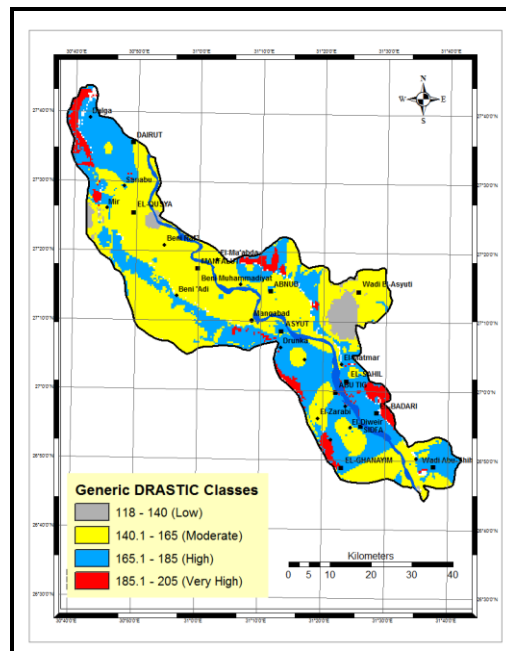


Figure 14: Vulnerability Map of Nile Aquifer in Study Area Generated By Generic DRASTIC Model

Table 12: Summary of Vulnerability Classes

| Generic DRASTIC | | |
|-----------------|---------------------|--------|
| Legend | Vulnerability level | Area % |
| 118 – 140 | Low | 3.8 |
| 140.1 – 165 | Moderate | 55.2 |
| 165.1 -185 | High | 35.4 |
| 185.1 - 205 | Very high | 5.6 |

From Figure 14 and referring to the legend illustrated in Table 12, it is found that about 3.8 % of the total area of Assiut governorate has low vulnerability level; on the other hand, 5.6 % of the total area is considered as very vulnerable level. The majority of study area is in between moderate vulnerable and high vulnerable; where 55.2 % of the area is moderately vulnerable and 35.4 % has high level of vulnerability.

With regard to Figure 14, it is seen that high vulnerability levels are concentrated on the south of the study area including districts of Sodfa, Abo-teej, and the western side of Assiut city towards Arab Al-Madabegh. As well as there are small areas in the eastern side on both east Abnoub city and Beni Muhammadyat city have high vulnerability level. Also, the high vulnerable areas can be clearly seen in the northern area beginning from Dayrout ending with Sanabuo village.

While the very high vulnerable areas are located on the eastern fringes of Al-Badary district as well as the western fringes of Al-Ghanayem and Dayrout districts. However, the northern areas beginning with Sanabuo ending with Assiut has moderate levels including Al-Qusya, Manfalut, and the western part of Abnoub district.

b) Groundwater Vulnerability Implemented By Pesticide DRASTIC Model

With regard to the groundwater vulnerability map illustrated in Figure 15 and Table 13, it is shown that about 64% of the study area has an extreme to high vulnerability to contamination, 34.6% has a moderate vulnerability and small areas occupy about 1.4% and has a low vulnerability.

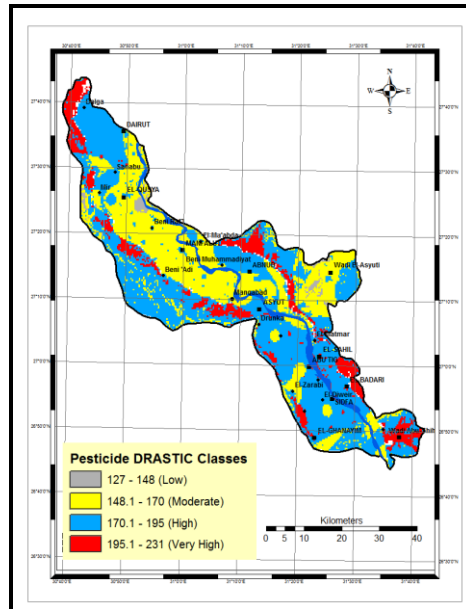


Figure 15: Vulnerability Map of Nile Aquifer in Study Area Generated by Pesticide DRASTIC Model

Table 13: Summary of Vulnerability Classes

| Pesticide DRASTIC | | |
|-------------------|---------------------|--------|
| Legend | Vulnerability level | Area % |
| 127 - 148 | Low | 1.4 |
| 148.1 - 170 | Moderate | 34.6 |
| 170.1 - 195 | High | 52 |
| 195.1 - 231 | Very high | 12 |

According to land use activities, it can be clearly seen that most areas which considered new reclaimed land are of very high vulnerability, while those which classified old agriculture lands vary between moderate to high vulnerability. The moderate levels areas lie in between the northern area of the governorate including Assiut, Manfalut, and Al-Qusya districts. Nevertheless, high vulnerable areas fully appear in the southern part of the study area including Sodfa, Abu-Teej, Al-Badary, Al-Sahel districts and the southern part of Assiut city.

5. Conclusion

Vulnerability Map of Nile aquifer along Assiut governorate was created by applying the DRASTIC model within GIS technique to find out the groundwater vulnerable zones to contamination. The vulnerability map generated by generic DRASTIC Model, demonstrates that about 3.8 % of the total area of Assiut governorate has low vulnerability level; on the other hand, 5.6 % of the total area is considered as very vulnerable level. The majority of study area is in between moderate vulnerable and high vulnerable; where 55.2 % of the area is moderately vulnerable and 35.4 % has high level of vulnerability. With regard to the groundwater vulnerability map generated by pesticide DRASTIC Model, it is shown that about 64% of the study area has an extreme to high vulnerability to contamination, 34.6% has a moderate vulnerability and small areas occupy about 1.4% and has a low

vulnerability. According to land use activities, it can be clearly seen that most areas which considered new reclaimed land are of very high vulnerability, while those which classified old agriculture lands vary between moderate to high vulnerability.

References

- [1] Sobih, M.A., Reem, D., Kamel, Y.Y., and El-Gharably, G.A. *Chemical and Bacteriological Evaluation of Drinking Ground Supplies in Assiut City, Assiut*. Vet Med J. Assiut University, Egypt. 1988. 38; 99-104.
- [2] Abu El Ella, E.M., Shamrukh. *Hydrogeochemical Evolution of Groundwater Aquifers in the Area East of Assiut Nile Basin, Egypt*. Bulletin of Faculty of Science, Assiut Univ., Egypt. 1999. 28; 1-16.
- [3] Bakheit, A.A., Ibrahim, H.A., Omran, A.A., Riad, S., and Senosy, M.A. *Application of the Resistivity Method to Study Groundwater Potentialities on a Part of the Entrance of Wadi El-Assiuti, Eastern Desert, Egypt*. Qatar University. SCI. J. 1993. 13 (2) 341-344.
- [4] Ebrahim, M.O. 1997: *Application of Surface Geoelectrical Methods for the Detection of Groundwater Contamination in the Area Northwest of Assiut City (El Madabegh)*. MSc Thesis, Assiut University, Egypt.
- [5] Sebaq, A.S., El-Hussaini, A.H., and Ibrahim, H.A. *Application of Electrical Resistivity and Self-potential for Groundwater Exploration and Contamination Study in the Area Northwest of Assiut City, Egypt*. J. King Saud Univ. 2003. 16 Science (1) 31-61.
- [6] Mohamaden, M.I.I., Abuo Shagar, S., and Abd. Allah, G. *Geoelectrical Survey for Groundwater Exploration at the Assuit Governorate, Nile Valley, Egypt*. JKAU: Mar. Sci. 2009. 20; 91-108.
- [7] Villeneuve, J.P., Banton, O., and Lafrance, P. *A Problematic Approach for the Groundwater Vulnerability to Contamination by Pesticides: the VULPEST Model*. Ecological Modelling. 1990. 51; 47-58.
- [8] Aller, L., Lehr, J.H., Petty, R., and Bennett, T. 1987: *DRASTIC: A Standardized System to Evaluate Groundwater Pollution Potential using Hydrogeologic Settings*. USEPA, Cincinnati, OH, USEPA. 622.
- [9] Clarke, K.C., 1997: *Getting Started with Geographic Information Systems*. New Jersey: Prentice Hall, Inc. 353.
- [10] Schmidt, R.R., 1987: *Groundwater Contamination Susceptibility in Wisconsin*. Wisconsin Groundwater Management Plan Report No. 5.
- [11] Nebert, D., and Anderson, D., 1987: *Utilization of Geographic Information Systems Technology in the Assessment of Regional Groundwater Quality in Irrigation Systems for the Twenty-First Century*. James, L.G. and M.J. English, ed. 370-377.
- [12] Petersen, G.W., Hamlett, J.M., Baumer, G.M., Miller, D.A., Day, R.L., and Russo, J.M., 1991: *Evaluation of Agricultural Non-Point Pollution Potential in Pennsylvania using a Geographic Information System: Final Report*. Pennsylvania Department of Environmental Resources, Penn State Environmental Resources Research Institute.

- [13] Atkinson, S.F., Thomlinson, J.R., Hunter, B.A., Coffey, J.M., and Dickson, K.L., 1992: *The Drastic Groundwater Pollution Potential of Texas*. Center for Remote Sensing and Landuse Analyses, University of North Texas, Denton, Texas. 41.
- [14] Zhang, R., Hamerlinck, J.D., Gloss, S.P., and Munn, L. *Determination of Nonpoint-Source Pollution using GIS and Numerical Models*. Journal of Environmental Quality. 1996. 25 (3) 411-418.
- [15] Al-Adamat, R.A., Foster, I.D., and Baban, S.M. *Groundwater Vulnerability and Risk mapping for the Basaltic Aquifer of the Azraq Basin of Jordan using GIS, Remote Sensing and DRASTIC*. Applied Geography. 2003. 23; 303-324.
- [16] Thapinta, A., and Hudak, P.F. *Use of Geographic Information Systems for Assessing Groundwater Pollution Potential by Pesticides in Central Thailand*. Environment International J. 2003. 29; 87-93.
- [17] Rahman, A. *A GIS Based DRASTIC Model for Assessing Groundwater Vulnerability in Shallow Aquifer in Aligarh, India*. Applied Geography. 2008. 28; 32-53 .
- [18] ALDAR, CH2M HILL, Spain, 2011: Study of Environmental and Social Impact Assessment Framework (ESIAF) of Assiut & Sohag Governorates, Executive Summary, Egypt. 82.
- [19] Dawoud, M.A., and Ewea, H.A. 2009: *Sustainable Development via Optimal Integration of Surface and Groundwater in Arid Environment: Nile River Quaternary Aquifer Case Study*. The International Conference on Water Conversation in Arid Regions. 12-14.
- [20] Conoco, 1987: Geologic Map of Egypt. Egyptian General Authority for Petroleum (UNESCO Joint Map Project), 20 sheets, scale 1:500 000. Cairo, Egypt.
- [21] Hohl, P., and Brad, M., 1997: *ArcView GIS Exercise Book*. 2nd edition. New Mexico: OnWord Press. 432.
- [22] DeMers, M.N., 2000: *Fundamentals of Geographic Information Systems*. 2nd edition. New York: John Wiley & Sons, Inc. 498.
- [23] Bernhardsen, T., 1999: *Geographic Information Systems: An Introduction*. 2nd edition. New York: John & Wiley & Sons, Inc. 372.
- [24] McCoy, J., and Johnston, K., 2001: Using Arcgis Spatial Analyst. Environmental Systems Research Institute, Inc., Redlands, California. 230.
- [25] Mehrjardi, T.R., Jahromi, Z.M., Mahmodi, Sh., and Heidari, A. *Spatial Distribution of Groundwater Quality with Geostatistics (Case Study: Yazd-Ardakan Plain)*. World Applied Sciences Journal. 2008. 4 (1) 9-17.
- [26] Moulton, D.L., 1992: *DRASTIC Analysis of the Potential for Groundwater Pollution in Pinal County, Arizona*. Arizona Geological Survey, Open-File Report. 92-13.
- [27] Piscopo, G., 2001: *Groundwater Vulnerability Map Explanatory Notes Castlereagh Catchment*. New South Wales (NSW) Department of Land and Water Conservation. 13.

Advances in Classification Techniques for Semi Urban Land Features using High Resolution Satellite Data

Srikrishna Shastri C.¹, Ashok Kumar T.², and Shiva Prakash Koliwad ³

¹Department of Electronics and Communication, Mangalore Institute of Technology, Moodabidri, Karnataka, India

²Department of Electronics and Communication, PES Institute of Technology, Shivamogga, Karnataka, India

³Department of Electronics and Communication, Vivekananda College of Engineering, Puttur, Karnataka, India

Publication Date: 14 March 2016

DOI: <https://doi.org/10.23953/cloud.ijarsg.49>



Copyright © 2016 Srikrishna Shastri C., Ashok Kumar T., and Shiva Prakash Koliwad. This is an open access article distributed under the **Creative Commons Attribution License**, which permits unrestricted use, distribution, and reproduction in any medium, provided the original work is properly cited.

Abstract Classification of satellite Images is one of the major research areas in remote sensing fields. Classification of remote sensed data is required for accurate classification of semi urban land features. Satellite image classification plays an essential role in proper monitoring and management of natural and manmade resources on the earth surface. However a good data set is required for the accurate classification of remotely sensed data. In this paper, to classify the data set, various image fusion techniques are used for fusing high resolution Panchromatic data with low resolution Multi-spectral data which gives better quality and more informative image data set. The performances of different fusion techniques are then evaluated to identify the best possible technique which gives better result for image classification.

Keywords *Remote Sensing; Image Fusion; High Resolution; Image Classification; Panchromatic; Multispectral*

1. Introduction

Remote sensing is the advancement in technique to obtain relevant data about earth's surface without being in direct contact with it. Sensors are used to receive and record information about an object without having any physical contact with it. These sensors are mounted on aerial vehicles like helicopters, planes, and satellites, and record the electromagnetic energy reflected from the objects surface. Unmanned aerial vehicles with sensors are also used to capture images remotely from earth surface.

With the availability of high quality satellite images and with improved image enhancement techniques, remote sensing technique has rapidly advanced over the years. Remote sensing science has always been an interesting topic over the years, and with the arrival of the earth observation satellite equipped with advanced instruments to monitor closely the land-air-ocean interactions, the field has expanded dramatically in the recent past. Due to the technical limitations of remote sensing satellites, they do not capture both high spatial and spectral images at the same time. Instead, dual images are captured;

one is a high resolution panchromatic image, which is used for identifying spatial details, and the other is a low resolution multispectral image, which is suitable for detecting spectral properties of image. The process of integrating high resolution panchromatic image with low resolution multispectral image is called Image fusion technique. The resultant fused image will be more informative and having better quality as compared to original multispectral data.

Usually image data is obtained from different types of camera with the region of interest (ROI) being the same. The quality of the image depends upon type of camera and its resolution. However to classify different objects in a scene, it is necessary to have a very high resolution camera. An alternative way to extract more information from the same region of interest is to fuse the images. Therefore, fusion techniques play an important role in getting a high quality image. Different fusion techniques have been adopted in RS data processing and the process results in the extraction of abundant information from the fused data. Hence, in our methodology we consider image data of different resolution of the same area and the images are panchromatic and multi-spectral image of the ROI.

Image fusion is a process of integrating two or more images to form a new and composite image using a certain algorithm in order to obtain more information than that can be derived from each of the single sensor data alone [1] [2]. In remote sensing, the fusion of a high resolution panchromatic (PAN) image with a low resolution multi-spectral (MS) image to produce a high resolution multi-spectral image. The PAN images have a very high spatial content while the MS images provide high spectral information. The main aim of fusing PAN and MS images is to create composite images of enhanced interpretability. The resultant image is a new image which is more suitable for human and machine perception or further image processing tasks such as segmentation, feature extraction and object recognition.

Several image fusion techniques are developed to improve the quality of a remote sensed data. The most commonly employed traditional fusion techniques are: Addition and Multiplication fusion, Transformation fusion, Filter fusion, and Multi-resolution analysis is also under investigation. In general, remote sensing fusion techniques can be classified into three different levels: The pixel/data level, the feature level and the decision level [1].

Pixel level is a low level of fusion which is used to analyze and combine data from different sources before original information is estimated and recognized. The pixel-level method works either in the spatial domain or in the transform domain. Feature level is a middle level of fusion which extracts important features from an image like shape, length, edges, segments and direction. Decision level fusion uses the outputs of initial object detection and classification as inputs to the fusion algorithm to perform the data integration. The most common and conventional fusion techniques are Principal Component Analysis (PCA), Intensity-Hue-Saturation (IHS) method, Brovey Transform (BT) and Multiplicative method (MT); currently the Wavelet Transformation method is widely used for study. Existing transformation based image fusion methods available are additive and multiplicative technique, multi-resolution method, filters fusion method, fusion based on inter-band relation [3].

Padwick et al. (2010) compared IHS, PCA, Gram Schmidt, and HCS (Hyperspherical Color Sharpening) algorithms for fusing WorldView-2 Pan and MS images and confirmed that Gram Schmidt, PCA, and IHS do not produce acceptable pan-sharpened natural colour MS images [4].

Luo and Kay (1988) introduced a generic data fusion structure based on multi-sensor integration. In this system, data from various sources were combined within embedded fusion centres in a hierarchical manner. They made a clear distinction between multisensory integration and multi-sensor fusion [6].

Chavez et al. (1991) applied IHS, PCA, HPF methods to merge multi-spectral and multi-resolution data, viz. Landsat TM (30m) and SPOT panchromatic (10m), and compared the methods [10]. The authors observed that IHS method distorts the spectral characteristics the most, PCA method distorts less while the HPF method distorts the data the least. An experiment conducted by Zhijun et al. (2005) on IKONOS-2 (1m) images too confirmed that the IHS, BT and PCA methods distort the spectral characteristics more than HPF, HPM, ATW and MRAIM methods [10].

Yun Zhang (2002) observes that the conventional fusion algorithms which have been successful for fusion of data from a particular sensor cannot effectively fulfil the fusion of the images collected from some other sensors [14].

Finally, it is also observed by the reviewers that the majority of the studies have shown greater concern for developing and evaluating fusion techniques using statistical metrics rather than developing application-specific techniques and assessments.

Image classification is viewed as the process of automatic categorization of all the pixels in an image into a finite number of land use/land cover classes (LU/LC). For example, LU built-up-land, building, road, for LC i.e., water, agriculture land forest, etc. Digital image processing techniques, also serves as a powerful quantitative data analysis tool for the regional mapping of natural resources. Image classification is a complex process that may be affected by many other factors. Effective use of multiple features of remotely sensed data and selection of suitable classification method play dominant role in improving classification accuracy. Non parametric classifiers such as fuzzy logic, neural network, decision tree classifier and knowledge based classifiers are the important approaches used by research scholars in recent years.

In general image classification can be grouped as

- Supervised and unsupervised
- Parametric and non-parametric
- Hard and soft (fuzzy) classification
- Pixel, sub-pixel and per-field classifications

Conventionally, the classification is based on “one-pixel-one-class relationship” i.e., obtaining a unique relationship between a given material or land cover class and its reflected radiation (reflectance) at certain wavelength contained in a spectral band of an image. It is commonly known as “hard” classification and is broadly grouped into two types: (i) Unsupervised classification (ii) Supervised classification. But the conventional methods such as Parallelepiped, Minimum Distance-to-Means, Mahalanobis distance, Maximum Likelihood Classifier, and Iterative Self-Organizing Data Analysis Technique (ISODATA) *only utilize spectral information*, and consequently have limited success in classifying high-resolution urban multi-spectral images for the reasons mentioned.

The Maximum Likelihood Classification (MLC) can obtain minimum classification error under the assumption that the spectral data of each class is normally (Gaussian) distributed. Under this assumption, the distribution of a category response pattern can be completely described by the mean vector and the covariance matrix, and the computation of the statistical probability of a given pixel value being a member of a particular land cover class is made. These probability density functions are used to classify an unidentified pixel. In theory, MLC is the most accurate technique, but slow in computation, and complex in mathematics. The MLC method itself cannot solve the problem of *spectral confusion*.

The principal drawback of the MLC is the assumption of normal distribution of data and requirement of large number of computations to classify each pixel particularly when a large number of spectral

channels are involved or a large number of spectral classes need to be differentiated. This poses problem when the ancillary data are added to the classification process since they violate the assumption of normal distribution of the training samples and give rise to multimodal distribution of data. However, the strength of the MLC is that it is not sensitive to sample size, and ensures medium accuracy which makes it adopt to various land cover classification, whereas its counterparts Classification And Regression Tree and Back Propagation Neural Network need adequate and good quality training samples.

Artificial Neural Networks (ANNs) also have been used in the field of image classification by many research scholars [16], [17], [18]. Back-Propagation (BP) algorithm is the most commonly used technique in ANN. Empirical evaluation has revealed that ANN is superior to the statistical methods used in terms of classification accuracy of training data but the classification time in neural network based classifier is linearly proportional to the size of the image. Even though this problem could be greatly reduced by implementing an adaptive back-propagation method and making classification faster, the main drawback of the network technique is its slow training phase [19].

Adoption of fuzzy concept as well as neuro-fuzzy classifiers attempts to resolve ambiguities that exists in RS classification and also increase classification accuracy [29], [21], [31]. Even though fuzzy classifiers exhibit satisfactory results, it is intuitive that they are mathematically complex and are not at ease in implementation. In complex fuzzy systems, manual determination and optimization of fuzzy membership parameters is highly difficult. Object-based classification has also been investigated extensively in remote sensing, but it demands for advanced segmentation techniques prior to classification.

Another promising classifier is Decision Tree (DT). DT classifiers are used successfully in many areas such as radar signal classification, character recognition, remote sensing, medical diagnosis, expert systems, speech recognition etc. This machine learning algorithm, based on “divide and conquer” strategy is a non-parametric classifier. Different variables and split-rules are used to split the subsets into further subsets.

For classification of features in urban area, the expected spatial resolution should be at least 5 m where buildings and roads can easily be distinguished. Following the enhanced spectral and spatial resolution of the sensors, the classification of urban and semi urban area is identified as one of the most challenging tasks in remote sensing for the following reasons. The classification accuracy is a function of two counteracting issues. The first issue is that the finer the spatial resolution the lesser the number of mixed pixels; however, this factor should increase the classification accuracy. But, on contrary to this, the finer the spatial resolution, the larger the number of detectable sub classes which implies that high within-class spectral variance of some classes decrease their spectral separability resulting in decrease in the classification accuracy. Because, the most of the urban land cover types such as roads, buildings, parking lots, grass, trees, shrubs and soil show spectral similarity. As the resolution is increased, the data exhibits abundant texture information and it becomes difficult to distinguish some geographical objects when area of interest has complicated texture information. Also, the spectral characteristic shows uncertainty if the geographical objects have complicated surroundings.

The existing traditional hard classification techniques are parametric in nature and they expect datasets to follow Gaussian distribution. Therefore hard classifiers exhibit lower accuracy in high resolution data where the assumption of Gaussian distribution of spectra is often violated, especially in the complex landscapes in high-resolution data. Another drawback of the parametric classifiers lies in the difficulty of integrating spectral data with ancillary data like digital elevation model, slope, surface temperature, texture and contextual information, etc as most of them are non-Gaussian in nature.

Therefore, parametric classifiers do not ensure of exploiting the best use of the information available through advanced sensor systems and various ancillary data at higher resolution.

The solution to the above problem is to go for the non-parametric classifiers. When non-parametric soft classification approach is proposed the ANN, Support Vector Machines (SVM), Decision Trees (DTs) and Fuzzy Soft Classifiers do gain importance. However, despite the fact that ANN and SVM show superior learning accuracy, they suffer from longer training time. This has made the rule based decision tree algorithms and fuzzy soft classifiers are attractive and promising approaches in classifying the spectrally overlapping classes [28].

Soft classifiers can be useful in describing forest boundaries, shorelines and other continuous classes. They can also bring out objects that cover small areas, which with conventional classifiers otherwise would have disappeared. In training and testing in a classification, mixed pixels are usually avoided. But it may be difficult to acquire a training set of an appropriate size if only pure pixels are selected for training, since large homogenous regions of each class are needed in the image. The training statistics defined, may not be fully representative of the classes and so provide a poor base for the remainder of the analysis.

2. Materials and Methods

2.1. Study Area and Data Characteristics

The study area considered for our work is Mangalore coastal region situated in Dakshina Kannada District, Karnataka State, India at geographical coordinates 13°00'41.5" N latitude and 74°47'35" E longitude as shown in Figure 1. The area considered for investigation is intensive and is dominated by agricultural, urban and tourism activities. It has a good mixture of classes comprising of man-made structures like concrete buildings, residential areas, roads, National highway, pool, and natural land cover features like barren land, coastal dunes, afforestation, wetlands, shrubs, sea and sea shore, etc. Also, the diverse environmental structures such as geology, soil, climate, hydrology and vegetation interact strongly with these land cover activities. This place is well connected to various important cities in the state via bus, rail and air. Moreover, the township is undergoing continuous changes over the past few years and hence selected for the study.

The image dimension of the study area is 277x255 pixels in MS data and 658x609 pixels in pan-sharpened data. Table 1 gives the specification of the image data products that has been used in the study. The data are of LISS-IV (Linear Mapping and Self Scanning) sensor of IRS P-6 (Indian Remote Sensing Satellite), Multi-spectral bands in Green, Red, Infrared and Blue.



Figure 1: Study Area: Mangalore Coastal Region, Dakshina Kannada District, Karnataka State, India

2.2. Evaluation of Image Fusion Techniques

In our research work, five different fusion techniques have been applied on the data set under study. Based on their performance, the best candidate is selected for fusing the MS and panchromatic data for the study of classification algorithms.

- Brovey Transform (BT)
- Principal Component Analysis (PCA)
- Multiplicative Technique (MT)
- Intensity Hue Saturation (IHS)
- High Pass Filtering (HPF)

2.3. Study of Classification Techniques

The motivation behind this research is the fact that accurate classification of remotely sensed data into various LU/LC is very essential in proper management and monitoring of natural as well as man-made resources on the Earth. The aim of this research is to improve the classification accuracy over semi-urban LU/LC features in high resolution satellite image by adopting soft classification algorithms and exploiting the spatial information inherent to the high resolution data.

3. Results and Discussion

The objective of evaluation of image fusion techniques is to determine the best fused data for classification of semi-urban LU/ LC features. Hence, the objective has been framed to carry out image fusion to integrate a multi-spectral image of 5.8 m and a panchromatic image of 2.5 m spatial resolution at pixel level by employing five of the commonly available data fusion algorithms and to evaluate the algorithms based on visual and statistical analysis, and finally substantiate the findings with classification accuracy.

3.1. Visual Analysis

Visual comparison of all the fused images has been used for the qualitative assessment since it is the most simple but very effective tool. When all the pan-sharpened images are compared visually with the original MS image, as far as the spatial quality is concerned, it is apparent that the spatial resolution of

the resultant/ fused images is higher than the original MS image and it is comparable to the resolution of the original PAN image. A few small and fine urban features such as roads, building edges, vehicles on high-way, flag post in front of the main building, slope of the roof, building shadows, separation between the buildings, individual tree crowns, array of trees in coconut farm etc. that are not discernible in the original 5.8m resolution MS image are identified individually in all the fused images. Other large features such as pools, tree clusters, roads and building blocks are much sharper than those seen in the original MS image.

3.2. Quantitative Analysis

The statistical analysis is necessary in order to examine the spectral information preservation in the resultant fused image. Therefore, mean value and the standard deviation were studied for all the fused images.

Table 1: Histogram-Means of the Bands of the Fused Images

| | MS | PCA | BT | MT | HIS | HPF | PAN |
|----------------|--------------|--------------|--------------|-------------|--------------|--------------|-------|
| Band 1 | 107.5 | 49.4 | 43.3 | 30.5 | 107.4 | 107 | |
| Band 2 | 75.5 | 110.9 | 41.2 | 42.2 | 115 | 75 | |
| Band 3 | 115.3 | 47.5 | 40.8 | 29.6 | 75.4 | 114.8 | 79.25 |
| Column Average | 99.43 | 69.26 | 41.76 | 34.1 | 99.26 | 98.93 | |

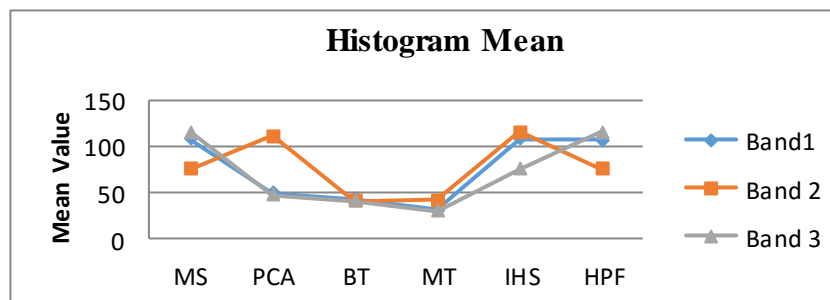


Figure 2: Histogram Means of Fused Image

From Figure 3 it is observed that in Band-1, the mean value is maximum for MS, HIS and HPF technique - while it is almost same for BT, MT and PCA techniques. In Band-2, the mean values are same for MS and HPF techniques - while it is almost same and it is maximum for PCA and HIS techniques. The mean values are minimum for BT and MT techniques. In Band-3, the mean values are maximum for MS and HPF techniques and it is most minimum for MT technique.

Standard deviation (SD) is an important index to measure the information content in any image. It reflects the deviation degree of values relative to the mean of the image. The computation of standard deviation of the original image and the fused images are carried out band-wise and is indicated in Table 2. Figure 3 shows graphical representation of standard deviation of all the bands of the MS and the fused images.

Table 2: Standard Deviation of the Bands of the Fused Images

| | MS | PCA | BT | MT | HIS | HPF | PAN |
|----------------|-------------|--------------|--------------|-------------|--------------|-------------|-------|
| Band 1 | 27.3 | 26.3 | 30.2 | 29.9 | 29.2 | 27.4 | |
| Band 2 | 15.3 | 41.7 | 20.2 | 26.7 | 20.8 | 15.4 | |
| Band 3 | 17.7 | 22.5 | 23.8 | 25.9 | 14.7 | 17.8 | 26.92 |
| Column average | 20.1 | 30.16 | 24.73 | 27.5 | 21.56 | 20.2 | |

Band 1: Green, Band 2: Red, Band 3: Infrared

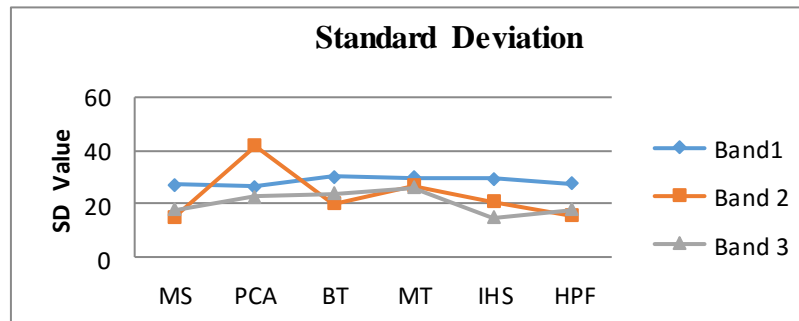


Figure 3: Standard Deviation of Fused Image

From the histogram statistics it is revealed that in PCA method, the histogram means of all bands are closer to the corresponding bands in MS bands. The value of SD varies very slightly with respect to MS data. The Multiplicative Technique indicates a major increase in statistical parameters. The Brovey Technique depicts major changes in the statistical parameters as the new pixel values are derived from the ratio of MS band and PAN band data. All the statistical values are found to be at lower end. In HPF fusion technique the mean and SD values are almost equal to the original MS bands. In IHS technique SD values are high, while the mean value remains almost same as that of MS data.

4. Conclusion

High-resolution and multispectral images are an important data source for acquiring large-scale and detailed geospatial information for a variety of applications. Image fusion techniques have proven to be effective tools for providing better image information for visual interpretation, image mapping, and image-based GIS applications.

To obtain better classification results, it is very essential to have a good fused image which retains both spectral and spatial properties of MS and panchromatic images, respectively. In this paper five different techniques are used to evaluate the performance of Image fusion method. Hence, having obtained the best fused image of MS and panchromatic data, the future work will concentrate on developing a classification methodology based on Ant Colony Optimization (ACO) algorithm and evaluate the same with the existing MLC and DT (Decision Tree) classification techniques.

Acknowledgements

The authors are grateful to the Department of Geo-informatics and Hydraulics, NITK, Surathkal for providing essential data to carry out the research work.

References

- [1] Pohl, C. and Van Genderen, J.L. *Multisensor Image Fusion in Remote Sensing: Concepts, Methods and Applications*. International Journal of Remote Sensing. 1998. 19 (5) 823-854.
- [2] Vyjayanthi Nizalapur. *Land Cover Classification Using Multi-Source Data Fusion of ENVISAT-ASAR and IRS P6 LISS-III Satellite Data- A Case Study over Tropical Moist Forested Regions of Karnataka, India*. The International Archives of the Photogrammetry, Remote Sensing and Spatial Information Sciences. XXXVII; Part B6b, Beijing, 2008.
- [3] Zhijun Wang, Djemel Zoiu, Costas Armenakis, Deren, Li. and Quingquan, Li. *A Comparative Analysis of Image Fusion Methods*. IEEE Transactions on Geoscience and Remote Sensing. June, 2005. 43 (6) 1391-1402.

- [4] Padwick, C., et al., 2010: *WorldView-2 Pan-Sharpener*. In: ASPRS 2010 Annual Conference, 26-30 April, San Diego, CA.
- [5] Thomopoulos, S.C., 1989: *Sensor Integration and Data Fusion*. In: Proceedings of the SPIE 1198, Sensor Fusion II: Human and Machine Strategies, 6–9 November, Philadelphia, PA. 178-191.
- [6] Luo, R.C. and Kay, M.G. *Multisensor Integration and Fusion: Issues and Approaches*. In: Proceedings of the SPIE on Sensor Fusion, 4–6 April, Orlando, FL, 1988. 931; 42-49.
- [7] Carvalho, H., et al. *A General Data Fusion Architecture*. In: Proceedings of the Sixth International Conference on Information Fusion (Fusion'03), 8-10 July 2003, Cairns, Australia. Piscataway, NJ: IEEE. 2003. 2; 1465-1472.
- [8] Cohen, O. and Edan, Y. *A Sensor Fusion Framework for Online Sensor and Algorithm Selection*. Robotics and Autonomous Systems. 2008. 56; 762-776.
- [9] Robert and Schowengerdt. *Remote Sensing: Models and Methods for Image Processing*. Academic Press, Elsevier. 2006.
- [10] Chavez, P.S., Sides, S.C. and Anderson, J.A. *Comparison of Three Different Methods to Merge Multiresolution and Multispectral Data: Landsat TM and SPOT Panchromatic*. Photogrammetric Engineering & Remote Sensing. 1991. 57 (3) 295-303.
- [11] Zhijun Wang, Djemel Ziou, Costas Armenakis, Deren, Li and Qingquan, Li. *A Comparative Analysis of Image Fusion Methods*. IEEE Transactions on Geoscience and Remote Sensing. June 2005. 43 (6) 1391-1402.
- [12] Saroglu, E., Bektas, F., Musaoglu, N. and Goksel, C. *Fusion of Multisensor Remote Sensing Data: Assessing the Quality of Resulting Images*. XXth ISPRS Congress, Geo-Imagery Bridging Continents, Istanbul, Turkey, 12-23 July 2004, Commission IV Papers. XXXV; B4.
- [13] Sanjeevi, S., Vani, K. and Lakshmi, K. *Comparison of Conventional and Wavelet Transform Techniques for Fusion of IRS 1 C LISS III and PAN Images*. 22nd Asian Conference on Remote Sensing, November 5-9, 2001, Singapore.
- [14] Yun Zhang. *Problems in the Fusion of Commercial High-Resolution Satellite as well as Landsat 7 Images and Initial Solutions*. Symposium on Geospatial Theory, Processing and Applications, Commission IV, WG IV/7. 2002.
- [15] Lu and Weng Q. *A Survey of Image Classification Methods and Techniques for Improving Classification Performance*, International Journal of Remote Sensing. 2007. 28 (5) 823-849.
- [16] Benediktsson, J.A., Swain, P.H. and Ersoy, O.E. *Neural Network Approaches versus Statistical Methods in Classification of Multisource Remote Sensing Data*. IEEE Transactions on Geoscience and Remote Sensing. July 1990. 28 (4) 540-552.
- [17] Dwivedi, R.S., Sreenivas Kandrika and Ramana K.V. *Comparison of Classifiers of Remote-Sensing Data for Land-Use/ Land-Cover Mapping*. Current Science. 2004. 86 (2) 328-335.
- [18] Gong, P. *Integrated Analysis of Spatial Data from Multiple Sources: Using Evidential Reasoning and Artificial Neural Network Techniques for Geological Mapping*. Photogrammetric Engineering & Remote Sensing. 1996. 62 (5) 513-523.

- [19] Philip Heermann, D., and Khazenic, Nahid. *Classification of Multispectral Remote Sensing Data Using a Back-Propagation Neural Network*. IEEE Trans. Geoscience and Remote Sensing. 1992. 30 (1) 81-88.
- [20] Justin Paola, D. and Robert Schowengerdt, A. *The Effect of Neural-Network Structure on a Multispectral Land-Use/ Land-Cover Classification*. Photogrammetric Engineering & Remote Sensing. 1997. 63 (5) 535-544.
- [21] Serpico, S.B., Bruzzone, L. and Roli, F. *An Experimental Comparison of Neural and Statistical Non-Parametric Algorithms for Supervised Classification of Remote-Sensing Images*. Pattern Recognition Letters 17, Elsevier Science. 1996. 1331-1341.
- [22] Mahesh Pal and Paul Mather, M. *A Comparison of Decision Tree and Backpropagation Neural Network Classifiers for Land Use Classification*. Geoscience and Remote Sensing Symposium. IEEE International Proceeding. 2002. 1; 503-505.
- [23] Michael Zambon, Rick Lawrence, Andrew Bunn and Scott Powell. *Effect of Alternative Splitting Rules on Image Processing Using Classification Tree Analysis*. Photogrammetric Engineering & Remote Sensing. 2006. 72 (1) 25-30.
- [24] Sameer Saran, Amit Bharti, Geert Sterk and Raju, P.L.N. *Comparing and Optimizing Land Use Classification in a Himalayan Area Using Parametric and Non-Parametric Approaches*. Journal of Geomatics, Indian Society of Geomatics. 2007. 1 (1) 23-32.
- [25] Mahesh Pal and Paul Mather, M. *An Assessment of the Effectiveness of Decision Tree Methods for Land Cover Classification*. Remote Sensing of Environment. 2003. 86 (4) 554-565.
- [26] Marc Simard, Saatchi, S.S. and De Grandi, G. *The Use of Decision Tree and Multiscale Texture for Classification of JERS-1 SAR Data Over Tropical Forest*. IEEE Transactions on Geoscience and Remote Sensing. 2000. 38 (5) 2310-2321.
- [27] Michael Zambon, Rick Lawrence, Andrew Bunn, and Scott Powell. *Effect of Alternative Splitting Rules on Image Processing Using Classification Tree Analysis*. Photogramm. Eng. Remote Sens. 2006. 72 (1) 25-30.
- [28] Philip Heermann, D. and Khazenic, Nahid. *Classification of Multispectral Remote Sensing Data Using a Back-Propagation Neural Network*. IEEE Trans. Geoscience and Remote Sensing. 1992. 30 (1) 81-88.
- [29] Andras Bardossy and Luis Samaniego. *Fuzzy Rule-Based Classification of Remotely Sensed Imagery*. IEEE Transactions on Geoscience and Remote Sensing. 2002. 40 (2) 362-374.
- [30] Hannes Taubenböck, Thomas Esch and Achim Roth. *An Urban Classification Approach Based on Object-Oriented Analysis of High Resolution Satellite Imagery for a Spatial Structuring Within Urban Areas*. 1st EARSeL Workshop of the SIG Urban Remote Sensing Humboldt-Universität zu Berlin, 2-3 March 2006.
- [31] Yoonsuk Choi, Ershad Sharifahmadian and Shahram Latifi Bruno. *Quality Assessment of Image Fusion Methods in Transform Domain*. International Journal on Information Theory. 2014. 3 (1) 7-18.

Application of RS and GIS for Land Use/Land Cover, Geomorphological Studies in Nalgonda District, Telangana, India

Ramadass G., Udaya Laxmi G., and Sriramulu G.

Department of Geophysics, Osmania University, Hyderabad, India

Publication Date: 5 March 2016

DOI: <https://doi.org/10.23953/cloud.ijarsg.46>



Copyright © 2016 Ramadass G., Udaya Laxmi G., and Sriramulu G. This is an open access article distributed under the **Creative Commons Attribution License**, which permits unrestricted use, distribution, and reproduction in any medium, provided the original work is properly cited.

Abstract The Land Sat 8 ETM+ satellite image of an area 17579 sq.km. Corresponding to the Nalgonda District and Ramadugu study region (1200 sq.km) in the northwestern part of Cuddapah basin, Telangana State was analyzed to determine the geological/structural configuration, land use land cover and geomorphology of the regions. The disposition of various faults, other lineaments and thirteen (1 to 13) radial drainage structures in the region were delineated. The findings are significant in view of the paucity of structural data in the region and form a geo structural data base for prognostication of lamproites.

Keywords *Domal Structures; Geomorphology; Lineaments; Satellite Image; Structural Configuration*

1. Introduction

Remote sensing a relatively new resource evaluation tool in geophysical surveys proves to be invaluable. The main advantage accruing from image interpretation is the 'overview' it affords. Linear features running for long distances such as dykes, fractures, joints, and faults are often indicators of mineral/groundwater resources. These features sometimes escape notice on ground as local morphological features such as weathering or vegetation cover and/or cultural features such as roads and buildings dominate them at places. The continuity of such partially obliterated features can very easily be traced from aerial photographs or satellite images and coupled together with other ground geophysical information can prove to be a valuable exploration tool.

The present work strategy consists of image analysis and interpretation to understand the LAND SAT 8 ETM map landuse, landcover, geomorphology and lineament studies of Nalgonda district and detailed structural and geomorphological studies, and prevailed drainage pattern with a view to compare with reported resources of Lamproites at Ramadugu, Somavari gudem and Vattikodu study region.

2. Data Base

The data have been collected from NRSC, Balanagar, Hyderabad and freely available on net source. The primary data collected are Survey of India (SOI) topo sheets at scale of 1:50,000 and 1:250,000 (Toposheet No's 56 K, 56 L, 56 O and 56 P) and multi spectral Satellite Imagery of the LANDSAT 8 ETM, 29-10-2011. Resolution 28.5 m number of band are 8 and path 144 and row is 48 of Nalgonda district.

The Land Sat 8 ETM+ satellite image of an area 17579 sq.km. Corresponding to the Nalgonda District and Ramadugu study region (1200 sq.km) in the northwestern part of Cuddapah basin, Telangana State was analyzed to determine the geological/structural configuration, land use land cover and geomorphology of the regions. The disposition of various faults, other lineaments and thirteen (1 to 13) radial drainage structures in the region were delineated. The findings are significant in view of the paucity of structural data in the region and form a geo structural data base for prognostication of lamproites

3. Study Area

The Nalgonda district is located in the northeastern part of the Proterozoic Cuddapah basin is located between latitudes $16^{\circ} 15' N$ to $17^{\circ} 45' N$ and longitudes $78^{\circ} 45' E$ to $80^{\circ} E$ lies in the State of Telangana, India (Figure 1). The district covers an area of 17,579 Sq.km and is bounded on the north by Medak and Warangal districts, on the east by Khammam and Krishna districts, on the south by Guntur and Mahabubnagar districts. In the southern part of the district along the northern bank of Krishna River the rocks of Archaean Peninsular Gneissic complex are unconformably overlain by sedimentary rocks of 1100-600 Ma, constituting the Cuddapah super group and Kurnool group. The geological formations (GSI, 1999) in the district comprises migmatites, granites granodiorite, tonalite-trondhjemite suite of rocks and hornblende-biotite schist, metabasalts, meta-rhyolite and banded hematite quartzite and Dharwar super group are exposed as linear belts near Peddavura on the Hyderabad-Nagarjuna sagar road and also around Fathepur village of Miryalaguda Mandal.



Figure 1: Location Map of Study Area

3.1. Image Processing and Analysis

The present study evaluates the effect land use land cover and structural studies in Nalgonda District. The work strategy consists of Image analysis and interpretation, detail analysis and methodology shown in Figure 2. The special database consists of survey of India (SOI) top maps and Indian Remote sensing Satellite images. The base map serves the purpose of demarcating district boundary,

natural and cultural features and for geo-referencing. The precision geo-coded data, Land Sat 8 ETM multi spectral scanning radiometer with eight bands and being capable of providing high resolutions were prepared using several band combinations and as many band rationing/indexing techniques mentioned by several authors (Goetz, 1975; Chavez et al., 1982; Singer, 1980; Miller and Pearson, 1971; Price, 1995) techniques of image information of the earth's surface. The ETM acquires the image data in visible (band1: 0.45-0.515 μm , band 2: 0.525-0.605 μm , band 3: 0.63-0.69 μm), near-infrared (band 4: 0.75-0.90 μm), mid-infrared (bands 5: 1.55-1.75 μm and band 7: 2.09-2.35 μm), far-infrared (band6: 10.4-12.5 μm) and panchromatic (band 8: 0.52-0.9 μm). The spatial resolution is 15m in the panchromatic band, 30m in the visible, near infrared, and mid-infrared bands, 60m in the far-infrared band and each scene represents the Earth in 183 by 170 kilometers. The data of satellite pass-over the area on 29-10-2011 and the standard data product corresponds to a scene with path/row numbers 144/48. Subsequently the image was geo-referenced and analyzed using appropriate software modules of ERDAS 9.1 and ArcGIS 9.2 software's are used for digital image processing and statistical analysis (Short, 1982; Hammond and McCullough, 1980; Castleman, 1978). Geometrical rectification for satellite data was done using ground control points (GCPs) extracted from the base map. The ground control points considered include road junctions, intersection of the drainage lines and manmade features. That allows one to display process, enhance, analyze and output raster as well as vector data for various applications. Landsat 8 ETM image of Nalgonda district is shown in Figure 3.

Visual interpretation of the satellite image analyses data have been used for preparation of land use land cover, lineaments maps of Nalgonda district and geomorphological map of the Ramadugu study area.

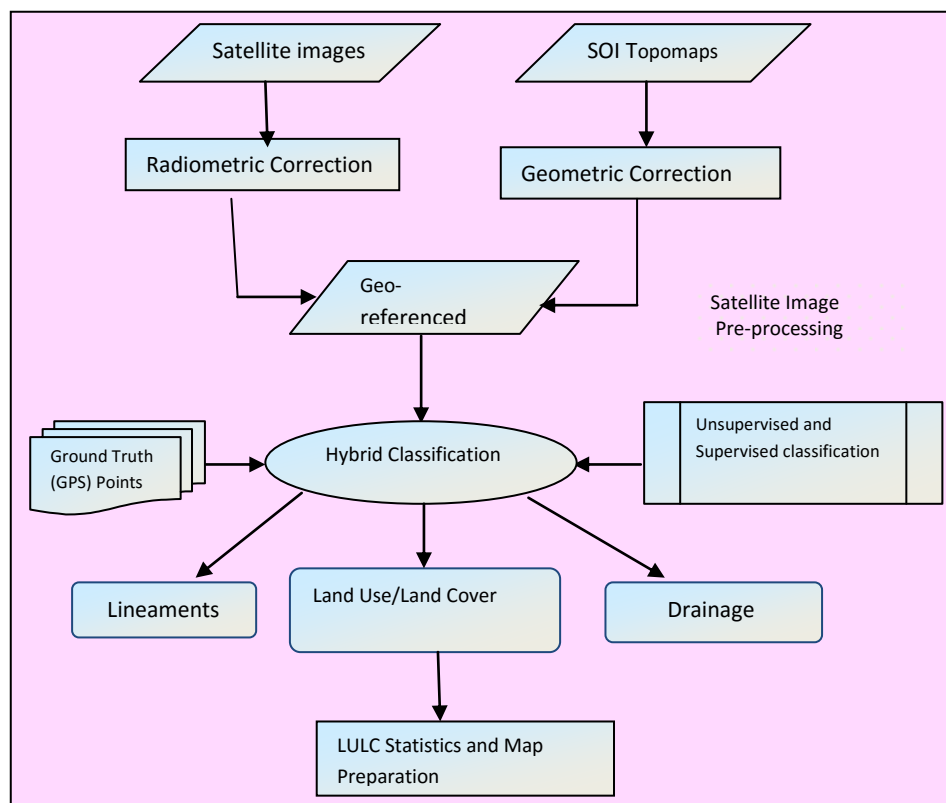


Figure 2: Shows the Flow Chart of Detailed Analysis of the Study Area

3.2. Land Use/Land Cover

The present classification is done with the help of Landsat 8 ETM Geocoded imageries to 1:250,000 scale by visual interpretation techniques.

The Nalgonda district situated in the heart of the Deccan Plateau is located between latitudes $16^{\circ} 15'$ N to $17^{\circ} 45'$ N and longitudes $78^{\circ} 45'$ E to 80° E, covering an area of more than 17579 Sq.km (Figure 3), at present district consists of fifty nine (59) mandals with 1175 Gram Panchayats. The entire district stands on pink and gray granites, these granite hills are spread all over the district and surrounding areas. Rivers Musi and Krishna rivers, which are the southerly flowing tributaries of the easterly flowing Krishna River. The Musi River begins in Anantagiri Hills near Vikarabad, Ranga Reddy district, 90 km to the west of Hyderabad and joins Krishan River near Wazirabad in Nalgonda district. Telangana is separated from Andhra Pradesh by the Krishna River, which acts as a geographical divider between the two. The Krishna River is the third longest river of the country. The river Krishna starts forming the delta downstream of Utsapalle village, once a famous gravel diamond-mining centre. The land use Land cover is made in to ten conventional divisions in the present study (1) Agricultural (2) canal (3) fallow land (4) forest (5) habitation (6) open land (7) plantation (8) river(9) road and (10) water body based on the colour, tone and texture shown in Figure 4.

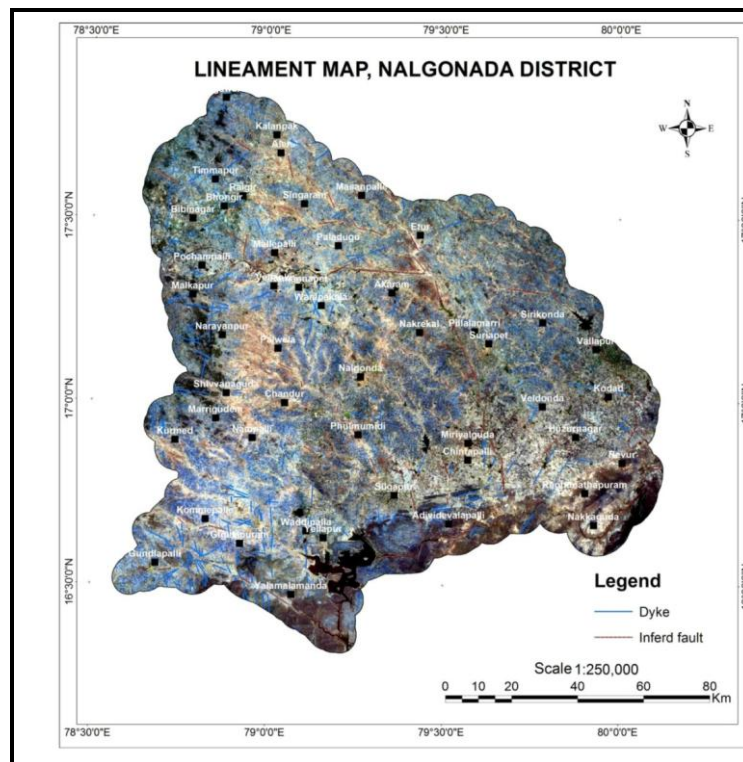


Figure 3: Landsat 8 ETM Image of Nalgonda District

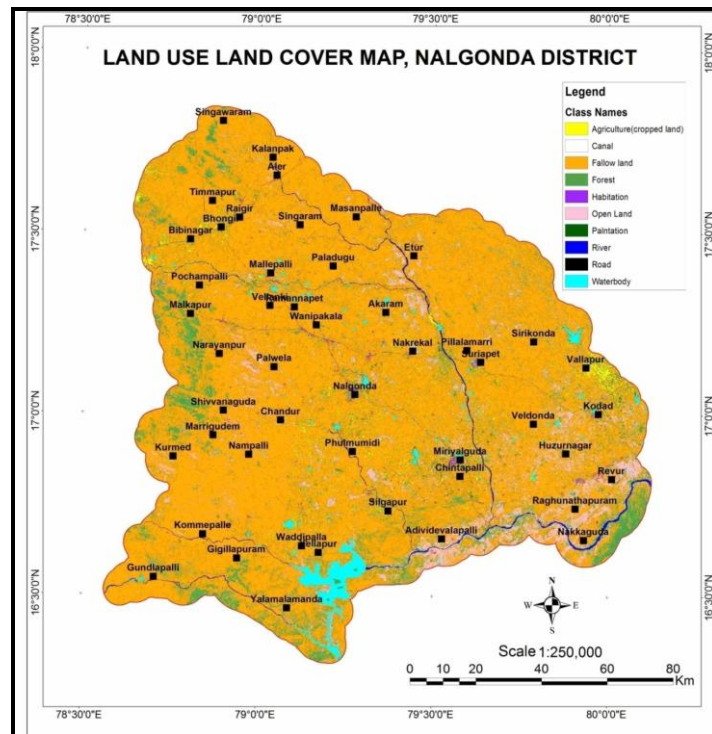


Figure 4: Land Use Land Cover map of Nalgonda District

The land use/land cover statistics of Nalgonda district for 2011 shown in Table 1.

Table 1: Land Use Land Cover statistics of Nalgonda District

| S. No. | Class Name | Area(Ha) | Area (Sq.Km) |
|--------|---------------------------|----------|--------------|
| 1. | Agriculture(Cropped land) | 27512 | 275 |
| 2. | Canal | 352 | 4 |
| 3. | Fallow land | 1391953 | 13920 |
| 4. | Forest | 169548 | 1695 |
| 5. | Habitation | 6999 | 70 |
| 6. | Open land | 107173 | 1072 |
| 7. | Plantation | 12281 | 123 |
| 8. | River | 10906 | 109 |
| 9. | Road | 1163 | 12 |
| 10. | Water body | 25860 | 259 |

Essentially the image has an intermediate tonal quality with fairly well distributed tonal unit agriculture /cropped land (yellow), canal (white), fallow land (yellow grey), forest (light green), Habitation (cyan to magenta), open land (pink), plantation (thick green), river (sky blue), road (black) and water body (light greenish). Further sub-classification of the landscape is guided by variations within these tonal units. Thus, light green signatures surrounding darker green tones correspond to weathered granite.

1) Agriculture (Cropped Land)

All the cultivated land with cropped (yellow color) is considered in this class in the district area the cropped lands have wet and dry cultivated lands. The areal extent of this land covered is 275Sq.km. Most of the land agricultural land in the study area is supported by peninsular gneissic complex.

2) Canals

Physiographically, the study area represents a pediplain with inselbergs and regional hills, which irrigated by a network of Nagarjuna Sagar canal only 4 sq.km, which has been caused the silty of the stream/river course in the Musi and Halia River drainage basin. Even some of the major stream course in the vicinity of canals turned out to be shallow marshy lands due to the continued anthropogenic activities.

3) Fallow Land

This class consists of areas of intensive use with much of the land occupied by man - made structures. This class consists of dense urban, low sub urban village, sub urban these are appearing in bluish ash tone having very coarse texture. It is defined as an area occupied by 13920 sq.km. However, due to non-agricultural use and which has a cover of buildings, roads and communications, utilities in association with water, vegetation and vacant lands.

4) Forest

Forest land are represent NNW-SSE trending structural hills in the western side of the Nalgonda district, sparse forest land located in an undulating terrain composed predominantly of granites, area occupied by the forest land is 1695 sq.km and the area to the north of Krishna is a pediplain terrain while its south is hilly terrain occupied by the Nallamala reserved forest.

5) Habitation

Habitations in the district were fluoride affected 70 sq.km. Out of 59 mandals 48 mandals are affected by fluoride, only 11 mandals are not effected by fluoride (Venkateshwarlu et al., 2014). High concentration of fluoride presence is up to 8 ppm in certain villages, Munugode, Nalgonda, Marriguda, Chandur, Chityal Nampally, Narayanpur, Narketpally, Choutuppall, Chinthapally, Peddavura and Tipparchy are severely affected mandals in the district, 1175 Gram Panchayats and about 32100 habitations in the district.

6) Open Land

Open or barren lands are of 1072 sq.km. Quasi open and open have little or no vegetation and limited to support vegetative communities due to human activity, areas such as agricultural, extractive and industrial land uses may be classed as barren land, therefore these areas must be explored very closely through the use of supplemental such as aerial photographs and topographical sheets included in this category are the sub categories of gardens, exposed rock and disturbed land, play grounds. They appeared in pale yellow colors fine textured.

An analysis of the nature and rate of land use change and its associated impact on groundwater quality is essential for a proper understanding of the present environmental problems.

7) Plantation

It describes mostly the natural vegetation occupied by 123 sq.km, which includes Grass lands, shrub, and mixed vegetation are sub categories. These areas become evident when large scale imagery is used. These areas generally appear in pale pinkish to bright red and dark reddish tone having smooth to mottled texture depending on the nature of plants, their distribution density, and moisture content.

8) River

Major rivers include Krishna, Dindi, Peddavagu, Aleru, Halia, Konga and Palleru, which form part of the Krishna river basin, total area covered is 109 sq.km, all the streams generally flow in southeastern direction and join the Krishna River. The district receives 50-70 cm rainfall per annum and experiences semi-arid climate. When we look at the Nalgonda district region, we find that the major river system draining this area consists of the Musi and its tributaries including Aleru vagu. For ease of examination, the region can be divided into the northwestern, northern, northeastern, eastern, southeastern, southern, southwestern, western and the central regions of Nalgonda Town.

9) Road

The total roads occupied in the district (12 sq.km) usually the built up roads lies in all types of terrain and waste lands in association with road, rail and artifact.

10) Water Bodies

The classification of water bodies (259 sq.km) is dependent upon scale and resolution characteristics of the remote sensing imagery used for interpretation. In some instances, a water body may be large enough to be identified as such or the water body may contain submerged or emergent vegetation. In this case that water body will be identified under the wetlands category. Water bodies are however very fine textured with their tone ranging from pale to cyan to almost black depending on the depths and turbidity.

3.3. Structural Analysis

The analysis of lineaments mapped from remote sensing data is a common reconnaissance tool for structural evaluation and follow-up geo -investigations. The relief, slope, extent of weathering, type of weathered material and overall assemblage of different land form is defined as Geomorphology which play an important role in modeling the land use land cover and structural (Sarala, 2013) elements associated with lineaments include fault zones, fractures (joint zones), and fault axes, linear igneous intrusions, apart from major features were delineated from geological map, satellite Imagery and field visits.

Geologically all faults, folds, joints, fractures etc. are considered to be lineaments. The drainage of the study area is easily visible on the Landsat 8 Satellite Image. These can be identifiable through remote sensing using lithological displacement, drainage pattern which follows faults (Trellis drainage pattern), bedding planes, folds which could be identifiable through its litho- logic similarities in the curvilinear bed, faults scraps, emplacement of dykes through fault planes, weathering pattern through joints. Many emphasized the importance of lineament interpretations and digital lineament analysis (Kutina, 1969; Katz, 1982; Liu et al., 2000) in localizing the major structural configuration of the region shown in Figure 5.

In buried pediments where granitic rocks with little soil cover and pediplains where soil cover is much high, these lineaments are not visible much through visual interpretation. Apart from the lithological composition of rocks the other element of geological interpretation is structural studies. However, through subjective (Moore and Waltz, 1983) a manual procedure is sometimes more reliable than their detection in the field. Structural interpretation in the present study has been lineaments, limited to limit mapping.

The present study area Nalgonda district is dominated by presence of biotitic granite associated with NW-SE and SW-NE. N-S and E-W directions and prominent linear features were inferred in Figure 5.

Seven linear-deep-seated faults are running NW-SE, N-S, E-W and NE-SW trending deep faults/fractures as well as margins of basic dykes which have persisted through time and influence the geological history of the area. Some of these lineaments correlate/or coincident with mapped structures such as faults, shear zones, dykes and foliation. There are eight deep seated regional faults have been identified on the satellite image, F1 fault is falling at south western side of the Nalgonda district running from South Yellapur to Gigivapuram trending E-W direction, F2 is located the N-S direction runs from west of Adavidevarapally to Silgapur, F3 trending from NE-SW side of Raghunathapur to Sirikond, F4 is long length trending in the NW-SE direction from waddipalli to Singawarm. Fault F5 (E-W), F6 NW-SE of Chintapalli to Miryalguda, F7 trending E-W of Nakrekal north to Sirikond and F8 is in between Nakrekal–Pulimamidi to Etur are trending in the E-W, NW-SE. E-W and N-S directions respectively.

The lamproites of Jaggayyapeta Lamproites field (Chalpathi Rao et al., 2004; Ramadass et al., 2015) occur in close spatial association with NNW-SSE and WNE-ESE trending dolerite dykes and fracture system and is mostly emplaced at the contact between dolerite and granite/gneisses.

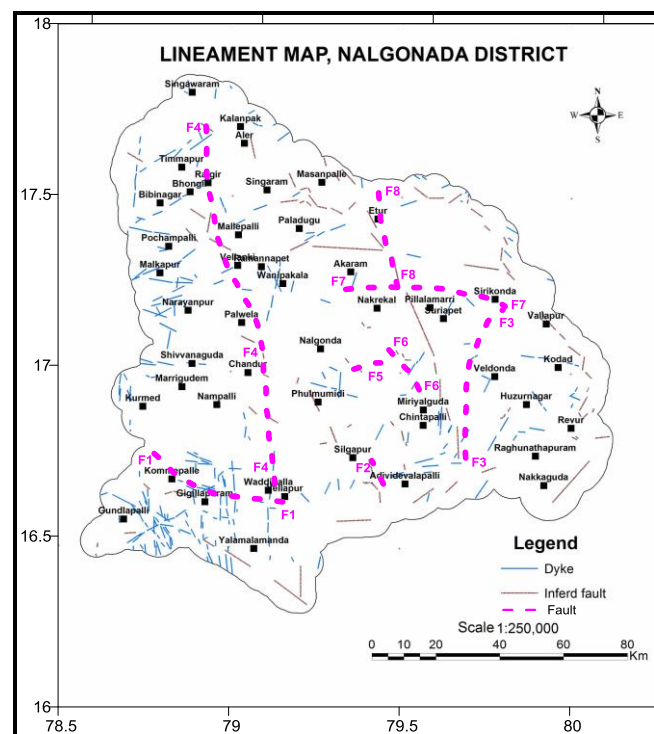


Figure 5: Lineament map of Nalgonda District

3.4. Ramadugu Study Area

The study area is situated in and around Ramadugu in Nalgonda district, the area is well known for the recent discovery lamproites clusters (Sridhar et al., 2005) are located north western part of Dharwar craton. Figure 6, Land Sat 8 ETM+ image (1:50,000 Scale) covering an area of approximately 1200 sq.km (Longitudes $79^{\circ} 5'$ to $79^{\circ} 25'$ and Latitudes $16^{\circ} 42'$ to $16^{\circ} 58'$) was digitally processed and visually interpreted to elucidate the structural fabric and geomorphology of the region comprising the geology and lineaments.

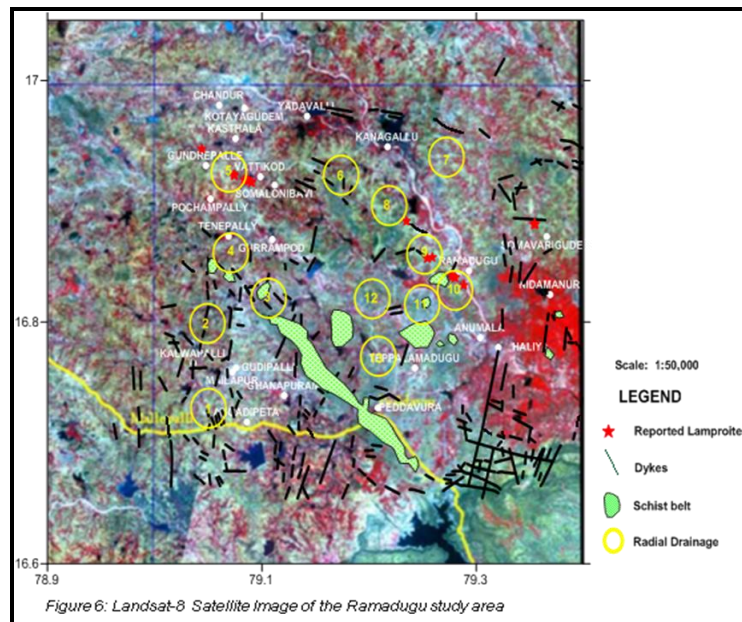


Figure 6: Landsat-8 Satellite Image of Ramadugu Area

The geomorphology map of the Ramadugu falls in Topo Sheet No. E44T1, E44T2 and E44T5 in parts of Nalgonda district of Telangana State is shown in Figure 7. The maximum elevation is varying from 242m to 150m south of Ramadugu village and north western side of Halia River.

There are number of dykes of dolerite, reefs of quartz and multiple fracture systems commonly trending N-S and ENW-WSE and NW-SE. The NW-SE trending dykes oldest followed by N-S and ENE–WSW trending dykes (Sridhar and Rau, 2005). These dykes run for tens of kilometers intermittently. The width of the dykes varies from less than a meter to 20 m. These dykes are massive and are mostly doleritic in composition, quartz veins traverse older rock unit and trend N-S and N 30° E, S 30° W, N 60° E-, S 60° W and N 75° W and S75° E are common in the area.

All of dykes in the region are associated with the younger granites and granitoids. The overall drainage is dendritic to sub-dendritic, dendritic homogenous nature of the area and controlled by numerous joints and fractures. The general slope of the area is observed trending toward the south east. The Peddavagu-Aliya River is also showing the flood plains in the study area even through this stream is dry throughout the year except few days after rains.

Ramadugu study areas there are seven (f1-f7) fault/lineament (Figure 6) have been identified. The fault/lineament f1 is observed is located in south western part of the study area which is contact zone between the younger granites and granite, graneodorite granite gneiss. The fault f2 indicating the contact between the western margin of Peddavura schist and granite, graneodorite granite gneiss. f3 is observed near Tenepalli it is abutting the north western part of the schist belt from the biotite gneiss. The fault f4 is trending in NE-SW direction, fault f5 (NW-SE) and f6 (NE-SW) are the important tectonic lineaments/fault zones in the study area which are highly disturbed nature. The emplacement of lamproites near Somvarigudem, Marepalli, Yacharam and Ramadugu regions are associated within fault/shear environment of f5 & f6. The f7 is separating the Lamproites of Vattikod from Gudrapalli Lamproites. The reactivation of these major crustal lineaments in this region, probably during upliftment of the Nallamala sub basin, caused mantle up-wrapping and facilitated the emplacement of mineralization (lamproites) (Alok Kumar et al., 2013) close to the E-W and the NNW-SSE trending faults/fractures.

The domal (radial) structures are reflected in the geomorphology of the region as elevated circular drainage pattern of the region from which the disposition and various geomorphological units are identified. The major drainage of the region is provided by the river Krishna and its tributaries. The well-developed weathered layer along with the final drainage density (Figure 7) give rise to numerous ponds in this region. Topographic highs and lows in turn were indicated by regions of circular or radial alignment of the drainage. Such radial structures taken in conjunction with faulted zones are contact between dolerite dykes, granite and gneisses are potential zones for lamproites indicators

Domal/radial structures are reflected in the geomorphology of the study region is elevated circular features, the Remote sensing approach to locate potential lamproites/kimberlites zones is to delineate region of domal geomorphology that is characterize by topography highs, higher intern and indicated by region of circular and radial alignment of the drainage. The general slope of the area is observed trending towards the south east Thus lineaments that fall within the migmatite gneisses show a concordant relation with the regional Dharwarian trend, i.e., NW-SE, whereas lineaments that fall over the biotite granites show both parallel as well as transverse relation, i.e., NW-SE, WNW-ESE, E-W, ENE-WSW and N-S.

Circular or radial alignment of the drainage structures taken in conjunction with the contact zone between the dyke environment and granitic gneisses and implying the involvement of distinct deep – seated faults/fractures in controlling their lamproite emplacement. Thirteen main circular zones have been identified numbered 1 to 13 details are given in Table 2. Among these seven zones (1, 2, 3, 7, 11, 12 and 13) no lamproites have been reported.

Zone five (5) is located at west of Vattikod region has already reported ten clusters of lamproites (Alok kumar et al., 2014) which is passing through the fault f6 and f7 trending in the NW-SE direction, most of these lamproites are emplaced at the contact zone between the Alkali Feldspar granite and biotite gneiss granitic–gneiss basement and in dolerite dykes.

Zone 6 is situated in between Samulonibavi and Kanagalu in Pulavay block reported few lamproites, similarly zone 8 represented by one lamproites near west of Marepally village, Zone 9 occurring east of Yacharam, this is the smallest zone reported two lamproites (Sridhar et al., 2005) and Zone 10 and zone 11 are located around Ramadugu passing through the NW-SE trending fault f5 has reported occurrence of Lamproites (Sridharar et al., 2005; Chalapathi Rao, 2013), which represents eight lamproites occur as dykes. Lamproites at Somavarigudem occur in close association with dolerite dykes and fault contact environment is observed in lamproite emplacement in the study area.

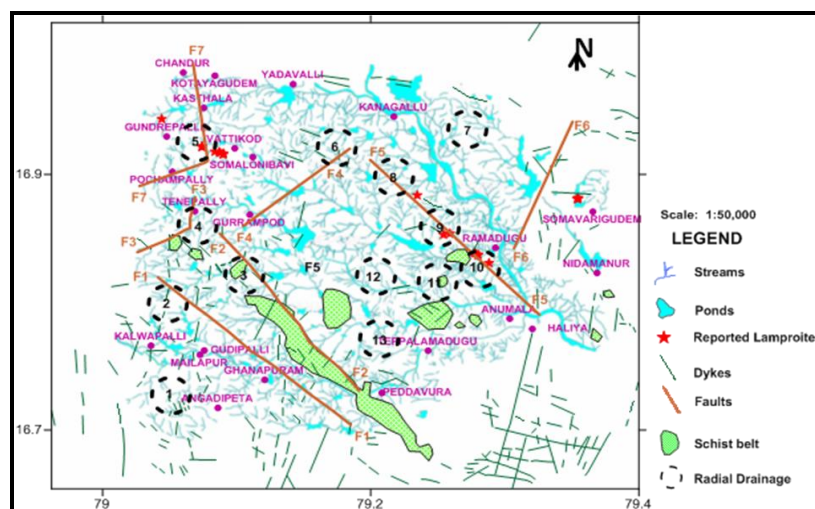


Figure 7: Drainage and Lineaments Pattern of the Ramadugu Study Area

Table 2: Identified Circular Zones in Ramadugu Study Area

| Circle No. | Location | Latitude in Degrees | Longitude in Degrees | Remarks |
|------------|----------------------------------|---------------------|----------------------|--|
| 1. | Angadipet | 16.72775724 | 79.05033432 | --- |
| 2. | Kalwapalle (North) | 16.79823752 | 79.04795858 | f1 fault(NW-SE) |
| 3. | Gurramphad (South) | 16.82041109 | 79.10576824 | f2 fault(NW-SE) |
| 4. | Between Tenepalle and Gurramphad | 16.85842293 | 79.07171598 | f2 fault (NW-SE) & f3 (NE-SW) |
| 5. | Vattikodu | 16.92510555 | 79.06955147 | Reported 9 Lamproite bodies (Alok Kumar et al., 2013) f7(NE-SW to N-S) fault |
| 6. | Between Samuloribai and Kanagalu | 16.92098407 | 79.17387278 | Reported Intrusive Lamproite bodies (Alok Kumar et al., 2013), fault f4 (NE-SW) |
| 7. | East of Kanagalu | 16.93365468 | 79.27286193 | --- |
| 8. | Marepalle | 16.89671022 | 79.21720719 | Reported one lamproite , fault f5(NW-SE) |
| 9. | Yacharam | 16.85763101 | 79.25227219 | Reported two Lamproite bodies (Chalapathi Rao et al., 2014) fault-f5(NW-SE) |
| 10. | Ramadugu (South west) | 16.82667477 | 79.27968791 | Reported 10 Lamproite bodies (Sridhar et al., 2005) Fault f 5 (NE-SE) |
| 11. | In between Ramadugu-Anumala | 16.81436376 | 79.24844205 | --- |
| 12. | -- | 16.81933294 | 79.20229964 | --- |
| 13. | Teppalamadugu | 16.76972864 | 79.20713314 | ---- |

4. Results and Discussion

Remote sensing Land Sat 8 satellite image analysis of the Nalgonda district facilitated preliminary elaboration of the land use land cover and structural elements, orientation and disposition of lineaments, dykes, minor/major shear zones and structural features. Lineament map (Figure 7) brought seven deep seated faults F1 to F7 lineaments, fractures and dyke NW-SE, NE-SW, N-S and E-W trends, which are responsible for the emplacement of the lamproites at contact between granite gneiss and dolerite dykes.

From geomorphic analysis of the drainage pattern in the Ramadugu region, thirteen (1 to 13) domal structures and seven faults f1 to f7 were identified. These structures in conjunction with the tectonic framework of the region indicated favorable location for lamproites.

Ramadugu lamproites occur as dykes, Lamproites at Somavarigudem and Vattikod occur in close association with dolerite dykes and fault region a contact environment is observed in lamproite emplacement in the study area.

Acknowledgements

The authors gratefully acknowledge the financial support extended by the UGC New Delhi for granting Emeritus professor.

References

- Alok Kumar, A., Ahmed, S., Priya, R., and Sridhar, M. *Discovery of Lamproites Near Vattikod Area, NW Margin of the Cuddapah Basin, Eastern Dharwar Craton, Southern India*. Journal of the Geological Society of India. 2013. 82; 307-312.
- Castleman, K.E., 1978: The Gray Level Histogram, Digital Image Processing, Prentice-Hall, Englewood, Cliffs, New Jersey. 68-84.
- Chalapathi Rao, N.V., Alok Kumar, Samarendra Sahoo, Dongre, A.N., and Debojit Talukdar. *Petrology and Petrogenesis of Mesoproterozoic Lamproites from the Ramadugu Field, NW Margin of the Cuddapah basin, Eastern Dharwar Craton, Southern India*. Lithos. 2014. 196-197; 150-168.
- Chavez, P.S, Jr., Berlin, G.L., and Sowers, L.B. *Statistical Method for Selecting Landsat MSS Ratios*. Journal of Applied Photographic Engineering. 1982. 8 (1) 23-30.
- Geological Survey of India, 2009: District resource map of Nalgonda district, Andhra Pradesh, 1:250,000 scale.
- Goetz, A.F.H, 1975: *Application of ERTS Images and Image Processing to Regional Geologic Problems and Geologic Mapping in Northern Arizona*. JPL Technical Report 32-1597, Jet Propulsion Laboratory, Pasadena, C.A.
- Hammond, R., and McCullagh, P.S. *Quantitative Techniques in Geography*, Oxford, England, Clarendon Press.
- Katz, M., 1982: *Lineament Analysis of Landsat Imagery Applied to Mineral Exploration*. In *Mineral Exploration Techniques in Tropical Forest Areas*. Edited by Laming, D.I.C. and Gibbs, A.K. Hiden Wealth. 157-166.
- Kutina, J. *Hydrothermal Ore Deposits in the Western United States: A New Concept of Structural Control of Distribution*. Science. 1969. 165; 1113-1119.
- Liu, C.C., Sousa, M.D.A Jr., and Gopinath, T.R. *Regional Structural Analysis by Remote Sensing for Mineral Exploration, Paraiba State, Northeast Brazil*. Geocarto International. 2000. 15 (1) 70-77.
- Miller, L.D. and Pearson, R.L. *Areal Mapping Program of the IBP Grassland Biome, Remote Sensing of the Productivity of the Short Grass Prairie as Input Into Bio System Model*. 7th Proceedings of the International Symposium. Remote Sensing of Environment. 1971. 1; 175-2005.
- Moore, G.K., and Waltz, F.A. *Objective Procedures for Lineament Enhancement and Extraction*. Photogramm Eng Remote Sens. 1983. 49; 641-647.
- Price, J.C. *Examples of High Resolution Visible to Near Infrared Reflectance Spectra and a Standardized Collection for Remote Sensing Studies*. International Journal of Remote Sensing. 1995. 16; 993-1000.
- Ramachandran, C., Kesavamani, M., and Prasad, R.M.C. *A Geophysical Prognostication of Primary Diamond Deposits in Peninsular India*. Jour. Geophysics. 1997. 20 (4) 155-178.

Ramadass, G., Satish Kumar, K., and Sri Ramulu, G. *Emplacement of Lamproites in North Western Margin of Cuddapah Basin (EDC), Nalgonda District (TS)- Regional Gravity Evidence*. Pelagia Research Library. 2015. 6 (8) 189-198.

Ramadass, G, Subhash Babu A., and Udaya Laxmi, G. *Structural Analysis of Airborne Radiometric data for Identification of Kimberlites in Parts of Eastern Dharwar Craton*. International Journal of Science and Research. 2013. 4; 2375-2380.

Reddy, T.A.K., Sridhar, M., Ravi, S., and Chakravarty, V. *Petrology and Geochemistry of the Krishna Lamproites Field, Andhra Pradesh*. Journal of the Geological Society of India. 2003. 61; 131-140.

Sarala, C., 2013: *Landuse/Land Cover and NDVI Analysis is for Halia Catchment*. IJARET. 4 (5) 126-133.

Short, N.M., 1982: *The Landsat Tutorial Workbook, Basis of Satellite Remote Sensing, Washington, DC*. NAASA. Scientific and Technical information Brands, NASA. 174-175.

Singer, R.B. 1980: *Near Infrared Spectral Reflectance of Mineral Mixtures, Systematic Combinations of Pyroxenes, Olivine and Iron Oxide*. PSD Publications. No.258, MIT, Cambridge, MA.

Sridhar, M. and Rau, T.K., 2005: *Discovery of a New Lamproite Field- Ramadugu Lamproite Field (RLF), Nalgonda district, Andhra Pradesh*. Proceedings of Group Discussion on Kimberlites and related rocks. Geol. Soc. India, Bangalore. 55-57.

Venkateswarlu, M.M., Rasheed, M.A, Reddy, U.V.B., and Kiran Kumar, A. *Assessment of Ground Water Quality in and around Miryalaguda area, Nalgonda District of Andhra Pradesh*. International Journal of Environmental Sciences. 2014. 4 (2) 259-260.

Land Use/Land Cover Change Detection and Classification using Remote Sensing and GIS Techniques: A Case Study at Siwa Oasis, Northwestern Desert of Egypt

Abd El hay Aly Farrag¹, El Sayed Ahmed El Sayed², and Hanaa Ahmed Megahed²

¹Geology Department, Faculty of Science, Assiut University, Egypt

²Geological Applications and Mineral Resources Division, National Authority for Remote Sensing and Space Sciences (NARSS) Egypt

Publication Date: 25 March 2016

DOI: <https://doi.org/10.23953/cloud.ijarsg.80>



Copyright © 2016 Abd El hay Aly Farrag, El Sayed Ahmed El Sayed, and Hanaa Ahmed Megahed. This is an open access article distributed under the **Creative Commons Attribution License**, which permits unrestricted use, distribution, and reproduction in any medium, provided the original work is properly cited.

Abstract Monitoring and analysis of the recent land cover/land use changes through the integration of remote sensing and GIS to detect change in land use and land cover pattern by providing more reliable direct quantitative information also could provide base information for documenting water salinity, soil change and expansion in surface lakes. Therefore in the present study an attempt is made on Siwa Oasis to bring out the quantitative information through field campaigns and the study of satellite imageries those freely available at National Authority for Remote Sensing and Space Sciences (NARSS) and Global Land Cover Forecasting (GLCF) site. The results obtained through this study using imageries of 1987, 2000 and 2014 of Siwa Oasis are presented.

Keywords *Land Use/Land Cover; Classification; Remote Sensing; GIS; Change Detection; Siwa Oasis.*

1. Introduction

Land cover and land use change detection is one of the most important application areas of remote sensing. Change detection involves the ability to quantify temporal changes in land use and landcover using multitemporal data sets (Singh, 1989; Ridd and Liu, 1998). During the past three decades, many change detection algorithms have been developed, and they vary widely in their sophistication and performance (Collins and Woodcock, 1996; Ola and Hay, 2003). The choice of a particular technique depends largely on the particulars of the study area, the nature of the expected landcover change, and the temporal and spatial resolution of the data (Kaufman and Seto, 2001). This paper is an attempt to assess the changes in land use/land cover at Siwa Oasis over a 27 year period.

1.1. Location and Description of the Study Area

Siwa Oasis is one of the depressions located in the northern part of the Western Desert of Egypt, to the west of the great Qattara Depression and continuing westward to the Gaghbub depression in Libya. It is about 300 km south of the Mediterranean Sea coast (Matrouh city) and extends in an E-W direction for approximately 82 km, with a width that varies between 9 and 28 km and has an area of about 2,950 km². It lies between latitudes 29° 07' 18" N and 29° 20' 36" N and longitudes 25° 18' 21" E and 26° 03' 05" E (Figure 1). It has an irregular elongate shape narrowing westward. The depression is bordered from the north by the steep escarpment of the Miocene Marmarica Limestone plateau attaining an elevation of about 150 m (a.s.l), which extends as far as the Mediterranean coast, while towards the south; it is limited by the dunes of the Great Sand Sea.

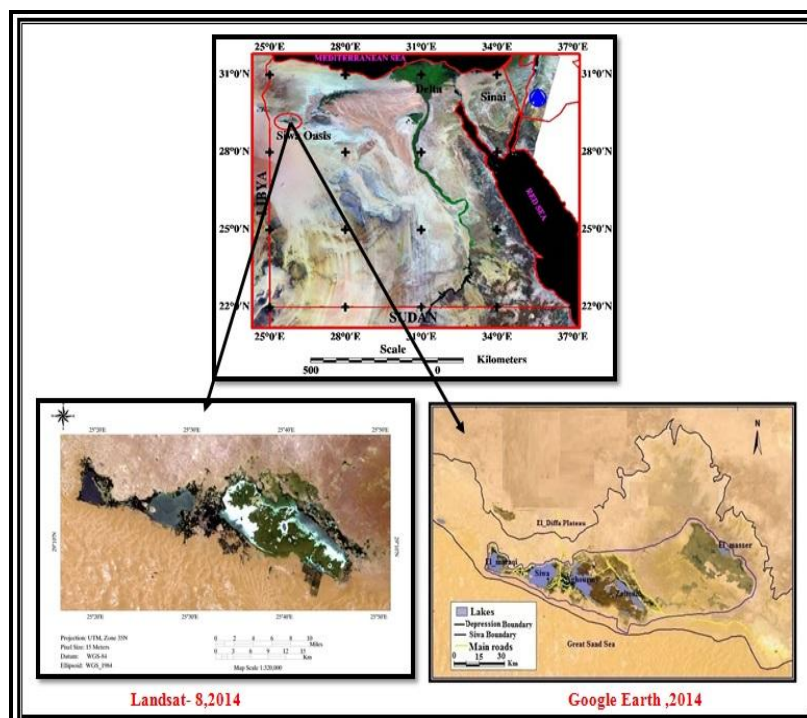


Figure 1: Location of the Investigation Area on Landsat -8 Image and Google Earth

Climatologically, the climate of Siwa Oasis is arid characterized by a short winter season and a long hot summer. The summer season is dry and very hot with maximum temperature reaching up to 30°C (Figures 2&3).

The monthly mean minimum temperatures range from 4°C in January to 21°C in July. The study of relative humidity values indicates that the monthly variations vary between 33.0 and 60.0 %. The annual relative humidity is 45.0 %.

Evaporation ranges from 283 mm/month in July to 76 mm/month in December (Figure 4). Because the oasis lies in a depression it is somewhat protected from the hot desert winds and evapotranspiration is slightly lower than in other desert environments. (Table 1)

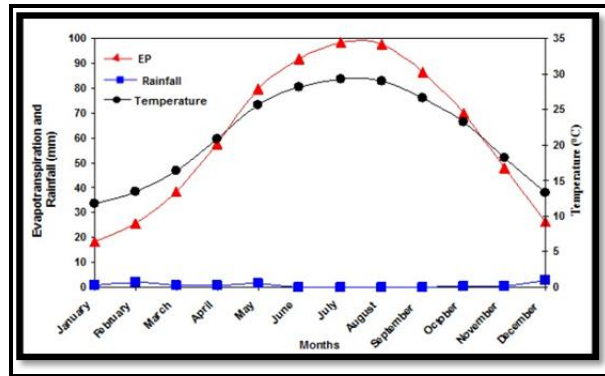


Figure 2: Relationship between Temperature, Rainfall, and Evapotranspiration

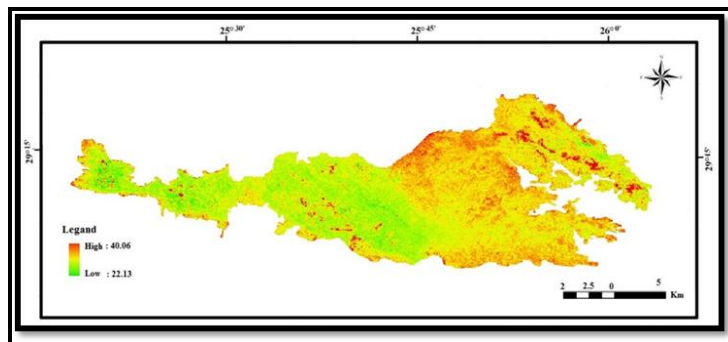


Figure 3: Land Surface Temperature Spatial Distribution in Siwa Oasis

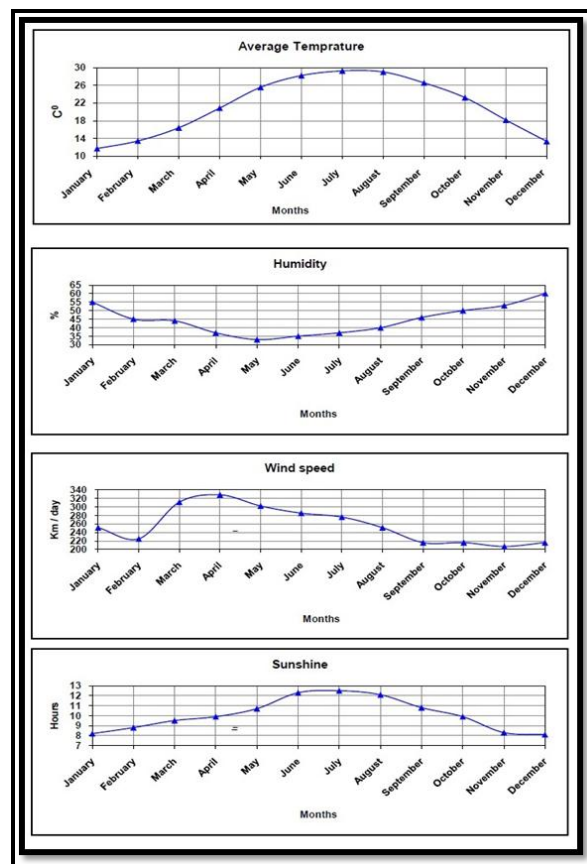


Figure 4: Climatological Diagram of the Study Area

Table 1: Climatological Data of Siwa Oasis, Monthly Averages during the Period (average of latest 20 years), Siwa Meteorological Station

| Meteorology Station; Siwa (20yr.) | | | | Altitude: - 13 m a.s.l | | | Co-ordinates: 29.12 N, 25.29 E | | | |
|-----------------------------------|---------------------|---------------------|--------------------|------------------------|---------------------------|---------------------------|--------------------------------|---|----------------|-----------------------------|
| Month | Temperature | | | Rainfall mm/month | Relative Humidity % | Wind velocity m/sec | Sunshine Hours | Solar. Radiation MJ/m ² _day | EP mm/Month | ET _o (mm/day) |
| | Max. Temp. °C | Min. Temp. °C | Mean Temp °C | | | | | | | |
| January | 19.60 | 3.80 | 11.70 | 0.80 | 55.0 | 2.90 | 8.20 | 13.90 | 62 | 3.20 |
| February | 21.50 | 5.30 | 13.40 | 2.00 | 45.0 | 2.60 | 8.80 | 16.90 | 101 | 3.90 |
| March | 24.80 | 8.0 | 16.40 | 0.70 | 44.0 | 3.60 | 9.50 | 20.90 | 175 | 5.60 |
| April | 29.70 | 12.0 | 20.85 | 0.90 | 37.0 | 3.79 | 9.90 | 23.70 | 229 | 7.40 |
| May | 34.50 | 16.60 | 25.55 | 1.50 | 33.0 | 3.49 | 10.70 | 25.80 | 274 | 8.70 |
| June | 37.30 | 19.10 | 28.20 | 0.00 | 35.0 | 3.30 | 12.30 | 28.50 | 276 | 9.30 |
| July | 38.0 | 20.50 | 29.25 | 0.00 | 37.0 | 3.19 | 12.50 | 28.50 | 283 | 9.20 |
| August | 37.70 | 20.30 | 29.0 | 0.00 | 40.0 | 2.90 | 12.10 | 27.10 | 255 | 8.40 |
| September | 35.10 | 18.0 | 26.55 | 0.00 | 46.0 | 2.50 | 10.80 | 23.30 | 192 | 6.70 |
| October | 31.80 | 14.60 | 23.20 | 0.30 | 50.0 | 2.50 | 9.90 | 19.20 | 151 | 5.30 |
| November | 26.30 | 10.0 | 18.15 | 0.60 | 53.0 | 2.39 | 8.30 | 14.60 | 100 | 3.80 |
| December | 21.10 | 5.50 | 13.30 | 2.80 | 60.0 | 2.50 | 8.10 | 13.10 | 67 | 2.90 |
| Annual mean | 29.80 | 12.80 | 21.30 | - | 45.0 | 2.97 | 10.10 | 21.30 | 188.75 | 74.40 |
| Annual total | - | - | - | 9.60 | - | - | - | - | 2265.0 | - |

Geologically, the study area is underlain and surrounded by sedimentary rocks, belonging to the Eocene, Pliocene, Pleistocene and Recent times (Figure 5). Stratigraphically, these sedimentary rocks can be divided into Upper, Lower and Middle Eocene, and Pleistocene and Holocene Deposits, (Said, 1990).

The same authors Gindy and El-Askary (1969) added that throughout the Siwa depression, three lithostratigraphic marine divisions can readily be recognized in the field, I-the lowest division (oasis member) which consists of shale and marl beds. The overall color is greenish buff, mostly khaki colored, II-the middle division (Siwa escarpment member) which consists mostly of relatively thick and snow-white chalky beds, with a pinkish stain common on the more weathered surfaces, and III- the upper-most division (plateau member) which consists of thin chalky limestone beds. The fossiliferous beds appear gray or grayish brown, but freshly broken surface range from white to cream color. The upper members (El-Diffa plateau and Siwa escarpment member) are equivalent to the Marmarica formation of western desert suggested by Said (1962).

2. Objectives

The study is aimed to identify the changes that happened in land use/land cover during the period of 1987-2014. The main observed changes could be expressed by: 1) - Enlargement of lake areas as a result of over-pumping from springs and wells and misuse of water for irrigation purposes, 2) - Change in wet sabkhas and dry areas and 3) - change in agriculture areas using remotely sensed data .

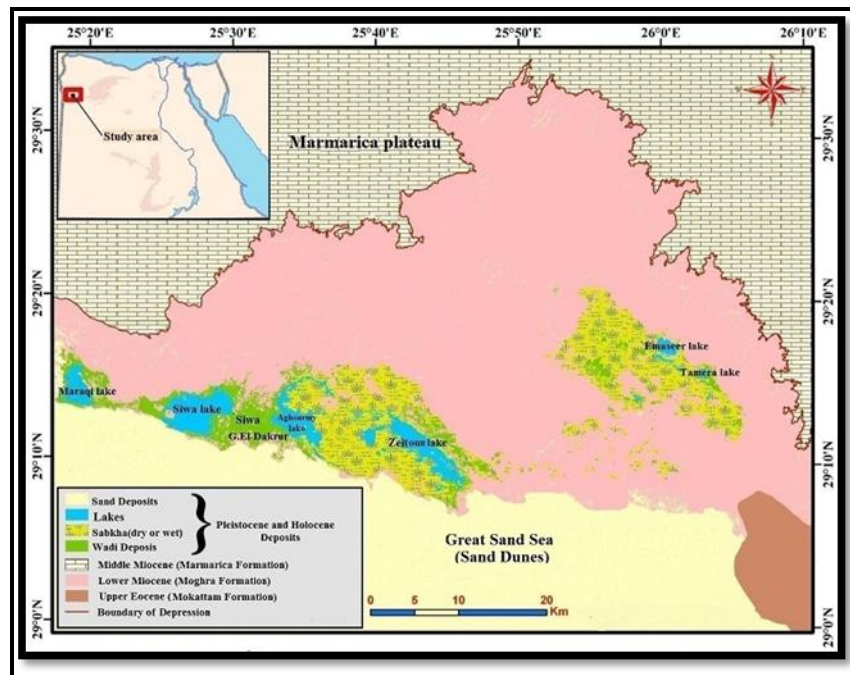


Figure 5: Schematic Geological Map of the Study Area. Digitized from Maps of CONOCO (1998) and Landsat-8 Image (2014)

3. Methodology

The methodology used in this work is summarized in the next flowchart; (Figure 6) includes supervised classification of landsat TM 1987, ETM+ 2000 & Landsat 8 (2014) images while the second will encompass change detection analysis.

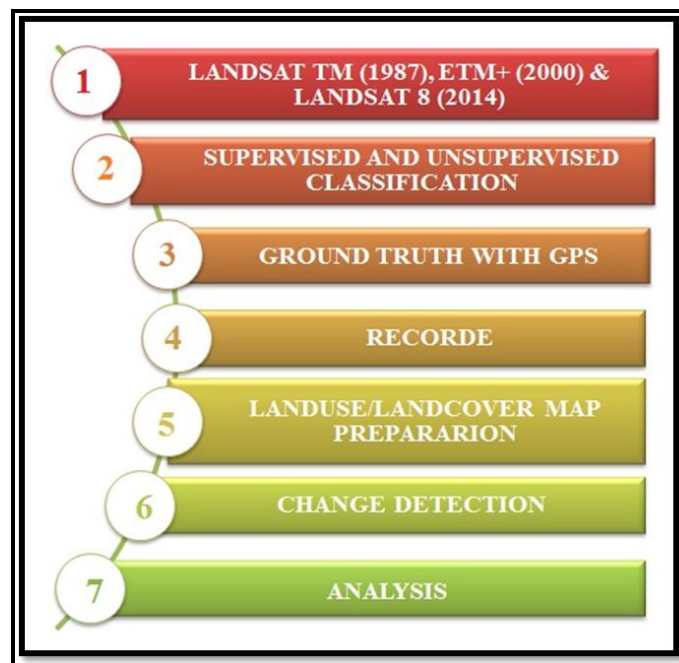


Figure 6: Flow Chart of Methodology

All images are collected from TM (1987), ETM+ (2000) & Landsat 8 (2014) Figures (7a, 7 b and 7c) where chronologically arranged and were subjected to unsupervised and supervised classification. An attempt was made to classify the images under four classes Vegetation, Water body, Wet sabkha-salt crusts and Dry sabkha. Out of the available modes of supervised classification Maximum likelihood classification algorithm technique is used considering its potential and suitability in the study planned. In this method care was taken to define signatures of each class after defining the signatures for each land cover category. The software uses those signatures to classify the remaining pixels. The classified land use/ land cover images were taken for ground truth. Ground truth was conducted by using GPS (Global Positioning System) and land use class was corrected by using recode technique, wherever it was needed based on the ground truth information.

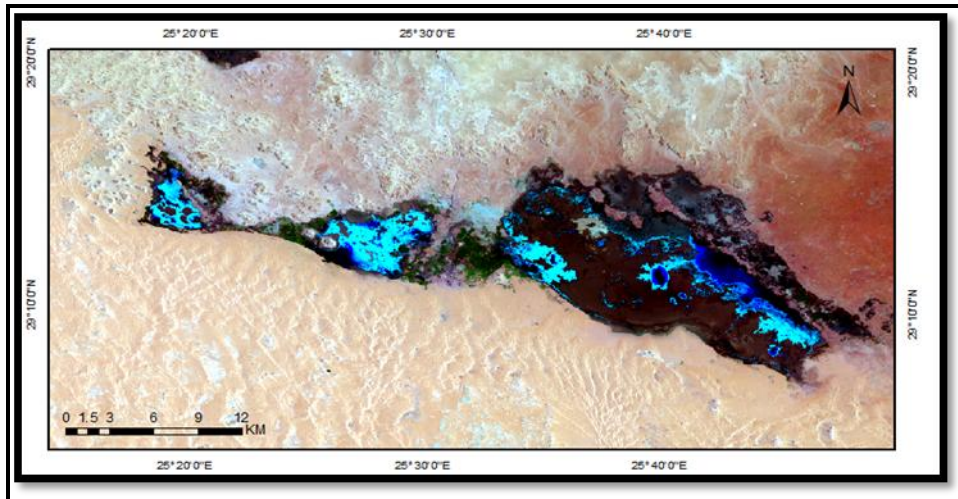


Figure (7a): Raw Image of Landsat TM, Band (RGB 7,4,2), (Acquisition Date: Nov, 1987)

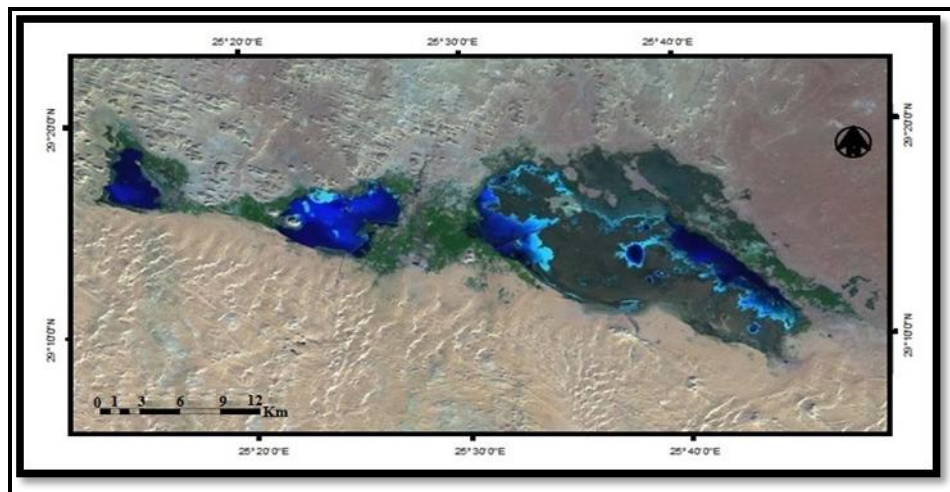


Figure (7b): Raw Image of Landsat ETM⁺, Band (RGB 7,4,2), (Acquisition Date: Oct, 2000)

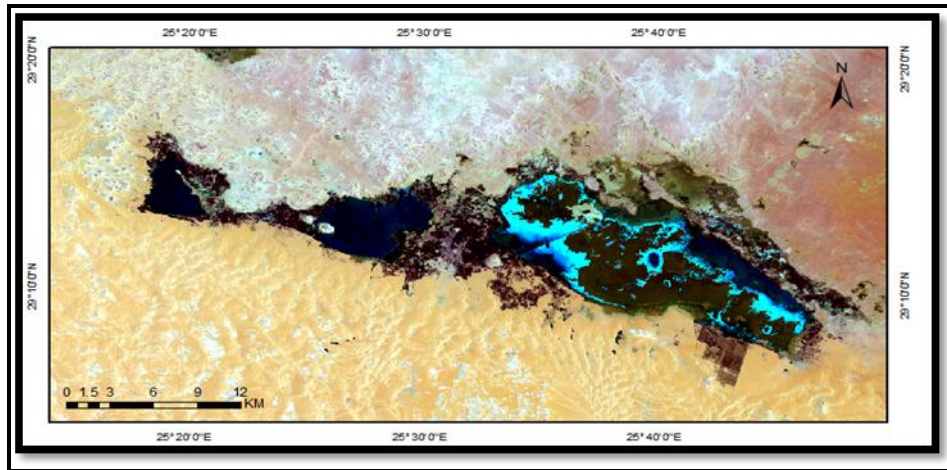


Figure (7c): Raw Image of Landsat 8, Band (RGB 7,4,2), (Acquisition Date: May, 2014)

4. Results and Discussion

The unsupervised classification techniques available are ISODATA and K-Means. ISODATA unsupervised classification calculates class means evenly distributed in the data space then iteratively clusters the remaining pixels using minimum distance techniques. This process continues until the number of pixels in each class changes by less than the selected pixel change threshold or the maximum number of iterations is reached. This method resulted in 7 classes as shown in Figure 8.

K-Means unsupervised classification calculates initial class means evenly distributed in the data space then iteratively clusters the pixels into the nearest class using a minimum distance technique. This process continues until the number of pixels in each class changes by less than the selected pixel change threshold or the maximum number of iterations is reached. This method resulted in 5 classes as shown in Figure 9.

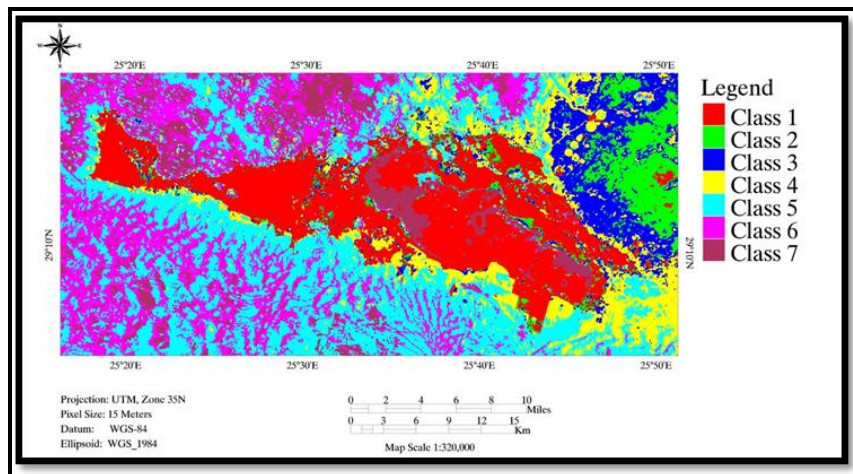


Figure 8: ISODATA Unsupervised Classification of the Study Area

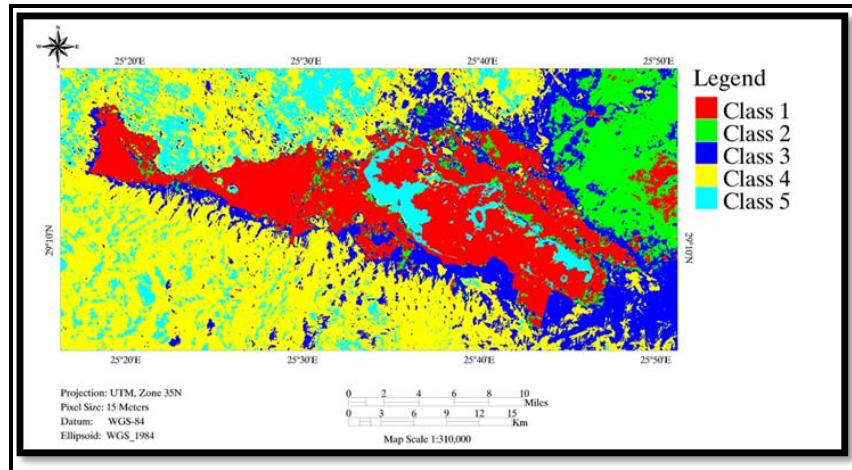


Figure 9: K-Means Unsupervised Classification of the Study Area

The result obtained through the study of imageries to evolve change in the land use and land cover of Siwa district are evaluated from 27 years of study period i.e. 1987, 2000, 2014 present in Figures 10, 11 and 12.

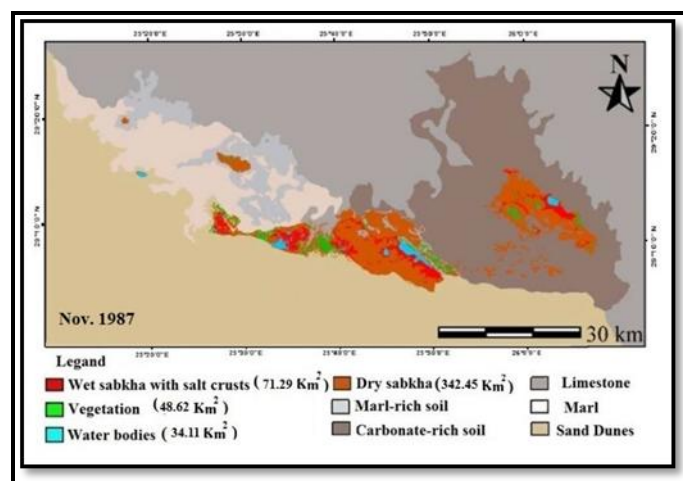


Figure 10: Land Use / Land Cover of Siwa District Year 1987

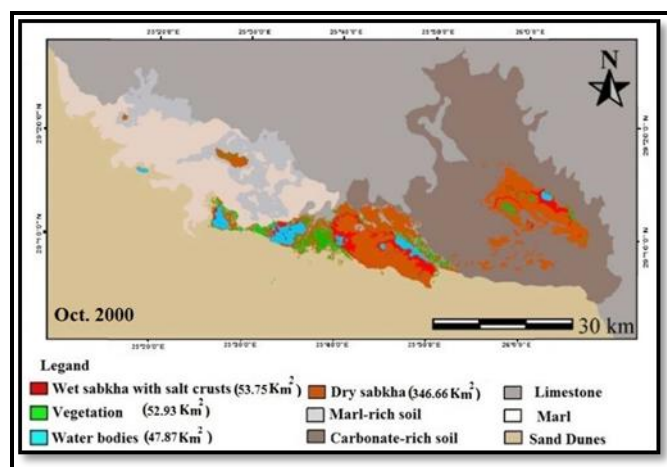


Figure 11: Land Use / Land Cover of Siwa District Year 2000

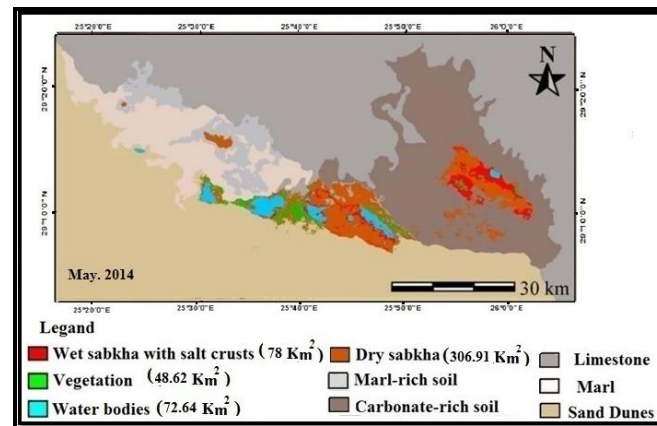


Figure 12: Land Use / Land Cover of Siwa District Year 2014

Spatio-temporal changes in different landcover classes, which were monitored in the whole area and surrounded the main four lakes in study area during three different dates 1987, 2000 and 2014, are shown in Figures 13, 14, 15 and Table 2. Change results confirmed a gradual increase in the extent of the surface waters in all of the study areas except Massir, which showed a slight decrease. For the 1987–2000 period of monitoring, an increase in water extent has resulted in an increase of vegetation cover in the study areas.

Moreover, a decrease in the extent of dry sabkha in Maraqi, Siwa, and Massir was observed, as was an increase in dry sabkha in Zaitun and the whole study area. Further, the extent of wet sabkha with salt crusts has increased in Zaitun and Massir but declined in Maraqi and Siwa as well as the whole study area. For the 2000–2014 period, the gradual increase in water extent resulted in a decrease in vegetation cover in the whole area.

In addition, a decrease in the extent of wet sabkha with salt crusts was observed in Maraqi, Siwa, and Zaitun, while in Massir and the whole study area it increased. The extent of dry sabkha showed a decline in Siwa, Zaitun, Massir, and in the whole study area, while a slight increase was observed in Maraqi. These results indicate that the direct proportional relationship between the extent of surface water and vegetation coverage reversed after the year 2000.

Field investigations, interviews with Siwa planners, and visual inspections of the 2000 and 2014 colour composite images showed that the only change in the infrastructure of the area is a road and drainage network that was set up after the year 2000. Such practices are thought to greatly affect the hydrologic characteristics of the surrounding lakes. Where the total coverage of the dry sabkha was lowered due to an increase in the surface extent of the lake waters in the study area, a considerable extension of the sabkha was near the vegetation cover and urban centers. Moreover, an increase in the clear-cut areas of the natural vegetation, including date palms and olive trees, was clear and at a high rate. Most of the vegetation was located in direct contact with the saline lake waters, the wet sabkhas, or near urban centers, thereby enhancing the evapo-transpiration rate of the nearby vegetation. The removal of vegetation cover significantly increases the soil moisture content due to reduced evapo-transpiration, which consequently raises the shallow water-table (Gates and Williams, 1988). In addition, the density of vegetation cover is of significant importance in governing the rate of evapo-transpiration. The edges of dense vegetation have a high rate of evapo-transpiration and hence are at-risk for dryness, and this is evident in the study area. Estimation of the vegetation coverage detected and predicted in the whole study area was carried out using GIS functions.

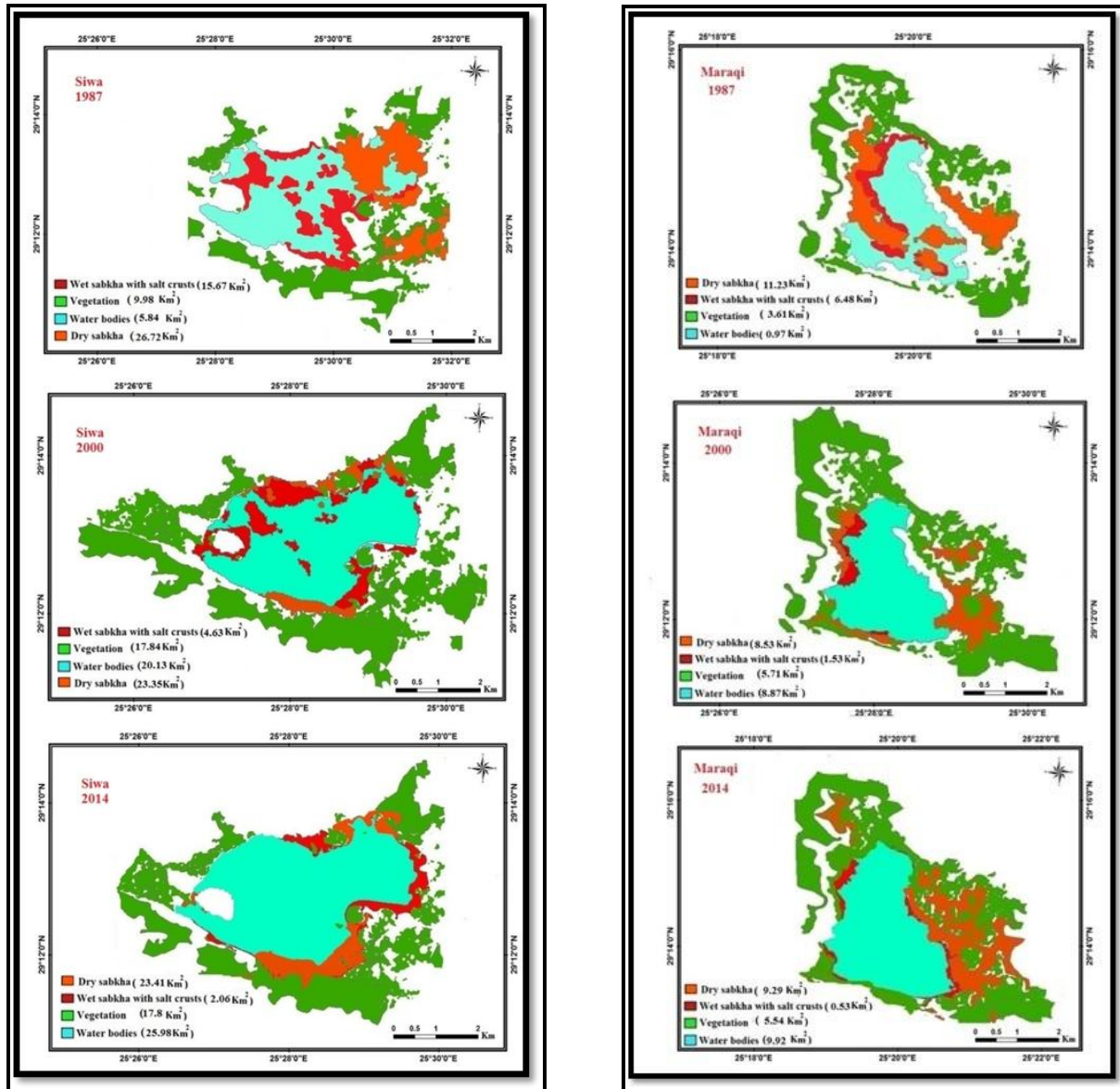


Figure 13: Change Detection (Km²) During the Period of 1987-2014 in El Maraqui and Siwa Lake

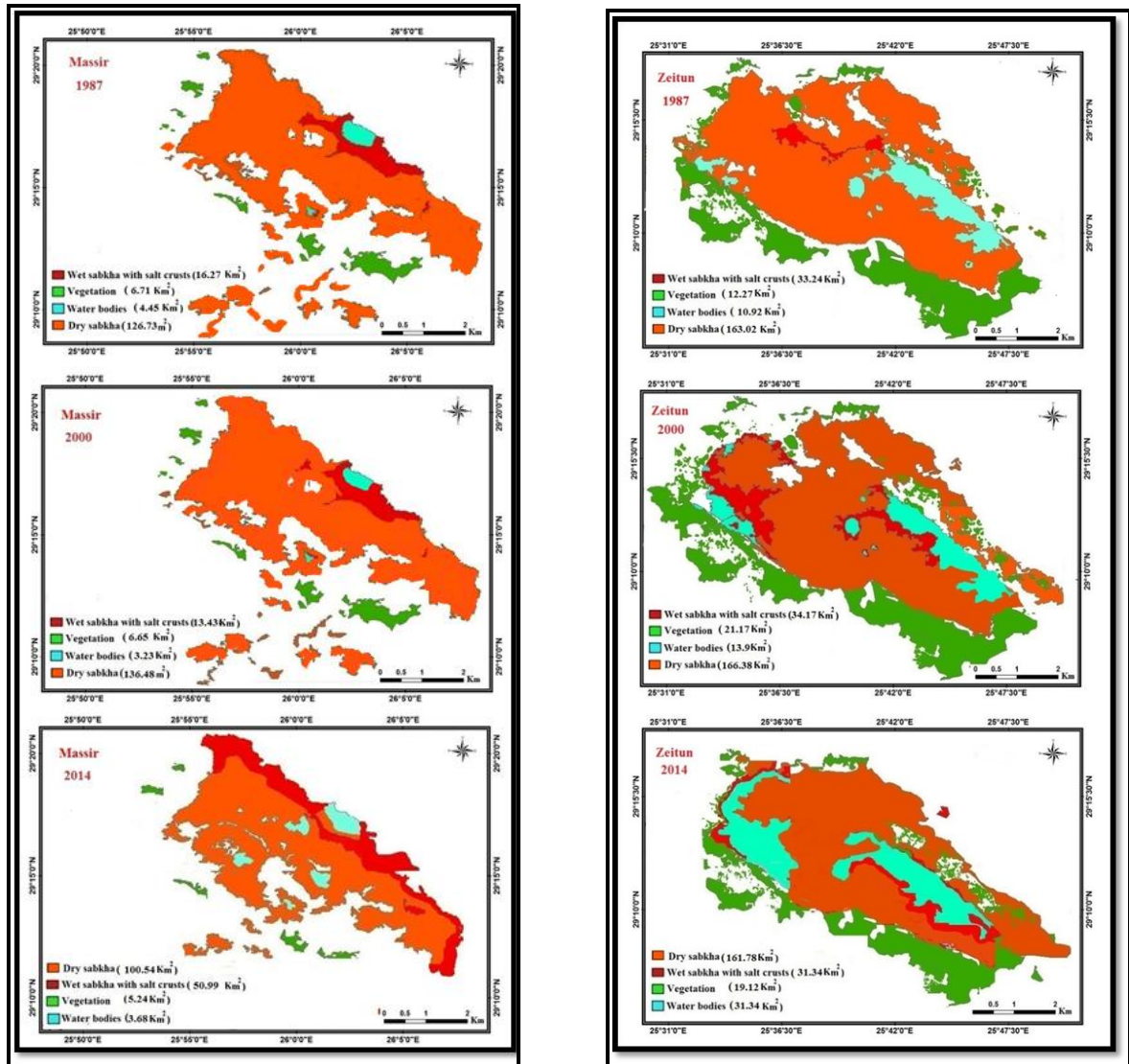


Figure 14: Change Detection (km²) during the Period of 1987-2014 in Zeitun and Massir Lake

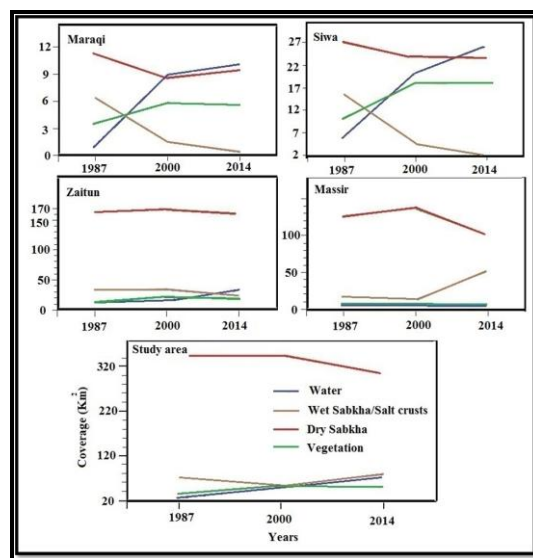


Figure 15: Diagrams Showing Temporal Changes in Different Landcover Classes in the Study Area and the Areas Surrounding the Main Four Lakes in Siwa Region

Table 2: Change Detection (Km²) Monitored in the 1987–2014 Period in the Study Area the Areas Surrounding the Main Four Lakes in Siwa Region

| Area /Years Lake/landcovers | Area/Km ² (1987) | Area/Km ² (2000) | Area/ Km ² (2014) | 1987/2000 Changes | 1987/2014 Changes | 2000/2014 Changes |
|--------------------------------|--------------------------------|--------------------------------|---------------------------------|----------------------|----------------------|----------------------|
| Maraq | | | | | | |
| Water bodies | 0.97 | 8.87 | 9.92 | 7.9 (Increase) | 8.95 (Increase) | 1.05 (Increase) |
| Wet sabkha-salt crusts | 6.48 | 1.53 | 0.53 | -4.95 (Decrease) | -5.95 (Decrease) | -1 (Decrease) |
| Dry sabkha | 11.23 | 8.53 | 9.29 | -2.7 (Decrease) | -1.94 (Decrease) | 0.76 (Increase) |
| Vegetation | 3.61 | 5.71 | 5.54 | 2.1 (Increase) | 1.93 (Decrease) | -0.17 (Decrease) |
| Siwa | | | | | | |
| Water bodies | 5.84 | 20.13 | 25.98 | 14.29 (Increase) | 20.14 (Increase) | 5.85 (Increase) |
| Wet sabkha-salt crusts | 15.67 | 4.63 | 2.06 | -11.04 (Decrease) | -13.61 (Decrease) | -2.57 (Decrease) |
| Dry sabkha | 26.72 | 23.35 | 23.41 | -3.37 (Decrease) | -3.31 (Decrease) | 0.06 (Increase) |
| Vegetation | 9.98 | 17.84 | 17.81 | 7.86 (Increase) | 7.83 (Increase) | -0.03 (Decrease) |
| Zeitun | | | | | | |
| Water bodies | 10.92 | 13.9 | 31.34 | 2.98 (Increase) | 20.42 (Increase) | 17.44 (Increase) |
| Wet sabkha-salt crusts | 33.24 | 34.17 | 24.3 | 0.93 (Increase) | -8.94 (Decrease) | -9.87 (Decrease) |
| Dry sabkha | 163.02 | 166.38 | 161.78 | 3.36 (Increase) | -1.24 (Decrease) | -4.6 (Decrease) |
| Vegetation | 12.27 | 21.17 | 19.12 | 8.9 (Increase) | 6.85 (Increase) | -2.05 (Decrease) |
| Massir | | | | | | |
| Water bodies | 4.45 | 3.23 | 3.68 | -1.22 (Decrease) | -0.77 (Decrease) | 0.45 (Increase) |
| Wet sabkha-salt crusts | 16.27 | 13.43 | 50.99 | -2.84 (Decrease) | 34.72 (Increase) | 37.56 (Increase) |
| Dry sabkha | 126.73 | 136.48 | 100.54 | 9.75 (Increase) | -26.19 (Decrease) | -35.94 (Decrease) |
| Vegetation | 6.71 | 6.65 | 5.24 | -0.06 (Decrease) | -1.47 (Decrease) | -1.41 (Decrease) |
| Study area | | | | | | |
| Water bodies | 22.78 | 47.87 | 72.64 | 25.09 (Increase) | 49.86 (Increase) | 24.77 (Increase) |
| Wet sabkha-salt crusts | 71.29 | 53.75 | 78 | -17.54 (Decrease) | 6.71 (Increase) | 24.25 (Increase) |
| Dry sabkha | 342.45 | 346.66 | 306.91 | 4.21 (Increase) | -35.54 (Decrease) | -39.75 (Decrease) |
| Vegetation | 34.11 | 52.93 | 48.62 | 18.82 (Increase) | 14.51 (Increase) | -4.31 (Decrease) |

5. Conclusion

Remote Sensing and Geographical Information System (GIS) are well accepted and more dependable advance techniques to detect change in land use and land cover pattern by providing more reliable direct quantitative information. Our results accurately quantify the land cover changes and delineate their spatial patterns, demonstrating the Utility of Landsat data in analyzing landscape dynamics over time. Such information is critical for making efficient and sustainable policies for resource management.

References

- Gates, G.W.B., and Williams, R.M. *Changes in Groundwater Levels, Southeast New South Wales*. Department of Water Resources, New South Wales, Technical Services Report. 1988. No. 80.
- Gindy, A.R., El Askary, M.A. *Stratigraphy, Structure and Origin of the Siwa Depression, Western Desert of Egypt*. Bull Am Assoc. Petrol Geol. 1969. 53; 603-625.
- Manonmani, R., and Mary Divya Suganya, G. *Remote Sensing and GIS Application in Change Detection Study in Urban Zone Using Multi Temporal Satellite*. International Journal of Geomatics & Geosciences. 2010. 1 (1).
- Ola, H., and Hay, G.J. *A Multiscale Object-Specific Approach to Digital Change Detection*. International Journal of Applied Earth Observation and Geoinformation. 2003. 4; 311-327.
- Patekar, P.R., and Patil, R.R. *Land Use-Land Cover Change Detection Using Remote Sensing and GIS Techniques; Solapur District of Maharashtra, India*. International Journal of Advanced Remote Sensing and GIS. 2014. 3 (1) 499-505.
- Phukan, P., Thakuria, G., and Saikia, R. *Land use Land Cover Change Detection Using Remote Sensing and GIS Techniques - A Case Study of Golaghat District of Assam, India*. International Research Journal of Earth Sciences. 2013. 1 (1) 11-15.
- Ridd, M.K. and Liu, J. *A Comparison of Four Algorithms for Change Detection in an Urban Environment*. Remote Sensing of Environment. 1998. 63; 95-100.
- Song, C., Woodcock, C.E., Seto, K.C., Lenney, M.P., and Macomber, S.A. *Classification and Change Detection using Landsat TM Data*. Remote Sensing of Environment. 2001. 75; 230-244.
- Said, R., 1990: *The Geology of Egypt*. Published for Egyptian Central Petroleum Corporation, Conco Hurgada Inc by Balkema, A.A. Rotterdam.
- Singh, A. *Digital Change Detection Techniques Using Remotely Sensed Data*. Int. J. Remote Sensing. 1989. 10 (6) 989-1003.
- Said, R., 1962: *The Geology of Egypt*. Amsterdam. New York, London: Elsevier Publishing Company.

Evaluating Lidar Point Densities for Effective Estimation of Aboveground Biomass

Zhuoting Wu¹, Dennis Dye¹, Jason Stoker², John Vogel¹, Miguel Velasco¹, and Barry Middleton¹

¹US Geological Survey, Western Geographic Science Center, United States

²National Geospatial Program, US Geological Survey, United States

Publication Date: 9 February 2016

DOI: <https://doi.org/10.23953/cloud.ijarsg.40>



Copyright © 2016 Zhuoting Wu, Dennis Dye, Jason Stoker, John Vogel, Miguel Velasco, and Barry Middleton. This is an open access article distributed under the **Creative Commons Attribution License**, which permits unrestricted use, distribution, and reproduction in any medium, provided the original work is properly cited.

Abstract The U.S. Geological Survey (USGS) 3D Elevation Program (3DEP) was recently established to provide airborne lidar data coverage on a national scale. As part of a broader research effort of the USGS to develop an effective remote sensing-based methodology for the creation of an operational biomass Essential Climate Variable (Biomass ECV) data product, we evaluated the performance of airborne lidar data at various pulse densities against Landsat 8 satellite imagery in estimating above ground biomass for forests and woodlands in a study area in east-central Arizona, U.S. High point density airborne lidar data, were randomly sampled to produce five lidar datasets with reduced densities ranging from 0.5 to 8 point(s)/m², corresponding to the point density range of 3DEP to provide national lidar coverage over time. Lidar-derived aboveground biomass estimate errors showed an overall decreasing trend as lidar point density increased from 0.5 to 8 points/m². Landsat 8-based aboveground biomass estimates produced errors larger than the lowest lidar point density of 0.5 point/m², and therefore Landsat 8 observations alone were ineffective relative to airborne lidar for generating a Biomass ECV product, at least for the forest and woodland vegetation types of the Southwestern U.S. While a national Biomass ECV product with optimal accuracy could potentially be achieved with 3DEP data at 8 points/m², our results indicate that even lower density lidar data could be sufficient to provide a national Biomass ECV product with accuracies significantly higher than that from Landsat observations alone.

Keywords 3DEP; Aboveground Biomass; Essential Climate Variable (ECV); Landsat; Lidar; Point Density; Quality Level

1. Introduction

Accurate estimation, mapping and monitoring of the amount of carbon stored in terrestrial vegetation is crucial to reliable analysis, understanding and projection of the global carbon cycle and its interactions with land use and climate change. Aboveground biomass is defined as an Essential Climate Variable (ECV) by the Global Climate Observing System (GCOS) (Bojinski et al., 2014). An accurate assessment of the amount of vegetation biomass is crucial for quantifying carbon stocks and the potential of vegetation to sequester carbon, which can have a direct influence on local, regional and

global climate. Aboveground biomass is a common input variable in ecosystem process and climate models, but large uncertainties as well as infrequent updating of biomass data are major potential sources of uncertainties in the model outputs.

It is widely recognized that active remote sensing systems, especially light detection and ranging (lidar), represent the future of large-scale estimation and mapping of terrestrial biomass (Chen et al., 2012; Evans et al., 2009; Zhao et al., 2009; Hall et al., 2005; Lefsky et al., 2002; Su et al., 2016; Gregoire et al., 2016), potentially supporting the operational production of a Biomass ECV product at the national scale. Lidar is an active remote sensing system that can measure the three-dimensional (3-D) structural characteristics of trees and other vegetation which are not directly captured by passive optical land imaging systems such as Landsat. Such 3-D structural information is critical for improved aboveground biomass estimation with greater accuracy (Dubayah and Drake, 2000; Gregoire et al., 2016). Past and ongoing research efforts have developed algorithms that use airborne lidar to quantify forest inventory variables (generally on local spatial scales), such as tree height (Hyypä et al., 2008; van Leeuwen and Nieuwenhuis, 2010; Næsset, 1997), stand structure (Lefsky et al., 2005; Næsset et al., 2005; Kane et al., 2010), leaf area index and cover (Morsdorf et al., 2006; Jensen et al., 2006), timber volume (Yu et al., 2004; Maltamo et al., 2006), and biomass (Boudreau et al., 2008; Lim and Treitz, 2004; Næsset and Gobakken, 2008; Lefsky et al., 2002; Zhao et al., 2009). Given lidar data with sufficiently high pulse density, determination of these fundamental biometric variables (tree height, tree density, fractional cover, and stand structure) with a low level of uncertainty is relatively straightforward. Yet, using these variables to estimate aboveground biomass introduces potentially large errors due to additional complexities and uncertainties, such as field sampling design, model selections and the accuracy of the allometric equations that are used in the estimation procedure (Gregoire et al., 2016).

In 2012, USGS initiated the 3D Elevation Program (3DEP), leveraging partnerships with other federal and state agencies, aiming to provide consistent, standardized national lidar coverage in the coming years (Sugarbaker et al., 2014). According to the National Enhanced Elevation Assessment study, the current level of lidar data availability is at a relatively low quality level (QL3) of <1 points/m² on a 25-year repeat cycle, although the quality level that provides the largest user satisfaction is high quality (QL1) at 8 points/m² on an annual cycle. However, high data quality / pulse density comes with high data acquisition cost, and therefore the most efficient cost-benefit recommendation is to acquire quality level 2 (QL2) at 2 points/m² lidar data on an 8-year cycle for the US (Sugarbaker et al., 2014). Typically, the lower the density of laser pulses, the less comprehensive the tree structure characteristics captured by the laser scanning systems, and therefore the higher the uncertainty of aboveground biomass estimates derived from lidar for individual trees. Yet, for the purpose of a Biomass ECV, it is less critical to accurately depict structure characteristics of each individual tree, and therefore lower pulse density at plot and stand levels can be a compromise to capture larger areas for a national scale operational product.

While the effectiveness of using lidar to map vegetation and estimate biomass has been demonstrated, the high cost of airborne lidar data acquisition poses practical limitations on their application to large-scale biomass mapping. Contrary to the high cost and sporadic acquisition of lidar, Landsat satellites provide wall-to-wall data coverage every 8 days with free access, and can be potential candidates for operational products such as a Biomass ECV. Landsat 8, the latest in the series of Landsat satellites, maintains similar spectral bands as the Operational Land Imager, and improvements in its radiometric performance (greater signal-to-noise ratio and 12-bit quantization) make it potentially more effective for mapping vegetation. However, the lack of 3-D structural information from Landsat data leads to relatively low accuracy in estimating aboveground biomass over large geographic areas (Foody et al., 2003; Hall et al., 2006; Lu, 2005; Avitabile et al., 2012). In the meantime, without suitable accommodations or modifications, the long acquisition cycle of the current 3DEP program and low point density may prevent development and implementation of a

feasible Biomass ECV product in the near future. Here, we aim to facilitate informed decision making and planning for a Biomass ECV product by examining the key factors that underlie this issue in a pilot study area. Specifically, we used our established research field sites in east-central Arizona (Wu et al., 2015) to (1) evaluate the impacts of different density/quality levels lidar data on aboveground biomass estimation accuracy, (2) compare the accuracies of aboveground biomass estimates derived from lidar and Landsat 8 data, and (3) consider the implications of our results for the opportunities and feasibility of an operational national Biomass ECV product.

2. Methods

2.1. Study Area

The study area is located near Point of Pines on the San Carlos Apache Reservation in east-central Arizona (33.39° N, 109.82° W, 1829 – 2134 m ASL). Vegetated landscapes in the study area are primarily comprised of forests and woodlands dominated by ponderosa pine (*Pinus ponderosa*), two-needle pinyon (*Pinus edulis*), alligator juniper (*Juniperus deppeana*), Arizona white oak (*Quercus arizonica*), and gambel oak (*Quercus gambelii*). 39 square plots of 30 m by 30 m each were established within the study area, including 21 woodland plots and 18 forest plots respectively. Ponderosa pine forests are continuous and extend throughout the study area; whereas pinyon, juniper and oak species are inter-mixed at lower elevation. Mixed woodland species plots usually have higher tree density and lower biomass than forest plots, which is consistent with the landscape characteristics of the study area.

2.2. Field Biometrics

Field biometric data were collected during three intensive field campaigns from June to August in 2013. To determine the corner coordinates of each plot, two survey-grade Global Positioning System (GPS) receivers were used; a base station GPS receiver was placed near each plot location, with a roving GPS receiver used to accurately map the plot corner points, referenced to the base station receiver. Tree species were recorded and individual tree heights were measured using a Nikon Forestry Pro Laser Range Finder 8381 for tall and mature trees, and an extension pole marked with 0.1 m increments for small and young trees. Tree heights were measured twice and the final tree height for each tree was determined as the average of the two measurements. Both methods achieved vertical accuracies of 0.3 m. The diameter at breast height (dbh) was measured at 1.37 m height for ponderosa pines, and no trees smaller than 1.4 m in height were included in the measurements. For woodland species, the root collar diameter of each stem was measured, and the equivalent diameter at root collar (edrc) was computed using the equation (1) below:

$$\text{edrc} = \sqrt{a^2 + b^2 + \dots + x^2}, \quad (1)$$

Where a, b, ..., x are diameter at root collar for each stem that is 3.8 cm or larger (Chojnacky and Ott, 1986).

Biomass of each individual tree measured in the field was calculated using validated species-specific allometric equations derived from field studies (Clary and Tiedemann, 1986; Grier et al., 1992; Kaye et al., 2005; Navar, 2009) in similar environments.

2.3. Remote Sensing Data

2.3.1. Airborne Lidar

Airborne lidar data were acquired through the U.S. Geological Survey Geospatial Product and Service Contract (GPSC), and the data collection was completed by Woolpert, Inc. (Dayton, OH). The lidar data were acquired using a Leica ALS70 Multiple Pulses in Air (MPiA) lidar sensor, onboard a Cessna 402 on August 8 – 9th, 2013 (Table 1). The Leica ALS70 system used in this study uses a laser that operates in the near infrared spectral region (1064 nm). A total of 52 flight lines were flown to provide comprehensive coverage of the study area at a specified minimum pulse density that equated to an average of 12 points/m² in open areas. When the sensor calibration, data acquisition, and GPS processing phases were complete, Woolpert then processed individual flight lines to derive a raw point cloud file in LASer (LAS) 1.2 format. Ground and non-ground classes were created using the calibrated point cloud files, and survey ground control data were imported and incorporated into an accuracy assessment. Woolpert calculated the vertical accuracy by comparing the lidar bare earth points to the ground surveyed QA/QC points, and reported a vertical accuracy of 0.072 m in flat, open areas, along with a bare-Earth DEM accuracy within 0.068 m, both at a 95 percent confidence level.

Table 1: Summary of Airborne Lidar Sensor and Flight

| Parameter | Performance |
|---|-------------|
| Post spacing (minimum) | 0.3 m |
| Aboveground level average flying height | 1,829 m |
| Mean sea level average flying height | 3,627 m |
| Average ground speed | 249 kph |
| Field of view (full) | 10 degrees |
| Pulse rate | 292.0 kHz |
| Scan rate | 72.6 Hz |
| Side lap (minimum) | 25% |

2.3.2. Landsat 8 Satellite Imaging

Cloud-free Landsat 8 surface reflectance data for September 24th, 2013 were acquired from USGS Earth Resources Observation and Science (EROS) Center Science Processing Architecture (ESPA). Normalized Difference Vegetation Index (NDVI) is the most widely used vegetation index for mapping vegetation, taking advantage of strong absorption at the visible spectral region and strong reflectance at the near-infrared spectral region of chlorophyll in the leaves (Rouse et al., 1974; Sellers, 1985; Tucker, 1979). NDVI has been used to estimate biomass (Labrecque et al., 2006; Zheng et al., 2004) as it is a sensitive indicator of canopy structure and leaf chemical content and leaf area, and is especially useful in low-biomass dryland forest and woodland ecosystem with low leaf area index (Gamon et al., 1995) where saturation of the NDVI is not typically observed. NDVI was computed using the red (R) and near-infrared (NIR) bands as $(NIR - R)/(NIR + R)$ using Landsat 8 surface reflectance data from ESPA. Surface reflectance of all 8 visible, near-infrared and shortwave infrared bands as well as computed NDVI were used to estimate aboveground biomass for forests and woodlands in our study area.

2.4. Aboveground Biomass Estimation

2.4.1. Lidar Derived Metrics

Because of the flight-lines overlap, superfluous lidar points were ignored, ensuring a more homogenous sampling density throughout the study area. To isolate the impacts of pulse density on various forest height metrics, a random thinning approach was applied to the original dataset at 12

points/m² to create a gradient of lower point densities at 8, 4, 2, 1 and 0.5 point(s)/m², respectively (Figure 1). For each reduced density point cloud dataset, ground points were classified and tree heights were then calculated relative to the ground surface. A common approach to generate aboveground biomass estimates from remote sensing is to establish statistical regression between laser height measurements and ground sampling plots (Gregoire et al., 2016). Various descriptive statistical metrics commonly used for estimating aboveground biomass (Lefsky et al., 1999; Means et al., 1999; Næsset, 1997; Zhao et al., 2009) were calculated from the entire vertical profile of the vegetation lidar returns to best capture the relationship between the lidar pulse data and field-based estimates of biomass at the plot level. All lidar data processing was conducted using LAStools (<http://lastools.org>) developed by Martin Isenburg (Isenburg and Schewchuck, 2007; Hug et al., 2004). Basic height statistics metrics, including maximum, minimum, mean, standard deviation, skewness, kurtosis, and quartic average, were computed from the canopy height point cloud data for each field plot. Canopy cover and tree density were computed from the number of vegetation returns versus total returns within each plot. Height percentiles can also be effective in capturing the different levels of laser beam penetration through the tree canopies and therefore reflect the structure characteristics of the vegetation, and have been demonstrated to be very useful in estimating aboveground biomass (Lim and Treitz, 2004). Using LAStools, 10th, 25th, 50th, 75th, and 90th percentiles of height were also calculated from the canopy height point cloud.

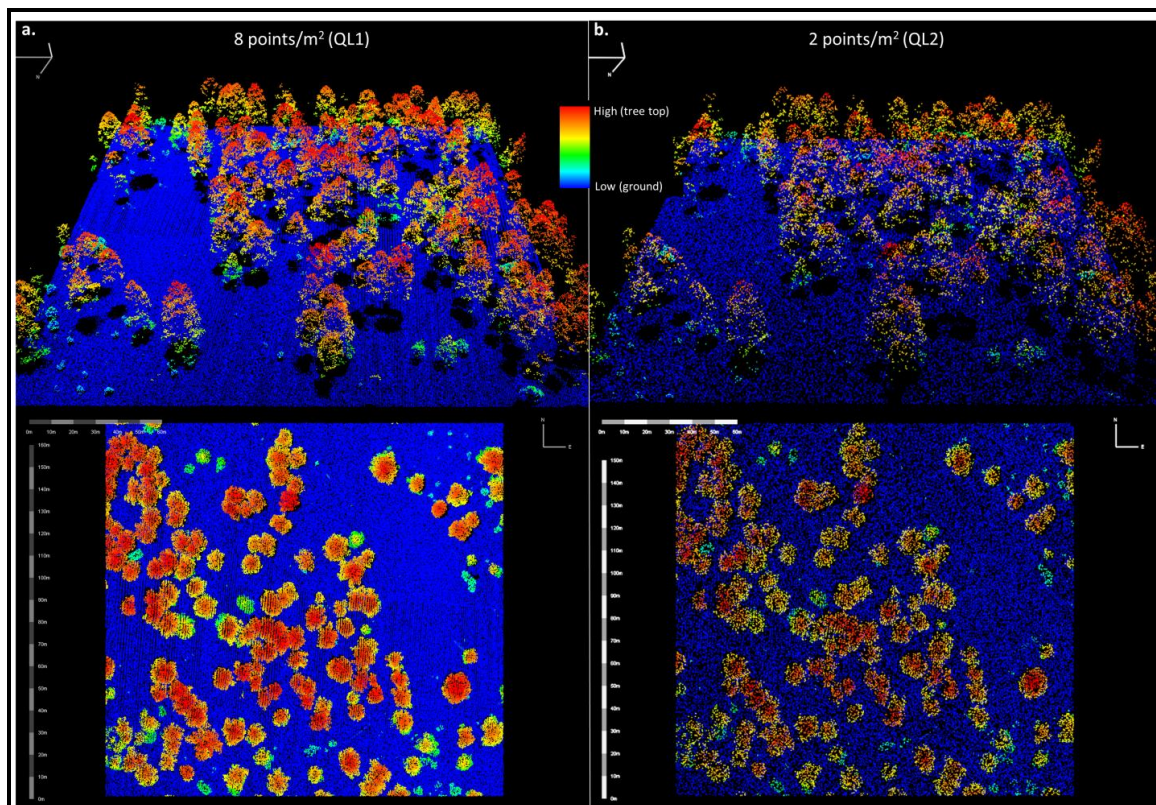


Figure 1: Lidar Point Clouds at (A) 8 Points/m² And (B) 2 Points/m² From Side View (Top) and Top View (Bottom), Corresponding to 3DEP Quality Level 1 (QL1) And QL2, Respectively

2.4.2. Regression Models

Multiplicative models were estimated as linear regressions using logarithmic transformations for predictor metrics and field-based aboveground biomass estimates, which have been found to be suitable to estimate vegetation biomass (García et al., 2010; Næsset and Bjerknæs, 2001; Næsset and Økland, 2002). The multiplicative model was formulated as equation (2):

$$AGB = a_0 p_1^{a_1} p_2^{a_2} p_3^{a_3}, \quad (2)$$

Whereas the linear form of equation (2) after logarithmic transformations is shown as equation (3):

$$\ln AGB = \ln a_0 + a_1 \ln p_1 + a_2 \ln p_2 + a_3 \ln p_3, \quad (3)$$

Where AGB is the field-based aboveground biomass in Mg ha^{-1} , and p_i is the predictor variable selected from the predictor metrics. Such linear regression models were created separately using lidar height derived metrics and Landsat 8 derived predictors.

Stepwise selection was used to select predictor variables to be included in the linear regression models. This method includes the predictor variables showing the highest coefficient of determination (R^2) with the estimator variable, and additional variables were incorporated into the model based on an F-test under the normality assumption of the variables, which was met using logarithmic transformations. To avoid overfitting the models and to identify the most critical predictors for aboveground biomass, a maximum of three predictors can be selected in a single regression model. The variance inflation factor (VIF) was used to identify the existence of collinearity in the selected model. It is commonly accepted that VIF values above 10 indicate multicollinearity which causes standard error inflation (Belsley et al., 2005). We applied a VIF threshold of 10 and the Pearson correlation coefficients to select optimal predictor variables for the aboveground biomass regression that minimized data dimensionality and the presence of multicollinearity within the predictor variables, and to overcome issues of over fitting. Upon model selections, the estimated aboveground biomass was converted back to the original scale, and the root-mean-square error (RMSE, in Mg ha^{-1}) was calculated. This regression modeling process was carried out for three different groups: (1) all forest and woodland plots ($n = 39$), (2) forest plots only ($n = 18$), and (3) woodland plots only ($n = 21$). Upon completion of the regression analysis, a 5 fold cross validation analysis was performed. The differences in the cross validation results and regression model results were evaluated to ensure consistency and accuracy of the regression models. Model performances of aboveground biomass estimates derived from lidar and Landsat 8 were evaluated using R^2 , RMSE, and cross validated RMSE values. All statistical analyses were performed in RStudio (version 0.97.237).

3. Results

3.1. Lidar-Derived Aboveground Biomass Models

We developed regression models to evaluate the statistical relationship between field-based biomass and lidar-derived predictor variables from multiple levels of point densities (Table 2). First, we developed biomass models for all forest and woodland plots, and found 8 points/ m^2 was the most optimal lidar point density level, producing the lowest error of 38 Mg/ha , which is equal to about 36% of average vegetation biomass in our plots (Table 2). Errors associated with the aboveground biomass estimates decreased as the lidar point density increased ($p = 0.03$, Figure 2). 5-fold cross validated RMSEs were slightly larger than the model RMSEs as we expected, yet they followed the similar trend along the point density gradient (Table 2). Out of all the metrics derived from the airborne lidar dataset, skewness and tree density were the two predictors that were consistently selected for high point densities including 4 and 8 points/ m^2 ; whereas standard deviation and kurtosis were the two metrics that were consistently used in the models derived from low density lidar data including 0.5, 1, and 2 points/ m^2 (Table 2).

Second, to account for biomass variation due to broad vegetation types within our study area and to test for differences among vegetation types, we developed separate regression models for forest and woodland plots (Table 2). Among all the models derived from a gradient of point densities, the smallest errors of 32.9 Mg/ha (33%) for the woodland plots and 31.8 Mg/ha (29%) for the forest plots were

produced at 8 points/m² density, respectively (Table 2). Both vegetation type-specific models demonstrated similar descending trends of estimated errors as lidar point density increases (Figure 2). From both model RMSEs and 5-fold cross validated RMSEs, forest plots exhibited a much sharper decline of errors of aboveground biomass estimates with increasing lidar point density than the woodland plots (Table 2 and Figure 2), indicating that the uncertainty associated with estimating forest biomass was more sensitive to source lidar data point density than woodland biomass estimation. Different predictor variables were selected for aboveground biomass models for forest and woodland plots. Forest aboveground biomass models consistently produced smaller errors than the woodland models except for at 1 point/m² (Figure 2). For woodland aboveground biomass models, maximum height and tree density were selected in the highest point density derived models at 8 points/m²; whereas standard deviation was selected in the low point density derived models at 0.5, 1 and 2 points/m² (Table 2). For forest aboveground biomass models, skewness and kurtosis were selected in the higher point density derived models at 4 and 8 points/m²; whereas standard deviation and kurtosis were selected in the lower point density derived models at 0.5, 1, and 2 points/m² (Table 2). For forest plots, kurtosis was proven to be crucial for estimating forest aboveground biomass. Overall, skewness and tree density were the most used metrics to estimate aboveground biomass when using high point density lidar data, while standard deviation and kurtosis were crucial for estimating aboveground biomass at low point density (Figure 3).

3.2. Landsat and Lidar Derived Aboveground Biomass Models Comparison

Using surface reflectance derived from Landsat 8 to estimate aboveground biomass in our study area, red and near infrared bands were selected when all plots were combined (Table 2). The Landsat 8 based model performed at a similar level to those derived from 0.5 – 1 point/m² lidar data when all forest and woodland plots were included (Table 2 and Figure 2). For separate forest and woodland models, Landsat 8 performed better in estimating woodland biomass than forest biomass (Table 2 and Figure 2). Green band and NDVI were used in the woodland aboveground biomass models, while coastal and green bands were selected in the forest models (Table 2). Landsat 8 produced larger 5-fold validated RMSEs than all lidar-derived models, including the lowest point densities of 0.5 – 1 point/m². Thus, Landsat 8 cannot be interchangeably used with lidar data to estimate forest or woodland aboveground biomass in our study area.

Table 2: Aboveground Biomass Models Derived from Multiple Lidar Point Densities and Landsat 8

| Point Density (points/m ²) | Predictable Variables * | R ² | RMSE (Mg/ha) | Percentage of Mean Biomass (%) | 5-fold Cross Validated RMSE (Mg/ha) |
|--|-------------------------|----------------|--------------|--------------------------------|-------------------------------------|
| All (n = 39) | | | | | |
| 8 | Skew, Density | 0.59 | 38.1 | 36.4 | 38.8 |
| 4 | Skew, Density, StdDev | 0.53 | 39.6 | 37.8 | 41.2 |
| 2 | StdDev, Kurtosis | 0.47 | 43.0 | 41.1 | 46.6 |
| 1 | StdDev, Kurtosis | 0.45 | 44.7 | 42.7 | 48.9 |
| 0.5 | StdDev, Kurtosis | 0.46 | 42.7 | 40.8 | 46.0 |
| Landsat 8 | Red, Near Infrared | 0.52 | 43.4 | 41.5 | 48.7 |
| Woodland (n = 21) | | | | | |
| 8 | Max, Density | 0.68 | 32.9 | 32.9 | 37.7 |
| 4 | Skew, QuarAvg | 0.67 | 34.4 | 34.4 | 43.8 |
| 2 | StdDev | 0.61 | 34.2 | 34.2 | 38.9 |
| 1 | StdDev | 0.61 | 34.9 | 34.9 | 40.3 |
| 0.5 | StdDev | 0.56 | 37.5 | 37.5 | 39.5 |
| Landsat 8 | Green, NDVI | 0.68 | 37.7 | 37.7 | 44.0 |
| Forest (n = 18) | | | | | |
| 8 | Skew, Kurtosis | 0.52 | 31.8 | 28.9 | 36.1 |
| 4 | Skew, Kurtosis, StdDev | 0.35 | 33.5 | 30.4 | 40.1 |
| 2 | StdDev, Kurtosis, P50 | 0.26 | 34.8 | 31.6 | 41.3 |

| | | | | | |
|-----------|------------------|------|------|------|------|
| 1 | StdDev, Kurtosis | 0.10 | 43.1 | 39.2 | 49.6 |
| 0.5 | StdDev, Kurtosis | 0.19 | 38.9 | 35.3 | 47.5 |
| Landsat 8 | Coastal, Green | 0.15 | 41.2 | 37.4 | 52.7 |

Skew = Skewness, Density = Tree density, StdDev = Standard Deviation, Max = Maximum height, QuarAvg = Quartic average, P50 = 50th percentile of height

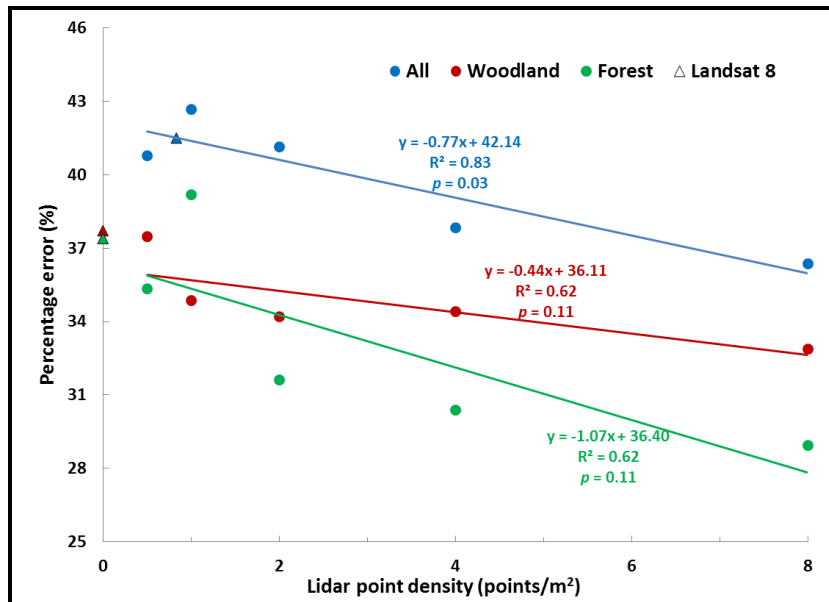


Figure 2: Errors in Aboveground Biomass Estimates at Various Lidar Point Densities, In Comparison to Landsat 8. The Errors were presented as the Percentage of the Root-Mean-Square Error (RMSE) of the Mean Biomass. Aboveground Biomass were Estimated for All Vegetation (Blue), Woodland (Red), And Forest (Green) from Lidar (Circle) and Landsat (Triangle). Linear Regressions between Percentage Error and Point Densities were applied to Lidar Derived Aboveground Biomass Models Only. When Landsat Derived Errors were Larger than Those Derived from All Lidar Data, Landsat Derived Errors Were Presented at 0 Point Density in the Graph for Reference

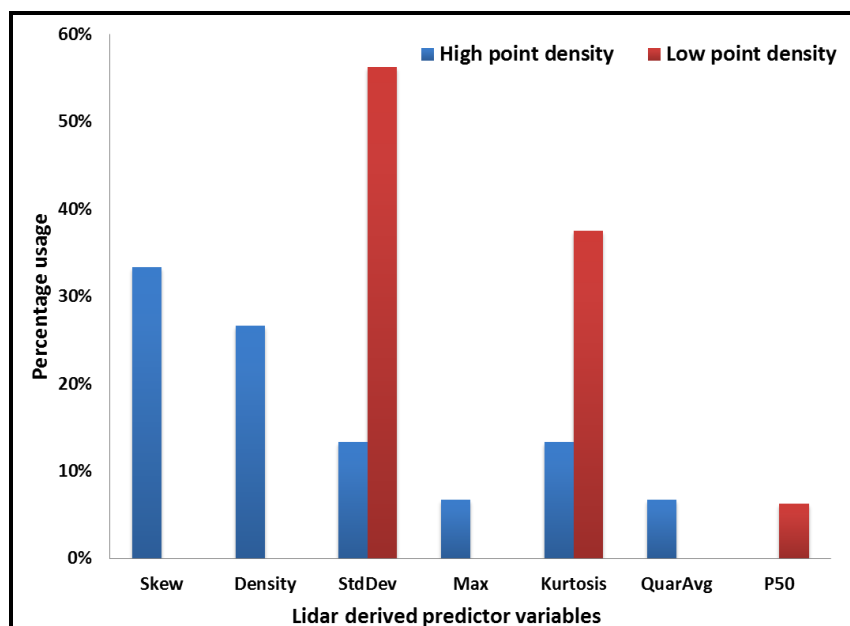


Figure 3: Usage of Lidar Derived Metrics in the Aboveground Biomass Models. High Point Density Includes 4 and 8 Points/m²; Low Point Density Includes 0.5, 1, and 2 Points/m²

3.3. Cost Considerations for Lidar-Derived Aboveground Biomass Estimates

Since airborne lidar acquisition over large areas is costly, lidar applications necessarily involve cost considerations and tradeoffs. The 3DEP is aiming to provide US national lidar coverage in the next decade, and the current target quality level (QL) is QL2 at 2 points/m², with an option to upgrade to QL1 at 8 points/m² (Sugarbaker et al., 2014). Obviously, the cost of lidar acquisition decreases as point density decreases, and uncertainty of aboveground biomass estimates generally increases as point density decreases, although not necessarily in a linear fashion or uniformly across vegetation types. We used the estimated cost information from 3DEP and the errors of aboveground biomass estimates from our plots to evaluate the cost efficiency of lidar acquisitions to estimate aboveground biomass at various quality levels (Figure 4). The aboveground biomass estimates error at per dollar investment increases linearly as the quality level increases (point density decreases), and QL1 at 8 points/m² provides the best efficiency for the lidar acquisition investment for aboveground biomass applications based on the results from our study area (Figure 4).

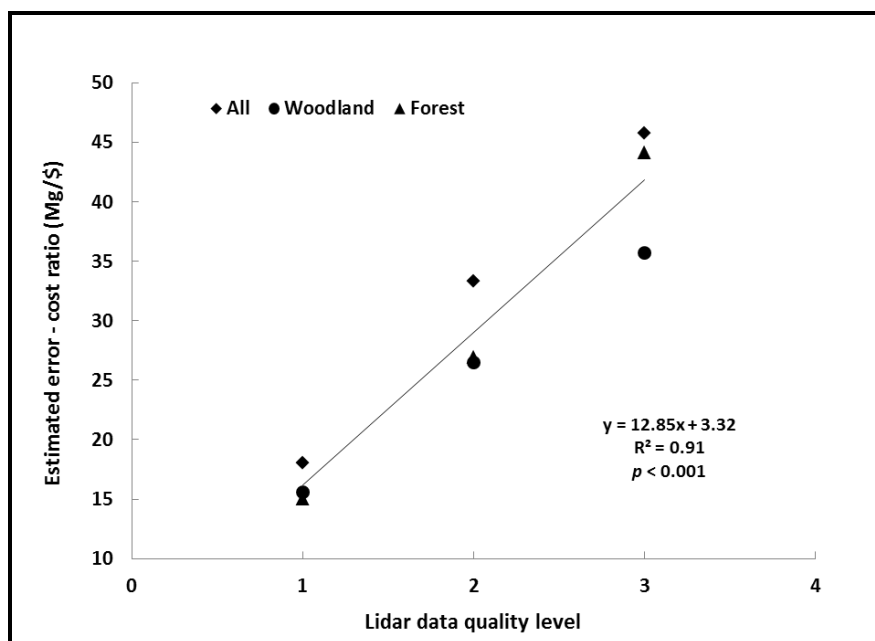


Figure 4: Estimate Errors – Acquisition Cost Ratios for Lidar Derived Aboveground Biomass. The Quality Levels (QL) Are: QL1 – 8 Points/m², QL2 – 2 Points/m², and QL3 – 1 Point/m²

4. Discussions

4.1. Lidar Point Density

An important question to ask when producing a large scale product such as a Biomass ECV is whether high point density lidar data are necessary to obtain sufficiently accurate results. From an operational perspective, broad scale (e.g., large regions, statewide, or national) lidar acquisition is usually obtained at low point density at <1 point/m² (Cunningham et al., 2004; Veneziano et al., 2012), which is much lower than the target forest research lidar acquisitions (1-8 points/m²). The next relevant question is whether these low point density lidar data that were intended to create elevation datasets are adequate to produce biomass products with acceptable accuracies.

From our results, the overall accuracies of biomass estimates increased as the source lidar data point density increased, but such trends were not statistically significant for the vegetation type specific models, although these trends may become significant given greater sample size. Some other

research found that high point density did not add much value to extracting forest canopy profiles at the stand level and estimating tree height or volume (Thomas et al., 2006; Goodwin et al., 2006; Lim et al., 2008; Jakubowski et al., 2013), unless the point density was simulated at very low levels (< 0.5 point/m²) where the errors grew significantly (Magnusson et al., 2007; Jakubowski et al., 2013). Results from analysis of our study area indicated that the optimal point density to achieve the best model performance and highest cost efficiency was 8 points/m². These studies are informative for evaluating the effects of point density on biomass estimation accuracy, however our random thinning approach may approximate but not perfectly replicate lower density data as they would be collected using the actual data sampling configurations of a multiple-return lidar sensor. In addition to pulse density, other factors of lidar acquisition such as sensors, flying altitudes, pulse repetition frequencies, and laser pulse power can also impact forest canopy metrics, although such effects are minor (Næsset, 2009; Chasmer et al., 2006).

Because of the rich information of 3-D structures of vegetation from lidar datasets, predictor metrics can be readily extracted from lidar datasets, while additional image analysis, personnel and software costs can occur while using other data sources. Especially for large areas where image processing and analysis workloads increase significantly, lidar can already be less expensive or comparable to image data analysis (Johansen et al., 2010). Another advantage of reduced density lidar data is the reduction of file size for data processing, especially for a large area such as the national Biomass ECV. It has been shown that a 40% reduction in lidar point density with a corresponding significant reduction in file size produced biomass estimates comparable to the full lidar dataset (Singh et al., 2015).

4.2. Lidar Metrics

Evaluation of multiple linear regression models in our analysis illustrated that descriptive statistics metrics such as skewness, kurtosis, and standard deviation explained more variance than direct canopy height related metrics, indicating that the overall summary of the canopy characteristics (kurtosis) and shape of height distribution (skewness) are crucial for aboveground biomass estimates. Only one height percentiles metric was selected in one final model for the forest aboveground biomass estimates (2 points/m²), and maximum height metrics were only used in the woodland aboveground biomass models derived from high point density data. Skewness and tree density were the most commonly used metrics in aboveground biomass models from the high point density lidar data, suggesting that effective estimates of tree density, and therefore accurate biomass estimates, requires higher point density lidar data. In contrast, standard deviation and kurtosis were the most commonly used metrics in the models derived from low point density lidar data, indicating that the variability of height distribution among neighboring points is important to ensure biomass estimate accuracy derived from low density lidar data. For woodland plots, it was challenging to select more than one metric (standard deviation) to predict woodland aboveground biomass using lower density lidar data at 0.5 – 2 points/m². Yet, the model performance was not substantially different with one-predictor in the low density models, when compared to two-predictor models from high density lidar data (Figure 2). Thus, low density lidar data can be used to estimate woodland-dominated areas with reasonably sufficient accuracy.

4.3. Aboveground Biomass Model Uncertainty

Quantifying the uncertainty of biomass estimates is crucial for identifying the appropriate data sources and algorithms for a potential national Biomass ECV. Errors can be introduced in multiple steps including tree measurements, allometric equations development, tree-level aboveground biomass prediction, plot-level aboveground biomass estimation, plot-level remote sensing metrics extraction, and remote sensing based model development. Although national scale allometric equations exist (Chojnacky et al., 2014), localized equations are preferred to reduce errors introduced into the field-

based biomass estimation (Chen et al., 2015). While the lack of field based biometrics and local diameter-based allometric equations limit the operational feasibility of a national Biomass ECV, data routinely collected by the U.S. Forest Service's Forest Inventory and Analysis (FIA) program have been successfully used in lidar-based forest biomass and carbon estimates (Johnson et al., 2014). Because of the comprehensive national sampling strategy of the FIA data, both training and validation sets can be generated from FIA datasets as long as they are independent. For example, national forest inventory data, in combination with spaceborne lidar and optical imagery, have been successfully used in a recent study to estimate biomass of China at the national scale (Su et al., 2016). However, mismatches in the timing of observations can be a source of error, as the years in which FIA plot surveys are performed can vary widely over large areas, and may rarely be coincident with the lidar acquisitions. An additional, potential shortcoming of FIA data for national-scale biomass estimation is that information on grassland or shrubland is not provided, and therefore models have not been developed to estimate grassland or shrubland biomass at a larger scale. Although grassland and shrubland typically have lower aboveground biomass compared to forests and woodlands, large geographic coverage and implications for land management decisions (e.g., grazing and fire management) makes the accurate estimation of their biomass an important issue. Differences between the structure of grasslands and forests/woodlands require different metrics derived from lidar to estimate aboveground biomass, and therefore additional research that extends beyond the scope of this study is needed.

4.4. Operational Feasibility

Although the 3DEP is aimed at accumulating, over time, airborne lidar data that approaches, if not fully achieves, comprehensive national coverage, the current spatial coverage remains far from that goal. In the interim, Landsat 8 surface reflectance data with national coverage and free access could be considered as an alternative candidate to support the creation of a national Biomass ECV. However, in the case of our pilot study area in Arizona, Landsat 8 generally produced higher errors than all lidar-based models, suggesting it cannot simply be used as a substitute of lidar data sources, although additional more sophisticated metrics can be extracted from Landsat data which required further processing and computing. Lidar-based vegetation type specific (forest and woodland) models produced lower errors than all-vegetation combined. Similar to our results, vegetation type specific models improved the aboveground biomass estimates in a mixed Mediterranean forest (García et al., 2010), and land cover maps have been used with other ancillary data to provide regional biomass estimates (Boudreau et al., 2008).

Until national-coverage lidar data are available, a practical approach to a national Biomass ECV product is to apply vegetation type specific models using existing land cover data (Stoker et al., 2014; Avitabile et al., 2012). In our pilot study area, for woodlands, lower point density lidar (e.g., QL3/QL2) were adequate to generate good estimates of woodland aboveground biomass given the small difference across point densities. For forested areas in the pilot plots, high point density lidar (e.g., QL1) for selected dominate forest species areas will be ideal for ensuring the accuracy of aboveground biomass estimates, but lower point density lidar data can also support the production of a Biomass ECV. Further, ponderosa pine forests in our pilot study area may require higher point density for accurate aboveground biomass estimate because of the "tall and thin" shape of conifer trees, and point density requirement may be lower for the broad leaf forests areas elsewhere. In addition, the average aboveground biomass in the semi-arid Southwest US is lower than forests in the Northeast and Northwest US, and therefore a lower point density may be adequate for other higher biomass areas to reach the same overall accuracy target.

Weighing cost and model performance, a high point density operational lidar dataset (e.g., 3DEP QL1) provides the most promising avenue to generating sufficiently accurate Biomass ECV products. Yet, lower point density lidar data still produced better estimates of aboveground biomass than optical data,

and therefore the current QL2 acquisition plan of 3DEP could adequately support the generation of an operational Biomass ECV product, with space for improvement in areas where higher density lidar datasets at 8 points/m² are available. Even though our study area only consists a number of species that are typical of the Southwest US, other research efforts that studied a range of different species (evergreen, deciduous, mixed, plantation, etc.) and stand conditions found similar results that point density decimation effect was minimal, and therefore low point density lidar data can be sufficient to estimate aboveground biomass (Singh et al., 2015; Gonzalez-Ferreiro et al., 2013; Gobakken and Næsset, 2008; Thomas et al., 2006). These findings reinforce our view that it is feasible to use the operational 3DEP QL2 lidar data to develop vegetation type specific aboveground biomass algorithm to create a national scale Biomass ECV given the limitation of current lidar data availability.

5. Conclusion

We compared the effectiveness of lidar data at multiple point densities to estimate aboveground biomass for forest and woodland plots on the San Carlos Apache Reservation in the Southwestern U.S. In general, estimated errors decrease as the point density increases, reaching a turning point at 8 points/m² where the best model performance and cost efficiency was achieved. Forest biomass estimates were more affected by point density levels than woodlands. Therefore, a high density lidar dataset can greatly improve the forest biomass estimates, whereas low density lidar datasets can be sufficient to ensure acceptable accuracy levels for estimating woodland biomass.

Although limited in geographic scope, results from our local scale plot-level research nevertheless provide insights that can be useful in planning effective, potential strategies for developing and implementing a national-scale Biomass ECV product from airborne lidar. Ideally, an operational national lidar dataset at 8 points/m² (QL1) would produce quality aboveground biomass estimates for forest and woodlands as an operational Biomass ECV. However, such high point density lidar data are not yet available at the national scale and the acquisition costs are high. For the near future, we recommend using low point density 3DEP QL2 lidar data, where it is available, to develop vegetation type specific aboveground biomass models, and leveraging higher point density lidar data for forested areas.

This study was conducted in the context of the feasibility of a national Biomass ECV, but it is also relevant to land managers who are potentially making decisions about lidar data acquisition parameters with a set budget. When considering lidar acquisition over large areas, land managers need to make decisions among cost, coverage, density, and accuracy standard. Our plots are located on the San Carlos Apache Reservation, where land managers are particularly interested in using lidar data to estimate vegetation biomass and carbon stocks to inform land management decisions. Our results will enable tribal land managers to make informed decisions on lidar acquisition specifications to maximize the data collection area and ensure reliable results.

Acknowledgements

This study is supported by the USGS Mendenhall, Land Remote Sensing and Land Change Science programs. Thanks to Robert Hetzler, Kelly Hetzler, Charles Truettner, Jacob Higgins, Beverly Maxwell and Terri Victor for providing help in field data collection. Thanks to Birgit Peterson for helpful comments to improve earlier drafts of this manuscript.

References

Avitabile, V., Baccini, A., Friedl, M.A., and Schullius, C. *Capabilities and Limitations of Landsat and Land Cover Data for Aboveground Woody Biomass Estimation of Uganda*. Remote Sensing of Environment. 2012. 117; 366-380.

- Belsley, D.A., Kuh, E., and Welsch, R.E., 2005: *Regression Diagnostics: Identifying Influential Data and Sources of Collinearity*. John Wiley and Sons.
- Bojinski, S., Verstraete, M., Peterson, T.C., Richter, C., Simmons, A., and Zemp, M. *The Concept of Essential Climate Variables in Support of Climate Research, Applications, and Policy*. Bulletin of the American Meteorological Society. 2014. 95; 1431-1443.
- Boudreau, J., Nelson, R.F., Margolis, H.A., Beaudoin, A., Guindon, L., and Kimes, D.S. *Regional Aboveground Forest Biomass Using Airborne and Spaceborne LIDAR in Québec*. Remote Sensing of Environment. 2008. 112; 3876-3890.
- Chasmer, L., Hopkinson, C., Smith, B., and Treitz, P. *Examining the Influence of Changing Laser Pulse Repetition Frequencies on Conifer Forest Canopy Returns*. Photogrammetric Engineering and Remote Sensing. 2006. 72; 1359-1367.
- Chen, Q., Vaglio Laurin, G., and Valentini, R. *Uncertainty of Remotely Sensed Aboveground Biomass over an African Tropical Forest: Propagating Errors from Trees to Plots to Pixels*. Remote Sensing of Environment. 2015. 160; 134-143.
- Chen, Q., Vaglio Laurin, G., Battles, J.J., and Saah, D. *Integration of Airborne Lidar and Vegetation Types Derived from Aerial Photography for Mapping Aboveground Live Biomass*. Remote Sensing of Environment. 2012. 121; 108-117.
- Chojnacky, D.C., and Ott, J.S. *Pinyon-Juniper Volume Equations for Arizona Hualapai and Havasupai Indian Reservations*. Research Note INT-363. 1986. 1-4.
- Chojnacky, D.C., Heath, L.S., and Jenkins, J.C. *Updated Generalized Biomass Equations for North American Tree Species*. Forestry. 2014. 87; 129-151.
- Clary, W.P., and Tiedemann, A.R. *Distribution of Biomass within Small Tree and Shrub form Quercus Gambelii Stands*. Forest Science. 1986. 32; 234-242.
- Cunningham, R., Gisclair, D., and Craig, J., 2004: *The Louisiana Statewide Lidar Project*. Louisiana State University, Baton Rouge, Louisiana.
- Dubayah, R.O., and Drake, J.B. *Lidar Remote Sensing for Forestry*. Journal of Forestry. 2000. 98; 44-46.
- Evans, J., Hudak, A., Faux, R., and Smith, A.M. *Discrete Return Lidar in Natural Resources: Recommendations for Project Planning, Data Processing, and Deliverables*. Remote Sensing. 2009. 1; 776-794.
- Foody, G.M., Boyd, D.S., and Cutler, M.E.J. *Predictive Relations of Tropical Forest Biomass from Landsat TM Data and Their Transferability between Regions*. Remote Sensing of Environment. 2003. 85; 463-474.
- Gamon, J.A., Field, C.B., Goulden, M.L., Griffin, K.L., Hartley, A.E., Joel, G., Penuelas, J., and Valetini, R. *Relationships between NDVI, Canopy Structure, and Photosynthesis in Three Californian Vegetation Types*. Ecological Applications. 1995. 28-41.

- García, M., Riano, D., Chuvieco, E., and Danson, F.M. *Estimating Biomass Carbon Stocks for a Mediterranean Forest in Central Spain Using Lidar Height and Intensity Data*. Remote Sensing of Environment. 2010. 114; 816-830.
- Gobakken, T., and Naesset, E. *Assessing Effects of Laser Point Density, Ground Sampling Intensity, and Field Sample Plot Size on Biophysical Stand Properties Derived from Airborne Laser Scanner Data*. Canadian Journal of Forest Research. 2008. 38; 1095-1109.
- Gonzalez-Ferreiro, E., Miranda, D., Barreiro-Fernandez, L., Bujan, S., Garcia-Gutierrez, J., and Dieguez-Aranda, U. *Modelling Stand Biomass Fractions in Galician Eucalyptus Globulus Plantations by use of Different Lidar Pulse Densities*. Forest Systems. 2013. 22; 510-525.
- Goodwin, N.R., Coops, N.C., and Culvenor, D.S. *Assessment of Forest Structure with Airborne Lidar and the Effects of Platform Altitude*. Remote Sensing of Environment. 2006. 103; 140-152.
- Gregoire, T.G., Naesset, E., McRoberts, R.E., Stahl, G., Andersen, H., Gobakken, T., Ene, L., and Nelson, R. *Statistical Rigor in Lidar-Assisted Estimation of Aboveground Forest Biomass*. Remote Sensing of Environment. 2016. 173; 98-108.
- Grier, C.C., Elliott, K.J., and McCullough, D.G. *Biomass Distribution and Productivity of Pinus Edulis-Juniperus Monosperma Woodlands of North-Central Arizona*. Forest Ecology and Management. 1992. 50; 331-350.
- Hall, R.J., Skakun, R.S., Arsenault, E.J., and Case, B.S. *Modeling Forest Stand Structure Attributes Using Landsat ETM+ Data: Application to Mapping of Aboveground Biomass and Stand Volume*. Forest Ecology and Management. 2006. 225; 378-390.
- Hall, S.A., Burke, I.C., Box, D.O., Kaufmann, M.R., and Stoker, J.M. *Estimating Stand Structure using Discrete-Return Lidar: An Example from Low Density, Fire Prone Ponderosa Pine Forests*. Forest Ecology and Management. 2005. 208; 189-209.
- Hug, C., Krzystek, P., and Fuchs, W. *Advanced Lidar Data Processing with LAStools*. 2004. 12-23.
- Hyypä, J., Hyypä, H., Leckie, D., Gougeon, F., Yu, X., and Maltamo, M. *Review of Methods of Small Footprint Airborne Laser Scanning for Extracting Forest Inventory Data in Boreal Forests*. International Journal of Remote Sensing. 2008. 29; 1339-1366.
- Isenburg, M., and Schewchuck, J. *LAStools: Converting, Viewing, and Compressing LIDAR Data in LAS Format*. 2007. Available at: <http://www.cs.unc.edu/~isenburg/lastools/>
- Jakubowski, M.K., Guo, Q., and Kelly, M. *Tradeoffs between Lidar Pulse Density and Forest Measurement Accuracy*. Remote Sensing of Environment. 2013. 130; 245-253.
- Jensen, J.L.R., Humes, K.S., Conner, T., Williams, C.J., and DeGroot, J. *Estimation of Biophysical Characteristics for Highly Variable Mixed-Conifer Stands using Small-Footprint Lidar*. Canadian Journal of Forest Research. 2006. 36; 1129-1138.
- Johansen, K., Phinn, S., and Witte, C. *Mapping of Riparian Zone Attributes using Discrete Return Lidar, Quickbird and SPOT-5 Imagery: Assessing Accuracy and Costs*. Remote Sensing of Environment. 2010. 114; 2679-2691.

- Johnson, K., Birdsey, R., Finley, A., Swantaran, A., Dubayah, R., Wayson, C., and Riemann, R. *Integrating Forest Inventory and Analysis Data into a LIDAR-Based Carbon Monitoring System*. Carbon Balance and Management. 2014. 9; 3.
- Kane, V.R., McGaughey, R.J., Bakker, J.D., Gersonde, R.F., Lutz, J.A., and Franklin, J.F. *Comparisons between field- and Lidar-Based Measures of Stand Structural Complexity*. Canadian Journal of Forest Research. 2010. 40; 761-773.
- Kaye, J.P., Hart, S.C., Fule, P.Z., Covington, W.W., Moore, M.M., and Kaye, M.W. *Initial Carbon, Nitrogen, and Phosphorus Fluxes Following Ponderosa Pine Restoration Treatments*. Ecological Applications. 2005. 15; 1581-1593.
- Labrecque, S., Fournier, R.A., Luther, J.E., and Piercey, D. *A Comparison of Four Methods to Map Biomass from Landsat-TM and Inventory Data in Western Newfoundland*. Forest Ecology and Management. 2006. 226; 129-144.
- Lefsky, M.A., Hudak, A.T., Cohen, W.B., and Acker, S.A. *Geographic Variability in Lidar Predictions of Forest Stand Structure in the Pacific Northwest*. Remote Sensing of Environment. 2005. 95; 532-548.
- Lefsky, M.A., Harding, D., Cohen, W.B., Parker, G., and Shugart, H.H. *Surface Lidar Remote Sensing of Basal Area and Biomass in Deciduous Forests of Eastern Maryland, USA*. Remote Sensing of Environment. 1999. 67; 83-98.
- Lefsky, M.A., Cohen, W.B., Harding, D.J., Parker, G.G., Acker, S.A., and Gower, S.T. *Lidar Remote Sensing of Above-Ground Biomass in Three Biomes*. Global Ecology and Biogeography. 2002. 11; 393-399.
- Lim, K., Hopkinson, C., and Treitz, P. *Examining the Effects of Sampling Point Densities on Laser Canopy Height and Density Metrics*. The Forestry Chronicle. 2008. 84; 876-885.
- Lim, K.S., and Treitz, P.M. *Estimation of above Ground Forest Biomass from Airborne Discrete Return Laser Scanner Data Using Canopy-Based Quantile Estimators*. Scandinavian Journal of Forest Research. 2004. 19; 558-570.
- Lu, D. *Aboveground Biomass Estimation using Landsat TM data in the Brazilian Amazon*. International Journal of Remote Sensing. 2005. 26; 2509-2525.
- Magnusson, M., Fransson, J.E.S., and Holmgren, J. *Effects on Estimation Accuracy of Forest Variables Using Different Pulse Density of Laser Data*. Forest Science. 2007. 53; 619-626.
- Maltamo, M., Eerikainen, K., Packalen, P., and Hyyppä, J. *Estimation of Stem Volume using Laser Scanning-Based Canopy Height Metrics*. Forestry. 2006. 79; 217-229.
- Means, J.E., Acker, S.A., Harding, D.J., Blair, J.B., Lefsky, M.A., Cohen, W.B., Harmon, M.E., and McKee, W.A. *Use of Large-Footprint Scanning Airborne Lidar to Estimate Forest Stand Characteristics in the Western Cascades of Oregon*. Remote Sensing of Environment. 1999. 67; 298-308.
- Morsdorf, F., Kotz, B., Meier, E., Itten, K.I., and Allgower, B. *Estimation of LAI and Fractional Cover from Small Footprint Airborne Laser Scanning Data Based on Gap Fraction*. Remote Sensing of Environment. 2006. 104; 50-61.

- Næsset, E., and Økland, T. *Estimating Tree Height and Tree Crown Properties Using Airborne Scanning Laser in a Boreal Nature Reserve*. Remote Sensing of Environment. 2002. 79; 105-115.
- Næsset, E. *Effects of Different Sensors, Flying Altitudes, and Pulse Repetition Frequencies on Forest Canopy Metrics and Biophysical Stand Properties Derived from Small-Footprint Airborne Laser Data*. Remote Sensing of Environment. 2009. 113; 148-159.
- Næsset, E. *Determination of Mean Tree Height of Forest Stands using Airborne Laser Scanner Data*. ISPRS Journal of Photogrammetry and Remote Sensing. 1997. 52; 49-56.
- Næsset, E., and Gobakken, T. *Estimation of Above-And Below-Ground Biomass Across Regions of the Boreal Forest Zone Using Airborne Laser*. Remote Sensing of Environment. 2008. 112; 3079-3090.
- Næsset, E., and Bjerknes, K. *Estimating Tree Heights and Number of Stems in Young Forest Stands Using Airborne Laser Scanner Data*. Remote Sensing of Environment. 2001. 78; 328-340.
- Næsset, E., Bollandsas, O.M., and Gobakken, T. *Comparing Regression Methods in Estimation of Biophysical Properties of Forest Stands from Two Different Inventories Using Laser Scanner Data*. Remote Sensing of Environment. 2005. 94; 541-553.
- Navar, J. *Allometric Equations for Tree Species and Carbon Stocks for Forests of Northwestern Mexico*. Forest Ecology and Management. 2009. 257; 427-434.
- Rouse, J.W., Haas, R.H., Schell, J.A., and Deering, D.W., 1974: *Monitoring Vegetation Systems in the Great Plains with ERTS*. NASA Goddard Space Flight Center 3d ERTS-1 Symposium. 309-317.
- Sellers, P.J. *Canopy Reflectance, Photosynthesis and Transpiration*. International Journal of Remote Sensing. 1985. 6; 1335-1372.
- Singh, K.K., Chen, G., McCarter, J.B., and Meentemeyer, R.K. *Effects of LiDAR Point Density and Landscape Context on Estimates of Urban Forest Biomass*. ISPRS Journal of Photogrammetry and Remote Sensing. 2015. 101; 310-322.
- Stoker, J.M., Cochrane, M.A., and Roy, D.P. *Integrating Disparate Lidar Data at the National Scale to Assess the Relationships between Height above Ground, Land Cover and Ecoregions*. Photogrammetric Engineering and Remote Sensing. 2014. 80; 59-70.
- Su, Y., Guo, Q., Xue, B., Hu, T., Alvarez, O., Tao, S., and Fang J. *Spatial Distribution of Forest Aboveground Biomass in China: Estimation through Combination of Spaceborne Lidar, Optical Imagery, and Forest Inventory Data*. Remote Sensing of Environment. 2016. 173; 187-199.
- Sugarbaker, L.J., Constance, E.W., Heidemann, H.K., Jason, A.L., Lukas, V., Saghy, D.L., and Stoker, J.M. *The 3D Elevation Program initiative—A Call For Action*. No. 1399. 2014. 1-35.
- Thomas, V., Treitz, P., McCaughey, J.H., and Morrison, I. *Mapping Stand-Level Forest Biophysical Variables for a Mixed Wood Boreal Forest Using Lidar: An Examination of Scanning Density*. Canadian Journal of Forest Research. 2006. 36; 34-47.
- Tucker, C.J. *Red and Photographic Infrared Linear Combinations for Monitoring Vegetation*. Remote Sensing of Environment. 1979. 8; 127-150.

Van Leeuwen, M., and Nieuwenhuis, M. *Retrieval of Forest Structural Parameters using LiDAR Remote Sensing*. European Journal of Forest Research. 2010. 129; 749-770.

Veneziano, D., Hallmark, S., and Souleyrette, R., 2012: *Comparison of Lidar and Conventional Mapping Methods for Highway Corridor Studies*. Center for Transportation Research and Education, Iowa State University. Final Report.

Wu, Z., Middleton, B., Hetzler, R., Vogel, J., and Dye, D. *Vegetation Burn Severity Mapping Using Landsat-8 and WorldView-2*. Photogrammetric Engineering and Remote Sensing. 2015. 81; 143-154.

Yu, X., Hyypä, J., Kaartinen, H., and Maltamo, M. *Automatic Detection of Harvested Trees and Determination of Forest Growth Using Airborne Laser Scanning*. Remote Sensing of Environment. 2004. 90; 451-462.

Zhao, K., Popescu, S., and Nelson, R. *Lidar Remote Sensing of Forest Biomass: A Scale-Invariant Estimation Approach using Airborne Lasers*. Remote Sensing of Environment. 2009. 113; 182-196.

Zheng, D., Rademacher, J., Chen, J., Crow, T., Bresee, M., Le Moine, J., and Ryu, S.R. *Estimating Aboveground Biomass Using Landsat 7 ETM+ Data across a Managed Landscape in Northern Wisconsin USA*. Remote Sensing of Environment. 2004. 93; 402-411.

Community Exposure to Nighttime Heat in a Desert Urban Setting, El Paso, Texas

Maria A. Amaya¹, MacTar Mohammed², Nicholas E. Pingitore^{1,3}, Raed Aldouri⁴, and Barry Benedict⁵

¹School of Nursing, the University of Texas at El Paso, El Paso, Texas, USA

²Environmental Science & Engineering, The University of Texas at El Paso, El Paso, Texas, USA

³Department of Geological Sciences, the University of Texas at El Paso, El Paso, Texas, USA

⁴Geospatial Center, the University of Texas at El Paso, El Paso, Texas, USA

⁵Department of Mechanical Engineering, The University of Texas at El Paso, El Paso, Texas, USA

Publication Date: 10 February 2016

DOI: <https://doi.org/10.23953/cloud.ijarsg.42>



Copyright © 2016 Maria A. Amaya, MacTar Mohammed, Nicholas E. Pingitore, Raed Aldouri, and Barry Benedict. This is an open access article distributed under the **Creative Commons Attribution License**, which permits unrestricted use, distribution, and reproduction in any medium, provided the original work is properly cited.

Abstract The combination of global warming and urbanization is expected to exacerbate the well-established urban heat island effect. Unfortunately, little is known about nighttime urban heat retention and its possible health effects on residents. Here we use infrared satellite imagery to evaluate the distribution of nighttime heat and its decadal changes in a large desert metropolis.

Keywords *Human Health, Nighttime Heat; Heat Exposure; Global Warming; Desert Cities; Thermal Infrared (IR) Satellite Imagery; Community Risk; Urban Growth; Urban Heat Island; Change Detection*

1. Background – The Urban Heat Island

The urban heat island was first described in London by Howard nearly two centuries ago [1]. The importance of this phenomenon has increased with the acceleration of urbanization, first in the industrialized world and, since the Second World War, through much of the remainder of the globe. Population growth has been a key driver of urbanization. Such growth also drives global warming, a more recent and increasing contributor to urban heat [2]. Unplanned and unregulated urban growth alters such thermal regulators as albedo, and the roughness and heat capacities of the urban surface [3].

In general, the temperature contrast between the urban heat island and the surrounding region is greater at night than during the day [4], [5]. This results from such factors as heat capacity of the materials in the two compartments and decreases in air convection during the night. However, this relationship might not be as strong in sparsely vegetated arid or desert regions, or at higher elevations where heat convection is more effective.

2. Study Area – El Paso, Texas, USA

Post-World War II urbanization in El Paso, Texas, USA and in its contiguous (separated only by the

Rio Grande) sister city of Ciudad Juarez, Chihuahua, Mexico has created a bi-national urban metroplex with an estimated 2 million inhabitants (Figure 1). The region lies in the Chihuahuan desert, characterized by temperatures of 35-40° C in summer, high elevation of 600-1675 m, and annual rainfall of less than 250 mm.

We employed infrared band satellite imaging to establish the variation of nighttime neighborhood surface temperatures across the city of El Paso, as well as all of El Paso County [6]. Data were retrieved for the summer months of June, July, and August, which encompass the highest temperature regime in the annual cycle.

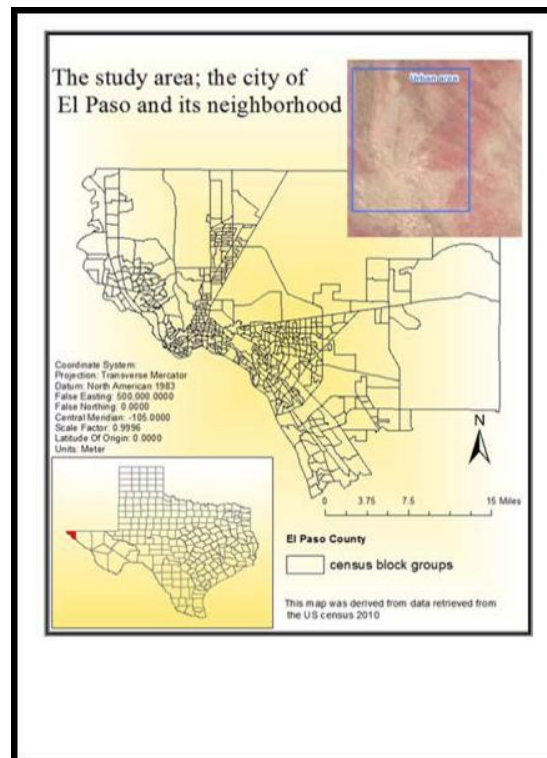


Figure 1: El Paso City and County, Far West Texas USA

3. Goal – Geography of Risk

Our continuing investigation asks a fundamental question: *do different neighborhoods pose different risks of exposure to high nighttime temperatures?* Posed more formally, we seek to define the geospatial distribution of morbidity risk consequent to elevated nighttime temperatures [7], [8]. The health risks associated with elevated temperature are well established, and can include heat stress, irritability, exacerbation of pre-existing medical conditions, and sleep deprivation, with possible resultant violence [9-11]. Exposure to heat at night is especially important because residents typically are in the home during these hours. Furthermore, some 90% of El Paso residents depend on evaporative or “swamp” coolers rather than the more effective conventional “refrigerated” air conditioning. Although evaporative coolers are much less expensive both to purchase and to operate, they raise the humidity of only partly cooled air and thus are less effective in cooling residents. Furthermore, their cooling ability falls sharply during El Paso’s late summer high-humidity “monsoon” period.

4. Procedures – Remote Imagery and Processing

Source materials for our study included: Advanced Spaceborne Thermal Emission and Reflection Radiometer), ASTER Global Digital Elevation Model V002, Landsat 7 Enhanced Thematic Mapper Plus, and Landsat 5 Thematic Mapper. From these we extracted and calculated Land Surface Temperature (LST); Land Surface Albedo (LSA), several Land Use Land Cover (LULC) classes, and the Normalized Difference Vegetation Index (NDVI). Processing packages included ArcMap version 10.1 and Environment for Visualizing Images (ENVI) version 5.0. Geographically Weighted Regression version 4.0. explored spatial relationships between LST and LSA, NDVI, elevation, and population density. We delineated the geographic distribution of social vulnerability relative to the LST via six social and biophysical indicators: total population, income, poverty, age over 65, LST, and NDVI.

5. Findings

The geographically weighted regression model revealed that day and nighttime land surface temperatures both were correlated with the normalized difference vegetation index, population density, and albedo. The index and albedo associations were stronger with daytime temperature and the population density association was stronger with nighttime temperature. Vegetation (negative) and population density (positive) were the strongest associations with temperature, followed by albedo and elevation.

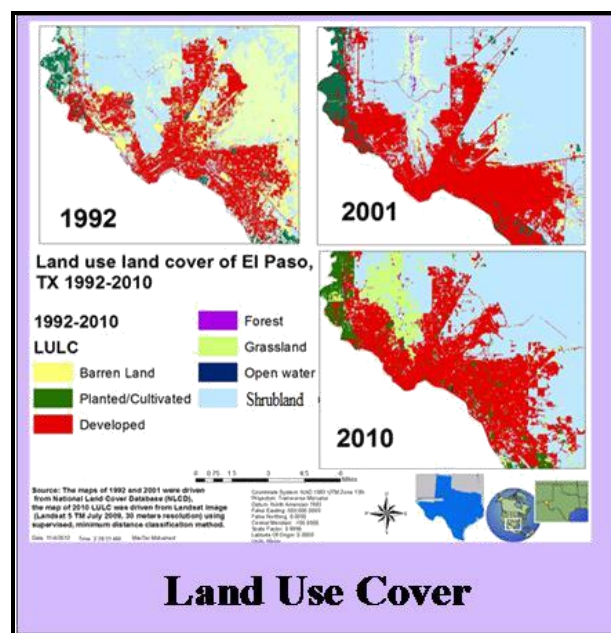


Figure 2: Decadal Sequence of Land Use in El Paso County

Large difference in land use over the past two decades reflects increasing urbanization (Figure 2). Development, indicated in red on the maps, is the key driver of the urban heat island effect.

Archived satellite imagery (Figure 3) indicated increases in both day and nighttime temperatures over the last two decades. With no expected change in urban growth and global warming, local residents will be at increasing risk in the future, as will residents in other urban centers in the desert southwest of the US.

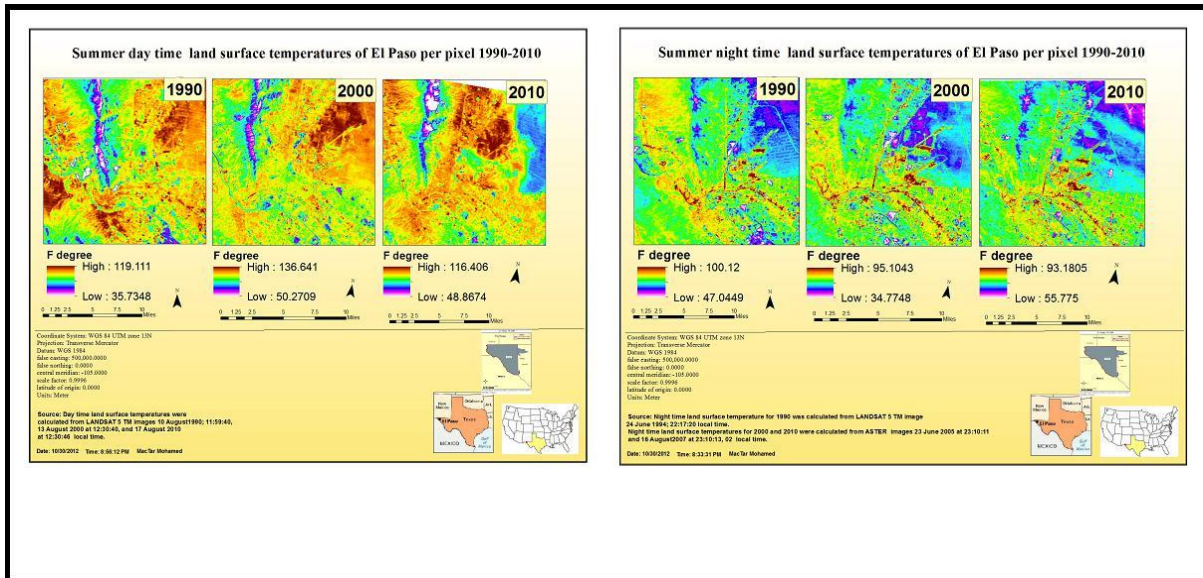


Figure 3: Decadal Sequence of Summer Day (Left) and Night (Right) Land Surface Temperatures in El Paso County

6. Public and Societal Health Implications

Socio-economic status, groups of people with the same income, power, and prestige, can be a powerful contributor to social vulnerability. Those of a lower socio-economic status tend to live in the poorer areas in low quality and often older housing with few resources available for heat mitigation [12]-[14]. Several studies have demonstrated higher heat-related mortality among people living in poor neighborhoods within cities [15], [16]. Here we combined the geographies of physical environmental and socio-economic data to create a nighttime and daytime vulnerability heat index (NVHI & DVHI) based on population density, income, % population below poverty level, population over 65 years, LST, and NDVI (Figure 4). It should be noted that the median El Paso income (2010) was \$37,152, with 25% of residents living below the national poverty line. Poverty in El Paso by and large follows population density.

In general, the proximal or urban core central, northeast, and eastside of the study area tend toward high vulnerability while the westside tends toward low vulnerability. This agrees with population density and economic status. This pattern is best seen in the “hot spot” maps (Figure 5). Also, there was a trend toward a shift in vulnerability from surrounding rural areas to the urban area between 2000 and 2010.

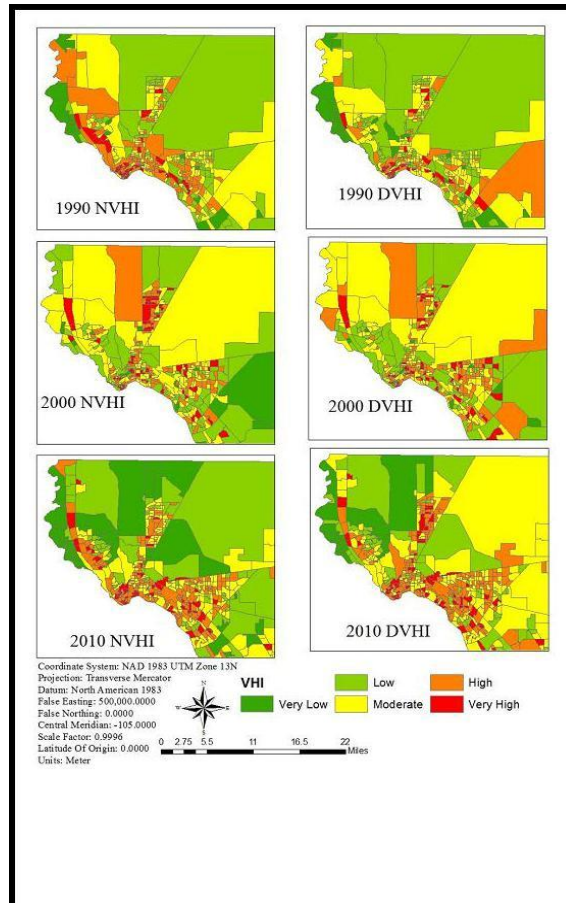


Figure 4: Decadal Sequence of Derived “Socio-Thermal” Nighttime and Daytime Vulnerability Heat Index

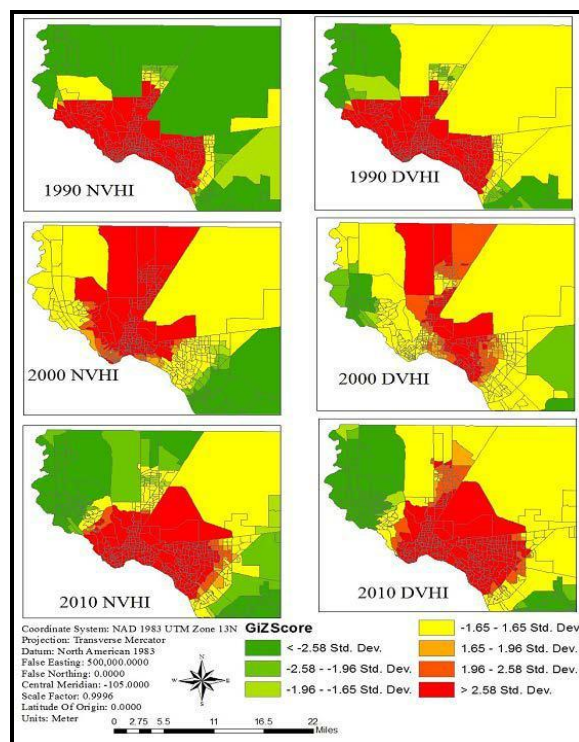


Figure 5: Decadal Sequence of El Paso County Heat Vulnerability “Hot Spots”

7. Mitigation Strategies

By 2060, the total population of El Paso County is projected to reach 1.5 million residents [17]. The overall pattern of our maps and global warming trends suggest that exposure and vulnerability to heat will continue to increase in this urban region in the near future. On a more positive note, the maps delineate the neighborhoods most likely to require heat prevention and intervention strategies because of both the ambient heat load and the special vulnerabilities of their residents (NVHI).

An obvious and relatively simple economic and political approach to slowing, stopping, or even reversing the trend toward higher nighttime temperatures in vulnerable neighborhoods is to increase greenspace in these critical areas. Such a program, carried out with the cooperation of the community could include streetside planting of native (xerophytic) trees and bushes; addition of park space, particularly numerous dispersed “pocket parks;” tax or other incentives for businesses to add native trees and bushes to their parking lots; similar programs for unoccupied private real estate lots; and so forth.

More intense immediate strategies could include educational and in-house servicing programs to ensure proper functioning of pre-existing evaporative cooling systems, assistance in purchasing and installing additional evaporative coolers, circulating fans, and window tinting. Longer-term strategies would include integration of heat vulnerability into local public-housing programs and medical assistance programs.

References

- [1] L. Howard. *The Climate of London, Deduced from Meteorological Observations, Made at Different Places in the Neighbourhood of the Metropolis*. London, UK, W. Phillips. 2; 1818-20.
- [2] Luber, G. and McGeehin, M. *Climate Change and Extreme Heat Events*. Amer. J. Preventive Med. Nov. 2008. 35; 429-435.
- [3] Baker, L.A. et al. *Urbanization and Warming of Phoenix (Arizona, USA): Impacts, Feedbacks and Mitigation*. Urban Ecosystems. Sept. 2002. 6; 183-203.
- [4] Chow, W.T.L. and Svoma, B.M. *Analyses of Nocturnal Temperature Cooling-Rate Response to Historical Local-Scale Urban Land-Use/Land Cover Change*. J. Appl. Meteor. Climat. Sept. 2011. 50; 1872-1883.
- [5] Giridharan, R., Lau, S.S.Y. and Ganesan, S. *Nocturnal Heat Island Effect in Urban Residential Developments of Hong Kong*. Energy Buildings. Sept. 2005. 37; 964-971.
- [6] Fung, W.Y. et al. *Derivation of Nighttime Urban Air Temperatures Using a Satellite Thermal Image*. J. Appl. Meteor. Climat. Apr. 2009. 48; 863-872.
- [7] Murphy, R.C. *Heat Stress Vulnerability as Predicted by Spatial Analysis of Remotely Sensed Imagery and Socioeconomic Data for Philadelphia, PA*. M.S. Thesis, Dept. Geog., U. Delaware, Newark, 2009.
- [8] Kestens, Y. et al. *Modelling the Variation of Land Surface Temperature as Determinant of Risk of Heat-Related Health Events*. Int. J. Health Geog. Jan. 2011. 10; 7-15.
- [9] Basu, R. and Malig, B. *High Ambient Temperature and Mortality in California: Exploring the Roles of Age, Disease, and Mortality Displacement*. Environ. Res. Nov. 2011. 111; 1286-1292.

- [10]Conti, S. et al. *General and Specific Mortality among the Elderly during the 2003 Heat Wave in Genoa (Italy)*. Environ. Res. Feb 2007. 103; 267-274.
- [11]Harlan, S.L. et al. *Neighborhood Microclimates and Vulnerability to Heat Stress*. Soc. Sci. Med. Nov 2006. 63; 2847-2863.
- [12]Cutter, S.L., Boruff, B.J. and Shirley, W. *Social Vulnerability to Environmental Hazards*. Soc. Sci. Quart. Jun 2003. 84; 242-261.
- [13]Emrich, C.T. *Social Vulnerability in United States Metropolitan Areas: Improvements in Hazard Vulnerability Assessment*. Ph.D. dissertation, Dept. Geog., Univ. South Carolina, Columbia, 2005.
- [14]Huang, G., Zhou, W. and Cadenasso, M.L. *Is Everyone Hot in the City? Spatial Pattern of Land Surface Temperatures, Land Cover and Neighborhood Socioeconomic Characteristics in Baltimore, MD*. J. Environ. Manag. Jul. 2011. 92; 1753-1759.
- [15]Johnson, D.P. and Wilson, J.S. *The Socio-Spatial Dynamics of Extreme Urban Heat Events: The Case of Heat-Related Deaths in Philadelphia*. Appl. Geog. Jul 2009. 29; 419-434.
- [16]Rosenthal, J.K. *Evaluating the Impact of the Urban Heat Island on Public Health: Spatial and Social Determinants of Heat-Related Mortality in New York City*. Ph.D. Dissertation, Dept. Urban Planning, Columbia Univ., NY, 2010.
- [17]Melanie, C. et al. *Water for Texas 2012 State Water Plan*. Texas Water Development Board, Austin, TX, 2012. Available: <http://www.twdb.texas.gov/waterplanning/swp/2012/index.asp>

Spatial Variability of Urban Heat Islands in Cairo City, Egypt using Time Series of Landsat Satellite Images

Islam Abou El-Magd¹, Ahmed Ismail² and Naglaa Zanaty¹

¹Environmental Studies Department, National Authority for Remote Sensing & Space Sciences Cairo, Egypt

²Environmental Science Department, Faculty of Science, Port Said University, Port Said, Egypt

Publication Date: 14 March 2016

DOI: <https://doi.org/10.23953/cloud.ijarsg.48>



Copyright © 2016 Islam Abou El-Magd, Ahmed Ismail and Naglaa Zanaty. This is an open access article distributed under the **Creative Commons Attribution License**, which permits unrestricted use, distribution, and reproduction in any medium, provided the original work is properly cited.

Abstract Global warming has obtained more attention because of increasing global mean surface temperature since the late 19th century. Urbanization is considered an important contributor to global warming in big cities. Cairo is one of the heavily populated cities in the world, which has rapid urbanization that resulted in remarkable temperature variation compared to the rural surrounding areas. This phenomenon is known as "Urban Heat Islands" (UHIs) that influence both local and regional climate, environment, and socio-economic development. In this research time series of satellite images were used to map the spatial variability of Land Surface Temperature (LST) and Heat Islands in Cairo city. Historical and contemporary record of Landsat images nearly 16 dates from 1990 to 2014 were used to retrieve LST and land cover categories. Results showed that LST was highly influenced by Land use and land cover changes; heat island effect was dominant in urbanized areas, bare/desert land and industrial zones (e.g. Shobra El-khema). The industrial zones, in particular, were possibly high due to the aluminum roof material plus the thermal energy from production activities and high emissions of air pollutants. The pattern of spatial distribution of heat islands has significantly changed from bare/desert land and built up areas (as warmer) to cultivated land and water bodies (as colder). To analyze the relationship between Heat Islands and land-cover changes a quantitative correlation between LST and Normalized Difference Vegetation Index (NDVI), Modified Normalized Difference Water Index (MNDWI) and Normalized Difference Build-up Index (NDBI) was employed. It was found that the correlation between LST and NDVI and MNDWI was negative with r^2 of 0.8 and 0.57 respectively; however, the correlation with NDBI was strongly positive with r^2 of 0.81. It is anticipated that the outcomes of this research will contribute to GEOSS for global integration and correlation.

Keywords *Remote Sensing; Land Surface Temperature; Mono Window Algorithm; Cairo*

1. Introduction

Global warming phenomenon has obtained more attention due to the recognized increase of the global mean surface temperature since the late 19th century. Urbanization is considered an important contributor to global warming in cities. Generally, the rapid population growth and urban expansion, to

meet such population, with dense urban infrastructure have significantly affected the quality of life of urban inhabitants and negatively changed the urban environment and climate [1, 2]. This has introduced the phenomenon of Urban Heat Islands (UHIs) that was first documented by Howard [3]. Since that time it has been studied in many cities around the world. Simply, this phenomenon is described as the alteration of temperatures in urban areas compared to their rural surroundings [4]. Throughout the last decade, heat islands have been observed and examined in many cities around the globe such as Łódź, Poland [5], Athens, Greece [6], Beijing, China [7], Hong Kong, China [8], Shanghai, China [9], Glasgow, UK [10], Leipzig, Germany [11], Nagoya city, Japan [12], in some Asian mega cities including Tokyo, Beijing, Seoul, Shanghai, Pyongyang, Bangkok, Manila and Ho Chi Minh City [13], the largest cities of Greece (Athens, Thessaloniki, Volos, Patra and Heraklion) [2], in addition to a total of 263 European cities were studied by [4].

Generally, UHIs in cities depend mainly on the size, population and industrial development of a city, topography, physical layout, regional climate and meteorological conditions [14]. Therefore, many factors are influencing the formation of the urban heat islands that includes a) construction materials of high heat capacity and low solar reflectivity (e.g. asphalt and concrete), b) reduced turbulent heat transfer and long-wave radiative heat loss due to street canyons geometry, c) reduced latent heat loss by evaporation due to the replacement of the natural green surfaces with dry surfaces and, d) increased anthropogenic heat emissions into the urban atmosphere [2].

Traditionally, urban heat islands could be recorded by measuring air temperature through the use of automobile transects and weather station networks. However, recently with the advancement of the remote sensing sensors, remote sensing used to measure the surface temperature [15, 16, 17, 18, 19, 20, 21]. Surface temperature is the cumulative effects of surface radiative and thermodynamic properties including surface moisture, surface emissivity, surface albedo, their radiative input at the surface, and the effects of the near surface atmosphere, in addition to the turbulent transfer from the surface [22]. It has strong relation with the changes of the land cover patterns especially changes associated with the urban expansion [23]. It has found that land surface temperature has direct link with the biophysical, such as built-up area and height [24], urban and street geometry [25], land use and land cover [17], vegetation [21], as well as population density and distribution [26, 27, 28] and the intensity of human activities [29].

The purpose of this study is to analyze the spatial variability of urban heat islands in Cairo as one of the highest populated cities in the world using time series of Landsat data in the last 24 years. It will also examine the changes of the pattern of land use and land cover to investigate the impact of such changes on the intensity and spatial pattern of the UHIs. This will enable to examine and understand the relationship between urban heat islands and the key bio-physical drivers in the city.

Area of Study

Cairo is the capital of the Arab Republic of Egypt and is one of the largest cities in Africa and the Middle East [30]. It is considered an important political and cultural focal point in the region. Geographically, it is located on the Nile River at the southernmost tip of the Nile delta nearly 165 km south of the Mediterranean Sea and 120 km to the west of the Gulf of Suez and Suez Canal [31, 32]. Figure 1 shows the location map of the study area and the administrative boundary of Cairo city in alignment with the surrounding governorates. Where the selected study area extends from 29°56'N, 31°10'E to 30°12'N, 31°29'E; including Cairo city, parts of Al-Giza and Al-Qalyubia Governorates, extends from Al-Obour city and Qalyob district at north to Al-Giza district and New Cairo city at south. The Nile River is located in the western part of the study area.

Cairo has a hot dry climate with limited rainfall and often high humidity due to the effects of the Nile River and its valley. The mean air temperature in Cairo ranges from 9°C to 24.8°C in the winter and

from 20.1°C to 34.7°C in the summer and may surpass more than 40°C in some hot days (analysis of the WMO – World Meteorological Organization- data from 1971-2000).

Cairo is a densely populated city due to the rapid increase in urbanization and population in the last few decades [33]. Its population count increased from 5,466,742 people in 1986 to 6,000,716 people in 1996 and 6,758,581 people in 2006 according to CAPMAS (Central Agency for Public Mobilization and Statistics) census data. In 2006 CAPMAS has estimated the projected population count of Cairo would be about 9,102,232 people in 2014. This in addition to about 10 million inhabitants just on the margin of the city and they have a daily interaction with the city.

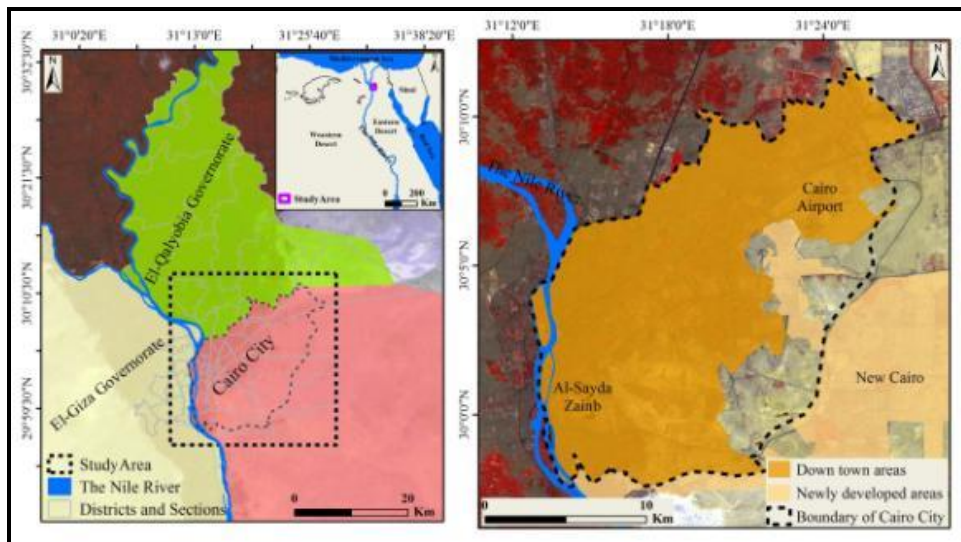


Figure 1: Area of Study – Cairo City

2. Materials and Methods

2.1. Satellite Data

In this research Landsat satellite data (i.e. Landsat TM/ ETM+ and Landsat8) was used in the last 24 years (from 1990 to 2014). The data is downloaded from the US Geological Survey (USGS) website (<http://glovis.usgs.gov/>) (Path 176 and Row 39). 16 dates were mainly downloaded to cover summer time (12 dates – July-August) and winter time (4 dates – December-January). Table 1 lists the sensor type and corresponding captured dates.

Table 1: List of the Landsat Data Used

| Sensor Type | Acquisition Date | Acquisition Hour | Season |
|---------------|------------------|------------------|--------|
| LandSat5 TM | 04 Aug. 1990 | 07:43:51 | Summer |
| | 13 Aug. 1999 | 08:01:29 | Summer |
| | 07 Jul. 2003 | 08:00:08 | Summer |
| LandSat7 ETM+ | 23 Aug. 2000 | 08:14:51 | Summer |
| | 30 Jan. 2001 | 08:14:21 | Winter |
| | 19 Dec. 2002 | 08:12:08 | Winter |
| | 17 Jul. 2004 | 08:12:49 | Summer |
| | 24 Aug. 2006 | 08:13:30 | Summer |
| | 10 Jul. 2007 | 08:14:04 | Summer |
| | 03 Dec. 2008 | 08:13:14 | Winter |
| | 04 Jan. 2009 | 08:13:29 | Winter |
| | 31 Jul. 2009 | 08:14:06 | Summer |

| | | | |
|----------|--------------|----------|--------|
| | 21 Jul. 2011 | 08:17:22 | Summer |
| | 24 Aug. 2012 | 08:19:04 | Summer |
| LandSat8 | 03 Aug. 2013 | 08:25:52 | Summer |
| | 22 Aug. 2014 | 08:23:56 | Summer |

2.2. Meteorological Data

Near surface air temperatures, relative humidity and wind speed for the study area were freely downloaded from Weather Underground website (<http://www.wunderground.com/wundermap/>). Weather Underground began as an Internet program to display worldwide weather data, developed by University of Michigan in 1991 that officially published in 1995. Data were downloaded for the same date and time of the Landsat data (Table 2).

Figure 2 shows the framework of the methodology adopted in this research. Initially the satellite data was geometrically corrected to the Universe Transverse Mercator (UTM) grid system (WGS, 1984). It has also radiometrically corrected based on the darkest pixel theory [34, 35, 36, 37]. Due to the Landsat sensor has had malfunction since 2003, therefore the data between 2003 and 2012 was having SLC-OFF problem that required GAP-FILL.

Table 2: List of the Meteorological Data used in this Research

| Date | Min. Air Temperature (C) | Max. Air Temperature (C) | Relative Humidity % | Wind Speed (Km/h) |
|------------|--------------------------|--------------------------|---------------------|-------------------|
| 04/08/1990 | 23 | 36.4 | 0.63 | 19.6 |
| 13/08/1999 | 24 | 37 | 0.64 | 16.8 |
| 23/08/2000 | 21 | 32 | 0.55 | 15.5 |
| 30/01/2001 | 7 | 23 | 0.54 | 8.4 |
| 19/12/2002 | 13 | 21 | 0.58 | 30.8 |
| 07/07/2003 | 25 | 37 | 0.60 | 21.0 |
| 17/07/2004 | 22 | 32 | 0.56 | 16.8 |
| 24/08/2006 | 25 | 38 | 0.59 | 13.8 |
| 10/07/2007 | 23 | 36 | 0.61 | 11.2 |
| 03/12/2008 | 14 | 27 | 0.61 | 16.8 |
| 04/01/2009 | 9 | 18 | 0.61 | 7.1 |
| 31/07/2009 | 24 | 35 | 0.65 | 13.8 |
| 21/07/2011 | 24 | 37 | 0.52 | 14.5 |
| 24/08/2012 | 23 | 35 | 0.56 | 17.5 |
| 03/08/2013 | 24 | 34 | 0.59 | 16.0 |
| 22/08/2014 | 24 | 36 | 0.59 | 14.0 |

2.3. Image Classification

To correlate the urban heat islands with the existing land cover, supervised classification with maximum likelihood algorithm was used to accurately classify and map the land cover categories. Four major classes were identified namely urban areas, cultivated lands, bare land/desert, and water bodies (Nile River and canals). Road networks were created using on-screen digitizing from high spatial resolution satellite image (IKONOS) to explore the correlation between these infrastructures and the urban heat islands. For further better accuracy, a post classification, technique including adjustments of the categories, was performed to improve the classification outputs.

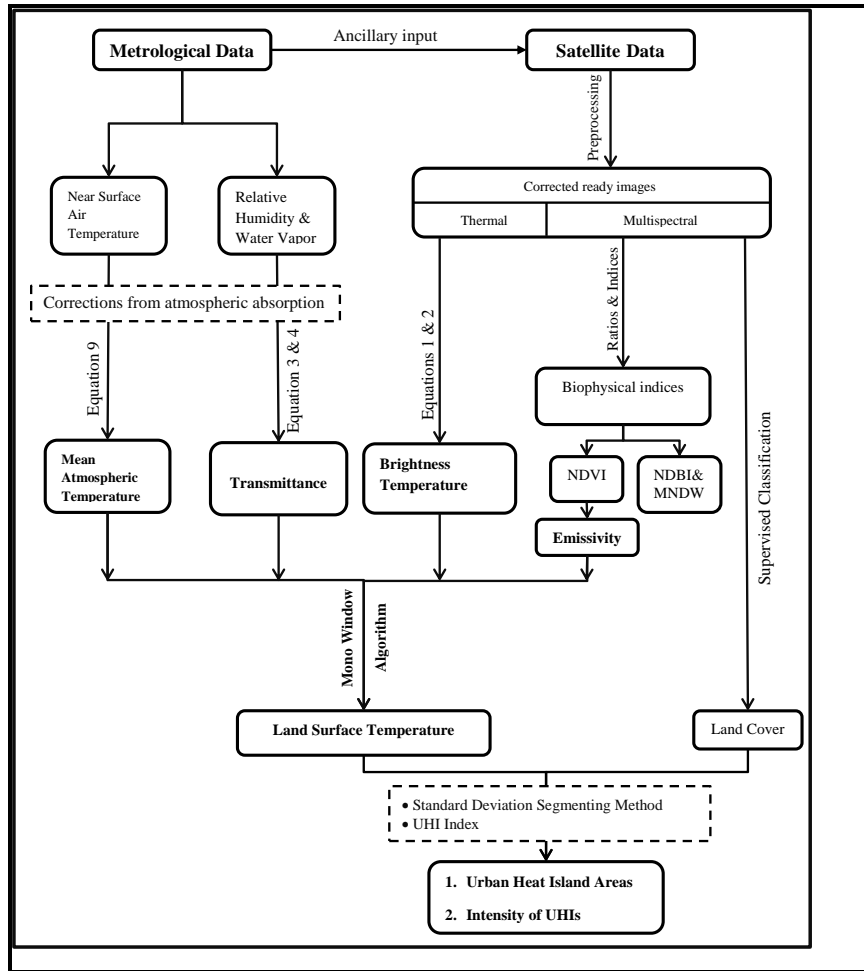


Figure 2: Framework of the Methodology Approach

2.4. Mono Window Algorithm for Retrieving Land Surface Temperature

Thermal Infrared in the electromagnetic spectrum ranges between (10.4–12.5 μm), which is covered by the thermal channels of the Landsat series, was used to estimate the at-sensor surface brightness temperature [38, 39, 36, 9, 40].

Figure 2 above shows the framework of the mono-window algorithm to estimate the surface temperature from the thermal infrared channels in combination with other variables and ancillary data. Equations (1 and 2) show the conversion of the DNs (Digital Numbers) to irradiance at sensor and then estimate the brightness temperature from the thermal channels.

$$L_{\lambda} = L_{\min} + \frac{(L_{\max} - L_{\min})}{(Q_{\text{calmax}} - Q_{\text{calmin}})} (Q_{\text{calDN}} - Q_{\text{calmin}}) \quad \text{Equation (1)}$$

Where:

L_{λ} = spectral radiance at sensor aperture [W/ (m². Sr. μm)],

$L_{\text{MIN}\lambda}$ = spectral at-sensor radiance that is scaled to Q_{calmin} or it is the minimum detected spectral radiance [W/ (m². Sr. μm)],

$L_{\text{MAX}\lambda}$ = spectral at-sensor radiance that is scaled to Q_{calmax} or it is maximum detected spectral radiance [W/ (m². Sr. μm)]

Q_{calDN} = quantized calibrated pixel value, represents the Landsat thermal band digital number (DN) values,

Q_{calmin} = the minimum quantized calibrated pixel value corresponding to $L_{MIN\lambda}$,

Q_{calmax} = the maximum quantized calibrated pixel value corresponding to $L_{MAX\lambda}$.

$$T_b = \frac{K_2}{\ln\left(\frac{K_1}{L_\lambda} + 1\right)} \quad \text{Equation (2)}$$

Where:-

T_b = effective at-sensor brightness temperature ($^{\circ}K$),

K_1 and K_2 are the calibration constants 1 and 2 (are equivalent to each sensor and obtained from the sensor specifications; for example for Landsat 5 “ $K_1=607.76$ ” & “ $K_2=1260.56$ ”),

L_λ = spectral radiance at the sensor's aperture ($W / (m^2 \cdot Sr \cdot \mu m)$),

To obtain a sensibly highly accurate Land Surface Temperature (LST) from at-sensor irradiance it is essential to implement some corrections from atmospheric absorption and re-emission; surface emissivity and surface roughness [22]. This includes:

Atmospheric Transmittance

Atmospheric transmittance is an essential input to the mono window algorithm that is estimated from equation (3). It is actually based on two air temperature profiles (High and Low air temperature) in which each temperature profile divided into two scales of water vapor content [41, 42]. The two profiles of High air temperature and Low air temperature were sub-classified into two categories according to the water vapor (i.e. 0.4-1.6 and 1.6-3.0 g/cm^2), which resulted in two transmittance value for each profile [43].

$$\tau_i = 1.031412 - 0.11536 * W_v \quad \text{Equation (3)}$$

Where τ_i = atmospheric transmittance and W_v = water vapor content.

Water vapor is the main factor controlling the estimation of atmospheric transmittance, which is estimated from equation (4) after [41, 42].

$$W_v = 0.0981 * \left\{ 10 * 0.6108 * \exp\left[\frac{17.27 * (T_o - 273.15)}{237.3 + (T_o - 273.15)}\right] * RH \right\} + 0.1697 \quad \text{Equation (4)}$$

Where W_v = water vapor content (g/cm^2);

T_o = near-surface air temperature in $^{\circ}K$ (taken from meteorological data)

RH = relative humidity (taken from meteorological data).

Land Surface Emissivity

Land surface emissivity (LSE) is an essential parameter for estimating the corrected land surface temperature. It is estimated from the Normalized Difference Vegetation Index (NDVI) as described in [44, 45, 46, 47]. Equation (5) is the basic equation to estimate the NDVI, then it is scaled to three main categories:

$$NDVI = \frac{\rho_4 - \rho_3}{\rho_4 + \rho_3} \quad \text{Equation (5)}$$

Where ρ_4 and ρ_3 are the reflectance of the near-infrared and red bands

- a) NDVI < 0.2: This category considers the pixel as non-vegetated areas (i.e. bare soil or built-up area or desert) and the emissivity is obtained from reflectivity values in the red region.
- b) NDVI > 0.5: This category considers the pixel as fully vegetated, and then a constant value for the emissivity is assumed to be 0.99.
- c) $0.2 \leq NDVI \leq 0.5$: This category considers the pixel as mixture of non-vegetated and fully vegetated areas;

Emissivity is calculated according to the following equation (6):

$$\epsilon = \epsilon_v F_v + \epsilon_u (1 - F_v) + d\epsilon \tag{Equation (6)}$$

Where ϵ_v = emissivity of vegetation,
 ϵ_u = emissivity of non-vegetated surface (in this study it was used as the emissivity of built-up surface),
 F_v = Fractional vegetation cover that computed from the equation (7):

$$F_v = \left(\frac{NDVI - NDVI_{min}}{NDVI_{max} - NDVI_{min}} \right)^2 \tag{Equation (7)}$$

Where $NDVI_{max}$ and $NDVI_{min}$ are the NDVI values in complete vegetation cover region and no vegetation cover region which considered as 0.5 and 0.2 respectively.

The term $d\epsilon$ in equation (6) includes the effect of the geometrical distribution of the natural surfaces and also the internal reflections. For plain surfaces, this term is negligible, but for heterogeneous and rough surfaces, as built-up areas, this term can reach a value of 2% [48]. A good approximation for this term can be estimated from equation (8)

$$d\epsilon = (1 - \epsilon_u) (1 - F_v) F \epsilon_v \tag{Equation (8)}$$

Where F is a shape factor whose mean value is 0.55, considering different geometrical distributions [49].

Mean Atmospheric Temperature

Mean atmospheric temperature is also a main parameter for estimating surface temperature from the Mono Window Algorithm. It was retrieved according to different global weather profile regions using Equation (9).

$$T_a = 16.0110 + 0.92621 * T_o \tag{Equation (9)}$$

Where T_a is the mean atmospheric temperature, T_o is the near-surface air temperature (°K)

Estimation of Land Surface Temperature

In order to estimate the final Land Surface Temperature in the area of study a spatial model was developed using the ArcGIS package based on the mono window algorithm. The three following equations were the main drivers of this model to estimate LST.

$$T_s = \{a(1 - C - D) + [b(1 - C - D) + C + C]T_b - DT_a\} / C \tag{Equation (10)}$$

$$C = \epsilon_i * \tau_i \tag{Equation (11)}$$

$$D = (1 - \tau_i)[1 + (1 - \epsilon_i) * \tau_i] \tag{Equation (12)}$$

$$a = -67.355351$$

$$b = 0.458606$$

Where T_s is the LST ($^{\circ}\text{K}$); (a and b) are constant values; T_b is the brightness temperature ($^{\circ}\text{K}$) which was obtained from equation (2); τ_i is the atmospheric transmittance, which was computed from equation (3); ϵ_i is the land surface emissivity which was either retrieved from equation (6) or got a constant value; and finally T_a represents the effective mean atmospheric temperature, which was applied using equation (9).

Finally in order to convert LST from degree Kelvin to degree Celsius, the following formula was used:

$$T_s (^{\circ}\text{C}) = T_s (^{\circ}\text{K}) - 273.15 \quad \text{Equation (13)}$$

Extraction of Heat Island Areas

Heat Island Areas (HIAs) reflect the spatial extent of Urban Heat anomaly. It actually estimated from land surface temperature by segmenting the urban surface temperatures from LST images. Standard deviation segmenting method was used to extract both the hot and cold islands by determining a threshold from the standard deviation of the surface mean temperature [50, 40, 43].

The principle of standard deviation segmenting method is to calculate values of threshold for each element of statistical series based on arithmetic mean and standard deviation of LST image using equation (14);

$$T = a \pm \chi * sd \quad \text{Equation (14)}$$

Where (T) represents the temperature threshold value, (a) is the mean value of the surface temperature for the area of study, χ ($\chi = -3, -2.5, -2, -1.5, -1, 0, -0.5, 0.5, 1, 1.5, 2, 2.5, 3$) is the times of standard deviation, while Sd is the standard deviation of LST image. Here thirteen values were prepared for χ and thirteen temperature threshold scales were calculated according to different values of χ ranging from -3 to 3 by the interval of 0.5 .

To precisely locate either the urban heat islands or the urban cool islands; the LST is classified into 13 slices (levels), which are then isolated using the mean LST +1 Stdv (to map the urban heat islands) and the mean LST -1 Stdv (to map the urban cool islands)

Urban Heat Islands Intensity Index (UHI Index)

The UHIs intensity index is a method to determine the spatial distribution of UHIs intensity [51]. In this research UHIs index was estimated using equation (15). The output is always scaled to 5 categories from extreme strong heat islands to weak heat islands. This will be illustrated in the result section.

$$T_r = \frac{T_i - T_a}{T_a} \quad \text{Equation (15)}$$

Where, T_r is the relative LST, T_i is LST at one site and T_a is the average LST.

Estimation of Normalized Difference Build-up Index (NDBI)

Normalized Difference Build-up Index (NDBI) is one of the widely used indices to precisely isolate the built-up areas [52]. The development of the index was based on the unique spectral response of built-up lands that have higher reflectance in MIR wavelength range than in NIR wavelength range [53]. In this research the NDBI was estimated using equation (16) [8].

$$NDBI = \frac{MIR - NIR}{MIR + NIR} \quad \text{Equation (16)}$$

Where, *MIR* and *NIR* are the middle infrared and the near-infrared bands of Landsat data, respectively.

Estimation of Modified Normalized Difference Water Index (MNDWI)

The Modified Normalized Difference Water Index was used to delineate open water features, which depends mainly on the higher reflectance in the green light wavelength and lower reflectance of *MIR* [53]. This index was estimated using equation (17).

$$MNDWI = \frac{G - MIR}{G + MIR} \quad \text{Equation (17)}$$

Where, *MIR* is a middle infrared band and *G* is Green band of Landsat data.

3. Results and Discussion

3.1. Land Cover Changes

Key element of studying the heat islands in big cities is to understand the changes of land cover. Table 3 lists the land cover changes in the last 24 years showing significant growth of the urbanized area. Such changes are analyzed to be correlated against the surface temperature and urban heat islands. The category of urban areas is merged with the road infrastructures due to they have similar behavior in heat emission.

Table 3: Land Cover Categories and their Changes in the Last 24 Years

| Class/ | Area (km ²) | | Changes | |
|-------------------|-------------------------|-------|-------------------------|-------|
| | 1990 | 2014 | Area (km ²) | % |
| Urban areas | 290.0 | 436.5 | + 146.4 | 16.6 |
| Cultivated lands | 196.6 | 172.6 | - 24.1 | -2.7 |
| Water bodies | 15.4 | 15.0 | - 0.5 | -0.1 |
| Bare land/ Desert | 381.5 | 259.6 | - 121.9 | -13.8 |
| Total | 883.6 | 883.6 | 0 | 0 |

3.2. Land Surface Temperature

The retrieved Land Surface Temperature (LST) from Landsat thermal channels for the summer of 1990 and 2014 shown in Figure (3-A and 3-B). Field observations and site visits aided in correlating the LST against the land cover categories, which indicated that the industrial estates, residential areas, development areas and bare land/ desert are places with the highest surface temperature compared with other categories of vegetation and water bodies. It was observed that northwestern and southwestern suburbs such (e.g. Qalyob, El-Qanater El-Khairia and Al-Giza districts), except the built-up areas, showed lower surface temperatures than eastern side with new built-up cities (e.g. Al-Obour, Al-Shrouk and New Cairo) and city center areas (e.g. Old Egypt, Nasser City, etc.). This could be explained that the surroundings of the new built-up areas in the eastern side are mostly desert landscape that accelerates heat advection and convection; however the other sides are fully surrounded with agriculture that cool down the surface temperature.

The large population density in old urban areas which increase the human activities and the percent of waste with heat emissions, play also a role in increasing LST in urban areas as pointed by [54]. For example (annotated in Figure 3), “Old Egypt district” that shows high LST, its population density is 22352 inhabitant/km² compared with “El-Zamalek” district that shows lower LST and population of 6450 inhabitant/km² [55].

Road networks in built up areas contribute to the thermal heat advection and showed also high surface temperature due to the impervious covering material (e.g. asphalt and concrete) [31]. In this context, in our research study area the road networks coupled with the heavy traffic of up to 4 million transportation vehicles has shown high anomaly of LST that nearly 10% higher than surroundings (Figure 4).

Fundamentally, the variation in LST in built-up areas returns to some essential factors: 1) building material (brick, concrete); 2) street canyons; 3) solar radiation and 4) sun elevation. To recognize this influence of these parameters, a cross section (A - B) in the NW-SE direction of about 40 Km length in the summer of 2000 is analyzed (Figure 5). The profile shows oscillation of LST that ranged from lower values in densely vegetated areas in the north region of Cairo to higher values in densely urbanized areas in Cairo city center as well as near the desert land in the south (above 50°C in summer). There is high anomaly in the middle of the curve, which is signposted by the letter (H) returns to the effect of the factories in area of Al-Ameria (industrial estate); while the observed low area of LST which is signposted by the letter (C) is due to the effect of green area in “Kids Park” in Nasser City district. This could explain the high presence of LST with human activities and anthropogenic emissions from industrial estates at Al-Ameria and Shoubra El-Kheima.

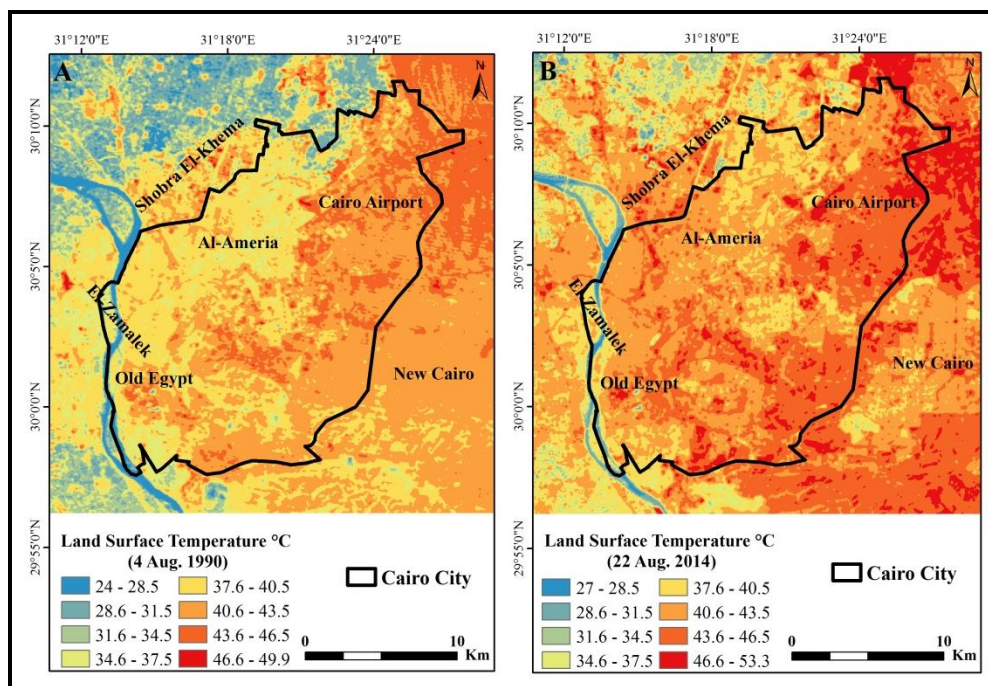


Figure 3: The Spatial Distribution of LST in °C (A summer of 1990 and B summer of 2014)

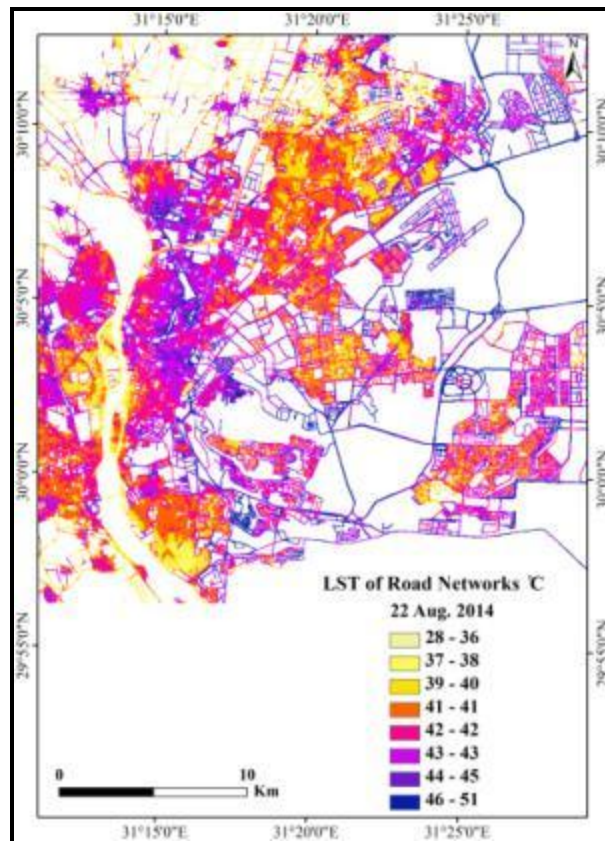


Figure 4: LST of Road Networks in summer 2014 in °C

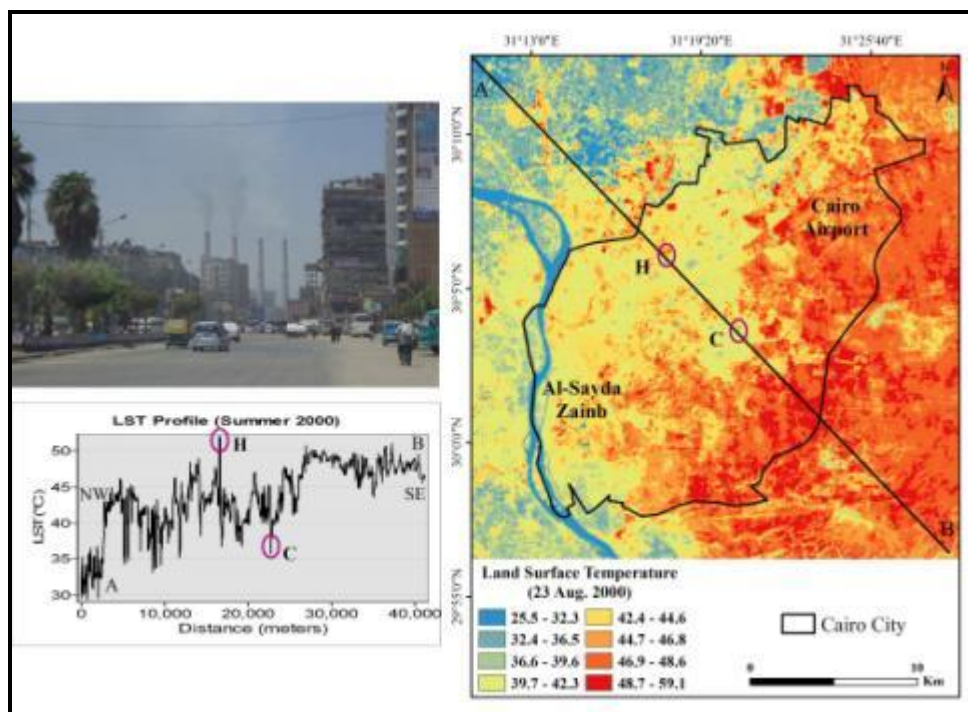


Figure 5: LST Profile for Shubra El-Kheima Industrial area in summer 2013

The trend line of the estimated LST (from 1990 to 2014) shows an increase of the summer temperature (Figure 6). In 1990 LST was ranged from minimum of 24 °C to a maximum of 49.9 °C;

however, in 2014 was ranged from minimum of 27 °C to a maximum of 53.3 °C. The slope of the LST increase in this period is projecting an increase of 2.5 °C by the end of this century, which is nearly agreeable with the global IPCC of global warming scenario of an increase of temperature from 1-2 °C per 100 years [56].

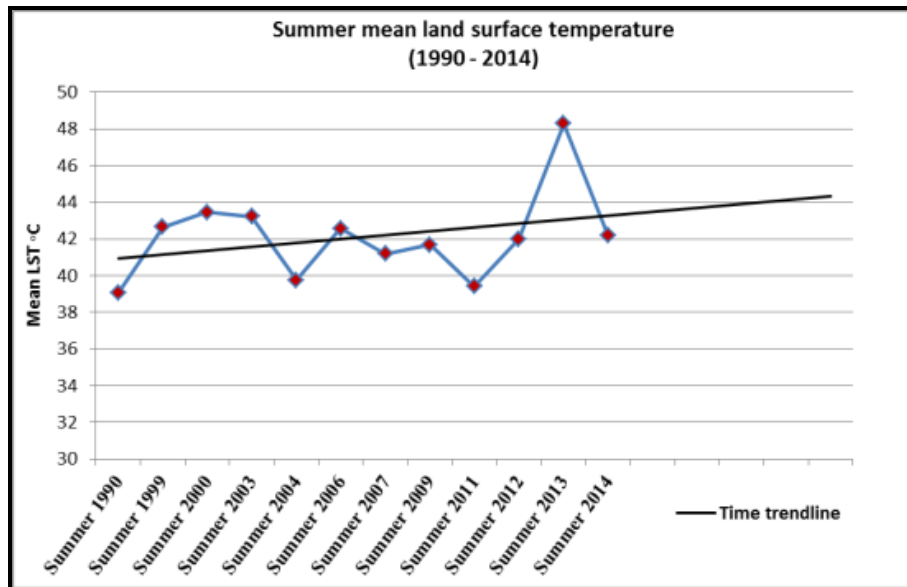


Figure 6: Slope of the LST Variations in the Last 24 Years

3.3. Segmentation of Heat Island Areas

Standard deviation segmenting approach was used to isolate the extreme heat islands in the last 24 years (Figure 7A and 7B). Then, it is correlated with land cover to show the direct link between both (Figures 7C). It is observed that most of the high surface temperature zones and heat islands in Cairo were concentrated in densely urbanized and populated areas, industrial zones, transportation networks and bare/desert land, particularly in the densely urbanized and populated city center and the eastern parts of Cairo.

The indirect solar heating and the anthropogenic heat that generated in the urban environment indirectly are the main causes of heat islands. Urban areas generate intense urban canopy heat island areas due to their physical properties including: urban structure, size of the city (population, density of built-up area), ratio of building height to distance with them, width of the streets, building materials, surface materials and sky-view factor.

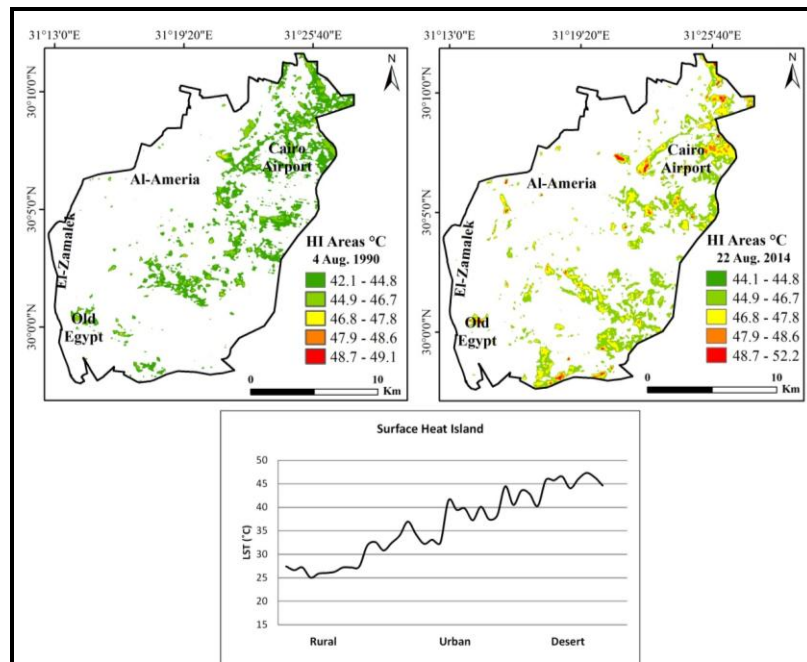


Figure 7: Comparison of the Intensity of Urban Heat Islands in 1990 and 2014 in Correlation with the Rural and Urbanized Areas

3.4. Urban Heat Island Intensity

Urban heat island Intensity is determined as the spatially averaged temperature difference between an urbanized and surrounding rural area [57, 58, 59]. The intensity of heat island differs from season to another and modulated by meteorological conditions such as wind speed and cloud cover as well as anthropogenic heat release. Some random observational points of LST values in both urban and rural areas in summer and winter seasons of 2009, for example, were extracted to show the intensity of UHIs in both seasons Figure (8 A&B). In summer the intensity was about 6.6°C while in winter it was about 1.7°C; surface UHIs in winter are much lower in magnitude and smaller in spatial extent than in summer which is agreed with [13]. As shown in Table 4 the difference between mean temperatures of urbanized and surrounding rural areas was 6.6°C, 7.9°C and 10.7°C in summer times of 1990, 2003 and 2013, respectively.

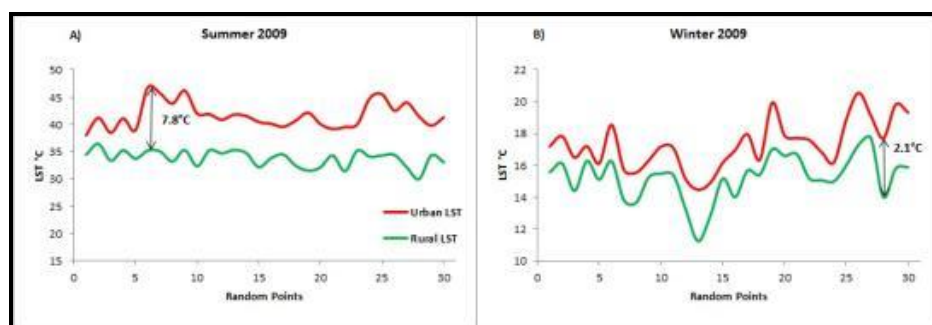


Figure 8: Variation of Heat Islands Intensity in Urbanized and Rural Areas in Summer and Winter 2009

Table 4: Estimated Surface Urban Heat Islands Intensity in (°C)

| Date | Mean Urban LST (°C) | Mean Rural LST (°C) | UHI Intensity (°C) |
|-------------|---------------------|---------------------|--------------------|
| 4 Aug. 1990 | 39.9 | 33.3 | 6.6 |
| 7 Jul. 2003 | 44.3 | 36.4 | 7.9 |
| 3 Aug. 2013 | 48.7 | 38 | 10.7 |

The spatial variability of UHIs over Cairo City was estimated using the UHI Index that showed that there are five dominant intensity levels (Figure 9):

- Level 1: less than 0, this level is considered as a very weak HI (green islands). This level occupies the western side of the study area with dominance of vegetation cover (Close to the Nile Delta agriculture land) and water mass (River Nile).
- Level 2: between 0 and 0.1, this level is considered as weak HI.
- Level 3: between 0.1 and 0.2, this level is considered as medium heat island. This level often occupies the eastern parts of Cairo.
- Level 4: between 0.2 and 0.4, this level is considered as a strong HI. This level found in the eastern side and in areas near “Imbaba” airport, and some parts near industrial zones.
- Level 5: more than 0.4, it is considered as extremely strong HI. This level found in some small scattered bare land areas and industrial estates.

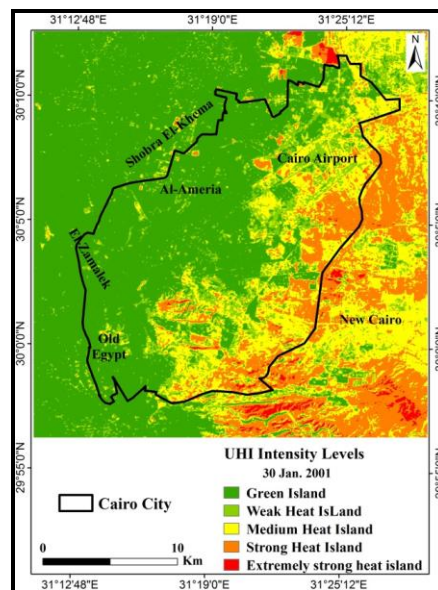
**Figure 9:** Example of the Spatial Variability of UHI over Cairo districts in winter 2002

Table 5 lists the area coverage and statistical analysis of the seasonal UHIs in the last 24 years. The maximum LST in 1990 was in the range of 48- 49.14°C that occupied a small area of nearly 0.03 km². However, in 2014 the maximum LST was in the range from 50- 52.2°C that occupied an area of 0.08 km². This indicates for an increase in the temperature by about 2°C and in the area by about 0.05 km². This table reflects that the maximum area of UHIs was in the summer (August) of 2012 was 65 km² with a maximum temperature of 55.7°C. Alternatively; the maximum temperature in the summer (August) was 58.3°C in the summer of 2013 that occupied an area of 36.1 km².

The magnitude and extent of UHIs were found highly positively correlated to population size of the cities, indicating the significant impacts of urban growth on the UHI problem. It was also found that the

spatial variability of UHIs in Cairo city was a function of urban surface properties, which in turn was characterized by land covers, most importantly, by vegetation cover and built-up density. The relationship between surface properties and UHIs, confirmed the importance of vegetation and in some degree, urban density in the partition of sensible and latent heat fluxes in humid environment of Cairo city.

Table 5: UHIs Intensities and Area Coverage in Cairo City in the Last 24 Years

| Season | Date | Cairo City | | | Statistics | |
|--------|--------------|------------------------|------|------|------------|--------------------|
| | | HIA (Km ²) | Min. | Max. | Mean | Standard deviation |
| Summer | 04 Aug. 1990 | 47.3 | 42.1 | 49.1 | 44.2 | 0.66 |
| | 13 Aug. 1999 | 47.9 | 45.6 | 53.0 | 48.2 | 0.64 |
| | 23 Aug. 2000 | 47.0 | 45.7 | 54.6 | 49.0 | 0.72 |
| | 07 Jul. 2003 | 58.1 | 44.2 | 52.8 | 47.9 | 0.84 |
| | 17 Jul. 2004 | 45.0 | 39.0 | 53.3 | 44.4 | 1.03 |
| | 24 Aug. 2006 | 53.5 | 43.5 | 56.3 | 47.3 | 0.93 |
| | 10 Jul. 2007 | 59.0 | 41.1 | 51.7 | 45.3 | 0.89 |
| | 31 Jul. 2009 | 54.2 | 41.3 | 54.7 | 46.6 | 0.89 |
| | 21 Jul. 2011 | 48.3 | 39.7 | 53.9 | 44.3 | 1.1 |
| | 24 Aug. 2012 | 65.0 | 41.7 | 55.7 | 46.6 | 0.98 |
| | 03 Aug. 2013 | 36.1 | 50.8 | 58.3 | 53.4 | 0.66 |
| | 22 Aug. 2014 | 55.6 | 44.0 | 52.2 | 46.6 | 0.73 |
| Winter | 30 Jan. 2001 | 51.2 | 22.5 | 35.9 | 27.5 | 1.2 |
| | 19 Dec. 2002 | 63.8 | 17.8 | 25.5 | 21.0 | 0.7 |
| | 03 Dec. 2008 | 66.4 | 23.9 | 34.0 | 27.9 | 0.96 |
| | 04 Jan. 2009 | 39.9 | 16.4 | 27.2 | 20.3 | 0.85 |

3.5. Correlation between Land Surface Temperature and Bio-Physical Indices

A correlation analysis between UHIs and set of bio-physical indices including: Normalized Difference Vegetation Index (NDVI), which indicates green areas; Normalized Difference Build-up Index (NDBI), which represents the build-up land; and Modified Normalized Difference Water Index (MNDWI) which indicates water surfaces and land surface temperature. This correlation was performed in order to compare the different effects of vegetation, build-up areas and water bodies on surface temperature variation and heat islands formation. About 100 points were selected randomly from the LST images and correlated with its corresponding values of NDVI, NDBI, MNDWI (Figure 10 & Table 6). The correlation coefficient “r” ranges between -0.53 and -0.9 for (NDVI), from -0.58 to -0.93 for (MNDWI), and from 0.55 to 0.93 for (NDBI). These correlation coefficients “r” were evaluated by Ramadan [60] as follow: 0.0 (no); 0.3-0.5 (low); 0.5-0.7 (medium); 0.7-0.9 (high); 0.9-1 (very high). So, it is clear that LST had medium to very high negative correlation with both of NDVI and MNDWI. This indicated that the impacts of green land or water bodies on surface temperature is negative and lead to decrease the probability of occurrence of heat islands. This is good indication that green land can reduce the heat islands effect and could be used as a method of mitigation or reduction of heat islands. Conversely, there was a medium to highly significant positive correlation between LST and NDBI which indicates that the built-up land and impervious surfaces can maximize the heat islands effect and increase the probability of urban heat islands formation as proved by Liu and Zhang [8]. It was also found that horizontal expansion of urban has less impact on the presence of UHIs on the fringes of the city and the newly developed suburbs rather than the vertical expansion with high population density and high traffic in the city Centre.

Table 6: Correlation Coefficient (r) between LST and Bio-Physical Indices

| Date | Correlation Coefficient (r) between | | |
|--------------|-------------------------------------|--------------|---------------|
| | LST and NDVI | LST and NDBI | LST and MNDWI |
| 04 Aug. 1990 | -0.90 | 0.93 | -0.91 |
| 13 Aug. 1999 | -0.83 | 0.90 | -0.92 |
| 23 Aug. 2000 | -0.86 | 0.87 | -0.86 |
| 30 Jan. 2001 | -0.71 | 0.72 | -0.86 |
| 19 Dec. 2002 | -0.79 | 0.75 | -0.83 |
| 07 Jul. 2003 | -0.85 | 0.86 | -0.81 |
| 17 Jul. 2004 | -0.75 | 0.82 | -0.82 |
| 24 Aug. 2006 | -0.64 | 0.85 | -0.83 |
| 10 Jul. 2007 | -0.76 | 0.79 | -0.73 |
| 03 Dec. 2008 | -0.76 | 0.67 | -0.83 |
| 04 Jan. 2009 | -0.56 | 0.55 | -0.65 |
| 31 Jul. 2009 | -0.53 | 0.81 | -0.93 |
| 21 Jul. 2011 | -0.64 | 0.77 | -0.73 |
| 24 Aug. 2012 | -0.67 | 0.76 | -0.85 |
| 03 Aug. 2013 | -0.87 | 0.91 | -0.73 |
| 22 Aug. 2014 | -0.82 | 0.85 | -0.86 |

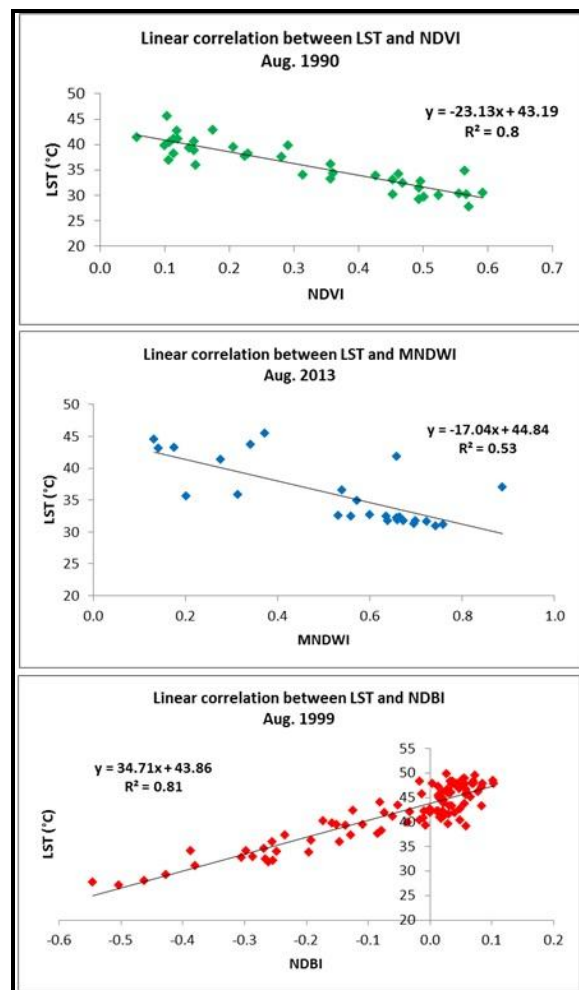


Figure 10: Correlation between UHIs and Bio-Physical Indices

4. Conclusion

This study has demonstrated the use of thermal remote sensing from time series of Landsat satellite to well-understand and map the intensity and variability of UHIs in Cairo and the main drivers in the last 24 years. Most of the previous studies on urban heat islands in Cairo and the surrounding areas have been either limited to few *in-situ* observations, or limited to small geographical coverage or limited to narrow time dimension. This study attempted to fill in the gaps and overcome these shortcomings. It is attempted to use readily available freely accessed high temporal resolution of Landsat images to monitor, assess and map urban climates in a mega city “Cairo” and create wide area coverage with wide time dimension of 24 years.

UHIs patterns and its seasonal variation in both intensity and spatial extent over Cairo demonstrated that the driving forces of land cover dynamics and socioeconomic showed high correlation with an enormous increase of LST with dense urbanization, higher population density and industrial activities. It was found that the extreme UHIs inner the city was in the industrial estates of Al-Ameria due to the building materials and emission. Indeed, such understanding and findings could help urban planners and decision-makers to consider such correlation to plan for mitigation and reduction of the LST.

Spatially, there were significant LSTs gradients from the city center and urbanized areas to the surrounding rural areas. This was observed in the correlation with bio-physical indices. The recently emerging urbanizing area and the intensive industrial estates inside the city and at the urban fringe exhibited higher LSTs and remarkable variation in LSTs. Conversely, the surrounding rural areas to the west and northwest exhibited lower LSTs and relative lower variation in LSTs. Moreover, there were significant relationships between LST and fractional vegetation cover, population density, and road density.

It could be concluded that the Landsat data has provided useful free access information for studying UHIs. Understanding the global climate changes phenomena requires more comprehensive data to the city level that would enable to project the implications on human being. This has challenged us to integrate this study in the Global Earth Observation System of Systems (GEOSS) to enable for global integration, comparison and modelling. Future work is needed to improve uncertainties using in-situ data from meteorological station networks and air quality monitoring stations to provide more understanding of the process and mechanism of UHIs associated with LULC and the air quality. However, further studies in the detailed LST–urban surface relationship addressing the urban morphology and air quality in big cities such as Cairo is necessary in order to have insights into the genesis of the surface UHIs and its linkage with the air quality and urban health environment.

References

- [1] Giannaros, T.M. and Melas, D. *Study of the Urban Heat Island in a Coastal Mediterranean City: The Case Study of Thessaloniki, Greece*. Atmospheric Research. 2012. 118; 103-120.
- [2] Stathopoulou, M. and Cartalis, C. *Daytime Urban Heat Islands from Landsat ETM+ and Corine Land Cover Data: An Application to Major Cities in Greece*. Solar Energy. 2007. 81; 358-368.
- [3] Howard, L. *The Climate of London*. London Harvey and Dorton: London, UK. 1833. 2; 1818-1820.
- [4] Schwarz, N., Lautenbach, S. and Seppelt, R. *Exploring Indicators for Quantifying Surface Urban Heat Islands of European Cities with MODIS Land Surface Temperatures*. Remote Sensing of Environment. 2011. 115; 3175-3186.

- [5] Klysik, K. and Fortuniak, K. *Temporal and Spatial Characteristics of the Urban Heat Island of Łódź, Poland*. Atmospheric Environment. 1999. 33; 3885-3895.
- [6] Livada, I., Santamouris, M., Niachou, K., Papanikolaou, N. and Mihalakakou, G. *Determination of Places in the Great Determination of Places in the Great Athens Area Where the Heat Island Effect is Observed*. Theoretical and Applied Climatology. 2002. 71; 219-230.
- [7] Miao, S., Chen, F., LeMone, M.A., Tewari, M., Li, Q. and Wang, Y. *An Observational and Modeling Study of Characteristics of Urban Heat Island and Boundary Layer Structures in Beijing*. Journal of Applied Meteorology and Climatology. 2009. 48; 484-501.
- [8] Liu, L. and Zhang, Y. *Urban Heat Island Analysis Using the Landsat TM Data and ASTER Data: A Case Study in Hong Kong*. Journal of Remote Sensing. 2011. 1535-1552.
- [9] Li, J., Song, C., Cao, L., Zhu, F., Meng, X. and Wu, J. *Impacts of Landscape Structure on Surface Urban Heat Islands: A Case Study of Shanghai, China*. Remote Sensing of Environment. 2011. 115; 3249-3263.
- [10] Emmanuel, R. and Krüger, E. *Urban Heat Island and Its Impact on Climate Change Resilience in a Shrinking City: The Case of Glasgow, UK*. Building and Environment. 2012. 53; 137-149.
- [11] Schwarz, N., Schlink, U., Franck, U. and Grobmann, K. *Relationship of Land Surface and Air Temperatures and its Implications for Quantifying Urban Heat Island Indicators—An Application for the City of Leipzig (Germany)*. Ecological Indicators. 2012. 18; 693-704.
- [12] Kato, S. and Yamaguchi, Y. *Analysis of Urban Heat–Island Effect Using ASTER and ETM+ Data: Separation of Anthropogenic Heat Discharge and Natural Heat Radiation from Sensible Heat Flux*. Remote Sensing of Environment. 2005. 99; 44-54.
- [13] Hung, T., Uchihama, D., Ochi, S. and Yasuoka, Y. *Assessment with Satellite Data of the Urban Heat Island Effects in Asian Mega Cities*. International Journal of Applied Earth Observation and Geoinformation. 2006. 8; 34-48.
- [14] Oke, T.R., 1987: *Boundary Layer Climates*. Second Edition, Methuen, London, New York. 262-330.
- [15] Gallo, K.P., McNab, A.L., Karl, T.R., Brown, J.F., Hood, J.J. and Tarpley, J.D. *The Use of NOAA AVHRR Data for Assessment of the Urban Heat Island Effect*. Journal of Applied Meteorology. 1993. 32; 899-908.
- [16] Gallo, K.P. and Owen, T.W. *Assessment of Urban Heat Island: A Multi-Sensor Perspective for the Dallas-Ft. Worth, USA Region*. Geocarto International Journal. 1998. 13; 35-41.
- [17] Dousset, B. and Gourmelon, F. *Satellite Multi-Sensor Data Analysis of Urban Surface Temperatures and Land Cover*. ISPRS Journal of Photogrammetry and Remote Sensing. 2003. 58; 43-54.
- [18] Roth, M., Oke, T.R. and Emery, W.J. *Satellite– Derived Urban Heat Islands from 3 Coastal Cities and the Utilization of Such Data in Urban Climatology*. International Journal of Remote Sensing. 1989. 10 (11) 1699-1720.

- [19] Streutker, D.R. *A Remote Sensing Study of the Urban Heat Island of Houston, Texas*. International Journal of Remote Sensing. 2002. 23 (13) 2595-2608.
- [20] Streutker, D.R. *Satellite–Measured Growth of the Urban Heat Island of Houston, Texas*. Remote Sensing of Environment. 2003. 85; 282-289.
- [21] Weng, Q., Lu, D. and Schubring, J. *Estimation of Land Surface Temperature, Vegetation Abundance Relationship for Urban Heat Island Studies*. Remote Sensing of Environment. 2004. 89 (4) 467-483.
- [22] Voogt, J.A. and Oke, T.R. *Thermal Remote Sensing of Urban Climates*. Remote Sensing of Environment. 2003. 86 (3) 370-384.
- [23] Zaki, R., Zaki, A. and Ahmed, S. *Land use and Land Cover Changes in Arid Region: The Case New Urbanized Zone, Northeast Cairo, Egypt*. Journal of Geographic Information System. 2011. 3; 173-194.
- [24] Bottyán, Z. and Unger, J. *A Multiple Linear Statistical Model for Estimating the Mean Maximum Urban Heat Island*. Theoretical and Applied Climatology. 2003. 75 (3-4) 233-243.
- [25] Eliasson, I. *Urban Nocturnal Temperatures, Street Geometry and Land Use*. Atmospheric Environment. 1996. 30 (3) 379-392.
- [26] Fan, H. and Sailor, D.J. *Modeling the Impacts of Anthropogenic Heating on the Urban Climate of Philadelphia: A Comparison of Implementations in Two PBL Schemes*. Atmospheric Environment. 2005. 39 (1) 73-84.
- [27] Weng, Q., Lu, D. and Liang, B. *Urban Surface Biophysical Descriptors and Land Surface Temperature Variations*. Photogrammetric Engineering and Remote Sensing. 2006. 72 (11) 1275-1286.
- [28] Xiao, R., Weng, Q., Ouyang, Z., Li, W., Schienke, E.W. and Zhang, W. *Land Surface Temperature Variation and Major Factors in Beijing, China*. Photogrammetric Engineering and Remote Sensing. 2008. 74 (4) 451-461.
- [29] Elvidge, C.D., Baugh, K.E., Kihn, E.A., Kroehl, H.W., Davis, E.R. and Davis, C.W. *Relation Between Satellites Observed Visible–Near Infrared Emissions, Population, Economic Activity and Electric Power Consumption*. International Journal of Remote Sensing. 1997. 18 (6) 1373-1379.
- [30] Molina, M.J. and Molina, L.T. *Critical Review: Megacities and Atmospheric Pollution*. Journal of Air Waste Management Association. 2004. 54; 644-680.
- [31] Marey, H.S., Gille, J.C., El-Askary, H.M., Shalaby, E.A. and El-Raey, M.E. *Study of the Formation of the “Black Cloud” and its Dynamics Over Cairo, Egypt, Using MODIS and MISR Sensors*. Journal of Geophysical Research. 2010. 115 (D21206) 1-10.
- [32] El-Metwally M., Alfaro, S.C., Abdel-Wahab, M.M., Favez, O., Mohamed, Z. and Chatenet, B. *Aerosol Properties and Associated Radiative Effects Over Cairo (Egypt)*. Atmospheric Research. 2011. 99; 263-276.

- [33] Yin, Z.Y., Stewart, D.J., Bullard, S. and MacLachlan, J.T. *Changes in Urban Built-Up Surface and Population Distribution Patterns during 1986–1999: A Case Study of Cairo, Egypt*. Computers, Environment and Urban Systems. 2005. 29; 595-616.
- [34] Chavez, P.S. *Image-Based Atmospheric Correction-Revisited and Improved*. Photogrammetric Engineering and Remote Sensing. 1996. 62; 1025-1036.
- [35] Lu, D., Mausel, P., Brondizio, E. and Moran, E. *Assessment of Atmospheric Correction Methods for Landsat TM Data Applicable To Amazon Basin LBA Research*. International Journal of Remote Sensing. 2002. 23 (13) 2651-2671.
- [36] Chander, G., Markham, B.L. and Helder, D.L. *Summary of Current Radiometric Calibration Coefficients for Landsat MSS, TM, ETM+, and EO-1 ALI Sensors*. Remote Sensing of Environment. 2009. 113 (5) 893-903.
- [37] Li, Y., Zhang, H. and Kainz, W. *Monitoring Patterns of Urban Heat Islands of the Fast-Growing Shanghai Metropolis, China: Using Time-series of Landsat TM/ETM+ Data*. International Journal of Applied Earth Observation and Geoinformation. 2012. 19; 127-138.
- [38] Barsi, J.A., Schott, J.R., Palluconi, F.D., Helder, D.L., Hook, S.J. and Markham, B.L., Chander, G. and O'Donnell, E.M. *Landsat TM and ETM+ Thermal Band Calibration*. Canadian Journal of Remote Sensing. 2003. 29 (2) 141-153.
- [39] Chander, G. and Markham, B. *Revised Landsat-5 TM Radiometric Calibration Procedures and Post Calibration Dynamic Ranges*. IEEE Transactions on Geo-science and Remote Sensing. 2003. 41 (11) 2674-2677.
- [40] Zhang, J. and Wang, Y. *Study of the Relationships between the Spatial Extent of Surface Urban Heat Islands and Urban Characteristic Factors Based on Landsat ETM+ Data*. Sensors. 2008. 8; 7453-7468.
- [41] Sun, Q., Tan, J. and Xu, Y. *An ERDAS Image Processing Method for Retrieving LST and Describing Urban Heat Evolution: A Case Study in the Pearl River Delta Region in South China*. Environmental Earth Sciences. 2010. 59; 1047-1055.
- [42] Qin, Z., Karnieli, A. and Berliner, P.A. *Mono-Algorithm for Retrieving Land Surface Temperature from Landsat TM Data and Its Application to the Israel-Egypt Border Region*. International Journal of Remote Sensing. 2001. 18; 583-594.
- [43] Zhang, J., Wang, Y. and Wang, Z. *Change Analysis of Land Surface Temperature Based on Robust Statistics in the Estuarine Area of Pearl River (China) from 1990 to 2000 by Landsat TM/ETM+ Data*. International Journal of Remote Sensing. 2007. 28 (10) 2383-2390.
- [44] Griend, A.A. and Owe, M. *On the Relationship between Thermal Emissivity and the Normalized Difference Vegetation Index for Natural Surfaces*. International Journal of Remote Sensing. 1993. 4 (6) 1119-1131.
- [45] Valor, E. and Caselles, V. *Mapping Land Surface Emissivity from NDVI: Application to European, African and South American Areas*. Remote Sensing of Environment. 1996. 57; 167-184.
- [46] Sobrino, J.A. and Raissouni, N. *Toward Remote Sensing Methods for Land Cover Dynamic Monitoring Application to Morocco*. International Journal of Remote Sensing. 2000. 21; 353-366.

- [47] Sobrino, J.A., Jiménez–Muñoz, J.C. and Paolini, L. *Land Surface Temperature Retrieval from LANDSAT TM 5*. Remote Sensing of Environment. 2004. 90 (4) 434-440.
- [48] Sobrino, J.A., 1989: Desarrollo de un modelo teórico para implementar la medida de la temperatura realizada mediante teledetección. Aplicación a un campo de naranjos, PhD dissertation, University of Valencia, Valencia, Spain, 170.
- [49] Sobrino, J.A., Caselles, V. and Becker, F. *Significance of the Remotely Sensed Thermal Infrared Measurements Obtained over a Citrus Orchard*. ISPRS Journal of Photogrammetry and Remote Sensing. 1990. 44 (6) 343-354.
- [50] Rhinane, H., Hilali, A., Bahi, H. and Berrada, A. *Contribution of Landsat TM Data for the Detection of Urban Heat Islands Areas Case of Casablanca*. Journal of Geographic Information System. 2012. 4; 20-26.
- [51] Xu, L.Y., Xie, X.D. and Li, S. *Correlation Analysis of the Urban Heat Island Effect and the Spatial and Temporal Distribution of Atmospheric Particulates Using TM Images In Beijing*. Environmental Pollution. 2013. 178; 102-114.
- [52] Lu, Y., Feng, P., Shen, C. and Sun, J., 2009: *Urban Heat Island in summer of Nanjing Based on TM Data*. In Proceedings of 2009 Joint Urban Remote Sensing Event, Shanghai, China, 20-22 May. 1-5.
- [53] Xu, H. *Extraction of Urban Built up Land Features from Landsat Imagery using a Thematic–Oriented Index Combination Technique*. Photogrammetric Engineering and Remote Sensing. 2007. 73 (12) 1381-1391.
- [54] Shangming, D. and Bo, D., 2001: Analysis of the Effects of Urban Heat Islands by Satellite Remote Sensing. Asian Conference of Remote Sensing, 5-9 November, Singapore.
- [55] Central Agency for Public Mobilization and Statistics, 2013: The Annual Statistical Book, Egypt, CAPMAS, 332.
- [56] International Panel of Climate Change (IPCC), 2007: *Summary for Policymakers*. In: Solomon, S., Qin, D.; Manning, M.; Chen, Z.; Marquis, M.; Averyt, K.B.; Tignor, M. and H.L. Miller (eds.). Climate Change 2007: The Physical Science Basis. Contribution of Working Group I to the Fourth Assessment Report of the Intergovernmental Panel on Climate Change, Cambridge University Press: Cambridge, United Kingdom and New York, USA, 327.
- [57] Magee, N., Curtis, J. and Wendler, G. *The Urban Heat Island Effect at Fairbanks, Alaska*. Theoretical and Applied Climatology. 1999. 64 (1) 39-47.
- [58] Kim, Y.H. and Baik, J.J. *Spatial and Temporal Structure of the Urban Heat Island in Seoul*. 2005. Journal of Applied Meteorology. 44, 591-605.
- [59] Memon, R.A., Leung, D.Y.C. and Chunho, L. *A Review on the Generation, Determination and Mitigation of Urban Heat Island*. Journal of Environmental Sciences. 2008. 20; 120-128.
- [60] Ramadan, A. *Heavy Metal Pollution and Biomonitoring Plants in Lake Manzala, Egypt*. Pakistan Journal of Biological Sciences. 2003. 6 (13) 1108-1117.

Assessment of the Spectral Characteristics of Different Physiological Stages of Some Olive cvs and Its Relation with Productivity

Amany F. ELwesemy¹, Nazmy A. Abdelghany², Ayman F. Abohadid², and Mohamed A. Aboelghar¹

¹Agricultural Applications Department, National Authority for Remote Sensing and Space Sciences, Cairo, Egypt

²Horticulture Department, Faculty of Agriculture, Ain Shams University, Cairo, Egypt

Publication Date: 5 March 2016

DOI: <https://doi.org/10.23953/cloud.ijarsg.45>



Copyright © 2016 Amany F. ELwesemy, Nazmy A. Abdelghany, Ayman F. Abohadid, and Mohamed A. Aboelghar. This is an open access article distributed under the **Creative Commons Attribution License**, which permits unrestricted use, distribution, and reproduction in any medium, provided the original work is properly cited.

Abstract Remote sensing satellite imagery is the tool to obtain synoptic, multi-temporal, dynamic and timely efficient information about any target on Earth. The main objective of the current study is to use remote sensing satellite data and field spectral reflectance measurements to identify the spectral pattern of the different cultivars of olives and to statistically correlate this spectral reflectance pattern with crop productivity. The study was carried out in El-Beheira governorate (Wadi El Natrun) city during the whole year of 2014. The three observed varieties were Picual, Manzanillo and Kalamata. Measurements were carried out for five growth stages: dormancy stage, flowering stage, fruit sat stage, mature stage and ripening stage. The spectral reflectance pattern for each cultivar through the different growth stages was identified. Then, seven vegetation indices (normalized difference vegetation index (NDVI), modified chlorophyll absorption ration index (MCARI), triangular vegetation index (TVI), modified chlorophyll absorption ration index-1 (MCARI-1), modified chlorophyll absorption ration index-2 (MCARI-2), modified triangular vegetation index-2 (MTVI2) and chlorophyll index (CI)) were calculated through the five growth stages for each cultivar and then were observed as estimators for crop yield modeling. Analysis of the result based on the comparison of the correlation coefficient (r^2) for all generated models, the target is to identify the optimal vegetation index and the optimal growth stage to predict yield for each variety. Generally, Manzanillo variety showed the highest reflectance followed by Picual and Kalamata. The result showed that the highest (r^2) was with the two cultivars Picual and Kalamata during mature stage, while the highest (r^2) was with cultivar Manzanillo during fruit sat stage. While the lowest (r^2) was found during dormancy stage for the three cultivars.

Keywords Olive Tree; Spectroradiometer; Spectral Characteristics

1. Introduction

Olive (*Olea europaea L.*) is one of the most important crops in Egypt. In 2014, Olive in Egypt occupies 82047.63 hectare with a total product of 563070 tons as of 2014. The top olive producers' areas in Egypt are the west coast, the province of Faiyum, Siwa Oasis, northern Sinai and Wadi El Natrun. Because of the importance of Olive cultivation for national economy, there is a high need to facilitate using remote sensing techniques in monitoring and predicting the yield of olive through remotely sensed statistical empirical models.

Remote sensing is the science to detect, measure, record and analyze energy in a selected portion of the electromagnetic spectrum. Remote sensing techniques, in particular, multispectral visible and Infra-Red (IR) reflectance and emission can provide an instantaneous, non-destructive, and quantitative assessment of crops ability to intercept radiation and photosynthesize [1].

There have been a lot of efforts worldwide to employ remote sensing techniques in crop monitoring and crop yield prediction. Most of these works showed that remote sensing technology was encouraging and promising crop yield as a key element for rural development. Statistical model process is based on Vegetation Indices (VI) such as (Normalized Difference Vegetation Index (NDVI), modified chlorophyll absorption ration index (MCARI), triangular vegetation index (TVI), modified chlorophyll absorption ration index-1 (MCARI-1), modified chlorophyll absorption ration index-2 (MCARI-2), modified triangular vegetation index-2 (MTVI2) Chlorophyll Index (CI)). These could be calculated from remote sensing satellite data as well as remotely sensed ground observation tools.

Gong et al. [2; 5] concluded that remote sensing statistical models are chiefly based on using various regressions that compute the crop yield empirically. The explicit and clear description of the mechanism or the effect of each input on crop yield is one of the significant factors of this group of models. Spectral characteristics in the form of vegetation indices could be used with this group of models. Simply, vegetation indices are algebraic combinations of remotely sensed spectral bands that can tell something useful about vegetation. These vegetation indices have proved to be very useful factors for explaining variability of the crop yield, which can be available for use in yield forecasting models. Lately, hyper spectral remote sensing techniques enlarged significantly the applications of remote sensing techniques. Govender et al. [6] Hyperspectral remote sensing imagers acquire many, very narrow, contiguous spectral bands throughout the visible, near-infrared, mid-infrared, and thermal infrared portions of the electromagnetic spectrum. Hyperspectral sensors typically collect 200 or more bands enabling the construction of an almost continuous reflectance spectrum for every pixel in the scene. Contiguous, narrow bandwidths characteristic of hyperspectral data allow for in-depth examination of earth surface features which would otherwise be 'lost' within the relatively coarse bandwidths acquired with multispectral scanners. Maselli et al. [7] extracted olive tree Normalized difference vegetation index (NDVI) values from MODIS imagery and used a modified parametric model (C-fix) and a bio-geochemical model (BIOME-BGC) to enable the prediction of daily olive tree gross primary production and olive tree net primary production (NPP). Guzmán et al. [8] used infrared machine vision system to detect olive fruit quality. Brilli et al. [9] estimated olive (*Olea europaea L.*) gross primary production (GPP) combining ground measurements and multi-sensor satellite data.

Ariana & Lu, [10] used Hyper spectral imaging to detect the defect internal option for pickling, however, the technique still cannot meet the online speed requirement because of the need to acquire and analyze a large amount of image data. Hyper spectral reflectance characteristics was used to discriminate different geographical origins of *Jatropha curcas L.* seeds to estimate chlorophyll content and to detect macronutrients content in oil seeds. Garcia-Maraver et al. [11] used hyperspectral technique to analyze the relation between the cellulose, hemi cellulose and lignin content and the thermal behavior of residual biomass from olive trees.

The main objectives of the current research are to study the spectral properties of the three cultivars of olive leaf during the whole season 2014 and determine the best spectral bands to separate the olive plantations as well as study aims to link crop productivity by spectral reflectance, research is a first step towards limiting the cultivation of olives at the State level. The objective of this study is Field spectral measurements and identifies the spectral signature of the different cultivars of olives, linking productivity of the olive crop with different spectral characteristics.

2. Materials and Methods

The study was carried out in olive farm located in Wadi El Natrun area, El-Beheira governorate between longitudes $30^{\circ}14'37.43''$ and $30^{\circ}14'58.07''$ E and latitudes $30^{\circ}19'54.69''$ and $30^{\circ}19'43.57''$ N. The Farm covers about 12.6 hectare where shown in Figure 1. The soil of the farm is Sandy clay and ratio of Calcium carbonate is 10%.

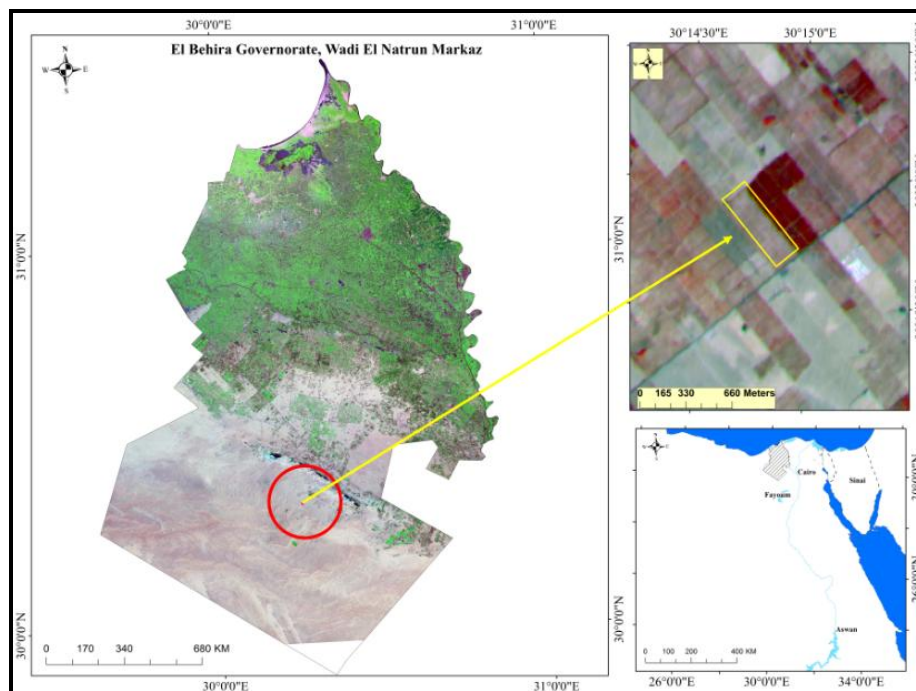


Figure 1: Field Experiment Location

Land surface temperature in the study area ranged from 5 to 15 Celsius degree in January and increased gradually to range from 28 to 38 Celsius degree in August as shown in Figure 2.

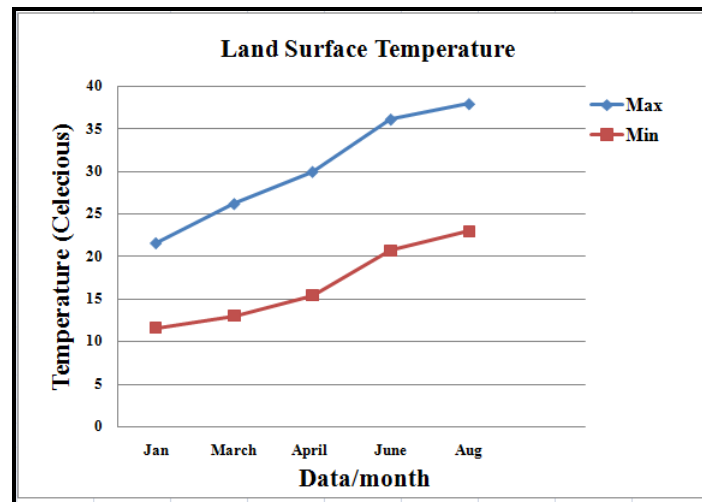


Figure 2: Mean Maximum & Minimum Land surface Temperature of Study Area

Analytical field spectroradiometer (ASD Field Spec) was used to measure the reflection of the different olive trees under investigation. Data were collected on cloudless days from 10 am clock to 2 pm in order to minimize the atmospheric effects. Measurements were carried out in a full optical spectral range (Visible – Near Infrared – Short Wave Infrared) starting from 350 nm to 2500 nanometer (nm). The sampling interval is 1.4 nm at the spectral range (350-1050 nm) while it is 2 nm at the spectral range (1000-2500 nm). These are the intervals which the device is capturing the reflectance. The device automatically performs an interpolation for the data and gives the final data output with (1 nm) interval for the all spectrum range (350-2500 nm). The spectrum characteristics of the device are shown in Table 1. The protocol used for the collection of spectral data is based on measuring radiance from a Spectralon® panel. A designed probe was attached to the instrument's fiber-optic cable to be used to ensure standardized environmental conditions for reflectance measurement. The fiber-optic cable provides the flexibility to adapt the instrument to a wide range of applications. Bare fore optic 25 degrees used for outdoor measurements resulting circular field of view with 3 cm diameter as measurements were taken at 5 cm height in nadir position (90 degrees) over the measured plants. In the current study, the measurements were performed by holding the pistol grip by hand. As recommended in the instructions of using the device, the Spectralon® was tilted directly towards the sun during optimization.

Table 1: The ASD Field Spec 3 Specifications

| | |
|----------------------------|---|
| Spectral Range | 350 - 2500 nm |
| Spectral Resolution | 3 nm at 700 nm and 8.5 nm @ 1400 nm and 6.5 nm @ 2100 nm. |
| Sampling Interval | 1.377 nm for 350 - 1000 nm and 2 nm for 1000 - 2500 nm |

The farm was divided into five spots, each spot contains twelve olive trees belong to the three observed cultivars. Each growing stage was covered by sixty (60) hyper spectral measurements with a total of three hundred (300) measurements overall the whole year of 2014. Table 2 shows the scheduled time for the field measurements while Figure 3 shows the location of measurements within the location.

Table 2: Scheduled Time for Field Measurements

| Stage | Time |
|-----------------|-----------|
| Dormancy Stage | 20/1/2014 |
| Flowering Stage | 10/3/2014 |
| Fruit Sat Stage | 28/4/2014 |
| Mature Stage | 9/6/2014 |
| Ripening Stage | 13/8/2014 |

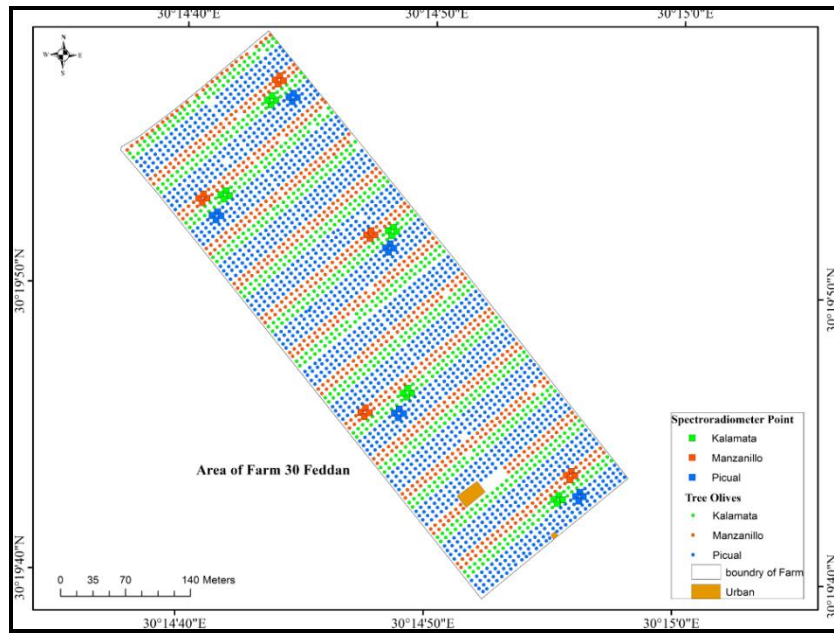


Figure 3: Location of the Measurements

As the first step of the analysis, spectral reflectance pattern for each cultivar in each growing stage was identified and compared. Seven vegetation indices were calculated to be tested as estimators for crop yield. Finally, accuracy assessment was carried out to identify the optimal vegetation index and the optimal growing stage to predict crop yield for each cultivar. Equations that were used to calculate the different indices and the references for each index are explained in Table 3.

Table 3: The Used Vegetation Indices (VIs)

| VIS | Equation | Reference |
|--------|--|-----------------------|
| NDVI | $\frac{(R800 - R670)}{(R800 + R670)}$ | Rouse et al. [12] |
| MCARI | $[(R700 - R670) - 0.2(R700 - R550)] * \left(\frac{R700}{670}\right)$ | Daughtry et al. [13] |
| TVI | $0.5[120(R750-R550)-200(R670-R550)]$ | Broge & Leblanc [14] |
| MCARI1 | $1.2[2.5(R800-R670)-1.3(R800-R550)]$ | Haboudane et al. [15] |
| MCARI2 | $\frac{1.5[2.5(R800 - R670) - 1.3(R800 - R550)]}{\sqrt{(2R800 + 1)^2 - (6R800 - 5\sqrt{R670})} - 0.5}$ | Haboudane et al. [15] |

| | | |
|-------------------|--|-----------------------|
| MTVI2 | $\frac{1.5[1.2(R800 - R500) - 2.5(R670 - R550)]}{\sqrt{(2R800 + 1)^2 - (6R800 - 5\sqrt{R670})} - 0.5}$ | Haboudane et al. [15] |
| Chlorophyll index | $\frac{R750}{(R700 + R710) - 1}$ | Gitelson et al. [16] |

For modeling process, descriptive statistics were applied to characterize the parameters of continuous environmental variables such as mean, median, standard deviation, minimum and maximum. Were imported to the Statistical Package of the Social Sciences (SPSS) version 18 statistical software for descriptive statistical analysis? We made relationships between the dependent (yield) (Kg) and independent (vegetation indices biophysical parameters) variables involved in the simple regression analysis.

The stepwise simple linear regression method was used to model Normalized difference vegetation index (NDVI), Modified chlorophyll absorption ratio index (MCARI), Triangular vegetation index (TVI), Modified chlorophyll absorption ratio index 1 (MCARI1), Modified chlorophyll absorption ratio index 2 (MCARI2), Modified triangular vegetation index (MTVI2), Chlorophyll index and grain yield predictions. To avoid the danger of too many parameters being included, the stepwise Forward method was used. The production function: or Grain Yield = f (vegetation indices biophysical parameters).

$$Y = a + b \cdot x \quad (\text{Linear regression model})$$

Where, Y is the actual grain yield and X are VIS. A is intercept, b is the regression coefficients. The final regression equation was derived through a researcher controlled trial, error approach and the impact of grain yield constraints on grain yield. Two main assumptions were used to check the relationships between the dependent (grain yield) and independent (vegetation indices biophysical parameters) variables involved in the simple regression analysis.

Regression analysis also has an assumption of linearity. The relationship between the dependent variable and the independent variables for a linear relationship was tested and was the basis of the correlation of the variables [17]. The relationship between predict and the predictors is linear. The simple linear regression models were applied to linear relationships. The linearity between grain yield and vegetation indices biophysical parameters was done using SPSS 18.

The square of the correlation coefficient (R^2) was computed to measure the goodness-of-fit of the model. It takes values between 0 (the points are completely random) and 1 (all the points lie exactly on the regression line). (R^2) describes the proportion of the total variability of grain yield (Y) which is explained by the linear relationship of Y on the entire vegetation indices biophysical parameters, and gives an indication of the goodness-of-fit of a model. However, every time another independent variable is added, the value (R^2) of is necessarily increased.

Three spectral regions of Spectroradiometer data (Visible, near infra-red and Shortwave infra-red) and seven spectral vegetation indices (NDVI, MCARI, TVI, MCARI1, MCARI2, MTVI2 and Chlorophyll Index) were used in the modeling process with crop yield. All generated models were validated using the correlation coefficient between the actual and predicted yields (r^2).

3. Results and Discussion

3.1. Analysis of Spectral Reflectance Characteristics

Spectral reflectance of plant leaves is characterized and uniquely identified by very low spectral reflectance in the red band followed by high spectral reflectance in near infra-red band and low spectral reflectance in the shortwave infra-red. Near infra-red band usually shows the highest reflectance value while visible bands show the lowest ones. The spectral zones for the three cvs showed that the highest spectral reflectance was in near infra-red infrared spectral zone (700–1300 nm), relatively low reflectance in the spectral zone (1450–1800 nm) while the lower reflectance was found in the spectral zone (1950–2300 nm). The lowest reflectance was found in the spectral zone (350–650).

Analysis of the spectral reflectance characteristics for each growing stage showed that in the dormancy stage, in visible bands Kalamata cultivar showed the highest spectral reflectance followed by Picual when Manzanillo cultivar showed the lowest spectral reflectance. In near infra-red bands, Kalamata cultivar showed the highest reflectance while Manzanillo cultivar was the lowest. Kalamata cultivar showed also the highest reflectance in short wave infrared (AWIR-1 and SWIR-2) while Manzanillo cultivar showed the lowest reflectance. Spectral reflectance pattern for the three cultivars in the dormancy stage is shown in Figure 4.

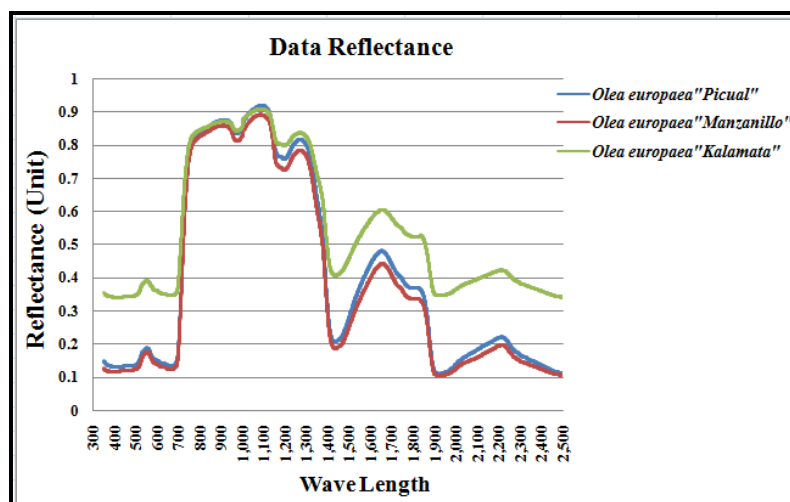


Figure 4: Spectral Reflectance in All Cultivar in Dormancy Stage

In flowering stage, Kalamata cultivar showed the highest spectral reflectance in all bands. In near infra-red band, Picual showed the lowest reflectance, however, no significant difference was found in the reflectance of Picual and Manzanillo in visible bands as shown in Figure 5.

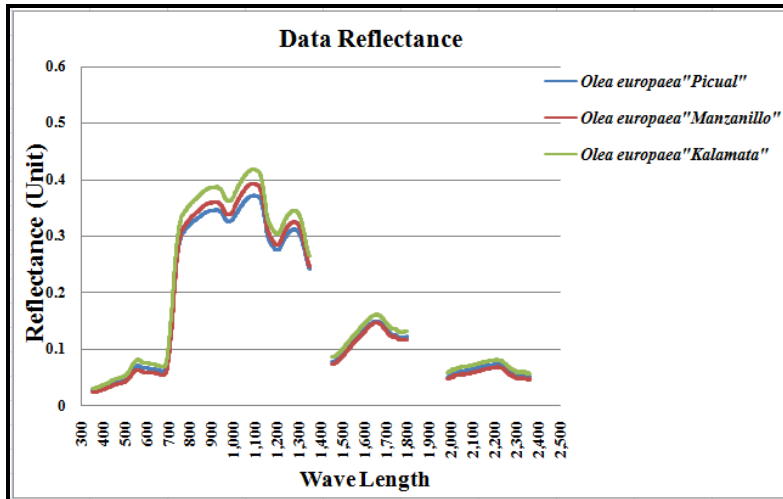


Figure 5: Spectral Reflectance in All Cultivar in Flowering Stage

In fruit sat stage, Manzanillo cultivar showed is highest spectral reflectance with while Kalamata cultivar showed the lowest reflectance as shown in Figure 6.

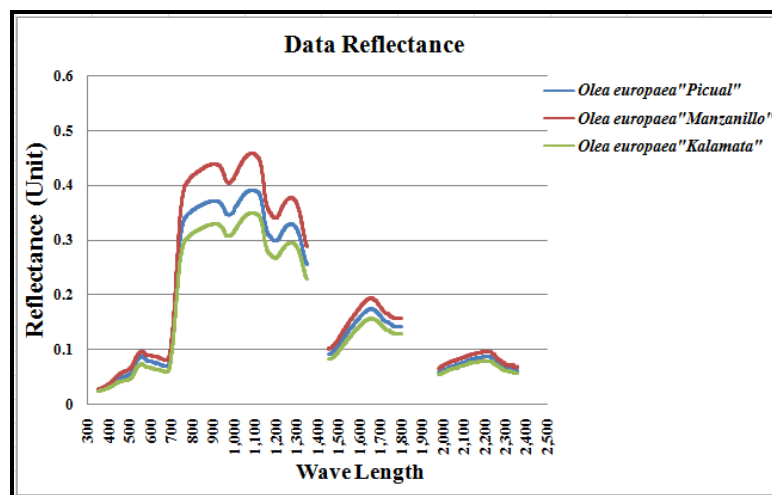


Figure 6: Spectral Reflectance in All Cultivar in Fruit Sat Stage

In mature stage, Manzanillo cultivar showed the highest spectral reflectance in all bands followed by Picual cultivar in near infrared and shortwave infrared. No significant difference in the reflectance of the three cultivars in visible spectral region as shown in Figure 7.

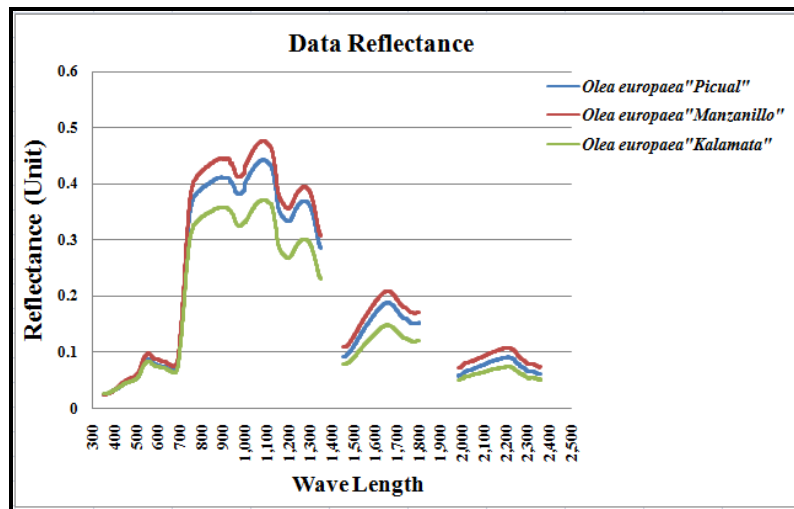


Figure 7: Spectral Reflectance in All Cultivar in Mature Stage

In ripening stage, Kalamata cultivar showed the highest reflectance in visible region while Manzanillo showed the lowest reflectance. Manzanillo showed the highest reflectance in near infra-red spectral region while Picual showed the lowest reflectance. In (SWIR-1 and SWIR-2), Kalamata cultivar showed the highest spectral followed by the other two cultivars that gave almost the same reflectance as shown in Figure 8.

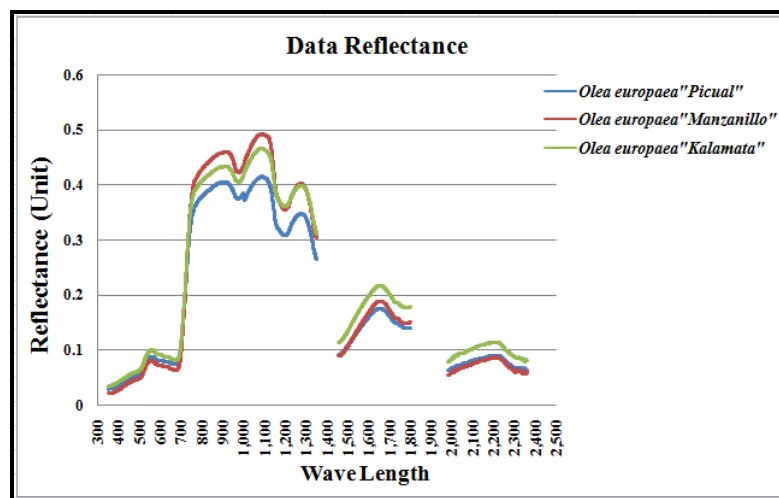


Figure 8: Spectral Reflectance in All Cultivar in Mature Stage

3.2. Yield Prediction Modeling

Modeling process in the current study is focusing on statistical empirical models that are limited to the conditions of the experiment. Data for the whole season of 2014 were used in the current study. Three hundred (300) spectral measurements (one hundred for each cultivar) were considered in the modeling process. Vegetation indices (VIs) and yield data were the main inputs in the modeling process. As the first step, each individual factor was used in a simple regression analysis to estimate Olive yield.

Total of Fifteen models were produced, yield prediction for each cultivar was estimated using the data from the five growing stages. It was found that the highest correlation coefficient for the two cultivars

Kalamata and Picual was presented in mature stage (Tables 4 and 5) while the highest correlation coefficient for Manzanillo cultivar was found during fruit sat stage (Table 6). The lowest correlation coefficient for all cultivars was found in dormancy stage. Table 7 showed the highly accurate model for each cultivar.

Table 4: Simple Regression Models for Picual Yield Prediction in Mature Stage

| Input factor | Intercept(a) | Slope Coefficient (b) | Generated Model | Correlation Coefficient (R ²) |
|-------------------|--------------|-----------------------|-----------------------------------|---|
| NDVI | -274.008 | 473.422 | Y=-274.008+473.422*NDVI | 0.851 |
| MCARI | 7.065 | 975.649 | Y=7.065+975.649*MCARI | 0.981 |
| TVI | -45.614 | 5.810 | Y=-45.614+5.810*TVI | 0.779 |
| MCARI1 | -51.494 | 223.087 | Y=-51.494+223.087*MCARI1 | 0.779 |
| MCARI2 | -51.364 | 57.304 | Y=-51.364+57.304*MCARI2 | 0.774 |
| MTVI2 | -23.839 | 68.901 | Y=-23.839+68.901*MTVI2 | 0.769 |
| Chlorophyll index | 27.078 | 81.214 | Y=27.078+81.214*Chlorophyll Index | 0.827 |

Table 5: Simple Regression Models for Kalamata Yield Prediction in Mature Stage

| Input factor | Intercept(a) | Slope coefficient (b) | Generated model | Correlation coefficient (R ²) |
|-------------------|--------------|-----------------------|-----------------------------------|---|
| NDVI | -98.902 | 239.018 | Y=-98.902+239.018*NDVI | 0.862 |
| MCARI | 13.771 | 985.786 | Y=13.771+985.786*MCARI | 0.941 |
| TVI | -10.977 | 4.928 | Y=-10.977+4.928*TVI | 0.752 |
| MCARI1 | -12.268 | 180.619 | Y=-12.268+180.619*MCARI1 | 0.748 |
| MCARI2 | -10.232 | 45.840 | Y=-10.232+45.840*MCARI2 | 0.787 |
| MTVI2 | 10.881 | 55.394 | Y=10.881+55.394*MTVI2 | 0.777 |
| Chlorophyll index | 39.973 | 68.333 | Y=39.973+68.333*Chlorophyll Index | 0.824 |

Table 6: Simple Regression Models for Manzanillo Yield Prediction in Fruit Sat Stage

| Input Factor | Intercept(A) | Slope Coefficient (b) | Generated Model | Correlation Coefficient (R ²) |
|-------------------|--------------|-----------------------|-------------------------------------|---|
| NDVI | 260.482 | 449.042 | Y=-260.482+449.042*NDVI | 0.969 |
| MCARI | -40.140 | 1975.960 | Y=-40.140+1975.960*MCARI | 0.894 |
| TVI | -242.221 | 15.755 | Y=-242.221+15.755*TVI | 0.877 |
| MCARI1 | -271.964 | 622.285 | Y=-271.964+622.285*MCARI1 | 0.779 |
| MCARI2 | -291.462 | 168.073 | Y=-291.462+168.073*MCARI2 | 0.744 |
| MTVI2 | -183.170 | 182.507 | Y=-183.170+182.507*MTVI2 | 0.777 |
| Chlorophyll index | -24.488 | 177.067 | Y=-24.488+177.067*Chlorophyll Index | 0.903 |

Table 7: Showed the Highest R² to Every Cultivar

| Cultivar | Intercept(A) | Slope Coefficient (B) | Generated Model | Correlation Coefficient (R ²) |
|------------|--------------|-----------------------|-------------------------|---|
| Picual | 7.065 | 975.649 | Y=7.065+975.649*MCARI | 0.981 |
| Manzanillo | -260.482 | 449.042 | Y=-260.482+449.042*NDVI | 0.969 |
| Kalamata | 13.771 | 985.786 | Y=13.771+985.786*MCARI | 0.941 |

According to the presented results, mature and fruit sat are the optimal growing stages for olive monitoring and yield prediction. At the same time, dormancy stage did not show sufficiency in either monitoring crop or predicting the yield. Most of vegetation indices showed high efficiency as estimators for crop yield, however, (MACARI - yield) and (NDVI - yield) models were the highly accurate models for yield prediction. These results agreed with Noureldin et al. [18] and Aboelghar et al. [19].

4. Conclusions

The main objective of the current study is to use hyperspectral remotely sensed data to identify the spectral signature of the different olive cultivars and to link productivity of the olive crop with different hyperspectral vegetation indices that were calculated from spectral characteristics to predict olive yield. The study was carried out in an observation site in Wadi El-Natron city using the dataset from season 2014.

Seven vegetation indices were tested in the current study: normalized difference vegetation index (NDVI), modified chlorophyll absorption ratio index (MCARI), triangular vegetation index (TVI), modified chlorophyll absorption ratio index 1 (MCARI1), modified chlorophyll absorption ratio index 2 (MCARI2), modified triangular vegetation index (MTVI2) and Chlorophyll index. Modeling and validation process were carried out for each cultivar. The most accurate models were generated during mature stage in the case of the two cultivars Picual and Kalamata and in fruit sat stage in the case of Manzanillo cultivar. The lowest accuracy was found during dormancy stage with all cultivars.

References

- [1] Ahamed, T., Tian, L., Zhang, Y., and Ting, K.C. *A Review of Remote Sensing Methods for Biomass Feedstock Production*. Biomass and Bioenergy. 2011. 35 (7) 2455-2469.
- [2] Gong, P., Pu, R., Biging, G.S., and Larrieu, M.R. *Estimation of Forest Leaf Area Index Using Vegetation Indices Derived from Hyperion Hyperspectral Data*. IEEE Transactions on Geosciences and Remote Sensing. 2003. 41 (6) 1355-1362.
- [3] Guréif, M., and Duke, C.L. *Adjustment Procedures of a Crop Model to the Site Specific Characteristics of Soil and Crop Using Remote Sensing Data Assimilation*. Agriculture, Ecosystems and Environment. 2000. 81; 57-69.
- [4] Hamar, D., Ferncz, C., Lichtenberger, J., Tarcsai, G., and Ferncz, A. *Yield Estimation for Corn and Wheat in the Hungarian Great Plain Using Landsat MSS Data*. International Journal of Remote Sensing. 1996. 17; 1689-1699.
- [5] Walthall, C., Dulaney, W., Anderson, M., Norman, J., Fang, H., and Liang, S. *A Comparison of Empirical and Neural Network Approaches for Estimating Corn and Soybeans Leaf Area Index from Landsat ETM₊ Imagery*. Remote Sensing of Environment. 2004. 92; 465-474.
- [6] Govender, M., Chetty, K., and Bulcock, H. *A Review of Hyperspectral Remote Sensing and Its Application in Vegetation and Water Resource Studies*. Water Sa. 2007. 33 (2) 145-151.
- [7] Maselli, F., Chiesi, M., Brilli, L., and Moriondo, M. *Simulation of Olive Fruit Yield in Tuscany through the Integration of Remote Sensing and Ground Data*. Ecological Modelling. 2012. 244; 1-12.
- [8] Guzmán, E., Baeten, V., Pierna, J.A.F., and García-Mesa, J.A. *Infrared Machine Vision System for the Automatic Detection of Olive Fruit Quality*. Talanta. 2013. 116; 894-898.
- [9] Brilli, L., Chiesi, M., Maselli, F., Moriondo, M., Gioli, B., Toscano, P., and Bindi, M. *Simulation of Olive Grove Gross Primary Production by the Combination of Ground and Multi-Sensor Satellite Data*. International Journal of Applied Earth Observation and Geoinformation. 2013. 23; 29-36.

- [10] Ariana, D.P., and Lu, R. *Hyperspectral Waveband Selection for Internal Defect Detection of Pickling Cucumbers and Whole Pickles*. Computers and Electronics in Agriculture. 2010. 74 (1) 137-144.
- [11] Garcia-Maraver, A., Salvachúa, D., Martínez, M.J., Diaz, L.F., and Zamorano, M. *Analysis of the Relation between the Cellulose, Hemicellulose and Lignin Content and the Thermal Behavior of Residual Biomass from Olive Trees*. Waste Management. 2013. 33 (11) 2245-2249.
- [12] Rouse, J.W., Haas, R.H., Schell, J.A., Deering, D.W., and Harlan, J.C., 1974: *Monitoring the Vernal Advancements and Retrogradation of Natural Vegetation*. NASA/GSFC, Final Report, Greenbelt, MD, USA. 1-137.
- [13] Daughtry, C.S.T., Walthall, C.L., Kim, M.S., Brown de Colstoun, E., and McMurtrey, J.E., III. *Estimating Corn Leaf Chlorophyll Concentration from Leaf and Canopy Reflectance*. Remote Sensing of Environment. 2000. 74; 229-239.
- [14] Broge, N.H., and Leblanc, E. *Comparing Prediction Power and Stability of Broadband and Hyperspectral Vegetation Indices for Estimation of Green Leaf Area Index and Canopy Chlorophyll Density*. Remote Sensing of Environment. 2000. 76; 156-172.
- [15] Haboudane, D., Miller, J.R., Pattey, E., Zarco-Tejada, P.J., and Stachan, I.B. *Hyperspectral Vegetation Indices and Novel Algorithms for Predicting Green LAI of Crop Canopies: Modeling and Validation in the Context of Precision Agriculture*. Remote Sensing of Environment. 2004. 90; 337-352.
- [16] Gitelson, A.A., Viña, A., Ciganda, C., Rundquist, D.C., and Arkebauer, T.J. *Remote Estimation of Canopy Chlorophyll Content in Crops*. Geophysical Research Letters. 2005. 32; L08403.
- [17] Ostrom, C.W., 1990: *Time Series Analysis and Regression Techniques*. Second Edition, Quantitative Applications in the Social Sciences, V. 07-009: Newbury Park: SAGE Publications, Inc. 95.
- [18] Noureldin, N.A., Aboelghar, M.A., Saady, H.S., and Ali, A.M. *Rice Yield Forecasting Models Using Satellite Imagery in Egypt*. The Egyptian Journal of Remote Sensing and Space Science. 2013. 16 (1) 125-131.
- [19] Aboelghar, M., Ali, A.R., and Arafat, S. *Spectral Wheat Yield Prediction Modeling Using SPOT Satellite Imagery and Leaf Area Index*. Arabian Journal of Geosciences. 2014. 7 (2) 465-474.

MODIS Derived Vegetation Index for Drought Detection on the San Carlos Apache Reservation

Zhuoting Wu, Miguel Velasco, Jason McVay, Barry Middleton, John Vogel, and Dennis Dye

Western Geographic Science Center, U.S. Geological Survey, United States

Publication Date: 13 February 2016

DOI: <https://doi.org/10.23953/cloud.ijarsg.44>



Copyright © 2016 Zhuoting Wu, Miguel Velasco, Jason McVay, Barry Middleton, John Vogel, and Dennis Dye. This is an open access article distributed under the **Creative Commons Attribution License**, which permits unrestricted use, distribution, and reproduction in any medium, provided the original work is properly cited.

Abstract A variety of vegetation indices derived from remotely sensed data have been used to assess vegetation conditions, enabling the identification of drought occurrences as well as the evaluation of drought impacts. Moderate Resolution Imaging Spectroradiometer (MODIS) Terra 8-day composite data were used to compute the Modified Soil Adjusted Vegetation Index II (MSAVI₂) of four dominant vegetation types over a 13-year period (2002 – 2014) on the San Carlos Apache Reservation in Arizona, US. MSAVI₂ anomalies were used to identify adverse impacts of drought on vegetation, characterized as mean MSAVI₂ below the 13-year average. In terms of interannual variability, we found similar responses between grassland and shrubland, and between woodland and forest vegetation types. We compared MSAVI₂ for specific vegetation types with precipitation data at the same time step, and found a lag time of roughly two months for the peak MSAVI₂ values following precipitation in a given year. All vegetation types responded to summer monsoon rainfall, while shrubland and annual herbaceous vegetation also displayed a brief spring growing season following winter snowmelt. MSAVI₂ values of shrublands corresponded well with precipitation variability both for summer rainfall and winter snowfall, and can be potentially used as a drought indicator on the San Carlos Apache Reservation given its wide geographic distribution. We demonstrated that moderate temporal frequency satellite-based MSAVI₂ can provide drought monitoring to inform land management decisions, especially on vegetated tribal land areas where in situ precipitation data are limited.

Keywords *Drought; Modified Soil Adjusted Vegetation Index II (MSAVI₂); MODIS; Precipitation; Vegetation Index Anomaly*

1. Introduction

Drought cycles are complex natural climate phenomena. The Southwestern United States has experienced persistent drought conditions since the 1990s, the severity and duration of which has not been seen in over 800 years (Cook et al., 2004; Meko et al., 2007). Climate change is projected to increase the severity and frequency of droughts in the Southwestern United States (Schwalm et al., 2012; Seager and Vecchi, 2010). Mean annual temperature is expected to increase by as much as 2 degrees Celsius by 2100 globally (IPCC, 2013). Warmer air temperatures increase atmospheric

evaporative demand, further reducing available moisture for vegetation (Weiss et al., 2009). Precipitation in the Southwest US typically follows a bi-modal pattern: winter and early spring bring snow to high elevation forests and rain to lower regions, and the North American monsoon season generates rain in the summer. Climate change is expected to disrupt this existing weather patterns and hydrological cycle. Warmer temperatures will cause more winter precipitation to fall as rain instead of snow (Knowles et al., 2006), snow to melt earlier in the spring (Clow, 2010; Harpold et al., 2012) and an overall decrease in precipitation as winter storm tracks shift to the north (Christensen et al., 2004). Forest communities of the Southwest US are known to be sensitive to changes in precipitation and moisture availability (Breshears and Barnes, 1999). Trees that are stressed by drought are more prone to fire, disease outbreaks, and mortality (Williams et al., 2010). Vegetation stressed by drought can result in a decrease in net primary production (NPP) – the transfer of carbon from the atmosphere to terrestrial biomass, which reduces the overall amount of carbon stored by vegetation. A reduction in NPP over North America in the early 2000s has been attributed to large-scale droughts in the region (Zhao and Running, 2010). Thus, understanding drought impacts on vegetation can help inform natural resources management decisions, and predict carbon cycle feedback to climate change (Friedlingstein et al., 2006).

In Arizona, summer monsoon moisture is important for vegetation growth, accounting for most of the rainfall during the year (Higgins et al., 1997). Droughts appear mainly because of irregularities in the amounts of summer monsoonal rainfall and winter snowfall. Detecting the emergence of drought is difficult because of its slow onset and lagged impacts. Direct assessment of drought usually requires climate data such as the Palmer drought severity index (Palmer, 1965), but this index has been criticized for its simplicity and for the manner in which potential evapotranspiration is modeled (Sheffield et al., 2012). In situ precipitation data from sparsely distributed stations hinder the drought analysis and the ability to map spatial patterns of drought. Satellite-based information has often been used in drought studies in recent decades because of its efficiency in identifying, monitoring and assessing drought conditions on the spatiotemporal scale (Zhang and Jia, 2013; Rhee et al., 2010; Vicente-Serrano, 2007). In addition, a number of satellite-based vegetation indices have been developed for monitoring drought from space (Anderson et al., 2011; Wang and Qu, 2007; Bayarjargal et al., 2006), taking advantage of the large spatial coverage and high temporal frequency of the satellite data.

Measurements of decreased vegetation productivity through remotely sensed satellite images can serve as a proxy for monitoring drought. For example, recent insect outbreaks (Meddens and Hicke, 2014; Walter and Platt, 2013; Dennison et al., 2010) and forest die-off events (Anderegg et al., 2013; Allen et al., 2010) in western North America observed through satellite imagery have been attributed to persistent drought conditions over the region. Remote sensing data derived vegetation Indices are often used to measure vegetation response to climatic conditions over time, and therefore time-series data are crucial for monitoring vegetation response as it relates to variabilities of temperature and precipitation. Because actively photosynthesizing vegetation is highly absorptive in the red spectrum and highly reflective in the near infrared, the Normalized Difference Vegetation Index (NDVI) is one of the most widely used vegetation indices for monitoring drought and vegetation health (Tucker, 1979; Ji and Peters, 2003; Anyamba and Tucker, 2005; Yengoh et al., 2015). In dryland environments, however, background soil and exposed surface reflectance can blur the vegetation signal (Lu et al., 2015). To control for this effect, the Modified-Soil Adjusted Vegetation Index (MSAVI₂) was developed to account for differences in soil brightness that can be found in arid to semi-arid regions (Qi et al., 1994). Although MSAVI₂ has been used to monitor vegetation growth in various ecosystems (Mariotto and Gutschick, 2010; Heiskanen, 2006; Gonsamo and Chen, 2014), it has less commonly been used for drought detection and monitoring vegetation temporal responses to drought.

The impacts of drought on vegetation depend on the local climatic regimes and vegetation types in the region, so it is almost impossible to develop a universal drought monitoring approach that spans

different regions. For our study area of San Carlos Apache Reservation in the semi-arid Southwest US, we developed a drought monitoring approach using high temporal frequency MODIS-derived MSAVI₂, which is particularly effective in arid and semi-arid regions (Qi et al., 1994). We established a 13-year mean MSAVI₂ as a baseline for four vegetation cover types over the entire San Carlos Apache Reservation and compared annual MSAVI₂ variability to the baseline (as anomalies) for drought detection. Specifically, our objectives were to: (1) assess the severity of drought in the past 13 years using MSAVI₂ anomalies, (2) compare drought impacts on different vegetation types, (3) identify time lags between vegetation responses and precipitation, and (4) identify indicator vegetation types for drought detection on the San Carlos Apache Reservation.

2. Methods

2.1. Study Area

The study area encompassed the entire San Carlos Apache Reservation (33.82°N, -110.75°W – 32.86°N, -109.48°W, Figure 1) in east-central Arizona. The reservation covers approximately 7,447 km², with elevation ranging from 600 to 2,400 meters above sea level (ASL). Its diverse habitat includes high desert grasslands and shrublands, pinon-juniper/chaparral/oak woodlands and is dominated by ponderosa pine forests. The coldest month in the town of San Carlos (33.351°N, -110.452°W, 819 m ASL) is January with a mean low temperature of 0° C and high of 13° C; July is the warmest month with mean low and high temperatures of 17° C and 35° C, respectively. Mean yearly rainfall ranges from 300 to 560 mm per year, with both precipitation and temperature dependent on elevation and season. From November through March, storms originating from the Pacific generally bring snowfall to the higher elevation ponderosa pine forests. The North American Monsoon brings summer rainfall from moisture originating in the Gulf of Mexico and the Gulf of California, usually lasting from late June through September (Higgins et al., 1997).

2.2. MODIS Satellite Imagery

We used 8-day composite surface reflectance data from the MODIS satellite at 250-meter spatial resolution for a 13-year study period (2002-2014). A maximum of 46 dates were available each year. Each image date was visually examined for cloud/cloud-shadow related artifacts. If these artifacts covered more than 10% of the reservation land, the image date was excluded from use in our analysis. In addition, the average of the two nearest valid dates was used to minimize effects of any missing scenes.

To understand the effects of climate on vegetation within the reservation land area, band 1 (red) and band 2 (near infrared) of the 8-day composite MODIS surface reflectance data were used to calculate MSAVI₂ for each date. The MSAVI₂ index was calculated as follows:

$$MSAVI_2 = \frac{2 * NIR + 1 - \sqrt{(2 * NIR + 1)^2 - 8 * (NIR - RED)}}{2},$$

Where NIR and RED are the surface reflectance of the near infrared and red bands, respectively. For each individual year, the mean MSAVI₂ value was calculated for the whole Reservation using the 8-day composite MODIS data. The resultant annual mean MSAVI₂ images were used to calculate a mean MSAVI₂ value for the 13-year study period as a baseline to generate MSAVI₂ anomalies. The MSAVI₂ anomalies were defined as the difference between the annual mean MSAVI₂ value of a given year and the 13-year MSAVI₂ average for a given pixel (Figure 1). On a pixel-by-pixel basis, each annual anomaly image was classified, highlighting areas within the reservation that had experienced drought impacts (negative MSAVI₂ anomalies) for the study period. A cumulative drought image was generated by quantifying the number of years out of the 13-year period that had experienced

vegetation stress due to drought (negative MSAVI₂ anomalies). The cumulative drought image was then classified into six classes to characterize the drought impacts on various vegetation types on the San Carlos Apache Reservation (Table 1).

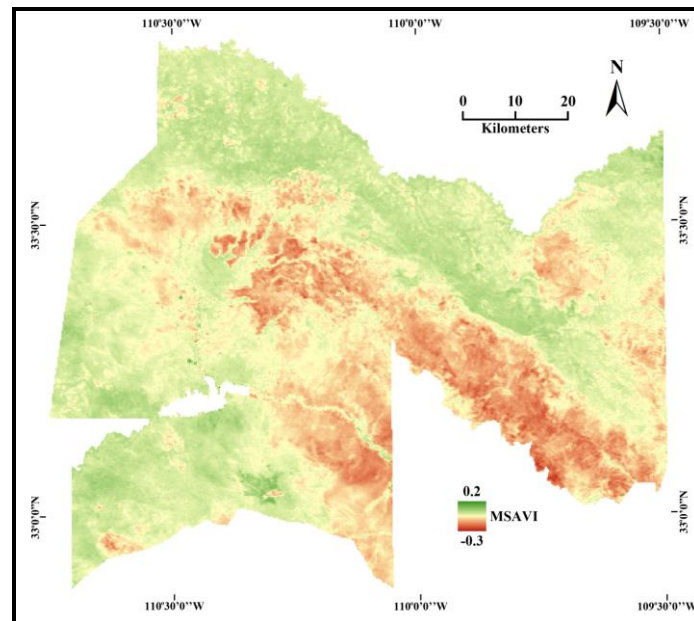


Figure 1: Sample MODIS-Derived MSAVI₂ Anomaly (year 2009) of the San Carlos Apache Reservation

2.3. LANDFIRE Vegetation Layer

We obtained the 2012 Landscape Fire and Response Management Tools (LANDFIRE) vegetation layer (<http://LandFire.gov>). LANDFIRE, a shared program between the wildland fire management programs of the U.S. Department of Agriculture and U.S. Department of Interior, provides several geospatial layers for natural resource management (Rollins and Frame, 2006). The 2012 LANDFIRE vegetation layer consist of several specific vegetation types. For this study, we consolidated the LANDFIRE vegetation classes into the following categories: grassland, shrubland, woodland, forest and others (e.g. developed, water) (Figure 2).

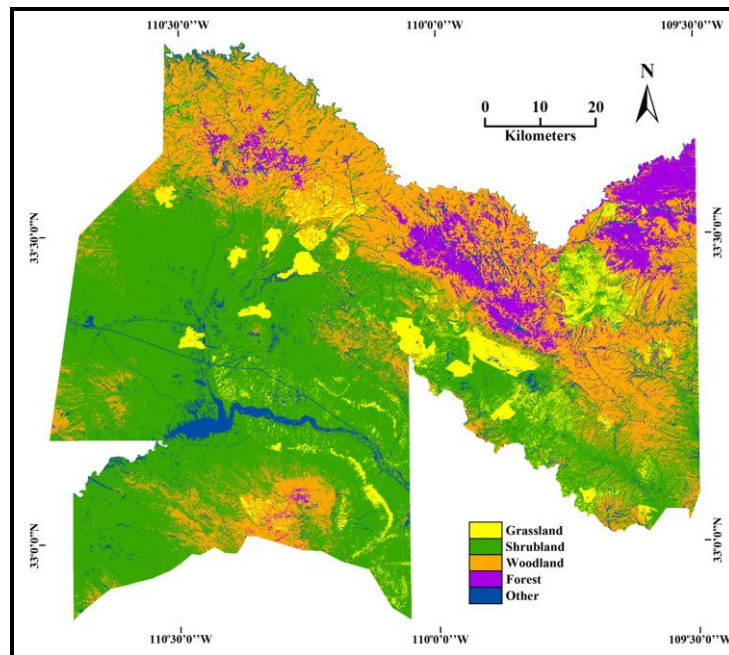


Figure 2: LANDFIRE Derived Vegetation Types of the San Carlos Apache Reservation Consolidated into Five Simplified Land Cover Types

2.4. PRISM Precipitation Data

Precipitation, from either winter snowfall or summer rainfall is the driving factor for vegetation green-up response (Davenport and Nicholson, 1993). Accurate and timely measurements of precipitation are important for the assessment of vegetation response. However, there are no currently established long-term weather stations on the San Carlos Apache Reservation and very few exist nearby. Instead, we obtained 4-km gridded precipitation data from the Parameter-elevation Relationships on Independent Slopes Model (PRISM) Climate Group at the Oregon State University (<http://prism.oregonstate.edu>). The PRISM datasets use a digital elevation model and point data to produce daily estimates of precipitation and temperature (Daly et al., 2002), especially the incorporation of radar data to produce the enhanced hybrid gridded precipitation data from 2002 on (http://www.prism.oregonstate.edu/documents/PRISM_datasets.pdf). The daily precipitation data were averaged into 8-day composite values to correspond with the composite MODIS data for the study period of 2002 to 2014.

2.5. Statistical Analysis

The lag between precipitation and vegetation response can vary depending on land cover type (Wang et al., 2003). For each individual date of the study period (2002-2014), mean MSAVI₂ values of each vegetation type were computed using MODIS-derived MSAVI₂ and vegetation classes from LANDFIRE. Using the same drought impacts classes identified for MSAVI₂ values, the mean MSAVI₂ value for each of the four vegetation types that fell within the medium to severe impact classes (Table 1) was calculated and compared with 8-day precipitation data from PRISM. Recognizing the inherent variability within the 8-day MSAVI₂ data, a running average of five image dates was calculated to best represent the vegetation response throughout the entire study period. To evaluate the most appropriate time lag between vegetation responses and precipitation events, we compared Pearson correlation coefficients between MSAVI₂ and precipitation for seven different time lags (32 – 80 days).

All image processing was performed using ERDAS Imagine 2014 (Hexagon Geospatial, GA, US) and statistical analyses were conducted in Microsoft Excel 2010 (Microsoft Corporation, WA, US).

Table 1: Drought Impacts Classification and Vegetation Composition

| Drought Impacts | Drought years | Grassland | Shrubland | Woodland | Forest | Other | Total |
|-----------------|---------------|-----------------|-----------------|-----------------|-----------------|-----------------|-----------------|
| | # years | km ² | km ² | km ² | km ² | km ² | km ² |
| Low | 1 -4 | 16 | 31 | 121 | 55 | 16 | 239 |
| Low-Medium | 5 | 82 | 268 | 401 | 116 | 63 | 930 |
| Medium | 6 | 204 | 972 | 781 | 168 | 143 | 2,268 |
| Medium-High | 7 | 179 | 1,500 | 627 | 118 | 135 | 2,559 |
| High | 8 | 55 | 869 | 191 | 37 | 57 | 1,209 |
| Severe | 9 -11 | 7 | 193 | 25 | 4 | 12 | 242 |

Drought years are defined as years with mean MSAVI₂ values below the 13-year average as negative anomalies

3. Results

3.1. Drought Impacts on Vegetation

Drought impacts were evaluated using the number of years with mean annual MSAVI₂ values below the 13-year (2002-2014) average (negative anomalies) (Table 1). The entire San Carlos Apache Reservation experienced at least one drought year out of the 13-year study period. The most severely impacted areas experienced drought conditions 11 out of 13 years. The total area in each drought impact class followed a normal distribution, with most areas in the medium and medium-high impact classes, followed by high and low-medium classes, and severe and low classes covering the smallest area (Table 1).

Drought impacts varied across vegetation types. Woodland and forest areas showed a decreasing trend along a drought impact gradient (Figure 3), indicating they were more buffered during drought occurrences. Shrubland as the most prevalent land cover type in the study area, showed the opposite trend from woodland/forests (Figure 3). When compared to other vegetation types, shrubland was the dominant land cover type in the medium-high drought impact category, and it became more predominant as the drought impact increased to the severe level, suggesting that shrubland can be used as a drought indicator vegetation type for the San Carlos Apache Reservation. Meanwhile, grasslands and other land areas did not show a significant trend along the drought impact gradient (Figure 3).

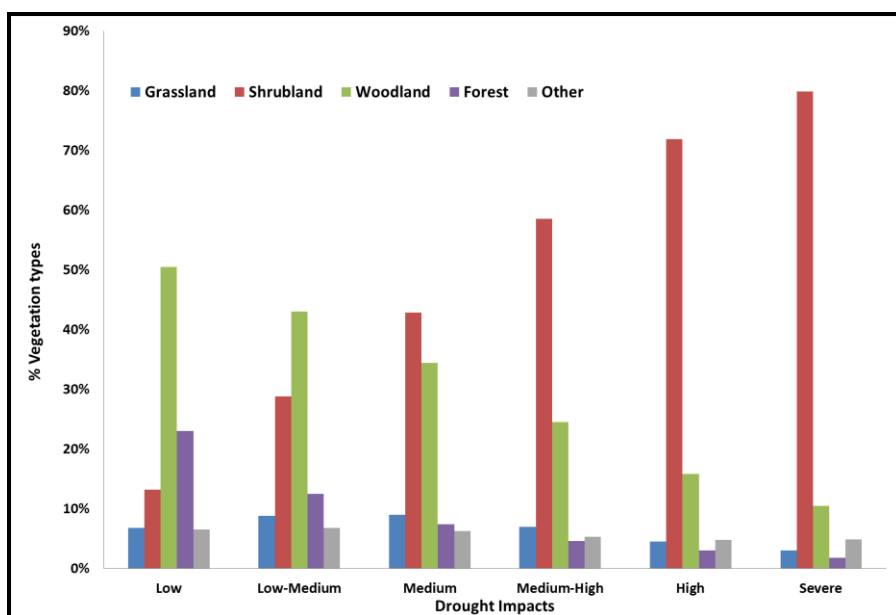


Figure 3: Vegetation Type Distribution within Each Drought Impact Category

3.2. Interannual Variability of Vegetation Response

All four vegetation types showed fluctuating interannual variability (Figure 4). However, grasslands and shrublands displayed a larger range of variability on an annual basis compared to woodlands and forests on the San Carlos Apache Reservation. The relatively “muted” response of woodlands and forests corresponded to the lower percentage of these two vegetation types in the higher drought impact classes (Figure 3). The differences between the two vegetation groups – grassland/shrubland and woodland/forest, were more obvious when we compared the mean MSAVI₂ values of the two vegetation groups (Figure 4, insert). Therefore, from here on, we used the two broader vegetation groups – grassland/shrubland and woodland/forest to further probe the mechanisms of the vegetation response to drought.

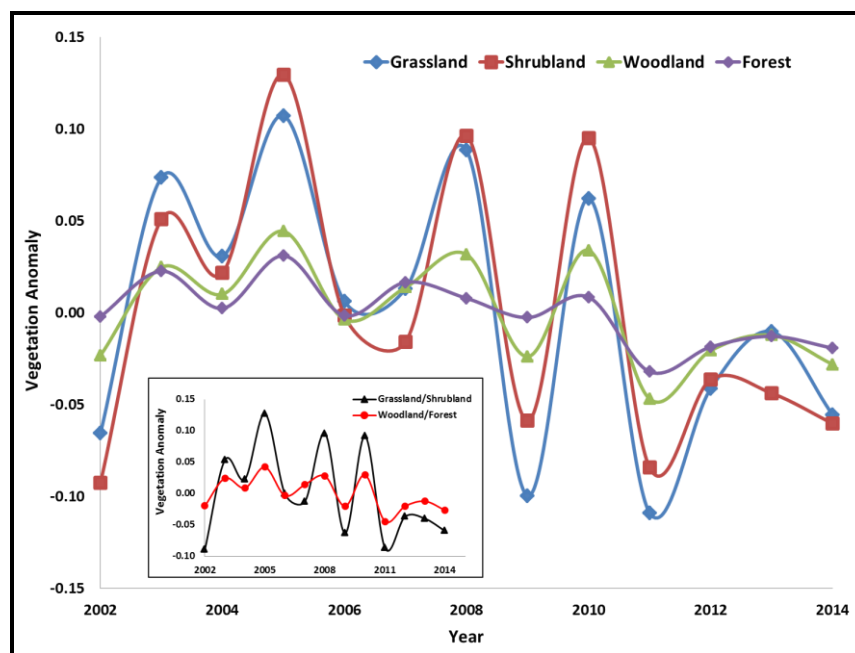


Figure 4: Mean Annual Vegetation Anomalies for 2002-2014. The Vegetation Anomalies were averaged across Medium to Severe Drought Impacts Classes Identified in Table 1. The Insert Graph Shows the Grouped Vegetation Anomalies of Grassland/Shrubland and Woodland/Forest, Respectively

3.3. Precipitation Variability and Vegetation Response

Correlation coefficients between vegetation responses and precipitation increased as lag time increased and tended to level off after the 64-day lag time (Figure 5). Although the correlation coefficients increased slightly beyond lag time of 64 days, the explanatory power of the relationship between precipitation and MSAVI₂ did not substantially increase, especially for the woodland/forest areas (Figure 5). The lag time referred here is defined as the onset of the precipitation event to the initiation of MSAVI₂ peak, which may occur after the initial vegetation growth. The peak MSAVI₂ date corresponded well with the peak precipitation date during the summer monsoon using a lag time of 64 days (Figure 6, shaded monsoon periods). With the 64-day lag time, both grassland/shrubland and woodland/forest vegetation groups showed a strong growth response to the summer monsoon rainfall, with woodland/forest having a higher mean MSAVI₂ value and a longer growing season following the onset of the monsoon (Figure 6). Overall, grassland/shrubland showed a higher correlation coefficient with precipitation than that from the woodland/forest vegetation group (Figure 5), mostly due to the C₃ shrubland green-up in response to the winter snowmelt (Figure 6, between shades). Grass species on the San Carlos Apache Reservation are dominated by C₄ grasses that are dormant during the cold winter season and respond rapidly to summer monsoon; whereas C₃ shrub and forb species green-up

after winter snow melt, followed by a longer and more dominant growing season during summer monsoon. Thus, shrubland and annual herbaceous vegetation can be used as a proxy for precipitation variability for both summer rainfall and winter snowfall.

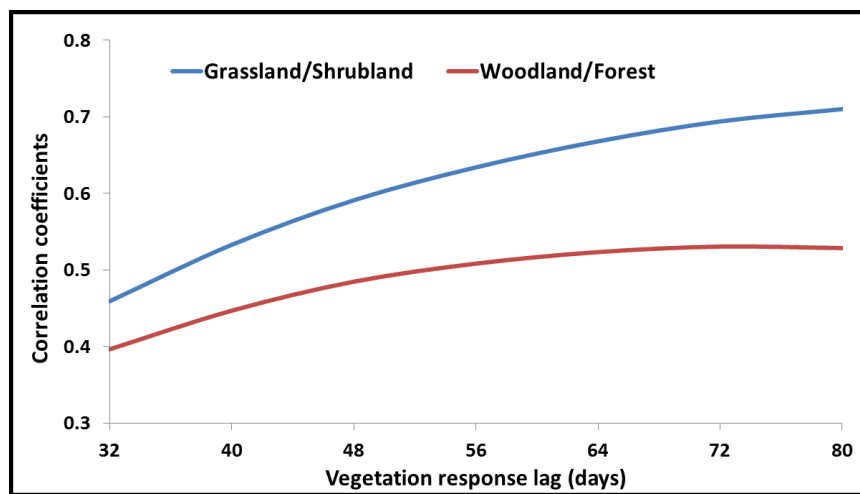


Figure 5: Correlation Coefficients between MSAVI₂ and Precipitation along a Gradient of Lag Time. All Correlation Coefficients Have P-Values <0.001

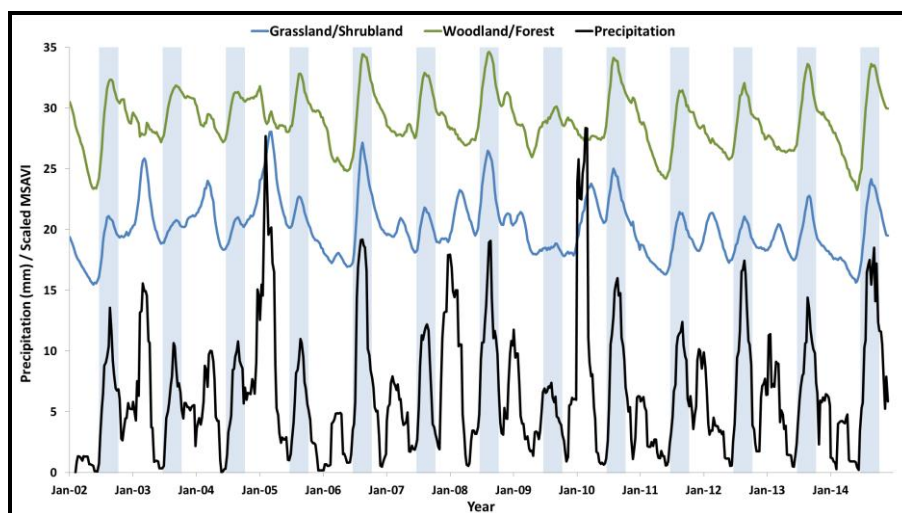


Figure 6: Vegetation Responses and Precipitation Variability from 2002 to 2014. Scaled MSAVI₂ Values are Mean MSAVI₂ Values for Grassland/Shrubland and Woodland/Forest Multiplied by 50 for Visual Display with the Precipitation in Millimeters. The Shaded Areas Highlight the Summer Monsoon in Arizona, Which Runs Roughly from June 26th to September 30th Each Year

4. Discussion

4.1. Effectiveness of MODIS-derived MSAVI₂ for Drought Monitoring

The MODIS-derived MSAVI₂ was effective in our study area for detecting different responses of vegetation types to changes in precipitation and drought. This index can serve as a useful drought monitoring tool, especially on tribal lands like the San Carlos Apache Reservation where ground-based weather data are sparse. Like the majority of the Southwestern US, dryland ecosystems deserve special attention because they are sensitive to changes in temperature and precipitation, and MSAVI₂ is particularly effective in monitoring vegetation responses to climate change in such environments.

For example, MSAVI₂ has been used to effectively monitor desertification in China at a large scale (Aixia et al., 2007). The related Soil Adjusted Vegetation Index (SAVI) has also been used to monitor changes in vegetation cover and processes contributing to desertification (Badreldin et al., 2014). Although NDVI has been used to monitor a host of vegetation responses to drought (Karnieli et al., 2010; Zhang et al., 2010; Yuhua and Scuderi, 2009; Yengoh et al., 2015), MSAVI₂ has great potential to be widely used for drought monitoring in the semi-arid Southwest US.

4.2. Grassland and Shrubland Response

Grassland and shrubland areas were more sensitive to changes in precipitation. In particular, grassland/shrubland vegetation group experienced a short green-up following winter snowmelt and an additional green-up following summer monsoon precipitation. A similar spring and summer peak in grassland greenness values as well as the general sensitivity of grasses to changes in annual precipitation has been observed in the Southwestern US (Pennington and Collins, 2007). In addition, sporadic and extreme rainfall events, brought on by climate change, can negatively impact grasslands by reducing net carbon cycling (Fay et al., 2008; Wu et al., 2011). Another consequence of decreased or sporadic rainfall will be the proliferation of invasive grass species in the southwest such as *Eragrostis lehmanniana*, already present in Arizona, which are more drought resistant than native grasses (Scott et al., 2010). Grasslands are increasingly susceptible to shrub encroachment in the semi-arid ecosystems in the Southwest US, due to the ability of shrubs to take advantage of the wide range of soil moisture conditions (Throop et al., 2012), especially in the face of increasing drought frequency and intensity in the Southwest US (Cayan et al., 2010).

Grassland above-ground productivity has long been strongly tied to precipitation, especially in regions where annual precipitation is low (Gilgen and Buchmann, 2009). This is because semi-arid grass rooting depth is typically limited to the top half meter of the soil depth, and roots are generally fine and spread widely below the surface to extract most of their moisture from the upper half meter of the soil profile (Eggemeyer et al., 2009). The shallow nature and wide distribution of roots allows C₃ grasses and annual forbs to quickly take up water and photosynthesize when moisture is available following snowmelt and summer rainfall. When immediate moisture is limited, semi-arid C₃ grasses lack the necessary root depth to draw moisture and subsequently enter into senescence. This bi-modal seasonal cycle of vegetation greenness has been observed throughout the Southwest US (Notaro et al., 2010). However, C₄ grasses dominated grassland on the San Carlos Apache Reservation usually displays a unimodal growing season during the summer monsoon, and therefore the early season green-up response displayed by the grassland/shrubland vegetation group was mostly dominated by C₃ shrub. In addition, shrubland in the Southwestern US have also been used as a proxy to indicate historic moisture availability (Mensing et al., 2004). Thus, shrubland dominated vegetation communities can serve as an effective indicator cover type or group for the onset of drought conditions for both winter and summer precipitation.

4.3. Woodland and Forest Response

Historically, increases in temperature, not precipitation, have been a leading cause of forest stress and mortality (Williams et al., 2013). In our study area, woodland and forested areas were less sensitive in their response to changes in precipitation. This could be due to deeper roots, which allow access to soil moisture that grasses and shrubs cannot access. A slower growth rate of established woodlands and forests may serve to buffer the effects of shortfalls in precipitation, especially during short-term droughts. However, for prolonged drought condition, forests can respond to severe water shortage and drought via a host of ecophysiological adaptations (Bréda et al., 2006).

Droughts in the Southwestern US are accompanied by increased temperature (IPCC, 2013), which may raise the risk of hydraulic failure and reduced carbon uptake, leading to stress or death even in

drought tolerant species (McDowell et al., 2008). In ponderosa pine forests, root growth often occurs in the spring before the production of new needles (Misson et al., 2006). Although the forested areas did not show an increase in MSAVI₂ in the spring following snowmelt, growth likely occurred in the roots underground. Increased greenness indicated by increasing MSAVI₂ occurred during the summer monsoon season when both woodland and forests reached their peak MSAVI₂. Similarly, in the Sierra Nevada Mountains, the highest observed rates of photosynthesis in individual ponderosa pine trees occurred following summer rains when soil temperatures were warm and soil moisture levels were ideal for growth (Misson et al., 2006).

4.4. Climate Change Implications for Tribal and the Southwest Land Management

Climate change is expected to increase the frequency, severity, and duration of droughts in the Southwest US (Seager and Vecchi, 2010). Along with a general increase in temperature, precipitation is expected to become more sporadic, possibly bringing less frequent, but more intense precipitation events (IPCC, 2007). Proper management of vegetation on tribal lands will be important in order to best mitigate the impacts of climate change and existing anthropogenic activities. Predicted future droughts in this century coupled with elevated temperature can reduce the spring snowpack and summer soil moisture (Cayan et al., 2010), which will negatively impact vegetation growth. Yet, forest resources management practices such as reducing forest canopy cover and tree density, more snow is allowed to accumulate and persist into the spring (Sankey et al., 2015). Thus, forest restoration efforts can help to mitigate some of the adverse impacts of drought and climate change by maximizing the existing winter snow accumulation.

Vegetation Indices have the potential to inform broad landscape natural resources management. In the Southwestern US, water management strategies must incorporate the maintenance of natural ecosystem functions in addition to agriculture and human demand in the face of climate change (Gleick, 2010). Drought will limit existing native vegetation's ability to serve as a net carbon sink (Zhao and Running, 2010), and persisting drought conditions and warmer temperature are also expected to contribute to larger and more catastrophic forest fires (Westerling et al., 2006). Effective management of ponderosa pine ecosystems should seek to reduce stand density and reduce the buildup of understory vegetation. Such treatments have already proven to be effective. For example, forested areas that were thinned prior to the 2002 Rodeo and Chedeski fires in Arizona burned less severely and exhibited altered fire behaviors (Finney et al., 2005).

5. Conclusion

Climate change is expected to bring on more frequent and severe droughts to the Southwestern US. Drought monitoring will be essential for proper and efficient management of vegetation and water resources in this region. MODIS-derived MSAVI₂ can serve as an effective drought monitoring tool in regions where in situ precipitation data are sparse or not available. We created time series of MODIS-derived MSAVI₂ spanning 2002–2014, and paired them with PRISM precipitation data to detect drought and to measure vegetation response to bi-modal precipitation patterns that are common to the San Carlos Apache Reservation and much of the Southwestern US in general. Drought conditions, defined as negative annual MSAVI₂ anomalies, occurred 1-11 years out of the 13-year study period on the Reservation land, and such persistent drought condition is likely to continue throughout this century (Cayan et al., 2010). We found that C₃ shrubland dominated vegetation types experienced a brief green-up following winter snowmelt, and a second, more pronounced green-up following rainfall from the North American monsoon in late summer/early fall. Forest and woodland ecosystems were less sensitive to short term drought conditions, possibly because of deeper root networks that allow them to access deep soil moisture that grassland and shrubland vegetation cannot access. Thus, grassland/shrubland, with their higher sensitivity to changes in precipitation, can serve as indicator vegetation types for drought in this region when monitored through MODIS-derived MSAVI₂. Tribal

forest management efforts should aim to reduce the risk of catastrophic wildfire and to mitigate the negative effects of climate change by increasing the adaptation of land management practices that prolong winter snowmelt and increase soil moisture across the landscape.

Acknowledgements

This work is supported by the US Geological Survey Land Change Science program. Thanks to Chris Soulard and Leila Gass for helpful comments to improve earlier drafts of the manuscript. The use of trade, product, or firm names is for descriptive purposes only and does not constitute endorsement by the U.S. Government.

References

- Aixia, L., Changyao, W., Jing, W., and Xiaomei, S. *Method for Remote Sensing Monitoring of Desertification Based on MODIS and NOAA/AVHRR Data*. Transactions of the Chinese Society of Agricultural Engineering. 2007. (10).
- Allen, C.D., Macalady, A.K., Chenchouni, H., Bachelet, D., McDowell, N., Vennetier, M., Kitzberger, T., Rigling, A., Breshears, D.D., Hogg, E.T., and Gonzalez, P. *A Global Overview of Drought and Heat-Induced Tree Mortality Reveals Emerging Climate Change Risks for Forests*. *Forest Ecology and Management*. 2010. 259; 660-684.
- Anderegg, W.R., Kane, J.M., and Anderegg, L.D. *Consequences of Widespread Tree Mortality Triggered by Drought and Temperature Stress*. *Nature Climate Change*. 2013. 3; 30-36.
- Anderson, M.C., Hain, C., Wardlow, B., Pimstein, A., Mecikalski, J.R., and Kustas, W.P. *Evaluation of Drought Indices Based on Thermal Remote Sensing of Evapotranspiration over the Continental United States*. *Journal of Climate*. 2011. 24; 2025-2044.
- Anyamba, A., and Tucker, C. *Analysis of Sahelian Vegetation Dynamics using NOAA-AVHRR NDVI Data from 1981–2003*. *Journal of Arid Environments*. 2005. 63; 596-614.
- Badreldin, N., Frankl, A., and Goossens, R. *Assessing the Spatiotemporal Dynamics of Vegetation Cover as an Indicator of Desertification in Egypt Using Multi-Temporal MODIS Satellite Images*. *Arabian Journal of Geosciences*. 2014. 7; 4461-4475.
- Bayarjargal, Y., Karnieli, A., Bayasgalan, M., Khudulmur, S., Gandush, C., and Tucker, C. *A Comparative Study of NOAA–AVHRR Derived Drought Indices Using Change Vector Analysis*. *Remote Sensing of Environment*. 2006. 105; 9-22.
- Bréda, N., Huc, R., Granier, A., and Dreyer, E. *Temperate Forest Trees and Stands under Severe Drought: A Review of Ecophysiological Responses, Adaptation Processes and Long-Term Consequences*. *Annals of Forest Science*. 2006. 63; 625-644.
- Breshears, D.D., and Barnes, F.J. *Interrelationships between Plant Functional Types and Soil Moisture Heterogeneity for Semiarid Landscapes within the Grassland/Forest Continuum: A Unified Conceptual Model*. *Landscape Ecology*. 1999. 14; 465-478.
- Cayan, D.R., Das, T., Pierce, D.W., Barnett, T.P., Tyree, M., and Gershunov, A. *Future Dryness in the Southwest US and the Hydrology of the Early 21st Century Drought*. *Proceedings of the National Academy of Sciences of the United States of America*. 2010. 107; 21271-21276.

- Christensen, N.S., Wood, A.W., Voisin, N., Lettenmaier, D.P., and Palmer, R.N. *The Effects of Climate Change on the Hydrology and Water Resources of the Colorado River Basin*. Climatic Change. 2004. 62; 337-363.
- Clow, D.W. *Changes in the Timing of Snowmelt and Streamflow in Colorado: A Response to Recent Warming*. Journal of Climate. 2010. 23; 2293-2306.
- Cook, E.R., Woodhouse, C.A., Eakin, C.M., Meko, D.M., and Stahle, D.W. *Long-Term Aridity Changes in the Western United States*. Science New York, N.Y. 2004. 306; 1015-1018.
- Daly, C., Gibson, W.P., Taylor, G.H., Johnson, G.L., and Pasteris, P. *A Knowledge-Based Approach to the Statistical Mapping of Climate*. Climate Research. 2002. 22; 99-113.
- Davenport, M., and Nicholson, S. *On the Relation between Rainfall and the Normalized Difference Vegetation Index for Diverse Vegetation Types in East Africa*. International Journal of Remote Sensing. 1993. 14; 2369-2389.
- Dennison, P.E., Brunelle, A.R., and Carter, V.A. *Assessing Canopy Mortality during a Mountain Pine Beetle Outbreak Using Geoeye-1 High Spatial Resolution Satellite Data*. Remote Sensing of Environment. 2010. 114; 2431-2435.
- Eggemeier, K.D., Awada, T., Harvey, F.E., Wedin, D.A., Zhou, X., and Zanner, C.W. *Seasonal Changes in Depth of Water Uptake for Encroaching Trees Juniperus Virginiana and Pinus Ponderosa and Two Dominant C₄ Grasses in a Semiarid Grassland*. Tree Physiology. 2009. 29; 157-169.
- Fay, P.A., Kaufman, D.M., Nippert, J.B., Carlisle, J.D., and Harper, C.W. *Changes in Grassland Ecosystem Function Due to Extreme Rainfall Events: Implications for Responses to Climate Change*. Global Change Biology. 2008. 14; 1600-1608.
- Finney, M.A., McHugh, C.W., and Grenfell, I.C. *Stand-and Landscape-Level Effects of Prescribed Burning on Two Arizona Wildfires*. Canadian Journal of Forest Research. 2005. 35; 1714-1722.
- Friedlingstein, P., Cox, P., Betts, R., Bopp, L., von Bloh, W., Brovkin, V., Cadule, P., Doney, S., Eby, M., Fung, I. and Bala, G. *Climate–Carbon Cycle Feedback Analysis: Results from the C4MIP Model Intercomparison*. Journal of Climate. 2006. 19; 3337-3353.
- Gilgen, A., and Buchmann, N. *Response of Temperate Grasslands at Different Altitudes to Simulated Summer Drought Differed but Scaled with Annual Precipitation*. Biogeosciences. 2009. 6; 2525-2539.
- Gleick, P.H. *Roadmap for Sustainable Water Resources in Southwestern North America*. Proceedings of the National Academy of Sciences of the United States of America. 2010. 107; 21300-21305.
- Gonsamo, A., and Chen, J.M. *Continuous Observation of Leaf Area Index at Fluxnet-Canada Sites*. Agricultural and Forest Meteorology. 2014. 189; 168-174.
- Harpold, A., Brooks, P., Rajagopal, S., Heidbuchel, I., Jardine, A., and Stielstra, C. *Changes in Snowpack Accumulation and Ablation in the Intermountain West*. Water Resources Research. 2012. 48 (11).
- Heiskanen, J. *Estimating Aboveground Tree Biomass and Leaf Area Index in a Mountain Birch Forest Using ASTER Satellite Data*. International Journal of Remote Sensing. 2006. 27; 1135-1158.

Higgins, R., Yao, Y., and Wang, X. *Influence of the North American Monsoon System on the US Summer Precipitation Regime*. Journal of Climate. 1997. 10; 2600-2622.

Intergovernmental Panel on Climate Change (IPCC). *Climate change 2007: the physical science basis-summary for policy makers. Contribution of Working Group I to the Fourth Assessment Report of the Intergovernmental Panel on Climate Change*. IPCC WGI 4th Assessment Report. 2007.

Intergovernmental Panel on Climate Change (IPCC). *Climate Change 2013: the Physical Science Basis. Contribution of Working Group I to the Fifth Assessment Report of the Intergovernmental Panel on Climate Change. Long-term Climate Change: Projections, Commitments and Irreversibility*. Cambridge Univ. Press, Cambridge, UK, and New York. 2013.

Ji, L., and Peters, A.J. *Assessing Vegetation Response to Drought in the Northern Great Plains using Vegetation and Drought Indices*. Remote Sensing of Environment. 2003. 87; 85-98.

Karnieli, A., Agam, N., Pinker, R.T., Anderson, M., Imhoff, M.L., Gutman, G.G., Panov, N., and Goldberg, A. *Use of NDVI and Land Surface Temperature for Drought Assessment: Merits and Limitations*. Journal of Climate. 2010. 23; 618-633.

Knowles, N., Dettinger, M.D., and Cayan, D.R. *Trends in Snowfall versus Rainfall in the Western United States*. Journal of Climate. 2006. 19; 4545-4559.

Lu, L., Kuenzer, C., Wang, C., Guo, H., and Li, Q. *Evaluation of Three MODIS-Derived Vegetation Index Time Series for Dryland Vegetation Dynamics Monitoring*. Remote Sensing. 2015. 7; 7597-7614.

Mariotto, I., and Gutschick, V.P. *Non-Lambertian Corrected Albedo and Vegetation Index for Estimating Land Evapotranspiration in a Heterogeneous Semi-Arid Landscape*. Remote Sensing. 2010. 2; 926-938.

McDowell, N., Pockman, W.T., Allen, C.D., Breshears, D.D., Cobb, N., Kolb, T., Plaut, J., Sperry, J., West, A., Williams, D.G. and Yezpe, E.A. *Mechanisms of Plant Survival and Mortality during Drought: Why do Some Plants Survive While Others Succumb to Drought?* New Phytologist. 2008. 178; 719-739.

Meddens, A.J., and Hicke, J.A. *Spatial and Temporal Patterns of Landsat-Based Detection of Tree Mortality Caused by a Mountain Pine Beetle Outbreak in Colorado, USA*. Forest Ecology and Management. 2014. 322; 78-88.

Meko, D.M., Woodhouse, C.A., Baisan, C.A., Knight, T., Lukas, J.J., Hughes, M.K. and Salzer, M.W. *Medieval Drought in the Upper Colorado River Basin*. Geophysical Research Letters. 2007. 34 (10).

Mensing, S.A., Benson, L.V., Kashgarian, M., and Lund, S. *A Holocene Pollen Record of Persistent Droughts from Pyramid Lake, Nevada, USA*. Quaternary Research. 2004. 62; 29-38.

Misson, L., Gershenson, A., Tang, J., McKay, M., Cheng, W., and Goldstein, A. *Influences of Canopy Photosynthesis and Summer Rain Pulses on Root Dynamics and Soil Respiration in a Young Ponderosa Pine Forest*. Tree Physiology. 2006. 26; 833-844.

Notaro, M., Liu, Z., Gallimore, R.G., Williams, J.W., Gutzler, D.S., and Collins, S. *Complex Seasonal Cycle of Ecohydrology in the Southwest United States*. Journal of Geophysical Research: Biogeosciences (2005–2012). 2010. 115 (G4).

- Palmer, W.C. *Meteorological Drought*. US Department of Commerce, Weather Bureau Washington, DC, USA. 1965.
- Pennington, D.D., and Collins, S.L. *Response of an Aridland Ecosystem to Interannual Climate Variability and Prolonged Drought*. *Landscape Ecology*. 2007. 22; 897-910.
- Qi, J., Chehbouni, A., Huete, A.R., Kerr, Y.H., and Sorooshian, S. *A Modified Soil Adjusted Vegetation Index*. *Remote Sensing of Environment*. 1994. 48; 119-126.
- Rhee, J., Im, J., and Carbone, G.J. *Monitoring Agricultural Drought for Arid and Humid Regions using Multi-Sensor Remote Sensing Data*. *Remote Sensing of Environment*. 2010. 114; 2875-2887.
- Rollins, M.G., and Frame, C.K. *The LANDFIRE Prototype Project: Nationally Consistent and Locally Relevant Geospatial Data for Wildland Fire Management*. 2006.
- Sankey, T., Donald, J., McVay, J., Ashley, M., O'Donnell, F., Lopez, S.M., and Springer, A. *Multi-Scale Analysis of Snow Dynamics at the Southern Margin of the North American Continental Snow Distribution*. *Remote Sensing of Environment*. 2015. 169; 307-319.
- Schwalm, C.R., Williams, C.A., Schaefer, K., Baldocchi, D., Black, T.A., Goldstein, A.H. Law, B.E., Oechel, W.C. and Scott, R.L. *Reduction in Carbon Uptake during Turn of the Century Drought in Western North America*. *Nature Geoscience*. 2012. 5; 551-556.
- Scott, R.L., Hamerlynck, E.P., Jenerette, G.D., Moran, M.S., and Barron-Gafford, G.A. *Carbon Dioxide Exchange in Semidesert Grassland through Drought-Induced Vegetation Change*. *Journal of Geophysical Research: Biogeosciences (2005–2012)*. 2010. 115 (G3).
- Seager, R., and Vecchi, G.A. *Greenhouse Warming and the 21st Century Hydroclimate of Southwestern North America*. *Proceedings of the National Academy of Sciences of the United States of America*. 2010. 107; 21277-21282.
- Sheffield, J., Wood, E.F., and Roderick, M.L. *Little Change in Global Drought over the Past 60 Years*. *Nature*. 2012. 491; 435-438.
- Throop, H.L., Reichmann, L.G., Sala, O.E., and Archer, S.R. *Response of Dominant Grass and Shrub Species to Water Manipulation: An Ecophysiological Basis for Shrub Invasion in a Chihuahuan Desert Grassland*. *Oecologia*. 2012. 169; 373-383.
- Tucker, C.J. *Red and Photographic Infrared Linear Combinations for Monitoring Vegetation*. *Remote Sensing of Environment*. 1979. 8; 127-150.
- Vicente-Serrano, S.M. *Evaluating the Impact of Drought Using Remote Sensing in a Mediterranean, Semi-Arid Region*. *Natural Hazards*. 2007. 40; 173-208.
- Walter, J.A., and Platt, R.V. *Multi-Temporal Analysis Reveals that Predictors of Mountain Pine Beetle Infestation Change During Outbreak Cycles*. *Forest Ecology and Management*. 2013. 302; 308-318.
- Wang, J., Rich, P., and Price, K. *Temporal Responses of NDVI to Precipitation and Temperature in the Central Great Plains, USA*. *International Journal of Remote Sensing*. 2003. 24; 2345-2364.
- Wang, L., and Qu, J.J. *NMDI: A Normalized Multi-Band Drought Index for Monitoring Soil and Vegetation Moisture with Satellite Remote Sensing*. *Geophysical Research Letters*. 2007. 34 (20).

- Weiss, J.L., Castro, C.L., and Overpeck, J.T. *Distinguishing Pronounced Droughts in the Southwestern United States: Seasonality and Effects of Warmer Temperatures*. Journal of Climate. 2009. 22; 5918-5932.
- Westerling, A.L., Hidalgo, H.G., Cayan, D.R., and Swetnam, T.W. *Warming and Earlier Spring Increases Western U.S. Forest Wildfire Activity*. Science. 2006. 313 (5789) 940-943.
- Williams, A.P., Allen, C.D., Macalady, A.K., Griffin, D., Woodhouse, C.A., Meko, D.M. Swetnam, T.W., Rauscher, S.A., Seager, R., Grissino-Mayer, H.D. and Dean, J.S. *Temperature as a Potent Driver of Regional Forest Drought Stress and Tree Mortality*. Nature Climate Change. 2013. 3; 292-297.
- Williams, A.P., Allen, C.D., Millar, C.I., Swetnam, T.W., Michaelsen, J., Still, C.J. and Leavitt, S.W. *Forest Responses to Increasing Aridity and Warmth in the Southwestern United States*. Proceedings of the National Academy of Sciences of the United States of America. 2010. 107; 21289-21294.
- Wu, Z., Dijkstra, P., Koch, G.W., Penuelas, J., and Hungate, B.A. *Responses of Terrestrial Ecosystems to Temperature and Precipitation Change: A Meta-Analysis of Experimental Manipulation*. Global Change Biology. 2011. 17; 927-942.
- Yengoh, G.T., Dent, D., Olsson, L., Tengberg, A.E., and Tucker III, C.J. *Recommendations for Future Application of NDVI. In Anonymous Use of the Normalized Difference Vegetation Index NDVI to Assess Land Degradation at Multiple Scales*. Springer. 2015. 57-59.
- Yuhas, A.N., and Scuderi, L.A. *MODIS-Derived NDVI Characterisation of Drought-Induced Evergreen Dieoff in Western North America*. Geographical Research. 2009. 47; 34-45.
- Zhang, A., and Jia, G. *Monitoring Meteorological Drought in Semiarid Regions using Multi-Sensor Microwave Remote Sensing Data*. Remote Sensing of Environment. 2013. 134; 12-23.
- Zhang, X., Goldberg, M., Tarpley, D., Friedl, M.A., Morisette, J., Kogan, F., and Yu. Y. *Drought-Induced Vegetation Stress in Southwestern North America*. Environmental Research Letters. 2010. 5; 024008.
- Zhao, M., and Running, S.W. *Drought-Induced Reduction in Global Terrestrial Net Primary Production from 2000 through 2009*. Science New York, N.Y. 2010. 329; 940-943.

Vegetation Loss and Ecosystem Disturbances on Kedargad Mandakini Subwatershed in Rudraprayag District of Uttarakhand due to Torrential Rainfall during June 2013

Neelam Rawat, Asha Thapliyal, Saurabh Purohit, Govind Singh Negi, Sourabh Dangwal, Santosh Rawat, Ashok Aswal and Kimothi M.M.

Uttarakhand Space Application Centre, Dehradun, Uttarakhand, India

Publication Date: 5 April 2016

DOI: <https://doi.org/10.23953/cloud.ijarsg.50>



Copyright © 2016 Neelam Rawat, Asha Thapliyal, Saurabh Purohit, Govind Singh Negi, Sourabh Dangwal, Santosh Rawat, Ashok Aswal and Kimothi M.M. This is an open access article distributed under the **Creative Commons Attribution License**, which permits unrestricted use, distribution, and reproduction in any medium, provided the original work is properly cited.

Abstract Uttarakhand is one of the hilly states in the Indian Himalaya. It lies in the Northern part of India between the latitudes 28° - 31° N to longitudes 77° - 81° E having a maximum dimension of east - west 310 km and 255 km; north - south covering an area of 53,484 km² with the elevation ranging from 210 to 7817 msl. It is the home to many holy rivers originating from the nearly 1439 glaciers. In view of the changing climate followed by factors responsible for varying nature of climate and its effect on environment basically related to vegetation phenology, biodiversity as well water resources especially in mountain region of Uttarakhand Himalaya which is well known for its rich biodiversity in perspective of socio-economic well-being of the rural people and forest dwellers; the natural devastation or any kind of calamity affect the native of the region due to their dependencies in the services provided by the nature which we call ecosystem services. The devastation caused during 16th & 17th June 2013 in Kedarnath valley on Kedargad micro watershed, of Mandakini sub watershed in Mandakini valley of Rudraprayag district, Uttarakhand Himalaya is one of the major devastations that have ruined the climate and ecosystem of the area to a greater extent. In the present study it is studied that how this devastation has affected vegetation by perturbing ecosystem services. It was noticed that after devastation forests and alpine is major region where a remarkable change was detected. A major change in river is also noticed.

Keywords *Vegetation; Ecosystem Services; Kedargad; Rudraprayag; Climate Change*

1. Introduction

Global change, whether generated from climate, land use change, biological invasion, global economic forces etc., will certainly affect the relationships that are part of the land and economies of the Himalayan region. Recognizing that global change and in particular global warming has and will have serious impacts on biophysical environment and the socio-economic conditions and livelihoods of people in Himalaya and adjacent plain areas. It will also affect species composition and diversity, habitats and the occurrence of rare and endangered species as well as invasive species in high

altitude areas, thus jeopardizing the conservation value of Himalayan protected areas and their wider environment (Maikhuri et al., 2000, 2001; Rao et al., 2002; Nautiyal et al., 2001). Further it is impacting glacial retreat – thereby affecting freshwater supplies etc. The Himalayan region is one of the most dynamic and complex mountain ranges in the world due to tectonic activity and they are vulnerable to global climate change and increasing human activities. Recent climate changes have had significant impact on high-mountain glacial environment. The previous study shows that the formation and expansion of moraine-dammed lakes, creating a potential danger from dammed lake outburst floods are the result of rapid melting of snow/ice and heavy rainfall (Dobhal et al., 2013). Because of altitudinal variation in the Himalaya, climate differs from high to low elevations, similarly natural resources, water etc.

Uttarakhand is one of the hilly states in the Indian Himalaya. It lies in the Northern part of India between the latitudes 28° - 31° N to longitudes 77° - 81° E having a maximum dimension of east - west 310 km and 255 km north - south covering an area of 53,484 km² with the elevation ranging from 210 to 7817 msl. It is the home to many holy rivers originating from the nearly 1439 glaciers. Total snow and ice reserves of the State constitute about 20% of its total area. Due to rich biodiversity this area provides many ecosystem services, in a strict sense, all those services generated as a result of interaction and exchange between biotic and abiotic components.

1.1. Ecosystem Service in the Mountain of Uttarakhand

The flow of energy is mediated by interacting organisms within ecosystems, and material which contribute towards many ecological services and goods to all the organisms including human beings. The important, undetectable but essential services include formation of good humus soil, decomposition of raw material, carbon sequestration and exchange of gases and their balance in atmosphere, derivative of climate and mitigation of climatic change, nutrient cycling, facilitation, assembly of community and succession and climax, water recycling recharge structure and air filtration, flood and drought control, regulation of water supply and many other services such as of recreation, aesthetic and religious values. The important Ecosystem goods and services include food, fodder, fiber, resin and drugs derived from many valuable plants or medicinal plants. This results in high biodiversity, forest cover up to considerable altitude, dominance of evergreen forest, rapid soil formation, agriculture, sericulture and many more.

1.2. Natural Disaster; Its Vulnerabilities in the Region

The region is seismically and ecologically very sensitive and fragile and even small disturbances (natural or anthropogenic) triggers changes that rapidly assumes dimension of the disaster.

The region has history of natural devastations i.e. various landslides and flash floods in the past. The occurrence of recent devastation caused due to torrential rainfall during 16th to 17th June 2013 in Kedarnath (one of the important pilgrims place out of four Religious places/Dhams situated in Uttarakhand State) witnessed unprecedented damage to the life and property, infrastructure, and landscape. The well exposed central crystalline rocks groups in the Higher Himalaya of Kedarnath valley form the oldest crystalline basement of the Himalaya, which shows fragile nature of this region. This might be one of the triggering agents in the region for landslides etc., which lead to further devastation.

The mountain region of Uttarakhand Himalaya which is well known for its rich biodiversity in perspective of socio-economic well-being of the rural people and forest dwellers, needs an understanding the impacts of this devastation and its forthcoming climatic effect in relation to vegetation phenology, biodiversity as well water resources there is a need of carrying study and analyzing climate implication vegetation loss and perturbing ecosystem services on Kedargad micro

watershed, of Mandakini subwatershed in Rudraprayag district, Uttarakhand Himalaya after June devastation 2013.

2. Study Area

The present study was carried out along an altitudinal gradient in the temperate forest of Kedargad Micro watershed Mandakini Watershed of Rudraprayag district, Uttarakhand, India. It lies in the Central Himalaya between the latitude 30°37'45.47"N and 30°48'23.93"N and longitude 78°59'59.91"E and 79°2'7.582"E with a total area of 9515.46 hectare (95.15km²). A total study area lies from 1,648 m – 7,000m altitudes from msl.

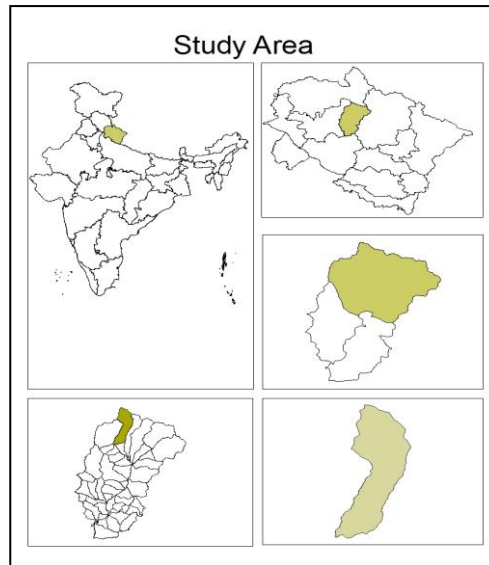


Figure 1: Study Area Locating Kedargad Microwatershed in Uttarakhand Himalaya, India

2.1. Geology of the Regions

The Kedarnath region is situated in the lap of two glaciers i.e., Chaurabari & Companion. The covered area of Chorabari glacier is nearly 4.23 sq.km upto a distance of 7 km approximately while that of Companion Glacier which is around 3.59 km in coverage and spreading upto a length of 5.79 km approximately (Dobhal et al., 2013). The area represents wide range of altitude (1600 m at Sonprayag to 6500 m at upper reaches), most of the area covered by snow-glaciers. Geomorphologically this area comes under valley glaciers and highly dissected hills and valley with moraines and piedmont slopes.

2.2. Climate & Soil

The elevation of the study area ranges from 1600 m to 6500 m from above sea level the climate of the region very largely depends on altitude. The winter season is from about mid-October to April. As most of the region is situated on the southern slopes of the outer Himalayas, monsoon currents can enter through the valley, the rainfall being heaviest in the monsoon from June to September. The slope of the study area is lies between 30-60° and towards the South-East aspect. The alpine habitat usually starts at timberline or the tree line i.e. 3500 masl and are characterized by the complete absence of tree. The soil of the Kedarnath valley is dark brown to brown at surface and brown to yellowish brown in the sub soil and endodynamorphic (Singh and Singh, 1992).

2.3. Floristic Composition of the Region

The floristic composition of study area shows mixed forest of *Rhododendron*, *Quercus leucotrichophora* (Banj), *Quercus floribunda* (Moru) and *Quercus semecarpifolia* (Kharsu), *Buxus wallichiana* (papri), *Acer spp.* (kaijal), *Betula alnoides* (katbhuj), Anyar (*Lyonia spp.*), *Alnus nepalensis* (Utis) upto an elevation and rest the alpine pasture. There are three distinct climatic seasons of Kedarnath, rainy season, summer season and winter season. Majority of the plant species having flowering and fruiting in rainy season, summer season is represented by lesser no plants than rainy season and the rest and very low plant species are representing to winter season. The area is very rich in Medicinal and aromatic plant diversity. This has traditionally occupied an important position in the socio-cultural, spiritual and medicinal arena of rural and tribal lives of India.

3. Methodology

In this study the High resolution remote sensing pre and post disaster satellite imageries (Table 1) acquired over the Kedargad a micro watershed (Kedarnath area to Sonprayag) of Mandakini watershed have been used for detail analysis and damage area assessment. The biomass study was done just a few month back in the area. The occurrence of medicinal plants wealth was also recorded from ground survey as well as literature consultation.

Table 1: Details of Satellites Data used for Analysis

| S. No. | Satellite Name | Resolution | Date of Acquisition | Pre and Post Event |
|--------|---------------------------|------------|---------------------|--------------------|
| 1. | LISS IV & Cartosat Merged | 2.5m | June 2011 | Pre-event |
| 2. | LISS IV & Cartosat Merged | 2.5m | June 2013 | Post-event |

Source: Satellite Data Sets were collected from NRSC, Hyderabad

3.1. Data Integration and Analysis

In the present work Integration of Satellite Data & SOI Toposheets by geometric correction was done for the micro watershed. The Digitization on pre and post image was done and Clipping and Marking of damaged area for Analysis and Interpretation of Data was done. Outset of all this was made for Assessment of Pasting vegetation and perturbing ecosystem services in the region.

4. Results

This study was based on pre and post satellite data analysis and a brief reconnaissance survey with additional information from previous research in the study area. The results are presented in form of maps, profiles, charts and statistical tables. The main objective of the present work was to know the loss of vegetation in the area due to flash flood and landslide. The Table 1 depicts the pre and post devastation area.

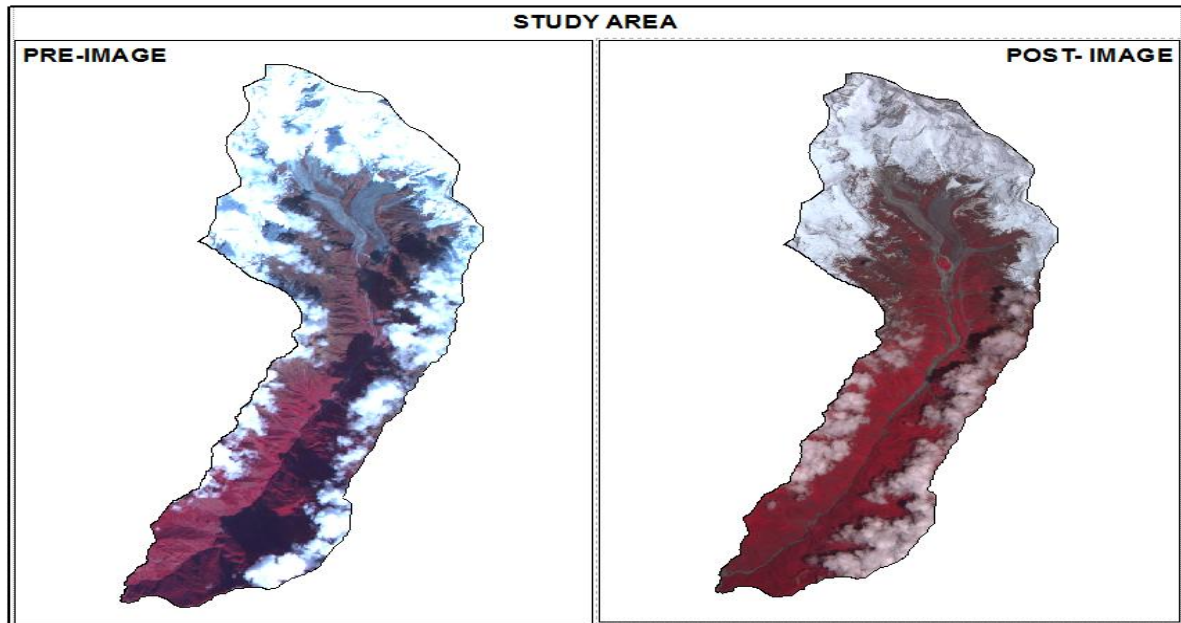


Figure 2: Kedargad Study Area Showing Pre and Post Image

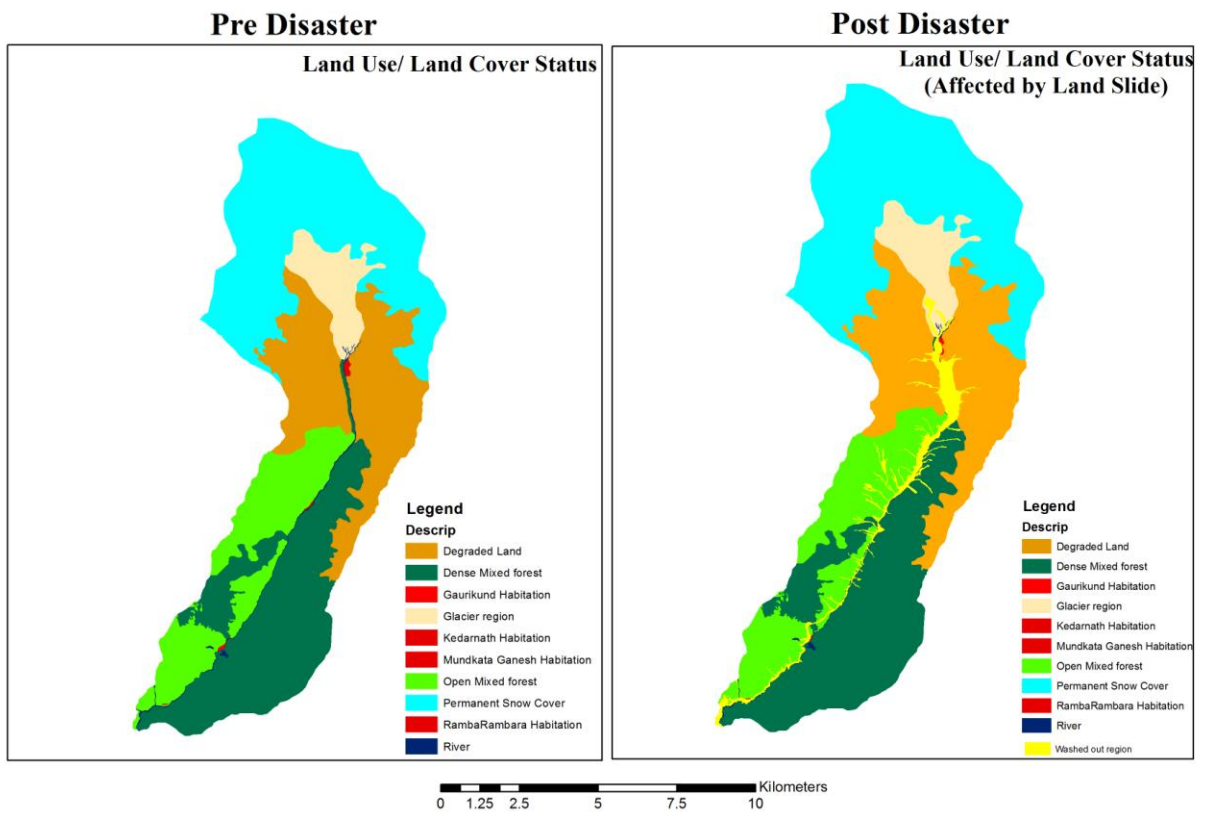


Figure 3: Landuse Landcover Status of Area Pre and Post Disaster

Table 2: Description of Study Area Analyzed and Devastated During Torrential Rainfall of 2013

| Description | Area (ha) (Before Devastation) | Washed out Area (ha) (After Devastation) | Total Remaining Area |
|------------------------------|-----------------------------------|--|-------------------------|
| Seasonal Snow Cover | 3425.76 | 270.55 | 3155.20 |
| Dense Mixed forest | 1240.98 | 33.16 | 1207.80 |
| Permanent Snow Cover | 3058.25 | 0.09 | 3058.20 |
| Wasteland | 92.88 | 2.23 | 90.60 |
| Rambara Habitation | 1.91 | 1.91 | 0.00 |
| Open Mixed Forest | 596.55 | 59.28 | 537.30 |
| Mundkatiya Ganesh Habitation | 0.66 | 0.25 | 0.40 |
| Kedarnath Habitation | 8.94 | 8.94 | 0.00 |
| Gaurikund Habitation | 2.84 | 2.79 | 0.00 |
| Rambara Habitation | 0.33 | 0.33 | 0.00 |
| River | 48.32 | 35.57 | 12.80 |

The result of present study area is depicting that the main region under seasonal and permanent snow cover. After that the major area is falling under forest and alpine pastures. The river and adjacent habitation are one of the main and affecting units in the region. The pre and post satellite image analysis is showing that there is a major change in seasonal snow cover. After that forests and alpine area is the major region where a remarkable change was detected. A major change in river is also noticed. The increasing river bank was the main cause of devastation of the region. The habitation of Kedarnath, Gaurikund and Rambara was totally washed out.

5. Discussion & Conclusion

In Himalayan region livelihood is directly related to its natural resources. Due to this recur devastation in the region the natural resources has lost to a greater extent. The upper Himalayan region is famous for alpine pastures (a region having rich bio diversity for medicinal and aromatic plants). The hilly region has also been associated with the local tradition and ethical culture. The damage in the region will therefore, will affect the ecological as well as socio-ethno culture of the region. These affect and damage will impact the following as:

5.1. Ecological Damage

The effect of this devastation resulted in ecological damage and further trigger to climate changes that will have significant impact on high-mountain glacial environment. The disturbance in dense mix forest (33.16 ha) and open mixed forest (59.28 ha) clearly indicate a greater loss to ecological cycling. As forests are important natural resources and play a vital role in social, cultural, historical, economic and industrial development of any country and in maintaining its ecological balance. Besides it forests also maintain and improve the moisture regime and provide fresh air and help in nutrient cycling. Floods and perennial streams are moderated by forest. Soil fertility, diversity in climatic and physical setting produces a markedly diverse flora and fauna. Due to this catastrophes (mass wasting, cloud bursts, avalanches) forests have been severely fragmented at many places degraded, causing threat to local extinction to many wild species of plants.

5.2. Climatic Implication/Biomass Loss in the Forest Area

In the present area the biomass estimation study were conducted during 2012 by sampling at ten random plot laid at open and dense forest site. The biomass obtained from that study had shown the 242.24 to 322.97 ton/hac for the mixed forest at the area. The total washed out area from forest was nearly an average 92.44 (open and dense forest). This showed that nearly 22392.66 to 29855.35 tons biomass from the total area is lost at a glance. In natural condition for vegetation growth and

productivity it will take many thousands of years for regeneration. The biomass and thus carbon sequestration process are directly linked to an ecosystem. From the present area the loss in biomass from the available species extinction is a greater loss for the ecological cycle.

5.3. Medicinal and Aromatic Plants Wealth Loss

This region is well known for the medicinal plants wealth. The high altitude areas are the habitats of medicinally important plants due to the varied /or microclimatic condition. The presence of many species according to a survey conducted earlier had shown a greater loss in the region. The plant list present in the area is as follows:

Abies pindrow, *Aconitum balfourii*, *Adhatoda zeylanica*, *Aesculus indica*, *Angelica glauca*, *Artemisia roxburghiana*, *Boehmeria rugulosa*, *Boerhavia diffusa*, *Brugmansia suaveolens*, *Centella asiatica*, *Foeniculum vulgare*, *Geranium nepalense*, *Geranium wallichiana*, *Berginia ciliata*, *Bidens pilosa*, *Berberis aristata*, *Berberis lycium*, *Oberonia falconeri*, *Ocimum tenuiflorum*, *Ajuga lobata*, *Polygonatum multiflorum*, *Polygonatum verticillatum*, *Rosa sericea*, *Satyrium nepalens*, *Sida rhombifolia*, *Stephania glabra*, *Swertia chirayita*, *Taxus baccata*, *Vanda cristata*, *Vitex negundo* etc (Bhatt and Vashishta 2008).

5.4. Cloudburst and Landslide Proximity and Losses

The melting of snow and glacier and heavy rainfall has resulted in the formation and expansion of moraine-dammed lakes, creating a potential danger from dammed lake outburst floods. The heavy rains together with moraine dammed lake (Chorabari Lake) burst caused flooding of Saraswati and Mandakini Rivers in Rudraprayag district of Uttarakhand, completely washed away Gaurikund (1990 m asl), Rambara (2740 m asl) and Kedarnath (3546 m asl) towns. The roads and footpath between Gaurikund and Kedarnath were also damaged. There are reports of loss of large number of human lives and damage to the property and livestock.

5.5. Socio-ethno Damage and Livelihood Insecurity

This region is socio ethnically very rich and thus is considered highly vulnerable to climate change, not only because of high physical exposure to climate-related disasters but also because of the dependency of its economy on climate-sensitive sectors (e.g. agriculture, forests, tourism, animal husbandry, fisheries etc.). The dependency on natural resources is highly conferred to local people. The cloud burst has washed out the forest area to greater extent. These forest areas are rich sources of flora and fauna. Beside it the loss in seasonal snow cover and alpine pastures shows a possibility of extinction of the important medicinal and alpine herb of the area. Their socio-ethnic culture depends on the local surrounding which shows that the loss in this region will negatively affect the people. The effects of Climate change lead by disaster was directly on people in their livelihoods, health, and natural resource security. Poverty, poor infrastructure (roads, electricity, water supply, education and health care services, communication, and irrigation), reliance on subsistence farming and forest products for livelihoods all were affected by this disaster.

Recommendation

The natural regeneration process takes many years for a particular area with many changes. The present day environmental condition and demand for today's need can be fulfilled by knowing and utilizing the today's natural wealth.

References

Bhatt, V.P. and Vashishta, D.P. *Indigenous Plants in Traditional Healthcare System in Kedarnath Valley of Western Himalaya*. Indian Journal of Traditional Knowledge. 2008. 7 (2) 300-310.

Dobhal, D.P., Gupta, A.K., Mehta, M. and Khandelwal, D.D. *Kedarnath Disaster: Facts and Plausible Causes*. *Current Science*. 2013. 105 (2)

Maikhuri, R.K., Nautiyal, S., Rao, K.S., Chandrasekhar, K., Gavali, R. and Saxena, K.G. *Analysis and Resolution of Protected Area-People Conflicts in Nanda Devi Biosphere Reserve*. *Environmental Conservation*. 2000. 27; 43-53.

Maikhuri, R.K., Semwal, R.L., Rao, K.S., Saxena, K.G. and Das, A.K. *Indigenous Techniques of Agricultural Soil Fertility Maintenance in the Central Himalaya*. *Ecol. Environ. Cons.* 2001. 7 (1) 15-20.

Nautiyal, S., Maikhuri, R.K., Rao, K.S. and Saxena, K.G. *Medicinal Plant Resources in Nanda Devi Biosphere Reserve in the Central Himalaya*. *J. Herbs, Species Med. Plants*. 2001. 8, 47-64.

Singh, J.S. and Singh, S.P., 1992: *Forest of Himalaya: Structure, Functioning and Impact of Man*. Gyanodaya Prakashan, Nainital.

Land Use and Land Cover Change Detection for Urban Sprawl Analysis of Ahmedabad City using Multitemporal Landsat Data

Minakshi Goswami and Khire M.V.

Centre of Studies in Resources Engineering, Indian Institute of Technology, Mumbai, Maharashtra, India

Publication Date: 12 April 2016

DOI: <https://doi.org/10.23953/cloud.ijarsg.51>



Copyright © 2016 Minakshi Goswami and Khire M.V. This is an open access article distributed under the **Creative Commons Attribution License**, which permits unrestricted use, distribution, and reproduction in any medium, provided the original work is properly cited.

Abstract Land use and land cover change is the important factor for the urban growth analysis, and because of urban growth the city is sprawling in the haphazard manner. Because of urban growth and urban expansion there is loss of agricultural land and green area and this is directly responsible for the loss of water body. Here Ahmedabad city has taken as case to study the urban expansion and land cover change that took place in a span of 12 years from 1999 to 2009. Remote sensing methodology is adopted to study the geographical land use changes occurred during the study period. Landsat images of TM and ETM+ of Ahmedabad city area are used in this study. After image processing, supervised image classification has been performed to classify the images in to different land use categories. So knowledge about the land use and land cover is very important and useful for the urban planners and the government for preparation of future master plans and to implement these plans in the proper way.

Keywords *Land Use/Land Cover; Urban Sprawl; Urbanization; Remote Sensing*

1. Introduction

Land use land cover is the important factor for the urban expansion and the growth of the city. Land cover change directly affect the environment because of loss of green are and agricultural land the water body also becomes down. The reason behind the change in land cover is also the increase in the population of the city and because of this the city is spreading everywhere in the haphazard way. The transmutation in land cover occurs even in the absence of human activities through natural processes whereas land use change is the manipulation of land cover by human being for multiple purposes- pabulum, fuel wood, timber, fodder, leaf, litter, medicine, raw materials and recreation. So many socio-economic and environmental factors are involved for the vicissitude in land use and land cover. Land use and land cover change has been reviewed from divergent perspectives in order to identify the drivers of land use and land cover change, their process and consequences. Urban magnification, categorically the kineticism of residential and commercial land to rural areas at the periphery of metropolitan areas, has long been considered a designation of regional economic vitality. Geographical information systems (GIS) and remote sensing are well-established information Technologies, whose applications in land and natural resources management are widely apperceived.

Current technologies such as geographical information systems (GIS) and remote sensing provide a cost efficacious and precise alternative to understanding landscape dynamics. Digital change detection techniques predicated on multi-temporal and multi- spectral remotely sensed data have demonstrated a great potential as an expedient to understanding landscape dynamics to detect, identify, map, and monitor differences in land use and land cover patterns over time, irrespective of the causal factors. Recent ameliorations in satellite image quality and availability have made it possible to perform image analysis at much more immensely colossal scale than in the past. The information about the land use and land cover from past and present gives details of the land cover change. All the researchers identified that urban environments are most dynamic in nature. Information on urban growth, land use and land cover change study is very useful to local government and urban planners for the betterment of future plans of sustainable development of any area.

2. Study Area and Objective

The city of Ahmedabad was founded in 1411 AD as a walled city on the eastern bank of the river Sabarmati, now the seventh largest metropolis in India and the largest in the state. The present Ahmedabad City lies between 23.03°N 72.58°E. The city has no main physical feature only Sabarmati River is there and which divides the city into two parts one is walled city means old city and other is new Ahmedabad city which we can see in Figure 1.

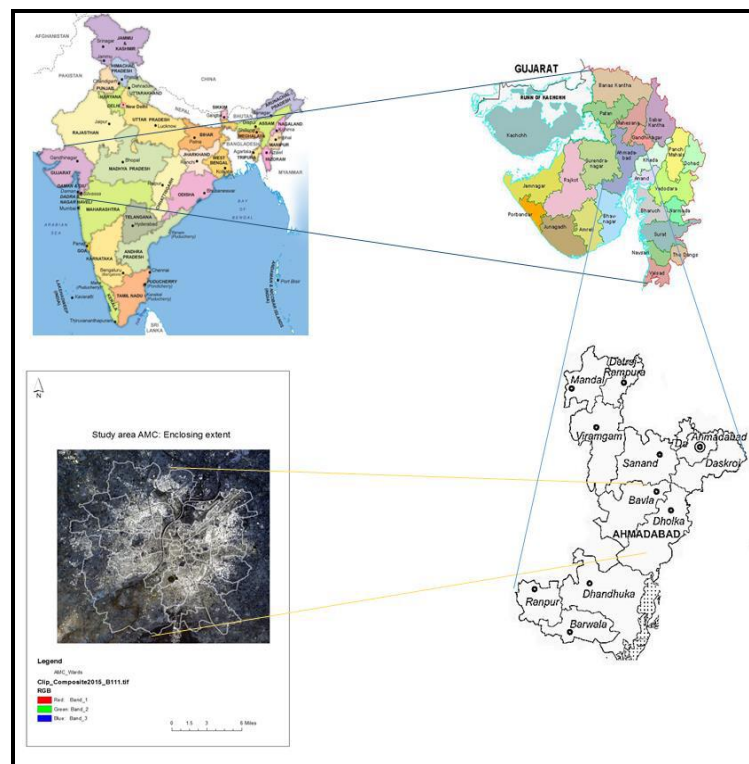


Figure 1: Location of the Study Area

Historically Ahmedabad has been one of the most important centers of trade and commerce in western India. The urban agglomeration (UA) population has increased from 3.31 Million in 1991 to 4.5 million in 2001 and the current population is 5.57 million (census 2011). The area of the city has also accordingly increased and is at present is 464 sq.km. as per Ahmedabad city master plan.

Objective of this study is analysis of the land use pattern and changes of land use pattern in Ahmedabad city between 1999 to 2011.

3. Material and Methods

Land use and Land cover maps is done in ARC GIS 10.1 software. The LU/LC pattern are studied and analyzed to detect the change in urban expansion and urban sprawl. The methodology adopted in detail is shown in the Figure 2.

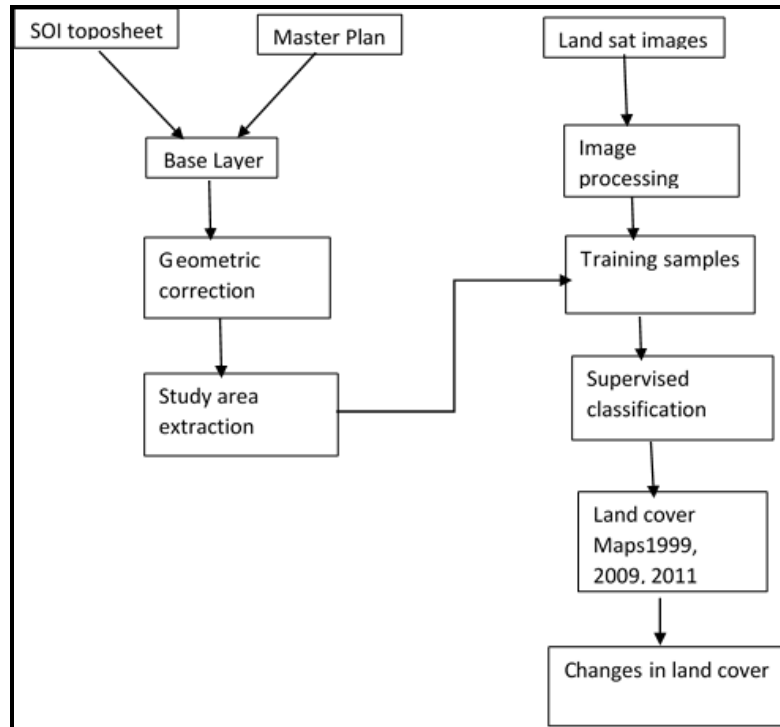


Figure 2: Methodology Chart

3.1. Data and Source

Urban growth was analyzed using temporal remote sensing data of the period 1999 to 2011. The time series spatial data acquired from Land sat look viewer (30m) sensors for the period 1999 to 2011 were downloaded from public domain (landsatlookviewer.org landsat.usgs.gov.in). Survey of India (SOI) topo-sheets of 1:50000 and 1:250000 scales were used to generate base layers of city boundary, etc. City map with ward boundaries were digitized from the Ahmedabad Municipal corporation map. The details of data collected is in Table 1.

Table 1: Details of Data Collected

| Name | Data | Source |
|-----------|--------------------|-----------------|
| Primary | Satellite images | Land Sat 5TM |
| | May 1999,2009,2011 | 30 m resolution |
| Secondary | Master Plan, CDP | AUDA, AMC |

The method involves i) Image analysis of remote sensing data (bands – green, red and NIR). ii) Selection of training samples (iii) loading these training polygons co-ordinates into pre-calibrated GPS, vi) collection of the corresponding attribute data (land use types) for these polygons from the field. GPS helped in locating respective training polygons in the field, iv) supplementing this information with Google Earth v) 60% of the training data has been used for classification, while the balance is used for validation or accuracy assessment. Land use analysis was carried out using supervised pattern classifier Accuracy assessment to evaluate the performance of classifiers (Mitrakis et al., 2008; Ngigi

et al., 2008; Gao and Liu, 2008), was done with the help of field data by testing the statistical significance of a difference, computation of kappa coefficients (Congalton et al., 1983; Sha et al., 2008) and proportion of correctly allocated cases (Gao & Liu, 2008). Recent remote sensing data (2010) was classified using the collected training samples. Statistical assessment of classifier performance based on the performance of spectral classification considering reference pixels is done which include computation of kappa (κ) statistics and overall (producer's and user's) accuracies. For earlier time data, training polygon along with attribute details were compiled from the historical published topographic maps, vegetation maps, revenue maps, etc. Application of maximum likelihood classification method resulted in accuracy of 80% in all the datasets. Land use was computed using the temporal data through ARC GIS. Land use categories include i) area under vegetation (parks, botanical gardens, grass lands such as golf field.), ii) built up (buildings, roads or any paved surface, iii) water bodies (lakes/tanks, sewage treatment tanks), iv.) Non built up barren land.

4. Results and Discussions

The Ahmedabad Urban Development Authority is in charge of land utilize arranging inside of its jurisdictional breaking points. As expressed over, the territory under AUDA might be seen as different subunits relying upon the authoritative jurisdictional cutoff points and degree of advancement. Of this, the region outlined as Ahmedabad Urban Complex comprising of AMC, outgrowth connecting AMC and territory liable to create in the ten years has been assigned as Ahmedabad Urban Complex This AMC city area has been taken for the study of land us land cover changes

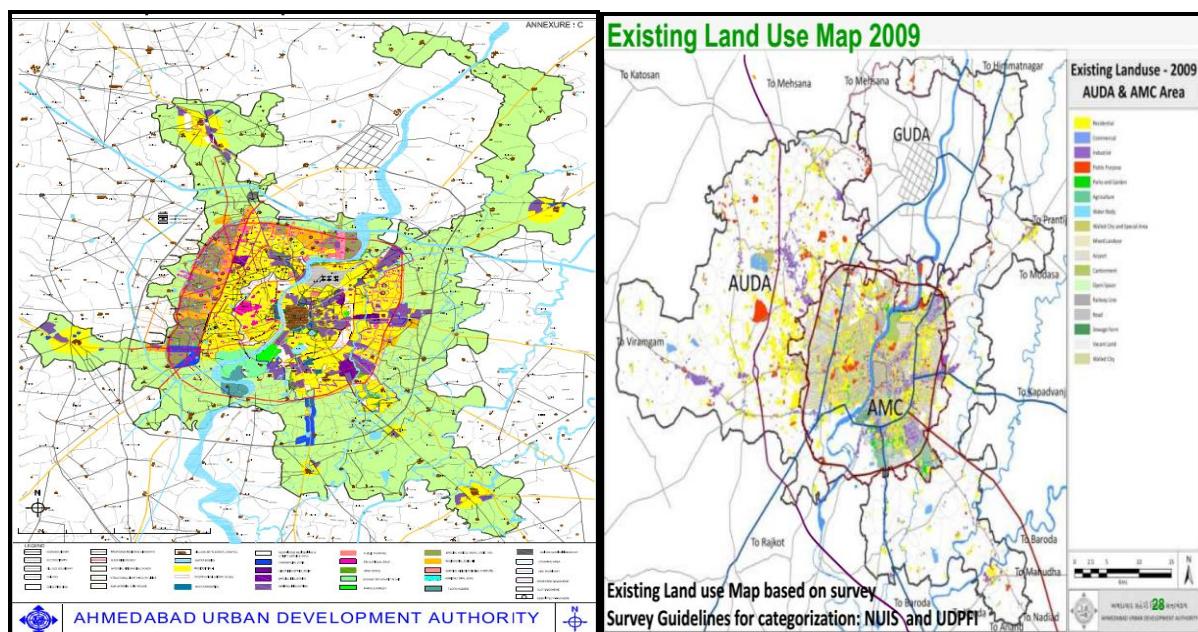


Figure 3: Ahmedabad Urban development Master Plan (2009-2011)

According to the State Government Policy, no major modern improvement inside of 24 kms of AMC point of confinement is allowed in AUDA zone. Considering existing advancement conditions a specific zone for modern utilize is assigned for light industry and in addition for general industry, alongside existing commercial enterprises at Vatwa, Naroda and Odhav (all lying within AMC), which forms nearly 10.38 percent. As per existing land use, more than one third (43%) of the total area is under residential use, followed by 15 percent of the area under the industries (Refer Figure 3).

Table 2: Land use of the AUDA area

| Land uses | Total area (ha.) | % of Total area |
|---|------------------|-----------------|
| Residential | 8340.22 | 43.7 |
| Walled city and village sites | 645.56 | 3.38 |
| General industrial | 2006.51 | 10.51 |
| Special Industrial | 786.72 | 4.12 |
| Commercial | 263.06 | 1.38 |
| Agricultural/recreational/open space | 1643.6 | 8.61 |
| Education | 387.3 | 2.03 |
| Area reserved | 1955.37 | 10.25 |
| Roads & highways | 2117.67 | 11.1 |
| water body | 937.97 | 4.92 |
| Total area | 19084 | 100 |

Information on land use - land cover pattern, especially the extent and spatial distribution of the same is important for the preparation of the prospective Development Plan. The land use - land cover information helps in formulation of policies for urban development and to know the growth pattern of city. Using the classification system and employing both visual and digital analysis techniques and with limited field checks, the urban land use/land cover maps were prepared for the entire city region.

The classified images obtained after preprocessing and supervised classification which are showing the land use and land cover of the Ahmedabad city are given in the following Figures 5, 6 and 7. These images provide the information about the land use pattern of the study area. The yellow colour represents the urban built-up area, dark green colour shows the vegetation, blue colour shows the water bodies and tan color shows the Non built up barren land. Land cover map is also superimposed with the master plan map with the Google images which helps in accuracy checking in Figure 8.

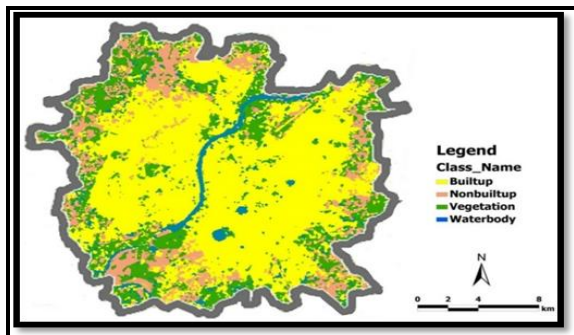


Figure 5: LU/LC Classified Image of 1999

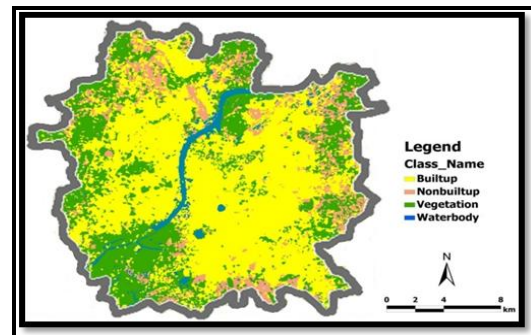


Figure 6: LU/LC Classified Image of 2009

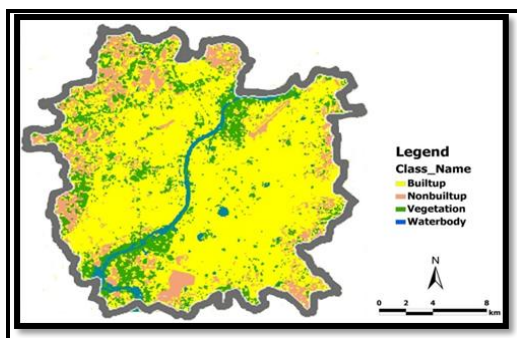


Figure 7: LU/LC Classified Image of 2011

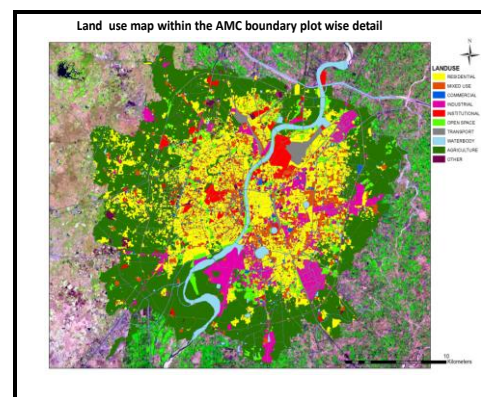


Figure 8: Land Use Map within AMC Boundary

4.1. Classification Accuracy Assessment

Each of the land use and land cover map was compared to the reference data to assess the accuracy of the classification. The reference data was prepared by considering random sample points, the field knowledge and Google earth. During the field visits a hand held GPS (Global Positioning System) is used to identify the exact position of the place under consideration with Latitude and Longitude and its type by visual observation. The ground truth data so obtained was used to verify the classification accuracy. Over all classification accuracy for 1999, 2009, and 2011 are 86%, 88% and 90% respectively. The Kappa coefficient for 1999, 2009, and images are 0.88, 0.79 and 0.81 respectively.

4.2. Change Detection Analysis

The urban change analysis presented in this paper was based on the statistics extracted from the four land use and land cover maps of the Ahmedabad city. The changes in land cover during the study period (four dates) can be observed clearly from the pie diagrams shown in Figure 9 to Figure 12.

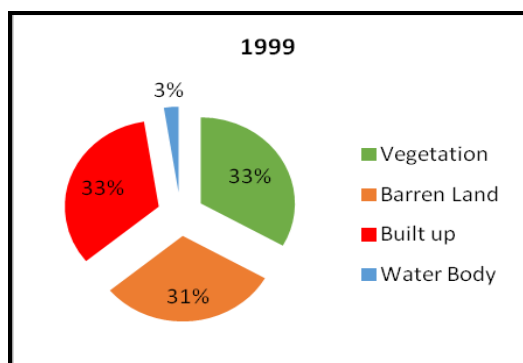


Figure 9: Land cover in 1999

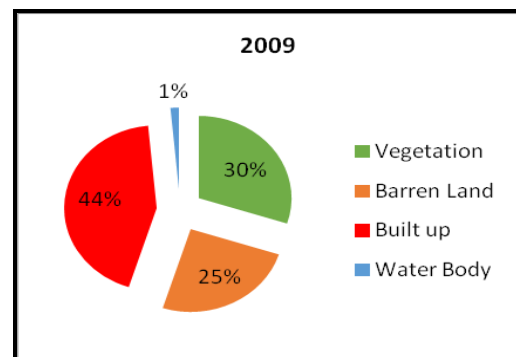


Figure 10: Land cover in 2009

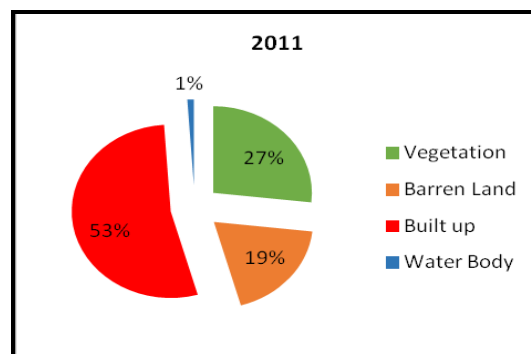
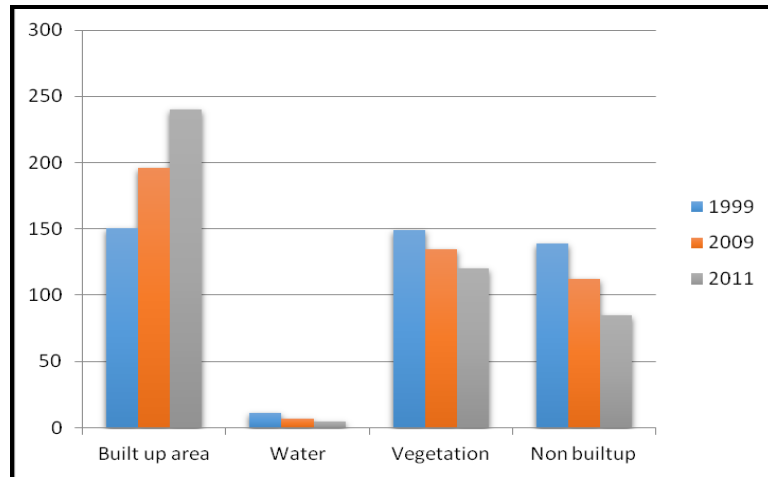


Figure 11: Land Cover in 2011

The built-up area as well as vegetation area has been changed drastically from 1999 to 2011. Built-up area has been increased by 22.51%, Vegetation has been decreased by 28.19% and barren area reduced by 24.26% the increase in built-up area has many reasons. Ahmedabad is famous for manufacturing industries, large numbers of industries are coming in to existence and corresponding infrastructure development leads to the increase of built-up area. Increase in institutional establishments and low cost housing are contributing to the loss of agriculture. There is a decrease in water body also by 28% over the study period. It was observed that real estate development is taking place along the Sabarmati river, because of that river water level got decreased and many chemical industries dumping their waste into the river. The results of change detection analysis are presented in the Table 3.

Table 3: Land Use Changes Matrix of Ahmedabad City (1999-2011)

| Class | Area in Sq.km | | | Changes in Percentage Area | |
|----------------------|---------------|--------|--------|----------------------------|-----------|
| | 1999 | 2009 | 2011 | 1999-2009 | 2009-2011 |
| Built up area | 150.42 | 196.05 | 240.19 | 30.33506 | 22.51466 |
| Water | 11.26 | 6.713 | 4.82 | -40.3819 | -28.199 |
| Vegetation | 149.25 | 134.64 | 120.53 | -9.78894 | -10.4798 |
| Non built-up | 138.82 | 112.13 | 84.92 | -19.2263 | -24.2665 |

**Figure 12:** Land Cover Changes (1999-2011)

The proportion of land-use changes especially the percentage built-up area, which is a key metric to measure sprawl, were estimated across all the Ahmedabad Municipal corporation area. The corresponding land-use changes within the AMC region are shown in Table 2. It was clearly evident that on an average the increase in built-up area from 33% to 53%, decrease in vegetation area from 33% to 27%. Growth of the built up area in the outer region of the city in 2009, towards North (Gota and Gandhinagar) and East Changodar and Sanand. Growth of the built up area in the outer region of the city in 2011, towards West (Ogani) and south East (Vatva). So it shows the increase in the urban area of the city from all the directions. North side city is growing because of Gandhinagar city and all the government and IT industries are situated there. The development along West side is due to the large number of manufacturing industries along this corridor specially Sanand Tata nano plant, and South east is due to the location of existing industrial estate Vatwa and Odhav.

5. Conclusions

Ahmedabad is the largest city and former capital of Gujarat. With a population of more than 6.3 million and an extended population of 7.2 million, it is the sixth largest city and seventh largest metropolitan area of India. Ahmedabad is located on the banks of the Sabarmati River, 30 km from the state capital Gandhinagar. It is experiencing a rapid urbanization. The urban sprawl is seen as one of the potential threats to sustainable development. This study attempted to identify such urban sprawls change for 1999-2011. Information on land use/land cover and possibilities for their optimal use is essential for the selection, planning and implementation of land use schemes to meet the increasing demands for basic human needs and welfare. This information also assists in monitoring the dynamics of land use resulting out of changing demands of increasing population.

References

Ahmedabad Urban Development Authority, City Development Plan (2006-12) and (2011-2021).

Congalton, R.G., Oderwald, R.G., and Mead, R.A. *Assessing Landsat Classification Accuracy using Discrete Multivariate Analysis Statistical Techniques*. Photogrammetric Engineering and Remote Sensing. 1983. 49; 1671-1678.

Gao Y. Liu. *Mapping Land Degradation from Space: A Comparative Study of Landsat ETM+ and ASTER Data*. International Journal of Remote Sensing. 2008. 29; 4029-4043.

Mitrakis, N.E., Topalogou, C.A., Alexandridis, T.K., Theocharis, J.B., Zalidis, G.C. *A Novel Self Organising Neuro-Fuzzy Multilayered Classifier for Land Cover Classification of a VHR Image*. International Journal of Remote Sensing. 2008. 29; 4061-4087.

Sudhira, H.S., Ramachandra, T.V., Wytzisk, A., and Jeganathan, C., 2005: *Framework for Integration of Cellular Automata and Agent-based Models for Simulating Urban Sprawl Dynamics*. CES Technical Report No. 100. Bangalore, India: Centre for Ecological Sciences, Indian Institute of Science, Bangalore.

Analysis of Land Use/Land Cover Changes Using Remote Sensing and GIS Techniques in Parbhani City, Maharashtra, India

Nayana S. Ratnaparkhi¹, Ajay D. Nagne² and Bharti Gawali²

¹D.S.M. Art's, Communication and Science College, Jintur, Maharashtra, India

²Department of Computer Science & Information Technology, Dr. Babasaheb Ambedkar Marathwada University Aurangabad, Maharashtra, India

Publication Date: 30 April 2016

DOI: <https://doi.org/10.23953/cloud.ijarsg.54>



Copyright © 2016 Nayana S. Ratnaparkhi, Ajay D. Nagne and Bharti Gawali. This is an open access article distributed under the **Creative Commons Attribution License**, which permits unrestricted use, distribution, and reproduction in any medium, provided the original work is properly cited.

Abstract Land use and land cover is an important factor in understanding the relations of human activities with the environment and thus is necessary to be able to simulate change. The focus of this paper is to map and study the land use and land cover pattern and change among 2002 and 2013 satellite imagery. It also produces a land use land cover maps of Parbhani city in Maharashtra at two epochs in order to detect the changes that take place in the diverse natural resources. After analysis of the image, supervised maximum likelihood algorithm was used to classify the imagery into different land use categories. Five land use classes have been recognized as vegetation, fallow land, barren land, residential area, and water body. The classification of image shows major change in residential areas. The change detection analysis shows that residential area in 2002 is 7.34 % and 14.25 % in 2013, it has been enlarged by 7.11 % similarly change detection for remaining areas has been done. The information on urban growth, land use land cover change study is extremely useful to local government and urban planners for the betterment for future plans of sustainable progress of the city.

Keywords GIS; LULC; LISS-III; LISS-IV; NRSC; Remote Sensing

1. Introduction

The land use/land cover of a region is a conclusion of natural and socio-economic factors and their consumption by man in time and space [1]. The term "land use" and "land cover" are often used simultaneously to depict maps that afford information about the types of features existing on the Earth's surface. Land cover refers to the physical individuality of Earth's surface, which is captured by vegetation, soil, water bodies and other physical features of the land. Land use refers to the way in which land has been used by humans and their habitat, usually for economic activities [2]. Land cover is an important input constraint for a number of agricultural, ecological models, which compose necessary tools for enlargement planning and management of natural resources in the area. To use land optimally, it is necessary to have information not only on existing land use/ land cover but also the capability to monitor the dynamics of land use resulting out of changing demands. If the area is small then land cover is based on ground surveillance and survey. However, if the area is large, then such

method are found to be less realistic [3]. In earlier study toposheet, censuses, demographic data may be used for reference but are not sufficient for the analysis of multi-complex environmental study. To handle multidisciplinary data set, we require new technologies like Satellite remote sensing and geographical information system [4].

Remote sensing has become an important tool appropriate to rising and understanding the global, physical processes affecting the Earth. Use of satellite data is to take advantage of increasing amounts of geographical data available in combination with GIS to aid in an interpretation. Digital change detection technique based on multi-temporal and multispectral remotely sensed data have been used to understand landscape dynamics to detect, identify, map and monitor difference in land use land cover pattern over time [5]. The basic principle in using satellite images for change detection is that changes in land cover result in changes in radiance values that can be remotely sensed. A wide variety of digital change detection techniques have been developed over the last two decades. These include mono-temporal, post classification comparison or change delineation, image differencing, image ratioing, change vector analysis, image regression, multi-temporal biomass index and background subtraction, digitization etc. Along all these methods, the post classification method is most widely used for change detection. This approach classifies and labels two images from different periods [2002 and 2013]. Such monitoring technique is based on multi-temporal satellite data. The area of change is considered through direct comparison of the classification results. The accuracy of the investigation depends upon accuracy of the classification of individual images [6] [7] [8].

The main objective of this paper is to notice and analyze the land use / land cover of Parbhani city between 2002 and 2013 using satellite imagery. The study also views the implementation of image processing and statistical techniques for the analysis of LULC in view of change detection changes that have taken place in LULC of study area. The paper uses remote sensing and geographic information system approach for the recognition, measurement and analysis of LULC changes in the study area.

2. Study Area

The selected study area was Parbhani city in Marathwada region of Maharashtra State of India shown in Figure 1. It is located between latitude 19.30'N and 19.50'N and longitude 76.45'E and 76.75'E. Parbhani district occupies an area about 6,511.58 km² and has population 1,835,982 in 2011 and 1,527,715 in 2001. The Population growth rate over the decades 2001-2011 was 20.18% [09].



Figure 1: Parbhani District: A Study Area

3. Methodology

To recognize the change detection between LISS III image of December 2002 and LISS IV Image of December 2013. The data have been collected from the National Remote Sensing Centre (NRSC) Hyderabad. Figure 2 shows a detailed Methodology. LISS III Image has the Spatial Resolution of 23.5 m and LISS IV image having 5.8 m Spatial Resolution. The selection of the images was constrained to similar season to avoid seasonal differences. Multispectral and multi-temporal images were chosen because they enclosed the period of intended study and their resolutions are suitable for classification of images. The land cover maps are executed only for these images.

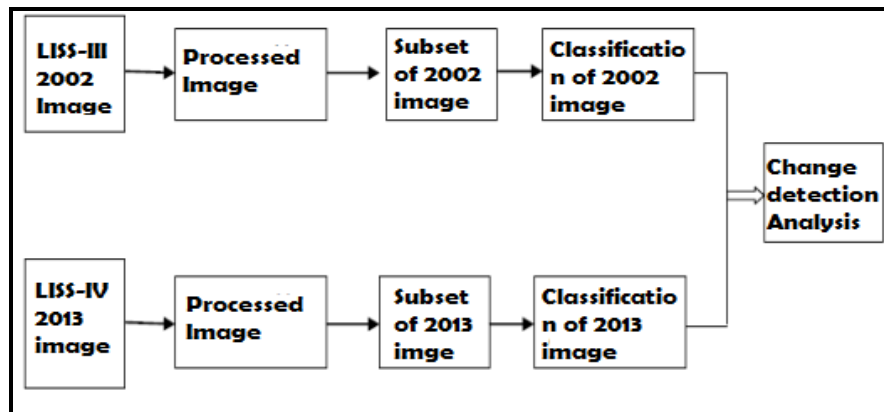


Figure 2: Experimental Workflow for Change Detection Analysis of Study Area

3.1. Pre-Processing of Images

In the analysis of imagery, the image pre-processing was carried out. Each pre-processing of an image consists of restoration and rectification of an image. The downloaded image LISS-IV Dec. 2013 contains image stacking, scenes mosaicking, and subsetting of the image and was done to get essential study area. The base layer so formed is used to subset of images. To position ground features of an image, image enhancement and extraction was used. Similarly LISS-III DEC. 2002 imagery contains four bands. To get composite image, image stacking is made in ENVI software.

3.1.1. Sub Setting and Mosaicking

Many times we do not interpret whole area of satellite image; we only interpret certain areas of the satellite image. In these cases the part we are interested in should be cut from the whole image to reduce the speed and size of an image and improve the reliability of the calculations. This cutting of an image has many names depending on the software: cut, clip (ArcGIS), extract (ArcGIS), subset (ERDAS), etc. Subset is the term used by ERDAS Imagine, satellite-image interpreting software. Subsetting can be done in most software programs by giving coordinates, i.e. in the case of a square sub-settable part, the coordinates of two opposite corners or by drawing a polygon over the area of the image you are interested in and using that for sub-setting.

Images in the same co-ordinate system can be drawn correctly positioned to each other based on their coordinates by most GIS software's. Images of adjacent areas will appear next to each other and can be saved as one large image. This is the process of mosaicking. Mosaicking does not only mean putting the images next to each other. Mosaicking is one of the techniques of image processing which is helpful for tiling digital images. Mosaicking is blending together of several randomly balanced image so that the boundaries between original images are not seen. Any number of geo-coded images can be blended together along use specified cut lines (polygons). Mosaicking is special case of geometric correction where registration takes place in the existing image [10].

3.1.2. Layer Stacking

Several types of measurement may be made from the ground area enclosed by a single pixel. Each type of measurement forms an image which carries some specific information about the area. By “stacking” these images from the same area together, a multilayer image is formed. Each component image is a layer in the multilayer image. Stacking is a process of combining in layers the bands required for various types of studies into a single output file [11].

3.2. Land Cover Image Classification

Image classification is the process of assigning pixels of continuous raster image to pre-defined land cover classes. The land cover classes generated were Residential Area, Fallow land, Water bodies, Vegetation. The classification gives the land use / land cover image of the area. Table 1 show the nomenclature used for the land covers.

Table 1: Land Covers Nomenclature

| Sr No. | LULC Classes | Colors Assign to Classes |
|--------|--------------|--------------------------|
| 1. | Water Bodies | Blue |
| 2. | Vegetation | Green |
| 3. | Barren Land | Yellow |
| 4. | Fallow land | Red |
| 5. | Residential | Magenta |

The result of Classification affected by the values of input images, classification methods, algorithm etc. To increase classification accuracy selection of appropriate classification method is necessary. Image classification is performing to recognize and allocate real world thematic classes to the image pixels. In this study image classification was done by performing supervised maximum likelihood classification method and classified image is shown in Figure 3. The maximum likelihood classification algorithm was chosen because it has the capability to incorporate the statistics of the training samples before conveying the land covers to each pixel. The training data given by the user tells the software, that what types of pixels are to be selected for certain land cover type.

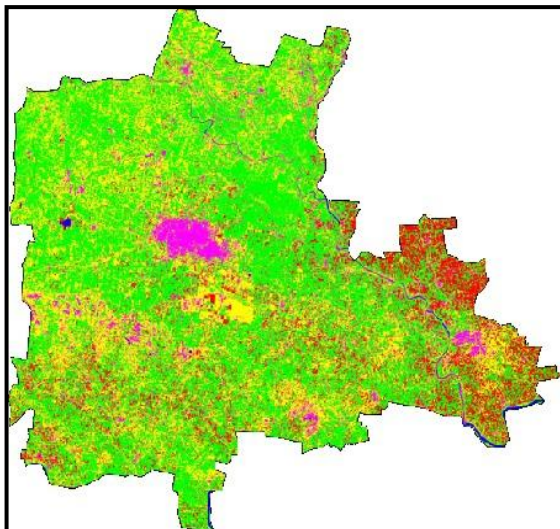


Figure 3: LISS-III 2002 Image Classification

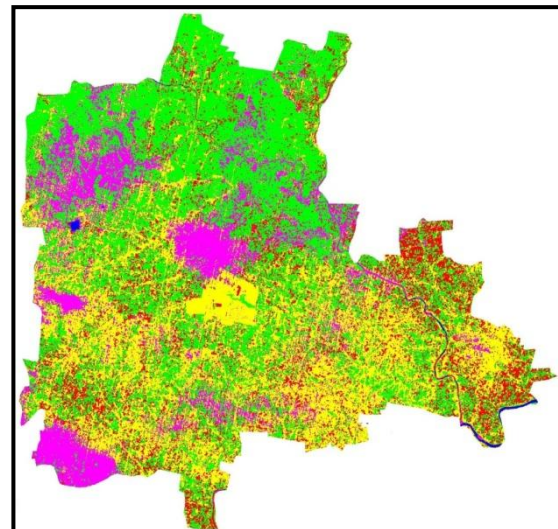


Figure 4: LISS-IV 2013 Image Classification

3.3. Change Detection Analysis

Change detection analysis describes and quantifies difference among imagery of the same scene at different epoch. The process of change detection depends on the phenomenon or scene at different times. The change detection process adopted for this study is the post feature under investigation. This is because the method is simple to implement and it provide thorough “from to” statistics suitable for decision making. The method was executed by using the two land cover maps generated for 2002 and 2013. The outcome was a land cover change map from 2002 and 2013. Table 2 shows the statistical analysis of change detection of both the imagery.

Table 2: Land Covers Statistics Using Maximum Likelihood Classification

| Class Name | 2002 Area in % | 2013 Area in % | Change Area In % |
|-------------|-------------------|-------------------|---------------------|
| Water Body | 0.34 | 0.24 | -0.10 |
| Vegetation | 46.94 | 39.26 | -7.68 |
| Barren Land | 34.91 | 31.82 | -3.09 |
| Fallow_Land | 10.47 | 14.23 | 3.76 |
| Residential | 7.34 | 14.45 | 7.11 |

Percentage of each class was calculated separately for each class of both the images. The statistical calculation of the classes is as follows:

Area in Percentage = $\text{Category} * 100 / (\text{Sum of area of all number of points})$ where category assign each individual class of the image

The Table 2 shows positive and negative changes. The positive changes showed that there is increase in particular area and negative changes showed that there are decreased in particular area.

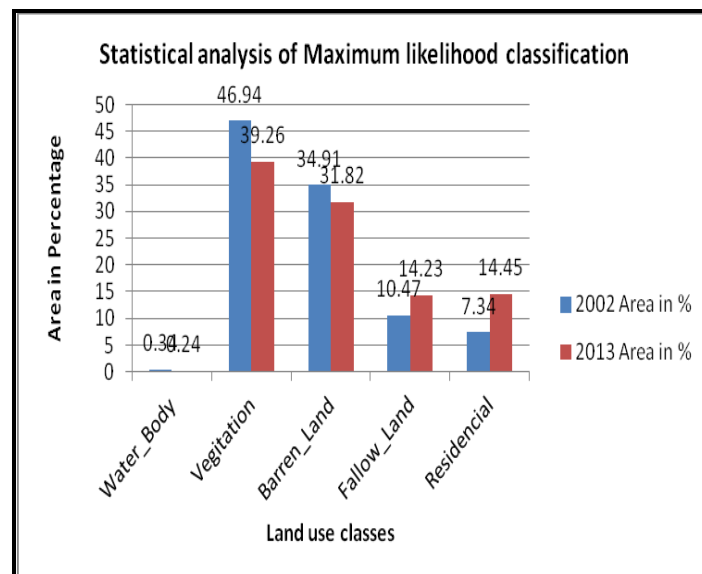


Figure 5: Statistical Analysis of Maximum Likelihood Classification

4. Results and Discussion

Land use and land cover of the study area have been analyzed for the time periods of 2002 and 2013. The results are presented in the form of maps, charts and statistical tables. The result of the land use/land cover change was analyzed using post classification approach which is based on a supervised maximum likelihood classification method. Statistical means prove that there were positive as well as negative changes in LULC classification. The post classification map indicates the city originally evolved in oval shape from the centre. An estimation area of each classified LULC type or surface was complete on the basis of the number of accessible pixels. The statistical analysis shows that water body is decrease by -0.10 %. Water body includes lakes, reservoirs, ponds, rivers and streams. Water body area in 2002 is 0.34 % and in 2013 it is 0.20 %. The area was decreased due to less rain fall and alteration of water spread area into built up area or human development area. Vegetation area was also decreased by -7.68 % during the study period. As shown in table 2 residential area was increased by 7.11 %. Such urban expansion was takes place due to expenses of barren land and vegetation. There are several factors that include directly and indirectly caused substantial changes to Parbhani LULC such as population increase is a major one. Colonization for employment and better living opportunities is another factor that has contributed in increasing urban growth. The study area is surrounded by number of small villages so that to get better educational facility many rural peoples migrate in the city place.

5. Conclusion

The current study aims to investigate land use/land cover change that occurred in Parbhani city during 2002 and 2013 using remote sensing and GIS. The study of land use and land cover classification establish the fact that the accurate land use data can be obtained from the satellite imagery more resourcefully and precisely than traditional methods. By using image processing techniques, the different land use classes are analyzed and mapped easily. The land use category compares with 2002 and 2013; it shows that there is expansion in residential area (7.11%). The increase in the area under residential land may lead to a lot of environmental and ecological problem. Water body and vegetation area were decreased due to less rain fall. The land use and land cover changes are important elements of the larger problem of global and regional environmental changes. Land use and land cover data is essential for planners, decision makers and those concerned with land resource management. Monitoring and analyzing of urban environment formulate use of up-to-date land use and land cover information for capable and sustainable management of urban areas. Change detection techniques with temporal remote sensing data provide complete information to detect and assess land use dynamics.

References

- [1] Tiwari Kuldeep and Khanduri Kamlesh. *Land Use/Land Cover Change Detection in Doon Valley, Uttarakhand: using GIS and Remote Sensing Technique*. International Journal of Geomatics and Geosciences.2011.2 (1).
- [2] Ramchandra, T.V. and Uttam Kumar, 2004: *Geographic Resources Decision Support System for Land Use, Land Cover Dynamics Analysis*. Proceeding of FOSS/GRASS User Conference, Bangkok, Thailand, 12-14 Sep.
- [3] Monalisa Mishra, Kamalkant Mishra, and Subadhi, A. *Urban Sprawl Mapping and Land Use Change Analysis using Remote Sensing and GIS*.
<http://www.geospatialworldforum.org/2011/proceeding/pdf/Monalisha.pdf>

- [4] Praveen Kumar Malluattu, Jayarama Reddy and Sreeniasula Reddy. *Analysis of Land Use/Land Cover Changes Using Remote Sensing Data and GIS at an Urban Area*. The Scientific World Journal. 2013. 6.
- [5] Harika, M., Aspiya Begum, S.K., and Yamini, S. *Land Use/Land Cover Change Detection and Urban Sprawl Analysis*. International Journal of Advanced Scientific Research and Technology. 2006. 2 (2)
- [6] Aduah, M.S. and Baffoe, P.E. *Remote Sensing for Mapping Land-Use/Cover Changes and Urban Sprawl*. The International Journal of Engineering and Science. 2013. 2 (10) 66-73.
- [7] Jay Gao, 2009: *Digital Analysis of Remotely Sensed Imagery*. The McGraw-Hill Companies.
- [8] Punyatoya Patra. *Remote Sensing and Geographical Information System (GIS)*. The Association for Geographical Studies.
- [9] Nayana, S. Ratnaparkhi, Ajay D. Nagne, and Bharti Gawali. *A Land Use Land Cover Classification System Using Remote Sensing Data*. International Journal of Scientific & Engineering Research. 2014. 5 (7)
- [10] Chen, D.M. and Rogan, J. *Remote Sensing Technology for Mapping and Monitoring Land Cover and Land Use Change*. Progress in Planning. 2004. 61 (4) 301-325.
- [11] Aruna Saxena, Manish K. Tiwari and Vivek Katara. *Mapping and Evaluation of Urban Sprawl using an Integrated Approach of Remote Sensing and GIS Techniques*. 2012 2 (1) 22-29.
- [12] Singh, A. *Review Article Digital Change Detection Techniques using Remotely Sensed Data*. International Journal of RS. 1989. 10 (6) 989-1003.
- [13] Lu. D., Mausel, P., Brondizio, E. and Moran, E. *Change Detection Techniques*. International Journal of Remote Sensing. 2004. 25 (12) 2365-2401.
- [14] Abdullah F. Al Qurashi and Lalit Kumar. *A Review, Investigation the use of Remote Sensing and GIS Techniques to Detect LULC Change*. Advances in Remote Sensing. 2013. 2; 193-204.
- [15] Alfredo Huete and Emilio Chuvieco, 2009: *Fundamentals of Satellite Remote Sensing*. CRC Press Textbook. 448.
- [16] Ernest E. Hardy, James R. Anderson, John T. Roach and Richard E. Witmer. *A Land Use and Land Cover Classification System for use with Remote Sensor Data*. U.S. Geological Survey Circular 671. Professional Paper 964.
- [17] A Canada Center for Remote Sensing Tutorial. *Fundamental of Remote Sensing*. <http://pcmas1.ccrs.nrcan.gc.ca/fundamental/258>
- [18] Mahesh Kumar Jat, Garg, P.K. and Deepak Khare. *Monitoring and Modeling of Urban Sprawl Using Remote Sensing and GIS Technique*. International Journal of Applied Earth Observation and Geoinformation. 2008. 10 (1) 26-43.

Representation of Geochemical Data in Geospatial Domain

Ashok Kumar Joshi¹ and Sisodiya D.S.²

¹Regional Remote Sensing Centre, NRSC, Dept. of Space, ISRO, Nagpur, Maharashtra, India

²Geological Survey of India, Central Region, Nagpur, Maharashtra, India

Publication Date: 16 August 2016

DOI: <https://doi.org/10.23953/cloud.ijarsg.66>



Copyright © 2016 Ashok Kumar Joshi and Sisodiya D.S. This is an open access article distributed under the **Creative Commons Attribution License**, which permits unrestricted use, distribution, and reproduction in any medium, provided the original work is properly cited.

Abstract Geochemical surveys are integral part of systematic geological survey to cover mineral provinces and geological basin. These surveys have indicated new mineral occurrences in different geological terrains. Large amount of data collected in the field is finally submitted as report in the hard copy format as part of the annual field survey plan. It takes many years to complete the geochemical survey of a geological basin by several parties working on different aspects. Geographical Information System (GIS) facilitates input, editing and display of spatial data collected in various forms (location, traverses, and boundaries) and analyse in most efficient way. However, large amount of geochemical data collected from various sources poses several challenges to represent and analyse the data in a meaningful way. This paper addresses all such difficulties in handling unformatted inputs and most optimal method for display, analysis and integration of geological data from various sources.

Keywords *Geochemical Exploration; GIS; Remote Sensing; Sakoli Basin*

1. Introduction

Geological mapping of mineral belts is carried out to suggest potential zones for further detailed exploration using geophysical and geochemical methods. Systematic geochemical sampling is carried out depending upon the type of mineralization and its extent. Organizations world over are also involved in collection of rocks samples for geochemical assessments at regional scale. Geochemical mapping has been successfully used as a tool to target mineral deposits in geologically diverse environments.

Geochemical data collected in the field is contoured and geochemical patterns are compared with geological map to locate probable anomalies. With increasing data volume and parameters being collected, representation of the datasets has been attempted in different ways (Bjorklund and Gustavasson, 1987). Innovative techniques of computer database structure and analysis termed as 'Data Mining' has been employed by Grunsky, 2007, emphasizing the role of multi-variate geo-statistical techniques in identification of geochemical anomalies. These techniques have been successfully employed in different parts of the world (Sisodiya, 1993; Sisodiya & Joshi, 2002; Samal et al., 2011; El-Makky and Sediek, 2012; Yilmaz et al., 2015). New techniques of data processing such as fractal analysis and fry analysis have been tested over known mineral deposits (Carranza, 2009).

Under various programmes of the government institutions in the world a repository of geochemical data has been created for geo-environmental studies to advice local governments over anomalous metal concentrations in some areas (Darnley et al., 1985; Timo, 1996).

Initially most of the surveys were carried out to detect a metal anomaly over a potential target; however, today most of the geochemical surveys are done to identify multi-metal anomalies over the large mineral provinces. Few geochemical surveys are also carried out to delineate the source of environmental degradation due to natural or man-made features.

Data collected through geochemical surveys over the years are sometime too voluminous to be analysed using simple tools. Visualization of these data to derive any inference becomes a challenge at times while studying geological basins on 1:50,000 scale. Multi-metal/temporal data collected from different sources presents many challenges in analyses of these data. Traditional way of representing these data is by graphs and grids which results in loss of spatial information and its comparison with other available maps.

With the availability of Geographic Information System (GIS) it is now possible to preserve the spatial relationship of the geochemical data collected over the years and with different parameters, however optimally representing the data and modeling is still a challenge to the geologists. A large amount of spatial maps/data are available from various sources which needs integration in a GIS. Several demonstrative studies have been carried out in a limited way over small regions however studies covering geological/mineral basin/province are rare.

Importing large amount of geochemical data into a GIS poses several challenges in terms of their positional accuracy, calibration, formatting and validation which takes away most of the project time. Today with much awareness about geomatic tools and techniques the data can be collected and imported into a GIS using defined templates very easily and analysed in a shorter time.

A demonstrative study has been carried out for Sakoli Basin in Central India involving large amount of geochemical data collected through stream sediments and bedrock samples during several field seasons toposheets-wise by various teams of Geological Survey of India. Chemical analyses data later has been appended for each sample analysed for Cu, Pb, Zn, Ni & Co; and analysed. An approach for representation of complex geochemical data along with other thematic maps has been demonstrated for deriving the inference on geochemical anomalies in a given geological basin/province.

2. Study Area

The area of study includes rocks of Sakoli Fold Belt (SFB) and adjacent gneisses of Nagpur, Bhandara and Gadchiroli districts of Maharashtra, in Central India (Figure 1). The area is bounded between latitude 20°25' N and 21°33'N and longitude 79°20'E and 80°10'E. Geographically the area spreads in a total of 13 Survey of India toposheets (55 O/8, 12, 15 & 16; 55P/5, 9, 13 & 14; 64C/3 & 4; 64D/1, 2 & 3.) on 1:50,000 scale.

3. Database

The core of the spatial database is geochemical data. Systematic geochemical surveys in the Sakoli Basin by stream sediment and bed rock sampling over 4060 sq km resulted in collection of a total of 11,491 samples (7815 Nos. of stream sediment and 3676 Nos. of bed rock) which have been analysed by Atomic Absorption Spectrometer for Cu, Pb, Zn, Ni & Co generating about 57,455 items of analytical data. Other spatial database includes lithology, structure, mineral map, gravity, geomorphology, drainage, slope, elevations, roads & settlements. IRS LISS-III satellite data was used

as image base to correct, update and refine vectorized thematic maps such as drainage, water body, roads, settlements etc.

Since most of the thematic database was in hard copy maps, all the maps were converted into softcopy, digitized and coded in a GIS database depending upon point, line and polygon features. In case of geochemical maps, the sample locations were digitized from the toposheets and were numbered using a standardised procedure maintaining the unique number for each location throughout the basin. Accordingly these unique numbers were also generated in the analytical attribute database. Unique number assigned was used to retrieve the geochemical value of respective metal for each sample location. Data for sample locations with metal values are treated separately for stream sediments and bedrock and GIS database was generated for further analysis.

3.1. Creation of Attribute Database

The availability of enormous amount of geochemical data collected over the Sakoli Basin has been compiled as analytical attribute database in commercially available GIS SW. The database contained field sample number, field season, toposheet number, rock description (in case of bedrock), metal content in ppm, and block name. This data was available in different files with inconsistencies in format. As a first step to rectify all the errors, all the database files are imported into common tabular format and corrected. A unique new code was given to each sample location for stream sediment and bedrock. The cartographic coordinates of each sample location with unique number were extracted from the point coverages (geospatial thematic database) of stream sediment and bedrock files. Using unique number the analytical data from the tabular sheet were appended with x, y locations derived from the coverage. Thus an analytical attribute database was generated with 11,491 records with 57,455 items of analytical data with geographic coordinates.

To ensure correctness of point data with geological and drainage map a proximity analysis was run and marginal errors in point location corrected. Also an error check was run on the values of various elements to ensure that the data falls in defined data bounds.

3.2. Representation of Geochemical Data

Geochemical Maps

The geochemical maps show distinct chemical concentration pattern that can be correlated with geological features, and the zones with higher metal abundance can be targeted for probable mineral deposit.

The geochemical map in this project has been prepared based on the dispersion of various metals in the stream sediments collected from first and second order drainage and also from bedrock samples. Separate point coverages have been prepared for each metal in stream sediments and bedrock samples. For better representation of geochemical data different methods have been adopted. Maps have been generated for stream sediments and bedrock separately to represent one or more metals at a time. A brief description of the methodology adopted is given in the following text.

Stream Sediments

As a first step the analytical data of stream sediments has been subjected to statistical analysis and based on standard deviation of the metal content in ppm a threshold has been calculated for each of the metal. The results of statistical analysis are given below:

Table 1: (n=7815, metal values in ppm)

| Serial No. | Element | Minimum | Maximum | Mean | Standard Deviation | Threshold Value |
|------------|---------|---------|---------|-------|--------------------|-----------------|
| 1 | Copper | 5 | 500 | 32.27 | 27.73 | 87.73 |
| 2 | Lead | 5 | 500 | 22.00 | 19.69 | 61.38 |
| 3 | Zinc | 5 | 500 | 36.52 | 34.76 | 106.04 |
| 4 | Nickel | 5 | 250 | 36.68 | 23.68 | 84.08 |
| 5 | Cobalt | 5 | 450 | 21.98 | 21.25 | 64.48 |

(Very high anomalous values were excluded from statistical treatment)

The number of stream sediment samples is very high and due to this high density of points they could not be represented with appropriate markers in the map. For better representation the metal values in ppm stream sediment data were contoured. For contouring the data, various methods of interpolation have been used and spatial maps generated.

The first procedure involved contouring the points using TIN (Triangular Irregular Network) module with various options and then smoothening the output. Such outputs have very angular contour lines and large number of contour lines around a high or low value.

Another procedure involved converting the TIN output to lattice and then applying low-pass filters to the grid. This resulted in smoother contour lines and were also matching with the point data.

The last procedure involved contouring using TOPOGRID (ARC/Info) module which generated an output matching the real world situation using drainage maps and watersheds. This method can be employed with different options and constraints; and that is why a better contour map could be produced. Care shall be exercised while contouring the stream sediment sample data across the ridge line/watershed divide. A high value on the other side of the ridge can greatly influence the contour value and will depict a misplaced/displaced anomaly. Many other statistical techniques can also be employed for contour interpolation, however care shall be exercised that most of the input values are justified in the interpolated surface.

The contours from the interpolated surface have been calculated for an interval of 20 ppm for all the metal maps. However, for an effective presentation of these contours thresholds were selected for creating the Isogrades of different metals. The thresholds adopted are given in respective outputs.

Bedrock

The analytical data of the bedrock samples for each metal has been subjected to the statistical treatment. The various parameters arrived at are as follows:

Table 2: (n=3676, metal values in ppm)

| Serial No. | Element | Minimum | Maximum | Mean | Standard Deviation | Threshold Value |
|------------|---------|---------|---------|-------|--------------------|-----------------|
| 1 | Copper | 5 | 1000 | 77.12 | 159 | 395.12 |
| 2 | Lead | 5 | 1000 | 28.45 | 89.42 | 207.29 |
| 3 | Zinc | 5 | 1000 | 52.55 | 92.96 | 238.47 |
| 4 | Nickel | 5 | 1000 | 36.79 | 52.85 | 142.49 |
| 5 | Cobalt | 5 | 1000 | 21.90 | 56.61 | 135.12 |

(Stray high values of the metals have been excluded from the statistical analysis)

Since bedrock samples represent the value at the sampling location within a particular litho-unit, this data cannot be contoured to delineate anomalous zones. The representation in such cases can be

limited only to point markers. Various methods of representation of these point markers have been carried out to optimally bring out the anomalies from the background for one or more metals at a time.

After extensive tests of alternative techniques of representation of the contents at sampling sites, technique based on the use of continuously increasing dot size with increasing contents was found to give satisfactory results in representation on the map (Bjorklund et al., 1987). An exponentially increase in diameter of the dots with exponentially increasing in metal content has been found to be better for visualisation of the pattern of metal content variation.

The above representation has been again modified since the larger dots mask the smaller dots thus hindering the true depiction. The open circles with increasing diameter proportional to the metal content were found more useful than dots and in this case all the circle sizes were distinct and could display the pattern in a more effective way. Such representations also hold good when overlaid on the geological map of the area.

The above type of representations are good for one metal, however in this case since at each location five metals are to be represented another approach has been adopted. The whole range of the metal content of all the sample points cannot be represented, which makes the output very clumsy. To avoid this problem the metal contents have been grouped in to four ranges (<50 ppm, 50 to 200 ppm, 200 to 400 ppm and >400 ppm), and the diameter of the circles (or patterns such as triangle, square etc.) has been decided accordingly. This helps correlating the size of the symbol directly with the range of the metal content. Such maps when overlaid on other themes clearly bring out the relationships. For multi metal representation different marker symbols have been assigned to each metal with range categories plotted in different sizes.

An effort was made to draw the isogrades of various metals as primary dispersion within a lithologic unit. However, in the small and narrow units the representation was not adequate. Also due to large discontinuity in terms of metal concentration across two litho-units the outputs were difficult to understand. Several modifications of this approach were experimented but did not yield good results. This was also due to the erratic distribution of metals (especially base metals) which are often structurally controlled.

Few software provides provision for softlines or hardlines (faults etc.) while interpolating the data but contoured outputs do not match the geological environment or human logic.

Figure 2, 3 & 4 show the distribution of copper, lead and zinc metals in stream sediments (contours) and bedrock samples (markers) over geology of the Sakoli basin.

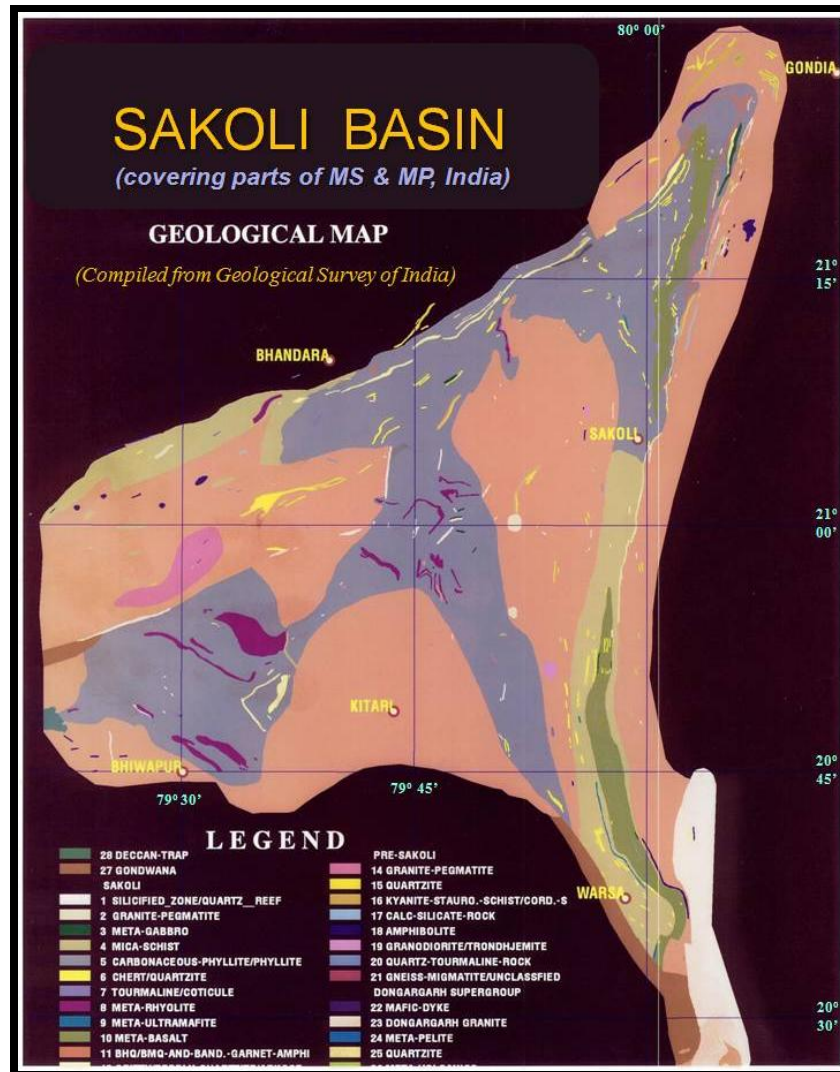


Figure 1: Geological Map of Sakoli Basin (After GSI). Survey of India 1:50,000 grid is overlaid on the map along with major towns

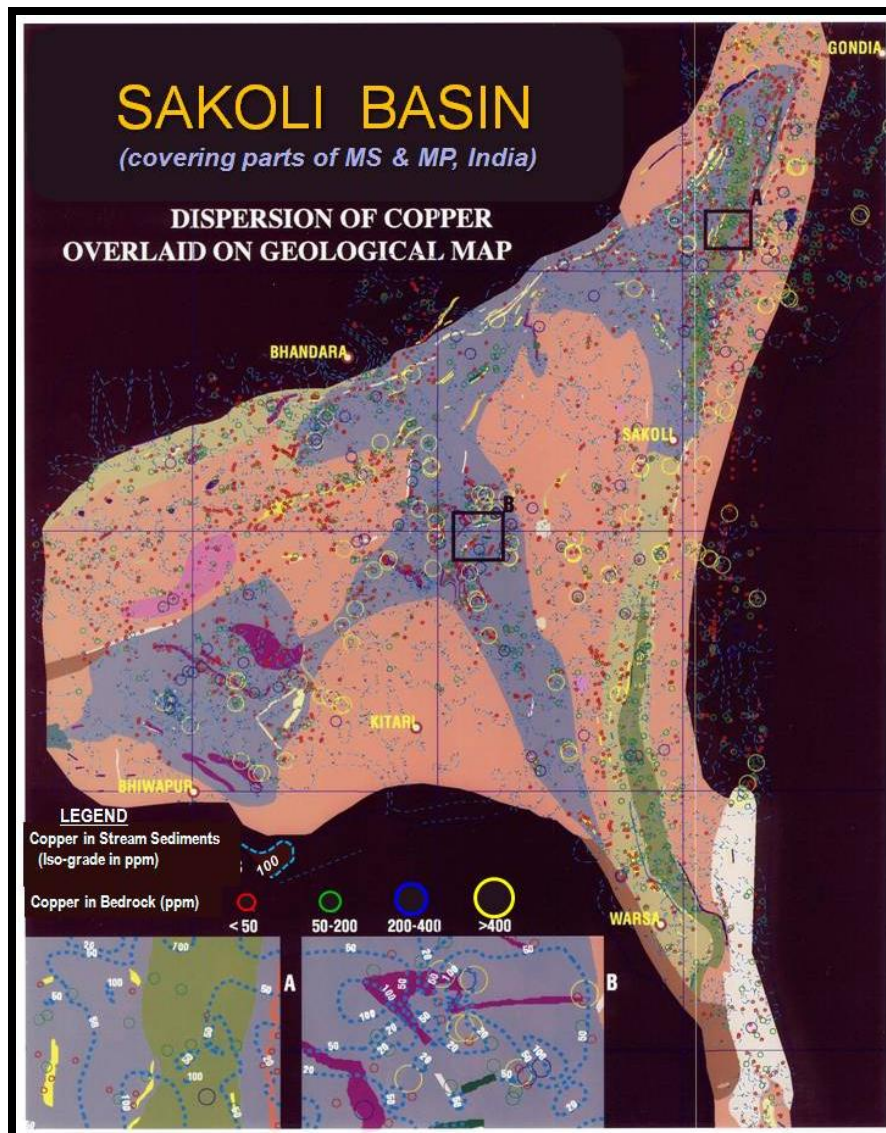


Figure 2: Map showing the dispersion of copper metal in Sakoli Basin area over geological map. Circles of different colour represent Cu concentration in ppm in bedrock. The dashed line with contour value shows distribution of Cu in stream sediments. Interesting Areas A and B marked on map are shown in detail in insets

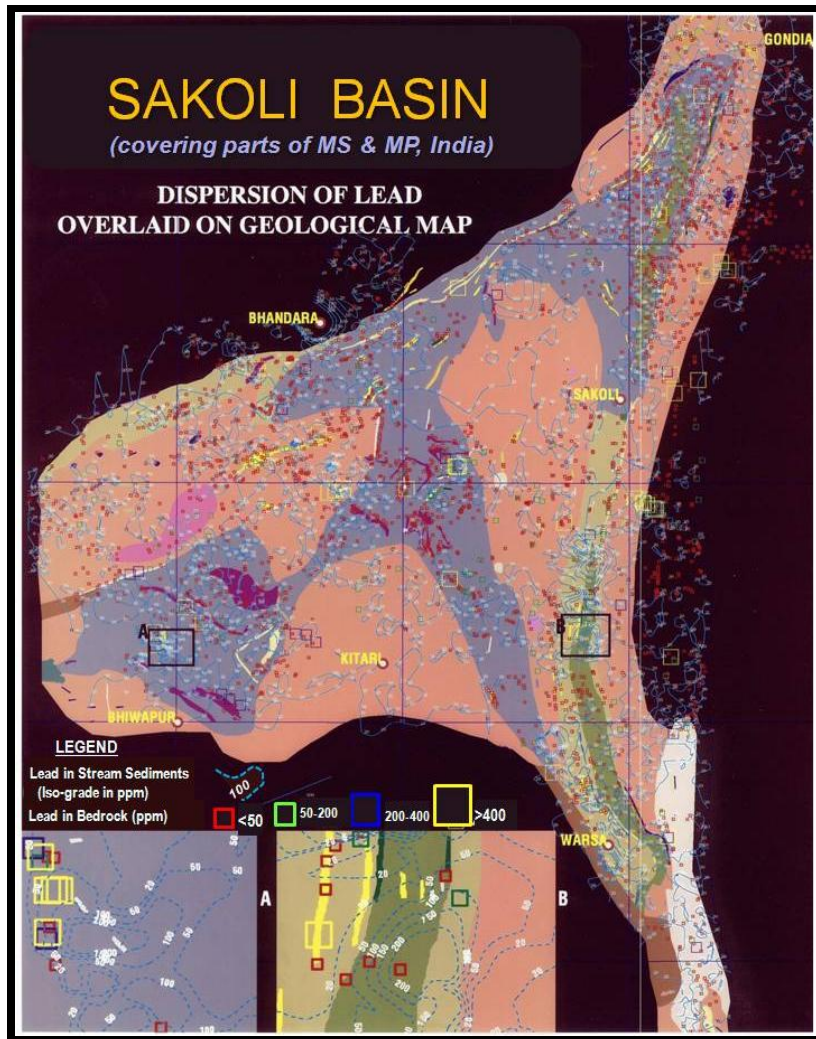


Figure 3: Map showing the dispersion of lead metal in Sakoli Basin area over geological map. Squares of different colour represent Pb concentration in ppm in bedrock. The dashed line with contour value shows distribution of Pb in stream sediments. Interesting Areas A and B marked on map are shown in detail in insets

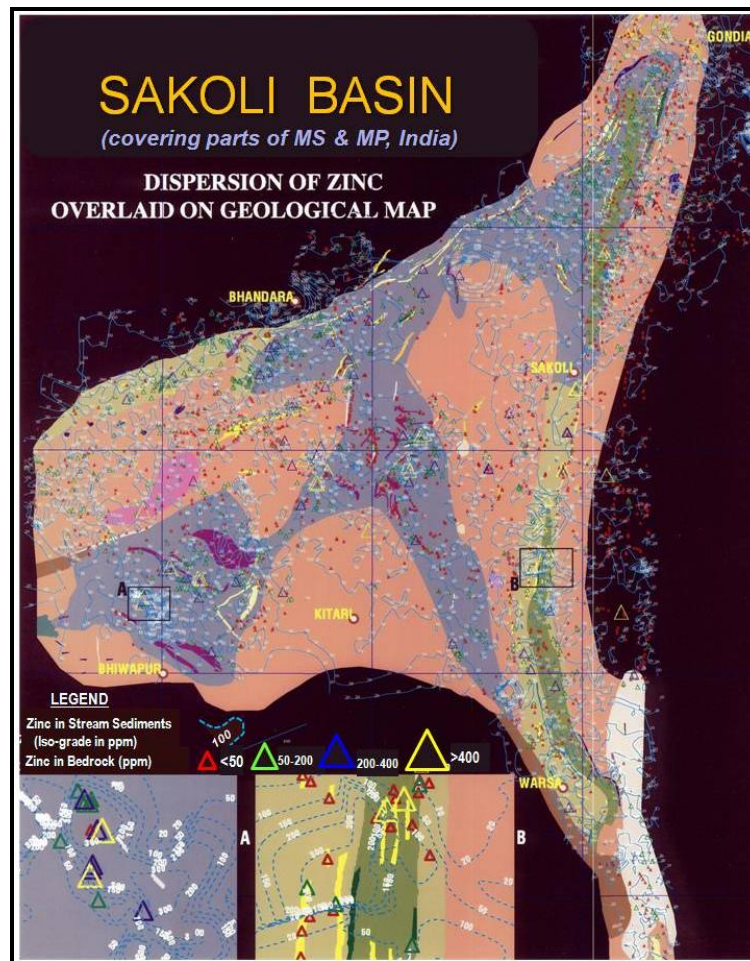


Figure 4: Map showing the dispersion of zinc metal in Sakoli Basin area over geological map. Triangles of different colour represent Zn concentration in ppm in bedrock. The dashed line with contour value shows distribution of Zn in stream sediments. Interesting Areas A and B marked on map are shown in detail in insets

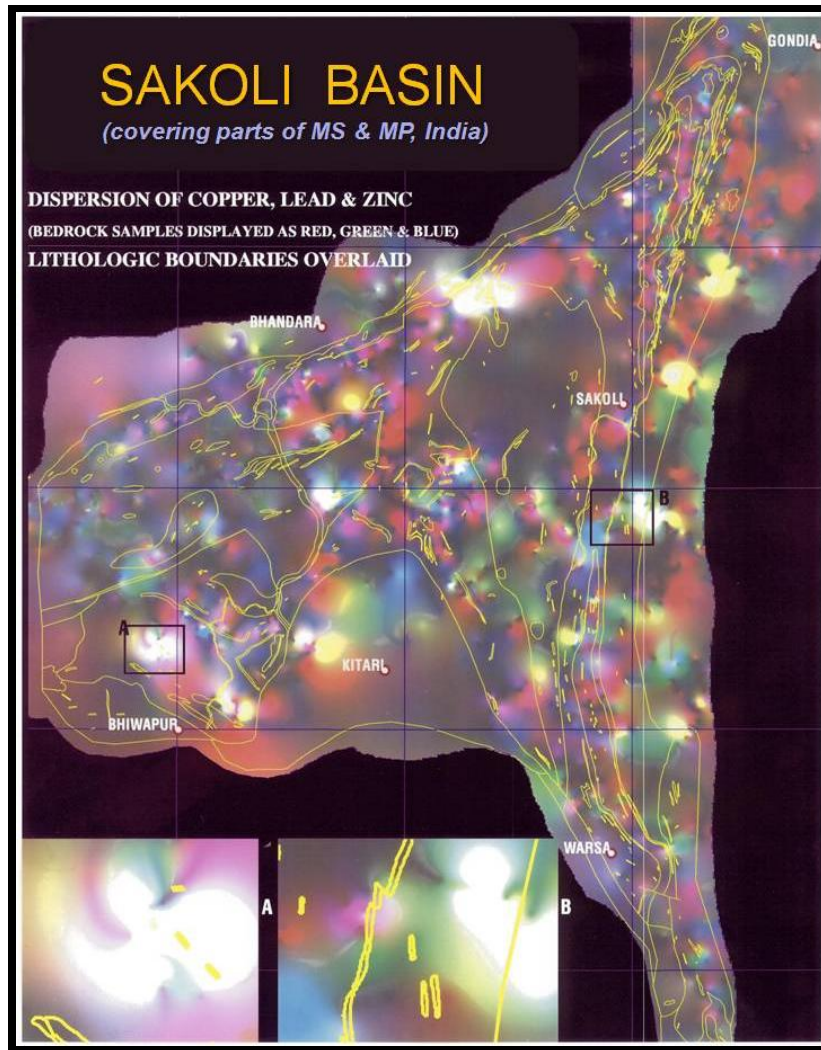


Figure 5: Dispersion of Copper, Lead & Zinc in bedrock shown as continuous surface (DEM) in RGB combination. White areas depict high concentration of all the three metals. Other colors are combination of two or three metal high anomalies. Geological map has been overlaid as line feature in yellow. Interesting Areas A and B marked on map are shown in detail in insets

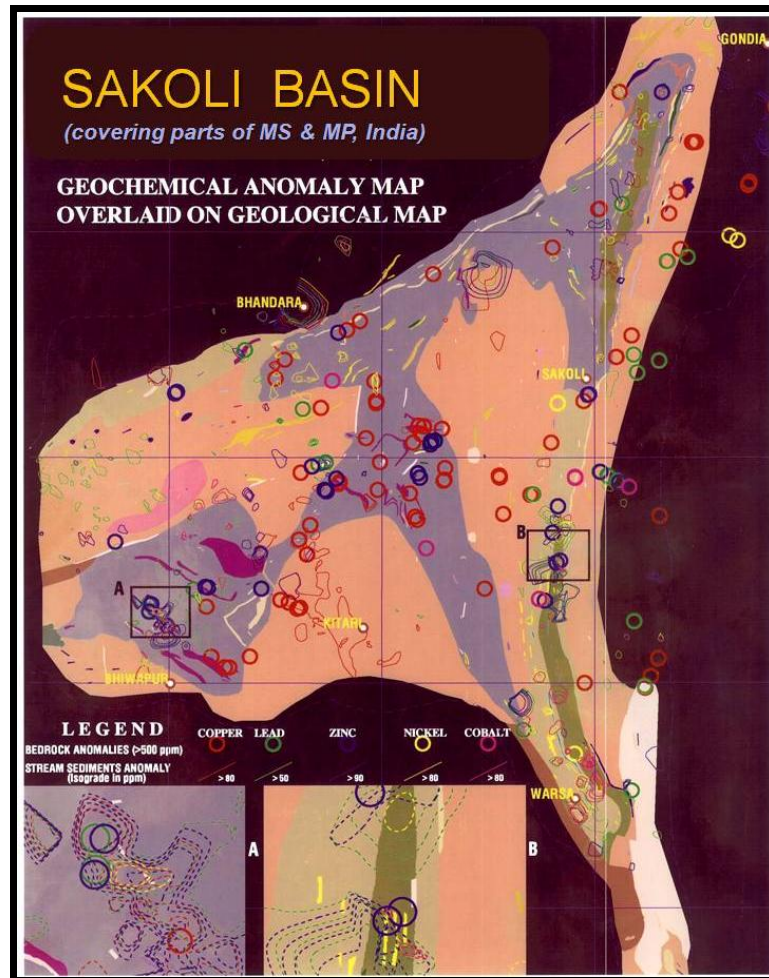


Figure 6: Metal concentration above the threshold has been shown as circles for bedrocks and contours as stream sediments. Red color of copper, green for lead, blue for zinc, yellow for nickel and magenta for cobalt has been used to depict bedrock and stream sediments anomalies. Geological map displayed in background to correlate geochemical anomalies to draw inferences

4. Integration and Modelling

The geographical information system is a powerful tool for integrating information (coverages) on points, lines and polygons for a digital cartographic database. The thematic maps can be overlaid, combined and intersected in any way one desires (such as points with line, points with polygon, line with polygon, polygon with polygon etc). The integration of several layers results in creation of n-dimensional database which can be used to derive the maps based on decision rules to arrive at the final map for a particular application. Modelling helps in performing the tasks in a systematic way to achieve the final results. Due to these important capabilities GIS plays a significant role in integrating data such as geological, geophysical, geochemical, geomorphological, slope, drainage, watershed etc. for mineral prognostics.

After extensive analysis of these datasets in a GIS using overlaying, unioning, buffering, proximity analysis, 3-D modelling etc., good correlation has been observed between primary and secondary dispersion patterns in certain areas leading to delineation of potential mineralized zones (Figure 2, 3, & 4).

Contours above the threshold values in stream sediment samples for each metal were extracted and correlated with bedrock values above the threshold in the Sakoli Basin in conjunction with geological map and gravity map (Figure 5 & 6).

The above exercise of extracting only anomalies in stream sediments and bedrock samples was done for all the five metals at a time and visualized with geological map in the background to ascertain the important (real) anomalies due to multimetal mineral occurrences. These anomalies were also checked with drainage and watershed map to differentiate correlated primary and secondary dispersion patterns.

Following conclusions have been drawn after analysis of results:

- An attempt has been made to represent various metals with varying ranges in two different sample media viz. Stream sediments and bedrock on a single map maintaining clarity and proper representation of the data using dots and symbols of different sizes (Figure 2, 3 & 4).
- The multi-metal anomaly zone thus brought out by superposition reflects the general dispersion of metal ions of higher order in meta-sediments as compared to gneisses. In gneisses the higher metal content is noted along shear and silicified zones due to remobilization (Figure 6).
- The anomaly between Sakoli and Tirka is significant, overlying the meta-basic + phyllitic rock with several primary spots of high values in the bedrock (Figure 6). Although prominent gossanisation is not seen the reported slag dumps and clay retorts indicate mineralized zone in the area. This anomaly is also substantiated by pitting and trenching near Tirka wherein the metal content (Pb +Zn) increases with depth (Sisodiya, 1993). Incidence of gold values with this anomaly further enhances the potentiality of this mineralisation.
- The Kitari Anomaly supported by gravity interpretation is important with prospecting point of view for gold, tungsten as base metal sulphides have good correlation with gold and tungsten as supported by the mineral map (Figure 5).
- The digital cartographic database thus created following extensive standardization procedure and integrated in a GIS environment provides wider scope for interpretation, integration and modelling of various thematic maps and forms a base for future scientific use related to Sakoli Basin or another such area.

5. Future Work

With the advancement in technology the geochemical sampling locations can be captured through mobile and field data can be directly integrated in a GIS along with photographs. While capturing the location of bedrock, input geological map can be used as background to precisely know the geological environment. Associated structures can also be recorded and sent to the Server through mobile application.

To optimize the sampling geomorphological maps can be used depicting degree of weathering which controls the movement of metals from the bedrock into stream sediments. Therefore, it is important to realize that lithology, structure, geomorphology, drainage, slope and watershed form a system which needs to be analysed in details before proceeding for a geochemical survey. Also the traditional concept of grid sampling needs modification to optimally sample the area in less number of samples.

Acknowledgements

This paper is an outcome of a major project on “Sakoli Basin” involving GSI and RRSC, Nagpur. Authors would like to thank then Director, RRSC, NNRMS and Deputy Director-General, GSI, Central Region for encouragement and taking up this project as collaborative venture. Former Head, RRSC, Nagpur and Director, Geology, GSI provided support along with technical guidance in carrying out this important project as demonstrative study after Project Vasundhara. Help rendered by colleagues from two organizations in some or the other way are duly acknowledged.

References

- Bjorklund, A. and Gustavasson, N. Visualisation of Geochemical Data on Maps. New Option. *Journal of Geochemical Exploration*. 1987. 29; 89-103.
- Carranza, E.J.M. Controls on Mineral Deposit Occurrence Inferred from Analysis of their Spatial Pattern and Spatial Association with Geological Features. *Ore Geology Reviews*. 2009. 35; 383-400.
- Damiey, A.G. Plenary Session Lecture-International Geochemical Mapping- A Review. *Jour. Geochem. Expln.* 1995. 55; 5-10.
- Darnley, A.G., Bjiirklund, A., Belviken, B., Gustavsson, N., Koval, P.V., Plant, J.A., Steenfelt, A., Tauchid, M., and Xie Xuejing, 1995: *A Global Geochemical Database for Environmental and Resource Management, Recommendations for International Geochemical Mapping*. Final Report of IGCP Project. 259. 122.
- Dunn, C.E. *Biogeochemistry in Mineral Exploration*. Handbook of Exploration and Environmental Geochemistry. 2007. 9; xiii–xviii, 1-460.
- El-Makky, A.M. and Sediek, K.N. Stream Sediments Geochemical Exploration in the Northwestern Part of Wadi Allaqi Area, South Eastern Desert, Egypt. *Natural Resources Research*. 2012. 21 (1) 95-115.
- Grunsky, E.C. *The Interpretation of Regional Geochemical Survey Data. Advances in Regional-Scale Geochemical Methods*. In Proceedings of Exploration 07: Fifth Decennial International Conference on Mineral Exploration. Edited by Milkereit, B. 2007. 139-182.
- Hakim, A. Structural and Tectonics of the Sakoli Belt in the Light of Gravity and Magnetic Data. *Indian Minerals*. 1995. 49 (4) 269-276.
- Hawkes, H.E., 1957: *Principles of Geochemical Prospecting, Contributions to Geochemical Prospecting for Minerals*. USGS Bulletin 1000-F. 225-355.
- Project Vasundhara, 1994: *Geoscientific Analysis, Data Base Creation and Development of GIS for Parts of South Indian Peninsular Shield*. National Workshop, Volume 1994.
- Roy, et al., 1995: *A Report on the Geological Mapping under Multidisciplinary Studies of Sakoli Basin*. Unpub. GSI Report.
- Saha, A.B. and Sathyanarayna, B., 1986: *A Report on the Regional Integrated Surveys for Base metal and Allied Mineralisation around Umarjhari and Other Areas*. Bhandara District, Mah. FS 1980-82. Unpub. GSI Report.

Samal, A.R., Sengupta, R.R. and Fifarek, R.H. Modelling Spatial Anisotropy of Gold Concentration Data Using GIS-Based Interpolated Maps and Variogram Analysis: Implications for Structural Control of Mineralization. *J. Earth Syst. Sci.* 2011. 120 (4) 583-593.

Sarkar, S.N., 1958: *Stratigraphy and Tectonics of the Dongargarh System*. A New System in Precambrian of Bhandara-Durg-Balaghat Area, Bombay and Madhya Pradesh. *Ind. Inst. Tech. Jour. Sci. Engr. Res.*, Kharagpur. 237-268.

Sinclair, A.J. Selection of Threshold Values in Geochemical Data Using Probability Graphs. *Jour. Geochem. Expl.* 1974. 3; 129-149.

Sisodiya, D.S., 1993: *Regional Geochemical Prospecting for Base metal Mineralisation in the Sakoli Basin and Older Metamorphites in Parts of Bhandara and Gadchiroli Districts of Maharashtra*. F.S. 1984-89.

Sisodiya, D.S. and Joshi, A.K., 2002: *Compilation of Geochemical Map of Sakoli Basin on 1:125,000 Scale - GIS and Remote Sensing Integration*, Technical Report, Published by GSI.

Timo Tarvainen, 1996: *Environmental Applications of Geochemical Databases in Finland*. Geological Survey of Finland.

Yilmaz, H., Sonmez, F.N., and Carranza, E.J.M. Discovery of Au–Ag Mineralization by Stream Sediment and Soil Geochemical Exploration in Metamorphic Terrain in Western Turkey. *Journal of Geochemical Exploration*. 2015. 158; 55-73.

Flash Flood Risk Susceptibility in Gagas River Watershed - Kumaun Lesser Himalaya

Sapna Bisht¹, Subrat Sharma² and Smita Chaudhry¹

¹ Institute of Environmental Studies, Kurukshetra University, Kurukshetra, Haryana, India

² G.B. Pant Institute of Himalayan Environment & Development, Almora, Uttarakhand, India

Publication Date: 23 May 2016

DOI: <https://doi.org/10.23953/cloud.ijarsg.55>



Copyright © 2016 Sapna Bisht, Subrat Sharma and Smita Chaudhry. This is an open access article distributed under the **Creative Commons Attribution License**, which permits unrestricted use, distribution, and reproduction in any medium, provided the original work is properly cited.

Abstract Himalayan region is highly susceptible to natural hazards particularly those that are triggered by the action of water. Due to the vast topographical diversity, events of 'peak runoff' pose various risks to small villages located at the watershed's foot area. In this study, for the purpose to estimate flash flood risk along the Gagas River in Kumaun lesser Himalaya, high-resolution Digital Elevation Model (DEM) coupled with Geographical Information Systems (GIS) were utilised. The region experiences frequent storm events especially in the monsoon season. The river basin is also an evolving HELP basin endorsed by UNESCO as part of its global efforts for restoration of languishing river systems. Variability in the climatic conditions has imposed undue pressure on the livelihoods for survival. Relevant morphometric, topographic parameters and maximum runoff of the sub-watersheds of Gagas river watershed were computed in the GIS environment and were analysed to understand the drainage basins susceptibility to the flash flood hazards. These measurements allowed prioritising the sub watersheds in the presence of a series of rainstorms that generate unusual runoff volumes. Map representing hazard zones of sub-watersheds were identified and classified into four susceptibility groups (very high, high, moderate and low). The knowledge of flash flood susceptibility is important in mitigating the losses incurred to agriculture, irrigation systems, watermills, and recreational activities; and in the proper management of water resources.

Keywords *Morphometry; Flash Floods; Himalaya; Prioritisation*

1. Introduction

In complex mountainous environment such as Himalayas, due to their high susceptibility to natural hazards such as debris flows, debris floods, and flash floods, hydric analysis is very important, so that appropriate risk management could be initiated. The unprecedented rate of Climate Change causing increase in high intensity rainfall and decrease in low and medium intensity events renders the situation more vulnerable to the after effects (Goswami et al., 2006; ICIMOD, 2007).

Flows hastened by intense rainfalls are often referred to as "flash floods", these, according to IAHS-UNESCO WMO (1974) are defined as sudden floods with high peak discharges, produced by severe

thunderstorms that are generally of limited areal extent. However, the actual time threshold may vary depending on particular hydrological characteristics such as small basins; steep slopes in the catchment, low infiltration capacity combined with meteorological events (Georgakakos, 1986).

In the Himalayas, this is a frequent phenomenon, especially the peak discharge in the monsoon season, with very severe implication to life and infrastructure developments and shall require appropriate adaptation measures to be taken up (Sharma, 2012). Management of flood occurrences requires information about both climatic conditions (i.e. rainfall, temperature, storm occurrences) and a watershed's physiographic characteristics (i.e. slope, elevation, drainage density etc.). Various morphometrical parameters including linear, areal and relief aspects are used worldwide for the characterisation of fluvial originated drainage basin (Chalam et al., 1996) and due to its perspective view Remote Sensing (RS) and Geographical Information System (GIS) applications has been useful for monitoring and management of watersheds. It outplays conventional studies since these techniques coupled with high-resolution Digital Elevation Model (DEM) measure a number of terrain and morphometric parameters efficiently, precisely and rapidly to characterise the stream network and watersheds (Vijith and Satheesh, 2006).

In order to study this approach in a hilly watersheds with steep overland, stream slopes and areas inclined to the flood phenomena, this study was undertaken in the Gagas Watershed, a hilly sub-watershed of the Ramganga River Basin, in the Kumaun Lesser Himalaya. The region experiences frequent storm events almost every year in the monsoon season (June 4, 1977; June 25, 1978; June 20, 1981; July 31, 1982; August 11, 1983; August 31, 1984; August 10, 1985; August 15, 1985) (Kumar and Kumar, 2008). Due to its high dependence on the River system, the basin has been endorsed by HELP (Hydrology for Environment, Life and Policy), under UNESCO's International Hydrological Program as part of its global efforts for restoration of languishing river systems (www.unesco.org/water/ihp/help/). In this paper, stream properties, basin characteristics and maximum stream discharge of the Gagas watershed and its sub watersheds have been analysed for their risk of flash floods and for prioritisation.

2. Study Area

The Gagas watershed covers an area of 511.19 Km² having perimeter 129.59 Km. It is the largest tributary basin of the Himalayan Ramganga River in the South-Western portion of Almora district of Uttarakhand, India, extending from 29°51'55" N and 29°35'49" N and longitudes 79°20'36" E and 79°33'15" E (Figure 1). The topography of the region varies from 2742 m amsl in the head reaches of the Gagas River in the North-Eastern part to 727 m amsl at the mouth of the Gagas River in the western part of the basin. The river originates in the sacred forests of Pandukholi in Almora district of the Kumaun lesser Himalaya.

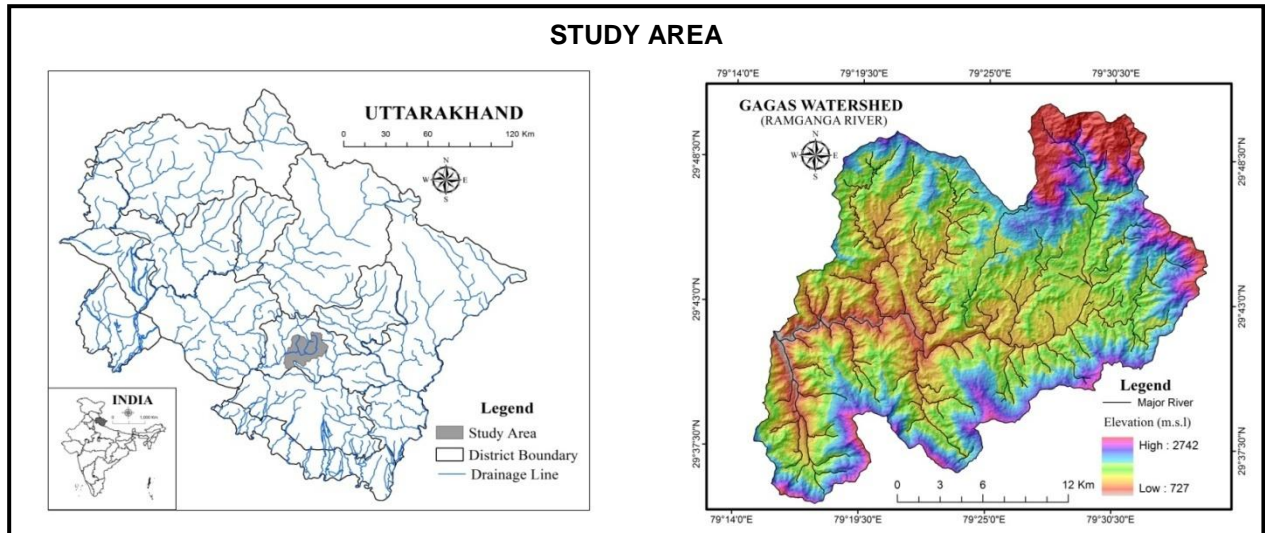


Figure 1: Study Area of Gagas Watershed

The study area lies in the Dudhatoli syncline range and constitutes a variety of meta-sediments like slate, phyllite, quartzite, mica-schist, gneiss, granite etc. that have suffered multiple phases of deformation and metamorphism (Pal, 2002). The area is dissected by major thrusts (North Almora, South Almora, Ramgarh) along the boundaries of major rock groups (Figure 2). The North Almora Thrust (NAT) is dissected by faults, which are transverse to the Himalayan orographic trend and are known as seismically active structures (Paul and Pant, 2003). The watershed is characterised by coarse textured soils and a number of tributaries spread the entire watershed having dendritic pattern. Morphologically the region is characterized by a series of deeply incised river valleys and high ridges (Kharkwal, 1993).

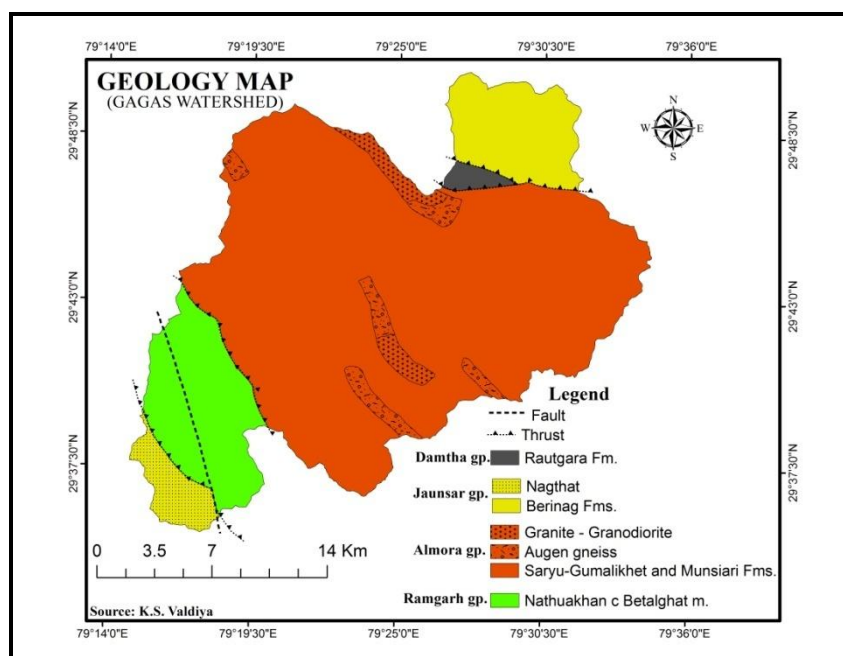


Figure 2: Geology Map of the Study Area
(Source: K.S. Valdiya, 1980)

In the watershed, the mean annual rainfall varies from 903 to 1,281 mm, with a mean value of 1,067 mm (Kumar and Kumar, 2008). Approximately, more than 80% of the annual precipitation in the region occurs during the South-West monsoon, which starts in the third week of June and can last till mid-October. Of the remaining, 15% rainfall is caused by cyclones and 5% by local thunderstorms distributed over the rest of the year (Jalal, 1988). Since, in the mountains, the topography has a major role in affecting the orographic precipitation, which varies significantly over small spatial scales (Shrestha et al., 2012). The phenomenon is resurrected by using the high resolution Bioclim data; it is observed that in the Gagas watershed the distribution of rainfall is effected by altitude variations, slope, aspect, and trends of mountain ranges. Duration of 50 years (1950-2000) of climatic data is classified into three seasons. The maximum average rainfall was observed in July (449.6 mm). Seasonal distribution of rainfall and temperature is represented with the maps (Figure 3), and monthly variations of the climatic data are shown with a hyetograph along with temperature isotherms (Figure 4).

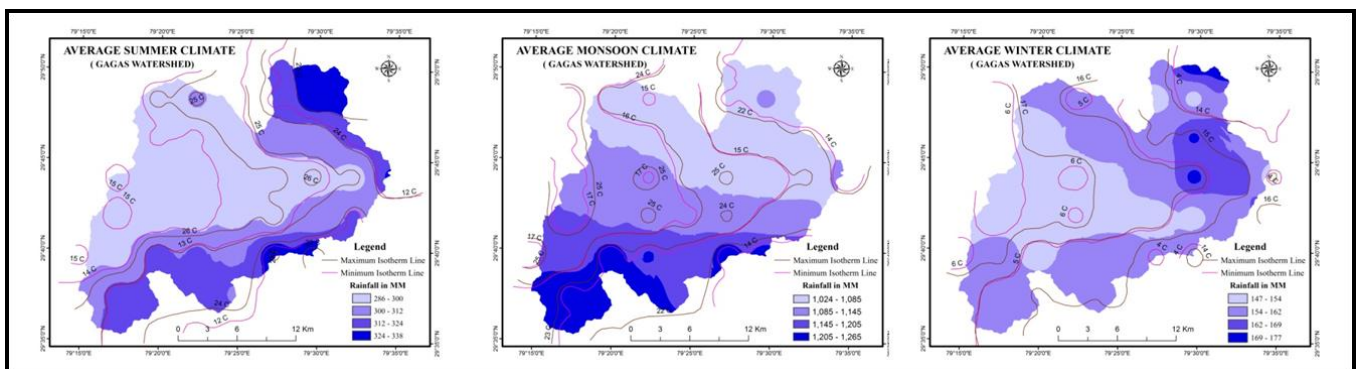


Figure 3: Seasonal Climatic Maps of Gagas Watershed (1950-2000) (Source: www.worldclim.org)

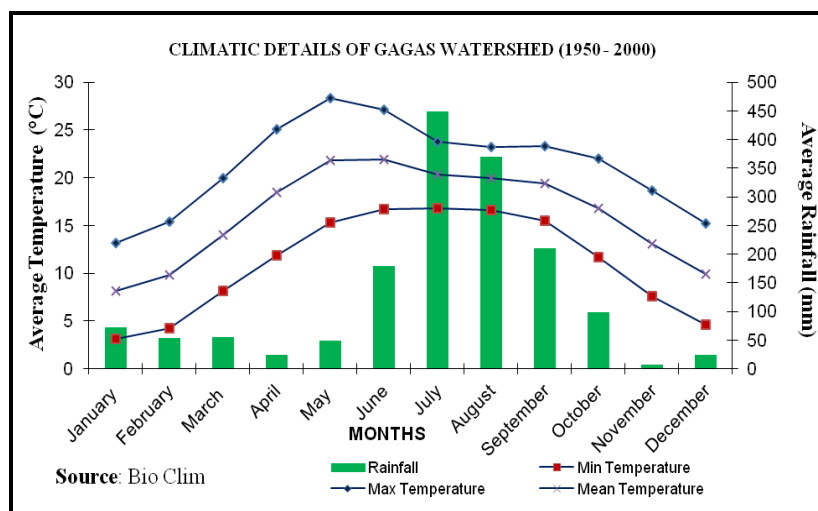


Figure 4: Average Monthly Profile of Gagas Watershed (1950-2000) (Source: www.worldclim.org)

3. Data Used and Methodology

The present study includes following approaches (1) Survey of India (SOI) topographic maps (No. - 530/5, 530/6, 530/9, 530/10) of 1958 (1:50,000 scales) to outline the natural drainage (2) ASTER data, with 30 m spatial resolution for DEM generation (Figure 5).

Strahler's scheme for stream ordering was used to digitize the drainage, by the use of toposheets on 1:50000 scale and were updated using remote sensed data (Landsat 8, Feb 2015). In the study, along with perennial streams, ephemeral streams were also digitised as a geomorphic agent during flash floods (Moges and Bhole, 2015). A 30 m resolution ASTER DEM was used to delineate the Gagas River watershed, subwatersheds and to extract altitude and slope layers using Arc Map and Arc Hydro tools. Table 1 describes the standard methods and formulae used for calculating the morphometric parameters in the 13 sub watersheds of the Gagas basin and the results are given in Tables 2, 3, 4.

Table 1: Definitions and Formulae of Morphometrical Parameters, Slope Categories, Wetness Index and Maximum Discharge used for the Analysis

| S. No. | Parameters | Definitions | Units | References |
|---|--|---|---------------|----------------------------------|
| Drainage Network Characteristics | | | | |
| 1 | Total number of streams (Nu) | The number of stream segments of various orders in a sub-watershed. | Dimensionless | Strahler (1957) |
| 2 | Stream orders (u) | Hierarchical ordering | Dimensionless | Strahler (1957) |
| 3 | Stream length (Lu) | Length of the stream orders. | Km | Horton (1945) |
| 4 | Total stream length | The lengths of total number of stream segments of various orders in a sub-watershed | Km | Horton (1945) |
| 5 | Longest flow path (Ls) | Length of main stream. | Km | |
| 5 | Stream grade (Sg) | $(H_s - H_d) / L_s * 100$ | % | Hack (1957) |
| 6 | Bifurcation ratio (Rb) | $Nu / N(u+1)$, where Nu is number of streams of any given order and N (u+1) is number in the next higher order | Dimensionless | Horton (1945) |
| 7 | Weighted mean bifurcation ratio (WRbm) | Total of $Rb * (Nur) / \text{Total of } (Nu-r)$; Nur=Number of stream used in the ratio | Dimensionless | Strahler (1953) |
| 8 | Drainage texture (Dt) | Total no. of stream segments in all order/ P | Km^{-1} | Horton (1945) |
| 9 | Drainage density (D) | $\sum Lt / A$, where $\sum Lt$ is the total length of all the ordered streams | $Km Km^{-2}$ | Horton (1945) |
| 10 | Length of overland flow (Lg) | $1/2Dd$ | Km | Horton (1945) |
| Basin Geometry | | | | |
| 11 | Basin area (A) | Area of watershed | Km^2 | |
| 12 | Basin length (Lb) | Maximum length of the watershed measured parallel to the main drainage line. | Km | Schumm (1956) |
| 13 | Perimeter (P) | Length of the watershed boundary | Km | |
| 14 | Perimeter of circle of watershed (Pc) | $2\pi r$ | Km | |
| 15 | Form factor (Rf) | A / Lb^2 | Dimensionless | Horton (1945) |
| 16 | Elongation ratio (Re) | $\sqrt{(A/\pi)} / Lb$ | Dimensionless | Schumm (1956) |
| 17 | Circulatory ratio (Rc) | $4\pi A / P^2$ | Dimensionless | Miller (1953) |
| 18 | Compactness coefficient (Cc) | Perimeter/ Perimeter of Circle of Watershed | Dimensionless | Gravelius (1914) |
| Relief Characteristics | | | | |
| 19 | Relative relief (Rr) | Basin Relief/Perimeter*100 | Dimensionless | Huggett and Cheesman (2002) |
| Slope Aspects | | | | |
| 20 | Slope categories | Different slope categories | Degree | NRCC (1998) |
| Wetness Index (WI) | | | | |
| 21 | Wetness Index (WI) | $\ln (A / \tan \beta)$; where, A is the upslope contributing area per unit contour length (| Dimensionless | Digital Terrain Analysis Manual, |

a/c) and $\tan \beta$ is the local slope

University of Minnesota (2013)

| Stream Flow | | | | |
|-------------|-----------------------|--|---------|---|
| 22 | Maximum Discharge (Q) | $Q = C.A^{0.75}$, where $C = 2.342 \log (0.6T) \log (1185/P) + 4$ and $P = 100 (6) / A$ | m^3/s | Punmia et al., 2009; Dawdy et al., 2012; Rijal 2014 |

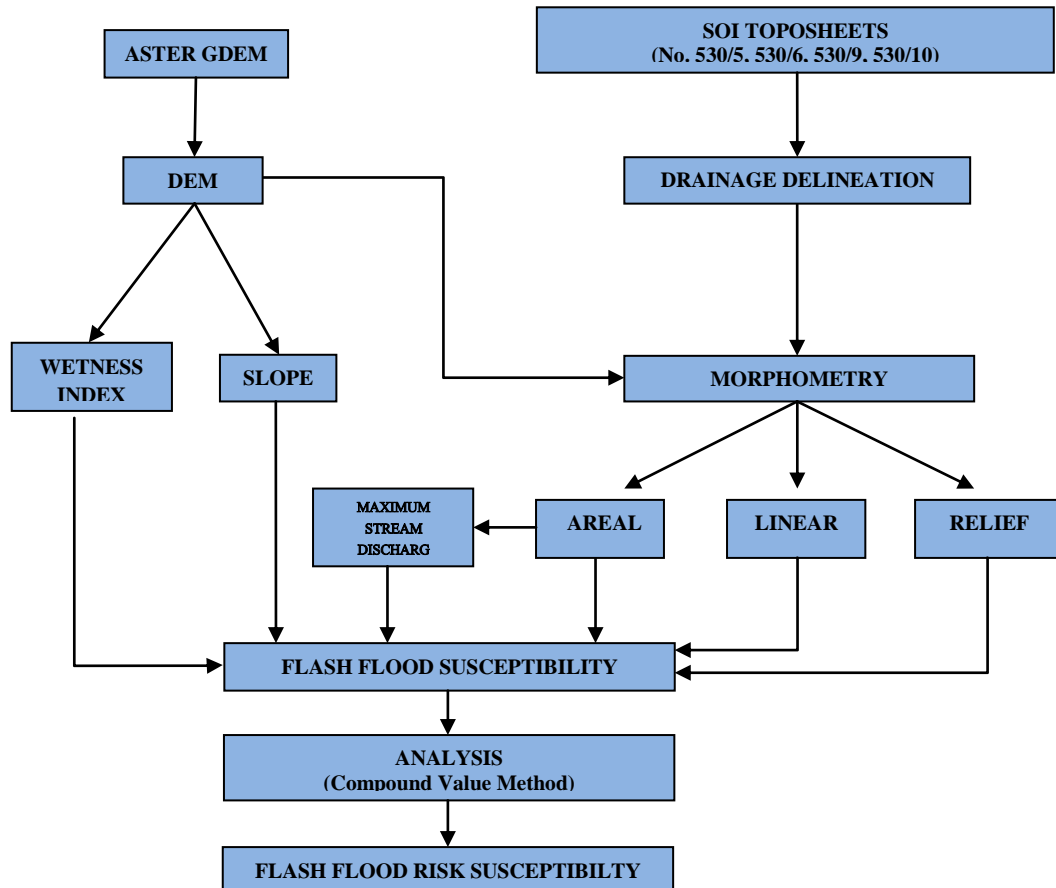


Figure 5: Flow Chart of Steps in Analysis for Evaluating Flashflood Susceptibility of Gagas Sub Watersheds

For the slope analysis, a standard slope classification is adopted to establish the relation between slopes and flash floods using Surface Analysis Tool in ArcGIS-9.3 (NRCC, 1998). The areas of sub watersheds were categorized into the following 10 slope classes: level (0° – 0.3°), nearly level (0.3° – 1.1°), very gentle slope (1.1° – 3.0°), gentle slope (3.0° – 5.0°), moderate slope (5.0° – 8.5°), strong slope (8.5° – 16.5°), very strong slope (16.5° – 24°), extreme slope (24° – 35°), steep slope (35° – 45°), and very steep slope (45° – 90°). For the purpose of analysis of its impact on surface runoff, ranking were given on the basis of percent area in the specific slope class, assuming that runoff in a particular slope class remains same in the sub watersheds.

In the study as an important parameter secondary topographic factor, wetness index (WI), has been applied for the flash flood susceptibility in the region. It considers catchment area and slope gradient and controls the flow accumulation in a terrain (Qin et al., 2011). It is helpful to delineate water saturation zone and determine water table conditions, and is calculated using the following formula:

$$TWI = \ln (A / \tan \beta) \quad (1) \quad (\text{Anon.}, 2013)$$

Where, A is the upslope contributing area per unit contour length (a/c) and $\tan \beta$ is the local slope.

A regional analysis of stream flows is performed that is based on relation between discharges to drainage area (Dawdy et al. 2012). Modified Dicken's Method was used to calculate maximum discharge for the region:

$$Q_{\max} = CA^{0.75} \quad (2) \quad (\text{Rijal, 2014; Punmia et al., 2009})$$

Where, Q_{\max} = maximum discharge (m^3/sec); A = drainage area (Km^2); and C = coefficient related to the region.

Wherein C is calculated using the formula:

$$C = 2.342 \log (0.6T) \log (1185/P) + 4 \quad (3)$$

And

$$P = 100 (6) / A \quad (4) \quad (\text{Rijal, 2014})$$

Here, A is the total catchment area (Km^2) respectively and T is return period in years (i.e. yearly).

For assessing the combined role of morphometrical and topographical parameters on the hydrological behaviour at sub watershed scale, a comparative runoff ranking methodology has been used. A compound value (C_p) was given to the parameters of sub watersheds to analyze the flash flood discharge susceptibility. This approach is based on the principles of knowledge-driven modeling and converts the qualitative understanding of a phenomenon based on scientific knowledge into a quantitative estimation. This method is one of the best approaches to compare land surface processes between similar entities (such as watersheds) (Ratnam et al., 2005).

In the study area, the total number of ranks assigned is based on the number of watersheds. Since there are 13 sub-watersheds, ranks were assigned from 1 to 13. For the purpose of analysis, rank 1 was assigned in a way that the value of the parameter represents maximum run off potential and vice versa. Same values of the parameters were assigned with similar rankings. The average of the ranks represents the collective impact of all the parameters on run off susceptibility of a sub-watershed. It is denoted as C_p and is calculated from following formula.

$$C_p = \sum R / n \quad (5)$$

Wherein,

C_p is Compound value of a particular watershed, R is Rank of a particular sub watershed for a parameter, n is Number of parameters.

Comparison of Different Parameters for Prioritizing Flash flood Susceptibility

In the ranking, the factors such as weighted mean bifurcation ratio (R_{bm}), drainage texture (D_t), drainage density (D), length of overland flow (L_g), shape factors (form factor (R_f), elongation ratio (R_e), circulatory ratio (R_c), compactness coefficient (C_c)), and relative relief (R_r), slope categories having a major role in the flash flood formation are calculated. Other important parameters such as stream grade, watershed area or the size, wetness index and empirical maximum stream discharge are derived using RS/GIS techniques, these have not been utilised for such studies till now in the Uttarakhand Himalayan region.

4. Results and Discussion

In the Gagas watershed, the drainage patterns is dendritic, indicating uniformly dipping bedrock, those are impervious and non-porous (Lambert, 1998). It also indicates less percolation and maximum runoff especially in the high areas. Table 2 represents the basic morphometric characteristics of the Gagas watershed. In the watershed, there are a total number of 3240 streams of total length of 1790.11 Km.

Table 2: Basic Watershed Characteristics of the Study Area

| | | Linear Parameters | | | | | Areal Parameters | | | | |
|------|---------|-------------------|--------|--------|------|------|------------------|----------------------|---------|--------|---------|
| Nu | Lu (Km) | Rb | | | | | Rbm | A (Km ²) | Lb (Km) | P (Km) | Pc (Km) |
| | | I/II | II/III | III/IV | IV/V | V/VI | | | | | |
| 3240 | 1790.11 | 4.3 | 4.4 | 4.7 | 2.5 | 5.5 | 4 | 511.19 | 24.31 | 129.59 | 80.13 |

Stream Number (Nu), Stream length (Lu), Bifurcation ratio (Rb) Mean bifurcation ratio (Rbm), Basin area (A), Basin length (Lb), Perimeter (P), Perimeter of circle of watershed (Pc)

4.1. Morphometric Analysis

Morphometry has a substantial affect on the watershed hydrology viz. the basin area determines the amount of water yield; the length, shape and relief, affect the rate at which water is discharged from the basin (Tucker and Bras, 1998) (Table 3).

Table 3: Quantitative Morphometry Parameters used in Ranking of Gagas Sub Watersheds

| Sub-Watersheds | Order of Tributaries | Drainage Network and Texture | | | | | Basin Geometry | | | | |
|----------------|----------------------|------------------------------|------|------------------------|-----------------------|---------|----------------------|------|------|------|------|
| | | Sg (%) | WRbm | Dt (Km ⁻¹) | D (Km ⁻¹) | Lg (Km) | A (Km ²) | Rf | Re | Rc | Cc |
| Bainali | 5 | 7.52 | 4.74 | 6.63 | 3.71 | 0.135 | 16.53 | 0.34 | 0.33 | 0.56 | 1.34 |
| Bhikiyasen | 3 | 10.41 | 5.89 | 3.51 | 3.59 | 0.139 | 5.25 | 0.64 | 0.45 | 0.59 | 1.30 |
| Dusad | 5 | 5.27 | 4.53 | 5.18 | 3.25 | 0.154 | 26.46 | 0.26 | 0.29 | 0.36 | 1.67 |
| Gagas Sub | 5 | 11.7 | 4.61 | 9.35 | 3.76 | 0.133 | 63.05 | 0.48 | 0.39 | 0.43 | 1.53 |
| Jamgad | 5 | 9.94 | 4.07 | 8.68 | 3.66 | 0.136 | 41.13 | 0.67 | 0.46 | 0.58 | 1.32 |
| Kali | 4 | 15.02 | 3.60 | 4.08 | 3.64 | 0.137 | 6.78 | 0.37 | 0.34 | 0.53 | 1.38 |
| Kaneri | 4 | 13.56 | 3.72 | 4.98 | 3.21 | 0.156 | 15.65 | 0.41 | 0.36 | 0.56 | 1.33 |
| Khar | 6 | 5.49 | 4.04 | 9.22 | 3.41 | 0.147 | 62.14 | 0.4 | 0.36 | 0.55 | 1.35 |
| Khiraon | 4 | 7.26 | 4.07 | 4.53 | 3.59 | 0.139 | 27.27 | 0.22 | 0.26 | 0.26 | 1.96 |
| Makraon | 6 | 13.76 | 3.36 | 6.18 | 3.96 | 0.126 | 13.82 | 0.57 | 0.43 | 0.68 | 1.21 |
| Malla | 5 | 5.88 | 4.41 | 9.13 | 3.33 | 0.150 | 47.49 | 0.52 | 0.41 | 0.57 | 1.32 |
| Narora | 6 | 10.48 | 4.33 | 12.19 | 3.83 | 0.131 | 59.52 | 0.92 | 0.54 | 0.64 | 1.25 |
| Riskan | 5 | 3.74 | 4.55 | 9.42 | 3.84 | 0.130 | 51.17 | 0.3 | 0.31 | 0.44 | 1.51 |
| Total Gagas | 6 | 4.21 | 4.32 | 25 | 3.5 | 0.143 | 511.19 | 0.86 | 0.52 | 0.38 | 1.62 |

Stream grade (Sg), Weighted mean bifurcation ratio (WRbm), Drainage texture (Dt), Drainage density (D) Length of overland flow (Lg), Basin area (A), Form factor (Rf), Elongation ratio (Re), Circulatory ratio (Rc), Compactness coefficient (Cc)

4.1.1. Drainage Network Analysis

The Gagas watershed was observed of having three 'sixth' order tributaries, and six 'fifth' order tributaries, three 'fourth' order tributaries and one 'third' order tributary. In the watershed more number of higher stream order tributaries shows the association with more discharge and higher velocity of the stream flow.

Stream Grade (Sg)

As an important parameter defined by slope of the channel, it influences most aspects of flood-plain geomorphic and hydrologic processes (Hack, 1957 and 1973). A high stream grade 15.02 (Kali) shows increased flow velocity leading to extensive flood damage on the high-gradient reaches than on the more gentle reaches (Hupp, 1982).

Weighted Mean Bifurcation Ratio (WRbm)

A mountainous or highly dissected terrain has a high bifurcation ratio and vice versa, which suggests that its value is related to geomorphic factors such as relief ratio, drainage density, etc. (Horton, 1945). Basins of high WRbm are elongated in shape, which in turn gives sufficient time for infiltration and ground water recharge, and low probability of flooding and vice versa (Barseem et al., 2013). According to Strahler (1953), WRbm give more representative bifurcation indexes, in the watershed it varies between 5.89 (Bhikiyasen) and 3.36 (Makraon). The sub watersheds with closer range in the variations are ascribed to the similar rock group composition and tectonic history, uniform climate conditions and in similar stage of development (Pakhmode et al., 2003).

Drainage Texture (Dt)

Drainage texture is the measure of the channel spacing and depends upon a number of natural factors such as climate, rainfall, vegetation, rock and soil type, infiltration capacity, relief and stage of development of a basin. A fine texture expresses soft or weak rocks uncovered by vegetation, whereas coarse textures represent massive and resistant rocks (Dornkamp and King, 1971). Based on the classification of Smith (1950), Narora (12.19 Km^{-1}) with fine texture show lower infiltration and higher runoff; while Bhikiyasen (3.51 Km^{-1}) followed by Kali (4.08 Km^{-1}) have coarse textures, with a large basin lag time.

Drainage Density (D)

Drainage density (D) indicates how dissected the landscape is by channels and in the formation of flood flows (Horton, 1932; Gardiner and Gregory, 1982). It is higher in weak/impermeable rocks with sparse vegetation cover. It increases with increasing probability of heavy rainstorms, rapid storm response, less infiltration and moderate erodibility of surface materials and vice versa (Betson, 1964). The values in Gagas sub watersheds varies from 3.21 (Kaneri) to 3.96 (Makaraun) KmKm^{-2} , with an average value of 3.6 KmKm^{-2} showing high drainage density.

Length of Overland Flow (Lg)

Length of overland flow (Lg) is the length of the run of rainwater on the ground surface before it is localized into definite channels and is roughly equal to half of drainage density (Horton, 1945). If a basin is well drained the Lg is short and the surface runoff concentrates quickly. Lg in the Gagas watershed varies from 0.126 (Makraun) to 0.156 Km (Kaneri) indicating gentler slopes and longer flow paths in the latter.

4.1.2. Basin Geometry

Basin geometry is a means of numerically analyzing different areal aspects of a drainage basin. These parameters affect the stream flow hydrographs and peak flows of the basins.

Area (A)

Watershed's area is an important parameter like the stream lengths of the drainage. As basin enlarges, the stream length increases and there is a delay in arrival of flow after heavy rain (Hack, 1957). Basin area vary from 63.05 Km² (Gagas sub) to 5.25 Km² (Bhikiyasen). Out of the total, nine sub watersheds fall in the range of 10-50 Km² of area.

Watershed Shape

Basin shape is a dimensionless factor that characterises the value range from 0 (a line, highly elongated shape) to unity (a circle) (Miller, 1953). The form factor (Rf) values vary from 0.22 (Khirao) to 0.92 (Narora) which shows the variations from elongated to perfectly circular shapes, the latter being more susceptible to peak runoff of shorter duration (Chopra et al., 2005). Gagas watershed has an average Rf of 0.47. Elongation ratio (Re) varies from 0.26 (Khirao) to 0.54 (Narora). Higher value of Re indicates active denudational processes with high infiltration capacity and low run-off in the basin, whereas, lower Re values indicate higher elevation of the basin susceptible to high headward erosion along tectonic lineaments (Avinash et al., 2011). Gagas watershed has an average Re of 0.38 which indicate moderate slope. The circularity ratio (Rc) is used for the out-line form of watershed as a quantitative method (Miller, 1953). Its low, medium and high values are indicative of the youth, mature and old stages of the life cycle of the tributary basins. In the sub watersheds, the Rc ranges from 0.26 (Khirao) to 0.68 (Makraon) (Table 4).

Compactness Coefficient (Cc)

Another dimensionless parameter, the compactness coefficient is independent of size of watershed and dependent only on the slope. For a circular basin Cc=1, and a deviation from the circular nature will have values greater than 1 (Gravelius, 1914). The runoff hydrograph is expected to be sharper with a greater peak and shorter duration, in a more compacted watershed i.e. more closer to 1 (Avery, 1975). Its values range from lowest in Makraon (1.21) to highest in Khirao (1.96) sub watersheds.

In an analysis of comparison between the average values of form factor (Rf), elongation ratio (Re) and circularity ratio (Rc) with order of tributaries >3. It is observed that order of tributaries is directly proportional with these ratios i.e. with increasing order of tributaries, the tendency of sub watersheds to be more circular in shape and hence increasing vulnerability to flash floods. The compactness coefficient (Cc), however show as indirect proportional to order (Figure 6). The analysis depicts these as significant parameters in drainage-basin evolution, expressing increases in the order of the main stream, in the area and in other parameters of elongated basins in relation to circular ones.

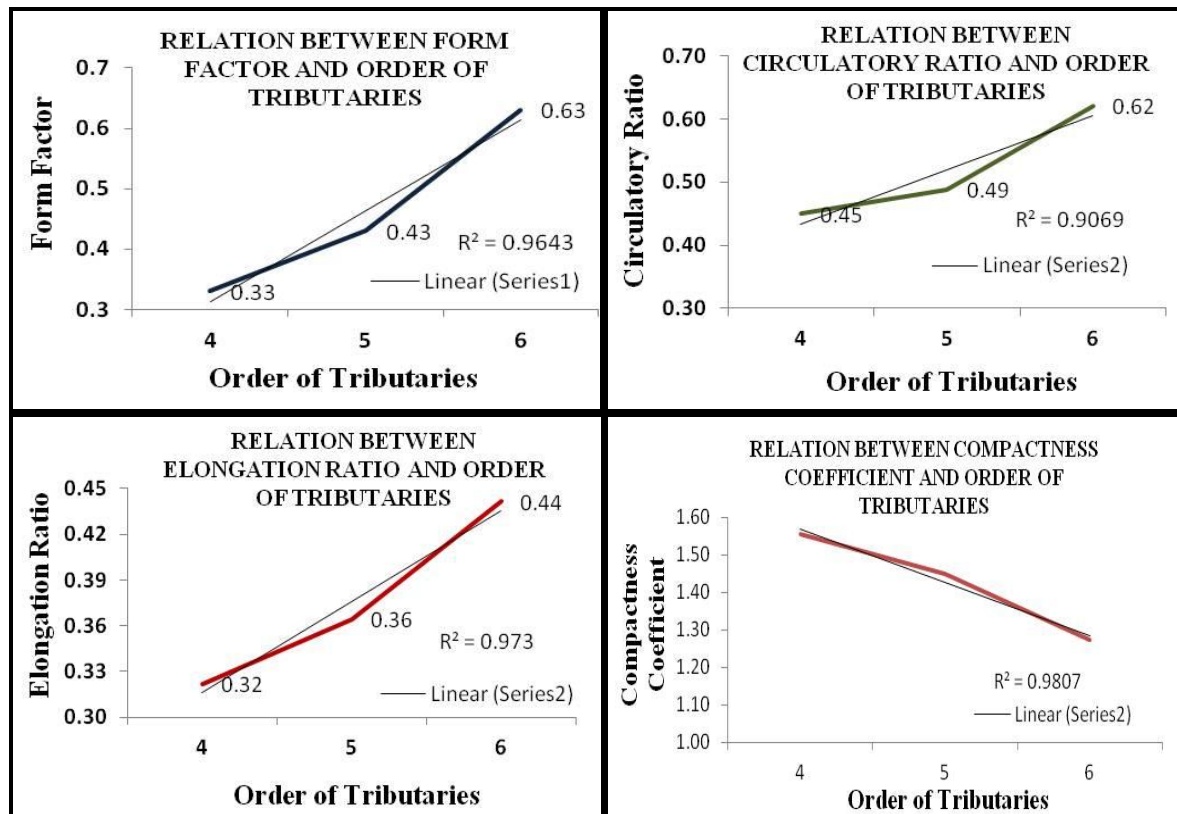


Figure 6: Graphs Showing Relation between Different Basin Shape Parameters and Order of Tributaries.

4.1.3. Relief Characteristics

Relative Relief (R_r) is an important morphometric variable used for the general estimation of morphological characteristics of terrain (Melton, 1957). The relative relief for watersheds varies from 1.97% (Riskan) to 6.60% (Kali) indicating higher runoff potential in Kali than others (Table 4).

4.2. Slope Categories and Wetness Index

In the hill slope estimation, the steep slope zones enhance the quick runoff during rains or storm events (Tucker and Bras, 1998). In the Gagas watershed, maximum 36.5% of the total area falls in slope range of 24° – 35° under extreme slope category, while minimum 0.01% falls in the lowest slope category of 0° – 0.3° (Table 4).

Another important parameter to quantify topographic control on hydrological processes is wetness index (WI) or topographic wetness index (TWI). Soil moisture is considered as the most important soil factor for rapid runoff and flash flooding. The higher WI empirically represents the spatial distribution of soil moisture, surface saturation and hence surface runoff which is an important factor to simulate soil erosion processes as well (Kienzel, 2004). It is expressed as the movement of water in terrain slope or local drainage by downslope topography. Sub watershed Gagas sub have been observed with highest value (11378) expressing potentially wetter region thus more runoff generation from such saturated areas, whereas Kali with the lowest value (5112) depicts a dry landscape (Table 4).

4.3. Maximum Discharge

As a function of the contributing area of a watershed, maximum flood have been derived by using the modified Dicken's method that helps in estimating the range of peak discharges in different

watersheds (Dawdy et al., 2012). However these values show the highest range, the sub watershed Gagas sub (49.87 m³/s) is most vulnerable to flash floods as compared to Bhikiyasen (8.82 m³/s) according to the estimated values (Table 4).

Table 4: Relief Ratio, Slope Categories, Wetness Index and Maximum Discharge used in Ranking of Gagas Sub Watersheds

| Sub-Watersheds | Relative relief (Rr) | Wetness Index (WI) | Slope (Area in %) | | | | | | | | | | Maximum Discharge (Q) (m ³ /s) |
|----------------|----------------------|--------------------|-------------------|------------|------------|------------|------------|-------------|------------|----------|----------|-------|---|
| | | | 0 – 0.3° | 0.3 – 1.1° | 1.1 – 3.0° | 3.0 – 5.0° | 5.0 – 8.5° | 8.5 – 16.5° | 16.5 – 24° | 24 – 35° | 35 – 45° | > 45° | |
| Bainali | 4.303 | 9900 | 0.00 | 0.11 | 0.78 | 1.94 | 4.85 | 18.58 | 28.52 | 38.52 | 6.53 | 0.17 | 19.68 |
| Bhikiyas | 5.379 | 8464 | 0.01 | 0.04 | 0.19 | 0.72 | 2.42 | 13.15 | 31.07 | 44.26 | 8.06 | 0.07 | 8.82 |
| Dusad | 2.145 | 10476 | 0.01 | 0.18 | 1.28 | 2.94 | 7.98 | 28.90 | 31.68 | 24.64 | 2.66 | 0.02 | 27.31 |
| Gagas Sub | 3.658 | 11378 | 0.01 | 0.35 | 2.28 | 2.83 | 4.90 | 16.98 | 23.41 | 32.82 | 14.19 | 2.23 | 49.87 |
| Jamgad | 3.489 | 10950 | 0.00 | 0.04 | 0.42 | 0.92 | 3.06 | 18.35 | 32.72 | 39.11 | 5.25 | 0.12 | 37.09 |
| Kali | 6.604 | 5112 | 0.01 | 0.02 | 0.48 | 0.97 | 3.28 | 20.59 | 31.90 | 35.28 | 6.97 | 0.49 | 10.56 |
| Kaneri | 5.633 | 9946 | 0.00 | 0.04 | 0.28 | 0.70 | 2.22 | 15.08 | 34.14 | 42.19 | 5.21 | 0.13 | 18.94 |
| Khar | 2.494 | 11345 | 0.01 | 0.13 | 0.82 | 1.73 | 4.70 | 23.52 | 34.49 | 29.67 | 4.62 | 0.32 | 49.37 |
| Khira0 | 3.347 | 10281 | 0.02 | 0.23 | 2.04 | 4.77 | 12.68 | 33.48 | 24.20 | 19.29 | 3.27 | 0.12 | 27.88 |
| Makrao | 5.485 | 9851 | 0.01 | 0.12 | 0.78 | 1.60 | 5.24 | 30.40 | 35.39 | 22.67 | 3.55 | 0.24 | 17.37 |
| Malla | 3.105 | 11043 | 0.00 | 0.10 | 0.78 | 1.68 | 5.13 | 22.39 | 30.50 | 34.27 | 5.05 | 0.11 | 40.98 |
| Narora | 3.630 | 11311 | 0.01 | 0.14 | 0.86 | 1.61 | 4.09 | 17.14 | 30.57 | 37.61 | 7.53 | 0.43 | 47.92 |
| Riskan | 1.968 | 11130 | 0.00 | 0.12 | 0.86 | 1.89 | 5.24 | 23.91 | 33.65 | 30.00 | 4.17 | 0.15 | 43.16 |
| Total Gagas | 1.536 | 13462 | 0.01 | 0.17 | 1.15 | 2.08 | 5.25 | 21.56 | 30.43 | 32.46 | 6.38 | 0.51 | 209.83 |

5. Assessing Flash Flood Risk Vulnerability

Flash flood risk susceptibility assessment of the sub watersheds of Gagas watershed was performed by the summation of the runoff ranks of relevant influencing parameters i.e., morphometric (linear, areal and relief), slope, wetness index and maximum discharge (Table 5). A compound value (Cp) representing the runoff susceptibility was calculated for different watersheds accordingly. A Cp of 5–6 is categorised as with very high priority, 6–7 as high priority, 7–8 with moderate priority and 8 and above with low priority.

Analysis of ranking by Cp values show that sub watersheds viz. Makraon has very high susceptibility to flash floods. The sub watersheds will have the quickest hydrological response in rainfall or storm events leading to lesser lag time. Four sub watersheds viz. Jamgad, Kali, Kaneri and Narora have shown high flash flood susceptibility and high downstream flood vulnerability, as compared to the sub watersheds showing moderate hazard such as Bainali, Bhikiyasen, Gagas sub, Khar, Malla and Riskan sub watersheds. Among the 13 sub watersheds Dusad and Khira0 are least susceptible to the flash flood risks, which make this group as having a good potential for groundwater recharge as well (Figure 7).

Table 5: Ranking of Flash Flood Susceptibility of Different Sub Watersheds of Gagas Basin

| Sub Watersheds | Gagas Basin | | | | | | | | | | | | |
|----------------|-------------|------------|-------|---------|------|--------|------|--------|----------|-------|--------|--------|----|
| | Bainali | Bhikiyasen | Dusad | Jamga-d | Kali | Kaneri | Khar | Khira0 | Makra-on | Malla | Narora | Riskan | |
| Sg | 8 | 6 | 12 | 4 | 7 | 1 | 3 | 11 | 9 | 2 | 10 | 5 | 13 |
| WRbm | 11 | 12 | 8 | 10 | 5 | 2 | 3 | 4 | 5 | 1 | 7 | 6 | 9 |
| Dt | 7 | 13 | 9 | 3 | 6 | 12 | 10 | 4 | 11 | 8 | 5 | 1 | 2 |
| D | 5 | 8 | 10 | 4 | 6 | 7 | 11 | 9 | 8 | 1 | 9 | 3 | 2 |
| Lg | 5 | 8 | 11 | 4 | 6 | 7 | 12 | 9 | 8 | 1 | 10 | 3 | 2 |
| A | 5 | 1 | 6 | 13 | 8 | 2 | 4 | 12 | 7 | 3 | 9 | 11 | 10 |

| | | | | | | | | | | | | | | |
|-------------------------|-------------------|-----------------|------------|-----------------|-------------|-------------|-------------|-----------------|------------|------------------|-----------------|-------------|-----------------|----|
| | Rf | 10 | 3 | 12 | 6 | 2 | 9 | 7 | 8 | 13 | 4 | 5 | 1 | 11 |
| | Re | 4 | 10 | 2 | 7 | 11 | 5 | 6 | 6 | 1 | 9 | 8 | 12 | 3 |
| | Rc | 6 | 3 | 11 | 10 | 4 | 8 | 6 | 7 | 12 | 1 | 5 | 2 | 9 |
| | Cc | 6 | 3 | 11 | 10 | 4 | 8 | 5 | 7 | 12 | 1 | 4 | 2 | 9 |
| | Rr | 5 | 4 | 12 | 6 | 8 | 1 | 2 | 11 | 9 | 3 | 10 | 7 | 13 |
| Slope Categories | 0 – 0.3 | 4 | 11 | 10 | 11 | 2 | 8 | 5 | 7 | 12 | 6 | 1 | 9 | 3 |
| | 0.3 – 1.1 | 6 | 2 | 11 | 13 | 4 | 1 | 3 | 9 | 12 | 8 | 5 | 10 | 7 |
| | 1.1 – 3.0 | 6 | 1 | 11 | 13 | 3 | 4 | 2 | 8 | 12 | 7 | 5 | 10 | 9 |
| | 3.0 – 5.0 | 10 | 2 | 12 | 11 | 3 | 4 | 1 | 8 | 13 | 5 | 7 | 6 | 9 |
| | 5.0 – 8.5 | 7 | 2 | 12 | 8 | 3 | 4 | 1 | 6 | 13 | 11 | 9 | 5 | 10 |
| | 8.5 – 16.5 | 8 | 13 | 3 | 11 | 9 | 7 | 12 | 5 | 1 | 2 | 6 | 10 | 4 |
| | 16.5 – 24 | 11 | 8 | 7 | 13 | 5 | 6 | 3 | 2 | 12 | 1 | 10 | 9 | 4 |
| | 24 – 35 | 4 | 1 | 11 | 8 | 3 | 6 | 2 | 10 | 13 | 12 | 7 | 5 | 9 |
| | 35 – 45 | 5 | 2 | 13 | 1 | 6 | 4 | 7 | 9 | 12 | 11 | 8 | 3 | 10 |
| | > 45 | 6 | 12 | 13 | 1 | 10 | 2 | 8 | 4 | 9 | 5 | 11 | 3 | 7 |
| | WI | 10 | 12 | 7 | 1 | 6 | 13 | 9 | 2 | 8 | 11 | 5 | 3 | 4 |
| | Q | 9 | 13 | 8 | 1 | 6 | 12 | 10 | 2 | 7 | 11 | 5 | 3 | 4 |
| Cp Value | 6.87 | 6.52 | 9.65 | 7.35 | 5.52 | 5.78 | 5.74 | 6.96 | 9.52 | 5.39 | 7.00 | 5.61 | 7.09 | |
| RANKING | Moderate | Moderate | Low | Moderate | High | High | High | Moderate | Low | Very High | Moderate | High | Moderate | |

Stream grade (Sg), Weighted mean bifurcation ratio (Rbm), Drainage texture (Dt), Drainage density (D), Length of overland flow (Lg), Basin area (A), Form factor (Rf), Elongation ratio (Re), Circulatory ratio (Rc), Compactness coefficient (Cc), Relative relief (Rr), Wetness Index (WI), Maximum discharge (Q)

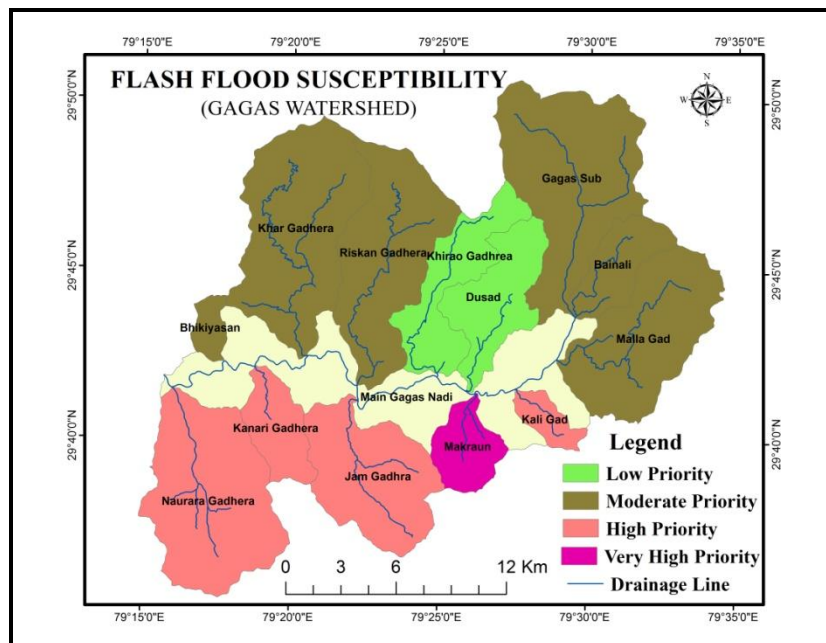


Figure 7: Map of Flash Flood Susceptibility in Gagas Watershed

6. Conclusion

In complex mountainous environment such as Himalayas, along with the topography having a major role in seasonal flooding, the effects of climate change render the region vulnerable to the natural hazards. As the primary determinants of running water systems functioning at the watershed scale, the physical (morphometrical, topographical) and climatic attributes were evaluated using remotely sensed data (ASTER-DEM) and GIS based approach.

The present study is carried out in the sixth order Gagas watershed in the Lesser Himalaya. In the study area, the drainage patterns are dendritic, that indicates impervious and non-porous bed rock. More number of higher order tributaries shows the association with more discharge and higher velocity of the stream flows. A detailed sub watershed study analysed 14 relevant parameters to assess flash flood susceptibility. The stream grade ranges from 3.74 % to 15.02 % showing the difference in the slope of the channel and thus the intensity of runoff at various reaches. The weighted mean bifurcation ratio ranges between 3.36 and 5.89, higher range show more elongated sub watersheds. Similar values express similar rock group composition and tectonic history, uniform climate conditions, infiltration rate and in similar stage of development. Drainage texture shows coarse (Bhikiyasen) texture showing massive and resistant rocks to very fine texture (Narora) expressing soft or weak rocks uncovered by vegetation. A relatively higher Drainage density (Makraun) shows a high density of streams, low infiltration and higher peak runoff. The sub watersheds sizes vary between 5.25 - 63.05 Km² affecting the lag time after heavy rainfall. In the analysis of relation between the order of tributaries; and shape factors (form factors, circulatory ratios, elongation ratios and compactness coefficient), it is observed that these are significant parameters in drainage-basin evolution as well as in influencing runoff.

The watershed has an average relative relief of 3.96%. The basin is characterised with level to very steep slope of the terrain ranging from lowest 0°–0.3° (01%) to >45° (0.51%). In the watershed maximum area falls in the slope category of 24°–35° (36.5%). Another important parameter of wetness index represents the spatial distribution of soil moisture, surface saturation and surface runoff. Its values range between 11378 (Gagas sub) showing potentially wetter region and more runoff generation and lowest 5112 (Kali) depicting a dry landscape. As a function of area, maximum discharge was calculated to estimate the potential hazard of flash floods. It varied between 49.87 m³/s (Gagas sub) to 8.82 m³/s (Bhikiyasen) and an average maximum discharge 30.69 m³/s.

The RS/GIS techniques have been efficient tools in the understanding of drainage characteristics that help in the hazard risk mapping and having more accurate and reliable results as compared to conventional methods. In the study, one sub watershed (Makraun) have shown very high susceptibility to flash floods, while four sub watersheds viz. Jamgad, Kali, Kaneri and Narora have shown high susceptibility and high downstream flash flood vulnerability, as compared to those with moderate hazards such as Bainali, Bhikiyasen, Gagassub, Khar, Malla and Riskan. Among the 13 sub watersheds, Dusad and Khirao are least susceptible to flash flood risks and having a good potential for groundwater recharge. As a management technique, various adaptive mechanisms to hazards such as water stress as well as peak runoff should be followed up. Building up of check dams, small ponds, storage water tanks, proper agriculture calendar could serve as measures for the prevention of losses occurred due to flash floods and mitigation of the water related disasters.

References

- Anonymous, 2013: Digital Terrain Analysis Manual. University of Minnesota United States. 1-64.
- Avery, T.E., 1975: *Natural Resources Measurements*. New York: McGraw-Hill Book Company. 339.

Avinash, K., Jayappa, K.S. and Deepika, B. *Prioritization of Sub-Basins Based on Geomorphology and Morphometric Analysis Using Remote Sensing and Geographic Information System (GIS) Techniques*. Geocarto International. 2011. 26 (7) 569-592.

Barseem, M.S.M., El Tamamy, A.M. and Masoud, M.H.Z. *Hydrogeophysical Evaluation of Water Occurrences in El Negila Area, Northwestern Coastal Zone–Egypt*. Journal of Applied Sciences research. 2013. 9 (4) 3244-3262.

Betson, R.P. *What is Watershed Runoff?* Journal of Geophysical Research. 1964. 69 (8) 1541-1552.

Chalam, B.N.S., Krishnaveni, M. and Karmegam, M. *Correlation of Runoff with Geomorphic Parameters*. Journal of Applied Hydrology. 1996. 9 (3-4) 24-31.

Chopra, R., Dhiman, R.D. and Sharma, P. *Morphometric Analysis of Sub-Watersheds in Gurdaspur District, Punjab Using Remote Sensing and GIS Techniques*. Journal of the Indian Society of Remote Sensing. 2005. 33; 531–539.

Dawdy, D.R., Griffis, V.W. and Gupta, V.K. *Regional Flood-Frequency Analysis: How we got here and where we are going*. Journal of Hydrologic Engineering. 2012. 17 (9) 953-959.

Doornkamp, J.C. and Cuchlaine, A.M.K., 1971: *Numerical Analysis in Geomorphology—an Introduction*. Edward Arnold, London. 372.

Gardiner, V. and Gregory, K.J., 1982: *Drainage Density in Rainfall-Runoff Modelling*. In: Singh, V.P., (Ed.), *Rainfall-Runoff Relationships*. Littleton (Colorado): Water Resources Publications. 449-76.

Georgakakos, K.P. *A Generalized Stochastic Hydrometeorological Model for Flood and Flash-Flood Forecasting: 1 Formulation*. Water Resources Research. 1986. 22 (13) 2083-2095.

Goswami, B.N., Venugopal, V., Sengupta, D., Madhusoodanan, M.S. and Xavier, P.K. *Increasing Trend of Extreme Rain Events Over India in a Warming Environment*. Science. 2006. 314 (5804) 1442-1445.

Gravelius, H., 1914: *Flusskunde* Goschen Verlagshandlung Berlin. In: *Morphometry of Drainage Basins*. Amsterdam: Elsevier.

Hack, J.T. *Stream-Profile Analysis and Stream-Gradient Index*. Journal of Research of the U.S. Geological Survey. 1973. 1 (4) 421-429.

Hack, J.T. *Studies of Longitudinal Stream Profiles in Virginia and Maryland*. Geological Survey Professional Paper (United States). 1957. 294 (B) 45-97.

Horton, R.E. *Drainage Basin Characteristics*. Transactions - American Geophysical Union. 1932. 13 (1) 350-361.

Horton, R.E. *Erosional Development of Streams and Their Drainage Basin: Hydrophysical Approach to Quantitative Morphology*. Geological Society of America Bulletin. 1945. 56; 275-370.

Huggett, R.J. and Cheesman, J., 2002: *Topography and the Environment*. Pearson Education. 292.

Hupp, C.R. *Stream-grade Variation and Riparian-Forest Ecology along Passage Creek, Virginia*. Bulletin of the Torrey Botanical Club. 1982. 488-499.

- IAHS-UNESCO-WMO, 1974: Flash Floods. In: *Proceedings of the Paris Symposium*, Paris: UNESCO. 112.
- ICIMOD, 2007: *Flash Flood Hotspot Mapping in the Hindu Kush-Himalayan Region*. Kathmandu: International Centre for Integrated Mountain Development (ICIMOD).
- Jalal, D.S., 1988: *Kumaun: The Geographical Perspective of Kumaun*. In: KS Valdiya (Ed.), *Kumaun: Land and People*, Nainital, India: Gyanodeya Prakshan.
- Kharkwal, S.C., 1993: *Physico-Cultural Environment and Development in U.P.*, Kotdware, India: Nutan Publications. 299.
- Kienzle, S. *The Effect of DEM Raster Resolution on First Order Second Order and Compound Terrain Derivatives*. Transactions in GIS. 2004. 8 (1) 83-111.
- Kumar, A. and Kumar, D. *Predicting Direct Runoff from Hilly Watershed Using Geomorphology and Stream-Order-Law Ratios: Case Study*. Journal of Hydrologic Engineering. 2008. 13 (7) 570-576.
- Lambert, D., 1998: *The Field Guide to Geology*. Checkmark Books. 130-131.
- Melton, M.A., 1957: *An Analysis of the Relations among Elements of Climate, Surface Properties, and Geomorphology* (No. CU-TR-11). New York: Columbia Univ.
- Miller, V.C. 1953: *A Quantitative Geomorphic Study of Drainage Basin Characteristics in the Clinch Mountain Area, Virginia and Tennessee*. Technical Report (3), Dept. of Geol. New York: Columbia University. 389-402.
- Moges, G. and Bhole, V. *Morphometric Characteristics and the Relation of Stream Orders to Hydraulic Parameters of River Goro: An Ephemeral River in Dire-dawa, Ethiopia*. Universal Journal of Geoscience. 2015. 3 (1) 13-27.
- NRCC, 1998: *The Canadian System of Soil Classification*. In: Soil Classification Working Group. 3rd edn. Canada: NRC Research Press, 149.
- Pakhmode, V., Kulkarni, H. and Deolankar, S.B. *Hydrological-Drainage Analysis in Watershed-Programme Planning: A Case from the Deccan Basalt, India*. Hydrogeology Journal. 2003. 11; 595-604.
- Pal, D., 2002: *Water Regimes of Uttaranchal*. In: Pandey et al. (Eds.), *Watershed Management in Himalaya*, Nainital, India: Gyanodaya Prakshan.
- Paul, A. and Pant, P.D. *Seismic Hazard Estimation in Northeastern Kumaun Himalaya*. Journal of the Geological Society of India. 2003. 61; 477-482.
- Punmia, B.C., Lal, P.B.B., Jain, A.K. and Jain, A.K., 2009: *Irrigation and Water Power Engineering*. Laxmi Publications Ltd. 986.
- Qin, C.Z., Zhu, A.X., Pei, T., Li, B.L., Scholten, T., Behrens, T. and Zhou, C.H. *An Approach to Computing Topographic Wetness Index Based on Maximum Downslope Gradient*. Precision Agriculture. 2011. 12 (1) 32-43.

Ratnam, K.N., Srivastava, Y.K., Rao, V.V., Amminedu, E. and Murthy, K.S.R. *Check Dam Positioning by Prioritization of Micro-Watersheds Using SYI Model and Morphometric Analysis—Remote Sensing and GIS Perspective*. Journal of the Indian Society of Remote Sensing. 2005. 33 (1) 25-38.

Rijal, K.P. *Comparative Study of Flood Calculation Approaches, a Case Study of East Rapti River Basin, Nepal*. Hydro Nepal: Journal of Water, Energy and Environment. 2014. 15; 60-64.

Schumn, S.A. *Evolution of Drainage Systems and Slopes in Badlands at Perth Amboy, New Jersey*. Geological Society of America Bulletin. 1956. 67; 597-646.

Sharma, S. *Catastrophic Hydrological Event of 18 and 19 September 2010 in Uttarakhand, Indian Central Himalaya—an Analysis of Rainfall and Slope Failure*. Current Science. 2012. 102 (2) 327-332.

Shrestha, D., Singh, P. and Nakamura, K. *Spatiotemporal Variation of Rainfall over the Central Himalayan Region Revealed by TRMM Precipitation Radar*. Journal of Geophysical Research: Atmospheres. 2012. (117) D22.

Smith, K.G. *Standards for Grading Texture of Erosional Topography*. American Journal of Science. 1950. 248 (9) 655-668.

Strahler, A.N. *Quantitative Analysis of Watershed Geomorphology*. Transactions-American Geophysical Union. 1957. 38; 913-920.

Strahler, A.N. *Revisions of Horton's Quantitative Factors in Erosional Terrain*. Transactions - American Geophysical Union. 1953. 34; 345.

Tucker, G.E. and Bras, R.L. *Hillslope Processes Drainage Density and Landscape Morphology*. Water Resources Research. 1998. 34 (10) 2751-2764.

UNESCO, 2005: *Hydrology for the Environment, Life and Policy—HELP Brochure*, Paris. 20. <http://www.unesco.org/water/ihp/help>.

Vijith, H. and Satheesh, R. *GIS based Morphometric Analysis of Two Major Upland Sub-Watersheds of Meenachil River in Kerala*. Journal of the Indian Society of Remote Sensing. 2006. 34 (2) 181-185.

WorldClim, Global Climate Data: <https://www.climond.org/BioclimData.aspx>

Impact of Port Structures on the Shoreline of Karnataka, West Coast, India

Deepa Naik¹ and Pravin D. Kunte²

¹Geography Department, Pune University, Pune, Maharashtra, India

²National Institutes of Oceanography, Council of Scientific and Industrial Research (CSIR), Goa, India

Publication Date: 23 May 2016

DOI: <https://doi.org/10.23953/cloud.ijarsg.56>



Copyright © 2016 Deepa Naik and Pravin D. Kunte. This is an open access article distributed under the **Creative Commons Attribution License**, which permits unrestricted use, distribution, and reproduction in any medium, provided the original work is properly cited.

Abstract The changes in shoreline positions and geomorphic features along the Karnataka, West coast of India, were studied for the period from 1973 to 2014, using multi-dated satellite images and topographic maps. The ten hotspots which are mainly areas nearer to the port region were specially studied for the quantification of erosion and accretion. Dredging for port development normally lead to noteworthy changes in the configuration of the seabed. These changes can meaning fully modify the currents, waves and water quality. The statistical method incorporated with GIS has been used to estimate the rate of change and net shore movement of the coast. The study indicates that gradual recession and accretion at Tadri, Bhatkal, Honnavar, etc. Shorelines extracted for the years 1973, 1998, 2000, 2003 and 2014 indicate that the coastline adjacent to port area experienced both the erosion and accretion. Shoreline change rate of Karnataka coastline is estimated as -1.2354 m/year. Erosion and accretion of shoreline are major impacts of port/harbor. However, minor impacts are like an increase in pollution due to waste dumping and port-related industries, increase in coastal population and related activities and degradation of surrounding environment due to dredging and dumping material. Most of the shoreline sites, though largely get affected due to port structures, during monsoon season, achieve natural partial equilibrium during the non-monsoon season due to reversing currents and wind pattern. And hence, it may be concluded that port/harbors have limited impact on the coastal shoreline.

Keywords *Port Impact; Reversing Wind; Shoreline Change; Geospatial Studies; Karnataka Coast*

1. Introduction

Shoreline changes induced by erosion and accretion are natural processes that take place over a range of timescales. Coastal erosion causes extensive damage to public and private property and to natural resources and jeopardizes human lives. This has resulted in significant economic losses to individuals, private businesses, and the state's economy. Coastal erosion damage has necessitated large public expenditures to remove debris and crumbling structures, and to replace crucial public facilities and services. The management of coastal erosion hazard areas supports to protect coastal

habitat areas, inland natural resources, homes, businesses, and communities from wind, water erosion and storm-induced high water.

Construction and development of ports and accompanied civil structures, at different locations in the world, brings about shoreline, environmental, and socio-economic changes. Like Newport harbor which is situated 16 km south of downtown Santa Ana once supported maritime industries such as boatbuilding, shipbuilding, and commercial fishing, but today it is used mostly for recreation. The shoreline movement has been studied for the period of 1874 to 2002. The accretion has been observed almost 200m from 1901-1983 because of disposal and dredge material and subsequent reclamation of land. During the 1980s and 1990s the accretion pattern continued. During 1983-2002 the shoreline retreated about -10m as in the winter season, the large volume of sand accreting in the offshore, and not coming ashore during summer. Developments at Rous Head prevent any residual dredge material from moving onto Port Beach from the south (Department of Planning and Infrastructure 2004).

Similarly, Port IJmuiden is located at the mouth of the North Sea Canal to Amsterdam, and situated about 17 km north of Haarlem is a deep water port suited to fully laden Panamax ships, and is fourth port of the Netherlands. The Port of IJmuiden has been constructed around 1870 and initially had a length of about 1.5 km. After the construction two breakwaters accretion occurred against both breakwaters and erosion at some more distance on either side of the port. During the study, it is observed that in the period 1840 – 1950, the accretion just north of the port was significantly larger than just south, given the fact that the net longshore transport along the Dutch coast is northward directed. After the extension of the harbor moles in 1965 the accretion has been started with a high rate at the coast south while further accretion at the north of the port remained limited. At present, the seaward movement of the shoreline against the southern breakwater since port construction is about 800 m and close to the northern breakwater about 700 m. The inclusion of sediment bypass improves the coastline response north of the port significantly, and the south the transition point between accretion and erosion of the coastline is reproduced well (Luijendijk et al., 2011).

Damietta Port is located at the Damietta branch, a tributary of the Nile, 15 km from the Mediterranean Sea, approximately 200 km north of Cairo has three distinct zones: (1) the western zone is noticeable by shoreline accretion; (2) the central zone which has mixed erosion and accretion; and (3) the eastern zone which is categorized by minor erosion with minor and localized accretion areas. Frihy (1988) stated that much of the eroded material from the tip of Rosetta and Damietta promontory is transported eastward by littoral drift and accreted on the eastern parts of the promontories. Moreover, there has been the formation of a spit on the same (eastern) side of Damietta promontory. Frihy et al. (1991) concluded that the maximum erosion occurred at the tip of the promontory, with accretion taking place to the east along its bank. The accretion has taken the form of a sand spit growing in the eastern direction. The eastern zone which extends from 22 km east of the mouth of the Damietta to Port Said, and is characterized by slight erosion with minor and localized accretion areas (EL-Raey et al., 1999).

Developments of major/minor ports and fishery harbors consist of the construction of coastal structures like break waters, jetties, groins and reclamation bunds. Improvements of the ports also involve the dredging and disposal activities to maintain these essential depths for navigation. These coastal structures and the dredging activities interfere in the coastal processes of the region. Alterations in the coastal processes have a large impact on the coast line (Kudale, 2010).

Natural forces such as wind, waves and currents are constantly influencing the coastal regions. The combined energy of these forces transports land materials. And the effects of waves, currents, tides and wind are primary natural factors that influence the coastline. The other features eroding the coastline include the sand sources and sinks, changes in relative sea level, slope, geomorphological

characteristics of the shore and sand, etc. Anthropological activities that trigger beach erosion are the construction of artificial structures, mining of beach sand, offshore dredging or building of dams or rivers. The major coastal process like littoral drift plays an important role in deciding the areas of coastal erosion and deposit, in shaping and orienting coastal landforms and finally in the evolution of the coast (Kunte and Wagle, 2000).

The shoreline changes between Ohtsu Fishery Harbor and Hitachi Port along the Joban Coast are studied during the period 1947-1966, 1966-1975, 1975-1984, and 1947-1984. Cyclic beach changes of accretion or erosion were observed on both sides of the headlands located between Ohtsu Fishery Harbor and Unomisaki Cape. This is because of the predominant wave direction changes seasonally from northeast to the southeast on the coast. Severe beach erosion and accretion were observed because of the elongation of the offshore breakwater at Ohtsu Fishery Harbor and Oharai Port. Along the Kashimanada Coast beach erosion is severe at the south site of Oharai Port, the north of Kashima Port and Hazaki Fishery Harbor. The slope of the beach face becomes steep and the armoring of the bed materials on the shore is under way on the eroded beach on the down drift side of the structure. It is observed that a large amount of sand accumulated inside Hazaki Fishery Harbor with the elongation of the breakwater. Especially the shoreline advanced very much after the completion of the construction work of the parallel offshore breakwater with respect to the shoreline. Regarding the cause of the beach changes inside the harbor, the deposition of a part of the sediment outflow from the Tone River is considered to be important because of the formation of the calm water inside the harbor (Sumiya et al., 2007).

During the last two decades, remote sensing and geographical information system (GIS) techniques have been widely employed in various coastal morphodynamic studies as they are less costlier, reduce manual error, and are useful in the absence of field investigations. The applications of remote sensing and GIS have proved particularly effective in delineation of coastal configuration and coastal landforms, finding of shoreline positions, assessment of shoreline and land form changes, extraction of shallow water bathymetry (White and El Asmar, 1999; Ryu et al., 2002; Siddiqui and Maaajid, 2004; Maiti and Bhattacharya, 2009; Chaudhari et al., 2013; Salvan et al., 2014). The Digital Shoreline Analysis System (DSAS) is a freely available software application that works with the Environmental Systems Research Institute (ESRI) Geographic Information System (ArcGIS) software, has been used. DSAS computes rate-of-change statistics for a time series of shoreline vector data (Himmelstoss, E.A. 2009). Digital Shoreline Analysis System (DSAS) version 4.0 — An ArcGIS extension for calculating shoreline changes (U.S. Geological Survey Open-File Report 2008-1278).

1.1. Study Site

Karnataka State is located between 11°30' and 18°30' N latitudes and 74° and 78°30' E longitude. The State is bounded by Maharashtra and Goa States in the north. Karnataka's coastline extends over a length of 320 km. It is one of the most indented shorelines with numerous river mouths, lagoons, bays, creeks, promontories, cliffs, spits, sand dunes and long beaches (Figure 1). The coastal stretch of Karnataka has no major delta formations. The shelf off Karnataka has an average width of 80 km and the depth of shelf break is between 90 and 120 m. There are a few islands off the coast, the major group being St. Mary's Island. Fourteen rivers drain their waters into the shore waters of Karnataka. The important estuaries include the Netravati-Gurpur, Gangolli, Hangarkatta, Sharavthi, Aganashini, Gangavali, and Kalinadi. Sand bars have developed in most of the estuaries. There are a number of barrier spits at Tannirbavi, Sasithitlu, Udyavara, Hoode, Hangarkatta and Kirimanjeswara formed due to migration of coastal rivers. There are 90 beaches out-of-which 22 beaches are classified as unfit for use due to erosion, human settlements and activities linked to ports/harbors, industries, and fisheries. Coastal zone comprises of districts of Uttara Kannada, Udupi and Dakshina Kannada. The coastal plain experiences a tropical humid climate with very hot summer and high monsoon rainfall. The

average annual maximum temperature is 30.9° C and a minimum of 23.7° C. On an average, annual rainfall is ~3,900 mm (Kumar et al., 2010).

During June–September, a period referred to as the summer monsoon, the general direction of winds, to the north of the equator, is southwesterly and its strength is considerably larger than that during the rest of the year. During November–March, referred to as the winter monsoon, winds over the same region have overall northeasterly direction. October and April–May are times of transition between the two monsoons (Shetye et al., 1985). The coastal segment along the study region is bounded by the Western Ghats in the east and the Arabian Sea in the west. The coastline at Karwar is inclined to the west by 24° from the true north. The bathymetry contours aligned approximately parallel to the coastline. The coastline at Honnavar and Malpe are inclined to the west by 17° from the true north. There are a few islands off the coast, the major one being St. Mary's Island, 4 km off the coast near Malpe. The coast is exposed to the seasonally reversing monsoon winds and the annual rainfall is 3 m. The tides in this region are mixed semi-diurnal dominant, the range of which increases towards the north (Kumar et al., 2011a). The monthly mean sea level at Karwar varies from 1.06 m in September to 1.3 m in January. The average tidal range at Karwar is 1.58 m during springs and 0.72 m during neaps. During the summer monsoon along the west, coast of India, significant wave height ($Hm0$) up to 6 m has been reported (Kumar et al., 2006), $Hm0$ is normally <1.5 m during rest of the period (Kumar et al., 2003)

The main aim of this investigation is to provide systematic and accurate historical measurements on shoreline change along the Karnataka coast using multi-resolution, multi-date satellite data and Geographic Information System (GIS) as the location of the shoreline and its historical rate of change can provide important information for the design of coastal protection, plans for coastal development, coastal and social vulnerability study, and the calibration and verification of numerical models, etc. A further attempt is also made to study the impact of port-related structures on shoreline changes of Karnataka coast, India.

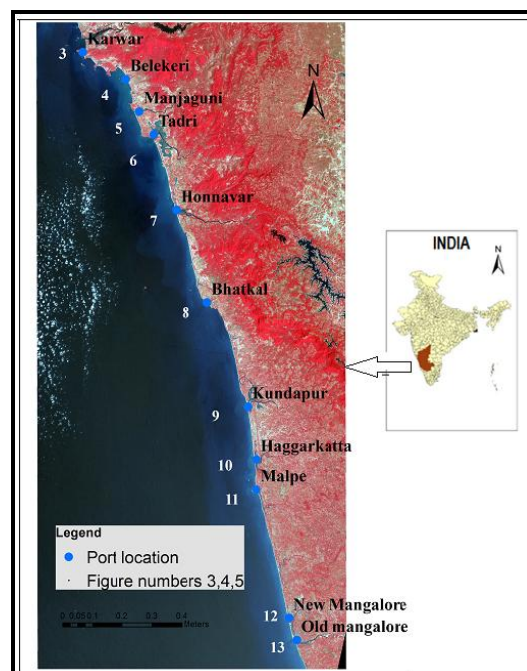


Figure 1: Karnataka, West Coast of India

2. Materials and Methods

For the present study, Geospatial techniques have been used to analyze the shoreline changes. As remote sensing data provide synoptic coverage and GIS helps in the analysis of more temporal data sets, so that dynamic areas, which are changing due to the erosion-accretion processes can be identified easily. The details of the data products used in this study are listed in Table 1.

Table 1: List of the Data Product Used for the Study

| Data | Date and Year | Sensor | Source |
|---------------------------------|----------------|---|---------------------------------------|
| Satellite images | 2 March 1973 | Landsat-MSS | www.usgs.gov.in |
| | 17 March 1998 | Landsat-TM | |
| | 14 March 2000 | Landsat-TM | |
| | 23 March 2003 | Landsat-TM | |
| | 8 January 2014 | Landsat-OLI | |
| Topo graphic maps (1:50,000) | 1975 | Grids:48J/1,6,7,12 48K/9,10,11,15,16, 48L/13 | Survey of India |
| Nearshore Bathymetry | ----- | ----- | National Institute of oceanography |
| Geomorphology map | 8 January 2014 | Landsat-OLI | Self-prepared |

2.1. Methods

The shoreline changes for 5 different years (1973, 1998, 2000, 2003 and 2014) have been studied using statistical method incorporated with GIS. Normalized difference water index has been calculated using ERDAS imagine software which enhances the water body so as to differentiate from land masses. The shorelines for 5 different years have been digitized using ArcGIS10. Survey of India topographic maps (1975) was geo-referenced in ERDAS Imagine 9.2 and reprojected to UTM, WGS 84, 43 north zones and used as a source of reference. Erosion-accretion maps were produced using these digitized shorelines. Geomorphology map has been created in ERDAS imagine using Landsat OLI 2014 Image. Contour map has been prepared to study the coastal region slope, as geomorphology and slope play an important role in understanding erosion and accretion processes. The rate of shoreline change and net shoreline movement has been estimated using digital shoreline analysis system (DSAS) tool which is a freely available software application (USGS 2005) that works within the Environmental Systems Research Institute (ESRI) Geographic Information System (ArcGIS) software.

DSAS requires more than two shorelines and those must reside in a single feature class. DSAS also requires that the feature class be in meter units in a projected coordinate system. The baseline i.e. simple vector line has been drawn, onshore, and parallel to the shorelines (Himmelstoss, 2009). The techniques involve the computation of the change in the position of the shoreline through time by drawing perpendicular transects to the baseline. Accordingly, 300 m long transects at a spacing of 500 m were casted along the 320 km long shoreline of Karnataka with the help of the DSAS TOOLBAR in ArcGIS 9.3 (Figure 2). The different methods used to calculate the rate of shoreline change include the End Point Rate (EPR), Net Shoreline Movement (NSM), Average of Rates (AOR), Linear Regression (LR), and Jackknife (JK). The advantage of the EPR method is its ease of computation, as it considers only two shoreline positions to calculate the rate of shoreline change (Dolan et al., 1991). At each transect along the shoreline, the NSM and EPR were estimated and the rate of shoreline change and associated risk ratings were calculated.

Shorelines extracted for the years 1973, 1998, 2000, 2003 and 2014 from Indian Remote Sensing satellite (IRS) data and using DSAS tool, were examined for possible shoreline change. The study estimates the area which experienced both the erosion and accretion, adjacent to ports. Net erosion

and accretion rate for the period 1973 to 2014 is shown in Figures 3-12, with red and green color respectively. The eroded and accreted areas for periods 1973-1998, 1973-2000, 1973-2003, and 1973-2014 are shown in red and green color, in four maps of each figure. The cumulative Shoreline change rate for the period 1973-2014 for every port is estimated and mentioned in Table 2.

Table 2: Net Shoreline Movement During 1973 to 2014 adjacent to Ports/harbors of Karnataka State

| Net Shoreline Movement during 1973_2014 | | |
|---|---------------|------------------|
| Ports/harbours | Net Recession | Net Progradation |
| 1 Karwar | -1.6497m | 3.3082m |
| 2 Belekeri | -51.7700m | 162.4500m |
| 3 Manjaguni | -42.9891m | 51.2880 |
| 4 Tadri | -80.1070m | 50.6750m |
| 5 Honnavar | -52.5720m | 32.5733m |
| 6 Bhatkal | -182.5083m | 22.2600m |
| 7 Kundapur | -58.0925m | 62.4367m |
| 8 Hangarkatta | -50.3829m | 62.5900m |
| 9 Malpe | -95.4862m | 43.9900m |
| 10 New Mangalore | -4.8400m | 2.1500m |

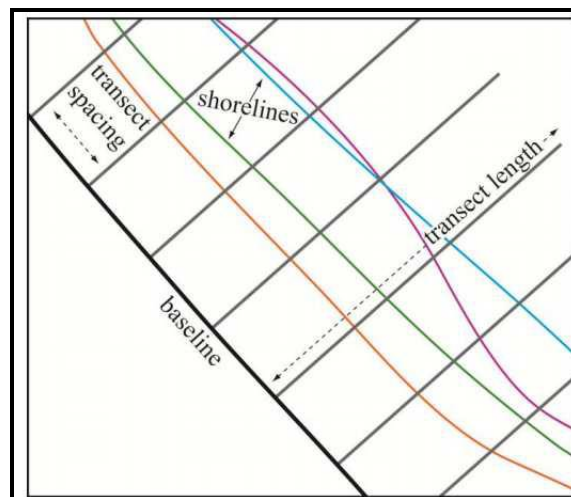


Figure 2: DSAS Input Data Structure

3. Results

The coastal zone of Karnataka is one of the better-developed geographical areas of the state with a high degree of economic development and density of population. The coastline is dotted with one major port at Mangalore, nine minor ports at Karwar, Belekeri, Tadri, Honavar, Bhatkal, Kundapur, Hangarkatta, Malpe and New & old Mangalore Port. Besides, there are 110 fish landing centers and 150 fishing villages. A single major intervention in the coastal zone is the project Sea Bird, where an area of around 32 sq. km. is being converted into an area with several structures. The port-wise study is presented as below.

3.1. Karwar Port

Karwar port is located at Baithkol, Karwar Bay. Karwar is one of the major fishing zones in Karnataka. The Kali River flows through Karwar which is also a prominent tourist destination. The entire city of Karwar is situated on beach ridges formed due to the influence of Kali River and the Arabian Sea confluence during the past. The area covered geomorphology classes such as tidal flat, spit, Marine

Island, sandy beach, creek, coastal plain, Channel Island and alluvial plain. Spit shows a gradual decrease in the area. Sediment discharge takes place near the river mouth, it is very dynamic and changes seasonally; long-term observation shows a shift of Kali River mouth towards the north. The area surrounding Karwar port (Figure 3) has the rate of erosion -1.6497m/yr and rate of accretion $+3.3082\text{m/yr}$ during the period of 1973 to 2014. Net shoreline recession during this period is -71.2837m and net pro gradation is $+114.7100\text{m}$.

Hills and coastal islands make the port a natural harbor, sheltered from the Arabian Sea. The length of the port is 355 m. The quay has two berths, with a draft capacity of 9.25 m. Karwar port also berths coastal vessels and there is a jetty for fishing vessels. The Government of Karnataka has planned to develop Karwar port on a Public Private Partnership (PPP) basis to provide six additional berths, a container terminal, and a rail link to Shirwad railway station. The port is able to handle all types of commodities, including "B" and "C" class petroleum products. The port has liquid storage tanks for bitumen, furnace oil, molasses, and HSD. A ban on iron ore mining and export in Karnataka state reduced congestion at the port. The port has arrangements for berthing coastal vessels, and a jetty for fishing boats (<http://en.wikipedia.org/wiki/Karwar>).

In 2012, the Government of Karnataka carried out maintenance dredging in the port, the approach channel, and the nearby anchorage. INS-Kadamba is an Indian Navybase located near Karwar in Karnataka. INS Kadamba is currently the third largest Indian naval base and is expected to become the largest naval base in the eastern hemisphere after completion of expansion Phase IIB. Erosion accretion areas surrounding Karwar port is shown in Figure 3.

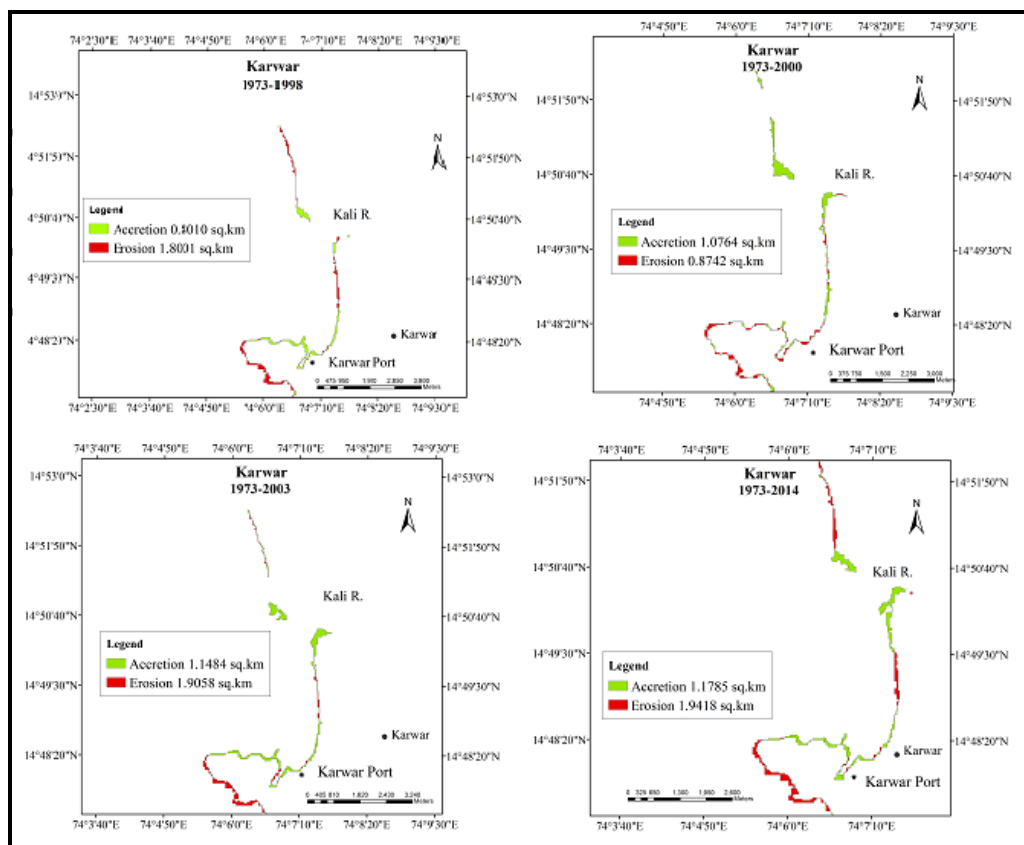


Figure 3: Erosion and Accretion Adjacent to Karwar Port

3.2. Belekeri Port

Belekeri Port is located 8 km north of Ankola and 15 km South of Karwar, in Uttara Kannada District of Karnataka. The Port is built on a rocky head land and is well protected from the southern side. It is built on the bank of Kalinadi River and has spits on north and south side of the river. It is second biggest port after Mangalore Port in Karnataka. This port is mainly used for exporting of Iron Ore. The area surrounding port shows (Figure 4) rate of erosion as 1.267m/y and the rate of accretion +3.977 m/y for the period 1973-2014. The shoreline retreats by -51.77m and is prograded by +162.45m.

The tidal inlets and the river mouths are located on littoral transport shore lines; they are often in a natural equilibrium with respect to bypassing of the littoral drift, which normally occurs on a shallow bar across the inlet. The area is characterized by sandy beaches and coastal plain. Erosion is noticed on one side of the port and accretion is observed on another side. This port is mainly used for exporting iron ore. Ore is transported to ships in the sea by barges. For now, three jetties are available for barge loading. Recent filings and reclamation works by the iron ore exporting companies have aggravated the intensity of erosion. Survey showed that the coastal dunes, which play a key role in preventing erosion, have been dug up for creating fields by the local farmers, thereby making the sea coast more prone to sea erosion (EMPRI 2007).

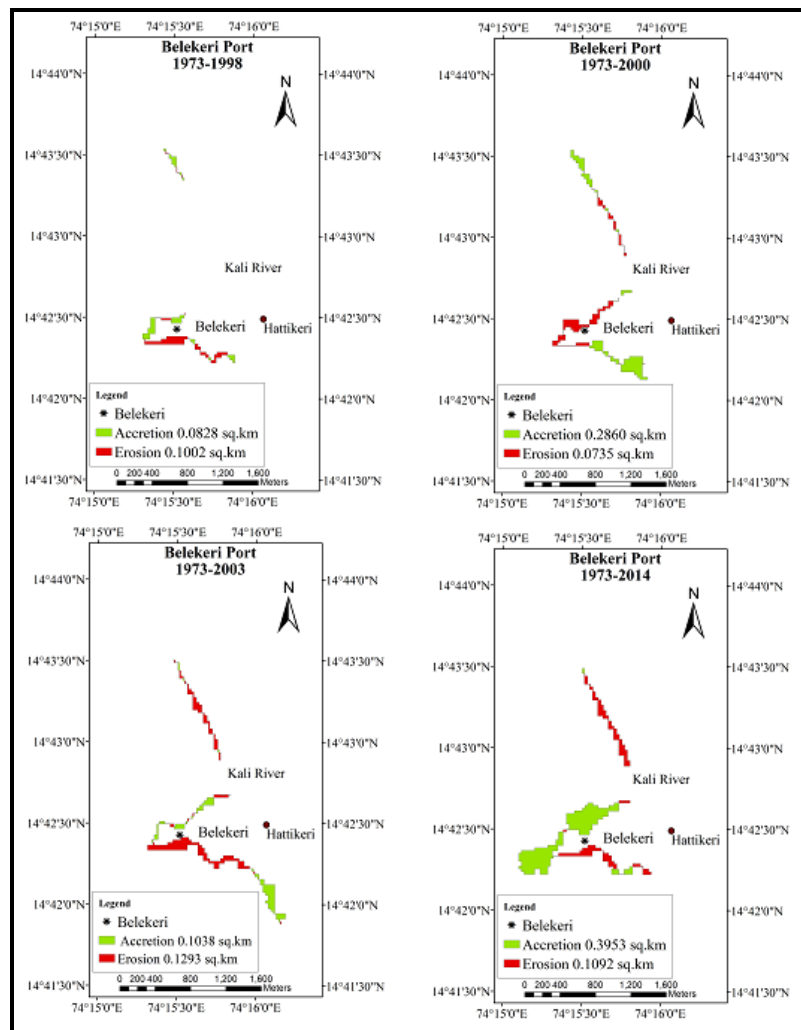


Figure 4: Erosion and Accretion near Belekeri

3.3. Manjaguni Port

Manjaguni port is located in the Uttara Kannada districts of Karnataka state. The port is on Gangavalli River. The surrounding area shows a (Figure 5) rate of erosion-1.0545m/y and rate of accretion is +1.2560m/y for the period of 1973 to 2014. During this period shoreline is retreated -42.9891m and pro graded +51.2880m.shows erosion and accretion at Manjaguni port area. Due to the northward growth of sand spit across the river Gangavalli, the river mouth has shifted northwards.

The Northern most side of the river is characterized by sand and followed by a rocky structure which suggests less erosion and near mouth, spit formation which indicates the source of sediment as a river rather than littoral drift. Sand dunes are dominantly observed in this area. At the Gangavalli, the long shore current mostly persisted around 0.2 - 0.25 m/s in October, November and December and about 0.25 - 0.3 m/s in January, February, May, July, August and September (Tirodkar et al., 2014).

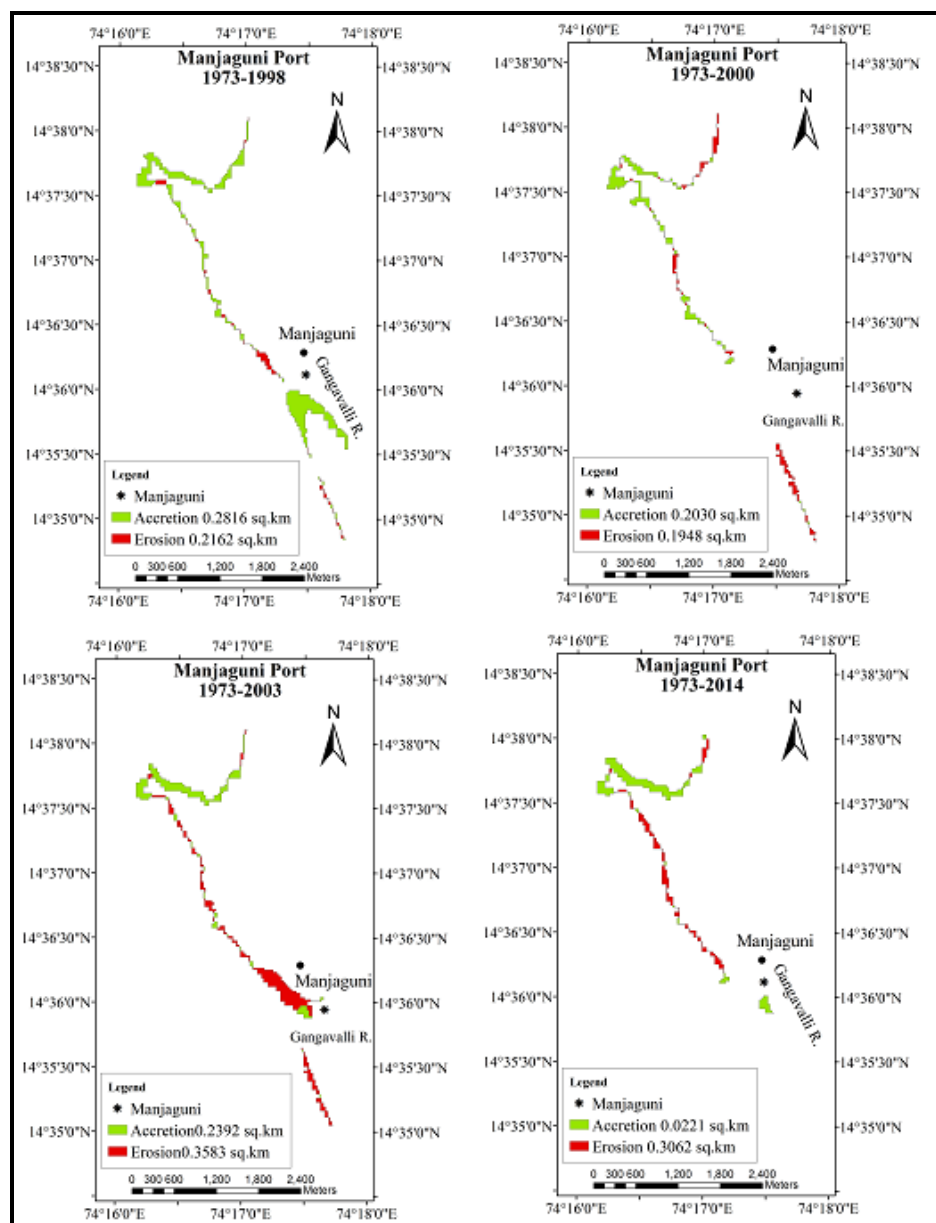


Figure 5: Erosion and Accretion near Manjaguni

3.4. Tadri Port

The Tadri port is located on the bank of Tadri/Aghanashini River. The rocky structure with a small fillet of sand has been observed at the northern side of the port. Sandy beach is observed at the southern side of the port. This port is projected for development under the BOOST (Build, Own, Operate, Share, and Transfer) concept through private participation. The coast shows a (Figure 6) rate of erosion -1.9992m/y and rate of accretion is $+1.4150\text{m/y}$ for the period of 1973 to 2014. About -80.1070m shoreline recession has been recorded and shoreline progradation is recorded about $+50.6750\text{m}$ for the period of 1973-2014.

The coast has a high productive ecosystem and is ecologically sensitive. The area is covered with the sandy beaches and cliffs. Sedimentation at river mouth has led to an arrowing of river mouths. The shoreline erosion on another hand is responsible for shifting of the mouth. From February to August the direction of longshore current was southward, whereas in December it is northward. Long shore currents are erratic in January and September (Tirodkar et al., 2014).

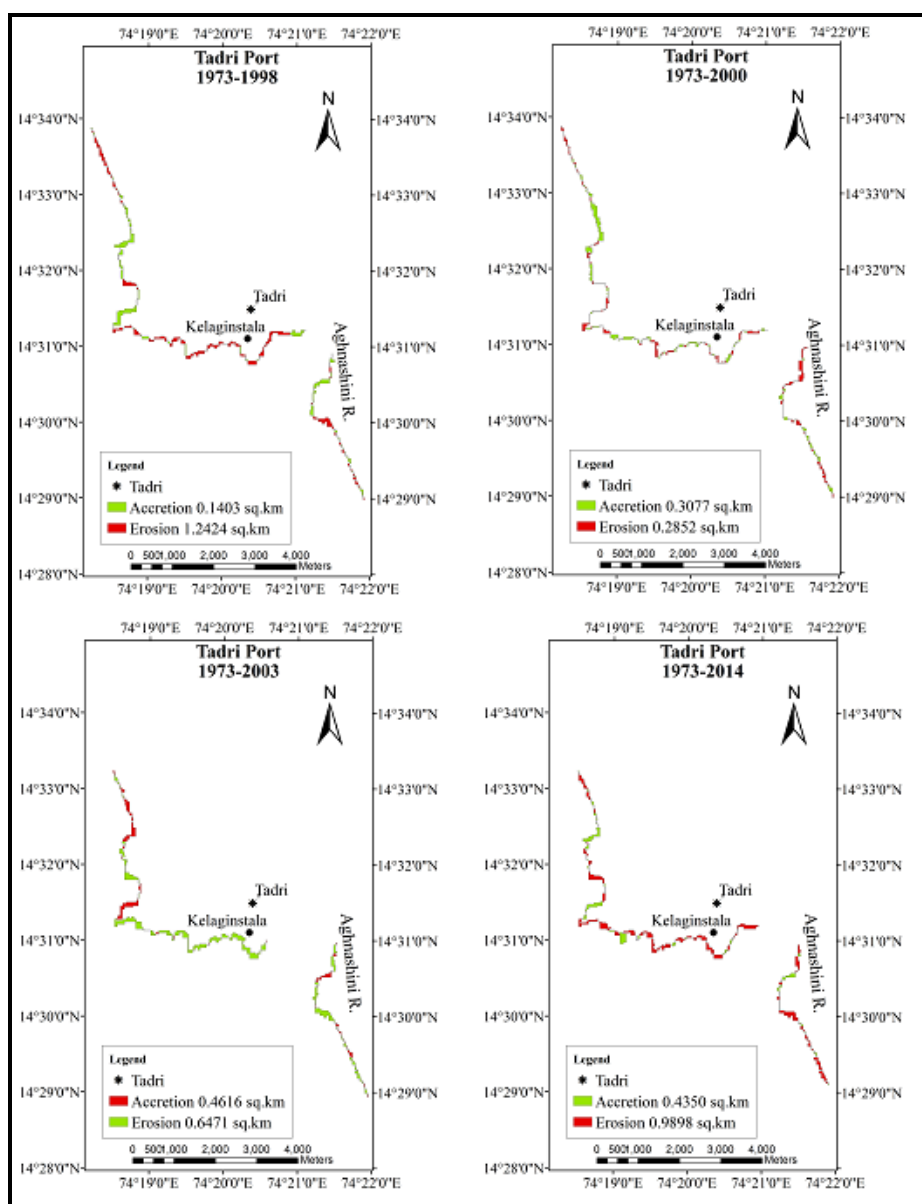


Figure 6: Erosion and Accretion near Tadri Port

3.5. Honnavar Port

Honnavar port is located on 10 km long Kasarkode stabilized spit pointing northwards at the mouth of Sharavati River. The port is near to the town of Honnavar in Uttara Kannada district. Honnavar shows (Figure 7) the rate of erosion is -1.2875m/y and rate of accretion is $+0.7967\text{m/y}$ during the period 1973 to 2014. It is a major fishing harbor. Pavinakurve spit is to the northern side of the river mouth and is affected by erosion. Kasarkode spit which situated on the southern bank of Sharavati River shows accretion. Northerly drift prevailing during the post-monsoon season favors spit growth across the river mouth from south to north. Detached breakwater is a coast-parallel structure located inside or close to the surf-zone. Groins are normally built perpendicular to the shoreline for protecting a section of the shoreline by blocking (part) littoral transport, whereby sand is accumulated on the upstream side of the groin and the erosion shifts to the downstream area.

A spit on the northern side of the Sharavati River mouth is affected by erosion and the spit on the southern side shows accretion. The shoreline recession is observed about -52.5720m and $+32.5733\text{m}$ progradation is recorded for the period of 1973-2014. Northerly drift prevailing during the post-monsoon season favors spit growth across the river mouth from south to north, whereas the southerly drift during December to February is responsible for the erosion of the portion of the beach to the north of the river mouth. The spit growth across river mouths is narrowing river mouth.

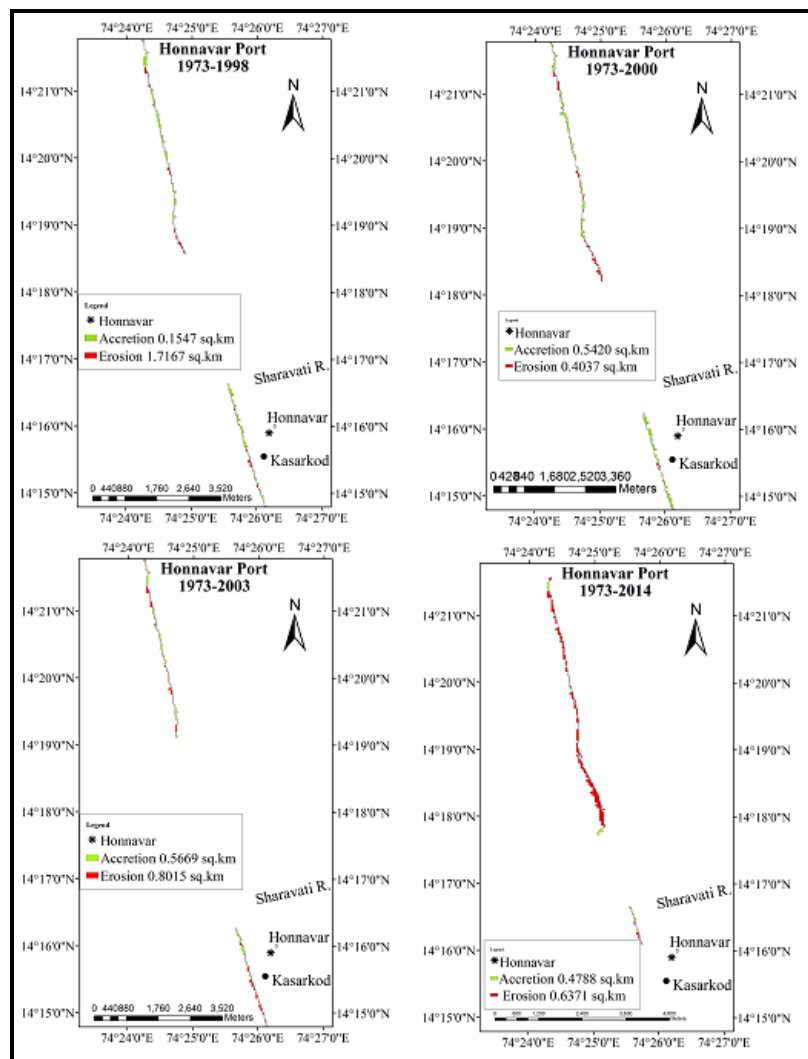


Figure 7: Erosion and Accretion at Honnavar

3.6. Bhatkal Port

This port is situated at the mouth of Bhatkal River. The Bhatkal port is protected from northward longshore by constructing a breakwater at the southern side of river mouth which is built perpendicularly to the coast. The rocky headland at northern side stops southward drift from clogging river mouth. Presently fishing vessels are utilizing the facilities of this port. This port could be developed as a modern fishing harbor with full-fledged fish handling facilities. The Port is surrounded by hills and river.

Figure 8 shows the area of erosion and accretion 0.534481 km^2 erosion and 0.005247 km^2 accretion are observed during 1973-1998. The coastline is characterized by the head land, shore line, and river mouth, beaches. The threat to the port is not much due to shore drift but is due to sediment siltation due to River. The shoreline is shifted backward about -182.5083m and forward about $+22.2600\text{m}$. The two breakwaters are observed at river mouth to stabilize the mouth, as the shifting of river mouth is very common along this coast. Erosion is observed at the north side of the port because of the northerly drift is dominant over the southerly drift and during monsoon the north side of the river mouth experiences more severe erosion than the southern side (Nayak et al., 2010).

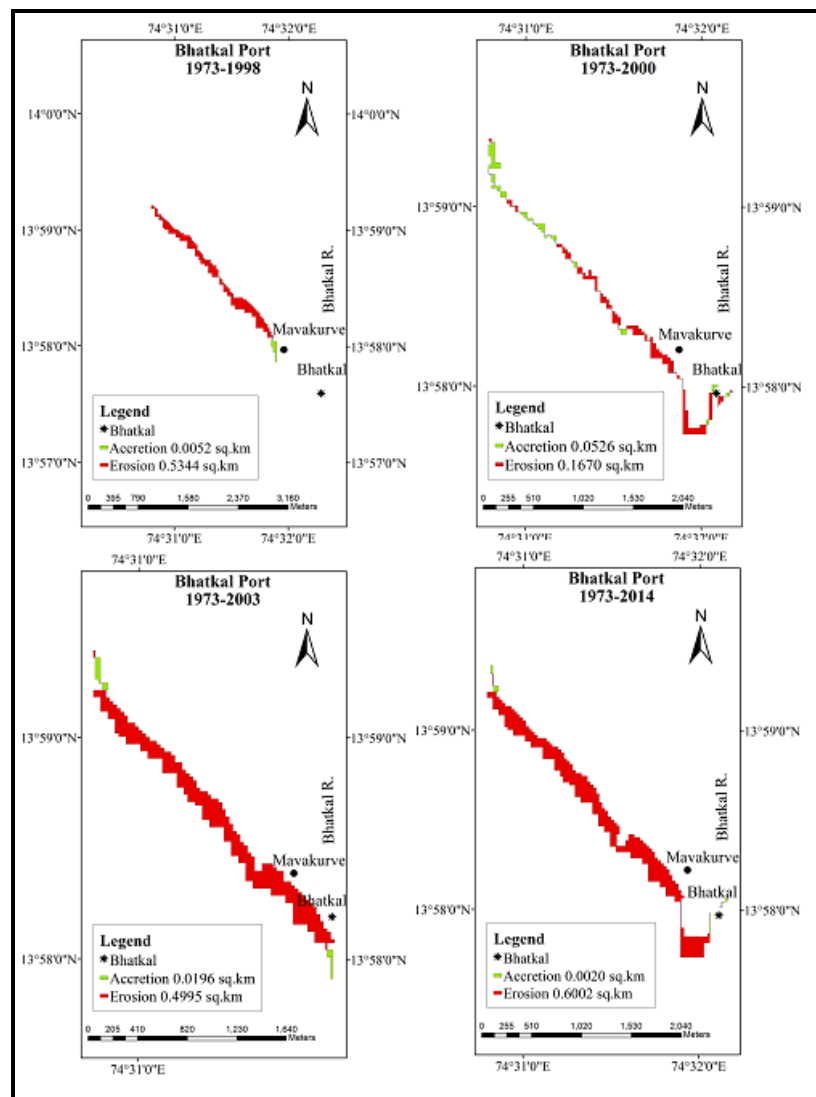


Figure 8: Erosion and Accretion at Bhatkal

3.7. Kundapur Port

The port area covers 7.644 Km and is situated on the confluence of Kollur-Chakkara and Haladi rivers and the Arabian Sea. At Kundapur, spits namely Koravadi and Gangoli are situated on either bank of the river, which play an important role in coastline changes. The port is surrounded by sandy beaches which lead to erosion. The wide estuary which supplies sediment in greater amount is the main reason for accretion and thus both processes balance each other, in this region. Kundapur shows (Figure 9) the rate of erosion is -1.5065m/y and rate of accretion is $+1.5300\text{m/y}$ during the period 1973 to 2014. During this period shoreline is retreated -58.0925m and prograded $+62.4367\text{m}$.

Rocky beach, sandbar and alluvial plane are the characteristics of Kundapur morphology. No changes have been detected in rocky beaches, Marine Island, and alluvial plain. It is detected that the coastal plain and channel Island have gradually increased. Coastal plain area increased by 0.159 Km^2 (Jayappa and Kumar, 2009).

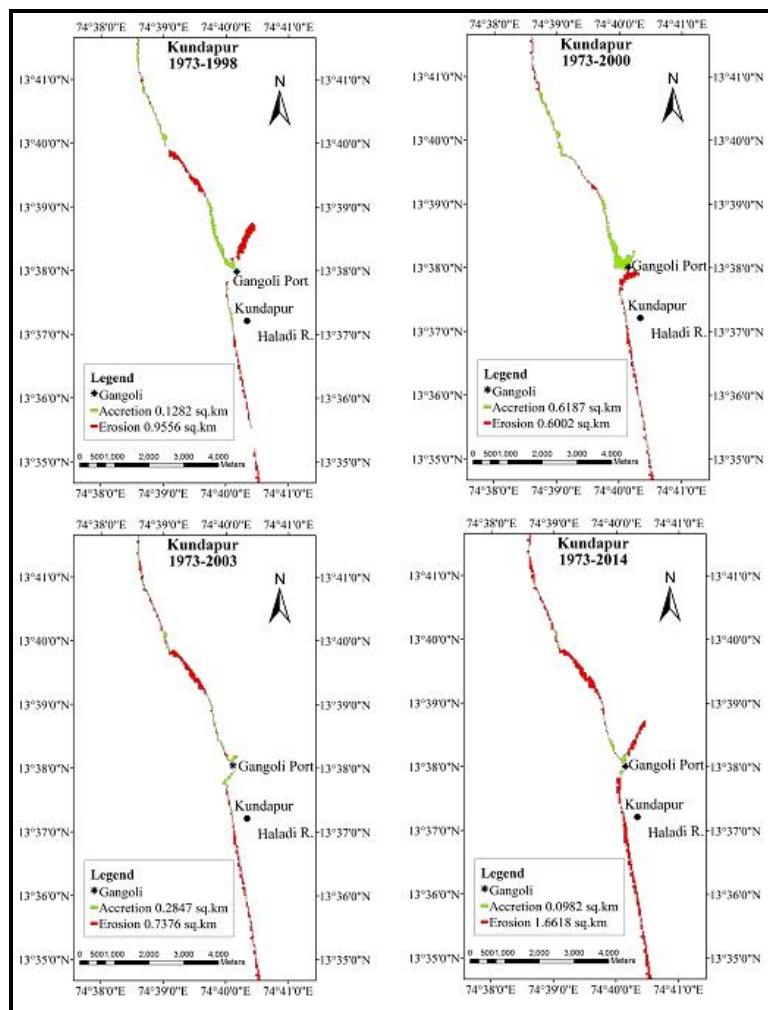


Figure 9: Erosion and Accretion near Kundapur

3.8. Hangarkatta Port

This port is located in Udipi district of Karnataka state. Hangarkatta port is mainly used by fishing boats. Hangarkatta Port is located on the bank of Sita and Swarna rivers. Prominent spits namely Kodi Bengre and kodithale are located at the southern side and at the northern side of the river mouth respectively. The growth of these spits is responsible for narrowing the river mouth. Mud flats are

observed in the middle region of the estuary. Shallow sand bars are observed at the inlet. Overall accretion is dominant in this region. The sediments removed from the foreshore are caught in the circulation cells and are re-circulated locally, which provide stability to the beaches during the season.

The area shows (Figure 10) the rate of erosion is -1.2343m/y and rate of accretion is +1.5300m/y during the period of 1973 to 2014. During this period, the shore line retreats by -50.3829m and prograded is +62.5900m. The estimate and pattern of erosion and accretion are shown in Figure 10. The area covers geomorphic classes like as andy beach, spit etc. Accretion is observed on the left bank of the river and on the other bank of river, erosion is noticed. Erosion and accretion pattern is unpredictable for this region.

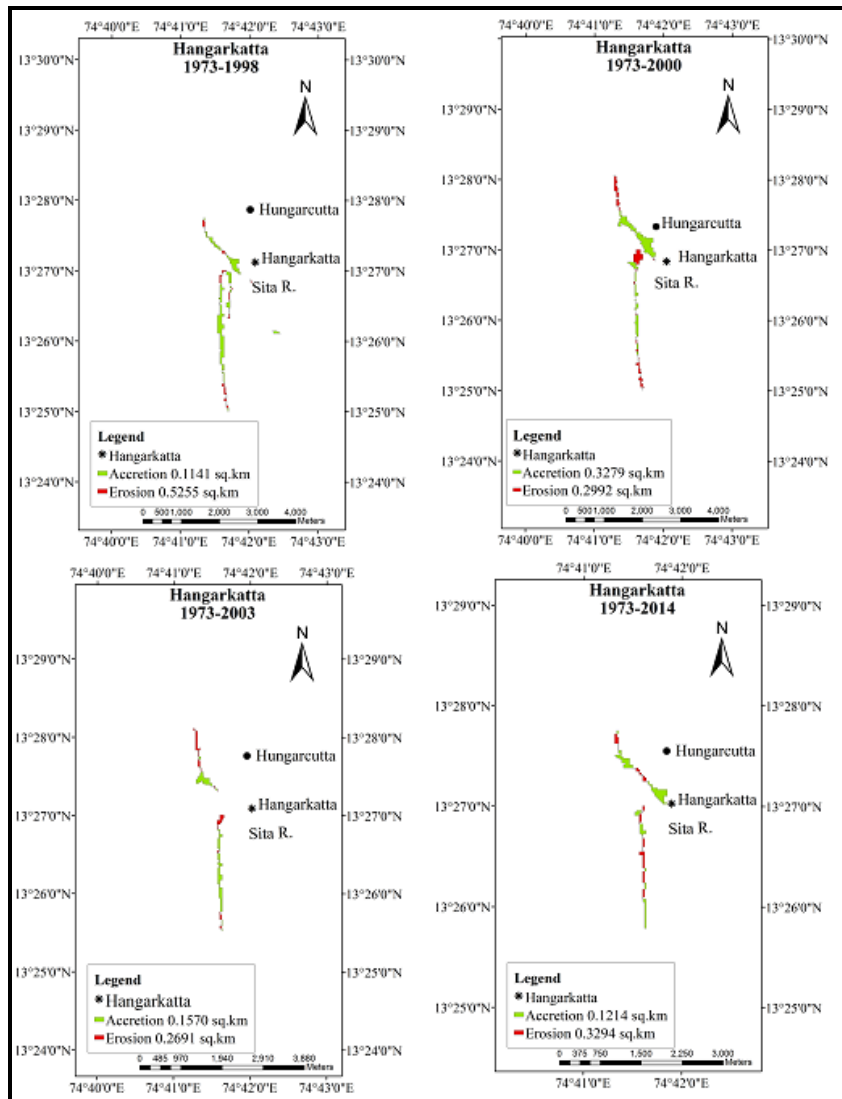


Figure 10: Erosion and Accretion near Hangarkatta

3.9. Malpe Port

Malpe fishing harbor is situated near the town of Udupi. Shoreline covers 14.383 Km and it lies at the confluence of Udyavara river and the Arabian Sea. The port mostly handles fishing activities and sometimes cargo also. Malpe is the largest fishing harbor in Karnataka. The shoreline retreats - 95.4862m and forwarded +43.9900m during the period 1973-2014.

The estimate and pattern of erosion and accretion are shown in Figure 11. The port is protected from southerly drift by constructing breakwater on the northern bank of River Udayyara. Whereas, long narrow stabilized Udapi beach protects the harbour from northerly shore drift. The northerly drift prevailing during the post-monsoon season favors Udapispit growth across the river mouth from south to north.

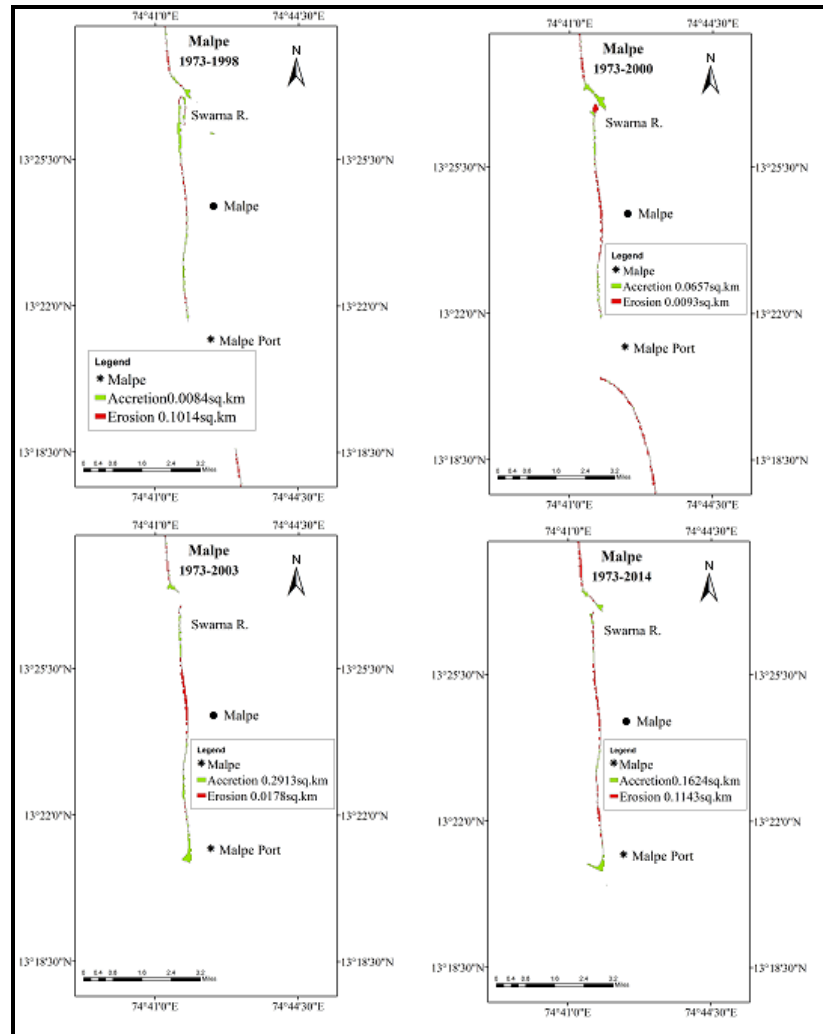


Figure 11: Erosion and Accretion near Malpe

3.10. New Mangalore Port

Mangalore is located at 12.87°N - 74.88°E in the Dakshina Kannada district of Karnataka. Panambur is the site of seaport called New Mangalore Port. It is located to the north of the Gurupura river confluence with the Arabian Sea. There is a beautiful beach on the shore of the Arabian Sea at Tanniru Bhavi to the south of sea port at Panambur (Figure 12). Gurpur River is to the south of Panambur. Panambur has an average elevation of 22 meters (72 feet) above mean sea level. It is the administrative headquarters of the Dakshina Kannada district, the largest urban coastal center of Karnataka. The government operates the deep-water, all-weather port at Panambur, Mangalore in Karnataka state. It is the only major port of Karnataka and is currently the ninth largest port in India.

The major commodities exported through the Port are Iron Ore Concentrates & Pellets, Iron Ore Fines, POL Products, granite stones, containerized cargo, etc. The major imports of the Port are Crude and POL products, LPG, wood pulp, timber logs, finished fertilizers, liquid ammonia,

phosphoric acid, other liquid chemicals, containerized cargo, etc. Geomorphologically, the area covers classes such as rocky cliffs, alluvial plain, sand beaches, lagoon and sand spits.

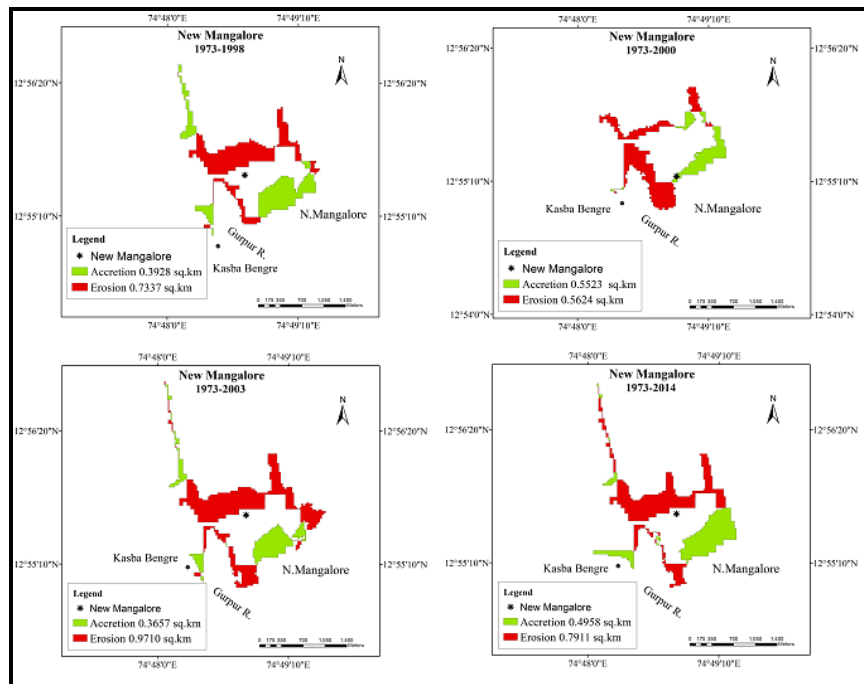


Figure 12: Erosion and Accretion Adjacent to New Mangalore Port

3.11. Old Mangalore Port

The Old Mangalore Port is located to the south of New Mangalore Port. It is popularly known by the name of Bunder. The port was used to ferry goods and passengers to Lakshadweep Island and Middle East countries. Now fishing has become main activity of this harbor. Old Mangalore port has the rate of accretion is +1.2900m/yr and rate of erosion is not recordable during the period of 1973 to 2014. Net accretion during this period is +52.6550m. The study area covers geomorphological classes such as rocky cliffs, alluvial plain, sand beaches, sand spits and manmade feat. In Netravati estuary contributed a major amount of sediments for the growth of spits.

The net shoreline movement during 1973 to 2014 adjacent to Ports/harbors of Karnataka state is mentioned in Table 2. Ports like Karwar, Belekeri, Manjaguni, Kundapur and Hangarkatta show prograding shoreline movement whereas, Tadri, Honnavar, Bhatkal, Malpe and New Mangalore show receding shoreline movement.

4. Discussion

During the study, it was observed that the Karnataka coast is subjected to three types of erosion; erosion along open beaches, along river/estuaries mouth, and the tidal reaches of rivers, causing loss of land, vegetation and revenue. Around 60 Km of the beach is confronted with appreciable or severe erosion. Erosion is more severe in Dakshina Kannada and Udupi coasts, where about 28 % of the total stretch is critical. In Uttar Kannada region, just 8% of this is subjected to severe erosion. The erosion becomes severe due to synchronization of high flood in the rivers and strong wave activity during the southwest monsoon. Erosion/bank collapse in the tidal reaches of the river is also severe and extends at least to about 12 Km. The maritime port requires transportation corridors for conveyors and road and rail access, a container terminal, staging yards, dry bulk stockpiles, a bulk liquid tank farm, and port administration buildings to manage which causes lot of landform changes at the particular site.

Subsequently, anthropogenic pressure increases which triggers the coastal erosion. Major development has been observed along the harbor/port region of the coast line channel and the port basin which is also a cause of erosion.

Above cumulative erosion makes huge sediments available for alongshore sediment transport process to distribute sediments along the shore line. Along Karnataka coast, it was observed that all ports are located at or near the river mouth. Now the ports are invariably made up of structures like breakwater wall, groins etc. These port structures act as a barrier against along shore transport (Kunte, 1994). These man-made structures accumulate sediments on the updrift side and the down drift side experiences sediment starvation and subsequent erosion (Taggart & Schwartz, 1988). The entire Karnataka coast is exposed to an onslaught of the southwest monsoon and so the coast has to face high wave conditions during the period which develops strong southwards littoral currents. These littoral currents, with the easy availability of sediments, distribute sediments along the shoreline. The ports obstruct sediment flow and get sediment enriched on updrift side whereas down drift side gets eroded during the monsoon period. The seasonally reversing wind pattern influences northward drift during northeastern monsoon which gradually redistributes the sediments and regain sediments at eroded sites.

Karnataka ports like Belekeri, Manjaguni, Tadri, Honnawar, Kundapur, Hangarkatta, Malpe and old Mangalore ports are all situated in the estuary, well inside the coastline. These ports are well protected due headlands or large spits exits at the mouth of the estuary. Alongshore currents have little or no impact on these ports, however, for coastal erosion, accretion and estuary mouth closer, alongshore currents are accountable. Siltation of river-transported sand is a major worry for port maintenance. Karwar port is within headland and safe and protected. New Mangalore port is facing Open Ocean but for protecting port two large breakers are constructed. These breakers are responsible for shoreline change.

Unplanned development surrounding port areas and industrial locations leads to objectionable and use practices. Expanding infrastructure facilities, surrounding the port area, lead to the transformation of a large tract of agricultural land to built-up areas. These are more pronounced in areas adjacent to industrial centers, fish landing centers and big projects like Seabird at Karwar. Conversion and reclamation of wetlands have caused coastal biodiversity loss.

The increased use of trawl nets accentuates deprivation of non-target groups along with juveniles and sub-adults of needed fishes and another benthic organism. Most of the bycatches are of low economic value but are vital for the food web. The discarded by-catches are thrown overboard which adds to pollution. The haphazard dumping of fish wastes near fish landing centers, processing of fish catch and a large number of ice factories cause water pollution. Improper solid waste disposal and inadequate treatment of sewage contribute to the water pollution. The marine pollution, though low at present, may lead to bioaccumulation of toxic chemicals in the long run. Selective scooping by trawl nets has exerted tremendous pressure on benthic organisms and their survival, as these are thrown overboard and are discarded dead which adds to pollution. Increased pumping of water required by port and other affiliated industries, in the coastal sandy areas, lead to landward movement of saline water-freshwater interface and upcoming of saline water in dug wells.

Eighty-eightpercent of rainfall received during four months of the rainy season leads to dis-appropriate run off. Reduced flow in rivers during non-rainy periods hinders proper flushing. Excessive siltation consequently raises the riverbed. Tidal inlets and river mouths are often, by nature, becomes shallow and are sometimes blocked due to excessive sediments, which make them unsuitable for navigation. In order to improve navigational conditions and, flushing sediments, many tidal inlets, and river inlets have regulated mouths. The regulation may consist of maintenance dredging programs. In this region, near Belekeri, Tadri, Majaguni and Honnavar ports, this is common practices. The siltation is also high

at New Mangalore Port, where the annual maintenance dredging varied from 1.67 million cubic meters to 4.28 million cubic meters during the last ten years.

The dredging leads to habitat disruption due to the removal of bottom sediments and/or accumulation of sediments. The water quality change subsequently leads to habitat inhibitions. As a result of dredging, re-suspension of bottom sediments, accumulation of/dispersion of toxic substances, oxygen depletion, reduced primary production, temperature alteration, increased nutrient level and bed load movement take place. This will alter the benthic community system.

Though sediment transport activity along Karnataka coast is very high, the presence of bi-direction littoral drift maintains natural equilibrium to the utmost extent. The results of the Coastal Vulnerability index study of Karnataka shoreline indicate this equilibrium. The CVI results reveal that, except a spot in Uttara Kannada, Karnataka coast has no Very High Vulnerability shore; the large extent of the coastline, 57% is classified as Low Vulnerability; medium and high vulnerable classes recorded 31.76% and 9.54% respectively (INCOIS 2007). CVI study carried out at Mangalore coast from Talapay to Surathkal indicate that Ullal coast is highly vulnerable, followed by Tannirbavi and most other segments are less vulnerable (Hegde and Reju, 2007). Udupi coast CVI study, also show that out of 95 km stretch of coastline, 59% Very high vulnerable, 7% high, 4% moderate, and 30% low vulnerable (Dwarakish et al., 2009).

5. Conclusions

Shorelines extracted for the years 1973, 1998, 2000, 2003 and 2014 and processed using DSAS software indicates that the coastline near port area experienced both the erosion and accretion. Shoreline change rate of Karnataka coastline is estimated as -1.2354m/year even though sediment transport along the Karnataka is dynamic. Dynamic equilibrium of erosion and accretion are observed along the coast during the study. Erosion is observed during monsoon season and accretion is observed during the non-monsoon season. Long shore currents and river sediment transport are mainly responsible for shoreline changes. Karwar, Belekeri, and new Mangalore ports are Open Ocean facing, the ports are well protected either by headlands or breakwaters and hence are safe. Other all ports/harbors are located well within estuary mouth are protected from alongshore transport by headlands or largely stabilized spits. Riverine erosion and sediment transport is a major threat for sediment siltation surrounding ports/harbors. Erosion and accretion of shoreline are major impact of port/harbor. However, minor impacts are like an increase in pollution due to waste dumping and port-related industries, increase in coastal population and related activities and degradation of surrounding environment due to dredging and dumping material. Most of the shoreline sites, though largely get affected due to port structures, during monsoon season, achieve natural partial equilibrium during the non-monsoon season due to reversing currents and wind pattern. And hence, it may be concluded that port/harbor has some impact on the coastal shoreline.

Port structures play an important role in erosion and accretion. This study estimates the amount of erosion and accretion in the neighborhood of Karnataka ports and also provides spatial visualization at one glance; this study will be useful for future development and management of these ports and similar ports elsewhere in the world.

Acknowledgments

The first author would like to thank Dr. V.S. Kale, Prof. and Head of the Department of Geography and Dr. S.D. Pardeshi, Associate Prof. in Geography and teacher-in-charge in Geoinformatics, for encouraging to undertake this study. The second author expresses his gratitude to the Director of the National Institute of Oceanography, Goa for his encouragement. The authors would like to thank the Global Land Cover Facility, <http://www.landcover.org> for the Landsat TM and ETM+ data, as well as

the USGS for the making available the Digital Shoreline Analysis Software (DSAS) available on their website.

References

Choudhari, R., Gowthaman, R., and Sunil Kumar, V. *Shoreline Change Detection from Karwar to Gokarna – South West Coast of India Using Remotely Sensed Data*. International Journal of Earth Sciences and Engineering. 2013. 6 (3) 489-494.

DPI (Department for Planning and Infrastructure) 2004: Port Beach – Coastal Erosion Study, DPI Report No. 427, New Coastal Assets Directorate Marine House, Western Australia 6959. 68.

Dwarakish, G.S., Vinay, S.A., Natesan, U., Asano, T., Kakinuma, T., Venkataramana, K., Jagadesha, Pai, B., and Babita, M.K. *Coastal Vulnerability Assessment of the Future Sea Level Rise. In: Udupi Coastal Zone of Karnataka State, West Coast of India*. Ocean & Coastal Management. 2009. 52; 467-478.

Dolan, R., Fenster, M.S., and Holme, S.J. *Temporal Analysis of Shoreline Recession and Accretion*. Journal of Coastal Research. 1991. 7; 723-744.

EL-Raey, M., Sharaf EL-DIN, S.H., Khafagy, A.A., and Abo zed, A.I. *Remote Sensing of Beach Erosion/ Accretion Patterns along Damietta-Port Said Shoreline, Egypt*. Int. J. Remote Sensing. 1999. 20 (6) 1087-1106.

EMPRI, 2007: Short Term Study Report on Environmental Issues of Belekeri Port, Environmental Management and Policy Research Institute, May.

Hegde, A.V. and Reju Vijaya Radhakrishnan. *Development of Coastal Vulnerability Index for Mangalore Coast, India*. Journal of Coastal Research. 2007. 23 (5) 1106-1111.

Himmelstoss, E.A., 2009: *DSAS 4.0 Installation Instructions and User Guide*. In: Thieler, E.R., Himmelstoss, E.A., Zichichi, J.L., and Ergul, A. Digital Shoreline Analysis System Version 4.0- An ArcGIS Extension for Calculating Shoreline Change: U.S. Geological Survey Open-File Report 2008-1278.

INCOIS, 2009: Report on Use of Satellite Data for Detection of Violation of Land Use along the Coastal Regulation Zone and Impact of Port structures on Shoreline Changes, Ministry of Earth Science ICMAM Project Directorate, Chennai and Indian National Centre for Ocean Information Services (INCOIS), Hyderabad.

Jayappa, V.K. and Kumar, A. Evolution of Coastal Landforms, Southern Karnataka—A Remote Sensing Approach, In: Jayappa, K.S. and Narayana, A.C. (Eds). Coastal Environmental Problems and Perspectives, I.K. international Publishing House Pvt. Ltd., New Delhi. 2009. 79-96.

Johannessen, J.W., Maclennan, A., and McBride, A., 2005: Inventory and Assessment of Current and Historic Beach Feeding Sources/Erosion and Accretion Areas for the Marine Shorelines of Water Resource Inventory Areas 8&9, Prepared by Coastal Geologic Services, Prepared by King Country Department of Natural Resources and Parks, Seattle, WA.

Kudale, M.D. *Impact of Port Development on the Coastline and the Need for Protection*. Indian Journal of Geo-Marine Sciences. 2010. 39 (4) 597-604.

Kumar, A. and Jayappa, K.S. *Long & Short-term Shoreline Changes along Mangalore Coast, India*. International Journal of Environmental Remote Sensing. 2009. 3 (2) 177-188.

Kumar, A., Narayana, A.C., and Jayappa, K.S. *Shoreline Changes & Morphology of Spits along Southern Karnataka, West Coast of India: A Remote Sensing and Statistics-based Approach*. Geomorphology. 2010. 120; 133-152.

Kunte, P.D. *Sediment Transport along the Goa-north Karnataka Coast, Western India*. Marine Geology. 1994. 118 (3/4) 207-216.

Kunte, P.D., Wagle, B.G. and Sugimori, Y. *Littoral Transport Studies along West Coast of India – A Review*. Indian Journal of Marine Sciences. 2001. 30; 57-64.

Kunte, P.D., and Wagle, B.G. *Spitbase of West Coast of India: Potential Appraisal*. Giornale Di Geologia, ser. 2000. (3^a, 62) 29-36.

Luijendijk, A., Vroeg, H.D, Swinkels, C., Walstra, D.J. *Coastal Response on Multiple Scales: A Pilot Study on the Ijmuiden Port*. In: The Proceedings of the Coastal Sediments 2011, Ed: Wang, P., Rosati, J.D., Roberts, T.M., Pub: World Scientific Publishing Co. Pte. Ltd., Singapore. 602-615.

Maiti, S. and Bhattacharya, A. *Shoreline Change Analysis and its Application to Prediction: A Remote Sensing and Statistics Based Approach*. Marine Geology. 2009. 257; 11-23.

Nayak, S.R., Hegde, V.S., Shalini, G., Rajawat, A.S., Girish, K.H., Jayakumar, S., and Suryanarayana, A. *Geomorphic Processes in the Vicinity of the Venkatapur River Mouth, Central West Coast of India: Implications on Estuarine Sedimentation*. Journal of Coastal Research. 2010. 26 (5) 925-934.

Ryu, J., Won, J., and Min, K. *Waterline Extraction from Landsat TM Data in a Tidal Flat: A Case Study in Gosmo Bay, Korea*. Remote Sensing of Environment. 2002. 83; 442-456.

Shetye, S.R., Shenoi, S.S.C., Antony, A.K., and Kumar, V.K. *Monthly-Mean Wind Stress along the Coast of the North Indian Ocean*. Journal of Earth System Science. 1985. 94-129.

Siddiqui, M. and Maajid, S. *Monitoring of Geomorphological Changes for Planning Reclamation Work in Coastal Area of Karachi, Pakistan*. Advances in Space Research. 2004. 33; 1200-1205.

Selvan, C.S., Kankara, R.S., and Rajan, B. *Assessment of Shoreline Changes Along Karnataka Coast, India Using GIS & Remote Sensing Techniques*. Indian Journal of Marine Sciences. 2014. 43 (7) 1-6.

Sumiya, M., Uda, T., Kumada, T., and Serizawa, M., 2006: *Simultaneous Prediction of Beach Changes and Grain Size Distribution on Coast with Artificial Headlands*. Coastal Engineering 2006, Proceedings of the 30th International Conference San Diego, California, USA, 3-8 September 2006. 3079-3091.

Taggart, B.E. and Schwartz, M.L. *Net Shore-Drift Direction Determination: A Systematic Approach*. Journal of shoreline Management. 1988. 4; 285-309.

The Department of Ecology and Environment, Coastal Zone Management Plan for Karnataka, State of the Environment Report-2003 (Karnataka), and Karnataka Coastal Zone Management Authority.

Tirodkar, G.M., Pathak, K.C., and Vaz, S. *Coastal Changes Along the Coast of Tadri River, Karnataka West Coast of India and Its Implication*. Indian Journal of Marine Sciences. 2014. 43 (7).

USGS, 2005: *The Digital Shoreline Analysis System (DSAS) version 3.0, an ArcGIS Extension for Calculating Historic Shoreline Change*. U.S. Geological Survey.

Vinayaraj, P., Glejin, J., Udhatha Dora, G., Sajiv Philip, C., Sunil Kumar, V., and Gowthaman, R. *Quantitative Estimation of Coastal Changes along Selected Locations of Karnataka, India: A GIS and Remote Sensing Approach*. International Journal of Geosciences. 2011. 2; 385-393.

White, K., and El Asmar, H. *Monitoring Changing Position of Coastlines using Thematic Mapper Imagery, An Example from the Nile Delta*. Geomorphology. 1999. 29; 93-105.

Morphometric Analysis of a Phulambri River Drainage Basin (Gp8 Watershed), Aurangabad District (Maharashtra) using Geographical Information System

Tribhuvan, P.R. and Sonar, M.A.

Govt. Institute of Science, Nipat Niranjan Nagar, Caves Road, Aurangabad, Maharashtra, India

Publication Date: 27 June 2016

DOI: <https://doi.org/10.23953/cloud.ijarsg.62>



Copyright © 2016 Tribhuvan, P.R. and Sonar, M.A. This is an open access article distributed under the **Creative Commons Attribution License**, which permits unrestricted use, distribution, and reproduction in any medium, provided the original work is properly cited.

Abstract Geographical information system (GIS) has emerged as a professional tool in demarcation of drainage pattern and ground water potential and its planning. GIS and image processing techniques can be utilized for the identification of morphological characteristics and investigating properties of basin. The morphometric parameters of basin can deal with linear, areal and relief features. The present study deals mainly with the geometry, more importance being given on the evaluation of morphometric parameters such as stream order (Nu), stream length (Lu), bifurcation ratio (Rb), drainage density (D), stream frequency (Fs), texture ratio (T), elongation ratio (Re), circularity ratio (Rc), and form factor ratio (Rf) etc. Study area is Phulambri river basin located in Aurangabad district of Maharashtra state in India. The GIS based Morphometric analysis of this drainage basin revealed that the Girja-Purna is 6th order drainage basin and drainage pattern mainly in dendritic type thereby indicates homogeneity in texture and lack of structural control. Total number of streams is 1616, in which 895 are first order, 391 are second order, 196 are third order and 97 are fourth order streams and 36 of the fifth order and 1 of the sixth order. The length of stream segment is maximum for first order stream and decreases as the stream order increases. The drainage density (Dd) of study area is 0.030 km/km².

Keywords *Morphometric Analysis; Girija-Purna Basin; GIS; Aurangabad District; Maharashtra*

1. Introduction

The present paper describes the drainage characteristics of Phulambri area in Aurangabad district obtained through RS GIS based morphometric analysis. It is felt that the study will be useful to understand hydrological behavior of basin. The area under study is located in Girja-Purna river basin in Aurangabad district, Maharashtra, situated between North Latitude 20°10' and 75°25', and East Longitude 20°0' and 75°30' (Figure 1a & b). It covers an area of 227.5 sq.km. The average annual rainfall in this area is about 500mm to 840mm and temperature goes up to 40°C in summer and comes down to 10.3°C in winter season. Various important hydrologic phenomena can be correlated with the physiographic characteristics of drainage basins such as size, shape, slope of drainage area, drainage density, size and length of the tributaries etc. (Rastogi et al., 1976). Remote sensing data can be used

in conjunction with conventional data for delineation of characterization, problem identification, assessment of potentials and management needs, identification of erosion prone areas, evolving water conservation strategies, selection of sites for check dams and reservoirs etc., (Dutta et al., 2002).

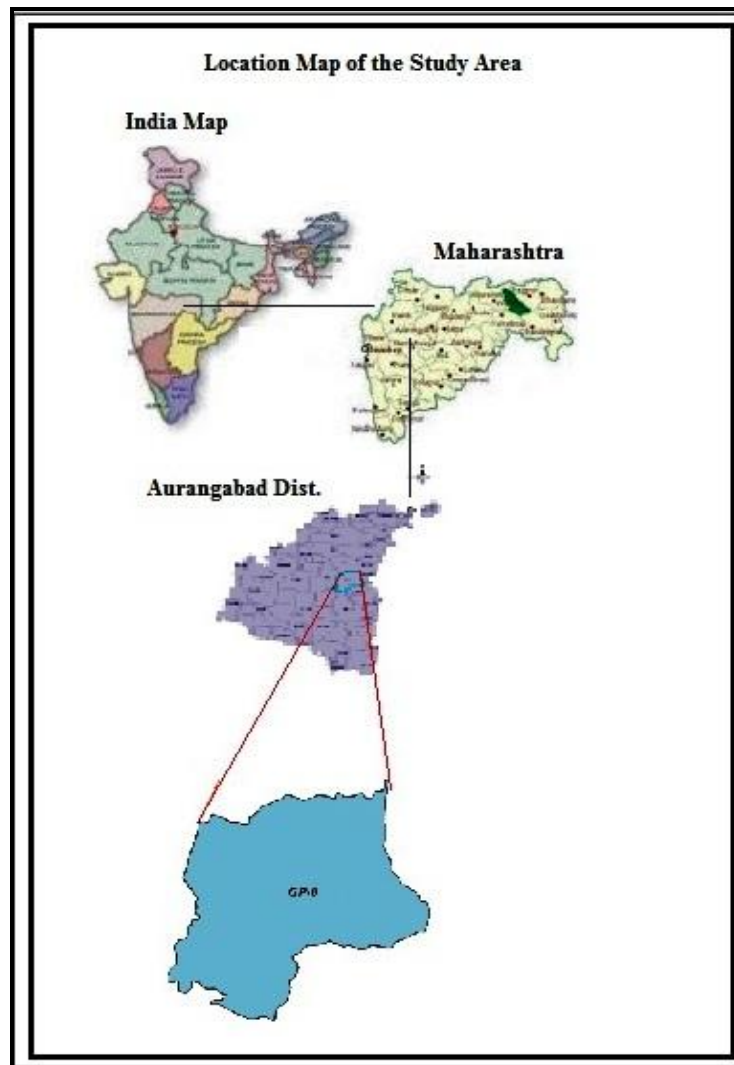


Figure 1a: Location Map of Phulambri River Area Showing GP8 Watershed

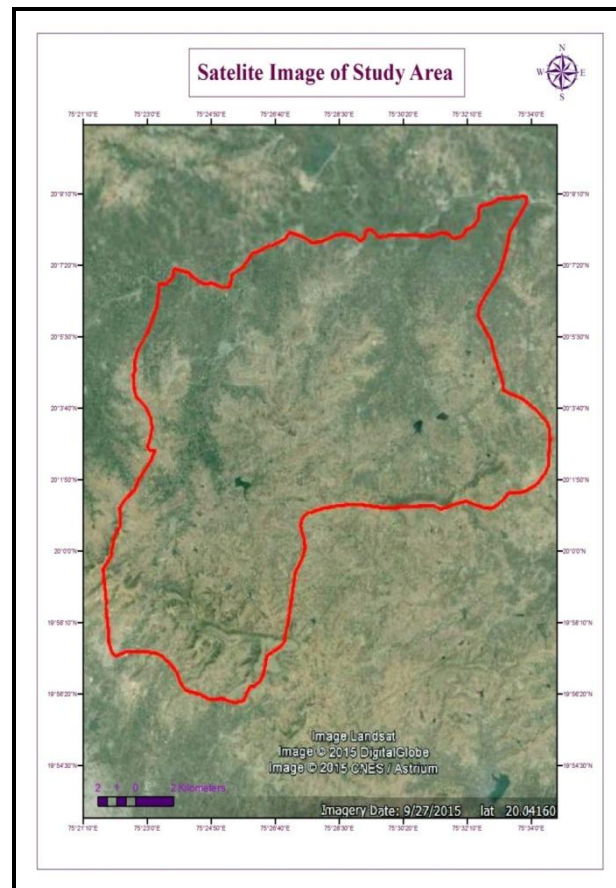


Figure 1b: Satellite Imagery (Courtesy of G.S.D.A.)

2. Materials and Methods

2.1. Geology

The whole area is covered by Deccan trap lava flows of upper cretaceous to lower Eocene age (Figure 2). The basaltic lava flows are covered with thin alluvial deposits along the Kham and Sukhna River. These flows belonging to the Deccan trap is the single major geological formation present in Aurangabad. The flows are gently inclined or nearly horizontal and each flow has two different components. The upper portion is made up of vesicular and amygdaloidal basalt whereas the lower portion is of compact basalt. The lava flows individually diverse in their ability to receive as well as hold water in storage and to transmit it. The difference in productivity of ground water in various flows occurs as a result of their inherent physical characters such as porosity and permeability. The ground water is present in the zone of saturation and is mostly controlled by the extent of its secondary porosity i.e. thickness of weathered rock and spacing of joints and fractures. The highly weathered vesicular basalt and lower jointed and fractured compact basalt contains the ground water potential zone (Water Res. Rep., 2015).

2.2. Methodology

The total study area is demarcated from Survey of India toposheets no. 46 p/8, 46 p/12 and 47 m/5 on 1:50000 scale with the help of Arc-GIS-10. Morphometric analysis of a drainage pattern needs the demarcation of all the existing streams. Digitization of the drainage basin was carried out for morphometric analysis in GIS environment using Arc GIS-10 software. The attributes were allocated to generate the digital data base for drainage layer of the river basin. Various morphometric parameters

such as linear aspects and aerial aspects of the drainage basin were computed. Digitization work was carried out for complete analysis of drainage morphometry. The diverse morphometric parameters have been determined as shown in Table 4.

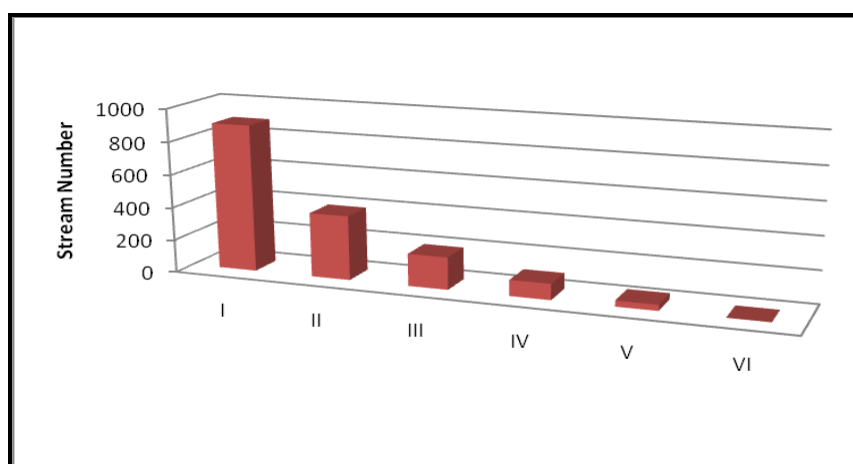
3. Results and Discussion

The subsequent subsections illustrate the substantial significance of various morphometric parameters. Further values of these parameters are obtained as per methods proposed by various researchers for the study area and indicated in respective descriptions. The morphometric analysis of the Gp-8 watershed was carried out on the Survey of India topographical maps. The lengths of the streams, areas of the watershed were measured by using ArcGIS-10 software, and stream ordering has been generated using Strahler (1953) system, and in ArcGIS-10 software. The linear aspects were studied using the methods of Horton (1945), Strahler (1953), Chorley (1957), the areal aspects using those of Schumm (1956), Strahler (1956, 1968), Miller (1953), and Horton (1932), and the relief aspects employing the techniques of Horton (1945), Melton (1957), Schumm (1954), Strahler (1952), and Pareta (2004). The average slope analysis of the watershed area was done using the Wentworth (1930) method. The Drainage density and frequency distribution analysis of the watershed area were done using the spatial analyst tool in ArcGIS-10 software.

3.1. Linear Aspects

3.1.1. Stream Order (S_u)

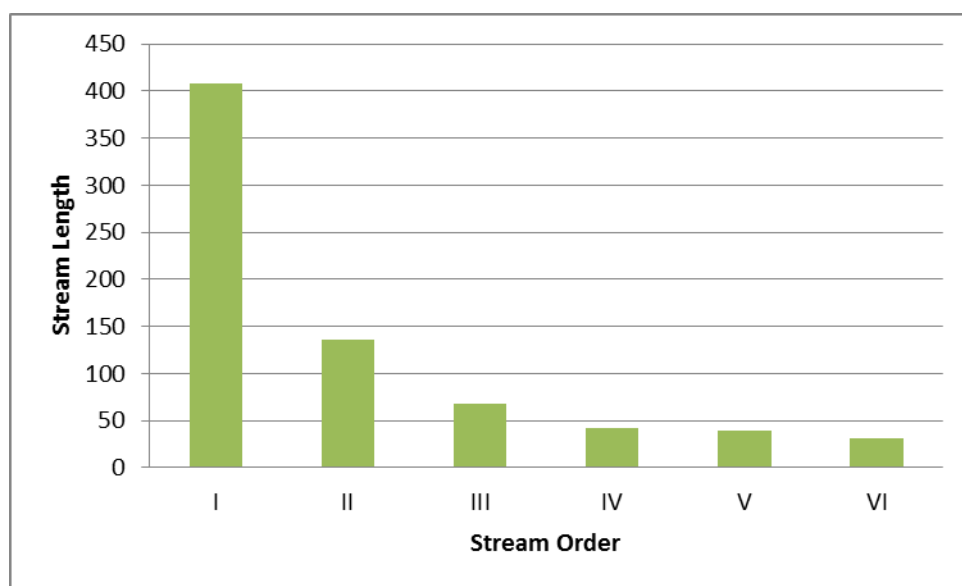
There are four different system of ordering streams that are available (Gravelius, 1914; Horton, 1945; Strahler, 1952; Schideggar, 1970). Strahler's system, which is a slightly modified of Hortons system, has been followed because of its simplicity, where the smallest, un-branched fingertip streams are designated as 1st order, the confluence of two 1st order channels give a channels segments of 2nd order, two 2nd order streams join to form a segment of 3rd order and so on. When two channel of different order join then the higher order is maintained. The trunk stream is the stream segment of highest order. It is found that Godavari river tributaries are of 6th order. In all 1616 streams were identified of which 895 are first order, 391 are second order, 196 are third order, and 97 in fourth order and 36 of the fifth order, 1 of sixth order. Drainage patterns of stream network from the basin have been observed as mainly of dendritic type which indicates the homogeneity in texture and lack of structural control. The properties of the stream networks are very important to study basin characteristics (Strahler, 2002).



Stream Number Vs Stream Order

3.1.2. Stream Length (L_u)

The stream length (L_u) has been calculated on the basis of the Horton's law. Stream length is one of the most important hydrological characters of the area as it gives information about surface runoff characteristics. The river of fairly smaller length is characteristics of regions with steep slopes and better textures. Rivers having longer lengths are commonly suggestive of smoother slope. In general, the total length of river section is highest in first order stream and the length is inversely proportional to the stream order. The numbers of streams are of various orders in a watershed are counted and their lengths from mouth to drainage divide are measured with the help of GIS software. The length of first order stream is 407.7 Km, second order stream is 135.2 Km, third order stream is 67.7 Km, and fourth order stream is 41.5 Km, fifth order stream 39.25 Km, and sixth order stream 30.8 Km. The change may indicate flowing of streams from high altitude, lithological variation and moderately steep slopes (Singh, 1997). The examination of stream order validates the Horton's law of stream number i.e. the number of stream segment of each order forms an inverse geometric sequence with order number.



Stream Length Vs Stream Order

3.1.3. Mean Stream Length (L_{um})

The mean stream length is a characteristic property related to the drainage network and its associated surfaces (Strahler, 1964). The mean stream length (L_{sm}) has been calculated by dividing the total stream length of order by the number of stream. The mean stream length of first order stream is 455.5 Km, second order stream is 346.0 Km, third order stream is 345.5 Km, and fourth order stream is 428.2 Km and 1090.3 Km, 30872 Km. The mean stream length of stream increases with increase of the order.

3.1.4. Stream Length Ratio (L_{urm})

Horton (1945, 291) states that the length ratio is the ratio of the mean (L_u) of segments of order (S_o) to mean length of segments of the next lower order (L_{u-1}), which tends to be constant throughout the successive orders of a basin. His law of stream lengths refers that the mean stream lengths of stream segments of each of the successive orders of a watershed tend to approximate a direct geometric sequence in which the first term (stream length) is the average length of segments of the first order (Table 2). Changes of stream length ratio from one order to another order indicating their late youth stage of geomorphic development (Singhand Singh, 1997).

Table 1: Stream Order, Streams Number, and Bifurcation Ratios in Gp-8 Watershed

| Su | Nu | Rb | Nu-r | Rb *Nu-r | Rbwm |
|-------|------|-------|-------|----------|-------|
| I | 895 | 2.28 | 1286 | 2,932.08 | 2.126 |
| II | 391 | 1.99 | 587 | 1,168.13 | |
| III | 196 | 2.02 | 293 | 591.86 | |
| IV | 97 | 2.69 | 133 | 357.77 | |
| V | 36 | 1.63 | 58 | 94.54 | |
| VI | 1 | ----- | ----- | | |
| Total | 1616 | 10.63 | | | |
| Mean | | 2.126 | | | |

Su: Stream order, **Nu:** Number of streams, **Rb:** Bifurcation ratios, **Rbm:** Mean bifurcation Ratio*, **Nu-r:** Number of stream used in the ratio, **Rbwm:** Weighted mean bifurcation ratios

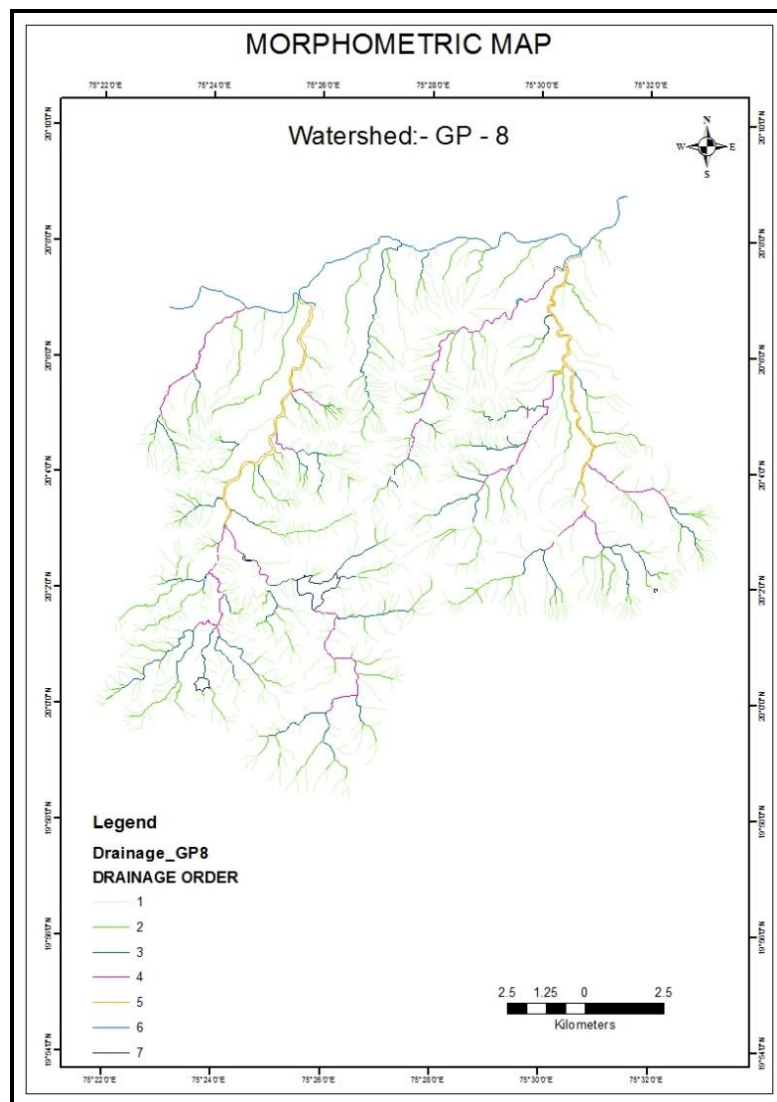


Figure 2: Map Showing Drainage Orders in GP-8 Watershed Area

Table 2: Stream Length, and Stream Length Ratio in Gp-8 Watershed

| Su | Lu | Lu/su | Lur | Lur-r | Lur*Lur-r | Luw _m |
|-------|--------|-------|-------|----------|-----------|------------------|
| I | 407.70 | 0.45 | | | | |
| II | 135.29 | 0.34 | 0.75 | 542.99 | 3,676.04 | |
| III | 67.73 | 0.34 | 1 | 203.02 | 1,374.44 | |
| IV | 41.53 | 0.42 | 1.23 | 109.26 | 739.69 | 6.76 |
| V | 39.25 | 1.09 | 2.59 | 80.78 | 546.88 | |
| VI | 30.87 | 30.87 | 28.32 | 70.12 | 474.71 | |
| Total | 722.37 | 33.51 | 33.89 | 1,006.17 | 6,811.76 | |
| Mean | | | 6.77* | | | |

Su: Stream order, Lu: Stream length, Lur: Stream length ratio, Lur_m: Mean stream length Ratio*, Lur-r: Stream length used in the ratio, Lu_{wm}: Weighted mean stream length ratio

3.1.5. Bifurcation Ratio (R_b)

Bifurcation ratio (R_b) may be defined as the ratio of the number of stream segments of given order to the number of segments of the next higher order (Schumm, 1956). Horton (1945) considered the bifurcation ratio as an index of relief and dissections. Strahler (1957) demonstrated that the bifurcation ratio shows a small range of variation for different regions or different environmental conditions, except where the geology dominates. It is observed that R_b is not the same from one order to its next order. In the study area mean R_b varies from 1.63 to 2.28; the mean R_b of the entire basin is 2.126. Usually these values are common in the areas where geologic structures less disturbing the drainage pattern.

3.1.6. Weighted Mean Bifurcation Ratio (R_{bwm})

To arrive at a more representative bifurcation number Strahler (1953) used a weighted mean Bifurcation ratio obtained by multiplying the bifurcation ratio for each successive pair of orders by the total numbers of streams involved in the ratio and taking the mean of the sum of these values. Schumm (1956, 603) has used this method to determine the mean bifurcation ratio of the value of 2.12 of the drainage of Perth Amboy, N.J. The values of the weighted mean bifurcation ratio this determined are very close to each other (Gp-8 watershed) Table 1.

3.1.7. Rho Coefficient (ρ)

The Rho coefficient is an important parameter relating drainage density to physiographic development of a watershed which facilitate evaluation of storage capacity of drainage network and hence, a determinant of ultimate degree of drainage development in a given watershed (Horton, 1945). The climatic, geologic, biologic, geomorphologic, and anthropogenic factors determine the changes in this parameter. Rho value of the Gp-8 watershed is 3.19. This is suggesting higher hydrologic storage during floods and attenuation of effects of erosion during elevated discharge

3.2. Basin Geometry

3.2.1. Length of the Basin (L_b)

Several people defined basin length in different ways, such as Schumm (1956) defined the basin length as the longest dimension of the basin parallel to the principal drainage line. Gregory and Walling (1973) defined the basin length as the longest in the basin in which are end being the mouth. Gardiner (1975) defined the basin length as the length of the line from a basin mouth to a point on the perimeter equidistant from the basin mouth in either direction around the perimeter. The author has determined length of the Gp-8 watershed in accordance with the definition of Schumm (1956) that is 25.80 Kms.

3.2.2. Basin Area (A)

The area of the watershed is another important parameter like the length of the stream drainage. Schumm (1956) established an interesting relation between the total watershed areas and the total stream lengths, which are supported by the contributing areas. The author has computed the basin area by using ArcGIS-10 software, which is 227.5Sq kms.

3.2.3. Basin Perimeter (P)

Basin perimeter is the outer boundary of the watershed that enclosed its area. It is measured along the divides between watershed and may be used as an indicator of watershed size and shape. The author has computed the basin perimeter by using ArcGIS-10 software, which is 96.97 Kms.

3.2.4. Length Area Relation (Lar)

Hack (1957) found that for a large number of basins, the stream length and basin area are related by a simple power function as follows: $Lar = 1.4 * A^{0.6}$

3.2.5. Lemniscates (k)

Chorely (1957), express the Lemniscate's value to determine the slope of the basin. In the formula $k = Lb^2 / 4 * A$. Where, Lb is the basin length (Km) and A is the area of the basin (km²). The Lemniscates (k) value for the watershed is 0.03 which shows that the watershed occupies the maximum area in its regions of inception with large number of streams of higher order.

3.2.6. Form Factor (Ff)

According to Horton (1932), form factor may be defined as the ratio of basin area to square of the basin length. The value of form factor would always be less than 0.754 (for a perfectly circular watershed). The watershed will be more stretched because the value of form factor reduces. The watershed with excessive form factors have elevated crest flows of lesser period, but lengthened watershed having minimal form factor varies from 2.03 representing them to be stretched out in shape and flow for longer period.

3.2.7. Texture Ratio (Rt)

According to Schumm (1965), texture ratio is an important factor in the drainage morphometric analysis which is depending on the underlying lithology, infiltration capacity and relief aspect of the terrain. The texture ratio is expressed as the ratio between the first order streams and perimeter of the basin ($Rt = Nl / P$) and it depends on the underlying lithology, infiltration capacity and relief aspects of the terrain. In the present study, the texture ratio of the watershed is 9.22 and categorized as moderate in nature

3.2.8. Elongation Ratio (Re)

According to Schumm (1965, 612), elongation ratio is defined as the ratio of diameter of a circle of the same area as the basin to the maximum basin length. Strahler states that this ratio runs between 0.6 and 1.0 over a wide variety of climatic and geologic types. The varying slopes of watershed can be classified with the help of the index of elongation ratio, i.e. circular (0.9-0.10), oval (0.8-0.9), less elongated (0.7-0.8), elongated (0.5-0.7), and more elongated (<0.5). The elongation ration of Gp-8 watershed is 0.60 which is represented the watershed is less elongated

3.3. Drainage Texture Analysis

3.3.1. Stream Frequency (F_s)

The drainage frequency introduced by Horton (1932, 357 and 1945, 285) means stream frequency (or channel frequency) F_s as the number of stream segments per unit area. In the present study, the stream frequency of the Gp-8 watershed is 7.90.

3.3.2. Drainage Density (D_d)

Drainage density is the stream length per unit area in region of watershed (Horton, 1945, 243 and 1932, 357; Strahler, 1952 and 1958; Melton, 1958) is another element of drainage analysis. Drainage density is a better quantitative expression to the dissection and analysis of landform, although a function of climate, lithology and structures and relief history of the region can finally use as an indirect indicator to explain, those variables as well as the morphogenesis of landform. Author has calculated the drainage density by using Spatial Analyst Tool in ArcGIS-10, which are 3.53 Km/Km² indicating moderate drainage densities (Table 5). It is suggested that the moderate drainage density indicates the basin is moderate permeable sub-soil and thick vegetative cover (Nag, 1998).

3.3.3. Constant of Channel Maintenance ($1/D$)

Schumm (1956) used the inverse of drainage density or the constant of channel maintenance as a property of landforms. The constant indicates the number of Kms² of basin surface required to develop and sustain a channel 1 Km long. The constant of channel maintenance indicates the relative size of landform units in a drainage basin and has a specific genetic connotation (Strahler, 1957). Channel maintenance constant of the watershed is 0.28 Kms²/Km.

3.3.4. Drainage Intensity (D_i)

Faniran (1968) defines the drainage intensity, as the ratio of the stream frequency to the drainage density. This study shows a low drainage intensity of 2.23 for the watershed. This low value of drainage intensity implies that drainage density and stream frequency have little effect (if any) on the extent to which the surface has been lowered by agents of denudation. With these low values of drainage density, stream frequency and drainage intensity, surface runoff is not quickly removed from the watershed, making it highly susceptible to flooding, gully erosion and landslides.

3.3.5. Infiltration Number (I_f)

The infiltration number of a watershed is defined as the product of drainage density and stream frequency and given an idea about the infiltration characteristics of the watershed. The higher the infiltration number, the lower will be the infiltration and the higher ran-off. The study shows 27.88 infiltration.

3.3.6. Drainage Pattern (D_p)

In the watershed, the drainage pattern reflects the influence of slope, lithology and structure. Finally, the study of drainage pattern helps in identifying the stage in the cycle of erosion. Drainage pattern presents some characteristics of drainage basins through drainage pattern and drainage texture. It is possible to deduce the geology of the basin, the strike and dip of depositional rocks, existence of faults and other information about geological structure from drainage patterns. Drainage texture reflects climate, permeability of rocks, vegetation, and relief ratio, etc. Howard (1967) related drainage patterns to geological information. Author has identified the dendritic pattern in the study area. Dendritic pattern is most common pattern is formed in a drainage basin composed of fairly homogeneous rock without

control by the underlying geologic structure. The longer the time of formation of a drainage basin is, the more easily the dendritic pattern is formed.

3.3.7. Length of Overland Flow (L_g)

Horton (1945) used this term to refer to the length of the run of the rainwater on the ground surface before it is localized into definite channels. Since this length of overland flow, at an average, is about half the distance between the stream channels, Horton, for the sake of convenience, had taken it to be roughly equal to half the reciprocal of the drainage density. In this study, the length of overland flow of the Gp-8 watershed is 73.78 Kms, which shows low surface runoff of the study area.

3.4. Relief Characterizes

3.4.1. Relief Ratio (R_{hl})

Difference in the elevation between the highest point of a watershed and the lowest point on the valley floor is known as the total relief of the river basin. The relief ratio may be defined as the ratio between the total relief of a basin and the longest dimension of the basin parallel to the main drainage line (Schumm, 1956). The possibility of a close correlation between relief ratio and hydrologic characteristics of a basin suggested by Schumm who found that sediments loose per unit area is closely correlated with relief ratios. In the study area, the value of relief ratio is 11.70. It has been observed that areas with low to moderate relief and slope are characterized by moderate value of relief ratios. Low value of relief ratios are mainly due to the resistant basement rocks of the basin and low degree of slope.

3.4.2. Relative Relief (R_{hp})

The maximum basin relief was obtained from the highest point on the watershed perimeter to the mouth of the stream. Using the basin relief (302m), a relief ratio was computed as suggested by Schumm (1956), which is 11.70 Melton's (1957) relative relief was also calculated using the formula: $R_{hp} = (H^*100) / P$, where P is perimeter in meters'. This comes to 311.4 for Gp-8 watershed.

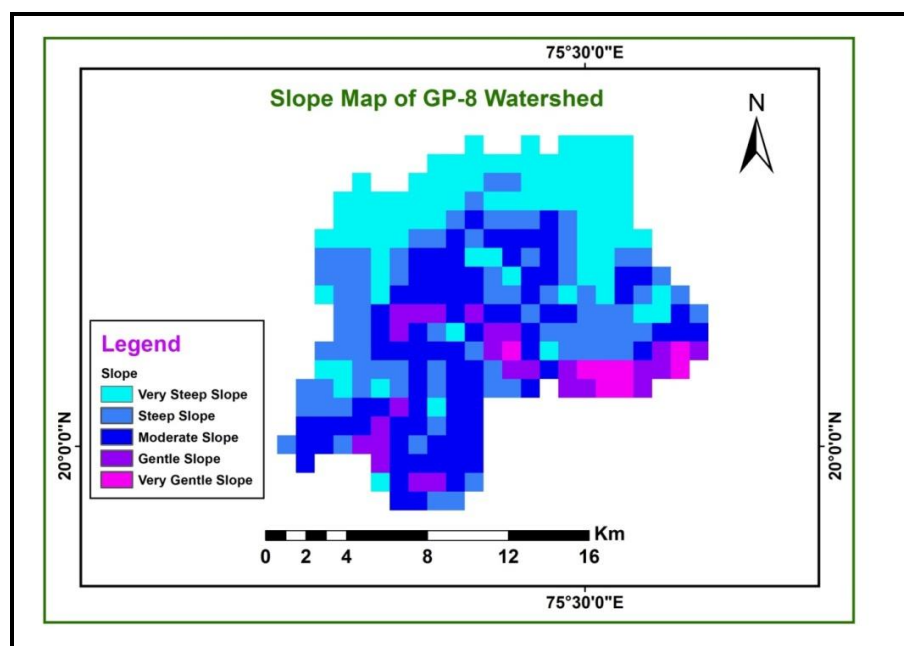


Figure 3: Slope Map of GP-8 Watershed Area

3.4.3. Ruggedness Number (Rn)

Strahler's (1968) ruggedness number is the product of the basin relief and the drainage density and usefully combines slope steepness with its length. Calculated accordingly, the Gp-8 watershed has a ruggedness number of 1.06. The low ruggedness value of watershed implies that area is less prone to soil erosion and have intrinsic structural complexity in association with relief and drainage density.

3.4.5. Melton Ruggedness Number (MRn)

The MRn is a slope index that provides specialized representation of relief ruggedness within the watershed (Melton, 1965). Gp-8 watershed has an MRn of 21.12. According to the classification of Wilford et al. (2004), this watershed is debris flood watersheds, where bed load component dominates sediment under transport.

3.4.6. Gradient Ratio (Rg)

Gradient ratio is an indicator of channel slope, which enables assessment of the runoff volume (Sreedevi, 2004). Watershed has an Rg of 11.70 which reflects the mountainous nature of the terrain. Approximately 83% of the main stream flows through the plateau and the relatively low values of Rg confirm the same.

3.5. Hypsometric Analysis (Hs)

Langbein et al. (1947) appear to have been the first to use such a line of study to collect hydrologic data. However, again Strahler (1952) popularized it in his excellent paper. According to Strahler (1952) topography produced by stream channel erosion and associated processes of weathering mass-movement, and sheet runoff is extremely complex, both in the geometry of the forms themselves and in the inter-relations of the process which produce the forms. In topographic profile, the nature of hypsometric curve and the value of the integral are fundamental elements. It shows remarkable differences in areas conflicting in phase of evolution and geologic formation, since the phase of youth hypsometric integral is large but it decreases as the landscape is denuded towards a stage of maturity and old age (Strahler, 1952, 118). The author used the percentage hypsometric curve method, and calculated the hypsometric integral (Hi). In late mature and old stages of topography, despite the attainment of low relief, the hypsometric curve shows no significant variations from the mature form, and a low integral results only where monadnock remain. After monadnock masses are removed, the hypsometric curve may be expected to revert to a middle position with integrals in the general range of 40 to 60 percent. (Strahler, 1952B, 1129-1130.) In the present study hypsometric integral (Hi) is 50.00, which indicate that the basin is in early mature stage.

Table 3: Hypsometric Data of Hypsometric Integrals

| S. No. | Altitude range(m) | Height(m)h | Area (Kms ²) a | h /H | a /A |
|--------|-------------------|------------|-------------------------------|-------|------|
| | | Z= 921 | z=619 | H=302 | |
| 1. | 900 | 301 | 7.5 | 0.006 | 0.03 |
| 2. | 800 | 181 | 62.5 | 0.59 | 0.27 |
| 3. | 700 | 81 | 50.6 | 0.26 | 0.22 |
| 4. | 680 | 61 | 54.7 | 0.20 | 0.24 |
| 5. | 660 | 41 | 40 | 0.13 | 0.17 |

| | | | | | |
|-----------|-----|----|------|------|------|
| 6. | 640 | 21 | 10.5 | 0.06 | 0.04 |
| Remaining | | | 1.97 | | |

Where, Maximum Height of the Basin = (Z) m, Height of Basin Mouth= (z) m Total Basin Relief=(H)m

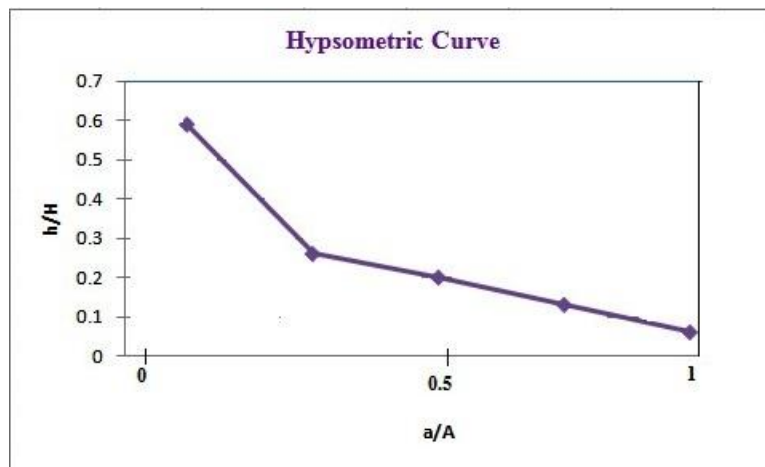


Figure 4: Hypsometric Curve of the Study Area

3.6. Comparison of Drainage Basin Characteristics

The details of the morphometric analysis and comparison of drainage basin characteristics of Gp-8 watershed is present in Table 4.

Table 4: Morphometric Analysis of Gp-8 Watershed - Comparative Characteristics

| Sr. No. | Morphometric Parameter | Formula | Reference | Result |
|---------|--|------------------------------|-----------------|-------------|
| 1 | Stream Order (Su) | Hierarchical Rank | Strahler (1952) | 1 to 6 |
| 2 | 1st Order Stream (Suf) | Suf = N1 | Strahler (1952) | 895 |
| 3 | Stream Number (Nu) | Nu = N1+N2+ ...Nn | Horton (1945) | 1616 |
| 4 | Stream Length (Lu) Kms | Lu = L1+L2 Ln | Strahler (1964) | 722.37 |
| 5 | Stream Length Ratio (Lur) | see Table 1 | Strahler (1964) | 0.7 to 28.3 |
| 6 | Mean Stream Length Ratio (Lurm) | see Table 1 | Horton (1945) | 6.77 |
| 7 | Weighted Mean Stream Length Ratio (Luwm) | see Table 4 | Horton (1945) | 2.12 |
| 8 | Bifurcation Ratio (Rb) | see Table 4 | Strahler (1964) | 1.6 to 2.6 |
| 9 | Mean Bifurcation Ratio (Rbm) | see Table 4 | Strahler (1964) | 2.12 |
| 10 | Weighted Mean Bifurcation Ratio (Rbwm) | see Table 4 | Strahler (1953) | 2.12 |
| 11 | Rho Coefficient (ρ) | ρ = Lur / Rb | Horton (1945) | 3.19 |
| B | Basin Geometry | | | |
| 12 | Basin Length (Lb) Kms | 1.312*A ^{0.568} | Schumm(1956) | 25.80 |
| 13 | Mean Basin Width (Wb) | Wb = A / Lb | Horton (1932) | 7.91 |
| 14 | Basin Area (A) Sq Kms | GIS Software Analysis | Schumm(1956) | 227.5 |
| 15 | Basin Perimeter (P) Kms | GIS Software Analysis | Schumm(1956) | 96.97 |
| 16 | Relative Perimeter (Pr) | Pr = A / P | Schumm(1956) | 2.10 |
| 17 | Length Area Relation (Lar) | Lar = 1.4 * A ^{0.6} | Hack (1957) | 34.06 |

| | | | | |
|----|---|-------------------------------|-----------------------|--------------|
| 18 | Lemniscate's (k) | $k = Lb^2 / A$ | Chorley (1957) | 0.30 |
| 19 | Form Factor Ratio (Rf) | $Ff = A / Lb^2$ | Horton (1932) | 3.26 |
| 20 | Shape Factor Ratio (Rs) | $Sf = Lb^2 / A$ | Horton (1956) | 0.3 |
| 21 | Elongation Ratio (Re) | $Re = 2 / Lb * (A / \pi) 0.5$ | Schumm(1956) | 0.60 |
| 22 | Texture Ratio (Rt) | $Rt = N1 / P$ | Schumm(1965) | 9.22 |
| 23 | Circularity Ratio (Rc) | $Rc = 12.57 * (A / P^2)$ | Miller (1953) | 0.27 |
| 24 | Circularity Ration (Rcn) | $Rcn = A / P$ | Strahler (1964) | 2.10 |
| 25 | Drainage Texture (Dt) | $Dt = Nu / P$ | Horton (1945) | 16.66 |
| 26 | Compactness Coefficient(Cc) | $Cc = 0.2841 * P / A 0.5$ | Gravelius (1914) | 1.92 |
| C | Drainage Texture Analysis | | | |
| 27 | Stream Frequency (Fs) | $Fs = Nu / A$ | Horton (1932) | 7.90 |
| 28 | Drainage Density (Dd) Km / Kms ² | $Dd = Lu / A$ | Horton (1932) | 3.53 |
| 29 | Constant of Channel Maintenance (Kms ² / Km) | $C = 1 / Dd$ | Schumm(1956) | 0.28 |
| 30 | Drainage Intensity (Di) | $Di = Fs / Dd$ | Faniran (1968) | 2.23 |
| 31 | Infiltration Number (If) | $If = Fs * Dd$ | Faniran (1968) | 27.88 |
| 32 | Drainage Pattern (Dp) | | Horton (1932) | |
| 33 | Length of Overland Flow (Lg) Kms | $Lg = A / 2 * Lu$ | Horton (1945) | 73.78 |
| D | Relief Characterizes | | | |
| 34 | Height of Basin Mouth(z) m | GIS Analysis / DEM | | 619 |
| 35 | Maximum Height of the Basin (Z) m | GIS Analysis / DEM | | 921 |
| 36 | Total Basin Relief (H) m | $H = Z - z$ | Strahler (1952) | 302 |
| 37 | Relief Ratio (Rhl) | $Rhl = H / Lb$ | Schumm(1956) | 11.70 |
| 38 | Relative Relief Ratio (Rhp) | $Rhp = H * 100 / P$ | Melton (1957) | 311.4 |
| 39 | Gradient Ratio (Rg) | $Rg = (Z - z) / Lb$ | Sreedevi(2004) | 11.70 |
| 40 | Watershed Slope (Sw) | $Sw = H / Lb$ | - | 11.70 |
| 41 | Ruggedness Number (Rn) | $Rn = Dd * (H / 1000)$ | Patton & Baker (1976) | 1.06 |
| 42 | Melton Ruggedness Number (MRn) | $MRn = H / A0.5$ | Melton (1965) | 21.12 |
| 43 | Contour Interval (Cin) m | GIS Software Analysis | --- | 20 |
| 44 | Relative Height (h/H) | see Table 3 (h/H) | Strahler (1952) | 0.66 to 0.99 |
| 45 | Relative Area (a/A) | see Table 3 (a/A) | Strahler (1952) | 0.00 to 0.01 |
| 46 | Hypsometric Integrals (Hi) % | Hypsom Curve h/H & a/A | Strahler (1952) | 50.00 |

4. Conclusion

GIS softwares have demonstrated that they have great significance in the morphometric analysis of the drainage basins. On the basis of the drainage orders, the Phulambri river Basin has been classified as sixth order basin. The mean Rb indicates that the drainage pattern is not much affected by geological structures. Drainage density (Dd) and stream frequency (Fs) are the most important criterion for the morphometric categorization of drainage basins which unquestionably control the runoff pattern, sediment yield and other hydrological parameters of the drainage basin. The Dd and Dt of the basin reveal that the nature of subsurface strata differs from fairly permeable to permeable. This is a distinctive element of drainage basin having Dt varying from fine to course as the texture value is 16.66. The study reveals that the drainage areas of the basin are passing through premature stage of

the fluvial geomorphic cycle. Lower order streams mostly control the basin. The developments of stream segments in the basin area are more or less affected by rainfall. Rc, Ff and Re show the somewhat elongated shape of the basin, having low degree of runoff and low relief of the terrain. It is observed that stream sectors up to 3rd order pass through parts of the high altitudinal regions with high virtual relief, which are characterized by steep slopes, while the 4th, 5th and 6th order stream segments occur in comparatively average relief regions in which maximum penetration of runoff occurs; these are main spots for constructing check dams. The outcome of our study illustrates the rocks in a region shows advantageous condition and good water bearing characteristics which might be useful for groundwater investigation.

Acknowledgements

The authors are thankful to Dr. A.K. Joshi, Head, Regional Remote Service Centre, Nagpur for providing a training in Remote Sensing and GIS and extending the lab facilities to the first author for this work. Further, the authors are also grateful to Dr. M.D. Babar, Dnyanopasak College, Parbhani for his critical remarks and suggestions on morphometric analysis. Dr. P.L. Salve, Deputy Director, G.S.D.A. Marathwada region for providing relevant literature is gratefully acknowledged.

References

- Back, W. and Hanshaw, B.B. *Chemical Geohydrology*. Adv. Hydro Science. 1965. 1; 49-109.
- Baker, C.P. and Panciera, E.C. *A Geographic Information System for Groundwater System Planning*. Jour. Soil and Water Conservation. 1990. 45; 246-248.
- Chorley, R.J., 1972: *Spatial Analysis in Geomorphology*. Methuen and Co. Ltd., London.
- Chorley, R.L., 1967: *Models in Geomorphology*. In Chorley, R.J. and Haggett, P. (eds.) *Models in Geography*, London. 59-96.
- Dutta, D., Sharma, J.R., and Adiga, S. (2002). Watershed characterization, development planning and monitoring remote sensing approach, technical report ISRO- NNRMS-TR-103-2002 Bangalore: ISRO.
- Faniran, A. *The Index of Drainage Intensity - A Provisional New Drainage Factor*. Australian Journal of Science. 1968. 31; 328-330.
- Gardiner. V., 1975: *Drainage Basin Morphometry*. British Geomorphological Group, Technical Bulletin. 14; 48.
- Gravelius, H., 1914: *Grundrifi der gesamten Gewissserkunde*. B and I: Flufikunde (Compendium of Hydrology, Vol. I. Rivers, in German). Goschen, Berlin, Germany.
- Hack, J.T., 1957: *Studies of Longitudinal Profiles in Virginia and Maryland*. US Geological Survey Professional Paper. 294 (B) 45-97.
- Howard. A.D. *Drainage Analysis in Geologic Interpretation: A Summation*. Bulletin of American Association of Petroleum Geology. 1967. 21; 2246-2259.
- Gregory, K.J. and Walling, D.E. *The Variation of Drainage Density within a Catchment*. International Association of Scientific Hydrology- Bulletin. 1968. 13; 61-68.
- Horton, R.E. *Drainage Basin Characteristics*. Trans. Am. Geophys. Union. 1932. 13; 350-361.

- Horton, R.E. *Erosional Development of Streams and Their Drainage Basins, Hydrological Approach to Quantitative Morphology*. Bull. Geophys. Soc. Am. 1945. 56; 275-370.
- Langbein, W.B., 1947: *Topographic Characteristics of Drainage Basin*. U.S. Geol. Surv. Water-Supply Paper 986 (C) 57-159.
- Govt. of Maharashtra. *Master Plan for IDWMR of Arunawati Sub-Basin (2015) Report*. Water Resource Dept. Govt. of Maharashtra, Hydropneum System, Pune. 17-29.
- Melton, M.A., 1957: *An Analysis of the Relations among the Elements of Climate, Surface Properties and Geomorphology*. Technical Report 11, Department of Geology, Columbia University, New York.
- Miller, V.C., 1953: *A Quantitative Geomorphic Study of Drainage Basin Characteristics in the Clinch Mountain Area, Virginia and Tennessee*. Project NR 389-042, Technical Report: 3, Columbia University, Dept. of Geology, ONR, Geography Branch, New York.
- Patton P.C., 1988: *Drainage Basin Morphometry and Floods*; In: Flood Geomorphology, Baker, V.R. and Kochel, R.C. and Patton, P.C. (eds) New York: John Wiley. 51-64.
- Rastogi, R.A. and Sharma, T.C. *Quantitative Analysis of Drainage Basin Characteristics*. J. Soil and Water Conservation in India. 1976. 26 (1&4) 18-25.
- Reddy, P.R., Vinod Kumar, K. and Seshadri, K. *Use of IRS-1C Data in Ground Water Studies*. *Current Science*. Special session: IRS-1 C. 1996. 70 (7) 600-605.
- Schidggar. A.E., 1970: *Theoretical Geomorphology*. 2nd edn. Berlin-Heidelberg New York: Springer.
- Schumm, S.A. *The Relation of Drainage Basin Relief to Sediment Loss*. International Association of Scientific Hydrology. 1954. 36; 216-219.
- Schumm, S.A. *Evolution of Drainage Systems & Slopes in Badlands at Perth, New Jersey*. Bulletin of the Geological Society of America. 1956. 67; 597-646.
- Schumm, S.A. *Sinuosity of Alluvial Rivers on the Great Plains*. Bulletin of the Geological Society of America. 1963. 74; 1089-1100.
- Singh, S. and Singh, M.C. *Morphometric Analysis of Kanhar River Basin*. National Geographical. J. of India. 1997. 43 (1) 31-43.
- Smith, K.G. *Standard for Grading Texture of Erosional Topography*. Amer. Jour. Sci. 1950. 48; 655-668.
- Smith, G.H. *The Morphometry of Ohio: The Average Slope of the Land* (abstract). Annals of the Association of American Geographers. 1939. 29; 94.
- Strahler, A.N. *Hypsometric Analysis of Erosional Topography*. Bulletin of the Geological Society of America. 1952. 63; 1117-42.
- Strahler, A.N. *Quantitative Slope Analysis*. Bulletin of the Geological Society of America. 1956. 67; 571-596.

Strahler, A.N., 1964: *Quantitative Geomorphology of Drainage Basin and Channel Network*. Handbook of Applied Hydrology. 39-76.

Shreve, R.L. *Statistical Law of Stream Numbers*. Journal of Geology. 1966. 74; 17-37.

Smith, G.H. *The Morphometry of Ohio: The Average Slope of the Land* (abstract). Annals of the Association of American Geographers. 1939. 29; 94.

Sreedevi, P.D., Srinivasulu, S. and Raju, K.K. *Hydro Geomorphological and Groundwater Prospects of the Pageru River Basin by Using Remote Sensing Data*. Environ. Geol. 2001. 40; 880-1094.

Wilford, D.J., Sakals, M.E., Innes, J.L. Sidle, R.C. and Bergerud, W.A. *Recognition of Debris Flow, Debris Flood and Flood Hazard through Watershed Morphometrics*. Landslide. 2004. 1 (1) 61-66.

Todd, D.K., 1980: *Groundwater Hydrology*. 2nd edn. New York: John Wiley. 535.

Calculation of Urban Morphology Parameterisations for London for use with the ADMS-Urban Dispersion Model

Mark Jackson, Christina Hood, Chris Johnson and Kate Johnson

CERC, Cambridge, UK

Publication Date: 12 April 2016

DOI: <https://doi.org/10.23953/cloud.ijarsg.52>



Copyright © 2016 Cambridge Environmental Research Consultants. This is an open access article distributed under the **Creative Commons Attribution License**, which permits unrestricted use, distribution, and reproduction in any medium, provided the original work is properly cited.

Abstract Two algorithms have been developed to parameterise the urban morphology of a large urban area, for use with the ADMS-Urban dispersion model. One algorithm calculates parameterisations of the urban canopy, as gridded values of average building height; average street canyon width; ratio of building plan area to grid cell area; and for a user-specified set of wind direction sectors, the ratio of the frontal area of the buildings to grid cell area. The second algorithm calculates parameterisations of the street canyon for individual streets for both sides of the street: canyon height, width, and length. The input data for both algorithms are detailed vector datasets of building and road geometry. The algorithms have been implemented as ArcPy Python tools within ArcGIS. Results are presented for London, calculated for the project Coupled Urban and Regional processes: Effects on AIR quality (CUREAIR). These results used building and road geometry from Ordnance Survey MasterMap Topography.

Keywords *Urban Morphology; Street Canyon; Urban Canopy*

1. Introduction

In urban areas, high traffic flows and congestion lead to large pollutant emissions. The resultant concentrations depend on the morphology of the urban area; wind speeds at ground level reduce where there are densely packed buildings and street canyons, resulting in increased concentrations. Further, the urban fabric alters the local climate so that the temperature gradient is rarely stable. Within street canyons, there may be channelling of the flow and a recirculation region driven by the component of the above-canopy flow perpendicular to the street; for street canyons with high aspect ratios, flow velocities may reduce significantly near the ground.

The atmospheric dispersion model ADMS-Urban contains modules to improve the model's predictions of concentrations in urban areas (CERC 2016; Hood 2014). The urban canopy module calculates a spatially varying flow field due to variations in building density and geometry at neighbourhood scales. The advanced street canyon module allows for detailed calculation of the effects of a wide range of individual street canyon geometries on the dispersion of pollution from road sources. These modules require input data characterising the urban morphology of the study domain.

The urban canopy module in ADMS-Urban requires a raster dataset containing gridded values of the average building height, the average street canyon width (\hat{g}), the ratio of the plan area of buildings to grid cell area (λ_P) and, for a user-specified set of wind direction sectors, the ratio of the frontal area of buildings to grid cell area (λ_F). Grid cell dimensions are set so that these parameters are able to represent the features of distinct urban neighbourhoods (typically 500 m to 2 km).

The advanced street canyon module in ADMS-Urban requires values of the following parameters for each road, for each side of the road centreline: building height, distance from road centreline to canyon wall and length of road with adjacent buildings.

This paper presents algorithms to derive these parameterisations from vector datasets of building and road geometry. These algorithms have been implemented as software tools and are now included as part of the ADMS-Urban modelling suite.

2. Data

The algorithms presented in this paper require vector datasets of building and road geometry. The building dataset must contain features for individual buildings, with polygons for their horizontal footprint and attributes for the height of the building. The road geometry dataset should contain features for individual roads and streets, with poly-line vector geometry for the road centreline and attributes for the road width (kerbside to kerbside). Such datasets are widely available for modern cities.

Practical complications can arise from building datasets which may contain multiple features for individual buildings. For example there may be one dataset for building podia and a separate dataset for the accompanying main buildings. This building configuration is found on some skyscrapers such as Lever House in New York which has a wide, single-story podium at the base and a narrower, multiple-story tower above (Figure 1).



Figure 1: Lever House in New York

Another possible source of practical challenges arises from generalisation: the simplification of the representation of geographical data to produce a map at a certain scale. To be readable at a smaller scale, some objects are removed; others are enlarged, aggregated and displaced one to another, and all objects are simplified (Shekar and Xiong, 2008). Complications can arise if the building dataset has

been generalised to a different scale than the road dataset; the relative positions and distances between roads and buildings might not be accurate and in extreme cases road features might intersect building features.

The results for London presented in this paper make use of building and road datasets from the Ordnance Survey MasterMap (Ordnance Survey 2014). The building dataset is the MasterMap Topography Layer and the road dataset is the Integrated Transport Network Layer. The building and road datasets have been generalised to the same scale so there were no issues in using these data. The road dataset is the same one used for the London Atmospheric Emissions Inventory 2010 (Greater London Authority 2013). The Building Height Attribute is an alpha release and is supplied as a separate comma-separated-variable format file which had to be joined to the building data in the Topography Layer. There are several height fields in the data (Figure 2). We used the field RelH2, relative height from ground level to base of the roof (m).

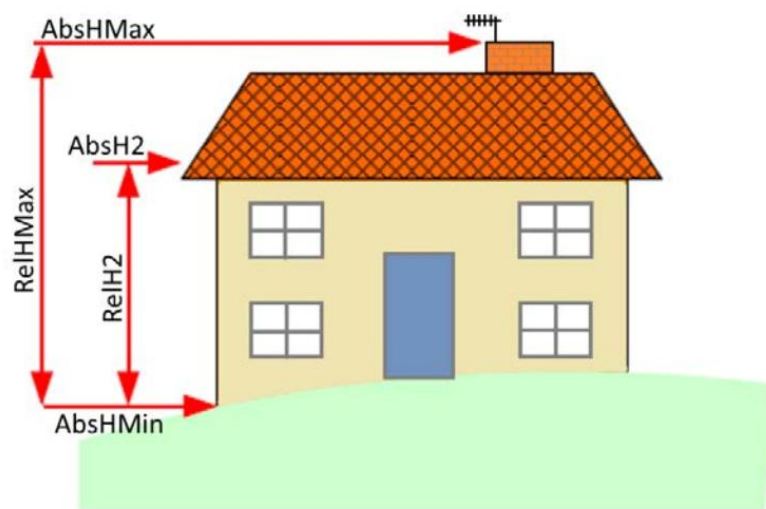


Figure 2: Height fields in the OS MasterMap Building Height Attribute dataset

3. Algorithms

3.1. Urban Canopy Algorithm

The algorithm presented here draws on the work by Stephen Evans of UCL (Evans, 2009), who developed methods to calculate urban canopy parameterisations for the LUCID project; the development of a Local Urban Climate Model and its Application to the Intelligent Development of Cities.

The input data for the algorithm are shown in Table 1.

Table 1: Input Data for the Urban Canopy Algorithm

| Input data | Notes |
|----------------------------------|---|
| Road Layer | Shapefile containing road geometry and road width (m) |
| Buildings Layer | Shapefile containing primary building geometry and building height (m) |
| Additional building layers | Shapefile(s) containing additional building layers each with building height (m). These additional layers contain additional features such as building podia. |
| Lambda F Directions | Wind direction sectors in degrees (°) for the λ_F calculation |
| Output grid extent and cell size | The output grid extent (minimum and maximum x- and y-coordinates) and cell size (m) |

The output data produced by the algorithm are shown in Table 2. These parameters are calculated as raster data, with separate values for each cell in the rectangular output grid, describing the urban canopy in the neighbourhood of the grid cell.

Table 2: Output Data from the Urban Canopy Algorithm

| Output data | Notes |
|-----------------|---|
| Road width | Average road width within the grid cell (m) |
| Building height | Average building height within the grid cell |
| Lambda P | λ_P – a measure of building coverage at ground level |
| Lambda F | λ_F – a measure of building frontage for particular wind directions |

The road width calculation proceeds as follows. For each cell, all of the road features in the Road Layer which intersect the cell are identified and clipped to only include sections within the cell. The average or neighbourhood-scale road width for the cell is calculated as the average value of the widths of all road features within that cell, weighted by the length of each road feature.

λ_P is calculated as follows. For each cell, all of the building features in the Buildings Layer which intersect the cell are identified and clipped to only include sections within the cell. The value λ_P is calculated as the ratio of the horizontal area in the cell taken up by building features to the total area of the grid cell.

λ_F is calculated as follows. For each cell, all of the building features in the Buildings Layer which intersect the cell are identified and clipped to only include sections within the cell. The calculations are performed for each of the wind directions provided by the user. The vertical area for each building, for each direction, is calculated from the product of the cross-wind area of the building (see Figure 3) and its height. λ_F is the ratio of the sum of these vertical areas divided by the total horizontal area of the grid cell.

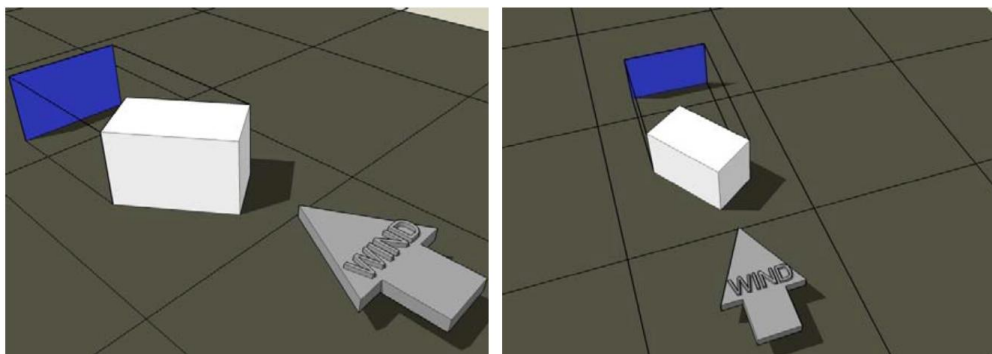


Figure 3: An example of cross-wind area (blue) for a building (white) that is not aligned to the wind direction

Figure taken from Evans 2009

The input dataset may contain two or more buildings or buildings of varying height in the same location. This data might represent a building comprised of a podium and a main building element as shown in Figure 1. The algorithm treats these cases by apportioning the height and length of each part of the building(s) into multiple segments. If one building feature completely contains a higher building, the tool assumes the overlapping feature represents part of one continuous building and that the actual height above ground level at each point is the maximum height (not the sum). The approach is illustrated in Figure 4.

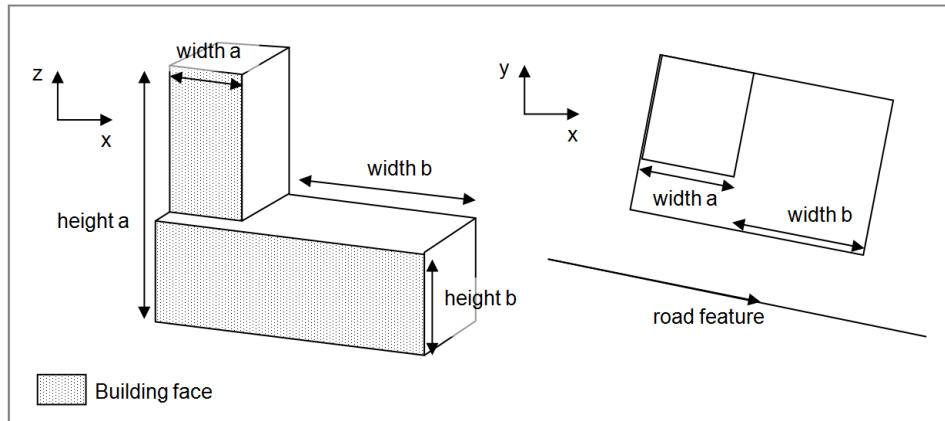


Figure 4: Illustration of the approach taken with varying building height

Adjoining (touching) buildings are counted separately for λ_F , not merged. The algorithm does not treat internal building faces; it only takes into account the widest points of a building perpendicular to the wind direction. The tool does not support buildings data in which multiple buildings overlap without one building completely containing another.

The value of λ_F is then determined from the sum of the building vertical areas, divided by the total area of the cell, giving the ratio of the cross-wind vertical area to cell size.

3.2. Street Canyon Algorithm

The input data for the algorithm are shown in Table 3.

Table 3: Input data for the street canyon algorithm

| Input data | Notes |
|--|---|
| Road Layer | Shapefile containing road geometry |
| Buildings Layer | Shapefile containing primary building geometry and building height (m) |
| Additional building layers | Shapefile(s) containing additional building layers each with building height (m). These additional layers contain additional features such as building podia. |
| Building distance tolerance (proportion) | Building distance tolerance as a proportion f |
| Building distance tolerance (m) | Building distance tolerance as a distance in metres b |
| Precision | Precision to use when processing coordinates (m) |
| Target minimum proportion of road with buildings | The target minimum proportion of road with buildings as a proportion |
| Maximum distance to the nearest building | Maximum distance to the nearest building (m) |

The output data produced by the algorithm are shown in Table 4. These parameters are calculated for each individual road feature in the input data.

Table 4: Output data from the street canyon algorithm: street canyon properties

| Output data | Notes |
|---------------|---|
| Canyon height | Minimum, maximum and mean canyon height are calculated for each side of the road (m) |
| Canyon width | Width from road centreline to the street canyon for each side of the road (m) |
| Canyon length | Length of the road which is considered as a street canyon for each side of the road (m) |

These output data are illustrated in Figure 5.

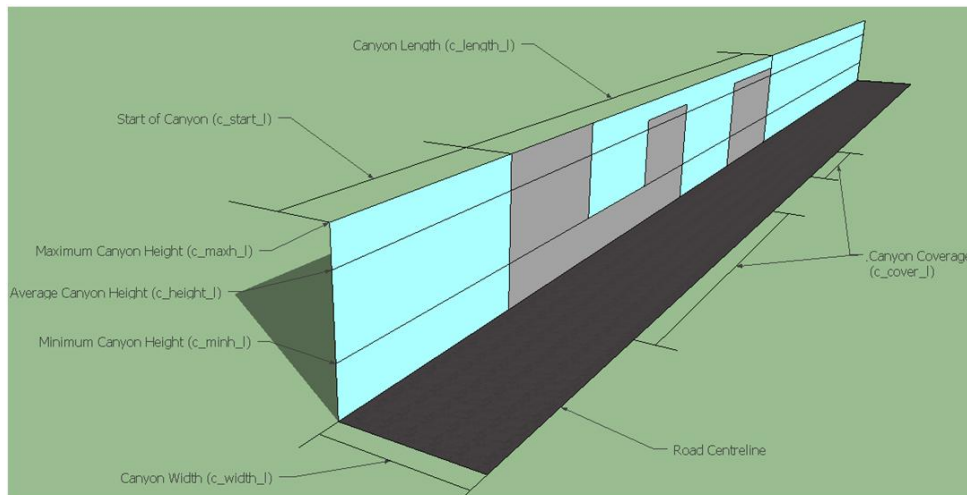


Figure 5: Illustration of the output parameters from the street canyon tool for a particular street, showing the left hand side of the street

The algorithm treats each road in turn in the input road dataset.

The algorithm first identifies all buildings that may affect the road. It starts by finding all buildings within the tolerances defined by the user. The building distance tolerance settings define a region beyond the base building. Any buildings, or building parts, in this region will be included in the canyon height calculations.

The **Building distance tolerance** is a combination of a proportion of the minimum distance (from the road centreline to the nearest building) and a constant distance. The **Building distance tolerance (proportion)** defines the proportion used. For example, a proportion of 0.5 would include buildings that are within half the minimum distance beyond the nearest building. The **Building distance tolerance (metres)** defines the constant component of the distance tolerance. For example, a setting of 2 would include buildings that are within 2 metres beyond the nearest building. These tolerances are illustrated in Figure 6.

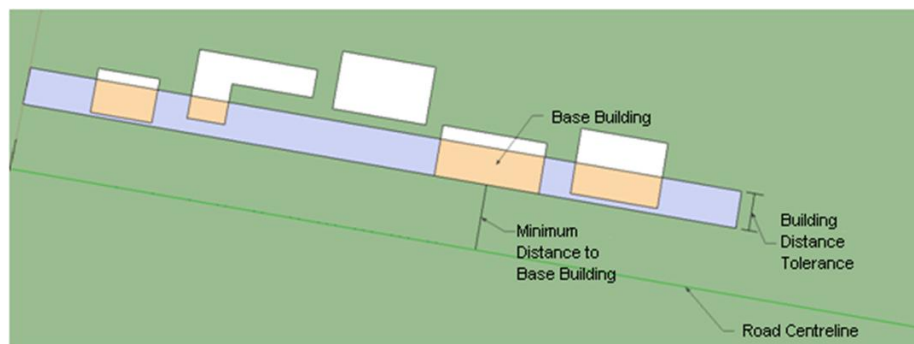


Figure 6: Illustration of the building distance tolerance settings

The left and right side calculations are carried out independently. For each road segment and each side of the road, the algorithm:

- Finds a suitable base building close to the road on that side. If the **Target minimum proportion of road with buildings** is set to 0.0, the base building will be the nearest building to the road. For other values of **Target minimum proportion of road with buildings**, the selected base building may be further away in order to achieve better coverage. It selects the nearest building likely to satisfy the target minimum proportion, or if no building is likely to satisfy that proportion, it chooses the building likely to give the highest coverage.
- Calculates a buffer distance:

$$\text{Buffer} = (1 + f)x + b$$

where,

x is the minimum distance from the base building to the road centreline,

f is **Building distance tolerance (proportion)**, and

b is **Building distance tolerance (metres)**.

- Locates all building faces within the buffer distance, perpendicular to the road centreline.
- Stores the height and length of each building face as projected onto the road centreline, as illustrated in Figure 7.

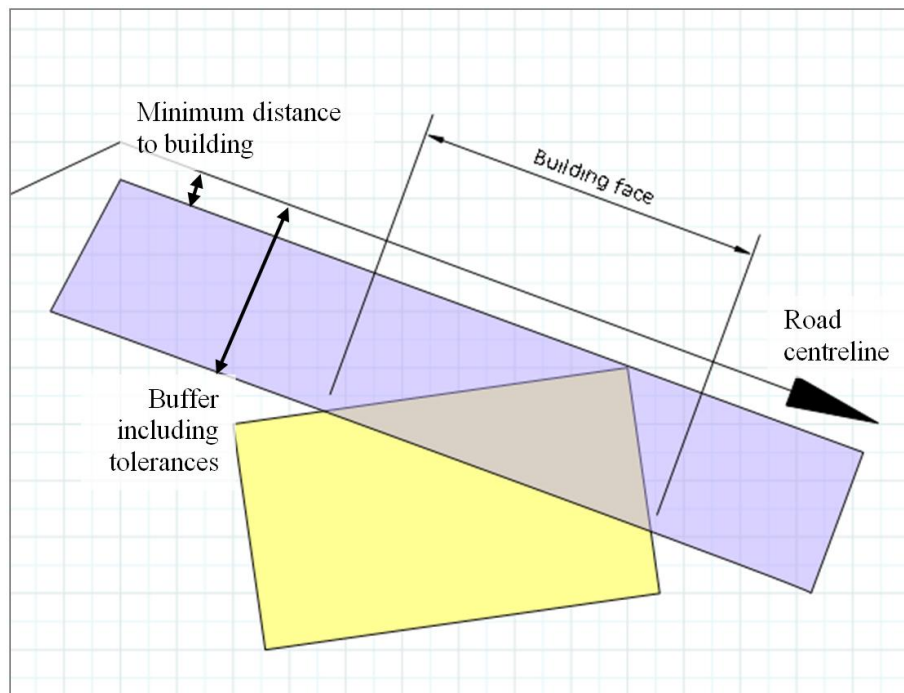


Figure 7: Example tolerance distance for the right hand side of a road feature

When two or more buildings or buildings of varying height are found in the same location, the height and length of each part of the building(s) is apportioned into multiple segments. The approach is illustrated in Figure 4 above.

Buildings that touch or cross the road centreline are ignored for the relevant road segment.

The output parameterisations from the algorithm, as shown in Figure 5, are calculated from the projected extent of the buildings that are deemed to affect the road, for each road feature and side of the road, based on the user-defined tolerances. The start of the canyon is defined as the distance from the first road vertex to the first building within the buffer calculated from the building distance tolerances. The length of the canyon is determined from that start point to the last building within the buffer around the road, such that it includes gaps. The canyon width and maximum, minimum and average height are only calculated for sections of the road considered to be within a canyon (where a building occurs within the buffer region). There is no double-counting: if a portion of the road is affected by multiple buildings, the width to the nearest point of the nearest building is used. The length of buildings in a canyon is calculated as the length of buildings within the canyon length, excluding gaps between buildings.

3.3. Implementation of both Algorithms as ArcPy Python Tools in ArcGIS

Both the algorithms have been implemented as user-friendly tools using the ArcPy Python package which enables geographic data analysis to be automated with Python in the ESRI ArcGIS platform (ESRI, 2016). The use of ArcPy simplified the implementation since (1) it was possible to take advantage of geoprocessing tools such as clipping a set of features to a polygon and (2) it was straightforward to create a user-friendly user interface for the tools. Figure 8 shows the user interface for the urban canopy tool.

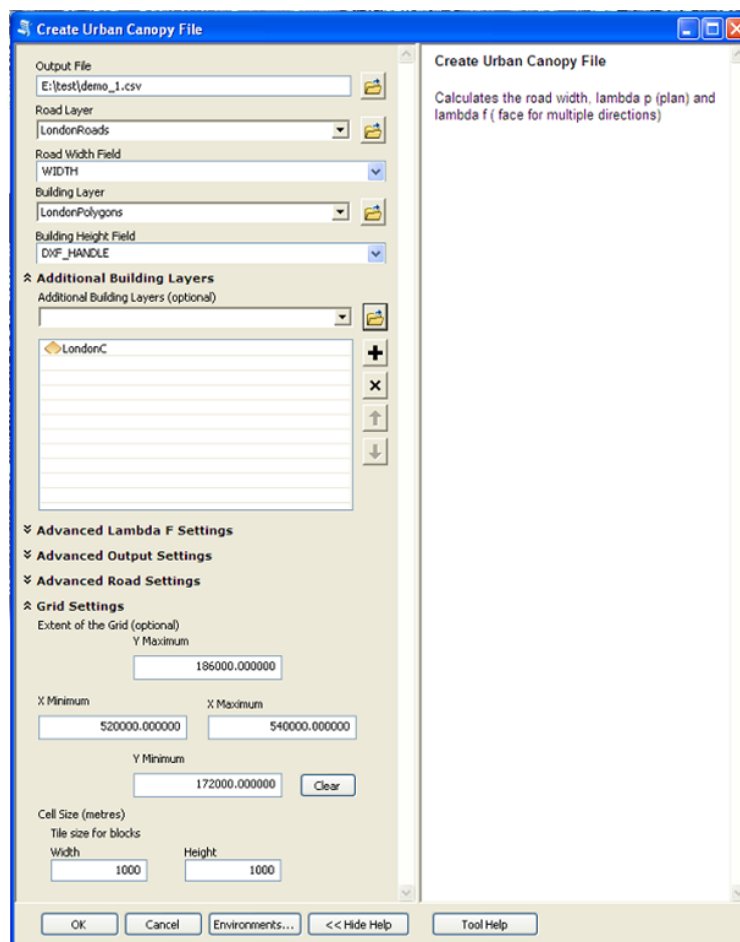


Figure 8: the user interface for the urban canopy ArcPy tool

4. Results, Discussion and Conclusions

The urban canopy and street canyon tools have been used to calculate parameterisations for London. The input road and building vector datasets were taken from OS MasterMap as described above. The study region was Greater London, covering an area of approximately 60km x 50 km which contains over 4 million buildings. The previous study (Hood et al., 2014) used a study area of 10 km x 15 km in central London.

The urban canopy grid resolution is 1 km and the wind direction sectors are 0° , 90° , 180° and 270° . The street canyon building tolerance proportion was 0.3 and the distance was 14 m. The coordinate precision was rounded to the nearest metre, the target minimum proportion of roads with buildings was 0.4 and the maximum distance to the nearest building was 50 m.

The results were as follows. The average building height across the study region was 5.5 m. The street canyon tool indicated that 65,136 of the 72,894 roads in the study are street canyons; with average canyon height of 9 m and width of 19 m. Around 19 % of the canyons are fully asymmetric, with a canyon wall on only one side. Figures 9 and 10 show the average building height and canyon width over the study area.

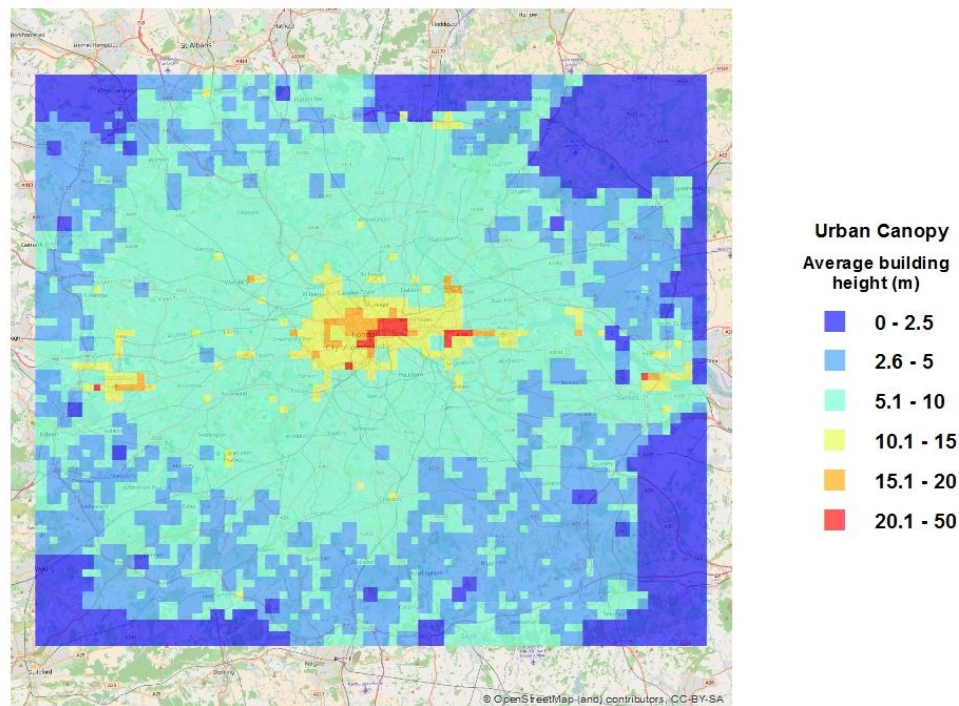


Figure 9: Urban canopy results showing average building height in each 1 km² grid cell

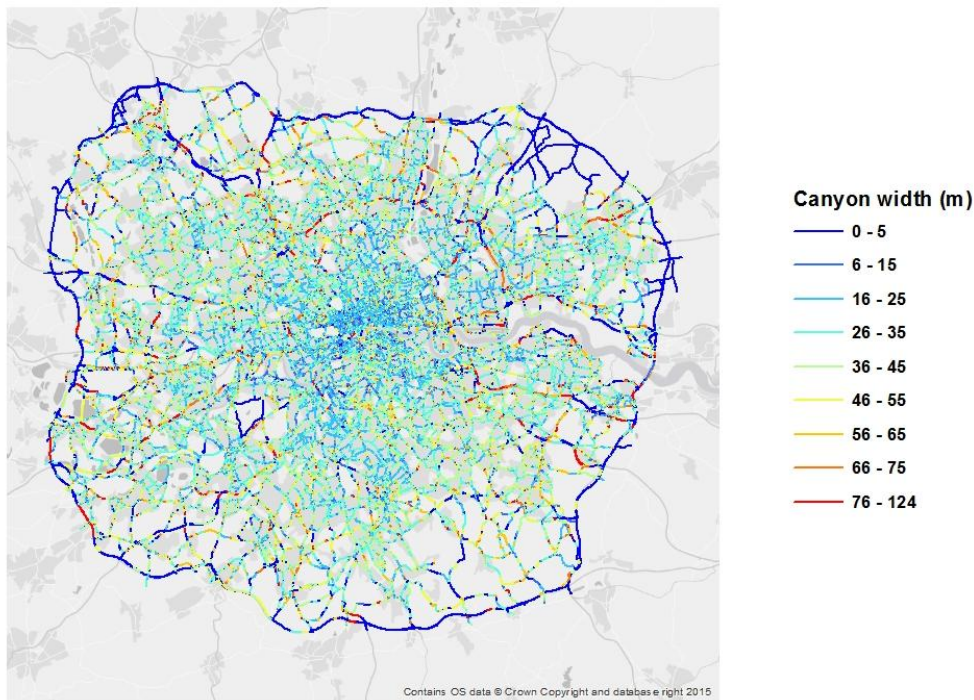


Figure 10: Canyon width results for each road against a grey background map. It can be seen that there are significant variations throughout the domain

The output urban morphology parameterisations for London are available to download from <http://www.cerc.co.uk/IJARSG2016> as supplementary data to accompany this paper. The data are in the correct format for use with ADMS-Urban.

Acknowledgements

Part of this work was funded by the UK NERC under grant NE/M002381/1.

References

- CERC, 2016: *ADMS-Urban*. <http://www.cerc.co.uk/ADMS-Urban>
- ESRI, 2016: *What is ArcPy?* <http://pro.arcgis.com/en/pro-app/arcpy/get-started/what-is-arcpy-.htm>
- Evans, S., 2009. *3D Cities and Numerical Weather Prediction Models: An Overview of the Methods Used in the LUCID Project*. UCL Working Papers Series, Paper 148, May 2009.
- Greater London Authority, 2013, London Atmospheric Emissions Inventory 2010, <http://data.london.gov.uk/dataset/london-atmospheric-emissions-inventory-2010>
- Hood, C. et al., 2014, *Urban Canopy Flow Field and Advanced Street Canyon Modelling in ADMS-Urban*. 16th International Conference on Harmonisation within Atmospheric Dispersion Modelling for Regulatory Purposes. 8-11 September 2014, Varna, Bulgaria
- Ordnance Survey MasterMap Integrated Transport Network Layer and Topography Layer (GML geospatial data), Coverage: London, Updated 18 December 2014, Ordnance Survey, GB. Using: EDINA Digimap Ordnance Survey Service, <http://digimap.edina.ac.uk>, Downloaded: May 2015.
- Shekar, S. and Xiong, H., 2008: *Encyclopedia of GIS*. Springer-Verlag, 1370.

A Geospatial Approach to Analyze the Impact of Population Growth on Bundelkhand Landscape, Central India

Lavkush Kumar Patel^{1,2} and Shashikant Tripathi²

¹ESSO-National Centre for Antarctic and Ocean Research, Vasco-da-Gama, Goa, India

²Mahatma Gandhi Chitrakoot Gramodaya Vishwavidyalaya, Satna, Madhya Pradesh, India

Publication Date: 10 June 2016

DOI: <https://doi.org/10.23953/cloud.ijarsg.58>



Copyright © 2016 Lavkush Kumar Patel and Shashikant Tripathi. This is an open access article distributed under the **Creative Commons Attribution License**, which permits unrestricted use, distribution, and reproduction in any medium, provided the original work is properly cited.

Abstract Population growth drives the process of urbanization and associated landscape changes. The conversion of natural landscape to anthropogenic landscape represents the most visible and pervasive form of human impact on the environment. The impact of population growth on Bundelkhand Landscape, Central India was analyzed using Landsat series satellite and MODIS Terra products. Population growth (total, urban and rural), landscape changes and variability in land surface temperature were analyzed for the last decades. The population has been increased manifold since 1901 and urbanization has also increased with the rate of $1.4\text{km}^2\text{a}^{-1}$ during last 24 years. This increase was rapid in current years (2000-2013) as compared to previous years (1989 - 2000). Due to rapid population growth, forest cover has been reduced by ~54% while agricultural land has been increased by ~76%. The mean land surface temperature has also increased by $\sim 0.5^\circ\text{C}$ during last 14 years (2001-2014). It is observed that the population growth was proportional to the growth of agriculture land ($r = 0.91$, $p < 0.05$, $n = 4$) and the built up area ($r = 0.94$, $p < 0.05$, $n = 4$) while inversely proportional to the forest resources ($r = -0.99$, $p < 0.001$, $n = 4$). The study indicates the phenomena “human environment interaction” where rapid population growth has lead LULC changes. This study also reveals that population growth is imposing an increasing burden on the limited and continually degrading natural resources thus altering the local environment.

Keywords *Geospatial Techniques; Urbanization; Landscape Changes; Bundelkhand; North Central India*

1. Introduction

Rapid population growth and accelerated demographic shift has made urbanization a significant increasingly global phenomenon [1]. Between one-third and one-half of the land surface has been transformed by human action [2]. The use of land to yield goods and services represents the most substantial human alteration of the earth system. Human use of land alters the structure and functioning of ecosystems, interacts with the atmosphere, with aquatic systems and with surrounding land. Moreover, land transformation interacts strongly with the components of global environment change [2]. With their speed, fragile ecologies and limited natural resources the impact of environmental change are more visible in developing regions [3].

Insights into human drivers of landscape change are crucial to understand the effect of human pressures on the structure and function of ecosystems [4]. Similarly, understanding the impact of anthropogenic activities on natural landscape is crucial for developing effective management plan [5]. The increasing variability, especially in the developing countries calls for the use of monitoring systems like Geospatial modelling. Geospatial techniques with integration of temporal satellite data sets and statistical analysis, it has become more efficient to observe the landscape changes [6], [7], [8]. Geospatial techniques have already shown their value in mapping urban areas, and as data sources for the analysis and modelling of urban growth and land use change [9], [10]. Studies were carried out to analyze the population growth and its impacts on environment using geospatial techniques [10], [11], [12]. The impact of disorganized urbanization on agriculture, ground water resources and on regional climate has been analyzed through geospatial technique [13], [14].

Bundelkhand region having an area of 7.1 million hectares comprises of seven districts of Uttar Pradesh (UP) and six districts of the Madhya Pradesh (MP) is among the least developed regions of Central India [15]. It has several historical places and tourist attractions. The region, with current human population $\sim 21 \times 10^6$, is lagging behind in terms of social and economic development and also affected by several drought years. The frequency of droughts has increased dramatically during recent years in this region, from one in 16 years during 18th and 19th centuries to virtually per year in recent times [16]. Banda, the largest and highly populated district of this region is influenced by several environmental problems such as rainfall uncertainty, ground water depletion, drought and global warming [16]. In the Bundelkhand region, very few studies have been done using geospatial techniques to analyse the urbanization growth and its impact on natural resources as well in local climate and are limited to explore the basal topography and water resources management [16], [17], [18]. Hence the study were undertaken to analyze the population growth, urbanization trend, landscape changes with respect to land surface temperature changes for the sustainability of the Bundelkhand region, Central India.

2. Study Area

Banda district ($80^{\circ}07'-81^{\circ}34'$ E and $24^{\circ}53'-25^{\circ}55'$ N) is the eastern most district of Bundelkhand region, Central India (Figure 1). It covers an area of $\sim 4460 \text{ km}^2$ and total human population of 1.8×10^6 (Census of India, 2011). The elevation in the area ranges from 400 to 600 m above mean sea level. It is drained by the Yamuna River and its tributaries (Ken and Baghein rivers). Over $\sim 80\%$ of population is dependent on agriculture and on an average $\sim 96\%$ of the farmer's income is being earned from the crop and livestock (agriculture economy). Its most of the area is irrigated by Ken canal network and groundwater through shallow and moderately deep tube wells. It is mostly covered by massive sandstone and limestone (high ground water yield) along with basement crystalline, impermeable or hard igneous and metamorphic rocks (poor aquifer and high runoff) exposed in the south-eastern part of the region. The region forms northern fringe of the peninsular India coming in contact with the Gangetic alluvium. Its major area is covered by Bundelkhand Granite Complex (Archean to Proterozoic) exposed in the south-eastern part of the region and overlain by alluvium soils; it is divided into two parts unconsolidated older (Pleistocene) and consolidated newer (Holocene) Alluvium. The general slope of the district is from southwest to north-east [19]. Climate of the district is characterized by hot summer, pleasant monsoon and cold seasons. The climate of the area is dry. The area lies in the semi-arid zone of Bundelkhand region. The annual rainfall is around $\sim 950 \text{ mm}$, with maximum precipitation (80%) received between July and September from the south-east monsoon (20). It has an average temperature of $13-36^{\circ}\text{C}$, minimum average temperature of $5.6-12^{\circ}\text{C}$ in winters (January-February) and maximum average temperature $32-44^{\circ}\text{C}$ in summers (March-May).

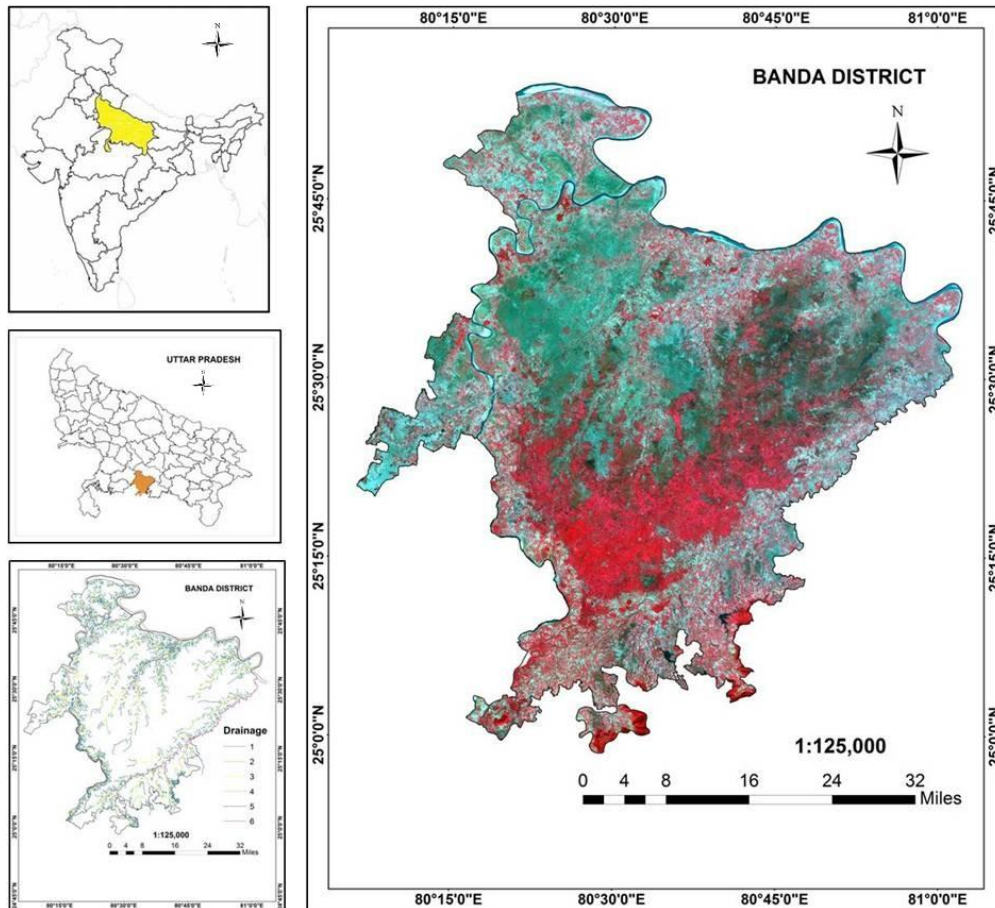


Figure 1: Location map of Banda district, Bundelkhand landscape, Central India, drainage network and synoptic view by Landsat 8 (PAN merged) operational land imager sensor data

3. Data and Methods

The census data of the district were collected from the Census survey of India for period of 1901-2011. The population growth and decadal variation were analysed for the urban, rural and total population of the district. Images from Landsat satellites series of different resolutions were used for the spatio-temporal data generation. Multispectral images of Landsat thematic mapper (TM) from 1989, enhanced thematic mapper (ETM⁺) from 2000 and Landsat 8 Operational Land Imager (OLI) image from 2013 were acquired from United States Geological Survey (USGS, <http://earthexplorer.usgs.gov/>). Additionally, the topographic maps of 1961 (1:50000) and administrative map of Banda district obtained from Survey of India were used as secondary data for the location identification and interpretation in satellite data. Landsat OLI satellite image was pansharpned by using its band 8 (Panchromatic band) and Brovey transform algorithm with bilinear interpolation re-sampling method. Pansharpned Landsat OLI satellite image (2014) was used as a reference to co registered satellite images of different time period to UTM Zone 44 North projection with WGS-84 datum within 0.5 pixel error. The built up area was manually extracted from the satellite data for different years (1989, 2000 and 2013) for the nine major populated regions of the district (Banda, Atarra, Baberu, Tindwaree, Badausa, Bisanda, Oran, Narainee, and Kamasin). In the selected populated regions, Banda, Atarra, Narainee and Baberu are the main towns and rest spots are the main villages of the district. The urbanization for last four decades (1989 to 2013) of the district was analysed. Annual expansion rate for the different time periods (1989-2000, 2000-13 and 1989-2013) were calculated and urbanization index were prepared for district and selected towns using following equation [21]:

$$Ire = \frac{\Delta U \times 100}{TLA \times \Delta t}$$

Where I is intensity index, ΔU is expansion area of urban land during a certain period, TLA is the total area of the research area, and Δt is time span of certain duration.

Satellite images were studied thoroughly to ascertain the probable land use classes and their range of reflectance values (DN). Six land use and land cover types were identified and used in this study, including: (1) urban or built-up land, (2) Open land and rocks, (3) Agriculture, (4) Forest (5) Grass land and shrubs, and (6) water. Supervised classification using maximum likelihood classification algorithm was performed for the classification of satellite data of different years in the Erdas Imagine 2015 environment. Accuracy (80-86 %) of the classified images was assessed, by comparing the classified data with ground truth GPS data. The land Use land cover changes (LULCC) were analysed by comparing the classified land use land cover maps of each year. Linear regression analysis was carried out in between variables like population growth, built up area, forest cover, and agriculture land to understand the impact of population growth on environment.

MODIS Land surface temperature (LST) product 8 day L3 Global 1 km (MOD11A2) was used to analyze the land surface temperature of the region. These data have been downloaded from the Land Processes Distributed Active Archive Centre: (<https://lpdaac.usgs.gov/>). The orbit of Terra around the Earth is scheduled to pass from north to south across the equator at about 10:30 a.m. and p.m. local solar time. The MODIS land surface temperature (LST) is derived from two thermal infrared band channels, i.e. 31 (10.78–11.28 μm) and 32 (11.77–12.27 μm) using the split-window algorithm [22] which corrects for atmospheric effects and emissivity using a look-up table based on global land surface emissivity in the thermal infrared [23].

4. Results and Discussions

The Banda district, one of the main landscapes of the Bundelkhand, covers major areas and is the major contributor of its economy. As per the analysis of district census data, the population of the district has been increased manifold since 1901 (Figure 2). The results for the population growth indicated increasing trend since 1901. The changes in population for each decade were calculated and it was observed that there was an increment in the population by approximately three times in last six decades (1961-2011). The growth in the urban population is comparatively high as compared to the rural population in the same time period. The decadal variation of the urban population (13-97%) was higher as compared to rural population (18-24%) during last six decades (1961-2011) (Figure 2). In the year 1961, decadal urban population decreased significantly as compared to rural population, the reason of this drift has remained unclear. In the following years (1971 and 1981), the decadal population of urban areas has increased dramatically. Most of the population tend to migrate towards urban areas for the better facilities which could be the reason of this higher population in urban. Increasing urban population could be also due to the natural growth of population in urban areas, rural to urban migration and reclassification of rural areas as urban in course of time [1]. The results of urbanization analysis of the district showed an annual expansion rate of $1.4 \text{ km}^2\text{a}^{-1}$ during 1989-2013, noticeably, 2000-2013 had higher annual expansion rate ($3.4 \text{ km}^2\text{a}^{-1}$) as compared to 1989-2000 ($1 \text{ km}^2\text{a}^{-1}$). Similar results were observed for urbanization index which was higher during 2000-2013 (0.1) as compared to that during 1989-2000 (0.02). The annual expansion in the major towns of the district was higher as compared to the villages. Banda, Atarra, Narainee and Baberu showed high annual expansion rate as (0.2, 0.04, 0.03, and $0.02 \text{ km}^2\text{a}^{-1}$ respectively) while villages showed a constant expansion rate $0.01 \text{ km}^2\text{a}^{-1}$ (Table 1). The increased urbanization is indicating increased land consumption and land excessive rate. Considering the built up expansion rate for selected urban towns of the district (Table 1), Banda city is the main town of the district and showed maximum changes (expansion) in built up area ($\sim 8 \text{ km}^2$) and had highest expansion rate $0.2 \text{ km}^2\text{a}^{-1}$ and

urbanization index of 1.1. Atarra and Baberu are the second and third highest developed town of district, which also had high annual expansion rate ($0.04 \text{ km}^2\text{a}^{-1}$, $0.03 \text{ km}^2\text{a}^{-1}$ respectively) and urbanization index (0.2 and 0.1 respectively) (Table 1). Major development like construction of institutions, hospitals, government buildings etc. was done during 2000-2013 in the district. Increase in built up area with population growth indicates that land was being used for urbanization at faster rate.

Table 1: Changes in the built up area, annual expansion rate and urbanization index of the selected nine urban towns of the Banda district during 1975-2013

| | Changes in Area (1989-2013) km^2 | Annual rate (1989-2013) km^2a^{-1} | Built up Index |
|----------|---|--|----------------|
| Banda | 8.0 | 0.2 | 1.0 |
| Atarra | 1.4 | 0.04 | 0.2 |
| Baberu | 0.9 | 0.02 | 0.1 |
| Tindwari | 0.4 | 0.01 | 0.1 |
| Badausa | 0.3 | 0.01 | 0.03 |
| Bisanda | 0.2 | 0.00 | 0.02 |
| Oran | 0.2 | 0.00 | 0.02 |
| Narainee | 0.7 | 0.02 | 0.1 |
| Kamasin | 0.2 | 0.01 | 0.03 |

As per the results of LULCC, the agriculture land comprised 73.9% of the area while forest cover comprised 8.1% area of district in 1989. From 1989 to 2013, the area of agriculture was found to increase while forest cover decreased (Table 2). In India and other developing countries, large areas had been partially cleared for agriculture. The degradation of forest cover was high in the period 1989-2000 (2.2%) as compared to 2000-2013 (2.1%) while agriculture land showed increment of 0.01% during the same period (Table 2 and Figure 3). The major LULC changes during 1880-2010 in India, which includes loss of forests, expansion of cropland and urbanization was studied by Tian et al. 2014 [24]. They have proposed that the greater deforestation occurred during 1880–1950 due to British rule policies to increase income from the timber products and cropland, however, deforestation decreased after the 1980s due to formulation of government policies to protect forests. Booth et al. (2002) [25] have reported the changing rates for the Southeast Asia forests (0.8 to -0.9%), Latin America (0.4 to 0.5%) and for the humid forests of Africa (0.4 to 0.5% per year). Richards and Flint (1994) [26] have reported that total forest area decreased from 100 million ha to 81 million ha while cropland area increased from 100 million ha to 120 ha during 1880–1950. New cultivation, population increase and poverty were found as the major cause of this deforestation. Built-up area showed increasing trend, however it had higher growth in 2000-2013 (1%) as compared to 1989-2000 (0.2%). There was increment in built up area (0.3% - 1.6%) since 1989-2013 especially along the roads. Although not significant, agriculture land and built up area were inversely correlated to the deforestation.

A continuous decrease in open land, rocks, grass and shrubs were observed in between 1989-2000 (0.7% and 2.1%) and 2000-2013 (0.04% and 2.8%). The area of surface water bodies of the district were seen fluctuating. It could be due to several drought years in between 1975-2013. Similar observations were reported for the Bundelkhand region [16]. The results showed agricultural expansion and intensification were the major drivers of LULCC. Reduction in the forest cover, grass and shrub land and increment in agriculture and built up land indicate unplanned development and anthropogenic activities in the district.

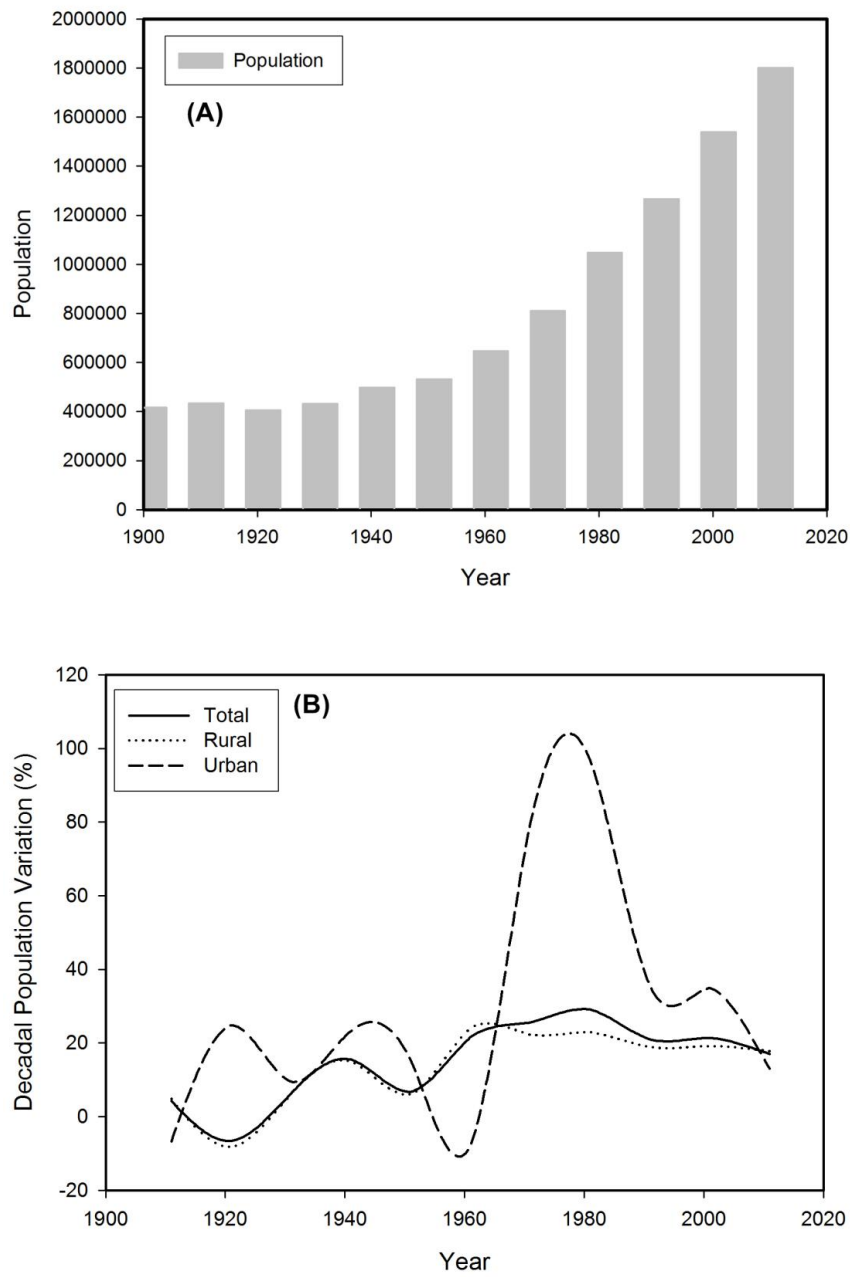


Figure 2: A) Population of the Banda district during each census since 1901-2011. (B) Decadal population variation for rural, urban and total (rural and urban) population of the Banda district

Table 2: Changes in the land use and land cover of the district for the period 1989-2013

| LULC | 1989 | | 2000 | | 2013 | |
|---------------------|--------|--------|--------|--------|--------|--------|
| | % Area | Area | % Area | Area | % Area | Area |
| Water bodies | 0.9 | 40.2 | 1.0 | 44.4 | 1.6 | 70.9 |
| Forest cover | 8.1 | 361.5 | 5.8 | 259.8 | 3.7 | 166.7 |
| Agriculture | 73.9 | 3296.1 | 77.2 | 3442.2 | 80.4 | 3587.8 |
| Open land and rocks | 3.9 | 177.1 | 4.7 | 209.8 | 4.8 | 211.8 |
| Grass and Shrubs | 12.8 | 569.9 | 10.7 | 477.7 | 7.9 | 353.1 |
| Built-up | 0.3 | 15.2 | 0.6 | 26.1 | 1.6 | 69.8 |

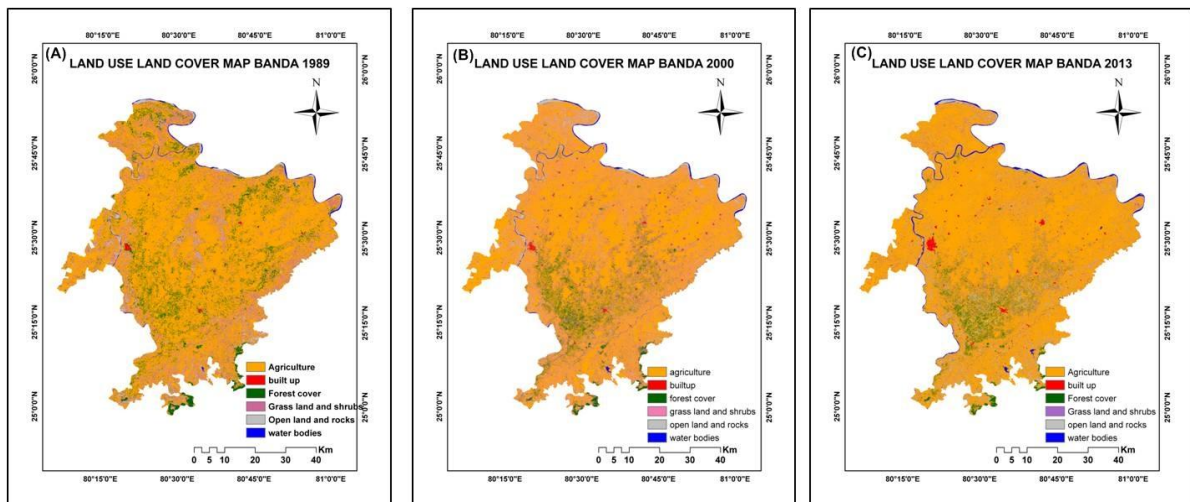


Figure 3: Landscape changes in the Banda District, (A) LULC map of 1989, (B) LULC map of 2000, and (C) LULC map of 2013

To understand the impact of increasing population and disorganized urbanization on landscape, a linear regression analysis was carried out. The analysis of population growth and others indicates decrement in the forest resources and substantial increment in the built up and agriculture land (Figure 4). Increase in population growth was significantly correlated to increasing agriculture land ($r = 0.91$, $p < 0.05$, $n = 4$) and built up area ($r = 0.94$, $p < 0.05$, $n = 4$). However, increasing populations significantly affected the forest cover ($r = -0.99$, $p < 0.001$, $n = 4$). The Figure 4 indicates the negative correlation of population and forest cover. With the growing population the forest cover showed a continuous decrease while population growth has positive correlation with agriculture and built up land. The changes of landscapes indicate the social and economic needs of growing population. Deforestation has been associated with increases in population density [5]. It indicates negative effect of population pressure on natural landscape of the district. Increasing human population and climate variability is affecting not only the district but also the other parts. Similarly, Badreldin and Goossens, (2014) [27] have also analyzed the LULC changes in the Egypt, where climate and human activities were the main causes for landscape change.

To analyze impact of human induced changes in LST, the MOD11A2 data for the period 2001 to 2014 were analysed and significant increment in the LST were observed (Figure 5). In 2001, ~59% of the district area represented 24°C to 26°C LST range, ~26% area represented 22°C to 24°C LST range, ~13% area represented 26°C to 28°C LST range and ~1% area represented 28°C to 30°C LST range. As compared to 2001, increment in LST was observed in 2007. In 2007, ~50% area represented 24°C to 26°C LST range; ~48% area represented 26°C to 28°C LST range, ~2% area represented 28°C to 30°C LST range, and ~1% area represented 23°C to 24°C LST range. Similarly for 2014, ~70% area represented 26°C to 28°C LST range, ~22% area represented 24°C to 26°C LST range, and ~8% area represented 28°C to 30°C LST range. The lowest land surface temperature range for the district increased 2°C and highest land surface temperature range increased 1°C (Figure 6). The overall mean land surface temperature of the district has been increased by 0.5°C (Figure 5). Mohan and Kandya, (2015) [28] have analyzed the diurnal temperature range (DTR) of the Delhi city for period 2001 to 2014 and reported that the converging trend of DTR which is primarily due to the increase in the minimum temperatures as a consequence of built structures in the cities. Similarly, Zhang et al., (2009) [29] had analyzed the effect of human induced changes and land surface temperature rise in the non-urban areas, and reported that the LULC changes has altered the land surface temperature of the Fuzhou city China. Chen et al., (2006) [30] had also reported changes in the temperature of the Pearl River Delta, caused by the LULC changes. So, the impact of rapid urbanization is not limited to urban

areas but it has impact on non-urban areas (rural) also. So, it indicated the impact of rapid population growth and disorganized urbanization on the LULC changes, which has altered the local climate.

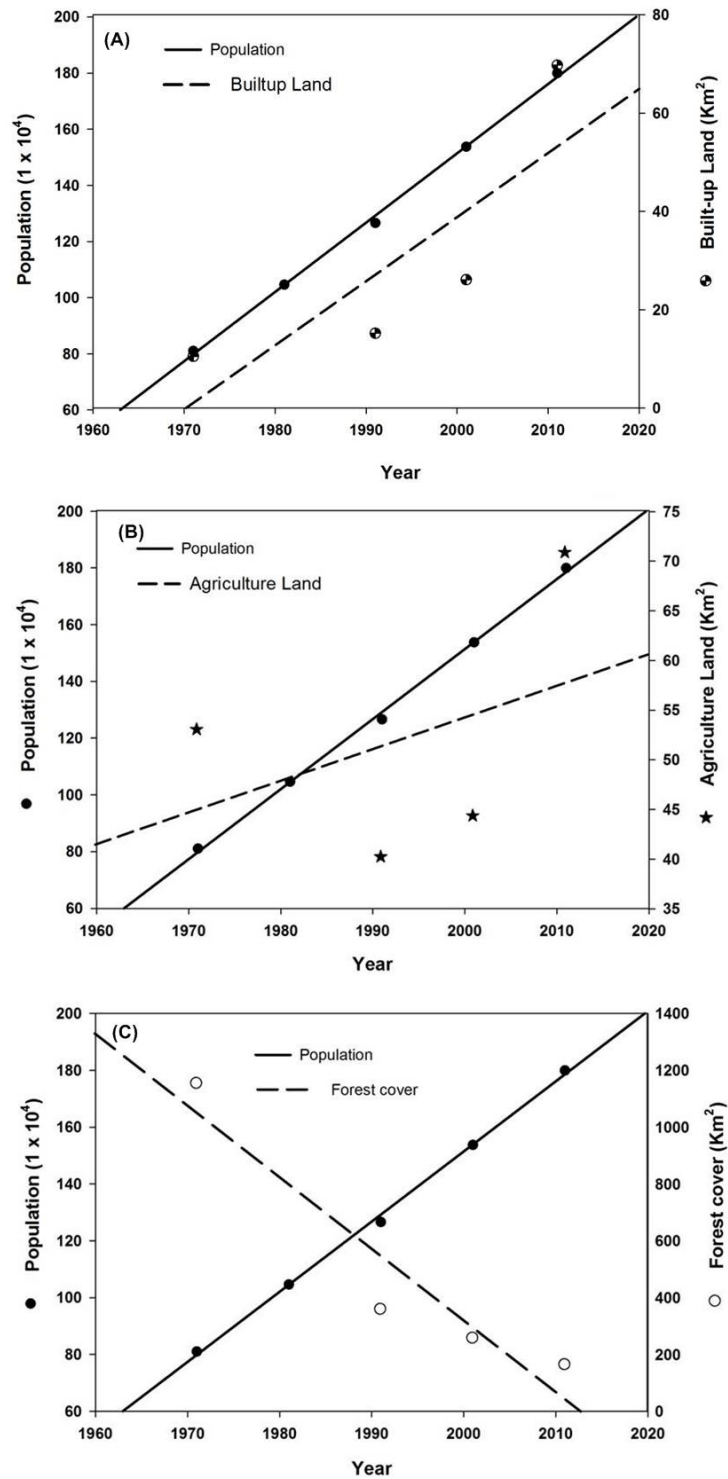


Figure 4: Population growth and its correlation with landscape changes (A) with built-up land, (B) with agriculture, and (C) with forest cover

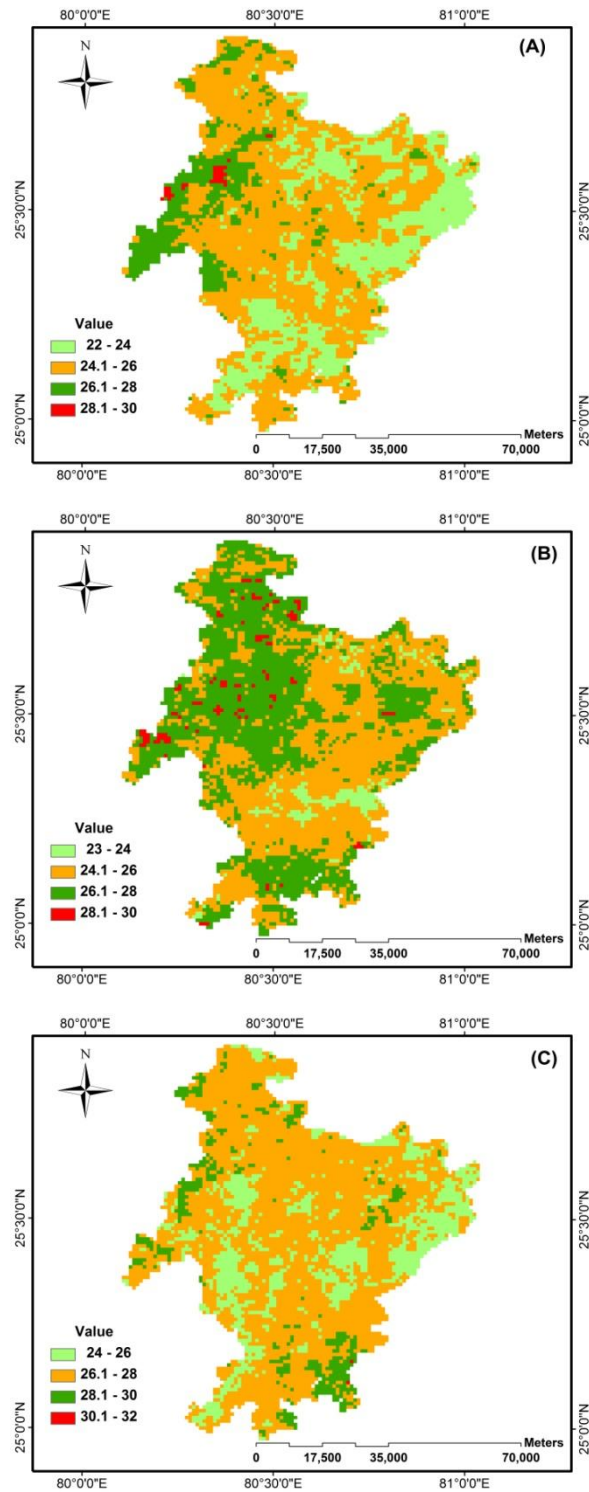


Figure 5: Land surface temperature (LST) obtained via MODIS Terra product for the period 2001-2015 over the Banda district (A) mean LST map of 2001, (B) mean LST Map of 2007, and (C) mean LST map of 2014

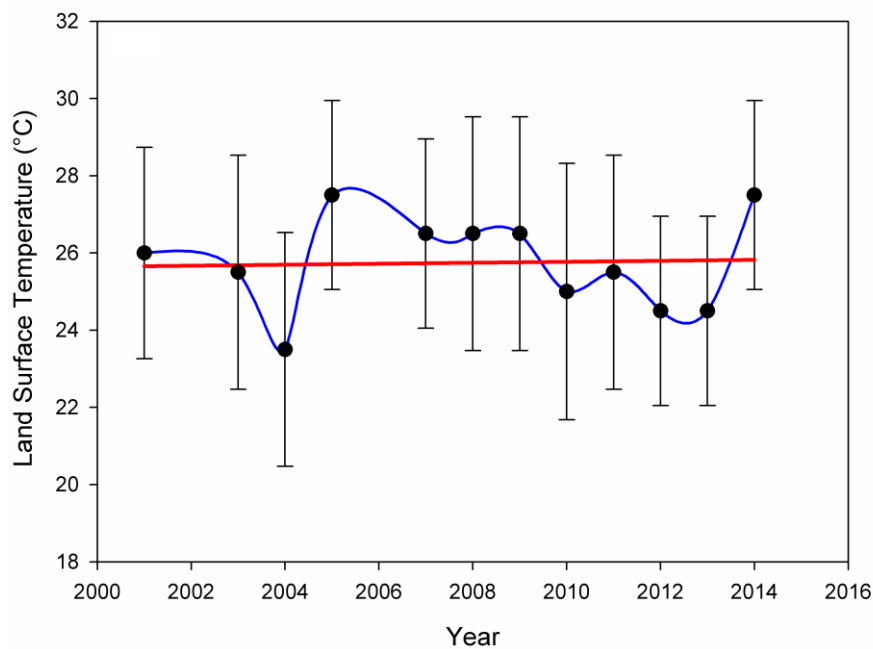


Figure 6: Mean Land surface temperature trend in the Banda district for the period 2001-2014

5. Conclusions

This study highlights the impact of population growth and urbanization on the Bundelkhand landscape of Central India. Temporal satellite data products were used for the estimation of urbanization and its impact on landscape. The population of the district has been increased manifold and agriculture and built-up area were increased by 8.8% and 358.7% respectively however forest cover was reduced by 53.9%, from 1989 to 2013. The conversion of natural lands to croplands, pastures, urban areas, reservoirs, and other anthropogenic landscapes represents the most visible and pervasive form of human impact on the environment. The population has been increased four times compared to 1901 and urbanization rate was higher ($1.4 \text{ km}^2\text{a}^{-1}$) for the current period (2000-2013). The decrement in the natural resources and increment in the land surface temperature of the district could be due to population growth, and urbanization. Regular monitoring of natural resources of the region is a prime need and also a recommendation. The path for sustainability might be achieved through the conservation and management of resources (forest, ground water and geological). Geospatial techniques can be used to explore the landscape dynamics, artificial ground water recharge zone and impact of urbanization for the sustainability of district. A systematic analysis of local-scale land use studies to provide an explanation for effective planning is required.

Acknowledgements

The Authors are grateful to the Vice-Chancellor MGCGV Chitrakoot and the Director, NCAOR for their support. We are also grateful to USGS, Census of India, for providing datasets. This is the NCAOR contribution number 09/2016.

References

- [1] Jenerette, G.D. and Potere, D. *Global Analysis and Simulation of Land-Use Change Associated with Urbanization*. Landscape Ecology. 2010. 25 (5) 657-670.
- [2] Vitousek, P.M., Mooney, H.A., Lubchenco, J. and Melillo, J.M. *Human domination of Earth's ecosystems*. 1997. Science. 277; 494-499.
- [3] Rasul, G. *Food, Water, and Energy Security in South Asia: A Nexus Perspective from the Hindu Kush Himalayan Region*. Environmental Science and Policy. 2014. 39; 35-48.
- [4] Wear, D. and Bolstad, P. *Land-use Changes in Southern Appalachian Landscapes: Spatial Analysis and Forecast Evaluation*. Ecosystems. 1998. 1; 575-594.
- [5] Turner, B.L., Meyer, W.B. and Skole, D.L. *Global Land-Use Land-Cover Change - Towards an Integrated Study*. Ambio. 1994. 23 (1) 91-95.
- [6] Taubenböck, H., Esch, T., Felbier, A., Wiesner, M., Roth, A. and Dech, S. *Monitoring Urbanization in Mega Cities from Space* 2012. Remote Sensing of Environment. 117; 162-176.
- [7] Paudel, S. and Yuan, F. *Assessing Landscape Changes and Dynamics Using Patch Analysis and GIS Modeling*. International Journal of Applied Earth Observation and Geoinformation. 2012. 16; 66-76.
- [8] Liu, H. and Weng, Q. *Landscape Metrics for Analysing Urbanization-Induced Land Use and Land Cover Changes*. Geocarto International. 2013. 28 (7) 582-593.
- [9] Liu, H. and Weng, Q. *Seasonal Variations in the Relationship between Landscape Pattern and Land Surface Temperature in Indianapolis, USA*. Environmental Monitoring and Assessment. 2008. 144 (1-3) 199-219.
- [10] Sharma, R., Ghosh, A. and Joshi, P.K. *Spatio-temporal Footprints of Urbanisation in Surat, the Diamond City of India (1990-2009)*. Environmental Monitoring and Assessment. 2013. 185; 3313-3325.
- [11] Sharma, R., Ghosh, A. and Joshi, P.K. *Analysing Spatio-Temporal Footprints of Urbanization on Environment of Surat City Using Satellite-Derived Bio-Physical Parameters*. Geocarto International. 2014. 1-19.
- [12] Sun, Y., Tong, S.T.Y., Fang, M. and Yang, Y.J. *Exploring the Effects of Population Growth on Future Land Use Change in the Las Vegas Wash Watershed: An Integrated Approach of Geospatial Modeling and Analytics*. Environment, Development and Sustainability. 2013. 15 (6) 1495-1515.
- [13] Liu, Y., Lv, X., Qin, X., Guo, H., Yu, Y., Wang, J. and Mao, G. *An Integrated GIS-Based Analysis System for Land-Use Management of Lake Areas in Urban Fringe*. Landscape and Urban Planning. 2007. 82; 233-246.
- [14] Pielke, R.A., Pitman, A., Niyogi, D., Mahmood, R., McAlpine, C., Hossain, F., Goldewijk, K.K., Nair, U., Betts, R., Fall, S., Reichstein, M., Kabat, P. and de Noblet, N. *Land Use/Land Cover Changes and Climate: Modeling Analysis and Observational Evidence*. Wiley Interdisciplinary Reviews: Climate Change. 2011. 2 (6) 828-850.

- [15] Chengappa, C., Edwards, R., Bajpai, R., Shields, K.N. and Smith, K.R. *Impact of Improved Cookstoves on Indoor Air Quality in the Bundelkhand Region in India*. Energy for Sustainable Development. 2007. 11 (2) 33-44.
- [16] Gupta, A.K. and Singh, A. *Traditional Intellect in Disaster Risk Mitigation: Indian Outlook – Rajasthan and Bundelkhand Icons*. Indian Journal of Traditional Knowledge. 2011. 10; 156-166.
- [17] Avtar, R., Singh, C.K., Shashtri, S., Singh, A. and Mukherjee, S. *Identification and Analysis of Groundwater Potential Zones in Ken-Betwa River Linking Area using Remote Sensing and Geographic Information System*. Geocarto International. 25 (5) 379-396.
- [18] Singh, R., Garg, K.K., Wani, S.P., Tewari, R.K. and Dhyani, S.K. *Impact of Water Management Interventions on Hydrology and Ecosystem Services in Garhkundar-Dabar Watershed of Bundelkhand Region, Central India*. Journal of Hydrology. 2014. 509; 132-149.
- [19] Radhakrishna, T., Chandra, R., Srivastava, A.K. and Balasubramonian, G. *Central/Eastern Indian Bundelkhand and Bastar cratons in the Palaeoproterozoic Supercontinental Reconstructions: A Palaeomagnetic Perspective*. Precambrian Research. 2013. 226; 91-104.
- [20] Srivastava, A., Tripathi, N.K. and Gokhale, K.V.G.K. *Basement Topography and Aquifer Geometry around Ken Graben, India*. International Journal of Remote Sensing. 1999. 20 (11) 2295-2305.
- [21] Zhou, D., Shi, P., Wu, X., Ma, J. and Yu, J. *Effects of Urbanization Expansion on Landscape Pattern and Region Ecological Risk in Chinese Coastal City: A Case Study of Yantai City*. The Scientific World Journal. 2014. 1-9.
- [22] Wan, Z., Zhang, Y., Zhang, Q. and Li, Z. *Validation of the Land-Surface Temperature Products Retrieved from Terra Moderate Resolution Imaging Spectroradiometer Data*. Remote Sensing of Environment. 83 (1-2) 163-180.
- [23] Vancutsem, C., Ceccato, P., Dinku, T. and Connor, S.J. *Evaluation of MODIS Land Surface Temperature Data to Estimate Air Temperature in Different Ecosystems over Africa*. Remote Sensing of Environment. 114 (2) 449-465.
- [24] Tian H., Banger K., Bo, T. and Dadhwal V.K. *History of Land Use in India During 1880-2010: Large-Scale Land Transformations Reconstructed from Satellite Data and Historical Archives*. Glob Planet Change. 2014. 121; 78-88.
- [25] Booth, D.B., Hartley, D. and Jackson, R. *Forest Cover, Impervious-Surface Area, and the Mitigation of Stormwater Impacts*. Journal of the American Water Resources Association. 2002. 38; 947-835.
- [26] Richards, J.F. and Flint, E.P. *Historic Land Use and Carbon Estimates for South and Southeast Asia 1880-1980*. In: Daniel, R.C. (ed.), ORNL/CDIAC-61, NDP-046. Oak Ridge National Laboratory, Tennessee, USA. 326.
- [27] Badreldin, N. and Goossens, R. *Monitoring Land Use/Land Cover Change using Multi-Temporal Landsat Satellite Images in an Arid Environment: A Case Study of El-Arish, Egypt*. Arabian Journal of Geosciences. 2014. 7; 1671-1681.

- [28] Mohan, M. and Kandya, A. *Impact of Urbanization and Land-Use/Land-Cover Change on Diurnal Temperature Range: A Case Study of Tropical Urban Airshed of India Using Remote Sensing Data*. The Science of the Total Environment. 506-507, 453-65.
- [29] Zhang, Y., Odeh, I.O.A. and Han, C. *Bi-temporal Characterization of Land Surface Temperature in Relation to Impervious Surface Area, NDVI and NDBI, using A Sub-Pixel Image Analysis*. International Journal of Applied Earth Observation and Geoinformation. 2009. 256-264.
- [30] Chen, X.L., Zhao, H.M., Li, P.X. and Yin, Z.Y. *Remote Sensing Image-Based Analysis of the Relationship Between Urban Heat Island and Land Use/Cover Changes*. Remote Sensing of Environment. 104 (2) 133-146.

Hydrogeological Mapping and Identification of Groundwater Recharge Potential Zone of Reamal Block Deogarh District, Odisha - A Geospatial Technology Approach

Kamal Kumar Barik¹, Rupeli Jeet¹, R. Annaduari² and Jagadish Kumar Tripathy¹

¹Dept. of Earth Sciences, Sambalpur University, Odisha, India

²School of Civil Engineering, SRM University, Chennai, Tamil Nadu, India

Publication Date: 28 June 2016

DOI: <https://doi.org/10.23953/cloud.ijarsg.63>



Copyright © 2016 Kamal Kumar Barik, Rupeli Jeet, R. Annaduari and Jagadish Kumar Tripathy. This is an open access article distributed under the **Creative Commons Attribution License**, which permits unrestricted use, distribution, and reproduction in any medium, provided the original work is properly cited.

Abstract Assessment of potential zone of groundwater recharge is extremely important for the protection of water quality and the management of groundwater systems. Groundwater Potential Zones (GPZ) are demarcated with the help of geospatial techniques. The parameters, considered for identifying the GPZ such as geology, geomorphology, slope, drainage density, lineament density, rainfall, soil maps and LULC are generated using the satellite data and toposheet. Later they are integrated with each other applying weighted overlay in ArcGIS. Suitable ranks are assigned for each category of these parameters. For the various geomorphic units, weight factors are decided based on their capability to store groundwater. This procedure is repeated for all the other layers and resultant layers are reclassified. The groundwater potential zones are classified into three categories like poor, good and excellent. The use of aforesaid methodology is demonstrated in a selected study area in Reamal Block of Deogarh District, Odisha. The thematic layers were first digitized from satellite imagery, supported by ancillary data such as toposheet, finally all thematic layers were integrated using ArcGIS software to identify the groundwater recharge potential zones for the study area and generate a map showing these groundwater recharge potential zones namely 'poorly suitable', to 'most suitable' on knowledge based weightage factors.

Keywords *Geomorphology; Lineament Density; Slope*

1. Introduction

In the India, the quantity and quality of groundwater have deteriorated year by year, especially in the large developing cities. The over-extraction of groundwater resources has led to lower the water table by more than one metre on average during the last two decades, while seawater intrusion is increasing in the coastal areas (Alsharhan et al., 2001). Groundwater quality in a region is largely determined by both natural processes (dissolution and precipitation of minerals, groundwater velocity, quality of recharge waters and interaction with other types of water aquifers) and anthropogenic activities (Mohamed et al., 2007; Al Asam, 1996; Mohamed et al., 2010a,b; Elmahdy and Mohamed, 2012a). Geophysical and field survey over regional scale was probably time and economic consuming (Sherif

et al., 2011). In consequence, remote sensing and geographic information system (GIS) often played, at least in remote access locations, a vital role in mapping and groundwater potential and groundwater management (Singh and Singh, 2005). These days, remote sensing specialist and hydrologists confirm that remote sensing data and GIS are only used rudimentarily in their daily routine (Van De Griend and Owe, 1993). For this reason it is important to demonstrate the value of remote sensing data and GIS technology for groundwater potential mapping. With the wide scale of remote sensing data, various techniques have been applied using an integration of various geomorphometric, geological and hydrogeological parameters not only to delineate new groundwater potential zones, but also solve other problems related to the groundwater quality (Prasad et al., 2008). Jaiswal et al. (2003) had used the GIS techniques for the generation of groundwater prospective zones for rural development. Sahoo et al. (1998), Singh and Prakash (2002), Elmahdy and Mohamed (2013c) and Elmahdy and Mohamed (2014b) had used the GIS to delineate groundwater potential zones. Rao and Jugran (2006) have applied GIS for processing and interpretation of groundwater quality data. The GIS had also been considered for multicriteria analysis in resource evaluation. Boutt et al. (2001) and Saraf et al. (2004) have carried out groundwater modelling through the use of GIS. Elmahdy and Mohamed (2014b) used probabilistic frequency Model for groundwater potential mapping. The GIS were used widely to estimate groundwater quality and transport modelling of a noncreative solute material in ground water flow, in groundwater vulnerability (Liggett and Talwar, 2009; Boughriba et al., 2010) and identification of groundwater potential zones (Elmahdy and Mohamed, 2014c).

The main goal of this study is to map groundwater potential zone based on terrain, hydrological and geological parameters employing multi criteria approach. These parameters are very closely associated with groundwater accumulation.

2. Study Area

The study area Reamal block is 908 km² of in Deogarh district of Odisha, India, which lies in Survey of India toposheet bearing nos. F45M11, F45M15, F45M12 and F45M16 falling between the latitude 21° 7' 51.67" to 21°29' 46.13"N and longitude 84°32'50" to 85° 0'16.39"E. The District consists of 3 Blocks namely Riamal, Barkote and Tileibani. It is situated in the Western region of the state. It is situated 192m meters above the sea level. The average annual rainfall of the District is 1142.3mm. The maximum temperature of the District is 43°C and minimum temperature is 8°C. The entire district comes under North-western Plateau Zone and belongs to one agro-ecological situation i.e. Low rainfall lateritic soil. The climate of the district is characterized by a very hot dry summer and erratic distribution of rains by the South-West monsoon.

3. Materials and Methodology

Two satellite images were employed in this study. The first data set was the updated version of Shuttle Radar Topography Mission (SRTM) DEM of ~90 m spatial resolution is currently available in the database of the Consortium for Spatial Information (<http://srtm.csi.cgiar.org/Index.asp>). The second data set was Landsat 8 (OLI) images of a 30 m spatial resolution and acquired on June-2015. Landsat images were downloaded from the USGS (<http://www.earthexplorer.usgs.gov>). The lithology map was collected from Geological Survey of India (GSI), Bhubaneswar and was later scanned, rectified and digitized on Arc GIS to prepare the of lithology thematic layer of the study area. The rainfall data was collected from regional office of Indian Meteorological Department, Bhubaneswar.

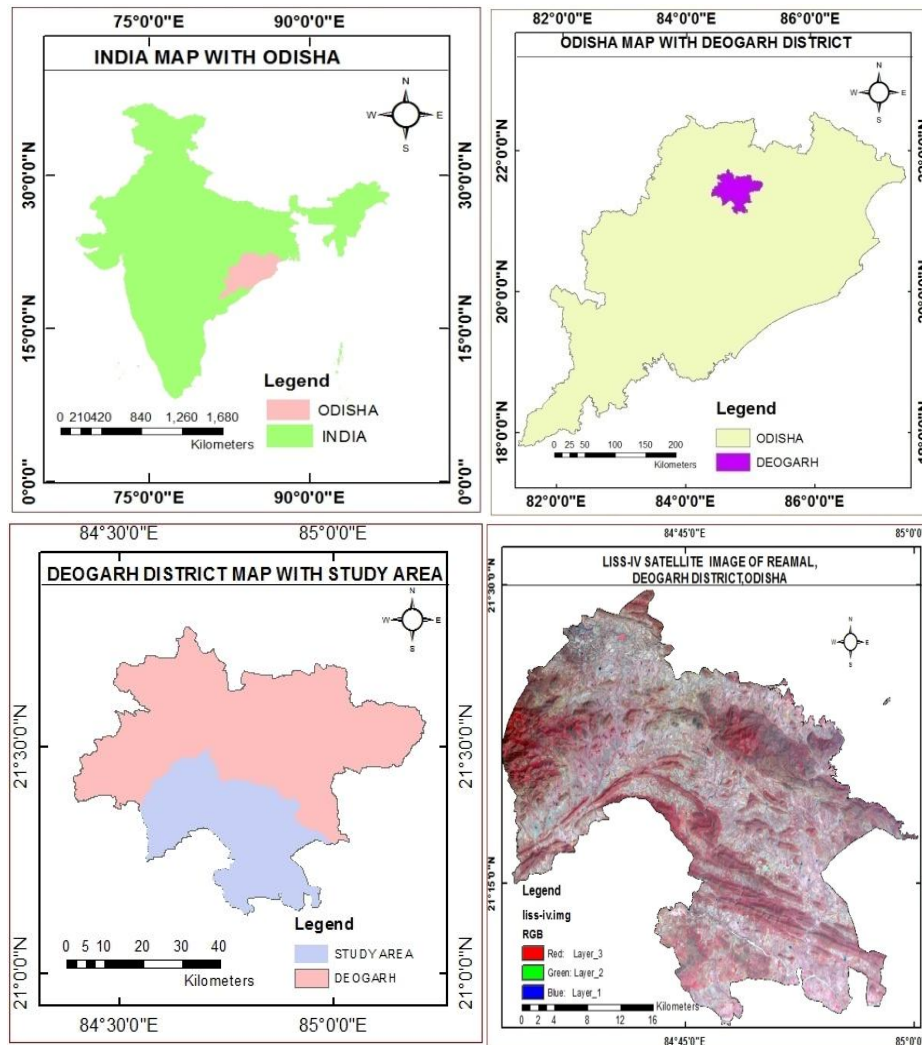


Figure 1: Location map predict the study area

The slope map was generated from SRTM DEM. The digital (FCCS) of Landsat OLI were visually interpreted for preparing different thematic layers like Geomorphological map, Landuse and Landcover and lineament density map of study area. The drainage map was prepared from SOI toposheet and the drainage density map was prepared from Arc GIS software. In order to access groundwater Potential zones, different thematic layers Viz. Geomorphology, LULC, Drainage density, Lineament density, Slope and Soil were generated from satellite imagery and the conventional data were in corporate with the help of Arc GIS 9.3 software. The methodology adopted flowchart for the present study is shown in Figure 2. GIS packages are used creation for digital data base, data integration and analysis. All thematic maps are digitized in continuous manner in vector format and the digitized values were then assigned. Different polygons in the thematic maps were labelled separately. Initially each one of the polygons in the final thematic layers was qualitatively visualized into one of the category Viz. (i) Excellent, (ii) Good, (iii) Moderate and (iv) Poor, in terms of their importance and occurrence of groundwater. Then suitable weights were assigned to each thematic feature after considering their characteristics. Knowledge based weight assignment was carried out for each feature and they were integrated and analyzed using the weighted aggregation method (ESRI 1988 & 1989). In this method, the total weights of the final integrated polygon were derived as sum or product of the weights assigned to different layers according to their suitability. Finally the groundwater prospect or Potential zone map was generated.

3.1. Categorization of Thematic Layers

To assess the groundwater prospect of an area, it is necessary to understand different types of landforms, geology, soil characteristics, slope and recent land utilization of that area. The information in groundwater characteristic of the various parameters is initially generated in descriptive forms, which reveals the parameters support the occurrences of groundwater. The criteria adopted for different thematic layers are given below.

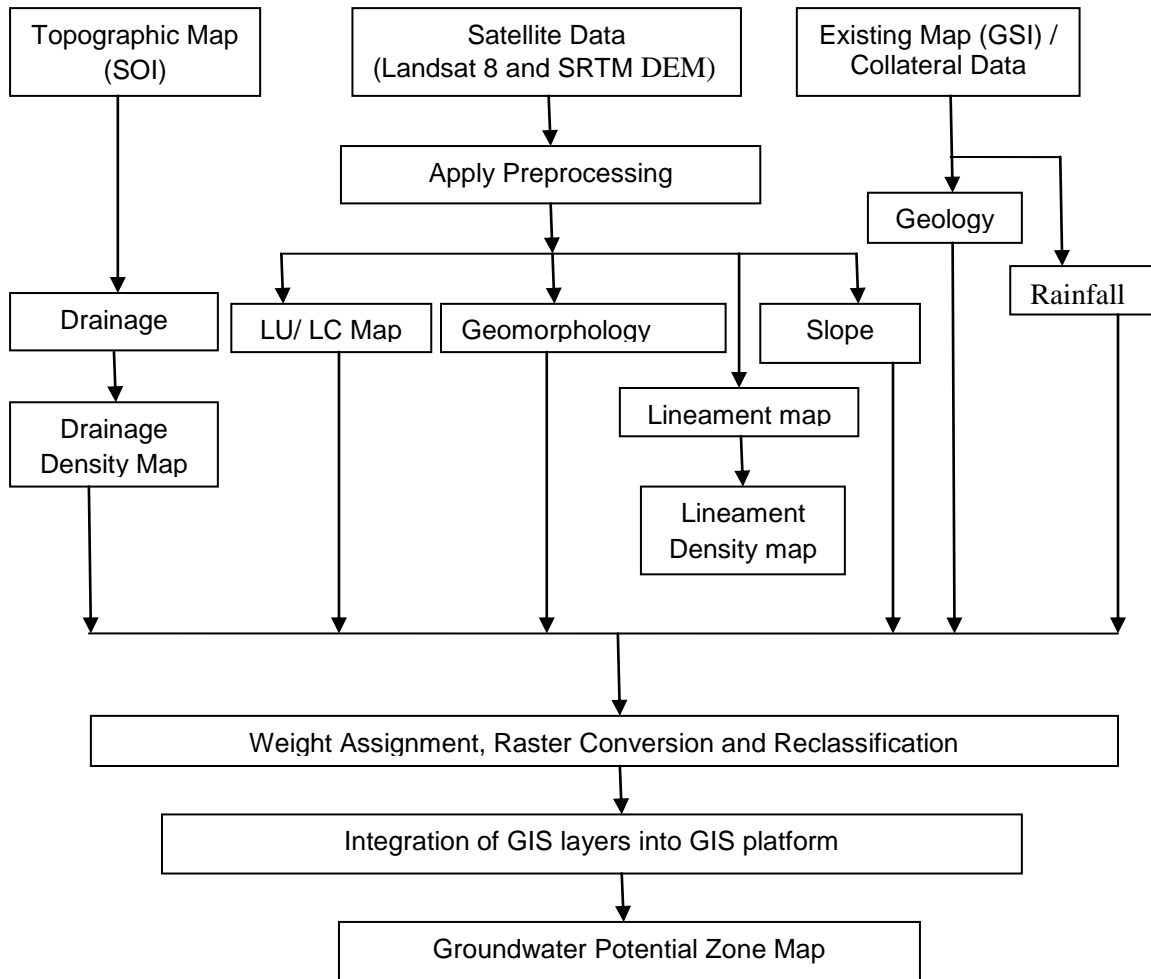


Figure 2: Flow chart assigning the groundwater Potential of the study area

2.2. Delineation of Groundwater Potential Zone

Considering all the themes and features in an integrated layer, the groundwater potential index (GWPI) is calculated as.

$$GWPI = GwGr + LwLr + DwDr + Llwlr + RwRr + SwSr + GMwGMr$$

Where Gw represents weight of geology and Gr represents rank on the theme;

Lw represents weight of LULC and Lr represents rank on the theme;

Dw represents weight of drainage density and Dr represents rank on the theme;

Llw represents weight of lineament density and LlR represents rank on the theme;

Rw represents weight of rainfall and Rr represents rank on the theme;

Sw represents weight of soil and Sr represents rank on the theme;
GMw represents weight of geomorphology and GMr represents rank on the theme.

4. Results and Discussion

The occurrence of groundwater in an area is governed by several factors, such as topography, geology, geomorphology, landuse, soil, rainfall, drainage density, and lineament density for which thematic layers are prepared for their input into a GIS.

4.1. Lithology

Lithology refers to an individual rock type, which is a basic geologic unit. The role of lithology in ground water studies needs no emphasis. In the unconsolidated/semi consolidated sediments and some rocks which have primary porosity and permeability, the lithology exercises major control on the ground water regime. Under favourable morphologic and recharge condition they form very good aquifers. Remote sensing provides the basis for discrimination and differentiation of rock types. Though, direct identification is limited to a few contrasting rock types, many of the rocks can be discriminated based on their spectral and morphological characteristics. Once rock types are identified, their physical continuity of individual rock units could be easily traced and the exact shape, size and geometry can be identified and mapped more accurately by using satellite imagery. By extraction of various classes of lithology, a thematic map for lithology is generated as per Figure 3 below. The ranks were assigned to the individual rock type, according to its respective influence of groundwater occurrence, holding and recharge, as per Table 1 below.

Table 1: Area and Ranking for Lithology

| Sl. No. | Lithology Unit | Ranking (in word) | Ranking (in Number) | Area in Sq.Km |
|---------|--|----------------------|------------------------|---------------|
| 1 | Biotite-Granite gneiss | Poor | 3 | 216.608796 |
| 2 | Charnockite | Poor | 3 | 202.723631 |
| 3 | Granite gneiss/Biotite-granite gneiss | Poor | 3 | 63.631938 |
| 4 | Khondalite | Poor | 3 | 222.543829 |
| 5 | Qurtzite | Poor | 3 | 121.001818 |
| 6 | Sandstone/ conglomerate | Good | 1 | 77.485732 |

4.2. Landuse and Land Cover

The study area consists of different types of forest, agricultural lands, built up land, wasteland and water bodies. From the landuse point of view agricultural lands are good sites for groundwater exploration. The areas occupied by water bodies are coming under good categories and the Reserve Forests are coming under poor categories. Lands which are not used for any purpose are treated or classified as wasteland and hence it is categorized as Poor for groundwater prospects. Lands with scrub are categorized as poor categories groundwater occurrence, holding and recharge, as per Table 2 below. By extraction of various classes of LULC, a thematic map is generated as per Figure 4 below.

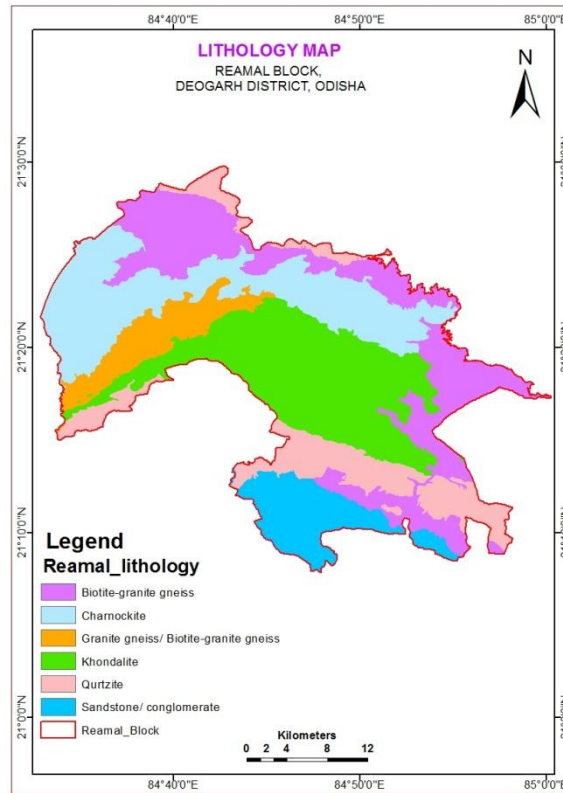


Figure 3: Lithology Map of the Study Area

Table 2: Area and Ranking for Landuse/Landcover

| Sr. No. | Land use land cover | Ranking (in word) | Ranking (in number) | Area in Sq.Km |
|---------|---------------------|-------------------|---------------------|---------------|
| 1 | DENSE FOREST | Poor | 3 | 224.39261 |
| 2 | SCRUB FOREST | Poor | 3 | 20.748576 |
| 3 | OPEN FOREST | Poor | 3 | 82.25220 |
| 4 | SCRUB LAND DENSE | Poor | 3 | 39.82270 |
| 5 | SCRUB LAND OPEN | Poor | 3 | 33.29237 |
| 6 | WASTELAND | Poor | 3 | 21.77518 |
| 7 | AGRICULTURAL LAND | Good | 1 | 458.70161 |
| 8 | BARREN ROKY | Poor | 3 | 2.17570 |
| 9 | BUILT UP | Moderate | 2 | 15.64627 |
| 10 | CANAL/DRAIN | Good | 1 | 0.29099 |
| 11 | RIVER | Good | 1 | 7.85328 |
| 12 | WATERBODIES | Good | 1 | 1.63047 |

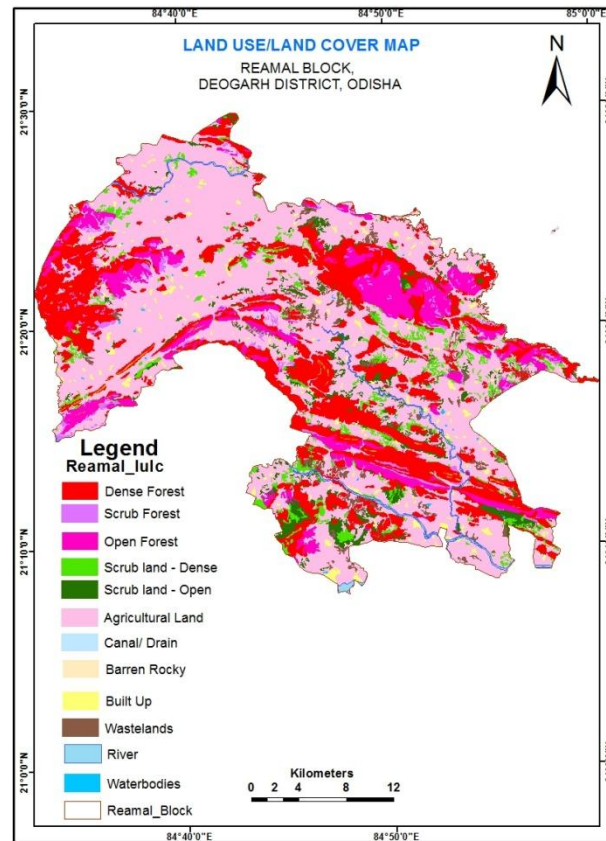


Figure 4: LULC Map of the study area

4.3. Geomorphology

The identification and characterisation of various landforms and structural features in the study area was very important from geomorphological study point of view. Many of these features are favourable for occurrence and recharge of groundwater and are classified in terms of groundwater recharge potentiality. Geomorphologic units are delineated based on the image characteristics such as tone, texture, shape, colour and associations. By overlapping the base map over the geocoded FCC image, the geomorphologic units and landforms, the structural information and structural trend lines are incorporated. Structural hills are observed on South and west part of the study area, which are the linear or acute hills exhibiting definite trend lines and mostly act as runoff zones due to its sloping topography. This shows poor potentiality for groundwater occurrence and recharge. Valleys are low lying depressions formed longitudinally along the streams or amongst the ridge portions, which shows excellent potential for groundwater occurrence and recharge. Weathered Pediplain are broad gently sloping or nearly flat erosion surface or plain of low relief, typically developed by running water; it is considered as moderate for groundwater occurrence and recharge. By extraction of various classes of geomorphology, a thematic map for geomorphology is generated as per Figure 5 below. The ranks were assigned to the individual landform, according to its respective influence of groundwater occurrence, holding and recharge, as per Table 3 below.

Table 3: Area and Ranking of Geomorphological unit

| Sl. No. | Geomorphic Unit | Ranking (In word) | Ranking (In number) | Area in Sq.Km |
|---------|---------------------|-------------------|---------------------|---------------|
| 1 | Vally Fills | Good | 1 | 37.2948 |
| 2 | Intermontane Vally | Good | 1 | 0.73158 |
| 3 | Structural Vally | Good | 1 | 0.81167 |
| 4 | Denudetional Hill | Poor | 3 | 37.11737 |
| 5 | Weathered Pediplain | Moderate | 2 | 215.70298 |
| 6 | Laterstic Uplands | Moderate | 2 | 32.03990 |
| 7 | Pediment | Moderate | 2 | 260.69416 |
| 8 | Hogback | Poor | 3 | 3.07401 |
| 9 | Residual Hill | Poor | 3 | 4.83740 |
| 10 | Structural Hill | Poor | 3 | 283.06020 |
| 11 | Quarry | Moderate | 2 | 9.30802 |
| 12 | Sand Bar | Good | 1 | 1.02726 |
| 13 | Waterbodies | Good | 1 | 4.33787 |
| 14 | Reservoir | Good | 1 | 0.63474 |
| 15 | River | Good | 1 | 5.35730 |

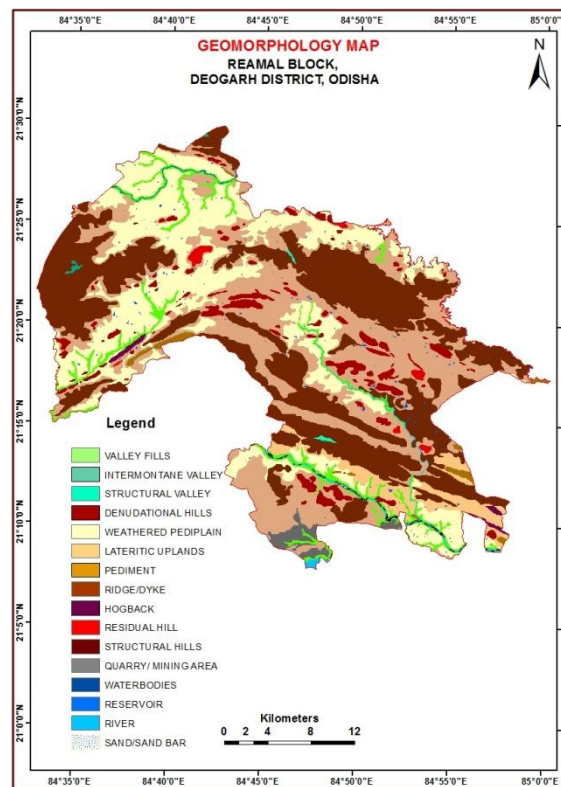


Figure 5: Geomorphology Map of the study area

4.4. Drainage Density

The drainage of the study area is hilly with steep slope on NW - SE part. A drainage basin is a natural unit draining runoff water to a common point. This map consists of water bodies, rivers, tributaries, perennial & ephemeral streams, ponds. High drainage density values are favorable for runoff low groundwater Potential zone. High ranks are assigned to low drainage density area and vice versa. The coarse drainage texture indicates highly porous and permeable rock formations; whereas fine drainage texture is more common in less pervious formations. Drainage density (in terms of Km/Km²) indicates

closeness of spacing of channel as well as the nature of surface material, thus providing a quantitative measure of average length of stream channel for whole basin. It has been observed from drainage density measurement made over a wide range of geologic and climatic type that a low drainage density is more likely to occur in region and highly resistant of highly permeable subsoil material under dense vegetative cover and where relief is low. High drainage density is the resultant of weak or impermeable subsurface material, sparse vegetation and mountainous relief. By extraction of drainage features, a thematic map generated drainage and drainage density, which is as per Figure 6 below.

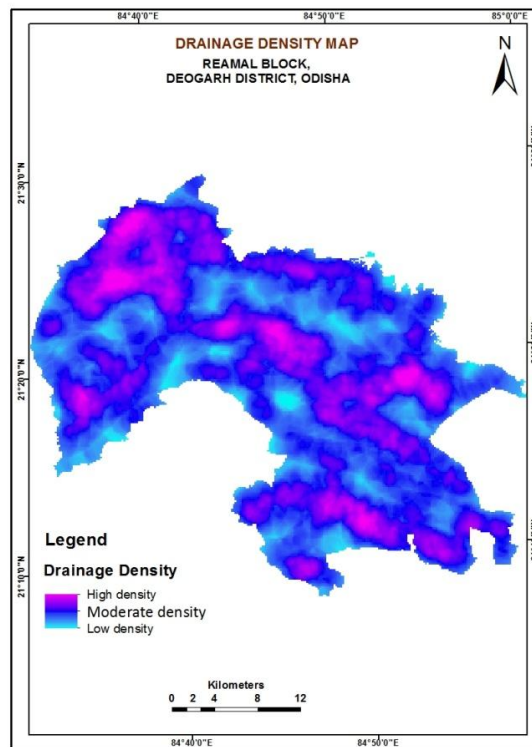


Figure 6: Drainage density Map of the study area

4.5. Lineament Density

In the hard rock areas the movement and occurrence of groundwater depends mainly on the secondary porosity and permeability resulting from structural discontinuities like lithologic contacts, bedding and cleavage planes, unconformities, folds, faults, fractures, joints etc. These structurally weak planes act as conduits for ground water movement and introduce an element of directional variation in hydraulic conductance. Using satellite data, different structural features can be studied on a scale commensurate with their size. It has the unique capability of providing direct evidence for regional level structures like major folds, faults and lineaments, which cannot be directly observable on the ground because of the limited field of view. The most structural features that are important from the point of groundwater are lineaments. They are seen on the satellite imagery as linear alignments of structural, lithologic, topographic, vegetation or drainage anomalies, either as straight lines or curvilinear features. They can be further classified into faults, fractures, joints, bedding traces, lithologic contacts, shear-zones, etc. In hard rock areas, faults and fractures mainly act as interconnecting channel ways for groundwater movement and form prospective ground water zones. All these linear features are interpreted from the satellite data and the lineament map is prepared for the study area. Lineaments are any linear features that can be picked out as lines in aerial or satellite imagery. From satellite imagery, lineament data is extracted and then lineament map is generated, which is as per Figure 8 below. Some lineaments are associated with geomorphic lineament i.e.

drainage parallel. The study area is covered by major and minor lineament. The lineament map is then converted into zones of different lineament density. Lineament density map is a measure of quantitative length of linear feature expressed in (Km/Km²). Lineament density of an area has direct influence on groundwater prospectiveness of that area. In the present study area, with very high lineament density having good groundwater potential whereas area with very low lineament density having poor groundwater potential. The entire map classified in to high to low lineament density.

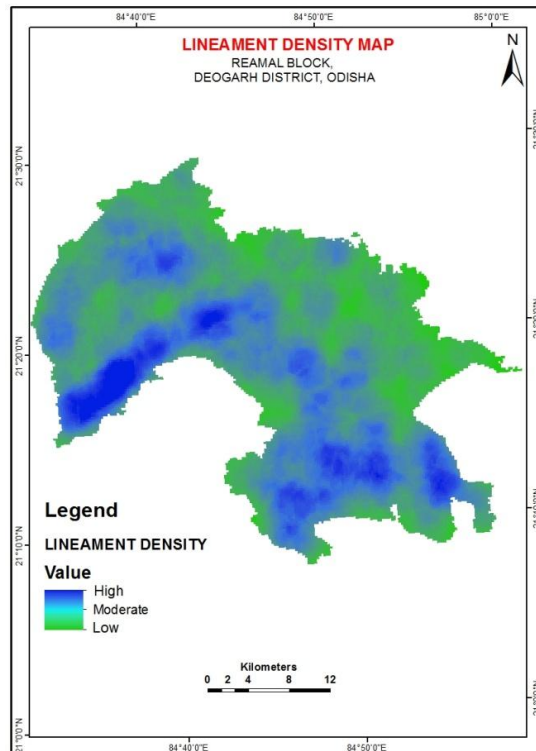


Figure 7: Lineament density Map of the study area

4.6. Slope

The precipitous terrain causes rapid runoff and does not store water easily. Slope of any terrain is one of the factors allowing the infiltration of groundwater into subsurface or in other words groundwater recharge. In the gentle slope area, the surface runoff is slow allowing more time for rainwater to percolate, whereas, steep slope area facilitates high runoff allowing less residence time for rainwater to percolate and hence comparatively less infiltration. The slope map of the study area is derived from SRTM DEM 30 m and slope of the study area is classified into six classes, which is as per Figure 8 below. The ranks are assigned to the individual slope class, according to its respective influence of groundwater occurrence, holding and recharge, as per Table 4 below

Table 4: Ranking for % Slope

| Sr. No. | Slope (%) | Description | Ranking (In word) | Ranking (In number) |
|---------|------------|-----------------------|-------------------|---------------------|
| 1 | < 1 | Nearly levelled | Good | 1 |
| 2 | 1% to 3% | Nearly Gently sloping | Good | 1 |
| 3 | 3% to 5% | Gently sloping | Good | 1 |
| 4 | 5% to 10% | Moderately sloping | Moderate | 2 |
| 5 | 10% to 30% | Strongly sloping | Poor | 3 |
| 6 | 30% to 90% | Steep sloping | Poor | 3 |

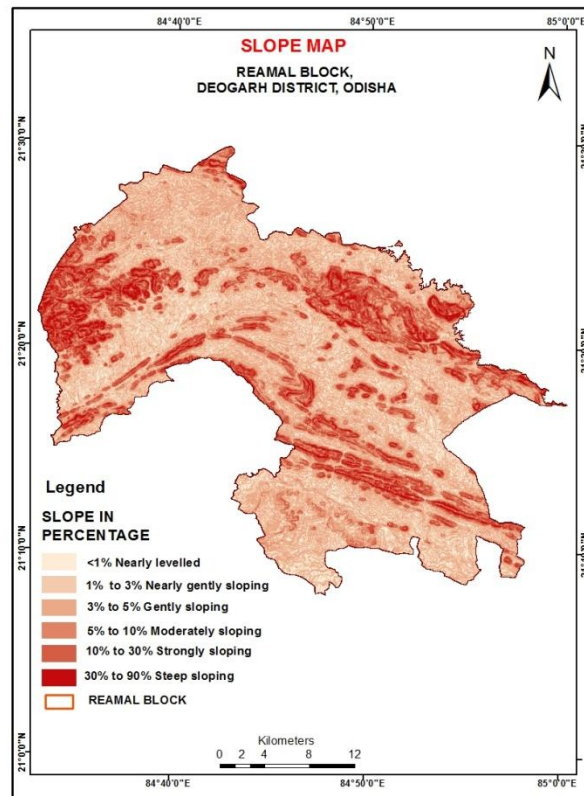


Figure 8: Slope Map of the study area

4.7. Groundwater Prospects Mapping

Being a hidden resource, ground water is not directly amenable to remote sensing. However, remote sensing data provide integrated information on several factors which directly or indirectly control the movement and occurrence of water below the ground. The synopticity of the satellite data helps in mapping different lithologic, structural and morphological units in their correct spatial relationship, and multispectral data provides certain additional information which is not otherwise easily observable on the ground. The satellite data provide information on different factors that control the groundwater regime and offers a common database for integrated study of all the factors to evaluate the groundwater potential and prospects besides understanding the relative significance of each factor. By integrating the information on the above factors i.e. lithology, geological structural and recharge conditions, ultimately the ground water prospects map has to be prepared.

Table 5: Statistic of Groundwater potential zones of study area

| Sl. No. | Potential Zone | Area {Km ² } | Area (%) |
|---------|----------------|-------------------------|----------|
| 1 | Very Good | 4.407 | 0.485 |
| 2 | Good | 42.558 | 4.687 |
| 3 | Moderate | 248.178 | 27.332 |
| 4 | Poor | 252.598 | 27.819 |
| 5 | Poor to Nil | 6.254 | 0.688 |
| 6 | Nil | 328.622 | 36.195 |
| 7 | Quarry | 10.302 | 1.134 |
| 8 | Reservoir | 1.634 | 0.179 |
| 9 | River | 8.244 | 0.907 |
| 10 | Water bodies | 5.212 | 0.574 |

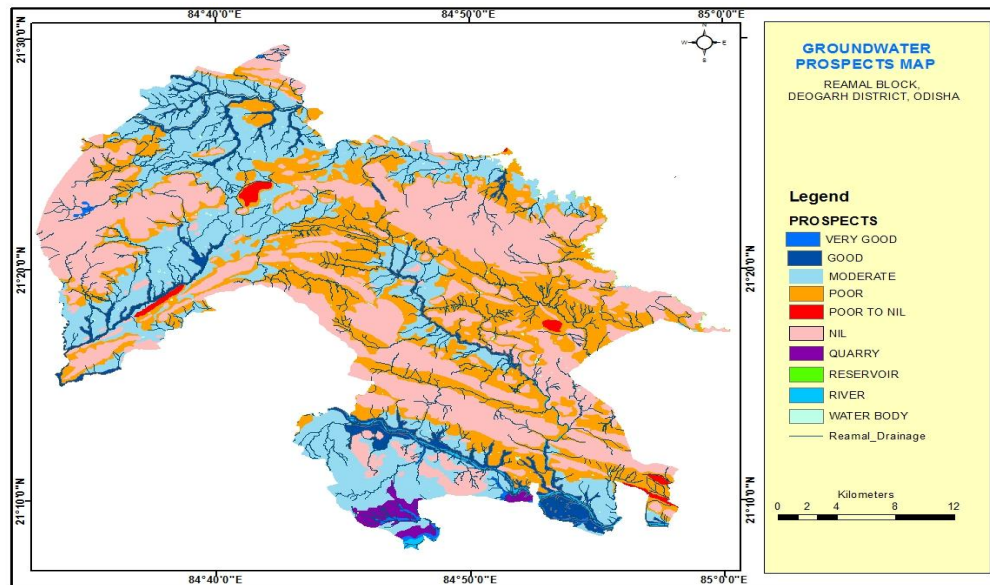


Figure 9: Groundwater Prospect Map of the study area

4.8. Overlay Analysis for Recharge Zone

Recharge is the most important factor in evaluating the groundwater prospects. Recharge to groundwater depends on precipitation, surface water bodies like reservoir, lakes, tanks, streams, canals, favourable lithologic, landforms and structural set up, etc. By providing integrated lithologic, structural, geomorphic and hydrologic data, satellite imagery facilitates better appreciation of recharge conditions. Satellite imagery provides information on surface water bodies, canals and irrigated fields which directly contribute groundwater recharge. Based on geomorphic and hydrologic analysis the area can be classified into runoff, recharge, storage and discharge zones, and the amount of recharge to groundwater from different sources can be estimated. Overlay analysis is a multi-criteria analysis wherein analysis can be carried out with complex things for finding out certain theme with the help of assignment of rank to the individual class of feature and then assigning weightage to the individual feature considering its influence over theme. All the thematic maps were converted into raster format and superimposed by weighted overlay method, which consists of rank and weightage wise thematic maps and integration of them through GIS. Integration of thematic maps for carrying out overlay analysis in GIS environment was done using ArcGIS software.

This study analyzed the hydro geologic and geographic attributes of the study area and identified five major factors influencing groundwater recharge potential, viz. slope (%), geomorphology, land use land cover, drainage density and lineament density. Each factor was examined was assigned an appropriate weight. Each recharge potential factor may influence the groundwater recharge process to a different degree. Overlay analysis is carried out, using weighted overlay analysis tool provided in the ArcGIS software, to integrate various thematic maps viz. geomorphology map, slope (%) map, landuse/landcover map, drainage density map and lineament density map, which are being very informative and plays important role in the study for groundwater recharge potential zones of study area. The various thematic maps were assigned with different weightage of numerical value to derive groundwater recharge potential zones. On the basis of weightage assigned to these maps and bringing them into the function of spatial analyst for integration of these thematic maps, a map indicating groundwater recharge potential zones is obtained, which is as per Figure 11 below. This map has been categorized into three zones viz. poorly suitable, moderately suitable and most suitable from groundwater recharge potential point of view.

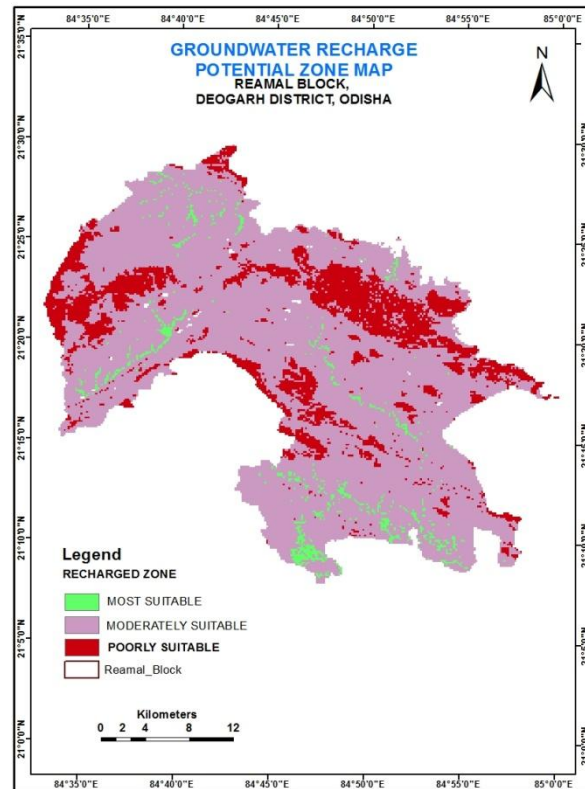


Figure 10: Groundwater Recharge Potential Map of the study area

5. Conclusions

This study produced a groundwater recharge potential map for study area. The results indicate that the most effective groundwater recharge potential zone is located on the map of the study area. In most suitable region, weathered pediplain and agricultural land have high infiltration ability. Also the concentration of drainage also indicates the ability of stream flow to recharge the groundwater system. The poorly suitable of study area is least effective for groundwater recharge, mainly due to its steep sloping topography. The occurrence and recharge of groundwater in the study area is prominently controlled by the geomorphology, LULC and slope (%) as revealed from GIS analysis. remote sensing and GIS technique used to integrate various thematic maps proves to be very important to map the groundwater occurrence and movement for recharge potential mapping and management plan on a scientific basis. Overall result demonstrate that the use of remote sensing and GIS technique provides powerful tool to study groundwater resources and design suitable exploration plan for recharge of groundwater in study area. The integrated groundwater recharge potential zones map for the study area has been categorized into 'poorly suitable', to 'most suitable', on the basis of the ranks and weightage assigned to different features of the thematic maps. From this study it is observed that remote sensing and GIS technique can be used effectively to delineate groundwater recharge potential zones map, which can be used for improvement in the groundwater recharge and holding for the study area and later on may be for various purposes like identification of location of structures for artificial recharge, locations of new tube wells and efficient groundwater management for betterment of the society.

References

- Al Asam, M.S., 1996: *UAE Water Resources Use in Agriculture and Conservation*. In: International Desalination Association (IDA) Conference of Desalination. 625-637.
- Alsharhan, A.S, Rizk, Z.S., Nairn, A.E., Bakhit, D.W., and Alhajari, S.A., 2001: *Hydrogeology of an Arid Region: The Arabian Gulf and Adjoining Areas*. Amsterdam: Elsevier. 331.
- Boughriba, M., Barkaoui, A., Zarhloule, Y., Lahmer, Z., and Verdoya, M. *Groundwater Vulnerability and Risk Mapping of the Angad Transboundary Aquifer using DRASTIC Index Method in GIS Environment*. Arabian Journal of Geosciences. 2010. 3 (2) 207-220.
- Boutt, D.F., David, W.H., Bryan, C.P., and David, T.L. *Identifying Potential Land Use-Derived Solute Sources to Stream Base Flow using Ground Water Models and GIS*. Ground Water. 2001. 39 (1) 24-34.
- Elmahdy, S.I. and Mohamed, M.M. *Geological Lineament Detection, Characterization and Association with Groundwater Contamination in Carbonate Rocks of Musandam Peninsular using Digital Elevation Model (DEM)*. Open Hydrol J. 2012b. 6; 45-51.
- Elmahdy, S.I. and Mohamed, M.M. *Influence of Geological Structures on Groundwater Accumulation and Groundwater Salinity in Musandam Peninsula, UAE and Oman*. Geocarto Int. 2013c. 28; 453-472.
- Elmahdy, S.I, and Mohamed, M. *Relationship between Geological Structures and Groundwater Flow and Groundwater Salinity in Al Jaaw Plain, United Arab Emirates; Mapping and Analysis by Means of Remote Sensing and GIS*. Arab J Geo. 2014b. 7; 1249-1259.
- Elmahdy, S.I and Mohamed, M. *Groundwater Potential Modelling using Remote Sensing and GIS: A Case Study of the Al Dhaid Area, United Arab Emirates*. Geocarto Int. 2014c. 29; 433-450.
- Jaiswal, R.K., Mukherjee, S., Krishnamurthy, J., and Saxena, R. *Role of Remote Sensing and GIS Techniques for Generation of Groundwater Prospect Zones towards Rural Development-An Approach*. Int J Remote Sens. 2003. 24; 993-1008.
- Liggett, J.E. and Talwar, S. *Groundwater Vulnerability Assessments and Integrated Water Resource Management*. Streamline Watershed Management Bulletin. 2009. 13 (1) 18-29.
- Mohamed, M., Hatfield, K., and Perminova, I.V. *Evaluation of the Biological Parameters in the Subsurface Using Moment Analysis: Theory and Numerical Testing*. Advances in Water Resources. 2007. 30 (9).
- Mohamed, M., Saleh, N., and Sherif, M. *Sensitivity of Natural Attenuation to Variations in Kinetic and Transport Parameters*. Bulletin of Environmental Contamination and Toxicology. 2010b. 84 (4) 443-449.
- Prasad, R.K., Mondal, N.C., Pallavi, Banerjee, M.V., and Nandakumar, V.S. *Deciphering Potential Groundwater Zone in Hard Rock through the Application of GIS*. Environmental Geology. 2008. 55 (3) 467-475.
- Rao, N.S., 2006: *Groundwater Potential Index in a Crystalline Terrain using Remote Sensing Data*. Environmental Geology. 50 (7) 1067-1076.

Sahoo, P.K., Kumar, S., and Singh, R.P. *Estimation of Stress using IRS - 1B Data of NW Himalaya*. Current Science. 1998. 74 (9) 781-786.

Saraf, A.K., Choudhury, P.R., Roy, B., Sarma, B., Vijay, S., and Choudhury, S. *GIS based Surface Hydrological Modelling in Identification of Groundwater Recharge Zones*. Int J Remote Sens. 2004. 25 (24) 5759–5770.

Sherif, M., Mohamed, M., Kacimov, A., and Shetty, A. *Assessment of Groundwater Quality in the Northeastern Coastal Area of UAE as Precursor for Desalination*. Desalination. 2011. 273 (2) 436-446.

Van De Griend, A.A. and Owe, M. *On the Relationship between Thermal Emissivity and the Normalized Difference Vegetation Index for Natural Surfaces*. Int. J. Rem. Sens. 1993. 14; 1119-1137.

Mapping Changes in Desert Pavement Surfaces of the Lower Colorado Desert of Southern California using Landsat Time Series Analysis

Christopher Potter

NASA Ames Research Center, United States

Publication Date: 9 June 2016

DOI: <https://doi.org/10.23953/cloud.ijarsg.57>



Copyright © 2016 Christopher Potter. This is an open access article distributed under the **Creative Commons Attribution License**, which permits unrestricted use, distribution, and reproduction in any medium, provided the original work is properly cited.

Abstract Potential disturbance of desert soils from renewable energy development in southern California is receiving increasing attention due to potential impacts on air quality and greenhouse gas emissions. This study was designed to quantify and map, for the first time, changes in desert pavement surface area using 20 years of Landsat satellite image data across the Lower Colorado Desert. Landsat-derived maps of geomorphic surface classes from 1990 to 2014 for the Lower Colorado Desert area showed that a relatively stable area of around 1920 km² was covered by well-developed desert pavements prior to 2014. Based on 2014 Landsat imagery, coverage of well-developed pavements within solar energy development boundaries of the Lower Colorado Desert area totaled to 421 km², the majority of which (>82%) were located in eastern Riverside County. If disturbed as a result of construction activities, these desert pavements could become a source of dust from exposure of the underlying fine particle layer.

Keywords *Landsat; Desert Pavements; Solar Energy Development; Lower Colorado Desert; DRECP*

1. Introduction

A desert pavement is an arid land surface that is covered with closely packed, interlocking angular or rounded rock fragments of pebble and cobble size (Cooke and Warren, 1973). A notable feature of desert pavements is the development of the so-called “vesicular A” (or Av) soil horizon just below the surface of pebbles, gravels, and small stones that form the ground surface of desert pavement. The Av layer consists of dust-sized wind-deposited particles underneath the pavement. Most of the particulate matter consists of very fine silt and fine sand. The fine-textured layer of particulates at the top of the soil profile contrasts notably with the underlying soil layer.

One theory for the formation of desert pavements is based on the shrink/swell properties of the clay underneath the surface stones and gravel. Trapped by slowing wind speed due to surface roughness, dust particles land on the surface and subsequently work their way down between surface gravels. The physical shrinking and swelling processes of clay stemming from drying and wetting result in lifting a gravel layer to the surface and form a desert pavement. Shrinking and swelling are also most likely

the cause of air trapped in the clay-rich layer creating disconnected air “vesicles” or air pockets in the Av layer (Yonovitz and Drohan, 2009).

Av horizons are characterized by an abundance of vesicular pores. Vesicular horizons are of interest to ecologists and hydrologists because they regulate the distribution of water by reducing infiltration rates and increasing water retention near the soil surface (Young et al., 2004). Fine clay particulates once weakly cemented to each other in the Av horizon contribute to stabilizing arid land surfaces (McFadden et al., 1998). At the same time, the gravel fragments above interlock and secure the underlying dust that may have been accumulating for millennia (Sweeney and Mason, 2013).

In a study of dust emissions from different Mojave Desert soil surfaces (including dry washes, dunes, playa margins, distal alluvial fans, and pavements), Sweeney et al. (2011) found that undisturbed desert pavements were the lowest emitters of dust, due to tightly-packed gravel that armors the surface and prohibits fine soil particles from being entrained by wind. However, if the Av horizon protected by pavements is partially exposed due to major mechanical disturbance, then these fine soils can become among the highest emitters of dust in desert landscapes (Bacon et al., 2011).

Renewable energy in newly proposed Development Focus Areas (DFAs) of southern California is receiving increasing attention due to potential impacts on air quality and greenhouse gas emissions. To mitigate and monitor the impacts of solar facility construction projects, the Desert Renewable Energy Conservation Plan (DRECP, 2010) has become a major component of the State of California Renewables Portfolio Standard. The DRECP is intended to provide effective environmental protections and natural resource conservation of desert ecosystems as appropriate development of renewable energy projects advances in southern California. The DRECP covers parts of seven California counties: Imperial, Inyo, Kern, Los Angeles, Riverside, San Bernardino, and San Diego. Approximately 91,000 km² of federal and non-federal California desert land are part of the DRECP Area. By the end of 2016, the Final DRECP Environment Impact Statement (EIS) will be completed for public lands under agency jurisdictions within the DRECP area. The objective of this remote sensing data analysis for southern California deserts was to quantify and characterize, for the first time, changes desert pavement surface area using 20 years of Landsat satellite image data across the Lower Colorado Desert region (Figure 1).

2. Study Area

The area of interest for this Landsat data study of desert pavements within the southern DRECP region was the Lower Colorado Desert of California (Figure 1). This area is bounded on the west by the Laguna, Santa Rosa, and San Jacinto mountain ranges, on the east by the California-Arizona state line, on the north by the gradual transition to the Mojave Desert, and on the south by the California-Mexico border (Marks, 1950). Low annual rainfall (50 – 300 mm) and high temperatures (reaching 45°C in the summer) make this area one of the most arid in North America. Vegetation communities in the Colorado Desert have been classified into seven basic types: creosote bush scrub, cactus scrub, saltbush scrub, alkali sink, microphyll woodland, psammaophytic scrub, and palm oasis (Schoenherr and Burk, 2007).

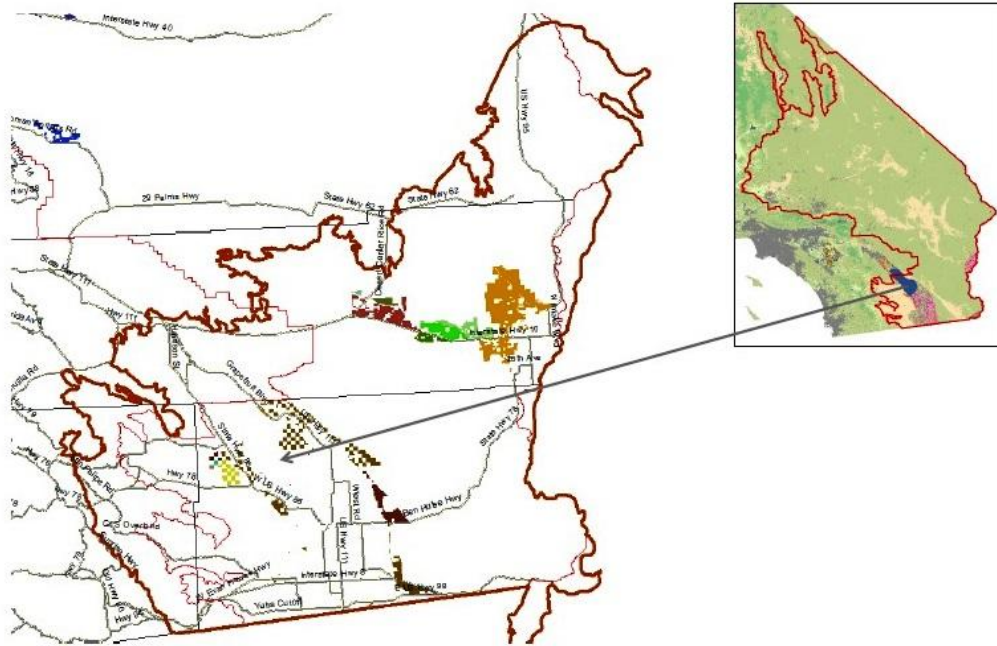


Figure 1: Map of the Lower Colorado Desert (brown line) and DRECP (red line) study area, with Development Focus Areas (DFAs) in other shaded polygon outlines. Smaller map in the right panel shows vegetation cover types for the entire DRECP area from the USDA CropScape map of 2014 (available online at nassgeodata.gmu.edu/CropScape/), with shrublands in light green, barren sand dunes in tan, developed urban areas in grey, croplands in magenta, and open water in blue

3. Methods

3.1. Satellite Imagery

For this study, near cloud-free imagery from the Landsat sensor was selected from the United States Geological Survey (USGS) Earth Explorer data portal (available online at earthexplorer.usgs.gov). Landsat scenes from path/row 39/37 were acquired between July and September of each year, well after the peak flowering period in the Lower Colorado Desert growing season (Schoenherr and Burk, 2007). All images used in this study were geometrically registered (UTM Zone 10) using terrain correction algorithms (Level 1T) applied by the USGS EROS Data Center.

For the Landsat 4-5 Thematic Mapper (TM) images acquired between 1985 and 2011, 30-m resolution surface reflectance data were generated from the Landsat Ecosystem Disturbance Adaptive Processing System (Masek et al., 2006). Moderate Resolution Imaging Spectroradiometer (MODIS) atmospheric correction routines were applied to Level-1 TM data products. Water vapor, ozone, geopotential height, aerosol optical thickness, and digital elevation are input with Landsat data to the Second Simulation of a Satellite Signal in the Solar Spectrum (6S) radiative transfer models to generate top of atmosphere (TOA) reflectance, surface reflectance, brightness temperature, and masks for clouds, cloud shadows, adjacent clouds, land, snow, ice, and water. Landsat 8 (after 2012) surface reflectance products were generated from the L8SR algorithm, a method that uses the scene center for the sun angle calculation and then hard-codes the view zenith angle to 0. The solar zenith and view zenith angles are used for calculations as part of the atmospheric correction.

3.2. Desert Pavement Detection

Beratan and Anderson (1998) developed an approach to map alluvial geomorphic surfaces in California. Visible bands and the near infrared (NIR) band of Landsat TM images were used to compose a new spectral space, which provided information about the composition and topography of desert surfaces. This spectral space can be classified as young, intermediate, or old in terms of stages of development. This methodology was successfully applied to mapping in the southern Whipple Mountains portion of the Mojave Desert in California.

Landsat image processing was carried out using the Environment for Visualizing Images software package (ENVI version 5.1, Research Systems, Inc.). A combination of processing techniques was required to delineate compositional differences between the three major geomorphic surfaces. Of primary interest in this study were surfaces covered by well-developed desert pavements and rock varnishes (Stage 2 surfaces). According to Beratan and Anderson (1998), Stage 2 surfaces display spectra that are strongly modified by the reflection spectrum of rock varnish. Such varnishes decrease surface reflectance and albedo, and result in a steep positive slope in between Landsat bands 1 and 5 due to a strong suppression of short wavelength radiance by the presence of oxidized transition metals (mainly Fe and Mg). In contrast, Stage 1 active washes are more commonly dominated by sand (quartz and feldspar crystals), which results in an increased reflectance (higher albedo) in all Landsat bands (Beratan and Anderson, 1998).

Figure 2 shows the image processing flowchart and definitions of surface classifications from Beratan and Anderson (1998) applied for the present study. Before applying these image analysis steps, pixels with non-pavement land cover features were masked out (e.g., vegetation, roads, and river channels, based on the United States Department of Agriculture (USDA) national land cover map of 2014; Figure 1).

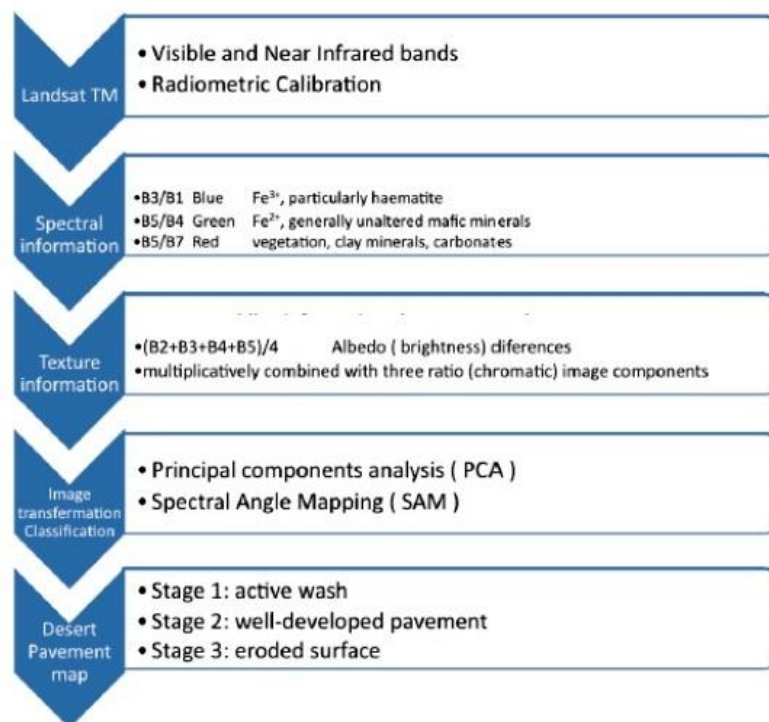


Figure 2: Image processing flowchart of desert pavements based on the four-component methodology from Beratan and Anderson (1998)

Spectral Angle Mapper (SAM) is a spectral classification in the ENVI software application that uses an n-D angle to match pixels to reference spectra (Kruse et al., 1993). The algorithm determines the spectral similarity between two spectra by calculating the angle between the spectra and treating them as vectors in a space with dimensionality equal to the number of bands. Endmember spectra used by the SAM were specified by Beratan and Anderson (1998) in their Figure 5. SAM compares the angle between the endmember spectrum vector and each pixel vector in n-D space. Smaller angles represent closer matches to the reference spectrum. Pixels further away than the specified maximum angle threshold in radians are not classified.

A clustering approach was used to further divide the areas as Stages 1 and 3 of desert pavement development. Stage 1 included young alluvial fan deposits with active channels and depositional fan surfaces. This stage of development is identified by the presence of distinct bar and swale topography. Stage 3 included old alluvial fan deposits that have been highly dissected, leaving virtually no trace of the original fan surface.

4. Results and Discussion

Landsat-derived maps of geomorphic surface classes from 1990 to 2014 for the southern DRCEP Colorado Desert area (Figure 3) showed that a relatively stable area of around 1920 km² was covered by Stage 2 well-developed pavements prior to 2014. Between 2010 and 2014 image dates, the Stage 2 well-developed pavements fraction evidently increased in area by 10% (to 2145 km²), whereas the Stage 3 fraction decreased in area by 10% (Figure 4). The majority of this recent area change between Stage 3 and Stage 2 surface classes was detected in the Granite Mountain and Palen Valley washes of eastern Riverside County (Figure 5).

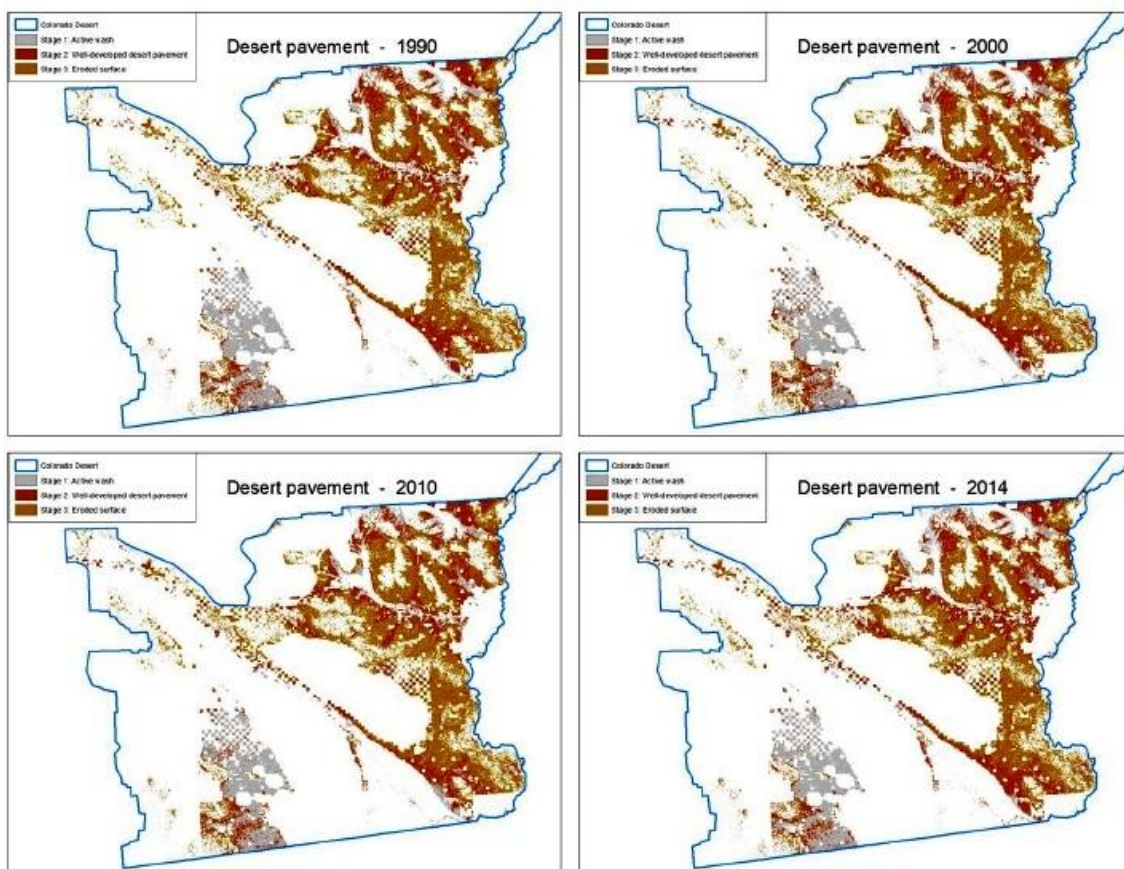


Figure 3: Landsat-derived maps of geomorphic surface classes in southern DRCEP Lower Colorado Desert area

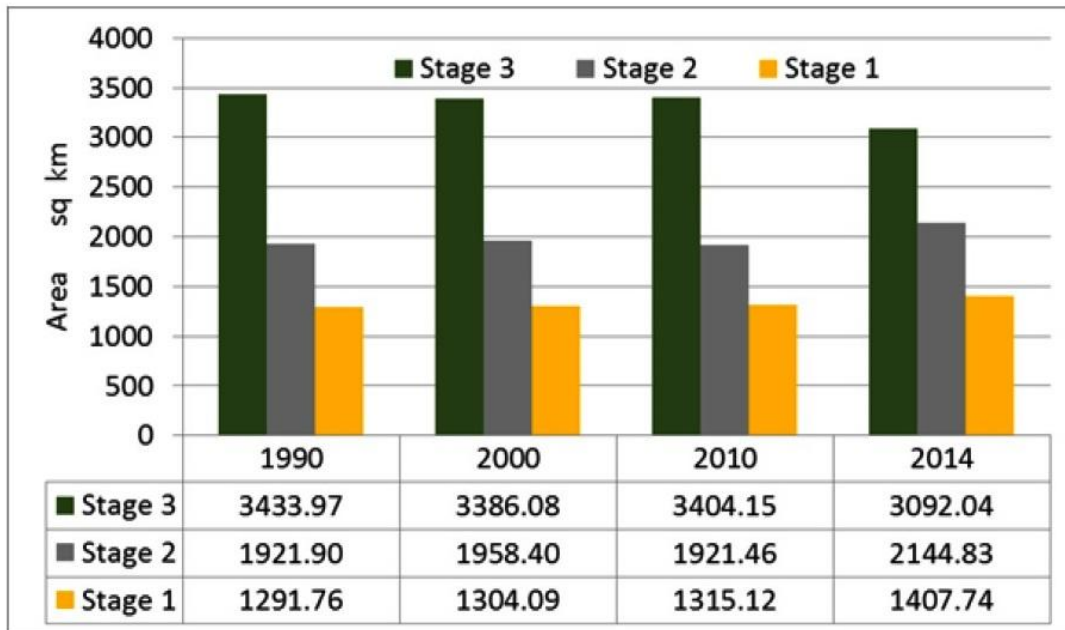


Figure 4: Changes in Landsat-derived geomorphic surface classes in the southern DRCEP Lower Colorado Desert area

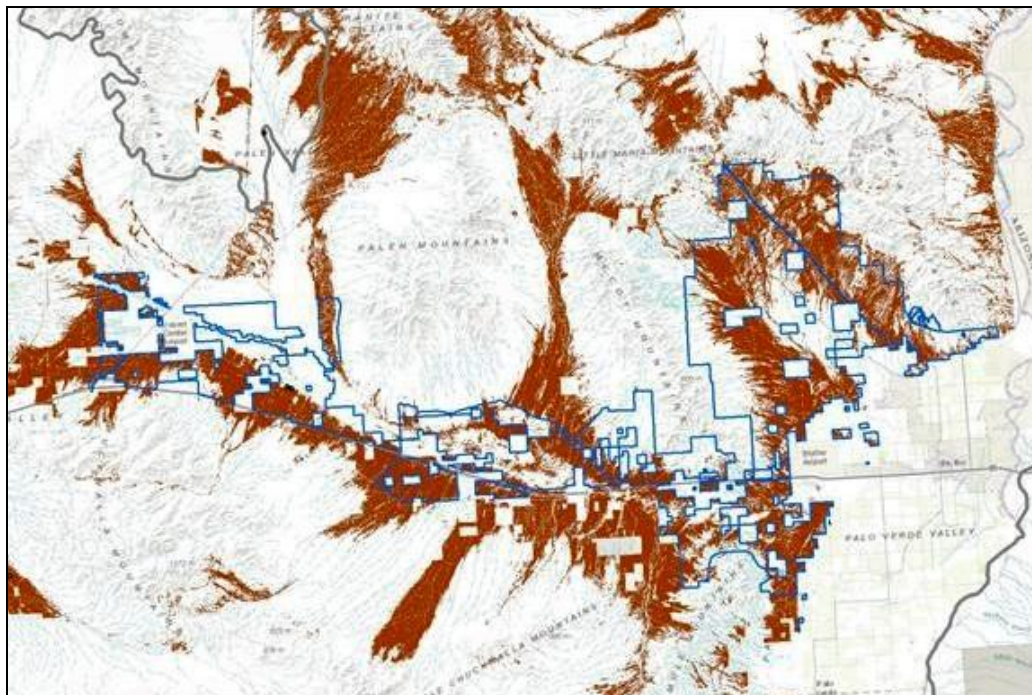


Figure 5: Landsat-derived coverage of Stage 2 well-developed pavements in 2014 for Riverside County areas of the Lower Colorado Desert (outlined in gray), with DFA boundaries outlined in blue

Generally speaking, increases detected in Stage 2 well-developed pavements may conceivably result from prior confusion in the satellite image classification process with Stage 3 eroded surfaces. According to Beratan and Anderson (1998), Stage 3 surfaces display the greatest relief, the presence of gullies and shadows, and strong linear features among pixels. These properties of Stage 3 eroded surfaces could contribute to misclassification errors into the other two geomorphic classes.

With reference to other transition types, it is conceivable that Stage 2 well-developed pavements could transition into Stage 1 active washes or into Stage 3 eroded surfaces, and that Stage 3 eroded surfaces could transition into Stage 1 active washes, or vice-versa. It is not easily conceivable, however, that Stage 1 active washes could transition into Stage 2 well-developed pavements in less than 25 years.

Based on 2014 Landsat imagery, coverage of Stage 2 well-developed pavements within DFA boundaries of the DRCEP Colorado Desert area totaled to 421 km², the majority of which (> 82% or 347 km²) were located in eastern Riverside County (Figure 5). About 217 km² of Stage 2 well-developed pavements were located in the DFA zones in washes of the eastern McCoy Mountains alone (as listed in Table 1). Within DFAs of Imperial County east of the Salton Sea, namely those in the Pope, Alamo River, and German Diggins Wash drainages, 51 km² were covered by Stage 2 well-developed pavements, based on 2014 Landsat imagery. If disturbed as a result of construction activities within these DFAs, these desert pavements could become a source of dust and surface erosion from exposure of the underlying fine particle layer.

Table 1: Coverage areas greater than 1 km² of Stage 2 well-developed pavements in 2014 within individual drainage basins (delineated by Seaber et al., 1987) of DFAs of eastern Riverside County

| Predominant Drainage | km ² |
|----------------------|-----------------|
| Aztec Mines | 20.5 |
| Ford Well | 17.6 |
| Lower Big Wash | 58.8 |
| Eagle Creek | 3.6 |
| McCoy Wash | 217.2 |
| Hopkins Well | 28.1 |

5. Conclusions

Disturbance to the desert pavement surfaces could “unlock” the stabilizing surface and readily generate fugitive dust and surface erosion from a dry, exposed Av layer. Ecological destabilization and human health problems with the increase in airborne particulate matter are adverse impacts that the DRECP seeks to avoid. Site hydrology may also change as soils may become more permeable for water, at least initially after disturbance. The multiple connections of dust in the environment to performance of solar facilities make management of disturbances to desert pavements critical to sustaining original energy production goals. Solar energy project developers can benefit from the satellite image mapping of locations of desert pavements in advance, so that the design of project footprints excludes desert pavements at the start.

Acknowledgements

The author is grateful to James Weigand (BLM, Sacramento, CA) for continual guidance in all aspects of this work. Satellite image processing and application of mathematical algorithms for soil map product figures and plots in this report was carried out primarily by Shuang Li of California State University Monterey Bay.

References

Bacon, S.N., McDonald, E.V., Amit, R., Enzel, Y. and Crouvi, O. *Total Suspended Particulate Matter Emissions at High Friction Velocities from Desert Landforms*. Journal of Geophysical Research. 2011. 116; F03019.

Beratan, K.K. and Anderson, R. *The Use of Landsat Thematic Mapper Data for Mapping and Correlation of Quaternary Geomorphic Surfaces in the Southern Whipple Mountains, California*, International Journal of Remote Sensing. 1998. 19 (12) 2345-2359.s.

Cooke, R.U. and Warren, A., 1973: *Geomorphology in Deserts*. London: B.T. Batsford Ltd. 120.

DRECP, 2010: Recommendations of Independent Science Advisors for The California Desert Renewable Energy Conservation Plan (DRECP) prepared for Renewable Energy Action Team.

Lentile, L., Holden, A., Smith, A., Falkowski, M., Hudak, A., Morgan, P., et al. *Remote Sensing Techniques to Assess Active Fire Characteristics and Post-Fire Effects*. International Journal of Wildland Fire. 2006. 15; 319-345.

Kruse, F.A., Lefkoff, A.B., Boardman, J.B., Heidebrecht, K.B., Shapiro, A.T., Barloon, P.J. and Goetz, A.F.H. *The Spectral Image Processing System (SIPS) - Interactive Visualization and Analysis of Imaging Spectrometer Data*. Remote Sensing of Environment. 1993. 44; 145-163.

Marks, J.B. *Vegetation and Soil Relations in the Lower Colorado Desert*. Ecology. 1950. 31; 176-193.

Masek, J.G., Vermote, E.F., Saleous, N., Wolfe, R., Hall, F.G., Huemmrich, F., Gao, F., Kutler, J. and Lim, T.K. *A Landsat Surface Reflectance Data Set for North America, 1990-2000*. Geoscience and Remote Sensing Letters. 2006. 3, 68-72.

McFadden, L.D., McDonald, E.V., Wells, S.G., Anderson, K., Quade, J. and Forman, S.L. *The Vesicular Layer and Carbonate Collars of Desert Soils and Pavements: Formation, Age and Relation to Climate Change*. Geomorphology. 1998. 24; 101-145.

Schoenherr, A.A. and Burk, J.H., 2007: *Colorado Desert Vegetation*. In: Barbour, M.G., Keeler-Wolf, T. and Schoenherr, A.A. (Eds.), *Terrestrial Vegetation of California*, 3rd ed. Berkeley, California: University of California Press. 657-682, 712.

Seaber, P.R., Kapinos, F.P. and Knapp, G.L., 1987: *Hydrologic Unit Maps: U.S. Geological Survey Water-Supply Paper 2294*. 63.

Sweeney, M.R., McDonald, E.V. and Etyemezian, V. *Quantifying Dust Emissions from Desert Landforms, Eastern Mojave Desert, USA*. Geomorphology. 2011. 135 (1-2) 21-34.

Sweeney, M.R. and Mason, J.A. *Mechanisms of Dust Emission from Pleistocene Loess Deposits, Nebraska, USA*. Journal of Geophysical Research - Earth Surface. 2013. 118; 1460-1471.

Yonovitz, M. and Drohan, P.J. *Pore Morphology Characteristics of Vesicular Horizons in Undisturbed and Disturbed Arid Soils; Implications for Arid Land Management*. Soil Use Management. 2009. 25; 293-302.

Young, M.H., McDonald, E.V., Caldwell, T.G., Benner, S.G. and Meadows, D.G. *Hydraulic Properties of a Desert Soil Chronosequence in the Mojave Desert, USA*. Vadose Zone J. 2004. 3; 956-963.

Analysis of the Fitting Accuracy of the 3d Affine Transformation Applied to Cartosat-1 (IRS P5) Satellite Stereo Imagery

Farzaneh Dadras Javan and Ali Azizi

Dept. of Photogrammetry, Faculty of Geomatics, University College of Engineering, University of Tehran, Iran

Publication Date: 27 June 2016

DOI: <https://doi.org/10.23953/cloud.ijarsg.59>



Copyright © 2016 Farzaneh Dadras Javan and Ali Azizi. This is an open access article distributed under the **Creative Commons Attribution License**, which permits unrestricted use, distribution, and reproduction in any medium, provided the original work is properly cited.

Abstract Since few years ago it has been generally accepted without any dispute that the 3D affine transformation applied to high-resolution satellite imageries (HRSI), produces results as accurate as those obtained by the RPCs derived from rigorous photogrammetric model. However, as the higher order terms are absent in the affine transformation, the degree of success of this model obviously hinges upon the geometric nature of the imagery to be geo-rectified. In authors view, there are a latent confusion and misunderstanding in the minds of the photogrammetric practitioners as regards the potential of the 3D affine transformation as a replacement model for the geometric correction of the HRSI. The main intention of this paper is, therefore, to analyse the 3D affine transformation by concentrating more on its limitations. To obtain deeper insight into the nature of the 3D affine model, it is applied to images with larger field of view as well as the images of highly mountainous terrains. The geo-coding success of the affine model is then evaluated by comparing the object coordinates of a dense cloud of homologous points derived by the affine model with the object coordinates of the same points obtained by the standard terrain-independent rational functions. Extensive tests conducted over excessively mountainous as well as the hilly terrains indicate that there are clear distortion trends in the residual ground coordinates that cannot be fully absorbed into the 3D affine coefficients. The sources of these non-linear trends such as the satellite attitude and position variations, the terrain relief, the earth curvature and their impact on the final accuracy are analysed using the scatter patterns of the residual errors.

Keywords *3D Affine Transformation; High Resolution Satellite Imagery; Cartosat-1; Rational Polynomial Functions; RPCs; Geometric Accuracy; Perspective to Affine Transformation; Parallel Projection*

1. Introduction

In recent years, the major trends in sensor orientation and geo-positioning solutions for high resolution satellite imageries have been dominantly confined to the fitting rational function coefficients to the rigorous photogrammetric collinearity equations (Tao et al., 2001; Dial and Grodecki, 2005; Grodecki, 2001). This approach proved to be accurate, flexible and easy to implement and hence the main stream photogrammetric software developers did not hesitate to tailor the RPC-based 3D ground reconstruction into their systems.

The suitability of RPC approach can be justified based on the following reasons:

- 1) The on-board GPS/INS-star tracker facilities provide precise attitude and satellite position data to serve as observational data for the exterior orientation parameters in collinearity model leading to direct-geo positioning (Grodecki and Dial, 2003),
- 2) Decades of research proved the excellence of the Collinearity Equation for rigorously modelling the geometry of the satellite linear array imaging systems (Valadan Zoej and Petrie, 1998),
- 3) After bias and drift is removed, the fitted RPCs are effectively as accurate as the collinearity model itself (Grodecki and Dial, 2003; Fraser and Hanly, 2003),
- 4) The problematic bias and drift parameters are easily tackled by a very few GCPs (Grodecki and Dial, 2003; Fraser and Hanly, 2003; Hanley and Fraser, 2004),
- 5) 3D ground reconstruction with RPCs is easy to implement with well-established formulations (Grodecki et al., 2004),
- 6) The user may easily develop his own bundle adjustment to calculate the object coordinates,
- 7) The manual 3D displacements of the floating mark in Photogrammetric work stations can be controlled via the fitted RPCs.

On the other hand, there has been a second main stream research trends that chose to go on different direction, and that is the famous 3D affine projection model initially suggested by Okamoto (Okamoto et al., 1998). This approach also indicated to be attractive in its simplicity and its outstanding potential to give “accuracies equal to and in cases superior to those obtained via the RPC approach” (Fraser and Yamakawa, 2004). The affine projection offers the following advantages:

- 1) Easy to implement,
- 2) No initial values are required for the solution of the affine transformation coefficients and the ground coordinates,
- 3) The solution is non-iterative,
- 4) No oscillation and collapsing occurs in the equation,
- 5) Normalization and regularization are not essential,
- 6) Few GCPs are needed to solve the sensor orientation.

Now, bearing in mind the reported accuracy figures obtained by the simple 3D affine projection approach (Fraser and Yamakawa, 2004; Elashmawy et al., 2005; Willneff et al., 2008), one could logically conclude that the eight coefficients of the 3D affine transformation are effectively equivalent to the 80 RPCs in the rational function model, i.e. the geometric non-linearities of the HRSIs under the test are negligible. This, obviously, has no mathematical justification. If, on the other hand, there are some distortion patterns that cannot be perfectly eliminated by the affine transformation, then what are those influential factors that the affine transformation fails to eliminate and in which situations this transformation can produce compatible results with the RPC approach?

To answer these questions, it is necessary to expose the affine transformation to the situations in which significant higher order distortions in the images are available. In the present research project, this is achieved by using the Cartosat-1 (IRS-P5) satellite image which has larger FOV compared to the other existing HRSIs. Moreover, the P5 stereo images used in this project are taken over a terrain with very high relief variations leading to the corresponding high relief displacements. To be able to determine the rate of success of the affine transformation, it is of crucial importance not to rely solely on RMSE's and the min/max of the residual errors.

The reason for this is that, depending on the number and distribution of the GCPs and bearing in mind the fact that the error patterns may be symmetrical; the resulted accuracy figures could be misleading.

Instead, in this project, the accuracy evaluation has been conducted using point clouds with regular distribution over the entire image plane. In this way, it has been possible to realistically analyse the rate of success of the affine projection model and its limitations using the scatter patterns of the residual errors for the point clouds.

To establish a firm theoretical basis for further analysis, the first section of this report derives the 3D affine transformation based on the parallel projection theorem. The 3D affine is then diagnosed in some detail to clarify the problems and limitations associated with this transformation as applied to the HRSIs. After a short introduction to the main characteristics of the Cartosat-1 (IRS-P5) images, different sources that generate higher order distortion patterns in these images are identified and analysed. These are then followed by detailed examination of the significance of these nonlinear terms using several tests carried out on Cartosat-1 toolkit stereo imageries.

1.1. Rigorous Parallel Projection and 3d Affine Transformation

The mathematical formulation for the rigorous parallel projection has been thoroughly discussed by Morgan (Morgan, 2004). It can be briefly stated as follows: With reference to Figure 1, it is assumed that the points in the image space are formed by the projecting rays that are parallel, i.e. the projection centre lies at infinity. This projective geometry, obviously, differs from the customary perspective projection in which the projecting rays converge to a point located at a finite distance. For parallel projection geometry, similar to the perspective geometry, it is possible to derive a rigorous mathematical model. Consider the image point a' and its corresponding point A on the ground, the rigorous parallel projection is then given by (details are given in Morgan, 2004):

$$\begin{pmatrix} x' \\ y' \\ 0 \end{pmatrix} = S \left(\lambda \bullet R \begin{bmatrix} L \\ M \\ N \end{bmatrix} + R \begin{bmatrix} E_A \\ N_A \\ h_A \end{bmatrix} \right) + \begin{pmatrix} \Delta x \\ \Delta y \\ 0 \end{pmatrix} \quad (1)$$

where, x' , y' are the image coordinates; L , M , N are the three components of the unit direction vector; R is the scene rotation matrix; S is the scale factor; E_A , N_A , h_A are the object coordinates of the point A ; Δx , Δy are the shifts in image space and λ is the distance between the object point and its corresponding image point.

Now, if λ is eliminated and under the constant velocity and constant attitude (CVCA) assumption, Equation 1 reduces to the familiar form of the 3D affine transformation, i.e.

$$\begin{aligned} x' &= A_1 E + A_2 N + A_3 h + A_4 \\ y' &= A_5 E + A_6 N + A_7 h + A_8 \end{aligned} \quad (2)$$

where, x' , y' are the pixel coordinates; E , N , h are the object coordinates and A_i are the 3D affine transformation coefficients. Similar pair of equations may be obtained for the corresponding right image points leading to four 3D affine equations for each homologous point. It should be noted that, the 3D affine transformation may be regarded as the parametric form of the rigorous parallel projection, if and only if the following conditions are fulfilled:

- E , N plane is not curved;
- The rays are parallel, i.e. the projection centre is at infinity;
- Satellite moves with constant velocity and constant attitude.

If any of the aforementioned conditions are not satisfied, the affine transformation cannot represent faithfully the parallel projection model. The section that follows lists and discusses the factors that influence the fidelity of the affine model.

1.2. Geometric Limitations of the 3d Affine Transformation

(A) General Considerations

There are certain well known factors that violate the parallel nature of the affine transformation. These are:

- (1) Internal errors of the CCD lines: These are mainly, CCD scan line rotation and bending in focal plane, lens distortion, principal point displacement and scale variation in scan and line directions respectively. These errors are taken into account in the collinearity equations and subsequently are catered for in the rational RPCs but are normally ignored in the 3D affine transformation.
- (2) Height variations in the scan direction (i.e. linear array direction) are projected according to the central perspective geometry and therefore the perspective to parallel transformation (PTP) is required (Okamoto et al., 1998; Fraser and Yamakawa, 2004; Morgan et al., 2004).
- (3) Scan line rotation around the z axis (yaw rotation) introduces an effect similar to the CCD rotation in the focal plane.
- (4) The vertical line passing through the projection centre does not remain parallel from one scan line to the other because of the curvature of the satellite route.
- (5) Map projection used for the object coordinates, introduces additional non-linear distortions.
- (6) As discussed before, the 3D affine transformation rigorously models the parallel projection geometry under the restrict proviso of CVCA condition. Any deviation in the satellite route and any attitude variations disturb the parallel projection requirements.

(B) Earth Curvature Considerations

The earth curvature, normally, does not conform to the nature of the 3D affine transformation. This is due to the fact that a curved surface mapped into a 2D image plane, inevitably imposes distortions on this plane. With the physical 3D reconstruction models, however, this distortion does not pose a difficulty. This is because the original pair of image forming incoming rays, irrespective of the complexities associated with the object surface, are regenerated in a reverse mode to reconstruct the object points. Therefore, with a selection of an appropriate object coordinate system, the planar image plane can be re-projected into a curved object surface without any significant distortion. However, the affine transformation is not flexible enough to perform similar task. In other words, the affine transformation, which is parametric and not physical, maps a 2-D space into a 3D space with 8 parameters with a property that a curve with a given degree is transformed into another curve with the same degree. That is, the mapped object surface must hold true in a plane given by:

$$AX + BY + CZ + D = 0.$$

This indicates that there are limitations inherent in the 3D affine transformation if the object space is a curved surface. This fact is demonstrated in Figure 1. As the Figure indicates, assuming no height variation, each scan line inevitably maps a curved surface. From this, it can be deduced that the points with the same height values are not mapped into the same scan line and therefore effectively different x-parallaxes are introduced to the points with the equal heights leading to the height distortion on the generated object space. Distortions in the regenerated planimetric coordinate of the object points also occur but with a smaller rate.

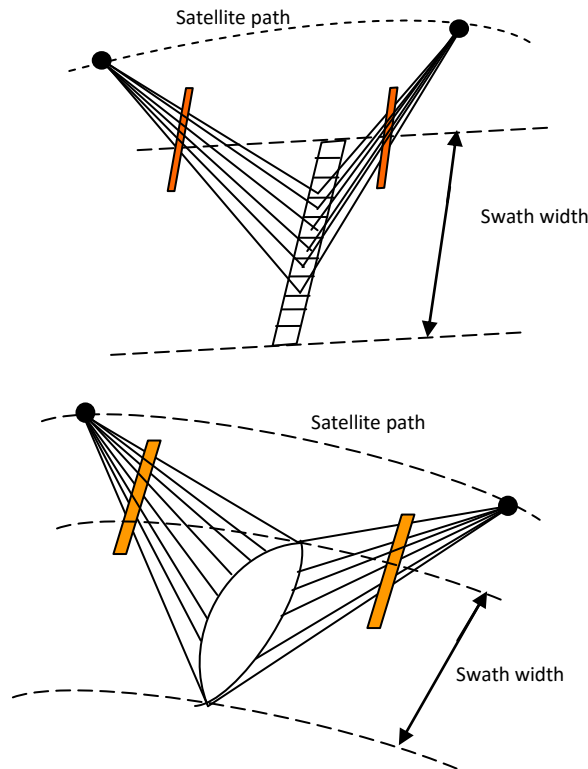


Figure 1: Image geometry for a flat surface (above) and a curved surface (below)

2. Accuracy Evaluation Strategy

The current approaches for accuracy assessment of the generated 3D points in object space for satellite imageries generally rely on the control and check points that are identified on the HRSI and measured on the ground using GPS or other geodetic surveying techniques. Alternatively, the GCPs may be identified and measured using existing maps. These approaches, however, suffer from certain ambiguities and uncertainties that result from the fact that the imaging system's point spread function smoothes the well-defined points. Hence ambiguity occurs during the point measurement process. Correlatively, the corresponding ground point identification undergoes the same ambiguities and the object point positioning uncertainties become inevitable. Moreover, due to the nature of the ground and other prohibiting factors, it is not always possible to extend the measurement to cover the entire area with uniform distribution of the points. This in turn weakens the accuracy assessment outcomes. To avoid these ambiguities in accuracy assessment and to reach a definite conclusion as regards the accuracy figures, this research adopts a fitting approach based on the procedures given in Figure 2.

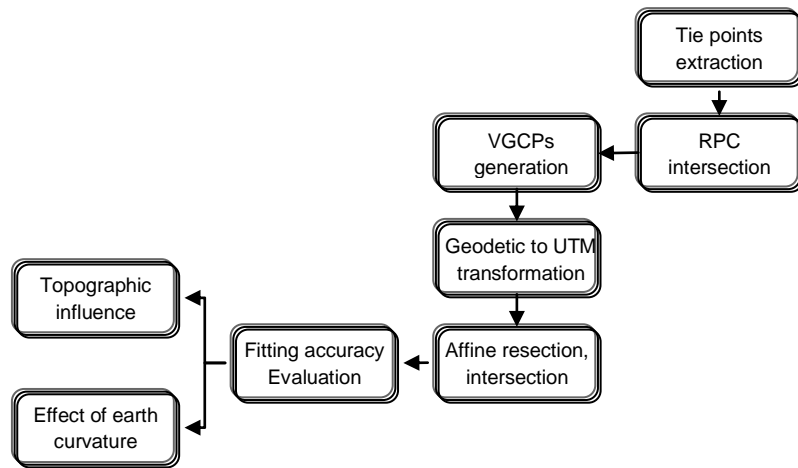


Figure 2: Accuracy evaluation strategy

As the Figure indicates, the procedure starts by measuring well distributed arbitrarily chosen homologous point clouds covering the entire stereo pair overlap area. The measurements are performed both manually and automatically. Both of the manual and automatic homologues point measurements can be performed with sub-pixel accuracy (see the section: “preliminary data analysis”). Using the available RPCs, the object space coordinates are then calculated by adopting the well-established RPC object point reconstruction formulation given by the following linearized rational equations: Grodecki et al., 2004,

$$s = s_o + s_s \begin{pmatrix} \frac{\partial K}{\partial X} & \frac{\partial K}{\partial Y} & \frac{\partial K}{\partial Z} \end{pmatrix} \begin{pmatrix} \frac{1}{\varphi_s} & 0 & 0 \\ 0 & \frac{1}{\lambda_s} & 0 \\ 0 & 0 & \frac{1}{h_s} \end{pmatrix} \begin{pmatrix} d\varphi \\ d\lambda \\ dh \end{pmatrix} \tag{3}$$

$$l = l_o + l_s \begin{pmatrix} \frac{\partial J}{\partial X} & \frac{\partial J}{\partial Y} & \frac{\partial J}{\partial Z} \end{pmatrix} \begin{pmatrix} \frac{1}{\varphi_s} & 0 & 0 \\ 0 & \frac{1}{\lambda_s} & 0 \\ 0 & 0 & \frac{1}{h_s} \end{pmatrix} \begin{pmatrix} d\varphi \\ d\lambda \\ dh \end{pmatrix}$$

where K and J denote the rational function equations respectively; s , l are the scan line and pixel coordinates; The subscripts o and s indicate the shifts and scale factors respectively used for the normalization process; the column vector comprises the unknown latitude, longitude and height differentials. Equation 3 can be written for each homologue point leading to four equations in three unknowns and solved iteratively. The generated object coordinates of the measured points provide well distributed ground points. Bearing in mind the fact that the RPCs are derived from the satellite auxiliary data by accurately fitting a rational function to the rigorous photogrammetric model, they are as accurate as the rigorous model itself. Therefore, the ground coordinates that are generated by the RPCs can be regarded as the virtual ground coordinate points (VGCPs). Consequently, these VGCPs are utilized as control points to determine the eight affine projection parameters after they have been transferred to the UTM coordinate system. This step is then followed by space intersection using all 16 affine transformation parameters determined in the previous stage. The ground coordinates for

previously measured homologous points are subsequently determined by the following linear 3D affine intersection:

$$\begin{pmatrix} x' - A_4' \\ y' - A_8' \\ x'' - A_4'' \\ y'' - A_8'' \end{pmatrix} = \begin{pmatrix} A_1' & A_2' & A_3' \\ A_5' & A_6' & A_7' \\ A_1'' & A_2'' & A_3'' \\ A_5'' & A_6'' & A_7'' \end{pmatrix} \begin{pmatrix} E \\ N \\ h \end{pmatrix} \quad (4)$$

Having calculated the object coordinates by affine intersection, it is then possible to determine the residual errors which are simply the differences between the ground coordinates of the homologous points calculated by the 3D affine and the ground coordinates of the same points determined by the RPCs, i.e.

$$\begin{pmatrix} dE \\ dN \end{pmatrix} = \begin{pmatrix} E - E' \\ N - N' \end{pmatrix} \quad (5)$$

Where E, \dots, N' are the calculated object coordinates by the affine and the rational functions respectively. As can be seen from the preceding discussion, it seems that there should be no ambiguity present in the analysis, because the same homologous and ground points are used for the solution of the affine coefficients. Moreover, regarding the fact that the fitted RPCs to the rigorous photogrammetric model are effectively as precise as the rigorous model, one can consider the VGCPs derived by the terrain-independent rational function, practically equivalent to the points generated by the rigorous model itself. In other words, this strategy measures the degree of the fitness of the affine transformation to the rational function model. Any remaining trend in the residual errors for the generated point clouds can also be easily observed by displaying the residual errors in a scatter diagram. Scatter diagrams are excellent means for revealing any trend in the residual errors.

2.1. Description and Analysis of the Data Sets

To be able to fully evaluate the potential of the 3D affine transformation, two sets of Cartosat-1 ortho-rectified stereo images have been selected. These datasets belong to the areas with different topography. The first data set belongs to a highly mountainous terrain and the second data set covers a hilly area. Before describing the datasets, it seems pertinent to briefly describe the Indian Cartosat-1 satellite: It is a near polar sun synchronous satellite launched in 5 May 2005, accommodating two 2.5 meters resolution forward and afterward linear array cameras. These cameras are mounted in the satellite flight. Cartosat-1 sensor specifications are given in Table 1.

Table 1: Geometric specifications of Cartosat-1 stereo imagery

| | Fore camera | Aft camera |
|----------------------|-------------|------------|
| Looking angle | +26 degree | -5 degree |
| Camera field of view | 2.4 degree | 2.4 degree |
| Swath width | 29 km | 26 km |
| Number of detectors | 12000 | 12000 |
| Focal length | 1945 mm | 1945 mm |
| Approximate altitude | 618 km | 618 km |

Dataset (A)

The first dataset is stereo images acquired over the area of Roodehen in Iran with a range of 1345 to 3236 meters height variation for the area covered by the stereo pair. The images have been acquired

in 13 August 2007. Nearly 400 homologous points with a uniform distribution over the entire stereo-pair are measured manually. Figures 3(left) and 3(right) indicate the distribution of the homologous points measured in the fore and aft stereo images respectively.

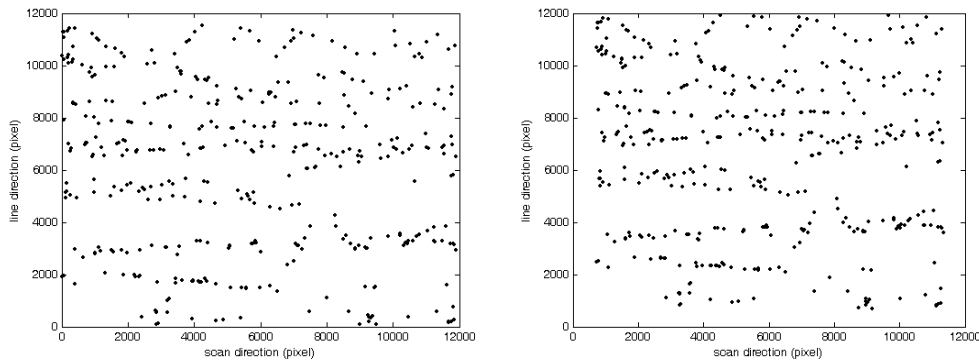


Figure 3: Measured homologous points: (left) aft image, (right) fore image – dataset A

For the same stereo-pair, 112 homologous points are also matched automatically using image correlation techniques. Due to the excessive height variation, the matched points were sparse and smaller in number than the manual measurements. Nevertheless, the distribution of the points was still uniform.

Dataset (B)

The second data sets are the orthokit stereo images taken over the city of Arak which is rather a hilly area with a height variation between 1624 to 1863 meters. The images have been acquired in 7 November 2006. In contrast to the first dataset in which, the automatic image matching did not succeed to produce dense homologous point cloud, in the second data set because of the smaller range of the height variations, the image matching procedures was carried out successfully and nearly 1000 homologous points were generated automatically. Figure 4 gives the distribution of the points in the fore and aft images respectively.

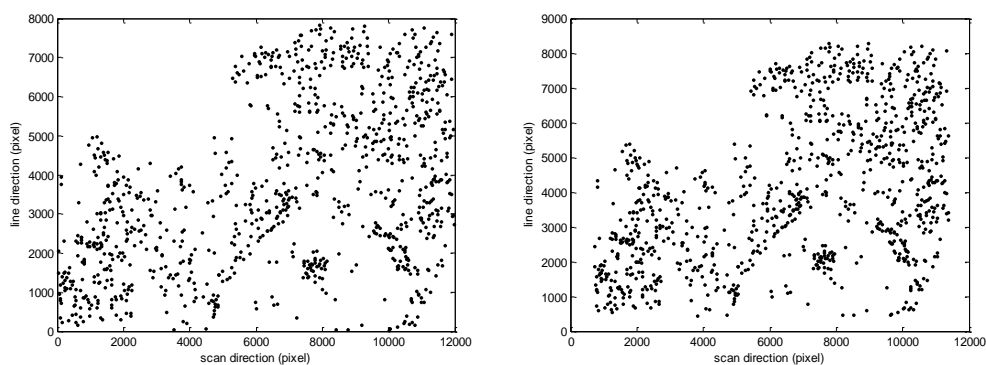


Figure 4: Measured homologous points: (left) aft image, (right) fore image (dataset B)

2.2. Preliminary Data Analysis

To determine a preliminary validation for the precision of the measured image points, y-parallaxes are computed based on the following relations:

$$py = p_A - p_F \quad (6)$$

Where p_A and p_F are the pixel coordinates in the scan direction for the corresponding homologue points in aft and fore images respectively. Figure 5 (left) shows the row y-parallaxes versus line direction (i.e. satellite movement direction) for manual measurements determined by Equation 6. The linear trend in the y-parallaxes is the result of a shift and a scale factor. The shift is due to the different sample numbers for the corresponding features and the scale factor (drift) seems to be due to the scale differences in the pixel direction between the fore and aft images. After fitting a line to the raw y-parallaxes, a value of shift equal to 716 pixels and a drift equal to 0.89 is obtained. Eliminating the linear trend, the new y-parallaxes are presented in Figure 5(left). The rmse of the y-parallaxes after the removal of the linear trend is about 0.3 pixel. This indeed shows that the homologous point measurements have been performed with sub-pixel precision. The rmse for the automatically measured points is slightly smaller than the manual measurement method indicating the superiority of the automatic matching to the manual measurement approach.

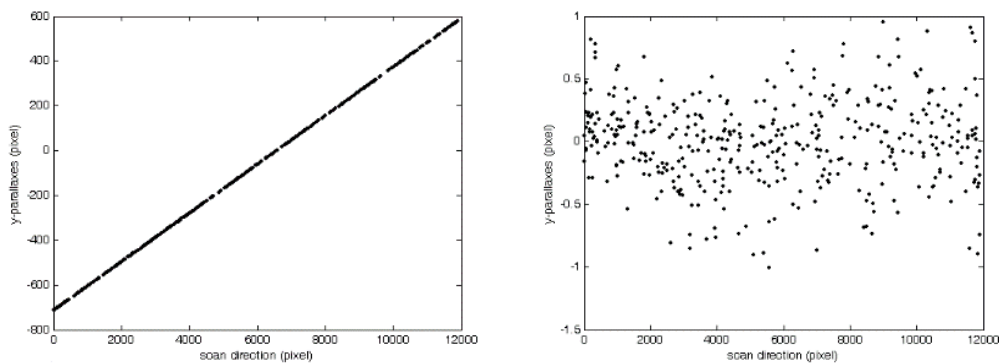


Figure 5: Raw y-parallax versus scan direction before (left) and after linear trend is removed (dataset A)

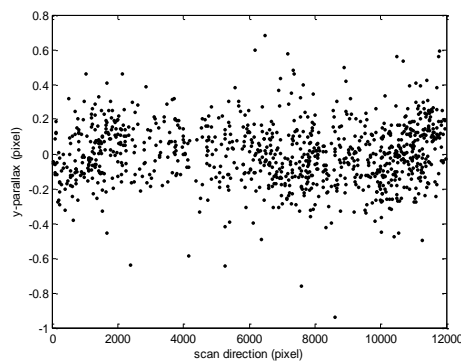


Figure 6: y-parallax versus scan direction after the linear trend is removed (dataset B)

Bearing in mind the fact that variations in satellite yaw, roll and pitch causes corresponding variations in y-parallaxes, the y-parallaxes can be then taken as an indication of the validity of the constant attitude assumption during the image acquisition. However, the y-parallax versus the line number indicates a very small systematic trend in the line direction (Figure 7). This small shift in y-parallaxes along the line direction (i.e. in the direction of the satellite movement) may be due to the small variations in the satellite altitude during the image acquisition (equivalent to classical BZ).

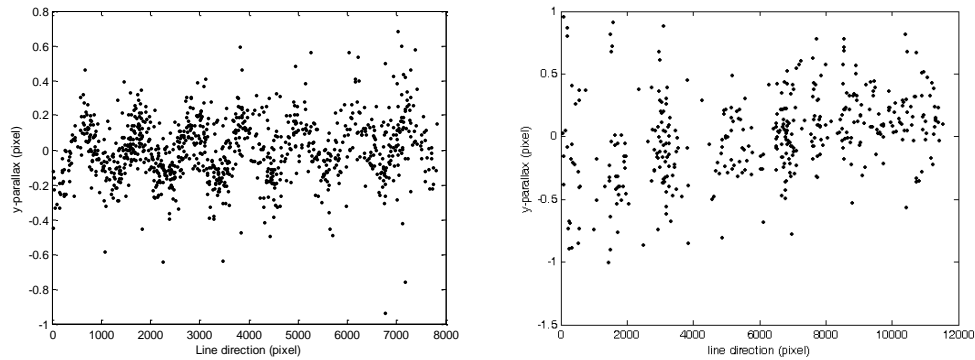


Figure 7: (left): *y-parallax versus line direction (dataset B)*, (right): *y-parallax versus line direction (dataset A)*

3. Accuracy Results and Evaluation

Based on the strategy for the accuracy evaluation discussed in the earlier section, the first stage, with reference to Figure 2, involves calculating the object coordinates of the measured homologous points. As stated before, this stage is carried out based on the RPC intersection formulation given by Equation 3. The solution of this Equation requires initial values for the unknown 3D object coordinates. The initial values may be obtained using a truncated rational function retaining only linear terms leading to a relation similar to a simple DLT intersection. This approach is adopted and implemented with satisfactory result. However, due to the fact that during a single frame image acquisition, the CVCA condition is reasonably fulfilled (see the preceding section), our tests indicate that even very approximate initial values (e.g. the orthokit rough geodetic coordinates for the longitude and latitude and the average terrain height) can fulfil the convergence requirements (Dadrass and Azizi, 2008).

After the solution of equation 3, it was noticed that the misclosure errors in the scan directions were quite high (about 30 pixels for the fore image and 27 pixels for the aft image) indicating a systematic bias in the scan direction. Table 2 gives the min, max and mean values for the disclosure errors for the fore and aft stereo images. After the bias is removed, the residual misclosure errors were reduced to a pixel level. Nevertheless, they still show a systematic trend. This may suggest that the RPCs have not been determined by a bundle adjustment solution. Figure 10 presents the scatter pattern of the misclosure errors for the fore and aft images respectively.

Table 2: Misclosure (pixels) in scan direction (P), line direction (L), before the shift removal for the fore and aft stereo images

| Mean residual fore image (L) | Max residual fore image (L) | Min residual fore image (L) | Mean residual aft image (L) | Max residual aft image (L) | Min residual aft image (L) |
|------------------------------|-----------------------------|-----------------------------|-----------------------------|----------------------------|----------------------------|
| -7E-5 | +11E-4 | -16E-4 | 30.78 | 31.5 | 29.9 |

| Mean residual fore image (P) | Max residual fore image (P) | Min residual fore image (P) | Mean residual aft image (P) | Max residual aft image (P) | Min residual aft image (P) |
|------------------------------|-----------------------------|-----------------------------|-----------------------------|----------------------------|----------------------------|
| 7E-5 | +17E-4 | -11E-4 | 27.4 | -26.7 | -28.2 |

Table 3: Misclosure (pixels) in scan direction (P), after the bias removal for the fore and aft stereo images

| Mean residual fore image (P) | Max residual fore image (P) | Min residual fore image (P) |
|------------------------------|-----------------------------|-----------------------------|
| 8E-5 | +0.8 | -0.8 |
| Mean residual aft image (P) | Max residual aft image (P) | Min residual aft image (P) |
| -9E-5 | +0.7 | -0.7 |

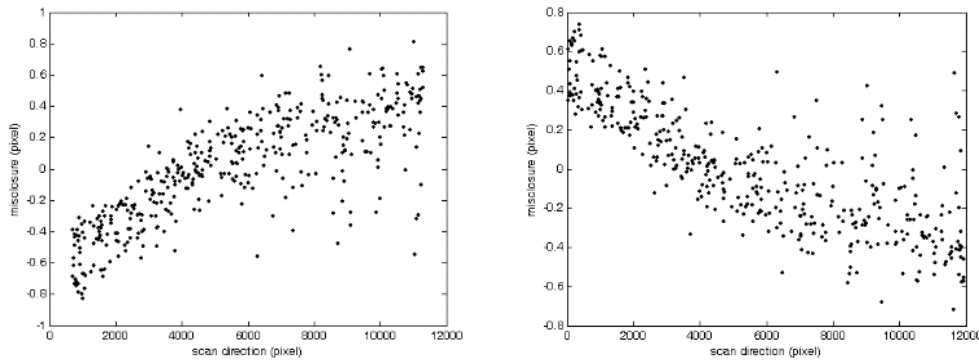


Figure 8: Residual errors in the scan direction after the bias is removed for the fore (left) and aft (right) images

After the solution of the RPC intersection, the UTM coordinates as optimum choice for the object coordinates discussed by Fraser et al., 2004, was adopted and, therefore, the calculated geodetic coordinates were transferred to the UTM coordinate system.

The 3D affine resection is then performed through which the affine coefficients are calculated. This stage is followed by the 3D affine intersection (equation 4) by which the 3D object coordinates are determined in the UTM coordinate system.

The following sub-sections present the accuracy results before and after the correction for the topographic influence:

3.1. Accuracy Evaluation before Eliminating the Effect of Topography

As mentioned in the previous sections, there are several factors that contribute to the deviation of the HRSI from the parallel projection geometry. The initial tests conducted on the P5 stereo-images are intended to highlight the total influence of all of these factors.

In the first stage, the dataset (A), which belongs to a highly mountainous terrain (see the Section: description of the datasets), used for the 3D affine accuracy evaluation. The residual discrepancies between the ground coordinates determined by the RPCs and the ground coordinates of the same points determined by 3D affine is determined based on equation 5. The rmse for E, N and h are given in Table 4. The residual error patterns for these parameters are presented in a kind of scatter diagram in Figures 9, 10 and 11 respectively. These scatter diagrams are very appropriate for revealing any trend in the residual errors.

Table 4: rmse of the E, N, h residual errors for dataset A (without height and Earth curvature corrections)

| Rmse (E) – (meter) | Rmse (N) – (meter) | Rmse (h) – (meter) |
|--------------------|--------------------|--------------------|
| 4.67 | 1.77 | 4.53 |

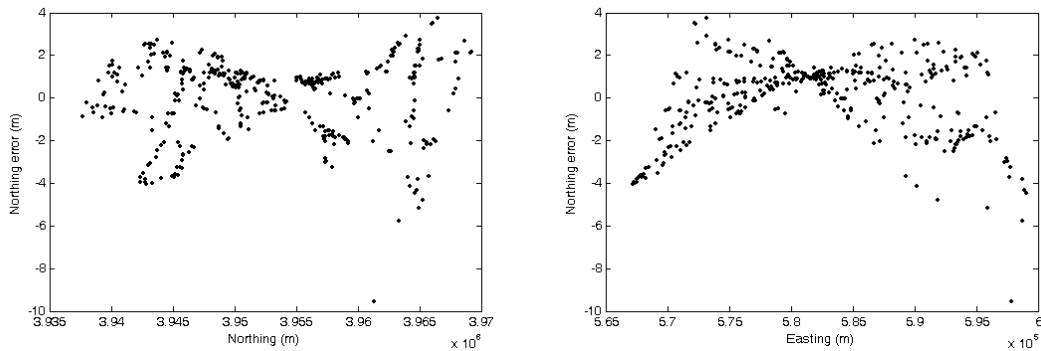


Figure 9: (left): Northing error versus Northing, (right): Northing error versus Easting

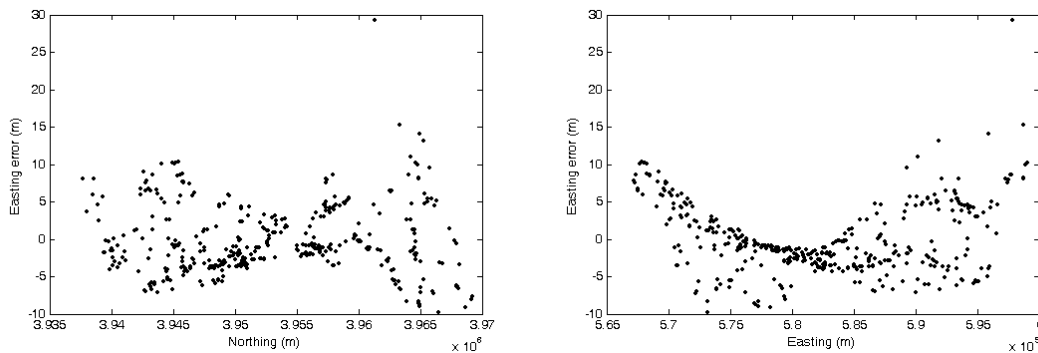


Figure 10: (left): Easting error versus Northing, (right): Easting error versus Easting

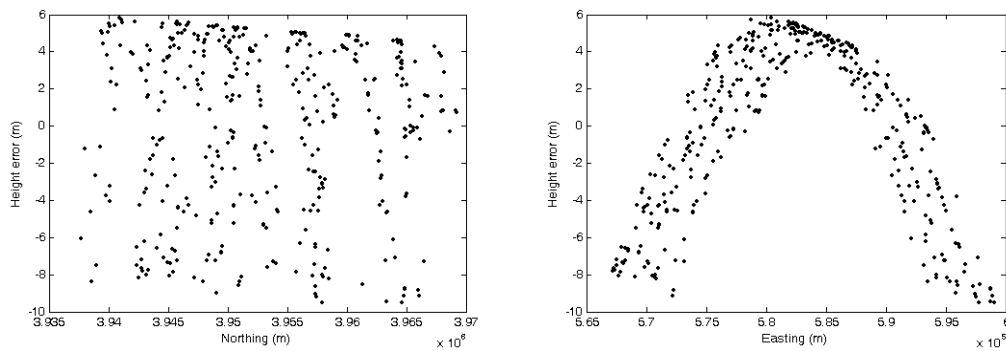


Figure 11: (left): Height error versus Northing, (right): Height error versus Easting

As the Figures indicate, the simple 3D affine is incapable to produce a good fit to the rational function in a highly mountainous terrain. This is, of course, in full agreement with the nature of the affine transformation. The main sources of errors in planimetry are due to the relief variations. As it was discussed earlier, the relief variation violates the parallel geometry in the scan line direction. This is clearly demonstrated in the scatter patterns presented in Figures 10(left & right). Nevertheless, Figures 9(left & right) also suggest that the relief variation has had some impact, although with a lower magnitude, on the line direction.

Figure 11(right) indicates a nearly curved pattern for the height discrepancies. This clearly suggests that the terrain topography does not play a decisive role on the height accuracy and this is the Earth curvature that dominantly affects the height residuals.

To further indicate the influence of topography on the performance of the 3D affine transformation, dataset B belonging to a hilly area is used. The results are presented in Table 5 and Figure 12 respectively. As can be seen from the Table and the residual scatter patterns, the accuracy improvement is clear. The max/min errors are less than a meter for all of the points indicating a sub-pixel fitting accuracy in the image space. This, of course, proves the considerable influence of the terrain height fluctuation in the fitting accuracy of the 3D affine transformation. It is important to notice that although rmse values are considerably reduced in dataset B as compared to the first dataset, the systematic trend in the E and N residual errors still is detectable which indicates that the influence of the height variations in the dataset B is still significant.

As Table 5 indicates, the errors in height have not been improved as compared to the dataset A. This is due to the fact that the errors due to the Earth curvature have remained intact.

Table 5: Rmse of the E, N, h residual error for dataset B (without height and Earth curvature corrections)

| Rmse (E) – (meter) | Rmse (N) – (meter) | Rmse (h) – (meter) |
|--------------------|--------------------|--------------------|
| 0.35 | 0.28 | 5.17 |

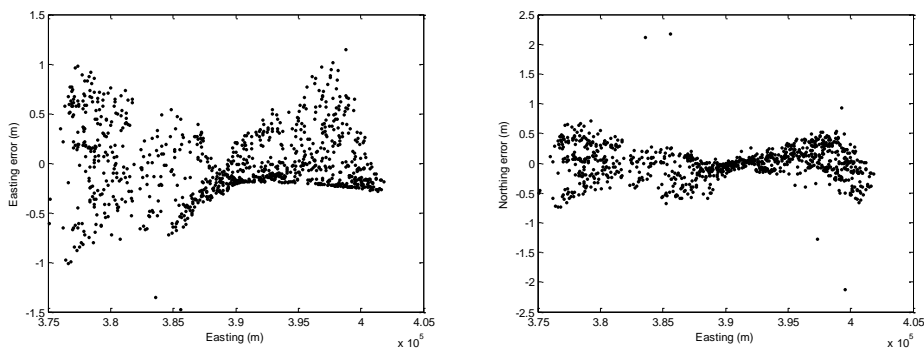


Figure 12: N and E residual errors (hilly terrain, dataset B)

3.2. Accuracy Evaluation after Eliminating the Effect of Topography

The next step involves the elimination of the influence of the terrain topography. This is achieved via the familiar perspective to parallel transformation, (Fraser and Yamakava, 2004):

$$y' = \frac{y}{1 - \frac{y}{f} \tan \omega} \pm [\tan(\omega + \alpha) - \tan \omega] \Delta Z \cos \omega$$

where y and y' are the pixel coordinates in the scan direction before and after the perspective to parallel transformation; ΔZ is the height variations brought into a scale close to the image scale; ω is the roll angle; α is the angle between the camera optical axis and the line connecting each pixel to the perspective centre and f is the camera focal length. However, as the roll angle, for the along track stereo images is nearly zero, the perspective to parallel transformation equation reduces to:

$$\Delta y = \Delta Z \tan \alpha \tag{7}$$

Where Δy is the perspective to parallel corrections applied to the pixel coordinates in the scan direction.

After applying Equation 7 to the measured image coordinates in the fore and aft images, the affine space resection followed by the affine space intersection is carried out and the ground points are generated. The rmse for E and N are presented in Table 6. The planimetric accuracy improvements as compared to the results obtained before PTP can be clearly seen in Table 6. However, as expected, the rmse value for the height discrepancies has not changed, i.e. rmse of heights are 4.51 and 4.53 meters before and after applying PTP respectively. This again shows that the height accuracy is less sensitive to the terrain topography.

Table 4: Rmse of the E, N, h residual error for dataset A, before and after perspective to parallel transformation

| Rmse (E) – (mster) (before PTP) | Rmse (N) – (mster) (before PTP) | Rmse (E) – (mster) (after PTP) | Rmse (N) – (mster) (after PTP) |
|---------------------------------|---------------------------------|--------------------------------|--------------------------------|
| 4.67 | 1.77 | 0.34 | 0.86 |

As it was mentioned earlier, the scatter diagram should be checked to detect the possible trends in the residual errors. Figures 13 and 14 show the scatter patterns of the errors in planimetry.

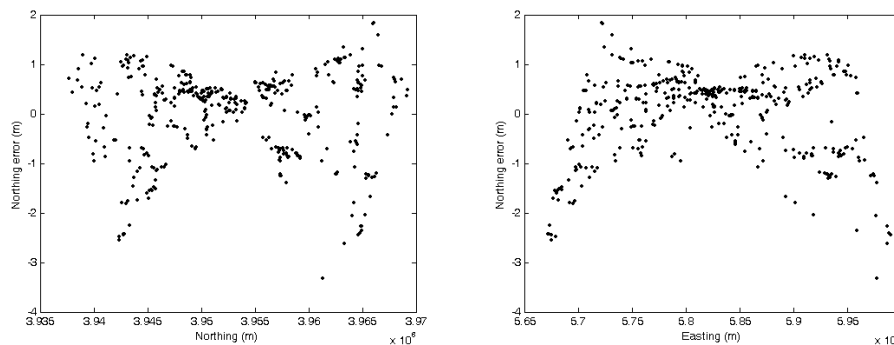


Figure 13: (left): N error versus N, (right): E error versus E, (dataset A)

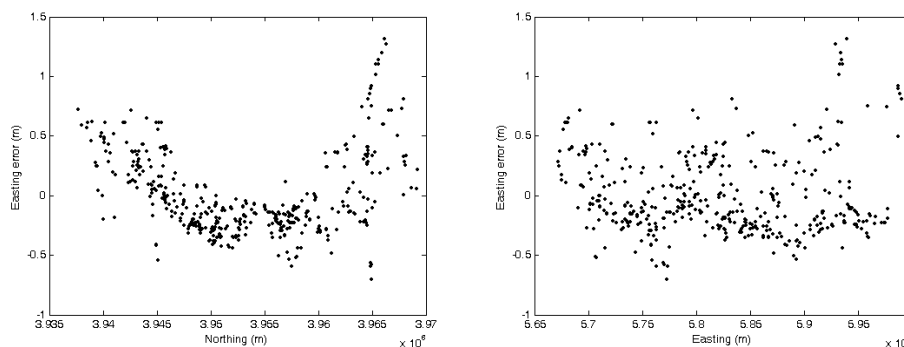


Figure 14: (left): E error versus N, (right): E error versus E, (dataset A)

3.3. Issues Related to the Earth Curvature

It was demonstrated in the preceding sections, that the displacements due to the Earth curvature on the object coordinates are inevitable when the 3D affine transformation is at issue. It was also demonstrated that this displacement is dominant over the height coordinates.

To remove the displacement effect of the Earth curvature, two different approaches have been adopted, namely, image space and object space solutions: In the first approach, the displacements due to the Earth curvature are formulated in the image space. To model the image point displacement due to the Earth curvature, it is assumed that the imaging geometry for each scan line is identical to the diagram depicted in Figure 15.

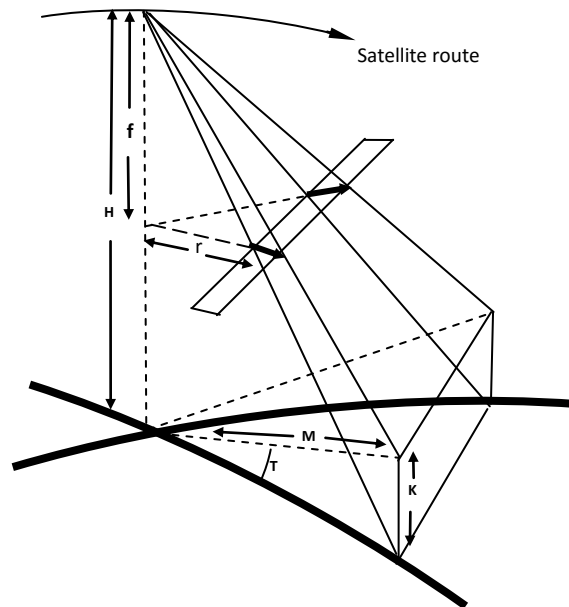


Figure 15: Image displacements due to Earth Curvature along the scan lines

With reference to Figure 16, it can be shown that the following relation holds true:

$$K = R - R \cos(2T) \tag{8}$$

Where R is the Earth radius; K is the vertical displacement of a point on the Earth surface and the planar surface formed on the object space by the affine transformation. This surface is indicated in Figure 15 by the dashed lines that are tangent to the Earth surface at the ground nadir point; and T is the angle between the tangent to the Earth surface and the planar surface generated by the affine transformation. This angle may be expressed as:

$$\sin(2T) = \frac{M}{R} \tag{9}$$

Where M is the horizontal distance between the object point and the ground nadir point. From Equations 8 and 9 it can be deduced that:

$$K = 2R \frac{M^2}{4R^2} = \frac{M^2}{2R} \tag{10}$$

M may be expressed as a function of the radial distance, r , from the image nadir point:

$$M = r * H / f \tag{11}$$

Where H is the satellite flying height and f is obtained via: $f' = f \cos \theta$ in which f and θ are the camera focal length and the satellite pitch angle respectively. By replacing Equation 11 in 10, we get:

$$K = \frac{r^2 \frac{H^2}{f^2}}{2R}$$

The image displacement, Δr , due to the value of K can then be expressed as:

$$\Delta r = \frac{r^3 H^2}{2Rf^2} \tag{12}$$

This relation is identical to the classical formulation in photogrammetry for the Earth curvature for frame photography. Based on the equation 12, the theoretical displacement is determined and is presented in Figure 16.

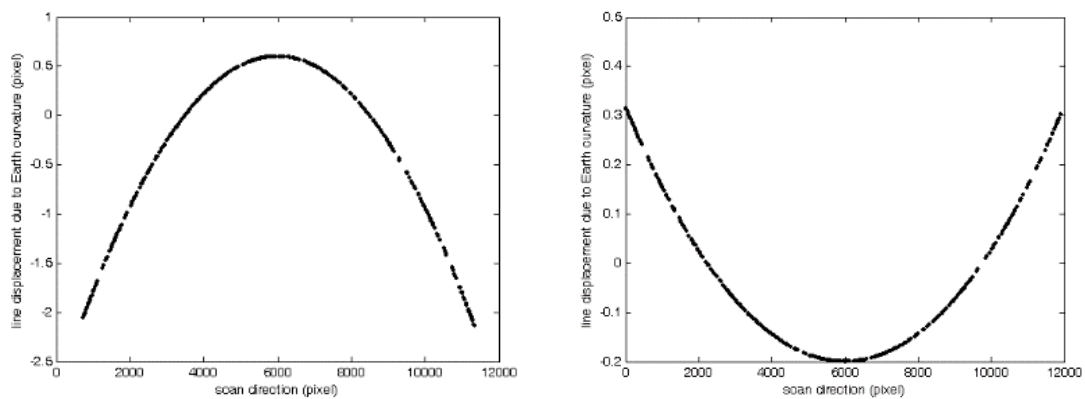


Figure 16: Image displacement due to Earth Curvature evaluated via equation 12, (left): fore image, (right): aft image

The theoretical formulation given by equation 12 is validated by the actual determination of the pixel displacements due to the Earth curvature for the dataset (A). This is achieved by the inverse solution of the affine transformation. That is, the object points are transformed to the image space via inverse affine parameters. The object coordinates in this case are the E, N values already computed by the affine intersection. However, the height values for each object point are replaced by the heights generated by the RPCs that are free from the Earth curvature displacements. The image space residuals due to the Earth curvature are then the differences between the transformed image coordinates and the originally measured image points. Figure 17 show these displacements for the fore and aft images respectively. As can be seen, the image coordinates distortion curves are in the sample direction and they are in conformity with the scatter diagrams depicted in Figure 16. From these figures it can be also seen that because of the smaller oblique viewing angle, the amplitude of the image displacement due to the Earth curvature in aft image is smaller than that of the fore image.

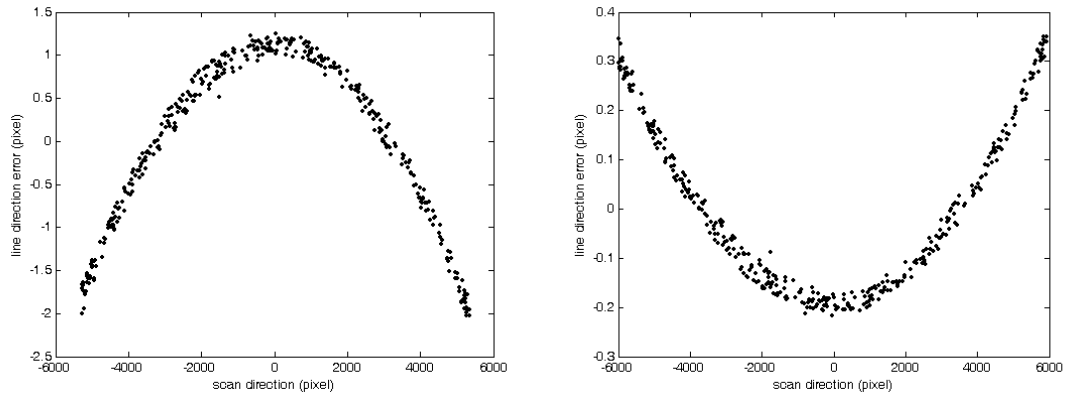


Figure 17: line direction displacement due to the Earth curvature, (left) fore scene, (right) aft scene

The second approach formulates the Earth curvature directly on the 3D affine generated height values on the object space. This alternative approach entails the direct utilization of Equation 10, in which the value of K is taken to directly represent the height displacement due to the Earth curvature. The value of M in Equation 10 is interpreted in this case as the shortest distance of the object points to the satellite ground track (SGT). To implement this approach, the SGT is determined. This is achieved by transferring the middle pixels of the images to the object space. Alternatively the SGT may be determined via the satellite heading from the metadata. After the computation of the shortest distance to the SGT for all generated object points, the Earth curvature is computed based on Equation 10. Figure 18 presents the residual height scatter diagram after removing the Earth curvature effect. The RMSE of the residual height errors has been reduced to 0.41 meter which is significantly better than 4.53 meters before eliminating the Earth curvature effect. Nevertheless, Figure 18 shows a systematic trend in the Northing direction. This may suggest that the height errors are also proportional to the direction of the satellite movement in which the satellite undergoes a slight altitude variation. The inclusion of the term (NZ) in the affine model, therefore, may improve the result. This is a matter for further investigation.

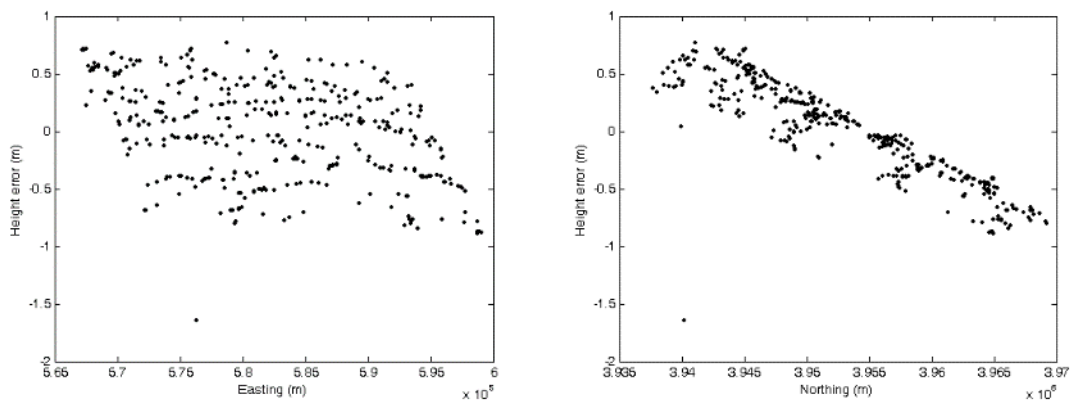


Figure 18: (left): height residuals versus Easting, (right): height residuals versus Northing, after the elimination of the Earth curvature effect

The overall achieved fitting accuracy of the 3D affine transformation before and after height correction and Earth curvature removal for comparison is given in Table 7.

Table 7: The overall accuracy figures for dataset (A) and (B) before and after applying the height and earth curvature corrections

| | Before corrections applied | | | After corrections applied | | |
|------------|-----------------------------|-----------------------------|-----------------------------|-----------------------------|-----------------------------|-----------------------------|
| | δE (m) - min/max | δN (m) - min/max | δh (m) - min/max | δE (m) - min/max | δN (m) - min/max | δh (m) - min/max |
| Dataset(A) | 0.01/29 | 0.002/9.5 | 0.08/9.6 | 8E-4/1.4 | 1E-4/3.3 | 5E-4/2.4 |
| Dataset(B) | 1E-3/1 | 1E-5/0.6 | 1E-3/20 | 2E- 4/1.07 | 6E-4/0.8 | 3E-5/0.3 |

The section that follows summarizes the whole theme of the paper and draws the necessary conclusions.

4. Concluding Remarks

Based on the results and the discussions presented in the preceding chapters, the following conclusions may be made:

- (1) Affine transformation can indeed approach the accuracy of the rational function with sub-pixel level.
- (2) The accuracy results deteriorate with increase in the camera field of view and increase in the terrain relief undulation.
- (3) Based on the theoretical concepts and the conducted tests, it seems unlikely that the pure 3D affine model can generate data with accuracies equal to the RPCs. The theoretical justification of this statement, moreover, lies in the fact that even in the absence of the errors such as the attitude and altitude and relief variations, still Earth curvature intervenes in the computational process.
- (4) The height variation in mountainous terrain does not seem to solely affect the scan direction. The conducted tests indicate that the line direction also receives some influence from the terrain relief undulation.
- (5) Even if the effect of the height variation by PTP transformation is eliminated and the earth curvature removed, still some trends, though very marginal, can be observed in the scatter pattern.
- (6) The RMSE and max/min errors cannot adequately indicate the quality of the residual errors. In fact, this is the scatter pattern for the point clouds that indicates the presence or the absence of the trends in the final output and the success of the 3D affine transformation cannot be realistically judged with small and uneven distribution of the GCPs.

References

- Dadrass, F. and Azizi, A. *The Affine Projection Model as a Tool for Rapid Geo-Coding of IRS-P5 Satellite Imagery*. The International Archives of the Photogrammetry, Remote Sensing and Spatial Information Sciences. 2008. 37 (B4) 1317-1322.
- Dial, G. and Grodecki, J. *RPC Replacement Camera Models*. International Archives of Photogrammetry, Remote Sensing and Spatial Information Sciences. 2005. 34; Part XXX.
- Elashmawy, N., Elmanadili, Y., and Barakat, H., 2005. *Comparative Analysis and Evaluation of Various Mathematical Models for Stereo IKONOS Satellite Images*. FIG Working Week and Gsdi-8, Cairo, Egypt. 1-16.
- Frase, C.S. and Hanley, H.B. *Bias Compensation in Rational Functions for IKONOS Satellite Imagery*. Photogrammetric Engineering and Remote Sensing. 2003. 69 (1) 53-57.

- Fraser, C.S. and Yamakawa, T. *Insights into the Affine Model for Satellite Sensor Orientation*. ISPRS Journal of Photogrammetry and Remote Sensing. 2004. 58 (5-6) 275-288.
- Grodecki, Jacek, 2001: *IKONOS Stereo Feature Extraction-RPC Approach*. Proceedings of ASPRS 2001 Conference, St. Louis, April 23-27. 7.
- Grodecki, J. and Dial, G. *Block Adjustment of High Resolution Satellite Images Described by Rational Polynomials*. Photogrammetric Engineering and Remote Sensing. 2003. 69 (1) 59-68.
- Grodecki, J., Dial, G., and Lutes, J., 2004: *Mathematical Model for 3d Feature Extraction from Multiple Satellite Images described by RPCs*. ASPRS Annual Conference Proceedings May 2004, Denver, Colorado.
- Hanley, H.B. and Fraser, C.S. *Sensor Orientation for High-Resolution Satellite Imagery: Further Insights into Bias-Compensated RPCs*. International Archives of the Photogrammetry, Remote Sensing and Spatial Information Sciences. 2004. 35 (B1) 24-29.
- Morgan, M., 2004: *Epipolar Resampling of Linear Array Scanner Scenes*. Ph.D. Dissertation, Department of Geomatics Engineering, University of Calgary, Canada.
- Morgan, M., Kim, K., Jeong, S., and Habib, A., 2004: *Indirect Epipolar Resampling of Scenes using Parallel Projection Modeling of Linear Array Scanners*. XXth Congress of ISPRS. July 2004.
- Okamoto, A., Fraser, C., Hattori, S., Hasegawa, H., and Ono, T. *An Alternative Approach to the Triangulation of Spot Imagery*. International Archives of Photogrammetry and Remote Sensing. 1998. 32 (B4) 457-462.
- Tao, C.V. and Hu, Y. *A Comprehensive Study of the Rational Function Model for Photogrammetric Processing*. Photogrammetric Engineering and Remote Sensing. 2001. 67 (12) 1347-1357.
- Valadan Zoej, M.J. and Petrie, G. *Mathematical Modeling and Accuracy Testing of Spot Level 1b Stereo-Pairs*. Photogrammetric Record. 1998. 16 (91) 67-82.
- Willneff, J., Weser, T., Rottensteiner, F., and Fraser, C.S. *Precise Georeferencing of Cartosat Imagery via Different Orientation Models*. The International Archives of the Photogrammetry, Remote Sensing and Spatial Information Sciences. 2008. 37 (B1) 1287-1294.

Population Estimation in an Urban Area with Remote Sensing and Geographical Information Systems

Dimitris Kaimaris¹ and Petros Patias²

¹School of Spatial Planning and Development (Eng.) Aristotle University of Thessaloniki, Greece

²School of Rural and Surveying Engineering, Aristotle University of Thessaloniki, Greece

Publication Date: 27 June 2016

DOI: <https://doi.org/10.23953/cloud.ijarsg.61>



Copyright © 2016 Dimitris Kaimaris and Petros Patias. This is an open access article distributed under the **Creative Commons Attribution License**, which permits unrestricted use, distribution, and reproduction in any medium, provided the original work is properly cited.

Abstract Population estimation with questionnaires and demographic models is time consuming and usually accompanied by high costs. Geoinformation tools constitute key tools towards the solution of this problem, and, therefore, studies have started to emerge in the early 70s. In this paper a brief reference to the methods of population estimation, which are based totally or in combination with statistical analysis methods on products of Remote Sensing and their processing with GIS is cited. Afterwards, the capability of stereoscopic satellite images of high spatial resolution for the determining of the height of buildings and the performance of their plans, which are essential data for the estimation of the population of each building is highlighted. The study area is the municipality of Thessaloniki (Northern Greece, Region of Central Macedonia), and the estimation accuracy of the population reaches 97.06%.

Keywords *Population Estimation; Remote Sensing; Ikonos-2; DSM; DTM; GIS*

1. Introduction

In Greece, the responsible principal for the documentation of the population census is the Greek Statistical Authority (ELSTAT). The methodology is costly, time consuming and relies on processing of census/residences questionnaires (method of interview within the respondents residence), in combination with their statistical study and processing.

The last census took place in Greece in 2011, and the preceding one in 2001 (short-term analysis). On the internet, freely available data for 2001 are provided at municipal districts' level (large spatial areas within municipalities); while for 2011 they are provided only at the municipal level (even larger territorial areas, since municipalities consist of districts or sections). Data at building level do not exist at all, and free data at blocks' level are not provided. However, apart from the demographic models for population estimation, Remote Sensing and Geographic Information Systems (GIS) are also utilized for this purpose.

The benefits of population estimation, beyond urban and regional planning, are obvious and have been described in many studies (Smith and Mandell, 1984; Benn, 1995; Smith et al., 2002; Liu, 2003;

Qiu et al., 2003; Lang et al., 2010; Deng et al., 2010). The estimation of daytime population, which is required, for example, in the case of constructing an evacuation plan of a city during rush hours, is currently difficult to tools of geoinformatics. The first attempts to estimate the residential population by means of Remote Sensing (and with the help of Geographical Information Systems, GIS) started in the 70s. The methodologies are distinguished, according to Wu et al. (2005), in areal interpolation methods (with subcategories auxiliary information are used) and statistical modeling methods (with subcategories based on the relationship between the population with urban areas, land uses, characteristics of satellite imagery and other natural or socio-economic characteristics).

An improvement of areal interpolation methods is the implementation of Pycnophylactic interpolation, dasymetric-mapping method or/and a combination of both (Langford, 2006; Mennis and Hultgren, 2006; Kim and Yao, 2010).

As far as statistical modeling methods are concerned, ordinary least squares (OLS) regression is the most commonly used method, while geographically weighted regression (GWR) provides better results (Harvey, 2002; Qiu et al., 2003; Wu and Murray, 2007; Dong et al., 2010; Deng et al., 2010).

The methodologies that include processing (eg classification) of satellite images for the exportation of dwelling units (and other coverages) give better population estimation results (Lo, 1995; Harvey, 2002; Wu et al., 2005; Li and Weng, 2005; Bagan and Yamagata, 2015). Nighttime images from the Defense Meteorological Satellite Program's Operational Linescan System (DMSP OLS) and the International Space Station (ISS) have been combined with census population data, and by the use of simple linear regression methods it has been proved that there is a correlation between the intensity of pixel brightness and the population data, but the assessment of both the urban population and its density is not satisfactory. Progress is expected due to their spatial resolution improvement beyond today's 50 m (Sutton, 1997; 2003; Anderson et al., 2010). In conclusion, through the visual interpretation of images (Lo, 1986; Yagoub, 2006) for the detection of dwelling units, the insertion of remote sensing products in predictive mathematical models (Al-Garni, 1995; Qiu et al., 2003), the correlation of specific spectral regions with urban space and, therefore, the population (Iisaka and Hegedus, 1982; Lo, 1995; Harvey, 2002; Li and Weng, 2005; Joseph et al., 2012; Zhu et al., 2015), and the statistical analysis and combination of demographic data with the Earth's surface coverages (Qiu et al., 2003; Lo, 2008; Avelar et al., 2009; Dong et al., 2010; Deng et al., 2010; Mao et al., 2012; Zhu et al., 2015), Remote Sensing is a powerful tool on the supply of data for assessment procedures on residential population (Tatem et al., 2007; Doll, 2008; Chand et al., 2009; Azar et al., 2010). The improvement of the spatial resolution of (daytime) satellite images (Yagoub, 2006; Lang et al., 2010), the use of object-orientated classification (Lang, 2010; Silvan-Cardenas et al., 2010) for land coverages exportation, and the utilization of Lidar data (Lu et al., 2006; Wu et al., 2008; Xie et al., 2008; Aubrecht et al., 2009; Chen et al., 2009; Silvan-Cardenas et al., 2010; Lu et al., 2010; Dong et al., 2010), which enable both the identification and rendering of the outline of the buildings and the correlation of their height with the population have helped towards this direction.

However, the supply of Lidar data is accompanied by high costs. It would be advantageous to use stereoscopic satellite images, which could provide a twofold benefit as it would allow the production of the necessary DSM (Digital Surfaces Model) for the extraction of building heights and the differentiation of buildings through image classification. This study moves towards this direction (use of stereoscopic images), where an effort is made to assess the population with the urban limits of the Municipality of Thessaloniki (Greece, Figure 1). The spatial processing of satellite images aims at the identification of the location and height of each building, information which will be used for the population assessment with the use of GIS. Moreover, the population census information will be used to verify the final result.

2. Study Area

The prefecture of Thessaloniki (Central Macedonia, Greece, Figure 1 and 2) has a population of 1,110,312 residents (census of ELSTAT 2011), essentially concentrating 9.4% of the Country's population. The Municipality of Thessaloniki (Figure 2), which will be the study area, is the second largest municipality of Greece. The former plan "Kapodistrias" (1997-2010, a plan for the optimization of public administration at local government level) divided the municipality in 5 municipal districts (Figure 3). The existing plan "Kallikratis" (2011 until present), on the one hand, merged municipalities so as to create larger administrative entities and, on the other hand, renamed from municipal districts to municipal units. The population estimation of the municipality of Thessaloniki through remote sensing and GIS cannot utilize population data from the municipal section of the historical center of the city (identified with the municipal district 1 in Figure 3), and this is due to the pure commercial use of the buildings. In fact, only a small percentage of the buildings in the historical center appear to be residential. The last population census (ELSTAT) of the historical center (and all municipal districts of the country) was conducted in 2001. In the new 2011 census, population information appears only at municipality level and not at municipality unit level. Therefore, comparative data for the municipality of Thessaloniki, deducting the population of the historical center, can be retrieved only for the census of 2001. Specifically, according to the census of 2001, the municipality of Thessaloniki has a population of 363,987 and the municipal district of the historical center (1 in Figure 3) has a population of 53,017. Therefore, the population of the municipal districts 2 to 5 (Figure 3) of the municipality of Thessaloniki is 310,970.



Figure 1: Thessaloniki's position in Greece



Figure 2: With dotted line are the boundaries of the Region of Central Macedonia, with green line the boundary of the prefecture of Thessaloniki and with red line the municipality of Thessaloniki

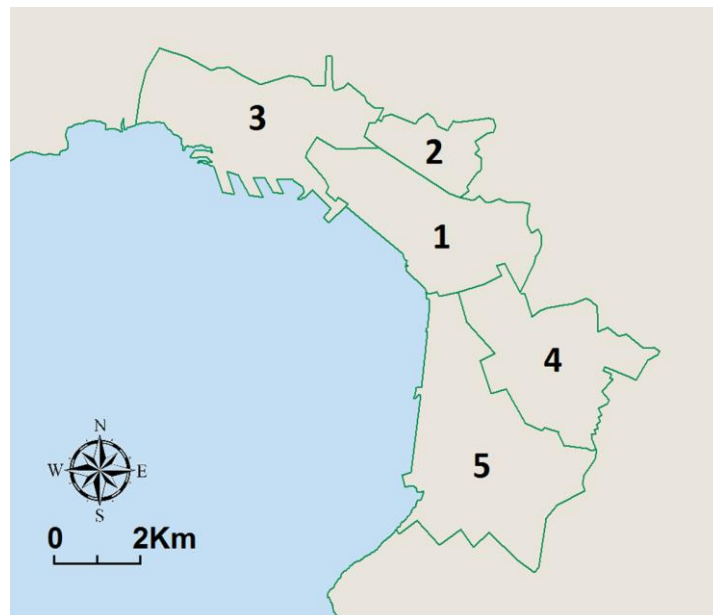


Figure 3: The municipal districts 1 to 5 of Thessaloniki

Subsequently in this study satellite images before 2011 will be used for the exportation of suitable products, which after their insertion and processing in GIS will allow the population estimation of the municipality of Thessaloniki (without the historic center). The result will be compared with the population of 310,970, which was mentioned at the end of the previous paragraph.

3. Methodology of Population Estimation

To begin with, the empirical equation (Eq.1) which was created for the population estimation of each building is presented, and afterwards the way that Remote Sensing and GIS allow for the export and processing of the necessary data.

$$\text{Building population} = \frac{(NFB - A) * E_{\text{building}}}{E_{\text{person}}} \tag{1}$$

Where NFB = Number of Floors of the Building = $\frac{H_{\text{building, max}} - H_{\text{building, min}}}{H_{\text{floor}}}$,

$H_{\text{building, max}}$ the highest altitude of the building,

$H_{\text{building, min}}$ the lowest altitude of the building (building's base altitude),

H_{floor} the nominal height of each floor in m,

A the reduction coefficient for the building floors (Table 1),

E_{building} the area of the building plot, and

E_{person} the average area per capita of each property.

Table 1: Value of the number of floors of the building (NFB) and coefficient A

| NFB Value | A Value | Justification |
|-----------|---------|---|
| 1 | 1 | The category is about ground floor buildings that are ancillary municipal structures, retail use constructions, etc. With value NFB=1 and by the coefficient A = 1 in the building, no population is attached (Eq. 1). |
| 2 | 1 | One of the two floors is the roof of the property. With value NFB=1 and by the coefficient A = 1 in the building, population is attached only to the ground floor (Eq. 1). |
| >2 | 2 | The top floor of the building is the roof that contains the installation and the mechanism of the lift or is the floor of the lifting mechanism installation. The ground floor in the majority of buildings in the municipality of Thessaloniki, in case of NFB> 2, is used for retail, for the parking, etc., and not as a residence. With value NFB>2 and by the coefficient A = 2, the building's ground floor and top floor are excluded from the estimate of the population (Eq. 1). |

Coefficient A values in Table 1 are adjusted each time in each study area, according to construction rationale of buildings and the use of the floors. Random selection of A values brings population results that have nothing to do with reality.

In equation (1) $H_{\text{floor}} = 3.5m$, and according to Greek urban planning standards (FEK 285/5 March 2004, states that "the accepted indicator, under the applied program for sustainable development, for the first residence is considered to vary between 28-45 sqm / person") the average area per capita is $E_{\text{person}} = 36.5$ sqm. So the equation (1) transforms in:

$$\text{Building population} = \frac{(\frac{H_{\text{building, max}} - H_{\text{building, min}}}{3.5} - A) * E_{\text{building}}}{36.5} \tag{2}$$

Through the classification of satellite images the identification and the extraction of each building plan of the city can be conducted. The result will be the calculation of the area of each building plan (E_{building}), while through the processing of stereoscopic satellite images the DSM (Digital Surface Model) and DTM (Digital Terrain Model) of the city will be determined. These products, after their insertion in GIS will allow for the calculation of the maximum (from DSM) and the minimum altitude

(from DTM) of each building. Then utilizing equation (2) and Table 1 (A coefficient), the processing of the population estimation of each building can be conducted (Figure 4).

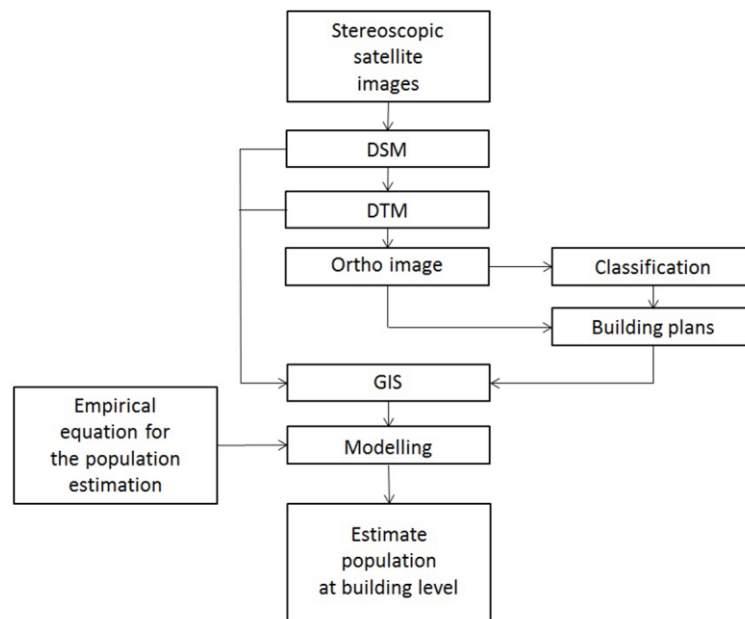


Figure 4: The flow chart of the operations carried out for population estimation

4. Satellite Data

Stereoscopic satellite data before 2011 and up to 2001 were searched. The used data are presented in Table 2 and Figure 5.

Table 2: Stereoscopic satellite images

| Type | Acquisition Date/Time | Bands | Nominal Collection Elevation | Spatial resolution |
|----------|-------------------------|--------|------------------------------|--------------------|
| Ikonos-2 | 2008-07-18 09:23 GMT | RGBNIR | 69.24175 degrees | 1 m |
| Ikonos-2 | 2008-07-18 09:23 GMT | RGBNIR | 74.73024 degrees | 1 m |

5. Processing of Satellite Images

5.1. Production of DSM, DTM and Ortho Satellite Images

For the satellite triangulation, fractional polynomials (RPC) of satellite images were used, 12 GCPs (Ground Control Points) and 13 CPs (Check Points, Figure 6), which were measured in the field with horizontal and vertical accuracy of 10 cm and 20 cm respectively. The utilized software was LPS 2011[®] (a photogrammetric suite of Erdas Imagine 2011[®]).

According to the results of the satellite triangulation, the marking precision in satellite images is:

$$\sigma_o = 0.305 \text{ pixel} = 0.3m, \text{ as } 1 \text{ pixel} = 1m.$$

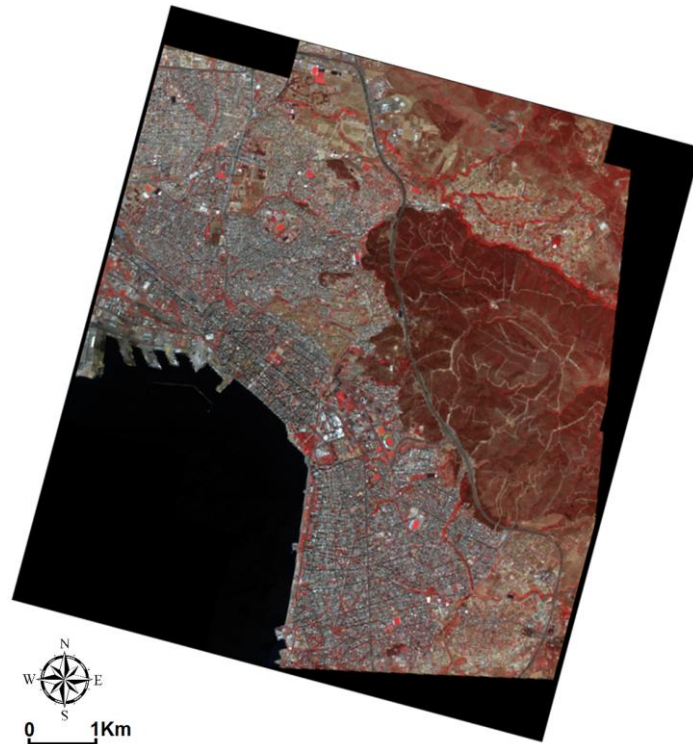


Figure 5: The satellite image of stereo pair Ikonos-2, RGBNIR

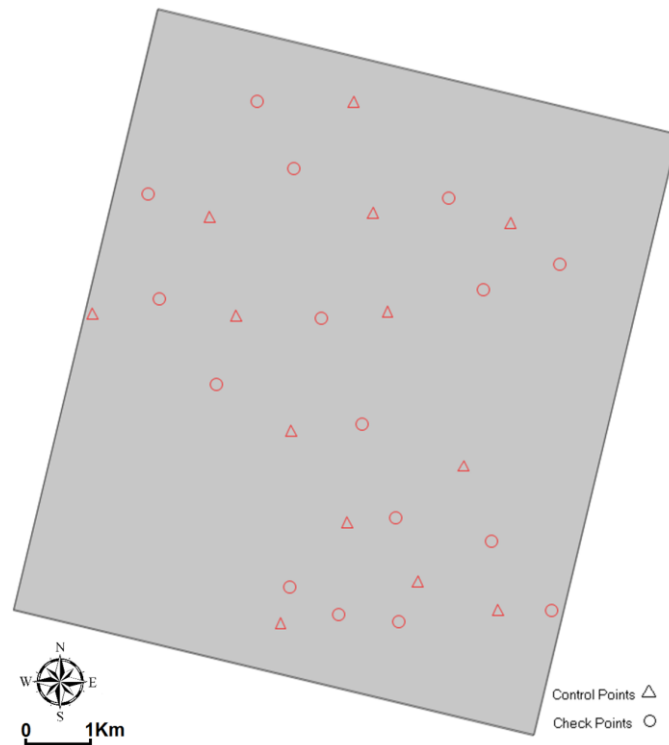


Figure 6: Distribution of GCPs and CPs in the stereoscopic images

For Check Points (CPs) the horizontal and vertical standard deviation is:

$$\sigma_{XY,triang.} = \sqrt{0.851^2 + 1.041^2} = 1.34m$$

and

$$\sigma_{z,triang.} = \sigma_z = 1.36m$$

Afterwards, during the production of DSM (Figure 7) Table 3 was calculated for the entire usable area of stereo images.

Table 3: Accuracy Information: General Mass Point Quality

| | |
|------------|---------|
| Excellent | 56.86 % |
| Good | 31.30 % |
| Fair | 0.00 % |
| Isolated | 0.00 % |
| Suspicious | 11.84 % |

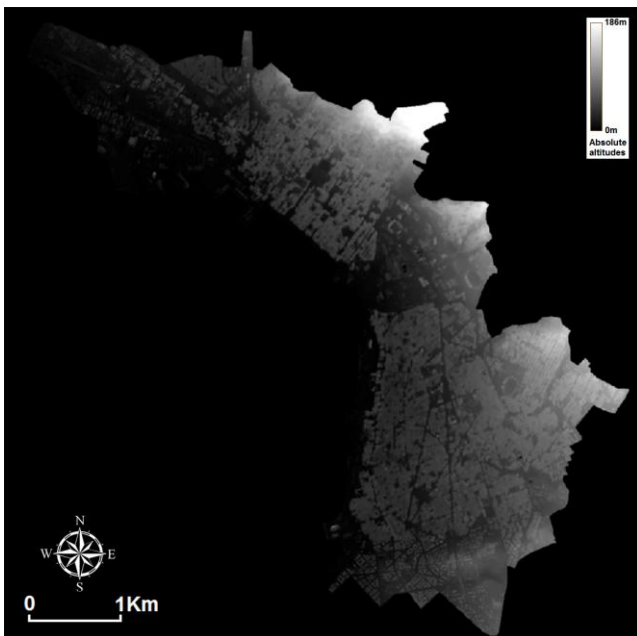


Figure 7: The DSM of the Municipality of Thessaloniki, Greece

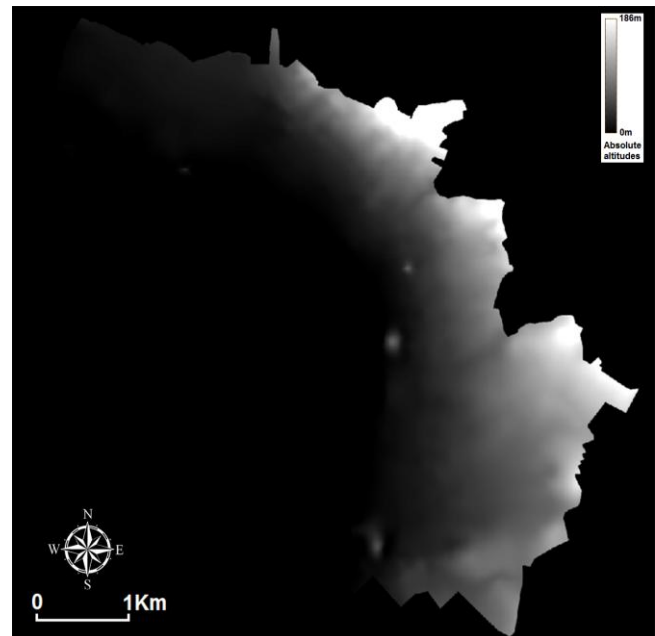


Figure 8: The DTM of the Municipality of Thessaloniki, Greece

The assessment of the necessary for this research variation of altitude differences follows. The assessment of altitude differences is retrieved from the equation:

$$\hat{\Delta}z = \frac{\sum_{i=1}^n \delta z_i}{n} = \frac{\sum_{i=1}^n |z_{DSM,i} - z_{CP,i}|}{n}$$

where δz_i represents the differences in the altitudes of check points within the calculated *DSM* and the field, $z_{DSM,i}$ the altitudes of check points within the calculated *DSM*, $z_{CP,i}$ the altitudes of check points measured in the field, and n the number of observations.

Thus: $\hat{\Delta z} = 1.3m$

For the assessment of the standard deviation of altitude differences the following equation is used:

$$\hat{\sigma} = \sqrt{\frac{1}{n-1} \sum_{i=1}^n (\hat{z}_i - \hat{\Delta z})^2} = \sqrt{\frac{1}{n-1} \sum_{i=1}^n (|z_{DSM,i} - z_{CP,i}| - \hat{\Delta z})^2}$$

and eventually results in:

$$\hat{\sigma} = 0.9m$$

However, it is necessary that: $\hat{\sigma} \leq \sigma_{DSM} = 2 \frac{h}{b} \sigma_o$

Where σ_{DSM} is the expected accuracy of the generated *DSM* , h the vertical distance of the stereo pair from the stereoscopic central point on the ground, and b the base of the stereo pair.

For a calculation of the ratio $\frac{h}{b}$ angles of the satellite images acquisition (Nominal Collection Elevation) are used. Table 2 provides the relative information:

$$A_1 = 69.24175 \text{ degrees and } A_2 = 74.73024 \text{ degrees.}$$

Angle A_3 (Figure 9) is derived as follows:

$$A_3 = 180^\circ - (A_1 + A_2) = 36.02801 \text{ deg rees}$$

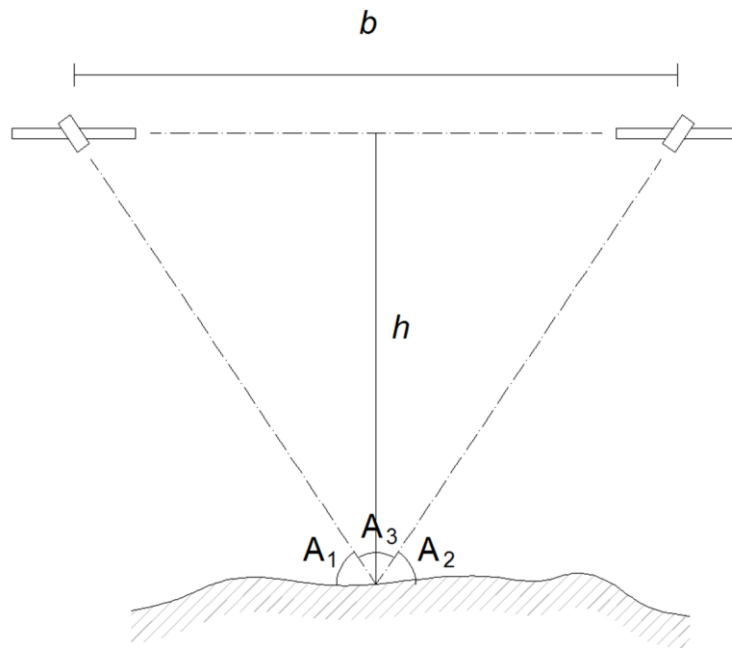


Figure 9: The acquisition angles, the base of the stereo pair and the vertical distance of the stereo pair from the main stent point

The base of the stereo pair is the basis of a theoretical isosceles triangle (due to long distances the two sides of the triangle are considered equal), and thus:

$$\tan \frac{A_3}{2} = \frac{b/2}{h} \Rightarrow \frac{h}{b} = \frac{1}{2 \tan \frac{A_3}{2}}$$

Where eventually is calculated that: $\frac{h}{b} = \frac{1}{0.65}$

Replacing the calculated values it becomes clear that the test is valid, as:

$$\hat{\sigma} \leq \sigma_{DSM} = 2 \frac{h}{b} \sigma_o = 2 \frac{1}{0.65} 0.305 = 0.94m \Rightarrow 0.92m < 0.94m$$

There after the assessment of the standard deviation of the estimated height differences (standard error of height differences) is calculated:

$$\hat{\sigma}_{\Delta z} = \frac{\hat{\sigma}}{\sqrt{n}}$$

$$\hat{\sigma}_{\Delta z} = 0.23m$$

The confidence interval for the actual height differences Δz is:

$$\hat{\Delta z} - \hat{\sigma}_{\Delta z} t_{n-1}^{\alpha/2} < \Delta z \leq \hat{\Delta z} + \hat{\sigma}_{\Delta z} t_{n-1}^{\alpha/2}$$

In the case of normal distribution, and especially in the case of t distribution. That calculation was A confidence factor of $1 - \alpha = 0.90$ (probability 90%) was set for the calculations, i.e. $\frac{\alpha}{2} = 0.05$. Also, $n - 1 = 15$. Therefore:

$$t_{n-1}^{\alpha/2} = t_{15}^{0.05} = 1.753$$

Resulting in:

$$P(0.91m < \Delta z \leq 1.70m) = 0.90$$

The above interval of values is acceptable for research, as each floor has a nominal height of 3.5m (from the confidence interval max = 1.70m $< \frac{1}{2}$ of 3.5m), i.e. such floor cannot be excluded from calculations. The creation of DTM follows by utilizing strategies of buildings removal and keeping the altitudes of the ground surface (Xu et al., 2008; Stournara et al., 2015) (Figure 8). The DSM and DTM were transformed in shapefile (or shp file) in the same software. The process was completed by the production of the ortho satellite image within the limits of the municipality, with a spatial resolution of 1m (Figure 10).



Figure 10: Ortho satellite image Ikonos-2, 1: B, 2:G, 3:NIR, within the limits of the municipality of Thessaloniki. with dotted line is the historic center of the city, which was excluded by the research

5.2. Buildings Identification-Supervised Classification

Supervised classification in Erdas Imagine 2011[®] was undertaken (Figure 11) on the generated ortho image within the limits of the municipality. A total of 27 classes of covers were used (11 buildings classes, 6 road classes, 4 land classes, 4 urban green classes, 1 class for shadow, and 1 class for water). The result on the accuracy of the classification is: Classification accuracy 81.58%, Kappa Statistics = 0.8118 (Masek et al., 2000; Ward et al., 2000; Zhang et al., 2002; Xian and Crane, 2005; Yuan et al., 2005; Lu and Weng, 2005; Xu, 2007; Lee et al., 2010; Ukwattage and Dayawansa, 2012). The outlines of the buildings were converted into shp file in the same software.

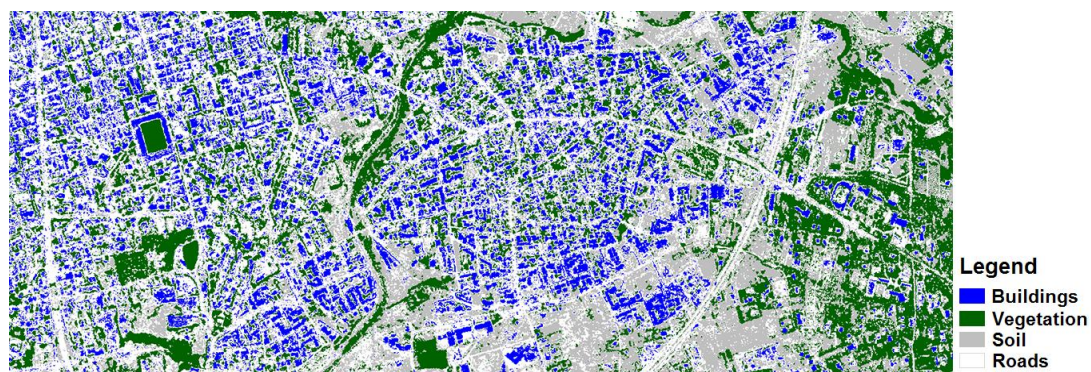


Figure 11: Abstract from the supervised classification. In blue color are the buildings, in white the roads, in gray the soil and in green the vegetation

6. Import of Remote Sensing Products in GIS, and Population Estimation

The shp files of the DSM, DTM and outlines of the buildings were imported in ArcMap[®]. In about 70% the separation of the adjacent buildings of the same kind was not allowed. For example, two buildings that are in contact and have the same shell coverage appeared as a single building in the final shp file. Such buildings may actually have different number of floors, therefore, could not be used to estimate

the population. Moreover, many roofs have different shell coverages, which also do not allow the accurate demarcation of the building plans. Finally, false detections of buildings and / or buildings that were not identified by the classification were spotted. Therefore, 85% (approximately) of the buildings of the study area were re-digitized in GIS with the help of ortho image (Figure 10). Then, purely public services, education, health, shopping malls, etc. were removed, keeping only the structures which are inhabited. The creation of the dynamic estimation model for the Number of Floors of the Building (NFB) for each building of the municipality of Thessaloniki is the next step (Figure 12).

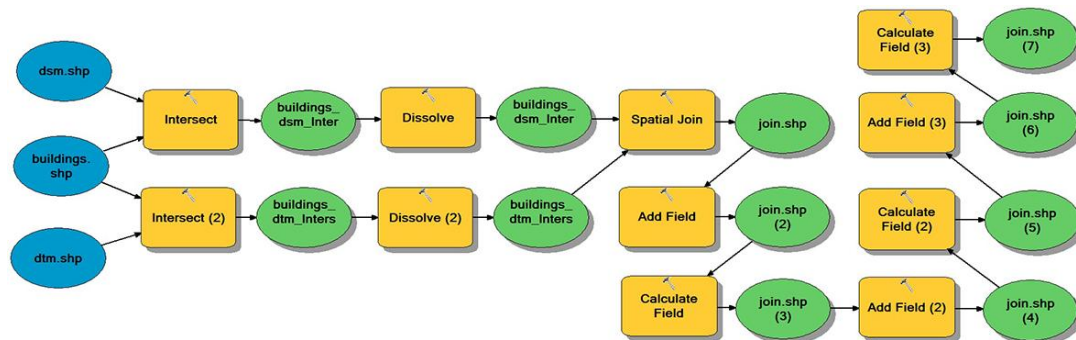


Figure 12: Estimation model for the Number of Floors of the Building (NFB)

According to the model, initially the intersection (Figure 12: Intersect, Figure 13c) of each building (Figure 13b) with DSM polygons (Figure 13a) is calculated. So each building now consists of all contiguous polygons (Figure 13c), each having the same or different altitude with the rest. Then, all polygons of each building are consolidated (Figure 12: Dissolve, Figure 13d), thereby yielding the border, while the total altitude of the original polygons is selected and the highest altitude of the building is maintained. The same procedure is conducted for the DTM, while, at the end, from all altitudes of the original polygons the smallest is selected and maintained for the building. Afterwards, the two new shp files are joined (Figure 12: Spatial Join) so as to produce a building file that contains the lowest and the highest altitude of each building. A new field (area, Figure 12: Add Field, join.shp (2)) is then created for the calculation of each building's area (Figure 12: Calculate Field, join.shp (3)), and a new field (NFB) for the estimation of the number of floors of each building (Figure 12: Add Field (2), join.shp (4), Calculate Field (2), join.shp (5)). At this point the results of NFB might be decimal numbers, and this is due to the estimation error of altitude differences which was described in preceding paragraphs. However, as already described, it is impossible to erase a floor. These errors can lead to decimal numbers of floors, which can then yield integer floors, if they are rounded to the nearest integer (eg NFB = 4.65 -> NFB true = 5 or NFB = 6.35 -> NFB true = 6). For this reason another field (NFB true) was created for the calculation of integer number of the floors of each building (Figure 12: Add Field (3), join.shp (6), Calculate Field (3), join.shp (7)).

The export of the attribute table of the shp file of buildings (including NFB true field) to excel followed, where the calculation of the population utilizing estimation equation (2) was performed. Rounding of the each building's population to the nearest integer was carried out (eg if the estimated population of the building is 21.12 then the final value is 21 or if the population is estimated up to 45.78 then the final value is 46), and the procedure lead to the value of 301,814. The difference from 2001 census (population 310,970) is 2.94%.

Additionally, new additional information can be drawn (Table 4). The structured surface of 20.601 buildings of the Municipality of Thessaloniki (apart from the historic center) is 3.66 km². The total volume of constructions is 75,297,940 m³. Finally, maps on the number of floors and the population per building (Figure 14 and 15 respectively) of the municipality of Thessaloniki (excluding the historical center) were created.

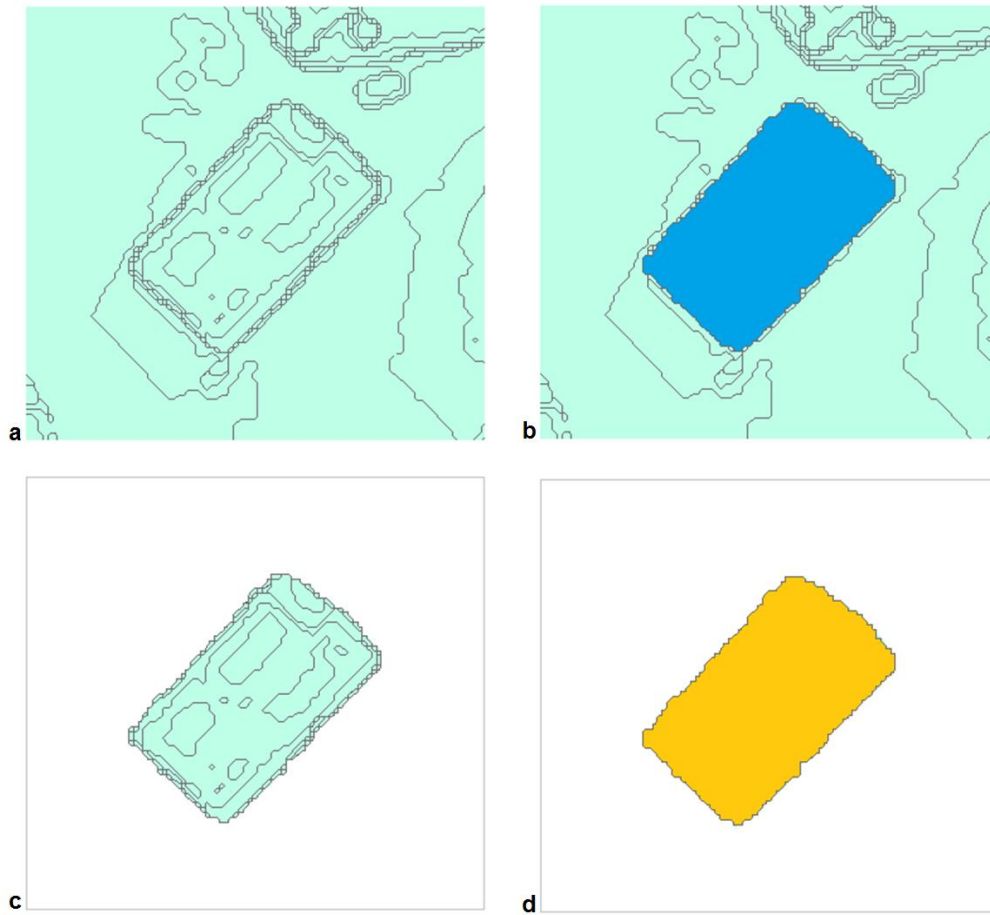


Figure 13: a. Polygons of DSM, b. the overlay of the building, c. the intersection of the building with the DSM (the building consists of contiguous polygons), and d. polygon outline of the building by keeping the higher altitude

Table 4: The distribution (percentages) of floors over buildings of the Municipality of Thessaloniki (apart from the historic center)

| Floor | Percentages of buildings with respective floors |
|--------------|---|
| Ground floor | 3.90 % |
| 2-storey | 6.00 % |
| 3-storey | 9.81 % |
| 4-storey | 9.17 % |
| 5-storey | 26.32 % |
| 6-storey | 18.85 % |
| 7-storey | 18.11 % |
| 8-storey | 4.76 % |
| 9-storey | 3.02 % |
| 10-storey | 0.05 % |
| 12-storey | 0.01 % |



Figure 14: Abstract of the study area. Number of floors per building



Figure 15: Abstract of the study area. Population per building

7. Conclusions

Studies on population estimation with geoinformatics tools date back to the early 70s. Among all developed methodological approaches up to date, those that are based on high resolution satellite image processing, in combination with statistical analysis of remote sensing products, as geographically weighted regression (GWR), usually provide better results. Errors occur when building altitudes are disregarded, a fact that is treated nowadays by the use of high resolution Lidar data. However, due to the cost of Lidar data, the study proposes and demonstrates that the use of modern stereo satellite images of high spatial resolution (lower cost) results in high-precision buildings' altitude data, apart from their automated extraction of their building plans through classification.

This study takes place in the city of Thessaloniki, within the limits of its municipality. Its historic center is excluded due to its almost total commercial use of buildings.

Stereoscopic satellite images of high spatial resolution Ikonos-2 processing, led to the calculation of buildings altitudes with accuracy between 0.91m to 1.70m, an interval which is considered satisfactory

as it marginally does not allow the exclusion of one floor (standard floor height 3.5m). Also, the produced ortho image of the study area has horizontal accuracy of about 1.35m.

Supervised classification was conducted on the ortho satellite image to identify and extraction of the building plans. Where the detection and / or the extraction of the building plans were incorrect, they were extracted manually in GIS.

GIS is a valuable tool for processing and analyzing of remote sensing products, modeling the procedures for the assessment of the population, and presentation of research results. Utilizing the above remote sensing products and the empirical equation developed to calculate population per building, the estimation of the population for the municipality of Thessaloniki reaches 97.06%.

The following research refers to tests on the estimation of the population on block level in city areas with different population density, and in areas with mixed use (commercial and residential). Tests on population change as a function of value changes of the coefficients of the empirical equation will be conducted as well.

References

- Al-Garni, A.M. *Mathematical Predictive Models for Population Estimation in Urban Areas using Space Products and GIS Technology*. Mathematical and Computer Modeling. 1995. 22; 95-107.
- Anderson, J.S., Tuttle, B.T., Powell, R.I., and Sutton, C.P. *Characterizing Relationships between Population Density and Nighttime Imagery for Denver, Colorado: Issues of Scale and Representation*. International Journal of Remote Sensing. 2010. 31 (21) 5733-5746.
- Aubrecht, C., Steinnocher, K., Hollaus, M., and Wagner, W. *Integrating Earth Observation and GIScience for High Resolution Spatial and Functional Modeling of Urban Land Use*. Computers, Environment and Urban Systems. 2009. 33; 15-25.
- Avelar, S., Zah, R., and Tavares-Correa, C. *Linking Socioeconomic Classes and Land Cover Data in Lima, Peru: Assessment Through the Application of Remote Sensing and GIS*. International Journal of Applied Earth Observation and Geoinformation. 2009. 11; 27-37.
- Azar, D., Graesser, J., Engstrom, R., Comenetz, J., Leddy, R.M., Schechtman, N.G., and Andrews, T. *Spatial Refinement of Census Population Distribution using Remotely Sensed Estimates of Impervious Surfaces in Haiti*. International Journal of Remote Sensing. 2010. 31 (21) 5635-5655.
- Bagan, Yamagata. *Analysis of Urban Growth and Estimating Population Density using Satellite Images of Nighttime Lights and Land-Use and Population Data*. GISRS. 2015. 52; 765-780.
- Benn, H., 1995: *TCRP Synthesis of Transit Practice 10: Bus Route Evaluation Standards*. Technical Report, Transportation Research Board, National Research Council, Washington, DC.
- Chand, T.R.K., Badarinath, S.V.K., Elvidge, D.C., and Tuttle, T.B. *Spatial Characterization of Electrical Power Consumption Patterns over India using Temporal DMSPOLS Night-Time Satellite Data*. International Journal of Remote Sensing. 2009. 30: 647-661.
- Chen, Y., Su, W., Li, J., and Sun, Z. *Hierarchical Object Oriented Classification using Very High Resolution Imagery and LiDAR Data Over Urban Areas*. Advances in Space Research. 2009. 43; 1101-1110.

Deng, C., Wu, C., and Wang, L. *Improving the Housing-Unit Method for Small-Area Population Estimation Using Remote-Sensing and GIS Information*. International Journal of Remote Sensing. 2010. 31 (21) 5673-5688.

Doll, N.H.C., 2008: *CIESIN Thematic Guide to Night-Time Light Remote Sensing and Its Applications*. Available online at: http://sedac.ciesin.columbia.edu/binaries/web/sedac/thematic-guides/ciesin_nl_tg.pdf.

Dong, P., Ramesh, S., and Nepali, A. *Evaluation of Small-Area Population Estimation using LiDAR, Landsat TM and Parcel Data*. International Journal of Remote Sensing. 2010. 31 (21) 5571-5586.

Harvey, J.K. *Population Estimation Models Based on Individual TM Pixels*. Photogrammetric Engineering and Remote Sensing. 2002. 68; 1181-1192.

Iisaka, J. and Hegedus, E. *Population Estimation from Landsat Imagery*. Remote Sensing of Environment. 1982. 12; 259-272.

Joseph et al. *Using Landsat Imagery and Census Data for Urban Population Density Modeling in Port-au-Prince, Haiti*. GISRS. 2012. 49; 228-250.

Kim, H. and Yao, X. *Pycnophylactic Interpolation Revisited: Integration with the Dasymetric-Mapping Method*. International Journal of Remote Sensing. 2010. 31 (21) 5657-5671.

Lang, S., Tiede, D., Holbling, D., Fureder, P., and Zeil, P. *Earth Observation (EO)-based Ex Post Assessment of Internally Displaced Person (IDP) Camp Evolution and Population Dynamics in Zam Zam, Darfur*. International Journal of Remote Sensing. 2010. 31 (21) 5709-5731.

Langford, M. *Obtaining Population Estimates in Non-Census Reporting Zones: An Evaluation of the 3-Class Dasymetric Method*. Computers, Environment and Urban Systems. 2006. 30; 161-180.

Lee, A.J., Lee, S.S., and Chi, K.H., 2010: *Development of an Urban Classification Method using A Built-Up Index*. Selected Topics in Power Systems and Remote Sensing, Japan. 39-43.

Li, G. and Weng, O. *Using Landsat ETM Imagery to Measure Population Density in Indianapolis, Indiana, USA*. Photogrammetric Engineering & Remote Sensing. 2005. 71 (8) 947-958.

Liu, X., 2003: *Estimation of the Spatial Distribution of Urban Population using High Spatial Resolution Satellite Imagery*. PhD Thesis, University of California, Santa Barbara, CA.

Lo, C.P., 1986: *Accuracy of Population Estimation from Medium-Scale Aerial Photography*. In American Congress on Surveying and Mapping and American Society for Photogrammetry and Remote Sensing, Falls Church, VA. 1-10.

Lo, C.P. *Automated Population and Dwelling Unit Estimation from High-Resolution Satellite Images: a GIS Approach*. International Journal of Remote Sensing. 1995. 16: 17-34.

Lo, C.P. *Population Estimation using Geographically Weighted Regression*. GIScience and Remote Sensing. 2008. 45; 131-148.

Lu, D. and Weng Q. *Urban Classification Using Full Spectral Information of Landsat ETM+ Imagery in Marion County, Indiana*. Photogrammetric Engineering & Remote Sensing. 2005. 71 (11) 1275-1284.

- Lu, D., Weng, Q., and Li, G. *Residential Population Estimation using a Remote Sensing Derived Impervious Surface Approach*. International Journal of Remote Sensing. 2006. 27; 3553-3570.
- Lu, Z., Im, J., Quackenbush, L., and Halligan, K. *Population Estimation Based On Multi-Sensor Data Fusion*. International Journal of Remote Sensing. 2010. 31 (21) 5587-5604.
- Masek, J.G., Lindsay, E.F., and Goward, N.S. *Dynamics of Urban Growth in the Washington DC Metropolitan Area, 1973-1996, from Landsat Observations*. International Journal of Remote Sensing. 2000. 21; 3473-3486.
- Mennis, J. and Hultgren, T. *Intelligent Dasymetric Mapping and Its Application to Areal Interpolation*. Cartography and Geographic Information Science. 2006. 33; 179-194.
- Mao et al. *Using Land Use Data to Estimate the Population Distribution of China in 2000*. GISRS. 2012. 49; 822-853.
- Qiu, F., Woller, K.L., and Briggs, R. *Modeling Urban Population Growth from Remotely Sensed Imagery and TIGER GIS Road Data*. Photogrammetric Engineering & Remote Sensing. 2003. 69 (9) 1031-1042.
- Shuo-sheng, W., Xiaomin, Q., and Wang, Le. *Population Estimation Methods in GIS and Remote Sensing: A Review*. GIScience and Remote Sensing. 2005. 42 (1) 58-74.
- Silvan-Cardenas, L.J., Wang, L., Rogerson, P., Wu, C., Feng, T., and Kamphaus, D.B. *Assessing Fine-Spatial-Resolution Remote Sensing For Small-Area Population Estimation*. International Journal of Remote Sensing. 2010. 31 (21) 5605-5634.
- Smith, S., and Mandell, M. *A Comparison of Population Estimation Methods: Housing Unit versus Component II, Ratio Correlation, and Administrative Records*. Journal of the American Statistical Association. 1984. 79 (386) 282-289.
- Smith, S., Nogle, J., and Cody, S. *A Regression Approach to Estimating the Average Number of Persons per Household*. Demography. 2002. 39; 697-712.
- Stournara, P., Georgiadis, C., Kaimaris, D., Tsakiri-Strati, M., and Tsioukas, V., 2015: *Feature Extraction from Geoeye-1 Stereo Pairs Data for Forested Area*. In Proceedings the 36th International Symposium on Remote Sensing of Environment, Berlin, Germany, ISRSE36-67-2.
- Sutton, P.C. *Modeling Population Density Using Nighttime Satellite Imagery and GIS*. Computers, Environment and Urban Systems. 1997. 21; 227-244.
- Sutton, P.C. *An Empirical Environmental Sustainability Index Derived Solely from Nighttime Satellite Imagery and Ecosystem Service Values*. Population and Environment. 2003. 24; 293-312.
- Tatem, A.J., Noor, M.A., Vonhagen, C., Digregorio, A., and Hay, S. *High Resolution Population Maps For Low Income Nations: Combining Land Cover and Census in East Africa*. PloS ONE. 2007. 2; e 1298.
- Ukwattage, L.N. and Dayawansa, N.D.K. *Urban Heat Islands and the Energy Demand: An Analysis for Colombo City of Sri Lanka Using Thermal Remote Sensing Data*. International Journal of Remote Sensing and GIS. 2012. 1 (2) 124-131.

- Ward, D., Phinn, S.R., and Murray, A.T. *Monitoring Growth in Rapidly Urbanizing Areas Using Remotely Sensed Data*. Professional Geographers. 2000. 52 (3) 371-386.
- Wu, C. and Murray, T.A. Population Estimation using Landsat Enhanced Thematic Mapper Imagery. *Geographical Analysis*. 2007. 39; 26-43.
- Wu, S., Wang, L., and Qiu, X. *Incorporating GIS Building Data and Census Housing Statistics for Sub-Block-Level Population Estimation*. The Professional Geographer. 2008. 60; 121-135.
- Xian, G. and Crane, M. *Assessment of Urban Growth in the Tampa Bay Watershed using Remote Sensing Data*. *Remote Sensing of Environment*. 2005. 97 (2) 203-205.
- Xie, Z., Roberts, C., and Johnson, B. *Object-based Target Search using Remotely Sensed Data: A Case Study in Detecting Invasive Exotic Australian Pine in south Florida*. *ISPRS Journal of Photogrammetry and Remote Sensing*. 2008. 63; 647-660.
- Xu, F., Woodhouse, N., Xu, Z., Marr, D., Yang, X., and Wang, Y. *Blunder Elimination Techniques in Adaptive Automatic Terrain Extraction*. The International Archives of the Photogrammetry, Remote Sensing and Spatial Information Sciences. 2008. Vol. XXXVII. Part B1. Beijing.
- Xu, H. *Extraction of Urban Built-up Land Features from Landsat Imagery Using a Thematic-oriented Index Combination Technique*. *Photogrammetric Engineering & Remote Sensing*. 2007. 73 (12) 1381-1391.
- Yagoub, M.M. *Application of Remote Sensing and Geographic Information Systems (GIS) to Population Studies in the Gulf: A Case of Al Ain City (UAE)*. *Journal of the Indian Society of Remote Sensing*. 2006. 34 (1) 7-21.
- Yuan, F., Sawaya, K.E., Loeffelholz, B.C., and Bauer, M.E. *Land Cover Classification and Change Analysis of the Twin Cities (Minnesota) Metropolitan Area by Multitemporal Landsat Remote Sensing*. *Remote Sensing of Environment*. 2005. 98 (2-3) 317-328.
- Zhang, Q., Wang, J., Peng, X., Gong, P., and Shi, P. *Urban Built-Up Land Change Detection with Road Density and Spectral Information from Multi-Temporal Landsat TM Data*. *International Journal of Remote Sensing*. 2002. 23 (15) 3057-3078.
- Zhu, H., Li, Y., Liu, Z., and Fu, B. *Estimating The Population Distribution in a County Area in China Based on Impervious Surfaces*. *Photogrammetric Engineering & Remote Sensing*. 2015. 81 (2) 155-163.

Identification and Area Measurement of the Built-up Area with the Built-up Index (BUI)

Dimitris Kaimaris¹ and Petros Patias²

¹School of Spatial Planning and Development (Eng.) Aristotle University of Thessaloniki, Greece

²School of Rural and Surveying Engineering, Aristotle University of Thessaloniki, Greece

Publication Date: 29 June 2016

DOI: <https://doi.org/10.23953/cloud.ijarsg.64>



Copyright © 2016 Dimitris Kaimaris and Petros Patias. This is an open access article distributed under the **Creative Commons Attribution License**, which permits unrestricted use, distribution, and reproduction in any medium, provided the original work is properly cited.

Abstract The calculation and determination of the built-up area with the highest possible accuracy is of major importance in urban, suburban and agricultural studies. Until present, different methodologies of satellite image processing in their multispectral space (eg pixel-based classification) have been developed and used in Remote Sensing, allowing the identification and area measurement of the built-up area with very high accuracy. Accordingly, the indexes that have been developed are able to provide the identification and area measurement of the built-up area immediately and quickly, but with less space and measuring accuracy than other methodologies. In this paper the main indexes that are used in Remote Sensing are initially presented. Afterwards, a new index, BUI (Built-Up Index), is presented, whose development is based on the combination of the bands of Landsat ETM+: RED (band 3), SWIR1 (band 5) and SWIR2 (band 7). Its comparison with other indexes takes place in the urban, suburban and agricultural area of a Greek city, and its effectiveness is tested in four other cities (in Greece and Palestine). The results are encouraging, since this index allows the identification of the built-up area more accurately than the others. Finally, the accuracy of area measurement of the built-up area approaches accuracies obtained with other methodologies of Remote Sensing.

Keywords *Landsat ETM+; Built-up Area; Index*

1. Introduction

The identification (location, distribution and size) of the built-up area is of major importance in urban, suburban and agricultural studies. The calculation of its change throughout the time to the detriment of the non-built-up area constitutes a highly important indicator of urban change and environmental degradation (Xian and Crane, 2006; Kaufmann et al., 2007; Xu, 2008; Melesse et al., 2007; Weng, 2008). Remote sensing provides reliable scientific tools for the calculation of the built-up area, using intertemporal satellite images and studying the multispectral space. The main technics on the determination of the built-up area from satellite images utilize neural networks (Seto and Liu, 2003), supervised or unsupervised image classifications (Masek et al., 2000; Ward et al., 2000; Zhang et al., 2002; Xian and Crane, 2005; Yuan et al., 2005; Lu and Weng, 2005; Yang, 2011; Ukwattage and Dayawansa, 2012), object-based classifications (Guindon et al., 2004; Zhou et al., 2012), support vector machines (Huang and Lee, 2004; Melgani and Bruzzone, 2004; Pal and Mather, 2005; Griffiths

et al., 2010; Kamusoko et al., 2013) and Tasseled Cap transformation (Deng and Wu, 2012). Besides the above, the indexes that have been developed up to date for the determination of the built-up area are easy, rapid and, therefore, valuable tools. Their use is independent, they allow the calculation of the built-up area in a simple manner without requiring special previous satellite image processing and, lastly, they utilize multispectral bands in which there is both a strong reflection of the built-up area, and a satisfactory spectral distinction among the Earth's surface different land uses (Xu, 2010). Likewise, the images they create can be used by classification techniques to calculate the built-up area (Xu, 2007; Lee et al., 2010).

In this paper, a new combination of satellite images' bands of Landsat-7 ETM+, which can determine the built-up area as an index (BUI-Built-Up Index) directly and with satisfactory accuracy will be presented. Specifically, the following Bands are utilized: RED (band 3), SWIR1 (band 5) και SWIR2 (band 7). A comparison with the indexes that have been developed up to date is carried out in the urban, suburban and agricultural area of Thessaloniki (Central Macedonia, Greece). Moreover, the cities of Katerini (Central Macedonia, Greece), Corinth and Patras (Peloponnese, Greece) are tested in scope of proving the effectiveness of BUI.

2. Indexes and Study Area

The main Remote Sensing indexes for rapid mapping of built-up areas are the Urban Index (UI) (Kawamura et al., 1996), the Normalized Difference Built-Up Index (NDBI) (Zha et al., 2003), the Index-based Built-Up Index (IBI) (Xu, 2008), the New Built up Index (NBI) (Jieli et al., 2010) and the Enhanced Built-Up and Bareness Index (EBBI) (As-syakur et al., 2012). Landsat ETM+ bands have been used for their calculation, using the spectral regions G, R, NIR, SWIR και TIR. Particularly in the last three (NIR, SWIR και TIR) significant contrast reflection range and absorption in built-up and bare land areas is observed (Herold, 2003; Zha et al., 2003; Herold et al., 2004; Weng, 2008; Lu and Weng, 2006; As-syakur et al., 2012).

The mathematical equations between the bands of Landsat ETM+ images used for the calculation of the above indexes are presented in Table 1. Index IBI is complex, and is derived from indexes NDBI, soil adjusted vegetation index (SAVI) (Huete, 1988) and modified normalized difference water index (MNDWI) (Xu, 2005; Xu, 2006). Moreover, the normalized difference vegetation index (NDVI) can be used in index IBI (Rouse et al., 1973) instead of SAVI, when plant cover is over 30% (Ray, 1994).

Table 1: Index Analysis

| Remote Sensing Indices | Equations between bands (Landsat 7) | |
|---|---|--|
| UI (Urban Index) | $\frac{\text{Band 7} - \text{Band 4}}{\text{Band 7} + \text{Band 4}}$ | |
| NDBI (Normalised Difference Built-Up Index) | $\frac{\text{Band 5} - \text{Band 4}}{\text{Band 5} + \text{Band 4}}$ | |
| IBI (Index-based Built-Up Index) | $\frac{[\text{NDBI} - (\text{SAVI} + \text{MNDWI})/2]}{[\text{NDBI} + (\text{SAVI} + \text{MNDWI})/2]}$ If the plant cover is < 30% | $\frac{[\text{NDBI} - (\text{NDVI} + \text{MNDWI})/2]}{[\text{NDBI} + (\text{NDVI} + \text{MNDWI})/2]}$ If the plant cover is ≥ 30% |
| | $\frac{2\text{Band5}/(\text{Band5} + \text{Band4}) - [\text{Band4}/(\text{Band4} + \text{Band3}) + (\text{Band2}/(\text{Band2} + \text{Band5}))]}{2\text{Band5}/(\text{Band5} + \text{Band4}) + [\text{Band4}/(\text{Band4} + \text{Band3}) + \text{Band2}/(\text{Band2} + \text{Band5})]}$ | |
| NBI (New Built up Index) | $\frac{\text{Band 3} * \text{Band 5}}{\text{Band 4}}$ | |

| | |
|---|--|
| EBBI (Enhanced Built-Up and Bareness Index) | $\frac{\text{Band 5} - \text{Band 4}}{10\sqrt{\text{Band 5} + \text{Band 6}}}$ |
| Band analysis Landsat ETM+ | Band 2: Visible Green (G), Spectral Range: 0.53-0.61 μm |
| | Band 3: Visible Red (R), Spectral Range: 0.63-0.69 μm |
| | Band 4: Near Infrared (NIR), Spectral Range: 0.78-0.90 μm |
| | Band 5: Short Wave Infrared 1 (SWIR1), Spectral Range 1.55-1.75 μm |
| | Band 6: Thermal Infrared (TIR), Spectral Range 10.4-12.5 μm |
| | Band 7: Short Wave Infrared 2 (SWIR2), Spectral Range 2.09-2.35 μm |

The study and application area of Table's 1 indexes is the city of Thessaloniki (Central Macedonia, Greece), and its suburban and agricultural area. Thessaloniki is the second most populated city in Greece. The urban area of Thessaloniki, according to the census of 2011, has 788,952 permanent inhabitants. The prefecture of Thessaloniki has a population of 1,110,312 inhabitants, which corresponds to 9.4% of the national population. The city's position in Greece and the section of the satellite image of Landsat ETM+ (atmospherically corrected) used with elements ID: 220-336, WES P/R: 2 184/032, Acq. Date: 28/07/2005, Producer: USGS (GLCF 2014), are presented in Figures 1 and 2. Additionally, Figure 2 shows that the plant cover is over 30%, and so NDVI index will be used for the calculation of IBI. Figure 3 portrays the polygons that enclose buildings as well as the major road network of the study area, which were detected in the satellite image.

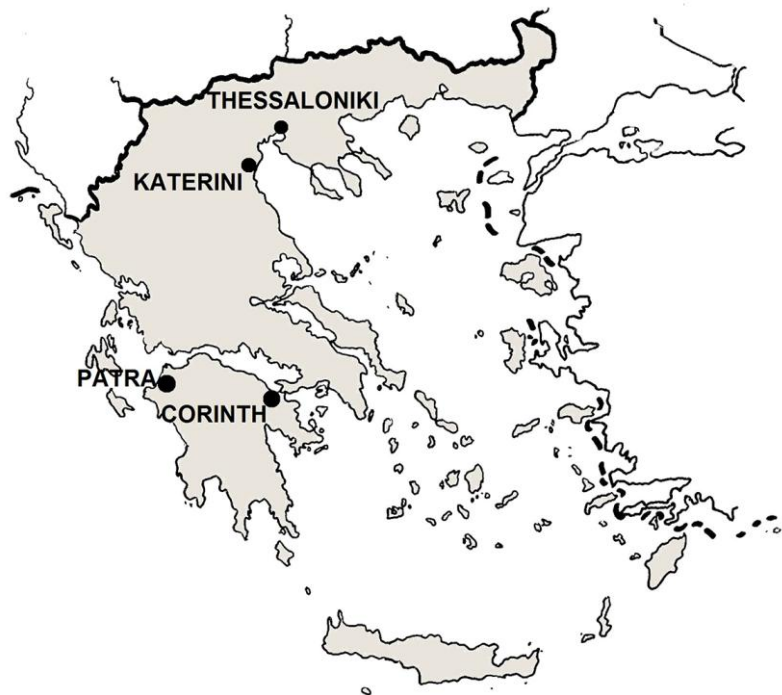


Figure 1: Study areas



Figure 2: Landsat ETM+ of the city (right) of Thessaloniki and its suburban and agricultural area, false colour image RGB=421, 28/07/2005

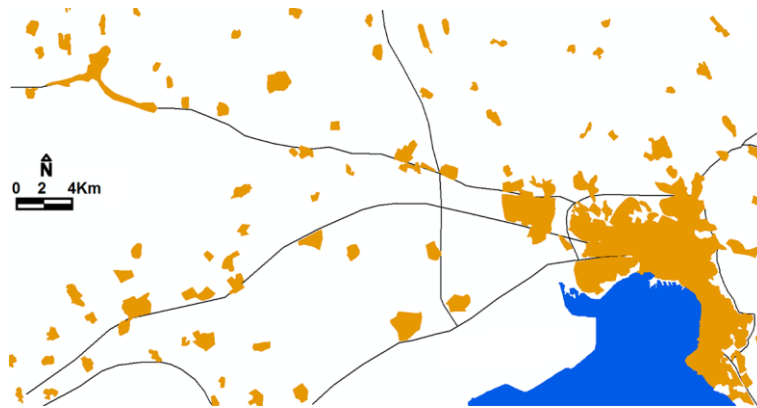


Figure 3: Polygons enclosing buildings (continuous / discontinuous construction and the major road network of the study area

3. Implementation of Existing Indexes and the New Index BUI

The urban, suburban and agricultural area of the study area (Figure 1 and 2) were divided into four categories/coverages, i.e., built-up area (e.g. residential, commercial, services, industrial, transportation), green vegetation (e.g. forest, shrubs and bushes, parks, cultivated land), bare soil (Ridd, 1995), and water (e.g. river, sea). In the two-dimensional spectral space, among all the combinations of Landsat ETM+ bands, the least spectral overlap between the above coverages is observed in combinations (Figure 4): RED-SWIR1, NIR- SWIR1 and SWIR1- SWIR2.

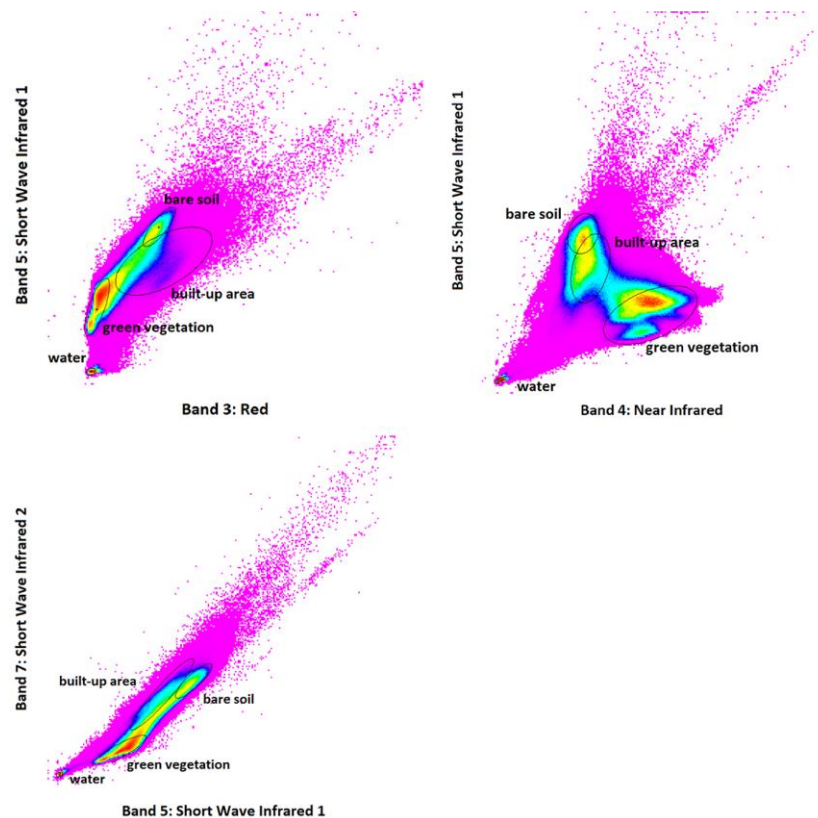


Figure 4: Scatter plot of the four major land use classes: built-up area, green vegetation, bare soil, and water surfaces

Optimal differentiation of the four coverages, based on the reflection of radiation (Figure 5) is observed at wavelengths NIR (Band 4) and SWIR1 (Band 5). Wavelengths RED (Band 3) and SWIR2 (Band 7) come next. In wavelength SWIR2 (Band 7) only a marginal distinction between the built-up area and the bare soil, and between green vegetation and water is observed, while the block: built-up area / bare soil is separated satisfactorily from the block: green vegetation / water. In the rest wavelengths BLUE (Band 1), GREEN (Band 2), TIR1 (Band 61) and TIR2 (Band 62), the distinction of the coverage is difficult.

The NIR spectrum region is utilized in every index of Table 2. The new index presented in this study, does not take into account this spectral region, although, as mentioned above, the region allows for the distinction of coverages (Figure 5). Specifically, among all bands of Landsat ETM+ image 4 only RED bands, SWIR1 and SWIR2 will be used, as their combination leads to a new optimal construction index. Figure 5 indicates that the subtraction of Band3 (RED) from Band5 (SWIR1) to their sum, and the addition of the subtraction of Band7 (SWIR2) from Band5 (SWIR1) to their sum, lead to high positive values for water, high negative values for bare soil and green vegetation, and minor negative values for the built-up area. Thus it becomes clear that the new index focuses on the last finding, i.e. in values ranging around 0.0, isolating the irrelevant information (green vegetation, bare soil and water) to high positive or negative values. This may not follow the logical boundary of the built-up area values adopted in indexes that have been developed so far (Ridd, 1995; Kawamura et al., 1996; Zha et al., 2003; Xu, 2007; Xu, 2008; As-syakur et al., 2012), but allows for the best distinction of constructions. The new index, BUI, is calculated according to the formula:

$$\frac{\text{Band3} - \text{Band5}}{\text{Band3} + \text{Band5}} + \frac{\text{Band7} - \text{Band5}}{\text{Band7} + \text{Band5}} = \frac{2 * [(\text{Band3} * \text{Band7}) - (\text{Band5} * \text{Band5})]}{(\text{Band3} + \text{Band5}) * (\text{Band5} + \text{Band7})}$$

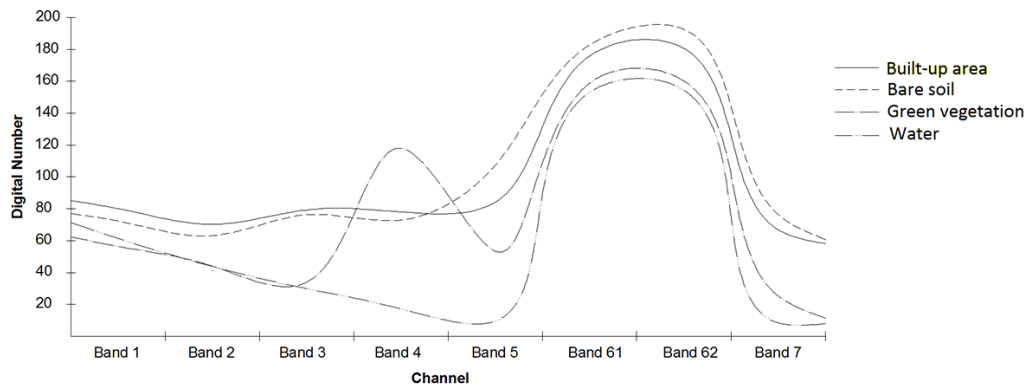


Figure 5: Spectral profiles for four classes of land cover in Thessaloniki city and its suburban and agricultural area

The results from the application of indexes UI, NDBI, IBI, NBI, EBBI and the new index BUI in the study area are shown in Figure 6.

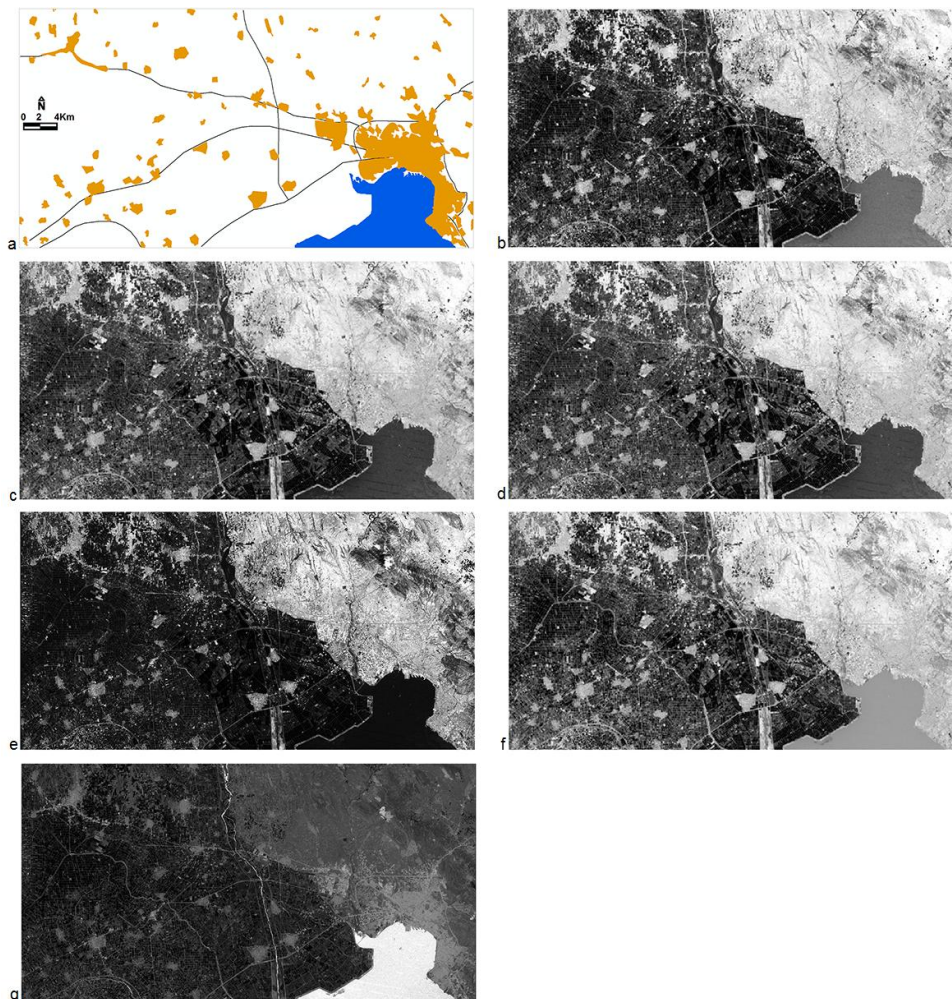


Figure 6: The application of Table 1 indexes in the city of Thessaloniki and its suburban and agricultural area. (a) Figure 4 in reduction. (b) UI (Urban Index). (c) NDBI (Normalized Difference Built-Up Index). (d) IBI (Index-based Built-Up Index). (e) NBI (New Built up Index). (f) EBBI (Enhanced Built-Up and Bareness Index). (g) BUI (Built-Up Index)

In scope of distinguishing the built-up area from index images (Figure 6), a minimum and maximum limit of pixel values is manually specified. In particular, the original multispectral image and the image of the index is utilized each time. Building and road positions (80-120 building and 80-120 road positions) are selected randomly but well distributed across the surface of the multispectral image. In the same positions the brightness values for each pixel of the index image are specified. These values determine the final range of the values of the index image, which corresponds to the built-up area. The range of these values for each index is presented in Table 2, and the results are the binary-images outputs shown in Figure 7.

Table 2: Pixel values of indexes for the identification of each construction's characteristics

| Remote Sensing Indices | Between -1 - 1 | Between 0 - 255 |
|---|-----------------|-----------------|
| UI (Urban Index) | -0.117 - -0.008 | 145 - 162 |
| NDBI (Normalised Difference Built-Up Index) | 0.021 - 0.072 | 164 - 172 |
| IBI (Index-based Built-Up Index) | 0.027 - 0.063 | 184 - 190 |
| NBI (New Built up Index) | - | 70 - 100 |
| EBBI (Enhanced Built-Up and Bareness Index) | 0.127 - 0.713 | 122 - 130 |
| BUI (Built-Up Index) | -0.225 - -0.013 | 98 - 114 |

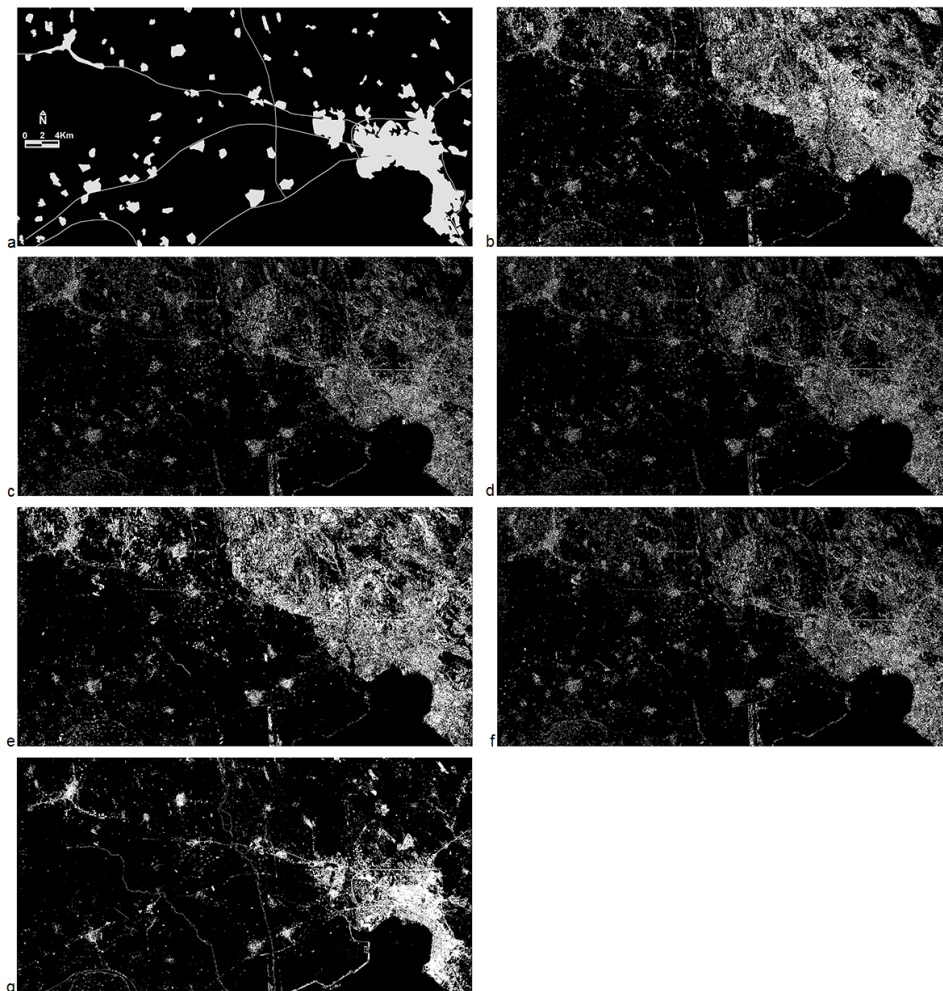


Figure 7: Index images after the application of the brightness pixel limits for the identification of constructions. (a) Negative colours of Figure 4. (b) UI (Urban Index). (c) NDBI (Normalized Difference Built-Up Index). (d) IBI (Index-based Built-Up Index). (e) NBI (New Built up Index). (f) EBBI (Enhanced Built-Up and Bareness Index). (g) BUI (Built-Up Index)

4. Results

For the calculation of the accuracy of the distinction between built-up area and open spaces, a random sampling method was used, and a total of 120 pixels were sampled (60 points within built-up areas, and 60 points within non built-up areas: green vegetation, bare soil, and water) in new index images (Figure 7), and compared to the corresponding points of the original Landsat ETM+ image (Figure 2). The results are presented in Table 3.

Table 3: Index accuracy

| Remote Sensing Indices | | Constructions | Not constructions | Total | User's accuracy |
|------------------------|---------------------|---------------|-------------------|-------|-----------------|
| UI | Constructions | 24 | 6 | 30 | 80.00% |
| | Not constructions | 36 | 54 | 90 | 60.00% |
| | Total | 60 | 60 | 120 | |
| | Producer's accuracy | 40.00% | 90.00% | | |
| | Overall accuracy | 65.00% | | | |
| | Kappa | 0.3000 | | | |
| NDBI | Constructions | 34 | 4 | 38 | 89.47% |
| | Not constructions | 26 | 56 | 82 | 69.29% |
| | Total | 60 | 60 | 120 | |
| | Producer's accuracy | 56.67% | 93.33% | | |
| | Overall accuracy | 75.00% | | | |
| | Kappa | 0.5000 | | | |
| IBI | Constructions | 34 | 2 | 36 | 94.44% |
| | Not constructions | 26 | 58 | 84 | 69.05% |
| | Total | 60 | 60 | 120 | |
| | Producer's accuracy | 56.67% | 96.67% | | |
| | Overall accuracy | 76.67% | | | |
| | Kappa | 0.5667 | | | |
| NBI | Constructions | 18 | 0 | 18 | 100.00% |
| | Not constructions | 42 | 60 | 102 | 58.82% |
| | Total | 60 | 60 | 120 | |
| | Producer's accuracy | 30.00% | 100% | | |
| | Overall accuracy | 65.00% | | | |
| | Kappa | 0.2600 | | | |
| EBBI | Constructions | 40 | 4 | 44 | 90,91% |
| | Not constructions | 20 | 56 | 76 | 73,68% |
| | Total | 60 | 60 | 120 | |
| | Producer's accuracy | 66.67% | 93.33% | | |
| | Overall accuracy | 80.00% | | | |
| | Kappa | 0.6000 | | | |
| BUI | Constructions | 50 | 2 | 52 | 96.15% |
| | Not constructions | 10 | 58 | 68 | 85.29% |
| | Total | 60 | 60 | 120 | |
| | Producer's | 83.33% | 96.67% | | |

| | | | | | |
|--|------------------|---------------|--|--|--|
| | accuracy | | | | |
| | Overall accuracy | 90.00% | | | |
| | Kappa | 0.8000 | | | |

5. Testing the New Index in Other Areas

5.1. Built-up Area Identification

The effectiveness of the index as far as its ability to identify the built-up area is concerned (as no other measurements existed for the areas below) was tested in two other sites in Greece, in the wider region of the cities of Katerini and Corinth (Figure 1). The city of Katerini is located in Macedonia and according to 2011 census has 55,997 inhabitants. The city of Corinth is located in Peloponnese, and according to 2011 census has 30,176 inhabitants. For both regions the index led to producer's accuracies up to 82.5% and 84.2% for the built-up area (Figure 8 and 9).

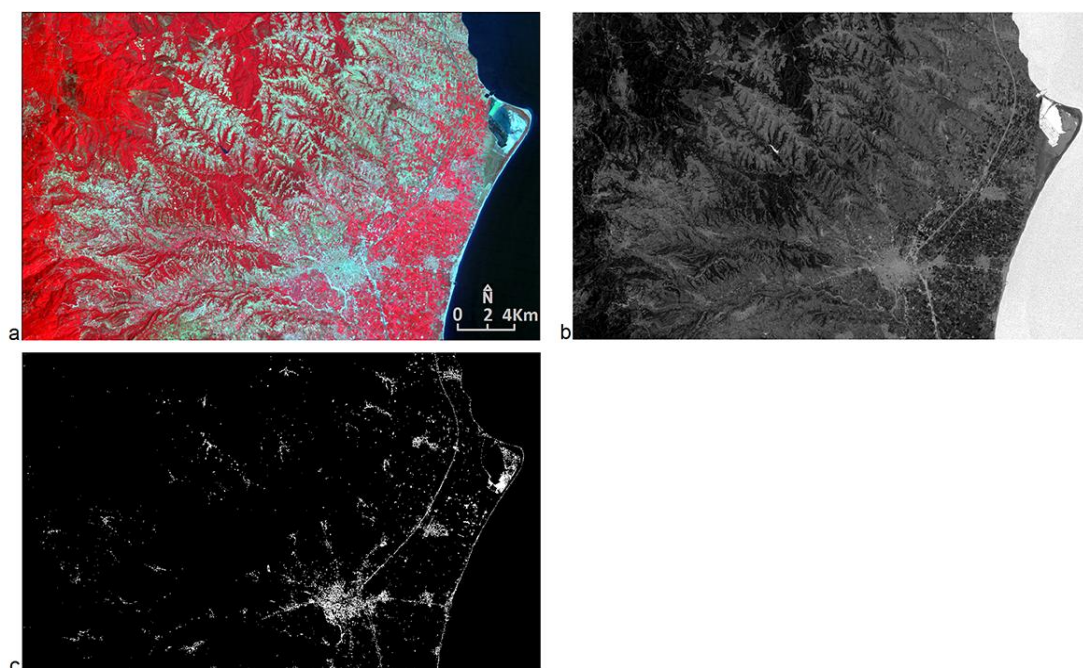


Figure 8: (a) Landsat ETM+ (ID: 220-336, WES P/R: 2 184/032, Acq. Date: 28/07/2005, Producer: USGS), in the city of Katerini and its suburban and agricultural area. (b) The application of the new index. (c) Index image after the application of brightness pixel limits for the identification of constructions

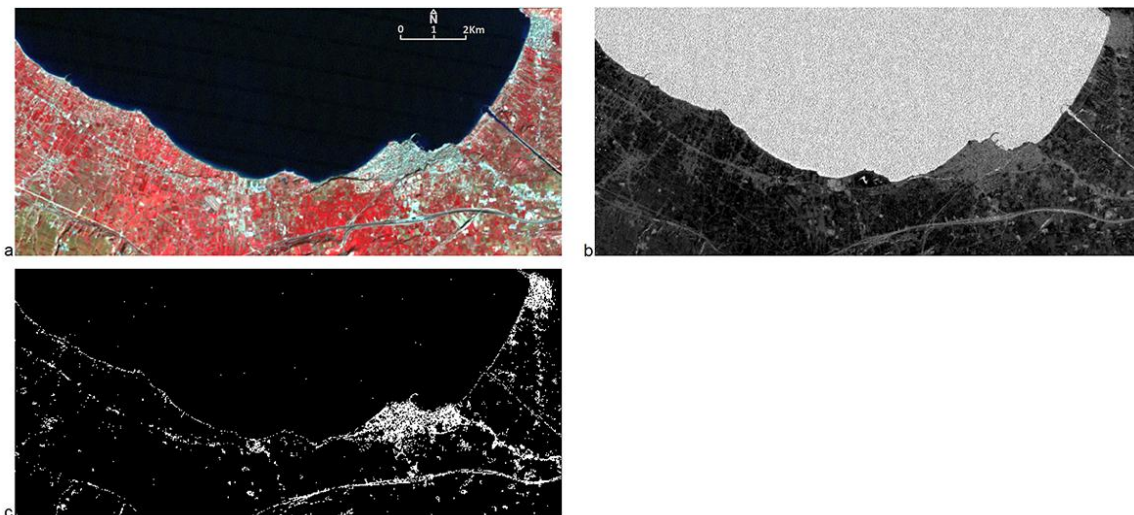


Figure 9: (a) Landsat ETM+, (ID: 220-285, WES P/R: 2: 183/034, Acq. Date: 10/01/2005, Producer: USGS), in the city of Corinth and its suburban and agricultural area. (b) The application of the new index. (c) Index image after the application of brightness pixel limits for the identification of constructions

5.2. Area Measurement of the Built-up Area

The index efficiency and accuracy, as far as area measurement is concerned, was tested with the use of data from the international research program LocalSats (2007-2013 ENPI CBC Mediterranean Sea Basin Programme, Table 4). The city of Patras is located in Peloponnese (Figure 1), and its urban area is the third largest area in population in Greece (according to 2011 census, the city is inhabited by 168,034 people), following the urban area of Athens and Thessaloniki. The information of Table 4 is provided by the international research program LocalSats, which is the result of modern city surveying. Bethlehem is a Palestinian city located in the central West Bank, about 10 kilometers south of Jerusalem, and has about 22,000 inhabitants. The information of Table 4 is provided by the international research program LocalSats, which is the result of photogrammetric processing of aerial images of 2010.

Table 4: Constructions areas and boundaries within statutory urban limits

| City | Way of recording | Areas (Km ²) | | | |
|----------------|-----------------------|--------------------------|--------|-----------|-------|
| | | City limits | Blocks | Buildings | Roads |
| Patras, Greece | Surveying (2006) | 24.28 | 21.88 | 4.83 | 2.40 |
| Bethlehem | Photogrammetry (2010) | 5.8 | 3.0 | 2.8 | |

The portion of the Landsat ETM+ satellite images (atmospherically corrected) used for the city of Patras with ID elements: 220-337, WES P / R: 2: 184/033, Acq. Date: 13/08/2005, Producer: USGS (GLCF 2014), and for the city of Bethlehem (Palestine) with ID elements: 296-233, WES P / R: 2: 174/038, Acq. Date: 15/04/2010, Producer: USGS (GLCF 2014) are shown in Figures 10 (a) and Figure 11 (a) respectively. The multispectral images were corrected geometrically according to each country’s national coordinate system (so that the results -areas- of the index are comparable with the data of Table 4). Afterwards, the new index BUI was applied (Figures 10 (b) and Figure 11 (b)). The minimum (Patra = 72, Bethlehem = 130) and maximum (Patra = 102, Bethlehem = 191) limits of brightness pixel values (in the range 0-255) were defined manually in scope of extracting the built-up areas from the index images (Figure 10 (b) and Figure 11 (b)). Thereafter, parts of the images enclosed within statutory limits of the urban areas were isolated (Figures 10 (c, d, f) and Figure 11 (c, d, f)). The size of the built-up area (Figure 10 (f)) for the city of Patras is 8.26 km². Compared with

Table 4 (buildings and roads cover a total area of 7.23Km^2) the area measurement error amounts to 14.2%. Finally, the size of the built-up area (Figure 11 (e)) for Bethlehem is 2.67 km^2 , and compared to Table 4 (buildings and roads cover an area of 2.8Km^2) the area measurement error reaches 4.6%.

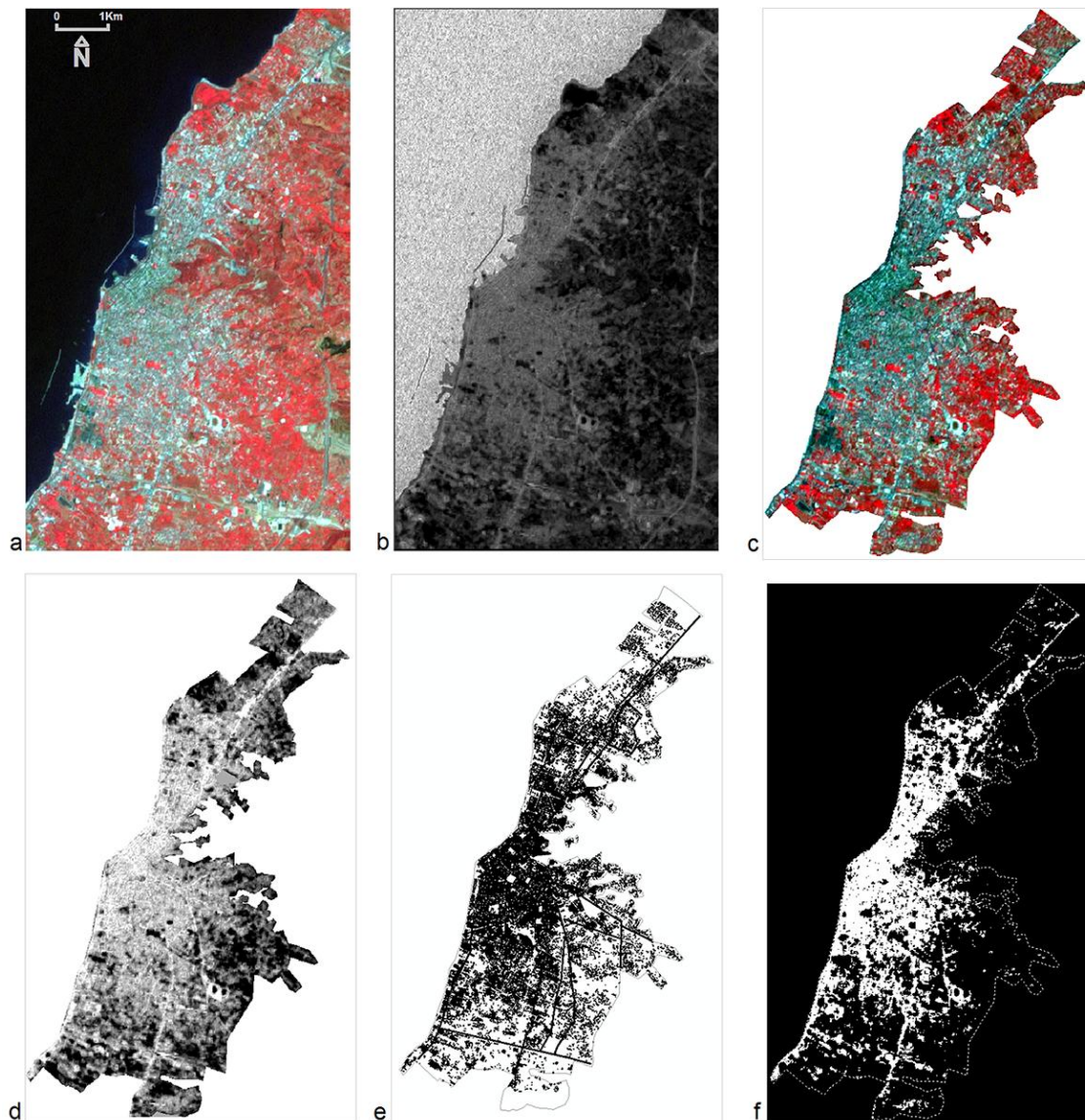


Figure 10: (a) The multispectral satellite Landsat ETM+ image (B, G, NIR) of the city of Patras. (b) Application of BUI index. (c, d) Portion of the multispectral image (a) and the image of BUI index (b) within the statutory limits of the urban structure. (e) Surveying of buildings and roads. (f) The index image (b) after the application of brightness pixel limits to determine the built-up area within the urban area

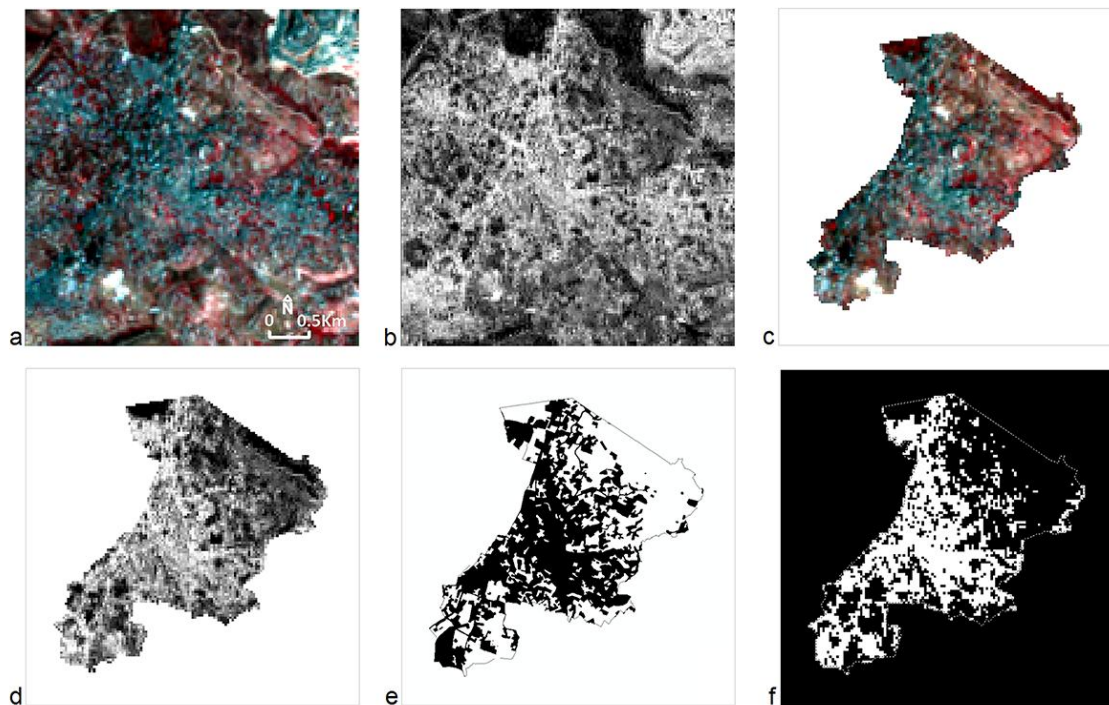


Figure 11: (a) The multispectral satellite Landsat ETM+ image (B, G, NIR) of Bethlehem. (b) Application of BUI index. (c, d) Portion of the multispectral image (a) and the image of BUI index (b) within the statutory limits of the urban structure. (e) Surveying of buildings and roads in black. (f) The index image (b) after the application of brightness pixel limits to determine the built-up area within the urban area

6. Conclusions

The new index BUI (Built-Up Index) which was developed and presented in this paper combines the bands of Landsat ETM+: RED (band 3), SWIR1 (band 5) and SWIR2 (band 7). NIR region of the spectrum (band 4) of the multispectral image of Landsat ETM+ was not utilized, differentiating from other indexes for the calculation of the built-up area which are developed up to date. The results of applying the index in five cities are encouraging, since the index allows the identification and area measurement of the built-up area in short time and with sufficient spatial and measuring accuracy. Specifically, the distinction accuracy (producer's accuracy) of the built-up area ranges from 82.5% to 84.2%, while the error of calculation of the area of the built-up area ranges from 4.6% to 14.2%.

Acknowledgements

We would like to thank Mona Banayout Ishaq, head of the Good Governance Program Manager, Applied Research Institute Jerusalem (ARIJ), partner of the research project LocalSats (2007-2013 ENPI CBC Mediterranean Sea Basin Programme), for the grant of geospatial data of Bethlehem (Table 4).

References

- As-syakur, A.R., Adnyana, I.W.S., Arthana, I.W., and Nuarsa, I.W. *Enhanced Built-Up and Bareness Index (EBBI) for Mapping Built-Up and Bare Land in an Urban Area*. Remote Sensing. 2012. 4 (10) 2957-2970.
- Deng, C. and Wu, C. *BCI: A Biophysical Composition Index for Remote Sensing of Urban Environments*. Remote Sensing of Environment. 2012. 127; 247-259.

GLCF, 2014: *Global Land Cover Facility*. Available online at: <http://www.landcover.org/>

Griffiths, P., Hostert, P., Gruebner, O., and Linden, S. *Mapping Megacity Growth with Multi-Sensor Data*. *Remote Sensing of Environment*. 2010. 114 (2) 426-439.

Guindon, B., Zhang, Y., and Dillabaugh, C. *Landsat Urban Mapping Based on a Combined Spectral-Spatial Methodology*. *Remote Sensing of Environment*. 2004. 92 (2) 218-232.

Herold, M., Roberts, D.A., Gardner, M.E., and Dennison, P.E. *Spectrometry for Urban Area Remote Sensing-Development and Analysis of A Spectral Library from 350 to 2400 nm*. *Remote Sensing of Environment*. 2004. 91; 304-319.

Herold, M., Gardner, M.E., and Roberts, D.A. *Spectral Resolution Requirements for Mapping Urban Areas*. *IEEE Transactions on Geoscience and Remote Sensing*. 2003. 41; 1907-1919.

Huang, Z. and Lee, G.B. *Combining Non-Parametric Models for Multisource Predictive Forest Mapping*. *Photogrammetric Engineering and Remote Sensing*. 2004. 70 (4) 415-425.

Huete, A.R. *A Soil-Adjusted Vegetation Index (SAVI)*. *Remote Sensing of Environment*. 1988. 25 (3) 295-309.

Jieli, C., Manchun, L., Yongxue, L., Chenglei, S., and Wei, H., 2010: *Extract Residential Areas Automatically by New Built up Index*. Theme Paper for the 18th International Conference on Geoinformatics, IEEE, 1-5.

Kamusoko, C., Gamba, J., and Murakami, H. *Monitoring Urban Spatial Growth in Harare Metropolitan Province, Zimbabwe*. *Advances in Remote Sensing*. 2013. 2; 322-331.

Kaufmann, R.K., Seto, C.K., Schneider, A., Liu, Z., Zhou, L., and Wang, W. *Climate Response to Rapid Urban Growth: Evidence of a Human-Induced Precipitation Deficit*. *Journal of Climate*. 2007. 20; 2299-2306.

Kawamura, M., Jayamana, S., and Tsujiko, Y. *Relation between Social and Environmental Conditions in Colombo Sri Lanka and the Urban Index Estimated by Satellite Remote Sensing Data*. Theme Paper for the International Archives of the Photogrammetry, Remote Sensing and Spatial Information Sciences. 1996. 31 (Part B7) 321-326.

Lee, A.J., Lee, S.S., and Chi, H.K. 2010: *Development of an Urban Classification Method using a Built-Up Index*. Theme Paper for the Selected Topics in Power Systems and Remote Sensing, Japan, 39-43.

Lu, D. and Weng, Q. *Urban Classification using Full Spectral Information of Landsat ETM+ Imagery in Marion County, Indiana*. *Photogrammetric Engineering & Remote Sensing*. 2005. 71 (11) 1275-1284.

Lu, D. and Weng, Q. *Use of Impervious Surface in Urban Land-Use Classification*. *Remote Sensing of Environment*. 2006. 102; 146-160.

Masek, J.G., Lindsay, F.E., and Goward, S.N. *Dynamics of Urban Growth in the Washington DC Metropolitan Area, 1973-1996, from Landsat Observations*. *International Journal of Remote Sensing*. 2000. 21; 3473-3486.

Melesse, A.M., Weng, Q., Thenkabail, P.S., and Senay, G.B. *Remote Sensing Sensors and Applications in Environmental Resources Mapping and Modelling*. *Sensors*. 2007. 7; 3209-3241.

- Melgani, F. and Bruzzone, L. *Classification of Hyper-spectral Remote Sensing Images with Support Vector Machines*. IEEE Transactions on Geoscience and Remote Sensing. 2004. 42 (8) 1778-1990.
- Pal, M. and Mather, M.P. *Support Vector Machines for Classification in Remote Sensing*. International of Remote Sensing. 2005. 26 (5) 1007-1011.
- Ray, T.W., 1994: *A FAQ on Vegetation in Remote Sensing*. California Institute of Technology. Pasadena, California, USA.
- Ridd, M.K. *Exploring a VIS (vegetation-impervious surface soil) Model for Urban Ecosystem Analysis through Remote Sensing: Comparative Anatomy for Cities*. International Journal of Remote Sensing. 1995. 16 (12) 2165-2185.
- Rouse, J.W., Haas, R.H., Schell, J.A., and Deering, D.W., 1973: *Monitoring Vegetation Systems in the Great Plains with ERTS*. Theme Paper for the Third ERTS Symposium, NASA SP-351, I, 309-317.
- Seto, K.C. and Liu, W. *Comparing ARTMAP Neural Network with the Maximum-Likelihood Classifier Detecting Urban Change*. Photogrammetric Engineering and Remote Sensing. 2003. 69 (9) 981-990.
- Ukwattage, L.N. and Dayawansa, K.D.N. *Urban Heat Islands and the Energy Demand: An Analysis for Colombo City of Sri Lanka Using Thermal Remote Sensing Data*. International Journal of Remote Sensing and GIS. 2012. 1 (2) 124-131.
- Ward, D., Phinn, R.S., and Murray, T.A. *Monitoring Growth in Rapidly Urbanizing Areas using Remotely Sensed Data*. Professional Geographers. 2000. 52 (3) 371-386.
- Weng, Q., 2008: *Remote Sensing of Impervious Surfaces: An Overview*. In Remote Sensing of Impervious Surfaces; Weng, Q., (ed.) Boca Raton, FL, USA: CRC Press, Taylor & Francis Group.
- Xian, G. and Crane, M. *Assessment of Urban Growth in the Tampa Bay Watershed using Remote Sensing Data*. Remote Sensing of Environment. 2005. 97 (2) 203-205.
- Xian, G. and Crane, M. *An Analysis of Urban Thermal Characteristics and Associated Land Cover in Tampa Bay and Las Vegas using Satellite Data*. Remote Sensing of Environment. 2006. 104; 147-156.
- Xu, H. *A Study on Information Extraction of Water Body with the Modified Normalized Difference Water Index (MNDWI)*. Journal of Remote Sensing. 2005. 9 (5) 589-595.
- Xu, H. *Modification of Normalized Difference Water Index (NDWI) to Enhance Open Water Features in Remotely Sensed Imagery*. International Journal of Remote Sensing. 2006. 27; 3025-3033.
- Xu, H. *Extraction of Urban Built-up Land Features from Landsat Imagery using a Thematic Oriented Index Combination Technique*. Photogrammetric Engineering & Remote Sensing. 2007. 73 (12) 1381-1391.
- Xu, H. *A New Index for Delineating Built-Up Land Features in Satellite Imagery*. International Journal of Remote Sensing. 2008. 29; 4269-4276.
- Xu, H. *Analysis of Impervious Surface and Its Impact on Urban Heat Environment Using the Normalized Difference Impervious Surface Index (NDISI)*. Photogrammetric Engineering and Remote Sensing. 2010. 76 (5) 557-565.

Yang, X. *Parameterizing Support Vector Machines for Land Cover Classification*. Photogrammetric Engineering and Remote Sensing. 2011. 77 (1) 27-37.

Yuan, F., Sawaya, E.K., Loeffelholz, C.B., and Bauer, E.M. *Land Cover Classification and Change Analysis of the Twin Cities (Minnesota) Metropolitan Area by Multitemporal Landsat Remote Sensing*. Remote Sensing of Environment. 2005. 98 (2-3) 317-328.

Zha, Y., Gao, J., and Ni, S. *Use of Normalized Difference Built-Up Index in Automatically Mapping Urban Areas from TM Imagery*. International Journal of Remote Sensing. 2003. 24; 583-594.

Zhang, Q., Wang, J., Peng, X., Gong, P., and Shi, P. *Urban Built-Up Land Change Detection with Road Density and Spectral Information from Multi-Temporal Landsat TM Data*. International Journal of Remote Sensing. 2002. 23 (15) 3057-3078.

Zhou, X., Jancsó, T., Chen, C., and Veróné, W.M., 2012: *Urban Land Cover Mapping Based on Object Oriented Classification using WorldView 2 Satellite Remote Sensing Images*. Theme Paper for the International Scientific Conference on Sustainable Development & Ecological Footprint, 1-10, Sopron, Hungary.

Creation of Soil Spectral Library for Marathwada Region

Ramdas D. Gore, Reena H. Chaudhari, and Bharti W. Gawali

Department of Computer Science and IT, Dr. Babasaheb Ambedkar Marathwada University, Aurangabad, Maharashtra, India

Publication Date: 27 June 2016

DOI: <https://doi.org/10.23953/cloud.ijarsg.60>



Copyright © 2016 Ramdas D. Gore, Reena H. Chaudhari, and Bharti W. Gawali. This is an open access article distributed under the **Creative Commons Attribution License**, which permits unrestricted use, distribution, and reproduction in any medium, provided the original work is properly cited.

Abstract This paper reports the development of the soil spectral library using Analytical Spectral Device (ASD) FieldSpec 4 Spectroradiometer with 350-2500 nm wavelength band. In this experiment we have used visible and Near-infrared band. The particular instrument is used to analyze the chemical properties of soil such as Carbon (C), Nitrogen (N), Phosphorus (P), and physical properties of soil such as soil texture (sand, silt, clay) and moisture content. It is observed that physical and chemical properties can be analyzed using hyperspectral band. The database used for experiment have 80 samples of soil which are collected from Aurangabad, Jalna, Parbhani, Hingoli, Nanded, Lature, Osmanabad and Beed from Marathwada region of Maharashtra state with their GPS coordinates. Linear Discriminant Analysis (LDA) technique is implemented for classification of soil spectral signature of chemical properties. Soil texture of Marathwada region comes under the silt clay loam. We got the 100% accuracy of Phosphorus content, where as Carbon and Nitrogen content found 75%, 87% respectively for Marathwada region.

Keywords *LDA; Spectral Signature; Spectroradiometer; Soil Property*

1. Introduction

There are many natural things on or surrounding of the earth like water, soil and air which are necessary for survival of living being. Soil is a natural form and it is a combination of minerals, organic matter, gases, liquids, and the countless organisms. Life on the earth can be supported by these things together. Soil is used as a medium for plant growth, as water storage, as a modifier of earth's atmosphere and also helpful for supply and purification. Soil continually undergoes development by way of numerous physical, chemical and biological processes, which include weathering with associated erosion [1]. This work is concentrated on soil and its properties.

The three basic types of soil properties are physical, chemical and biological. The physical properties of soil are texture, structure, density, consistency and color. Chemical properties of soil are Cation-Exchange Capacity (CEC), soil pH, minerals and organic matter (carbon, nitrogen and phosphorus) [2]. Biological property include soil biota, including flora (plants), fauna (animals) and microorganisms which perform functions that contribute to the soil's development, structure and productivity [3]. Soil properties are influenced by texture such as drainage, water holding capacity, Cation-Exchange

Capacity (CEC), pH buffering capacity and organic matter content. It was best effected on management and productivity of soil.

The physical and chemical properties of the soil are essential nutrients which are important for crops and basic resource for maintaining the Earth's ecosystems [4]. In agriculture field or in natural resources like ecosystem, requires the appropriate use of soil which having good physical, chemical and biological properties. Different crops need different type of soils, different types and amounts of nutrients, and different types and amounts of water. The amount of water required by the plant is also dependent on the growing season and the climate where it is grown. By selecting the right crop for the given soil conditions and climate, one can optimize yields and save water requirements for irrigation. Soil texture refers to the size of the particles that make up the soil and depends on the proportion of sand, silt and clay-sized particles and organic matter in the soil. Sandy soils feel gritty when rubbed between the fingers. Silts feel smooth – a little like flour. Most clays are sticky and moldable. Soils that are a mixture of sand, silt and clay are called loams [5]. Black soil contains a large amount of clay which have moderate amount of phosphorous but is poor in nitrogen. This type of soil is also used for rice, wheat, sugarcane and cotton. It is additionally used to grow groundnut, millet and oilseeds. Sandy and dry soils contain nitrogen, but are suitable for agriculture only if there is a sufficient water supply. Generally only drought-resistant crops such as barley and millet can grow in this type of soil [6]. The nitrogen, phosphorus and potassium (K) plays very important role for the production of rice crop [7]. For getting information about physical, chemical, biological, and fertility properties of soils, soil science is useful. It has found to develop techniques that help for better characterization of soil types.

In recent studies, Remote sensing techniques for soil application have gained much concentration, because these techniques have been shown to generate faster and cheaper characterizations. The application of remote sensing techniques in soil studies started in the 1960s and developed for various applications, including fast and nondestructive quantification of soil properties [8]. The basic requirement for this is the creation of a spectral signature database. We have created our own soil spectral signature database for Marathwada region.

When soil absorbs the energy from energy source then it reflects that radiation differently in various bands. The soil spectral signature is the radiation reflected as a function of the wavelength [9]. Recent researchers have indicated that visible and near-infrared, diffuse reflectance spectroscopy (VINR-DRS) and specific band from hyperspectral sensor data [10, 11-15]. Near-Infrared spectroscopy can be used to analyze heavy metal contents in soil such as zinc (Zn), copper (Cu), lead (Pb), chrome (Cr), and nickel (Ni) [16].

China has large area of rice fields and created Chinese Soil Spectral Library (CSSL). Spectral library data achieved that consist of spectral signatures measured on selected natural soil. 1st derivative, 2nd derivative, savitzky-Golay method, multiplicative scatter correction (MSC) and standard normal variate (SNV) are the pretreatment methods. Spectroradiometer has used for the measurement, soil physical and chemical properties such as clay, sand content, moisture content, carbon, nitrogen and phosphorus. Near-infrared is used to assess clay, sand, moisture content and other soil properties and small studies area [10, 12, 17, 18]. The soil spectral library developed in the artificial dark room. Landsat Thematic Mapper (TM) six band 1, 2, 3, 4, 5 and 7 used for soil analysis. Partial least square regression and artificial neural network used mathematical tools in the analysis of soil properties [19-21].

2. Materials and Methods

2.1. Creation of Database and Study Area

For this experiment we created soil database, which consists of 80 samples of soil from farms. The samples include top soil (0-20 cm depth from land surface) denoted as A and sub soil (20-40 cm depth

from land surface) denoted as B in Table 1. Soil samples were collected from the Marathwada region of India during Oct-Nov 2015 between 10: 00 am to 4: 00 pm on a sunny day. Soil samples collected from 8 districts such as Aurangabad, Jalna, Parbhani, Hingoli, Nanded, Lature, Osmanabad, Beed and details of sample is presented in Table 1. It has been collected from different cropping systems, including arable. A global position system (GPS) was used to determine the coordinates of the sampling point. Distance between two samples is 2-3 km. We have collected 5 soil samples from each district of Marathwada region. The samples were stored in air tight bags to restore the moisture.

Table 1: Details of soil samples from study area

| Sr. No. | City/Village Name | Presented Crop | Top Soil | Subsoil |
|---------|--------------------------|---------------------|----------|---------|
| 1.1 | Hingoli | Red gram, Soybean | A | B |
| 1.2 | Risol, Hingoli | Cotton | A | B |
| 1.3 | Savarkheda, Hingoli | Soybean | A | B |
| 1.4 | Savarkheda, Hingoli | Jowar | A | B |
| 1.5 | Savarkheda, Hingoli | Soybean | A | B |
| 2.1 | Ardhapur, Nanded | Green Gram | A | B |
| 2.2 | Nanded | Banana | A | B |
| 2.3 | Nanded | Vegetables (Chilly) | A | B |
| 2.4 | Nanded | Soybean | A | B |
| 2.5 | Nanded | Black soil | A | B |
| 3.1 | Khanapur, Parbhani | Soybean | A | B |
| 3.2 | Parbhani | Black soil | A | B |
| 3.3 | Parbhani | Jowar | A | B |
| 3.4 | Parbhani | Jowar | A | B |
| 3.5 | Parbhani | Soybean | A | B |
| 4.1 | Bharahnpur, Latur | Lady Finger | A | B |
| 4.2 | Latur | Jowar | A | B |
| 4.3 | Malwati, Latur | Jowar | A | B |
| 4.4 | Kasarkheda, Latur | Black soil | A | B |
| 4.5 | Chikalthana, Latur | Soybean | A | B |
| 5.1 | Thoki, Osmanabad | Soybean | A | B |
| 5.2 | Rui, Osmanabad | Black soil | A | B |
| 5.3 | Kavadgaon, Osmanabad | Black soil | A | B |
| 5.4 | Bhadachiwadi, Osmanabad | Corn, Sugarcane | A | B |
| 5.5 | Upala, Osmanabad | Soybean | A | B |
| 6.1 | Anandwadi, Beed | Black soil | A | B |
| 6.2 | Ramnagar, Beed | Black soil | A | B |
| 6.3 | Pendgaon, Beed | Jowar | A | B |
| 6.4 | Palwan chowk, Beed | Jowar, soybean | A | B |
| 6.5 | Palwan, Beed | Cotton | A | B |
| 7.1 | Badnapur Tahsil, Jalna | Cotton | A | B |
| 7.2 | Badnapur, Jalna | Cotton | A | B |
| 7.3 | Selgaon, Jalna | Corn | A | B |
| 7.4 | Jalna | Cotton, Red gram | A | B |
| 7.5 | Jalna Toll Plaza | Soybean | A | B |
| 8.1 | Aurangabad | Wheat | A | B |
| 8.2 | Kanchanwadi, Aurangabad | Red gram | A | B |
| 8.3 | Gevrai Tanda, Aurangabad | Bajra (millets) | A | B |
| 8.4 | Gevrai, Aurangabad | Black soil | A | B |
| 8.5 | University, Aurangabad | Back soil | A | B |

2.2. Spectral Measurement through FieldSpec 4

FieldSpec 4 Spectroradiometer is scanned and absolute reflectance of samples is recorded for 350-2500 nm wavelength and collects spectra at the rate of 0.1 seconds per spectral scan. Spectral resolution is 3 nm @ 700 nm (350-1000 nm) and 10 nm/ 8 nm/ 30 nm @ 1400/2100 nm (100-2500 nm). Data sampling interval is 1.4 nm (350-1000 nm) and 2 nm (1000-2500 nm) and spectral resolution of 3 nm at 700 nm and 10 nm at 1400 nm and 2100 nm. The total number of 2151 data points per spectrum using FieldSpec 4 Spectroradiometer (Analytical Spectral Devices Inc., Boulder, Colorado, USA). Its input is 1.5m permanent fiber optic cable and it is having 25 degree, 8 degree and 1 degree field-of-view (FOV). Fiber optic cable is flexible. FieldSpec 4 is a very flexible instrument, it can use in lab and on the field. It has some accessories like pistol grip tripod, lamp, reference panels, backpack, battery, AC power supply and laptop. The laptop is required to communicate the instrument through Ethernet wired interface or Wi-Fi Ethernet interface. It has some software such as RS3, ViewSpec Pro, Indico Pro and third party software. RS3 software is used for data collection and file saves as .asd extension.

ViewSpec Pro software is used for data analysis and pre-process data. It has the same tools like reflectance, absolute reflectance, log 1/ T, log 1/ R, 1st and 2nd derivative, and parabolic correction and so on. It can export .asd file into the ASCII code (text file) and shows the latitude and longitude coordinates of the field location (GPS).

Each soil sample was scanned 5 times. Database is created by FieldSpec 4 Spectroradiometer. Database size is 400. The reflectance of each sample was calculated by taking the average of 100 scans performed by the sensor. The spectrum of the sample was the average of 30 successive scans. Soil samples are scanned with a spectral range of 350-2500 nm; Soils were scanned from below using a high intensity source instrument FieldSpec 4 and Spectralon panel for white reference. It is used 8°FOV. It was placed on a tripod with a nadir position. Distance between optical head and soil sample was 20 cm with a lamp mounted on distance 45 cm form sample. All spectral data were collected by RS3 software.

2.3. Spectral Characteristic Analysis

It is non imaging hyperspectral data and able to predict the soil properties. ViewSpec Pro software was used for pretreatment and each spectral signature transformed into ASCII format by using the ViewSpecPro software. The analysis is conducted for five spectral signature. The wavelength bands for carbon is (2040-2260 nm), nitrogen (1702 nm, 1870 nm and 2052 nm), and phosphor (2021-2025 nm, 2240-2400 nm), texture Particles (1323 nm, 2081 nm) and water contents (1400 nm, 1900 nm, 2200 nm). Figure 1 shows the reflectance of all soil samples and Table 2 represents soil texture of all soil samples. Mean of reflectance value of soil is calculated for statistical analysis which is shown in Table 3.

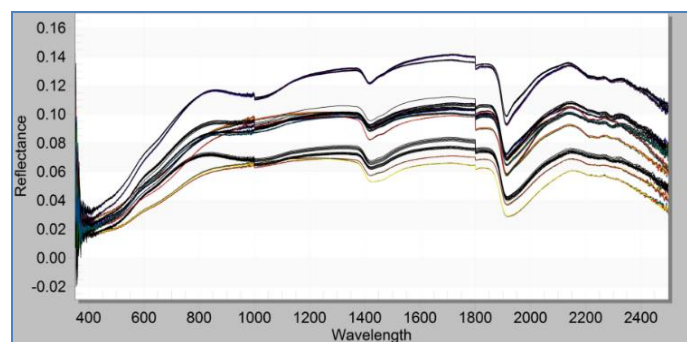


Figure 1: Reflectance of all soil samples

Table 2: Soil texture of all soil samples

| Marathwada Region | Sand % | Clay % | Silt % | Total |
|-------------------|--------|--------|--------|-------|
| Beed | 23 | 37 | 40 | 100 |
| Hingoli | 20 | 29 | 51 | 100 |
| Jalna | 9 | 28 | 63 | 100 |
| Latur | 13 | 26 | 61 | 100 |
| Nanded | 15 | 27 | 58 | 100 |
| Osmanabad | 18 | 26 | 56 | 100 |
| Parbhani | 17 | 52 | 31 | 100 |
| Aurangabad | 29 | 22 | 49 | 100 |

Table 3: Statistic of carbon, nitrogen, phosphorus and water contents

| Soil Properties | Beed | Hingoli | Jalna | Latur | Nanded | Osmanabad | Parbhani | Aurangabad |
|-----------------------------|-------------|-------------|-------------|-------------|-------------|-------------|-------------|-------------|
| Range of Carbon content | 0.058-0.079 | 0.125-0.135 | 0.062-0.073 | 0.082-0.092 | 0.096-0.104 | 0.048-0.061 | 0.124-0.133 | 0.09-0.105 |
| Range of Nitrogen content | 0.059-0.071 | 0.129-0.137 | 0.064-0.082 | 0.084-0.1 | 0.097-0.103 | 0.05-0.066 | 0.125-0.141 | 0.092-0.099 |
| Range of Phosphorus content | 0.054-0.065 | 0.118-0.126 | 0.058-0.069 | 0.073-0.085 | 0.09-0.098 | 0.044-0.058 | 0.115-0.125 | 0.082-0.097 |
| Water content | 0.043-0.066 | 0.106-0.128 | 0.046-0.071 | 0.064-0.092 | 0.078-0.1 | 0.034-0.058 | 0.101-0.127 | 0.067-0.098 |

2.4. Linear Discriminant Analysis (LDA) Technique Implemented for Soil Properties

Linear Discriminant Analysis (LDA) is simple, mathematically robust and often produces models whose accuracy is good. It is based upon the concept of searching for a linear combination of variables (predictors) that best separates the two classes (targets). LDA is a transform-based method which attempts to minimize the ratio of within-class scatter to be between class scatter. The mathematical formulation involved in the theory of LDA is explained in the following sections. A within-class scatter matrix defines the scatter of samples around their respective class centers (means) [22].

We applied LDA classification technique on soil spectral signature classification of chemical properties with reference the wavelengths.

3. Results Analysis and Conclusion

All the soil samples which are tested in this study have similar reflectance spectra. Figure 1 represents the reflectance of soil samples which is a spectral signature of the soil. It shows each wavelength band of the soil. From different band we can get different chemical and/or physical content of the soil. For following wavelength 1323 nm, 1400 nm, 1702nm, 1870 nm, 2052 nm and 2081 nm, we got high reflectance peaks in the spectral signature. As previously mentioned several pretreatments are considered among all, the 1st derivative good result.

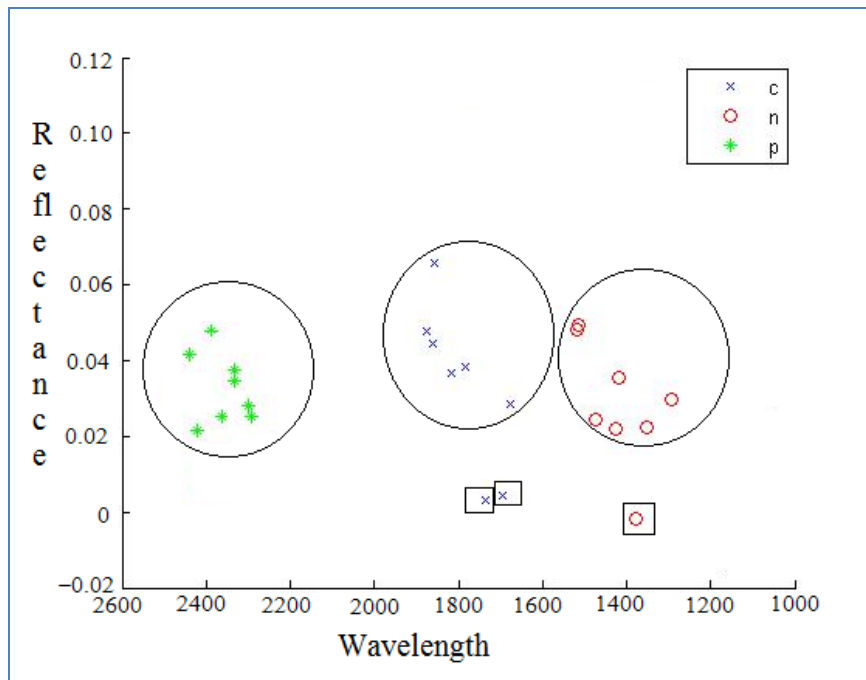


Figure 2: LDA implementation for soil spectral signature for Carbon, Nitrogen and Phosphorus

Table 2 presents the soil texture of all the study area. It is observed that silt percentage in the soil more than sand and clay. The percentage of sand in soil for Aurangabad region is 29%, clay 22%, and silt 49%, due to less rainfall in Aurangabad district. Parbhani districts have 17% sand, clay is more, it is 52% and silt is 31% as generally on an average, there is good rainfall in Parbhani of Marathwada region. The results got for remaining regions are depend upon the rainfall, the geographical condition and structure of that area. Soil texture class depends on percentage of sand, silt and clay. These classes again subdivided into loam, sandy loam, clay loam, sandy clay, silt clay, silt clay loam and sandy clay loam.

The chemical analysis result of the concentrations of Carbon, Nitrogen, Phosphorus and water contents are presented in Table 3 for the calibration and prediction sets respectively. Linear Discriminant Analysis (LDA) classification technique is applied to the soil properties. C, N and P of soil spectral signature are resulted and seen in Figure 2. Reflectance value of Carbon (C), Nitrogen (N) and Phosphorus (P) are shown on X-axis, whereas Wavelength range placed on Y-axis. It is observed that the reflectance value of phosphorus for all the soil samples found to be similar. The accuracy of carbon is 75%. Reflectance value of the carbon for Osmanabad and Beed region is low. For nitrogen is 87%. The reflectance value Osmanabad region is less and for Parbhani and Hingoli, it is near about same. The accuracy rate of soil chemical properties is seen in Table 4.

This paper analyzes the soil properties of eight districts of Marathwada region of Maharashtra state. These districts are Aurangabad, Jalna, Beed, Parbhani, Hingoli, Nanded, Latur and Osmanabad. The distance between the selected areas is approximate (60-100 km). From the result, we have concluded that for the Beed and Hingoli regions, the texture class is clay loam. Jalna, Latur, Nanded and Osmanabad comes under silt clay loam. Aurangabad is loam and Parbhani is Clay texture class. The Carbon reflectance is high (0.128) in Parbhani. Nitrogen (0.133) and Phosphorus (0.123) is high in Hingoli. Carbon, Nitrogen and Phosphorus reflectance is poor in Osmanabad.

Linear Discriminant Analysis (LDA) classification technique is used to classify Carbon, Nitrogen and Phosphorus. Phosphorus got 100% accuracy. We have concluded that the content of phosphorus in soil for Marathwada region is more prominent than nitrogen and carbon. With the help of collected soil

samples, Soil Spectral Library is created for Marathwada region. Osmanabad and Beed regions carbon content showed the difference, in reflectance spectra for nitrogen. Parbhani and Hingoli found to be similar whereas Osmanabad region showed the less reflectance value for nitrogen.

References

- [1] Wikimedia Foundation, Inc. Wikipedia®. Available at <https://en.wikipedia.org/wiki/Soil>.
- [2] Ramdas D., Gore, Sunil S., Nimbhore, and Bharti W., Gawali. *Understanding Soil Spectral Signature Through RS and GIS Techniques*. International Journal of Engineering Research and General Science. 2015. 3 (6) 866-872.
- [3] My Agriculture Information Bank. Available at <http://agriinfo.in/?page=topic&superid=1&topicid=373>
- [4] Shuo, Li, Wenjum, Ji, Songehao Chen, Jie Peng, Yin Zhou, and Zhou Shi. *Potential of VIS-NIR-SWIR Spectroscopy from the Chinese Soil Spectral Library for Assessment of Nitrogen Fertilization Rates in the Paddy-Rise Region, China*. Remote Sensing. 2015. 7; 7029-7043.
- [5] Demand Media. *Types of Soil & Crops Grown in India*. Available at <http://www.gardenguides.com/128581-types-soil-crops-grown-india.html>
- [6] Science Learning Hub, The University of Waikato. Soil Properties. Available at <http://sciencelearn.org.nz/Contexts/Soil-Farming-and-Science/Science-Ideas-and-Concepts/Soil-properties>
- [7] Henrique Bellinaso, Jose Alexandre Melo Dematte and Suzana Araujo Romeiro. *Soil Spectral Library and Its Use in Soil Classification*. Scielo, Revista Brasileira de Ciencia do Solo. 2010. 34 (3).
- [8] Zejian Lei, Mingyin Yao, Muhua Liu, Qiulian Li and Hanping Mao. *Comparison between Fertilization N, P, K and No Fertilization N, P, K in Paddy Soil by Laser Induced Breakdown Spectroscopy*. IEEE Intelligent Computation Technology and Automation. 2011. 1; 363-366.
- [9] Shuo, Li, Wenjum, Ji, Songehao Chen, Jie Peng, Yin Zhou, and Zhou Shi. *Potential of VIS-NIR-SWIR Spectroscopy from the Chinese Soil Spectral Library for Assessment of Nitrogen Fertilization Rates in the Paddy-Rise Region, China*. Remote Sensing. 2015. 7; 7029-7043.
- [10] European Space Agency. Spectral Signatures. Available At http://www.esa.int/SPECIALS/Eduspace_EN/SEMPNQ3Z2OF_0.html
- [11] Davin J. Brown. *Using a Global VNIR Soil-Spectral Library for Local Soil Characterization and Landscape Modeling in a 2nd-Order Uganda Watershed*. Geoderma. 2007. 140 (4) 444-453.
- [12] Linker, R. *Soil Classification via Mid-Infrared Spectroscopy*. Chapter in Computer and Computing Technologies in Agriculture, Vol. 2. The International Federation for Information Processing Series Vol. 259. 2008. 1137-1146.
- [13] Gholizadeh, A., Amin, M.S.M., Boruvka, L., and Saberioon, M.M. *Models for Estimating the Physical Properties of Paddy Soil using Visible and Near Infrared Reflectance Spectroscopy*. Journal of Applied Spectroscopy. 2014. 81 (3) 534-540.

- [14] Todorova, M., Mouazen, A.M., Lange, H., and Astanassova, S. *Potential of Near-Infrared Spectroscopy for Measurement of Heavy Metals in Soil as Affected by Calibration Set Size*. *Water Air Soil Pollut.* 2014. 225 (8) 1-19.
- [15] Haiqing Yang, Boyan Kuang, and Abdul M. Mouazen. *Affect of Different Preprocessing Methods on Principal Component Analysis for Soil Classification*. *ICMTMA*. 2011. 1; 355-358.
- [16] Viscarra Rossel, R.A., Walvoort, D.J.J., McBratney, A.B., Janik, L.J., and Skjemstad, J.O. *Visible, Near Infrared, Mid Infrared or Combined Diffuse Reflectance Spectroscopy for Simultaneous Assessment of Various Soil Properties*. *Geoderma*. 2006. 131 (1-2) 59-75.
- [17] Josea M., Dematte, Peterson R., Fiorio, and Suzana R., Araújo. *Variation of Routine Soil Analysis When Compared with Hyperspectral Narrow Band Sensing Method*. *Remote Sensing*. 2010. 2 (8) 1998-2016.
- [18] Changwen Du and Jianmin Zhou. *Evaluation of Soil Fertility Using Infrared Spectroscopy: A Review*. 2009. 7 (2) 97-113.
- [19] Rossel, R.A.V., Jeon, Y.S., Odeh, I.O.A., and McBratney, A.B. *Using a Legacy Soil Sample to Develop a mid-IR Spectral Library*. *Soil Research*. 2008. 46 (1) 1-16.
- [20] Gehl, R.J. and Rice, C.W. *Emerging Technologies for in situ Measurement of Soil Carbon*. *Climatic Change*. 2007. 80 (1) 43-54.
- [21] David J. Brown, Keith D. Shepherd, Markus G. Walsh, M. Dewayne Mays and Thomas G. Reinsch. *Global Soil Characterization with VNIR Diffuse Reflectance Spectroscopy*. *Geoderma*. 2006. 132 (3-4) 273-290.
- [22] Sebastian Raschka. *Linear Discriminant Analysis*. Available at http://sebastianraschka.com/Articles/2014_python_lda.html

Use of GIS Mapping for HFMD Cases in Sarawak, Malaysia

Noraishah M.S.^{1,2}, and Krishnarajah I.^{2,3}

¹Environmental Health Research Centre, Institute for Medical Research, Kuala Lumpur, Malaysia

²Laboratory of Computational and Operational Research, Institute for Mathematical Research, Universiti Putra Malaysia, Serdang, Selangor, Malaysia

³Department of Mathematics, Faculty of Science, Universiti Putra Malaysia, Serdang, Selangor, Malaysia

Publication Date: 14 October 2016

DOI: <https://doi.org/10.23953/cloud.ijarsg.72>



Copyright © 2016 Noraishah M.S., and Krishnarajah I. This is an open access article distributed under the **Creative Commons Attribution License**, which permits unrestricted use, distribution, and reproduction in any medium, provided the original work is properly cited.

Abstract GIS is widely used to observe health data. However, there is limited study of Hand, Foot and Mouth Disease (HFMD) focusing into this area. This study aim to describe the disease spread geographically in eleven divisions of Sarawak, Malaysia. GIS was used to observe the spatial pattern of the disease in Sarawak from year 2006 to 2013. A Spatial Analyst tool of ArcGIS software was applied to locate and present if any potential clustering of HFMD occur between the divisions. An Inverse Distance Weighted (IDW) spatial interpolation method was used to illustrate HFMD spread in the state. This study also observes the locality factors that could influence by the disease. The urban divisions show a high-risk pattern of HFMD during the outbreak year when we used the number of notified cases as the basis. However, there is no significant difference of urban and rural population when IDW was applied to the incidence proportion of HFMD (p -value = 0.84). From this study, we found that GIS approach is very useful to the health authorities before they decide to implement any activities in reducing the disease transmission for the particular area.

Keywords GIS; IDW; HFMD; Sarawak, Malaysia

1. Introduction

HFMD could be easily transmitted from the infected person through coughing or sneezing, close personal contact, contact with feces or contaminated objects and surfaces (CDC, 2013). The disease is contagious in Sarawak compared to other state in Malaysia. One component of other infectious diseases in Malaysia Health Facts 2015 reported that the incidence rate of HFMD in Malaysia for year 2014 is 104.7 per 100,000 population (Ministry of Health, 2015). This value increase at 33.3 percent compared to 2014 which it was only 78.52 per 100,000 population. Therefore, the disease is one of the crucial infectious disease especially to the children as the management protocols aimed at reducing transmission and the number of cases in Malaysia. The disease commonly affects children below ten years old and resulted in a number of deaths (Sarawak State Health Department, 2006).

In order to prepare the appropriate control measures for HFMD in time, it is very important to determine the spatial pattern of HFMD whether the disease is spatially autocorrelated among the divisions in Sarawak. This information will further help in curtailing the disease more specifically by

tracking the disease spread and also maximizing the use of control measure facilities. Epidemiologist used Geographical Information Systems (GIS) in order to visualize epidemiological data in terms of spread and clustering as well as ongoing trends. GIS has been applied for analyzing the spread of various infectious diseases (Noraishah et al., 2014; Bhunia et al., 2013; Bie et al., 2010; Nakhapakorn and Jirakajohnkool, 2006; Chaikaew, 2009; Dom et al., 2010).

A study on application of GIS by Bhunia et al. (2013) showed that epidemiological measures can be used to differentiate high and low risk areas more efficiently which aids in optimizing resources and minimizing one of the leading causes of morbidity and mortality cases in Bihar, India. The study guided health authority with a more sophisticated tool to differentiate risk patterns of the epidemic disease by using spatial statistical approaches rather than relying on the annual cumulative incidence alone. This technique helped in identifying the high-risk areas at any time in the epidemic based on their integrated spatial–temporal profiles.

In China, Bie et al. (2010) found that the relationship between geographical factors and HFMD incidence are important factors in order to control and prevent HFMD outbreak and epidemic. Nakhapakorn and Jirakajohnkool (2006) explored the potential of GIS technology for analysis of spatial factors with regard to dengue fever (DF) and dengue haemorrhagic fever (DHF). Chaikaew et al. (2009) revealed spatial patterns and hotspots of diarrhea in the Chiang Mai province, Thailand between the years 2001 and 2006. Numerous studies have been conducted to explore the linkages between infectious disease and spatial-temporal patterns in Malaysia (MohdHussin et al., 2003; Shafie, 2011; Hamed et al., 2011; Hafiz et al., 2012). The study in Malaysia showed no significant distribution pattern for the dengue intensity index as the higher values tend to stay at the same locality throughout the year in Subang Jaya, Malaysia (Dom et al., 2010)..

However, to our best knowledge, there was only one study on HFMD using GIS regarding HFMD in Malaysia. In year 2012 which is the outbreak year, Noraishah et al. (2014) had shown that spatial autocorrelation exist in 11 districts of Sarawak due to HFMD. Hence, this study was carried out to identify how the localities factors could influence the disease spread in the state. As a result, it could help the health authorities in surveillance and suggesting appropriate control strategies in reducing the disease transmission in particular area.

2. Materials and Methods

The eight-year period (2006 to 2013) of HFMD epidemiological data were used in this study which covered eleven divisions of Sarawak. The weekly basis data was compiled by the Crisis Preparedness and Response Centre (CPRC), Sarawak State Health Department.

Sarawak divisions are divided into two classes (rural and urban) based on the definitions. The proportion of rural population in Sarawak, Malaysia is 30% less than the urban population from 2006 to 2013 (DOS, 2010). Urban was defined based on Department of Statistics, Malaysia (2010) as follow:

"Gazetted areas with their adjoining built-up areas, which had a combined population of 10,000 or more at the time of the Census 2010 or the special development area that can be identified, which at least had a population of 10,000 with at least 60% of population (aged 15 years and above) were involved in non-agricultural activities."

The built-up areas were next to a gazetted area and had at least 60% of their population (aged 15 years and above) engaged in non-agricultural activities. Special development areas are areas of development that can be identified and separated from any gazetted area or built-up area more than 5 km and the area had a population of at least 10,000 with 60 percent of the population (aged 15 years and above) were involved in non-agricultural.

For rural, it is defined as an area with population less than 10,000 people having main activities related to agriculture and natural resources in which its population either is clustered, linear or scattered (Rural Master Plan, 2010). Therefore, Kuching, Samarahan, Sibul, Bintulu and Miri were considered as the urban areas in Sarawak whereas Sri Aman Betong, Sarikei, Mukah, Kapit and Limbang were the rural areas.

2.1. Geographical Information System (GIS) Procedure

GIS has been beneficial in order for us to understand the data by visualizing the spread and clustering within areas in Sarawak. To study a particular infectious disease, GIS is a valuable tool especially for mapping the spread of disease geographically and the trend of the disease can be seen clearly. Spatial Analyst is one of the ArcMap tool which is used in order to observe the spatial pattern and the spatial autocorrelation of the disease. The ArcMap which is primary application based on ArcGIS used to display, query, edit, create and analyzing data. This study utilized the ArcMap application in order to locate and present potential clustering of HFMD in different divisions in Sarawak. ArcGIS version 10.1 was used for this study.

2.2. Inverse Distance Weighted (IDW) Interpolation Methods

A spatial sampling approach called interpolation used to predict the unknown values for cells in a raster format from a limited sample geographical point dataset (Lai et al., 2009). This method assumed that spatially distributed objects are correlated and the closer they are the chances for them to have similar values will be higher. There are three common methods of spatial interpolation namely as Inverse Distance Weighted (IDW), spline and kriging.

This study applied the IDW interpolation method which is known to be more accurate as it is able to sustain the entire probability distribution of incidence values compared to other methods (Kheirandish et al., 2012). IDW is also known as moving average or distance weighted average methods. IDW weights the contribution of each input point by a normalized inverse of the distance from the control point to the interpolated point. IDW interpolation method also assumes that each input point has local influence that decreases with distance (Fisher et al., 1987).

There are two parameters that are important to handle IDW; namely as power and radius. A power can be any real number. It is advised to use a range of 0.5 to 3 which can lead to the most reasonable results (ESRI, 2015). Power also controls the significance of surrounding points on the interpolated value where higher power results in less influence from distant points. Our study used a power of 2 as default power. Another operating parameter, radius is used to determine the number of known points to estimate an unknown value. This study used Sarawak boundary as a fixed radius where the output raster will be created.

3. Results

3.1. Spatial Data Analysis

According to Table 1, year 2006 had the highest total number of HFMD notified cases, followed by 2012, 2008, 2009, 2013, 2007, 2010 and 2011. Incidence proportion is also a good indicator to apply while comparing and estimating the risk of a disease since we took the population of Sarawak into account. Therefore, this study also demonstrated the spatial autocorrelation of HFMD in Sarawak by using the incidence proportion. It showed that the incidence proportion of HFMD in year 2006 was the highest compared to other years. There were about 631 cases for every 100,000 people in Sarawak for year 2006.

Table 1: HFMD notified cases and incidence proportion, 2006-2013, Sarawak, Malaysia

| | 2006 | 2007 | 2008 | 2009 | 2010 | 2011 | 2012 | 2013 |
|-----------------------|--------|--------|--------|--------|--------|--------|--------|--------|
| Notified cases | 14,875 | 6,571 | 10,435 | 9,655 | 5,010 | 2,900 | 13,495 | 8,571 |
| Incidence proportion* | 630.97 | 273.31 | 428.54 | 390.76 | 199.88 | 114.72 | 525.63 | 327.22 |

*per 100,000 population

A summary of HFMD notifications based on the locality distributions in Sarawak from year 2006 to 2013 was presented in Table 2 where 54,796 (76.62%) of the total notified cases were urban cases. The rural areas accounted for only 16,716 (23.38%) of the total notified cases.

Table 2: Numbers and rates of HFMD notification by localities, 2006-2013, Sarawak, Malaysia

| Year | Number of notifications | | | | Rate/100,000 | | Urban/Rural Rate ratio (RR) | 95%CI for RR | |
|-------|-------------------------|-------|--------|-------|--------------|--------|-----------------------------|--------------|-------|
| | Rural | % | Urban | % | Rural | Urban | | LCL | UCL |
| 2006 | 3,434 | 23.09 | 11,441 | 76.91 | 544.12 | 621.78 | 1.14 | 1.03 | 1.26 |
| 2007 | 1,440 | 21.91 | 5,131 | 78.09 | 228.17 | 278.85 | 1.22 | 1.05 | 1.40 |
| 2008 | 1,881 | 18.03 | 8,554 | 81.97 | 298.04 | 464.88 | 1.56 | 1.41 | 1.71 |
| 2009 | 1,921 | 19.90 | 7,734 | 80.10 | 304.38 | 420.32 | 1.38 | 1.23 | 1.53 |
| 2010 | 1,307 | 26.09 | 3,703 | 73.91 | 207.09 | 201.25 | 0.97 | 0.78 | 1.17* |
| 2011 | 679 | 23.41 | 2,221 | 76.59 | 107.59 | 120.70 | 1.12 | 0.86 | 1.38* |
| 2012 | 3,853 | 28.55 | 9,642 | 71.45 | 610.51 | 524.01 | 0.86 | 0.74 | 0.98 |
| 2013 | 2,201 | 25.68 | 6,370 | 74.32 | 348.75 | 346.19 | 0.99 | 0.84 | 1.14* |
| Total | 16,716 | 23.38 | 54,796 | 76.62 | 331.08 | 372.25 | 1.12 | 0.98 | 1.27* |

*p<0.05; CI = Confidence Interval; LCL = Lower Confidence Limit; UCL = Upper Confidence Limit; RR = Rate Ratio between notification rates of urban to rural

This study also took into account the proportion of the urban and rural populations in Sarawak. The notification rate of urban HFMD was 372.25 per 100,000 population, compared to 331.08 per 100,000 population in rural areas. HFMD notification rates were significantly higher in urban areas, with an urban to rural rate ratio of 1.12 (95%CI: 0.98 – 1.27; p<0.05). The rate ratios of urban to rural HFMD notification increase from 1.14 (95%CI: 1.03 – 1.26; p<0.05) in 2006 to 1.56 (95%CI: 1.41 – 1.71; p<0.05) in 2008. However, the rate ratios fluctuated from year 2009 to 2013.

IDW method was used for both variables; number of notified cases and the incidence proportion of HFMD for the eight-year study period to illustrate the spatial distribution of the interpolated estimates as shown in Figure 1 and Figure 3. Moreover, Figure 2 and Figure 4 addressed the locality of HFMD occurrence in Sarawak. The color from green to red is directly related to the intensity of HFMD occurrence in the state. It means that the red color represent a high risk of HFMD in the respected division.

In Figure 1, we observed that the high-risk area were found in Kuching, Sibul, Bintulu and Miri for the outbreak year 2006. The low-risk patterns were found for the non outbreak year; 2007, 2010 and 2011. In 2008, 2009, 2012 and 2013, there were a moderate-risk of HFMD for each division in Sarawak. The urban divisions of Sarawak comprises of Kuching, Sibul and Miri are the most affected divisions by HFMD compared to rural divisions during the eight-years study period as seen in Figure 2. This figure showed similar result as the rate ratio of urban to rural of 1.12 in Table 2.

By using the incidence proportion shown in Figure 3, a high-risk were spatially illustrated on the north-west areas of Sarawak during the outbreak year (2006, 2008 and 2009). However, in year 2012 it seems that the south-east areas had only a moderate-risk of HFMD. Other years (2007, 2010, 2011 and 2013) showed a low-risk of the disease.

The incidence proportion of HFMD of urban population and rural population did not show much difference in Sarawak (Figure 4). This could be due to other causes of disease transmission rather than population itself. The Moran's *I* value also showed statistically not significant at the level of 90 percent (p -value = 0.84).

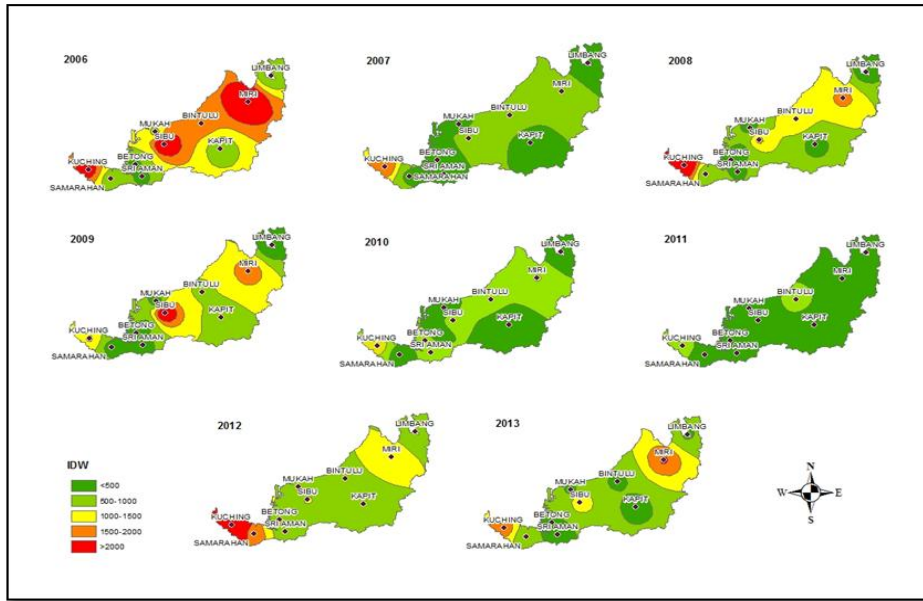


Figure 1: Mapping of inverse distance weighting interpolation based on notified cases of HFMD by divisions in Sarawak

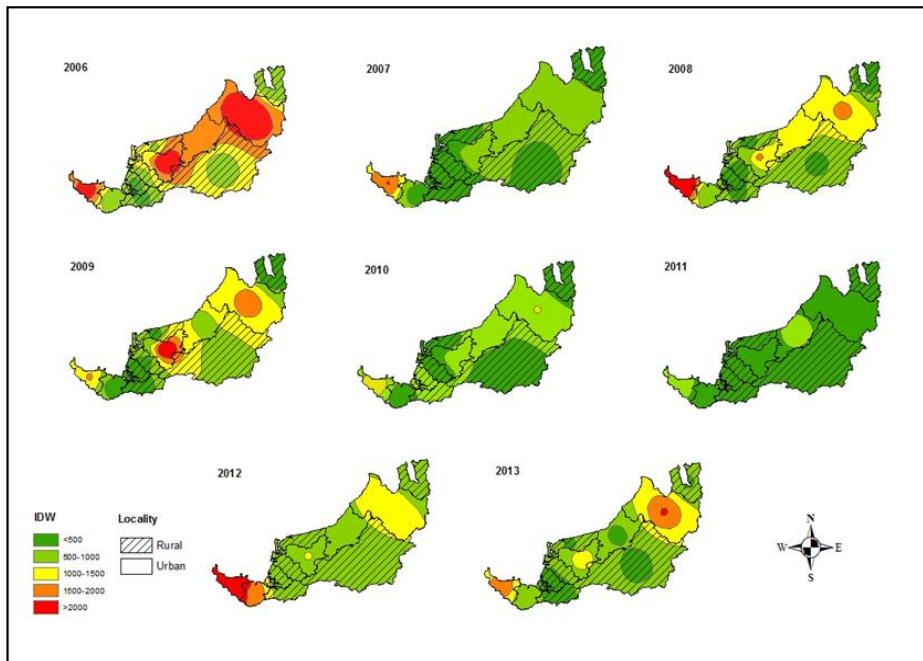


Figure 2: Mapping of inverse distance weighting interpolation based on notified cases of HFMD by divisions and locality in Sarawak

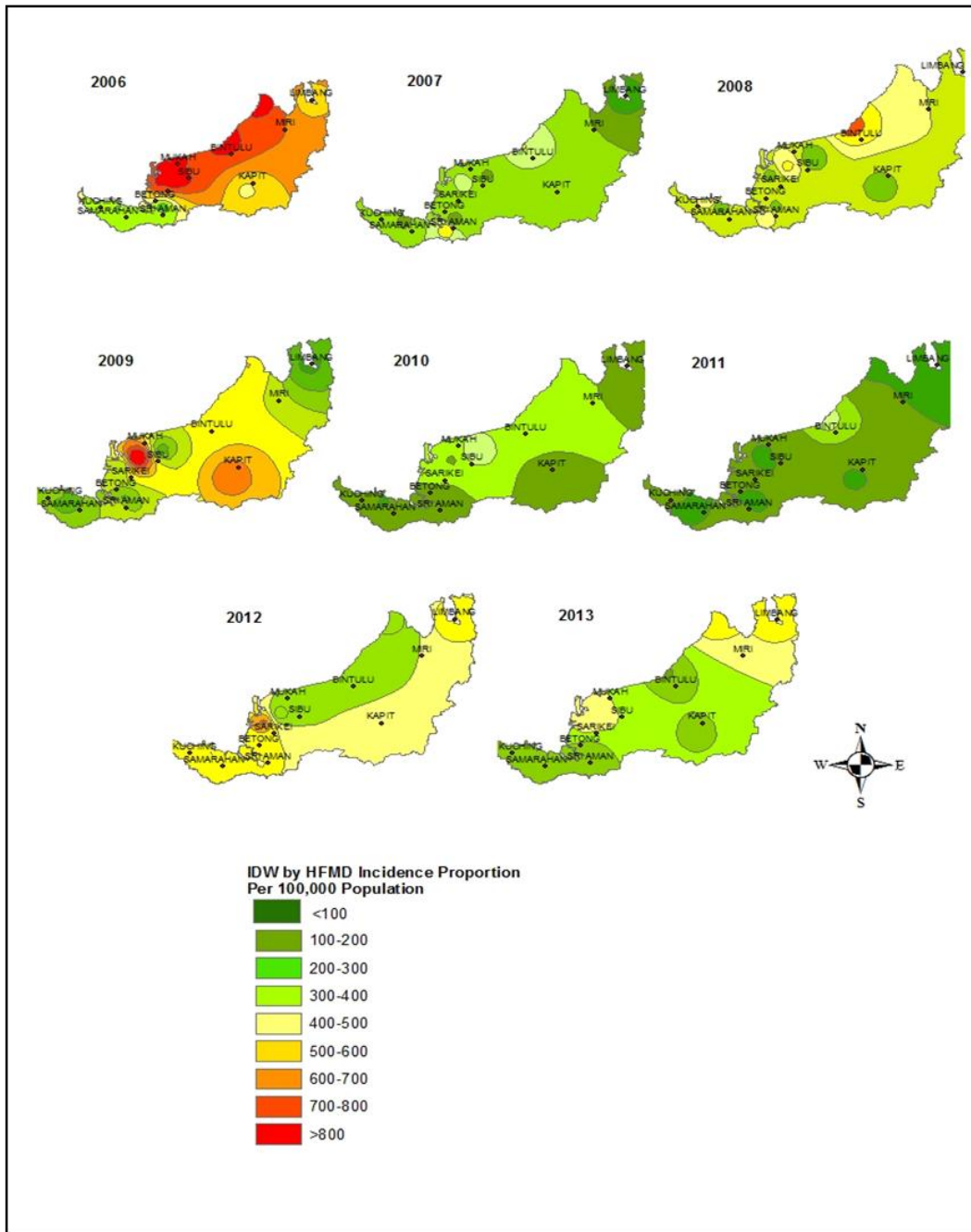


Figure 3: Mapping of inverse distance weighting interpolation based on the incidence proportion of HFMD by divisions in Sarawak

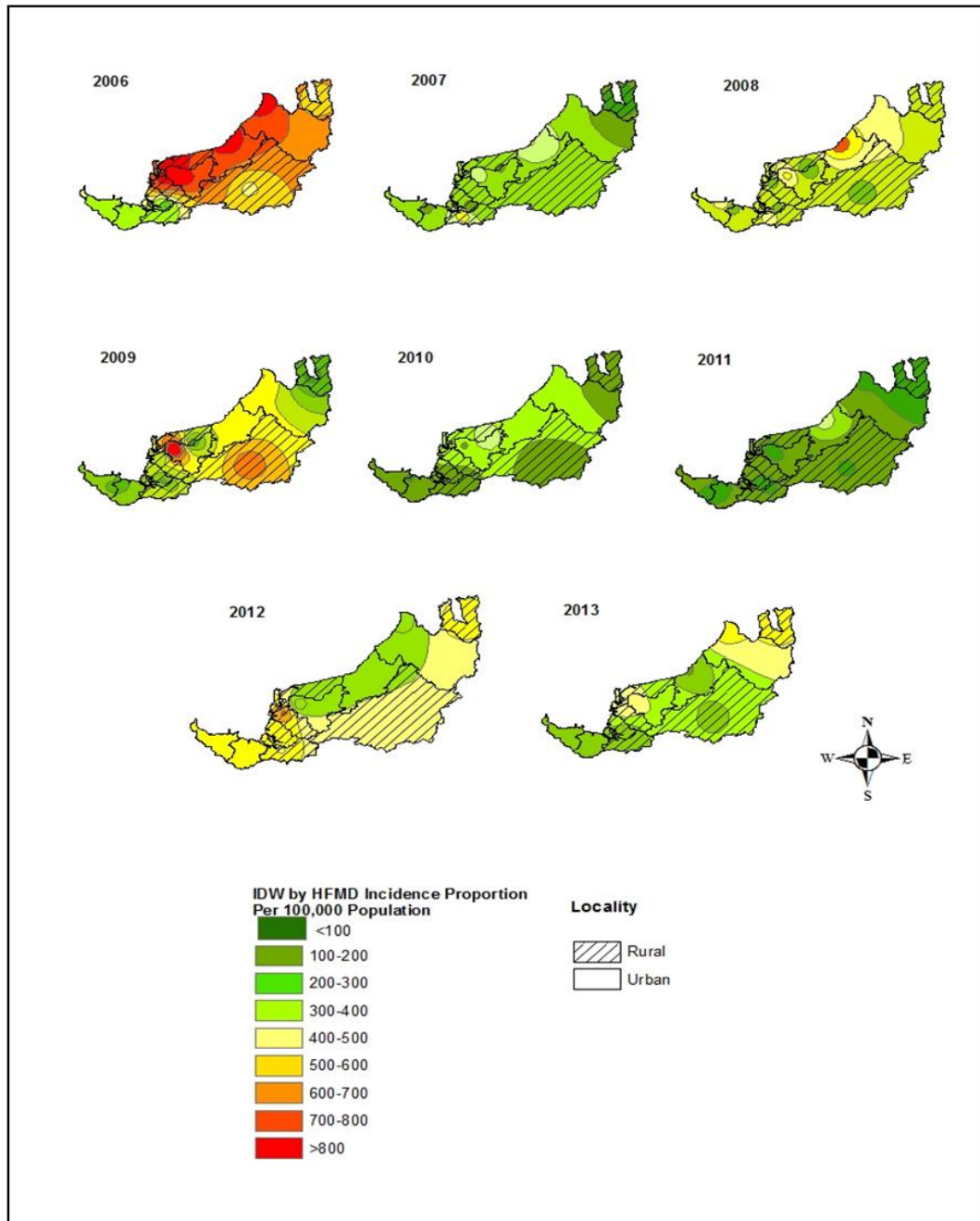


Figure 4: Mapping of inverse distance weighting interpolation based on the incidence proportion of HFMD by divisions and locality in Sarawak

4. Discussion

A spatial analysis involves few sequence of operational steps in order for us to achieve the main objective which is GIS-based health analyses. First, we need to identify the study area. Next, the sources of spatial and disease data to include in the study. Then, the appropriate spatial analyses to be used will be selected. Finally, to conclude and determine if the chosen method is adequate to summarize our data. With all these questions, we can provide sufficient information that helps the health authorities to choose the right timing and strategy for the implementation of control activities.

The limitation of this study is when we only used the central coordinate of each division to locate area in Sarawak. To have a good GIS-based analysis, we should have the full address of each notified cases so that we can project the best solution in reducing the disease transmission in the future. Besides, this study covered only the divisions in Sarawak due to the limited availability of surveillance data and also the period of study covered is only eight years. In future, it is hoped that a study for the whole country with full geographical information of each cases could be carried out.

5. Conclusion

Spatial sampling approach by using the spatial interpolation will generate statistical surfaces of varying degrees of smoothness. The IDW method used in this study showed the disease spread according to the HFMD notified cases and incidence proportion by divisions in Sarawak. It shows that, when it comes to control strategy, the health authorities should focus on the urban area rather than the rural area although there was only a little different. As a result, it could help to curb the spread of the disease and reduce the number of HFMD notified cases in Sarawak.

Acknowledgements

We thank the Director-General of Health Malaysia for his permission to present the results of this study. We also would like to thank the Crisis Preparedness and Response Centre, Communicable Disease Control Section, Sarawak State Health Department for the invaluable assistance on compiling the dataset; many thanks to Institute for Medical Research for the financial support.

References

- Bhunja, G.S., Kesari, S., Chatterjee, N., Kumar, V., and Das, P. Spatial and Temporal Variation and Hotspot Detection of Kalaazar Disease in Vaishali district (Bihar), India. *BMC Infectious Diseases*. 2013. 13; 64.
- Bie, Q., Qiu, D., Hu, H., and Ju, B. Spatial and Temporal Distribution Characteristics of Hand-Foot-Mouth Disease in China. *Journal of Geo-information Science*. 2010. 12 (3)
- CDC, 2013. Hand, Foot and Mouth Disease: <http://www.cdc.gov/hand-foot-mouth/about/transmission.html>
- Chaikaew, N., Tripathi, N.K., and Souris, M. Exploring Spatial Patterns and Hotspots of Diarrhea in Chiang Mai, Thailand. *Int J Health Geogr*. 2009. 8 (1) 36-36.
- Department of Statistics, Malaysia, 2010: Population and Housing Census Malaysia, 2010 Report.
- Dom, N., Ahmad, A., Nasir, R., and Ismail, R. Spatial Mapping of Temporal Risk Characteristic of Dengue Cases in Subang Jaya. *International Conference on Science and Social Research*. 2010. 361-366.
- ESRI, 2015: Interpolates A Surface from Points using an Inverse Distance Weighted (IDW) Technique. http://resources.esri.com/help/9.3/arcgisdesktop/com/gp_toolref/spatial_analyst_tools/idw.htm
- Fisher, N.I., Lewis, T., and Embleton, B.J.J., 1987: *Statistical Analysis of Spherical Data*. Cambridge University Press.
- Hafiz, H., Shohaimi, S., and Hashim, N.R. Risk Mapping Of Dengue in Selangor and Kuala Lumpur, Malaysia. *Geospatial Health*. 2012. 7 (1) 21-25.

Hamed, B., and Salim, N. Prediction of Dengue Outbreak in Malaysia using the Combination of Clinical, GIS and Meteorological Data and Machine Learning Techniques. Postgraduate Annual Research Seminar (PARS 2015), Universiti Teknologi Malaysia.

Kheirandish, S., Liaghat, M., Azahar, T.M., and Gohari, A. Comparison of Interpolation Methods in Prediction the Pattern of Basal Stem Rot Disease in Palm Oil Plantation. *Geoinformatica- An International Journal*. 2012. 2 (1) 12-16.

Lai, P.C., So, F.M., and Chan, K.W., 2009: *Spatial Epidemiological Approaches in Disease Mapping Analysis*. CRC Press.

Ministry of Health, Malaysia, 2015. Health Fact 2015.

MohdHussin, Z.A., Abdul Majid, N., Md Said, M.A., Baharudin, S.H., and Mahmood, N.N. The Application of Geographic Information System (GIS) and Remote Sensing Techniques in Mapping of Children with Malnutrition – An Introduction. 7.
Available at http://www.medic.usm.my/~helic/gis_files/Malnutrition%20Mapping.pdf

Nakhapakorn, K., and Jirakajohnkool, S. Temporal and Spatial Autocorrelation Statistics of Dengue Fever. *Dengue Bulletin*. 2006. 30; 177.

Noraishah, M.S., Krishnarajah, I., Ibrahim, N.A., and Lye, M.S. Temporal and Spatial Mapping of Hand, Foot and Mouth Disease in Sarawak, Malaysia. *Geospatial Health*. 2014. 8 (2) 503-507.

Sarawak State Health Department, 2006: HFMD.
http://jknsarawak.moh.gov.my/en/modules/mastop_publish/?tac=91

Shafie, A. Evaluation of the Spatial Risk Factors for High Incidence of Dengue Fever and Dengue Hemorrhagic Fever Using GIS Application. *Sains Malaysiana*. 2011. 40 (8) 937-943.

Web-GIS based Framework for Solid Waste Complaint Management for Sustainable and Smart City

Yadvendra P. Singh¹, Singh A.K.², and Singh R.P.³

¹GIS Cell, Motilal Nehru National Institute of Technology, Allahabad, India

²Department of Civil Engineering and Member GIS Cell, Motilal Nehru National Institute of Technology, Allahabad

³Department of Civil Engineering, Motilal Nehru National Institute of Technology, Allahabad, India

Publication Date: 14 October 2016

DOI: <https://doi.org/10.23953/cloud.ijarsg.71>



Copyright © 2016 Yadvendra P. Singh, Singh A.K., and Singh R.P. This is an open access article distributed under the **Creative Commons Attribution License**, which permits unrestricted use, distribution, and reproduction in any medium, provided the original work is properly cited.

Abstract Geographical information system (GIS), data management and digital technology play a key role in the development of sustainable city. These technologies help administrator and planner to increase performance, utilize resources efficiently, reduce cost and engage the citizen in the system, which makes the city smarter. Basic infrastructure component that makes the city smarter include transport, energy, healthcare, water and waste management. The present study is aimed to develop Web-GIS based framework for the lodging complaint, visualization and monitoring for solid waste in an urban area. A Web-GIS based framework is presented that uses free open-source software (FOSS) such as open layer, Javascript, Apache tomcat, Geoserver and PostgreSQL/PostGIS for visualization and monitoring of geospatial data. Using this framework a Geo-locator tool is developed to find the locations of facility (bins) to end user for reporting and lodging complain etc. It also develops automatic report for municipal officers to quickly respond to the complaints.

Keywords *MSW; Geoserver; Open Layer; Open Source; PostGIS; WebGIS*

1. Introduction

Web-GIS is also known as Internet GIS, which is the combination of Internet and GIS. It is a conventional GIS which uses the Internet as a basic information infrastructure for spatial data dissemination. Internet GIS is regarded as an interactive, distributed, dynamic, cross-platform and client/server computing system which has the capability to access various forms of GIS data and functions in an interoperable environment [1].

There has been many WebGIS based system and decision support system for geospatial mapping for map visualization [1], assessment of health [2, 3], transportation [4] and for decision making that include the public participation [5].

GIS and Internet technology are useful in monitoring the urban system. GIS improves the monitoring and visualization experience and makes possible to monitor and visualize the city in spatial context.

With the help of GIS, it has become possible to visualize the physical entities in a virtual environment using different models.

The basic goals of smart cities are efficient organization, recycling and reuse of already developed solutions, better and quick decision making, easier to contact the governing organization (eg. Municipality, Nagar Nigam etc.) and improve the participation of citizen for longer sustainable environment.

In the present study web-GIS based has been developed that works as information system as well as used for monitoring the solid waste complaint. Free open source softwares have been used in development of system.

2. Architecture of WebGIS based Framework

Web-GIS based architecture and used software in each phase is shown in Figure 1, which is based on client-server architecture. A generalized Web-GIS architecture includes three basic components: client layer, server layer, and data layer. For developing a WebGIS based framework html, openlayer, javascript and Java server page (JSP) are used at client layer. Apache tomcat and Geoserver is used as server layer and PostgreSQL with PostGIS are used as database for data storage and management.

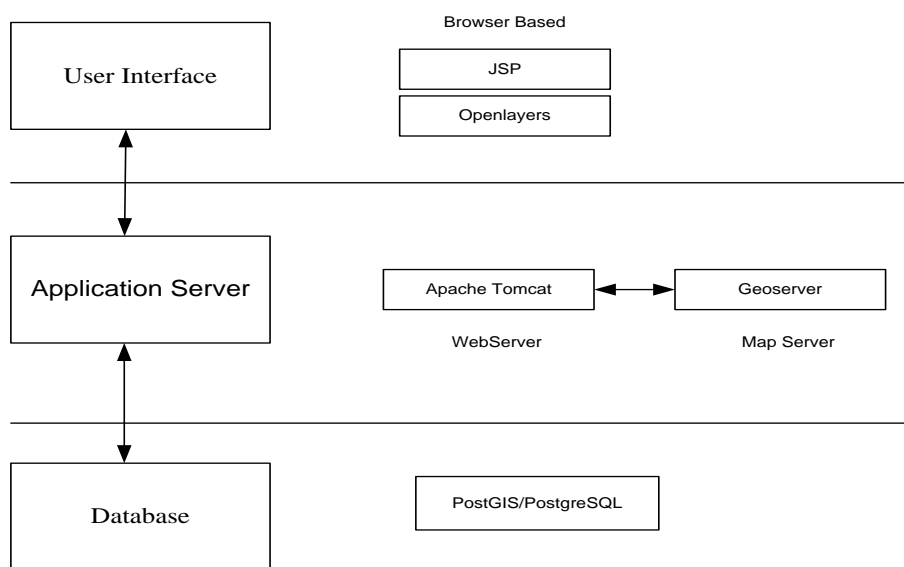


Figure 1: WebGIS Framework Architecture

Descriptions of open source software used in developed framework are as follows:

2.1. OpenLayers

Open Layers is an open-source JavaScript library for displaying map data in web browsers. It provides an API for building rich web-based geographic applications similar to Google Maps and Bing Maps. The library was originally based on the prototype JavaScript Framework [7]. Openlayers support GeoRSS, Keyhole markup language (KML), geography markup language (GML), GeoJSON and map data from any source using OGC standards as Web Map Services(WMS) or Web Feature service(WFS).

2.2. Apache Tomcat

Apache Tomcat software is an open source implementation of the Java Servlet and Java Server Pages technologies [8]. It is a web server and servlet container

2.3. GeoServer

Geoserver is an open source server for sharing geospatial data which provide the interoperability. It publishes data from any major spatial data source using open standards. GeoServer can access a variety of spatially enabled databases such as Oracle Spatial, ArcSDE and PostGIS [2]. GeoServer also publish data from many sources such as PostGIS, shapefile, java property file as vector data sources ArcGrid, GeoTIFF, Gtopo30, Image Mosaic and World Image as Raster data sources and other. Geoserver can deliver these data to different formats such as GIF, GeoTIFF, JPEG, KML, PDF, PNG and OpenLayer [9].

2.4. PostGIS/PostgreSQL

PostgreSQL database coupled with the additional PostGIS package are OGC (open geospatial consortium) compliant and open source software [10]. Postgres is an enterprise class relational database system. PostGIS is a spatial add-on for Postgres [6]. PostGIS spatially enables the Postgres database by adding support for geographic objects, allowing it to understand coordinate systems, projections, transformations, etc. PostGIS is the most common data store used with GeoServer because both are open source applications as well as being OGC standards compliant [2].

3. Development of Framework

Web-GIS based framework is developed for visualization of geospatial data, named as Web GIS based Framework for Management and Monitoring of Municipal Solid Waste (WGFMM-MSW). Figure 2 gives the framework of proposed system. It includes three modules namely public, ward level administrator and city administrator. Modules are further subdivided into sub modules as shown in Figure 2.

In public module main concern is to lodge complain regarding the solid waste location with the help of geo-locator. It shows the latitude, longitude and closing matching address.

The Ward level admin module is divided into three sub modules as given below:

- 1) To assign jobs to employee based on lodged complaint about unattended garbage bins by waste collection agency/system.
- 2) To update the status based on served complaints by the employees.
- 3) To generate the ward wise report based on solid waste complaint.

The third module is 'Admin module' for the management authority of the city whose responsibility is to monitor the status of solid waste management of the entire city. System helps the authority to visualize entire city data at one place and to generate reports accordingly. This helps administrator to assess the solid waste efficiency of entire city which may be used for further planning and improving the system with time.

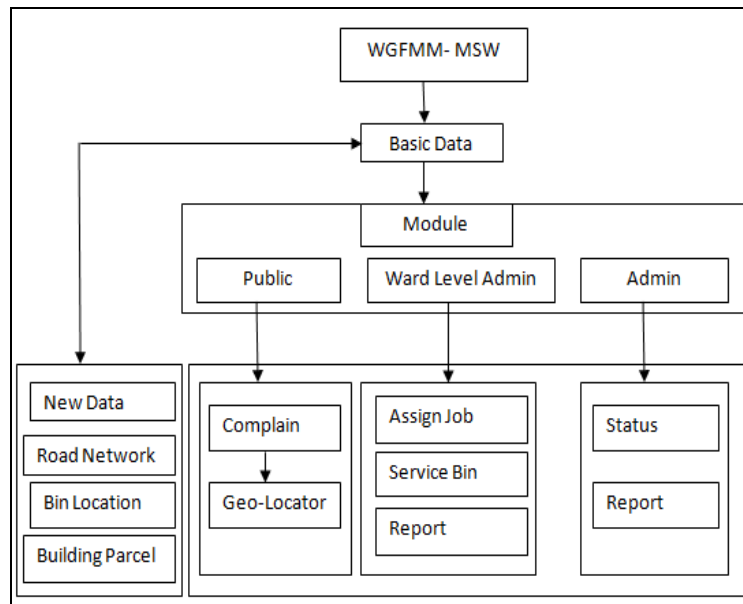


Figure 2: Framework for WGFMM-MSW

4. Implementation of Framework

Proposed Web GIS based framework has been implemented for complaint monitoring and management of municipal solid waste. For implementing the framework study area is Allahabad city. Basic data that have been used in system are road network and point vector data of bins location. The road network is created on survey of India (SOI) toposheet of scale 1:50000 using ArcGIS software. Bins location has been collected by field survey using the GPS receiver and then plotted in ArcGIS software. These data have been exported in PostGRES/PostGIS database using the pgShapeLoader graphical interface. Publish these layers in GeoServer from PostGIS. These published layers are shown in Figure 3 and 4 respectively.

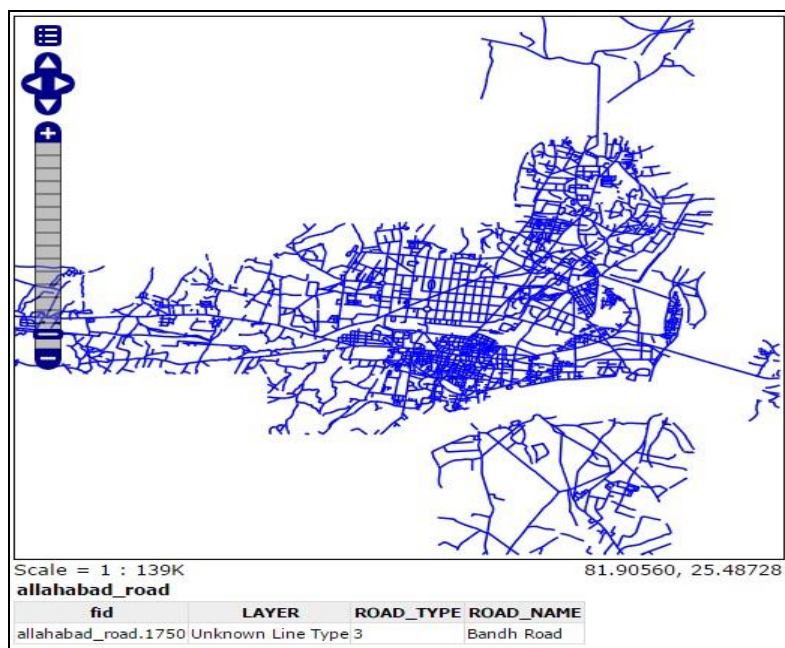


Figure 3: Road network of Allahabad

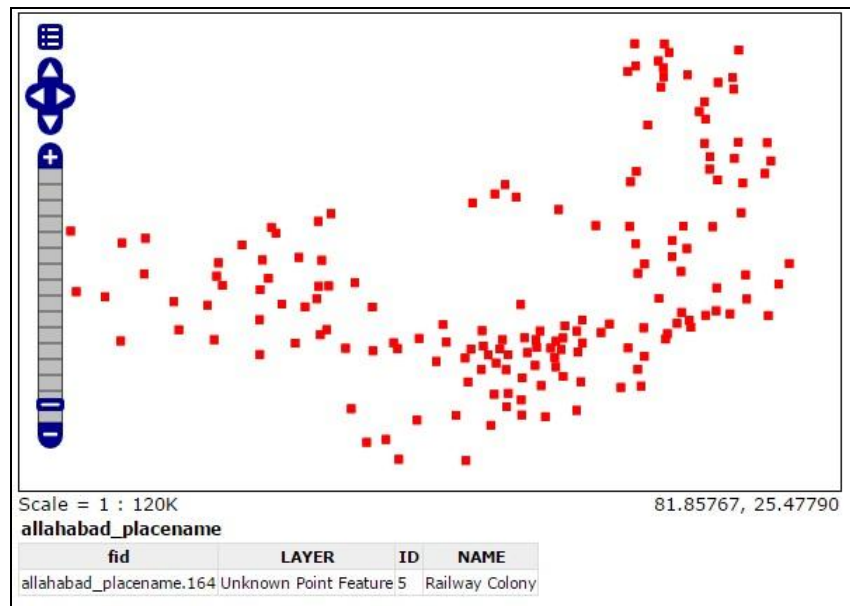


Figure 4: Bins location published in Geoserver

These layers are meaningful when the base layers are added in web application and overlaid these layers on the base map. Base layer can be added using the Open street map or Google map. Visualization of map and features with base layer provide the realistic view of environment. Google map is used as a base layer in application. A snapshot of home page is shown in Figure 5 to explain the implemented framework. Home page consists of the module links as indicated in Figure 2.

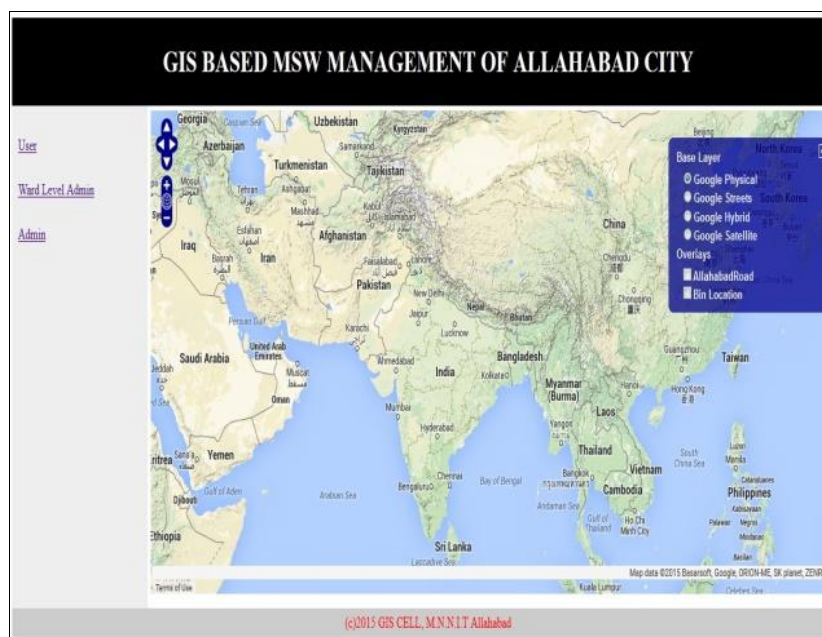


Figure 5: Home page of implemented Framework

First module for lodging the complaint by user is named as Geo-locator. Geo-locator tool is developed for public participation and feedback. It shows the Geo-locator status, location in form of longitude and latitude and close matching address across the roads. Figure 6 shows the location and close matching address of the user who lodged the complaint about the unattended solid waste bins or unestimated garbage generated at any location due to activities such as demolition, public events etc. Geo-locator

works when it moves with mouse point and it shows the status of attributes. Marker status attribute is at drag ended it shows the correct information about attributes. This information is used by the end user to lodge complaint by clicking on submit button as shown in Figure 6.

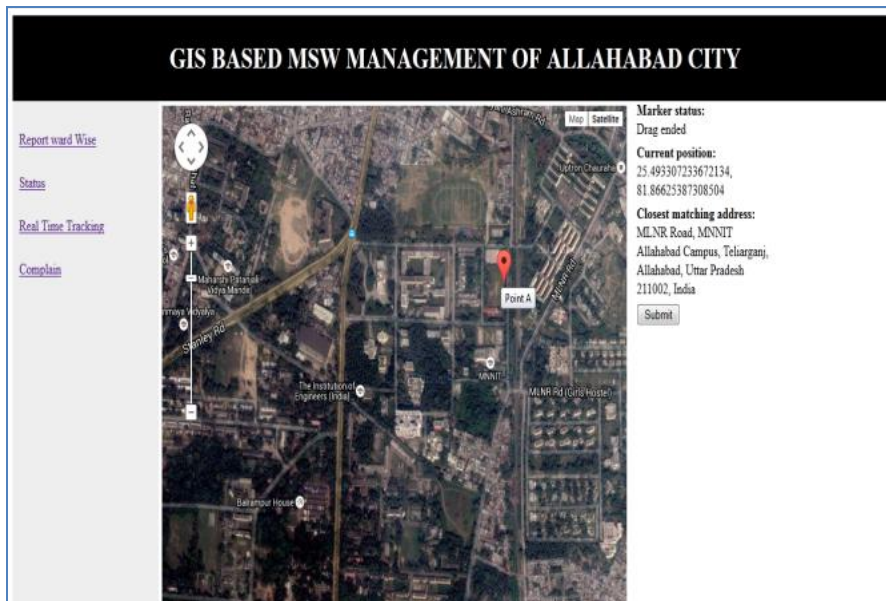


Figure 6: Geo-locator tool for citizen to report and lodge complain of solid waste

Geo-locator for administrator works when address is put in textbox and then clicked on Geo-code button; it generates the marker on the map at given address. Figure 7 shows the location of complaints to the administrator on the map. This may be helpful to the administrator when complains about solid waste are lodged through telephone or from other communicated system. This information is used by the administrator for providing the service to the end user by communicating address to employee who is serving at that location.

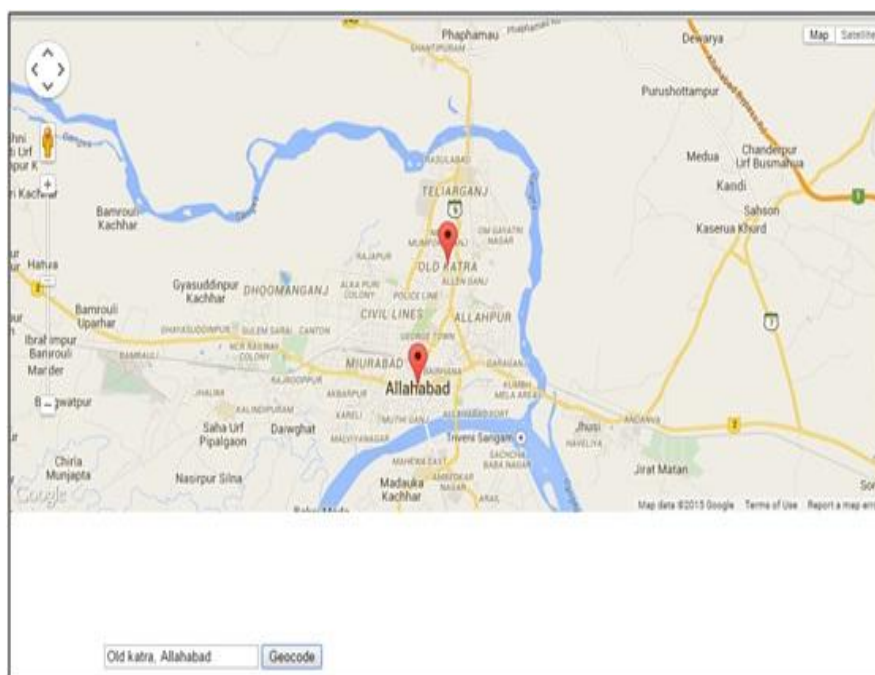


Figure 7: Geo-Locator for Administrator to know Position on Map

These lodged complaints are saved in database which is used by administrator at different levels to monitor the system. Ward level admin responsibility is to distribute the jobs to employee based on lodged complaints. At the end of the day status is updated based on attended complaints by employee. This updated information is saved in the database and used by city administrator to check the status of entire city and can generate the report accordingly.

5. Conclusions

In this paper WebGIS based framework is introduced for solid waste complaint monitoring and management. For public participation to easily lodge complaints online with help of GIS tool a Geo-locator marker is developed. Geo-locator marker helps the user to easily find the exact location with close matching address for lodging complaints. This lodged complaint is saved in a central database and this helps the different levels of administrator to see the status of city on map to improve the decision making capability of administrator. With the help of this tool, collection of solid waste becomes easy and the service level and satisfaction of citizen is improved. This may also be helpful in finding the waste generation in city.

References

- [1] Huang, B., Jiang, B., and Li, H. An Integration of GIS, Virtual Reality and the Internet for Visualization, Analysis and Exploration of Spatial Data. *Int. J. Geographical Information Science*. 2001. 15 (5) 439-456.
- [2] MacEachren, A.M., Crawford S., Akella, M., and Lengerich, G. Design and Implementation of a Model, Web-based, GIS Enabled Cancer Atlas. *The Cartographic Journal*. 2008. 45 (4) 246-260.
- [3] Abdullahi, F.B., Lawal, M.M., and Agushaka, J.O. Design and Implementation of a Web-Based GIS for Public Healthcare Decision Supports System in Zaria Metropolis. *IJRRAS Healthcare Decision Support System*. 2010. 4 (4) 435-439.
- [4] Ziliaskopoulos, A.K., and Waller, S.T. An Internet Based Geographic Information System that Integrates Data, Models and Users for Transportation Applications. *Transportation Research, Part C*: 8, 427-444.
- [5] Peng, Z. Internet GIS for Public Participation. *Environment and Planning B: Planning and Design*. 2001. 28, 889-905.
- [6] Akbari, M., and Peikar, S.R.H. Evaluation of Free/Open Source Software using OSMM Model Case Study: WebGIS and Spatial Database. *Advances in Computer Science: An International Journal*. 2014. 3 (5) 34-43.
- [7] OpenLayers 3. <http://openlayers.org/>.
- [8] The Apache Software Foundation, Apache Tomcat. <http://tomcat.apache.org/>.
- [9] Open Source Geospatial Foundation. GeoServer. <http://geoserver.org/>.
- [10] OSGeo, Oregon, United States. PostGIS. <http://postgis.refractory.net/>.

Decadal Impact Study of Saharan Dust Transport using Multi Sensor Measurements

Sriharsha Madhavan, John J. Qu, and Xianjun Hao

Environmental Science and Technology Center, Department of Geography and Geoinformation Sciences, George Mason University, 4400 University Drive, Fairfax, Virginia, USA

Publication Date: 13 July 2016

DOI: <https://doi.org/10.23953/cloud.ijarsg.65>



Copyright © 2016 Sriharsha Madhavan, John J. Qu, and Xianjun Hao. This is an open access article distributed under the **Creative Commons Attribution License**, which permits unrestricted use, distribution, and reproduction in any medium, provided the original work is properly cited.

Abstract Dust monitoring is one of the most challenging issues in today's aerosol remote sensing. Aerosol loading of dust predominantly in the arid regions is highly variable and thus poses challenges that are several magnitudes larger while compared to the monitoring of continental aerosols. This paper addresses the time varying aspects of the Saharan dust. A time series analysis from 2002-2013 of the Saharan dust region using multi-sensor measurements is done to capture the dust transport mechanisms that have been proven to have far reaching consequences in shaping the climatology of the Northern Atlantic region. Based on over decadal measurement datasets it was found that temporal and amount of dust transport were found to be a chief catalyst in the large number of storm systems (28) that occurred in 2005. Similarly, a time lag, slight change in spatial location, coupled with a reduction in the amount of dust transport had reduced the number of storm systems (11) that occurred in 2009. Relationship studies of the surface air temperatures and Aerosol Optical Thickness (AOT) over the study area showed a reduction in the correlation between the two geophysical parameters in 2005 compared to 2009. This means the large AOT values tended to slightly decrease the surface air temperatures. This also gave an idea of the location in terms of height of the dust to be in the upper troposphere and lower stratosphere (approximately between 2 km - 4 km above ground surface).

Keywords *Time Series; Multi-Sensor; AOT; MODIS; AIRS; Saharan Dust*

1. Introduction

Dust aerosol transport over the globe has far reaching effects in shaping the climate apart from affecting the air quality. Saharan dust is a major source of atmospheric dust found in the North (N.) Atlantic Ocean and coast of West Africa. It accounts for more than 50% of annual dust globally and ranges between 2 to 4 billion tons that get transported into the N Atlantic Ocean [1]. One of the radiative effects of Saharan dust is known to increase or decrease precipitation locally based on deep convection [2]. Also, found through the research reported by Perlwitz et al., [3] is that the dust emission, transport and climate forcing depends on the optical properties (i.e. absorption and transmission properties) of dust aerosol. The importance of understanding the radiative forcing of Saharan dust aerosols is further exemplified by the following reported results. Miller et al., in [4] demonstrated that while global precipitation is reduced in response to surface radiative forcing of dust,

precipitation may be enhanced locally over desert regions. In another work performed by Yoshika et al., [5] stated that for weakly absorbing dust rainfall is reduced globally as well as regionally over the Sahel region in response to the dust radiative effects. It was estimated about 30% of the observed precipitation reduction in Sahel from the 1950-1960s to the 1970-1980s are attributed to dust. Finally, Solomon et al., [6] found by modeling that the precipitation response over West Africa to dust radiative forcing is highly sensitive to the radiative properties of dust. Therefore, dust aerosol radiative forcing heavily influence the climate globally particularly in the regions of West (W) Africa, Atlantic, and Caribbean (WAAC).

This paper presents an in depth decadal time series of the Saharan dust transport using key geophysical parameters. Multiple sensors used in this work comprise of remotely based Earth Observing Systems (EOS) such as Terra (T) and Aqua (A) platforms and ground based AErosol RObotic NETwork (AERONET). The remote sensing based instruments include T- and A- MODerate-resolution Imaging Spectroradiometer (MODIS), and the A- Atmospheric InfraRed Sounder (AIRS). A unique geographical dust region is selected that covers the coastal W. African countries as well as several miles of the N. Atlantic Ocean. This allowed the analysis to capture the dust properties both at the origin and eventually at the transported dust location in the ocean. As found from previous literatures the importance of dust transport and its mitigation in the formation of Atlantic storm systems. The time series analysis is first done using the information on the statistics of the various Atlantic storm systems that have impacted in the last decade. Figure 1 presents a time series of the number of Atlantic systems formed since 2000, also shown is and the number of major hurricanes for each of those these years. The statistics shown are compiled from data archived at the National Hurricane Center (NHC) in National Oceanic and Atmospheric Administration (NOAA) (<http://www.nhc.noaa.gov/>). From Figure 1, two distinct types of pattern are observed. First, peak storm system formation years can be identified notably in 2005 and 2010. Second, 2002 and 2009 are found to be valley system years where in the total numbers of hurricanes formed where were significantly less than the average of 6.5/year compared to other years. Figure 2 shows the storm systems path (courtesy, NASA and NOAA (NHC)) for an example case of peak and valley system years respectively. It's quite clear that 2005 was quite a dynamic year in terms of hurricane formation and eventually recorded a historical high 28 storm systems of which 15 culminated into hurricane systems of varying categories. In contrast, 2009 was a barren year for Atlantic storm system activities as only 11 systems were formed of which only 3 contributed to becoming a hurricane. Hence, these two typical cases will be further examined in greater details using multi-sensor measurements that comprise of both remotely based and ground sensor based measurements.

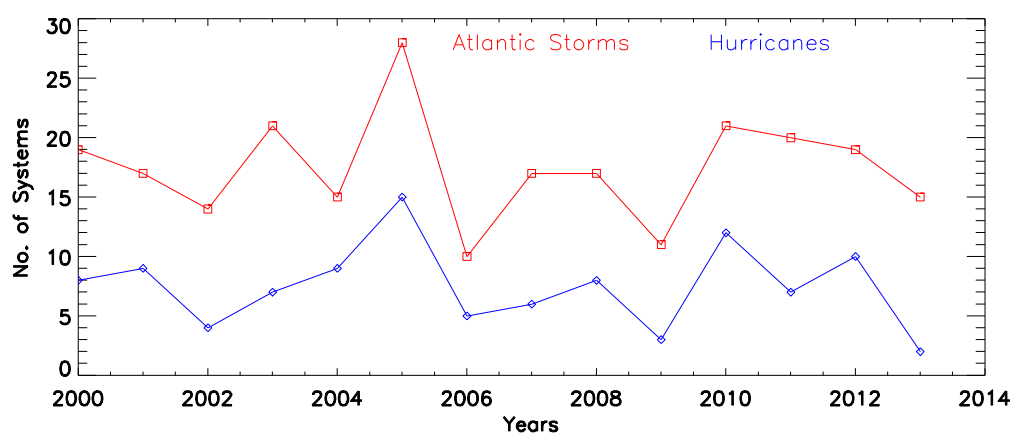
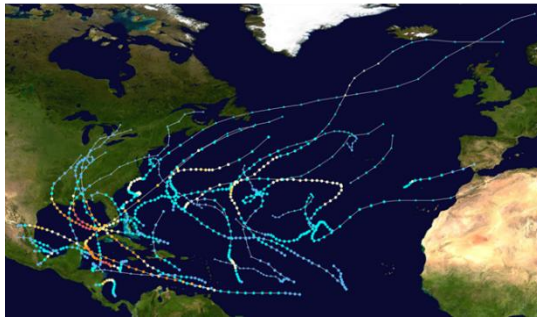


Figure 1: Number of the Atlantic storm systems from 2000-2013

2005 Systems Path



2009 Systems Path

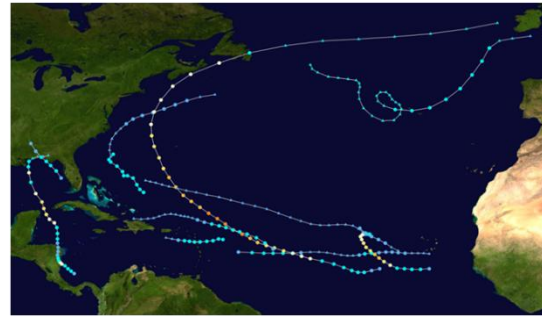


Figure 2: Example cases of N. Atlantic storm systems path. a. Peak system (2005), b. Valley system (2009).

Courtesy: <http://www.nhc.noaa.gov/>

2. Datasets and Methodology

In order to perform the analysis on the afore mentioned case study involving the N. Atlantic Ocean site, a sweet spot region needs to be carefully selected. One of the requirements of the sweet spot region is to guarantee enough coverage from the coast of the W. Africa to the center location of the transported dust in the ocean basin. Such a region would allow the study to focus on the properties of the dust and other geophysical parameters both at the origin and the final transported location. This was achieved by mimicking the test site locations used by the NASA African Monsoon Multidisciplinary Analyses (NAMMA) in 2006 [7-8], the field research investigation was set up 350 miles off the coast of Senegal. With the given knowledge, a field region with geographical co-ordinates (-44.12° W, 36.42° N, 5.02° S, 15.72° E) was set that covered all the requirements to perform the Saharan dust analysis. Figure 3 gives the corresponding satellite image view of the region used for further analysis.

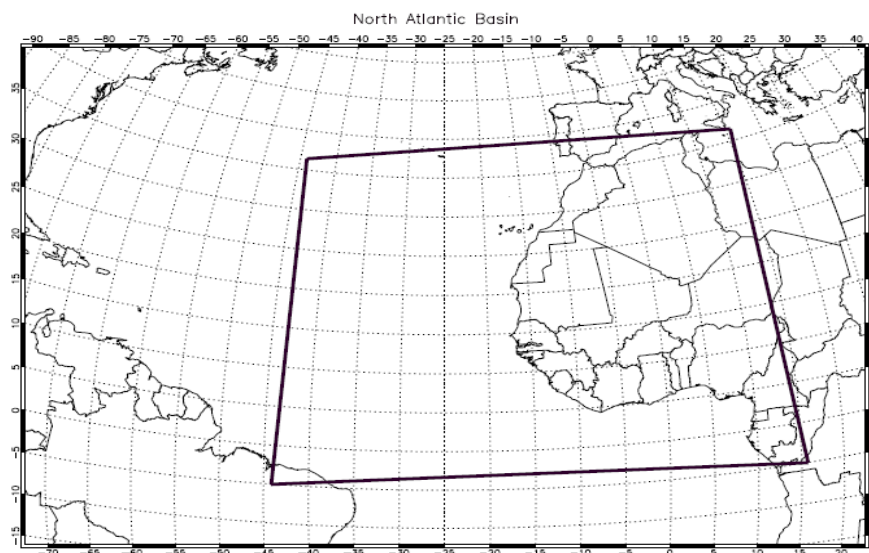


Figure 3: Saharan dust analysis region with geographical co-ordinates (-44.12° W, 36.42° N, 5.02° S, -15.72° E)

The ensuing paragraphs briefly but succinctly describes the various scientific data products that are used in the study.

The MODIS is a whisk broom scanning radiometer which is on board the T- and A- spacecrafts. Both MODIS instruments have successfully completed more than 12 years of on-orbit flight and collected a

decadal amount of high quality remotely sensed information in both reflective and thermal wavelengths on almost a 100% duty cycle [9-10]. Together, both instruments cover the entire globe every 2 days. Since, the T- spacecraft is on a descending orbit with an equatorial crossing time of approximately 10 am and the A- spacecraft is on an ascending orbit with an afternoon crossing of the equatorial plane at about 2 pm gives a unique opportunity to take measurements by the same instrument roughly twice within a day. About 40 science products are derived on different time scales i.e. daily, 8-day composite, and monthly; the products are compiled using the Level 1B (L1B) radiometrically and geo-location calibrated Top Of Atmosphere (TOA) radiance [11-15]. Hence, MODIS is a versatile instrument and is considered as the benchmark remote sensing instrument for the 2000s. Thus, the use of MODIS science products over a decade has ensured a high fidelity of the derived scientific parameters, in examining the various climate variables.

The primary MODIS Level 2 (L2) daily atmospheric products provide the AOT for each granule at a 10 km by 10 km resolution. The AOT measurements are reported in 7 spectral wavelengths varying from blue center wavelength of approximately 466 nm to shortwave Infrared center wavelength of approximately 2120 nm. The AOT retrieval algorithms employ a Look-Up Table (LUT) for radiative inversion. The LUT consists of various parameterizations that simulate the actual given conditions at the time of acquisition by the sensor [16]. Further, the monthly Level 3 (L3) products are assimilated from the L2 products and are weighted averages, with the exclusion of any instrument related anomalies or activities. The L [1-3] products were obtained from <http://ladsweb.nascom.nasa.gov>, the monthly data and subsequent charts are collected from the NASA's web based application for the Geospatial Interactive Online Visualization ANd aNalysis Infrastructure (GIOVANNI).

The AIRS instrument is a hyperspectral imaging sounder aboard the A- spacecraft. AIRS collects variety of measurements in a spectral range varying from about 3700 nm to 15400 nm. The AIRS instrument covers close to 80% of the globe with measurements collected in both the day (ascending) and night (descending) orbits. The AIRS uses a cross track scanning mechanism with acquisitions acquired in a coarser resolution of 15 km in comparison to the 1 km resolution of MODIS [17-18]. The AIRS L2 standard product provides physical retrieval of a variety of climate properties such as profiles of surface skin and air temperatures, total column water vapor, and total column ozone. The L2 products for the analysis presented in this paper were obtained from <http://disc.sci.gsfc.nasa.gov> while the L3 monthly data and charts for AIRS were obtained from the NASA GIOVANNI web based tool. Data archived at the National Hurricane Center (NHC) in National Oceanic and Atmospheric Administration (NOAA) (<http://www.nhc.noaa.gov/>) are used to provide the charts as shown in Figures 1 and 2.

In order to confirm the above satellite based AOT analysis a ground based reference was used. AERONET is a conglomerate of ground based remote sensing aerosol network providing globally distributed observations of spectral aerosol optical depth [19-20]. A group of 8 AERONET sites within the sweet spot region was selected. The geographical co-ordinates of each of these sites are provided in Table 1. Sites such as Cape Verde, Santa Cruz, Azores, are part of a chain of islands located a few 100 miles of the W. African coast. On the other hand, sites such as Dakhla are located at the very tip of the Saharan area. This allows the analysis to capture the dust amounts close to the source location as well as a few 100 miles into the ocean basin.

The AOT and skin / air temperature measurements, both remote sensing based and ground based, are significant indicators of the dust pattern and the amount of dust particle transported into the atmosphere. The L2 and L3 MODIS and AIRS products were used in assimilating the information. First, the geographical locations of the Saharan dust origin are ascertained, followed by the time scales required for the dust transport. By correlating the time scales and the amount of dust transport through the AOT measurements with the timing of the various Atlantic systems that were formed one would get a detailed understanding on the dust transport mechanism.

Table 1: List of AERONET Sites in the Sweet Spot Saharan Dust Region

| No. | Aeronet Site | Latitude | Longitude |
|-----|--------------|----------|-----------|
| 1 | Azores | 38.53 | -28.63 |
| 2 | Cape Verde | 16.73 | -22.94 |
| 3 | Dakhla | 39.09 | -15.95 |
| 4 | Graciosa | 28.48 | -28.03 |
| 5 | La Laguna | 28.48 | -16.32 |
| 6 | Lzana | 28.31 | -16.50 |
| 7 | Praia | 14.95 | -23.48 |
| 8 | Santa Cruz | 28.47 | -16.25 |

Next, a correlation study is performed between the AOT and skin / air temperatures to identify the possible dust locations in the atmosphere during the peak and valley dust transport years. Finally, a correlation study between the AERONET and remote sensor based measurements allows the study to be validated. With the afore mentioned studies a detailed understanding of the temporal and vertical and horizontal distribution of the dust transport will be achieved. The next subsection presents the results and analysis.

3. Results and Discussion

The decadal time series of AOT over the Saharan sweet spot region indicate interesting patterns when observed on a monthly scale. A couple of key instances are noted and presented here. Figure 4 presents the time series trend for AOT measurements from both MODIS instruments over the last decade since 2000 (with the exception A- MODIS as the satellite was launched only in 2002). The AOT is reported at 550 nm wavelength. Based on the figure, each data point is monthly averaged estimate over the study region. The x-axis is given in years with the start and mid months highlighted for each of the years is provided in the tick marks at the top. It is noted from the chart that the AOT measurements have seasonal oscillations with peak and minimum occurrences within each year. A careful introspection of both Figure 1 and Figure 4 reveals that peak storm system could have a periodicity of approximately 5 years and a valley storm system periodicity of approximately 5.5 years. It is however noted that the time span is short to make a strict claim as more climatic patterns need to be observed before this can be concluded. However, in order to tease out meaningful climatic interpretations the geophysical parameters noted earlier were synergistically combined.

As mentioned earlier, two key years 2005 and 2009 will be closely studied as they presented unique storm system patterns. One was a peak year while the other was a valley year. The AOT measurements on a monthly scale are shown in Figure 5. Also, the spatial distributions of the AOT for the two years are shown in Figures 6 and 7.

For the year 2005, the yearly averaged AOT value in the W. African Coast is typically higher and range between 0.55 and 1.2. In January 2005, the highest presence of Saharan dust is observed over the coast of W. Africa and the nearby Atlantic basin. AOT values typically averaged about 1.1 during this period which marks the start of the dust transport. By June 2005, an increased geographical extent of the Saharan dust is seen. The Saharan dust transport by now has peaked and is found close to the middle of the N. Atlantic Ocean. This triggered the start of the Atlantic storm season. By comparing the time scales for the start of dust transport to the 1st Atlantic system formed the incubation period for storm formation could be assessed.

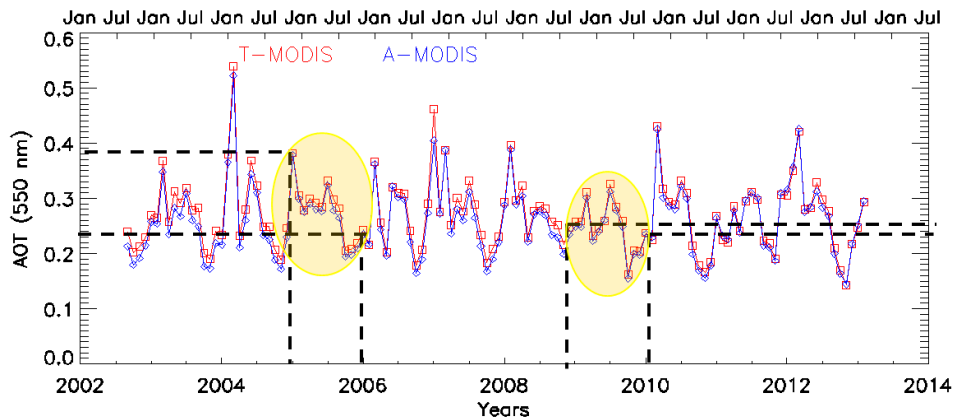


Figure 4: Time series of AOT measurements from the sweet spot region as shown in Figure 6

A higher amount of dust transport has resulted in a smaller incubation period of only 128 days. In October 2005, a cooling period is observed with a lower dust activity in the N. Atlantic basin which would mark the end of the dust transport. Also, noticed is the change of seasons as a heavy biomass burning activity causes the AOT value to increase in the Southern regions of Africa and parts of South America. As mentioned before since T-MODIS and A-MODIS are on morning and afternoon orbits this provides a unique advantage to look at the dust transport within a span of 3 to 4 hours. A slow transport of dust from the eastern shores of W. Africa to the N. Atlantic Ocean is observed through the two MODIS sensors. Very identical AOT measurements are seen for the same three months by A-MODIS.

In contrast to 2005 which is considered as the peak storm system year, 2009 was drastically apart. Significantly lower dust presence is observed as the AOT values varied from about 0.4 to 0.7 only. In comparison to January 2005 the AOT values only were as high as 0.8 in the Saharan dust region. On the contrary AOT values picked up in June of 2009 and averaged about 1.1. This showed a phase shift in the timing of the dust presence. As a consequence, to this shift, weak storm systems were formed and this further caused suppression or delay in formation of storm systems. Similar observations were reported by Kamal, M., et al., [21] who showed that presence of dust in hurricane systems tended to reduce the energy of the developing system. Hence, the out of phase and lower amount of dust transport caused the incubation period to about 192 days before the 1st Atlantic storm was observed. Again, the dust amount in terms of AOT and the transport mechanism was found to be very consistent with A-MODIS.

Based on several years of data (not shown) it was generally found that the start of dust formation is by end of November or early December, and by mid-January the Saharan dust has gathered enough energy to get transported into the N. Atlantic Ocean. This process takes about roughly 150 days to finally culminate into storm systems. Clearly, the amount and the pattern of the Saharan dust transport is a significant contributor to the storm system activity in the Atlantic region.

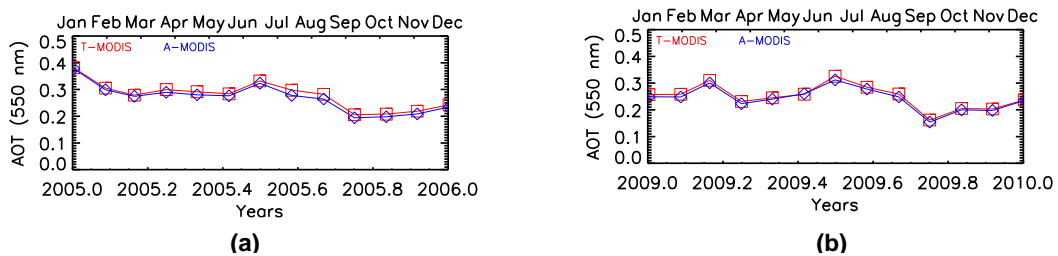


Figure 5: Monthly mean AOT measurements from 2005 and 2009

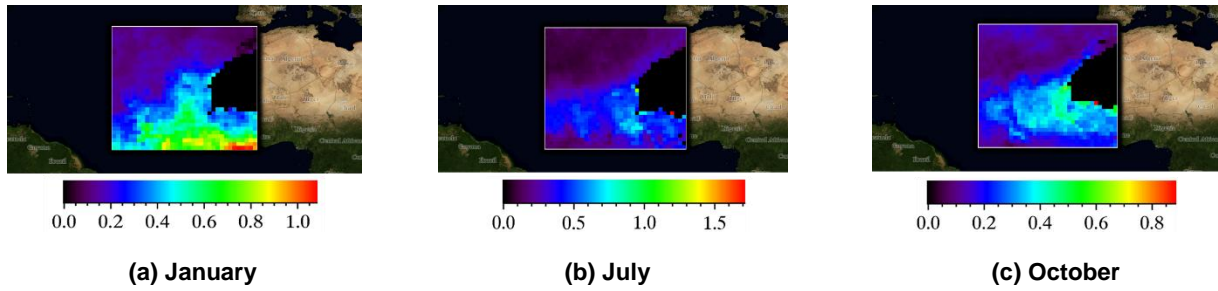


Figure 6: AOT measurement in 2005 over the African and the Atlantic regions using T-MODIS

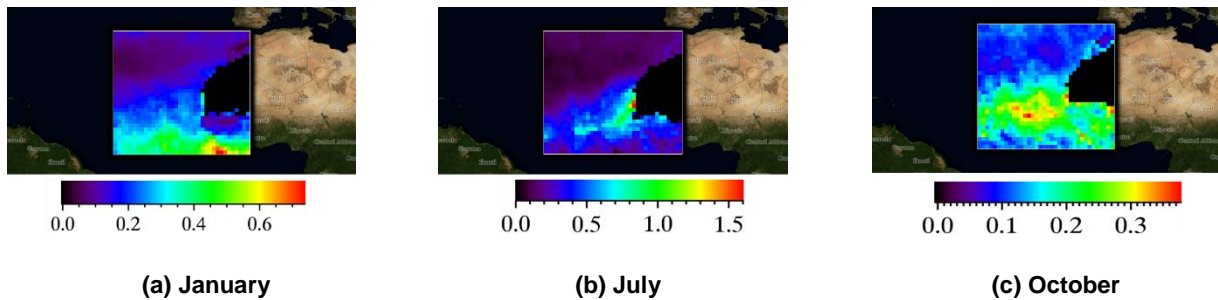


Figure 7: AOT measurement in 2009 over the African and the Atlantic regions using T-MODIS

Next, the measurements from the ground based AERONET sites are used to validate the measurements from the remote based time series measurements. The AERONET measurements are acquired every 15 minutes. For the purpose of this analysis, the AOT values at 550 nm were averaged daily and then assimilated into monthly averaged values for all the available data. In some instances, the AERONET was only commissioned for a brief period and hence only sporadic data was available. Sites such as Azores, Graciosa had only limited measurements of only 5 years starting 2000 and 2 years starting 2009 respectively. However, the overall trends could be well established by using all the 8 site locations. Cape Verde had the longest data record spanning for 11 years starting 2001. Figure 8 shows the AOT time series over a period of 12 years starting from 2000. The AOT measurements are provided in 550 nm from each of the ground based AERONET sites. The trends observed from Cape Verde, Laguna, and Santa Cruz show remarkable similarity with the MODIS based AOT measurements. This directly confirms the correlation between the time scale of heavy dust and the number of Atlantic Storm activity recorded for that year. The key highlight being the high AOT value in the month of January in 2005 which resulted in a peak storm system and a shift of high AOT values to the month of June in 2009 which attributed to the suppression of storm activities in that year.

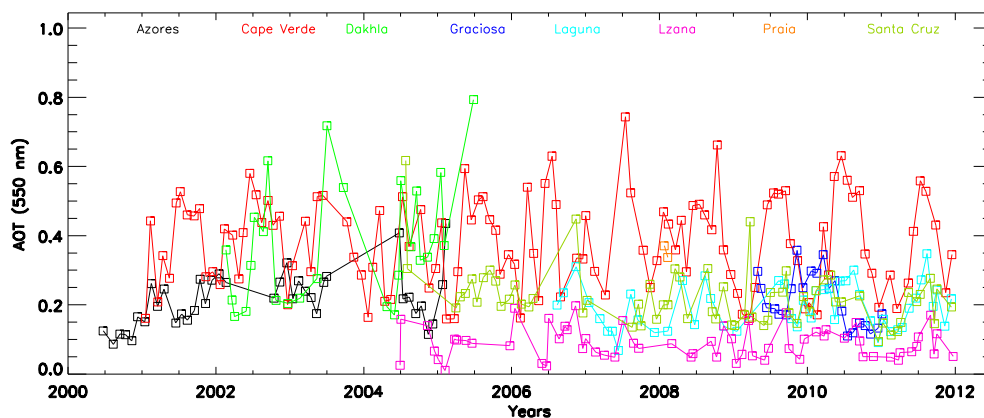


Figure 8: Time series of AOT measurements from the ground based AERONET sites within the sweet spot region

The above presented results and analysis covered the temporal and horizontal distribution of the Saharan dust which helped in correlating with the hurricane system formations. The second key aspect of the Saharan dust transport is to understand the vertical distribution of the dust during the two study years. This is enabled by studying the relationship of the skin and air temperature measurements from AIRS measurements and the AOT from both MODIS and Aeronet measurements. The air temperature is a critical geophysical parameter as the temperatures vary with height. The changes in air temperatures with height are what allow the stratification of the various atmospheric layers. This classic characterization is well described in [22]. Figure 9 shows the variation of air temperature above ground surface as a function of both heights in Km and air pressure given in mb.

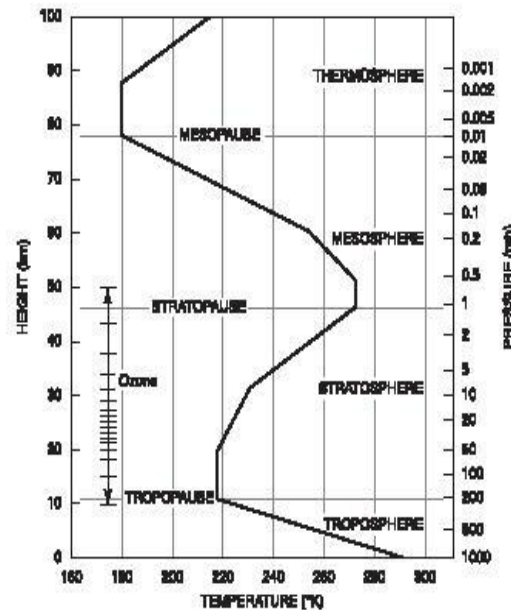


Figure 9: General relationship of air temperature with height above sea level [Liou, K.N., 2002]

In principle, in clear sky conditions AOT and air temperatures correlate very well. This implies that the aerosol particle size is so minute ($\ll 1 \mu\text{m}$) that the relationship of AOT and air temperature are monotonic and highly correlated. However as reported in [23], dust particles such as the Saharan dust are greater than $5 \mu\text{m}$ in diameter, work reported in [24] showed that dust particles in the Saharan region could be greater than $75 \mu\text{m}$ in diameter. Under these conditions, the correlation of the AOT and air temperatures significantly reduces and in many cases is even negatively correlated. Roy, S.S., [25] reported that the “AOD–temperature relationship was predominantly negative, meaning that higher AOD concentrations resulted in lower temperatures for both seasons over northeastern India and the west coast, in the vicinity of Mumbai”. Keeping the above framework in mind, a correlation is performed using the yearly averaged AOT and the air temperatures at varying heights over the Saharan dust region for 2005 (given in red) and 2009 (given in blue). In addition, the correlations are also provided for the ten-year period between 2002-2013 (shown in black). Figure 10 shows the correlation plot of the AOT both as a function of height and air pressure. It is clearly observed, that the correlation of yearly averaged AOT and air temperature is mostly reduced in 2005 when compared to 2009. This is also seen at varying heights with the exception at 25 km in height (middle stratosphere), where the correlation is pretty high. Several key observations are made from Figure 10. Consistent with the previous study reported in [25] the presence of high AOT concentrations (in this case heavy dust suspension) causes the correlation with air temperature to be lowered, the lowest being approximately -0.02 at a height of about 12 km above sea level. The consistent low correlation at heights of 2 km to 4 km in comparison to 2009 strongly suggests a heavy dust presence at these heights. The negative correlation at the 12 km could be chiefly attributed to clouds which are generally

seen at such heights. In 2009, when the dust suspension activity is the lowest, the correlation with air temperature is the highest. Thus, the Saharan dust in many ways is bound to have a cooling effect on the air temperature levels. The decadal correlation of AOT and air temperature is generally low and also found to be relatively constant at varying heights. On average, the correlation could vary between 0.25 and 0.35. Based on the MODIS and AIRS TOA measurements, the Saharan dust suspension in 2005 could be largely lifted to the lower- to middle Troposphere (approximately 2~5 km). The conditions described above are further tested and validated using the ground based AERONET and AIRS measurements. Figure 11, shows a similar correlation plot to Figure 10, and presents the study for the two years 2005 and 2009 respectively, over the ground site at Cape Verde. It is to be noted that ground based measurements are highly accurate at skin level (2 Km above surface level) and are good up to the upper to mid stratosphere. Also, the TOA measurements are generally over a wide spatial region, while AERONET measurements are highly localized.

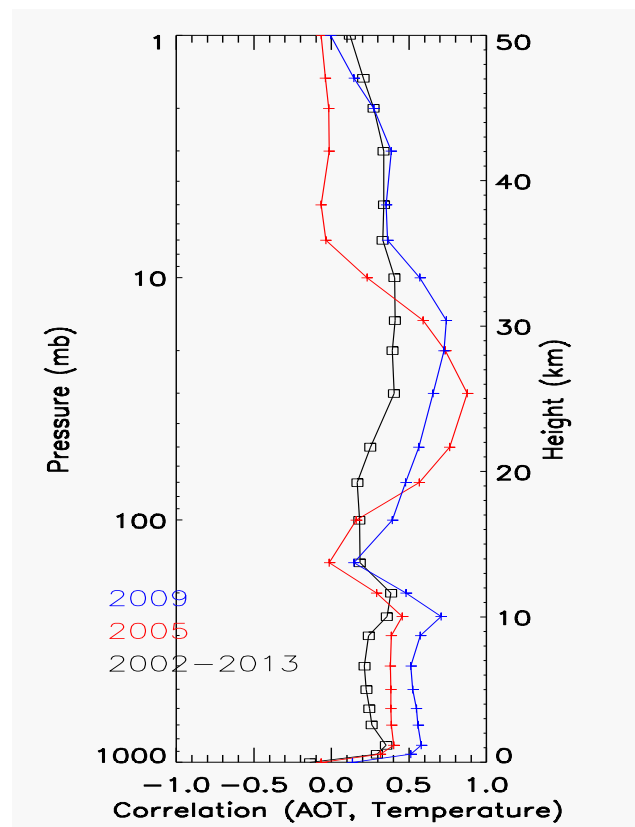


Figure 10: Correlation Plot of AOT measurement from MODIS and air temperature measurements from AIRS

Despite these differences, results based on Figure 11 correlate very well with the results from Figure 10. In other words, a similar dip in correlation between AOT and air temperature is observed around the 13~14 km vertical height above sea level. Further, another observation is also made. A large dip in 2005 is observed at a height of approximately 4 km above ground. An exact similar observation was made by Prospero, J.M., and Carlson T.N. [26]. In their work they reported “Most airborne Saharan dust of smaller particle size, lifted off the surface in a few local regions like Lake Chad. It typically reached and altitude of 4 km by the time it blows out over the Atlantic.” A very similar observation at Cape Verde confirms that the dust particles very near to the African coast is suspended at an altitude of about 4 km which is the middle troposphere and gets suspended to the higher troposphere over the North Atlantic Ocean. Further, in order to validate the above discovery, an independent measurement source was used to spot check. The NASA CALIPSO, a LIDAR sensor that provides backscattered attenuation is quite useful in determining the height of the suspended dust particles.

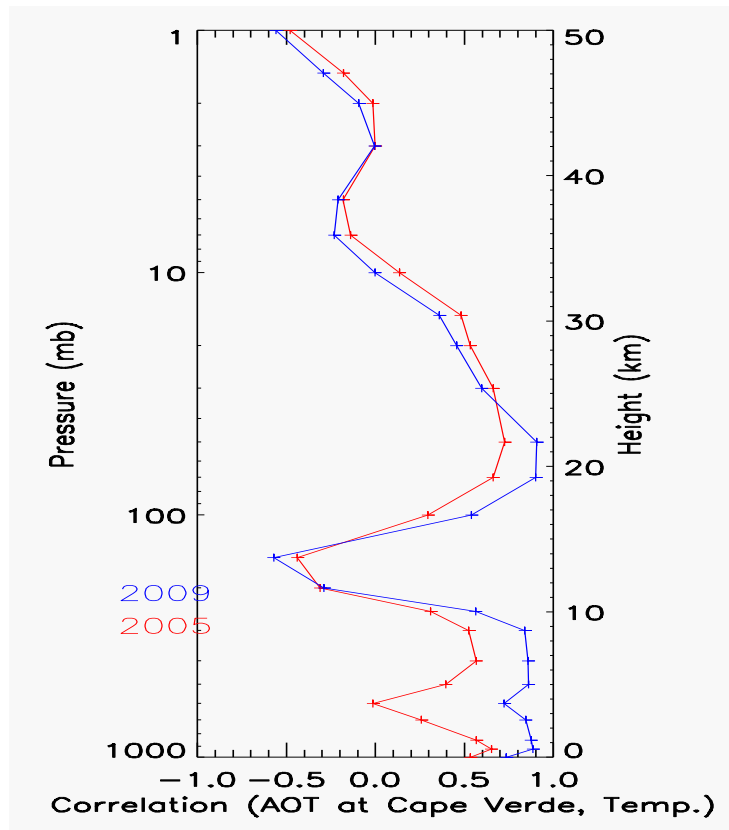


Figure 11: Correlation Plot of AOT measurement from AERONET site (Cape Verde) and air temperature measurements from AIRS

A simultaneous satellite observation of both A-MODIS and CALIPSO are used on the Saharan dust emission example dated July 30th 2013. Figure 12a shows the MODIS image with the overlapping CALIPSO pixels (shown by the dark pink line). Figure 12b gives the CALIPSO backscatter at 532 nm. Based on Figure 12b it is quite clear that the location of the dust on the left hand side (Figure 12a) corresponds to latitudes varying from approximately 18° to approximately 20.5°. At these locations, the backscatter attenuation is intense at heights of 2 km, 4-6 km. This corresponds to the lower and mid troposphere. Further, another set of attenuation cluster of lesser intensity is observed at 12 km that corresponds to the lower stratosphere which would signify presence of stratospheric clouds. This single event validates the earlier discoveries made through the AIRS and MODIS measurements.

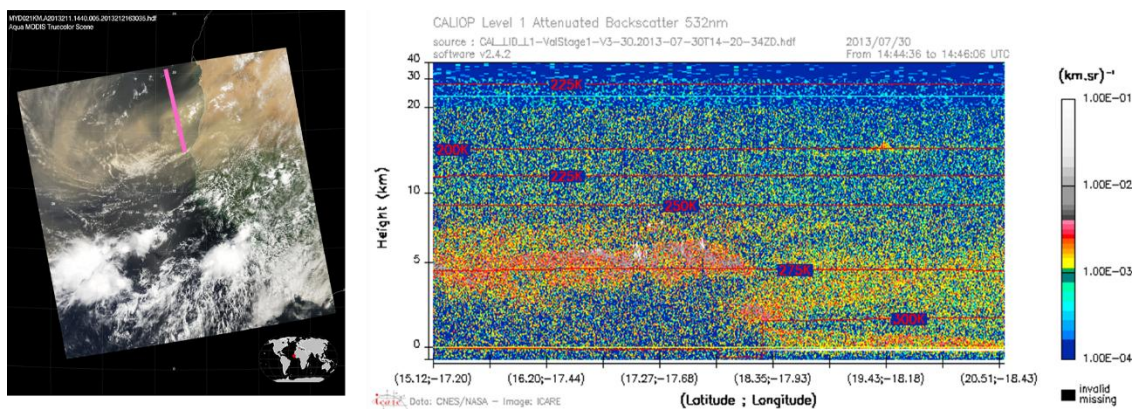


Figure 12: a. Simultaneous Satellite observations of MODIS and CALIPSO. b. Attenuated backscatter at 532 nm corresponding to the dark pink line shown in a

Since 2005 and 2009 are quite different in terms of the total amount and the spatial and vertical distribution of dust, a third analysis is performed. This study was intended to capture the correlation of the dust as measured by the ground site and the TOA measurements.

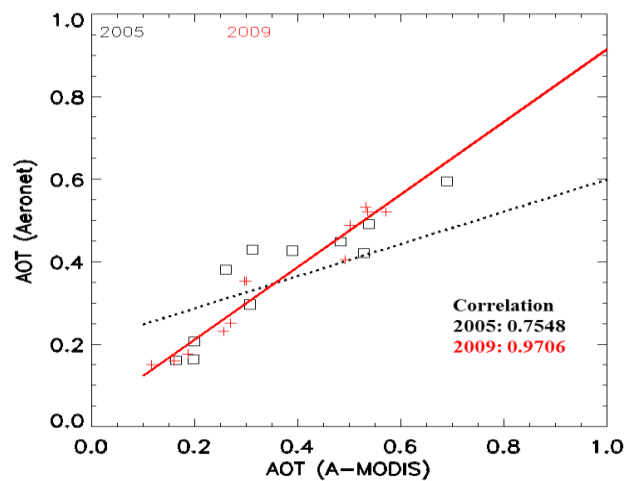


Figure 13: One-to-One Chart of AOT measurement from Aeronet and A-MODIS over Cape Verde

Figure 13 shows a one-to-one correlation plot for the monthly averaged AOT measurements between A-MODIS and AERONET at Cape Verde for 2005 (black squares and dotted fitted line) and 2009 (red plus symbol and solid fitted line) respectively. The correlation study shows that in 2005 the dust amount present in the TOA significantly different from the ground based measurement. This is suggestive by the lower correlation value of approximately 0.75. In 2009, the dust amounts are lower yielding to very good correlation (correlation coefficient of 0.97) between the TOA measurements and the ground based measurements. The detailed analysis presented here strongly suggests that the Saharan dust presence is quite significant for the climatology of the North Atlantic Ocean.

4. Conclusions

This paper focused on the time series study of the Saharan dust impact on the formation of the various weather systems for well over a decade. Two years '2005' and '2009' were identified as the 'Peak' and 'Valley' Storm formation years. Analysis was conducted by studying the relationship of geophysical quantities such as AOT, surface / air temperatures using multi sensors. Multi -sensor measurements from T- and A-MODIS, A-AIRS, and the ground based AERONET were employed. In general, the correlation of AOT and the air temperatures gave a fair idea of the exact lift off for the dust particles. The dust particles generally tended to be lifted from 2-4 km above surface level in the peak storm system year of 2005. A negative correlation was found between the AOT and air temperatures leading to a convincing conclusion that the suspended dust particles tended to cool the upper atmosphere. Also, the time series of the actual dust outbreak season was very critical to the storm formation intensities. The temporal and amount of dust transport were found to be a chief catalyst in the large number of storm systems (28) that occurred in 2005. Similarly, a time lag coupled with a slight change in spatial location of dust outbreak had reduced the amount of dust transport into the North Atlantic Ocean. This caused a significant reduction in the number of storm systems (11) that occurred in 2009. Finally, the heavy dust formation in the month of January 2005 is the probable cause for the incubation of storm energy. Dust accumulation was quite low in 2009 that reduced the capacity for the formation of storm system years.

Acknowledgments

The authors would like to thank Dr. Mike Summers (Department of Physics and Astronomy, GMU) and Dr. Donglian Sun (Department of Geography and Geoinformation Sciences, GMU) for their helpful comments and suggestions.

References

- [1] Goudie, A.S. and Middleton, N.J. *Saharan Dust Storms: Nature and Consequences*. Earth-Sci. Rev. 2001. 56; 179-204.
- [2] Miller, R.L. and Tegen, I. *Climate Response to Soil Dust Aerosols*. J. Climate. 1998. 11; 3247-3267.
- [3] Perlwitz, J., Tegen, I., and Miller, R.L. *Interactive Soil Dust Aerosol Model in the GISS GCM I. Sensitivity of the Soil Dust Cycle to Radiative Properties of Soil Dust Aerosols*. J. Geophys. Res. 2001. 106; 18167-18192.
- [4] Miller, R.L., Tegen I., and Perlwitz J. *Surface Radiative Forcing by Soil Dust Aerosols and the Hydrologic Cycle*. J. Geophys. Res. 2004. 109; D04203.
- [5] Yoshioka, M., Mahowald, N., Conley, A.J., Collins, W.D., Fillmore, D.W., Zender, C.S., and Coleman, D.B. *Impact of Desert Dust Radiative Forcing on Sahel Precipitation: Relative Importance of Dust Compared to Sea Surface Temperature Variations, Vegetation Changes and Greenhouse Gas Warming*. J. Climate. 2007. 16; 1445-1467.
- [6] Solomon, F., Mallet, M., Elguindi, N., Giorgi, F., Zakey A., and Konar'e, A. *Dust Aerosol Impact on Regional Precipitation Over Western Africa, Mechanisms and Sensitivity to Absorption Properties*. Geophys. Res. Lett. 2008. 35; L24705.
- [7] Chen, G., et al. *Observations of Saharan Dust Microphysical and Optical Properties from the Eastern Atlantic during NAMMA Airborne Field Campaign*. Atmos. Chem. Phys. 2011. 11; 723-740.
- [8] Jeong, M., et al. *Ground-based Measurements of Airborne Saharan Dust in Marine Environment during the NAMMA Field Experiment*. Geophys. Res. Lett. 2008. 35; L20805,
- [9] Salomonson, V.V., Barnes, W.L., Xiong, X., Kempler, S., and Masuoka, E. *An Overview of the Earth Observing System MODIS Instrument and Associated Data Systems Performance*. Proc. IGARSS. 2002. 2; 1174-1176.
- [10] Barnes, W.L., Xiong, X., and Salomonson, V.V. *Status of Terra MODIS and Aqua MODIS*. Proc. IGARSS. 2002. 2; 970-972.
- [11] Tanré, D., Kaufman, Y.J., Herman, F., and Mattoo, S. *Remote Sensing of Aerosol Properties over Oceans using the MODIS/EOS Spectral Radiances*. J. Geophys. Res. 1997. 102 (D14) 16971-88.
- [12] Kaufman, Y.J., Tanré, D., Remer, L.A., Vermote, E.F., Chu, A., and Holben, B.N. *Operational Remote Sensing of Tropospheric Aerosol over Land from EOS Moderate Resolution Imaging Spectroradiometer*. J Geophys Res. 1997. 102; 17051-67.

- [13] Justice, C.O., Vermote, E., Townshend, J.R.G., Defries, R., Roy, D.P., Hall, D.K., Salomonson, V.V., Privette, J.L., Riggs, G., Strahler, A., Lucht, W., Minnie, R.B., Lewis, P., and Barnsley, M.J. *The Moderate Resolution Imaging Spectroradiometer (MODIS): Land Remote Sensing for Global Change Research*. IEEE Trans. Geosci. Remote Sensing. 1998. 36; 1228-1249.
- [14] King, M.D., Menzel, W.P, Kaufman Y.J., et al. *Cloud and Aerosol Properties, Precipitable Water, and Profiles of Temperature and Humidity from MODIS*. IEEE Trans. Geosci. Remote Sens. 2003. 41; 442-58.
- [15] Parkinson, C.L. *Aqua: An Earth-Observing Satellite Mission to Examine Water and Other Climate Variables*. IEEE Trans. Geosci. Remote Sensing. 2003. 41 (2) 173-183.
- [16] Remer, L.A., Kaufman, Y.J., Tanre, D., et al. *The MODIS Aerosol Algorithm, Products and Validation*. Journal of the Atmospheric Sciences-Special Edition. 2005. 62; 947-973.
- [17] Aumann, H.H. and Strow, L. *AIRS: the First Hyper-Spectral Infrared Sounder for Operational Weather Forecasting*. Proc. of IEEE Aero. Conf., Mar 10-17. Big Sky MT Conference Publication. 2001. 4; 1683-92.
- [18] Qu, J.J., Gao, W., Kafatos, M., Murphy, R.E., and Salomonson, V.V. *Earth Science Satellite Remote Sensing*. Science and Instruments. Vol. 1. Springer Publishing Company. 2006. 408.
- [19] Dubovik, O., Smirnov, A., Holben, B.N., King M.D., Kaufman, Y.J., Eck, T.F., and Slutsker, I. *Accuracy Assessments of Aerosol Optical Properties Retrieved from AERONET Sun and Sky-Radiance Measurements*. J. Geophys. Res. 2000. 105; 9791-9806.
- [20] Holben, B.N., Tanre, D., Smirnov, A., Eck, T.F, Slutsker, I., Abuhassan, N., Newcomb, W.W., Schafer, J., Chatenet, B., Lavenue, F., Kaufman, Y.J., Vande Castle, J., Setzer, A., Markham, B., Clark, D., Frouin, R., Halthore, R., Karnieli, A., O'Neill, N.T., Pietras, C., Pinker, R.T., Voss, K., and Zibordi, G. *An Emerging Ground-Based Aerosol Climatology: Aerosol Optical Depth from AERONET*. J. Geophys. Res. 2001. 106; 12 067-12 097.
- [21] Kamal, M.M., Qu, J.J., and Hao, X. *A Study of Dust Aerosols Impact on Hurricanes with Multi-Sensors Measurement from Space*. The Open Remote Sensing Journal. 2012. 5; 73-82.
- [22] Liou, K.N., 2002: *An Introduction to Atmospheric Radiation*. 2nd Edition. International GeoPhysics Series. Academic Press, Elsevier, USA. 84; 365.
- [23] Shettle, E., 1984: *Optical and Radiative Properties of a Desert Aerosol Model*. In Proceedings of the Symposium on Radiation in the Atmosphere. Perugia, Italy, 21-28 Aug.
- [24] Wald, A.E. *Modeling Thermal Infrared (2-14 μm) Reflectance of Frost and Snow*. J. Geophys. Res. 1995. 99; 24, 241-24, 250.
- [25] Sen, S.R. *Impact of Aerosol Optical Depth on Seasonal Temperatures in India: A Spatio-Temporal Analysis*. International Journal of Remote Sensing. 2008. 29 (3) 727-740.
- [26] Prospero, J.M. and Carlson, T.N. *Dust Concentration in the Atmosphere of the Equatorial North Atlantic Ocean*. J. Geophys. Res. 1972. 77; 5255-5265.

Urban Built-up Area Extraction and Change Detection of Adama Municipal Area using Time-Series Landsat Images

Priyakant Sinha¹, Niva Kiran Verma², and Eskindir Ayele³

¹School of Environmental and Rural Science, University of New England, Armidale, NSW 2351, Australia

²School of Science and Technology, University of New England, Armidale, NSW 2351, Australia

³Department of Surveying, Dire Dawa Institute, Dire Dawa University, P.O. BOX 1362, Ethiopia

Publication Date: 16 August 2016

DOI: <https://doi.org/10.23953/cloud.ijarsg.67>



Copyright © 2016 Priyakant Sinha, Niva Kiran Verma, and Eskindir Ayele. This is an open access article distributed under the **Creative Commons Attribution License**, which permits unrestricted use, distribution, and reproduction in any medium, provided the original work is properly cited.

Abstract Urban built-up area information is required in various applications of land use planning and management. However, urban built-up area extraction from moderate spatial resolution Landsat time-series data is challenging because of significant intra-urban heterogeneity and spectral confusion between other landcover types. This paper proposes a technique to extract urban built-up area from time-series Landsat Thematic Mapper (TM) and Enhanced Thematic Mapper Plus (ETM+) imageries and determines urban area changes between 1984 to 2015 of Adama Municipal Area of Ethiopia. The study selected three indices, the Enhanced Built-Up and Bareness Index (EBBI), Soil Adjusted Vegetation Index (SAVI) and Modified Normalized Difference Water Index (MNDWI), to represent three major urban land-use classes: built-up and barren/bare land, open waterbody, and vegetation, respectively. The built-up area was extracted by taking the difference between EBBI, SAVI and MNDWI to remove the vegetation and water noises, and the resulted index image was spectrally segmented to separate built-up area from the non-urban built-up lands. The derived index was used to map built-up area for 1984, 1995, 2005 and 2015 periods. The expansion of the built-up area has been revealed as a major change in the area when city area expanded substantially by 293% between 1984 to 2015 periods. The advantage of the method was to use almost the entire spectral range of Landsat imageries which cause less spectral confusion between land cover classes and hence resulted in higher accuracies compared to other indices. The method was effective and simple to implement, and can be used for built-up extraction in other areas.

Keywords *Remote Sensing; Built-up Area; Spectral Indices; Urban Study; Landsat*

1. Introduction

Like any other cities in the developing world, Adama city has been gradually expanding both physically and in terms of its population and has been the locus of economic activity and transportation nodes in Ethiopia. Urban areas are dominated by built-up lands with impervious surfaces (Xu et al., 2000). Since the expansion of urbanized areas results in encroachment of surrounding valuable natural lands, the conversion of the nature lands into impervious built-up area may have significant impacts on the ecosystem, hydrologic system and biodiversity in the area (Xu, 2007). The study of urban spatial

expansion always needs accurate, quick and timely information on urban built-up areas in the form of size, shape, and spatial context for urban land use planners and decision makers. The information on pattern and extent of built-up area expansion in past few decades even becomes more important for various decision making process in terms of resource and utility allocation and distribution to attain urban landuse sustainability. Time-series satellite remote sensing data with different spatial and spectral resolutions have been found very promising to meet these requirements and have been used in several built-up area mapping and urban studies (e.g., Batty and Howes, 2001).

Mapping urban built-up areas using moderate resolution remote sensing data such as from Landsat TM/ETM+ data is complex because urban areas comprise of manmade and natural features like vegetation, waterbody, bareland etc. These urban areas often display heterogeneous spectral characteristics and significant spectral confusion between land cover classes and as a result reduce mapping accuracy. For example, barren land and asphalt concrete share similar spectral properties and, as a result, can be readily confused. To overcome this spectral confusion, numerous techniques have been developed for built-up and urban landcover mapping using satellite data. These techniques can be broadly grouped into two categories (He et al., 2010): (a) classification-based that involves use of different classification algorithms to improve mapping accuracies at pixel- and object-levels (e.g., Cleve et al., 2008) and (b) index-based that involve development of different indices to enhance a particular built-up area and determination of optimal threshold level to separate built-up areas from other landcover types (e.g., He et al., 2010; Zhang et al., 2005). Several indices for mapping the built-up and other landcover types in urban areas, such as the Normalised Difference Built-Up Index (NDBI) (He et al., 2010), Index-based Built-Up Index (IBI) (Xu, 2008), Urban Index (UI) (Kawamura et al., 1996), Normalised Difference Bareness Index (NDBal) (Zhao and Chen, 2005), and Bare soil index (BI) (Rikimaru and Miyatake, 1997) have been employed in various studies. However, each has its own advantages and disadvantages. For example, NDBI and UI were used for mapping of built-up or bare land areas, however, they were found ineffective in differentiating built-up area from bare land areas (Zha et al., 2003; He et al., 2010; Sukristiyanti et al., 2007) and therefore the universality of the approach needed to be tested in other geographic areas. He et al. (2010) improved the accuracy of the original approach using the automatic segmentation method. They noted that the complex spectral response pattern of vegetation, bare land, and built-up areas resulted in spectral confusion between classes and hence made it difficult to separate them on NDBI image. Varshney (2013) improved this method by setting an optimal threshold value by allocating improved positive difference values of continuous NDBI and Normalized Difference Vegetation Index (NDVI) to built-up areas. Xu (2008) developed the index-based built-up index (IBI) to detect asphalt and concrete surfaces.

In this study, a new technique is applied for the extraction of urban built-up area from Landsat data based on new image derived from three thematic indices, Enhanced Built-Up and Bareness Index (EBBI) (As-syakur, 2012), Soil Adjusted Vegetation Index (SAVI) (Huete, 1988), and Modified Normalized Difference Water Index (MNDWI) (Xu, 2005). The method is demonstrated through the extraction of urban built-up area of Adama Municipality from Landsat TM/ETM+ images for 1984, 1995, 2005 and 2015, and identification of changes in built-up areas between 1984-2015 periods. The study is important because Adama city is characterized by low density and low-rise development and like any third world city, leap frogging and sporadic developments are common in Adama. Therefore, common built-up area mapping indices do not look very promising in this case and there is need to develop alternative built-up mapping method for such area. Further, excessive alteration of landuse has been taking place without formal procedures. Therefore, information on built-up area change spatially would allow urban planner and decision makers to understand and evaluate municipal growth pattern in relation to landcover changes and management for sustainable usage of invaluable nature lands.

2. Study Area

Adama Municipal Area (AMA) comprises of city area and its surrounding covering a total area of 43.2 square km and characterized by a very good agricultural land in the vicinity. Adama city is located in central Ethiopia about 100 km south east of country capital Addis Ababa at $8^{\circ}35'$ to $8^{\circ}36'N$ latitude and $39^{\circ}12''$ to $39^{\circ}21'15''E$ longitude at an average altitude of 1620 m above sea level. It is situated in Rift valley system in the upper Awash River Basin. Figure 1 shows location map of the study area and Figure 2 shows urban built-up area for the year 1984 and 2005.

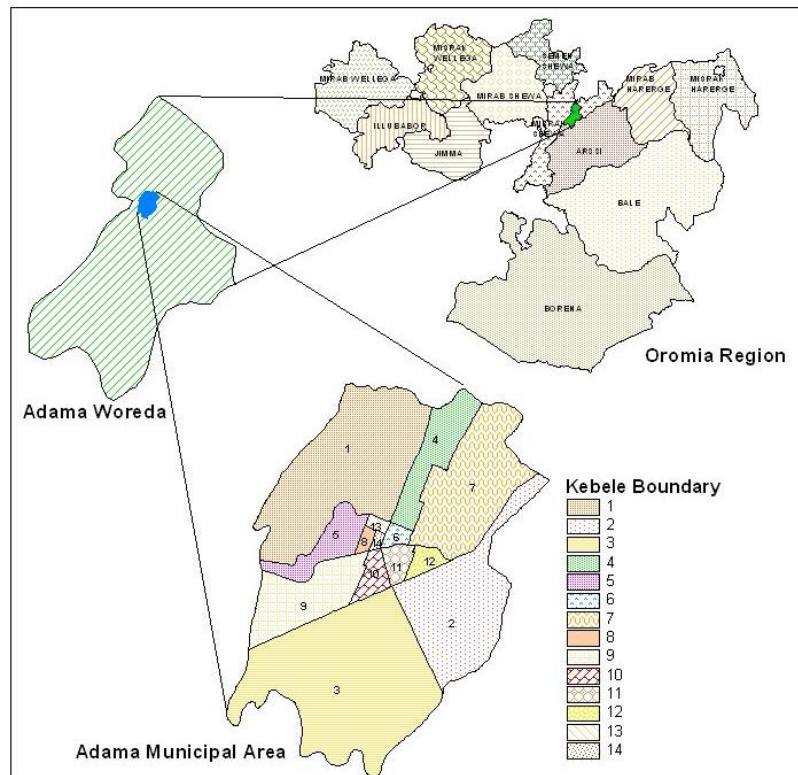


Figure 1: Location map of the Adama Municipal Area with Kebele boundaries

The urbanized area, which for many years was confined near and around the railway station, in the last three decades, has spread out in to the outer zones mainly to the southern fringes along the roads from Addis to the Awash. The area is covered by soil which is built up of light and fine clay which is easily blown in the storms during the dry months. The annual rainfall which mostly comes in the month of June-August ranges between 700-900 mm.

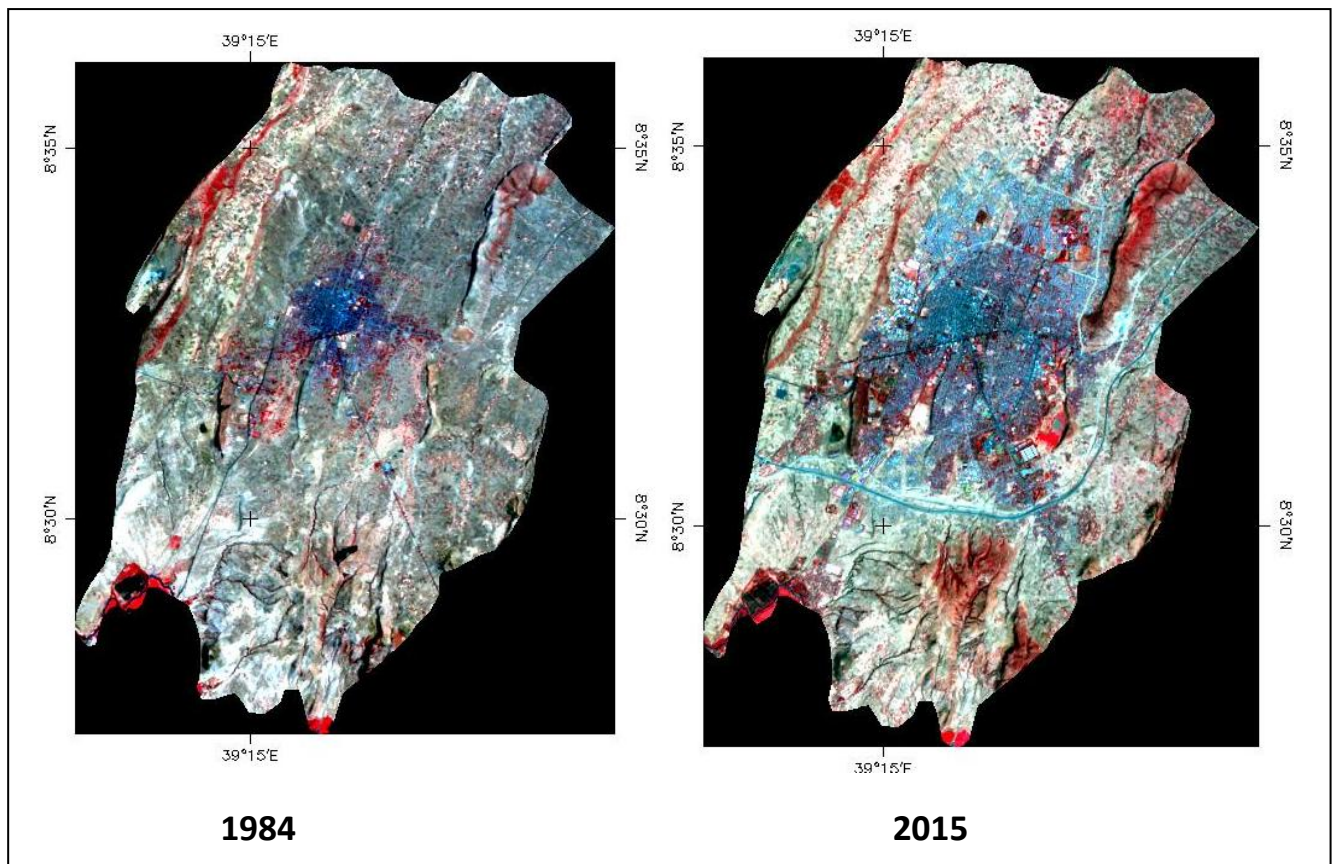


Figure 2: Adama City area in the year for 1984 and 2015 as shown on Standard False Colour Composite (FCC) of Landsat images. (FCC bands R:G:B–4:3:2)

3. Material and Methods

3.1. Image Acquisition and Pre-processing

Landsat time-series Thematic Mapper (TM) data of April 1984 and March 1995 and Enhanced Thematic Mapper plus (ETM+) data of January 2005 and February 2015 (path 168, row 54) – were acquired for built-up area extraction and change detection for the study. All image processing tasks were implemented in ENVI 5.0. The purpose of image pre-processing was to make all of the images similar so that they can be considered to be taken at the same environmental conditions, and by the same sensors (Hall et al., 1991). In the current study, the images were geometrically referenced to the UTM Zone 37 N projection system. Conversion of digital numbers (DNs) into radiance or surface reflectance is a requirement for quantitative analysis of multiple images acquired on different dates (Lu et al., 2004; Sinha et al., 2012). All four image DNs were converted to top-of-atmosphere (TOA) reflectance values using the equation suggested by Chander and Markham (2003). Further, a linear regression method was adopted for normalizing images on two different dates assuming the image pixel values on date 1 to be a linear function of the values of the same area on date 2 (Eckhardt et al., 1990; Jha and Unni, 1994).

3.2. New Built-Up Index (NBUI)

The concept of NBUI is based on the understanding that the urban area is a complex ecosystem composed of four main heterogeneous components: impervious surface material, green vegetation, exposed soil or bare soil and waterbody. Therefore, NBUI applies almost the entire wavelengths of Landsat images to represent these major urban landuse classes and computed as:

$$NBUI = \frac{B5-B4}{10 \times \sqrt{B5+B6}} - \left(\frac{(B4-B3) \times (1+l)}{B4-B3+1} + \frac{B2-B5}{B2+B5} \right) \quad (1)$$

where $l = 0$ to 1 depending upon high density vegetation ($l = 0$) to low density vegetation ($l = 1$). The first part of equation 1 uses near-infrared (NIR) ($0.83 \mu\text{m}$), shortwave-infrared (SWIR) ($1.65 \mu\text{m}$), and thermal-infrared (TIR) ($11.45 \mu\text{m}$) of Landsat images to highlight the contrast reflection range and absorption in built-up and bare land areas (e.g., Chen et al., 2003; Zha et al., 2003). The second part of NBUI uses SAVI to highlight vegetation by taking ratio of NIR (B4) to a red (B3) band to take advantage of high vegetation reflectance in NIR and high pigment absorption of red light (Jensen, 2007). The study used SAVI to map vegetation in place of commonly used Normalized Difference Index (NDVI) due to its advantage over NDVI when applied in an area with low plant cover such as the Adama Municipal Area. The SAVI was found effective even in area with vegetation cover as low as 15 percent, while NDVI is effective in area where vegetation cover is above 30 percent (Ray, 1994). The final expression of NBUI is used to map water, a major component in urban landuse, using a SWIR (B5) and green band (B2) as suggested by Xu (2005). Finally, density slicing was carried on NBUI image to create binary images separating built-up area from other landcover types for the year 2005 (Sinha and Kumar, 2013; 2014). The process was repeated for other change years (1984, 1995 and 2015) and the extracted built-up areas were compared to determine the change. To compare the effectiveness of NBUI in built-up area extraction, the results were compared with other commonly used built area mapping indices such as the Normalized Difference Built-up index (NDBI) (Zha et al., 2003) and Urban Index (UI) (Zhang et al., 2013) computed as:

$$NDBI = \frac{B5-B4}{B5+B4} \quad (2)$$

$$UI = \frac{B7-B4}{B7+B4} \quad (3)$$

3.3. Accuracy Assessment

High resolution IKONOS image (4 m spatial resolution) of Adama city for the year 2005 was used to assess the accuracy of extracted built-up area from different indices. The extracted built-up binary images were overlaid on the IKONOS image, and then visually inspected on pixel basis. The built-up areas were vectorized based on visual interpretation of IKONOS image, which was then converted into 30×30 m pixels in raster form in order to compare the results. A random sampling technique was applied to collect 75 sample pixels to compare the accuracies of built-up extraction from different indices and to evaluate the difference between them. The mapping accuracies were reported in the form of overall accuracy (OA) and kappa coefficient (κ) (Congalton and Green, 2009).

4. Results and Discussion

The mean spectral response of four landcover classes (Built-up, vegetation, barren land and waterbody) of Adama municipal area is shown in Figure 3.

Values area derived by taking mean of 20 pixels for each class.

It can be seen that built-up areas reflectance to be higher at SWIR and TIR wavelengths (B5, B6-1,2) and low in NIR (B4), and therefore these band associated with a high contrast for detecting built-up and bare land areas. Further, there exists an inverse reflectance relationship in B4 and B5 between built-up or bare land areas and vegetation. Vegetation has a high reflectance in B4 than the reflectance of built-up or bare land, while in B5 the reflectance of built-up is higher than vegetated areas (Herold et al., 2003). The TIR band has ability to distinguish high and low levels of albedo in built-up objects (Zhao and Chen, 2006), which can be used for mapping built-up areas based on a low albedo, which eliminates the effect of shadows and water while high albedo demonstrates built-up and

bare land (Weng, 2008). The use of SWIR in this study in place of NIR band in commonly used normalized difference water index (NDWI) is due to high built-up area reflectance in SWIR compared to NIR. Thus the resulting index will have negative values for the built-up area and positive values for the water features, which makes water features free from built-up area noise on index image. The index will not impact on vegetation due to negative value for vegetation. Therefore, by taking difference between index highlighting built-up area and bare land with indices highlighting vegetation and water as shown in equation 1, will result in positive values for built-up and barren pixels and will result in negative values for vegetation and water.

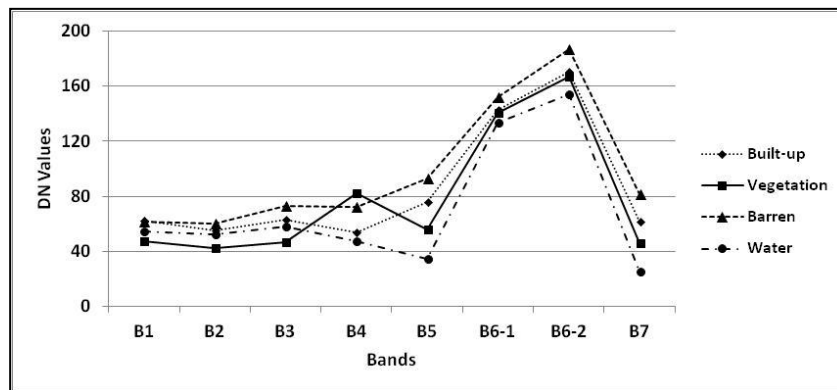


Figure 3: Spectral profiles for four land cover classes of Adama Municipal area for the year 2005

Figure 4 shows the built-up area extracted from NBUI (proposed method) and the two commonly used built-up indices, normalized difference built-up index (NDBI) and the urban index (UI) for the year 2005. The patterns of built-up area extraction were found similar in the three cases, however, the built-up area were more in case of NDBI and UI compared to NBUI. This is because of inability of NDBI and UI to differentiate between built-up and barren land or bare soil and most of the barren area in the adjacent land got mixed with the built area. However, high spectral reflectance of built-up area in B5 than vegetated areas and the ability of TIR band to distinguish high and low levels of albedo in built-up objects allowed built-up area to be separated from barren land in NBUI image. Further, by taking the difference between index highlighting built-up area and bare land and vegetation and water indices, separated built-up area from vegetation and water, resulting in higher accuracy in case of NBUI. The overall accuracy (OA) and kappa for NBUI image in built-up area extraction was found to be 93.2% and 0.91, respectively, which was much higher than NDBI (OA = 88.4%, kappa = 0.86) and the UI (OA = 86.1%, kappa = 0.83) images. The built-up areas as determined by each remote sensing indices and from the IKONOS data for the year 2005 were compared to determine the difference in area accuracies. The analysis results showed that the total built-up area obtained from the NBUI was 1074.6 ha, which was 124.5 ha more than the area determined from the IKONOS imagery. However, the built-up area extracted from the other two indices NDBI and UI were much higher (378.3 ha and 412.5 ha, respectively) as compared to IKONOS image based built-up area.

4.1. Built-Up Area Expansion from 1984 to 2015

The proposed method (NBUI) was most accurate in terms of built-up area extraction as compared to other two indices, and hence was used for built-up area mapping for the years 1984, 1995 and 2015, which were then compared to determine the built-up area expansion between 1984–2015 periods. Figure 5 shows built-up area expansion map highlighting the change occurring between two dates.

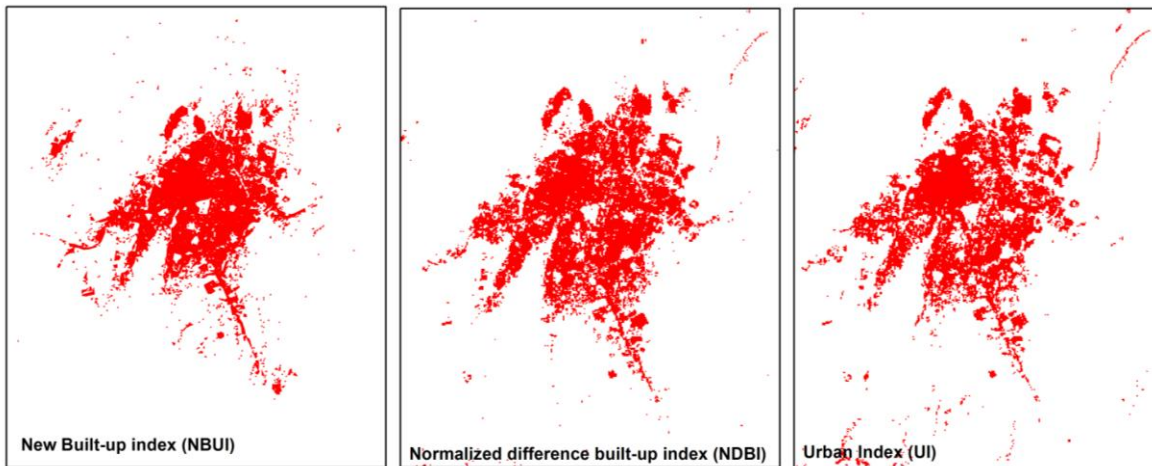


Figure 4: Built-up area extracted for Adama Municipal Area from NBUI (proposed method) and the two commonly used built-up indices, normalized difference built-up index (NDBI) and the urban index (UI) for the year 2005

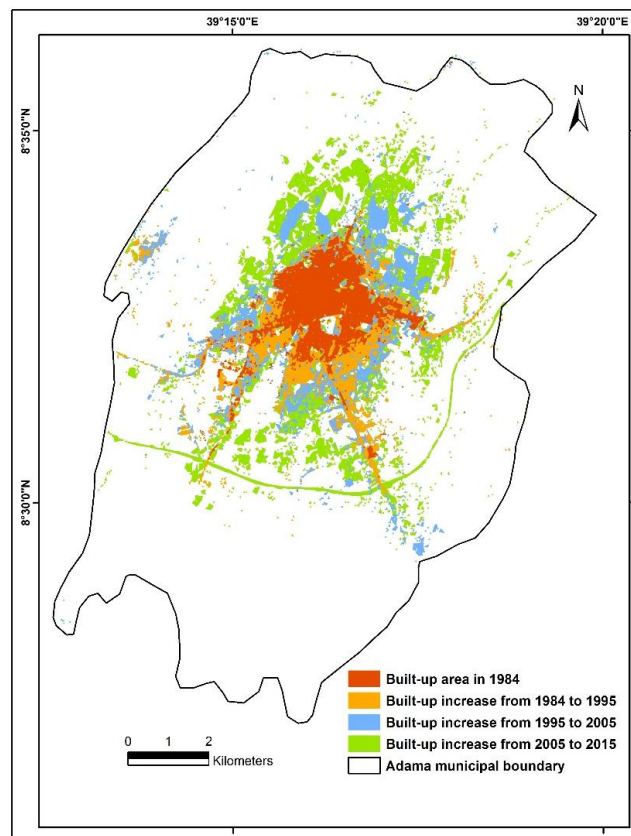


Figure 5: Built-up area expansion from 1984 to 2015 in Adama Municipal Area extracted from the proposed method (NBUI). Different shades of colour highlighting the change occurring between two dates

The comparison of class statistics shows that there has been marked land cover change in a span of 32 years. However, the results show a substantial increase in only two land use classes namely built up area and sparse vegetation. Built-up area showed an overall increase of almost 293% in a span of 32 years. The increase however was significantly higher (67.52 %) in the first decade of our study period, i.e. between 1984-1995. The increase in built-up area between 1995-2005 and 2005–2015 were also very significant (38.62% and 30%, respectively). The statistics for year 1984 shows city area

to be spread in only 578 ha which was only 4.23 % of the total municipal area, which increased to 2275 ha by the year 2015 accounting for nearly 17% of the total area. The increase in city area spread over the years was mostly on barren land concentrated towards the northern and western part of the area. The rest of the region depicted dispersed built-up land patterns.

5. Conclusions

Remote sensing based indices in urban areas are generally used to distinguish different urban landuse features such as built-up, barren land, vegetation and waterbody. However, accurate extraction of these landuse features is very challenging because of high intermixing between classes, especially in urban areas. This study proposed a method (NBUI) that highlights built-up area by first highlighting built-up and barren land area based on information from near-infrared, shortwave-infrared and thermal infrared data, and then excluded the vegetation and water noises to extract built-up area. The index was applied in Adama municipal area, Ethiopia, to map built-up area from time series data from 1984 to 2015. The results obtained by the NBUI were compared with those from commonly used built-up indices, the NDBI and UI and improvement in accuracy was found in case of NBUI over the two in terms of built-up area extraction. The method was found very simple to compute and easy to implement, however, it needs more testing particularly for more complex heterogeneous landscapes in terms of differentiating landcover classes. It can be used as one of the spectral bands along with original bands, or with other indices to improve the classification accuracy which warrant subsequent study. In a period of 32 years (1984-2015), the built-up area in Adama municipality has increased almost by 293% which showed excessive alteration of landuse occurring in the area. The results from this study on built-up area change would allow urban planner to understand and evaluate municipal growth for sustainable usage of urban land system.

References

- As-Syakur, A.R., Adnyana, I., Arthana, I.W., Nuarsa, I.W. Enhanced Built-Up and Bareness Index (EBBI) for Mapping Built-Up and Bare Land in an Urban Area. *Remote Sensing*. 2012. 4; 2957-2970.
- Batty, M. and Howes, D. Predicting Temporal Patterns in Urban Development From Remote Imagery. In Donnay, J.P., Barnsley, M.J., and Longley P.A. (eds.), *Remote Sensing in Urban Analysis*. 2001. 185-204.
- Chander, G. and Markham, B. Revised Landsat-5 TM Radiometric Calibration Procedures and Post-Calibration Dynamic Ranges. *IEEE Transaction in Geoscience and Remote Sensing*. 2003. 41 (11) 2674-2677.
- Chen, X.L., Zhao, H.M., Li, P.X., and Yin, Z.Y. Remote Sensing Image-Based Analysis of The Relationship Between Urban Heat Island and Land Use/Cover Changes. *Remote Sensing of Environment*. 2006. 104; 133-146.
- Chen, J., Gong, P., He, C., Pu, R., and Shi, P. Land Use/Cover Change Detection Using Improved Change Vector Analysis. *Photogrammetric Engineering and Remote Sensing*. 2003. 69; 369-379.
- Cleve, C., Kelly, M., Kearns, F., and Moritz, M. Classification of the Wildland–Urban Interface: A Comparison of Pixel- and Object-Based Classifications using High-Resolution Aerial Photography. *Comp. Environment and Urban System*. 2008. 32; 317-326.
- Congalton, R.G. and Green, K., 2009: *Assessing the Accuracy of Remotely Sensed Data: Principles and Practices*. Boca Raton: CRC/Taylor & Francis.

- Eckhardt, D.W., Verdin, J.P., and Lyford, G.R. Automated Update of an Irrigated Lands GIS using SPOT HRV Imagery. *Photogrammetric Engineering and Remote Sensing*. 1990. 56; 1515-1522.
- Hall, F.G., Botkin, D.B., Strebel, D.E., Woods, K.D., and Goetz, S.J. Large-scale patterns of forest succession as determined by remote sensing. *Ecology*. 1991. 72; 628-640.
- He, C., Shi, P., Xie, D., and Zhao, Y. Improving the Normalized Difference Built-Up Index to Map Urban Built-Up Areas Using a Semiautomatic Segmentation Approach. *Remote Sensing Letters*. 2010. 1; 213-221.
- Herold, M., Roberts, D.A., Gardner, M.E., and Dennison, P.E. Spectrometry for Urban Area Remote Sensing-Development and Analysis of a Spectral Library from 350 to 2400 nm. *Remote Sensing of Environment*. 2004. 91; 304-319.
- Herold, M., Gardner, M.E., and Roberts, D.A. Spectral Resolution Requirements For Mapping Urban Areas. *IEEE Transaction in Geoscience and Remote Sensing*. 2003. 41; 1907-1919.
- Huete, A.R. A Soil-Adjusted Vegetation Index (SAVI). *Remote Sensing of Environment*. 1988. 25 (3) 295-309.
- Jha, C.S. and Unni, N.V.M. Digital Change Detection of Forest Conversion of Dry Tropical Forest Region. *International Journal of Remote Sensing*. 1994. 15; 2543-2552.
- Jensen, J.R., 2007: *Remote Sensing of the Environment: An Earth Resource Perspective*. 2nd ed. Upper Saddle River, NJ: Pearson/Prentice Hall.
- Kawamura, M., Jayamana, S., and Tsujiko, Y. Relation between Social and Environmental Conditions in Colombo Sri Lanka and the Urban Index Estimated By Satellite Remote Sensing Data. *International Archieve of Photogrammetry and Remote Sensing*. 1996. 31 (B7) 321-326.
- Lu, D., Batistella, M., Moran, E., and Mausel, P. Application of Spectral Mixture Analysis to Amazonian Land-Use and Land-Cover Classification. *International Journal of Remote Sensing*. 2004. 25; 5345-5358.
- Ray, T.W., 1994: *Vegetation in Remote Sensing FAQs, Applications*, ER Mapper, Ltd., Perth, unpaginated CD-ROM.
- Rikimaru, A. and Miyatake, S., 1997: *Development of Forest Canopy Density Mapping and Monitoring Model using Indices of Vegetation, Bare soil and Shadow*. In Proceeding of the 18th Asian Conf. Rem. Sens. (ACRS), Kuala Lumpur, Malaysia, 3, 20-25.
- Sinha, P., Kumar, L., and Reid, N. Seasonal Variation in Landcover Classification Accuracy in Diverse Region. *Photogrammetric Engineering and Remote Sensing*. 2012. 78 (3) 781-780.
- Sinha, P. and Kumar, L. Binary Images in Seasonal Land-Cover Change Identification: A Comparative Study in Parts of NSW, Australia. *International Journal of Remote Sensing*. 2013. 34 (6) 2162-2186.
- Sinha, P. and Kumar, L. Independent Two-step Thresholding of Binary Images in Inter-Annual Land Cover Change/No-Change Identification. *ISPRS Journal of Photogrammetry and Remote Sensing*. 2013. 81 (7) 31-43.

- Sukristiyanti, R. and Suharyadi Jatmiko, R.H. Evaluasi Indeks Urban pada citra Landsat Multitemporal dalam ekstraksi kepadatan bangunan. *Jurnal Riset Geologi dan Pertambangan*. 2007. 17; 1-10.
- Varshney, A. and Rajesh E. A Comparative Study of Built-up Index Approaches for Automated Extraction of Built-up Regions from Remote Sensing Data. *Indian Society of Remote Sensing*. 2013.
- Weng, Q., Hu, X., and Lu, D. Extracting Impervious Surface from Medium Spatial Resolution Multispectral and Hyperspectral Imagery: A comparison. *International Journal of Remote Sensing*. 2008. 29 (11) 3209-3232.
- Xu, H. A Study on Information Extraction of Water Body with the Modified Normalized Difference Water Index (MNDWI). *Journal of Remote Sensing*. 2005. 9 (5) 511-517.
- Xu, H., X. Wang, and G. Xiao. A Remote Sensing and GIS Integrated Study On Urbanization With Its Impact on Arable Lands, Fuqing City, Fujian Province, China. *Land Degradation & Development*. 2000. 11 (4) 301-314.
- Xu, H. Extraction of Urban Built-up Land Features from Landsat Imagery Using a Thematic-oriented Index Combination Technique. *Photogrammetric Engineering and Remote Sensing*. 2007. 73 (12) 1381-1391.
- Xu, H. A New Index for Delineating Built-Up Land Features in Satellite Imagery. *International Journal of Remote Sensing*. 2008. 29; 4269-4276.
- Zhao, H.M. and Chen, X.L., 2005: *Use of Normalized Difference Bareness Index in Quickly Mapping Bare Areas from TM/ETM+*. In Proceedings IEEE International Geoscience and Remote Sensing Symposium, Seoul, Korea, 25-29 July. 3; 666-1668.
- Zhang, Q., Schaaf, C., and Seto, K.C. The Vegetation Adjusted NTL Urban Index: A New Approach to Reduce Saturation and Increase Variation in Nighttime Luminosity. *Remote Sensing of Environment*. 2013. 129; 32-41.
- Zhang, Q., Pavlic, G., Chen, W., Fraser, R., Leblanc, S., and Cihlar, J. A Semi-Automatic Segmentation Procedure for Feature Extraction in Remotely Sensed Imagery. *Computer and Geoscience*. 2005. 31; 289-296.
- Zha, Y., Gao, J., and Ni, S. Use of Normalized Difference Built-Up Index in Automatically Mapping Urban Areas from TM imagery. *International Journal of Remote Sensing*. 2003. 24; 583-594.
- Zhao, H.M. and Chen, X.L. Use of Normalized Difference Bareness Index in Quickly Mapping Bare Areas from TM/ETM+. *Geoscience and Remote Sensing Symposium*. 2005. 3 (25-29) 1666-1668.

Emerging Urban Heat Islands in the New Capital Region of Andhra Pradesh, India - A Satellite based Evaluation

Kusuma Sundara Kumar¹, Pinnamaneni Udaya Bhaskar², and Kollipara Padma Kumari¹

¹Department of Civil Engineering, JNT University, Kakinada, Andhra Pradesh, India

²AP Public Service Commission, Prathibha Bhavan, Hyderabad, Andhra Pradesh, India

Publication Date: 14 October 2016

DOI: <https://doi.org/10.23953/cloud.ijarsg.69>



Copyright © 2016 Kusuma Sundara Kumar, Pinnamaneni Udaya Bhaskar, and Kollipara Padma Kumari. This is an open access article distributed under the **Creative Commons Attribution License**, which permits unrestricted use, distribution, and reproduction in any medium, provided the original work is properly cited.

Abstract Satellite-based estimation and evaluation of urban heat islands (UHI) are latest in the field of urban micro climate and environmental management. UHI is one of the serious upcoming climatological issues regarding the development of cities. Conversion of the vegetative area into the impervious surface is the root cause of this problem of development of urban heat. Large-area coverage, quick process, more economical, less energy and other requirements are the attractive features of the satellite-based studies. The present study deals with the formation of UHI in the new capital region of Andhra Pradesh, a recently formed state in India in the year 2015. Satellite images of Landsat-8 are procured and processed to develop LULC and land surface temperature (LST) images. Field data of about 100 points, collected in the study area is also used in this work and the classification accuracy obtained is about 93%. From LULC and LST images it was concluded that the capital region is experiencing severe UHI phenomenon. The two big cities Vijayawada and Guntur are emerged as hot spots. High and low LST obtained are 58^oC and 23^oC respectively. The corresponding areas of hot and cold regions were estimated and presented. The outcome of this research can be used as a scientific basis for urban planners in urban planning and management as well as to increase the community awareness in urban heating effect. Urban greening is an essential measure to be adopted by the urban planners to protect the citizens from the ill effects of UHI.

Keywords *Urban Heat Island; Land Surface Temperature; Landsat-8; Land Use; Land Cover*

1. Introduction

Urban heat island is an upcoming serious issue which causes discomfort to the city dwellers and increases the power consumption because of the increased requirements of cooling, etc. Increased heat waves also result in the rise of the death toll, particularly old age people. Urban heat island is also connected to other micro climatological factors like humidity, rainfall, etc. Large scale conversion of forests and agricultural lands into impervious surfaces comprising roads, buildings and other infrastructure amenities is the main cause to this issue. The conversion of vegetative land into impervious land is changing the energy budget and responsible for excess heat development. Normally green areas with vegetation receive sunlight and utilize in the process of photosynthesis, and the energy will be converted into mass in the form of carbohydrates. Whereas the rocky area or

concrete or asphaltic surfaces do not utilize the solar energy instead, the accumulated energy will be converted into heat. So the short wave light energy from the sun is received by the impervious surfaces and converts in to heat energy in the form of infrared long wave. The cooling effect of vegetation is mainly due to the evapotranspiration. Through evapotranspiration water escapes from the plant leaves which contributed to the loss of energy and causes cooling effect. This makes the surrounding environment cooler. Bare soil or impervious surfaces will not perform this phenomenon and thereby appear hotter always compared to vegetative or green surfaces.

Detection of urban heat island (UHI) is useful for protection of the urban area from the potential evil effects of UHI effect. Proper environmental management with suitable strategies to control deforestation and de-vegetation together with development of green spaces can reduce the intensity of the problem. Conventional measurement of temperatures with thermometers could be very cumbersome and their interpretation in the form of maps is very tedious. Application of Satellite images can be a right option for this. Several researchers used satellite technology for study of UHI effect. Satellite images with thermal band information can be processed to obtain land surface temperature. *Landsat* is one of the largest satellite supplying satellite images since 1970's with multi-spectral as well as thermal bands.

Analyzing the spatio-temporal characteristics of land use land cover change is essential for understanding the pattern of urbanization [1]. Multi-temporal satellite images can be used to detect and assess the changes in land use land cover [2]. Divine Odame Appiah et al. applied the techniques of geo information for change analysis of land use and land cover [3]. Lewoye Tsegaye analysed land use land cover change and its drivers using remote sensing data and GIS analysis [4]. Sahoo Satiprasad et al. monitored the urban land use land cover change by using multi temporal remote sensing satellite information [5]. Several researchers used multi-temporal and multi spectral satellite imagery for detecting, assessing and monitoring the land use land cover changes [6-11]. Satellite images are widely used to study the urban heat island phenomenon [12]. There are several methods of extracting land surface temperature from satellite data. One of the prominent techniques, which provide simple, easy and highly effective result called Mono-Window algorithm, was used in this study [13]. Evaluating urban heat is very important for gauging urban ecological environment, surface atmospheric interaction and energy fluxes between land surface and earth's atmosphere [14,15]. It also directly influences the health and comfort of urban dwellers. It is also connected to the mortality related to the heat waves [16,17].

1.1. Objective of the Present Study

Our objective is to identify the impact of land use land cover on the thermal environment of the capital region of Andhra Pradesh, using satellite images. Through the study of thermal environment, formation urban heat islands will be identified and their extent will be estimated which is useful for proper urban thermal environmental management. Hence development of land use and cover image and corresponding land surface temperature images from the satellite images are the key elements in this research work.

2. Study Area and Data

2.1. Capital Region of Andhra Pradesh

Andhra Pradesh is located in the south-eastern part of the country, bordered by Odisha & Chhattisgarh on the North, Telangana & Karnataka on the west, Tamil Nadu towards the south and Bay of Bengal on the east. With the bifurcation of Andhra Pradesh in to two states, Telangana and Andhra Pradesh, the new state of Andhra Pradesh has got tremendous potential for development in infrastructure, industrial and commercial sectors.

The new state of Andhra Pradesh is spread across an area of approximately 160,200 square kilometers and divided into 13 districts with a total population on base of approximately 49 million as per 2011 census. Andhra Pradesh is endowed with a variety of geographic features such as Eastern Ghats, Nallamala Forest and the state is fed by Krishna and Godavari rivers. The state boasts of vast arable fertile land and rich endowments of natural resources such as asbestos, coal, limestone, granite, bauxite, gypsum, manganese, etc. Some of the major urban centres in the Andhra Pradesh state include Visakhapatnam, Vijayawada, Tirupati, Guntur and Nellore.

The new Andhra Pradesh state is envisioning to build a new Capital City, close to Vijayawada and Guntur. Andhra Pradesh Government aspires to build a world class Capital City; the glowing pride for all the people of Andhra Pradesh. The development of the New Capital City will be on a green field site of 217.23 sq.km located centrally within the Capital Region. The Capital Region comprises of 8,603.32 sq.km including forest and hills, straddling on both sides of the Krishna River in both Krishna and Guntur Districts. The Capital Region is well connected to the surrounding economic hubs by air, rail, road, and ports. The Andhra Pradesh Capital Region Development Authority (AP-CRDA) was notified on December 30th, 2014 by the Government of Andhra Pradesh, which replaced the existing Vijayawada-Guntur-Tenali-Mangalagiri Urban Development Authority (VGTMUDA). The extent of the region is spread in 58 mandals, of which 29 are in Krishna district and 29 in Guntur district. The capital region covers 18 mandals fully and 11 mandals partially in Guntur district. In Krishna district, it covers 15 mandals fully and 14 mandals partially under the jurisdiction of AP-CRDA.

Within this new capital region, several infrastructural projects were already proposed. One outer ring road project and one inner ring road project, capital city development project, airport development project are some examples. All these projects will definitely consume lot of land and there will be a significant change in the land use and land cover. These changes can affect the environmental conditions of this area. For estimating the future scenario, we need to know the present status. Hence the effect of land use land cover on the environment is estimated in the present day context. Particularly impact of land use land cover on the local climate was focussed in this study. For this land surface temperature is estimated from satellite images. The location of the study area selected is shown in the Figure 1.

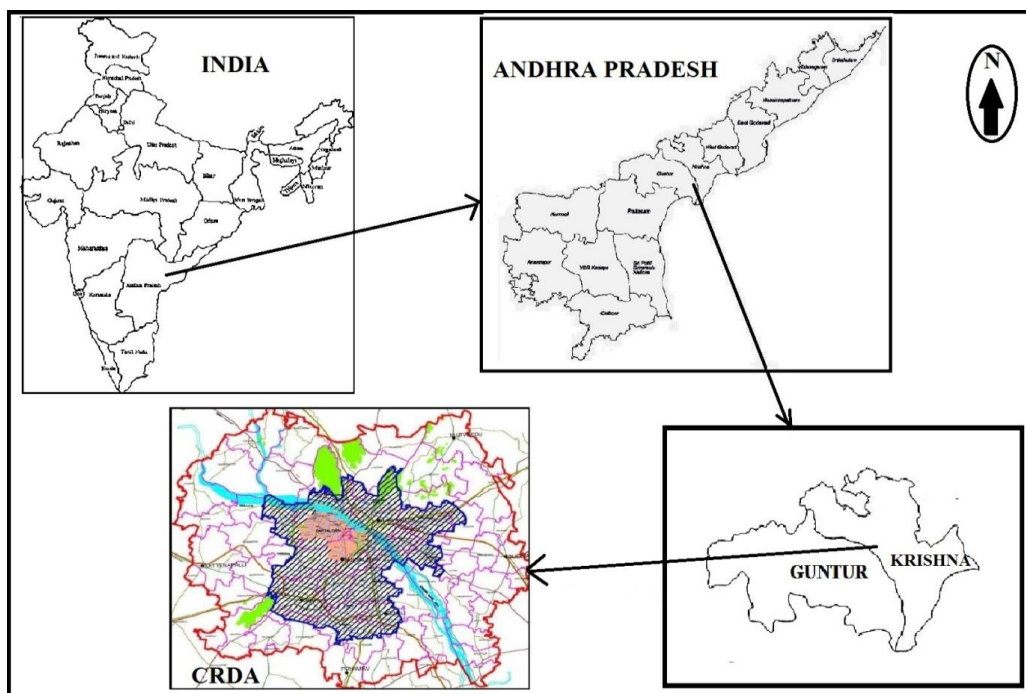


Figure 1: Location of the Study area: AP-CRDA







2.2. Data Collected







To carry out the present work first CRDA master plan proposed was collected from the authorities. Total 20 topo-maps were collected from Survey of India with the following numbers: 65 D/1 to 65 D/16, 65 H/1 to 65 H/4. The mosaic of these topo-maps after clipping the study area is obtained as a base map of the study area. Landsat-8, OLI-TIRS satellite image for the study area for the year 2015 was selected and downloaded from official website of USGS: <http://earthexplorer.usgs.gov/>. The details of satellite imagery collected were presented in the Table 1. For supplementing the image classification process with ground truth data, field visits were conducted in the entire study area and about 100 locations were identified and latitude and longitude were noted using hand held GPS. Some of the field data points collected were shown in the Table 2 as a sample.

Table 1: Details of satellite image collected

| Date | Time of Pass (GMT) | Satellite | Sensor | Reference System | Path/ Row (Scene centre) | Bands | Resolution in Meters |
|------------|--------------------|-----------|----------|------------------------------|--------------------------|-------|-------------------------------------|
| 2015-05-23 | 4:56:46 | Landsat-8 | OLI-TIRS | WRS-II WGS-84 Zone--44 | 142/49 | 11 | 30 (Both Reflective and Thermal) |

Table 2: Ground truth data collected by field visit in the study area (12 points were shown here as a sample)

| Point ID | Class ID | Latitude | Longitude | Place | Photo |
|----------|----------|---------------|---------------|------------|---|
| 1 | AL | 16 12 56.21 N | 80 46 17.38 E | Vellabadu |  |
| 2 | AL | 16 33 35.77 N | 80 41 46.32 E | Nunna |  |
| 3 | OD | 16 37 02.94 N | 80 25 14.69E | Kothapeta |  |
| 4 | BR | 16 39 42.42 N | 80 45 53.18E | Agiripalli |  |
| 5 | BR | 16 33 36.76 N | 80 49 34.91 E | Atkuru |  |
| 6 | FD | 16 13 13.53 N | 80 00 56.17 E | Kaza |  |

| | | | | | |
|----|----|---------------|---------------|----------------|--|
| 7 | WB | 16 20 56.73 N | 80 43 48.74 E | Krishna river |  |
| 8 | AL | 16 03 52.33N | 80 32 19.49 E | Kasukarru |  |
| 9 | BR | 16 28 00.58 N | 80 35 33.39 E | Yerrabale-m |  |
| 10 | OD | 16 23 52.37 N | 80 32 55.99 E | Chinnakka-ni |  |
| 11 | AL | 16 24 43.55 N | 80 36 38.55 E | Pedavadla-pudi |  |
| 12 | AL | 16 05 04.37 N | 80 46 40.59 E | Vemavaram |  |

WB- Water Bodies/Wet Lands, AL- Agricultural Land/Light Vegetation, FD- Forests/Dense Tree Clad Area, OD- Open Area/Dry Fields, BR- Barren Land/Rocky Area

3. Methodology

In this section, the methodology adopted in this work has been described briefly. As the main objective of the present research work is to determine the development of urban heat islands in the new capital region of Andhra Pradesh, the task completion involves the development of LULC image and LST image from the satellite images. The procured Landsat-8 satellite image which is in the form of 11 bands was first stacked and pre-processed for image enhancement using ERDAS Imagine. The blue, green red and near infrared bands were stacked to develop LULC. Supervised classification method was adopted using the maximum likelihood algorithm by selecting training sites within the study area. The entire study area has been classified into seven classes according to the site. The classification accuracy was also verified by performing the accuracy assessment using the collected field data. Field data from 100 points within the study area were collected using GPS and digital camera. Thus the LULC image of the study area was obtained. The process of LST image was explained below.

Cloud free Landsat-8 scene of the study area was downloaded from "earthexplorer" of USGS [18]. From the 11 bands of the image, band 11 was considered for generation of LST map. The band 10 image carries 16 bit information with digital numbers ranging from 0 to 65535. These digital numbers are brightness values in the thermal infrared region sensed by Landsat-8. Next step involves conversion of DN (Digital Number) to the physical measure of Top of Atmospheric Reflectance (TOA) and the Thermal band to At-Satellite Brightness Temperature. TIRS band data can be converted from spectral radiance to brightness temperature using the thermal constants provided in the Landsat8 data users handbook [19].

3.1. Calculation of Spectral Radiance

$$L\lambda = MLQ_{cal} + AL$$

where: $L\lambda$ = TOA spectral radiance (at the sensor's aperture) (Watts/(m²* sr * μ m))

ML = Band-specific multiplicative rescaling factor

AL = Band-specific additive rescaling factor

Q_{cal} = Quantized and calibrated standard product pixel values (DN)

3.2. Calculation of Brightness Temperature

$$TB = K_2 / \ln((K_1 / L\lambda) + 1)$$

where: TB = At-satellite brightness temperature (K)

K₁ = Band-specific thermal conversion constant (watts/m² * sr * μ m)

K₂ = Band-specific thermal conversion constant (in kelvin)

In this work Band-11 was considered for estimation of LST. From the metadata file the following constants were extracted for use in the above algorithm.

K₁ = 1201.14 and K₂ = 480.89 for Band 11

ML = 0.0003342 and AL = 0.1 for Band 11

3.3. Estimation of Land Surface Temperature

Estimation of Land Surface Temperature Contact measurements of emissivity values of the surfaces using thermal radiometers and spectral assessment of samples supplemented LST estimation procedures in this study. Since the temperature values obtained as at-satellite temperature TB, referenced to black bodies, the land cover classes were assigned emissivity values derived through field measurements. Thus the emissivity corrected land surface temperatures can be calculated as

$$LST = TB / [1 + [\lambda * TB / \rho] \ln \epsilon]$$

λ = Wavelength of emitted radiance,

$$\rho = h * c / \sigma = (1.438 * 10^{-2} \text{ m K})$$

h = Planck's constant (6.626 * 10⁻³⁴ Js)

σ = Stefan Boltzmann constant (5.67 * 10⁻⁸ Wm⁻² K⁻⁴)

c = velocity of light (2.998 * 10⁸ m/s)

From the metadata, λ = 0.0000113m.

In the above LST algorithm ϵ is the emissivity of the surface.

Emissivity depends on the characteristic of the surface and it is inherent property of the material. The energy received from sun will be emitted back to space in different quantities by different materials. The emissivity values depend on the LULC. Emissivity image is obtained by developing a model in ERDAS which uses LULC and corresponding emissivity values. The emissivity values used in the model are given in the Table 3 below.

Table 3: Emissivity values of different LULC classes

| S. No. | Material/LULC | Emissivity |
|--------|-------------------------------------|------------|
| 1 | Water Bodies - Wet Lands | 0.98 |
| 2 | Sand - River Course | 0.90 |
| 3 | Built Up - Rural & Urban | 0.75 |
| 4 | Forest - Dense Tree Clad Area | 0.99 |
| 5 | Agriculture Land - Light Vegetation | 0.97 |
| 6 | Open Area - Dry Fields | 0.92 |
| 7 | Barren Land - Rocky Area | 0.85 |

4. Results and Discussion

In this section the results obtained from the present work has been presented and discussed. The output LULC image obtained from the supervised classification in ERDAS was given in Figure 2. The seven LULC classes and corresponding areas are given in the Table 4. The classified images are assessed for accuracy using the field data. The overall classification accuracy obtained is 93% and the corresponding Kappa Statistic was found to be 0.9102. From the emissivity, and the thermal band data of Landsat-8, land surface temperature image was developed in ERDAS and was presented in Figure 3.

Table 4: Areas of different LULC classes in the study area

| S. No. | Land Use Type | Area in Hectares |
|--------|-------------------------------------|------------------|
| 1 | Water Bodies - Wet Lands | 8281.08 |
| 2 | Sand - River Course | 14008 |
| 3 | Built Up - Rural & Urban | 35750.3 |
| 4 | Forest - Dense Tree Clad Area | 73216.9 |
| 5 | Agriculture Land - Light Vegetation | 187164 |
| 6 | Open Area - Dry Fields | 338747 |
| 7 | Barren Land - Rocky Area | 58516.61 |
| | Total | 715683.89 |

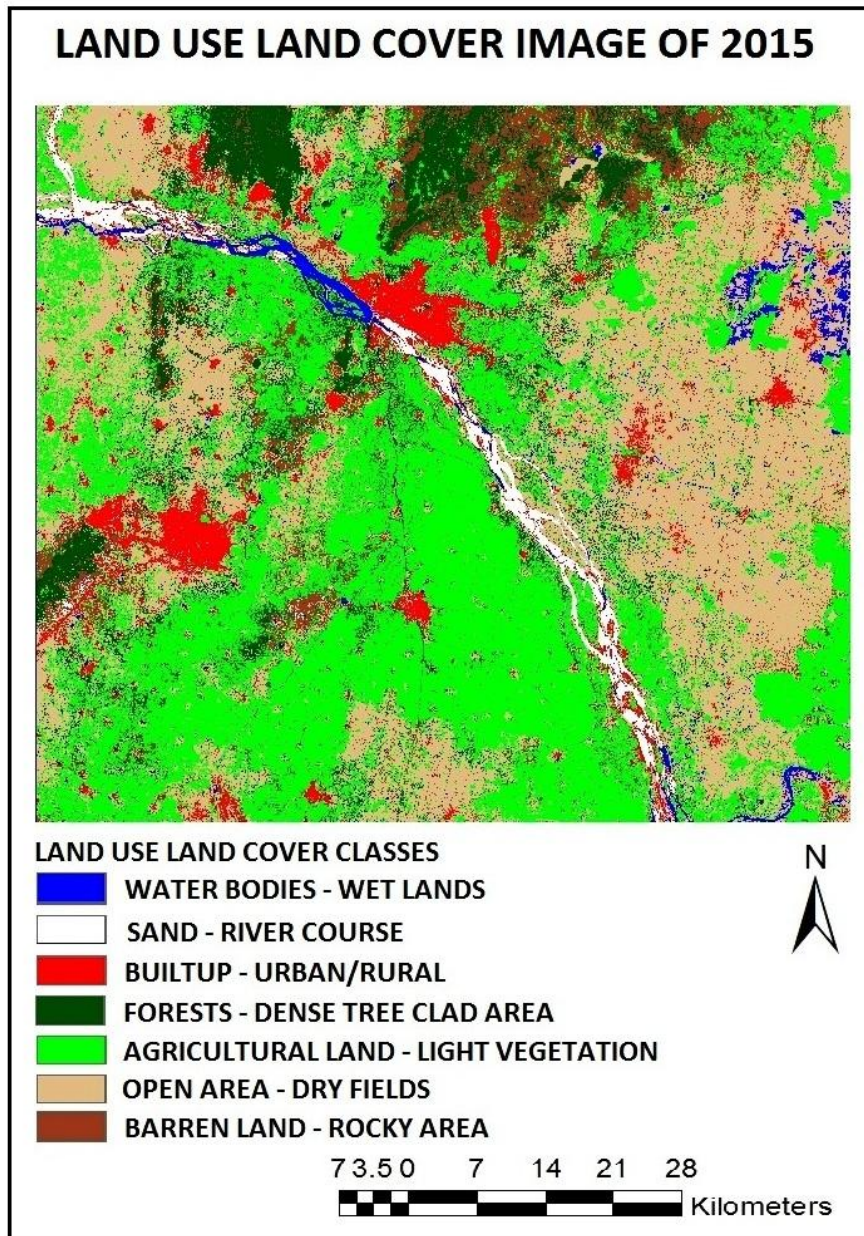


Figure 2: Land use Land cover image of the study area in the year 2015

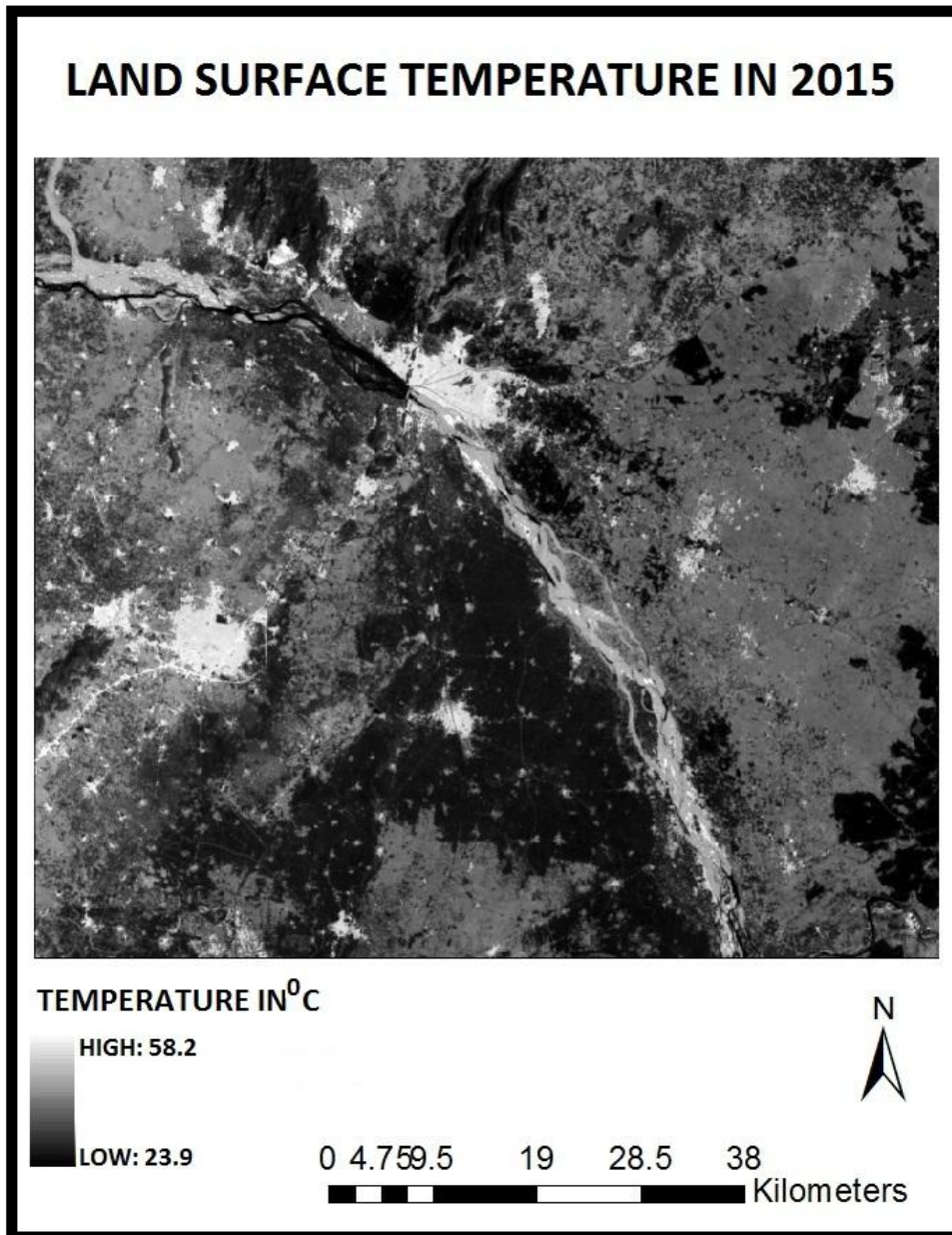


Figure 3: Land Surface Temperature image of the study area in the year 2015

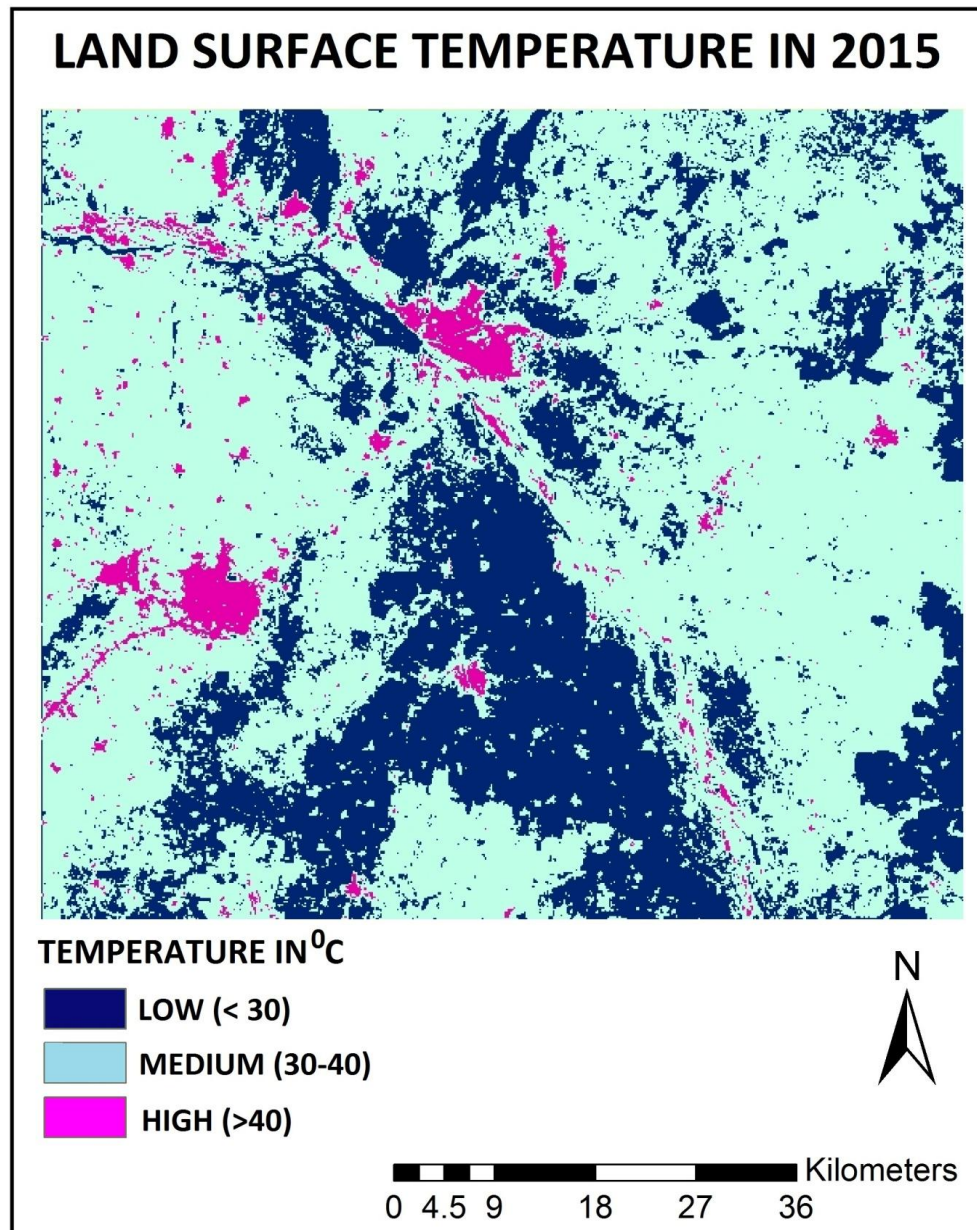


Figure 4: Classified Land Surface Temperature image of the study area in the year 2015

The LST image obtained from the ERDAS model has been classified into three classes: Low, Medium and High according to temperature ranges. Temperature less than 30°C was considered low, temperature in between 30 and 40 was considered medium and temperature greater than 40 were considered high. The satellite pass time on the study area is 4:56:46 GMT, which comes around 10.30 a.m. according to Indian Standard Time (IST). So at this time the maximum and minimum temperatures obtained in the study area are 58.2°C and 23.9 °C respectively. Low temperature was observed in water bodies-wet lands, forests-dense tree clad area and agricultural land-light vegetation. Medium temperature, which is around 40 °C was observed in sand-river course, open area-dry fields and barren land- rocky area. Similarly high temperature was observed in built-up-urban/rural area. The temperature levels and corresponding LULC classes were shown in a bar chart in Figure 5. The details of LST, corresponding LULC and respective areas in hectares are presented in Table 5.

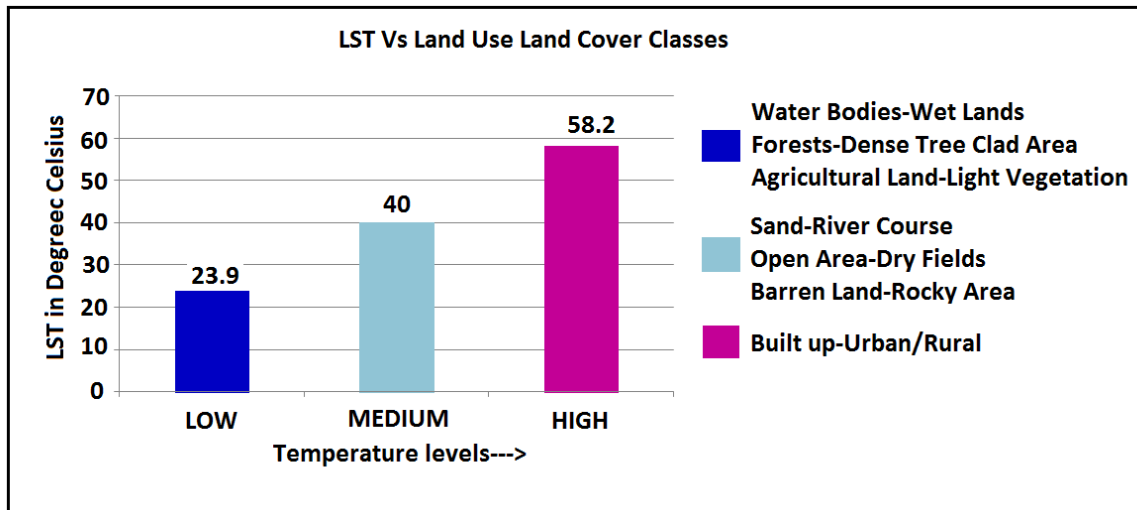


Figure 5: Land Surface Temperature Verses Land use Land Cover classes

Table 5: Land Surface Temperature and corresponding type of LULC classes and areas

| LST Level | LST IN °C | Area in Hectares | Type Of LULC |
|-----------|-----------|------------------|--|
| LOW | 23.9-30 | 186156.72 | Water Bodies-Wet Lands, Forests-Dense Tree Clad Area, Agricultural Land-Light Vegetation |
| MEDIUM | 30-40 | 385939.99 | Sand-River Course, Open Area-Dry Fields, Barren Land- Rocky Area |
| HIGH | 40-58.2 | 31892.68 | Built-up-Urban/Rural |

Urban Heat Island

From the LST image developed for the study area, it was clearly understood that there is a buildup of Urban Heat Island (UHI) in the core urban areas. In APCRDA region Vijayawada and Guntur cities are two major hot spots for the development of (UHI).

From the LST images it was clearly understood that the land surface temperature is inversely proportional to the vegetation cover. Higher values of LST were observed only at built up surfaces. Forests, agricultural areas and other light vegetative areas showed low temperature. The LST is increasing from rural areas to the urban areas. The non-evaporating and non-transpiring surfaces such as stone, metal and concrete brings up the surface radiant temperature. This is the root cause of the urban heat island phenomenon. To reduce this effect the trees must be grown and vegetation cover must be increased. In the APCRDA region, Vijayawada and Guntur are the two big cities which has lot of potential for development if UHI. In these cities a temperature rise of nearly 12 °C is observed.

The temperature profile across the two cities from north to south and east to west were prepared by taking transects and shown in Figures 6 to 9. From these figures also the UHI phenomenon is clearly evident. The field survey also confirms the absence or low density of green cover in the urban areas.

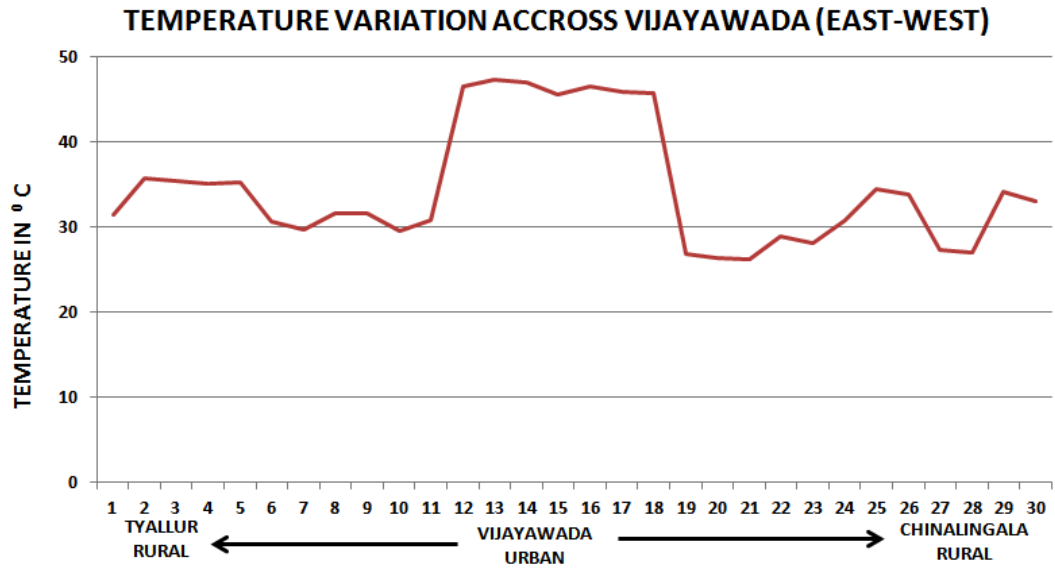


Figure 6: Land Surface Temperature variation across Vijayawada from East to West

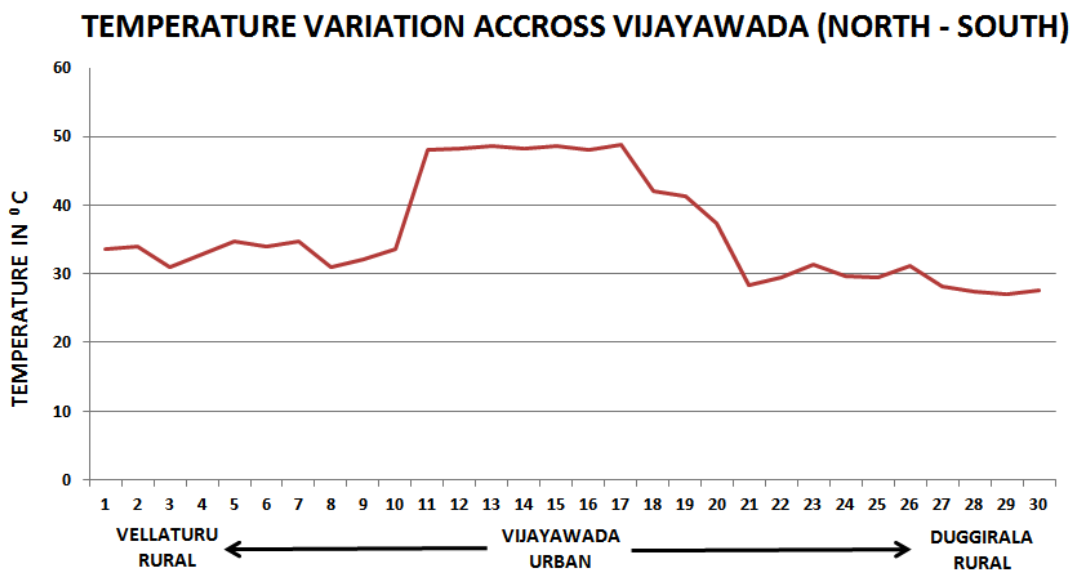


Figure 7: Land Surface Temperature variation across Vijayawada from North to South

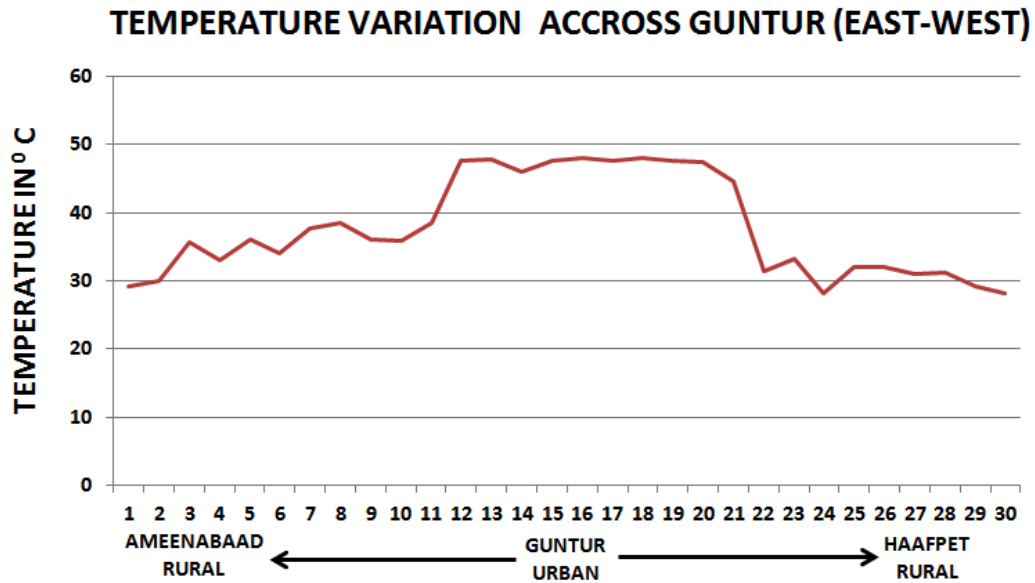


Figure 8: Land Surface Temperature variation across Guntur from East to West

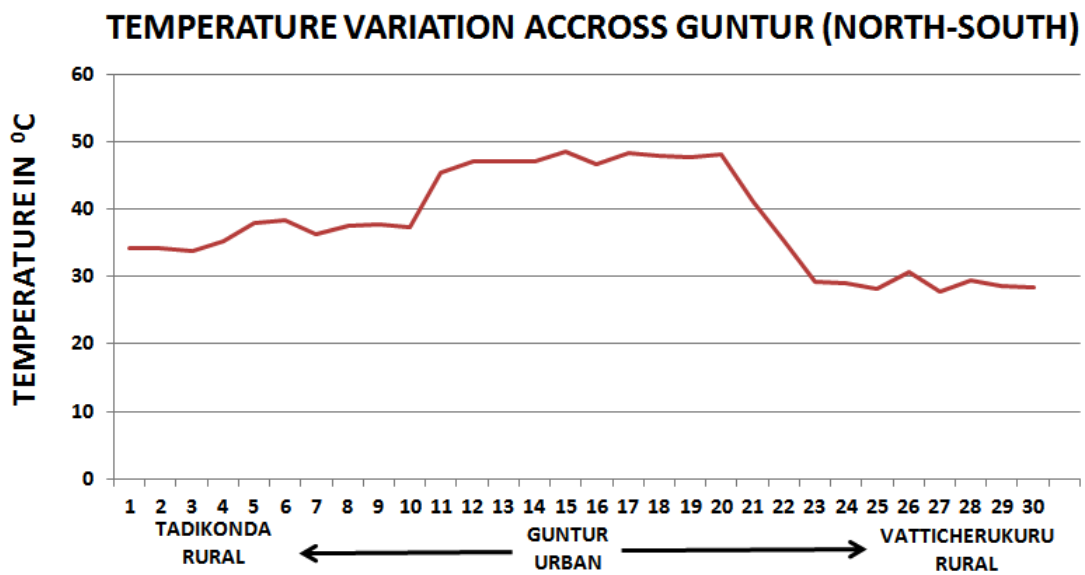


Figure 9: Land Surface Temperature variation across Guntur from North to South

5. Conclusion

The new capital of Andhra Pradesh state situated in APCRDA region is considered as a case study to examine the land use land cover (LULC) and land surface temperatures (LST). In this work Landsat-8 image for the date 23-05-2015 was collected and processed to develop LULC images. The area has been divided in to seven classes according to the type of land observed in the field. More than 100 points were selected in the study area and conducted field survey work with GPS. The field data was supplemented for LULC classification as well as for development of emissivity. The classification accuracy was obtained as 93%. From the thermal band and emissivity, LST image has been developed using ERDAS modelling. By studying the LULC image and LST image it is observed that high temperatures are developed in those areas where urban or built-up areas exist with less

vegetation. The low temperature and high temperature values observed are 23.9°C and 58.2°C respectively. Through this satellite based study it is concluded that the region experiences severe UHI phenomenon. The two big cities namely Vijayawada and Guntur are identified as hot spots. This research can be used as a reference or scientific basis for urban planners in urban planning and management as well as to increase the community awareness in urban heating effect.

Acknowledgement

The USGS official web site for distribution of satellite imagery “Earthexplorer” is duly acknowledged for making the requisite remote sensing satellite data, Landsat-8(OLI-TIRS) available for the study.

References

- [1] Xinchang Zhang, Tingjun Kang, Haiying Wang, and Ying Sun. Analysis on Spatial Structure of Landuse Change Based on Remote Sensing and Geographical Information System. *International Journal of Applied Earth Observation and Geoinformation*. 2010. 12S; S145-S150.
- [2] Md. Surabuddin Mondal, Nayan Sharma, Martin Kappas, and Garg, P.K. Critical Assessment of Land Use Land Cover Dynamics using Multi-Temporal Satellite Images. *Environments*. 2015. 2; 61-90.
- [3] Divine Odame Appiah, Dietrich Schroder, Eric Kwabena Forkuo, and John Tiah Bugri. Application of Geo-Information Techniques in Land Use and Land Cover Change Analysis in a Peri-Urban District of Ghana. *International Journal of Geoinformatics*. 2015. 4; 1265-1289.
- [4] Lewoye Tsegaye. Analysis of Land Use and Land Cover Change and Its Drivers Using GIS and Remote Sensing: The Case of West Guna Mountain, Ethiopia. *International Journal of Remote Sensing and GIS*. 2014. 3 (3) 53-63.
- [5] Sahoo Satiprasad. Monitoring Urban Land Use Land Cover Change by Multi-Temporal Remote Sensing Information in Howrah City, India. *International Research Journal of Earth Sciences*. 2013. 1 (5) 1-6.
- [6] Jin S. Deng, Ke Wang, Yang Hong, and Jia G. Qi. Spatio-temporal Dynamics and Evolution of Land Use Change and Landscape Pattern in Response to Rapid Urbanization. *Landscape and Urban Planning*. 2009. 92; 187-198.
- [7] Cetin, M. A Satellite Based Assessment of the Impact of Urban Expansion around a Lagoon. *Int. J. Environ. Sci. Tech*. 2009. 6 (4) 579-590.
- [8] Jieying Xiao, Yanjun Shen, Jingfeng Ge, Ryutaro Tateishi, Changyuan Tang, Yanqing Liang, and Zhiying Huang. Evaluating Urban Expansion and Land use Change in Shijiazhuang, China, by using GIS and Remote Sensing. *Landscape and Urban Planning*. 2006. 75; 69-80.
- [9] Fenglei Fan, Qihao Weng, and Yunpeng Wang. Land Use and Land Cover Change in Guangzhou, China, from 1998 to 2003, based on Landsat TM /ETM+ Imagery. *Sensors*. 2007. 7; 1323-1342.
- [10] Bin Quan, Zhikun Xiao, Romkens, M.J.M., Yijun Bai, and Shi Lei. *Spatiotemporal Urban Land Use Changes in the Changzhutan Region of Hunan Province in China*. *Journal of Geographic Information System*. 2013. 5; 136-147.

- [11] Sundara K. Kumar, Harika, M., Aspiya Sk. Begum, Yamini, S., Bala K. Krishna. Land use and Land cover Change Detection and Urban Sprawl Analysis of Vijayawada City using Multi-temporal Landsat Data. *International Journal of Engineering Science and Technology*. 2012. 4 (1) 170-178.
- [12] Sundara K. Kumar, Udaya P. Bhaskar, and Padma Kumari K. Estimation of Land Surface Temperature to study Urban Heat Island Effect Using Landsat ETM+ Image. *International Journal of Engineering Science and Technology*. 2012. 4; 807-814.
- [13] Qin, Z., Karnieli, A., and Berliner, P. A Mono-Window Algorithm for Retrieving Land Surface Temperature from Landsat TM Data and Its Application to the Israel-Egypt Border Region. *International Journal of Remote Sensing*. 2001a. 22 (18) 3719-3746.
- [14] Sobrino, J.A., Jiménez-Muñoz, J.C., and Paolini, L. Land Surface Temperature Retrieval from LANDSAT TM 5. *Remote Sensing of Environment*. 2004. 90 (4) 434-440.
- [15] Weng, Q. Remote Sensing of Impervious Surfaces in the Urban Areas: Requirements, Methods, and Trends. *Remote Sensing of Environment*. 2012. 117; 34-49.
- [16] Streutker, D.R. A Remote Sensing Study of the Urban Heat Island of Houston, Texas. *International Journal of Remote Sensing*. 2002. 23 (13) 2595-2608.
- [17] Daniel Oudin Åström, Bertil Forsberg, and Joacim Rocklöv. Heat Wave Impact on Morbidity and Mortality in the Elderly Population: A Review of Recent Studies. *Maturitas*. 2011. 69; 99-105.
- [18] USGS. EarthExplorer. U.S. Department of the Interior, U.S. Geological Survey. <http://earthexplorer.usgs.gov/>.
- [19] USGS. Landsat 8 (L8) Data Users Handbook. U.S. Department of the Interior, U.S. Geological Survey. <http://landsat.usgs.gov/documents/Landsat8DataUsersHandbook.pdf>

Geospatial Techniques in Health Survey to Overcome the Lack of Sampling Frame

Elangovan A., Elavarsu G., Ezhil R., Prabu R., and Yuvaraj J.

National Institute of Epidemiology (ICMR), Ayapakkam, Chennai, Tamil Nadu, India

Publication Date: 14 October 2016

DOI: <https://doi.org/10.23953/cloud.ijarsg.78>



Copyright © 2016 Elangovan A., Elavarsu G., Ezhil R., Prabu R., and Yuvaraj J. This is an open access article distributed under the **Creative Commons Attribution License**, which permits unrestricted use, distribution, and reproduction in any medium, provided the original work is properly cited.

Abstract Sampling frame is a complete list of items or population from which a sample is drawn. More often researchers face difficulties in getting an up to date line list of sampling units, especially in the field where rapid changes are frequent. In household surveys it is difficult as newly constructed houses are seen as a continuous process in urban as well as rural areas. To overcome this issue, in this paper, we proposed a novel method by using Google-Earth with the GIS technologies. A study was done with the primary objective to identify the health impact of people living in and around quarries/crusher units at Thiruneermalai region nearer to Chennai. Since the boundary of the study area is found to be radial, it was difficult in getting the complete line list of the people living within the required radius. To overcome the issue the entire region was divided into small 30 x 30 meter grid cells. A total of 43652 sampling units (grid cells) formed the sampling frame. Among them, the required sample size was selected for the study. This method of GIS based grid sampling serve as an alternate tool for developing sampling frame with no or least cost.

Keywords *Geographical Information System; Grid Sampling; Sampling Frame*

1. Introduction

Sampling is an easy scientific method for investigating the entire population for assessing the outcome of interest [1-2]. Though various methods are available for deriving the representative samples from the population, simple random sampling method is considered to be more generalizable that represents the whole population since each individual in the sampling frame has equal chance of getting selected for evaluation [1-2]. Availability of sampling frame is a pre-requisite for deriving a sample using this method [3]. However in resource limited settings availability of reliable sampling frame is unlikely [4]. The available resources such as census enumeration did not have the location/household identifier details moreover in the rapidly expanding population settings. The recent advances in technology related to Geographical Information System (GIS) and spatial analysis has paved way for overcoming limitations in the random sampling method. The GIS technology is being widely used in sampling natural resources and phenomena such as geological surveys, plant sampling, mineral deposition, bio-fuel exploration etc [5]. Spatial sampling does not rely on the sampling frame and building the sampling frame is not feasible in these cases. Sampling frame is

constructed in the spatial sampling by dividing the overlaid pattern into a defined number of units/grids/cells [5].

Further there is a paucity of literature, which demonstrates and depicts the usefulness and limitations of grid-sampling method in public health surveys. This method may reduce the cost of the survey to a considerable extent by minimizing the time, manpower and generating reliable estimates. With this background we explored the feasibility of using grid sampling method in estimating the health impact of hard stone quarry/crusher works in a sub-urban setting in Chennai in South India.

Public health is one of the major areas that have been made increasing use of Geographical Information System (GIS) techniques. In general, these efforts fall naturally within the domain of problems requiring use of spatial analysis as part of the solution [6-10]. GIS and other spatial analysis tools are therefore recognized as providing potentially transformational capabilities for public health efforts. A study used systematic GIS based grid sampling procedure for reconnaissance survey for assessing the percentage of positive for dengue and chikungunya caused mosquito breeding habitats [11], where the mean value of breeding habitats was calculated and assigned to each of the grid cells for mapping the mosquito breeding habitats. Efforts are continuously being done to improve the accuracy of grid based data and to find a simple and feasible method for treating population and housing grid data as the basis for sampling [12].

In order to fine tune the available methods, here we have proposed a novel sampling frame method, where we have included each and every point of the study area to form total sampling frame from where the required number of sampling units will be selected by simple random sampling method.

2. Study Area

The study area is identified as Thiruneermalai region nearer to Chennai which is located at 13°02'N 80°10'E/ 13.04°N 80.17°E on the southeast coast of *India* and in the northeast corner of *Tamil Nadu state* (Figure 1). It is located on a flat *coastal plain* known as the *Eastern Coastal Plains*. Our objective is to measure the health impact of quarry works among the residents living within 5 KM radius from the quarries and to measure the related environmental parameters in the study area with specific attention to Tuberculosis.

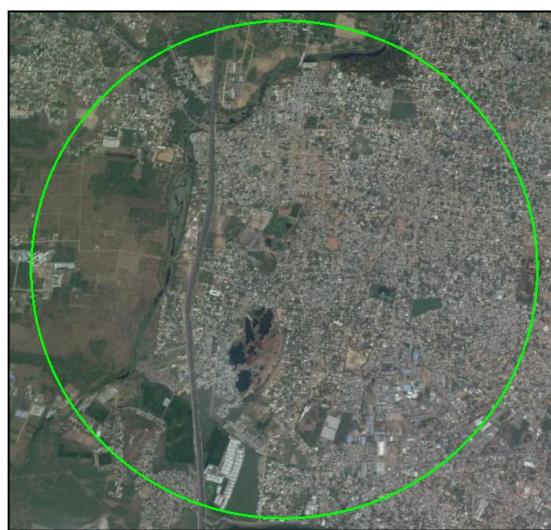


Figure 1: Study area with radial boundary

We tried to get a complete list of houses of the study area but end up with failures as our boundary of study area is circular and not part of any existing administrative boundaries. To overcome this problem, we found an alternative strategy to develop a sampling frame by using Google-Earth [13], GPS and GIS technologies.

3. Materials and Methods

GIS/GPS based grid sampling method is used for recruitment of community residing nearby quarries. We identified the quarry site and created a buffer zone of 5 KM around the quarry over Google-Earth (Figure 1). Google-Earth has been used all over the world along with GIS tools for better research in public health [14-16].

Once the study area is identified, we blocked all water bodies, forest area and other areas where people are not residing. Hence it is ensured that only those areas where people residing are considered for selection. The entire 5 KM buffer-zone was overlaid with 30x30 meter small grids developed using Keyhole Mark-up Language (KML) programme [17]. There were 43652 such grid cells created (Figure 2) and each cell has been assigned with a unique number. The longitude, latitude, distance from centre point (quarry) and their unique identification of each grid cells have been stored in a file, from where 300 grid cells have been selected by simple random sampling method. The sample size of 300 was arrived by considering the approximate prevalence of morbidity conditions required by the study. Samples of two selected grids are shown in Figure 3.

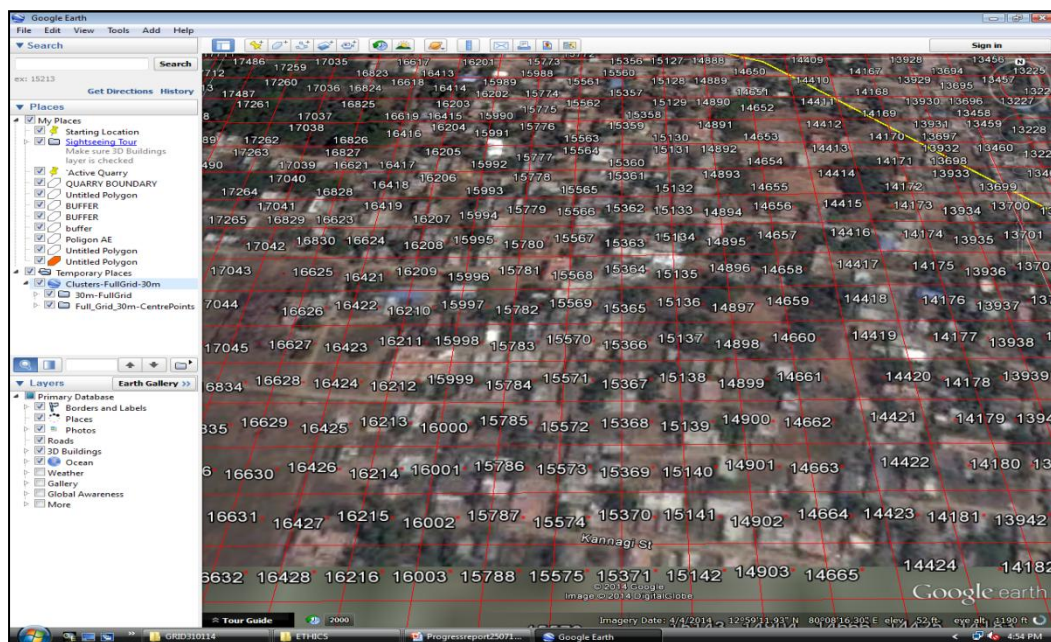


Figure 2: Study area divided by 30x30 meter grids

Our paramedical field teams who are well trained in using Global Positioning System (GPS) visited the selected grid with help of Tablet-PC, where all the 300 selected grids were overlapped on Google-Earth map [18]. Tablet-PC was used to assist the team in identifying the way and direction of the selected houses available in any particular grid of a street.

The longitude and latitude of grids were re-confirmed with the GPS readings before collecting the data from the particular households. Standard questionnaire was developed and the relevant information related to this study was collected. A maximum of 4 households were enumerated from each grid. If more numbers of household available in a single grid, we randomly selected 4 households as required

by the study. The study was initiated during February 2014 and a total number of 1905 subjects including 869 males and 1036 females were covered.



Figure 3: Samples of two selected grids

4. Results

Nearly 65 (22%) grids fall on empty land and the remaining 235 (78%) fall on structural buildings (Table 1). Hence one can expect that nearly 25% of grids may fall in vacant places in spite of the exclusion of water bodies, forest etc. Among the 235 grids whom fall on structural buildings, 208 (89%) grids were having residential structures and the remaining 27 (11%) grids fall on companies, schools, office etc., (Table 2). These factors have to be kept in mind while calculating the sample size and required number of extra grids has to be added with the sample size.

Table 1: Distribution of sampled grids (N=300)

| Grid | Description of grid | No. | % |
|-----------------------------|---------------------------------|------------|-----------|
| Fall on structural building | grids with habitations | 208 | |
| | companies, school, office etc., | 27 | |
| | total | 235 | 78 |
| Fall on empty land | vacant land | 53 | |
| | water bodies | 8 | |
| | roads | 4 | |
| | total | 65 | 22 |

Table 2: Distribution of grids having structural buildings (N=235)

| Grid | Description of grid | No. | % |
|-------------------------|---------------------------------|------------|-----------|
| Habitations | grids with eligible HH | 204 | |
| | exclusion criteria | 2 | |
| | refusal | 2 | |
| | total | 208 | 89 |
| In-eligible structurals | companies, school, office etc., | 27 | 11 |

The relevant information was entered into Mapinfo [19], GIS software to perform further advanced spatial analysis. Figure 4 shows the distribution of grids from where the samples were collected. The cases found within the grids fall between 3 and 5 KM is considered are controls and between 1 and 3 KM is considered as cases.

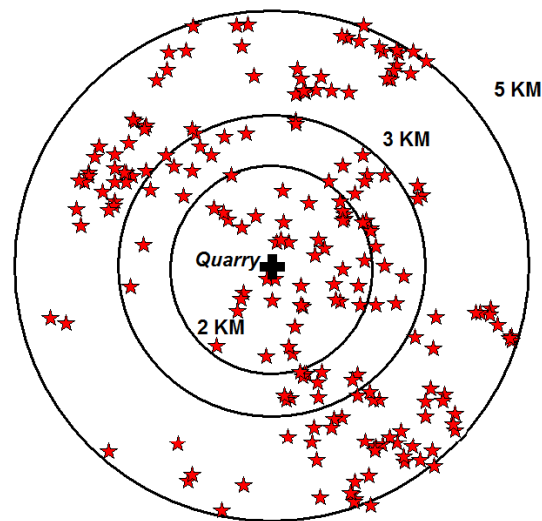


Figure 4: Distribution of households within 2, 3 and 5 KM radius (N=204)

5. Discussions

Use of spatial technology in identifying sampling units has been used in public health since many years. Baba Soumare et al. used computer software which randomly select a site to identify sheep/goats from that particular site [20], which may lead to have more number of empty points requiring more man power to search for a valid site/point and does not provide a complete sampling frame as large portion of areas are not been selected. Similar approach of creating random points was used by Kumar N. [5] to identify a household. These procedures may effective for collecting samples from ground water, soil, ambient air etc. It does not provide complete sampling frame as many of the points were not been selected. But the method proposed in this paper will form a complete sampling frame without leaving a single point/location as the entire study area is covered by grids. The size of the grid may vary depends upon the size of the sampling unit of any particular study.

Google-Earth is particularly very useful tool for public health, which can be used as free of cost. The new settlements can be viewed on the map as the Google-Earth is periodically updating their imagery data. Google Earth also provides higher resolution satellite images which can be used as a pre-navigation tool. Viewing grids or sample points in Google Earth before visiting the actual field helped field investigators to identify a right house without much difficulty and hence it reduces the cost, time and manpower.

6. Limitation

In the recent time GIS technology has been used in public health particularly in mapping mosquito breeding habitats, quantifying the ambient air pollution and in other socio-demographic surveys. Though there are many advantages of using grid-sampling method in public health surveys certain limitations exist such as a) empty cells which will take more manpower to find the valid cells; b) some households spread across two adjacent grids, which violates the principle of independence in the distribution within each grid; c) varying number of households across grids, which requires differential probability of inclusion by adding appropriate weight.

The important limitation is that the micro level Google imageries which include roads and structural building are available only for important regions/cities and not for all the regions. Removing non-residential areas like water bodies, companies etc., from being selected are considered as a big challenge.

7. Conclusions

House hold survey is often difficult as newly constructed houses are continues process in both urban and rural areas. Many times researchers find difficulties in getting up-to-date line list, especially in the field setting where rapid changes are frequent. Since Google-Earth capture periodical imageries of the globe along with their spatial locations, this demonstration of using grid sampling method with the combination of Google-Earth with other GIS technologies serve as an alternate tool for developing sampling frame with no or least cost.

References

- [1] Royal Geographical Society with IBG, London. Sampling Techniques. <https://www.rgs.org/OurWork/Schools/Fieldwork+and+local+learning/Fieldwork+techniques/Sampling+techniques.htm>
- [2] Stephen B., Hulley, 2001: *Designing Clinical Research- An Epidemiologic Approach*. Second Edition. Philadelphia, PA: Lippincott, Williams & Wilkins. 336.
- [3] Michelle C. Kondo, Kent D.W. Bream, Frances K. Barg, and Charles C. Branas. A Random Spatial Sampling Method in a Rural Developing Nation. *BMC Public Health*. 2014. 14; 338.
- [4] Mark V. Wilson and Oregon State University. Simple Random Sampling in the Field. <http://oregonstate.edu/instruct/bot440/wilsomar/Content/SRS.htm>
- [5] Kumar, N: Spatial Sampling Design for a Demographic and Health Survey. *Popul. Res. Policy Rev.* 2007. 26; 581-599.
- [6] Mona Choi, R.N. Spatial Analysis in Epidemiology. *Health Informatics Research*. 2013. 19 (2) 148-149.
- [7] Rushton, G. Public Health, GIS, and Spatial Analytic Tools. *Annual Review of Public Health*. 2003. 24 (1) 43-56.
- [8] Stefania Bertazzon. GIS and Public Health. *ISPRS International Journal of Geo-Information*. 2014. 3 (3) 868-870.
- [9] Riner, M.E., Cunningham, C., and Johnson, A. Public Health Education and Practice using Geographic Information System Technology. *Public Health Nursing*. 2004. 21 (1) 57-65.
- [10] Robinson, T.P. Spatial Statistics and Geographical Information Systems in Epidemiology and Public Health. *Advances in Parasitology*. 2000. 47; 81-128.
- [11] Palaniyandi, M., Anand, P.H., and Maniyosai, R. GIS Based Community Survey and Systematic Grid Sampling for Dengue Epidemic Surveillance, Control and Management: A Case Study of Pondicherry Municipality. *International Journal of Mosquito Research*. 2014. 1 (4) 30-38.

- [12] Ding Wenxiu, Xiaole, Li, Zhiqiang, Li, Donaixia, Zhang Yimei, and Temu Qile. Population and Housing Grid Spatialization in Yunnan Province based on Grid Sampling and Application of Rapid Earthquake Loss Assessment: The Jinggu Ms6.6 Earthquake. *Geodesy and Geodynamics*. 2014. 5 (4) 25-33.
- [13] Google Company. Google Earth, <https://www.google.com/earth/KML>.
- [14] Theodore B. Lefer, Matthew R. Anderson, Alice Fornari, Anastasia Lambert, Jason Fletcher and Maria Baquero. Using Google Earth as an Innovative Tool for Community Mapping. *Public Health Reports*. 2008. 123 (4) 474-480.
- [15] Raoul Kamadjeu. Tracking the Polio Virus down the Congo River: A Case Study on the use of Google Earth™ in Public Health Planning and Mapping. *International Journal of Health Geographics*. 2009. 8; 4.
- [16] Taylor, B.T., Fernando, P., Bauman, A.E., Williamson, A., Craig, J.C., and Redman, S. Measuring the Quality of Public Open Space using Google Earth. *Am J Prev Med*. 2010. 40 (2) 105-112.
- [17] Wikimedia Foundation, Inc. Keyhole Markup Language
https://en.wikipedia.org/wiki/Keyhole_Markup_Language
- [18] Ping Yu, Maximilian de Courten, Elaine Pan, Gauden Galea, and Jan Pryor. The Development and Evaluation of a PDA-based Method for Public Health Surveillance Data Collection in Developing Countries. *International Journal of Medical Informatics*. 2009. 78 (8) 532-542.
- [19] Pitney Bowes Software. MapInfo Pro. The World's Premier Desktop GIS and Mapping Application. www.mapinfo.com/product/mapinfo-professional/
- [20] Baba Soumare, Stefano Tempia, Vittorio Cagnolati, Abdullatif Mohamoud Guido Van Huylenbroeck, Dirk Berkvens. Screening for Rift Valley Fever Infection in Northern Somalia: A GIS based Survey Method to Overcome the Lack of Sampling Frame. *Veterinary Microbiology*. 2007. 121 (3-4) 249-256.

Flood Susceptibility Appraisal in Ponnaiyar River Basin, India using Frequency Ratio (FR) and Shannon's Entropy (SE) Models

Jothibas A. and Anbazhagan S.

Centre for Geoinformatics and Planetary Studies, Department of Geology, Periyar University, Salem, India

Publication Date: 14 October 2016

DOI: <https://doi.org/10.23953/cloud.ijarsg.73>



Copyright © 2016 Jothibas A. and Anbazhagan S. This is an open access article distributed under the **Creative Commons Attribution License**, which permits unrestricted use, distribution, and reproduction in any medium, provided the original work is properly cited.

Abstract In any Watershed management studies, demarcation of flood prone area is one of the key tasks. Flood management is essential to shrink the flood effects on human lives and livelihoods. Main goal of the present research is to investigate the application of the Frequency Ratio (FR) and Shannon's Entropy (SE) models for flood susceptibility appraisal of Ponnaiyar River basin in Tamil Nadu, India. Initially, the flood inventory map was prepared using overlay analysis (slope, 20 meter contour intervals and drainage patterns) and extensive field surveys. In total, 136 flood locations were noted in the study area. Out of these, 95 (70%) floods were randomly selected as training data and the remaining 41 (30%) floods were used for the validation purposes. Further, flood conditioning factors such as lithology, land-use, distance from rivers, soil depth, rainfall, slope angle, slope aspect, curvature, topographic wetness index (TWI) and altitude were prepared from the spatial database. Then, the receiver operating characteristic (ROC) curves were drawn for produced flood susceptibility maps and the area under the curves (AUCs) was computed. The final results indicated that the FR (AUC = 80.20%) and SE (AUC = 79.30%) models have almost similar and reasonable results. Therefore, these flood susceptibility maps can be useful for researchers and planner in flood mitigation strategies.

Keywords *Geographic Information System; Remote Sensing; Flood Susceptibility; Ponnaiyar River*

1. Introduction

Flood is one of the most common natural disaster events and it creates many environmental problems due to rapid urban growth and climate change (Kjeldsen, 2010). A deep tropical depression came through the Bay of Bengal and hit the south-eastern coast of India on 10-11 November 2015, causing heavy rain. Heavy rain resumed during Nov 16-19, with 30-37 cm of rain accumulating over the 9-day period. After pausing for several days, heavy rains have resumed in early December and in some locations rain is projected to continue until 8-10 December. Chennai received over 33 cm of rain in a 24-hour period from December 1-2, causing widespread flooding and damage. In Tamil Nadu, Chennai city, Cuddalore, Kanchipuram, and Tiruvallur districts are worst affected. Reports are estimating 347 people have lost their lives in Tamil Nadu which can be more. The floods which occurred are the worst in 100 years and the people got stranded in the midnight since flood water entered into the houses while they are asleep, especially in Chennai. The Government of India has

declared Chennai a National Disaster zone, and National Disaster Response Force carried out rescue operations in the city (JNA, 2015). It is motivated to demarcate flood prone area in the study area. Early warnings and emergency responses to floods are needed, so that governments and agencies can prevent as much damage as possible (Feng and Wang, 2011). In natural hazards research, enormous databases are habitually needed (Regmi et al., 2013). These are not easy to collect, and in some cases a lack of appropriate data can hamper research (Liu and De Smedt, 2004). Natural factors such as hydrological and meteorological characteristics, soil types, geological structures, geomorphology, and vegetation are the most influential contributors to flooding. Human interference in natural cycles by cutting trees and building with impervious materials can accelerate flooding.

From sustainable development point of view, the flood hazard management is very essential for future (Feng & Wang, 2011; Esteves, 2013; Schober et al., 2015). However, negative consequences of flood can be applied by integrated approaches to flood hazard management (Anbazhagan and Dash, 2003; Masood & Takeuchi, 2012; Jourde et al., 2014). Remote sensing techniques coupling with GIS tools can provide a good platform to combine, manipulate and analyses the information for the determination of potential hazard areas very quickly and more efficiently (Saha et al., 2005; Pradhan et al., 2011; Devkota et al., 2013; Wang et al., 2013; Pourghasemi et al., 2014). The most popular methods in natural hazard modeling are ANN (Pradhan and Buchroithner, 2010; Pradhan et al., 2010b), analytic hierarchy process (AHP) (Yalcin, 2008), frequency ratio (FR) (Pradhan et al., 2011), logistic regression (LR) (Pradhan, 2010a,b) and fuzzy logic (Pradhan, 2011). Shafapour Tehrani et al. (2013) compared the prediction performances of two different methods such as rule-based decision tree and combination of FR and logistic regression statistical models for flood susceptibility mapping at Kelantan, Malaysia. Their result demonstrated that the area under the curve (AUC) for decision tree and the ensemble FR and LR models was 87 and 90%, respectively. Lee et al. (2012a) applied FR model for flood susceptibility mapping in Busan, South Korea. The results showed that FR model is very efficient for flood susceptibility modeling. Shannon's entropy is the average unpredictability in a random variable, which is equivalent to its information content. The entropy of flood refers to the extent that the various controlling flood occurrences influence the flood susceptibility. Several influencing factors give extra entropy into the index system. Therefore, the entropy value can be used to calculate objective weights of the index system (Jaafari et al., 2014). The main objective of the present research was to assess and compare flood susceptibility maps produced using two statistical GIS-based approaches, i.e. FR and SE models in the Ponnaiyar river basin, Tamil Nadu, India.

2. Study Area

Ponnaiyar River basin an interstate river is one of the largest rivers of the state of Tamil Nadu, often reverently called 'Little Ganga of the South'. The river has supported many civilizations of peninsular India across the history and continues to play a vital role in supplying precious water for drinking, irrigation and industry to the people of the states of Karnataka, Tamil Nadu and Pondicherry. The study area extends over approximately of 11,595 sq.km, and lies between 11°35' and 12°35' N latitudes and 77°45' and 79°55' E longitudes (Figure 1). Ponnaiyar River originates on the south eastern slopes of Chennakesava Hills, northwest of Nandidurg of Kolar district in Karnataka State at an altitude of 1000m above mean sea level (amsl). The total length of Ponnaiyar River is 432km of which 85km lies in Karnataka state, 187km in Dharmapuri, Krishnagiri and Salem districts, 54km in Thiruvannamalai and Vellore districts and 106km in Cuddalore and Villupuram districts of Tamil Nadu. The Cuddalore and Villupuram districts are the most affected flood area in the river basin. The first spell witnessed intensive flooding in Cuddalore where most of the water bodies were full and the associated breaching affected the communities' life damaging houses and infrastructure etc., (Figure 2). The Ponnaiyar basin is predominantly built up with granite and gneisses rocks of Archean period. The fifteen years (2000-2014) average annual rainfall in the basin is 969 mm. The climate in general is hot; April and May being the hottest months of the year when the temperature rises to 34°C.

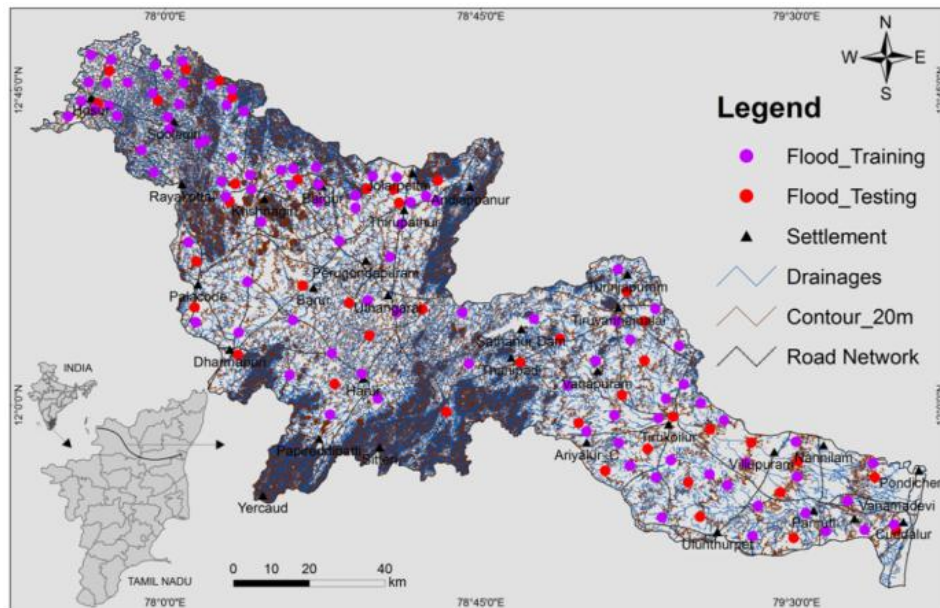


Figure 1: Study area and flood locations of Ponnaiyar river basin



Figure 2: Photographs shows the severity of the flood that occurred in 2015

3. Data Used and Methodology

3.1. Identify Flood Locations

A basin level flood-prone area map provides the regional level planners and decision makers with information useful in formulating broad policies to guide the future development of flood plains. In the context, the flood-prone map was prepared using SRTM satellite data were applied to create a digital elevation model (DEM) of the study area with spatial resolution of 90 m. The slope and contour maps were prepared using DEM. Which include contour lines with 20 m interval connecting points on the ground surface that have the same elevation showing the configuration and elevation of the land

surface. The areas subject to flooding were delineated from readily available information for quick appraisal rather than by detailed field surveys.

3.2. Flood Conditioning Factors

In order to execute flood susceptibility mapping it is necessary to find out the flood conditioning factors (Kia et al., 2012). Therefore, a flood related spatial database should be created. Through the knowledge gathered from the literature review and field investigation the conditioning factors were chosen (Smith and Ward, 1998). Hence, ten flood conditioning factors such as lithology, land use / land cover (LULC), soil depth, distance from main river, rainfall, altitude, curvature, slope, topographic wetness index (TWI) and aspect were selected for the susceptibility analysis and the spatial database of these factors was compiled. The lithology is considered as one of the most important indicators of hydro-geological features which play a fundamental role in both the porosity and permeability of aquifer materials (Ayazi et al., 2010; Charon, 1974). The analog lithology map (1:100,000) was obtained from the Geological Survey of India (GSI, 1998) and the digital lithology map was generated using ArcGIS 9.3 (Figure 3a). According to Geological Survey of India the lithology of the study area is varied and covered by twenty two rock types.

Land use types play a significant role, which directly or indirectly influence on some of hydrological processes components such as infiltration, evapotranspiration and run-off generation. Land use types within the study area are agriculture land, built-up land, forest cover, river, water body, barren land, and grass land (Figure 3b). Built-up areas, which are mostly made by impervious surfaces, increase the storm run-off and inundation (Shafapour Tehrany et al., 2013). On the other hand, agricultural areas are less prone to flooding due to the positive relationship between infiltration capability and vegetation density. The land use / land cover map was prepared from IRS P6 LISS III image through supervised classification using maximum likelihood algorithm, and false color composite (FCC) techniques in ENVI 4.3 software.

Distance from main rivers play significant roles in hydro-geological systems. It is one of the main conditioning factors due to its impact on the flood magnitude (Glenn et al., 2012). It controls the stability of a slope is the saturation degree of the material on the slope. The closeness of the slope to drainage structures is another important factor in terms of stability. Streams may adversely affect stability by eroding the slopes or by saturating the lower part of material until resulting in water level increases (Gokceoglu and Aksoy, 1996). The distance from river map was produced using the buffer tool in ArcGIS 9.3 and was classified into five classes (Figure 3c). Soil is a complex biogeochemical material on which plants may grow. Information on the type of soil is often needed as a basic input in hydrologic evaluation. Mapping soil usually involves delineating soil types that have identifiable characteristics. The delineation is based on many factors garment to soil science such as geomorphologic origin and conditions under which the soil formed (Vieux, 2004). Soil depth is one of the most important factors in the surface and subsurface runoff generation and infiltration process (Mogaji et al., 2014). The soil depth map was obtained from the Central Groundwater Board (CGWB, 2012). There are four classes of soil depth in the study area (Figure 3d).

The monsoon flooding takes place after heavy rain, so this factor should be considered as one of the main contributors in flood occurrence (Bajabaa et al., 2013). The monthly records of rainfall amount for thirty rain-gauge stations within the study area for a period of 15 years (2000–2014) were obtained from the Tamil Nadu State Surface and Groundwater Division database. The resulting map was classified into five major classes: 688-850, 850-923, 923-987, 987-1046 and 1046-1195 mm/year (Figure 3e). Average annual rainfall in the study area varies in the range of 688 mm to 1195 mm. North eastern and south western part receive high rainfall (>987mm) whereas southeastern and northwestern part receive low rainfall (<923mm).

The slope map of the study area was generated based on DEM using the Spatial Analysis tools in ArcGIS 9.3. Based on the quantile classification scheme (Tehrany et al., 2014), the slope angle map was grouped into six classes such as $<7^\circ$, 7° - 15° , 15° - 20° , 20° - 25° , 25° - 30° and $>30^\circ$ (Figure 3f). Aspect is related to the main precipitation direction and the physiographic trends (Ercanoglu and Gokceoglu, 2002). Slope aspect layer was extracted from DEM and divided into nine classes including ten directions and flat based on normal or common standard classification (Figure 3g). Curvature, (T_c) was calculated from the DEM (Figure 3h). The map comprises five classes ranging from very high class to very low class. Negative values for curvature (<-2) correspond concave and accumulation zones, zero values for curvature represent the flat and transitional zones and the positive values for curvature represent the convex and dissipation zones (Florinsky, 2000).

Topographic Wetness Index (TWI) has been widely used to explain the impact of topography conditions on the location and size of saturated source zones of surface runoff generation. It is defined as (Moore et al., 1991):

$$TWI = \ln\left(\frac{A_s}{\tan\beta}\right) \quad (1)$$

Where, A_s is the cumulative upslope area draining through a point (per unit contour length) and β is the slope gradient (in degree)

In this study, TWI map is grouped into four classes using quantile classification scheme (Tehrany et al., 2014) (Figure 3i). The tendency of water to accumulate at any point in the catchment (in terms of α) and the tendency of gravitational forces to move that water down slope (indicated in terms of $\tan \beta$ as an approximate hydraulic gradient) are considered by the $\ln \beta \tan \alpha$ index. Primarily, the water infiltration depends upon material properties such as permeability and pours water pressure on the soil strength.

Different altitudes have altered climate conditions, and this caused differences in soil condition and vegetation type (Aniya, 1985). Altitude map of the study area was created from the DEM. The altitude map was grouped into six classes: -4 to 205 m, 205–386 m, 386–556 m, 556–750 m, 750–1009 m, and 1009–1635 m based on the quantile classification method (Figure 3j) (Tehrany et al., 2013).

3.3 Frequency Ratio (FR) Model

Frequency ratio (FR) model is a bivariate statistical approach which can be used as a useful geospatial assessment tool to determine the probabilistic relationship between dependent and independent variables, including multi-classified maps (Oh et al., 2011). Recently, FR model has been successfully used for flood susceptibility mapping by Tehrany et al. (2014a), Rahmati et al. (2015). In fact, the FR is defined as the ratio of the area where flood occurred in the total study area. FR model structure is based on the correlation and observed relationships between each flood conditioning factor and distribution of flood locations. FR value in each class of the groundwater-related factor can be expressed based on Eq. 2:

$$FR = \left(\frac{A/B}{C/D}\right) \quad (2)$$

Where,

A is the number of flood training set for each factor;

B is the number of total flood training set in study area;

C is the number of pixels in the class area of the factor;

D is the number of total pixels in the study area

The complete calculation of weight determination for individual parameters is presented in Table 1. In a given pixel, flood susceptibility index (FSI) can be determined by summation of pixel values according to Eq. (3):

$$FSI = Li_{FR} + LU_{FR} + Dmr_{FR} + Sd_{FR} + Rf_{FR} + Sad_{FR} + Sa_{FR} + Tc_{FR} + TWI_{FR} + At_{FR} \quad (3)$$

3.4. Shannon's Entropy Model

The entropy index is a measure of “evenness” extent to which groups are evenly distributed among organizational units (Massey and Nancy, 1988). In the present study, an attempt has been made to assess flood susceptibility mapping using entropy. More precisely, Theil (1972) defined entropy index as a measure of the average difference between a unit's group proportions and that of the system as a whole. There is a one-to-one relationship between the quantity of entropy of a system and the degree of disorder called Boltzmann principle and has been used to represent the thermodynamic status of a system (Yufeng and Fengxiang, 2009). Shannon improved upon the Boltzmann principle and established an entropy model for information theory. The equations implemented to calculate the information coefficient (V_j) representing the weight value for the parameter as a whole (Bednarik et al., 2010) are given as following (Eqs. 4–8):

$$E_{ij} = \frac{FR}{\sum_{j=1}^{M_j} FR} \quad (4)$$

where, FR is the frequency ratio and E_{ij} is the probability density.

$$H_j = - \sum_{i=j}^{M_j} E_{ij} \log_2 E_{ij}, j = 1, \dots, n \quad (5)$$

$$H_{jmax} = \log_2 M_j, \quad M_j = \text{number of classes} \quad (6)$$

$$I_j = \left(\frac{H_{jmax} - H_j}{H_{jmax}} \right), I = (0,1), j = 1, \dots, n \quad (7)$$

$$V_j = I_j FR \quad (8)$$

Where, H_j and H_{jmax} are entropy values;

I_j is the information coefficient and

M_j is the number of classes

V_j depicts the resultant weight value for the parameter as a whole

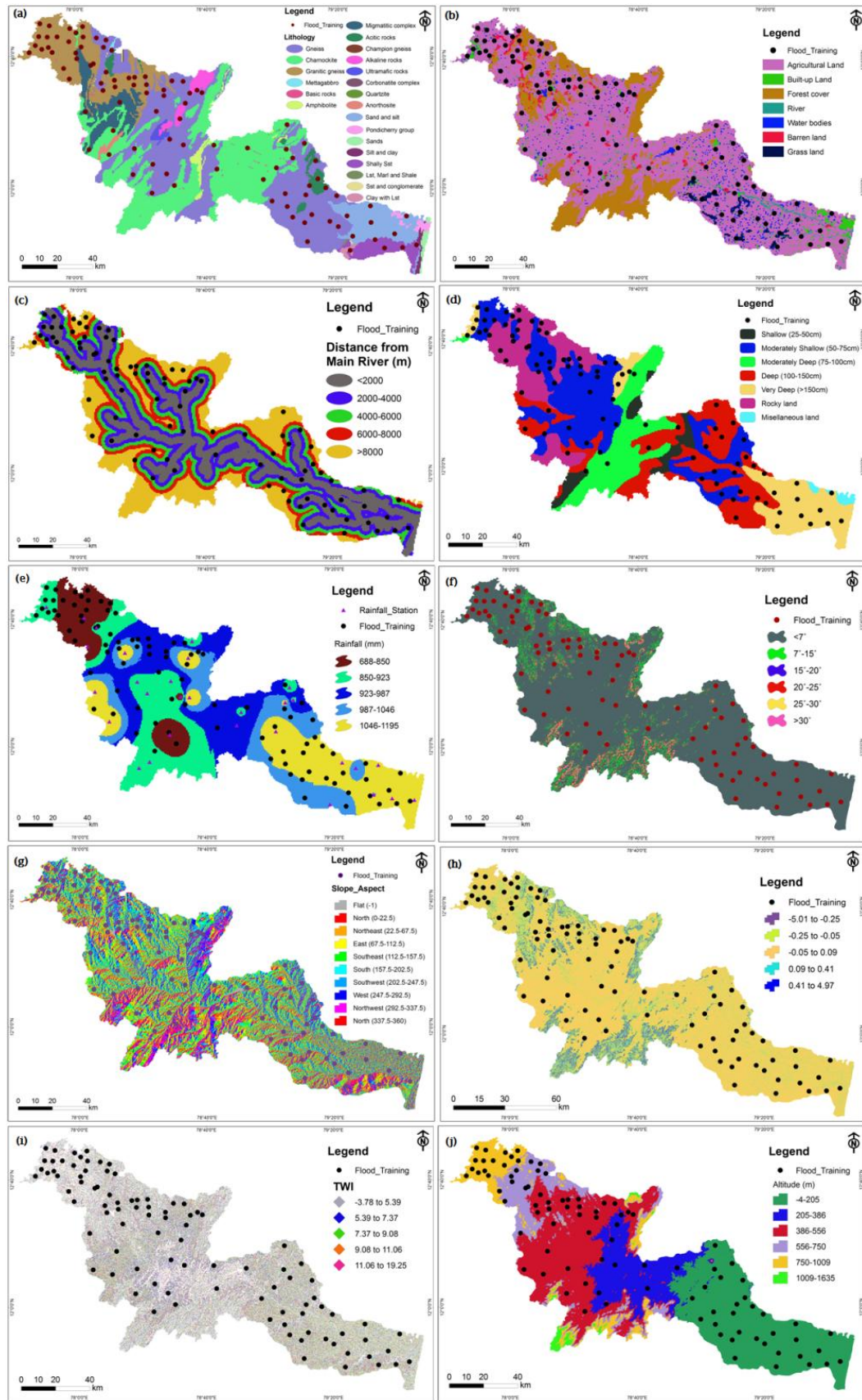


Figure 3: Flood conditioning factors of Ponnaiyar river basin; (a) lithology altitude (b) land use (c) distance from main river (d) soil depth (e) rainfall (f) slope angle (degree) (g) slope aspect (h) curvature (i) Topographic Wetness Index (TWI) and (j) altitude

Table 1: Frequency Ratio and Shannon's Entropy values for the considered flood condition factors

| Factors | No. of pixel in domain | Percent age of domain | No. of well l | Percent age of well | FR | Eij | Hj | Hmax | Ij | Vj | Vj final |
|------------------------------------|------------------------|-----------------------|---------------|---------------------|------|-------|-------|-------|-------|-------|----------|
| Lithology | | | | | | | | | | | |
| Gneiss | 11933 | 34.879 | 23 | 24.211 | 0.69 | 0.061 | 1.053 | 1.342 | 0.215 | 0.149 | 2.435 |
| Charnockite | 10057 | 29.395 | 29 | 30.526 | 1.04 | 0.092 | | | | | |
| Granitic gneiss | 4519 | 13.208 | 23 | 24.211 | 1.83 | 0.162 | | | | | |
| Mettagabbro | 25 | 0.073 | 0 | 0.000 | 0.00 | 0.000 | | | | | |
| Basic rocks | 66 | 0.193 | 0 | 0.000 | 0.00 | 0.000 | | | | | |
| Amphibolite | 377 | 1.102 | 2 | 2.105 | 1.91 | 0.169 | | | | | |
| Migmatitic complex | 1777 | 5.194 | 4 | 4.211 | 0.81 | 0.072 | | | | | |
| Granitic/acidic rocks | 663 | 1.938 | 2 | 2.105 | 1.09 | 0.096 | | | | | |
| Champion gneiss | 12 | 0.035 | 0 | 0.000 | 0.00 | 0.000 | | | | | |
| Alkaline rocks | 567 | 1.657 | 3 | 3.158 | 1.91 | 0.168 | | | | | |
| Ultramafic | 165 | 0.482 | 0 | 0.000 | 0.00 | 0.000 | | | | | |
| Ultrabasic syenite | 10 | 0.029 | 0 | 0.000 | 0.00 | 0.000 | | | | | |
| Quartzite | 5 | 0.015 | 0 | 0.000 | 0.00 | 0.000 | | | | | |
| Anorthosite | 153 | 0.447 | 0 | 0.000 | 0.00 | 0.000 | | | | | |
| Sand and silt | 2278 | 6.658 | 6 | 6.316 | 0.95 | 0.084 | | | | | |
| Pondicherry | 202 | 0.590 | 0 | 0.000 | 0.00 | 0.000 | | | | | |
| Sands | 150 | 0.438 | 0 | 0.000 | 0.00 | 0.000 | | | | | |
| Alter seq. of sand / silt and clay | 128 | 0.374 | 0 | 0.000 | 0.00 | 0.000 | | | | | |
| Shaly sand stone | 1001 | 2.926 | 3 | 3.158 | 1.08 | 0.095 | | | | | |
| Lime stone, marl and shale | 14 | 0.041 | 0 | 0.000 | 0.00 | 0.000 | | | | | |
| Sand stone and conglomerate | 7 | 0.020 | 0 | 0.000 | 0.00 | 0.000 | | | | | |
| Clay with limestone | 104 | 0.304 | 0 | 0.000 | 0.00 | 0.000 | | | | | |
| Land use | | | | | | | | | | | |
| Agricultural land | 24296 | 71.014 | 81 | 85.263 | 1.20 | 0.189 | 0.802 | 0.845 | 0.050 | 0.060 | 0.354 |
| Built-up land | 1153 | 3.370 | 0 | 0.000 | 0.00 | 0.000 | | | | | |
| Forest cover | 5859 | 17.125 | 6 | 6.316 | 0.37 | 0.058 | | | | | |
| River | 437 | 1.277 | 2 | 2.105 | 1.65 | 0.260 | | | | | |
| Water bodies | 1260 | 3.683 | 0 | 0.000 | 0.00 | 0.000 | | | | | |
| Barren land | 814 | 2.379 | 5 | 5.263 | 2.21 | 0.349 | | | | | |
| Grass land | 394 | 1.152 | 1 | 1.053 | 0.91 | 0.144 | | | | | |
| Soil Depth | | | | | | | | | | | |
| Shallow (25-50cm) | 1457 | 4.259 | 3 | 3.158 | 0.74 | 0.121 | 0.788 | 0.845 | 0.066 | 0.049 | 0.467 |
| Moderately shallow (50-75cm) | 10091 | 29.495 | 28 | 29.474 | 1.00 | 0.162 | | | | | |
| Moderately deep (75-100cm) | 4831 | 14.120 | 18 | 18.947 | 1.34 | 0.218 | | | | | |
| Deep (100-150cm) | 7802 | 22.804 | 12 | 12.632 | 0.55 | 0.090 | | | | | |
| Very deep (>150cm) | 4932 | 14.416 | 18 | 18.947 | 1.31 | 0.214 | | | | | |
| Rocky land | 4821 | 14.091 | 16 | 16.842 | 1.20 | 0.194 | | | | | |
| Miscellaneous land | 279 | 0.815 | 0 | 0.000 | 0.00 | 0.000 | | | | | |
| Distance from river (m) | | | | | | | | | | | |
| <2000 | 9219 | 26.946 | 33 | 34.737 | 1.29 | 0.250 | 0.712 | 0.778 | 0.084 | 0.108 | 0.504 |
| 2000-4000 | 7253 | 21.200 | 15 | 15.789 | 0.74 | 0.144 | | | | | |
| 4000-6000 | 5463 | 15.968 | 18 | 18.947 | 1.19 | 0.230 | | | | | |
| 6000-8000 | 4247 | 12.413 | 16 | 16.842 | 1.36 | 0.263 | | | | | |
| >8000 | 8031 | 23.474 | 13 | 13.684 | 0.58 | 0.113 | | | | | |
| Rainfall (Rf) | | | | | | | | | | | |
| 688-850 | 3947 | 11.537 | 10 | 10.526 | 0.91 | 0.184 | 0.695 | 0.778 | 0.105 | 0.096 | 0.634 |

| | | | | | | | | | | | |
|----------------------------------|---------|--------|-------|--------|------|-------|-------|-------|--------|-------|-------|
| 850-923 | 7505 | 21.936 | 20 | 21.053 | 0.96 | 0.193 | | | | | |
| 923-987 | 7937 | 23.199 | 22 | 23.158 | 1.00 | 0.201 | | | | | |
| 987-1046 | 6420 | 18.765 | 19 | 20.000 | 1.07 | 0.215 | | | | | |
| 1046-115 | 8404 | 24.564 | 24 | 25.263 | 1.03 | 0.207 | | | | | |
| Altitude | | | | | | | | | | | |
| (-4-205) | 463487 | 33.577 | 28 | 29.474 | 0.88 | 0.157 | 0.747 | 0.778 | 0.039 | 0.034 | 0.234 |
| 205-386 | 208941 | 15.136 | 13 | 13.684 | 0.90 | 0.162 | | | | | |
| 386-556 | 399278 | 28.925 | 25 | 26.316 | 0.91 | 0.163 | | | | | |
| 556-750 | 160107 | 11.599 | 14 | 14.737 | 1.27 | 0.227 | | | | | |
| 750-1009 | 133540 | 9.674 | 15 | 15.789 | 1.63 | 0.292 | | | | | |
| 1009-1635 | 15038 | 1.089 | 0 | 0.000 | 0.00 | 0.000 | | | | | |
| Total Curvature | | | | | | | | | | | |
| (-5.01--0.25) | 34153 | 2.474 | 2 | 2.105 | 0.85 | 0.182 | 0.669 | 0.903 | 0.259 | 0.220 | 2.071 |
| (-0.25--0.05) | 275679 | 19.971 | 18 | 18.947 | 0.95 | 0.203 | | | | | |
| (-0.05-0.09) | 947734 | 68.657 | 66 | 69.474 | 1.01 | 0.217 | | | | | |
| 0.09-0.41 | 102835 | 7.450 | 8 | 8.421 | 1.13 | 0.242 | | | | | |
| 0.41-4.97 | 19990 | 1.448 | 1 | 1.053 | 0.73 | 0.156 | | | | | |
| Slope angle (Degree) | | | | | | | | | | | |
| <7° | 1206725 | 87.419 | 80 | 84.211 | 0.96 | 0.193 | 0.698 | 0.778 | 0.103 | 0.099 | 0.618 |
| 7°-15° | 84829 | 6.145 | 11 | 11.579 | 1.88 | 0.378 | | | | | |
| 15°-20° | 35695 | 2.586 | 2 | 2.105 | 0.81 | 0.163 | | | | | |
| 20°-25° | 27425 | 1.987 | 1 | 1.053 | 0.53 | 0.106 | | | | | |
| 25°-30° | 18224 | 1.320 | 1 | 1.053 | 0.80 | 0.160 | | | | | |
| >30° | 7493 | 0.543 | 0 | 0.000 | 0.00 | 0.000 | | | | | |
| Topographic wetness index | | | | | | | | | | | |
| (-3.78-5.39) | 95719 | 6.934 | 17 | 17.895 | 2.58 | 0.369 | 0.844 | 0.845 | 0.0004 | 0.001 | 0.003 |
| 5.39-7.37 | 440145 | 31.886 | 31 | 32.632 | 1.02 | 0.146 | | | | | |
| 7.37-9.08 | 576050 | 41.731 | 21 | 22.105 | 0.53 | 0.076 | | | | | |
| 9.08-11.06 | 172320 | 12.483 | 16 | 16.842 | 1.35 | 0.193 | | | | | |
| 11.06-19.25 | 96157 | 6.966 | 10 | 10.526 | 1.51 | 0.216 | | | | | |
| Slope aspect | | | | | | | | | | | |
| Flat (-1) | 7252 | 0.525 | 1.00 | 1.05 | 2.00 | 0.171 | 1.07 | 1.146 | 0.066 | 0.133 | 0.930 |
| North (0-22.5) | 84014 | 6.086 | 11.00 | 11.58 | 1.90 | 0.162 | | | | | |
| Northeast (22.5-67.5) | 170927 | 12.383 | 15.00 | 15.79 | 1.28 | 0.109 | | | | | |
| East (67.5-112.5) | 210918 | 15.280 | 13.00 | 13.68 | 0.90 | 0.076 | | | | | |
| Southeast (112.5-157.5) | 218733 | 15.846 | 12.00 | 12.63 | 0.80 | 0.068 | | | | | |
| South (157.5-202.5) | 171230 | 12.404 | 13.00 | 13.68 | 1.10 | 0.094 | | | | | |
| Southwest (202.5-247.5) | 146330 | 10.601 | 9.00 | 9.47 | 0.89 | 0.076 | | | | | |
| West (247.5-292.5) | 145311 | 10.527 | 9.00 | 9.47 | 0.90 | 0.077 | | | | | |
| Northwest (292.5-337.5) | 158753 | 11.501 | 5.00 | 5.26 | 0.46 | 0.039 | | | | | |
| North (337.5-360) | 66923 | 4.848 | 7.00 | 7.37 | 1.52 | 0.129 | | | | | |

The result ranges between 0 and 1. The closer the value is to the number 1, the greater the imbalance is 0. The complete calculation of weight determination for individual parameters is presented in Table 1. In flood susceptibility mapping, the entropy measures and reflects the spatial association between the conditioning factors and flood occurrences. The flood susceptibility index can be determined by summation according to Eq. (9).

$$FSI = Li_{FR}2.435 + LU_{FR}0.354 + Dmr_{FR}0.504 + Sd_{FR}0.467 + Rf_{FR}0.634 + Sad_{FR}0.618 + Sa_{FR}0.930 + Tc_{FR}2.071 + TWI_{FR}0.003 + At_{FR}0.234 \quad (9)$$

3.5. Validation Method

From scientific significance viewpoint, validation is considered to be the most important process of modeling (Chung and Fabbri, 2003). Therefore, it is very important to evaluate the resultant FSI. The receiver operating characteristics (ROC) curve was applied to determine the accuracy of the FSI. The FSI delineated in the current study was verified using the flood locations in the validation datasets. Based on the flood inventory data, the accuracy assessment of the flood susceptibility mapping was made. In total, 136 flood locations were noted in the study area. Out of these, 95 (70%) floods were randomly selected as training data and the remaining 41 (30%) floods were used for the validation purposes. The ROC curves were then obtained by considering cumulative percentage of probability index maps (on the x axis) and the cumulative percentage of flood occurrence (on the y axis). The area under the curve (AUC) was calculated based on ROC curve analysis and it demonstrates the accuracy of a prediction system by describing the system's ability to expect the correct occurrence or non-occurrence of pre-defined "events" (Jaafari et al., 2014). Finally, using the quantitative and qualitative relationship between the AUC value and prediction accuracy can be grouped as very high, high, moderate, low and very low flood occurrences in the study area. The brief methodology used in the present study area shown in Figure 4.

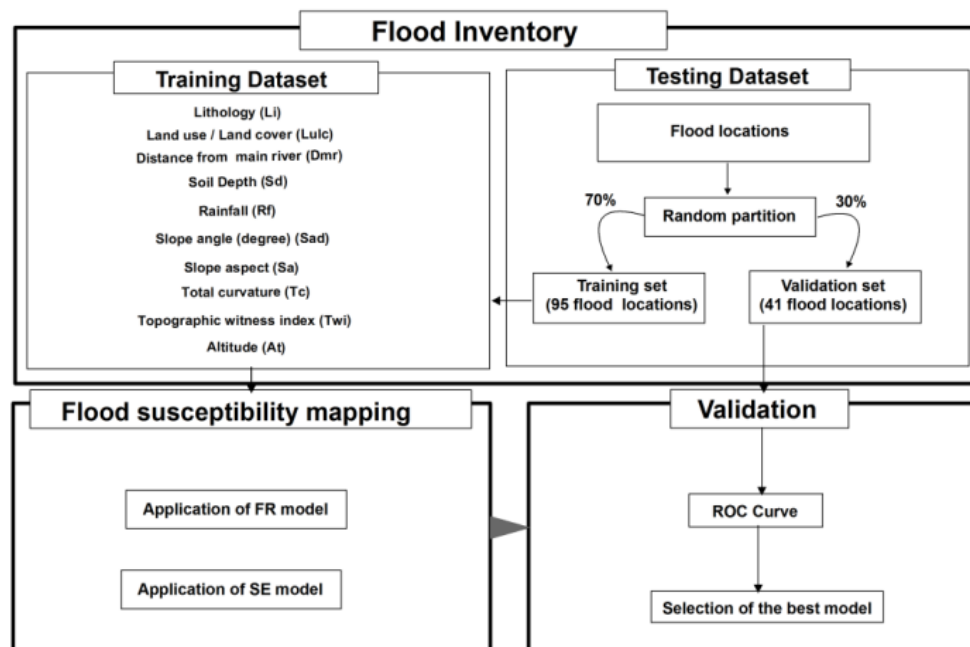


Figure 4: Flowchart showing the methodology adopted in this study

4. Results and Discussion

Frequency Ratio methods were applied to determine the level of relationship between flood locations and conditioning factors. In general, the FR value of 1 indicates an average correlation between flood locations and effective factors (Pradhan, 2010). If the FR value would be larger than 1, there is a high correlation, and a lower correlation equals to the FR value lower than 1 (Lee et al., 2012a). The analysis of FR for the relationship between flood location and lithology units indicates that amphibolites and Alkaline rocks have the highest FR value (1.91) have the most probability for flooding in the study area. The agricultural and barren lands have values of 1.20 and 2.21, respectively, indicating that the probability of flood occurrence in these land-use types is very high. For distance from river in the range 2000–4000 m and >8000 m, there is a low probability of flooding; in contrast, distances in the range <2000 m, 4000–6000 m and 6000–8000 m have the highest values (1.29, 1.19, and 1.36, respectively). These results demonstrated that the flooding mostly occurs near to the river bank and

rarely far from the rivers. The results of soil depth displayed that moderately deep, very deep and rocky land have the highest value of FR (1.34, 1.31 and 1.20 respectively).

The slope angle indicates that class 7° – 15° has the highest FR value (1.88), and other indicating a low probability. This means that flood occurrence probability decreases with increasing in slope angle. In the case of slope aspect, flood event is most abundant on flat (FR = 2.00) and northwest-facing slopes (FR = 0.46), have the lowest abundance. Based on the curvature, the (0.09-0.41) shape has the highest FR value (1.13) indicates that the most probability for flooding. That shape retains surface run-off for a longer period especially during heavy rainfall. Therefore, it is more prone for flooding compared to the other shapes. Flood locations are more concentrated in areas with a TWI (-3.78-5.39) (FR = 2.58) and altitude classes of 750-1009 m (FR = 1.63). In the case of altitude, analysis of FR values demonstrated that the flood occurrence cannot occur in the high elevation regions of the study area. Finally, based on Equation (2), the final flood susceptibility map obtained by the FR model is shown in Figure 5.

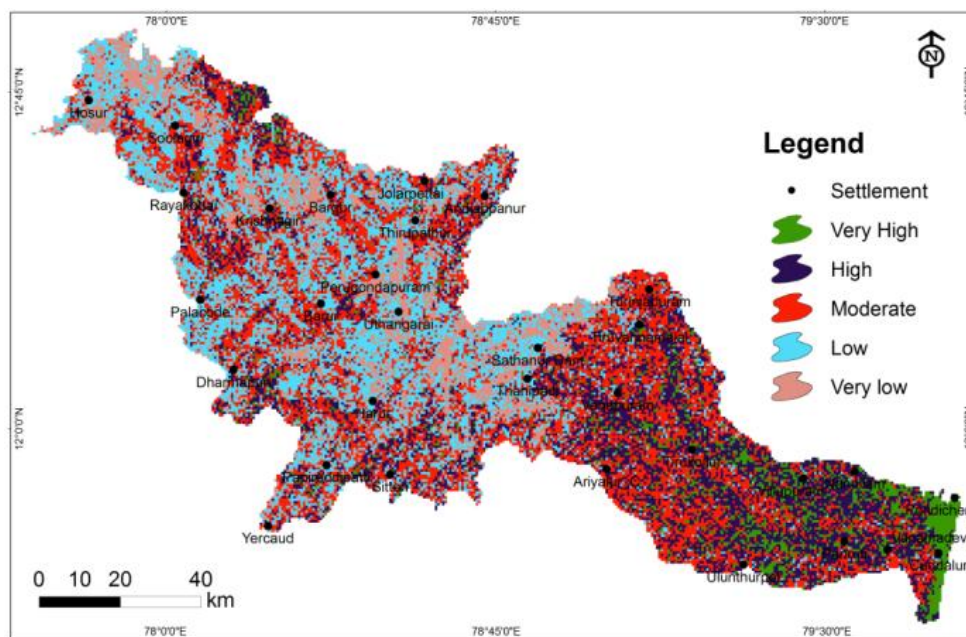


Figure 5: Flood susceptibility map of FR model in Ponnaiyar River basin

In the present study, all parameters of SE model were calculated for each conditioning factor, which is shown in Table 1. Based on the results obtained from the entropy, the lithology and curvature represented highest flood susceptibility in the study area (V_j final, 2.435, 2.071 respectively) showing maximum flood susceptibility. The land-use weights of factors were 0.802, 0.845, 0.050, and 0.060, respectively. The entropy values of distance from the river indicated positive influence in flooding. The analysis of SE for the relationship between flood occurrence and slope angle indicated that positive influences in flooding. In the case of slope aspect and plan curvature, flat area had a strong positive correlation with flood occurrence. E_{ij} values increases by increasing classes of TWI. Moore et al. (1991) stated that TWI represents the effect of topography on the location and size of saturated source areas of surface run-off generation under the assumption of steady-state conditions and uniform soil properties. In the case of altitude, the highest weight (0.292) was for the range of 750–1009 m that has positive effect in flood occurrence. Finally, based on Equation (9), the final flood susceptibility map created by the SE model is shown in Figure 6.

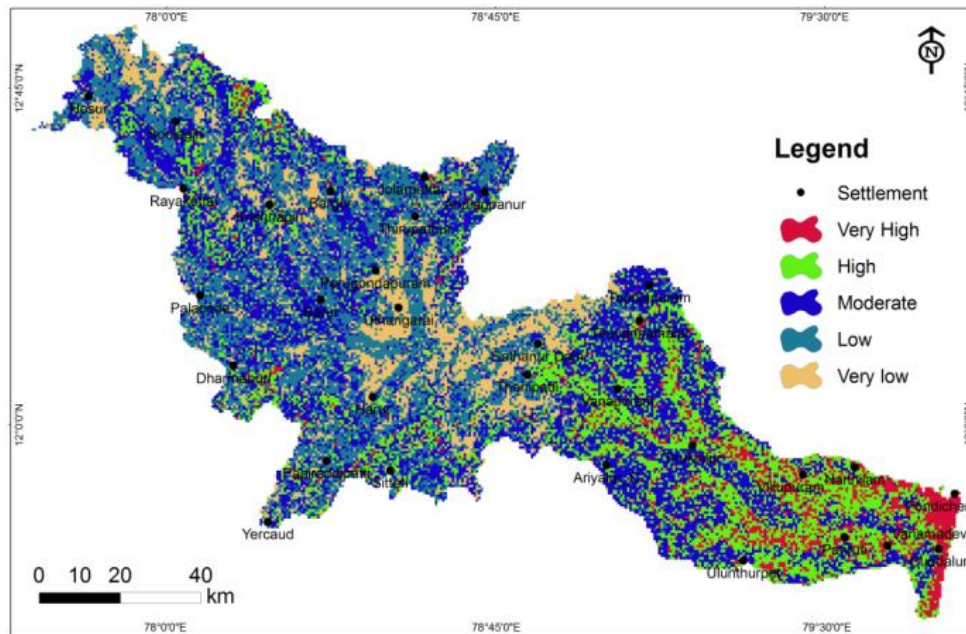


Figure 6: Flood susceptibility map of SE model in Ponnaiyar River basin

In flood susceptibility appraisal, the major aim was to find areas that may be affected by future floods. Thus, no matter which integration methodology is used, it is very important to validate the resultant flood susceptibility maps with respect to unknown future flood events (Chung & Fabbri, 2003). In this study, the flood locations that were not used during the model building/training were used to verify the flood susceptibility maps. The receiver operating characteristics (ROC) analysis was used (Egan, 1975; Swets, 1988; Pradhan & Lee, 2010; Pradhan et al., 2011; Pourghasemi et al., 2012a; Rahmati et al., 2014) to determine the accuracy of flood susceptibility maps produced using FR models. The ROC curve is a common methodology to determine the accuracy of a diagnostic test (Pourghasemi et al., 2012a), and it is considered as a graphical representation of the trade-off between the false-negative (X-axis) and false-positive (Y-axis) rates for every possible cut-off value (Pourghasemi et al., 2014). The AUC of ROC describes the accuracy of a prediction model by determining the system's ability to expect the correct occurrence or non-occurrence of pre-defined 'events' (Pourtaghi & Pourghasemi, 2015). The ROC curves for FR and SE models are shown in Figure 7 a & b respectively.

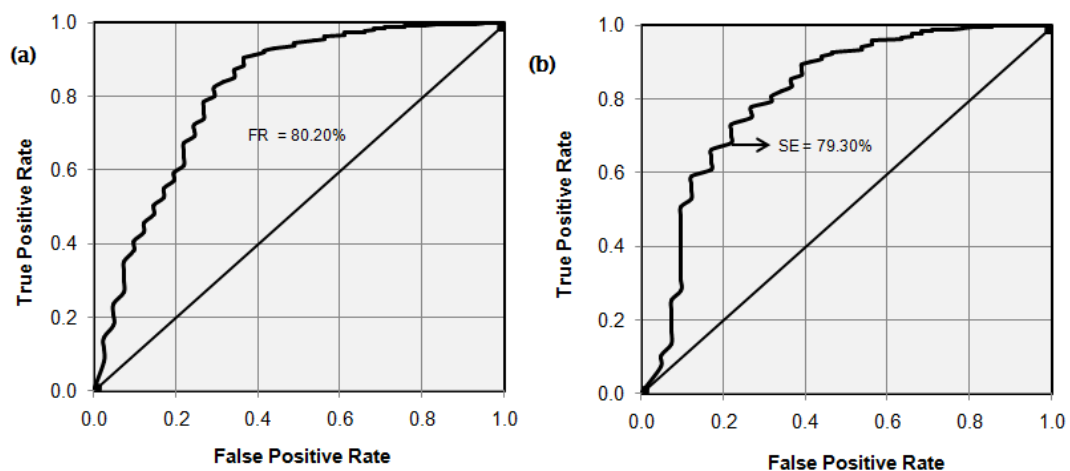


Figure 7: ROC curve for the flood susceptibility maps produced by FR and SE models of Ponnaiyar river basin

It is clear that in the flood susceptibility mapping using the FR model, the AUC is about 0.8020, which corresponds to the prediction accuracy of 80.20%, whereas in the flood susceptibility map using the SE model, the AUC is about 0.7930 and the prediction accuracy is 79.30%. Therefore, based on the calculated AUC, the FR and SE models indicated almost similar and reasonable results and can be used as simple tools in flood susceptibility mapping and flood mitigation when a sufficient number of data is obtained.

5. Conclusion

Industrial and agricultural expansion has been accompanied in recent decades by an ever increasing use of areas subject to flood, which has resulted in increased flood damages. Apart from studies related to investigations and improvements of river system, simultaneous action for studies of watersheds and adoption of measures aimed at runoff and water flow retardation is also required. Therefore, flood susceptibility mapping is necessary for integrated watershed management in order to have sustainable development. The validation of results indicated that the FR and SE models had almost similar and reasonable results in the study area. In the present study, flood susceptibility maps have been prepared using FR and SE methods with the integration of remote sensing and GIS. The application of the FR and SE models is divided into three steps: the construction of database, the calculation of weights and the data integration and verification procedure, in which the obtained FSI was verified with ROC and flood locations. In general, all used factors have relatively higher values of variation index implying the importance of all factors for accurate demarcation of flood prone areas. FR approach is in agreement with the result obtained by other researchers used in flood susceptibility appraisal and various environmental studies. FR model is effective and reliable approach for flood susceptibility mapping in the present study. According to Shannon's entropy results, it can be concluded that lithology and curvature have the strongest relationships with flood occurrence. Also, factors such as slope angle (degree) distance to from Main River, and slope aspect had the lowest importance on flood susceptibility map. From the analysis, it is seen that the FR model (AUC=80.20 %) performs better than SE (AUC=79.30 %) models. As a final conclusion, the results of the present study proved that FR and SE models can be successfully used in flood susceptibility mapping. So, the result of flood susceptibility map indicated that the Ponnaiyar river basin has undergone a significant amount of the flood occurrences are made in future. Based on the overall assessments, the proposed approaches in this study were concluded as objective and applicable. The scientific information derived from this study can assist governments, planners and engineers to perform proper actions in order to prevent and mitigate the flood occurrence in the future.

Acknowledgements

The first author acknowledges University Grants Commission (UGC), New Delhi, for granting a Post-Doctoral Fellowship. The authors thank the anonymous reviewers for their valuable comments and suggestions to improve the content of the article.

References

- Aniya, M. Landslide-susceptibility mapping in the amahata river basin, Japan. *Ann Assoc Am Geogr.* 1985. 75 (1) 102-114.
- Anbazhagan, S., and Dash, P. Environmental case study of Cauvery river flood plain. *GIS Development.* 2003. 7 (12) 30-35.
- Ayazi, M.H., Pirasteh, S., Arvin, A.K.P., Pradhan, B., Nikouravan, B., and Mansor, S. Disasters and risk reduction in groundwater: Zagros mountain southwest Iran using geo-informatics techniques. *Dis Adv.* 2010. 3 (1) 51-57.

- Bajabaa, S., Masoud, M., and Al-Amri, N. Flash flood hazard mapping based on quantitative hydrology, geomorphology and GIS techniques (case study of Wadi Al Lith, Saudi Arabia). *Arab. J. Geosci.* 2013. 1-13.
- Bednarik, M., Magulová, B., Matys, M., and Marschalko, M. Landslide susceptibility assessment of the Kraňovany–Liptovský Mikuláš railway case study. *Phys Chem Earth.* 2010. 35; 162-171.
- Charon, J.E., 1974: Hydrogeological applications of ERTS satellite imagery. In: Proc UN/FAO regional seminar on remote sensing of earth resources and environment. Commonwealth Science Council, Cairo. 439-456.
- Chung, J.F., and Fabbri, A.G. Validation of spatial prediction models for landslide hazard mapping. *Nat Hazards.* 2003. 30 (3) 451-472.
- Co, R.M., 1990: *Handbook of groundwater development.* New York: Wiley. 34-51.
- Central Ground Water Board (CGWB), (2012). Annual Report.
- Devkota, K.C., Regmi, A.D., Pourghasemi, H.R., Yoshida, K., Pradhan, B., Ryu, I.C., Dhital, M.R., and Althuwaynee, O.F. Landslide susceptibility mapping using certainty factor, index of entropy and logistic regression models in GIS and their comparison at Mugling–Narayanghat road section in Nepal Himalaya. *Nat Hazards.* 2013. 65; 135-165.
- Egan, J.P., 1975: *Signal detection theory and ROC analysis.* New York: Academic Press.
- Ercanoglu, M., and Gokceoglu, C. Assessment of landslide susceptibility for a landslide prone area (north of Yenice, NW Turkey) by fuzzy approach. *Environ Geol.* 2002. 41; 720-730.
- Esteves, L.S. Consequences to flood management of using different probability distributions to estimate extreme rainfall. *J Environ Manage.* 2013. 115; 98-105.
- Feng, C.C., and Wang, Y.C. GIScience research challenges for emergency management in southeast Asia. *Nat Hazards.* 2011. 59; 597-616.
- Florinsky, I.V. Relationships between topographically expressed zones of flow accumulation and sites of fault intersection: analysis by means of digital terrain modelling. *Environ Model Softw.* 2000. 15 (1) 87-100.
- Glenn C.R. et al., 2012: Lahaina Groundwater Tracer Study—Lahaina, Maui, Hawaii. Final Interim Report prepared from the State of Hawaii DOH, the U.S. EPA, and the U.S. Army Engineer Research and Development Center.
- Geological Survey of India (GSI) (1988). Annual report.
- Gokceoglu, C., and Aksoy, H. Landslide susceptibility mapping of the slopes in the residual soils of the Mengen region (Turkey) by deterministic stability analyses and image processing techniques. *Eng Geol.* 1966. 44; 147-161.
- Jaafari, A., Najafi, A., Pourghasemi, H.R., Rezaeian, J., and Sattarian, A. GIS-based frequency ratio and index of entropy models for landslide susceptibility assessment in the Caspian forest, northern Iran. *Int J Environ Sci Te.* 2014. 11 (4) 909-926.

Joint Needs Assessment (JNA) Report of Tamilnadu Floods-2015.

Jourde, H., Lafare, A., Mazzilli, N., Belaud, G., Neppel, L., Dörfliger, N., and Cernesson, F. Flash flood mitigation as a positive consequence of anthropogenic forcing on the groundwater resource in a karst catchment. *Environ Earth Sci.* 2014. 71; 573-583.

Kia, M.B., Pirasteh, S., Pradhan, B., Mahmud, A.R., Sulaiman, W.N.A., and Moradi, A. An artificial neural network model for flood simulation using GIS: Johor river basin, Malaysia. *Environ Earth Sci.* 2012. 67; 251-264.

Kjeldsen, T.R. Modelling the impact of urbanization on flood frequency relationships in the UK. *Hydrol. Res.* 2010. 41; 391-405.

Lee, S., Kim, Y.S., and Oh, H.J. Application of a weights-of-evidence method and GIS to regional groundwater productivity potential mapping. *Environ Manag.* 2012a. 96 (1) 91-105.

Liu, Y.B., Gebremeskel, S., De Smedt F. et al. A diffusive transport approach for flow routing in GIS-based flood modeling. *J Hydrol.* 2003. 283; 91-106.

Masood, M., and Takeuchi, K., Assessment of flood hazard, vulnerability and risk of mid-eastern Dhaka using DEM and 1D hydrodynamic model. *Nat Hazards.* 2012. 61; 757-770.

Massey, D.S., and Nancy, A.D. The Dimensions of Residential. *Social Forces.* 1988. 67 (2) 281-315.

Mogaji, K.A., Lim, H.S., and Abdullah, K. Regional prediction of groundwater potential mapping in a multifaceted geology terrain using GIS-based Dempster–Shafer model. *Arab J Geosci.* 2015. 8 (5) 3235-3258.

Moore, I.D., Grayson, R.B., and Ladson, A.R. Digital terrain modeling: a review of hydrological, geomorphological and biological applications. *Hydrol Process.* 1991. 5; 3-30.

Pourghasemi, H.R., and Beheshtirad, M. Assessment of a data-driven evidential belief function model and GIS for groundwater potential mapping in the Koohrang Watershed, Iran. *Geocarto Int.* 2014. 30 (6) 662-685.

Pourghasemi, H.R., Mohammady, M., and Pradhan, B. Landslide susceptibility mapping using index of entropy and conditional probability models in GIS: Safarood Basin, Iran. *Catena.* 2012a. 97; 71-84.

Pradhan, B., and Lee, S. Regional landslide susceptibility analysis using back-propagation neural network model at Cameron Highland, Malaysia. *Landslides.* 2010. 7 (1) 13-30.

Pradhan, B. Flood Susceptible Mapping and Risk Area Estimation Using Logistic Regression, GIS and Remote Sensing. *J Spatial Hydrol.* 2012a. 9 (2) 1-18.

Pradhan, B. Remote sensing and GIS-based landslide hazard analysis and cross-validation using multivariate logistic regression model on three test areas in Malaysia. *Adv Space Res.* 2010b. 45 (10) 1244-1256.

Pradhan, B., and Buchroithner, M.F. Comparison and validation of landslide susceptibility maps using an artificial neural network model for three test areas in Malaysia. *Environ. Eng. Geosci.* 2010. 16; 107-126.

- Pradhan, B., Youssef, A.M., and Varathrajoo, R. Approaches for delineating landslide hazard areas using different training sites in an advanced artificial neural network model. *Geospatial. Inf. Sci.* 2010b. 13; 93-102.
- Pradhan, B., Mansor, S., Pirasteh, S., and Buchroithner, M.F. Landslide hazard and risk analyses at a landslide prone catchment area using statistical based geospatial model. *Int. J. Remote. Sens.* 2011. 32; 4075-4087.
- Pradhan, B. Use of GIS-based fuzzy logic relations and its cross application to produce landslide susceptibility maps in three test areas in Malaysia. *Environ. Earth Sci.* 2011. 63; 329-349.
- Pourtaghi, Z.S., and Pourghasemi, H.R. GIS-based groundwater spring potential assessment and mapping in the Birjand Township, southern Khorasan Province, Iran. *Hydrogeol J.* 2015. 22; 643-662.
- Rahmati, O., Pourghasemi H.R. and Zeinivand, H. Flood susceptibility mapping using frequency ratio and weights-of-evidence models in the Golastan Province, Iran. *Geocarto International*, 2015. 31 (1) 42-70.
- Rahmati, O., Nazari Samani, A., Mahdavi, M., Pourghasemi, H.R., and Zeiniv, H. Groundwater potential mapping at Kurdistan region of Iran using analytic hierarchy process and GIS. *Arab J Geosci.* 2014a. 8; 1-13.
- Regmi, A.D., Devkota, K.C., Yoshida, K., Pradhan, B., Pourghasemi, H.R., Kumamoto, T., and Akgun, A. Application of frequency ratio, statistical index, and weights-of-evidence models and their comparison in landslide susceptibility mapping in central Nepal Himalaya. *Arab J Geosci.* 2013.
- Saha, A.K., Gupta, R.P., Sarkar, I., Arora, K.M., and Csaplovics, E. An approach for GIS-based statistical landslide susceptibility zonation with a case study in the Himalayas. *Landslides.* 2005. 2; 61-69.
- Schober, B., Hauer, C., and Habersack, H. A novel assessment of the role of Danube floodplains in flood hazard reduction (FEM method). *Nat Hazards.* 2015. 75; 33-50.
- Shafapour Tehrany, M., Pradhan, B., and Jebur, M.N. Spatial prediction of flood susceptible areas using rule based decision tree (DT) and a novel ensemble bivariate and multivariate statistical models in GIS. *J Hydrol.* 2013. 504; 69-79.
- Smith, K., and Ward, R., 1998: *Floods: Physical Processes and Human Impacts*. Chichester: Wiley. 382.
- Swets, J.A. Measuring the accuracy of diagnostic systems. *Science.* 1988. 240; 1285-1293.
- Tehrany, M.S., Pradhan, B., Jebur, M.N. Spatial prediction of flood susceptible areas using rule based decision tree (DT) and a novel ensemble bivariate and multivariate statistical models in GIS. *J Hydrol.* 2013. 504; 69-79.
- Tehrany, M.S., Pradhan, B., Jebur, M.N. Flood susceptibility mapping using a novel ensemble weights-of-evidence and support vector machine models in GIS. *J Hydrol.* 2014. 512; 332-343.
- Theil, H., 1972: *Statistical decomposition analysis*. Amsterdam: North-Holland Publishing Company.

Vieux, B.E., 2004: *Distributed hydrologic modeling using GIS*. Water Sci Tech Libr. Vol. 48. Kluwer Academic Publishers. 312.

Wang, H.B., Wu, S.R., Shi, J.S., and Li, B. Qualitative hazard and risk assessment of landslides: a practical framework for a case study in China. *Nat Hazards*. 2013. 69; 1281-1294.

Yalcin, A. GIS-based landslide susceptibility mapping using analytical hierarchy process and bivariate statistics in Ardesen (Turkey): comparisons of results and confirmations. *Catena*. 2008. 72. 1-12.

Yufeng, S., and Fengxiang, J. Landslide stability analysis based on generalized information entropy. *Int Conf Environ Sci Inf Appl Technol*. 2009. 2; 83-85.

Normalized Difference Vegetation Index (NDVI) Based Classification to Assess the Change in Land Use/Land Cover (LULC) in Lower Assam, India

Ravi Prakash Singh, Neha Singh, Saumya Singh, and Saumitra Mukherjee

School of Environmental Science, Jawaharlal Nehru University, New Delhi

Publication Date: 31 October 2016

DOI: <https://doi.org/10.23953/cloud.ijarsg.74>



Copyright © 2016 Ravi Prakash Singh, Neha Singh, Saumya Singh, and Saumitra Mukherjee. This is an open access article distributed under the **Creative Commons Attribution License**, which permits unrestricted use, distribution, and reproduction in any medium, provided the original work is properly cited.

Abstract The land use activities ultimately affect the land cover spatially and temporarily. The major factor responsible for the change in land use/land cover is to fulfill the growing demands of increasing population through agricultural intensification for food and clearing natural land cover like the forest for settlement and commercial activities. The change in land use and land cover also disturbs the other natural component soil fertility, soil erosion, ecology, biodiversity, air quality and water regime of the disturbed area. The remote sensing and GIS technology has been emerged as a good tool to analyze the change in land use and land cover of the area at spatial and temporal scale. In this study, the NDVI based classification has indicated about significant change in land use land cover between a year 1990 and 2014. The Major change has been found in the forest cover area where about 113 km² (2.9%) of forest have been degraded and about 115.4 km² area of wetland has been lost between year 1990 and 2014.

Keywords *NDVI; GIS; Landsat; LULC*

1. Introduction

Land cover refers to the physical state of the land surface including cropland, forest, wetland etc. (Di Gregorio & Jansen, 2000); whereas land use refers to biophysical assets used by the human (Cihlar & Jansen, 2001; Campbell, 2002). Land use/land cover analysis is important for agricultural planning, urbanisation and environmental studies (Turner, 1995; Goulding & Blake, 1998; Mahajan et al., 2001, Vitousek, 1994; Nunes et al., 2005; Huang & Siegert, 2006), and this information also helps to understand the relationship between cropland, forest land, settlement etc. In recent time, the modernisation and demographic pressure have increased the land use and simultaneously affected the land cover (Myers, 1984). Remote sensing data and GIS is an appropriate tool for the assessment of the global land use/land cover change and environmental monitoring because of its spatial and temporal coverage capabilities (Anderson et al., 1976; Green et al., 1994; Fraser, 2009; Mukherjee et al., 2010). Normalized difference vegetation index (NDVI) based comparison using multi date satellite data methods proposed for change detection in land use and land cover (Nielson et al., 1998; Stow et al., 1996; Yuan et al., 1999). The change detection and assessment of land use/land cover using geo-

informatics allow the user to monitor land cover over the large area and over a period of time. The change in land use and land cover (LULC) varying along regions, in rural areas is attributed due to agriculture expansion, forest fire and illegal tree cutting while in urban areas it is attributed to urbanization and commercialisation. The heterogeneous change in land use and land cover of an area is critically linked to other environmental parameters like groundwater quality and soil health (Rao et al., 1996; Turner, 1995). The normalised difference vegetation index (NDVI) is used for the mapping of changes in land cover (Woodcock et al., 2002; Lunetta et al., 2006). The change in land use/land cover were analysed by studying the difference between images derived by transforming multi-temporal images to digital numbers indicative of the changes (Maselli, 2004). In the present study, analysis of land use/land cover focuses on following 3 aspects Detection of changes in land use & land cover between 1990 and 2014, Identification of nature of changes & Assessment of the pattern of the changes.

2. Study Area

In the present study, lower western Assam area has been selected as the study area (Figure 1) which includes two districts Goalpara and Bongaigaoun. The district Goalpara, situated on the Southern bank of river Brahmaputra, covers an area of 1,842 sq km and is located between 25°53'N & 90°07'E and 26°15'N & 91°05'E. The district Bongaigaoun is situated on the northern bank of river Brahmaputra, adjacent to Goalpara district covering an area about 1725 sq km and is located between 26°30'N and 90°23'E and 26°10'N and 90° 52'E. The study area is occupied by both the hills and plains. The hills in the region occur as isolated inselbergs, areas varying from 1 to 15 sq km (e.g. Inselberg west of Goalpara town), and heights ranging from 60 to 300 m above msl. The hills are veneered by lateritic mantle and are deeply forested with evergreen mixed open jungles (CGWB, 2008). The district Goalpara and Bongaigaoun is a part of the alluvial plains which lies adjacent to the foot-hill ranges. Archaean inliers are present in the central and the eastern part of the district. with a gentle regional slope towards Brahmaputra river.

2.1. Geological Settings of Study Area

Both the districts of the study area (Goalpara and Bongaigaoun) are situated in foreland depression between the comparatively younger mountains chain of the Himalayas in the north and block Mountains of Shillong plateau in the south. The geological formation in the area are the Archean group of rock comprising Biotite-Hornblend gneiss, granulites, schists which are intruded by granite with pegmatites trending NE-SW with a moderate dip towards NW. The unconsolidated alluvium of quaternary age is divided into older and younger types. The major part of the area is lying under younger alluvial plain which consists of gravel, pebbles, sand, silt and clay while older alluvium is compact and contains limonitic clay, unsorted boulders, pebbles, gravel and sand (GSI, 2009).

3. Materials and Methods

3.1. Image Acquisition

The image of study area has been acquired during the month of November with minimum cloud cover.

Table 1: Details of the image used in the study

| Image | Path/row | Acquisition Date | Spatial Resolution |
|-----------|----------|------------------|--------------------|
| Landsat 5 | 137/43 | 11/11/1990 | 30 meter |
| Landsat 7 | 137/43 | 08/11/2014 | 30 meter |

3.2. Image Pre-processing

- Layer Stacking: The layer stacking of bands was performed on the Erdas Imagine 14 software.
- Mosaicking the layer stacked image tiles were mosaicked and then clipped with study area shapefile.
- Image rectification was done to correct distortions resulting from the image acquisition process.
- Projection: The image downloaded is in Universal Transverse Mercator projection and it is reprojected to Geographic WGS 84, spheroid and datum Everest.

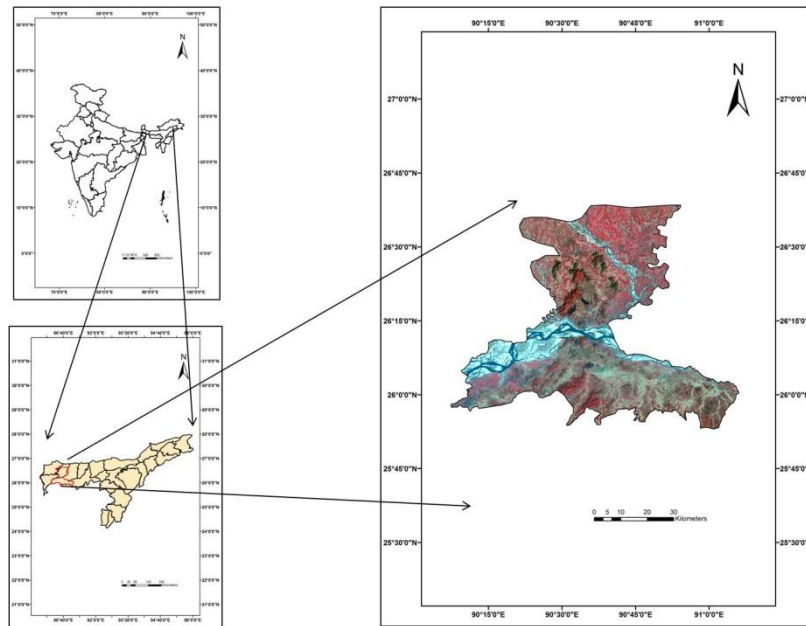


Figure 1: Study Area

3.3. Image Classification and Change Detection

Image classification for both years (1990 & 2014) was performed through supervised classification using maximum likelihood classifier, which includes following steps:

- Selection of signature of different features (training sites) by digitisation of selected area on the image. Selection of signature was based on field knowledge and existing literature and map.
- Obtained signatures act as an input for digital image classification. On the basis of given signature, the whole study area was classified into four classes.
- Based on the quality of results, training samples were refined until a satisfactory result was obtained.
- Classified images were recorded to respective classes (i.e. Forest, wetland vegetation, river, agricultural field)
- The normalised difference vegetation index was calculated on ERDAS Imagine14.0 for the year 1990 and 2014 of land sat image. The results of both the years were also compared, which show significant changes in land use/land cover over a period of time in the study area.

4. Results and Discussion

The pressure of increasing population and unplanned land use practices has great impact over natural land cover. The large vegetation cover has been converted into crop land, settlement and the natural wetlands are under the threat of dryness. The concern about the change in LULC has got attention after realizing the impact of change on climate and ecosystem of the area. In present study, two images (1990 and 2014) have been classified on the basis of normalised difference vegetation index (NDVI), a vegetation index calculated by

$$NDVI = \frac{NIR - RED}{NIR + RED}$$

NDVI is an index based on spectral reflectance of the ground surface feature. Each feature has its own characteristic reflectance varying according to the wavelength. NDVI value ranges between -1 to +1. A Higher value of NDVI infers the presence of healthy vegetation in the area while its lower value is the indicator of sparse vegetation. NDVI has been used for analysis of change detection in many studies (Huang and Siegert, 2006; Ahl et al., 2006; de Boer, 2000). The NDVI value calculated from Landsat satellite image of the year 1990 ranges from 0.85 to -0.02. The higher value of NDVI was found in the upper part of the district Bongaigaoun and in the periphery of Goalpara district in south of Brahmaputra river (Figure 2). The upper part of the area having higher NDVI value belongs to the Manas reserve forest. The lower values of NDVI were found in the rivers and wetland regions of the study area.

In comparison to the year 1990, the NDVI values of the year 2014 show a significant change across the whole region and its value ranges from 0.83 to -0.37 (Figure 2). Higher NDVI was found in scattered patches. The decrease in NDVI value indicates the change in land use of the area mainly due to the loss of forest area because of agricultural expansion and human encroachment.

4.1. Change in Land Use/Land Cover

Change in land use/land cover between 1990 and 2014 were evaluated using satellite images in the area. The whole area was classified under 4 classes by supervised classification (maximum likelihood method) using image processing software on Erdas 2014. The classes are as follows: Forest (2) River (3) Wetland (4) Agricultural field and sand. The classified satellite image of the year 1990 and 2014 shows a significant change in land use/land cover in the study area. The classified image of the year 1990 (Figure 3) shows that about 78% of the area is under agricultural field; while 10% of the area is drained by the rivers (Table 2). A dense forest has been observed in the north of the area lying near Manas forest reserve and along the hilly area of Bongaigaoun (north of Brahmaputra) and Goalpara district (South of Brahmaputra) (Figure 3). The classified image of the year 2014 (Figure 4) shows a significant change in the land use and land cover. A major change has been found in the forest cover area where about 113 km² (2.9%) of forest have been degraded between the year 1990 and 2014. The changes occur mainly due to the human encroachment and agricultural intensification.

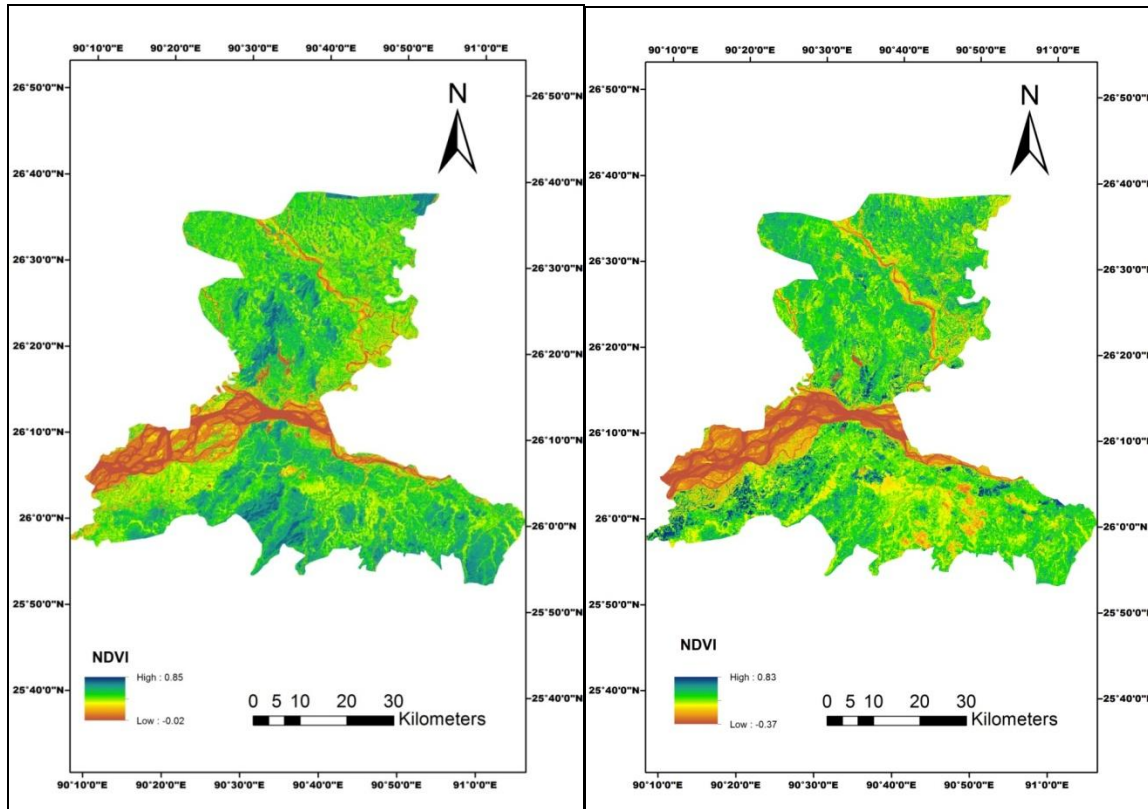


Figure 2: NDVI variation in the study area in 1990 (a) and 2014 (b)

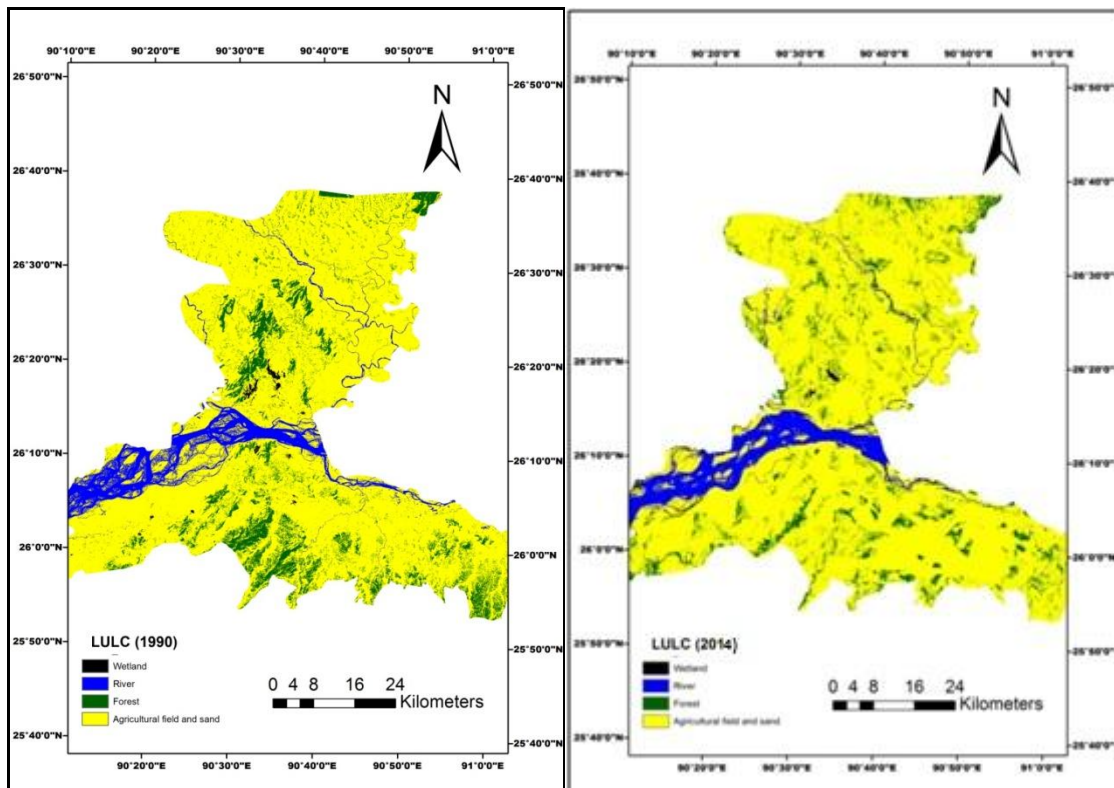


Figure 3: Change in Landuse and Landcover of the area in the year 1990(a) and 2014(b)

The increasing population has changed the land cover pattern through overexploitation of land resources for their livelihood because the population residing near forest depends on upon valuable timbers of forest and agriculture (Sharma, 2003; Bhattacharjee and Nayak, 2003). The agricultural expansion (mainly paddy crops) and settlement have become a threat for forest cover. The area of the agricultural field has increased in the year 2014 about 225 km² which is 5.8 % more than the year 1990 (Figure 4). The demographic pressure and illegal natural resource exploitation have not only affected the forest cover but also the wetland area. The wetlands, locally known as “Bils”, developed during geomorphic transformation and tectonic activities, are also the conspicuous features of flood plains in Brahmaputra river basin. In 1990, the wetland area was about 146.3 km² (3.75 %) of the total area while in the year 2014 it was found that about 115.4 km² area of wetland has been lost. In comparison to the year 1990, only 30.9 km² areas are covered by wetland which is about 0.79 % of total area (Table 2). Although there is no significant change in the area of river between 1990 and 2014, but the course of river Ai, and river Manas the northern flowing tributaries of Brahmaputra has changed which is clearly visible in Figure 3.

Table 2: Change in Land use/Land cover of the study area

| LULC category | Area(km ²) | | Percentage of total area | | Change | |
|--|------------------------|--------|--------------------------|-------|-----------------|------------|
| | 1990 | 2014 | 1990 | 2014 | km ² | Percentage |
| Total area =3903.2 km² | | | | | | |
| Forest | 408.2 | 294.6 | 10.46 | 7.55 | -113.6 | -2.91 |
| River | 283.5 | 287.3 | 7.26 | 7.36 | 3.8 | 0.1 |
| Agricultural field | 3065.2 | 3290.4 | 78.53 | 84.30 | 225.2 | 5.8 |
| Wetland | 146.3 | 30.9 | 3.75 | 0.79 | -115.4 | -2.96 |

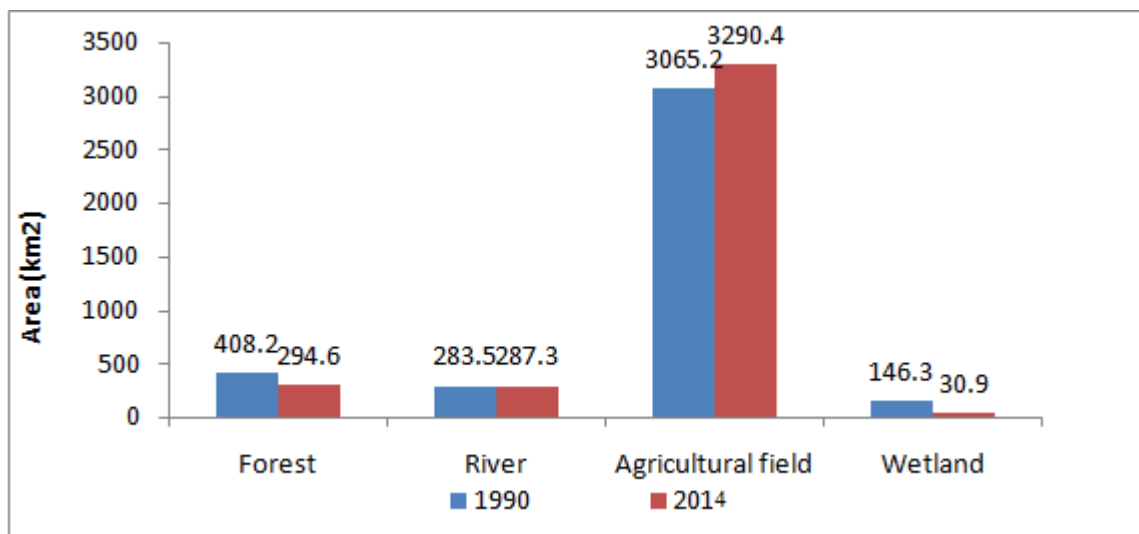


Figure 4: Graphical presentation of change in Land use/Land cover of study area

5. Conclusions

In comparison to the 1990 and 2014 show a significant change in land use and land cover. In recent time the modernisation, increasing demographic pressure, and over-exploitation of natural resources have become a major threat for degradation of forest cover and loss of wetland in the study area. The total 113 km² of forest cover and 115.4 km² wetland has been lost between the year 1990 and 2014 due agricultural intensification and human encroachment. This alarming condition is required a scientific management of land use for sustainable development in the area.

Acknowledgement

The lead author acknowledges Council of Scientific and Industrial Research (CSIR) for providing fellowship during research work. The authors also acknowledge to Jawaharlal Nehru University for providing instrumentation facilities.

References

- Ahl, D.E., Gower, S.T., Burrows, S.N., Shabanov, N.V., Myneni, R.B., and Knyazikhin, Y. Monitoring spring canopy phenology of a deciduous broadleaf forest using MODIS. *Remote Sensing of Environment*. 2006. 104; 88-95.
- Anderson, J.R., Hardy, E.E., Roach, J.T., and Witmer, R.E., 1976: A land use and land cover classification system for use with remote sensor data. Geological Survey Professional Paper No. 964, U.S. Government Printing Office, Washington, DC. 28.
- Bhattacharjee, P.R., and Nayak, P. Socio-economic rationale of a regional development council for the Barak Valley of Assam. *Journal of NEICSSR*. 2003. 27 (1) 13-26.
- Campbell, J.B., 2002: *Introduction to Remote Sensing*. London and New York: Taylor and Francis.
- CGWB, 2008: Ground Water Information Booklet Goalpara District, Assam.
- Chilar, J. Land Cover Mapping Of Large Areas from Satellites: Status and Research Priorities. *International Journal of Remote Sensing*. 2000. 21 (67) 1093-1114.
- De Boer, M.E., 2000: Landcover monitoring: an approach towards pan European land covers classification and change detection. Scientific report. Delft, Beleids Commissie Remote Sensing (BCRS)
- Di Gregorio, A., and Jansen, L.J.M., 2000: Land Cover Classification System (LCCS): Classification Concepts and User Manual.
- Fraser, R.H., Olthof, I., and Pouliot, D. Monitoring land cover change and ecological integrity in Canada's national parks. *Remote Sensing of Environment*. 2009. 113; 1397-1409.
- Geological Survey of India, 2009: Geology and Mineral Resources of Assam, Part 4, v.2.
- Goulding, K.W.T., and Blake, L. Land Use, Liming and the mobilization of potentially toxic metals. *Agriculture, Ecosystem and Environment*. 1998. 67; 135-144.
- Green, K., Kempka, D., and Lackey, L. Using remote sensing to detect and monitor land-cover and land-use change. *Photogrammetric Engineering and Remote Sensing*. 1994. 60; 331-337.
- Huang, S., and Siegert, F. Land cover classification optimized to detect areas at risk of desertification in North China based on SPOT VEGETATION imagery. *Journal of Arid Environments*. 2006. 67; 308-327.
- Lunetta, R.S., Knight, J.F., Ediriwickrema, J., Lyon, J.G., and Worthy, L.D. Land-cover change detection using multi-temporal MODIS NDVI data. *Remote Sensing of Environment*. 2006. 105 (2) 142-154.

- Mahajan, S., Panwar, P., and Kaundal, D. GIS application to determine the effect of topography on landuse in Ashwani Khad watershed. *Journal of Indian Society of Remote Sensing*. 2001. 29; 243-248.
- Maselli, F. Monitoring forest conditions in a protected Mediterranean coastal area by the analysis of multiyear NDVI data. *Remote Sensing of Environment*. 2004. 89 423-433.
- Mukherjee, S. Role of Satellite sensors in groundwater exploration. *Sensors*. 2008. 8 (3) 2006-2016.
- Myers, N., 1984: *The Primary Source: Tropical Forests and Our Future*. W.W. Norton: New York. 399.
- Nielsen, A.A., Conradsen, K., and Simpson, J.J. Multivariate alteration detection (MAD) and MAF post processing in multispectral, bitemporal image data: new approaches to change detection studies. *Remote Sensing of Environment*. 1998. 64; 1-19.
- Nunes, M.C.S., Vasconcelos, M.J., Pereira, J.M.C., Dasgupta, N., Alldredge, R.J., and Rego, F.C. Land cover type and fire in Portugal: do fires burn land cover selectively? *Landscape Ecology*. 2005. 20; 661-673.
- Sarma, P.K., Lahkar, B.P., Ghosh, S., Rabha, A., Das, J.P., Nath, N.K., and Brahama, N. Landuse and Landcover change and future implication analysis in Manas National Park, India using multi temporal satellite data. *Current Science*. 2008. 95; 2.
- Stow, D.A., Chen, D.M., Parrott, R., 1996: Enhancement, identification and quantification of land cover change. In: Morain, S.A., and Lopez Barose, S.V., Raster imagery in geographical information systems. 307-312.
- Turner, H.B.L., 1995: Linking the Natural and Social Sciences. The Land use/cover Change Core Project of International Geosphere-Biosphere Programme (IGBP) IGBP Newsletter, No. 22.
- Vitousek, P.M. Beyond global warming: ecology and global change. *Ecology*. 1994. 75; 1861-1878.
- Yuan, D., Elvidge, C.D., and Lunetta, R.S., 1999: Survey of multi-spectral methods for land cover change analysis. In: Lunetta, R.S., and Elvidge, C.D. Remote sensing change detection: Environmental monitoring methods and applications, Ann Arbor Press. 21-39.
- Woodcock, C.E., Macomber, S.A., and Kumar, L., 2002: Vegetation Mapping and Monitoring. In: Skidmore, A.K. Environmental Modelling with GIS and Remote Sensing. London, UK: Taylor and Francis.

Characterization of Potential Springs in the Lower Colorado Desert of Southern California using Satellite Radar and Landsat Time Series Analysis

Christopher Potter

Senior Scientist, NASA Ames Research Center, United States

Publication Date: 13 September 2016

DOI: <https://doi.org/10.23953/cloud.ijarsg.68>



Copyright © 2016 Christopher Potter. This is an open access article distributed under the **Creative Commons Attribution License**, which permits unrestricted use, distribution, and reproduction in any medium, provided the original work is properly cited.

Abstract Renewable energy development in southern California is receiving increasing attention due to potential impacts on wildlife habitats and water sources. This study was designed to quantify and map, for the first time, sub-surface water sources from springs in the Lower Colorado Desert area of southern California using satellite radar data and 30 years of Landsat satellite image data. Synthetic Aperture Radar (SAR) data was used to identify sub-surface water sources not already documented as springs or seeps in the National Hydrography Database. Landsat imagery starting in 1985 was used to characterize vegetation growth patterns at these suspected spring locations detected from SAR analysis. Results showed a total of 104 potential spring locations across the Lower Colorado Desert study area, 19 of which were detected within Solar Energy Zone (SEZ) development boundaries, roughly evenly split between Riverside East and Imperial East, and 13 of which (both inside and outside SEZs) showed relatively high green vegetation index values over the period of 1985 to 2015 that would depend on non-precipitation water sources associated with active springs.

Keywords *Radar; Landsat; Surface Water; Springs; Seeps; Solar Energy Development; Lower Colorado Desert; DRECP*

1. Introduction

Under the surface of the Mojave and Sonoran-Colorado Deserts of California is a complex system of groundwater stored in underground aquifer layers of fractured rock. The depth at which an aquifer becomes saturated is called the water table. A natural spring or seep occurs where the water table exceeds or breaches the soil surface from underneath. In general, if water from beneath the surface is regularly observed flowing upwards from a well-defined source, then it is called a spring. If it simply forms a constantly wet, ponded area on the surface from a poorly defined sub-surface source, then it is called a seep. Spring areas usually include the orifice area and out-flow stream or springbrook (Patten et al., 2007).

Springs and seeps in the southern California deserts support numerous sensitive and threatened plant and animal species (Randall et al., 2010). Human activities over the last 100 years, such as

groundwater pumping for agricultural irrigation and mining developments, have destroyed or profoundly altered many of these rare wetland habitats (Patten et al., 2007; USFWS, 2009).

Renewable energy in newly proposed Development Focus Areas (DFAs) of southern California is receiving increasing attention due to potential impacts on wildlife habitats and water sources. To mitigate and monitor the impacts of solar facility construction projects, the Desert Renewable Energy Conservation Plan (DRECP, 2016) has become a major component of the State of California Renewables Portfolio Standard. The DRECP provides effective environmental protections and natural resource conservation of desert ecosystems as appropriate development of renewable energy projects advances in southern California.

The DRECP covers parts of seven California counties: Imperial, Inyo, Kern, Los Angeles, Riverside, San Bernardino, and San Diego. Approximately 91,000 km² of federal and non-federal California desert land are part of the DRECP Area. By the end of 2016, the Final DRECP Record of Decision (ROD) will be completed for BLM public lands under agency jurisdictions within the DRECP area.

The objective of this remote sensing data analysis for southern California deserts was to quantify and characterize, for the first time, sub-surface water sources and potential springs in the Lower Colorado Desert area using satellite L-band Synthetic Aperture Radar (SAR) data together with 30 years of Landsat satellite reflectance data. Satellite SAR data were used to identify sub-surface water sources not already documented as springs or seeps in the National Hydrography Database (NHD; USGS, 1999), whereas Landsat imagery starting in 1985 was used to characterize vegetation growth patterns at these suspected spring locations detected from SAR analysis. The normalized difference vegetation index (NDVI) from Landsat has been closely correlated with percent cover measurements of green vegetation canopies in arid ecosystems, as reported in numerous published studies (Anderson et al., 1993; Elmore et al., 2000; Huang et al., 2010).

2. Study Area

The area of interest for this Landsat data study within the southern DRECP region was the Lower Colorado Desert of California (Figure 1). This area is bounded on the west by the Laguna, Santa Rosa, and San Jacinto mountain ranges, on the east by the California-Arizona state line, on the north by the gradual transition to the Mojave Desert, and on the south by the California-Mexico border (Marks, 1950). Low annual rainfall (50 – 300 mm) and high average daily temperatures (reaching 45°C in the summer) make this area one of the most arid in North America. Vegetation communities in the Colorado Desert have been classified into seven basic types: creosote bush scrub, cactus scrub, saltbush scrub, alkali sink, microphyll woodland, psammaophytic scrub, and palm oasis (Schoenherr and Burk, 2007).

The National Hydrography Database (USGS, 1999) includes 548 known spring features in the Lower Colorado Desert study area. The majority of these known springs in the NHD are located in eastern San Diego County. Only five of the known springs in the NHD are located in renewable energy DFA zones of the Lower Colorado Desert.

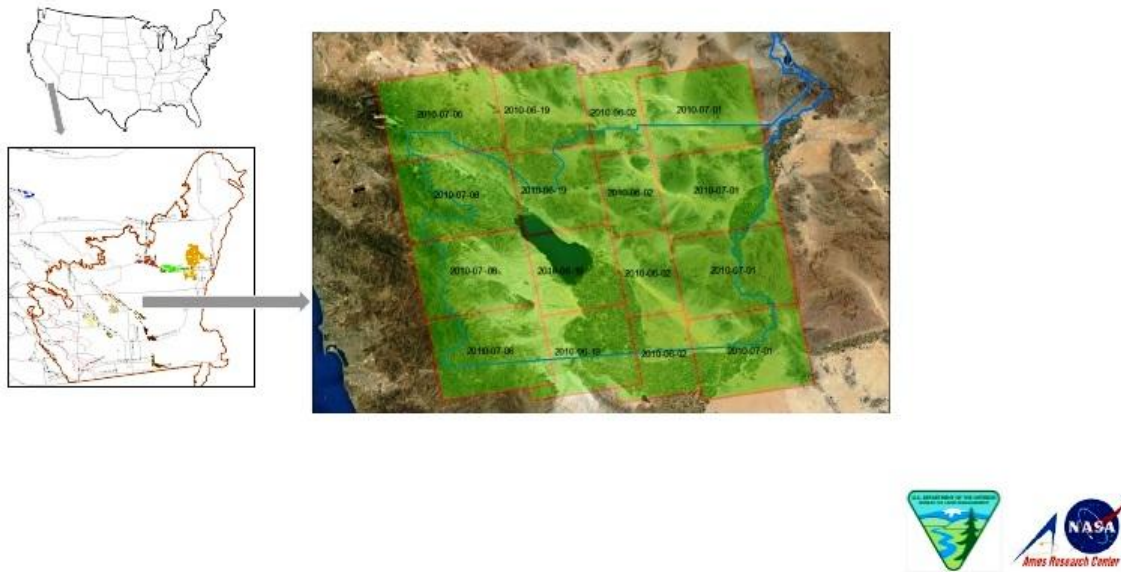


Figure 1: Lower Colorado Desert study area with the footprint of PALSAR images acquired in FBD mode

3. Methods

3.1. Sub-Surface Water Anomaly Detection from SAR

Spaceborne L-band SAR data from the Advanced Land Observing Satellite/Phased Array (ALOS/PALSAR) sensor was acquired for the Lower Colorado Desert study area. PALSAR data sets were acquired from the Japan Aerospace Exploration Agency (JAXA) with Fine Beam Single polarization (FBS, look angle 34.3°, HH-polarization, and a 6.25m×6.25m ground resolution) with Fine Beam Double Polarization (FBD, look angle 34.3°, HH- and HV-polarization, ground resolution approximately 12.5m×12.5m). In FBS mode, ALOS/PALSAR can be operated with either HH- or VV-polarization with a bandwidth of 28 MHz. In FBD mode, the polarization options are HH/HV or VV/VH at 14-MHz bandwidth. FBS polarization (HH or VV) and FBD polarization (HH+HV or VV+VH) of PALSAR data have a look angle varying between 7° and 51° (8-60° incidence angle). The operating sensor frequency is 1.27GHz, which corresponds to a wavelength of 23.6 cm (L-band). L-band images from PALSAR were acquired for June/July 2010 (12.5m, HH and HV polarization) coinciding with dry season, and for November/December 2010 (12.5m, HH and HV polarization) coinciding with wet season (as listed in Table 1 and Figure 1).

Table 1: Listing of PALSAR imagery datasets acquired for sub-surface soil water detection

| ID | Name | Observation Mode | Polarization | Capture Date |
|----|-----------------|------------------|--------------|--------------|
| 1 | ALPSRP231960640 | FBD | HH/HV | 2010-06-02 |
| 2 | ALPSRP231960650 | FBD | HH/HV | 2010-06-02 |
| 3 | ALPSRP231960660 | FBD | HH/HV | 2010-06-02 |
| 4 | ALPSRP231960670 | FBD | HH/HV | 2010-06-02 |
| 5 | ALPSRP234440640 | FBD | HH/HV | 2010-06-19 |
| 6 | ALPSRP234440650 | FBD | HH/HV | 2010-06-19 |
| 7 | ALPSRP234440660 | FBD | HH/HV | 2010-06-19 |
| 8 | ALPSRP234440670 | FBD | HH/HV | 2010-06-19 |
| 9 | ALPSRP236190640 | FBD | HH/HV | 2010-07-01 |

| | | | | |
|----|-----------------|-----|-------|------------|
| 10 | ALPSRP236190650 | FBD | HH/HV | 2010-07-01 |
| 11 | ALPSRP236190660 | FBD | HH/HV | 2010-07-01 |
| 12 | ALPSRP236190670 | FBD | HH/HV | 2010-07-01 |
| 13 | ALPSRP236920640 | FBD | HH/HV | 2010-07-06 |
| 14 | ALPSRP236920650 | FBD | HH/HV | 2010-07-06 |
| 15 | ALPSRP236920660 | FBD | HH/HV | 2010-07-06 |
| 16 | ALPSRP236920670 | FBD | HH/HV | 2010-07-06 |
| 17 | ALPSRP254570640 | FBD | HH/HV | 2010-11-04 |
| 18 | ALPSRP254570650 | FBD | HH/HV | 2010-11-04 |
| 19 | ALPSRP254570660 | FBD | HH/HV | 2010-11-04 |
| 20 | ALPSRP254570670 | FBD | HH/HV | 2010-11-04 |
| 21 | ALPSRP257050640 | FBD | HH/HV | 2010-11-21 |
| 22 | ALPSRP257050650 | FBD | HH/HV | 2010-11-21 |
| 23 | ALPSRP257050660 | FBD | HH/HV | 2010-11-21 |
| 24 | ALPSRP257050670 | FBD | HH/HV | 2010-11-21 |
| 25 | ALPSRP258800640 | FBD | HH/HV | 2010-12-03 |
| 26 | ALPSRP258800650 | FBD | HH/HV | 2010-12-03 |
| 27 | ALPSRP258800660 | FBD | HH/HV | 2010-12-03 |
| 28 | ALPSRP258800670 | FBD | HH/HV | 2010-12-03 |

The Alaska Satellite Facility (ASF) provided range compression using Fast Fourier Transform (FFT), secondary range compression using range migration compensation, range migration curvature corrections, azimuth compression, multi-look processing and performed conversion from slant to ground range (PALSAR User's Guide, 1st edition, March 2006). MapReady software version 3.1.22 (http://www.asf.alaska.edu/downloads/software_tools), developed by ASF, was used to process ALOS/PALSAR imagery, following the methodology steps from Li and Potter (2012):

Step 1: Radiometric Calibration Calibrating a SAR image involves the process of converting a linear amplitude image into a radiometrically calibrated power image. The input image starts in units of digital numbers (DNs), where the output image is in units of β° , γ° , or σ° . Backscatter is the portion of the outgoing radar signal that the target redirects directly back towards the radar antenna. It is a measure of the reflective strength of a radar target. The normalized measure of the radar return from a distributed target is called the backscatter coefficient, σ° , or sigma naught, and is defined per unit area on the ground. An undesired signal formed by backscatter is called clutter. Other portions of incident radar energy may be reflected and scattered away from the radar or absorbed.

The radar backscatter coefficient (σ°) is the ratio of the power that reflected from a patch of ground in relation to the power sent to the patch of ground, and serves as a quantitative reference measure to the ground. The coefficient can be retrieved from SAR images by using the following equation:

$$\sigma^\circ = a_2 (DN^2 - a_1 Nr)$$

where DN = the digital number of the original pixel value

Nr = the noise offset as a function of range

a_1 = the noise scale factor determined during processor calibration

a_2 = a linear conversion factor determined during processor calibration.

The σ^0 value resulting from the equation above is in a power scale. Conversion of these values into decibel (dB) values followed the relationship:

$$\text{dB} = 10 * \log_{10} (\text{power scale})$$

Step 2: Terrain Correction SAR images are acquired with side-looking geometry. This format leads to a number of distortions in the imagery: foreshortening, layover, and shadow (Figure 2). Terrain correction removes these geometry-induced distortions by using a digital elevation (DEM). The process of terrain correction includes geometric terrain correction and radiometric terrain correction. Geometric terrain correction adjusts the individual pixels of an amplitude image to be in their proper locations. Radiometric terrain correction adjusts the brightness of the pixels with respect to the observation geometry, defined by the incidence angle as well as the slope and aspect of the local terrain.

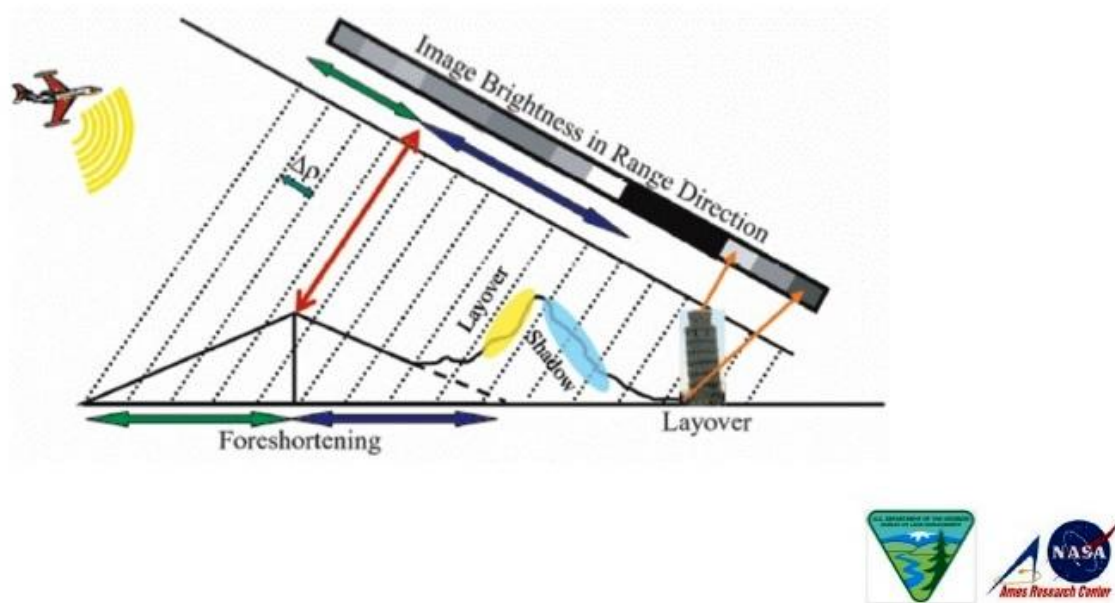


Figure 2: Schematic of terrain with foreshortening, layover, and shadow effects experienced in SAR image processing (from Li and Potter, 2012)

Step 3: Geocoding The geocoding step is essential to correlate the SAR image geometry to the actual terrain. By transforming the image from SAR geometry into one of the standard map projections, the SAR image can be imported into imager processing applications for further analysis. The geocoding step is invoked by turning on the “Geocode” module from MapReady with a UTM projection. For the PALSAR scene of the I-10 corridor, the parameters for UTM zone 11N and the WGS84 datum were used. As part of the transformation from SAR geometry into map-projected space, a bi-linear method was used to resample the data values. Compared to nearest-neighbor and bi-cubic approaches, the bi-linear interpolation scheme considers four neighboring pixel values.

Step 4: Speckle Filtering SAR images were filtered to reduce the effect of speckle by utilizing a Kuan filter with a 3x3 kernel. The resultant imagery preserved the mean values, while decreasing the standard deviation of homogeneous targets, and visually preserving the feature edges.

A threshold value (greater than -15 dB) of the preprocessed radar backscatter signals was set to detect pixels with sub-surface water anomalies across the study area. Single or scattered pixels were removed in the newly created sub-surface water anomaly layer. Only clustered pixels were retained for

further “hot spot” analysis. Using visual inspection, pixel clusters with known ground features (i.e. high radar backscatter coefficient caused by terrain relief, transmission towers, communication towers, single buildings, major roadways and river courses, developed residential areas, croplands, and known springs in the NHD) were eliminated from the water anomaly layer. All the suspected sub-surface water sources on slopes less than 10% were converted into potential spring point features for further historical evaluation with Landsat green vegetation index records, mainly to exclude rugged mountainous areas where future renewable energy development activities would not likely take place (Kwartin et al., 2012).

3.2. Landsat Imagery

For this study, near cloud-free imagery from the Landsat sensor was selected from the United States Geological Survey (USGS) Earth Explorer data portal (available online at earthexplorer.usgs.gov) for the years 1985 to 2015. Landsat scenes from path/row 39/37 were acquired during the period of April - May of each year, just following the peak flowering period in the Lower Colorado Desert growing season (Schoenherr and Burk, 2007). All images used in this study were geometrically registered (UTM Zone 11) using terrain correction algorithms (Level 1T) applied by the USGS EROS Data Center.

For the Landsat 4-5 Thematic Mapper (TM) images acquired between 1985 and 2011, 30-m resolution surface reflectance data were generated from the Landsat Ecosystem Disturbance Adaptive Processing System (Masek et al., 2006). Moderate Resolution Imaging Spectroradiometer (MODIS) atmospheric correction routines were applied to Level-1 TM data products. Water vapor, ozone, geopotential height, aerosol optical thickness, and digital elevation are input with Landsat data to the Second Simulation of a Satellite Signal in the Solar Spectrum (6S) radiative transfer models to generate top of atmosphere (TOA) reflectance, surface reflectance, brightness temperature, and masks for clouds, cloud shadows, adjacent clouds, land, snow, ice, and water. Landsat 8 (after 2012) surface reflectance products were generated from the L8SR algorithm, a method that uses the scene center for the sun angle calculation and then hard-codes the view zenith angle to 0. The solar zenith and view zenith angles are used for calculations as part of the atmospheric correction.

4. Results and Discussion

A total of 104 potential spring locations were identified from the 2010 PALSAR image analysis across the Lower Colorado Desert study area (Figure 3). There were 19 potential springs located within DFA boundaries, roughly evenly split between Riverside East and Imperial East Solar Energy Zones (SEZs).

Outside of the DFA zones, 10 potential spring locations were clustered along the Interstate Highway 10 in Riverside County, and about 15 other potential springs were located north of the Riverside East SEZ. Another 10 potential spring locations were clustered in western Imperial County, outside of any DFA zone.

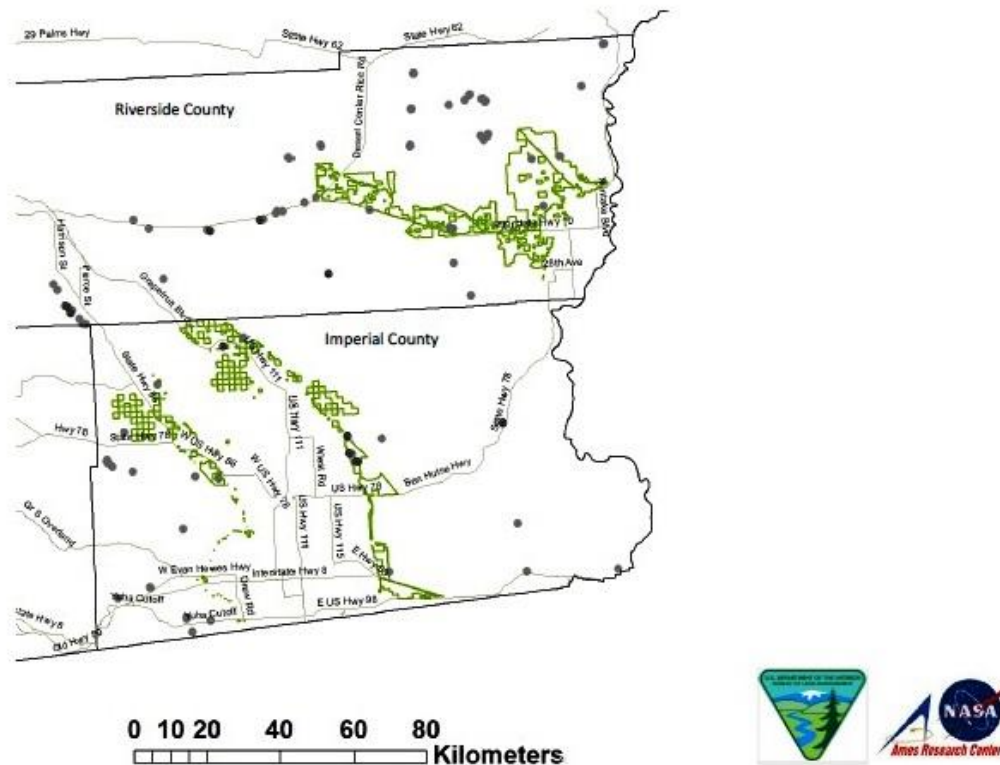


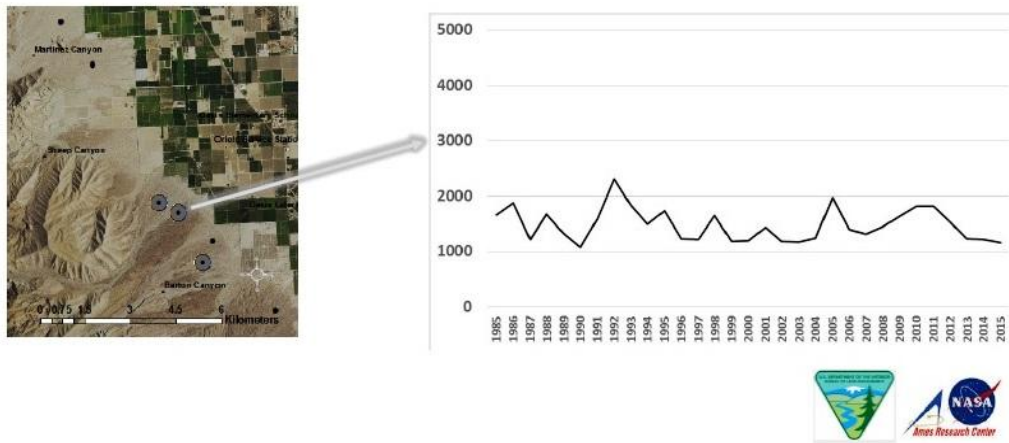
Figure 3: Potential spring locations (gray points) from 2010 PALSAR image analysis across the Lower Colorado Desert study area. Point labels with a dot in the center were those potential springs detected with Landsat green vegetation index values in excess of 2000 NDVI units during the period of 1985 to 2015. Solar energy zones (SEZ) DFA zones were outlined in green

Landsat NDVI time series data extracted for all 104 potential springs locations showed that only 13 (Figure 3) had green vegetation index values in excess of 2000 NDVI units during the period of 1985 to 2015. Potter (2016) reported that Landsat vegetation index values for desert shrub vegetation averaged across Lower Colorado study area never exceeded 2000 NDVI units, even during the relatively wet precipitation years of 1995, 1998, 2005, and 2010. In contrast, vegetation cover averaged from developed residential zones within the study did regularly exceed 2000 NDVI units, presumably due to urban irrigation practices, except during the driest precipitation years of 2000, 2003, 2007, and 2013-14. This baseline of 2000 NDVI units was therefore established as the indicator level for periodic vegetation growth that would depend on non-precipitation, sub-surface water sources associated with active springs.

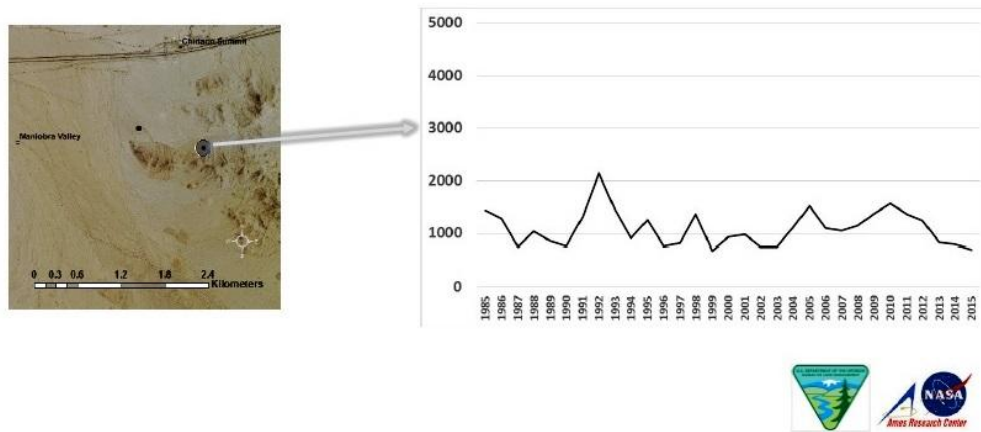
A closer examination of potential spring locations where the green vegetation index values periodically exceeded 2000 NDVI units showed highest green cover periods were consistently detected in the years 1992, 2005 and 2010 (Figure 4). The three locations detected in Riverside County were within the Barton Canyon drainage (Seaber et al., 1987) south of Palm Desert (Figure 4a), within the Maniobra Valley drainage south of Interstate Hwy 10 (Figure 4b), and within the Gulliday Well drainage (Figure 4c), for a total of five potential springs all outside of DFA zones.

One potential spring detected above the baseline of 2000 NDVI units in Imperial County (located north of Niland Marina, Figure 4d) was within a DFA zone and showed a different NDVI time series pattern from all the others. In this area, vegetation greenness levels remained below 1000 NDVI units until 2010, after which the green cover increased rapidly to NDVI values in excess of 4000 units by 2015. The true-color image of the areas in Figure 4d indicated that this sub-surface moisture source may

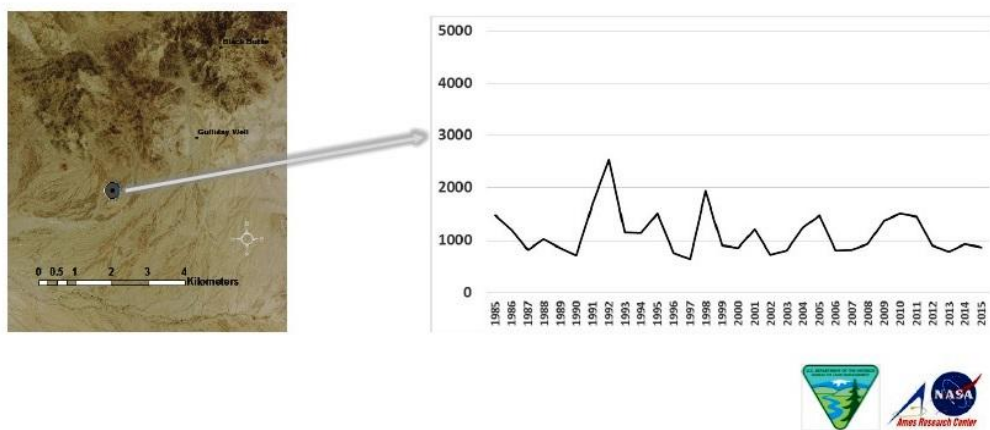
have resulted from a new flow pathway of water into the Salton Sea just to south of this potential spring location.



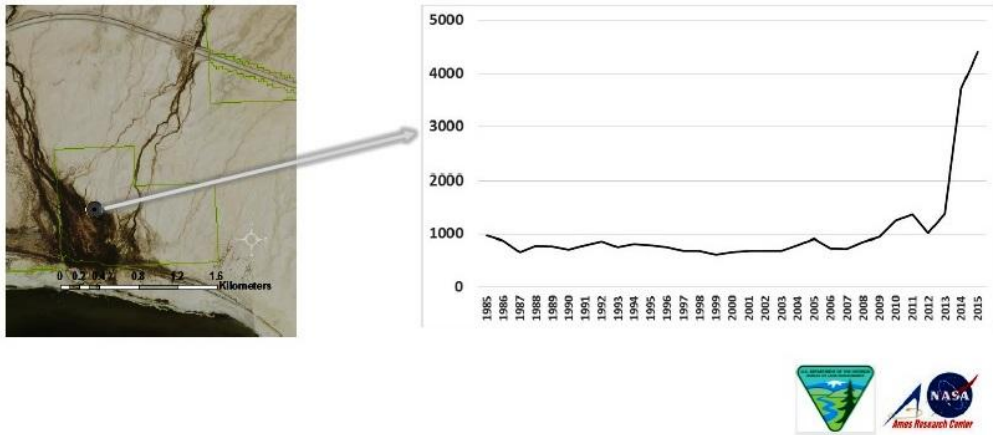
4a: Martinez Canyon to Barton Canyon south of Palm Desert, Riverside County (33.4731N, -116.1505 W)



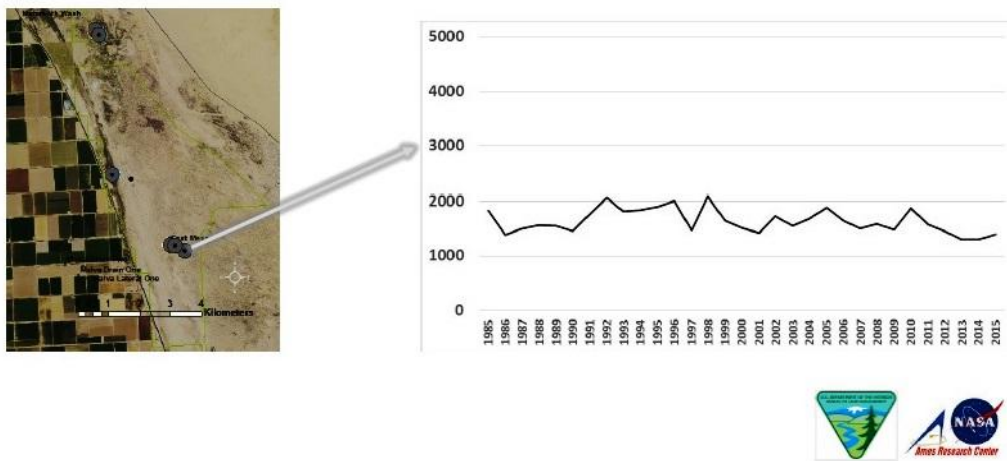
4b: Maniobra Valley south of Hwy 10, Riverside County (33.6133 N, -115.6769 W)



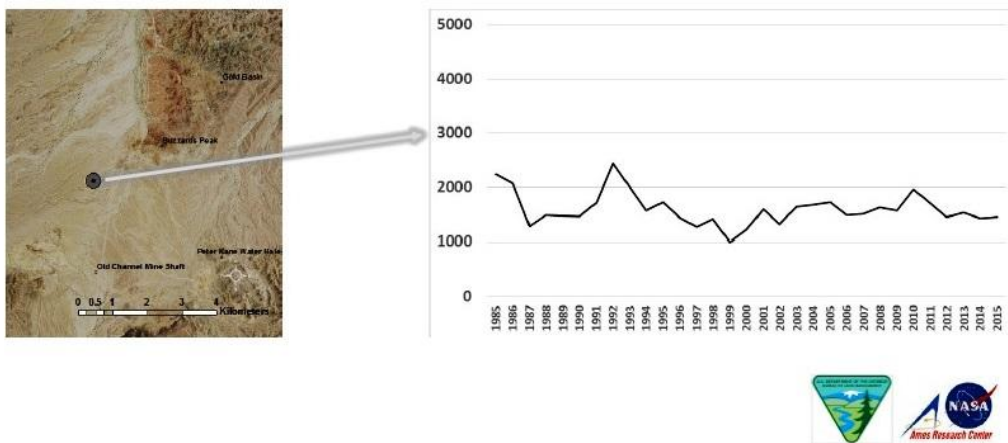
4c: Near Gulliday Well, southern Riverside County (33.4910 N, -115.3012 W)



4d: North of Niland Marina DFA, Imperial County (33.3599 N, -115.6954 W)



4e: East Mesa DFA, Imperial County (33.008 N, -115.2609 W)



4f: Peter Kane Water Hole near State Hwy 78, Imperial County (33.1349 N, -114.8869 W)

Figure 4: Time series plots for Landsat NDVI for the years 1985 to 2015 from the months of April–May for potential spring locations where the green vegetation index values periodically exceeded 2000 NDVI units. True color satellite image of the potential spring area and location markers (as in Figure 3) detected from PALSAR data analysis

The other two potential spring areas detected above the baseline of 2000 NDVI units in Imperial County were located in the East Mesa DFA zone (Figure 4e), and another potential spring farther to the east in the Midway Well drainage (Seaber et al., 1987) near State Hwy 78 (Figure 4f) outside of any DFA zone. Both of these locations showed highest green cover periods detected in the years 1992 and 2010.

The remaining 91 potential spring locations that did not show greenness levels above the baseline of 2000 NDVI units over the period 1985 to 2015 appeared to have vegetation cover patterns similar to the barren dune areas reported by Potter (2016) in the Lower Colorado Desert study area. In general, the yearly greenness levels for most of these potential spring locations remained at or below 1000 NDVI units. It is plausible that analysis of 2010 PALSAR images detected residual sub-surface moisture or ponded surface water in seep-like features at these locations, despite there being insufficient water from below the soil surface to support more than the growth of sparse desert shrub cover nearby.

It is plausible that some seep-like, largely unvegetated ponds detected using PALSAR image data in the Lower Colorado Desert actually corresponded to summer breeding habitats for amphibian species such as Couch's Spadefoot (*Scaphiopus couchi*) and Western Spadefoot (*Spea hammondi*). Spadefoots remain burrowed underground for most of the year and remain under-ground for consecutive years, but appear at the soil surface after the first heavy summer precipitation event to breed in temporary rain-fed ponds on the same night as the event occurs (Mayhew, 1965). Reports of this type of amphibian breeding habitat have been made in areas east of the Algodones Dunes and along State Hwy 78 (Dimmitt and Ruibal, 1980).

5. Conclusions

Satellite radar data sets were shown to successfully detect sub-surface water locations in the Lower Colorado Desert where Landsat NDVI was also measured at levels of vegetation growth that would depend on non-precipitation water sources associated with active springs.

None of the total 104 potential spring locations identified from PALSAR image analysis across the study area were previously listed in the National Hydrography Database (USGS, 1999).

A high priority for field-based verification of spring locations should be given to the 19 potential springs located within solar energy DFA boundaries.

In any case, solar energy project developers can benefit from the satellite image mapping of locations of potential springs and seeps in advance, so that the design of project footprints excludes these rare desert habitats for plants and animals at the start.

Acknowledgements

PALSAR image processing and application of mathematical algorithms for sub-surface water mapping was carried out primarily by Shuang Li of California State University Monterey Bay. This research was supported by funding from the BLM California State Office, Sacramento, CA.

References

- Anderson, G.L., Hanson, J.D., and Haas, R.H. Evaluating Landsat Thematic Mapper Derived Vegetation Indices for Estimating above Ground Biomass on Semiarid Rangelands. *Remote Sensing of Environment*. 1993. 45; 165-175.
- Cooke, R.U., and Warren, A., 1973: *Geomorphology in Deserts*. London: B.T. Batsford Ltd. 120.
- Dimmitt, M.A., and Ruibal, R. Environmental Correlates of Emergence in Spadefoot Toads (*Scaphiopus*). *J. Herpetol.* 1980. 14; 21-29.
- DRECP, 2010: Recommendations of Independent Science Advisors for The California Desert Renewable Energy Conservation Plan (DRECP) prepared for Renewable Energy Action Team.
- Elmore, A.J., Mustard, J.F., Manning, S.J., and Lobell, D.B. Quantifying Vegetation Change in Semiarid Environments: Precision and Accuracy of Spectral Mixture Analysis and the Normalized Difference Vegetation Index. *Remote Sensing of Environment*. 2000. 73; 87-102.
- Huang, S., Potter, C., Crabtree, R.L., Hager, S., and Gross, P. Fusing Optical and Radar Data to Estimate Sagebrush, Herbaceous, and Bare Ground Cover in Yellowstone. *Remote Sensing of Environment*. 2010. 114; 251-264.
- Lentile, L., Holden, A., Smith, A., Falkowski, M., Hudak, A., Morgan, P., et al. Remote Sensing Techniques to Assess Active Fire Characteristics and Post-Fire Effects. *International Journal of Wildland Fire*. 2006. 15; 319-345.
- Li, S., and Potter, C.S. Patterns of Aboveground Biomass Regeneration in Post-Fire Coastal Scrub Communities. *GIScience & Remote Sensing*. 2012. 49; 182-201.
- Kwartin, R., Alexander, S., Anderson, M., Clark, D., Collins, J., Lamson, C., Martin, G., Mayfield, R., McAlpine, L., Moreno, D., Patterson, J., Schultz, C., and Stiever, E. Solar Energy Development on Department of Defense Installations in the Mojave and Colorado Deserts, ICF International, San Jose, California, January 2012. 140.
- Marks, J.B. Vegetation and Soil Relations in the Lower Colorado Desert. *Ecology*. 1950. 31; 176-193.
- Masek, J.G., Vermote, E.F., Saleous, N., Wolfe, R., Hall, F.G., Huemmrich, F., Gao, F., Kutler, J., and Lim, T.K. A Landsat Surface Reflectance Data Set for North America, 1990-2000. *Geo-science and Remote Sensing Letters*. 2006. 3; 68-72.
- Mayhew, W.W. Adaptations of the Amphibian, *Scaphiopus Couchii* to Desert Conditions. *Am. Midl. Nat.* 1965. 74; 95-109.
- Patten, D.T., Rouse, L., and Stromberg, J.C. Isolated Spring Wetlands in the Great Basin and Mojave Deserts, USA: Potential Response of Vegetation to Groundwater Withdrawal. *Environmental Management*. 2008. 41 (3) 398-413.
- Potter, C. Landsat Time Series Analysis of Vegetation Changes in Solar Energy Development Areas of the Lower Colorado Desert, Southern California. *Journal of Geoscience and Environment Protection*. 2016. 4; 1-6.

Randall, J.M., Parker, S.S., Moore, J., Cohen, B., Crane, L., Christian, B., Cameron, D., MacKenzie, J., Klausmeyer, K., and Morrison, S., 2010: Mojave Desert Ecoregional Assessment. Unpublished Report. The Nature Conservancy, San Francisco, CA. 106.

Schoenherr, A.A., and Burk, J.H., 2007: *Colorado Desert Vegetation*. Pages 657-682 in Barbour, M.G., Keeler-Wolf, T., and Schoenherr, A.A. (Eds.), *Terrestrial Vegetation of California*, 3rd ed. University of California Press, Berkeley, California. 712.

Seaber, P.R., Kapinos, F.P., and Knapp, G.L., 1987: Hydrologic Unit Maps: U.S. Geological Survey Water-Supply Paper 2294. 63.

U.S. Fish and Wildlife Service (USFWS), 2009: Desert National Wildlife Refuge Complex Ash Meadows, Desert, Moapa Valley, and Pahrangat National Wildlife Refuges, Final Comprehensive Conservation Plan and Environmental Impact Statement Summary, Sacramento, CA. 42.

U.S. Geological Survey (USGS), 1999: Standards for National Hydrography Dataset, Reston, VA.

GIS Based Spatio-temporal Mapping of Groundwater Depth in Hisar District, Haryana State, India

Rani Reeta and Chaudhary B.S.

Department of Geophysics, Kurukshetra University, Kurukshetra, Haryana, India

Publication Date: 21 December 2016

DOI: <https://doi.org/10.23953/cloud.ijarsg.75>



Copyright © 2016 Rani Reeta and Chaudhary B.S. This is an open access article distributed under the **Creative Commons Attribution License**, which permits unrestricted use, distribution, and reproduction in any medium, provided the original work is properly cited.

Abstract Water Resource management is very important for sustained use of natural resources and is vital for existence of mankind. Groundwater plays a significant role due to its easy availability and low cost inputs for use. The present study deals with the monitoring of spatio-temporal changes in groundwater depth in Hisar district of Haryana state, India. A total of 92 observation wells were selected throughout the district for point observations. The groundwater depth (m, bgl) data from 1990 to 2014 of pre-monsoon for each year have been used in the present study. Change detection maps were generated using Inverse Distance Weighted (IDW) interpolation technique in Arc GIS. Depth to water level data at 4 year interval has been considered for monitoring the changes. Long-term variations have also been monitored by using data of 1990-2014 so as to understand the changing groundwater regime in the area. The study revealed uprising trend in average groundwater depth from 12.9 m bgl in 1990 to 8.10 m bgl in year 2014. The changes in the groundwater depth were more prominent in South (rising trend), East (rising trend) and North-east (rising trend) parts of the District. The probable reason for this trend is poor groundwater quality in southern and north-eastern parts of the district hampering the farmers from its use.

Keywords *Groundwater Fluctuation; Hisar; Spatial Distribution; GIS; India*

1. Introduction

Groundwater has an important role in the environment: it replenishes streams, rivers, and wetlands and helps to support wildlife habitat; it is used as primary source of drinking water and also in agricultural and industrial activities. Around the world, groundwater resources are under increasing pressure caused by the intensification of human activities and other factors such as climate changes. Groundwater is a significant part of the hydrologic cycle, containing 21 percent of Earth's freshwater. Groundwater comprises 97 percent of fresh water not tied up as ice and snow in polar ice sheets, glaciers, and snowfields. This greatly exceeds the amount of water in streams, rivers, and lakes. Excessive pumping of water from an aquifer may result in an area wide lowering of the water table (*Babu et al., 2011*). This will eventually occur any place where more water is pumped than is recharged by infiltrating precipitation. Over drafting from an aquifer may result in changes in groundwater quality, a reduction in groundwater availability (and hence the loss of water supply to current and future wells), and perhaps even a permanent loss of the aquifer's capacity to store water.

Many states in India use the water right process to manage groundwater quantity and to ensure that over drafting does not occur. Groundwater is the major source of drinking water in rural India. It is estimated that approximately one third of world's population use groundwater for drinking purpose. In addition to rural households, public water supplies in various parts of the world depend on wells and groundwater.

Water level fluctuations can result from a wide variety of hydrologic phenomena, some natural and some induced by man (*Bagher and Rasoul, 2010*). Good management practices demand adequate information on how this volume varies with time. The amount of groundwater in storage is obtained by periodic measurements of the depth to water level from some reference point and keeping track of these measurements over time. Rising water levels in the well means that more water is in storage and vice versa. Chaudhary (2003) explained the importance of groundwater depth data in overall planning and development and emphasized it as an integral component for resource planning.

1.1. Geo-Identity

The Hisar district is situated between 28°53'45" to 29°49'15" N latitudes and 75°13'15" to 76°18'15" E longitudes. The district covers an area of 4174 sq km and is bordered on the east by Rohtak district, on the west by Fatehabad district & Rajasthan state, on the south by Bhiwani district and on the north by Jind district. The location map of the study area is shown in Figure 1. The area is nearly level, with imperceptible slopes, except for the regions in and around the sand dunes locally known as tibbas. The general trend of gradient of the terrain is from north–east to south-west and then west (*Haryana district Gazetteer, Hisar*). Hisar district comprises of three major physiographic units i.e. Aeolian plain, Older alluvial plain and Chautang flood plain. Major physiographic sub-units occurring in the district are sand dunes, plains, old channels and basin. The west and south-west parts of district are affected by Aeolian activity, comprising of sand dunes, sandy plains and interdunal areas.

The district is a part of the Indo-Gangetic alluvial plain. The Indo-Gangetic alluvium owes its origin to a sag in the crust, formed contemporaneously with the uplift of the Himalayas. This depression has since been filled up by sediments derived from the rivers and channels of northern Himalayas and southern Aravali hills from Pleistocene to recent times. The sub-surface geology of the area has been a subject of speculation for a long time, as the alluvium effectively conceals the solid geology of the floor. The whole of the alluvial plain, with relict channel beds within which the Saraswati, Drishdawati and Ghaggar rivers have occasionally shifted their beds in Holocene times, are covered by Aeolian deposits in the recent past with increasing aridity. Some of the great rivers of fluvial age such as Saraswati and Drishdawati (Chautang) have receded leaving inter-locked alluvial fans along its receding course, which were later covered with Aeolian deposits, and resulted into present landscape scenery within varying monotonous plain having relict channel courses, levees, bars, depressions and sand dunes. The depth of the alluvium varies from 100 meters to more than 400 meters as observed from many geophysical and borehole data (*Haryana district Gazetteer, Hisar*).

2. Objectives of Study

The present study has been undertaken with the aim to understand the spatial distribution of depth to water table in the area from the year 1990 to 2014. The objectives are briefly enumerated as:

- 1) To understand the spatial distribution pattern of groundwater level since 1990 to 2014.
- 2) To understand the pattern of groundwater level fluctuations in the period of 1990-2014.

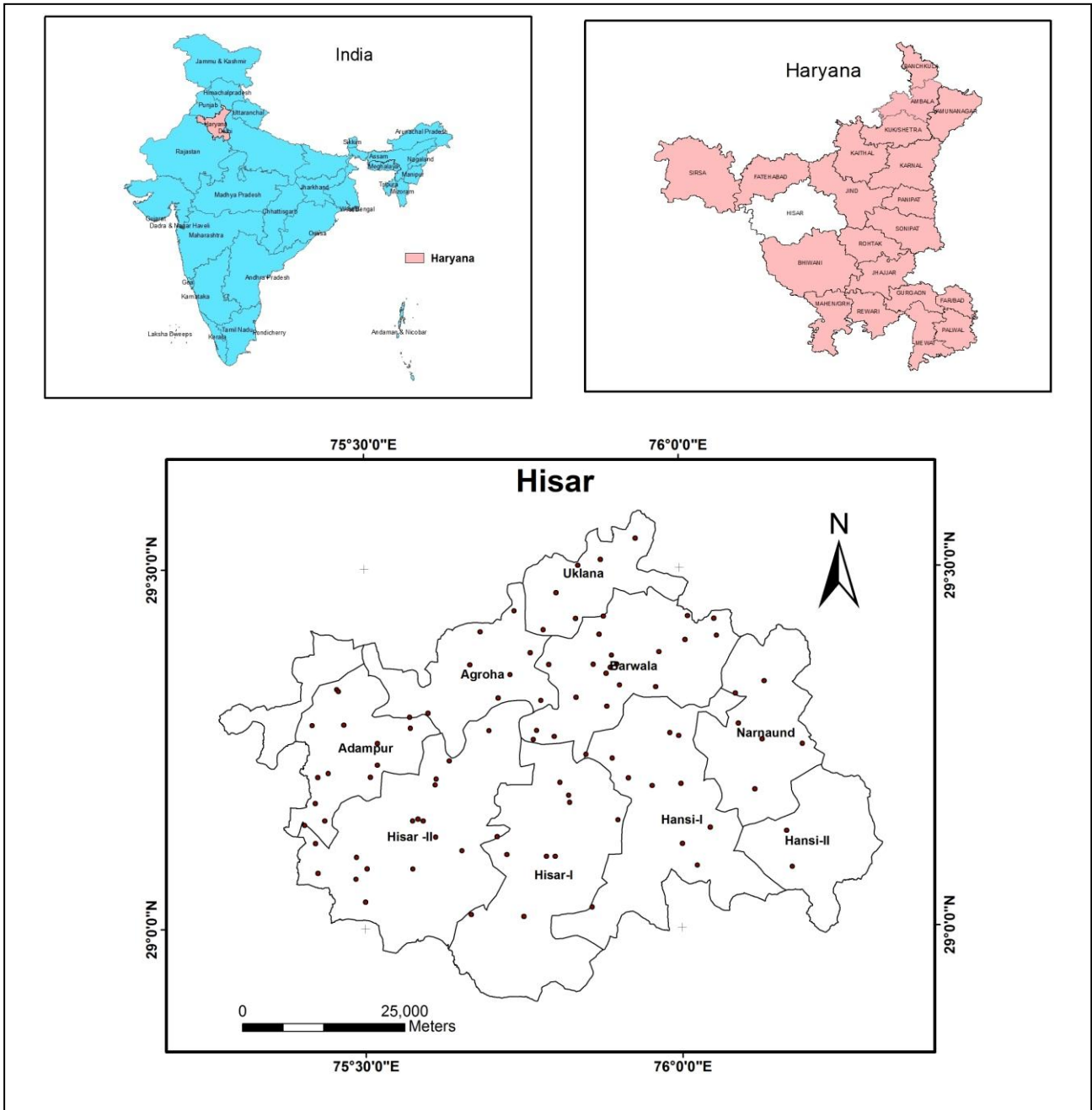


Figure 1: Location Map of Hisar District, Haryana

3. Materials

In present study, Survey of India Toposheet (1:50,000), well observation point data of groundwater level from the year 1990-2014 and other ancillary data in the form of published literature, reports and maps by different organizations involved in groundwater studies have been used. The observation point data has been collected from Groundwater Cell, Department of Agriculture, Govt. of Haryana.

4. Methodology

Base map of the study area was prepared using survey of India topographical maps. The well observation data was plotted on to the map by using location (latitude & longitude) of each well.

In total 92 observation wells were selected for further processing of the data for spatio-temporal analysis. These maps were prepared with the help of IDW spatial interpolation technique in Arc GIS Software (Srivastava *et al.*, 2012) and interpreted using standard methods (Haryana Groundwater Cell, 2014). In this study, IDW technique was used for spatial distribution of Groundwater level fluctuation (m bgl) for pre-monsoon (June) on five year interval (1990-94, 1994-98, 1998-2002, 2002-2006, 2006-2010, 2010-2014) and long term fluctuation (1990-2014). Different interpolation techniques like Krigging, Spline and Inverse Distance Weightage (IDW) were used but IDW was found to be best both in terms of spatial distribution representation and also from accuracy point of view. Inverse Distance Weighted (IDW) is a method of interpolation that estimates cell values by averaging the values of sample data points in the neighborhood of each processing cell. The closer a point to the center of the cell being estimated, the more influence, or weight; it has in the averaging process. Compared with regression analysis ($R^2 = 0.82$), IDW technique is giving more accurate results as compared to other techniques tried for interpolation purpose. The premonsoon data of groundwater depth levels have been used in the analysis as this is the true representation without predominant influence of seasonal recharges due to rains.

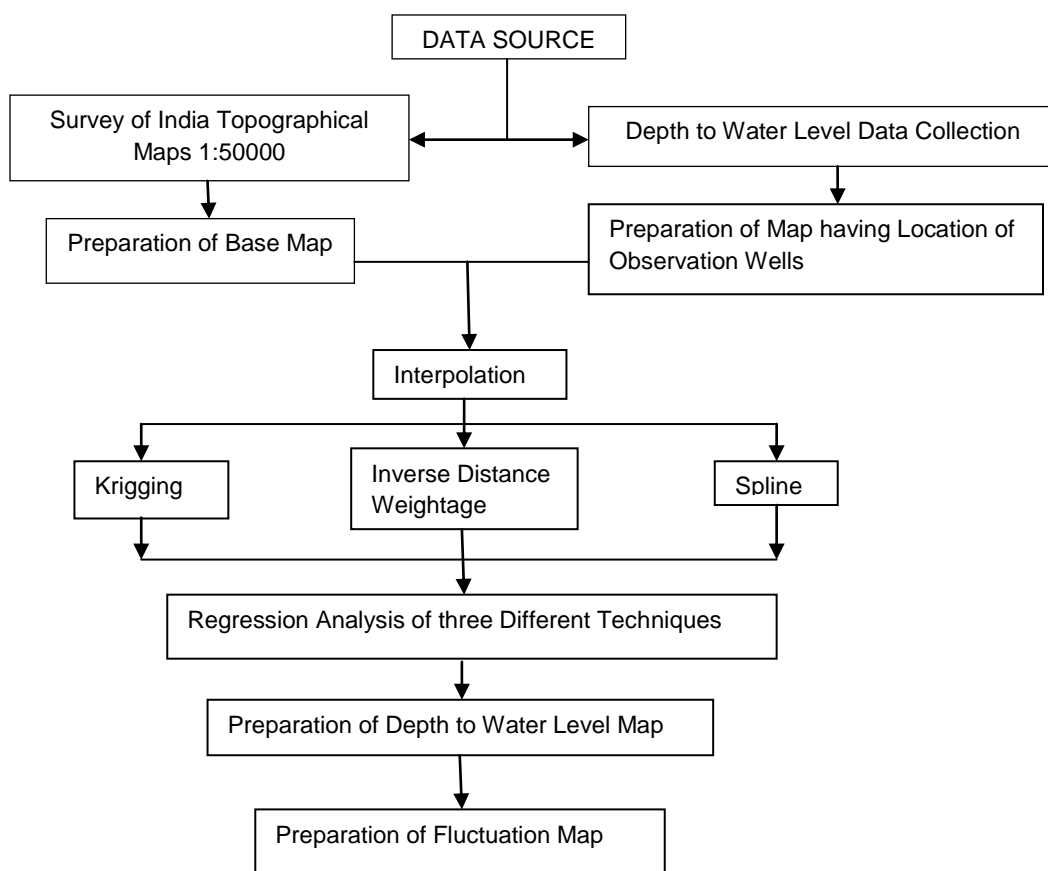


Figure 2: Methodology Chart for Analysis of Depth to water level data

5. Results and Discussion

The average value of depth to water level (m bgl) for different blocks for the year 1990, 1994, 1998, 2002, 2006, 2010 and 2014 is shown in Figure 3. The spatial distribution maps of the year 1990, 1994, 1998, 2002, 2006, 2010 and 2014 are shown in Figure 4 (a) and (b). Detailed comparison of these maps indicates that a lot of area which was in the range of 10-20 meter has come in to 3-10 meter which shows a general incline trend of groundwater in the area. The entire area in this category is wide across the district and has a particular pattern/trend along north-east to south-west in 1990.

A close look on the 1994 data shows that the area covered in depth of 20-30 meter in 1990 comes under the depth of 10-20 meter in 1994. Some parts of district also falls in depth range of 3-10 meter from depth 10-20 meter. 1998 data shows that there is inclination from depth of 3-10 meter to 0-3 meter in an area of about 360.46 sq kms. It may be due to heavy floods in the district in 1995 as reported by Chaudhary et al., 1999, Arya et al., 1996 that rainfall of about 600 mm was recorded in many parts of Haryana over a small period of one week from August 29-30 to September 5, 1995 and larger area in depth range of 10-20 meter in 1994 also came in depth range of 3-10 meter in 1998. The data from year 2002, 2006 and 2010 shows that most of the area of district was covered only in the depth of 3-10 meter and 10-20 meter. However in 1998, maximum area was covered in the depth range of 3-10 meter. A detailed listing of areas under different categories during these selected years is shown in Table 1.

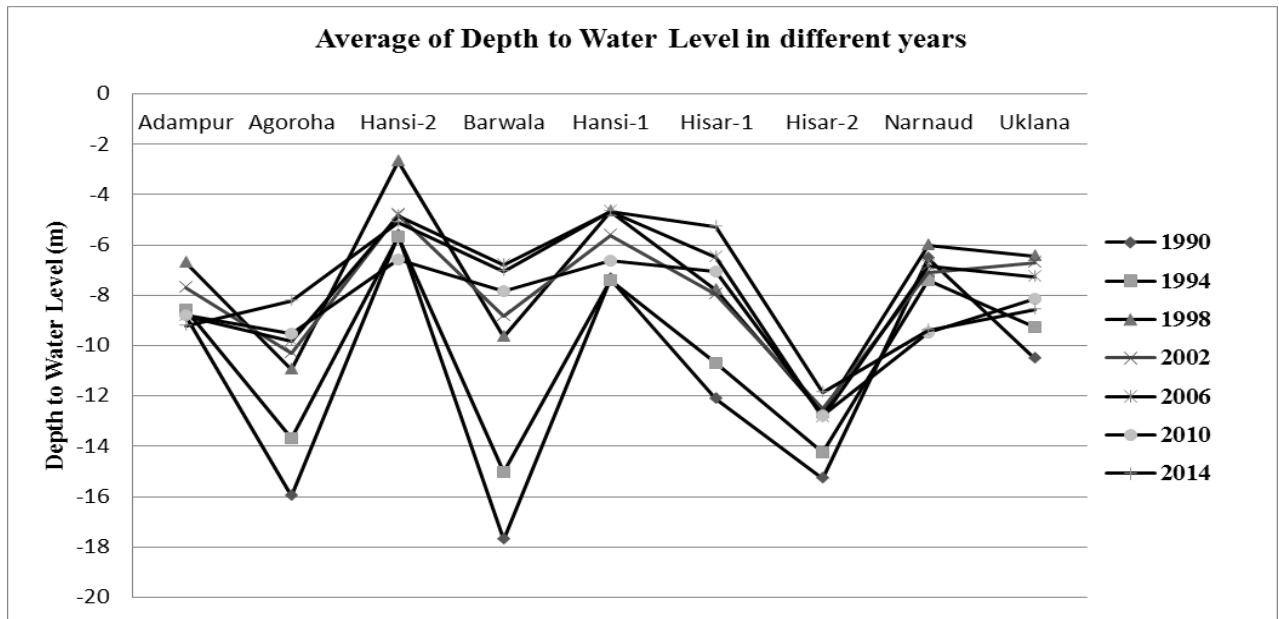


Figure 3: Average depth to water level in various block for years 1990, 1994, 1998, 2002, 2006, 2010 and 2014

Table 1: Area under Different Groundwater Depth zones in various years

| Sr. No. | Depth to Water Level (m, bgl) | Area (in km ²) | | | | | | |
|---------|-------------------------------|----------------------------|---------|---------|---------|---------|---------|---------|
| | | 1990 | 1994 | 1998 | 2002 | 2006 | 2010 | 2014 |
| 1 | 0 - 3 | 5.56 | 0.16 | 360.62 | 0.05 | 9.40 | 0.83 | 644.46 |
| 2 | 3.0 – 10.0 | 1583.15 | 1835.92 | 2820.30 | 3299.60 | 3400.91 | 3452.56 | 3461.36 |
| 3 | 10.01 – 20.0 | 2486.86 | 2333.92 | 993.56 | 874.86 | 764.20 | 721.12 | 67.47 |
| 4 | 20.01 – 30.0 | 98.95 | 4.51 | - | - | - | - | 1.21 |

The water level fluctuation maps (Figure 5) of 1990-94, 1994-98, 1998-2002, 2002-06, 2006-10, 2010-14 interval shows that a significant area has come in depth of 3-10 meter from depth of 10-20 meter and in the depth range of 10-20 meter from 20-30 meter which shows incline trend. Water level fluctuation Map (1990-94) shows that incline trend (0.01-1.5 m, bgl) in area of 2021.12 Km² which is 48.95 % area of the whole district. Water level fluctuation Map (1994-98) shows that incline trend (1.5-3.0 m, bgl) in area of 2468.11 Km² which is 58 % area of the whole district. Water level fluctuation Maps of 1998-2002, 2002-06, 2006-10 and 2010-14 clearly indicates general trend of inclination of depth of water level. The area statistics under different zones is shown in Table 2.

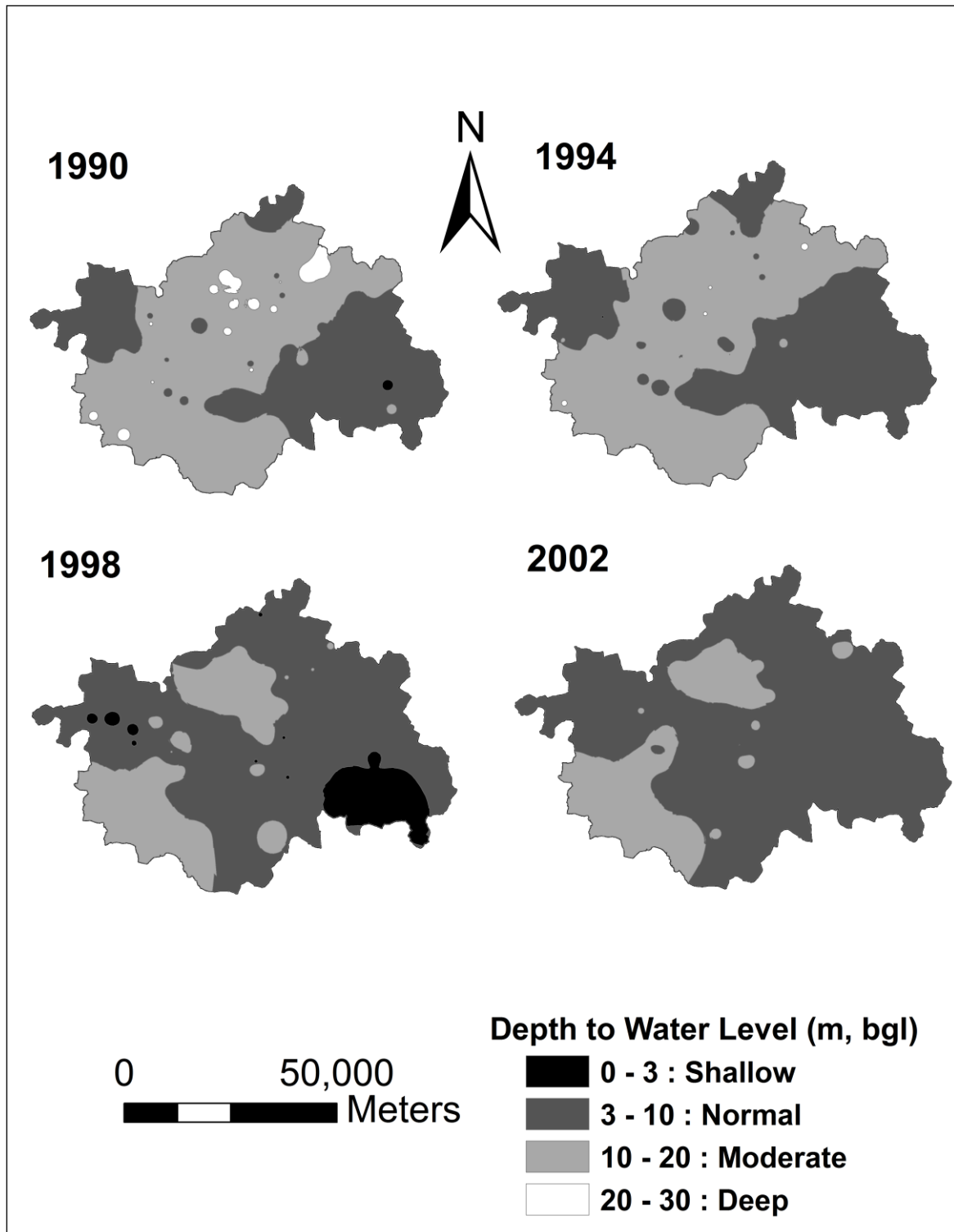


Figure 4 (a): Depth to water level maps for the years 1990, 1994, 1998 and 2002

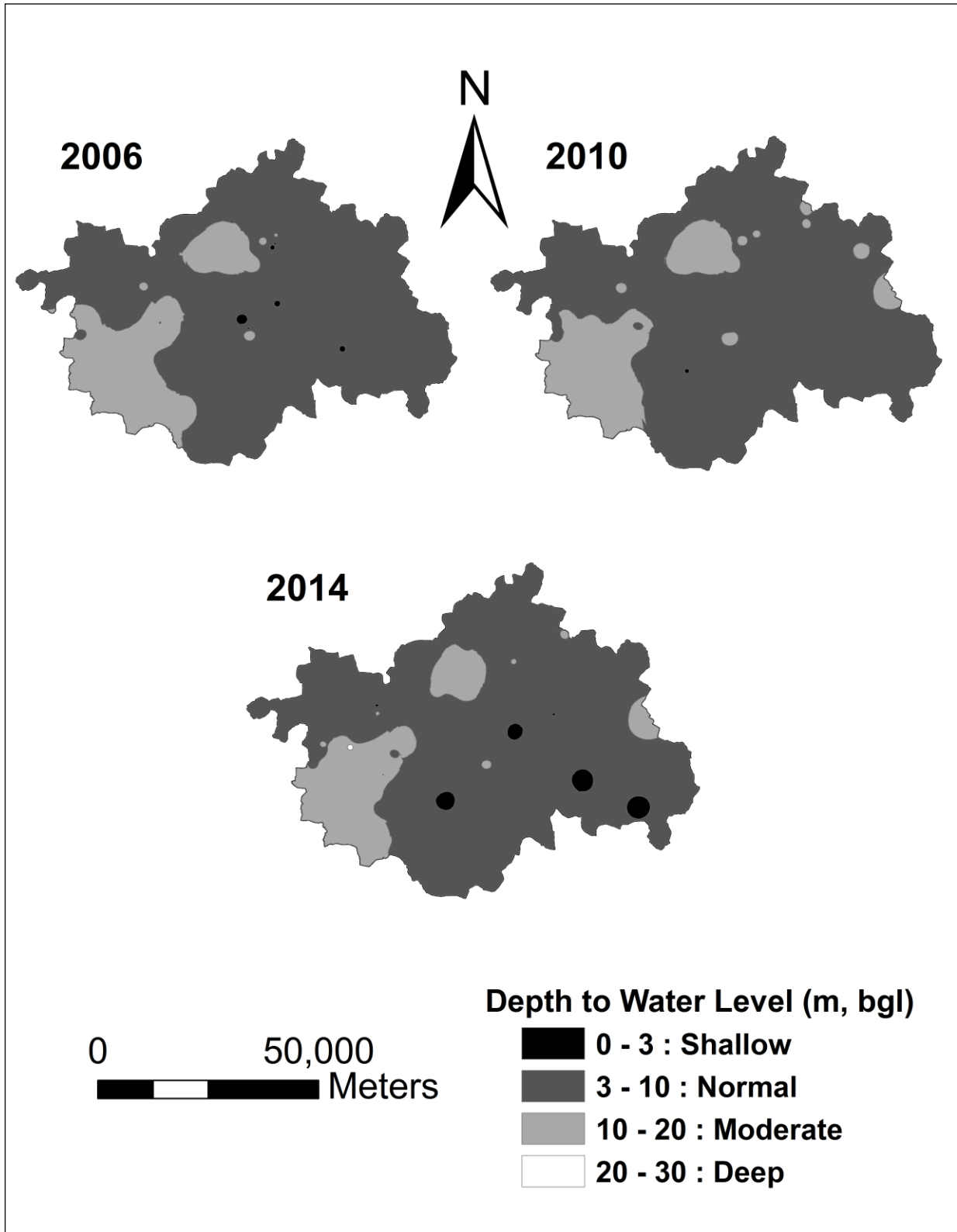


Figure 4 (b): Depth to water level maps for the years 2006, 2010, 2014

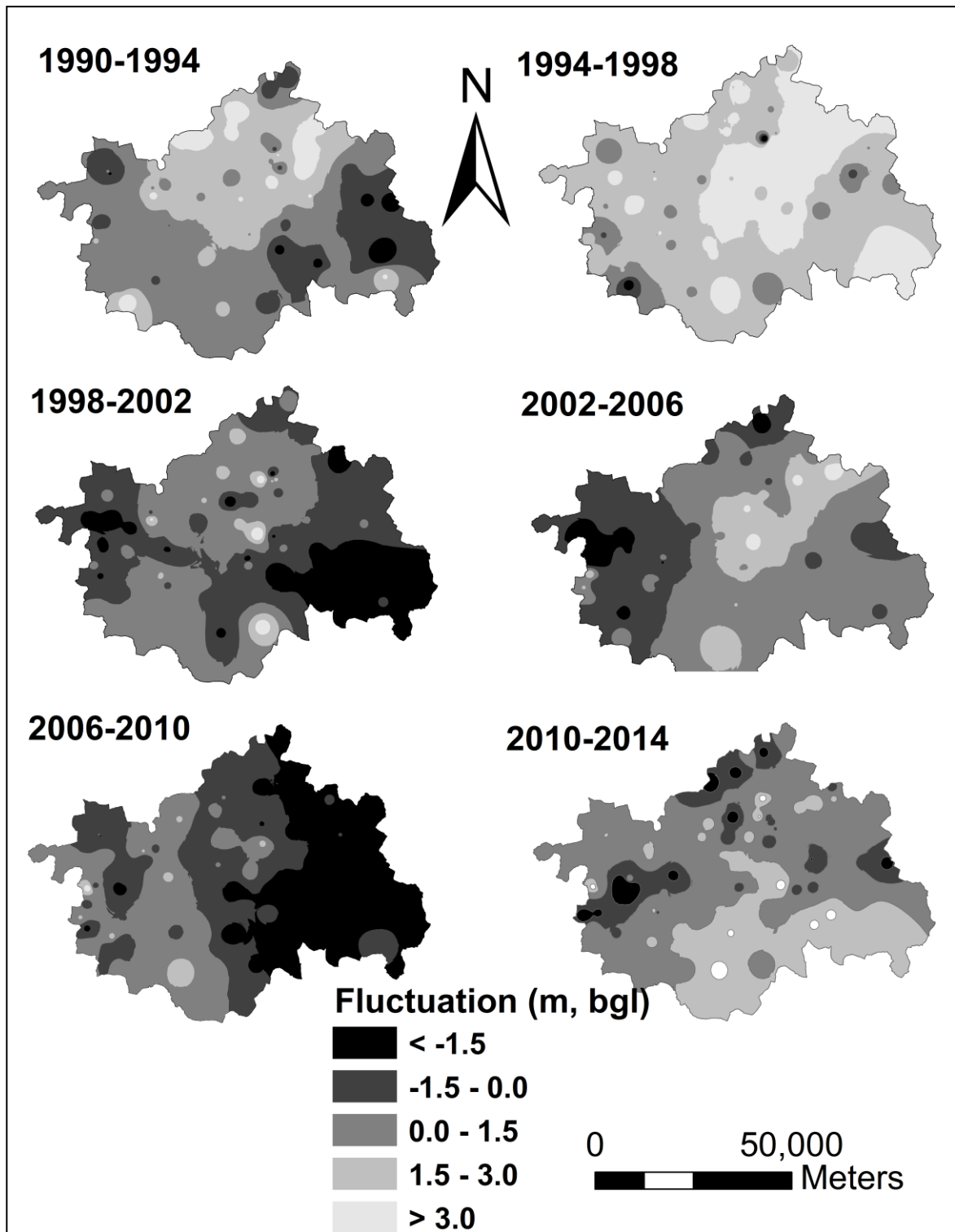


Figure 5: Water level Fluctuation Maps for 1990-94, 1994-98, 1998-2002, 2002-06, 2006-10 and 2010-2014 of Hisar District

Table 2: Area under Different Groundwater Depth Fluctuation in various years

| Fluctuation in depth to Water Level (meter, bgl) | Area (in km ²) | | | | | | Trend of Fluctuation | |
|--|----------------------------|---------|---------|---------|---------|---------|----------------------|-------------|
| | 1990-94 | 1994-98 | 1998-02 | 2002-06 | 2006-10 | 2010-14 | | 1990-14 |
| < -1.5 | 70.10 | 7.12 | 752.78 | 145.56 | 1502.34 | 100.41 | 319.86 | Declination |
| -1.51 – 0.0 | 723.45 | 28.90 | 1596.90 | 1109.27 | 1422.18 | 513.18 | 330.22 | |
| 0.01 – 1.5 | 2021.12 | 336.76 | 1692.17 | 2231.73 | 1187.95 | 2327.63 | 519.09 | Inclination |
| 1.51 – 3.0 | 1150.09 | 2468.11 | 109.91 | 650.98 | 59.98 | 35.15 | 531.41 | |
| > 3.0 | 209.77 | 1333.62 | 22.73 | 36.97 | 2.07 | 1198.13 | 2473.88 | |

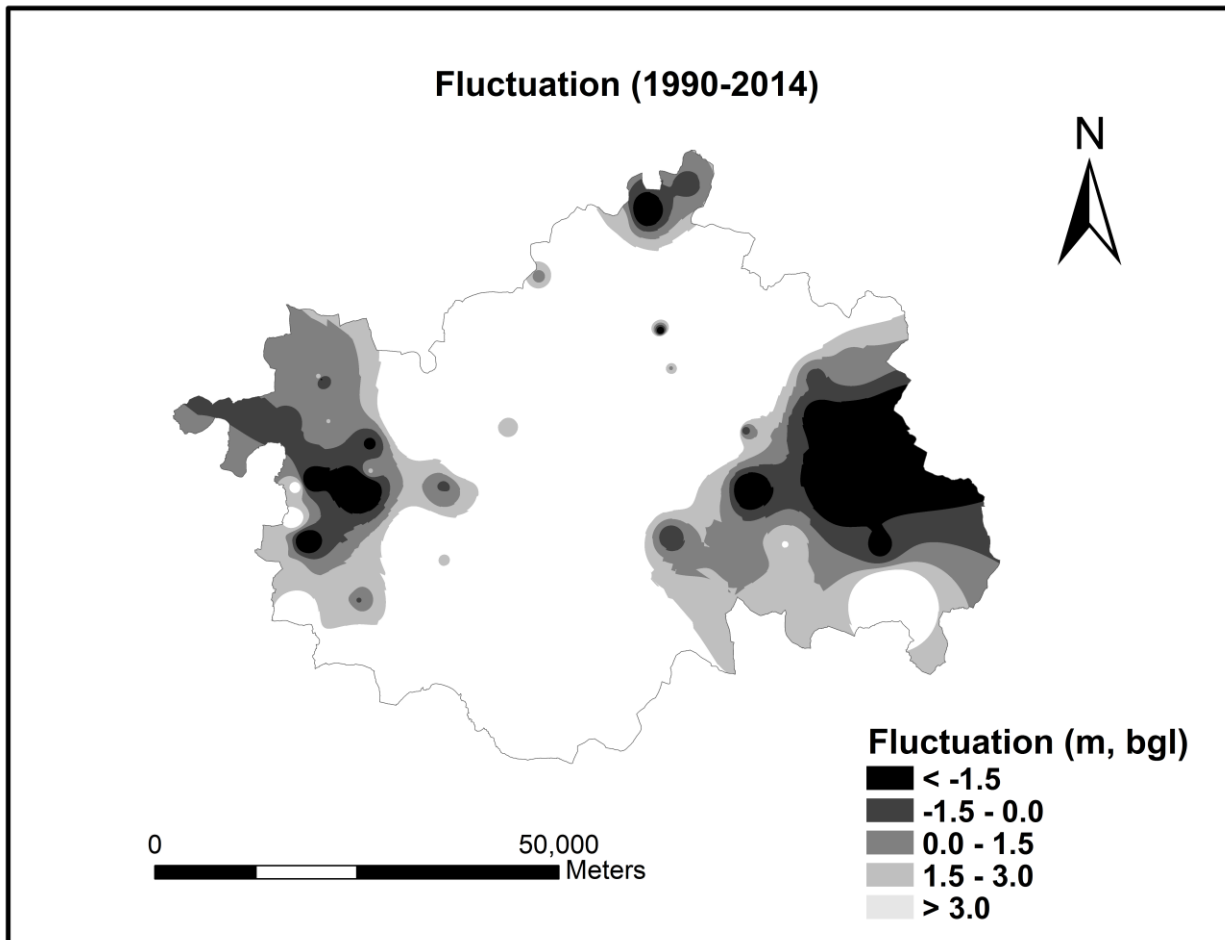


Figure 6: Water level Fluctuation Map for 1990-2014 of Hisar District

Water level fluctuation map (1990-2014) indicates an area of 2473.88 Km² shows inclination trend of depth to water level. This is shown in Figure 6. Long term fluctuation map (1990-2014) shows that about 91.1% area of district falls in the range of 3-10 m. It is due to poor drafting of groundwater in the district. The dominating factors among these are poor quality of ground water in these areas. The poor quality of groundwater restricts the farmers from its use in agriculture. Groundwater quality studies conducted in Hisar district (Rani & Chaudhary, 2015) and Kaithal district (Goyal *et al.*, 2010; Goyal and Chaudhary, 2010) also indicates an overall inclining trend in the areas having poor groundwater quality. These areas show a good network of canals and farmers mostly rely on the use of canal water for irrigation. Most prevalent method of irrigation in the area is flood irrigation which further recharges the groundwater due to return flow.

6. Conclusions

The study reflects overall inclining trend of depth to groundwater level over the study period. There is an increase of 1878 km² in the depth range of 3-10 meter from the year 1990 to 2014. In 1990, 60 % of total area was covered in the depth range of 10-20 meter out of which 40 % came in the depth range of 3-10 meter in 2014. An area of 85.42 % of the district comprising of north-west, south-west and south-east parts shows incline trend over the study period of 1990-2014. Rising trend in average depth in the district in the year 1998 is reflected due to heavy floods which occurred in 1995. The areas showing inclining trend on long term basis (1990-2014) are the areas having poor groundwater quality. Very small area of 15.58% shows decline trend and is confined around northern portion of Hansi II block, Narnaud block and parts of Adampur Block in the district over the period 1990 to 2014. The study demonstrates the subtle use of GIS in spatial distribution mapping and monitoring for groundwater quality in the area.

References

- Arya, V.S., Chaudhary, B.S., Beniwal, A., Babu, T.P., and Hooda, R.S., 1996: Satellite Surveillance for Disaster Mitigation, ACRS-1996 Colombo, Sri Lanka, PP ACRS C-7-1-6.
- Babu M.J. Ratnakanth, Das I.C., Jaisankar G., Rao E.N. Dhananjaya, and Kumar P.A. Assessment of Groundwater Pollution in Parts of Guntur District using Remote Sensing & GIS. *Int J. Earth Sci. and Engg.* 2011. 4 (6) 1024-1030.
- Bagher, R.M., and Rasoul, M. Effect of groundwater table decline on groundwater quality in Sirjan Watershed. *Arab. J Sci Engg.* 2010. 35; 197-210.
- Chaudhary, B.S., 2003: Integrated land and water resources management in southern part of Haryana using remote sensing and geographical information systems (GIS), Ph.D. Thesis, University of Rajasthan, Jaipur, India. 78-79.
- Chaudhary, B.S., Arya, V.S., Beniwal, A., Babu, T.P., and Ruhel, D.S., 1999: *Satellite applications for monitoring flood hazards in Haryana, India-A case study.* Proc.18th Earsel Symposium on Operational Remote sensing for sustainable development/Enchede/Netherlands. 281-284.
- Goyal, S.K., and Chaudhary, B.S. GIS based study of Spatio-Temporal changes in groundwater depth and quality in Kaithal district of Haryana, India. *J Ind Geophys Union.* 2010. 14; 75-87.
- Goyal, S.K., Chaudhary, B.S., Singh, O., Sethi, G.K., and Thakur, P.K. Variability analysis of groundwater levels-A GIS-based case study. *J. Indian Soc. Remote Sens.* 2010. 38; 355-364.
- Goyal, S.K., and Chaudhary, B.S. Groundwater depth and quality in Kaithal district: a GIS based study. AttiDella fondazina: Giorgio Ronchi (Italy), 2010. 823-830.
- Rani, R., and Chaudhary, B.S. Spatial Distribution Mapping and Assessment of Suitability of Groundwater Quality for Drinking Purpose in Hisar District of Haryana State, India. *SSARSC International Journal of Geo Science and Geo Informatics.* 2015. 2 (1) 1-8.
- Report of Central Groundwater Board, 2013-14.
- Rao Srinivasa, Y., and Jugran, D.K. Delineation of groundwater potential zones and zones of groundwater quality suitable for domestic purposes using remote sensing and GIS. *Hydrol. Sci. J.* 2003. 48; 821-833.
- Srivastava, V.K., Giri, D.N., and Bharadwaj, P. Study and Mapping of Groundwater Prospect using Remote Sensing, GIS and Geoelectrical resistivity techniques—a case study of Dhanbad district, Jharkhand, India. *J Ind Geophys Union.* 2012. 16; 55-63.

Block Level Micro Watershed Prioritization Based on Morphometric and Runoff Parameters

Kiran V.S.S.¹, Jai Sankar G.², Jagannadha Rao M.², and Vijaya Kumar G.T.³

¹GIS Specialist, Willis Towers Watson, Mumbai, India

²Andhra University, Visakhapatnam, India

³IIC Technologies Ltd, Hyderabad, India

Publication Date: 21 December 2016

DOI: <https://doi.org/10.23953/cloud.ijarsg.76>



Copyright © 2016 Kiran V.S.S., Jai Sankar G., Jagannadha Rao M., and Vijaya Kumar G.T. This is an open access article distributed under the **Creative Commons Attribution License**, which permits unrestricted use, distribution, and reproduction in any medium, provided the original work is properly cited.

Abstract Water is one of the most and essential natural resource in the globe, without which our life cannot exist. The demand of water is increasing with the increase of population day by day. We need water for regular activities, drinking, industry, agriculture, human and cattle consumption. Therefore, it is very important to manage with this resource as a sustainable manner. However, we need proper development and management planning to restore or recharge water where highly runoff exists due to various topographical conditions. In this paper we concern the block based micro watershed study with the help of morphometric and Runoff estimation method. Remote sensing and GIS tools very significant for prioritization of micro watershed studies. NRSC Runoff Curve Number method is a quantitative descriptor of the land use and land cover, soil characteristics of watershed and its computed, runoff through an empirical relation that requires the rainfall and watershed co-efficient namely runoff curve number. These Curve Number approach to runoff volume is typically thought of as a method for generating the storm runoff. Where we also applied the common morphometric analysis method which has been commonly applied to the prioritization of watersheds and sub watersheds. Hence we applied the morphometric parameters where linear and aerial shape have been determined for each micro watershed and assigned rank on the basis of value or relationship with erodibility so as to arrive at a compound value for final ranking of the sub-watersheds. The runoff and morphometric parameters were obtained with the help of Remote Sensing and GIS tools. Based on output results of both parameters the final results revealed of micro watershed priorities are shown into five categorizes very high, high, medium, low and very low priority.

Keywords *Morphometric Parameters; Watershed Prioritization; Runoff Estimation; Land Use/Land Cover; Remote Sensing and GIS*

1. Introduction

A watershed is an ideal unit for natural resources management system that also support in water and land for mitigation of the impact of natural disaster for achieving sustainable development. The significant factor for planning and development of a micro watershed are its physiography, drainage, geomorphology, soil, land use/land cover, surface runoff and available water resources. Remote

Sensing and GIS technology both are the most effective tools for watershed development, watershed management, and studies on prioritization of micro-watersheds.

Morphometric Analysis could be used for prioritization of micro-watersheds by studying different linear and aerial parameters of the watershed even without the availability of soil maps (Biswas et al., 1999). Remote Sensing and GIS tools have become proven tools for the management and development of water resources on block level micro watershed system (Kiran and Srivastava, 2010). Several studies have been carried out worldwide and they have shown excellent results. Due to advancement in satellites and sensing technology, it is possible to map clear details of the earth surface and provide scope for micro watersheds level management and planning.

The study area that is taken has severe water crises during the summer season. The terrain is highly undulated with very high runoff which causes minimum recharge of ground water in spite of 1750 mm average annual rainfall. This high runoff also causes very fertile soil erosion. The present study aims to prioritize micro watersheds based on Morphometric analysis and surface runoff analysis. In this study we attempt to increase the water potential for irrigation and drinking purpose.

2. Study Area

The study area Simlupal block, Bankura district, which is part of Silai River basin in West Bengal State is considered for the analysis. It is located on 22° 59' 38.84" North to 22° 50' 34.42" North latitude and 86° 55' 20.15" to 87° 13' 06.10" East longitudes. It has an average elevation of 57mtr (187 feet's) and area of this block is 309.20 Km² (Figure 1).

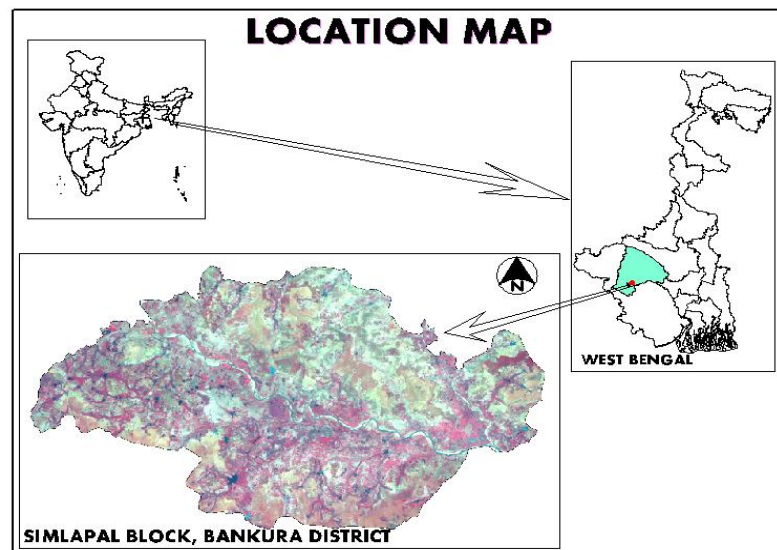


Figure 1: Location Map of Simlupal Region, West Bengal

3. Methodology

Remote Sensing and GIS tools have been used for the processing of satellite data and deriving of thematic maps and vector layers. Extracted thematic maps from the satellite images using remote sensing techniques and applied GIS tools for detailed analysis. Performed Morphometric analysis and Surface runoff for prioritization of micro-watersheds using GIS tools. The datasets used for study are Survey of India toposheets on 1:50,000 scale and IRS LISS I IV satellite imagery with 23.5 and 5 meter resolutions, NBSS soil data. SRTM digital elevation datasets and Seasonal rainfall data.

3.1. Morphometric Analysis

The morphometric analysis is one of the significant RSGIS tool for prioritization of micro-watershed even without soil map and land use/land cover map. This model is depends on the behaviour of total drainage system and its pattern (Nookaratanam et al., 2005). The drainage pattern refers to spatial relationship among area streams, which could be influenced in erosion by inequalities of soils rock resistance, slope, geologic history and structure of a region (Nag S.K., 1998). Prioritization of micro-watershed in a morphometric analysis uses, crucial linear morphometric parameters like Drainage density (Dd), Stream frequency (Fu), Texture ratio(T), Bifurcation ratio (Rb) Length of overland flow (Lo) and shape morphometric parameters are Form factor (Rf), Shape factor (Bs), Circularity Ratio (Rc), Elongated ratio (Re), Compactness coefficient (Cc). While computing morphometric parameters we also considered linear and aerial aspects. All these parameters were obtained with the help of GIS Software. The highest value of the linear parameters was priority rated rank 1 and next highest value was rated rank 2 and so on, similarly lowest value of aerial or shape factor was rated rank 1 and next lowest value a rating of rank 2. After rating of all parameter, the rating value for every micro-watershed was averaged to arrive at a compound value (Cp). The Compound value is based on the average of all parameters in single micro-watershed (Kiran and Srivastava, 2012).

Then priority fixation of all micro-watersheds were categorized into five equal groups based on range of compound value, these are very high (≤ 30), high ($>30 \leq 37$), medium ($>37 \leq 43$), low ($>43 \leq 50$), very low (>50). Thus, 14 micro watersheds out of 77, were given as very high priority since they have very low compound values, 19 micro watersheds were given high priority, with low Cp values. 15 micro watersheds were given medium priority having moderate compound values, 23 micro watersheds fall under low priority with high compound values and the remaining 6 micro watersheds are given very low priorities which have very high compounds values (Figure 2).

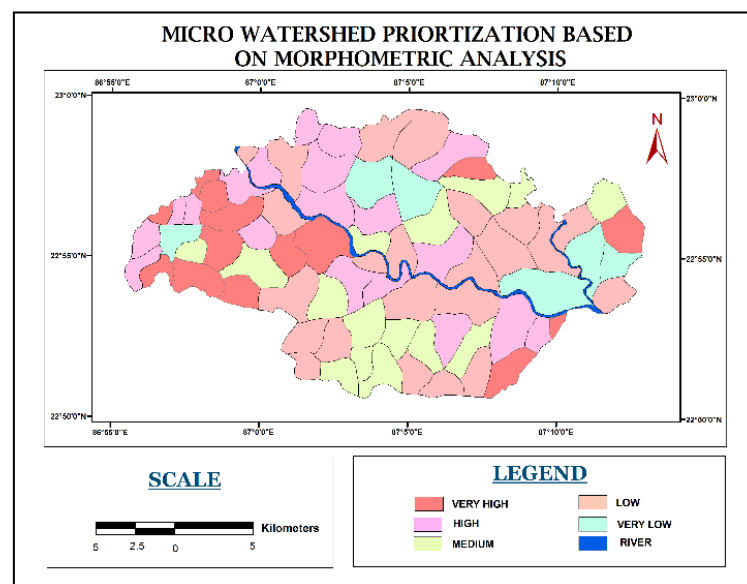


Figure 2: Morphometric Analysis Output Results

3.2. Runoff Calculation and Analysis

The SCS curve number approach to runoff volume is typically thought as a method for generating storm runoff and not for water quality design. Typically utilized with the assumption of average Anti Moisture Condition that will be appropriately analysed to study the moisture condition of every single micro-watershed. Soil Conservation Service is to be used with RSGIS tools to estimate the runoff from each Micro-Watershed. Curve Number model carried on hydrological soil groups, land use and land

cover features and daily rainfall data parameters. Soil Conservation Service Curve Number (USDA, 1985) method is a well accept tool in hydrology, which uses a land condition factor called the Curve Number.

This curve number is taken based on some important properties of catchments namely soil type, land use, surface condition, and antecedent moisture conditions, and also some desirable curve number in suitable land use/land cover features of Indian conditions (Kiran and Srivastava, 2014).

Soil Conservation Service Runoff Curve Number is a quantitative identification of the land use and land cover, soil characteristics of micro watershed and its computed direct runoff through an empirical relation that requires the rainfall and watershed co-efficient namely runoff curve number (Pramod Kumar et al., 1991). The SCS Curve Number approach to runoff volume is typically thought of as a method for generating storm runoff for rare events. The volume of runoff is expressed as:

$$VQ = (P-0.3S)^2 / (P+0.7S) \text{ ---- Runoff Hydrological Equation}$$

Where, VQ is volume of runoff and P is Accumulated rainfall and S is potential maximum relation of water by the soil.

To calculate the runoff of each micro watershed of study area analysed the study area soil and classified into three different hydrological soil groups based on antecedent moisture conditions of soil. It is very important in runoff estimation for prioritization of micro watershed. Soil properties influence the relationship between rainfall and runoff by affecting the rate of infiltration. Based on infiltration rates, soil texture and soil taxonomic conditions, soils in the study are divided into four hydrologic soil groups i.e. Well drained (Group-A), Moderate to well drain (Group-B), Poor to Moderate drained (Group-C) and Poorly drained (Group-D), However the study area classified only three categories based on geographic condition and soil factors i.e. Group A, B and D (Kiran and Srivastava, 2014), (Figure 3).

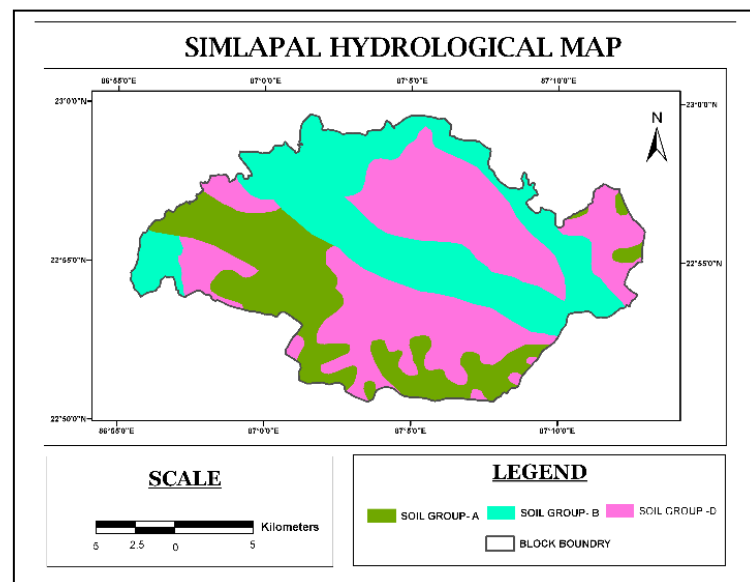


Figure 3: Hydrological Soil Groups of Study Area

As land use and land cover also important parameter for curve number, we classified the LISS IV data and prepared the land use and land cover map using supervised and hybrid classification techniques to overlay the vectorised data (Figure 4). With the help of hydrological groups and land use land cover curve number we calculated the ground Anti Moisture Condition, which is indicator of watershed

wetness and availability of soil moisture storage during the rain (Samah Al Jabari et al., 2009). The soil conservation service developed three antecedent soil-moisture conditions and named as AMC-I, AMC-II, AMC-III. The AMC condition I curve number is dry condition it can be denoted as CN-I, AMC condition II curve number is normal condition it can be denoted as CN-II, AMC condition III curve number is dry condition it can be denoted as CN-III. Using these curve number, we could estimate the soil vegetation land complex and antecedent soil moisture condition in a watershed. Using the hydrological Soil Groups (A, B and D), land use classes to create the curve number. The values of curve number for the all three antecedent moisture condition are listed in Table 1. To calculate the runoff estimation of each micro watershed by applying the above mentioned Runoff hydrological equation.

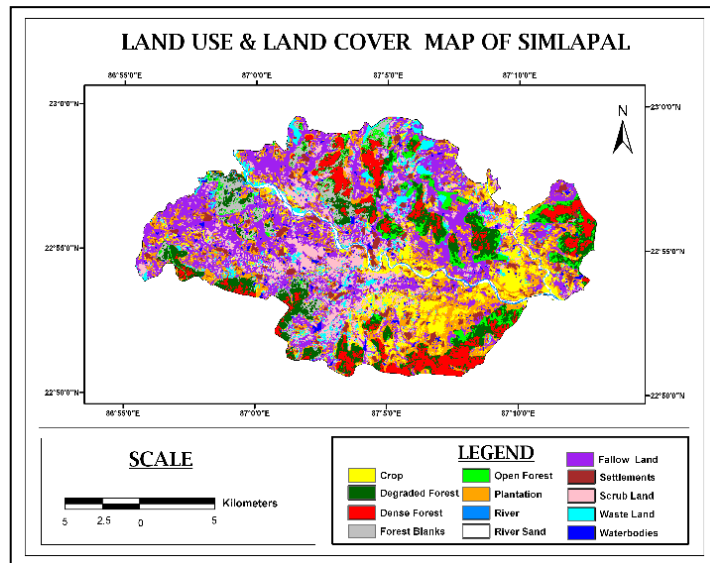


Figure 4: Land Use and Land Cover Map of Study Area

Based on rainfall and hydrological calculation of VQ values are arranged in order of priority into five categories. The final prioritize results are 4 micro-watersheds out of 77, were given very high priority, 4 MWS were given high priority, 14 MWS fall under medium priority, 32 MWS fall under low priority and remaining 23 MWS falling very low priorities (Figure 5).

Table 1: Hydrological Soil Group Curve Numbers

| LU/LC Classes | Curve Number(CN) | | |
|-----------------|------------------|---------|---------|
| | HSG - A | HSG - B | HSG - D |
| Agriculture | 55 | 69 | 83 |
| Plantation | 39 | 61 | 83 |
| Fallow | 59 | 70 | 81 |
| Scrub land | 77 | 86 | 94 |
| Wasteland | 45 | 66 | 83 |
| Water bodies | 94 | 94 | 94 |
| Open Forest | 19 | 40 | 63 |
| Forests Blank | 64 | 71 | 85 |
| Degraded Forest | 15 | 30 | 48 |
| Dense Forest | 36 | 58 | 80 |
| River | 94 | 94 | 94 |
| Sand Deposition | 96 | 96 | 96 |
| Settlement's | 59 | 74 | 86 |

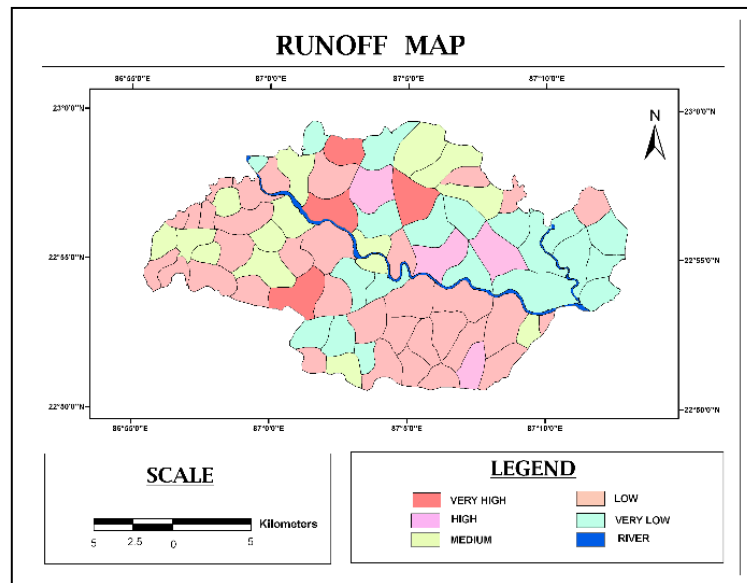


Figure 5: Runoff Results

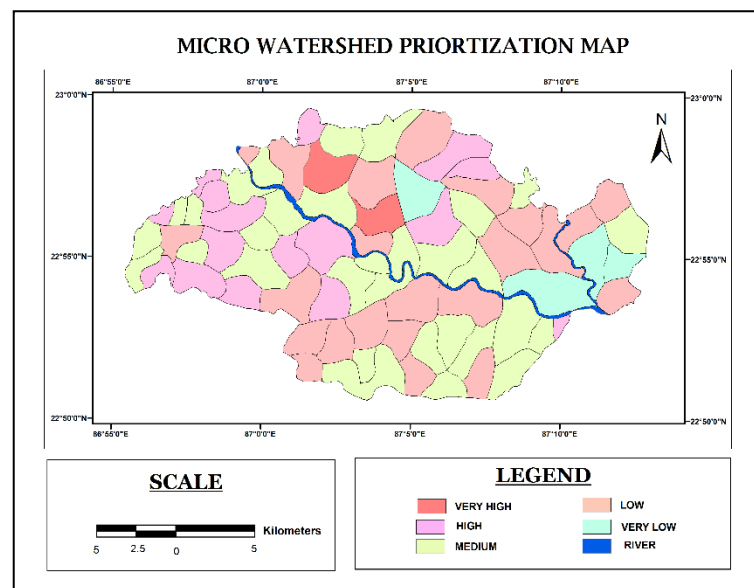


Figure 6: Final Results

4. Results and Discussion

Prioritization of Micro-Watershed has been done by using compound values by morphometric analysis and volume of runoff values by soil conservation service curve number method these are then integrated with two different prioritized attributes. Attributes of morphometric analysis is based on three aspects namely linear, aerial and shape. These three aspects are given ten parameters and computed the compound parameter values. According to these values the micro-watershed priorities are 14 micro-watersheds were found very high category, 19 micro-watersheds were found high priority, 15 micro-watersheds were found medium priority, 23 micro-watersheds were found low category and 6 micro watersheds were found very low priority (Figure 2). Based on SCS-CN method, the attributes of SCS are given in the seasonal runoff estimation of daily rainfall data we used it for the estimation of the runoff to prioritize. Estimated runoff weightage were 4 micro-watersheds out of 77, were given very

high priority, 4 MWS were given high priority, 14 MWS fall under medium priority, 32 MWS fall under low category and 23 MWS falling very low priorities (Figure 5). From the integrated study of SCS-CN method and Morphometric analysis, Out of 77 micro-watersheds 2 were identified as very high prioritized micro-watersheds. These have very high soil loss values and have excellent drainage density, highly runoff. Texture ratio values of these basins are also indicating the high. Out of 77 micro-watersheds 16 were given high priority with high runoff and good drainage pattern and drainage density, 32 fall under the medium priority with moderately drainage pattern and medium soil erosion, 23 micro-watersheds were given low priority and remaining 4 micro-watersheds were found very low priority, probably because of the area in plains. The prioritization of Micro-watershed decreasing from western side to eastern side because of the slope (Figure 6).

References

- Kiran, V.S.S., and Srivastava, Y.K., Check Dam Construction by Prioritization of Micro Watershed, using Morphometric Analysis as a Perspective of Remote Sensing and GIS for Simlatal Block, Bankura, W.B. *Bonfring International Journal of Industrial Engineering and Management Science*. 2012. 2 (Special Issue 1) 20-31.
- Kiran, V.S.S., and Srivastava, Y.K. Micro Watershed Level Water Resource Management Based on Three Years Runoff Estimation Using Remote Sensing and GIS Techniques for Simlatal Block, Bankura, West Bengal, India. *International Journal of Earth Science and Engineering*. 2014. 7 (1) 80-92.
- Biswas, S., Sudhakar, S., and Desai, V.R. Prioritization of Sub-watershed based on Morphometric Analysis of Drainage Basin: A Remote Sensing and GIS approach. *Journal of the Indian Society of Remote Sensing*. 1999. 155-166.
- USDA, Soil Conservation Service, 1985: National Engineering Hand Book, USA.
- Nookaratnam, K., Srivastava, Y.K., Venkateswara Rao, V., Amminedu, E., and Murthy, K.S.R. Check Dam Positioning by Prioritization of Micro-watershed using SYI Models and Morphometric Analysis: A Remote Sensing and GIS Approach. *Journal of Indian Society of Remote Sensing*. 2005. 33 (1).
- Nag, S.K. Morphometric Analysis using Remote Sensing Techniques in the Chakra sub-basin Purulia district. *Journal of Indian Society of Remote-Sensing*. 1998. 26 (1&2).
- Pramod Kumar et al., Tiwari, K.N., and Pal, D.K. Established SCS Runoff Curve Number from IRS Digital Data Base. *Journal of Indian Society of Remote Sensing*. 1991. 19 (4).
- Samah Al Jabari et al., Majed Abu Sharkh et al., Ziad Al-Mimi, 2009: Estimation of Runoff for Agricultural Watershed using SCS Curve Number and GIS. A Remote Sensing and GIS Approach Thirteenth International Water Technology Conference, IWTC 13, 2009, Hurghada, Egypt. 1213-1229.
- Kulkurni, A.A., Aggrawal S.P., and Das, K.K. Estimation of Surface Runoff using Rainfall-Runoff Modeling of Warasgaon Dam Catchment- A Geospatial Approach. Submitted to Map India Conference 2004, New Delhi, India.
- US Department of Agricultural, 1981: Predicting rainfall erosion losses, a guide to conservation planning, handbook no 537.
- Murthy, J.V.S., 1998: Watershed Management, New Age International, 21-34.
- Suresh, R., 1997: Soil and Water Conservation Engineering. Standard Published Distr., Delhi. 48-51.
- Smith and Wischmer, 1941: Interpretation of Soil Conservation Data for Field Use. Agriculture Engineering. 173-175.